

Lecture Notes in Mechanical Engineering

Kannan Govindan
Harish Kumar
Sanjay Yadav *Editors*

Advances in Mechanical and Materials Technology

Select Proceedings of EMSME 2020


 Springer

Lecture Notes in Mechanical Engineering

Series Editors

Francisco Cavas-Martínez, Departamento de Estructuras, Universidad Politécnica de Cartagena, Cartagena, Murcia, Spain

Fakher Chaari, National School of Engineers, University of Sfax, Sfax, Tunisia

Francesco Gherardini , Dipartimento di Ingegneria, Università di Modena e Reggio Emilia, Modena, Italy

Mohamed Haddar, National School of Engineers of Sfax (ENIS), Sfax, Tunisia

Vitalii Ivanov, Department of Manufacturing Engineering Machine and Tools, Sumy State University, Sumy, Ukraine

Young W. Kwon, Department of Manufacturing Engineering and Aerospace Engineering, Graduate School of Engineering and Applied Science, Monterey, CA, USA

Justyna Trojanowska, Poznan University of Technology, Poznan, Poland

Francesca di Mare, Institute of Energy Technology, Ruhr-Universität Bochum, Bochum, Nordrhein-Westfalen, Germany

Lecture Notes in Mechanical Engineering (LNME) publishes the latest developments in Mechanical Engineering—quickly, informally and with high quality. Original research reported in proceedings and post-proceedings represents the core of LNME. Volumes published in LNME embrace all aspects, subfields and new challenges of mechanical engineering. Topics in the series include:

- Engineering Design
- Machinery and Machine Elements
- Mechanical Structures and Stress Analysis
- Automotive Engineering
- Engine Technology
- Aerospace Technology and Astronautics
- Nanotechnology and Microengineering
- Control, Robotics, Mechatronics
- MEMS
- Theoretical and Applied Mechanics
- Dynamical Systems, Control
- Fluid Mechanics
- Engineering Thermodynamics, Heat and Mass Transfer
- Manufacturing
- Precision Engineering, Instrumentation, Measurement
- Materials Engineering
- Tribology and Surface Technology

To submit a proposal or request further information, please contact the Springer Editor of your location:

China: Ms. Ella Zhang at ella.zhang@springer.com

India: Priya Vyas at priya.vyas@springer.com

Rest of Asia, Australia, New Zealand: Swati Meherishi at swati.meherishi@springer.com

All other countries: Dr. Leontina Di Cecco at Leontina.dicecco@springer.com

To submit a proposal for a monograph, please check our Springer Tracts in Mechanical Engineering at <https://link.springer.com/bookseries/11693> or contact Leontina.dicecco@springer.com

Indexed by SCOPUS. All books published in the series are submitted for consideration in Web of Science.

More information about this series at <https://link.springer.com/bookseries/11236>

Kannan Govindan · Harish Kumar · Sanjay Yadav
Editors

Advances in Mechanical and Materials Technology

Select Proceedings of EMSME 2020

 Springer

Editors

Kannan Govindan
Department of Technology and Innovation
University of Southern Denmark
Odense, Denmark

Harish Kumar
Department of Mechanical Engineering
National Institute of Technology Delhi
New Delhi, India

Sanjay Yadav
Physico-Mechanical Metrology
CSIR—National Physical Laboratory
New Delhi, India

ISSN 2195-4356

ISSN 2195-4364 (electronic)

Lecture Notes in Mechanical Engineering

ISBN 978-981-16-2793-4

ISBN 978-981-16-2794-1 (eBook)

<https://doi.org/10.1007/978-981-16-2794-1>

© The Editor(s) (if applicable) and The Author(s), under exclusive license to Springer Nature Singapore Pte Ltd. 2022

This work is subject to copyright. All rights are solely and exclusively licensed by the Publisher, whether the whole or part of the material is concerned, specifically the rights of translation, reprinting, reuse of illustrations, recitation, broadcasting, reproduction on microfilms or in any other physical way, and transmission or information storage and retrieval, electronic adaptation, computer software, or by similar or dissimilar methodology now known or hereafter developed.

The use of general descriptive names, registered names, trademarks, service marks, etc. in this publication does not imply, even in the absence of a specific statement, that such names are exempt from the relevant protective laws and regulations and therefore free for general use.

The publisher, the authors and the editors are safe to assume that the advice and information in this book are believed to be true and accurate at the date of publication. Neither the publisher nor the authors or the editors give a warranty, expressed or implied, with respect to the material contained herein or for any errors or omissions that may have been made. The publisher remains neutral with regard to jurisdictional claims in published maps and institutional affiliations.

This Springer imprint is published by the registered company Springer Nature Singapore Pte Ltd.

The registered company address is: 152 Beach Road, #21-01/04 Gateway East, Singapore 189721, Singapore

Preface

International Conference on Energy, Materials Sciences and Mechanical Engineering (EMSME)—2020 conference is the first conference of its series organized by Department of Mechanical Engineering of National Institute of Technology Delhi, India. It has been considered as a forum to bring together scientists, university professors, graduate students, and mechanical engineers, presenting new science, technology, and engineering ideas and achievements. The conference attracted many participants working in various fields of engineering: design, mechanics, materials, etc. The success of the conference inspired the organizers to turn the conference into an annual event.

More than 370 papers were presented at the conference EMSME 2020. They covered topics ranging from the renewable energy, mechanics of machines, material engineering, structural strength, and tribological behavior to transport technologies, machinery quality, innovations etc. However, for this book, only 124 peer-reviewed papers, authored by research groups representing various universities and institutes, were selected for inclusion.

Furthermore, I thank the staff and management of the institute for their cooperation and support and, especially, Dr. Satish Kumar, Hon. Director, National Institute of Technology Delhi, and all members of the program committee and the organizing committee for their work in preparing and organizing the conference. Last but not least, I thank Springer for its professional assistance and particularly Priya Vyas who supported this publication.

Odense, Denmark
New Delhi, India
New Delhi, India

Kannan Govindan
Harish Kumar
Sanjay Yadav

Contents

A Mini State of Art Survey on Photovoltaic/Thermal Desalination Systems	1
Subbarama Kousik Suraparaju, Arivazhagan Sampathkumar, and Sendhil Kumar Natarajan	
Mathematical Modelling and Performance Analysis of Single Slope Solar Desalination System	17
Subbarama Kousik Suraparaju, Nirmal Jha, S. Manoj, and Sendhil Kumar Natarajan	
Analysis and Comparison of Various High Performance Folded Cascode OTA Topologies	35
Bhawna Aggarwal and Vaishali Sharma	
Grasping Force Analysis of 3-Fingered Gripper	47
Rohan Malik, Yashasvi Verma, Abhishek Verma, and Vikas Rastogi	
Simplification of Governing Equation for Fluid Flow Between Two Concentric Cylinders	59
Anamika Yadav and Pooja Pathak	
Optimization Techniques Used to Optimize Process Parameters of Submerged Arc Welding: A Review	67
Sameer Vishwakarma, V. K. Dwivedi, and Manoj Kumar Agrawal	
Free Vibration Analysis of FGM Conical Shell	83
Prabhat Mahawar and Pankaj Sharma	
Performance Improvement of Microsurfacing Machine: A Case Study	93
Kratika Ravekar and Santosh Jaju	

Squeeze Film Operation of Thrust Bearing Operating with Shear-Thinning Lubricants	103
Vivek Kumar, Vatsalkumar Ashokkumar Shah, Kuldeep Narwat, and Satish C. Sharma	
Feasibility and Performance Analysis of Earth-Tube Heat Exchanger	115
Rampal Singh and V. K. Dwivedi	
Combined Objective Optimization of FMS Scheduling by a Hybrid Genetic Algorithm	125
K. Gayathri Devi, R. S. Mishra, and A. K. Madan	
Comparison of Nature-Inspired Approaches for Path Planning Problem of Mobile Robots in MATLAB	141
Divya Agarwal and Pushpendra S. Bharti	
Evaluation of SFLA and TLBO Algorithm for Path Planning of Mobile Robots in MATLAB	151
Divya Agarwal and Pushpendra S. Bharti	
New Locking Mechanism for Safe Landing	161
N. Rakshith	
A Preliminary Assessment of Solar Industrial Process Heating for Cement Industry	171
Niranjan Sahoo, Anil Kumar, and Samsher	
Experimental Investigation of Drying Tomato in a Double Slope Solar Dryer Under Natural Convection	179
E. Elavarasan, Yogesh kumar, R. Mouresh, and Sendhil Kumar Natarajan	
Design of Zig-Zag 1–3 Viscoelastic Composite Layer for the Improved Passive Damping Treatment of Beam	191
Abhay Gupta, Rajidi Shashidhar Reddy, and Satyajit Panda	
Design and Simulation of Structural Components of Affordable, Automated Solar Panel Cleaning Mechanism	201
Shubham Jain and Rhythm Singh	
Influence of Number of Lobe on Dynamic Performance of Hydrodynamic Journal Bearing	211
Vivek Kumar, Kush Shrivastava, Kuldeep Narwat, and Satish C. Sharma	
Performance Assessment of Parabolic Trough Collectors with Variable Mass Flow Rates	225
Anshul Tewari and R. S. Mishra	
Influence of Nanoparticles in Different Types of Cutting Fluids: A Literature Review	237
Anurag Sharma, R. C. Singh, Ranganath M. Singari, and S. L. Bhandarkar	

The High Energy Concentration of Heat Pipe for Enhanced Electronic Cooling	253
P. Senthil Kumar, Syed Abudhagir Umar, and R. Balaji	
Effect of Block Location in a Suddenly Expanded Micro-combustor	261
Arees Qamareen, Shahood S. Alam, and Mubashshir A. Ansari	
An Analysis of the Effect of E-mobility Trend on the Traditional Suppliers in the Global Automotive Industry	273
Akshay Suhas Narkar and Tejas Pramod Naik	
Faster RCNN for Face Detection on a FACENET Model	283
U. Syed Abudhagir, Karne Anuja, and Jigar Patel	
Study of the Degradation in a Unitized Regenerative Fuel Cell	295
Amit C. Bhosale, Reeshab Goenka, and Prakash C. Ghosh	
Crashworthiness of Bird Inspired Fuselage of Small UAV	305
Rohit Naryal and Pankaj Dorlikar	
An Experimental Study to Determine the Optimum Order of Design Review Parameters for Designing Review in Immersive Virtual Environment	313
D. Shukla, A. Patil, P. Dholiya, S. J. Singh, and V. Vakharia	
Energy and Exergy Analysis of Poovan Banana Under Single Slope Forced and Natural Convection Solar Drying	321
E. Elavarasan, Anagh S. Bhanu, Yogesh Kumar, R. Mouresh, and Sendhil Kumar Natarajan	
Experimental Investigation of Surface Roughness in Electric Discharge Machining of Hybrid Metal Matrix Composite	333
Gurpreet Singh Matharou and B. K. Bhuyan	
Modeling and Simulation of Mechanical System for Power Generation Using Footsteps	345
Anmol Singh, Anshul Singh, and Arunesh Chandra	
Case Study on Bearing Fault Diagnosis in Liquid Rocket Engine Using Envelope Detection Technique	357
Debanjan Das, P. Padmanabhan, V. Kumaresan, and D. P. Sudhakar	
A Study on Machining Behaviour of Metal Matrix Composite: A Review	367
Nikhil Bharat and P. S. C. Bose	
Optimisation of E-Shell Heat Exchanger Using Multi-objective Evolutionary Algorithm NSGA-II	375
Abhisekh Kumar Maurya, Anubhav Agrawal, Robert Singh, Owais Ali Khan, and Brahma Nand Agrawal	

Integrated Approach for Flexible Job Shop Scheduling Using Multi-objective Genetic Algorithm	387
Sunita Nayak, Anoop Kumar Sood, and Abhishek Pandey	
Mathematical Analysis of Angular Distortion in GTAW of Stainless Steel 304 Sheets	397
Ayush Kumar, Udit Saini, Vivek Yadav, and Pradeep Khanna	
Development of a Programmable Contour Following Unit for TIG Welding	409
Palash Hazra, Ashish Kumar, Sanyam Jain, Sourabh Naskar, and Pradeep Khanna	
Modal Analysis of a Pre-stressed Quadcopter Propeller Using Finite Element Analysis	421
Faraz Ahmad, Pushpendra Kumar, and Pravin P. Patil	
Development of Mathematical Model for Prediction and Control of Weld Dilution in MIG Welded Stainless Steel 202 Plates	431
Prithu Mishra, Mayank Pandit, Shruti Sood, and Pradeep Khanna	
Artificial Neural Network-Based Classifier for Fault Detection in Photovoltaic Modules	445
Kritika Anuragi, Mohak Gaba, Ashir Raza Malik, Ritwik Gambhir, and Bhavnesh Kumar	
Improvement in Overall Equipment Effectiveness in Manufacturing Industry Using Autonomous Maintenance	455
S. Gurpreet Singh Bali, Gurvinder Singh, Balbir Singh, and Sanjay Mohan	
Design and Selection of Hydraulic Components for the Rotary Head System of Blasthole Drill Machine	469
Alok Vardhan and Ajay Pratap Singh	
A Simulation Method for the Behavior of Hybrid Mg-Based Composite Brake Caliper in Automobile Application	483
Sakshi Singh and Kamal Kant Singh	
Prediction of Tensile Strength of Hybrid Natural Fiber Reinforced Composites Using Machine Learning Approach	491
Murugappan Elango, V. Naveen Krishna, Adithyan Annamalai, and P. Harish	
Simulation Analysis for Minimizing Waiting Time of Patients in an Outpatient Department	503
Murugappan Elango, S. Sivalingam, Adithyan Annamalai, and Abinav Karthikeyan	

Material Removal Rate and Surface Roughness Prediction in Turning and Milling Operations Using Taguchi Analysis, Support Vector Machine and Gaussian Process Regression 515
 V. Vakharia, J. Sanghvi, and H. Thakker

Prediction of Angular Distortion in MIG Welding of Stainless Steel 202 Plates 525
 Laksha, Preksha Bharti, and Pradeep Khanna

Modeling and Simulation of Steering and Front Wheel Assembly for FSAE Vehicle 537
 Katyá Sah, Rashmi Kaushal, Parnika Chauhan, and Vivek K. Chawla

Design and Analysis of Pedal Assembly for an FSAE Vehicle 557
 Deepanshi Gupta, Pragya Mahajan, and Vivek K. Chawla

Design and Analysis of Drivetrain Assembly for FSAE Vehicle 571
 Sukriti Dhauni, Vanshita Sharma, and Vivek K. Chawla

Emission Analysis of Compression Ignition Engine with Induced Chemical Reaction Between Engine Exhaust and Slaked Calcium Hydroxide Solution 587
 Vadivel Ayyakkannu, Periyasamy Sivanandi, and Arivazhagan Sampathkumar

Modeling and Analysis of Sustainability Practices in Indian Apparel Industries Using Fuzzy Analytic Hierarchy Process (FAHP) 599
 Amit Vishwakarma, M. L. Meena, G. S. Dangayach, and Sumit Gupta

Numerical Comparison of Elliptical and Conical Cavity Receiver of Solar Parabolic Dish Collector System 607
 M. Tharun, S. R. Navin, K. Arjun Singh, Arivazhagan Sampathkumar, and Sendhil Kumar Natarajan

Optimization of Weld Parameters for Cladding Using Box–Behnken Design Method 619
 Amit Kumar Singh, Vivek Singh, Som Ashutosh, Abhishek Gupta, and Ajay Pratap Singh

A New Approach for Sustainability-Based Material Selection Model of Toxic Chemicals in Manufacturing Domain 629
 Ankush Anand, Amit Kumar Sinha, Falak Idrees Tak, Aafaq Amin Tak, and Raof Ahmad Khan

Zero Waste Concept: Recycling of Slag to Use as Flux in Submerged Arc Welding 641
 Deepanjali Nimker and Reeta Wattal

Study of High-Velocity Oxy-fuel Coating Technique and Fe-Based High-Velocity Oxy-fuel Coatings	649
Subrat Sharma, Paras Mahajan, and Sanjay Mohan	
Automation in Conventional Drilling Machine to Multi-spindle Drilling SPM	663
Vinay D. Patel, Mahendra Choudhary, Rushikesh Bhosale, Sarvesh Wapikar, Pranav Bhamare, and Ashish J. Chaudhari	
Mechanical Behavior of 3D Printed Polymeric Materials: Impact of Process Parameters	673
Aman Agrawal, Sunil Bhawnani, Anmol Sharma, Ankush Raina, and Mir Irfan Ul Haq	
Deformation Behaviours of Magnesium Alloy AZ41 Beyond Necking Using Extrapolation Method	683
Manish Kumar Gupta and N. K. Singh	
Thermal Analysis of Tank Gun Barrel	691
Nirav Shah, Aadish Meghani, Dhruvi Panchal, Dhruvit Patel, and Vinayak H. Khatawate	
Modelling and Simulation on Behaviours of Aluminium Alloys	703
Ravi Kumar and N. K. Singh	
Accelerometer Mass Effects on Vibration Frequencies of Magnesium Alloy Fixed–Fixed Beam	713
Anuj Yadav and N. K. Singh	
Prediction and Optimization of Weld Bead Geometry of MIG Welded Stainless Steel 202 Plates	723
Shruti Sood, Prithu Mishra, Mayank Pandit, and Pradeep Khanna	
Ultrasonic Metal Welding: A Novel Joining Technique for Phosphor Bronze Sheets	735
Bharat Sanga, Reeta Wattal, and D. S. Nagesh	
An Investigation to Different Methods of Health Assessment in Power Transformers	749
Anuj Banshwar, Naveen Kumar Sharma, Mohit Pathak, Bharat Bhushan Sharma, and Sujit Kumar	
Effect of MgO Powder Addition in Synthesis of Recycled Waste Bagasse Reinforced Green Composite Materials	757
Nitin Srivastava, Shashi Prakash Dwivedi, V. K. Dwivedi, and Rajat Yadav	
Low-Amplitude and High-Frequency Loading Influences Interstitial Fluid Flow in Osteogenesis Imperfecta Osteon	769
Nikhil Vivek Shrivastava, Abhishek Kumar Tiwari, Dharmendra Tripathi, and Santosh Patil	

DGA-Based Health Assessment of a 20 MVA Power Transformer	779
Naveen Kumar Sharma, Anuj Banshwar, Bharat Bhushan Sharma, Mohit Pathak, and Sujit Kumar	
Study of Fabrication Methods, Mechanical Features and Applications of Natural Fiber Composites	785
R. Muthalagu, V. Srinivasan, S. Sathees Kumar, and V. Murali Krishna	
Elastic Instability of the Functionally Graded Porous Cylindrical Panel	799
Abhay Gupta, Amit Kumar Mangoliwala, Rajidi Shashidhar Reddy, and Satyajit Panda	
Design and Development of Industry 4.0-Enabled Monitoring System	809
Abhimanyu Sharma, Parth Gahalot, Sharjil Talib, Sumit Gupta, Nipun Gautam, Atul Singh, Umananda Goswami, and Shubham	
Theoretical Modelling of Thin Air Film Thickness in Miscible Liquids	817
Vijayakumar Mathaiyan, R. Vijayanandh, and Dong Won Jung	
Analysis of Output Parameters of EDM: A Review	825
Akash Gupta and V. K. Dwivedi	
Biodiesel Prepared from Used Palm Oil Collected from Hostel Mess is a Promising Supplement for Diesel Fuel	841
Santosh Kumar Dash, P. S. Ranjit, Bhemuni Varaprasad, Nabam Hina Papu, and P. V. V. S. S. Manikanta	
Mapping, Trajectory Planning, and Navigation for Hexapod Robots Using ROS	851
Jovan Menezes, Shubhankar Das, Bhavik Panchal, Nitesh P. Yelve, and Praseed Kumar	
Voronoi Diagram Approximated Austenite Grain Mapping and Voronoi Algorithm-Based Microstructure Prediction of Quenched C35 Steel	867
S. Sanchu, N. Biju, and V. N. N. Namboothiri	
Development and Fabrication of Nylon 6 Standard and Asymmetric Spur Gear Using Injection Moulding	879
Mohit Jain, Santosh Patil, and S. S. Ghosh	
Investigates the Impact of Insulation Material on the Building Performance in Different Weather Zones of India	891
Shaheen Hasan, Sabah Khan, and Saif Uddin	

Performance Comparison Between Pure Diesel and 5% Butanol Blended Diesel in a Multi-cylinder Engine	903
Jitendra Kumar, Naushad Ahamad Ansari, Samsher, and Irwin Osmond Toppo	
Gamma Radiation Effects on Pre- and Post-welding SS304 and SS316 Stainless Steels' Ductility and Hardness	913
Parveen Kumar, Rajinder Kumar Soni, and B. S. Dehiya	
Design and Analysis of Multi-purpose Shopfloor Vice	925
Jash H. Patel, Jay S. Shah, Mili D. Shah, Monil K. Shah, and Vinayak H. Khatawate	
Selection of a Best Humanoid Robot Using "TOPSIS" for Rescue Operation	943
K. Krishna Kumar, Abinav Karthikeyan, and Murugappan Elango	
Experimental Investigation on Performance and Emission Characteristics of Low Heat Rejection Engine Operating on Biodiesel	955
A. Vadivel, S. Periyasamy, V. V. Mithun Kumar, and M. Praveen	
An Analytical Implementation of AHP in Supply Chain Working Environment	969
V. K. Pathak, N. Kumar, and R. K. Patel	
Simulation and Experimental Analysis of Multi-fragment Directional Warhead	981
Pankaj K. Choudha and A. Kumaraswamy	
FEA Analysis of the Knee Joint at Different Q Angle	995
Richa Rai and Vikas Rastogi	
Fault Diagnosis of Ball Bearing Using EEMD IMF Features, ReliefF, and Machine Learning	1009
V. Dave and V. Vakharia	
Design of External Wall Painting Robot for High-Rise Buildings	1021
Supreet Thale, Prathamesh Sawant, Saurabh Bagwe, and N. S. Chandrashekhhar	
Optimization of Wear Behaviour of Sugarcane Bagasse-Based Epoxy Particulate Composite Using Taguchi Method and Grey Relational Analysis	1033
Ankit, Rajesh, and Anil Kumar	
Parametric Investigation of Ballastless Railway Track for High-Speed Railway	1045
Yamika Patel, Vikas Rastogi, and Wolfgang Borutzky	

Determining the Fiber Loading on Mechanical Behavior of Kenaf and Sisal Fibers Reinforced Polyester Composites 1057
 R. Muthalagu, V. Srinivasan, S. Sathees Kumar, and V. Murali Krishna

An Experimental Investigation of Influence of Coated Piston Ring Surface Under Different Lubrication Condition Against Uncoated Surface on Diesel Engine 1069
 Anshul Kumar, Rajiv Chaudhary, and Ramesh Chand Singh

Numerical Study of Traction at Grouser–Soft Seabed Interface Incorporating Experimentally Validated Constitutive Model 1079
 S. Sumith, K. Shankar, and K. Kannan

Performance Characteristics of Asymmetric Body in Hypersonic Flow 1091
 D. Nithin and Vinod Kotebavi

Experimental and Theoretical Investigations of Support Structure Features and Build Time Management in PolyJet Technology 1101
 Arivazhagan Pugalendhi, Rajesh Ranganathan, and Balamurugan Gopalakrishnan

Fluid Flow Analysis of a Rotating Vaneless Diffuser Using CFD 1121
 Gnanadurai Ravikumar Solomon, R. Rahul, R. Balaji, and Ashish Selokar

Design and Performance of Wick-Type Solar Water Distillation Unit 1139
 Ashwini Shrivastava, Devendra Singh, Ajay Kumar Sharma, and Ashok K. Dewangan

Investigation of Tribological-Based Thermal Behaviours of Lubricating Oil of Worm Gearbox: A Review 1153
 J. S. Bhat, A. B. Chougale, and B. U. Sonawane

Prediction and Modelling of Nodal Temperature in Turning Operation 1163
 Rishish Mishra, Vineet Dubey, Rabesh Kumar Singh, and Anuj Kumar Sharma

Sensitivity of Al/Mg/Ti/Cu/SiC Hybrid Composite to Static Loads 1175
 Kumar Prakash and N. K. Singh

The Effect of Geometric Parameters of a Container on Thermal Charging of Latent Heat Thermal Energy Storage System: A Review 1185
 Jayesh Kumar, Pushpendra Singh, and Rajesh Kumar

Generation of a Versatile Discharge Formula for Multiple Parshall Flumes Using a Regression Technique	1197
D. Saran and N. K. Tiwari	
A Review on Bone Regeneration via Porosity Development Using Smart Manufacturing Techniques	1209
Mahesh Chaudhary, Jinesh Kumar Jain, and Toshit Jain	
Various Methods of Metal Transfer in the Welding Process	1223
Vinod Kumar Aswal and Jinesh Kumar Jain	
A Comparative Analysis of Different Algorithms for Optimizing Cutting Force Components in Turning Stainless Steel	1255
Toukir Ahmed, Ferdous Al Rafi, and Shahed Mahmud	
Computer Modelling of Loading-Induced Fluid Motion in 3D Osteon Model	1265
Naman Sharma and Rakesh Kumar	
Influence of Ultra-low Temperature Treatments on the Slurry Erosion Performance of Stainless Steel-316L	1273
Munish Kumar, Hazoor Singh Sidhu, and Buta Singh Sidhu	
Performance, Combustion, and Emission Characteristics of Diesel Engine Using Low-Temperature Combustion	1287
R. T. Sarathbabu, M. Kannan, R. Balaji, and Ashish Selokar	
A Review on Machining Potential of Composite Materials During Abrasive Water Jet Machining	1301
Anil Kumar Dahiya, B. K. Bhuyan, and Shailendra Kumar	
Theoretical and Experimental Estimation of Material Removal Rate of Electric-Spark Diamond Grinding of Difficult-To-Cut Materials	1317
Kumar Bhartendu, S. K. Jha, and B. K. Bhuyan	
An Inverse Technique to Estimate the Heat Flux of a Slab with Transient Heat Conduction	1335
Siddhartha Gollamudi and Pradeep S. Jakkareddy	
A Numerical Approach to Find Distinct Mechanisms of a Planar Kinematic Chain Using Linkage Coordinates	1347
Vinjamuri Venkata Kamesh, V. Srinivasa Rao, D. V. S. S. V. Prasad, and P. S. Ranjit	
Multi-objective Optimization of Machining Parameters in μ-EDM Drilling of SS317L Using Novel JAYA and TLBO Algorithms	1363
V. Rajashekar and Shivraj Narayan Yeole	

Effect of Inelasticity on Buckling of Axially Compressed Cylindrical Shell 1377
 Ishita

Analysis of Shock Trains in an Isolator Model 1389
 Choraghe Shweta Laxman and S. R. Nagaraja

Effect of Shear Work on Heat Transfer Characteristics of Gaseous Flow Between Two Micro-parallel Plates 1397
 Prathuk Balachandra Hegde and Hari Mohan Kushwaha

Prediction of Stable Cutting Range Using Local Mean Decomposition Merged with Statistical Approach 1409
 Pankaj Gupta, Bhagat Singh, and Yogesh Shrivastava

Thermoeconomic Analysis of Crossflow Printed Circuit Heat Exchanger 1421
 K. Manjunath

A Comparative Study on the Performance of Energy Storage Systems for Hybrid Electric Vehicles 1433
 Kanchan Yadav and Sanjay Maurya

Parametric Analysis of Friction Stir Welding of Pure Copper 1443
 Deepak Kaushal and Akhilesh Kumar Choudhary

Engineering and Ergonomics—An Important Aspect in Fruit Harvesting Systems 1453
 Suhail Nazir Wani, Sanjay Mohan, and Mohd. Kamal

Emission Reduction from Diesel Engine Using Alkali Solution, and Carbon Black in Union with Catalytic Convertor 1463
 Mohit Bhandwal and R. K. Tyagi

About the Editors




Prof. Kannan Govindan is currently a Professor and head of the Center for Sustainable Supply Chain Engineering, University of Southern Denmark, Odense, Denmark. He received 2018, 2019 highly cited researcher award from Thomson-Reuters/Clarivate Analytics (“one of only 204 researchers to be listed in the engineering category”). He received the Fyens Stiftstidende research award for 2019. He received the High-Level Overseas Innovative Talent to Tianjin award (Under 1000 talents program for High-Level Overseas Innovative Talent experts of Tianjin Province) from Tianjin Province, China. His research interests include digital supply chain, industry 4.0 on supply chain, sustainable development goals, reverse logistics, closed loop supply chain, digitalized sustainable circular economy, green supply chain management, and sustainable supply chain management. He has published more than 250 international journal articles (with total 21400 + citations and H-index of 82) in leading journals such as Nature, Omega, Journal of the Operational Research Society, Journal of Environmental Management, Renewable & Sustainable Energy Reviews, European Journal of Operational Research, Journal of Cleaner Production, Computers & Industrial Engineering, Ecological Indicators, Transportation Research Part E: Logistics and Transportation Review, Transportation Research Part D: Transport and Environment, Transactions on Systems, Man, and Cybernetics Part A: Systems and Humans, European Management Journal, Computers and OR, International Journal of Production Economics and *International Journal of Production Research*.

Dr. Harish Kumar is currently working as Assistant Professor in National Institute of Technology Delhi. He has more than 15 years of research and academic experience and served as Scientist at different grades in CSIR—National Physical Laboratory, India (NPLI). He has been an active researcher in the area of mechanical measurement and metrology. He has worked as Guest Researcher at National Institute of Standards and Technology, USA in 2016. He has been instrumental in ongoing redefinition of kilogram in India. He has authored more than 70 publications in peer reviewed journals and conferences. He has served as Guest Editors of different journals and conference proceedings volumes including Mapan—Journal of Metrology Society of India.

Dr. Sanjay Yadav is a Senior Principal Scientist and Head of the Pressure, Vacuum and Ultrasonic Metrology Section and Prof. Academy of Scientific and Innovative Research (AcSIR), CSIR—National Physical Laboratory, New Delhi, India. He received his Ph.D. in Physics from Meerut University in 1990. He has published more than 270 papers in international journals and conference proceedings and is the Editor-in-Chief of the journal MAPAN—Journal of Metrology Society of India, published by Springer. He is reviewer of many reputed journals including Measurement Science and Technology, Metrologia, Measurement, Review of Scientific Instruments, etc.

A Mini State of Art Survey on Photovoltaic/Thermal Desalination Systems



Subbarama Kousik Suraparaju , Arivazhagan Sampathkumar ,
and Sendhil Kumar Natarajan 

Abstract Water is a substantial need for the survival of mankind on Earth. It is impossible to envisage our life without water. In the present scenario, pristine water accessibility is the most faced problem in almost all countries. The only alternative to come out of this situation is converting the available seawater into pure water through several desalination practices. Desalination techniques powered with renewable energy sources are the most pertinent solution for the world water crisis as they do not deplete the existing energy sources which lead to ecological imbalance. In the realm of desalination, solar thermal desalination is the most preferable and economical technique because of its enormous advantages compared to others. The current trend in solar desalination is that coupling solar still to a photovoltaic system for more benefits. This PV/T integration to the desalination system not only satisfies the clean water needs but also fulfils the electricity demand in the remote and rural areas where there is power scarcity. In this context, this article elucidates a concise review of the solar desalination techniques powered by the incorporation of photovoltaic and thermal (PV/T) technologies.

Keywords Solar still · Desalination · Hybrid · Photovoltaic/thermal (PV/T)

1 Introduction

In the world, almost 844 million people suffer from a dearth of basic drinking water amenities, near to 159 million people are reliant on the surface water and at least 2 billion people are habituated to drink water that is contaminated with faeces that lead to diseases like diarrhoea, cholera, typhoid, dysentery and polio. A survey by WHO concluded that almost half of the population in the world will be living in water-stressed areas by 2025 [1]. In the current situation, the urge for fresh drinking water is increased, but the pure water reserves across the globe are already started depleting. One of the solutions to overcome this life-threatening

S. K. Suraparaju · A. Sampathkumar · S. K. Natarajan (✉)
Solar Energy Laboratory, Department of Mechanical Engineering, National Institute of
Technology Puducherry, Karaikal, UT of Puducherry 609609, India

© The Author(s), under exclusive license to Springer Nature Singapore Pte Ltd. 2022
K. Govindan et al. (eds.), *Advances in Mechanical and Materials Technology*,
Lecture Notes in Mechanical Engineering,
https://doi.org/10.1007/978-981-16-2794-1_1

glitch is to convert the available seawater into pure and drinkable water through some advanced desalination techniques with the environment. Among all the renewable energy sources, the present-day world is trending towards solar photovoltaics and fuel cells for better energy efficiency [2–5]. In this regard, García et al. and Ghaffour et al. conversed about the renewable energy-driven desalination system and their viability [6, 7]. Sharon et al. and Pouyfaucou et al. discussed solar energy-driven desalination systems [8, 9]. Pugsley et al. and Shatat et al. given a brief description of solar desalination across the globe [10, 11]. Manchanda et al. [12], Samuel et al. [13] and Kabeel et al. [14] studied various types of solar still designs for increasing productivity in desalination. Panchal et al. reviewed the various techniques to augment the efficiency of solar tubular still [15]. Kumar et al. analysed the efficacy of the multi-stage evacuated solar still and found it was comparatively given a better performance than the conventional solar still [16]. Suraparaju et al. analysed the influence of natural fibre in the solar still performance and found it is hindering the solar radiation [17]. Dinesh et al. reviewed the various effects of fin configuration parameters on the solar still for better efficiency [18]. Othman et al. and Francesco et al. examined the operation of the integrated photovoltaic/thermal solar collectors for poly-generation techniques [19, 20]. Gude et al. reviewed various energy storage methods for powering the desalination systems by storing thermal energy storage [21, 22]. Manju et al. studied the various renewable energy-powered desalination systems and suggested a viable way to overcome freshwater scarcity in India [23]. Mohsen et al. have given a brief description of the photovoltaic-based desalination systems [24]. In this regard, there is no particular literature about combined photovoltaic and thermal desalination. In this article, a short survey of integrated photovoltaic/thermal desalination systems and the recent developments in the particular approach has been discussed to address the above-mentioned research gap.

2 Solar Desalination Coupled with PV System

2.1 *Photovoltaic/Thermal (PVT)–Humidification and Dehumidification (HDH) Desalination*

Giwa et al. examined the technical feasibility and sustainability of the integrated PV-HDH desalination system. The outcomes of the investigation found that the heat recovered from the PV produced the freshwater about 2.28 L per m² of PV. Also, the environmental assessment of the PV-HDH system proved that there was a decrease of 83.6% environmental effects when compared to PV-RO system [25]. Amin M. Elsafi analysed the performance of combined CPVT collectors and humidification and dehumidification desalination systems for generation of electricity and freshwater. The results of the investigation showed that the system was capable of producing the freshwater of about 12 m³ and electricity of about 960 kWh annually for a location having 1.88 MWh/yr solar radiation. The cost of potable water was about 0.01\$/L,

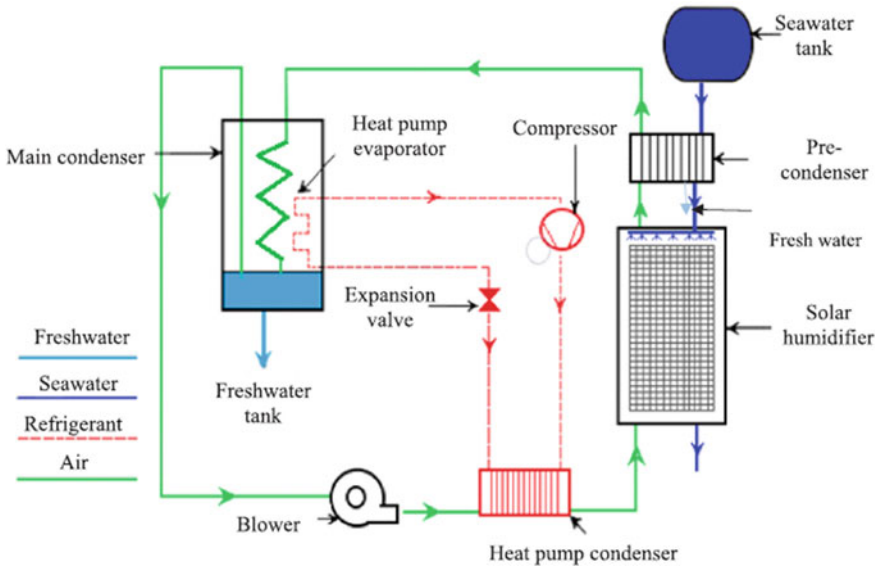


Fig. 1 Schematic of the PV-HDH desalination system with heat pump [28]

whereas the cost of electricity generation was about 0.289 \$/kWh [26]. Gabrielli et al. studied the working of PV-HDH system in generating electricity as well as water. The techno-economic assessment showed that the system is viable when compared with conventional solar HDH systems against the electricity prices, annual water production, ambient conditions and size of HDH system [27]. Pourafshar et al. inspected the effect of the heat pump in PV-HDH desalination as shown in Fig. 1 and found that the potable water production rates were about in between 0.56 and 0.99 kg/h/m², whereas the freshwater was produced at 0.018 US \$/kg [28].

2.2 Solar Still

2.2.1 Flat Plate Collector-Photovoltaic/Thermal Solar Desalination System

Kumar et al. assessed the heat transfer coefficients of the photovoltaic/thermal solar desalination system located in New Delhi. They proposed a thermal model and compared it with other models for the evaluation of internal heat transfer coefficients and percentage deviation. Also, it was noticed that their model named Kumar and Tiwari model (KTM) was best fitted with the results compared to other models [29]. Tiwari et al. determined the characteristic equation of a PV/T solar still, located in New Delhi, India, and compared theoretical values with experimental values

performed from April 2006 to March 2007. It was noticed that the output of the developed solar desalination system was increased by 3.5-folds than the passive solar still at 0.05 m basin water depth [30]. Kumar et al. designed, fabricated and examined the efficiency of the single-slope and double-slope hybrid photovoltaic/thermal solar desalination systems. It was detected that the day-to-day productivity obtained from the passive solar desalination system was about 2.26 kg, whereas for the similar operating conditions the productivity was about 7.22 kg for proposed hybrid photovoltaic/thermal solar desalination system at a depth of 0.05 m basin water. The output of the hybrid solar desalination system was 3.2 times greater in summer and winter, and it was 5.5 times greater than the passive solar desalination system. It was also noted that the proposed design has higher thermal efficiency about 20% compared to passive solar desalination system. The other active hybrid solar desalination system with double slope was designed, fabricated and analysed and resulted with 1.4 times increase in the productivity in comparison with single-slope active solar desalination system for similar conditions. In the later stage, the proposed set-up was economically analysed and reported that EPF and LCC efficiency was observed to be 5.9% and 14.5%, respectively, for the anticipated life of 30 years. The costs of energy and potable water production were found to be Rs.0.85/kWh and Rs. 0.75/L, respectively. The predicted payback period was 4.2 years if the yield was traded at the price of Rs. 6.0/L. Later, enviro-economic and exergy-economic analysis on partially covered photovoltaic-flat plate collector (PV-FPC) active solar desalination system resulted that the recommended active solar desalination system can encounter the day-by-day demand of pure water and DC electrical power [31–34]. Boubekri et al. modelled and simulated the single-slope solar desalination system coupled through two reflectors integrated with a PV/T solar water heater system in Algeria weather conditions. The effect of reflectors increased productivity by about 127.06% during winter, 10.1% during summer and 21.78% during spring. The nocturnal productivity increased when the system was integrated with either thermal or PV/T storage during sunshine hours. The productivity increase was estimated for thermal storage as 17.36% during winter, 28.34% during spring and 33.00% during summer. Similarly, the productivity enhancement was estimated for PV/T storage as 47.61% during winter, 137.06% during spring and 131.06% during summer [35]. Eltawil et al. came up with hybrid PV/T solar still equipped with a solar flat plate collector (FPC), spraying unit, a solar air collector, perforated tubes, and external condenser. Later, it was distinguished with conventional solar desalination system which lead to increase in the distillate productivity by a range of 51–148% for the several integrations to system. The developed solar desalination system exhibited better operation over conventional solar desalination system by 148% increase in productivity and about 29% increase in the daily efficacy [36]. Gaur et al. and Saeedi et al. optimized the influential parameters and no. of collectors for hybrid photovoltaic/thermal desalination systems to obtain a better energy efficiency [37, 38]. Singh et al. experimentally studied the partially covered PV/T-FPC solar desalination system and resulted that maximal values of energy, exergy, overall efficiency, electrical exergy and overall exergies are found to be 75%, 20.74%, 69.06%, 28.53%

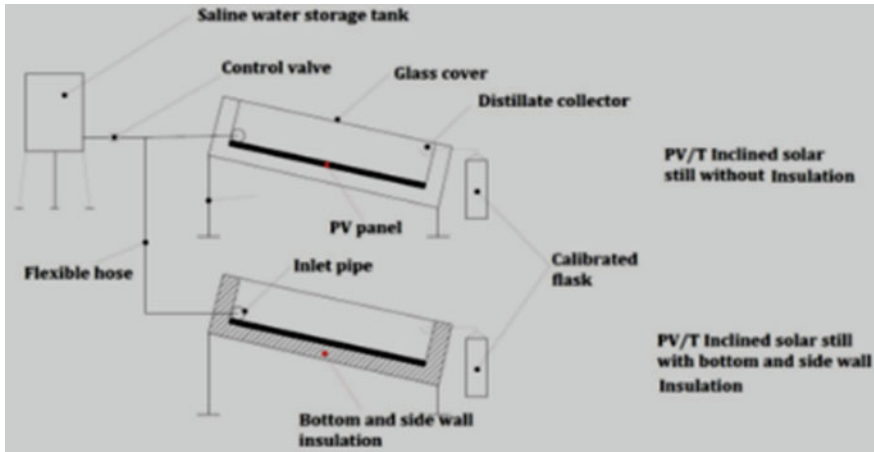


Fig. 2 Schematic of solar still with and without insulation [42]

and 25%, respectively [39]. Mehrnaz et al. numerically and experimentally investigated the integrated PV/T collector with stepped solar desalination system for energy efficiency. Also, the consequences of design and operating parameters on potable water productivity, energy efficacy and output electrical power were analysed. The proposed desalination system resulted in an increase in energy efficiency by 2 times and productivity by 20% [40]. Praveen Kumar et al. experimentally investigated and compared the hybrid PV/T active solar still at three diverse water depths of the basin (0.05 m, 0.10 m and 0.15 m) with conventional active solar still. Nickel–chromium (Ni–Cr) heater driven by solar photovoltaic (SPV) was equipped in the recommended model for better productivity. The productivity of a developed model was greater than the conventional solar desalination system by sixfolds, and overall thermal efficacy and electrical efficacy were also increased up to 25% when compared to conventional solar desalination system [41]. Muthu Manokar et al. examined the influence of insulation on the Inclined Solar Panel Basin (ISPB) as shown in Fig. 2, incorporated with the photovoltaic module and results depicted that maximal yield of 7.3 kg was attained when ISPB solar desalination system with the bottom and sidewall insulation. Also. It was noticed that ISPB with insulation has greater productivity and efficacy when compared to a desalination system without insulation [42]. Balachandran et al. examined the effect of hybrid natural fibre composite (HNFC) insulation on the efficiency of PV/T desalination system and the outcomes of the experiment proved that the HNFC insulation with 0.5 cm depth and glass cover cooling by water film increased the productivity by 35%, whereas the HNFC insulation with 1 cm depth and glass cover cooling by water film increased the productivity by 21% [43]. Kabeel et al. investigated the influence of cover cooling in inclined PV panel solar still on the yield. It was found that the yield was increased by 18.17% for partial cover cooling, whereas, for full cover cooling, there was an increase in the yield by 36.25% [44].

2.3 Concentrated Photovoltaic/Thermal Solar Desalination System

Al-Nimr et al. investigated the concentrated photovoltaic/thermal system that uses thermal energy refused by the photovoltaic cell to desalinate the water. This photovoltaic/thermal system was sophisticated with a porous evaporator and an internal condenser. It supplies the potable water along with electric power, and also it operates as a passive system as the rotation of water was driven by the thermosyphon effect. Also, investigation on process parameters like solar intensity, condenser temperature, ambient temperature, wind speed and PV cell used was done [45]. Singh et al. analysed the cost estimation of partially covered PV/T and CPC collector-coupled solar desalination system (Fig. 3). The influential parameters like mass flow rate and no. of PV/T-CPC collectors were optimized for better working of the system. The EPF, LCC efficiency and annual yield were observed to be greater by 12.73%, 22.22% and 5% for double-slope PV/T-CPC than single-slope PV/T-CPC desalination system at 0.14 m basin water depth. It was noticed that if the basin water depth was lesser than 0.19 m, then the double-slope PV/T-CPC performs better than the single-slope PV/T-CPC and vice versa. Later, the enviro-economic, exergo-economic and productivity analysis on basin-type solar stills by integrating N indistinguishable PV/T-CPC collectors depicted that enviro-economic parameter, exergo-economic parameter, cogeneration efficiency and productivity for double-slope PV/T-CPC active solar still were greater by 21.48%, 16.22%, 5.73% and 8.56% than single-slope still at 0.14 m basin water depth for the similar operating conditions [46, 47].

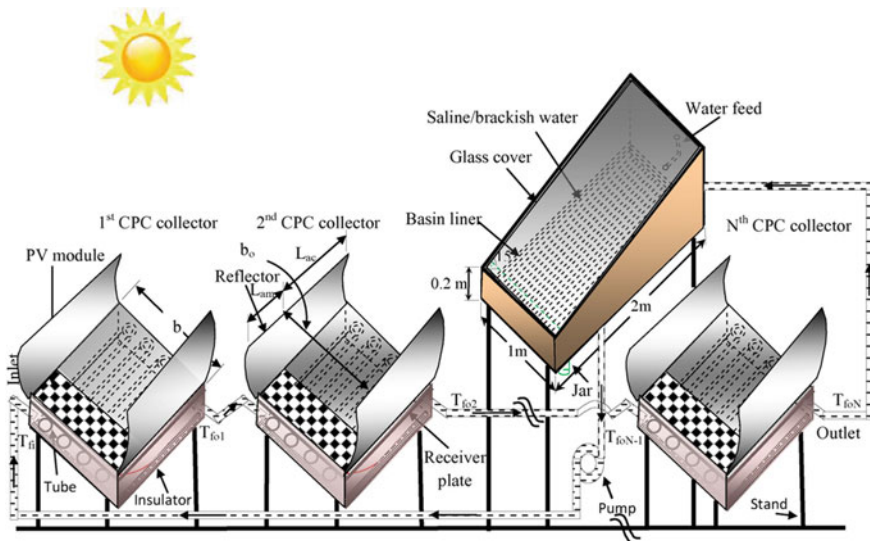


Fig. 3 Schematic of proposed PV/T solar desalination system [46]

Singh et al. examined the operation of three models, namely single slope comprised with N-PVT-FPC-SS; N-PV/T-CPC-SS and conventional single-slope (CSS) solar desalination systems and assessed the yearly yield, energy, exergy, production cost of potable water, energy metrics and cogeneration efficiency at a basin water depth of 0.14 m for New Delhi weather conditions [48]. Gupta et al. developed the characteristic equation for N indistinguishable fully covered PV/T-CPC combined solar desalination system which was analogous to Hottel-Whillier-Bliss equation. The proposed system addressed the limitations of partially covered PV/T for the identical watt peak [49].

2.4 Evacuated Collector—Photovoltaic/Thermal Solar Desalination System

Mazraeh et al. proposed and studied the solar still outfitted to evacuated tube collector and semi-transparent photovoltaic in natural convection mode. The system efficiency was evaluated by considering the several factors such as distillate yield, instantaneous energy and exergy efficiencies along with daily energy and exergy efficiencies, instantaneous electrical power production along with daily electrical power production concerning to six types of PV modules, number of tubes and different depths of basin water. It was observed that there is no influence of PV module type on the distillate output type, and increased tubes number enhances the distillate productivity. The maximal yield ($4.77 \text{ kg/m}^2 \text{ day}$) was attained for 0.07 m basin water depth with 30 tubes. It was observed that for the heterojunction with intrinsic thin layer—photovoltaic module (HIT-PV) resulted in the maximal instantaneous electrical power and overall electrical power of 70.48 W/m^2 and 483.2 W h/m^2 . Also, maximal daily exergy and energy efficacies were recorded as 16.65% and 6.86% for a basin water depth of 0.07 m with 10 tubes. Further, they proposed a new system coupled with evacuated tube collectors, semi-transparent photovoltaic and phase change materials and developed the numerical models to estimate the consequences of several PCM-PV modules, tube numbers and basin water depths on the thermoelectrical performance of the system. Later, the effect of several parameters was examined and resulted in that type of PV does not affect the distillate yield; however, it was an influential parameter on electrical power generation. Also, the no. of tubes enhanced the distillate yield in which it affects the energy efficacy and exergy efficacy inversely. On the other hand, PCM also enhanced energy efficacy but has no remarkable influence on exergy efficacy. The maximal distillate yield throughout a day was evaluated for the 0.03 m basin water depth and 30 tubes with paraffin wax PCM ($4.5503 \text{ kg/m}^2\text{-day}$) which was 20.32% higher than the instance without paraffin wax. Also, maximal daytime energy and exergy efficacies were disclosed as 17.93% and 6.95% for 0.03 m water depth and ten tubes with PCM [50, 51]. Singh et al. developed a double-slope solar desalination system coupled with N indistinguishable evacuated tube collectors (N-ETC-DS—Fig. 4) Further, the system was

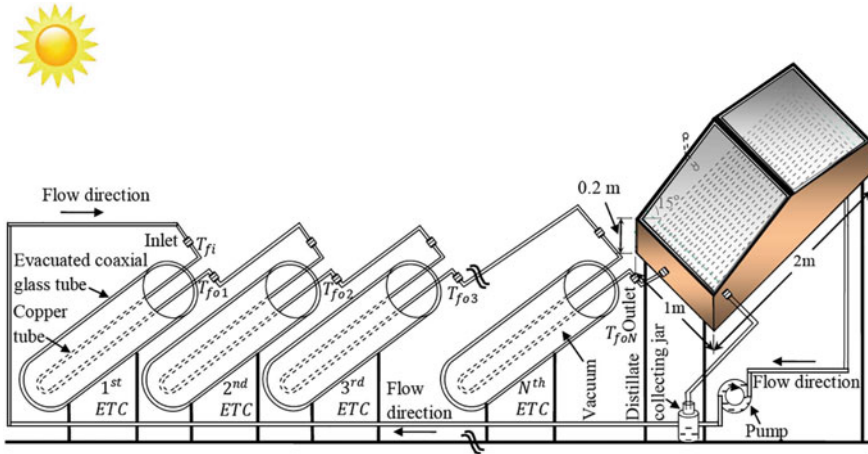


Fig. 4 Proposed evacuated tube—PV/T solar desalination system [52]

analysed during four types of climatic conditions at New Delhi and compared solar desalination systems incorporated with N indistinguishable PV/T flat plate collectors, compound parabolic collectors and conventional solar desalination system and concluded that evacuated tube collector has the best performance [52].

2.5 Other Novel Photovoltaic/Thermal Solar Desalination Systems

Riahi et al. examined the solar desalination system incorporated with the PV module and AC heater for viable freshwater production. A 500 W heater is coupled with a double-slope solar desalination system, and six photovoltaic modules were employed to generate 1.5 kW power which further allied with four batteries of each 150 Ah capacity. The key benefit of this proposed system is that it was able to yield distilled water indeed at low insolation due to the incorporation of the PV module and AC heater. The proposed system yielded 6 times greater than the conventional solar desalination system with a yield of 5.7 kg/m^2 [53]. Al-Nimr et al. developed a novel single-sloped solar desalination system with PV/T cell at the base of its basin, and the solar still was attached with the outside finned condenser and further developed a numerical model to evaluate the efficiency of the developed system [54]. Pounraj et al. investigated on the novel PV/T active solar still integrated with Peltier system. The results of performance analysis observed that the recommended desalination system produces about 6.5 times higher, and the payback period was 127 days lesser than the conventional desalination system [55]. Faramarz Sarhaddi examined the efficiency of stepped solar still by integrating PV and found that there was an increase of almost two times in the energy

efficiency, whereas the freshwater productivity was increased by 20% [56]. Abd Elbar et al. investigated the solar still with PV, black steel wool fibres (BSWF) and forced convection air cooling (FAC) for better productivity. The outcomes of the investigation showed that the solar still with BSWF and FAC achieved an increase in daily productivity and efficiency by 30% and 35%, respectively. The exergo-economic and exergo-environmental assessment of the system proved that the system is viable in all perspectives [57, 58]. Parsa et al. investigated the performance of solar still integrated with thermoelectric modules and PV for better efficiency at the height of 13,000 ft. The results found that the modified solar still achieved 27.8% higher instantaneous efficiency and 42.5% higher productivity than the solar desalination system at Tehran [59]. Haiping et al. analysed the performance of flash tank-coupled low concentrating photovoltaic/thermal system (FT-LCPVT) for the generation of electricity and potable water as shown in Fig. 5. The outcomes of the investigation depicted that the electricity generated was about 447.55 W, and the freshwater produced was about 23.65 L during 09.00 and 17.00 [60].

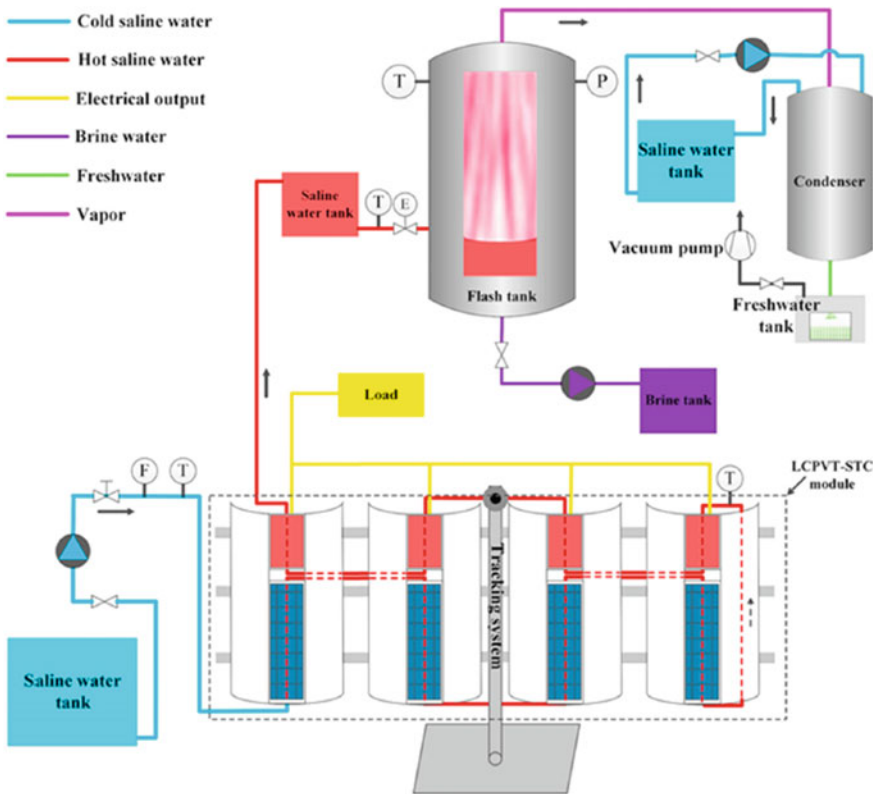


Fig. 5 Schematic of the proposed FT-LCPVT system [60]

3 Summary

According to the discussion, it was clear that the integration of photovoltaic/thermal system for desalination was comparatively effective than the conventional solar desalination systems in terms of economic and environmental assessments. Also, PV-HDH systems were evolved as better systems than PV-RO systems. The installation of PV/T-desalination systems is not only the solution for freshwater scarcity but also addresses the electricity problems. The various works regarding photovoltaic/thermal desalination were tabulated in Table 1 which leads the researchers to select appropriate desalination system according to the requirements.

4 Conclusions

Based on the above discussion, the conclusions of this short survey are as follows:

- Integrated PV/T solar still can produce water and electricity to fulfil the basic needs of the world's population who are living in a water and energy crisis.
- The efficiencies of PV panel and solar still both are influenced by parameters like radiation, ambient temperature, wind velocity, etc.
- Wind velocity had a greater impact on the PV/T system in which wind velocity enhances the system efficiency but high wind velocities lead to negative impacts on both solar desalination system and PV panel.
- At higher temperatures, the energy efficiency of the system decreases, and also high panel temperature leads to a negative impact on power production.
- The integration of PV with thermoelectric modules and some energy storage materials would be added benefit for the solar stills.
- Cooling of PVs in the integrated systems would increase productivity which turns the system into economically viable, and also the heat losses could be decreased.

Table 1 Various research works in PV/T desalination

S. No.	Authors	Proposed model	Remarks
1	Giwa et al. [25]	PV-HDH	2.28 L/m ² of PV 83.6% less environmental effects than PV-RO
2	Elsafi [26]	CPVT-HDH	Generated the freshwater of about 12 m ³ and electricity of about 960 kWh annually
3	Dev and Tiwari [30]	PV/T solar still	3.5 times greater yield than the conventional
4	Balachandran et al. [43]	HNFC insulation	Insulation with 0.5 cm depth increased 35% productivity, whereas the HNFC insulation with 1 cm increased the productivity by 21%
5	Singh et al. [46]	PV/T–CPC	Double-slope PV/T–CPC achieved 5% greater yield than single-slope PV/T-CPC desalination
6	Mazraeh et al. [50]	PV/T–evacuated collector	The maximal yield (4.77 kg/m ² day) was attained for 0.07 m basin water depth with 30 tubes
7	Riahi et al. [53]	PV module and AC heater	Proposed system yielded 6 times greater than the conventional solar desalination system
8	Faramarz Sarhaddi [56]	PV/T stepped solar still	The freshwater productivity was increased by 20%
9	Parsa et al. [59]	Thermoelectric modules and PV at the height of 13,000 ft	The modified solar still achieved 27.8% higher instantaneous efficiency and 42.5% higher productivity than the solar desalination system at Tehran
10	Haiping et al. [60]	FT-LCPVT	Electricity generated was about 447.55 W, and the freshwater produced was about 23.65 L during 09.00 and 17.00

References

1. WHO Drinking Water Facts
2. Dash AK, Gairola S, Agrawal S, Shukla S (2019) A novel investigation and comparative study on building integrated photovoltaic thermal (BIPVT) system. *Int J Math Eng Manage Sci* 4:460–470

3. Natarajan SK, Kamran F, Ragavan N, Rajesh R, Jena RK, Suraparaju SK (2019) Analysis of PEM hydrogen fuel cell and solar PV cell hybrid model. *Mater Today Proc* 17:246–253. <https://doi.org/10.1016/j.matpr.2019.06.426>
4. Natarajan SK, Kumar A, Mohamed R, Rathna R (2019) Design and development of dual axis sun tracking system for floating PV. In: *IOP Conference Series: Earth and Environmental Science*, p 312. <https://doi.org/10.1088/1755-1315/312/1/012001>
5. Natarajan SK, Suraparaju SK, Elavarasan E, Singh KA (2019) Performance analysis of solar photovoltaic panel at Karaikal weather conditions. In: *IOP Conference Series: Earth and Environmental Science*. <https://doi.org/10.1088/1755-1315/312/1/012007>
6. García-Rodríguez L (2002) Seawater desalination driven by renewable energies: a review. *Desalination* 143:103–113. [https://doi.org/10.1016/S0011-9164\(02\)00232-1](https://doi.org/10.1016/S0011-9164(02)00232-1)
7. Ghaffour N, Bundschuh J, Mahmoudi H, Goosen MFA (2015) Renewable energy-driven desalination technologies: a comprehensive review on challenges and potential applications of integrated systems. *Desalination* 356:94–114. <https://doi.org/10.1016/j.desal.2014.10.024>
8. Sharon H, Reddy KS (2015) A review of solar energy driven desalination technologies. *Renew Sustain Energy Rev* 41:1080–1118. <https://doi.org/10.1016/j.rser.2014.09.002>
9. Pouyfaucou AB, García-Rodríguez L (2018) Solar thermal-powered desalination: a viable solution for a potential market. *Desalination* 435:60–69. <https://doi.org/10.1016/j.desal.2017.12.025>
10. Pugsley A, Zacharopoulos A, Mondol JD, Smyth M (2016) Global applicability of solar desalination. *Renew Energy* 88:200–219. <https://doi.org/10.1016/j.renene.2015.11.017>
11. Shatat M, Worall M, Riffat S (2013) Opportunities for solar water desalination worldwide: Review. *Sustain Urban Areas* 9:67–80. <https://doi.org/10.1016/j.scs.2013.03.004>
12. Manchanda H, Kumar M (2015) A comprehensive decade review and analysis on designs and performance parameters of passive solar still. *Renewa Wind Water Solar* 2. <https://doi.org/10.1186/s40807-015-0019-8>
13. Kabeel AE, Manokar AM, Sathyamurthy R, Winston DP, El-Agouz SA, Chamkha AJ (2019) A review on different design modifications employed in inclined solar still for enhancing the productivity. *J Solar Energy Eng Trans ASME* 141:1–10. <https://doi.org/10.1115/1.4041547>
14. Samuel DGH, Nagarajan PK, Arunkumar T, Kannan E, Sathyamurthy R (2016) Enhancing the solar still yield by increasing the surface area of water—a review. *Environ Prog Sustainable Energy* 35:815–822. <https://doi.org/10.1002/ep.12280>
15. Panchal H, Sadasivuni KK, Israr M, Thakar N (2019) Various techniques to enhance distillate output of tubular solar still: a review. *Groundw Sustain Dev* 9:100268. <https://doi.org/10.1016/j.gsd.2019.100268>
16. Reddy KS, Kumar KR, Donovan TSO, Mallick TK (2012) Performance analysis of an evacuated multi-stage solar water desalination system. *DES* 288:80–92. <https://doi.org/10.1016/j.desal.2011.12.016>
17. Suraparaju SK, Natarajan SK (2020) Performance analysis of single slope solar desalination setup with natural fiber. *Desalin Water Treat* 193:64–71. <https://doi.org/10.5004/dwt.2020.25679>
18. Mevada D, Panchal H, Sadasivuni KK, Israr M, Suresh M, Dharaskar S, Thakkar H (2020) Effect of fin configuration parameters on performance of solar still: a review. *Groundw Sustain Dev* 10:100289. <https://doi.org/10.1016/j.gsd.2019.100289>
19. Othman MY, Yatim B, Sopian K, Abu Bakar MN (2007) Performance studies on a finned double-pass photovoltaic-thermal (PV/T) solar collector. *Desalination* 209:43–49. <https://doi.org/10.1016/j.desal.2007.04.007>
20. Calise F, Dentice M, Vanoli L (2012) Design and dynamic simulation of a novel solar trigeneration system based on hybrid photovoltaic / thermal collectors (PVT). *Energy Convers Manage* 60:214–225. <https://doi.org/10.1016/j.enconman.2012.01.025>
21. Gude VG (2018) Energy storage for desalination. Elsevier Inc. <https://doi.org/10.1016/B978-0-12-815244-7.00010-6>
22. Gude VG (2015) Energy storage for desalination processes powered by renewable energy and waste heat sources. *Appl Energy* 137:877–898. <https://doi.org/10.1016/j.apenergy.2014.06.061>

23. Manju S, Sagar N (2017) Renewable energy integrated desalination: a sustainable solution to overcome future fresh-water scarcity in India. *Renew Sustain Energy Rev* 73:594–609. <https://doi.org/10.1016/j.rser.2017.01.164>
24. Mohsen MS, Jaber JO (2001) A photovoltaic-powered systems for water desalination. *Desalination* 138:129–136. [https://doi.org/10.1016/S0011-9164\(01\)00254-5](https://doi.org/10.1016/S0011-9164(01)00254-5)
25. Giwa A, Fath H, Hasan SW (2016) Humidification-dehumidification desalination process driven by photovoltaic thermal energy recovery (PV-HDH) for small-scale sustainable water and power production. *Desalination* 377:163–171. <https://doi.org/10.1016/j.desal.2015.09.018>
26. Elsafi AM (2017) Integration of humidification-dehumidification desalination and concentrated photovoltaic-thermal collectors: energy and exergy-costing analysis. *Desalination* 424:17–26. <https://doi.org/10.1016/j.desal.2017.09.022>
27. Gabrielli P, Gazzani M, Novati N, Sutter L, Simonetti R, Molinaroli L, Manzolini G, Mazzotti M (2019) Combined water desalination and electricity generation through a humidification-dehumidification process integrated with photovoltaic-thermal modules: design, performance analysis and techno-economic assessment. *Energy Convers Manage X* 1:100004. <https://doi.org/10.1016/j.ecmx.2019.100004>
28. Pourafshar ST, Jafarinaemi K, Mortezaipoor H (2020) Development of a photovoltaic-thermal solar humidifier for the humidification-dehumidification desalination system coupled with heat pump. *Sol Energy* 205:51–61. <https://doi.org/10.1016/j.solener.2020.05.045>
29. Kumar S, Tiwari GN (2009) Estimation of internal heat transfer coefficients of a hybrid (PV/T) active solar still. *Sol Energy* 83:1656–1667. <https://doi.org/10.1016/j.solener.2009.06.002>
30. Dev R, Tiwari GN (2010) Characteristic equation of a hybrid (PV-T) active solar still. *Desalination* 254:126–137. <https://doi.org/10.1016/j.desal.2009.12.004>
31. Kumar S, Tiwari A (2010) Design, fabrication and performance of a hybrid photovoltaic/thermal (PV/T) active solar still. *Energy Convers Manage* 51:1219–1229. <https://doi.org/10.1016/j.enconman.2009.12.033>
32. Singh G, Kumar S, Tiwari GN (2011) Design, fabrication and performance evaluation of a hybrid photovoltaic thermal (PVT) double slope active solar still. *DES* 277:399–406. <https://doi.org/10.1016/j.desal.2011.04.064>
33. Kumar S (2013) Thermal-economic analysis of a hybrid photovoltaic thermal (PVT) active solar distillation system: role of carbon credit. *Urban Climate* 5:112–124. <https://doi.org/10.1016/j.uclim.2013.07.001>
34. Tiwari GN, Yadav JK, Singh DB, Al-helal IM, Abdel-ghany AM (2015) Exergoeconomic and enviroeconomic analyses of partially covered photovoltaic flat plate collector active solar distillation system. *DES* 367:186–196. <https://doi.org/10.1016/j.desal.2015.04.010>
35. Boubekri M, Chaker A, Chekneane A (2013) Modeling and simulation of the continuous production of an improved solar still coupled with a photovoltaic/thermal solar water heater system. *DES* 331:6–15. <https://doi.org/10.1016/j.desal.2013.09.027>
36. Eltawil MA, Omara ZM (2014) Enhancing the solar still performance using solar photovoltaic, flat plate collector and hot air. *DES* 349:1–9. <https://doi.org/10.1016/j.desal.2014.06.021>
37. Gaur MK, Tiwari GN (2010) Optimization of number of collectors for integrated PV/T hybrid active solar still. *Appl Energy* 87:1763–1772. <https://doi.org/10.1016/j.apenergy.2009.10.019>
38. Saeedi F, Sarhaddi F, Behzadmehr A (2015) Optimization of a PV/T (photovoltaic/thermal) active solar still. *Energy* 87:142–152. <https://doi.org/10.1016/j.energy.2015.04.062>
39. Singh DB, Yadav JK, Dwivedi VK, Kumar S, Tiwari GN, Al-helal IM (2016) Experimental studies of active solar still integrated with two hybrid PVT collectors. *Sol Energy* 130:207–223. <https://doi.org/10.1016/j.solener.2016.02.024>
40. Naroei M, Sarhaddi F, Sobhnamayan F (2018) Efficiency of a photovoltaic thermal stepped solar still: experimental and numerical analysis 441:87–95. <https://doi.org/10.1016/j.desal.2018.04.014>
41. Praveen Kumar B, Prince Winston D, Pounraj P, Muthu Manokar A, Sathyamurthy R, Kabeel AE (2018) Experimental investigation on hybrid PV/T active solar still with effective heating and cover cooling method. *Desalination* 435:140–151. <https://doi.org/10.1016/j.desal.2017.11.007>

42. Manokar AM, Winston DP, Kabeel AE, Sathyamurthy R (2017) Sustainable fresh water and power production by integrating PV panel in inclined solar still. *J Clean Prod*. <https://doi.org/10.1016/j.jclepro.2017.11.140>
43. Balachandran GB, David PW, Vijayakumar ABP, Kabeel AE, Athikesavan MM, Sathyamurthy R (2019) Enhancement of PV/T-integrated single slope solar desalination still productivity using water film cooling and hybrid composite insulation. *Environ Sci Pollut Res*. <https://doi.org/10.1007/s11356-019-06131-9>
44. Kabeel AE, Sathyamurthy R, El-Agouz SA, Muthu Manokar A, El-Said EMS (2019) Experimental studies on inclined PV panel solar still with cover cooling and PCM. *J Anal Calorimetry* 138:3987–3995. <https://doi.org/10.1007/s10973-019-08561-6>
45. Al-Nimr MA, Dahdolan ME (2015) Modeling of a novel concentrated PV/T distillation system enhanced with a porous evaporator and an internal condenser. *Sol Energy* 120:593–602. <https://doi.org/10.1016/j.solener.2015.08.006>
46. Singh DB, Tiwari GN (2016) Effect of energy matrices on life cycle cost analysis of partially covered photovoltaic compound parabolic concentrator collector active solar distillation system. *Desalination* 397:75–91. <https://doi.org/10.1016/j.desal.2016.06.021>
47. Singh DB, Tiwari GN (2017) Exergoeconomic, enviroeconomic and productivity analyses of basin type solar stills by incorporating N identical PVT compound parabolic concentrator collectors : a comparative study. *Energy Convers Manage* 135:129–147. <https://doi.org/10.1016/j.enconman.2016.12.039>
48. Singh DB (2018) Improving the performance of single slope solar still by including N identical PVT collectors. *Appl Therm Eng* 131:167–179. <https://doi.org/10.1016/j.applthermaleng.2017.11.146>
49. Sagar V, Bandhu D, Mishra RK, Kumar S, Tiwari GN (2018) Development of characteristic equations for PVT-CPC active solar distillation system. *Desalination* 445:266–279. <https://doi.org/10.1016/j.desal.2018.08.009>
50. Yari M, Mazareh AE, Mehr AS (2016) A novel cogeneration system for sustainable water and power production by integration of a solar still and PV module. *Desalination* 398:1–11. <https://doi.org/10.1016/j.desal.2016.07.004>
51. Mazraeh AE, Babayan M, Yari M, Sefidan AM, Saha SC (2018) Theoretical study on the performance of a solar still system integrated with PCM-PV module for sustainable water and power generation. *Desalination* 443:184–197. <https://doi.org/10.1016/j.desal.2018.05.024>
52. Singh DB, Al-helal IM (2018) Energy metrics analysis of N identical evacuated tubular collectors integrated double slope solar still. *Desalination* 432:10–22. <https://doi.org/10.1016/j.desal.2017.12.053>
53. Riahi A, Yusof KW, Singh B, Singh M, Isa MH, Olisa E, Atieya N, Zahari M (2016) Sustainable potable water production using a solar still with photovoltaic modules-AC heater. *Desalin Water Treat* 57:14929–21494. <https://doi.org/10.1080/19443994.2015.1070285>
54. Al-nimr MA, Al-ammari WA (2016) A novel hybrid PV-distillation system. *Sol Energy* 135:874–883. <https://doi.org/10.1016/j.solener.2016.06.061>
55. Pounraj P, Winston DP, Kabeel AE, Kumar BP, Manokar AM, Sathyamurthy R, Christabel SC (2018) Experimental investigation on Peltier based hybrid PV / T active solar still for enhancing the overall performance. *Energy Convers Manage* 168:371–381. <https://doi.org/10.1016/j.enconman.2018.05.011>
56. Sarhaddi F (2018) Experimental performance assessment of a photovoltaic/thermal stepped solar still. *Energy Environ* 29:392–409. <https://doi.org/10.1177/0958305X17751392>
57. Abd Elbar AR, Hassan H (2020) An experimental work on the performance of new integration of photovoltaic panel with solar still in semi-arid climate conditions. *Renew Energy* 146:1429–1443. <https://doi.org/10.1016/j.renene.2019.07.069>
58. Elbar ARA, Yousef MS, Hassan H (2019) Energy, exergy, exergoeconomic and enviroeconomic (4E) evaluation of a new integration of solar still with photovoltaic panel. *J Clean Prod* 233:665–680. <https://doi.org/10.1016/j.jclepro.2019.06.111>
59. Parsa SM, Javadi YD, Rahbar A, Majidniya M, Salimi M, Amidpour Y, Amidpour M (2020) Experimental investigation at a summit above 13,000 ft on active solar still water purification

- powered by photovoltaic: a comparative study. *Desalination* 476:114146. <https://doi.org/10.1016/j.desal.2019.114146>
60. Haiping C, Xinxin G, Heng Z, Yang L, Haowen L, Yuegang B (2019) Experimental study on a flash tank integrated with low concentrating PV/T (FT-LCPVT) hybrid system for desalination. *Appl Therm Eng* 159:113874. <https://doi.org/10.1016/j.applthermaleng.2019.113874>

Mathematical Modelling and Performance Analysis of Single Slope Solar Desalination System



Subbarama Kousik Suraparaju , Nirmal Jha, S. Manoj,
and Sendhil Kumar Natarajan 

Abstract The shortage of water is the main and perilous glitch faced by the world and to be addressed immediately with a sustainable solution for the sustenance of human life. In this regard, solar thermal desalination is one of the viable solutions for water scarcity, and single slope solar desalination setups are one of the most economic and efficient approaches of desalination. In this article, the single slope solar desalination system with fins and energy storage is considered, and it is mathematically analysed for its performance. Later, the analytical results are experimentally validated. It is observed that the physical properties like density, thermal conductivity, viscosity, and specific heat capacity are the influencing parameters of the productivity of the solar desalination system. The theoretical efficacy of the system was about 31.58%, and the experimental efficiencies of the conventional and modified desalination systems were about 36.28% and 78.86%, respectively. The change of absorber material to a high thermally conductive material such as copper showed the great impact in raising system temperatures and thus the efficiency of the system by increasing the yield.

Keywords Solar · Desalination · Single slope · Mathematical model · Performance analysis

1 Introduction

Nowadays, water has become the major prerequisite for living with which without water human life is unimaginable. As there is depletion of pure drinking water throughout the world, researchers are taking much effort to make the availability of pure water from the available seawater at low costs. The conversion of seawater into pure water through solar energy is one of the better methods of desalination.

S. K. Suraparaju · S. K. Natarajan (✉)

Solar Energy Laboratory, Department of Mechanical Engineering, National Institute of Technology Puducherry, Karaikal, UT of Puducherry, India

N. Jha · S. Manoj

Department of Mechanical Engineering, Sri Ramakrishna Engineering College, Coimbatore, Tamil Nadu, India

This system does not require more human effort as other processes do, but the output depends on the type of efficient desalination approach used in the system. In the realm of renewable energy, the present-day world is trending towards solar photovoltaics and fuel cells for better energy efficiency [1–3]. Solar desalination can be put into two ways with one using active and passive ways of solar energy. A solar still or solar thermal desalination system is the economic and easiest method of desalination relative to other solar desalination processes.

In this regard, Manju and Sagar outlined the water scarcity in the world and also the depletion of pure water in India due to the increase in population. They discussed various desalination techniques which could decrease the water crisis. The outcomes of the review revealed that the desalination plants had to be set near the seas and the oceans, and also depending upon the population of various places, there have to be some fixed sizes of the plant that are based on the availability of saline/brackish water to overcome the water crisis. This approach might decrease the amount of water scarcity with the superior quality of purified water available for daily living. Finally, it was also reported that the installation of desalination plants is impossible without the grants from the government which without desalination plants leads to an increase in the water scarcity problem [4]. Tiwari and Sahota took some theoretical models for testing the efficiency of solar still based on Nusselt number coefficients, and they proposed a model named Kumar and Tiwari model (KTM) to test the theoretical working of any solar still. The outcomes of the experiment resulted that less the depth of the water give rise to higher distillate output [5]. Kumar et al. investigated the various stills to gain more productivity. They investigated both passive and active solar stills and inferred that the active stills have much greater productivity than the passive stills. They also found that multi-effect stills had greater efficiency than the single-effect stills. The efficiency achieved was around 62% in overall productivity. The study concluded that the maximum yield depends on factors such as type of saline water, flow rates of water, the mean temperature, and area [6]. Kalita et al. discussed various parameters that increase the daily distillate efficiency of a solar desalination system. The major parameters were thermodynamic part of the solar desalination system. Thermodynamic analysis (energy and exergy analysis) was done to analyse the flow in the solar stills. The two different approaches to state the energetic efficiency of the system are presented, namely brute-force exergy and functional exergy efficiency. At last, they reported that further experimentation and study on parameters may give a better yield on the daily distillate productivity [7]. Suraparaju et al. investigated the influence of natural fibre in the solar still performance and found it is hindering the solar radiation [8]. Suraparaju et al. analysed the performance of solar still with bottom staggered fins. It was found that the modified solar still had an increase in efficiency by 24.26% compared to the conventional at 2 cm water depth [9]. Himanshu et al. briefly reviewed the effect of the several designs, operating and environmental parameters on the productivity of the desalination setup. It was claimed that the efficiency is higher at the water depth of 4 cm, and the increase in the water depth will decrease the internal convective heat transfer. The outcomes resulted that the yield was about 5.4 kg/m² at the input feed rate of water as 3.6 kg/h, and the productivity was improved by the glass cover cooling with a rate of flow

of water at 1.5 m/s. Also, other factors influence the productivity such as climatic conditions, design parameters etc., Beyond those factors by altering the depth of water, the inclination of the setup was also greatly influenced single slope solar still for greater efficiency [10, 11]. Rufus and Iniyan reviewed the alteration of certain parameters in the solar stills lead to an increase in the productivity of the distillate output. Later, installed the basin with wick/absorbers such as black granite gravel or jute cloth which led to an output of 6.5 L/m² day. They inferred an additional change in the phase change material (PCM) may give a desired increase in the output, so they used paraffin wax whose melting point is below 60 °C which was positioned beneath the liner [12]. Omara et al. discussed the effect of both external and internal reflectors in solar still among which the external was the one which gave higher efficiency. Reflectors played a significant role where the impact of insolation was weak, and the ambient temperature was low. They used external reflectors as an alternation in a conventional solar still to obtain better potable water output. The study concludes that the usage of reflectors was much simpler and cost-efficient to gain the desired output [13]. The incorporation of the phase change material (PCM) with additional properties such as carbon nanostructures (CNs) leads to an increase in the latent heat capacity for thermal storage. It was focussed to enhance the thermal conductivity and latent heat capacity of the PCM used in the desalination for better results [14]. Abdulateef et al. reviewed certain enhancement techniques between the PCM and the heat transfer fluid by the addition of fins beneath the PCM. The fins were used to assess the latent heat transfer energy storage (LHTES). The usage of circular fins leads to a rise in the relative heat transfer coefficient rather than the pinned fins. The discussion determined that there might be a difficulty in the phase transient behaviour of the PCM-LHTES system. So, the review concluded that future enhancement in the fins with less material could be made more efficient [15]. In the investigation of Ranjan et al., the energy and exergy analysis of a thermodynamic model was done by altering the external constraints. The performance of the passive solar still was examined in terms of efficiency and coefficients which was gained due to different parameters. Initially, the authors fixed a certain theoretical value to compare the test results. It was found that the value of energy is greater than the exergy as there is less energy in the setup. The instantaneous energy and exergy efficiency decreased with an increase in depth of water in the basin [16]. The solar stills can be incorporated with energy storage materials for the advancement in solar desalination systems and to increase efficiency. Panchal outlined that the energy from the sun is an essential and abundant and also unsteady. So, the use of energy storage materials results in the effective utilisation of solar energy and using certain materials also led to an increase in productivity enormously. In the review, it was found that charcoal particles gained 15% more yield, whereas the rubber mat, black-ink, and black dye resulted in increased efficiency by 38%, 45%, and 60%, respectively. It was also revealed that not only the variation of internal parameters, but also external parameters such as glass cover in the inclination angle, etc., also increase the daily distillate [17]. In the current research, single slope solar still with black-coated copper absorber basin with copper fins at the bottom is inserted in the paraffin wax energy storage material and is considered for analytical and experimental investigation.

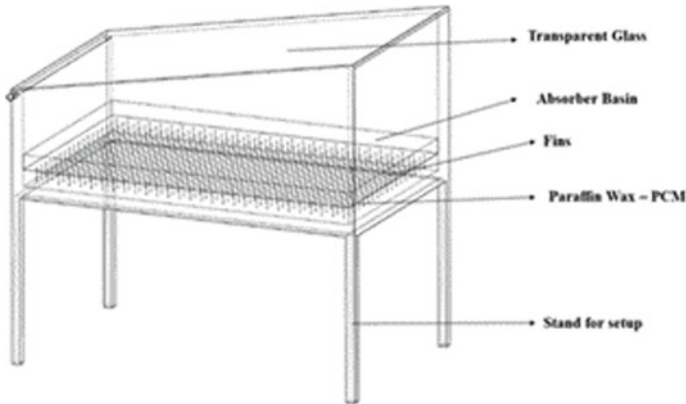


Fig. 1 Schematic of the desalination system

2 Solar Desalination System and Experimentation

2.1 Development of Solar Desalination System

Two single slope solar desalination systems were designed and developed for evaluating the performance at a constant water depth. The desalination systems considered for performance evaluation were (i) Conventional Single Slope Solar Desalination System (CSSSDS), (ii) Single Slope Solar Desalination System with Fins & PCM (SSSDSFP). The solar desalination systems were made of waterproof plywood, and the outer portion was sealed with polystyrene sheets to prevent the heat loss to the ambient. The inner portion was covered with 2 mm thick and black-coated aluminium sheets for more absorption of solar radiation. The absorber of the desalination systems was made of copper, and the absorber area was 0.6 m^2 with 110 cm (length) \times 60 cm (breadth) \times 5 cm (height). The desalination system was then covered with a glass on the top. The slope of the glass cover was 11° (Latitude of test location) for better results. The rate of heat transfer can be augmented by brazing the fins to the absorber basin. The fins of 5 mm diameter and 50 mm length and 220 numbers were brazed to the bottom of the absorber basins. Paraffin wax was used as the energy storage material in the system because of its effective physical properties as well as its economical benefits [18]. The absorber with bottom fins was integrated with energy storage as shown in the schematic (Fig. 1).

2.2 Experimentation

The performance analysis was carried out at the NIT Puducherry, Karaikal, India during January 2020 from 8.30 am and 06.30 pm. The seawater in the absorber

Fig. 2 Photograph of experimental setup



Fig. 3 Datalogger with thermocouples



basin was maintained at a height of 3 cm throughout the experiment. The fabricated three solar desalination setups were arranged for performance evaluation as shown in Fig. 2. The K type thermocouples were used to record the glass cover, water, absorber basin, paraffin wax, fins, and ambient temperature. The thermocouples were connected to “Datalogger” as shown in Fig. 3. Each thermocouple is calibrated using a multimeter before connecting to datalogger. The global radiation was measured by using Hukseflux Pyranometer as shown in Fig. 4. The productivity from the solar still is measured using measuring jars with least count of 5 ml. Each set of the data is collected for every 30 min for the precise analysis of the performance of solar still.

3 Mathematical Model

The respective inferences have been made for the mathematical modelling of heat balance equations for various components in a single slope solar desalination system:

Fig. 4 Pyranometer

1. The experimental setup is vapour leakage free, and depth of water is kept constant.
2. There is no thermal gradient across the condensing surface and water volume.
3. The condenser surface inclination is very small.
4. Heat loss occurs by conduction through the insulating wall and by radiation and convection from the glass surface to the atmosphere.
5. Convection, radiation, and evaporation heat transfer happens between the evaporating and condensing surface.

Equations of energy balance for the several constituents of the solar still are evaluated to get the real-time behaviour of passive solar still:

For Glass Cover:

Some part of the insolation is incident on glass cover and surface of the basin water. The glass cover rejects the radiation to the ambient through convection and radiation.

The heat balance equation on glass cover

$$I_1 + Q_{rg} + Q_{cg} = Q_{cw} + Q_{rw} + Q_{ew} + I_2 \quad (1)$$

where $I_1 = (1 - \alpha_g)$ and $I_2 = (1 - \alpha_g)(1 - \alpha_w)I$.

The conductive heat transfer coefficient between the condensing surface and the ambient relies on the velocity of the wind. The sky temperature is just 6 °C less than the ambient temperature ($t_{\text{sky}} = t_a - 6$).

For water mass in Solar still:

Some part of the transmitted insolation is absorbed by water in solar still basin. From absorbed radiation, some part is stored in the water because of its specific heat capacity, and remaining is transferred to the condensing surface through convection, evaporation, and radiation.

$$I_1 + Q_b + C_w \left(\frac{dt_w}{dt} \right) = Q_{cw} + Q_{rw} + Q_{ew} + I_2 \quad (2)$$

The convection heat transfer is directed upwards through the humid air present in the solar still. Stefan-Boltzmann's law guides to evaluate the radiative heat transfer that occurs between the water surface and condensing surface. This phenomenon occurs because of the temperature difference between these two surfaces.

For basin liner:

The heat balance equation on the basin liner:

$$I = Q_b + Q_{\text{bot}} \quad (3)$$

where Q_{bot} is the heat transfer rate from basin liner to the atmosphere through the bottom side.

Some portion of the transmitted energy is absorbed by the basin liner that strikes on it. Some of the absorbed heat is transferred to the basin water, whereas remaining heat is lost from basin liner to atmosphere through conduction and convection from the bottom and sides of the solar still.

The effective emittance between the condensing glass surface and the water surface is calculated by:

$$\varepsilon_{\text{eff}} = \left(\frac{1}{\frac{\varepsilon_g + 1}{\varepsilon_g - 1}} \right)^{-1} \quad (4)$$

Some amount of heat radiated from the water surface to the glass surface. The coefficient of radiation heat transfer between water and glass is given by [19]:

$$h_{rw} = \sigma (T_w^2 + T_g^2) (T_w + T_g) \varepsilon_{\text{eff}} \quad (5)$$

The total amount of heat energy involved in radiation between the water surface and the glass surface is related by the equation mentioned below:

$$Q_{rw} = h_{rw} A_w (T_w + T_g) \quad (6)$$

Because of the vaporisation, there is pressure arisen in the solar still, and the saturated partial pressure affects various properties of the fluids involved in solar still. The measure of the saturated partial pressure of the water is written as:

$$P_w = e^{\left(\frac{25.317 - 5144}{T_w} \right)} \quad (7)$$

$$P_g = e^{\left(\frac{25.317 - 5144}{T_g} \right)} \quad (8)$$

$$x = \frac{P_g}{P_w + P_g} \quad (9)$$

The density of the fluid depends on the temperature, and it affects productivity as it is directly related to the Grashoff number. The density of the water, dry air, and the moist air involved in the solar still is related by their corresponding temperature by the equations mentioned below [20]:

$$d_w = 1002.6 - 0.0505t_a - 0.0038t_a^2 \quad (10)$$

$$d_a = \frac{353}{T_a} \quad (11)$$

$$d_m = \frac{(3.484 - 1.3717x)(P_w + P_g)}{T_g} \quad (12)$$

As the temperature increases, random movement of molecules in fluid increases that tends to decrease the thermal conductivity. Hence, the following equations give the thermal conductivity of the corresponding fluid:

$$K_a = 0.001[(-2.277 \times 10^{-3}) + (1.260 \times 10^{-4} \times T_a) - (1.482 \times 10^{-7} \times T_a^2) + (1.736 \times 10^{-10} \times T_a^3) - (1.067 \times 10^{-13} \times T_a^4)] \quad (13)$$

$$K_v = 0.001(17.618 + 0.556t_g + 0.0001666t_g^2) \quad (14)$$

$$K_m = K_a + \frac{x(0.8534(K_v - K_a))}{1 - 0.1464x} \quad (15)$$

The specific heat capacity of the material is the reason for the storage of energy in it. In solar still the specific heat capacity of water in the basin, dry air and moist air changes according to the temperature so, it must be considered. This energy leads to evaporation–condensation of water in the solar still basin and directly relate to productivity.

$$C_{pa} = 1.034 - (2.849 \times 10^{-4} \times T_a) + (7.817 \times 10^{-7} \times T_a^2) + (4.971 \times 10^{-10} \times T_a^3) \quad (16)$$

$$C_{pv} = 1.869 - (2.578 \times 10^{-4} \times t_g) + (1.941 \times 10^{-5} \times t_g^2) \quad (17)$$

$$C_{pm} = C_{pa} + 0.622 \frac{P_g}{P_w} \quad (18)$$

The equation to estimate the viscosity of dry air, water, and moist air is given below:

$$\mu_a = [-0.986 + (0.0908 \times T_a) - (1.176 \times 10^{-4} \times T_a^2) + (1.235 \times 10^{-7} \times T_a^3) - (5.797 \times 10^{-11} \times T_a^4)] \times 10^{-6} \quad (19)$$

$$\mu_v = (80.581 + (0.400 \times t_w)) \times 10^{-6} \quad (20)$$

$$\mu_m = \frac{\mu_a + x(0.7887 \times (\mu_v - \mu_a))}{1 - 0.2213x} \quad (21)$$

T' is the effective temperature difference that is calculated by the equation given below

$$T' = (t_w + t_g) + \frac{(P_w + P_g) \times T_w}{268900 - P_w} \quad l_m = \frac{H_1 + H_2}{2} \quad (22)$$

and the average distance (l_m) between the water surface and the condensing surface.

The heat transfer coefficient is associated with the Nusselt number which is obtained by the correlation:

$$Nu = CRa^n = C(Gr \times Pr)^n \quad (23)$$

where Ra is Rayleigh number and the value of C and n depends on the Gr and Pr. The values of C and n are calculating by linear regression model developed in the Minitab software [21].

$$\ln\left(\frac{m_w}{R}\right) = \ln C + n \times \ln Ra \quad (24)$$

where L_{ev} and R is given by,

$$L_{ev} = (2501.67 - 2.389t_g) \times 1000, \quad R = \frac{0.016273(P_w + P_g) \times K_m}{l_m} \times \frac{1800}{L_{ev}} \quad (25)$$

Here, the Grashof number and Prandtl number is given by

$$Gr = \frac{(g\beta_m l_m T' d^2)}{\mu_m} \quad (26)$$

$$Pr = \frac{\mu_m C_{Pm}}{K_m} \quad (27)$$

After enumerating the Nusselt number, the heat transfer coefficients can be expressed by the relations:

Evaporation heat transfer in solar still from the water surface to glass surface:

$$Q_{ew} = \frac{(m_w \times L_{ev})}{1800 \times 1000} [\text{mass is converted into kg so, divided by 1000}] \quad (28)$$

The expression for convective heat transfer coefficient from water to glass is:

$$h_{cw} = \frac{Q_{ew}}{0.016273(P_w + P_g)} \quad (29)$$

And convective heat transfer within solar still from water to glass is: [22]

$$Q_{cw} = h_{cw} \times A_w \times (t_w - t_g) \quad (30)$$

Evaporation heat transfer coefficient from the water to glass can be calculated by:

$$h_{ew} = 0.016273 \times h_{cw} \times \frac{P_w + P_g}{t_w - t_g} \quad (31)$$

The radiative heat transfer from condensing surface to ambient is given by:

$$Q_{rg} = A_g \times \sigma \times \varepsilon_g \times (T^4 - T_{sky}^4) \quad (32)$$

$$h_{rg} = \frac{Q_{rg}}{A_g(t_g - t_a)} \quad (33)$$

And the equation reported by Agrawal is used to find the radiative heat transfer from condensing surface to ambient.

$$h_{cg} = 2.38 + 3.0V_{wind}; V_{wind} \leq 5 \text{ m/s} \quad (34)$$

$$h_{cg} = 5.70 + 3.8V_{wind}; V_{wind} > 5 \text{ m/s} \quad (35)$$

Convective heat transfer from the glass surface to ambient depends on both ambient and glass temperature, and it is related by the mentioned expression:

$$Q_{cg} = h_{cg} \times A_g(t_g - t_a) \quad (36)$$

Total heat loss coefficient can be found with the help of the equations below:

$$h_{tga} = h_{cg} + \sigma \varepsilon_g \left(\frac{T_g^4 - T_a^4}{T_g - T_a} \right) \quad (37)$$

$$h_{twg} = h_{tga} \frac{(t_g - t_a)}{(t_w - t_g)} \quad (38)$$

Other heat transfer coefficient from the bottom of the basin to the ambient and total loss coefficient for solar still is given, respectively.

$$h_b = \frac{\text{Nu} \times K_m}{l_m} \quad (39)$$

$$U_t = h_{tga} \times h_{twg} (h_{tga} + h_{twg}) \quad (40)$$

The efficiency of solar still is related by the expression as mentioned [23, 24]

$$\eta = \frac{m_{\text{theo}} \times L_{ev}}{A_b \times \Delta t \times \sum I(t)} \times 100 \quad \text{Where, } m_{\text{theo}} = \frac{h_{ew}(t_w - t_g) \times 1800}{L_{ev}} \quad (41)$$

The effect of PCM in the solar still is given by charging and discharging modes, where charging mode is of storing the energy in the form of sensible heat and latent heat of fusion by taking the energy from the sun and melting, whereas discharging mode is of releasing the energy by condensing to the normal position after sunset [25].

PCM in Charging Mode

The equations of energy balance during sunshine hours are as follows:

$$h_{lw} A_w (T_l - T_w) + I \tau_g \alpha_w A_w = A_w h_t (T_w - T_g) + h_{wc} A_f (T_w - T_f) + m_w F_w \frac{dT_w}{dt} \quad (42)$$

The energy balance between absorber and water is as follows:

$$I \tau_g \alpha_1 = h_{lw} (T_l - T_w) \quad (43)$$

During charging, the energy balance of PCM is as follows,

$$A_{sf} \frac{K_f}{Y_f} (T_f - T_{\text{PCM}}) = M_E \frac{dT_{\text{PCM}}}{dt} \quad (44)$$

PCM in Discharging Mode

The energy balance during sunset is as follows

$$h_{wc} A_f (T_f - T_w) = A_w h_t (T_w - T_g) m_w F_w \frac{dT_w}{dt} \quad (45)$$

$$A_{sf} \frac{K_f}{Y_f} (T_{PCM} - T_f) = h_{wc} A_f (T_f - T_w) \quad (46)$$

During discharging, the energy balance of PCM is as follows,

$$M_E \frac{dT_{PCM}}{dt} = A_{sf} \frac{K_f}{Y_f} (T_{PCM} - T_f) \quad (47)$$

where

$$M_E = m_{pcm} C_{S,pcm} \text{ for } T_{PCM} < T_f$$

$$M_E = m_{pcm} L_{S,pcm} \text{ for } T_{PCM} = T_f$$

$$M_E = m_{pcm} C_{l,pcm} \text{ for } T_{PCM} > T_f.$$

4 Results and Discussion

The thermophysical properties of the fluids involved in the system were varying with time and temperature and plotted in the following Fig. 5. It was found that the properties like viscosity, thermal conductivity, and specific heat capacity were changing significantly for moist air; whereas for air and vapour, it was almost constant. The following graphs (Fig. 5a–d) depicted the change in the properties concerning the time.

Convection, radiation, evaporation, and total heat transfer coefficients were analysed and plotted graphically as in Fig. 6a, and the heat transfer was plotted in Fig. 6b concerning time. The heat transfer and heat transfer coefficient were found at every 30 min, and the graph was plotted for the same. It was found that heat transfer coefficients were maximum during 12:00 to 13:00 when solar intensity was at the maximum.

The primary influencing parameters of the solar desalination system efficiency were the glass cover, absorber, water, and PCM temperatures. In Fig. 7a, all the experimental temperatures recorded were plotted against time for both conventional as well as the modified setup. The system temperatures were appeared to increase till noon and achieved maximum at 13:00 and then starts to lower and minimum in the night after 20:00. It was observed in the modified desalination system that the highest temperature of basin water was around 69 °C; for the condensing glass surface, it was about 55 °C, whereas the copper absorber basin recorded about 70 °C. The addition of copper fins and PCM to the system made a great impact that the water temperature was raised to a great extent which leads to more evaporation and hence more yield.

Theoretical and experimental productivity of the two solar desalination systems was calculated and compared graphically in Fig. 7b. It was observed that there was a concurrence between the theoretical and the experimental yield of the conventional system. However, the modifications in the solar desalination system showed a great impact on productivity, and the system yielded almost double when compared to the conventional system. The theoretical efficiency of the system was about 31.58%, and

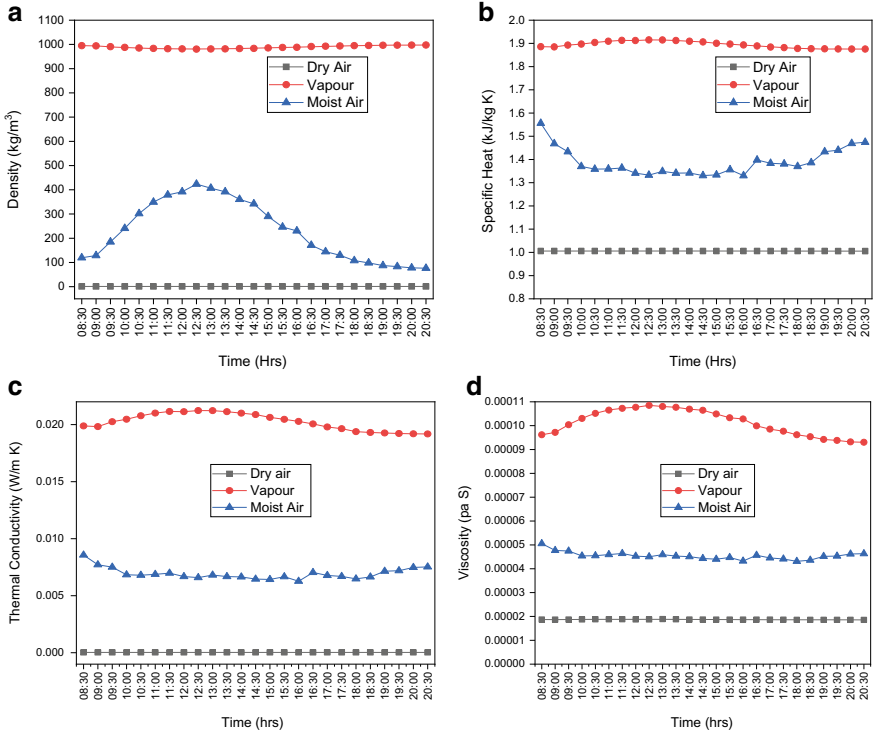


Fig. 5 Variation of **a** density, **b** specific heat capacity, **c** thermal conductivity, **d** viscosity with time

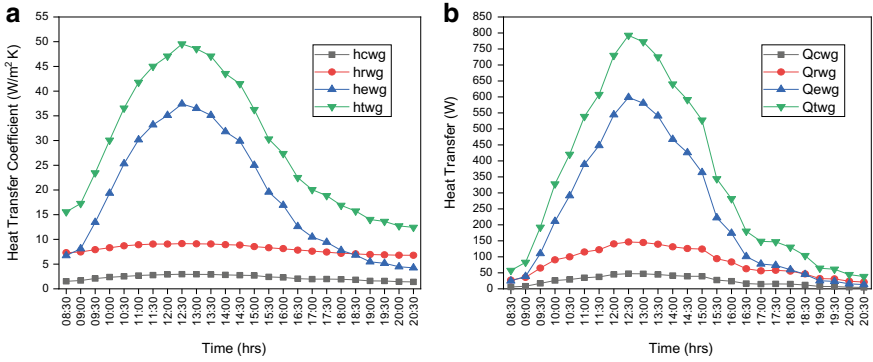


Fig. 6 Variation of **a** heat transfer coefficient, **b** heat transfer with time

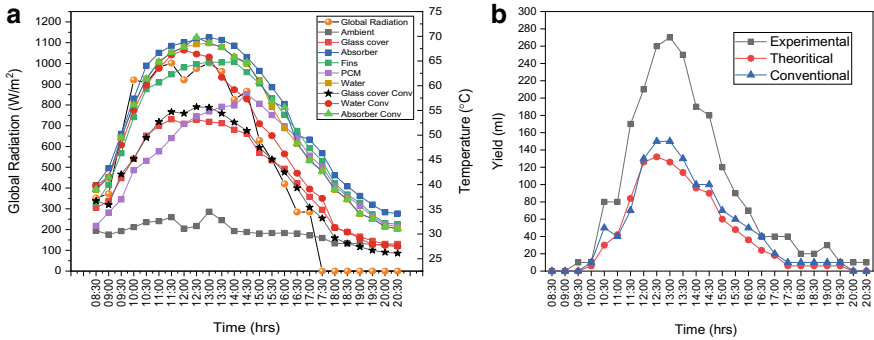
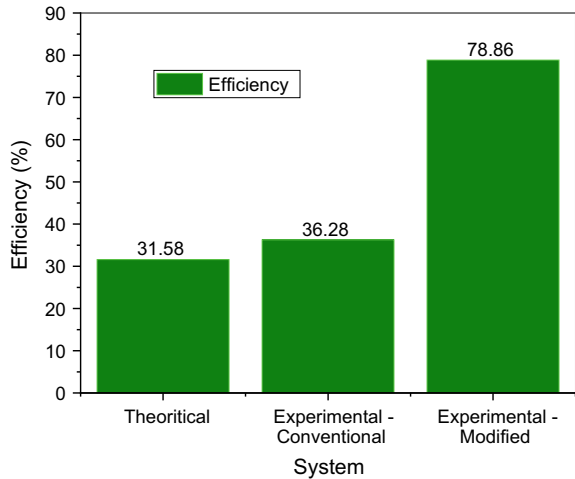


Fig. 7 Variation of **a** temperature, **b** productivity with time

the experimental efficiencies of the conventional and modified desalination systems were about 36.28% and 78.86%, respectively. The calculated efficiencies were plotted in Fig. 8, and it was depicted that the assumptions made for the analysis had an impact on the efficiency of solar still since experimental efficacy of the conventional system is slightly higher than theoretical efficiency. The efficiency of the modified desalination system was almost double than the conventional system due to the addition of high thermally conductive copper fins into the efficient phase change energy storage material.

Fig. 8 Comparison of theoretical and experimental efficiencies



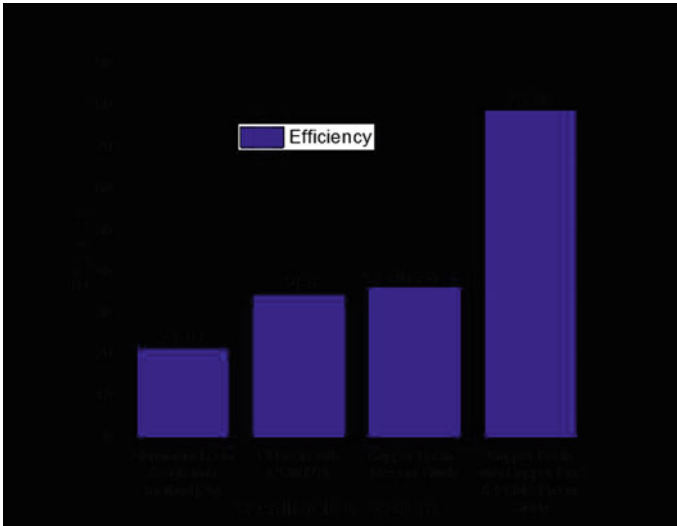


Fig. 9 Comparison of current research with previous researches

5 Comparing the Current Work with Existing Literature

The results of the investigation showed that the efficiency of the proposed setup was higher than the previous researches in the literature with modifications in the basin. It was noticed that the distillate output of single slope solar still with a basin made of aluminium and working on agitation method was 21.67% [26]. Also, the system with a basin made of GI sheet and aluminium powder with PCM was 34.6% [27]. The present system comprises of a high thermally conductive copper basin brazed with copper fins and inserted in phase change material that leads to the enhancement in the system temperatures, and hence, the augmented efficiency is attained. The previous works had a low thermally conductive material made basin which heat losses more, and the system had a lower efficiency. The comparison of literature for modifications showed that changing the basin material with higher conductivity like copper enhances the efficiency of the solar still up to an extent which makes the system viable. The comparison of efficiencies is shown in Fig. 9.

6 Conclusions

In this research, the influence of copper fins and PCM on the operation of a single slope solar desalination system was assessed to improve productivity. The desalination systems dealt for experimental assessment were as follows; (i) CSSSDS and (ii) SSSDSFP. The obtained experimental values were analysed and compared with

the output from the theoretical model of the solar desalination system. The major conclusions made from the current research are as follows:

1. The addition of high thermally conductive copper material to absorber basin and copper fins inserted in PCM had a greater impact in raising the temperatures of the system that leads to enhanced performance.
2. It was analysed that changing the basin material to material with higher conductivity enhances the productivity of solar desalination system when compared to other basin materials.
3. The mathematical model output and the experimental values were compared and found that there was a concurrence between both experimental and mathematical model. However, the modified desalination system showed improved performance.
4. The maximum distillate water was 0.215 kg at 13:00, and it was found to be 2.95 kg/m²day.
5. The theoretical efficiency of the system was about 31.58%, and the experimental efficiencies of the conventional and modified desalination systems were about 36.28% and 78.86%, respectively.

References

1. Natarajan SK, Kamran F, Ragavan N, Rajesh R, Jena RK, Suraparaju SK (2019) Analysis of PEM hydrogen fuel cell and solar PV cell hybrid model. *Mater Today Proc* 17:246–253. <https://doi.org/10.1016/j.matpr.2019.06.426>
2. Natarajan SK, Kumar A, Mohamed R, Rathna R, Mondal S, Suraparaju SK (2019) Design and development of dual axis sun tracking system for floating PV plant. In: IOP conference series: earth and environmental science, 312. <https://doi.org/10.1088/1755-1315/312/1/012001>
3. Natarajan SK, Suraparaju SK, Elavarasan E, Arjun Singh K (2019) Performance analysis of solar photovoltaic panel at Karaikal weather conditions. In: IOP Conference Series: Earth and Environmental Science, 312. <https://doi.org/10.1088/1755-1315/312/1/012007>
4. Manju S, Sagar N (2017) Renewable energy integrated desalination: a sustainable solution to overcome future fresh-water scarcity in India. *Renew Sustain Energy Rev* 73:594–609. <https://doi.org/10.1016/j.rser.2017.01.164>
5. Tiwari GN, Sahota L (2017) Review on the energy and economic efficiencies of passive and active solar distillation systems. *Desalination* 401:151–179. <https://doi.org/10.1016/j.desal.2016.08.023>
6. Vishwanath Kumar P, Kumar A, Prakash O, Kaviti AK (2015) Solar stills system design: a review. *Renew Sustain Energy Rev* 51:153–181. <https://doi.org/10.1016/j.rser.2015.04.103>
7. Kalita P, Dewan A, Borah S (2016) A review on recent developments in solar distillation units. *Sadhana* 41:203–223
8. Suraparaju SK, Natarajan SK (2020) Performance analysis of single slope solar desalination setup with natural fibre. *Desalin Water Treat* 193:64–71. <https://doi.org/10.5004/dwt.2020.25679>
9. Suraparaju SK, Natarajan SK (2021) Experimental investigation of single-basin solar still using solid staggered fins inserted in paraffin wax PCM bed for enhancing productivity. *Environ Sci Pollution Res*

10. Manchanda H, Kumar M (2015) A comprehensive decade review and analysis on designs and performance parameters of passive solar still. *Renew Wind Water Solar* 2. <https://doi.org/10.1186/s40807-015-0019-8>
11. Sharshir SW, Yang N, Peng G, Kabeel AE (2016) Factors affecting solar stills productivity and improvement techniques: a detailed review. *Appl Therm Eng* 100:267–284. <https://doi.org/10.1016/j.applthermaleng.2015.11.041>
12. Dsilva Winfred Rufuss D, Iniyan S, Suganthi L, Davies PA (2016) Solar stills: a comprehensive review of designs, performance and material advances. *Renew Sustain Energy Rev* 63:464–496. <https://doi.org/10.1016/j.rser.2016.05.068>
13. Omara ZM, Kabeel AE, Abdullah AS (2017) A review of solar still performance with reflectors. *Renew Sustain Energy Rev* 68:638–649. <https://doi.org/10.1016/j.rser.2016.10.031>
14. Amaral C, Vicente R, Marques PAAP, Barros-Timmons A (2017) Phase change materials and carbon nanostructures for thermal energy storage: a literature review. *Renew Sustain Energy Rev* 79:1212–1228. <https://doi.org/10.1016/j.rser.2017.05.093>
15. Abdulateef AM, Mat S, Abdulateef J, Sopian K, Al-Abidi AA (2018) Geometric and design parameters of fins employed for enhancing thermal energy storage systems: a review. *Renew Sustain Energy Rev* 82:1620–1635. <https://doi.org/10.1016/j.rser.2017.07.009>
16. Ranjan KR, Kaushik SC, Panwar NL (2016) Energy and exergy analysis of passive solar distillation systems. *Int J Low-Carbon Technol* 11:211–221. <https://doi.org/10.1093/ijlct/ctt069>
17. Panchal HN (2016) Use of thermal energy storage materials for enhancement in distillate output of solar still: a review. *Renew Sustain Energy Rev* 61:86–96. <https://doi.org/10.1016/j.rser.2016.03.043>
18. Haji-Sheikh A, Eftekhari J, Lou DYS (1983) Some thermophysical properties of paraffin wax as a thermal storage medium. *Prog Astronaut Aeronaut* 86:241–253
19. Agrawal A, Rana RS, Srivastava PK (2017) Heat transfer coefficients and productivity of a single slope single basin solar still in Indian climatic condition: experimental and theoretical comparison. *Resource-Efficient Technol* 3:466–482. <https://doi.org/10.1016/j.refit.2017.05.003>
20. Tsilingiris PT (2008) Thermophysical and transport properties of humid air at temperature range between 0 and 100 °C. *Energy Convers Manage* 49:1098–1110. <https://doi.org/10.1016/j.enconman.2007.09.015>
21. Kumar S, Tiwari GN (1996) Estimation of convective mass transfer in solar distillation systems. *Sol Energy* 57:459–464. [https://doi.org/10.1016/S0038-092X\(96\)00122-3](https://doi.org/10.1016/S0038-092X(96)00122-3)
22. El-Naggar M, El-Sebaii AA, Ramadan MRI, Aboul-Enein S (2016) Experimental and theoretical performance of finned-single effect solar still. *Desalin Water Treat* 57:17151–17166. <https://doi.org/10.1080/19443994.2015.1085451>
23. Gupta B, Kumar Mandraha T, Edla P, Pandya M (2013) Thermal modeling and efficiency of solar water distillation: a review. *Am J Eng Res (AJER)* 02:203–213
24. Cooper PI (1973) The maximum efficiency of single-effect solar stills. *Sol Energy* 15:205–217. [https://doi.org/10.1016/0038-092X\(73\)90085-6](https://doi.org/10.1016/0038-092X(73)90085-6)
25. Sonker VK, Chakraborty JP, Sarkar A, Singh RK (2019) Solar distillation using three different phase change materials stored in a copper cylinder. *Energy Rep* 5:1532–1542. <https://doi.org/10.1016/j.egy.2019.10.023>
26. Kumar RA, Esakkimuthu G, Murugavel KK (2016) Performance enhancement of a single basin single slope solar still using agitation effect and external condenser. *Desalination* 399:198–202. <https://doi.org/10.1016/j.desal.2016.09.006>
27. Chaichan MT, Kazem HA (2015) Using aluminium powder with PCM (paraffin wax) to enhance single slope solar water distiller productivity in Baghdad–Iraq winter weathers. *Int J Renew Energy Res* 5:251–257. <https://doi.org/10.20508/ijrer.87846>

Analysis and Comparison of Various High Performance Folded Cascode OTA Topologies



Bhawna Aggarwal and Vaishali Sharma

Abstract Operational transconductance amplifier (OTA) is an amplifying device that is widely being used as a basic building block in current mode and voltage mode devices. Folded cascode OTA is a preferred choice for circuit designers due to its high output impedance and low noise characteristic along with high output swing. Various techniques have been proposed in the literature to improve its performance characteristics. In this paper, various current recycling techniques have been studied and discussed that help in improving gain-bandwidth product and slew rate of folded cascode OTA without increasing the power or area requirement of the original folded cascode OTA. Moreover, adaptive biasing and superclass-AB topologies have also been discussed. These topologies further increase the gain and slew rate of OTA while operating at much lower biasing currents, and thereby, consuming much smaller static power. All these techniques have been discussed in detail with their advantages and disadvantages. Furthermore, to justify their effectiveness in the practical environment, simulation results under similar biasing environment have been carried out using Ltspice with the help of 0.18 μm CMOS technology.

Keywords Folded cascode OTA · Current recycling · Improved recycling · Enhanced recycling · Adaptive biasing · Superclass-AB

1 Introduction

Operational transconductance amplifier (OTA) is a voltage controlled current source (VCCS), which generates an output current proportional to applied differential input voltage [1]. It is a fundamental block for various circuits like voltage controlled amplifiers, active filters, analog and digital converters, delta-sigma modulators, etc. Its major performance parameters are differential transconductance gain (G_m), unity gain frequency (f_T), common mode rejection ratio (CMRR), input/output resistance, slew rate (SR), gain/phase margin, and supply voltage [2]. In the literature, various

B. Aggarwal (✉) · V. Sharma
Netaji Subhas University of Technology, New Delhi, India

techniques like Miller compensation [1], slew rate enhancement [2], stress memorization technique [3], current-shunt technique [4], switched-capacitor circuit [5], positive feedback technique [6], etc., have been reported to enhance OTA performance. Current recycling technique is a class of technique that increases the G_m of OTA without increasing its biasing current and chip area. However, these current recycling topologies need some additional MOSFETs and the biasing voltage supplies [2, 7, 8].

The motivation behind this work is to study and analyze various current recycling topologies and to identify their suitability for different applications. In this work, conventional folded cascode OTA (FC OTA) [2] has been chosen as it provides high output impedance along with high gain, bandwidth, and output swing. Various current recycling techniques like recycling folded cascode (RFC) OTA [9], improved recycling folded cascode (IRFC) OTA [6], enhanced recycling folded cascode (ERFC) OTA [6], adaptive biased [10], and superclass-AB RFC OTA [10] have been analyzed and compared. It has been observed that gain becomes twice in RFC OTA as compared to conventional FC OTA, with same biasing current, while using six extra MOSFETs. Addition of more shunt current sources to RFC further increases its gain. This new topology with additional MOSFETs is known as IRFC OTA. However, due to mismatch in its output stage, this topology leads to various problems like offset voltage and parasitic capacitances. To overcome these problems, adjustable floating voltage source (FVS) is used. This topology known as ERFC removes mismatch and improves bandwidth and gain-bandwidth product (GBW). All these topologies operate on the principle of utilizing biasing current efficiently to obtain improvement in G_m the amplifier. However, for large values of signal voltages, such circuits need high biasing currents. To overcome this, in the literature, various topologies have been suggested that depend on generation of large dynamic currents directly across output transistors, without internal replication. One such technique is superclass-AB which helps in achieving very high performance with low power consumption [10].

In the paper, all these techniques have been studied in detail and their comparison using SPICE has been presented. In the paper, Sect. 2 details the various current recycling and adaptive biasing topologies. This section also elaborates their advantages and disadvantages. Section 3 presents Ltspice-based simulation results and performance evaluation for all these circuits. Finally, Sect. 4 concludes the paper.

2 Various Current Recycling and Adaptive Biasing Topologies

2.1 *Folded Cascode OTA*

Cascode structures are used to achieve high gain in any amplifier. This gain increases as the cascading stages are increased due to increase in r_{out} . However, it causes extra voltage burden on the amplifier. To overcome this extra burden, a folded cascode

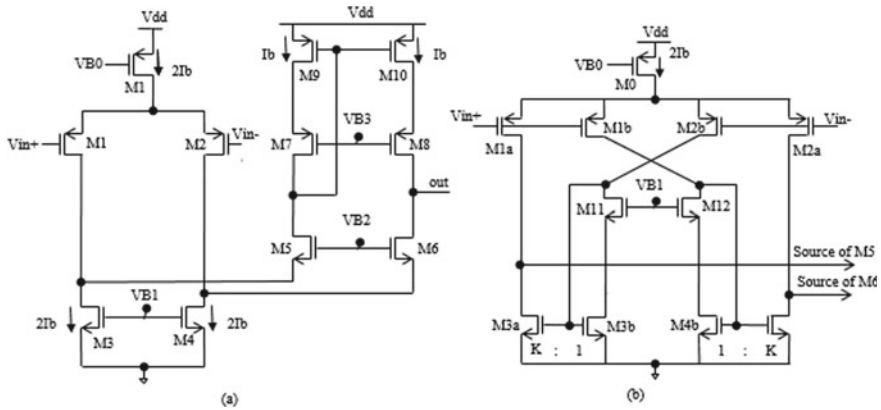


Fig. 1 a PMOS based folded cascode OTA. b Recycling folded cascode OTA

is used. It has been observed that PMOS amplifiers operate at lower noise and are preferred as compared to telescopic OTAs. Furthermore, these amplifiers offer higher dominating poles, speed, gain, and output swing [2, 11, 12]. The circuit of PMOS based folded cascode OTA is shown in Fig. 1a. Here, PMOS $M1$ and $M2$ perform the differential operation and convert the voltage signal into current form. NMOS $M0$ provides the necessary biasing current. Folding cascode operation is performed by common gate n-channel MOSFETs ($M5$ and $M6$). These MOSFETs fold the direction of current flowing in the amplifying transistors and transfer this current to a high impedance output node. Thereby, known as a folded cascode amplifier. The transconductance gain (G_m) and slew rate (SR) of folded cascode amplifier is given as [13]:

$$G_{mFC} = g_{m1}; \quad SR_{FC} = 2I_b/C_L \tag{1}$$

here, g_{m1} denotes the transconductance of MOSFET $M1$ and C_L represents the load capacitance of the amplifier.

In folded cascode amplifiers current flowing in amplifying transistors is folded up or down with the help of opposite polarity transistors. This folding leads to a requirement of additional biasing current sources. Thereby, leading to a large number of biasing current sources in the amplifier. This further increases the power dissipation of the circuit.

2.2 Recycling Folded Cascode

As discussed in the previous sub-section, a folded cascode amplifier needs additional biasing current sources. The performance of folded cascode amplifiers can be enhanced significantly if the MOSFETs used to implement these current sources

are used as driving transistors instead of appearing as ideal devices in signal path [13]. These techniques that utilize these MOSFETs for enhancing the performance of amplifier are termed as current recycling techniques in literature. The recycled folded cascode amplifier (RFC) proposed in [13] increases G_m and SR without increasing the power consumed or area required by the circuit.

The circuit of PMOS-based recycling folded cascode OTA is shown in Fig. 1b. In this circuit, MOSFETs $M3$ and $M4$ (of Fig. 1a), which were earlier used as current sink only, have been used as driving transistors. To achieve this, MOSFETs $M1$ and $M2$ are divided into 2 equal halves, $M1a$ & $M1b$ and $M2a$ & $M2b$, respectively. This splitting causes current I_b to be divided, leading to biasing current $I_b/2$ across each transistor. Similar process is carried out with $M3$ and $M4$ of FC OTA. Here, care is taken to maintain the same overall area requirement of the devices. Crossover connections have been made to maintain the polarity of the small-signal current. MOSFETs $M11$ and $M12$ are used to achieve improved voltage matching at drain terminals of $M3a:M3b$ and $M4a:M4b$. Here, if a ratio of $K:1$ is maintained across $M3a:M3b$ and $M4a:M4b$, G_m and SR for the amplifier are given as:

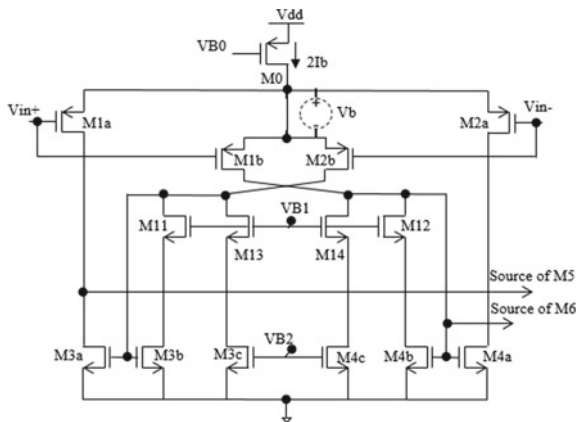
$$G_{mRFC} = g_{m1a}(1 + K); \quad SR_{RFC} = 2K I_b / C_L. \quad (2)$$

Comparison of Eq. (2) with Eq. (1) shows that gain, and thereby gain-bandwidth product (GBW) becomes twice and SR increases up to 3 times ($K = 3$), in RFC OTA. All these improvements are achieved without increasing power consumption or chip area requirement of the circuit [2, 12, 13].

2.3 Improved Recycling Folded Cascode (IRFC) OTA

In RFC OTA, enhancement in gain is achieved by splitting the transistors connected in current mirror configuration that make them operate as driving transistors in signal path. However, in RFC OTA, DC and AC currents flow through the same path and restrict the maximum gain achievable by the configuration. To overcome this limitation, IRFC configuration was proposed by Li et al. in 2010 [4]. The circuit of IRFC OTA is given in Fig. 2. Here, AC and DC paths are separated by splitting $M3b$ into $M3b$ and $M3c$ & $M4b$ into $M4b$ and $M4c$. This separation of AC and DC paths increases the signal swing at current mirror nodes. To materialize this splitting $M11$ and $M12$ (of Fig. 1a) are divided into $M11$, $M12$, $M13$, and $M14$. The path formed by $M13$, $M3c$, $M4c$, $M14$ offers high impedance to AC signal, while the path formed by $M11$, $M3b$, $M4b$, $M12$ is of low impedance. This leads to the improvement in signal flow through current mirror nodes. Moreover, MOSFETs $M3c$ and $M4c$ behave as shunt current paths [12]. These shunt current sources reduce the DC current flowing in recycled current mirrors and thereby provide the possibility for improving the recycling current mirror gain. To realize IRFC with the same DC currents, MOSFETs must be chosen with specific sizing ratio. The sizing ratio of $M1a:M1b$ ($M2a:M2b$) is kept to be $p:(1 - p)$, where $0 < p < 1$. The sizing ratios of

Fig. 2 Improved recycling folded cascode and enhanced recycling folded cascode OTA (with dotted circuit)



$M3a:M3b:M3c$ ($M4a:M4b:M4c$) is maintained as $(1 + p):q(1 - p):r(1 - p)$, where $q + r = 1$.

With these transistor sizing G_m and maximum SR of IRFC OTA are given as:

$$\begin{aligned} G_{m\text{IRFC}} &= g_{m1a}(p + (1 + p)/q); \\ \text{SR}_{\text{IRFC}} &= (1 + p)[2 - (1 - q)(1 - p)]I_b/[q(1 - p)C_L] \end{aligned} \quad (3)$$

In IRFC OTA, if $p = q = 1/2$, then comparison of Eqs. (1) and (3) show that gain of IRFC increases by 250% and maximum value of slew rate will be 425% higher as compared to that of FC OTA.

2.4 Enhanced Recycling Folded Cascode OTA

Enhanced recycling folded cascode (ERFC) OTA has been proposed by Khade et al. in 2019 [6]. In this technique, a floating voltage source (FVS), having small output impedance (ideally 0), is added in the input stage of IRFC OTA (shown dotted in Fig. 2). This adjustable FVS is used to bias differential pair constituted by MOSFETs $M1b$ and $M2b$. Here, MOSFETs forming outer differential pair ($M1a$ and $M2a$) are operated in weak or moderate inversion region, while $M1b$ and $M2b$ are operated in strong inversion region. This is done for identical MOSFETs driven by same input signal by adjusting the value of FVS. This unbalanced biasing helps in improving the GBW and SR of the amplifier. Moreover, in ERFC OTA, the gain can be changed just by adjusting the value of FVS. Addition of FVS also leads to improvement in high frequency performance of the circuit because of very low output impedance of the device. Though at low frequency, G_m of ERFC is equal to that of IRFC and can be expressed by Eq. (3).

The SR of ERFC OTA is expressed as:

$$SR_{ERFC} = 2((1 + p)/q) \cdot (I_b/C_L) \tag{4}$$

Equation (4) shows that for small values of p and q , high values of SR can be achieved with ERFC OTA. It can be summarized that ERFC improves the high frequency performance of the circuit. Though, at low frequencies, IRFC OTA and ERFC OTA operate with approximately the same gain. However, in ERFC, FVS is adjustable and can be adjusted to increase the recycling current mirror gain, GBW, and slew rate [6].

2.5 Recycling Folded Cascode OTA with Adaptive Biasing Technique

Current in all the recycling OTA techniques discussed so far was limited by the biasing DC current. Increasing this current will lead to an increase in the square of power consumed by the circuit. An adaptive biasing technique compatible with folded cascode OTA proposed in [7] and helps in dynamically controlling the biasing current of the amplifier. This not only helps in keeping the static power dissipation of the circuit at low levels rather it helps in generating large dynamic currents (greater than I_b) for large input signals.

Circuit of a RFC OTA with adaptive biasing technique is shown in Fig. 3a. It consists of two well matched transistors connected in cross-coupled fashion to the current source. These current sources must provide large current during the charging and discharging of large capacitive load. Here, MOSFET M0 is split into MOSFETs M1d, M1c, M2d, and M2c to form adaptive bias configuration. The differential circuits with adaptive biasing provide double transconductance at input stage and improve the GBW and provide an increase in current [10].

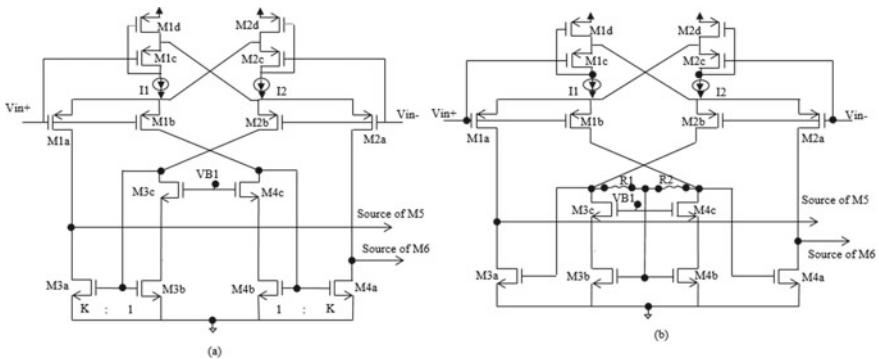


Fig. 3 a RFC OTA with adaptive biasing technique. b Superclass-AB RFC OTA

2.6 Superclass-AB Recycling Folded Cascode OTA

Adaptive biasing helps in achieving high output currents with large values of differential input voltage while utilizing small biasing currents. In 2005, A. J. López-Martín, et al. proposed superclass-AB technique that makes use of adaptive biasing technique to get output current proportional to v_{id}^4 , here, v_{id} represents the differential input voltage signal [14, 15]. This technique was implemented on RFC OTA by M. Pilar Garde in 2018 [10]. It has been observed that superclass-AB RFC OTA provides large dynamic current, very high GBW, and high current efficiency.

The circuit for superclass-AB RFC OTA is given in Fig. 3b. In this circuit, the input differential pair uses adaptive biasing configuration and MOSFETs forming active load for this differential pair ($M3b$ - $M3c$ and $M4b$ - $M4c$) are rearranged. A local common mode feedback (LCMFB) is provided via symmetrical resistors $R1$ and $R2$. This LCMFB provides additional current boosting and higher current efficiency, leading to significant increase in GBW. The most special part of this circuit is that all these improvements are achieved at low values of static biasing current. G_m and SR of superclass-AB FC OTA are given as:

$$G_{mAB} = 2 \cdot g_{m1a}(1 + g_{m3a}(R||r_{02B}));$$

$$SR_{AB} = \frac{\beta_{3,4A}}{2C_L} \left(\sqrt{\frac{\beta_{1,2B}}{2\beta_{3,4B}}} A + \frac{R_{1,2}\beta_{1,2B}}{4} A^2 \right)^2 \quad (5)$$

here, $R = R1 = R2$ used for LCMBF, r_{02B} is small-signal drain resistance of MOSFET $M2b$, $\beta_i = \mu C_{ox}(W/L)_i$ and A is the amplitude of differential step input signal.

From Eq. (5), it can be seen that SR and G_m and thereby GBW of the amplifier can be enhanced by increasing the value of R . However, very large values of R causes decrease in phase margin and thereby instability of the amplifier. Though due to biasing circuits, significant GBW can be achieved at optimal values of R .

3 Simulation Results

All the simulations have been carried out in Ltspice using 0.18 μm technology. To get a fair comparison among results of different circuits, they have been simulated on the same platform under similar conditions. However, due to low voltage and low biasing current requirement of adaptive biased and superclass-AB recycling folded cascode OTAs, they have been simulated at lower supply voltage and low biasing current. All these design parameters have been summarized in Table 1. Table 2 tabulates the aspect ratio of various MOSFETs used for designing of the OTAs.

To verify the behavior of presented circuits as voltage controlled current amplifier, their DC analysis has been carried out by varying differential input voltage (v_{id}) from

Table 1 Design parameter used for simulating the various folded cascode OTA topologies discussed in the paper

Design parameter	FC, RFC, IRFC, ERFC	Adaptive, superclass-AB
Technology	0.18 μm CMOS	0.18 μm CMOS
Resistance (RL)	100 k Ω	100 k Ω
Capacitor (CL)	10 pF	10 pF
Supply voltage	± 1.6 V	± 1 V
Bias current	200 μA	10 μA

Table 2 Aspect ratio of different MOSFETs used in simulating the various folded cascode OTA topologies

OTA type	MOSFET	W/L (μm)	MOSFET	W/L (μm)	MOSFET	W/L (μm)
FC OTA	M0	128/0.5	M3, M4	32/0.5	M7, M8	64/0.18
	M1, M2	128/0.36	M5, M6	16/0.18	M9, M10	64/0.5
RFC OTA	M1a, M2a	64/0.36	M3a, M4a	24/0.5	M11, M12	8/0.18
	M1b, M2b	64/0.36	M3b, M4b	8/0.5		
IRFC OTA	M1a, M2a	64/0.36	M3a, M4a	24/0.5	M3c, M4c	4/0.5
	M1b, M2b	64/0.36	M3b, M4b	4/0.5	M11-M14	4/0.18
ERFC OTA	M1a, M2a	64/0.36	M3a, M4a	24/0.5	M3c, M4c	12.5/0.5
	M1b, M2b	64/0.36	M3b, M4b	4/0.5	M11-M14	12.5/0.18
Adaptively biased & Superclass-AB	M1a-c, M2a-c	190/0.6	M3a, M4a	180/0.6	M5, M6	120/0.6
	M1d, M2d	60/0.6	M3b, M4b	60/0.6	M7-M10	200/0.6
	M1d, M2d	60/0.6	M3b, M4b	60/0.6	M7-M10	200/0.6

–200 to 200 mV and has been plotted in Fig. 4. Curves of Fig. 4 show the improvement achieved in transconductance factor of various configurations as discussed in Sect. 2. It shows that at very low biasing currents transconductance achieved in superclass-AB is significantly greater than what is achieved in other configurations at much higher biasing currents.

AC analysis for different OTA circuits for frequency range of 1 Hz to 100 MHz has been shown in Fig. 5. Again these curves show the improvements in gain, bandwidth, and GBW with advancement in OTA technique. Though, in these curves, the said

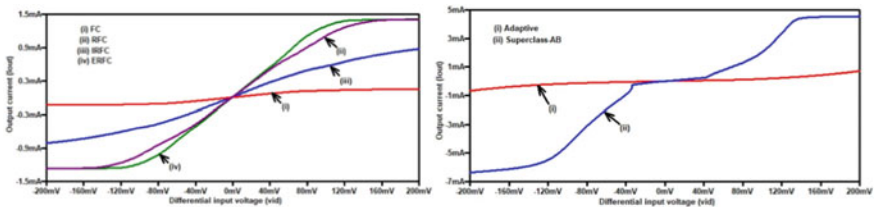


Fig. 4 DC response for various folded cascode OTA topologies

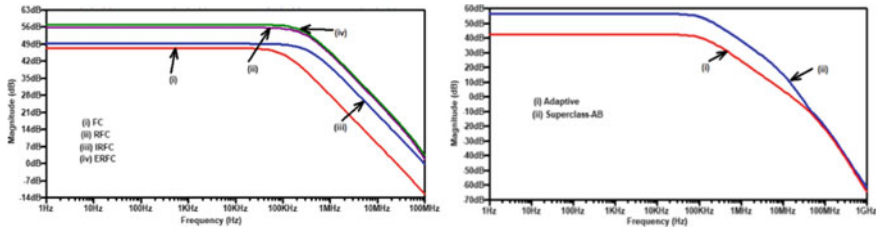


Fig. 5 AC response for various folded cascode OTA topologies

parameters for adaptive and superclass-AB RFC OTA appear to be of lower value, but actually for these OTAs, the results have been plotted at much lower biasing current and supply voltage. In case, comparison is carried out under the same biasing conditions, adaptive and superclass-AB OTAs will outperform other OTAs significantly. However, IRFC OTA does not show expected improvements in the parameters. This may be due to the condition of a similar simulation environment imposed by the authors, for fair comparison.

To calculate the slew rate and observe the response in a practical environment, transient analysis of the circuits has been performed and plotted in Fig. 6. All these results show that superclass-AB RFC OTA has a much higher slew rate as compared to the rest of all the OTAs. All these values obtained via simulations have been summarized in Table 3.

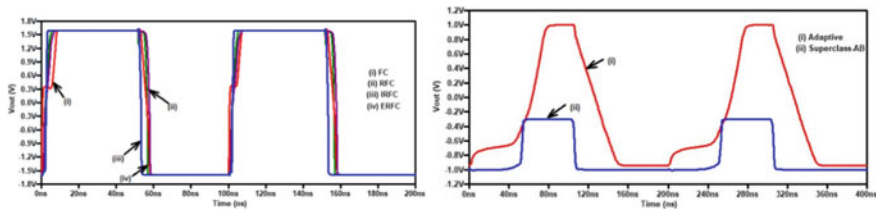


Fig. 6 Transient response for various folded cascode OTA topologies

Table 3 Comparative summary of simulated results for various folded cascode OTA topologies

OTA type	Gain (dB)	Bandwidth (kHz)	GBW (MHz)	SR + (V/ μ s)	SR- (V/ μ s)
FC	47.40	107.44	25.63	473.77	501.11
RFC	55.80	293.89	114.09	423.01	1413.90
IRFC	49.12	351.95	97.03	2328	1590
ERFC	57.04	276.75	133.38	746.88	1388.29
Adaptive	42.44	125.46	16.28	86.80	42.53
Superclass-AB	56.16	121.26	27.13	230.90	269.98

4 Conclusion

In this paper, various advanced techniques available in the literature for improving the OTA characteristics have been studied and compared. These techniques like RFC, IRFC, and ERFC are majorly based on current recycling concept, which helps in improving transconductance without increasing power consumption or chip area. Moreover, these techniques improve GBW and slew rate of OTA as well. Further, techniques like adaptive biasing and superclass-AB that reduce static power consumption while providing large dynamic range have also been discussed. These topologies not only operate at low biasing currents but also increase current efficiency and GBW of the circuit significantly. All these circuits have been simulated under a similar biasing environment in Ltspice using 0.18 μm CMOS technology. Results obtained clearly show the effectiveness of various techniques and represent their usefulness in the practical environment.

References

1. Zhao X, Fang H, Xu J (2012) A transconductance enhanced recycling structure for folded cascode amplifier. *Analog Integr Circ Sig Process* 72:259–263
2. Akbari M et al (2014) Design and analysis of DC gain and transconductance boosted recycling folded cascode OTA. *Int J Electron Commun (AEU)* 68(11):1047–1052
3. Saitoh M, Nakabayashi Y, Ota K, Uchida K, Numata T (2010) Understanding of short-channel mobility in tri-gate nanowire MOSFETs and enhanced stress memorization technique for performance improvement. In: *International electron devices meeting, San Francisco, CA*, 34.3.1–34.3.4
4. Li YL, Han KF, Tan X, Yan N, Min H (2010) Transconductance enhancement method for operational transconductance amplifiers. *Electron Lett* 46(19):1321
5. Akbari M (2015) Single-stage fully recycling folded cascode OTA for switched-capacitor circuits. *Electron Lett* 51(13):977–979
6. Akbari M, Biabanifard S, Asadi S et al (2015) High performance folded cascode OTA using positive feedback and recycling structure. *Analog Integr Circ Sig Process* 82:217–227
7. Sarkar A, Panda SS (2017) Design of a power efficient, high slew rate and gain boosted improved recycling folded cascode amplifier with adaptive biasing technique. *Microsyst Technol* 23:4255–4262
8. Deo N, Sharan T, Dubey T (2020) Subthreshold biased enhanced bulk-driven double recycling current mirror OTA. *Analog Integr Circ Sig Process*. <https://doi.org/10.1007/s10470-020-01689-8>
9. Zhao X et al (2015) Transconductance and slew rate improvement technique for current recycling folded cascode amplifier. *Int J Electron Commun (AEU)* 70(3):326–330
10. Garde MP, Lopez-Martin A, Carvajal RG, Ramírez-Angulo J (2018) Super class-AB recycling folded cascode OTA. *IEEE J Solid-State Circuits* 53(9):2614–2623
11. Assaad RS, Silva-Martinez J (2009) The Recycling folded cascode: a general enhancement of the folded cascode amplifier. *IEEE J Solid-State Circuits* 44(9):2535–2542
12. Khade AS et al (2019) Performance enhancement of advanced recycling folded cascode operational transconductance amplifier using an unbiased input stage. *Integr VLSI J* 69:242–250
13. Assaad R, Silva-Martinez J (2007) Enhancing general performance of folded cascode amplifier by recycling current. *Electron Lett* 43(23):1243–1244

14. Elwan H, Gao W, Sadkowski R, Ismail M (2000) CMOS low-voltage class-AB operational transconductance amplifier. *Electron Lett* 36(17):1439
15. Lopez-Martin AJ, Baswa S, Ramirez-Angulo J, Carvajal RG (2005) Low-voltage super class AB CMOS OTA cells with very high slew rate and power efficiency. *IEEE J Solid-State Circuits* 40(5):1068–1077

Grasping Force Analysis of 3-Fingered Gripper



Rohan Malik, Yashasvi Verma, Abhishek Verma, and Vikas Rastogi

Abstract The aim of our study is to understand the role of grip force on the object being manipulated by a robotic end effector. This was accomplished by the means of a threefold comprehensive approach. In the first stage, an expansive review of the existing literature was conducted to obtain the anthropometric measurements of human fingers. This measurement then became the foundation of our CAD model so as to encompass ergonomic considerations. The second stage of our project was the development of a model ideal for gripping our test object. Further, the model was 3D printed and assembled so as to conduct the physical experimentation. The model was made functional by means of Servo Motors and Arduino and fed commands via a laptop. The last stage of the project was to perform simulations on ANSYS pertaining to the grip force, the value for which was obtained by surveying the available literature to form specific simulations. The value of deformation in test piece was brought to the allowable limits and the ideal force values calculated. These were tested on the physically developed model. The final code will be able to provide motion to the hand in a way to grip various test pieces at the required optimal force values.

Keywords Robotic gripper · ANSYS · Force estimation

1 Introduction

The last few years have witnessed a paradigm shift in technological innovation that has successfully guided industrial automation. The integration of manufacturing ability with programming techniques has allowed effective utilization of automation to reduce lead times, improve productivity and enhance quality. This has been observed with a simultaneously reduced need for human intervention in the manufacturing process. We plan to add to this concept by building a three-fingered robot

R. Malik · Y. Verma (✉) · A. Verma
Delhi Technological University, Shahbad Daultapur, Delhi 110042, India

V. Rastogi
Mechanical Department, Delhi Technological University, Shahbad Daultapur, Delhi 110042, India

gripper model. Many such grippers are available today and the required model can be selected for operation. Egan et al. [1] patented a gripper for specialized grasping of objects. It included configurations that permitted the pivot or the presence of a pivotable member to allow for an object to be gripped between two movable and coupled arms. To reduce the grasping torque, the model employed a novel can that also led to a decreased level of complexity of the gripper. Peer et al. [2] present a comprehensive model for the control of a three-fingered gripper by means of the human hand. These efforts are bolstered by a force feedback via an exoskeleton, and the subsequent mappings have been appropriated to rectify for the differences in kinematic structures of a human hand and a robotic gripper. Factors such as stability of design and retention of object influence the grip. Zhou et al. [3] have developed a three-fingered novel soft gripper that has the versatility to grasp not only small objects, but convex shaped large objects as well. It has been found to overcome external disturbances in manipulation operations and provides considerable grasping force at low actuation pressure. Li et al. [4] expatiate over the development of a versatile gripper that can grasp objects of various sizes, but is easy to control as well. The proposed model has three fingers each consisting of three joints and actuation by two motors. The four bar linkage can be used to drive the multi-DOF fingers independently. Three finger grippers can be adapted to not only manoeuvre delicate objects but also for functions where strength and precision are requisites. Koustoumpardis et al. [5] have developed a gripper model containing three fingers, of which two were underactuated, for pinching and clamping fabrics in the apparel industry. This agile end effector permits the grasping of fabric from a flat surface by mimicking the movements of the human fingers. Manti et al. [6] talk about a three-fingered soft gripper that is adaptable and underactuated. It is capable of securely seizing objects of varying shape, size and materials using minimal control parameters. Such a design can find easy application in the field of bio-inspired robotics. The gripping function exerts certain forces on the said objects and may even cause deformation. Hence, depending upon the industry, the grip forces are required to be adjusted. There has been high-end research dedicated to robotic hands and gripper with optimized force control. Buss et al. [7] have expounded upon the development of a grasping force optimized dextrous hand. They propose achieving a balance of external forces to attain the grasp stability by applying appropriate internal forces. Pons et al. [8] furthered this concept with their work on the MANUS-HAND project. They use the underactuated principle and increase the number of active joints to evolve an upper limb prosthetic, which can have multi-functional utility. The clinical validation has seen successful generation of this mechanical design. Talasaz, Trejos and Patel [9] expand upon the force feedback mechanism of a robot gripper in performing a knot-tightening task in robotics-assisted minimally-invasive surgery (RAMIS). Three modes of feedback have been evaluated with respect to various parameters such as consistency, time of performance and tissues damage. Gazeau et al. [10] present a four-fingered robotic hand reinforced by a neural network that can estimate the contact force and aid fine manipulation of objects. The 4 DOF gripper is actuated by DC servos. Zhang et al. [11] have patented a robot that allows for the mating of the workpiece with an external object after assessing its location

and orientation. This is done with the aim of minimizing the contact force. Carrozza et al. [12] have expanded this concept into the field of biomechanics by integrating cybernetics to develop a wearable upper limb prosthetic that possesses motor capabilities. These versatile capabilities have been ingrained by sensory feedback for position and force. Birglen and Gosselin [13] discuss the ability of a robot equipped with underactuated fingers to securely seize any irregularly shaped object. The force capability of the 2-DOF gripper has been analyzed to reduce complexity of design and to develop sensory feedback. Attempts have been made to develop sensors that can be effectively employed in such applications. Kawasaki et al. [14] dwell upon integrating the human grasp reflex into a robotic gripper in order to facilitate manipulation of unknown objects. The suitable contact force is applied by means of joints, which can be independently controlled. Kinoshita et al. [15] have experimented on a set of individuals to analyze the grip force exerted by them in various stances of grasping operations. Flanagan and Wing [16] discuss the correlation of load force and grip force and postulate that upon movement of a grasped object the grip force plays a vital role. Sahu and Choudhary [17] have modified a six axis industrial robot for efficient application by analyzing the shear stress, natural frequency and modal shape. Natarajan et al. [18] have simulated the deformation of a soft object during grasping via a gripper. They have further utilized this simulation to minimize the contact force, whilst preventing slipping of object during gripping. Wang and Lan [19] propose an optimized gripper configuration that applies a constant gripping force using feedback regulation. The compliant gripper has been found to execute the required object manipulations. We plan to develop a versatile robotic hand that can modulate its grip strength depending upon the object it is expected to manoeuvre. The physical investigation presented in our paper is carried out as an extrapolation of simulated evaluations on relevant software and on intensive information obtained by reviewing literature.

2 Methodology and Design

To develop a robotic hand that responds and modulates its grip force depending upon the features of the object to be manipulated, we decided to tread with a threefold approach. The design began with an extensive research online, which was aimed at understanding the ergonomics of human fingers. Human hands have been anatomically designed to perform a variety of delicate as well as robust actions. Once this data were collected, it was used as a reference, whilst developing the gripper model. A three-fingered gripper was considered to be appropriate for the designated function by keeping in mind the ergonomic considerations and the capability of the design to securely hold an object without any slippage. The model was developed on Solidworks. Once the design was prepared, it was 3D printed. The individual parts were assembled to prepare the model hand. This was powered via 3 servomotors. Arduino Uno controlled the motion of the motors. The Solidworks model and the data regarding testing object were fed into ANSYS. Using ANSYS, simulations were

performed to conceive the contact force that the gripper applied in secure grasping of objects keeping in mind that the objects be deformed within an acceptable limit. The grasping force was validated by conducting an expansive literature review. These forces were modulated and the optimal forces were reached for minimal deformation in objects without any loss in capability to perform the grasping task. This was repeated for a few materials, and each data were noted. Finally, an interface code was developed to facilitate the movement of the model hand so that it applied the required optimal force to grasp the object successfully.

2.1 Anthropometric Data

The anthropometric data of the human fingers were obtained through a thorough perusal of research available on the subject. This was done with the aim to develop an ergonomically feasible design. Cakit et al. [20] have presented the data of biomechanics measurement of a multitude of people. This encompasses the quantification of hand dimensions of the said population. A website [21] illustrated the various measurements of a human hand. This includes the finger length data, which was divided according to the females and male percentile populous. Asadujjaman et al. [22] have conducted anthropometric measurements for nine hand parameters in their research with the aim to estimate stature of the Bangladeshi population on the basis of these measurements. Using these sources, we dwelled on the measurements for the proposed design and reached a consensus by keeping in mind the objects we had assumed for manipulation in our study. These measurements are indicated in Table 1.

Table 1 Comparison between the available and selected data

Dimension		Measurement	
		Available values (cm)	Considered (cm)
1st and 2nd Finger	Length	8.3	9
	• 1st Phalange	–	3
	• 2nd Phalange	–	3
	• 3rd Phalange	–	3
3rd Finger	Length	5.8	9
	• 1st Phalange	3.2	5
	• 2nd Phalange	2.6	4
Fingers	Width	1.5	2.15
	Breadth	1	1.5
Palm	Length	10.5	9
	Breadth	8.7	1
	Width	5	8

2.2 Design and Modelling

We decided to employ Solidworks for the modelling. The parameters became the basis for the constraints of the shape and geometry of our design. This was chosen to be a three-jaw gripper that imitated the configurations of a human hand and satisfied the ergonomic expectations placed on it. The gripper was designed so that when it seized an object, the object would be held in a secure grasp that prevented slipping. The orientation of the fingers came to be seen as a vital consideration. Since, the human hand inspired our design; the thumb was placed in opposition to the other two fingers so that it could provide not only manipulative function but also geometric support.

The 2 adjacent fingers spaced at a distance of 1 cm consisted of 3 phalanges each. The third finger, which supports the object from the opposite sides consisted of 2 phalanges. A base plate of 8 cm \times 9 cm was also provided to support the object being carried from below and to provide structural stability to the design, as a whole. The inter-phalange movements have been made possible with rivets of variable length, which also facilitate quick assembly. Small extensions on the back of the second phalange have been incorporated in the design to limit the maximum angle of engagement to 180 degrees, following the anthropological blueprint of a human finger. The fingers have also been made hollow to integrate the connection with the servomotor. The modelled gripper is shown in Fig. 1.

Assembly of the physical model. The CAD model was 3D printed to develop the physical model. The material for the model was chosen as Polylactic Acid or PLA. The assembled model is shown in Fig. 2. Once the solid model was prepared, the necessary control operations were added. A string imitating the tendonic operations in human fingers was attached to the hollow left inside the fingers. The free end of these strings was attached to servomotors (which were taken as MG90 in model). The servo was connected via a breadboard to the Arduino Uno microcontroller. The pulse waves of the servo were programmed using the Arduino IDE. The circuit diagram for the same is given in Fig. 3.

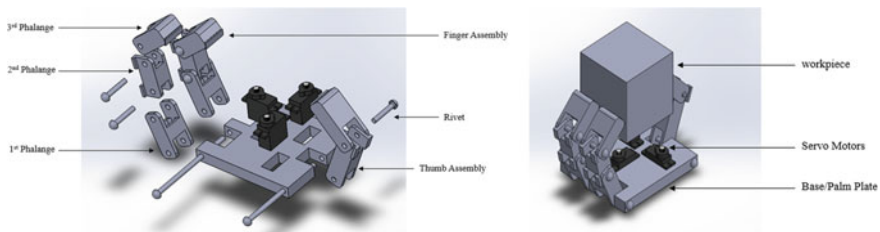


Fig. 1 Labelled diagram of CAD model

Fig. 2 Assembled model

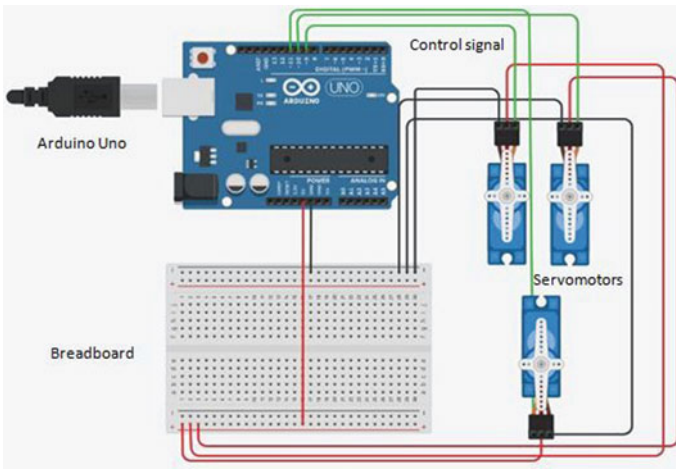
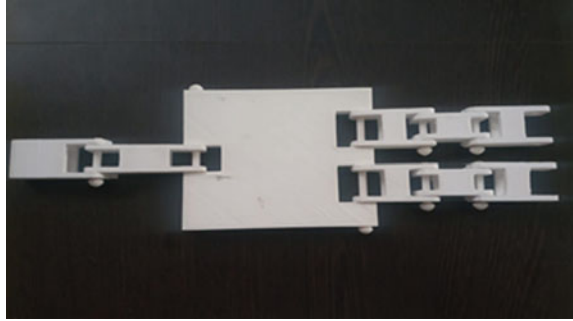


Fig. 3 Circuit diagram

3 Experimentation and Result

3.1 Finite Element Analysis

The modelled gripper was analysed on a finite element solver, ANSYS. It was assumed that during the entire operation, all the parts of the model remained mated. The boundary conditions were applied at the top of the base/palm plate and force was applied at the contact point of each phalange and the cube as shown in Fig. 4. Self-weight was added as vertically downwards. The forces applied by the gripper along with the friction ($\mu = 0.3$) [23] acts against the force of gravity. The material of the cube was taken to be PLA as well. The simulation results as shown in Fig. 5 were also performed on various other materials such as balsa wood, rubber in order to further validate the results. The various parameters required for judging were recorded as output in Table 2.

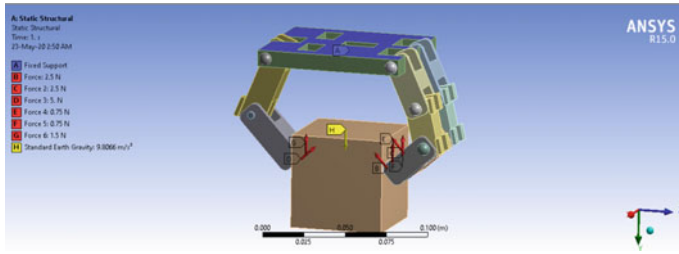


Fig. 4 Force application and boundary conditions

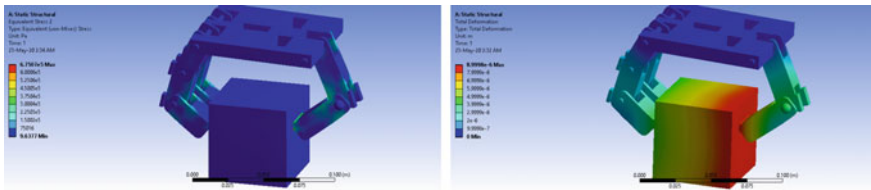


Fig. 5 Von-Mises stress and total deformation contours

Table 2 Results and values

Parameter	Value
Maximum Von-Mises stress	6.7×10^5 Pa
Maximum deformation	9×10^{-6} m
Ultimate strength	35 MPa
Poisson's ratio	0.38
Young's Modulus E	3.5 GPa

The results deduced that the deformation produced was very negligible and hence acceptable. The grasping force was in accordance to the equation:

$$2 \times F \times \cos \theta + m \times g = \mu \times m \times g \tag{1}$$

where,

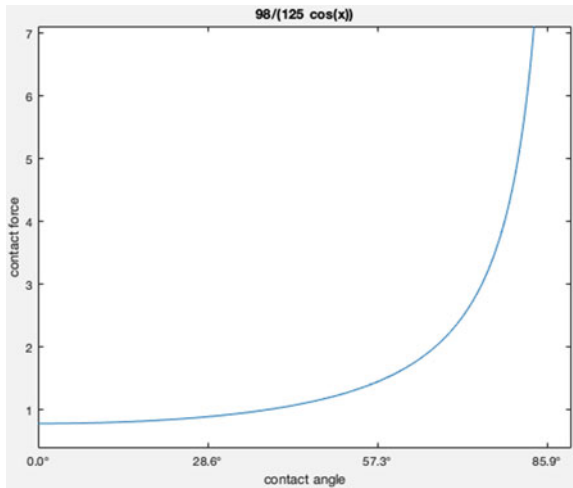
- m is mass of the block
- F is the grasping force
- θ is angle of contact with the horizontal
- G is earth's gravity
- μ is coefficient of friction.

After the analysis physical experimentation was carried out on a pliable material to check the effect of grasping force. The result as depicted in Fig. 6 proved that considerable deformation was being achieved.

Fig. 6 Deformation in material



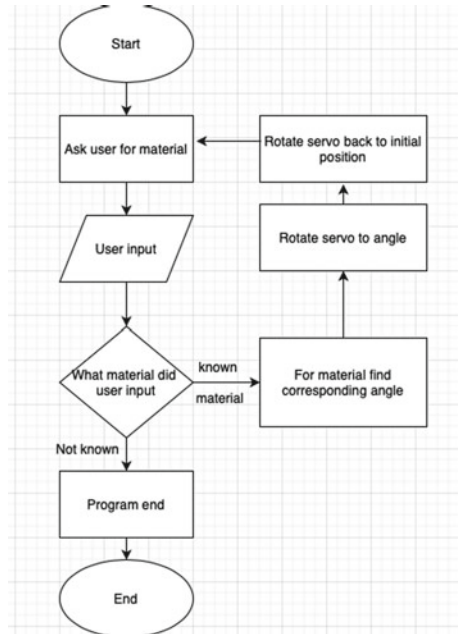
Fig. 7 Relation between grasping force and contact angle



Hence the relation was developed between the grasping force and angle of contact based on our governing Eq. (1) as shown in Fig. 7.

3.2 Algorithm

To build versatility in the gripper, the Arduino code was modified. This modification was done to introduce the control of angle of rotation of the servo. As seen above, there was a relation between the grasping force and angle of contact between the finger and the contacting surface of the object. This relation was taken as a basis for manoeuvring of different objects in the future. The code was rewritten to incorporate a precise control of grasping operation. Keeping in mind the acceptable level of deformation, the code made it possible to move the servo through the desired angle for the grasping particular object with the optimal grasping force that did not permit slipping of the object. The algorithm of the code is shown in Fig. 8.

Fig. 8 Novel algorithm

4 Conclusion and Future Development

For successful pursuit of the above-mentioned proposed model and design, the validation by the physical model was carried out and gave positive results. The following can be concluded

- Anthropometric measurements obtained by conducting a literature review were extrapolated and modified to build a versatile yet simple design for a three-fingered anthropomorphic gripper.
- The design was modelled on Solidworks and the parts were 3D printed and assembled as per the design and made operational by using Arduino. This made it very simple to mobilize the servomotors that in turn pulled on the tendonic strings to clench and unclench the fingers.
- It was made sure that the components in the abovementioned project were widely available and relatively inexpensive. This was an important consideration for achieving versatility aided with financial control.
- We proceeded to structurally simulate the model on ANSYS and reach an ideal optimal grasping force value considering the deformation in the test object on manipulation.
- The correlation of these force values with angle of contact was used as the basis to develop a code that would adapt the gripper to the particular object.

The proposed gripper had the following limitations

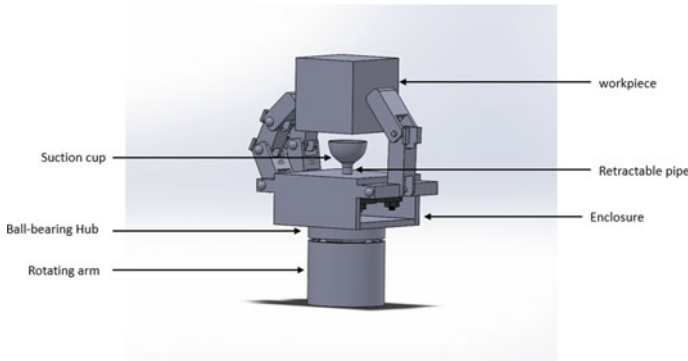


Fig. 9 Proposed CAD

- The weight of the object that could be manoeuvred using the versatile gripper is dependant on the material of the gripper and the torque capacity of the servomotors.
- No retracting mechanism was provided for the fingers to be brought back to their original position after grasping operation had been performed.
- There was a requirement for fail-proofing the system by including a force feedback mechanism. This could have been done by the incorporation of force sensing resistors.
- The grasping force analysis that became the sound basis for inducing versatility in the operation was defined specific to the pick and place operation.

In the future, this technology can be furthered and made more sophisticated. We propose the addition of a retractable vacuum cup mechanism on the palm plate that would enhance the grasping power of the gripper. This would allow for a multitude of shapes and sizes of objects to be manipulated easily with reduced grasping force and hence possible decreased deformations in delicate pick and place operations. A sample design is depicted in Fig. 9.

References

1. Egan BP et al (1993) Gripper apparatus for use in a robotics system. United States Patent, Patent no. 5,253,911
2. Peer A, Einkenel S, Buss M (2008) Multi-fingered telemanipulation—mapping of a human hand to a three finger gripper. In: 17th IEEE international symposium on robot and human interactive communication, pp 465–470
3. Zhou J, Chen S, Wang Z (2017) A soft-robotic gripper with enhanced object adaptation and grasping reliability. *IEEE Robot Autom Lett* 2(4):2287–293
4. Li G, Fu C, Zhang F et al (2015) A reconfigurable three-finger robotic gripper. In: *IEEE international conference on information and automation*, pp 1556–1561
5. Koustoumpardis PN, Nastos KX, Aspragathos NA (2014) Underactuated 3-finger robotic gripper for grasping fabrics. In: *23rd international conference on robotics*, pp 1–8

6. Manti M, Hassan T, Passeti G et al (2015) An under-actuated and adaptable soft robotic gripper. In: Wilson S, Verschure P, Mura A, Prescott T (eds) *Biomimetic and biohybrid systems. living machines 2015. Lecture Notes in Computer Science*, vol 9222. Springer
7. Buss M, Hashimoto H, Moore JB (1996) Dextrous hand grasping force optimization. *IEEE Trans Robot Autom* 12(3):406–418
8. Pons J, Rocon E, Ceres R (2004) The MANUS-HAND dextrous robotics upper limb prosthesis: Mechanical and manipulation aspects. *Auton Robot* 16(2):143–163
9. Talasz A, Trejos AL, Patel RV (2012) Effect of force feedback on performance of robotics-assisted suturing. In: Fourth IEEE RAS & EMBS international conference on biomedical robotics and biomechatronics, pp 823–28
10. Gazeau JP, Zehloul S, Arsicault M et al (2001) The LMS Hand: Force and position controls in the aim of the fine manipulation of objects. *IEEE International Conference on Robotics and Automation* 3:2642–2648
11. Zhang H et al (2007) Industrial robot with controlled flexibility and simulated force for automated assembly. United States Patent, Patent No. US 7,181,314 B2
12. Carrozza MC, Massa B, Micera S et al (2001) A “wearable” artificial hand for prosthetics and humanoid robotics applications. In: IEEE—RAS international conference on humanoid robots
13. Birglen L, Gosselin CM (2003) On the force capability of underactuated fingers. *IEEE International Conference on Robotics and Automation* 1:1139–1145
14. Kawasaki H, Mouri T, Takai J et al (2002) Grasping of unknown object imitating human grasping reflex. In: 15th IFAC triennial world congress, vol 3, issue 1, pp 247–252
15. Kinoshita H, Murase T, Bandou T (1996) Grip posture and forces during holding cylindrical objects with circular grips. *Ergonomics* 39(9):1163–1176
16. Flanagan JR, Wing AM (1993) Modulation of grip force with load force during point-to-point arm movements. *Exp Brain Res* 95(1):131–143
17. Sahu S, Choudhury BB (2019) Stress and modal analysis of six-axis articulated robot using ANSYS. In: *Information and communication technology for competitive strategies. Lecture notes in networks and systems*, vol 40. Springer, Singapore, pp 303–311
18. Natarajan S, Jegan A, Vivekananthan R (2019) The modelling of contact force of the robot gripper for deformable object using finite elements method. *Int J Mech Prod Eng Res Dev (IJMPERD)* 8(6):579–588
19. Wang JY, Lan CC (2014) A constant-force compliant gripper for handling objects of various sizes. *J Mech Des* 136(7):MD-13–1311
20. Cakit E, Durgun B, Cetik MO et al (2014) A survey of hand anthropometry and biomechanical measurements of dentistry students in Turkey. *Hum Factors Ergon Manuf Serv Ind* 24(6):739–753
21. Anthropometric Data, <http://limited-use-only.com/strategies/anthropometric-data/>. Last accessed on 2 Dec 2019
22. Asadujjaman M, Ali Molla MB, Al Noman SN (2019) Stature estimation from hand anthropometric measurements in Bangladeshi population. *J Forensic Leg Med*, 86–91
23. Tribology, <https://www.tribology-abc.com/abc/cof.html>. Last accessed on 15 May 2020

Simplification of Governing Equation for Fluid Flow Between Two Concentric Cylinders



Anamika Yadav  and Pooja Pathak 

Abstract The fluid film journal bearing has two parts, i.e., journal/shaft and the bearing. At stop position, journal is at rest on the bearing's inner surface. In ideal condition of journal bearing, the journal and bearing are concentric. But in actual running condition, the centers of the journal and bearing are at distance known as eccentricity. Eccentricity is necessary for generating pressure to lift the bearing in the marginal space of journal and inner surface of bearing. The pressure is calculated by the Reynolds governing equation of fluid flow between the concentric cylinder. Many researchers used complex solution to get the required solution to the non-dimensional governing Reynolds equations. The purpose of this paper is to simplify the governing equation used by the researchers so that it could be understood. In this paper, the authors have taken the complex equation of two researchers and converted in its simplified form.

Keywords Journal bearing · Fluid flow · Reynolds equation · Concentric cylinder

Nomenclature

P_s	Supply pressure
b	Clearance ratio
U	Linear Velocity
c	Clearance
P	Pressure
R_b	Radius of bearing
h	Film thickness
L	Length of bearing
D	Diameter of bearing
μ	Lubricant viscosity

A. Yadav · P. Pathak (✉)

Department of Mathematics, GLA University, Mathura, India

e-mail: pooja.pathak@gla.ac.in

ω Angular speed
 R_j Radius of journal

1 Introduction

Flow is very natural phenomenon for the existence of the universe. Researchers have studied the different flow pattern in their laboratory such as flow of wind to understand climate change and other natural and unnatural phenomenon. Flow of air leads to generation of power that can be used by wind turbine, whereas in steam turbine, high-pressure steam flow strike on the turbine blade to rotate the turbine and generates the power. To support these rotating turbo-machineries, fluid film bearing is employed in industries. These bearings support heavy shaft in rotation and also carry out the heat generated. These bearing also supports the shaft by pressure generation between clearance space with the help of external pump. Pressure is generated in the clearance space by the wedge action. Pressure is generated because of the flow of fluid between the marginal space of bearing and the shaft. Sometimes researcher uses very complex mathematics to present the flow of fluid in the journal bearing. The journal bearing is a noticeable area of research nowadays among the researchers due to its wide use in industry. This bearing becomes a heart of turbomachinery, because it supports the journal at high loads and high speeds. Due to rapid growth in transportation and space engineering between the nations, journal bearing attracts many researchers. These bearings support the load with help of lubricant supplied at prescribed pressure from oil supply holes at inlet point through one or many grooves. The position of the grooves plays important role to support the load, i.e., shaft/journal weight and stability of the bearing [1]. Researchers [2] use the finite element method (FEM) to study the loading direction's effect on the performance of twin axial bearing and find the optimum location of groove from the load line. Flow rate at every groove is important in creation of pressure within the journal bearing. To know the effect, the rate of flow at each groove should be measured [3]. In some cases, single groove journal bearing shows better performance if groove manufactured by the side of the load line [4]. Pressure generated within the journal bearing depends upon the size and shape of grooves [5]. Axial and circumferential grooves are mainly used in the journal bearing which depends upon the applications. Both groove configurations can also be used at different location in same bearing to get the advantages of the configuration for generating more load-bearing capacity of the journal bearing. Experimental setup was prepared by the researchers [6, 7] to analyze the effect of temperature and pressure of the lubricant in the bearings. They have observed that if the feed pressure of the lubricant increases, the flow rate is increased but if temperature of lubricant is decreased, then minimum film thickness and attitude angle are increased. Stability of the journal bearing is also resolved by choosing three axial groove in water lubricating journal bearing [8]. Bearing number [9] and eccentricity ratio are controlling parameters for the stability of the

journal bearing. By controlling synchronous, whirl stability can be achieved from 800 to 1666 rpm for 150 N load [10]. It is mentioned by a group of researchers [11] that under heavy load, the performance to twin axial groove configuration is better as compared to single groove bearing. It is because of the uneven pressure in the individual groove. The optimum location is a very important parameter to achieve the max load-bearing capacity of the journal bearing. There are no. of methods such as ANOVA and genetic algorithm [12] which are available to optimize the location of the groove to get minimum friction, mass coefficient, and maximize the load-carrying capacity. Flow regimes [13, 14] also affect the static and dynamic performance of bearing at start/stop and accelerating/decelerating condition of the journal bearing. To know the influence of temperature generation on the bearing's performance, the governing Reynolds energy equation and equation of heat conduction in the clearance zone between journal and bearing is solved [15]. ANSYS CFX software is also used to find the temperature profile of the journal bearing by using correct boundary condition [16]. Stability margin is also presented by the researcher for water [17] lubricated journal bearings with experimental validation.

In this paper, an attempt is to be made to derive the complex governing equation given by the researcher [2, 8] from the basic form of Reynolds equation [17].

2 Mathematical Model of Governing Equation

This section shows the mathematical model developed for the research of the performance of fluid flow between two concentric cylinders, i.e., journal bearing used in many industries. The basic geometry of the journal bearing is shown in Fig. 1.

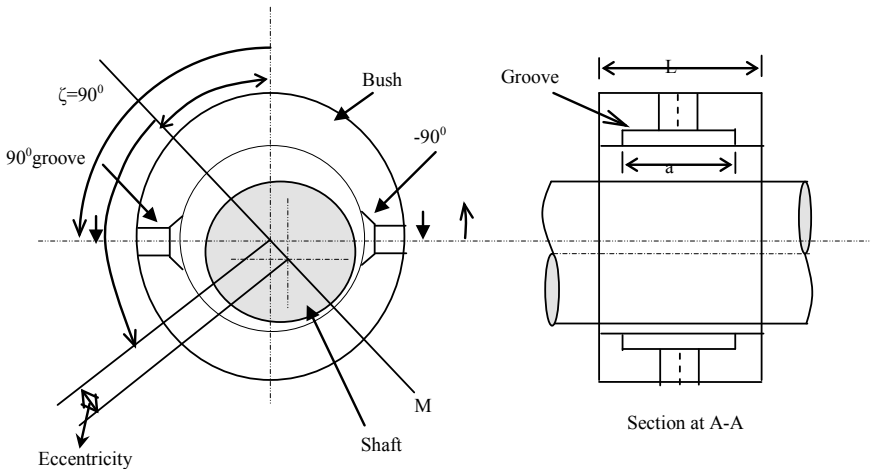


Fig. 1 Bearing geometry [14]

3 Flow Field Equation of Between Two Concentric Cylinders

The Reynolds equation governing the lubricating oil's flow in the margin space of a two concentric cylinders, i.e., hydrodynamic journal bearing using is given by Eq. (1) [18].

$$\frac{\partial}{\partial x} \left(\frac{h^3}{\mu} \frac{\partial p}{\partial x} \right) + \frac{\partial}{\partial z} \left(\frac{h^3}{\mu} \frac{\partial p}{\partial z} \right) = 6U \frac{\partial h}{\partial x} \quad (1)$$

Here, x is circumferential, and z is direction of length.

Reynolds equation taken by Kaye et al. [8] is as follows

$$\frac{\partial}{\partial \theta} \left(H^3 \frac{\partial y}{\partial x} \right) + \left(\frac{D}{L} \right)^2 H^3 \frac{\partial^2 P}{\partial Z^2} = S \frac{\partial H}{\partial \theta} \quad (2)$$

Now, the effort has made by the authors to convert the basic Reynolds equation with substituting the proper substitution in Eq. (1)

Put $x = R\theta$ in Eq. (1)

$$\frac{\partial}{R \partial \theta} \left(\frac{h^3}{\mu} \frac{\partial p}{R \partial \theta} \right) + \frac{\partial}{\partial z} \left(\frac{h^3}{\mu} \frac{\partial p}{\partial z} \right) = 6U \frac{\partial h}{R \partial \theta}$$

Or

$$\frac{\partial}{\partial \theta} \left(h^3 \frac{\partial p}{\partial \theta} \right) + R^2 \frac{\partial}{\partial z} \left(H^3 \frac{\partial p}{\partial z} \right) = 6\mu U R \frac{\partial h}{\partial \theta}$$

So

$$\frac{\partial}{\partial \theta} \left(h^3 \frac{\partial p}{\partial \theta} \right) + R^2 \frac{\partial}{\partial z} \left(h^3 \frac{\partial p}{\partial z} \right) = 6\mu \omega R^2 \frac{\partial h}{\partial \theta} \quad (3)$$

We know $U = R \omega$

Now, non-dimensional the above equation by substrng following value in Eq. (3)

$$H = \frac{h}{c} \text{ or } h = Hc; P = \frac{p}{p_s} \text{ or } p = P \cdot p_s \text{ and } Z = \frac{z}{L/2} \text{ or } z = \frac{ZL}{2}$$

$$\frac{\partial}{\partial \theta} \left(H^3 c^3 \right) \frac{\partial (P p_s)}{\partial \theta} + R^2 \frac{\partial}{\frac{L}{2} \partial Z} \left(H^3 c^3 \frac{\partial P p_s}{\partial Z} \right) = 6\mu \omega R^2 \left(c \frac{\partial H}{\partial \theta} \right)$$

$$c^3 p_s \frac{\partial}{\partial \theta} \left(H^3 \frac{\partial P}{\partial \theta} \right) + \left(\frac{4R^2}{L^2} \right) 4C^3 \frac{\partial}{\partial z} \left(H^3 \frac{\partial P}{\partial z} \right) = 6\mu \omega R^2 c \left(\frac{\partial H}{\partial \theta} \right)$$

Or

$$\frac{\partial}{\partial \theta} \left(H^3 \frac{\partial P}{\partial \theta} \right) + \left(\frac{D}{L} \right)^2 \frac{\partial}{\partial z} \left(H^3 \frac{\partial P}{\partial z} \right) = \frac{6\mu\omega R^2}{p_s c^2} \frac{\partial H}{\partial \theta}$$

Because $H \neq f(z)$ so

$$\frac{\partial}{\partial \theta} \left(H^3 \frac{\partial P}{\partial \theta} \right) + \left(\frac{D}{L} \right)^2 H^3 \left(\frac{\partial^2 P}{\partial z^2} \right) = S \frac{\partial H}{\partial \theta} \quad (4)$$

where

$$S = \frac{6\mu\omega R^2}{p_s C^2}$$

S = Dimensionless speed parameter.

Similarly, the authors have again converted the modified Reynolds equation as given by Fedor [2]

$$\frac{\partial}{\partial \theta} \left[\frac{(1 + b \cos \theta)^3}{\mu} \frac{\partial P}{\partial \theta} \right] + r^2 \frac{\partial}{\partial z} \left[\frac{(1 + b \cos \theta)^3}{\mu} \frac{\partial P}{\partial z} \right] = \frac{-6Urb \sin \theta}{C^2} \quad (5)$$

To get Eq. (5), from basic Reynolds Eq. (1)

$$\frac{\partial}{\partial x} \left(\frac{h^3}{\mu} \frac{\partial p}{\partial x} \right) + \frac{\partial}{\partial z} \left(\frac{h^3}{\mu} \frac{\partial p}{\partial z} \right) = 6U \frac{\partial h}{\partial x}$$

It is observed from Eq. (5) that it is in cylindrical coordinate system, whereas Eq. (1) is in Cartesian coordinate system. To convert Eq. (1) in the form of cylindrical coordinate system.

Put $x = r\theta$ and $h = c(1 + b \cos \theta)$ in Eq. (1).

where $c = R_b - R_j$, $b = \text{eccentricity ratio } \left(\frac{e}{c} \right)$

$$\frac{\partial}{r \partial \theta} \left[\frac{c^3(1 + b \cos \theta)^3}{\mu} \frac{\partial P}{r \partial \theta} \right] + \frac{\partial}{\partial z} \left[\frac{c^3(1 + b \cos \theta)^3}{\mu} \frac{\partial P}{\partial z} \right] = 6U \frac{\partial [c(1 + b \cos \theta)]}{r \partial \theta}$$

Or

$$\frac{\partial}{\partial \theta} \left[\frac{(1 + b \cos \theta)^3}{\mu} \frac{\partial P}{\partial \theta} \right] + c^3 \frac{\partial}{\partial z} \left[\frac{(1 + b \cos \theta)^3}{\mu} \frac{\partial P}{\partial z} \right] = -\frac{6Ucb \sin \theta}{r}$$

Or

$$\frac{\partial}{\partial \theta} \left[\frac{(1 + b \cos \theta)^3}{\mu} \frac{\partial P}{\partial \theta} \right] + r^2 \frac{\partial}{\partial z} \left[\frac{(1 + b \cos \theta)^3}{\mu} \frac{\partial P}{\partial z} \right] = -\frac{6Urb \sin \theta}{c^2} \quad (5)$$

4 Conclusion

A parametric study of the governing equation of fluid flow between two concentric cylinder Reynolds equation is solved analytically by using different substitution of parametric values. This paper is helpful to new researcher to understand the different non-dimensionalized term, e.g., speed parameters, eccentricity ratio, relative clearance, and radial clearance. This paper also gives the idea about the conversion of coordinate system from Cartesian to cylindrical system for better understanding of effect of geometrical specification on the journal bearing's static and dynamic characteristics.

References

1. Morton PG, Johnson JH, Walton MH (1987) The influence of grooves in bearing on the stability and response of rotating systems. *Tribol Series* 11:347–354
2. Basri H, Neal PB (1990) Oil flow in axial groove journal bearings. In: Proceedings of the seminar on developments in plain bearings for the '90s. IMechE Tribology Group, pp 11–17
3. Costa L, Mirinda AS, Fillon M, Claro JCP (2003) An analysis of the influence of oil supply condition on the thermo-hydrodynamic performance of a single groove journal bearing. *Ins Mech Eng Part J J Eng Tribol* 217:133–144
4. Desai CK, Patel DC (2005) Experimental analysis of pressure distribution of hydrodynamic journal bearing: a parametric study. In: International conference on advances in Mechanical Engineering, Dhaka, Bangladesh
5. Brito FP, Bouyer J, Fillon M, Miranda AS (2006) Thermal behavior and performance characteristics of a twin axial groove journal bearing as a function of applied load and oil supply temperature. *Tribologia-Finnish J Tribol* 3:22–24
6. Brito FP, Miranda AS, Bouyer J, Fillon M (2007) Experimental investigation of the influence of supply temperature and supply pressure on the performance of a two axial groove hydrodynamic journal bearing. *Trans ASME* 129:98–105
7. Kayar AFI, Salem EA, Khalil MF, Hegazy AA (1963) Two-dimensional finite difference solution for externally pressurized journal bearing of finite length. *Wear* 84:1–13
8. Kini MV, Pai RS, Rao DS, Shenoy SB, Pai R (2006) Effects of groove location on the dynamic characteristics of multiple axial groove water lubricated journal. *Acad Sci Eng Tech* 36:738–742
9. Navthar RR, Halegowda NV (2010) Stability analysis of hydrodynamic journal bearing using stiffness coefficient. *Int J Eng Sci Tech* 2(2):87–93
10. Brito FP, Miranda AS, Claro JCP, Fillon M (2012) Experimental comparison of the performance of a journal bearing with a single and a twin axial groove configuration. *Tribolo Int* 54:1–8
11. Roy L, Kakoty SK (2013) Optimum groove location of hydrodynamic journal bearing using genetic algorithm. *Adv Tribol*, Article ID 580367
12. Dwivedi VK, Chand S, Pandey KN (2014) Effects of turbulence on dynamic performance of accelerated/decelerated hydrodynamic journal bearing. *Int J Des Eng* 5(3):256–288
13. Dwivedi VK, Sand C, Pandey KN (2016) Stability analysis of twin axial groove hybrid journal bearing. *J Appl Fluid Mech* 9(6):2763–2768
14. Bhagat C, Roy L (2014) Steady state thermo hydrodynamic analysis of two axial groove and multilobe hydrodynamic bearings. *Tribol Ind* 36(4):475–487
15. Solghar A, Brito FP, Abdolzadeh, Frajpour MA (2015) Numerical study of twin groove journal bearings performance under steady state condition. *Lub Sci* 27(2):83–102

16. Ren T, Feng M (2016) Stability analysis of water lubricated journal bearing for fuel cell vehicle air compressor. *Tribol Int* 95:342–348
17. Constantinescu VN (1967) The pressure equation for turbulent lubrication. *Proc Inst Mech Eng Lond* 182(3A):383–400

Optimization Techniques Used to Optimize Process Parameters of Submerged Arc Welding: A Review



Sameer Vishwakarma, V. K. Dwivedi, and Manoj Kumar Agrawal

Abstract The welding has been used from very early ages of metal fabrication process. Various types of welding are used for different materials and also in different areas of applications. In spite of having many theories, researchers have been working in the way of optimization of various welding parameters for different welding methods. This paper is strictly concentrated on optimization of submerged arc welding (SAW) parameters and study has been done on 25 research articles. SAW process parameters can be optimized to achieve the best results at minimum cost that may help an organization to reduce their cost of production and also it is helpful in energy conservation.

Keywords SAW · Taguchi · ANOVA · ANN · Optimization · Mathematical modeling · Bead geometry · Shape factor · RSM

1 Introduction

Submerged arc welding is a welding process which is different from other arc welding processes like manual metal arc welding, tungsten inert gas welding, metal inert gas welding, etc. It uses flux to cover the weld pool which protects weld bead from being oxidized or reacting with environment. Different welding parameters like feed rate of wire, welding speed, current, and voltage can be controlled easily with onboard controllers to achieve the best possible welding output by using different fluxes. Because of easily controllable parameters many researchers have tried to optimize them for dilution, deposition rate [1–4], strength [5–7], and hardness [5, 7–10] by using different fluxes [7, 11] on different steels of different thickness with the help of different optimization techniques such as genetic algorithm [12, 13], particle swarm

S. Vishwakarma (✉)
University Polytechnic, GLA University, Mathura, India
e-mail: sameer.vishwakarma@gla.ac.in

V. K. Dwivedi · M. K. Agrawal
Department of Mechanical Engineering, IETGLA University, Mathura, India

© The Author(s), under exclusive license to Springer Nature Singapore Pte Ltd. 2022
K. Govindan et al. (eds.), *Advances in Mechanical and Materials Technology*,
Lecture Notes in Mechanical Engineering,
https://doi.org/10.1007/978-981-16-2794-1_6

optimization [12], Taguchi, artificial neural network [3, 11, 14, 15], and many more other optimization techniques.

2 Equipments of SAW Machine

Power Source: Both alternating current and direct current power source can be used. While using direct current in SAW direct current electrode positive (DCEP) or direct current electrode negative (DCEN), depending upon application could be used as DCEP is suitable for welding and DCEN is suitable for filling or hard-facing process [16].

Transformer: Heavy duty step down transformer is used. Some transformers have power switch, voltage, and current controller on board.

Rail: The trolley is moved on the rail. Rail is generally straight, but sometimes, when a single type welding for mass production is required the rail can be modified as per requirement.

Trolley: Trolley is the most important part of SAW machine. Trolley has the following equipments on it.

Chassis and Wheel—The base of trolley is important part because four wheels allow the trolley to travel on the rail. The wheel has a groove or wheel may be like a pulley. The rail fits into the groove allowing the trolley not to fall from rail.

Controller: A controller box is equipped on the trolley to control wire feed, carriage speed, forward-reverse direction control, welding start-stop switches, and wire up-down switches. Also, it consists of display for welding current, voltage, and carriage speed as shown in Fig. 1.

Gear Box: With the help of gear box, the movement of carriage can be switched between manual and auto.

Wire Electrode and Reel: Wire electrode is coated with copper to increase electrical conductivity, provides self-lubrication, and also protects the wire from environment. The wire is bound on the reel or spool for easy operation. Sizes of wire available are 1.6 mm, 2.0 mm, 3.0 mm, 4.0 mm, 5.0 mm, and 6.0 mm.

Fluxes: Fluxes play important role because they are the main protector and finisher of arc and weld pool. Fluxes can be fused, agglomerated, or mixture of two depending upon type of material.

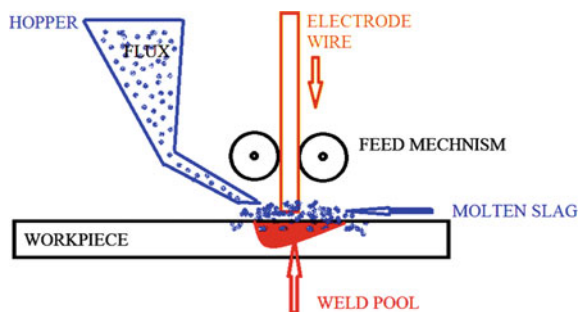
Fig. 1 SAW machine trolley and rail



3 Working of SAW

Submerged arc welding process is initiated after preparing the job by making grooves or keeping them straight depending upon thickness and capability of machine. The hopper throat is opened for fluxes to come out and connection between electrode and workpiece is checked. Machine is turned on by selecting manual or automatic movement of trolley along with setting the parameters. The flux covers the electrode pointing toward the workpiece. No sooner, electrode touches the workpiece an electric arc is generated and flux is melted. This molten flux or slag covers entire weld pool and electric arc to protect them from environment. The machine moves, flux continuously fed to cover the weld pool and welding is continued to make the joint. After welding completed, slag is gently removed and joint is further tested for flaws [16, 17], the working of SAW process is illustrated in Fig. 2.

Fig. 2 Working of SAW



4 Literature Review

SAW process is suitable for thickness of plate starting from 6 mm [18] to 34 mm [19] having different steel alloys like mild steel IS: 2062 steel [12, 14, 18, 20–23], low carbon steel [6, 11, 24], shipbuilding steels [25], X56 steel [19], stainless steel [1, 9, 26], ASME SA 516 Gr. 70 steel [4, 11], AISI 304 steel [6, 26], and ASTM 131 AH 31 steel [7]. Optimizing welding parameters current, arc voltage, wire feed rate, welding speed, standoff distance and flux becomes necessary in order to achieve the best output with optimum input which will help in conservation of the energy and materials. Many mathematical models [27], optimization methods such as Taguchi [1, 2, 5, 10, 12, 21, 27, 28], artificial neural network (ANN) [11, 15], and Jaya algorithm [24] are being used followed by regression analysis gray, analysis of variance (ANOVA) to optimize the parameters of SAW process. In recent years, Taguchi method has been in trend as it provides the effect of parameter directly on output as well as their interaction too.

Type and size of material with optimization method are clearly as shown in Table 1.

Welding current plays an important role in defining size of weld bead. Increasing the welding current increases reinforcement height [2, 3, 14, 18, 20, 21, 25, 27, 29], deposition rate [25], fused area [3, 4, 25], penetration [14, 18, 20, 25], dilution rate [1, 18], hardness [19], and decreased bead width [2, 18, 20, 21, 23, 24, 29], but in the starting of increasing current, the bead width first increases up to 700 A [25] and beyond it behaves uneven. Working range suitably may be 400 to 700 A. Voltage is the main factor that drives current for welding purpose. While optimizing an optimized voltage may reduce cost of production. Increasing arc voltage increases fused area [25], bead height [25], penetration [18], dilution [18], but deposit area and width behave uneven [25, 29]. Increasing voltage decreases reinforcement [18]. Working range for voltage may be 20 V [21] to 44 V [25] depending upon type and thickness of the workpiece. Since wire feed rate is associated with arc current as to melt wire at higher welding speed more current is required. Since wire feed rate is AC controllable factor, its effect should be studied and value must be optimized to achieve good weld quality. With increasing feed rate penetration, reinforcement [18, 22, 29] and dilution rate [18, 21] increases. Depending upon workpiece feed rate should be selected wisely. If not sure feed rate can be selected by performing some pilot test before going for final welding.

Welding speed helps in defining texture, size, mechanical properties, and aesthetic quality of welding. Welding speed is the only parameter that can be selected between manual and automatic in case of SAW process. Too fast welding will not be good for proper welding and too slow welding melts off the material. Penetration, reinforcement, dilution in percentage and weld width is decreased with increasing welding speed [18], and thus welding speed is said to be negative impact factor for weld bead [20]. Standoff distance or nozzle to plate distance, sometimes termed as strikeout, is the distance between the surfaces to be welded from the nozzle tip of welding machine from which feed wire is guided. Increasing standoff penetration, dilution,

Table 1 Materials and methods for optimization

Ref. No.	Optimization method	Material	Thickness of plate welded (in mm)
[25]	Self-adaptive offset neural network	Lloyd's Grade A Shipbuilding Steel	12.5
[18]	Response surface methodology	IS 2062 Carbon Steel	6
[19]	Finite element modeling	X56 Steel	38
[1]	Taguchi optimization followed by ANOVA	Martensitic Stainless Steel	30
[20]	Design of experiments (DOE)-based factorial technique	IS 2062 Carbon Steel	6
[2]	Comparison with GMAW, Taguchi	Mild Steel	9.5
[29]	Sensitivity analysis	Mild Steel	10
[21]	Taguchi optimization	IS 2062 Carbon Steel	6.5
[14]	Multi-regression and ANN	IS 2062A	15
[12]	Taguchi, PSO, and genetic algorithm	IS 2062 Carbon Steel	6
[3]	Comparative analysis, ANN	ASTM A709	20
[8, 28]	Taguchi optimization	Mild Steel	20
[27]	Mathematical model	Mild Steel	12
[22]	LabVIEW software for thermal profiling	IS 2062 Carbon Steel	16.5
[24]	Jaya algorithm	AISI 1023	12
[9]	Response surface methodology	Stainless Steel	10
[4]	Taguchi optimization	ASME SA516 Gr.70 Steel	34
[6]	Comparative analysis	AISI 304 Austenitic Steel	12
[7]	Comparative analysis by adding niobium to flux	ASTM 131 AH 36 Steel	...
[11]	Taguchi optimization, ANN	ASTM A516 Gr. 70 Steel	8
[15]	Taguchi and ANN with C++	Mild Steel	10

(continued)

Table 1 (continued)

Ref. No.	Optimization method	Material	Thickness of plate welded (in mm)
[13]	Genetic algorithm, ANOVA, RSM, and regression method	Mild Steel	15
[26]	Response surface methodology	SS316, SS 304	...
[23]	Fractional factorial design	IS 2062 A	10

and weld width decreases but reinforcement increases [18]. Hardness and micro-hardness can be improved by selecting suitable flux [7, 23, 24] also current and voltage are responsible for hardness and strength [9, 15]. Flux is used to cover the weld zone during welding. It melts down and forms slag to protect weldment from harmful gases of environment. Flux always baked before using [1, 7, 14, 21, 24, 28, 30]. Adding niobium to flux improves micro-hardness of weld zone [6]. Sometime, binary and ternary system made of TiO_2 , SiO_2 , MgO , and Al_2O_3 [7] helps in improving mechanical, chemical, and physical properties of the flux which further improves thermal diffusion, stabilizes arc, and improves mechanical properties of weld. While selecting the flux great care is to be taken care. The SAW welding parameter and their effects are tabulated in Table 2.

5 Conclusions

On viewing the research articles by many researchers, the following points can be said

1. SAW process can be used for variety of steels.
2. SAW process can be used for different thickness of plates starting from 6 to 34 mm with single side and double side weld with different groove type and angles. Most suitable are V-notch.
3. Input parameters welding current, welding voltage, wire feed rate, welding speed, standoff distance, angle of contact between workpiece, and electrode wire produce their own effect as well as with interacting other input parameters.
4. Current plays most important role in defining the weld bead structure and mechanical properties.
5. Different fluxes have different effects on weld properties. They are responsible for arc stability, microstructure, micro-hardness, slag formation, and ease in slag removal.
6. Input parameters including fluxes can be optimized by DOE, mathematical models, Taguchi method, ANN, Jaya algorithms, and many more followed by ANOVA and gray relational analysis for regression to achieve the best output.

Table 2 SAW welding parameters and their effect

Ref. No.	Input parameter	Quality parameter	Conclusion/result
[25]	Arc current Arc voltage Welding speed	Reinforcement height Penetration Bead width Deposited area Fused area	On increasing arc voltage, fused area, and bead height were increased, but deposited area and width were found to behave uneven
[18]	Arc voltage Welding speed Wire feed rate Standoff distance	Reinforcement height Penetration Bead width Dilution rate	With increasing voltage penetration, dilution, width increased but reinforcement decreased, all the outputs were increased with increasing feed rate, all outputs decreased with increasing welding speed and with increment in standoff distance all outputs except reinforcement were decreased
[19]	Arc current Arc voltage Welding speed Wire number Feed wire diameter	Residual stress and strain Displacement	Residual stresses, strain, and distortion can be optimized by FEM for thin walled pipelines by altering process parameters
[1]	Arc Current Arc Voltage Welding speed Standoff distance	Hardness deposition rate dilution rate	Deposition rate increased from 6.36 to 8.58 kg/h, dilution decreased from 18.8 to 12.8 percent, and hardness was improved from 53.2 to 53.5 HRC
[20]	Arc voltage Wire feed rate Welding speed Standoff distance	Reinforcement height Penetration Bead width	For pipes such models can easily be employed for manual and automatic welding to obtain good weld bead size and impact of wire feed rate was positive and welding speed had negative impact on weld bead

(continued)

Table 2 (continued)

Ref. No.	Input parameter	Quality parameter	Conclusion/result
[2]	Arc current Arc voltage Wire feed rate	Reinforcement height Penetration Bead width Deposition rate	SAW operation cost is lower than gas metal arc welding, though the total cost is high for SAW. Further, they suggest that between these two processes selection should be done carefully by taking care of the initial cost and operational span
[29]	Arc current Arc voltage Welding speed	Reinforcement height Penetration Bead width	All three parameters affect all three outputs directly, however, voltage has high effect on width and current and speed has high effect on penetration
[21]	Welding speed Wire feed rate Standoff Arc current	Reinforcement height Penetration Bead width	Taguchi method is best suited for submerged arc welding for optimization of process parameters
[14]	Heat input Wire feed rate	Penetration Reinforcement Width	ANN can be used for graphical analysis of bead geometry which is suitable for online welding processes
[12]	Arc current Arc voltage Welding speed Standoff distance	Weld width	Values: 360 and 390 A current, 25 and 30 V voltage, 400 and 420 mm/min welding speed, and 19 and 25 mm standoff distance. Best values are 360 A, 30 V, 420 mm/min, and 19 mm for current, voltage, welding speed, and standoff, respectively, produces minimum width of 12.5 mm

(continued)

Table 2 (continued)

Ref. No.	Input parameter	Quality parameter	Conclusion/result
[3]	Heat input	Reinforcement Deposition rate Penetration HAZ	Reinforcement, deposition rate, penetration, heat affected zone was increasing with heat input but contact angle was decreasing for single and tandem welding methods and also increasing heat input melted electrode faster but there was no significant variation on plate melting
[30]	Arc current	Heat input	Model could directly be employed to shipyards in order to reducing heat input as well as cost, they included cost also
[8, 28]	Ratio of NiO, MgO, and MnO Arc current	Hardness Impact strength	Hardness and impact strength MnO and MgO are main factors and using NiO, MgO, and MnO 80gms, 85gms, and 50gms will be most suitable for optimum hardness and impact strength at 500 amperes welding current
[27]	Altering polarity Wire feed rate Arc voltage Welding speed Standoff distance	Bead size Reinforcement form factor penetration size factor	Bead size and reinforcement form factor were high in electrode positive and weld penetration size factor was high in electrode negative position
[22]	Arc voltage Welding speed Wire feed rate Standoff distance Two temperature level zero and 30 degree celcius of environment	Penetration	Environmental temperature has not a big effect on penetration but welding parameters have
[24]	Arc voltage Wire feed rate Welding speed standoff flux status Thickness of material	Reinforcement height Bead width Penetration	Welding speed plays important role along with wire feed rate and voltage for quality of weld. Baked fluxes have positive effect on quality of weld

(continued)

Table 2 (continued)

Ref. No.	Input parameter	Quality parameter	Conclusion/result
[5]	Ratio of CaO, TiO ₂ , Al ₂ O ₃ and MgO Arc Voltage	Hardness Impact strength	Improvement in S/N ration from 0.187 to 0.13605 when voltage was changed to 32 from 28 V by using CaO, TiO ₂ , Al ₂ O ₃ , and MgO 600 gms, 300 gms, 750 gms, and 400 gms, respectively
[9]	Arc current Arc voltage Welding speed Standoff distance	Reinforcement height Bead width Hardness	Increasing voltage increased bead width but reduced penetration and current has reverse effect and for hardness current is more responsible as compared to other parameters
[4]	Arc current Arc voltage Welding speed Heat input	Tensile strength Hardness Deposition rate	Increasing voltage increased bead width but reduced penetration and current has reverse effect and for hardness current is more responsible as compared to other parameters
[6]	Current	Bead geometry	Dendrites were forming from base and moved toward center in majority. On increasing current width was increasing but stopped at higher current values. Increasing current increases reinforcement, penetration depth, tensile strength, and also heat input
[7]	Adding niobium to flux	Hardness Strength	Niobium was dissociated with its compound and formed niobium oxide along grain boundaries of fusion zone having higher content of Niobium at face and root and moderate at middle, micro-hardness was improved, yield strength was decreased and ductility in case Nb2O5 was improved

(continued)

Table 2 (continued)

Ref. No.	Input parameter	Quality parameter	Conclusion/result
[11]	Combinations of TiO ₂ , SiO ₂ , MgO, and Al ₂ O ₃	Thermal analysis Chemical Analysis Grain size of mixture Physical properties	Individual flux component affect density only but not other mechanical properties. Among all four individual compounds SiO ₂ -MgO only increased grain size of the mixture and other binaries were not good. TiO ₂ -SiO ₂ -MgO and SiO ₂ -MgO-Al ₂ O ₃ were found to be synergetic in aspects of grain size of mixture. Al ₂ O ₃ improves thermal diffusion process
[10]	Arc voltage Wire feed rate Welding speed	Strength Hardness	Optimized voltage, feed rate, welding speed, and standoff distance as 29 V, 5.5 m/minute, 0.4 m/minute, and 24 mm
[31]	Various	Various	Multi-pass welding improves tensile strength and hardness due to multiple thermal cycles. Adding manganese, sulfur, and silicon may improve properties of weld
[15]	Arc voltage Arc current Wire feed rate Welding speed	Hardness	Hardness by ANN as impact of current was highest among all inputs. Maximum error reported was at 450 amperes, 42 V, 70 mm/minute feed rate, and 1150 mm/min
[13]	Arc current Arc voltage Standoff Welding speed	Temperature Repair result	The results were obtained by four methods of optimization ANOVA, regression analysis, RSM, and genetic algorithm. The temperature is affected by generally with arc current and voltage
[26]	Arc current Arc voltage Welding speed	Width and height of weld bead	It was observed that arc voltage and current affect the width and height of bead while welding speed is not effective

(continued)

Table 2 (continued)

Ref. No.	Input parameter	Quality parameter	Conclusion/result
[23]	Arc voltage Welding speed Wire feed rate Electrode dia Flux	Bead height Bead width Penetration hardness	Bead height and penetration are most affected by electrode diameter and welding speed. Hardness can be controlled by arc voltage

References

1. Tarng YS, Juang SC, Chang CH (2002) The use of grey-based Taguchi methods to determine submerged arc welding process parameters in hardfacing. *J Mater Process Technol* 128(1–3):1–6
2. Correia DS, Ferraresi VA (2007) Welding process selection through a double criteria: operational costs and non-quality costs. *J Mater Process Technol* 184:47–55
3. Shen S, Oguocha INA, Yannacopoulos S (2012) Effect of heat input on weld bead geometry of submerged arc welded ASTM A709 grade steel joints. *J Mater Process Technol* 212(1):286–294
4. Ahmad MA, Sheikh AK, Nazir K (2019) Design of experiment based statistical approaches to optimize submerged arc welding process parameter. *ISA Trans* 94:307–315
5. Choudhary S, Shandley R, Kumar A (2018) Optimization of agglomerated fluxes in submerged arc welding. *Mater Today Proc* 5(2, Part 1):5049–5057
6. Sridhar PVSS, Biswas P, Mahanta P (2019) Influence of welding current and mechanical properties of double sided submerged arc welding of AISI 304 austenitic stainless steel. *Mater Today Proc* 19(part 2):831–836
7. Osorio AG, Souza D, dos Passos T, Dalpiaz L, Aires T (2019) Effect of niobium addition on the flux of submerged arc welding of low carbon steels. *J Mater Process Technol* 266:46–51
8. Kumar A, Maheshwari S, Sharma SK (2015) Fuzzy logic optimization of weld properties for SAW using silica based agglomerated flux. *Procedia Comput Sci* 57:1140–1148
9. Vedrtnam A, Singh G, Kumar A (2018) Optimizing submerged arc welding using response surface methodology, regression analysis and genetic algorithms. *Defence Technol* 14(3):204–212
10. Sailender M, Suresh R, Chandramohan Reddy G, Venkatesh S (2020) Prediction and comparison of the dilution and heat affected zone in submerged arc welding (SAW) of low carbon alloy steel joints. *Measurement* 150, article 107084
11. Sharm L, Chhibber R (2019) Investigation of physicochemical and thermophysical properties of submerged arc welding fluxes designed using TiO_2 - SiO_2 - MgO and SiO_2 - MGO - Al_2O_3 flux system for linepipe steels. *Ceramics Int* 45(2, Part A):1569–1587
12. Edwin Raja Dhas J, Kumanan S (2011) Optimization of parameters of submerged arc weld using non conventional techniques. *Appl Soft Comput* 11(8):5198–5204
13. Sahare P, Pradhan SK (202) Experimental Investigation and optimization of submerged arc weldiing on windmill tower using genetic algorithm. *Proceedings*, In press, Issue NA, Available online on 29 April 2020
14. Ghosh A, Chattopadhyaya S, Das RK, Sarkar RK (2011) Prediction of submerged arc welding yield parameters through graphical techniques. *Procedia Eng* 10:2797–2802
15. Singh RP, Singh A, Singh A (2020) Optimization of hardness of weld in submerged arc welding. *Materials Today: Proc*. In press as on 14 May, 2020, Issue NA, Available online on 18 April 2020
16. Houldcroft PT (1989) *Submerged arc welding*, 2nd edn. Woodhead Publishing Limited
17. Weman K (2012) *Submerged arc welding*. *Welding Processes Handbook*, pp 105–117
18. Gunaraj V, Murugan N (1999) Application of response surface methodology for predicting weld bead quality in submerged arc welding of pipes. *J Mater Process Technol* 88(1–3):266–275
19. Wen SW, Hilton P, Farrungia DCJ (2001) Finite element modelling of a submerged arc welding process. *J Mater Process Technol* 119(1–3):203–209
20. Murugan N, Gunaraj V (2005) Prediction and control of weld bead geometry and shape relationship in submerged arc welding of pipes. *J Mater Process Technol* 168(3):478–487
21. Ghosh A, Chattopadhyaya S, Sarkar PK (2011) Critical analysis of confounded parameters of saw process. *Procedia Eng* 10:2786–2790
22. Biswas A, Bhowmik A (2018) Study of heat generation and it's effect during submerged arc welding (SAW) on mild steel plate at zero degree celcius plate temperature. *Mater Today Proc* 5(5, Part 2):13400–13405

23. Rathi AK (2020) To study the effect of submerged arc welding parameters on bead geometry and hardness for mild steel (IS-2062A) using fractional factorial design. *Mater Today Proc.* Available online on 31 March 2020
24. Choudhary A, Kumar M, Unune DR (2018) Experimental investigation and optimization characteristics during submerged arc welding of AISI 1023 steel. *Defence Technol* 15(1):72–82
25. Li P, Fang MTC, Lucas J (1997) Modelling of submerged arc weld beads using self adaptive offset neural networks. *J Mater Process Technol* 71(2):288–298
26. Sharma P, Mohal S (2020) Parametric optimization of submerged arc welding process parameters by response surface methodology. *Mater Today Proc* 24(Part 2):673–682
27. Singh RP, Garg RK, Shukla DK (2016) Mathematical modelling of effect of polarity on weld bead geometry in submerged arc welding. *J Manuf Process* 21:14–22
28. Kumar A, Maheshwari S, Sharma S (2015) Optimization of Vickers hardness and impact strength of silica based fluxes for submerged arc welding by Taguchi Method. *Mater Today Proc* 2(4–5):1092–1101
29. Karaoglu S, Secgin A (2008) Sensitivity analysis of submerged arc welding process parameters. *J Mater Process Technol* 202(1–3):500–507
30. Lu Y, Chen JS, Jhang YM, Kvidahl L (2014) Predictive control based double-electrode submerged arc welding for fillet joints. *J Manuf Process* 16(4):415–426
31. Sharma H, Rajput B, Singh RP (2020) A review paper on effect of input welding parameters on structure and properties of weld in submerged arc welding process. *Mater Today Proc.* In press as on 14 May, 2020, Issue NA, Available online on 13 March 2020

Free Vibration Analysis of FGM Conical Shell



Prabhat Mahawar and Pankaj Sharma

Abstract Present study deals with modal behavior of FG material conical shell under different boundary conditions. Material properties are varied in the thickness direction with power law distribution. The modal analysis of isotropic and FGM conical shell is accomplished by using FEA software COMSOL Multiphysics (version 5.0). Modal values acquired by present work are validated with modal values computed using numerical method for reduce case. Effects of power law index and semi-cone angle on modal values are presented.

Keywords Vibration analysis · Conical shell · COMSOL

1 Introduction

The composite materials were used in many engineering fields, but they were not stable at high-temperature conditions. Later, a ceramic material was used in place of composite material. It was more stable at high-temperature conditions than composite materials but it mechanically unstable due to low toughness. To get rid of this instability, the new material has been invented in 1984 in Japan called as functionally graded material (FGM). It can withstand at high-temperature conditions up to 2000 °C and specially designed for aerospace industries. The FGM is referred as a material with changing porosity, microstructure, and composition through the volume of material [1]. The FGMs were designed by varying properties with the volume of bulk material regarding their area of application in which they can be used. There are different types of FGM available.

P. Mahawar (✉) · P. Sharma
Department of Mechanical Engineering, University Teaching Department, Rajasthan Technical University, Kota, Rajasthan, India

P. Sharma
e-mail: psharma@rtu.ac.in

2 Literature Survey

Fares et al [2] studied of FG truncated conical shell. The conical shell is made up of orthotropic material. Mori–Tanaka model was developed to analyze the modal behavior of conical shell. “Multiphase nano-composite viscoelastic laminated conical shell was developed by HadiHaj Mohammad et al [3]. Haar Wavelet differential method [HWDM] was employed to acquire mathematical results of laminated composite viscoelastic conical structure. Differential quadrature method (DQM) was employed by Ahmed Farrokhian et al [4]. Laminated reinforced conical shell has been taken into consideration to obtain the modal values. Final results were gained by using layerwise theory with DQM. Yasir Kiani et al [5] presented the free vibration study of composite conical panels reinforced with FG-CNT’s.” FGM was used as material of panels. All the mathematical equations were solved by Hamilton’s principle. Material properties of structure are variable with thickness and uniformly distributed with power law. Parametric instability analysis of truncated conical shell was studied by Qiyi Dai and Qingjie [6]. Mathematical formulation has been made by Haar Wavelet method and Bolotin’s method. Modal behavior of shell was analyzed by applying the Fourier series.

By using Galerkin method, Nguyen Dinh Duc et al. [7] presented the thermal and mechanical stability of FG conical shell reinforced by composite surrounded by the elastic foundation. The classical shell theory with FSDT has been adopted to describe the modal behavior of the conical structure. The modal behavior of FGM structures with and without graded properties is available in the literature [8–16].

3 Research Methodology

The mechanical parameters of the shell can be written as:

$$E(z) = (E_1 - E_2)V_1 + E_2 \quad (1)$$

$$\mu(z) = (\mu_1 - \mu_2)V_1 + \mu_2 \quad (2)$$

$$\rho(z) = (\rho_1 - \rho_2)V_1 + \rho_2 \quad (3)$$

where V_1 and V_2 are the volume fraction of ceramic and metal defined as:

$$\text{FGM}_1(m/n/o/p) : V_1 = [1 - m(0.5 + z/h) + n(0.5 + z/h)^o]^p \quad (4)$$

$$\text{FGM}_2(m/n/o/p) : V_1 = [1 - m(0.5 - z/h) + n(0.5 - z/h)^o]^p \quad (5)$$

Here $m, n, o,$ and p are the material parameters used in Ref. [18]. It is presumed that the sum of volume fractions of ceramic (V_1) and metal (V_2) is written as

$$V_1 + V_2 = 1$$

4 Result

Free vibration behavior of conical shell is considered where mechanical parameters are changing according to power law distribution. The mechanical constants are presumed to be changing in accordance with rule of mixture (P-FGM) along the thickness direction. The fundamental natural frequencies under fixed and fixed-free boundary conditions for different values of power law index (p) at different semi-cone angle (α) are reported. The FE software COMSOL is used to attain the natural frequencies. The volume fraction range is $p = 1$ to $p = 4$ considered in this work. Material properties are taken from [17]. The results are attained using FE software COMSOL Multiphysics® (version 5.0) for different semi-cone angle (α) and are displayed in Table 1. It could be seen that with the increase of semi-cone angle (α in degrees), the natural frequencies decrease under fixed-free boundary condition which is shown in Table 1, and modal values for FGM conical shell under fixed-fixed boundary condition are displayed in Table 2 for wide range of volume fraction index

Table 1 Natural frequencies (Hz) of FGM1 conical shell under fixed-free boundary condition under power law ($R1 = 0.5$ m, $L\sin \varphi = 2$ m, $\varphi = 50^\circ$, $m = 1$, $h/R1 = 0.10$)

Mode	p	Frequency (Hz)			
		$\alpha = 40$	$\alpha = 50$	$\alpha = 60$	$\alpha = 70$
1	1	174.35	110.47	62.541	30.362
2	2	181.7	116.56	64.830	30.916
3	3	191.78	124.29	67.898	31.842
4	4	203.52	131.79	71.496	33.004

Table 2 Natural frequencies (Hz) of FGM conical shell ($R1 = 0.5$ m, $L\sin \varphi = 2$ m, $\varphi = 50^\circ$, $m = 1$, $h/R1 = 0.20$)

Mode	p	Frequency (Hz)			
		$\alpha = 40$	$\alpha = 50$	$\alpha = 60$	$\alpha = 70$
1	2	196.72	123.82	68.305	33.564
2	3	207.30	131.02	71.529	34.461
3	4	219.58	138.89	75.299	35.728
4	5	232.75	146.80	79.473	37.293

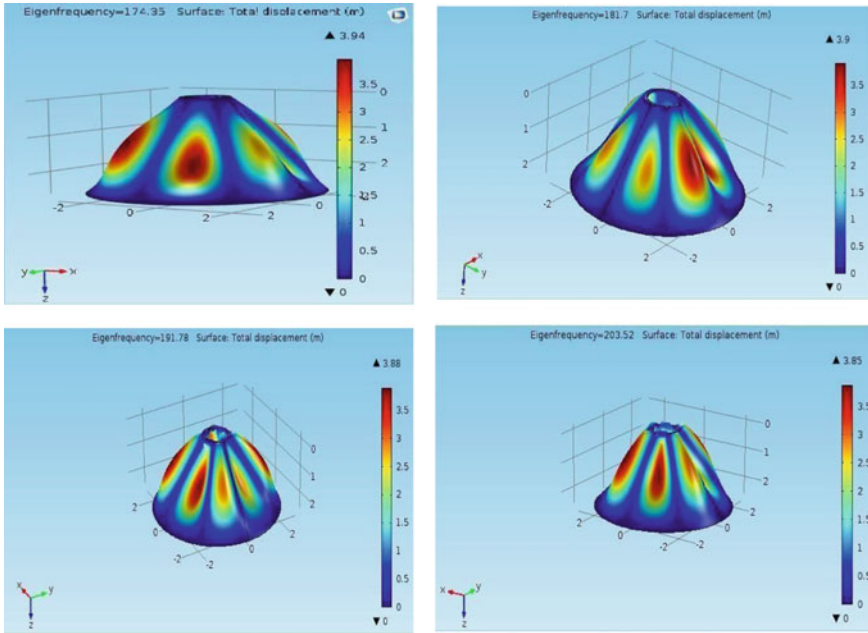


Fig. 1 Mode shapes of FGM conical shell under fixed-free end condition ($R_1 = 0.5$ m, $L \sin \varphi = 2$ m, $\varphi = 50^\circ$, $m = 1$, $h/R_1 = 0.10$) at ($\alpha = 40$)

and semi-cone angle. It might be observed that with increase in volume fraction index, the modal values increase. It may also be observed that with increase in semi-cone angle, the modal values decrease.

The mode shapes of FGM conical shell under fixed-free end condition are displayed in Fig. 1.

The variation of modal values with semi-cone angles (α) is displayed in Fig. 2 for different values of volume fraction indices.

5 Validation Study

The geometry of FG conical is shown in Fig. 3.

The geometric parameters are as small end radius ($R_1 = 0.5$ m), thickness ($h = 0.1$ m), $\varphi = 50^\circ$, $L \sin \varphi = 2$. The modal values attained by using FEM software under fixed-fixed end condition are exhibited in Table 3. The modal values reported by FEM are well satisfied with result published in [18].

The deform shape of FGM conical shell is displayed in Fig. 4. The results acquired by using FEM for FGM conical shell are exhibited in Table 4. The effective mechanical parameters are taken from [17].

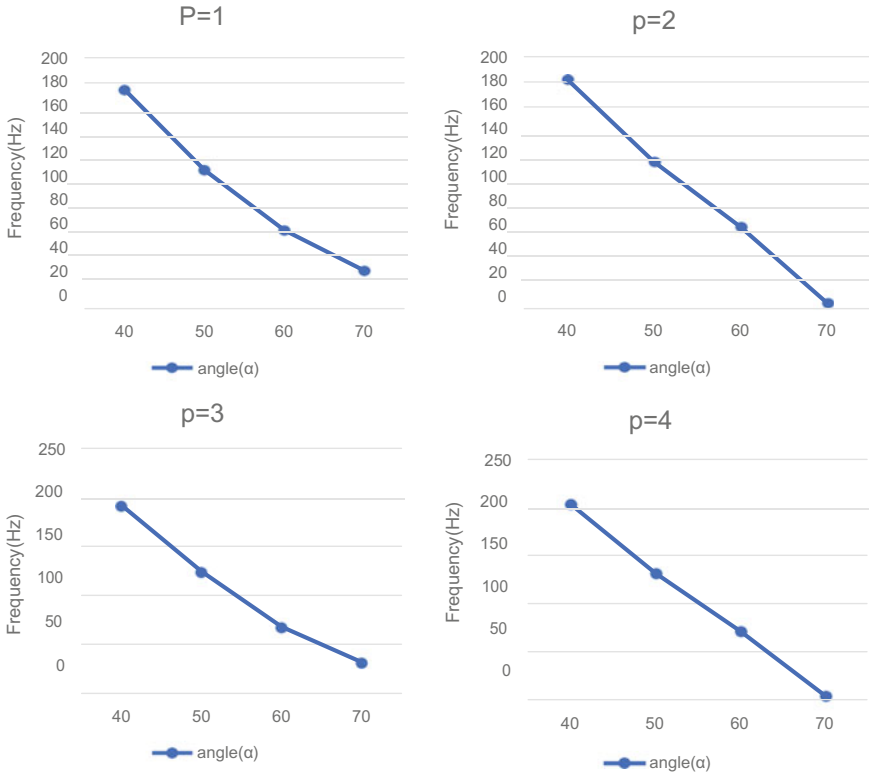


Fig. 2 Behavior of modal values versus α for FGM shell under fixed-free boundary condition

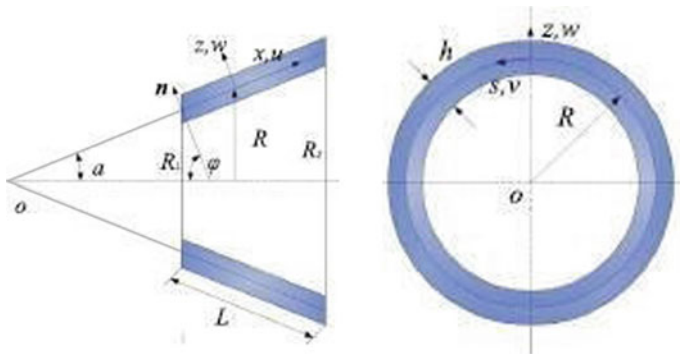


Fig. 3 Model of FGM shell [17]

Table 3 Validation of modal values of homogeneous conical shell

Frequency (Hz)	Ref. [18] [DQM]	Ref. [18] HWDM	FEM	Error (%)
F1	227.59	227.61	227.67	0.03
F2	227.59	227.61	227.0.67	0.03
F3	239.71	239.72	237.23	1.03
F4	239.71	239.72	237.23	1.03
F5	275.27	275.33	267.45	2.84
F6	275.27	275.33	267.45	2.84
F7	333.69	333.72	332.33	0.40
F8	333.69	333.72	332.33	0.40
F9	350.59	350.65	351.43	0.23
F10	350.59	350.65	351.43	0.23

6 Conclusion

Free vibration analysis FGM conical shell has been computed where mechanical parameters are graded continuously across thickness using power law distribution. The modal values of conical shell have been attained for fixed-free and fixed-fixed end condition. The modal values are computed using FEM software. The effect of geometric parameters, semi-cone angle, and power law index on fundamental modal values is explored. It could be seen that with the increase of semi-cone angle (α), the natural frequency decreases under fixed-free boundary condition. In now a day, conical shells are used in many engineering fields.

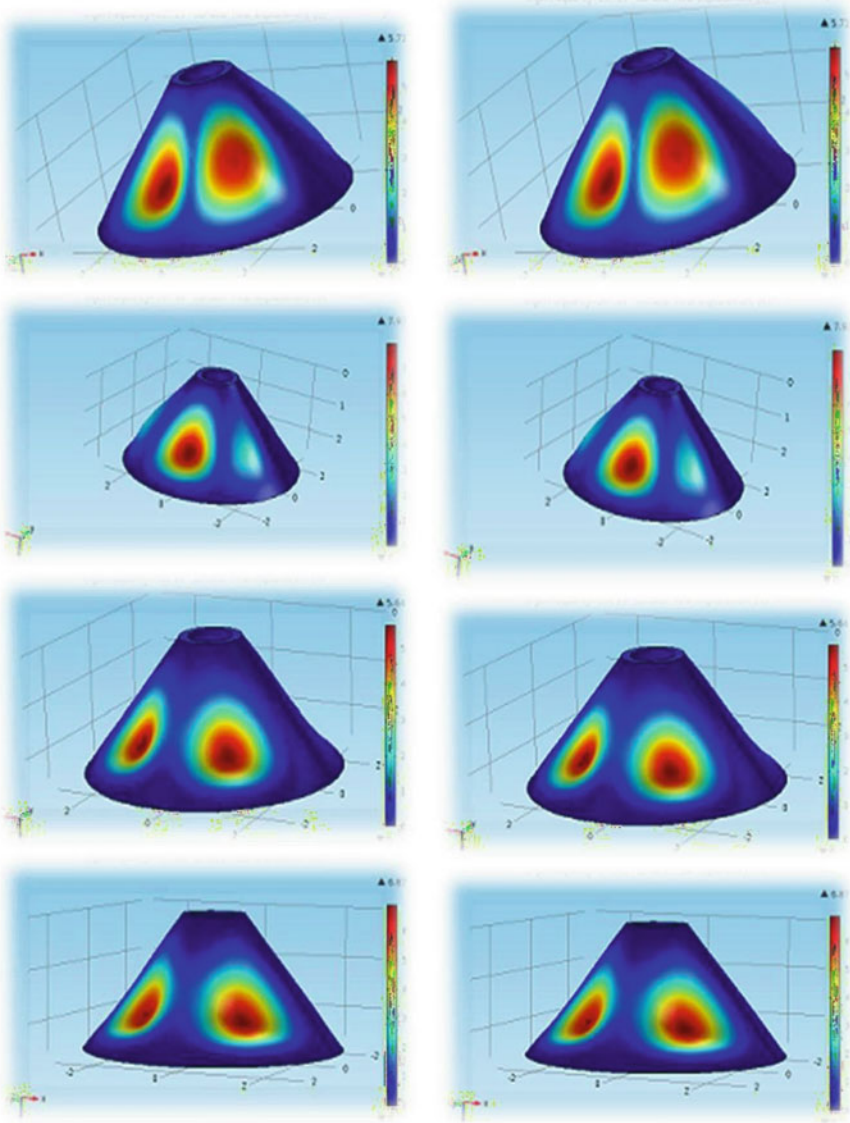


Fig. 4 Deform shapes of conical shell ($R1 = 0.5$ m, $h = 0.1$ m, $\varphi = 50$, $L \sin \varphi = 2$)

Table 4 Frequencies of FGM1 conical shell under ($R1 = 0.5$ m, $L\sin\varphi = 2$ m, $\varphi = 50^\circ$, $m = 1$) with fixed-free and fixed-fixed end condition

P	h/R1	Boundary condition	FGM1 ($m = 1/n = 0/o/p$)			
			Ref. [19] Exact	Ref. [18] HWDM	COMSOL	Error (%)
1	0.10	C-F	174.301	174.412	174.35	0.02
5	0.20	C-C	232.923	232.994	232.75	0.07

References

1. Bhavar V, Kattire P, Thakare S, Singh RK (2017) A review on functionally gradient materials (FGMs) and their applications. IOP Conf Ser Mater Sci Eng 229(1):012021
2. Fares ME, Youssif YG, Hafiz MA (2004) Structural and control optimization for maximum thermal buckling and minimum dynamic response of composite laminated plates. Int J Solids Struct 41(3–4):1005–1019
3. Zarei MS, Kolahchi R, Hajmohammad MH, Maleki M (2017) Seismic response of underwater fluid-conveying concrete pipes reinforced with SiO₂ nano particles and fiber reinforced polymer (FRP) layer. Soil Dyn Earth Eng 103:76–85
4. Hajmohammad MH, Zarei MS, Nouri A, Kolahchi R (2017) Dynamic buckling of sensor/functionally graded-carbon nanotubes reinforced laminated plates/actuator based on sinusoidal-viscopiezoelectricity theories. J Sandw Struct Mater (In press)
5. Kiani Y (2016) Free vibration of functionally graded carbon nanotube reinforced composite plates integrated with piezoelectric layers. Comput Math Appl 72:2433–2449
6. Zhang LW, Cui WC, Liew KM (2015) Vibration analysis of functionally graded carbon nanotube reinforced composite thick plates with elastically restrained edges. Int J Mech Sci 103:9–21
7. Duc ND, Cong PH, Anh VM, Quang VD, Phuong T, Tuan ND, Thinh NH (2015) Mechanical and thermal stability of eccentrically stiffened functionally graded conical shell panels resting on elastic foundations and in thermal environment. J Compos Struct 132:597–609
8. Parashar SK, Sharma P (2016) Modal analysis of shear-induced flexural vibration of FGPM beam using generalized differential quadrature method. Compos Struct 139:222–232
9. Sharma P, Parashar SK (2016) Free vibration analysis of shear-induced flexural vibration of FGPM annular plate using Generalized Differential Quadrature method. Compos Struct 155:213–222
10. Sharma P (2018) Efficacy of harmonic differential quadrature method to vibration analysis of FGPM beam. Compos Struct 1(189):107–116
11. Sharma P, Singh R, Hussain M (2020) On modal analysis of axially functionally graded material beam under hygrothermal effect. Proc Inst Mech Eng C J Mech Eng Sci 234(5):1085–1101
12. Sharma P (2019) Vibration analysis of functionally graded piezoelectric actuators. Springer, New York, NY
13. Sharma P, Parashar SK (2016) Exact analytical solution of shear-induced flexural vibration of functionally graded piezoelectric beam. In: AIP conference proceedings, 6 May 2016, vol 1728, no 1. AIP Publishing LLC, p 020167
14. Sharma P, Singh R (2019) Investigation on modal behaviour of FGM annular plate under hygrothermal effect. In: IOP conference series: materials science and engineering, Oct 2019, vol 624, no 1. IOP Publishing, p 012001
15. Singh R, Sharma P (2019) A review on modal characteristics of FGM structures. In: AIP conference proceedings 3 Sep 2019, vol 2148, no 1. AIP Publishing LLC, p 030037
16. Khinchi A, Sharma P (2020) Free vibration analysis of isotropic spherical cap and FG-spherical cap with cut-out using COMSOL. In: AIP conference proceedings, 4 May 2020, vol 2220, no 1. AIP Publishing LLC, p 130074

17. Liew KM, Ng TY, Zhao X (2005) Free vibration analysis of conical shells via the element-free kp-Ritz method. *J Sound Vib* 281:627–645
18. Tornabene F, Viola E, Inman DJ (2009) 2-D differential quadrature solution for vibration analysis of functionally graded conical, cylindrical shell and annular plate structures. *J Sound Vib* 328:259–290
19. Qu YG, Long XH, Yuan GQ, Meng G (2013) A unified formulation for vibration analysis of functionally graded shells of revolution with arbitrary boundary conditions. *Compos Part B Eng* 50:381–402

Performance Improvement of Microsurfacing Machine: A Case Study



Kratika Ravekar and Santosh Jaju

Abstract Microsurfacing has been used in the United States since 1980 as an upkeep treatment for asphalt. The paper shows the advantages, impediments and elements that add to effective utilizations of microsurfacing. The historical backdrop of microsurfacing, too as a definition and procedure portrayal of the treatment, is incorporated. The assemblage of logical work on microsurfacing is appeared to advance its utilization in preventative maintenance programs, and the potential for microsurfacing to meet fixing ecological and budgetary limitations. Recommendations are given for future exploration to extend microsurfacing's applications and adequacy. This case study consists of the different test and methodology used for the microsurfacing. It is shows that how different authors have used various method and tools to make microsurfacing more effective. The present work is showing that the microsurfacing machine which is present in the industry faces some problem, while working on site, i.e., sticking of microsurfacing material on the material discharge plate. Due to which machine has to stop for cleaning it and after that it is back to the further work. Some design modifications can be done to solve the problem of sticking microsurfacing material on discharge plate.

Keywords Microsurfacing · Microsurfacing machine · METONG machine · Requirements of microsurfacing mixture · Material discharge plate

1 Introduction

Microsurfacing is a fast traffic framework that permits traffic to return not long after arrangement. Microsurfacing ought to be fit for acting in factor thickness cross-segments, for example, grooves, scratch courses and processed surfaces. In the wake

K. Ravekar (✉) · S. Jaju
Department of Mechanical Engineering, G H Raisoni College of Engineering, Nagpur,
Maharashtra 440016, India
e-mail: Ravekar_kratika.ghrcemtechcad@raisoni.net

S. Jaju
e-mail: Santosh.jaju@raisoni.net

© The Author(s), under exclusive license to Springer Nature Singapore Pte Ltd. 2022
K. Govindan et al. (eds.), *Advances in Mechanical and Materials Technology*,
Lecture Notes in Mechanical Engineering,
https://doi.org/10.1007/978-981-16-2794-1_8

of relieving and starting traffic solidification, it should oppose further compaction. The smaller scale surfacing will be applied as a homogeneous tangle, hold fast solidly to the readied surface, and have a slide safe surface all through its administration life. In indistinguishable classification of asphalt medicines from seal covering and slender hot blend asphalt overlays, microsurfacing medicines spread the whole width of the street to which they are applied. For the most part microsurfacing is delegated a safeguard support treatment instead of a remedial upkeep treatment due to the huge capacity of microsurfacing to seal and re-establish asphalt surfaces however the powerlessness of microsurfacing to improve auxiliary defects [1].

1.1 Requirements of Microsurfacing Mixture

The mixture requires polymer modified bitumen emulsion, aggregates, synthetic polypropylene fiber to resist abrasion and crack, cement, water and additive.

(I) Bitumen Emulsion Properties

The sort of bitumen utilized has an effect on the blending and setting properties of the emulsion produced using it. The key execution attributes are the infiltration and corrosive estimation of the bitumen. For trench filling purposes, a 60/70 entrance grade bitumen was utilized instead of an 80/100-infiltration bitumen which is regularly utilized for overlay purposes. The base bitumen was gotten from center east unrefined which has low-corrosive qualities. An elastomeric SBR polymer was consolidated into the emulsion to improve the consistency and union of the microsurfacing and at last the solidness of the surfacing. For ideal emulsion quality, the engineered-elastic latex was presented by means of the water stage preceding processing during the emulsion preparing. The emulsion was uncommonly defined to give the ideal breaking time and to guarantee adequate setting properties of the blend during placing.

(II) Aggregate

The main necessity is to guarantee that the up-and-comer total can be dependably provided to the predetermined reviewing. The reactivity of the total impacts the emulsifier type and focus required to give a sufficient blending time. The methylene blue and sand proportionality tests were utilized to explore total movement. A mix of washed and unwashed smasher dust sourced from Alpha Stone's Pietermaritzburg quarry was chosen. Smasher dust adjusting to the 0/8 evaluating and meeting the prerequisites were utilized rather than the 0/6 reviewing which is utilized for overlays. The significant segment and generally condemning of the blend for long haul execution. Total source, degree and tidiness factor in the conduct of the framework. Total tests required for lab blend structure.

(1) Gradation, (2) Hardness, (3) Soundness, (4) Sand Equivalent, (5) Methylene Blue, (6) Water Absorption.

- (III) Polymer modification
Reduces the temperature helplessness, the blend can be put in thicker lifts while stays stable, the blend is speedy setting, enhanced toughness.
- (IV) Mineral fillers
Mineral filler—portland cement, hydrated Lime, or aluminim sulfate are utilized. The mineral filler contributes the ideal blending and setting attributes of the framework and improves the consistency of the micro surface blend.
- (V) Other system components
Chemical added substances used to hinder or quicken the break of the framework blend, application hardware and practices, environmental conditions, road conditions, weather, water—should be a consumable asset free of defiles that could influence the framework blend.

1.2 Advantages

- Pollution free as no warming is required.
- Very quick execution (up to 2 km/path/day) and could be opened for traffic inside 1–2 h (contingent upon climate conditions)
- Quick development
- Higher protection from scraped area
- Longer life as oxidation/maturing is diminished.
- No rolling and compaction are required
- Saving in regular assets
- Cost compelling
- Water opposition, slide obstruction
- Provide slip obstruction
- Improve feel
- Correct rutting and minor surface profile inconsistencies
- Average execution life: 5–7 years
- Minimize oxidation/maturing, diminish water invasion, right ravelling and enduring.

1.3 Breaking/Setting/Curing

- **Breaking**—An emulsion breaks when the black-top drops start to re-consolidate. Outwardly saw when the material changes from earthy colored to dark and can never again be hand worked. Breaking of microsurfacing blend ought to be in the middle of 2–3 min.
- **Setting**—As the total is covered by the bitumen, the slurry blend sets. This is the point at which the underlying removal of water happens. At the point when water leaves the framework and bitumen accomplishes its unique state. Setting of microsurfacing blend ought to be for the most part in a short time.

- **Curing**—Not the entirety of the water is ousted during the breaking and setting. Relieving is the term utilized for the ejection of a large portion of the water from the tangle through vanishing or substance response.

It ought to be noticed that last fix (all out lack of hydration) can take times of as long as about fourteen days; nonetheless, the vast majority of the water is removed inside 24 h after application. As of now the aggregate is completely secured with asphalt.

1.4 Site Process

- All raw materials, i.e., aggregates, fiber, emulsion, water, cement and additive are feeded in to the slurry truck.
- Calibrate the machine to ascertain required flow of all ingredients.
- All surface area should be clean to remove dust and debris with air compressor and should be mark with safety cones prior laying of mix.
- Arrange labors for monitoring and adjusting laying, thickness, etc.
- Set flows for all ingredients and start production [2].

2 Case Study on Approaches Adopted by Previous Research for Performance Improvement

Mahdi Zalnezhad and Ebrahim Hesami executed that microsurfacing surface treatment was estimated and surveyed by utilizing steel slag material and thought about it by siliceous totals.

- The total tests indicated that the steel slag has necessary properties to use for microsurfacing blends. The outcomes got from the union test, it was perceived that blends containing steel slag had more twist force and attachment than control blend, and therefore, it is increasingly reasonable for traffic reviving.
- The outcomes got from wet-track abrasion test (WTAT) for 6 days, blends contain steel slag that has much lower weight reduction than the control blend. As it were, steel slag total expands the obstruction of black-top blend against stripping occasion.
- The disfigurement of blends by means of loaded wheel test, it was perceived that siliceous blend in ideal bitumen has a more fragile presentation than the blends containing steel slag, and sometimes, it has surpassed the suggested limitations. Also, the “blend containing 100% of steel slag has more side long and vertical removal than the blend containing 60% steel slag” [7].

Dominique M. Pittenger & Douglas D. Gransberg stated that the total aggregate gathered from the Gurunanak smasher plant close by IIT-Guwahati had utilized in their investigation. Three kind of total example has gathered from smasher plant. “Test 1 is coarse total which is 9.5 mm passing and 4.75 held. Test 2 is fine total which is 4.75 mm passing. Test 3 is dust which is passing 4.75 mm passing”. To start with, the examination uncovers the estimation of long haul PPT field research, just as a need to join both execution information and cost information when PPTs are thought about. The investigation likewise exhibits the possible practicality of portland cement slurry seal (PCSS) as a groove filling pavement preservation treatments (PPT), giving quantitative proof to remembering it as a possibility for the common US department of transportation’s asphalt safeguarding program. The examination created field preliminary information that exhibited that both microsurfacing and PCSS perform viably and similarly based on surface rubbing under a similar traffic and climatic conditions. Both PPTs offer conceivably practical answers for filling grooves and expanding asphalt administration life. The significant commitment of the paper is to improve the asphalt support designer’s possibilities for stretch the department of transportation (DOT) financial plan by choosing the “right treatment” for a given asphalt safeguarding venture [3].

Mostafa Poursoltani and Saeid Hesami uses the Reclaimed asphalt pavement in microsurfacing blend. It was inspected as part of stone materials or every one of them and its exhibition was contrasted and that of the traditional microsurfacing blend. The utilization of reclaimed asphalt pavement in microsurfacing, aside from the positive natural impacts, could improve a portion of the properties of the blend. In addition, to accomplish better after effects of microsurfacing blend containing reclaimed asphalt pavement.

- Mixtures containing RAP indicated a more fragile exhibition contrasted with the blend containing 100% Virgin aggregate in both attachment test and WTAT (Wet-track abrasion test), proposing that the bond of bitumen emulsion with the matured bitumen spread over the RAP total surface was not as much as its attachment to the virgin aggregate and was disturbed in a wet domain.
- The effects of the wet stripping test, Reclaimed asphalt pavement consolidation in microsurfacing blends can take care of the issue of total non-covering generally. Likewise, in the attachment test, tests containing RAP showed a more noteworthy obstruction to keep up total covering. Concerning short opening time of microsurfacing, keeping up progressively total covering in the union test can be critical.
- Mixtures containing reclaimed asphalt pavement had a higher protection from flushing trouble. What is more, with an expansion in RAP substance of the blend, this marvel happens at a higher temperature.
- The ideal bitumen required for blends containing reclaimed asphalt pavement was higher than that of the blend containing completely virgin aggregate up to 1%.
- The blends containing 43%, 69%, and 95% RAP, the one with 69% RAP demonstrated a superior exhibition [4].

Shuguang Hou, Chen Chen, Junhui Zhang, Huajie Shen and Fan Gu described four distinctive cationic emulsifiers that were used to get ready black-top emulsions, and their impacts on the capacity strength and warm soundness were researched. Likewise, the impacts of an assortment of elements on the presentation of micro-surfacing blends were assessed, including blending time, demulsification time and wet-track abrasion test (WTAT). The objectives of the study were to “explore the correlations between different stability tests, and investigate the influence of different factors on the performances of microsurfacing mixtures properties”.

- Fresh asphalt emulsions would in general have little molecule size and more prominent explicit surface region. Black-top emulsion arranged with quaternary ammonium salt emulsifier yielded the small molecule size and most prominent explicit surface region, which demonstrated the most elevated stockpiling solidness, trailed by asphalt emulsions.
- The stockpiling solidness test results were in concurrence with molecule size and explicit surface region results, and there was a straight connection between square of molecule size and capacity strength results.
- Asphalt emulsion arranged with xylonamide emulsifier yielded the most noteworthy warm steadiness, and no predictable positioning was found between capacity dependability and warm soundness.
- All impact factors examined above affect blending time and demulsification time of blends, total degree, total temperature, extra water content, concrete substance and sand proportional.
- Mixtures with higher black-top emulsion substance and sand equal would in general have higher early quality and lower dampness helplessness [5].

3 Approach Adopted in the Present Work

Microsurfacing is used for the road construction, repairing and maintenance. When the emulsion falls on the discharge plate the emulsion (thick solution) sticks over material discharge plate which is presently in rubber form, due to its quick procedure the water gets evaporated and the residue left is only the bitumen which sticks over the material discharge plate. Material discharge plate has to be cleaned after every pass to remove the bitumen which gets struck over the plate. For removing the microsurfacing material along with water an opposite adhesive mixture is being used whose properties are just opposite to the adhesive which allows the material to clean over the plate. By using the opposite adhesives, the material is prevented from sticking of the bitumen. The material which is being stick over the plate can be removed by solvents which can be purchased from outside.

To remove this there is need of “Acetone, white spirit, dichloride and MTO chemical that is Mineral turpentine oil”. These solvents are used to remove stuck material discharge plate, but these material turns out to be costly and they are not eco-friendly it catches fire easily. So, the solvents cannot be used frequently to remove the stick bitumen from “material discharge plate which is of rubber material”, there is a way



Fig. 1 Material discharge plate of microsurfacing machine

in which material of the material discharge plate can be changed to cure the sticking problem which is caused in case of rubber. The other material can be used for the discharge plate so that the bitumen does not get stick over the material discharge plate used in the microsurfacing machine. For this, the material could be use such that it should not get reacted with the atmosphere and get stick over the discharge plate nor it should get hard enough to cause problem while operating. Figure 1 shows the “material discharge plate of microsurfacing machine” on which the microsurfacing materials gets stick.

3.1 Supreme Bituchem

Supreme is a company with experience in offering products and services in the construction sector. Throughout our history of more than two decades, industry has been successful in providing our customers with a variety of construction solutions and lots of quality work. Suprema Bituchem India Pvt. Ltd. has made its name on the list of the leading suppliers of paint and related products, bitumen in India. The supplier company is based in Nagpur, Maharashtra and is one of the main suppliers of listed products. Suprema Bituchem India Private Limited has been listed by Trade India providing the highest quality of water-based bituminous primer, reflective thermoplastic road marking paint, quick drying solvent-based road marking paint, etc.

Supreme Bituchem India Private Limited is a leading manufacturer of a wide range of technologically advanced products for the construction and infrastructure industry. Their conflicts include a better understanding of the class of financial products and class products and effective solutions. Supreme Bituchem fully justifies its appearance, creating an amazing spectrum of high-quality products such as pre-made torches and self-adhesive waterproof membranes; PVC membrane, liquid waterproof

membrane; Construction chemicals and building materials: Sealants, mixtures and grout; Full range of bituminous products; Thermal insulation and heat management products and anticorrosive coating and tape. They manufacture high-quality road emulsions and modified and oxidized bitumen for hydride and road exfoliation.

Figure 2 and Fig. 3 shows the compost seal/micro-coating machine from the METONG brand was recently developed in 2006 by the METONG company. Unlike the comparative model in domestic advertising, the METONG LMT5310TXF becomes increasingly practical, reliable and robust performance, maintenance and common sense through the use of imported high-caliber and domestic sectors with high cost. Smaller surfaces are good answer for roads that are in the early stage



Fig. 2 Microsurfacing machine

Fig. 3 Microsurfacing machine (back side)



of decay. A mixture of aggregate asphalt, water and fiber is applied to the existing asphalt in a top coat. Small-scale coating offers several advantages: incremental slip resistance, shade contrast, surface restoration and management life for fast, heavy roads. METONG's richness is based on quality, imaginative design and first-class customer care. The LMT5310TXF (with case) focusses on the general understanding of development and long- distance quality using 8×4 case. The power is 247 kW [6] (Fig. 3).

4 Conclusion

It is analysed that the case study which is discussed above is all about the different methods used in the field of microsurfacing to modify the microsurfacing mixture as Mahdi Zalnezhad and Ebrahim Hesami used the steel slag and bitumen for the performance of microsurfacing and Mostafa Poursoltani and Saeid Hesami uses the RAP in microsurfacing blend. And the present study justifies that some problem which industry is facing in the microsurfacing machine to reduce or eliminate that problem some designs and different material such as aluminum alloys or other type of rubber material should be used so that the loss which industry is facing, while the machine is stopped can reduced.

References

1. Lonbar MS, Nasrazadani SM, Shafaghat A (2015) Investigation of aggregate and binder types effects on the microsurfacing rutting properties. In: International conference on civil engineering architecture and urban infrastructure
2. Supreme BituChem, Microsurfacing. www.supremebituChem.com
3. Pittenger DM, Gransberg DD (2020) Life cycle cost analysis of Portland cement slurry seal and microsurfacing to correct rutting. *J Struct Integrity Maintenance*
4. Poursoltani M, Hesami S (2018) Performance evaluation of microsurfacing mixture containing reclaimed asphalt pavement. *Int J Pavement Eng*
5. Hou S, Chen C, Zhang J, Shen H, Gu F (2018) Thermal and mechanical evaluations of asphalt emulsions and mixtures for microsurfacing. *Constr Build Mater* 191:1221–1229
6. Microsurfacing and Sealcoating Machine, Hangzhou Sansan Metong Machinery Co. Ltd., www.metongchina.com
7. Zalnezhad M, Hesami E, Effect of steel slag aggregate and bitumen emulsion types on the performance of microsurfacing mixture. *J Traffic Transp Eng*

Squeeze Film Operation of Thrust Bearing Operating with Shear-Thinning Lubricants



Vivek Kumar , Vatsalkumar Ashokkumar Shah, Kuldeep Narwat, and Satish C. Sharma

Abstract This paper investigates the effect of shear-thinning behaviour of non-Newtonian lubricant on steady and dynamic performance of a control flow valve (CFV)-controlled hydrostatic thrust bearing. A generalized Reynolds equation for non-Newtonian lubricant is used to compute fluid film pressure in the flow domain. Finite element method is used to obtain simultaneous solution of the Reynolds equation, Rabinowitsch fluid model equation and lubricant supply equation through CFV device. The bearing performance has been evaluated using film pressure distribution, film reaction force, film stiffness coefficients, etc. The effect of shear-thinning behaviour of lubricant has been examined on these performance indices of bearing employing various recess geometry. It has been found that shear-thinning nature of lubricant has an adverse effect on static and dynamic behaviour of bearing. However, these effects can be partially minimized by a judicious selection of geometric shape of recess.

Keywords Thrust bearing · Control flow valve · Recess geometry · FEM

V. Kumar (✉) · V. A. Shah
Department of Mechanical Engineering, PDPU Gandhinagar, Gandhinagar 382007, India
e-mail: vivek.kumar@sot.pdpu.ac.in

V. A. Shah
e-mail: vatsal.smtmd19@sot.pdpu.ac.in

K. Narwat
School of Mechanical Engineering, Galgotias University, Greater Noida 203201, India
e-mail: Kuldeep.narwat@galgotiasuniversity.edu.in

S. C. Sharma
Department of Mechanical and Industrial Engineering, IIT Roorkee, Roorkee 247667, India
e-mail: sshmefme@me.iitr.ac.in

1 Introduction

Externally pressurized thrust bearing is generally used to support heavy axial load in applications [1] such as hydroelectric turbo-rotors, vertical pumps, lock gates, telescopes and ship propulsion system observatory domes. Compared to hydrodynamic bearing, design of hydrostatic bearing is more involved and requires specialized design and application practices. Some of the unique advantages offered by these bearings are low friction (no metal-to-metal contact), very low wear rate, high load carrying ability, etc. These bearings also provide good dynamic characteristics, which is quite desirable while operating precision instrument and measuring devices/machines.

The performance of such bearings can be suitably managed by an adequate selection of compensating device, pocket geometric configuration/dimensions and type/adequate quantity of lubricant [1, 2]. The compensating devices act as an integral component of a hydrostatic bearing system. Capillary and orifice are commonly used flow control devices in such bearings. These compensating devices are based on constant supply pressure system. Control flow valve is another compensating device which is based on constant flow system. Rectangular and circular shape [1–3] are most widely used recess configurations in these systems because of their ease in manufacturing and production. However, technological progress in manufacturing techniques, for instance, micro-stereolithography, micro-machining, laser surface modification [4, 5], etc. have enabled bearing designers to produce micro and macro-features with high degree of accuracy and repeatability. Normally, the recess as mentioned in hydrostatic bearing represents a macro-feature. The depth of recess is usually very large as compared to the nominal film thickness, whereas micro-features are dimples, grooves or patterns whose depth is of the order of film thickness. Laser surface texturing (LST) over the last decades has emerged as new technology to enhance tribological performance of fluid film bearings. Although, suitability of LST in improving performance of hydrodynamic bearings is widely accepted and recognized [5], yet a very limited number of studies [6, 7] are available dealing with investigation of LST in improving the performance of hydrostatic/hybrid bearings. It has been reported that providing micro-features in hydrodynamic/hybrid bearings [5–7] can substantially enhance load-supporting ability and reduce the film frictional power loss.

Lubricant used in commercial applications is subjected to severe operating conditions such as sustaining heavy loads at low speed and high temperature. For bearings to work satisfactorily under such operating conditions, stock oils are often blended with additive agents such as anti-wear additives, corrosion-resistant additives and viscosity improvers. The viscosity improvers are often added to stabilize viscosity variation of the lubricant at high strain rate [8]. The viscosity improvers are long-chain polymer additives. The use of additives imparts non-Newtonian character to the lubricant, making them exhibit nonlinear relation for shear stress and strain rate. Researchers have performed experimental studies [9–15] to investigate the friction and wear response of tribo-pairs operating with various non-Newtonian lubricants.

Initially, Wada and Hayashi [9] experimentally investigate the performance of a hydrodynamic journal bearing employing lubricant blended with viscosity improver additives. The author concluded that lubricant containing such additives behaves as Pseudoplastic fluids, which can be theoretically better described using cubic shear stress fluid model. Later, researchers have investigated the friction-reducing properties of additives in tribo-pairs such journal bearings [10], rubbing surfaces [11], clutch [12] and squeeze film [13]. Many theories such as couple stress [14], electrically conducting [15], power law [13], and Rabinowitsch model [16, 17] are available to describe the nonlinear characters of lubricants. Couple-stress model describes the effect of additives size, which is altogether neglected in classical Newtonian mechanics. Kumar and Sharma [14] investigated the effect of couple-stress additives on dynamic performance of annular recessed thrust bearing. The authors reported a marked improvement in stiffness and damping coefficient owing to the presence of couple-stress lubricant. Another investigation on squeeze film performance of the thrust bearing [15] reported an enhancement in damping coefficient and reduction in stiffness capabilities by use of electrically conducting fluids. Wu and Dareing [13] experimentally studied squeeze film performance of CFV controlled thrust bearing operating with non-Newtonian lubricant. The lubricant is formulated by adding traces of graphite powder in the ethylene glycol. The author reported that non-Newtonian nature of such lubricant can be expressed using power law model. Lin [16] and Singh et al. [17] performed a theoretically investigated on the static performance parameters of annular recessed thrust bearing lubricated with non-Newtonian fluid. The authors [16, 17] reported a substantial decrease in load-supporting ability of parallel annular disc due to shear-thinning effect of lubricant at high rotating speed.

The literature review compiled here indicates that Rabinowitsch fluid model [9] confirms well with experimental results, while describing the shear-thinning behaviour of non-Newtonian lubricants. Some studies are reported to regarding squeeze film operation of thrust bearing lubricated with Pseudoplastic lubricant. However, these studies are either confined to annular recessed thrust bearing [17] or uncompensated parallel plates [16]. Furthermore, there is dearth of studies related to the dynamic performance of thrust bearing, considering combined influence of recess configuration/dimension and Pseudoplastic lubricant. Therefore, present work is aimed to investigate the effect of recess configuration, and shear-thinning behaviour of lubricant rotor dynamic performance of CFV is compensated thrust bearing.

2 Governing Equations and Finite Element Formulation

The layout of a hydrostatic thrust bearing and configurations of recess under investigation is illustrated in Fig. 1a, b. The bearing system employs a control flow valve (CFV) to regulate the supply of lubricant into the bearing system. The flow of lubricant has been considered to be laminar, isothermal and incompressible. The lubricant is assumed to be non-Newtonian in nature. The shear-thinning behaviour of lubricant is theoretically described using Rabinowitsch fluid model. The flow of

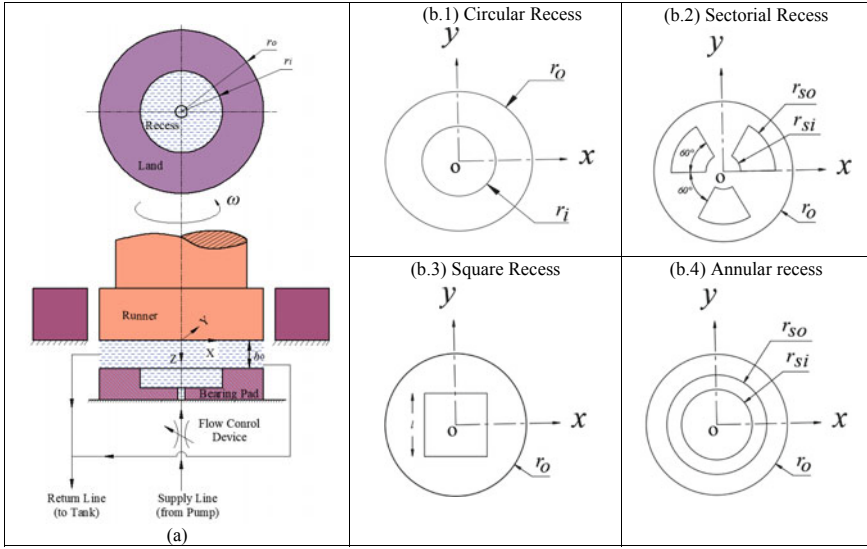


Fig. 1 a Layout of hydrostatic thrust bearing. b Recess geometric details

non-Newtonian fluid in narrow passage between thrust and runner surface has been expressed using a generalized Reynolds equation.

$$\frac{\partial}{\partial \alpha} \left(\bar{h}^3 \bar{F}_2 \frac{\partial \bar{p}}{\partial \alpha} \right) + \frac{\partial}{\partial \beta} \left(\bar{h}^3 \bar{F}_2 \frac{\partial \bar{p}}{\partial \beta} \right) = -\Omega \bar{r} \sin \theta \frac{\partial}{\partial \alpha} \left[\left(1 - \frac{\bar{F}_1}{\bar{F}_0} \right) \bar{h} \right] + \Omega \bar{r} \cos \theta \frac{\partial}{\partial \alpha} \left[\left(1 - \frac{\bar{F}_1}{\bar{F}_0} \right) \bar{h} \right] + \frac{\partial \bar{h}}{\partial \bar{t}} \quad (1)$$

$$\alpha = \frac{x}{r_o}; \beta = \frac{y}{r_o}; \bar{h} = \frac{h}{h_o}; \bar{r} = \frac{r}{r_o}; \bar{p} = \frac{p}{p_s}; \bar{\mu} = \frac{\mu}{\mu_r}; \Omega = \frac{\mu_r \omega r_o^2}{h_o^2 p_s}; \bar{t} = t \frac{h_o^2 p_s}{\mu_r^2}$$

\bar{F}_0 , \bar{F}_1 and \bar{F}_2 represent viscosity integrals of lubricant which can be expressed as follows:

$$\bar{F}_0 = \int_0^1 d\bar{z}; \quad \bar{F}_1 = \int_0^1 \frac{\bar{z}}{\bar{\mu}} d\bar{z}; \quad \bar{F}_2 = \int_0^1 \frac{\bar{z}}{\bar{\mu}} \left(\bar{z} - \frac{\bar{F}_1}{\bar{F}_0} \right) d\bar{z} \quad (2)$$

The present bearing system has been numerically simulated for squeeze film operation of bearing surfaces. As the system is at rest ($\Omega = 0$), therefore hydrodynamic term in Eq. 1 can be disregarded.

$$\frac{\partial}{\partial \alpha} \left(\bar{h}^3 \bar{F}_2 \frac{\partial \bar{p}}{\partial \alpha} \right) + \frac{\partial}{\partial \beta} \left(\bar{h}^3 \bar{F}_2 \frac{\partial \bar{p}}{\partial \beta} \right) = \frac{\partial \bar{h}}{\partial \bar{t}} \quad (3)$$

Finite element approach has been used to render partial differential equation (Eq. 3) into a set of linear algebraic equations. Four node quadrilateral elements have been used to discretize the pad surface. Primary field variable, i.e. fluid film pressure has been approximated to be varying bilinearly along x and y direction, within an element.

$$\bar{p} = \sum_{j=1}^4 [N_j \bar{p}_j]; \quad N_j = \frac{1}{4}(1 + \xi_i \xi)(1 + \eta_i \eta) \tag{4}$$

Weighted residual method and Galerkin approach have been used to obtain the weak form of Reynolds Eq. 3.

$$\iint N_j \left(\frac{\partial}{\partial \alpha} \left(\frac{\bar{h}^3}{\bar{\mu}} \bar{\varphi} \frac{\partial}{\partial \alpha} \left\{ \sum_{j=1}^4 (\bar{p}_j N_j) \right\} \right) + \frac{\partial}{\partial \beta} \left(\frac{\bar{h}^3}{\bar{\mu}} \bar{\varphi} \frac{\partial}{\partial \beta} \left\{ \sum_{j=1}^4 (\bar{p}_j N_j) \right\} \right) - \frac{\partial \bar{h}}{\partial \bar{t}} \right) d\alpha d\beta = 0 \tag{5}$$

Simplification of Eq. 5 yields global system of equation representing fluid flow over the pad surface:

$$[F_{ij}^e] \{\bar{p}\} = [Q_i^e] + \bar{h} [RS_i^e] \tag{6}$$

The shear-thinning behaviour of lubricant has been incorporated into above equation (Eq. 6) using Rabinowitsch fluid model. The constitutive flow equation for such lubricant is as follows:

$$\bar{\tau} + k\bar{\tau}^3 = \bar{\gamma} \tag{7}$$

$$\bar{\gamma} = \sqrt{\left[\frac{\bar{h}}{\bar{\mu}} \frac{\partial \bar{p}}{\partial \alpha} \left(\bar{z} - \frac{\bar{F}_1}{\bar{F}_0} \right) \right]^2 + \left[\frac{\bar{h}}{\bar{\mu}} \frac{\partial \bar{p}}{\partial \beta} \left(\bar{z} - \frac{\bar{F}_1}{\bar{F}_0} \right) \right]^2} \tag{8}$$

The next step is to integrate the flow control valve into the thrust bearing system. This can be achieved by locating all the nodes on the outer edge of recess. The sum of lubricant flow rate through all these nodes must be equated to the lubricant supply rate through the CFV device (\bar{Q}_{CFV}) in the bearing system. This enables coupling of CFV device to the pocket of bearing.

$$\begin{bmatrix} \bar{F}_{11} & \bar{F}_{12} & \dots & \bar{F}_{1j} & \dots & \bar{F}_{1n} \\ \bar{F}_{21} & \bar{F}_{22} & \dots & \bar{F}_{2j} & \dots & \bar{F}_{2n} \\ \vdots & \vdots & \vdots & \vdots & \vdots & \vdots \\ \bar{F}_{j1} & \bar{F}_{j2} & \dots & \bar{F}_{jj} & \dots & \bar{F}_{jn} \\ \vdots & \vdots & & \vdots & \vdots & \vdots \\ \bar{F}_{n1} & \bar{F}_{n2} & \dots & \bar{F}_{nj} & \dots & \bar{F}_{nn} \end{bmatrix} \begin{bmatrix} \bar{p}_{o1} \\ \bar{p}_{o2} \\ \vdots \\ \bar{p}_{oj} \\ \vdots \\ \bar{p}_{on} \end{bmatrix} = \begin{bmatrix} \bar{Q}_1 \\ \bar{Q}_2 \\ \vdots \\ \bar{Q}_R \\ \vdots \\ \bar{Q}_n \end{bmatrix} + \bar{h} \begin{bmatrix} \bar{RS}_1 \\ \bar{RS}_2 \\ \vdots \\ \bar{RS}_j \\ \vdots \\ \bar{RS}_n \end{bmatrix} \tag{9}$$

The swift-Stiber boundary condition is applied on all the nodes located at the outer edge of pad. This ensures conservation of mass at outer boundary of thrust pad, where fluid film pressure smoothly approaches to ambient pressure. In order to obtain steady-state performance parameters such as film pressure distribution and film reaction force, the squeeze terms in equation can be neglected. Thereafter, Gauss–Siedel iterative numerical technique is used to get film pressure distribution in land area of pad.

$$\text{Film Reaction : } \bar{F}_z = \sum_{e=1}^{n_e} \left\{ \int_{-1}^{+1} \int_{-1}^{+1} \left(\sum_{j=1}^4 \bar{p}_j N_j \right) |\bar{J}| d\xi d\eta \right\} + \sum_{e=1}^{n_p} \bar{A}_p \bar{p}_r \quad (10)$$

Afterwards, perturbation technique will be used to compute film pressure gradient with respect to change in film thickness and squeeze velocity. These pressure gradient will enable us to compute film stiffness and damping coefficients by performing integration using Gauss-Legendre, over the fluid flow domain as follows:

$$\text{Stiffness Coefficient : } \bar{K} = \sum_{e=1}^{n_e} \left\{ \int_{-1}^{+1} \int_{-1}^{+1} \left(\sum_{j=1}^4 \frac{\partial \bar{p}_j}{\partial \bar{h}} N_j \right) |\bar{J}| d\xi d\eta \right\} + \sum_{e=1}^{n_p} \bar{A}_p \frac{\partial \bar{p}_r}{\partial \bar{h}} \quad (11)$$

$$\text{Damping Coefficient : } \bar{D} = \sum_{e=1}^{n_e} \left\{ \int_{-1}^{+1} \int_{-1}^{+1} \left(\sum_{j=1}^4 \frac{\partial \bar{p}_j}{\partial \dot{\bar{h}}} N_j \right) |\bar{J}| d\xi d\eta \right\} + \sum_{e=1}^{n_p} \bar{A}_p \frac{\partial \bar{p}_r}{\partial \dot{\bar{h}}} \quad (12)$$

3 Solution Procedure

In the present work, finite element (FE) simulation of thrust bearing is carried out. The solution of flow governing equation has been obtained using Gauss-Siedel/Newton Raphson iterative technique. The geometric/operating condition of bearing system is listed in Table 1.

A source code is developed to solve flow governing equation for primary field variable, i.e. fluid film pressure. In order to ensure reliability of numerical results, grid independence test has been performed for each pocket shape. In addition to this, repeatability of numerical results has been achieved by setting a convergence of order of 10^{-04} on film pressure. Once the solution scheme gets terminated, performance variables of bearing would be computed using analysis presented in preceding section. The step-wise solution scheme adopted for present work is as follows:

Table 1 Bearing geometric and operating conditions

Input parameters	Dimensional value
Radius of pad (r_o)	100 mm
Circular pocket radius (r_i)	50 mm
Sectorial pocket details	$r_{so} = 75$ mm; $r_{si} = 25$ mm
Annular pocket details	$r_{so} = 71$ mm; $r_{si} = 50$ mm
Square pocket details	$l = 88.6$ mm
Film thickness	0.05 mm
Supply pressure	5 MPa
Lubricant viscosity	0.034 Pa s

1. Input geometric and operating parameters, discretize bearing domain, initialization of field variables.
2. Generation of gauss point within four-node iso-para element.
3. Compute viscosity integrals (F_0, F_1 and F_2) for lubricant.
4. Establish film thickness on elements.
5. Compute elemental matrices.
6. Perform assembly of elemental equation into global matrix equations.
7. Solution of global equation for pressure distribution using Gauss–Siedel and Newton Raphson method.
8. Check for convergence on primary field variable (film pressure). If convergence is not meet, jump back to step 3.
9. Computer bearing performance indices, once iterative scheme is terminated.

After establishing the solution scheme, the accuracy of newly developed mathematical model is verified by regenerating the numerical results for on hydrostatic thrust bearings (from the existing literature). Jain and Sharma [3] had derived series solution expressions for thrust bearing lubricated using Newtonian lubricant. The developed source code has been used to simulate the bearing system from reference study [3]. The comparison of numerical results and analytical results from reference study [3] is depicted in Table 2. This comparison indicates a good agreement and validates the developed numerical model for thrust bearing.

Table 2 Validation with published available literature on hydrostatic thrust bearing

Restrictor coefficient (\overline{CS}_2)		Non-dimensional performance indices			
		\overline{P}_o	\overline{F}_z	\overline{S}	\overline{D}
5	Ref. [3]	0.9220	1.5670	0.6770	0.8902
	Present	0.9218	1.5612	0.6808	0.8713
10	Ref. [3]	0.9780	1.6620	0.213	0.6810
	Present	0.9781	1.6564	0.2146	0.6645
15	Ref. [3]	0.9900	1.6820	0.0984	0.6342
	Present	0.9904	1.6767	0.1001	0.6174

4 Results and Discussion

In this section, numerical results are presented and discussed in details for externally pressured thrust bearing operating with non-Newtonian lubricant. Influence of recess configuration and shear-thinning behaviour of lubricant has been discussed on film pressure profile, film reaction force and film stiffness and damping coefficient. Four different configurations of recess: circular, sectorial, square and annular are compared w.r.t bearing performance indices. The shear-thinning behaviour of non-Newtonian lubricant is characterized by fluid flow index ($k = 0.2 \sim 1$). When the value of k approaches towards zero, the lubricant starts to approximate Newtonian behaviour in the bearing.

Figure 2 presents the effect of configuration of recess and value of flow index on film pressure profile. It can be seen that shear-thinning behaviour of lubricant tends to shrink film pressure envelope above the thrust surface. It could be attributed to a decrease in the apparent viscosity of the fluid. In addition to fluid flow index, the shrinkage in film pressure profile is noticed to vary considerably with respect to geometric configuration of recess, provided in the pad. This indicates that geometric

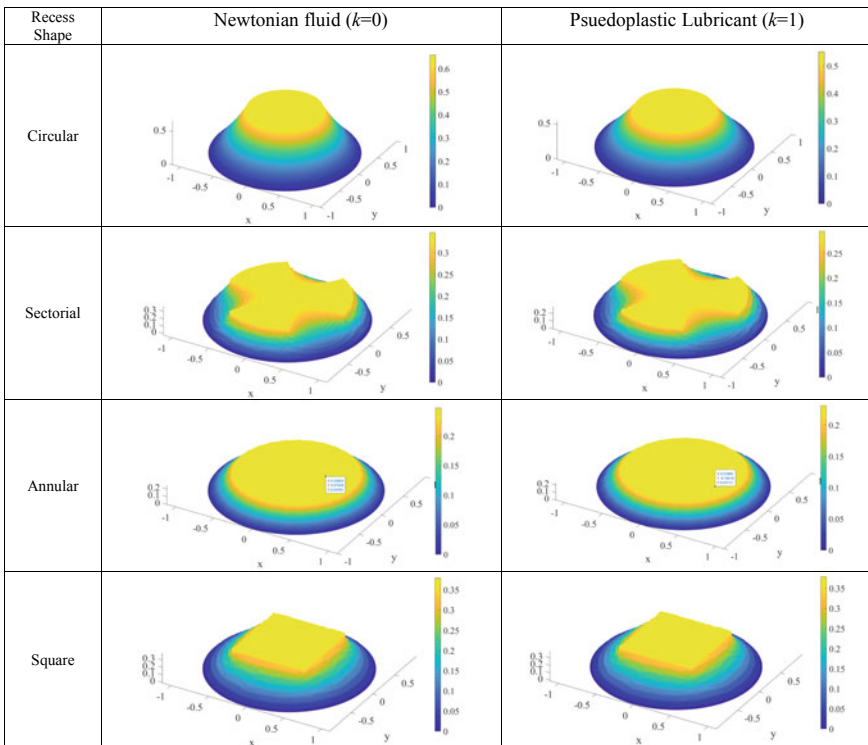


Fig. 2 Effect of geometric configuration of recess on film pressure envelope on thrust bearing lubricated using Newtonian and Pseudoplastic fluid

configuration of recess has a strong influence on film pressure distribution. Figure 3 depicts variation in pocket pressure with respect to fluid flow index for various recess configurations. Irrespective of recess configuration a continuous drop in recess pressure has been noticed with an increment in value of fluid flow index. It has been noticed that circular and square recess (vis-à-vis annular and sectorial recess) generates higher fluid pressure in the recess. The drop in circular and square recess pressure with respect to k is also noticed to be more step as compared to annular and sectorial recess. This indicates that annular and sectorial recess effectively counter a drop in apparent viscosity due to shear-thinning behaviour of lubricants.

Figure 4 presents variation in film reaction (force) with respect to an increase in Psuedoplastic nature of the lubricant. The result presented in Fig. 4 is closely following the trends of fluid film pressure profile and values depicted in Figs. 2 and 3. This is because film reaction is obtained by integrating film pressure over recess and land surface of thrust pad. It can be seen here that circular and sectorial recess configurations generate maximum and least film reaction while operating with both Newtonian lubricants ($k = 0$) and Psuedoplastic ($k < 1$) lubricants. Comparatively, using circular recess vis-à-vis sectorial recess enhances load carrying capacity by 52.8% and 52.3% while operating with Newtonian ($k = 0$) and Psuedoplastic ($k = 1$) lubricants, respectively. The numerical results in Fig. 4 can be described by using following trends.

$$\left| \overline{F}_z \right|_{\text{Psuedoplastic}} < \left| \overline{F}_z \right|_{\text{Newtonian}}$$

$$\left| \overline{F}_z \right|_{\text{Sectorial}} < \left| \overline{F}_z \right|_{\text{Annular}} < \left| \overline{F}_z \right|_{\text{Square}} < \left| \overline{F}_z \right|_{\text{Circular}} \Big|_{k=0 \rightarrow 1}$$

Fig. 3 Recess pressure versus flow index

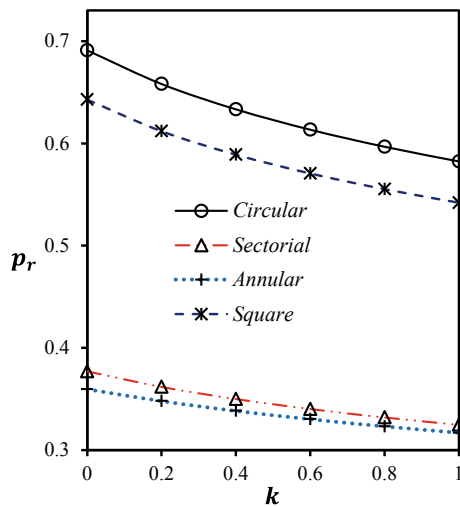


Fig. 4 Fluid film reaction versus flow index

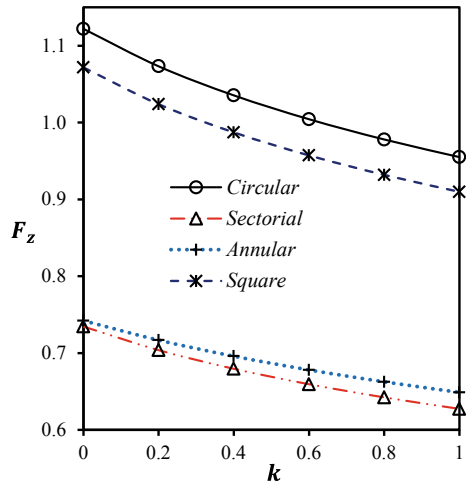


Figure 5 depicts influence of recess configurations on stiffness coefficient of bearing lubricated using non-Newtonian fluid. Among all recess configurations, circular recess is noticed to be imparting maximum stiffness capabilities to the bearing. A sharp reduction in stiffness coefficient is observed with respect to an increment in value of fluid flow index. This reduction in stiffness coefficient is noticed to be lying in range of -24.2% (*Annular*) to -28.1% (*Sectorial*). The numerical results from Fig. 5 can be summarized using following trends:

$$\left| \bar{S} \right|_{\text{Pseudoplastic}} \left(\bar{S} \right|_{\text{Newtonian}} \left| \right.$$

Fig. 5 Stiffness coefficient versus flow index

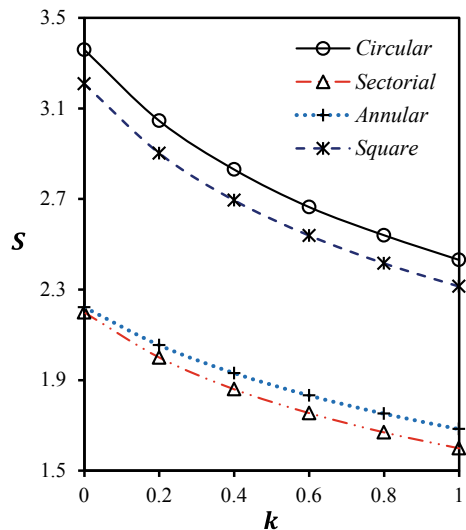
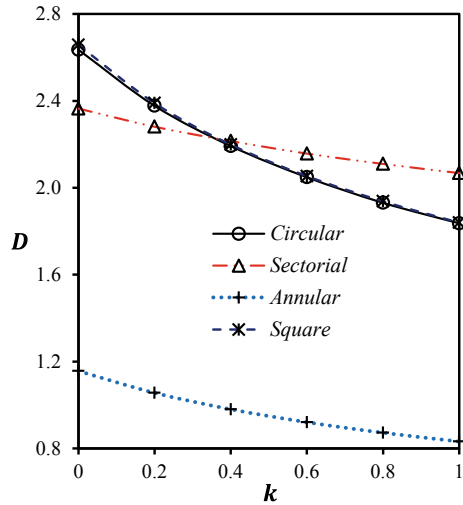


Fig. 6 Damping coefficient versus flow index



$$|\bar{S}|_{\text{Sectorial}} \langle \bar{S} |_{\text{Annular}} \langle \bar{S} |_{\text{Square}} \langle \bar{S} |_{\text{Circular}} \Big|_{k=0 \rightarrow 1}$$

The numerical results for damping coefficient of bearing system are presented in Fig. 6. It can be clearly seen that shear-thinning nature of lubricant has an adverse effect on damping capability of the system. However, this effect can be partially reduced by an adequate selection of geometric configuration of recess. The numerical results from Fig. 6 can be deduce as follows:

$$|\bar{D}|_{\text{Pseudoplastic}} \langle \bar{D} |_{\text{Newtonian}} \Big|_{k=0 \rightarrow 1}$$

$$|\bar{D}|_{\text{Annular}} \langle \bar{D} |_{\text{Circular}} \langle \bar{D} |_{\text{Square}} \Big|_{\text{Newtonian}; k \rightarrow 0}$$

$$|\bar{D}|_{\text{Annular}} \langle \bar{D} |_{\text{Circular}} \langle \bar{D} |_{\text{Square}} \langle \bar{D} |_{\text{Sectorial}} \Big|_{\text{Newtonian}; k \rightarrow 1}$$

The square and circular recess can be good choice if shear-thinning phenomenon is negligible, or the lubricant is exhibiting a Newtonian character. At high shear-thinning rate, the sectorial recess can be opted from the viewpoint of achieving better damping capabilities in the bearing.

5 Conclusions

Following conclusions could be deduced from the numerical simulation of thrust bearing:

- The shear-thinning effect in lubricant adversely affects the performance of a CFV-controlled thrust bearing.
- The loss in the performance level/indices of thrust bearing due to shear-thinning in lubricant can be partially mitigated by an appropriate selection of recess configuration.
- Under given operating conditions, circular/square recess should be preferred choice, when shear-thinning effects are negligible, and bearing design criteria are generating higher load carrying capacity/stiffness characteristics.
- The sectorial recess should be preferred, when bearing design criteria is primarily damping characteristics, and shear-thinning effects are profound during operation of bearing.

References

1. Rowe WB (2013) *Hydrostatic and hybrid bearing design*. Elsevier, London
2. Sinhasan R, Jain S (1984) Lubrication of orifice-compensated flexible thrust pad bearings. *Tribol Int* 17(4):215–221
3. Kumar V, Sharma SC (2018) Dynamic characteristics of compensated hydrostatic thrust pad bearing subjected to external transverse magnetic field. *Acta Mech* 229(3):1251–1274
4. Yang H, Ratchev S, Turitto M (2009) Rapid manufacturing of non-assembly complex micro-devices by microstereolithography. *Tsinghua Science Technology* 14:164–167
5. Etsion I (2005) State of the art in laser surface texturing. *Trans ASME F J Tribology* 127(1):248–253
6. Kumar V, Sharma SC (2019) Effect of geometric shape of micro-grooves on the performance of textured hybrid thrust pad bearing. *J Braz Soc Mech Sci Eng* 41(11):508
7. Kumar V, Sharma SC, Narwat K (2019) Influence of micro-groove attributes on frictional power loss and load-carrying capacity of hybrid thrust bearing. *Ind Lubric Tribol*. <https://doi.org/10.1108/ILT-07-2019-0278>
8. Stachowiak GW, Andrew WB (2013) *Engineering tribology*. Butterworth-Heinemann, Australia
9. Wada S, Hayashi H (1971) Hydrodynamic lubrication of journal bearings by pseudoplastic lubricants (part II, experimental studies). *Bull JSME* 14(69):279–286
10. Oliver DR (1988) Load enhancement effects due to polymer thickening in a short model journal bearing. *J Nonnewton Fluid Mech* 30:185–196
11. Spikes HA (1994) The behavior of lubricants in contacts: current understanding and future possibilities. *Proc Inst Mech Eng J J Eng Tribol* 28:3–15
12. Scott W, Suntiattana P (1995) Effect of oil additives on the performance of a wet friction clutch material. *Wear* 181:850–855
13. Wu Z, Dareing DW (1994) Non-Newtonian effects of powder-lubricant slurries in hydrostatic and squeeze film bearings. *Tribol Transaction* 37:836–842
14. Kumar V, Sharma SC (2017) Study of annular recess hydrostatic tilted thrust pad bearing under the influence of couple stress lubricant behaviour. *Int J Surf Sci Eng* 11(4):344–369
15. Kumar V, Sharma SC (2018) Finite element method analysis of hydrostatic thrust pad bearings operating with electrically conducting lubricant. *Proc Inst Mech Eng J: J Eng Tribol* 232(10):1318–1331
16. Lin JR (2012) Non-Newtonian squeeze film characteristics between parallel annular disks: Rabinowitsch fluid model. *Tribol Int* 52:190–194
17. Singh UP, Gupta RS, Kapur VK (2013) On the application of Rabinowitsch fluid model on an annular ring hydrostatic thrust bearing. *Tribol Int* 58:65–70

Feasibility and Performance Analysis of Earth-Tube Heat Exchanger



Rampal Singh and V. K. Dwivedi

Abstract The temperature of Mathura is as high as 50 °C in summer, and it is as low as below 10 °C in winter. So we may utilize the fact that the temperature of earth at a depth of 2–3 m is constant throughout the year irrespective of the season, and that constant temperature is called earth undistributed temperature (EUT) so this maybe utilized for heat rejection of air in the summer for cooling purpose (heat source) and heat addition of air in the winter for the heating purpose. Current setup is developed to explore possibility of EAHE installation for heating and cooling in Mathura region to curb demand of energy consumption. For this small setup of ETHE was developed at GLA University, Mathura. Tube or pipe MS/GI can be buried at above-mentioned depth, and air can be made to pass through these tubes by employing a blower into it. In present experiment, a setup is established at GLA University, Mathura. It consists of MS pipes and blower of 600 W. To analyze the performance of ETHE of current setup, measurement of atmospheric temperature and inside temperature of soil at depth of 6 feet in summer is done. This data is also calculated for winter season. Calculations of the amount of heat transfer and work input to blower were done by applying suitable thermodynamic formulae and data. Calculation of the coefficient of performance was also done.

Keywords ETHE · Constant soil temperature · Cabin heating cooling · Summer and winter temperature

1 Introduction and Literature Survey

A large amount of electrical energy is consumed in heating and cooling of residential building and commercial building by using conventional methods. Generally, conventional method used is VCRS, and refrigerant is used which causes damage to the environment. It causes greenhouse effect and global warming. ETHE could be a potentially proven method for heating and cooling purposes. As air is used as

R. Singh (✉) · V. K. Dwivedi
Department of Mechanical Engineering, IETGLA University, Mathura, India

working fluid, it does not have any depleting effect on environment. ETHE is efficient, economic and environmentally friendly [1]. The concept of constant temperature of earth surface below 2–3 m or inertia of ground which is called earth undistributed temperature can be utilized for heating/cooling to provide thermal comfort [2–4]. Two types of looping system can be used—vertical loop system and horizontal loop system. In vertical loop system, pipe has to be buried deep inside earth's surface. In horizontal loop, pipe has to be buried 1–3 m deep in earth's surface. Earth-tube heat exchanger can also be classified as open-type ETHE in which air passes through buried tubes for preheating and precooling later heated by convention units, and closed-type ETHE in which heat carrier medium is circulated within the tubes [5] Mathura is a potential region for it as the temperature variation is quite high. Researchers have suggested that it can be utilized in the regions where temperature difference is quite high which means temperature difference between summer and winter is high. On conventional energy, resources are better option of clean and sustainable energy. This kind of energy is, at principle, inexhaustible and can be founded and exploited equally well on the planet. Problem associated with ETHE is humid nature of climate in rainy season, and condensation takes place within the pipe and damages the system [6]. Greenhouse cultivation is also feasible with ETHE in hot and arid climate [7]. Experimental setup is designed to show temperature difference which is dependent on area also. If one provides fins' arrangement over the pipe, then heat transfer is more than without fin arrangement [8]. It has sufficient potential to cool outside air [9]. In present setup, feasibility analysis of ETHE is done, and also calculation for the performance of ETHE is made.

2 Experimental Setup

2.1 Components

- MS pipe is used to carry air inside and deliver it, which transfers heat to ground and delivers it to space where cooling and heating have to be done. It is of 2 inch diameter.
- Elbows are used to connect MS pipe at 90°, so that pipes could be connected as per the connection made in drawing.
- Blower is used to suck air from atmosphere and send it to underground pipes. Here blower used is
- Of 600 W, supplying air at 2.5 m³/min rotating at 15,500 rpm.
- Fiber sheets are used to make envelope where air is to be supplied.
- Adhesives are used at joint to prevent leakage of air.
- Pyrometer is used to measure the temperature.

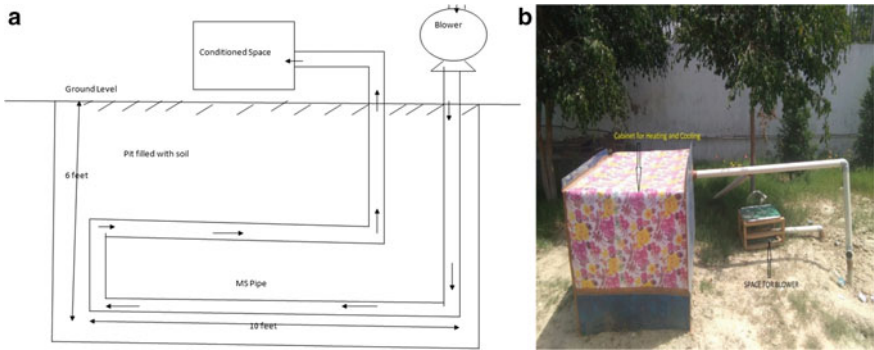


Fig. 1 a Schematic diagram of ETHE, and b actual image of practical ETHE above ground

2.2 Procedure

1. A pit is dug in the earth of dimension $10 \times 4 \times 6$ cubic feet.
2. In pipe arrangement, five MS pipes kept inside pit, and two PVC pipes on entry and exit point are put up inside the pit as shown in Fig. 1. Pipes were connected to each other through elbow. Along with elbow, adhesive was also used to prevent leakage of air at joints.
3. Backfilling the pit with soil extracted and ramming it.
4. Measure temperature and environment temperature of the pit by putting thermometer inside it.
5. Later on, we measure temperature inside the cabin after running the system for 15 min.

2.3 Thermodynamic Analysis

There are two processes involved:

1. **Adiabatic compression process**—Blower is a machine that takes in air at atmospheric pressure, compresses it by using centrifugal force and delivers it at higher pressure. This process is shown as process 1–2 on P–T diagram.
2. **Constant pressure heat absorption**—During winter, atmospheric air at lower temperature is made to pass through the soil at depth which is at higher temperature; hence, air will absorb heat from soil. This is constant pressure heat addition process. This process is shown as process 2–3 on P–T diagram as illustrated in Figs. 2, 3, 4, 5 and 6 and corresponding data is provided in Tables 1, 2 and 3.

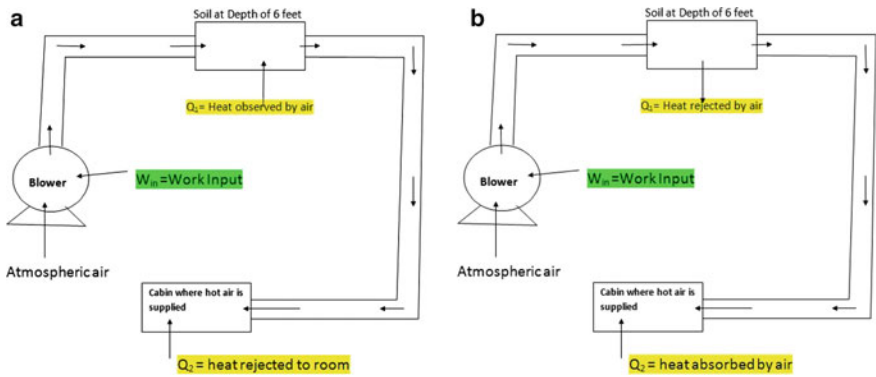


Fig. 2 a Thermodynamic cycle of ETHE for winter and b thermodynamic cycle of ETHE for summer

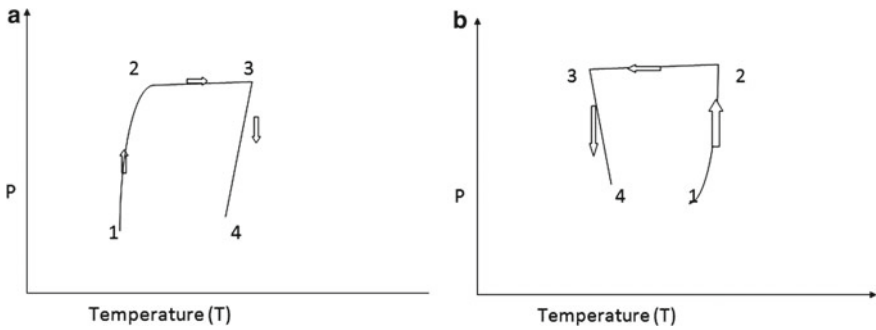


Fig. 3 a Pressure–temperature diagram of ETHE and b pressure–temperature diagram of ETHE

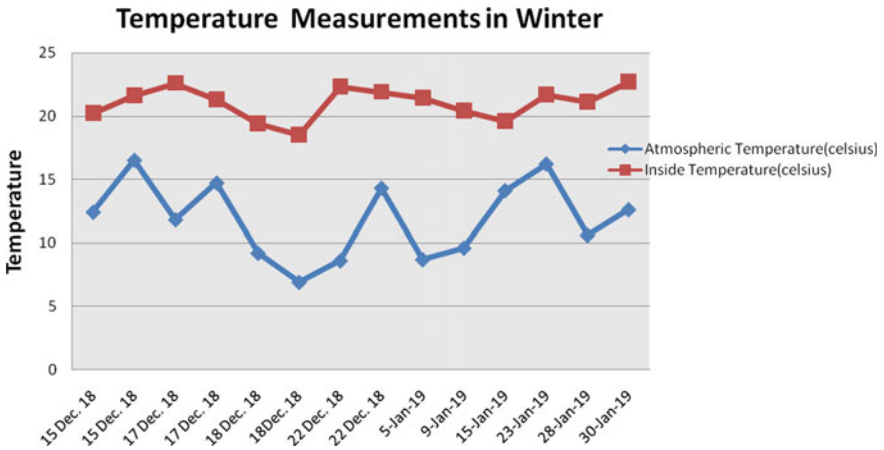


Fig. 4 Variation of temperature in winter

Fig. 5 Temperature variation between inside soil and outside

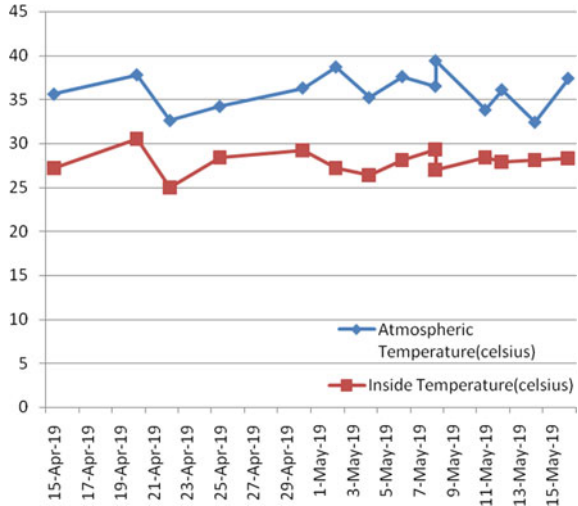
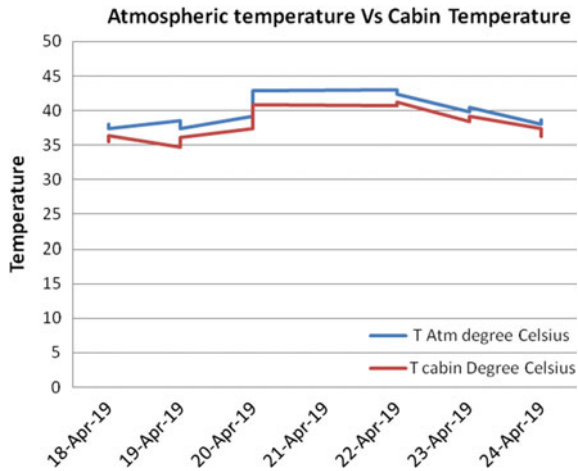


Fig. 6 Variation of cabin temperature and atmospheric temperature



2.4 COP Calculation

Performance of heating and cooling system can be gaged in terms of coefficient of performance (COP). It can be defined as the ratio of desired effect and work input. For cooling, desired effect is amount of heat absorbed from space where cooling has to be done. For heating, desired effect is amount of heat rejected to space where heating has to be done [10].

$$COP = \text{desired effect/work supplied.}$$

The coefficient of performance is calculated by formula proposed by ASHRAE

Table 1 Temperature measurement in winter

S. No.	Date	Day	Time	T_{atm} (°C)	T_{Inside} (°C)	ΔT (°C)
1	15-Dec-18	Saturday	9:00 AM	12.4	20.2	7.8
2	15-Dec-18	Saturday	11:00 AM	16.5	21.6	5.1
3	17-Dec-18	Monday	8:00 AM	11.8	22.6	10.8
4	17-Dec-18	Monday	2:00 PM	14.7	21.3	6.6
5	18-Dec-18	Tuesday	7:00 PM	9.2	19.4	10.2
6	18-Dec-18	Tuesday	9:00 PM	6.9	18.5	11.6
7	22-Dec-18	Saturday	10:00 AM	8.6	22.3	13.7
8	22-Dec-18	Saturday	4:00 PM	14.3	21.9	7.6
9	5-Jan-19	Saturday	8:00 AM	8.7	21.4	12.7
10	9-Jan-19	Wednesday	10:00 AM	9.6	20.4	10.8
11	15-Jan-19	Tuesday	4:00 PM	14.1	19.6	5.5
12	23-Jan-19	Tuesday	8:00 AM	16.2	21.7	5.5
13	28-Jan-19	Monday	9:00 AM	10.6	21.1	10.5
14	30-Jan-19	Wednesday	8:00 AM	12.6	22.7	10.1
Average temperature difference						9.17857

Table 2 Temperature measurement in summer

S. No.	Date	Day	Time	T_{atm}	T_{inside}	ΔT (°C)
1	15-Apr-19	Wednesday	10:00 AM	35.6	27.2	8.4
2	20-Apr-19	Monday	2:00 PM	37.8	30.5	7.3
3	22-Apr-19	Wednesday	8:00 AM	32.6	25	7.6
4	25-Apr-19	Saturday	3:00 PM	34.2	28.4	5.8
5	30-Apr-19	Thursday	11:00 AM	36.3	29.2	7.1
6	2-May-19	Saturday	3:00 PM	38.7	27.2	11.5
7	4-May-19	Monday	2:00 PM	35.2	26.4	8.8
8	6-May-19	Wednesday	4:00 PM	37.6	28.1	9.5
9	8-May-19	Friday	8:00 AM	36.5	29.3	7.2
10	8-May-19	Friday	4:00 PM	39.4	27	12.4
11	11-May-19	Monday	9:00 AM	33.8	28.4	5.4
12	12-May-19	Tuesday	10:00 AM	36.1	27.9	8.2
13	14-May-19	Thursday	5:00 PM	32.4	28.1	4.3
14	16-May-19	Saturday	11:00 AM	37.4	28.3	9.1
Average temperature difference						8.04286

Table 3 Temperature difference between cabin and outside air

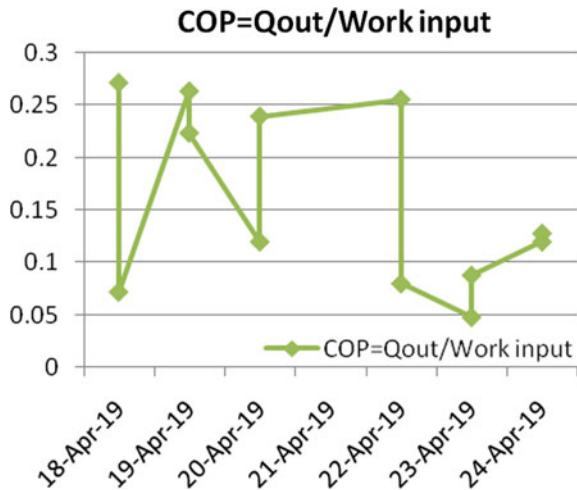
S. No.	Date	Day	Time	T_{atm}	T_{inside}	ΔT (°C)
1	18-Apr-19	Thursday	8:00 AM	38	35.5	2.5
2	18-Apr-19	Thursday	8:30 AM	37.4	36.3	1.1
3	19-Apr-19	Friday	11:00 AM	38.6	34.7	3.9
4	19-Apr-19	Friday	11:30 AM	37.4	36.1	1.3
5	20-Apr-19	Saturday	1:00 PM	39.2	37.4	1.8
6	20-Apr-19	Saturday	1:30 PM	42.9	40.8	2.1
7	22-Apr-19	Monday	11:00 AM	43	40.7	2.3
8	22-Apr-19	Monday	11:30	42.4	41.2	1.2
9	23-Apr-19	Tuesday	9:00 AM	39.8	38.4	1.4
10	23-Apr-19	Tuesday	9:30 AM	40.5	39.2	1.3
11	24-Apr-19	Wednesday	11:00 AM	38.1	37.4	0.7
12	24-Apr-19	Thursday	11:30	38.7	36.2	2.5
Average temperature difference						1.84167

$$COP = Q_{OUT}/W_{IN} \tag{1}$$

$$Q_{out} = mCp(T_{cabin} - T_{atm}) \tag{2}$$

For present blower used in setup, volume flow rate = 2.5 m³/min, W = 600 W (power of blower), density of air = 1.14 kg/m³ and volume flow rate = 2.5 m³/min (Fig. 7).

Fig. 7 Plot of COP



Cold air is used to heat the space, so small space of PVC fiber with a small door was created, now measure the temperature of ambient air and temperature of air inside the cabin, and we run the system for 15 min every time to measure the temperature, but temperature difference was not much, so we did not receive favorable results. Possible causes of it could be the unappropriated length of pipe, incorrect capacity blower velocity of air and depth of pit. It is evident from data collection that temperature difference between soil temperature and atmosphere temperature is 9.17 °C in winter, while in summer it is 8.04.

One may notice that in cabin, much temperature difference could not be obtained due to following reasons:

1. Size of pipe might not be sufficient enough to transfer heat from ground to air inside the pipe.
2. Thermal conductivity of soil might not be good enough to transfer heat from soil to MS pipe.
3. There were some leakage from cabin to outside; hence, some heat of outside air was continuously entering the cabin.
4. There might be time constraints, when air is flowing inside the tube it might not getting sufficient time to transfer heat from soil to air or vice versa.
5. Soil transfers heat slowly and has high thermal capacity, so temperature changes slowly.
6. Low thermal conductivity of soil.
7. Velocity of air is high.

Method for calculation of COP is suggested as mentioned in Table 4 [11].

3 Conclusion

Experimental study has been carried out on set developed. Various parameters like temperature, heat absorbed and coefficient of performance for the installation of ETHE have been measured/calculated using thermodynamic equations/formulae. Temperature variation between soil and atmospheric air is obtained after measurement, and depth of 2-3m is good enough to utilize it for heating and cooling purpose during winter and summer, respectively. Value of COP is low due to reasons mentioned in result. Results obtained were consistent with the research done at other part of world. One may conclude if properly designed ETHE could be potential alternative for building heating/cooling. One need to select design parameters accurately to make it of practical use.

Table 4 COP calculation

S. No.	Date	Day	Time	T_{Atm}	T_{CABIN}	ΔT	m (kg/s)	C_p (J/kgC)	$Q_{out} = mC_p(T_{cabin} - T_{atm})$ in Watt	Work input	COP = $Q_{out}/Work$ input
1	18-Apr-19	Thursday	8:00 AM	38.6	35.2	3.4	0.0475	1007	162.63	600	0.27
2	18-Apr-19	Thursday	8:30 AM	37.4	36.5	0.9	0.0475	1007	43.049	600	0.071
3	19-Apr-19	Friday	11:00 AM	38.2	34.9	3.3	0.0475	1007	157.847	600	0.26
4	19-Apr-19	Friday	11:30 AM	38.9	36.1	2.8	0.0475	1007	133.931	600	0.22
5	20-Apr-19	Saturday	1:00 PM	39.1	37.6	1.5	0.0475	1007	71.74	600	0.12
6	20-Apr-19	Saturday	1:30 PM	43.4	40.4	3	0.0475	1007	143.49	600	0.234
7	22-Apr-19	Monday	11:00 AM	43.5	40.3	3.2	0.0475	1007	153	600	0.255
8	22-Apr-19	Monday	11:30	42.6	41.6	1	0.0475	1007	47.83	600	0.0797
9	23-Apr-19	Tuesday	9:00 AM	39.1	38.5	0.6	0.0475	1007	28.69	600	0.048
10	23-Apr-19	Tuesday	9:30 AM	40.5	39.4	1.1	0.0475	1007	52.61	600	0.0877
11	24-Apr-19	Wednesday	11:00 AM	38.7	37.2	1.5	0.0475	1007	71.74	600	0.12
12	24-Apr-19	Thursday	11:30	38.2	36.6	1.6	0.0475	1007	76.53	600	0.127
									Average COP		0.159

References

1. Trombe A, Pettit M, Bourret B (1991) Air cooling by earth tube heat exchanger experimental approach. *Renew Energy* 1:699–707
2. Sharan G, Sahu RK, Jadhav R, Air cooling and heating system for tigers in zoo using earth tube heat exchanger, Centre for Management in Agriculture, Indian Institute of Management, Ahmedabad, 380015
3. Bisoniya TS, Design of earth air heat exchanger. Springer. <https://doi.org/10.1186/s40517-015-0036-2>
4. Khotakshay, Analysis of various designing parameters for earth air tunnel heat exchanger. *Int J Mech Eng Technol (IJMET)*. ISSN 0976-6359(ONLINE)
5. Chaturvedi AK, Bartaria (2015) Performance of earth tube heat exchanger cooling of air—review. *Int J Mech Eng Robotic Res* 4
6. Sobti J, Singh SK, Earth air heat exchanger as green retrofit for Chandigarh—a critical review. *Geothermal Energy: A Spring Open Journal*. <https://doi.org/10.1186/s40517-015-0034-4>
7. Sharan G, Prakash H, Jadhav R, Performance of greenhouse coupled to earth tube heat exchanger in closed loop mode. www.researchgate.net/publication/5113538
8. Rathi R, Ianjewar A (2015) Thermal performance analysis of EAHE with and without fin arrangements. *Int J Eng Appl Sci (IJEAS)* 2(6). ISSN: 2394-3661; Nitish S, Aruna K, performance analysis of a finned pipe air heat exchanger. *Int J Sci Res (IJSR)*. ISSN: 2319-7064
9. Soni SK, Pandey M, Bartaria VN (2015) Ground coupled heat exchangers review and applications. *Renew Sustain energy Rev* 47:83–92
10. Rasha SA (2014) Performance analysis of an earth tube heat exchanger for winter heating in erbil. *Int J Sci Eng Res* 5(3). ISSN: 2229:5518
11. Nitish S, Aruna K, Performance analysis of a finned pipe air heat exchanger. *Int J Sci Res (IJSR)*. ISSN 2319-7064

Combined Objective Optimization of FMS Scheduling by a Hybrid Genetic Algorithm



K. Gayathri Devi, R. S. Mishra, and A. K. Madan

Abstract Flexibility is an important character of flexible manufacturing systems (FMSs). All the developments made so far aims to improve the flexibility in FMS. Scheduling plays an important part in obtaining that flexibility while implementing a FMS. In real-world scenario, scheduling problems are more complex and hence solving single objective is not enough anymore. This article addresses one such problem where an attempt has been made to minimize the machine idle time and to minimize the overall penalty cost by combined optimization. A new novel hybrid method christened as GAPSOTS has been introduced in this paper. The hybrid technique is an amalgamation of three meta-heuristics approaches, namely genetic algorithm (GA), tabu search (TS) and particle swarm optimization (PSO). To determine the validity of the proposed approach, two large variety problems of 43 jobs 16 machines and 80 jobs 16 machines of FMS system taken from literature are solved for optimal scheduling. The feasibility and adaptability of the hybrid algorithm GAPSOTS are found by comparing experimental outcomes obtained from other hybrid techniques. The optimal schedule obtained by GAPSOTS surpasses other existing meta-heuristic techniques, thereby proving the proposed algorithm is superior in its performance.

Keywords Flexible manufacturing systems (FMS) · Scheduling · Genetic algorithm · Tabu search · Particle swarm optimization (PSO) · Hybrid meta-heuristics

1 Introduction and Literature Review

Increasing customer demand in the market leads to question the efficiency of mass production. Flexible manufacturing system has to achieve success by meeting up the highly increasing competition in the market. An efficient FMS must fulfil the demands of market where customized products are gaining importance. An efficient

K. Gayathri Devi (✉) · R. S. Mishra · A. K. Madan
Department of Mechanical, Delhi Technological University, New Delhi, India

© The Author(s), under exclusive license to Springer Nature Singapore Pte Ltd. 2022
K. Govindan et al. (eds.), *Advances in Mechanical and Materials Technology*,
Lecture Notes in Mechanical Engineering,
https://doi.org/10.1007/978-981-16-2794-1_11

125

FMS should have highly reliable flexibility. The scheduling optimization is one of the important problems in FMS as it decides the efficiency and capability of the system. It is highly complex. It differs from conventional scheduling by routing flexibility that is available in the FMS. Scheduling is critical as its primary goal is to minimize the time taken to finish a product within a deadline. The level of difficulty for sequencing and scheduling of FMS depends upon the type of FMS, its process constraints and the performance parameters. Scheduling is one of the “NP” (nondeterministic polynomial time) hard problems, and it is complex in both time-wise and computational-wise.

Scheduling is a problem where jobs are allocated to particular machines with processing times and specific sequence of operations. It has to be ensured that machines are available without any breakdown, and it has to process an operation uninterrupted [1]. The intricacy of scheduling problem in a FMS is difficult than conventional job shop scheduling, as it should allocate jobs among the set of machines available. It is a well-known NP hard problem.

1.1 Earlier Research

FMS can be classified as (a) design problems (b) planning problems (c) scheduling problems (d) control problems. Stecke [2] proposed a framework to study planning and scheduling problems of FMSs. FMS problems are solved by traditional techniques and non-traditional techniques like meta-heuristics. In our proposed approach, we have used meta-heuristic techniques. Hence, the review is mainly done for scheduling problems that used meta-heuristic techniques. Zhao et al. [3] have presented a genetic algorithm with the concepts of virtual and real operations. Chromosome coding and genetic operators of GAs are defined during the problem solving. A minimum weighted tardiness objective function is used to define code fitness, which is used for selecting species and producing a new generation of codes. Kumar et al. [4] have used ACO for the graph-based representation of the FMS scheduling problem. The authors have studied the performance of various parameters and validated it. Noorul Haq et al. [5] have contemplated production and MHS scheduling in combination. The authors studied different scheduling decisions of FMS to check its efficiency by GA and SA. Jerald et al. [6] have proposed four different approaches such as PSO, GA, SA and memetic algorithm (MA) for large variety of problems with 10–43 jobs and 8–16 machines. PSO showed its superior performance over other techniques. Gnavel Babu et al. [7] have made AGV as a part of the scheduling problem. The author demonstrated the effectiveness of proposed differential evolution in obtaining optimal solutions for simultaneous scheduling for the same. Udhayakumar and Kumanan [8] have adopted extended Giffler and Thompson to generate an optimal schedule by an ACO approach. Their algorithm was found to be superior as its results are better than other techniques found in the literature. Sreedhar kumar et al. [9] have solved a combined objective function by bacterial foraging algorithm (BFOA). They moderated the penalty by including a

reward and evaluated the effectiveness of objective function. Nidish Mathew Nidhry et al. [10] have attempted to solve a multi-objective problem. The authors considered 16 machines with 80 job varieties. And they have proved that their algorithm performs better than other algorithms. Reddy and Rao [11] considered the simultaneous scheduling of machine and automated guided vehicles for multi-objectives. The authors considered some benchmark problems reported in the literature and few case studies to test the proposed hybrid GA and found the algorithm to have a better performance. Burnwal and Deb [12] had developed a modified cuckoo search to solve a 43 jobs with 16 machines problem. They have proved that CS requires less time to converge and have the potential to explore further. Chawla et al. [13] have investigated the simultaneous scheduling of AGVs workload and its travel time. They have considered multi-objectives and obtained the optimal schedule by grey wolf optimization algorithm (GWO).

Literature review shows that various meta-heuristics have been applied in order to achieve the best optimization of benchmark problems. Though many meta-heuristic techniques have found success in finding optimal solution, there is still a scope to find better optimal result when we hybridize the meta-heuristic techniques. One such attempt has been made in this article, and an amalgamation of genetic algorithm (GA), particle swarm optimization (PSO), tabu search (TS) has been done. The resulting hybrid technique is christened as GAPSOTS. The main advantage of this hybrid technique is that we have used one global search and two local search methods, thereby preventing the trapping of local optima. GA has good probability for finding better global solutions, PSO is known for solving combinatorial optimization, and TS gives a better neighbourhood search. The novel algorithm GAPSOTS has been applied to generate optimal schedules for the FMS environment taken from the literature for combined objectives, which contradicts each other. The FMS environment considered in our paper is for two different set-ups, a 43 jobs 16 machine problem and 80 jobs 16-machine problem. The outcomes are then compared with existing optimal values taken from the literature for the same problems. The results and future scope have been discussed in results section.

2 Problem Definition

The FMS set-up considered in this work, the assumptions made and objective of the present work are adopted from [6] and are presented in the following points.

1. The FMS set-up taken in this work is shown in Fig. 1. It has five flexible machining cells (FMCs), with two to six computer numerical machines (CNCs) for each FMC, an autonomous tool magazine, one tool changer (ATC) that is automatic and one pallet changer (APC) that is automatic. One to three dedicated robots are assigned for intra cell movement of resources among the jobs. A loading and unloading stations are dedicated exclusively to release parts in batches when required and for moving the finished jobs to the storage. The

automatic storage and retrieval system (AS/RS) are utilized for stocking the jobs that are incomplete. The five FMCs are conjoined by a couple of similar AGVs. These AGVs move any unfinished products to AS/RS and FMC and move finished products to the unloading dock.

2. The following assumptions are made: i) The number of products considered vary from 40 to 80 jobs for a specific mix of tools in tool magazines. Each job must be processed in a specific order, lot size, due date, and a penalty cost is imposed when the product due date is not met. Every job has to follow a particular sequence in a particular machine for specified amount of time. A product mix with processing times is shown in Table 2.
3. This study aims to solve a combined optimization problem for minimization of idle time of a machine and total penalty cost.

Combined Objective Function (COF)

$$\text{COF} = (\omega_1) * \frac{\text{TPC}}{\text{Max PP}} + (\omega_2) * \frac{\text{TMI}}{\text{Max TE}} \quad (1)$$

where

ω_1 and ω_2	weights assigned. The value considered is 0.5 for both weights.
TPC	penalty cost incurred in total.
TMI	machine idle time.
Max PP	maximum penalty that is permissible.
Max TE	maximum elapsed time of the machine.

3 The Proposed Hybrid Algorithm (GAPSOTS)

3.1 GAPSOTS Algorithm Design

An effective multi-objective scheduling approach GAPSOTS is applied, which is a combination of the genetic algorithm (GA), particle swarm optimization (PSO) and tabu search (TS) algorithms (GAPSOTS algorithm). The purpose of using genetic algorithm with multiple objectives is to successfully resolve multiphase process scheduling in FMS setting. Then, PSO algorithm is applied for optimization the scheduling process and TS helps in solving combinatorial optimization issues. This new approach is made by hybrid method with multiple objectives to handle the flexible job scheduling complications with manifold goals. Investigational studies have been utilized to validate the method, and matching the results of the recommended method to specify the compliance/flexibility and supremacy of the present model does a comparative analysis. The proposed algorithms have been implemented and tested by using MATLAB R2016b or beyond, computing environment on an Intel Core™i7, with Windows 10.

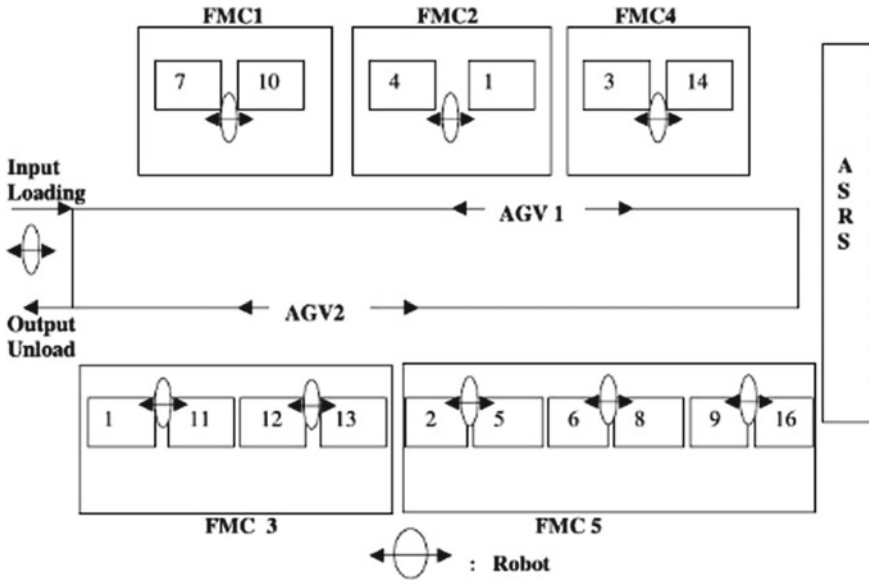


Fig. 1 FMS structure

The genetic algorithm (GA) is an adaptive heuristic exploration technique through which suitable answers to the problems of searching and optimizing can be made on the basis of a fitness function. It is a subsection of evolutionary algorithm, which provides responses to the optimizing issues by naturally stimulated algorithms and includes mutation, reproduction, and cross over, etc. In GA, there is a string of finite length called as chromosome that serves as representation of individual solution. There are position sets that are known as “genes” in a chromosome. Discrete values are given to those genes according to the solution. Crossover and mutation are genetic operators that are used to modify chromosome in order to create a new generation of “kids” that will have the characteristics of both “parents”. Every iteration results in moving towards the multi-objective optimization. Particle swarm optimization is mimicking the flock pattern of birds. In PSO, the probable solutions are termed as particles that will move in problem search space. Fitness values will be assigned to particles, which are then evaluated for fitness function that has to be optimized. Velocities will direct the path that should be taken by particles. The current feasible solutions will be pursued by the particles that will be flown in the problem space. Initialization of PSO is done randomly, and it moves towards optimum solution at each iteration by updating. The updated particles have two best values. One is “pbest”, the best solution achieved by a particular particle so far and “gbest”, the best solution achieved by any particle in the whole set (global best). Tabu search (Glover and Laguna, 1997) is a meta-heuristic method that has been effectively applied in several multi-objective optimization problems in scheduling. It is one of the popular local search algorithms that prevent the trapping of local optima. TS algorithm is

fundamentally a neighbourhood approach and offers a way to clear the inflexible combinatorial problems of optimizing. It helps to get rid of “local optima” problems for such ambience. The process of transfer of present solution to the adjoining solution is termed as move. The neighbourhood/nearby solution providing optimal solution is attained through a “move” in case of TS algorithm.

3.2 The Framework of GAPSOTS

The framework of our hybrid technique GAPSOTS is given as follows:

Step 1: Setting up of parameters.

Step 2: First initial population is generated by GA.

Step 3: The fitness function is evaluated.

Step 4: Has termination criteria been achieved?

If yes End program and display results.

Else goto Step 5.

Step 5: Generation of New populace.

Step 5.1: Application of genetic operators.

Step 5.2: Apply PSO for getting quality particles. Update global best solution.

Step 5.3: Check for termination criteria.

If yes End program.

Else goto step 5.4

Step 5.4: Generation of neighbourhood.

Step 5.5: If aspiration criterion is met, replace and update tabu list.

Step 5.6: Perform steps 5–5.5 until a termination condition is satisfied or reach maximum iteration.

The workflow process of GAPSOTS is given in Fig. 2. Detailed explanation of the proposed GAPSOTS is given in following paragraphs.

3.3 Genetic Operators for GA

To address the optimization problem, genetic operators that is used has to be very rich and so that we can achieve excellent individuals in the population. Selection, crossover and mutation are the three important genetic operators.

3.3.1 Reproduction

The method of rank selection is employed for reproduction. In rank selection method, first the entire population is ranked and the chromosomes are assigned fitness values. The least fitness will be given 1 and next will be 2 and the last will be N. The

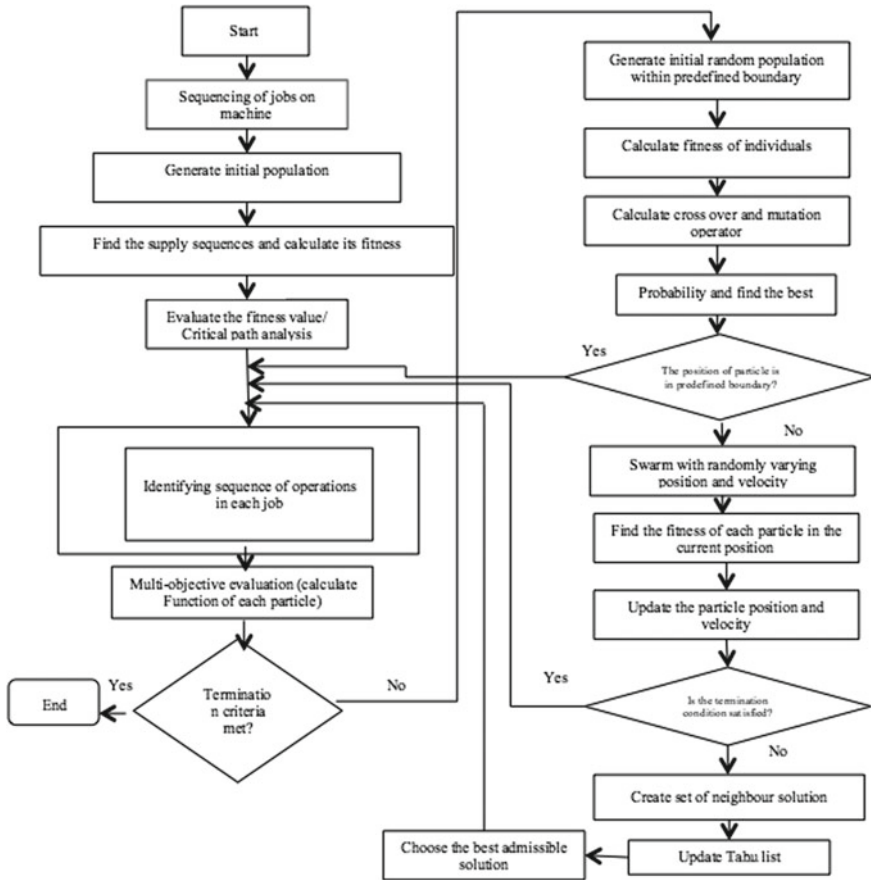


Fig. 2 Workflow process for proposed GAPSOTS

main advantage of rank selection method is it can avoid the algorithm to converge prematurely. Another advantage is that in this method the importance is given to ranks rather than the fitness values. That way the selection pressure is maintained. This method also helps to maintain diversity thereby enhancing the search. The fitness values assigned in this paper range from 0.4 to 1.6.

Once done with above calculation of every ranking, the reproduction is carried out using MATLAB simulation through employing arbitrary numbers.

3.3.2 Crossover

This operation is used after the reproduction is over. For this the “mating pool” is provided with strings. Generally, it is a convergence operation that is anticipated to have a value with regard to either “local” minimum or maximum.

- (1) Randomly select several positions of $R1$ and $R2$ and exchange the genes. Whereas other genes in other locations remain unchanged.
- (2) Check for any conflict to delete the same gene as the exchange position in the original parent gene.
- (3) Unused genes are then filled in the gene vacancy sequentially.

3.3.3 Mutation

Mutation is actually a dissimilarity task. It is just a process of tweaking the chromosome a little bit in order to maintain divergence. The mutation process is the “exploration” of the search universe. It is proposed to periodically break at least one individual from a populace out of a nearby least/greatest space and possibly find a superior least/most extreme space. A random variable is generated for each bit in a sequence to implement mutation. This random variable shows if a particular bit will be modified or not. The main objective of mutation is to avoid the chromosome population becoming too identical to each other thereby preventing the entrapment of local optima.

To boost the local search capability, the mutation operator is utilized and also maintained the population diversity ratio. The ratio of mutation probability is attained by,

$$\text{Mutate} - p = k_3 \frac{f_{\max} - f_i}{f_{\max} - f_{av}} \quad \text{if } f_i \geq f_{av} \quad (2)$$

$$\text{Mutate} - p = k_4 \quad \text{if } f_i < f_{av} \quad (3)$$

where

- $\text{Mutate}-p$ probability mutation.
- f_m maximal value of fitness in the population.
- f_{av} fitness value in average in the entire population.
- k_3 and k_4 are considered as a common value a ($0 < k_3 < 1$, $0 < k_4 < 1$).
- f_i the individual fitness value that will perform the mutation operator.

3.4 Particle Swarm Optimization (PSO) and Tabu Search (TS)

Particle swarm optimization (PSO) algorithm is a meta-heuristic technique based on evolution developed by Eberhart and Kennedy (1995). The mutation done in GA may bring us the good results. The mutation of gene is vital to maintain the divergence of population. But to improve the optimal strategies performance, we have applied PSO and tabu search algorithm.

In PSO, the individual solution is called “bird” in the searching space. They are referred to as “particles”. Each and every particle will have a value for fitness that is estimated using the function of fitness. These functions are to made optimum. There is a particular velocity to guide the movement of the particles. The particles will be flowing inside the problematic region in the direction next to the present particles with optimum functions. This algorithm has set of arbitrary particles at initial stage, which are the solutions and then begin to search for further possible optimum values by means of upgrading the generations. The particles are reorganized with new values at every step of iteration with two terms with best values, namely particles’ best, P_{best} and global best, g_{best} . One is the best fitness attained by the particle until then. The next one is the total best value of many such swarms. At every step, the velocity of every single particle is altered to stretch towards P_{best} and g_{best} . With the fresh values of velocity and location, the fitness function will be estimated with new-fangled ordinates.

The best solution with respect to the ordering structure and choosing is needed for the scheduling optimizing of flexibility oriented manufacture. The PSO and TS algorithms are hence utilized for clearing the issues related to “combinatorial” optimizing. The methodology will be adopted for arbitrarily created instances and for practical applications to exhibit the superiority of the suggested method.

The movement of the particle to find the optimal value is given by Eqs. 4 and 5

$$v_{id} = \omega \times v_{id} + G_1 \times r_1 \times (p_{idk}^{best} - p_{idk}) + G_2 \times r_1 \times (p_{gd}^{best} - p_{idk}) \quad (4)$$

$$v_{id} = \omega \times v_{id} + G_1 \times r_1 \times (p_{idk}^{best} - p_{idk}) + G_2 \times r_1 \times (p_{gd}^{best} - p_{idk}) \quad (5)$$

In Eq. (4), v_{id} means the distance moved by idk th particle for one iteration between $[-Mmax; Mmax]$ in which $Mmax$ is the maximum distance moved by a particle in one step. “ ω ” is called inertial weight that is a variable, which calculates the distance moved by a particle in each step. $G1$ is the self-learning factor, meaning a particle learn from its own knowledge p_{idk}^{best} . $G2$ is the social learning factor, meaning a particle’s knowledge globally, i.e. of the entire swarm p_{gd}^{best} . r_1 is a random number generated from an uniform distribution of $[0,1]$. p_{idk} denotes the position of idk th particle.

p_{idk}^{best} denotes the best personal value of idk th particle and p_{gd}^{best} denotes the best global value of all particles of a swarm. The newly generated velocity for idk th particle is obtained by Eq. 4, and updation of position is obtained by Eq. 5

A particle might leave the search area, to prevent this a maximum velocity factor is employed to the PSO so that the velocity is limited within a range. This allows the particle to move freely but in a constrained search area and is given by Eq. 6

$$v_{lmn}^t = \min\{M_{max}; \max\{-M_{max}; v_{lmn}^t\}\}, \quad m = 1, \dots, M; \quad l = 1, \dots, L \quad (6)$$

To achieve global optimum, a larger value of inertia weight ω is preferred and small inertia weight is preferred to explore locally and thus convergence happens

fast. In order to strike a balance between exploration and exploitation, a linear inertia weight that decreases with the convergence of algorithm evolving was adopted that has exhibited good global search ability initially and in later iterations good local search ability.

$$\omega[t] = (\omega_{\text{initial}} - \omega_{\text{final}}) \cdot \left(\frac{g-t}{g}\right)^m + \omega_{\text{final}} \quad (7)$$

where

ω_{initial} initial weight inertia
 ω_{final} final weight inertia
 g maximal number of iterations.
 $\omega_{\text{initial}} > \omega_{\text{final}}$, and $m \in [0.6; 1.4]$ are the nonlinear index [14, 15].

Then the process of tabu search (TS), which was introduced by Glover in 1986, overcomes the local optimality issues based on the evaluation function that has been selected with the highest evaluation solution at each iteration. The initial population of tabu search is done by taking the result of PSO, and some random solutions are introduced. Next step is neighbourhood structure where the existing solutions will be modified to obtain new solutions. The movement of solutions is accepted on the basis of probability function. A tabu list is created to store the properties of the accepted moves, and they will be avoided in later iterations thus called “taboo”. In the new neighbourhood, the best neighbour (solution) will be chosen that is not a tabu. This is applied to avoid cyclic movements. A strategy called forbidding is employed to control and update the tabu list. The parameters used for this hybrid technique GAPSOTS are given in Table 1.

Table 1 Parameters of proposed hybrid technique—GAPSOTS

Parameters	Value
Population size	500
Crossover probability	0.5
Mutation probability	0.9
The total number of generations	200
Length of tabu list	10
The maximum iteration size	800
Number of particles	20

Table 2 Part mix with due date and penalty cost

Part number	Processing sequence: Machine number (processing time in minutes)	Due date (days)	Batch size (No.)	Penalty (Rs/unit/day)
1	6(1)-7(1)-8(1)-10(2)	17	150	1.00
2	2(1)-6(1)-8(2)-9(2)-14(4)-16(2)	17	200	1.00
3	8(1)-11(3)-13(4)	14	800	1.00
4	9(4)	26	700	2.00
5	4(5)-5(3)-15(4)	11	150	1.00
6	6(5)-14(1)	16	700	1.00
7	3(5)-6(3)-16(5)	26	250	2.00
8	5(4)-6(5)-8(1)	26	850	2.00
9	4(1)-5(5)-8(1)-11(1)	1	100	0.00
10	2(2)-9(1)-16(4)	20	150	2.00
11	8(4)-12(2)	1	250	1.00
12	6(2)-8(4)-10(1)	19	1000	3.00
13	6(1)-7(5)-10(4)	25	700	400
14	4(2)-5(3)-6(2)-15(2)	22	1000	400
15	5(4)-8(3)	15	700	5.00
16	5(3)	27	750	3.00
17	3(1)-6(4)-14(1)	20	650	5.00
18	9(2)-6(3)	24	250	400
19	4(1)-5(5)-6(2)-8(2)-15(5)	5	450	1.00
20	8(2)-11(4)	11	50	5.00
21	4(5)-5(5)-8(4)-15(4)	16	850	3.00
22	12(5)	24	200	5.00
23	4(2)-5(1)-6(5)-8(4)	14	50	400
24	8(4)-11(4)-12(5)-14(4)	7	200	5.00
25	7(3)-10(2)	24	350	1.00
26	10(2)	27	450	0.00
27	8(5)-11(5)-12(4)	22	400	1.00
28	2(1)-8(1)-9(2)	3	950	5.00
29	4(1)-5(5)	7	700	1.00
30	11(3)-12(5)	18	1000	1.00
31	8(2)-10(2)	2	800	2.00
32	2(3)-6(4)-9(3)	15	800	1.00
33	5(4)-6(5)-15(3)	27	500	4.00
34	3(2)-6(2)	12	300	4.00
35	3(4)-14(1)	9	900	2.00

(continued)

Table 2 (continued)

Part number	Processing sequence: Machine number (processing time in minutes)	Due date (days)	Batch size (No.)	Penalty (Rs/unit/day)
36	3(2)	20	700	2.00
37	1(5)-2(2)-6(3)-8(3)-9(2)-16(4)	22	250	4.00
38	2(4)-8(3)-9(2)-16(5)	8	50	1.00
39	6(5)-10(5)	9	500	1.00
40	2(2)-6(4)-9(4)	7	250	5.00
41	5(1)-8(2)-15(1)	22	800	4.00
42	2(5)-6(4)-9(3)-16(1)	19	400	2.00
43	1(3)-5(2)-6(2)-8(2)-15(3)	15	550	3.00

4 Results and Discussions

The FMS problem considered in this work is taken from existing literature [6]. The hybrid procedure GAPSOTS is developed for 43 jobs and 80 jobs for 16 machines using combined objective optimization method. The problem matrix taken for this problem is given in Table 2. MATLAB software version R2016b and above is used for programming. The MATLAB helps the user to solve complex scheduling problems. TOMLAB/CPLEX is also used as it is a subproblem solver and handles quicker solving of mixed-integer linear and quadratic programming (MILP,MIQP), and linear and quadratic programming (LP,QP). Feasible schedule has been achieved for the combinatorial scheduling using the above hybrid approach. A comparison between the proposed GAPSOTS and other algorithms, namely GA, SA, memetic algorithm, cuckoo search (found in the literature) has been analysed and shown in Table 3 and Fig. 3 for 43 jobs 16 machine problem and Fig. 4 for 80 jobs 16 machine problem. The proposed algorithm has been run for different iterations. When the iterations numbers are less the results were not good, but as iterations increased we got better results. We stopped at 800 iterations, as there was no significant change in optimal value later.

5 Conclusion

The following points summarize the authors contribution made in this paper.

- A new hybrid technique named GAPSOTS has been developed by hybridizing GA, PSO, TS. A global search technique has been combined with two local search methods thereby balancing the drawbacks of the said techniques.

Table 3 Performance comparison of GAPSOTS with various techniques

Problem size	Objectives	Genetic algorithm	Simulated annealing	Memetic algorithm	Cuckoo search	GAPSOTS
43 jobs × 16 machines	COF	0.274	0.45936	0.35136	0.2646	0.11967
	Sequence	21; 28; 16; 42; 39; 25; 5; 23; 22; 35; 36; 37; 15; 1; 2; 9; 4; 3; 40; 20; 31; 11; 14; 30; 27; 43; 17; 10; 7; 26; 33; 18; 29; 8; 41; 32; 13; 12;	36 25 14 39 1 33 27 3 13 4 18 22 0 42 28 35 30 38 8 26 11 24 23 41 13 24 37 10 32 9 20 12 9 6 16 17 15 21 7 29 5	10 35 18 27 3 42 5 19 2 39 83 34 30 0 26 36 22 28 38 7 34 11 31 24 23 1 32 1 14 12 5 15 20 9 16 41 21 6 17 29 40 7	8, 14, 28, 31, 3, 42, 26, 33, 22, 20, 5, 24, 12, 41, 18, 7, 10, 19, 23, 38, 4, 35, 40, 37, 15, 15, 17, 39, 6, 2, 34, 1, 29, 27, 16, 36, 30, 25, 32, 13, 43, 11, 10, 9	30 29 8 26 13 31 38 24 37 20 33 7 11 36 23 12 39 18 34 42 35 21 28 36 17 25 5 4 15 22 9 40 2 1 27 14 10 32 19 41 16 43
80 jobs × 16 machines	COF	0.0959237	0.14738715	0.1067266	-	0.08537
	Sequence	34, 50, 59, 76, 48, 69, 31, 11, 1, 26, 56, 23, 47, 25, 62, 20, 3, 78, 55, 53, 24, 51, 70, 71, 75, 46, 58, 74, 4, 2, 28, 18, 38, 22, 54, 5, 72, 12, 13, 40, 10, 60, 65, 79, 43, 37, 66, 27, 42, 7, 64, 61, 29, 35, 36, 73, 39, 49, 67, 2, 41, 15, 17, 44, 45, 63, 21, 6, 80, 9, 19, 57, 14, 33, 16, 68, 52, 77, 8, 32	41, 53, 51, 70, 1, 71, 47, 58, 36, 61, 30, 4, 23, 54, 75, 77, 76, 52, 79, 31, 15, 78, 35, 59, 66, 72, 55, 56, 64, 28, 40, 13, 45, 17, 14, 48, 80, 49, 34, 25, 10, 20, 44, 29, 11, 60, 67, 38, 27, 9, 12, 32, 46, 5, 18, 43, 65, 37, 24, 21, 42, 2, 63, 19, 7, 22, 33, 74, 26, 57, 16, 62, 3, 39, 69, 6, 50, 73, 68, 8	69, 17, 36, 24, 74, 61, 20, 35, 75, 49, 25, 18, 58, 47, 3, 52, 28, 45, 51, 59, 46, 6, 16, 34, 31, 53, 70, 76, 22, 2, 40, 79, 15, 30, 62, 54, 38, 10, 43, 13, 80, 37, 71, 26, 66, 73, 72, 65, 56, 67, 12, 1, 4, 5, 21, 32, 77, 27, 29, 63, 33, 60, 64, 57, 41, 9, 14, 48, 55, 78, 7, 42, 11, 23, 39, 8, 50, 68, 19, 44	39, 26, 8, 32, 35, 78, 59, 27, 51, 18, 19, 31, 52, 71, 57, 5, 1, 74, 22, 13, 63, 58, 33, 34, 65, 29, 48, 42, 70, 17, 9, 56, 40, 49, 67, 30, 3, 66, 7, 45, 11, 23, 80, 38, 16, 46, 44, 21, 60, 75, 24, 10, 4, 53, 47, 15, 76, 20, 6, 54, 72, 43, 64, 50, 2, 14, 73, 25, 69, 77, 41, 28, 79, 61, 55, 68, 36, 12, 37, 62	

Fig. 3 Comparison of COF for 43 jobs by different approaches

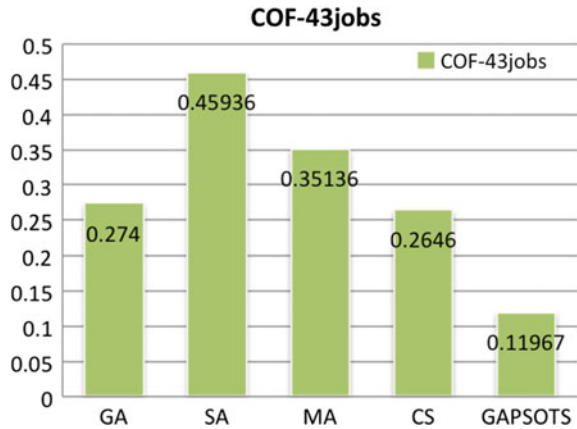
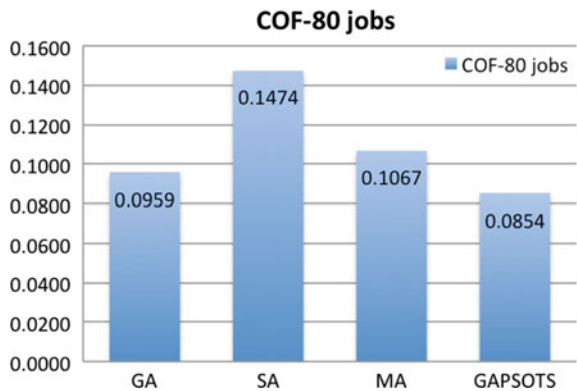


Fig. 4 Comparison of COF for 80 jobs by different approaches



- The developed technique was tested for benchmark problems taken from the literature, which consists of 2 problems of 43 jobs × 16-machine problem and 80 jobs × 16 machine problem.
- A less solved combinatorial optimization problem for minimizing the total penalty cost and total machine idleness has been evaluated.
- Optimal results were obtained with less computational time, and the results were found to be superior to other approaches found in the literature. The difference we got is subtle yet the results were promising to explore other adaptations of GA, PSO, TS.
- The main observation is with less number of generations we got a better optimal value. With adaptations made in genetic operators, the premature convergence of algorithm has been prevented.
- In future, the proposed GAPSOTS can be tested for integrated scheduling FMS and can be implemented for any FMS with different set-ups.

References

1. Mathew N, Saravanan NR (2012) Evaluation of genetic algorithm approach for scheduling optimization of flexible manufacturing systems. *Int J Eng Res Appl* 2:437–446
2. Stecke KE (1985) Design, planning, scheduling, and control problems of flexible manufacturing systems. *Ann Oper Res* 3:1–12. <https://doi.org/10.1007/BF02023765>
3. Zhao C, Wu Z (2001) A genetic algorithm approach to the scheduling of FMSs with multiple routes. *Int J Flex Manuf Syst* 13:71–88. <https://doi.org/10.1023/A:1008148313360>
4. Kumar R, Tiwari MK, Shankar R (2003) Scheduling of flexible manufacturing systems: an ant colony optimization approach. *Proc Inst Mech Eng Part B J Eng Manuf* 217:1443–1453. <https://doi.org/10.1243/095440503322617216>
5. Noorul Haq A, Karthikeyan T, Dinesh M (2003) Scheduling decisions in FMS using a heuristic approach. *Int J Adv Manuf Technol* 22:374–379. <https://doi.org/10.1007/s00170-002-1474-0>
6. Jerald J, Asokan P, Prabakaran G, Saravanan R (2005) Scheduling optimisation of flexible manufacturing systems using particle swarm optimisation algorithm. *Int J Adv Manuf Technol* 25:964–971. <https://doi.org/10.1007/s00170-003-1933-2>
7. Gnanavel Babu A, Jerald J, Noorul Haq A et al (2010) Scheduling of machines and automated guided vehicles in FMS using differential evolution. *Int J Prod Res* 48:4683–4699. <https://doi.org/10.1080/00207540903049407>
8. Udhayakumar P, Kumaran S (2010) Sequencing and scheduling of job and tool in a flexible manufacturing system using ant colony optimization algorithm. *Int J Adv Manuf Technol* 50:1075–1084. <https://doi.org/10.1007/s00170-010-2583-9>
9. Kumar AVSS, Veeranna V, Durgaprasad B, Sarma BD (2013) Combined objective optimization of FMS scheduling with non-traditional optimization techniques. *Int J Eng Res Technol (IJERT)* 2:1420–1428
10. Nidhish Mathew Nidhiry DRS (2012) A combined objective genetic algorithm for scheduling of machines in FMS. *Int J Eng Res Appl*
11. Reddy BSP, Rao CSP (2006) A hybrid multi-objective GA for simultaneous scheduling of machines and AGVs in FMS. *Int J Adv Manuf Technol* 31:602–613. <https://doi.org/10.1007/s00170-005-0223-6>
12. Burnwal S, Deb S (2013) Scheduling optimization of flexible manufacturing system using cuckoo search-based approach. *Int J Adv Manuf Technol* 64:951–959. <https://doi.org/10.1007/s00170-012-4061-z>
13. Chawla VK, Chanda AK, Angra S (2019) The scheduling of automatic guided vehicles for the workload balancing and travel time minimization in the flexible manufacturing system by the nature-inspired algorithm. *J Proj Manag* 4:19–30. <https://doi.org/10.5267/j.jpm.2018.8.001>
14. Chatterjee A, Siarry P (2006) Nonlinear inertia weight variation for dynamic adaptation in particle swarm optimization. *Comput Oper Res* 33:859–871. <https://doi.org/10.1016/j.cor.2004.08.012>
15. Durand FR, Abrão T (2013) Particle swarm optimization in WDM/OCDM networks with physical impairments. *J Microwaves Optoelectron Electromagn Appl* 12:336–352. <https://doi.org/10.1590/S2179-10742013000200008>

Comparison of Nature-Inspired Approaches for Path Planning Problem of Mobile Robots in MATLAB



Divya Agarwal and Pushpendra S. Bharti

Abstract Robot path planning is a significant research topic that comprises massive mathematical computations for generating an optimal shortest collision-free path from starting position to goal position within minimum processing time. Robotics is an interdisciplinary field that is directly related to automation. Automation requires planning and organization of workspace for the autonomous working of robots and machines. Recently, researchers' curiosity has increased to implement nature-inspired evolutionary (NIE) approaches for path planning and obstacle avoidance (PPOA) problem. NIE approaches allow robots to learn from elements of nature and perform better compared to conventional and heuristic PPOA approaches. This work draws a comparison between the IWO and ABC algorithm for the same set of environments and initial conditions for the PPOA problem. The results show that the IWO algorithm has a faster convergence rate and high precision than the ABC algorithm.

Keywords Path planning · Obstacle avoidance · Invasive weed optimization · Artificial bee colony optimization · Nature-inspired evolutionary optimization

1 Introduction

Robot path planning is a significant research topic that comprises massive mathematical computations for generating an optimal shortest collision-free path from starting position to goal position within minimum processing time [1]. Path planning is a method to formulate a collision-free path in a workspace with static or dynamic obstacles and optimizing the path as per objective function and constraints. Path planning is established through a workspace map, and path planning and obstacle avoidance (PPOA) approaches help robots to traverse through a workspace evading collision from obstacles [2].

D. Agarwal (✉) · P. S. Bharti
Guru Gobind Singh Indraprastha University, New Delhi 110078, India

There are numerous PPOA approaches available for researchers to adapt to their problems. However, their choice depends on the type of environment (static—fixed and known obstacles or dynamic—unknown obstacles), performance parameters (processing time and path length), size of robot and obstacles, the shape of obstacles, number of constraints or assumptions to be made depending on application and complexity of workspace [3]. Based on the above information, PPOA can be broadly categorized into global PPOA approach where all information is known to the robot at the start, and local PPOA approach where incomplete or no information is available to the robot, and it has to decide on its own based on the situation [4]. The core objective of any PPOA approach must be to give a smooth, optimal and complete path for the robot to traverse from start to end without collision. The PPOA approaches can be categorized into conventional approaches (such as bug algorithm, roadmaps, and bidirectional trees algorithms), heuristic approaches (such as artificial neural networks, genetic algorithm, harmony search), nature-inspired evolutionary (NIE) approaches (such as particle swarm optimization, whale optimization, shuffled frog leaping algorithm, artificial bee colony optimization (ABC), invasive weed optimization (IWO)) and hybrid approaches (which are a combination of two algorithms which are amalgamated to balance each other and give optimal results) [3, 5].

Recently, NIE approaches have gained much interest as they take inspiration from elements of nature, which makes these algorithms flexible and robust. These algorithms are better computational approaches to solve complex PPOA problems efficiently and effectively. They are flexible, dynamic and parallel in approach, and most importantly, their self-organizing and self-learning capability inspired researchers to exploit them for solving complex problems [3, 6].

This paper comprises a comparison of the performance of IWO and ABC algorithms for the PPOA problem on MATLAB 2020a. For simulation work, four workspaces were considered encompassing different combinations of fixed circular-shaped obstacles. The different workspaces were considered to illustrate the performance of IWO and ABC algorithm for different complexity workspaces or environments. This research work aims to illustrate how the robot would traverse towards the destination, evading obstacles in a 2D environment using MATLAB simulation platform. IWO and ABC algorithms were implemented due to their wide range of applications. The effectiveness and superiority of these algorithms are depicted through the simulation of these algorithms in MATLAB 2020a. Simulation results of IWO and ABC algorithms are compared with one another for the same environment to validate their application in the PPOA problem.

The paper is organized as follows. Section 2 comprises a brief description of IWO, and paper is organized as follows. Section 2 comprises a brief description of the IWO and ABC algorithm, and Sect. 3 deals with experimentation and problem formulation. Section 4 comprises results and discussion and simulation results on MATLAB 2020a. Section 5 entails the conclusion and future scope.

2 A Brief Background

This section outlines in brief IWO and ABC algorithms and discusses brief literature related to them and their implementation steps.

2.1 *Invasive Weed Optimization (IWO)*

Weed colonization and distribution inspired Mehrabian and Lucas [5] to propose a stochastic NIE algorithm named IWO. Weeds are unwanted plants but robust and adaptive [7]. IWO is a metaheuristic algorithm for solving multi-resource path planning (MRPP) problem in partially or unknown environments while avoiding obstacles. It comprises following principle steps [1, 7]: (1) initialization: population initialization of weeds or artificial robots, number of iteration steps and initializing path from the start point to goal location; (2) reproduction and mutation of weeds depending on the fitness level of weeds, i.e. weeds produce seeds depending on maximum seeds for fittest weed and minimum seeds for weed with reduced fitness level; (3) spatial dispersal of seeds generated in step 2 in such a way that fitter seeds are found in neighbourhood of parent weed and are clubbed together while weak seeds are eliminated [3], and (4) competitive exclusion means that reproduction and mutation of fitter seeds stop when iteration limit is reached. When this algorithm is applied for robot navigation, the fittest and weakest seeds are stored in robot programming. When it encounters an obstacle in path, it avoids collision from it and manoeuvres towards target location [2]. Robots here mimic how population of weeds reproduces in any big or small geographical terrain. This approach was tested and showed effective and robust results for complicated situations [6].

Advantages: Can solve linear as well as nonlinear multi-objective optimization problem with greater performance efficiency and randomness [3]; adaptability; computation effort and time are independent of nonlinear nature of problem [1]; robustness [7]; better results obtained compared to bacterial foraging algorithm [2] and efficient technique for accelerating convergence rate of optimization technique [6]. Limitation is premature convergence [6]. Steps of IWO algorithm for mobile robot navigation are briefly discussed below [2]:

- (1) Initialize start and goal position of robot.
- (2) Navigate robot towards goal until it encounters an obstacle
- (3) When obstacles obstruct the target path, implement IWO algorithm.
- (4) Generate initial population of weeds.
- (5) Calculate objective function value of each weed and then find fittest and weakest weed.
- (6) When population size is more than the maximum population, eliminate weeds with lower objective function values.
- (7) Navigate robot towards the best weed position.
- (8) Repeat steps (2–7) until robot avoids obstacle and reaches its goal.

2.2 Artificial Bee Colony Optimization (ABC) Algorithm

It is a swarm-based NIE approach proposed by Karaboga [8], which mimics the food searching strategy of honeybees. In this algorithm, artificial bees are classified into three classes: employed bees (EB), onlooker bees (OB) and scout bees (SB) [9]. The size of bee colony is twice the number of food positions. Bee colony is composed of EB and OB [10]. After several iterations, if EB cannot improve food position, then it becomes a scout bee.

Food searching strategy comprises (1) EB scans and evaluates nectar quality in search of food; (2) OB receives information from EB and thereby chooses better quality nectar as food; (3) SB then determines locations where food could be found based on motivation or external clues ([11, 12]. Scouts are regarded as low search costs and a low average in food source quality [10]. Local path searching operation is done by EB and OB, while global path search is carried out by OB and scout bees [4]. Contreras-Cruz et al. [10] implemented the ABC algorithm for RPP problem in a static environment. ABCO is easy to implement and can be easily modified as per application needs. Advantages: simple implementation and computational efforts; minimal processing time; broad applicability; high flexibility [13, 14]. Its limitation comprises requirement of new fitness tests on addition of new parameters. It may lose information, i.e. if the nectar amount of new food source is better than the previous source, then it forgets and memorizes new sources; relatively slow for sequential processes; computational costs increase with an upsurge in population [15].

Steps of this algorithm are as follows [14]:

1. Initialize population.
2. Evaluate population size.
3. Classify onlooker and employed bees based on ranking.
4. Generate new solutions with onlooker and employed bees.
5. Generate solutions using scout bees and
6. Update population size after every iteration.

These steps keep on repeating until all objectives are met.

3 Experimentation

Table 1 outlines four different workspaces which were designed to illustrate comparison of performance amongst IWO and ABC algorithms. The workspaces were designed based on different number of obstacles, starting and final position, to achieve unbiased comparison results. For better performance of algorithms, certain assumptions are made at initialization and are termed specific control parameters. The values for these control parameters for ABC and IWO algorithms are defined in Table 2. For unbiased comparison in simulation work, the following parameter values were kept similar and fixed:

Table 1 Types of workspace by initializing number of obstacles, start and final position

S. No.	No. of obstacles	Start position	Final position
1	6	0, 0	10, 10
2	13	3, 3	14, 14
3	30	3, 3	14, 14
4	45	0,0	15, 15

Table 2 Specific control parameter values for ABC and IWO algorithms

S. No.	Name of control parameter	Parameter value	
		ABC	IWO
1	No. of onlooker bees	150	
2	Abandonment limit parameter or trial limit	450	
3	Acceleration coefficient	1	
4	Initial population size		10
5	Minimum no. of seeds		0
6	Maximum no. of seeds		5
7	Variance reduction exponent		2
8	Initial value of standard deviation		0.5
9	Final value of standard deviation		0.001

1. *numberofhandlingpoints*(n) = 5,
2. *maximumnumberofiterations*(500), and
3. *numberofpopulation*(150)

The x and y coordinates values of location of obstacles and their size are defined in Table 3. The simulation work was carried out on MATLAB 2020a with following system specifications:

1. Intel (R) Core™ i5 – 4210U CPU@1.7-GHz,
2. 64Bitoperationprocessor
3. 12GBRAM.

4 Results and Discussion

This paper’s objective is to check and compare the shortest optimized path generated by IWO and ABC for the same set of conditions. Here, algorithms’ performance is compared in terms of optimal path length and processing time in static environments. It can be inferred from Table 4 that for all four workspace maps, IWO outperforms ABC. IWO is an NIE approach based on weed optimization, i.e. based on microorganisms while ABC takes inspiration from foraging behaviour of bees, i.e. based on insects. Since weeds are unplanned and random in approach, they perform better

than the ABC algorithm, which is justified from Table 4 and Figs. 1, 2, 3 and 4. The best values obtained after evaluation, from both algorithms has been highlighted as bold in Table 4.

For all four workspace maps simulated in MATLAB 2020a, five tests were conducted, and its result is displayed in Table 4. Table 4 shows that for workspace map 1, IWO outperformed ABC algorithm with best cost in the least processing time, i.e. 14.3096 units in 82.1242 s (See Fig. 1). It can also be seen that IWO is highly precise and repeatable, which is of interest in designing a PPOA algorithm. For workspace map 2 shown in Fig. 2, best cost generated by IWO was 16.5568 units and 17.2873 units by ABC. In workspace map 2, it can be seen that as the number of obstacles increased and size of obstacles varied, though IWO gave the best cost in the least possible time, ABC was more precise than IWO. In Fig. 3, there are 30 obstacles of 0.4 sizes. In this workspace map, ABC and IWO are highly precise and repeatable, and their best cost is also close enough, but ABC takes more time

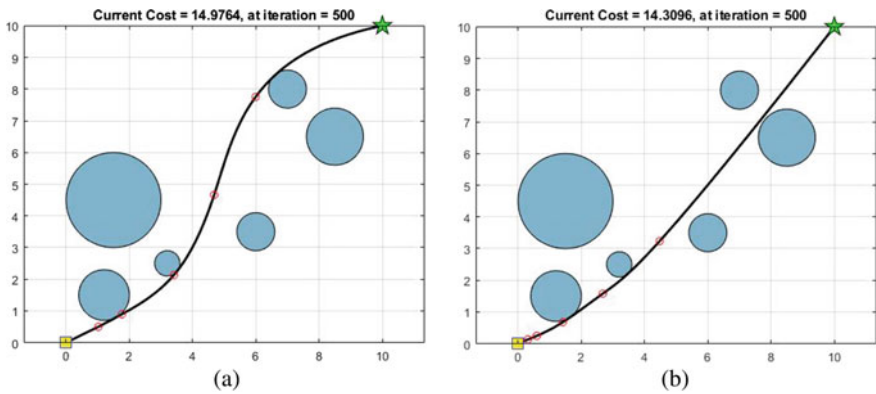


Fig. 1 Path generated for workspace 1: a ABC algorithm, b IWO algorithm

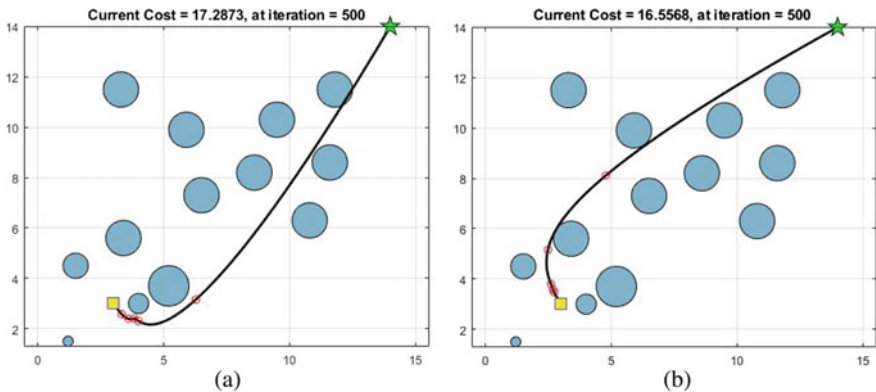


Fig. 2 Path generated for workspace 2: a ABC algorithm, b IWO algorithm

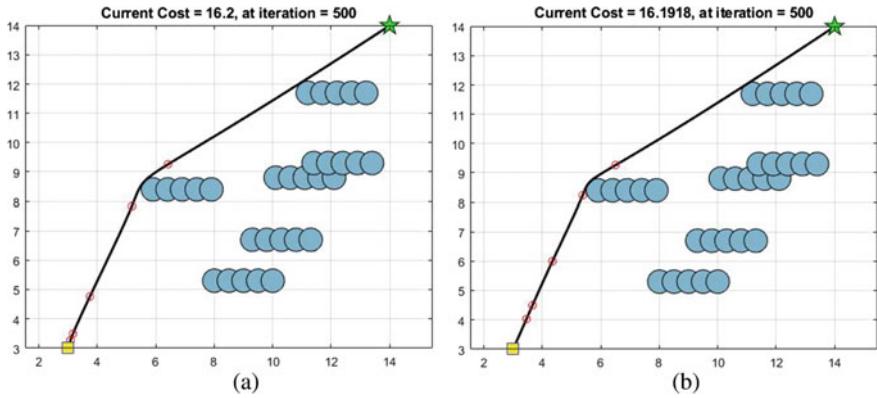


Fig. 3 Path generated for workspace 3: a ABC algorithm, b IWO algorithm

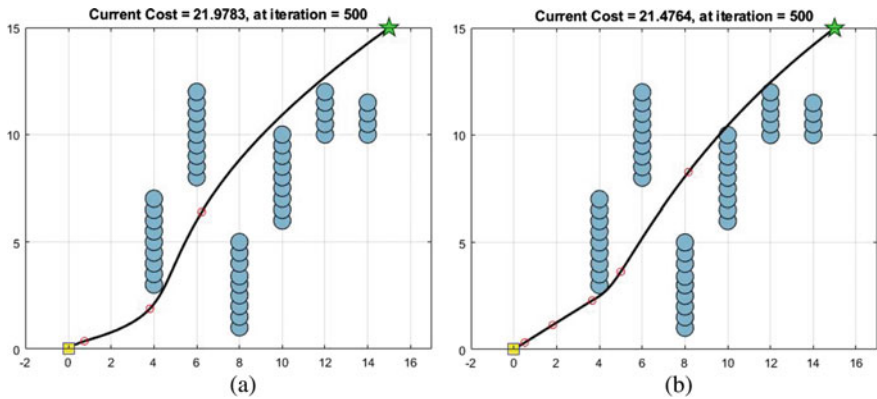


Fig. 4 Path generated for workspace 4: a ABC algorithm, b IWO algorithm

to process the best cost. Workspace map 4 is a complicated environment with 45 obstacles of 0.4 unit size shown in Fig. 4. In this workspace map, IWO not only outperforms ABC algorithm but is repeatable as well.

5 Conclusion and Future Scope

From the above simulation results, it can be concluded that both algorithms were complete approaches, optimal or near-optimal results and were able to evade local minima. It can be inferred from the results section that IWO algorithm is highly precise and repeatable, which must be of interest for application in PPOA domain. It can also be concluded based on results that IWO gave better performance for PPOA

optimization problem to produce optimal path with least cost in the least processing time, had population adjustment capabilities and could acclimatize quickly. In the future, work testing on the real mobile robot would be done to check the authenticity of the above-simulated results.

References

1. Ghalenoei MR, Hajimirsadeghi H, Lucas C (2009) Discrete invasive weed optimization algorithm: application to cooperative multiple task assignment of UAVs. In: Proceedings of the 48th IEEE Conference on Decision and Control (CDC) Held Jointly with 28th IEEE Chinese Control Conference, pp. 1665–1670 (2009)
2. Mohanty PK, Parhi DR (2016) A new efficient optimal path planner for mobile robots based on Invasive Weed Optimization algorithm. *Front Mech Eng* 9(4):317–330
3. Verma D, Saxena P, Tiwari R (2020) Robot navigation and target capturing using nature-inspired approaches in a dynamic environment. In: 10th international conference on cloud computing, data science & engineering (confluence), India, pp 629–636
4. Ma Q, Lei X (2010) Dynamic path planning of mobile robots based on ABC algorithm. In: International conference on artificial intelligence and computational intelligence. Springer, Berlin, pp 267–274
5. Mehrabian AR, Lucas C (2006) A novel numerical optimization algorithm inspired from weed colonization. *Eco Inform* 1(4):355–366
6. Panda MR, Das PK, Dutta S, Pradhan SK (2018) Optimal path planning for mobile robots using oppositional invasive weed optimization. *Comput Intell* 34(4):1072–1100
7. Sengupta A, Chakraborti T, Konar A, Nagar A (2011) Energy efficient trajectory planning by a robot arm using invasive weed optimization technique. In: IEEE Third world congress on nature and biologically inspired computing (NaBIC), pp. 311–316
8. Karaboga, D.: An idea based on honey bee swarm for numerical optimization. Technical report, Erciyes University, Computer Engineering Department, pp 1–6
9. Saffari MH, Mahjoob MJ (2009) Bee colony algorithm for real-time optimal path planning of mobile robots. In: *Soft computing, computing with words and perceptions in system analysis. Decision and control*, pp 1–4
10. Contreras-Cruz MA, Ayala-Ramirez V, Hernandez-Belmonte UH (2015) Mobile robot path planning using artificial bee colony and evolutionary programming. *Appl Soft Comput* 30:319–328
11. Xu C, Duan H, Liu F (2011) Chaotic artificial bee colony approach to Uninhabited Combat Air Vehicle (UCAV) path planning. *Aero Sci Technol* 14(8):535–541
12. Bhagade AS, Puranik PV (2012) Artificial bee colony (ABC) algorithm for vehicle routing optimization problem. *Int J Soft Comput Eng* 2(2):329–333
13. Ding L, Wu H, Yao Y (2015) Chaotic artificial bee colony algorithm for system identification of a small-scale unmanned helicopter. *Int J Aerospace Eng*, Article ID 801874
14. Liang JH, Lee CH (2015) Efficient collision-free path planning of multiple mobile robots system using efficient artificial bee colony algorithm. *Adv Eng Software* 79:47–56
15. Bhattacharjee P, Rakshit P, Goswami I, Konar A, Nagar AK (2011) Multi-robot path-planning using artificial bee colony optimization algorithm. In: *Third World Congress on Nature and Biologically Inspired Computing (NaBIC)*, pp 219–224

Evaluation of SFLA and TLBO Algorithm for Path Planning of Mobile Robots in MATLAB



Divya Agarwal and Pushpendra S. Bharti

Abstract Autonomous robots are employed in manufacturing units and industries as they can perform complex tasks in hazardous and harmful environments such as space explorations, submarines, and mining work. When a robot can traverse from start to goal location while evading obstacles, it is called an autonomous robot for which path planning is essential. All evolutionary and swarm intelligence approaches are probabilistic-based and entail few to many control parameters based on problem and application area. Shuffled frog leaping algorithm (SFLA) is one such example that requires six problem-specific parameters, while teaching learning-based optimization (TLBO) is a specific parameter-less algorithm. Thus, there is no burden of tuning control parameters in TLBO. In this work, comparison of both these algorithms is done on MATLAB 2018a to demonstrate the results that despite the usage of no specific parameters, TLBO outperforms SFLA algorithm for path planning and obstacle avoidance problem (PPOA).

Keywords Path planning · Obstacle avoidance · Shuffled frog leaping algorithm · Teaching learning based optimization

1 Introduction

Path planning and obstacle avoidance (PPOA) is an essential branch of robotics that is of research interest. PPOA comprises of sub-problems: to plan a path from start to end, to circumvent obstacles in the path, to devise smooth and shortest path within the least possible processing time [1]. Much research, exploitation, and exploration are done in this field by researchers in last six decades for devising an optimal PPOA approach, which is flexible, robust, and adaptable in many application fields [2]. Based on the robot's understanding of workspace, PPOA algorithms can be categorized into offline global PPOA (known environment and fixed obstacles) and online local PPOA (unknown or partially known environment with fixed as well as mobile

D. Agarwal (✉) · P. S. Bharti
Guru Gobind Singh Indraprastha University, New Delhi 110078, India

obstacles) [3]. Based on application, PPOA approaches can be broadly categorized into conventional approaches, (such as roadmap, random exploring trees, probabilistic roadmap approach, etc.) heuristic approaches, (such as genetic algorithm, neural networks, fuzzy approach, etc.) meta-heuristic-based nature-inspired evolutionary approaches (such as particle swarm optimization (PSO), invasive weed colony (IWO) optimization, shuffled frog leaping algorithm (SFLA), firefly algorithm, grey wolf optimization, etc.), and hybrid approaches [4]. Different algorithms depend on application need, performance parameters, workspace complexity, size and shape of obstacles, and known or unknown parameters; thus, one algorithm cannot be applied to problems of all types. Many conventional approaches fail to satisfy the PPOA problem in complex and dynamic situations because of non-flexibility, negligible robustness, and erratic behavior [5]. Specific heuristic approaches suffer from limitations such as high computational time for complex environment, low convergence speed and accuracy, and poor compliance to path map [6].

Different algorithms require different algorithm-specific parameters to be specified at the beginning of operation. For example, artificial bee colony algorithm requires parameters such as no. of onlooker bees, abandonment limit parameter or trial limit and acceleration coefficient [7]; IWO algorithm uses initial population size, minimum no. of seeds, maximum no. of seeds, variance reduction exponent, initial value of standard deviation and final value of standard deviation as initial parameters; PSO uses inertia weight, inertia weight damping ratio, personal learning coefficient, global learning coefficient, mutation coefficient rate, and SFLA uses memeplex size, number of memeplexes, number of parents, number of offsprings, maximum no. of offsprings iterations, and step size [6, 8] as necessary initial parameters. Performance of an algorithm is dependent on these parameters; hence, their values play a crucial role. Improper tuning of these parameters either increases computational effort or generates non-optimal solution, i.e., a solution that gets stuck in local optima. However, one such algorithm requires no such proper tuning of parameters as it is a specific parameters-less algorithm known as the teaching-learning-based algorithm (TLBO) [9]. Thus, researchers have gained interest in TLBO approach because of no burden of tuning control parameters, thereby reducing computational effort [5, 7].

In this work, comparison of SFLA and TLBO algorithm is done based on three maps comprising of different number of fixed round-shaped obstacles. Comparison work is simulated on MATLAB 2018a, and experimentation results are shown in Sect. 3. Brief literature work of both algorithms is discussed in Sect. 1. Results and discussions, along with simulated results, are discussed in Sect. 4, followed by conclusion in Sect. 5.

2 Literature Review

In this section, both algorithms, as mentioned above, are briefly discussed.

2.1 *Shuffled Frog Leaping Algorithm (SFLA)*

Food hunting behavior of frogs inspired Eusuff and Lansey [10] to develop an NIE approach called SFLA. It is a population-based cooperative search method that adopts a frog's natural hunting behavior to achieve quick and easy applications [2]. SFLA approach is composed of two algorithms in which a genetic-based memetic algorithm performs local search operation, and global search is performed by social behavior-based PSO approach [4]. In this approach, a group of virtual frogs is left in a workspace to explore and plan best possible shortest path within minimal processing time [11]. These virtual frogs are partitioned into separate memeplexes. Local search operation is performed independently in each memeplex [6]. In global search operation, shuffling procedure is done based on a memetic algorithm. This shuffling strategy helps to balance local and global search phenomena giving improved results [8]. SFLA approach can compute complex combinatorial optimization problems in the least possible time with better efficiency [2, 12]. To avoid getting trapped in local minima due to implementation of heuristic approaches for navigation and RPP problem, Ni et al. [8] implemented SFLA to achieve optimal path in dynamic environment. This approach is efficient in handling autonomous navigation and robot path planning compared to other heuristic and NIE approaches [3].

Advantages: Robust approach can achieve global convergence faster; an optimal solution with higher success rate even in uncertain environment; easy implementation; requires less initial knowledge; avoids local minima [4]; high time complexity with faster search capability [13]; parameter sensitive; more efficient than PSO [8]; minimal computation cost; efficiently handle complex nonlinear combinatorial optimization problems [13]. Limitations: Premature and slow convergence; it falls into local optima when implemented in multi-objective optimization problems [11]. Steps of this approach are [8, 11]:

1. Specifying optimization problem as minimization one,
2. Specifying information of positions,
3. Initialize pose of goal and obstacles utilized to define the frog's fitness function
4. This process is repeated several times to obtain best frog, which traverses through start to end without hitting fixed obstacles.

2.2 *Teaching Learning-Based Optimization (TLBO)*

It is a meta-heuristic, population-based evolutionary approach proposed by Rao et al. [14]. TLBO takes motivation from basic mathematical model of teaching and learning where students enrich themselves with knowledge gained in class [9, 14]. Number of students form population in TLBO and each student comprises several design variables (or subjects in which student is affluent) [1, 9]. An optimal solution is obtained from best student in the population, which becomes the teacher in next iteration until further best student is obtained in the population [14]. TLBO method is based

on two phases: teacher phase in which students gain knowledge of subjects (design variables) from teacher and student phase in which students gain knowledge based on level of interaction among each other [15]. The design variables or subjects are the parameters in the objective function, and the best solution obtained is the optimal solution. Advantages: Ease of use, effective with high precision, fast convergence speed, and it involves relatively less computational cost [5, 15]; it has a better search tendency compared to ABC or GA algorithm. Steps followed for implementation of TLBO are as follows [7]:

1. *Population Initialization*: Parameters such as population size (no. of students or set of solutions), number of iterations (generations), termination criterion, design variables, and their respective ranges are initialized.
2. *Population is randomly generated* based on number of teachers. Each population member, i.e., each student has knowledge of all design variables whose value is randomly selected in between the range specified.
3. *Computation of objective function*: Marks or score obtained by every student forms the objective function for TLBO.
4. *Teacher Phase or Greedy selection procedure*: In this phase, learner, i.e., students learn from teacher, and objective of the teacher is to obtain better results for the subject taught by him based on his abilities. Memorize and update new solutions (i.e., best learner becomes teacher) if it is better than previous or existing solutions. The difference between the actual mean result of each subject, and the teacher's corresponding result for each subject is computed to update a new solution.
5. *Learner Phase*: Knowledge of learners is enhanced based on their interaction capabilities. If a learner has more knowledge than others, they will interact to gain knowledge, and solution is updated using the above procedure. The objective function is obtained, and new solution takes over the existing solution if it is superior to it.
6. *Redundancy* of solution is done to identify and remove duplicate solutions.
7. Repeat 4–6 steps for all number of iterations or until stopping criterion is met.

3 Experimentation

Three maps with different complexity levels based on the different number of obstacles were formed in MATLAB 2018a. The environment considered for simulation was static with fixed round-shaped obstacles. The simulation was performed using both SFLA and TLBO algorithms. Simulation results demonstrated that both algorithms are complete and give an optimal solution, but TLBO is easy to implement and gives better results compared to SFLA depending on map complexity. Obstacle placement for three maps is shown in Table 1. Control parameters for tuning of TLBO and SFLA are displayed in Tables 2 and 3, respectively. Both algorithms were simulated for same number of handling points (5), maximum number of iterations (500), and number of population (150). The coordinates of the obstacle position and size

Table 5 Summary of path length in five tests each

S. No.	SFLA		TLBO	
	Path length	Processing time	Path length	Processing time
1	14.3035	118.1747	14.3278	113.7625
2	15.2184	110.9812	14.8681	134.3704
3	16.2424	111.8031	14.3445	129.5421
4	14.3023	112.1947	14.2988	118.7895
5	14.5146	115.2877	14.8995	112.4995
6	16.6943	122.6119	17.3286	134.9568
7	16.8959	128.9687	17.949	141.9778
8	16.8025	122.5669	16.7135	130.5413
9	16.9176	125.7421	17.0299	135.1254
10	17.1248	138.9877	17.6472	142.9575
11	16.1951	166.1817	16.1686	170.6517
12	16.1909	154.1965	16.2043	175.2730
13	16.1902	164.9244	16.2257	178.1866
14	16.2433	188.4260	16.1998	169.5413
15	16.2159	172.5659	16.2154	181.5478

4 Results and Discussion

There are many PPOA algorithms depending on application, research problem, and mode of operation. With the increasing number of complexity, many algorithms have specific parameters and assumptions to deal with it. Authors have considered two nature-inspired approaches among which SFLA requires six specific parameter values as input (Table 3), while TLBO does not require any (Table 2). In this paper, performance of SFLA and TLBO algorithms was simulated in MATLAB 2018a for PPOA problem of a mobile robot. 500 iterations were taken for five tests conducted per environment map (i.e., 15 tests for three maps). From the overall tests conducted per map shown in Table 5, it can be seen that for maps 1 and 3, TLBO outperformed SFLA while for the cluttered environment given in map 2, SFLA performed better by giving the best cost in less processing time. Also, from all the tests given in Table 5, it can be seen that TLBO takes more time to process the best cost path than SFLA, although the difference in processing time is less in TLBO.

In map 1, this had only six obstacles of different sizes, TLBO performed better than SFLA in all the five tests conducted with best cost to be 14.2988 units in 118.7895 s. In map 2, which had 13 obstacles of different sizes, SFLA gave better results than TLBO approach for all the five tests conducted for this map. From readings of map 3, it can be seen that both SFLA and TLBO were consistent in giving best cost values. However, the best cost conducted for five tests is 16.1686 given by TLBO approach.

Fig. 1 SFLA map 1 path generated

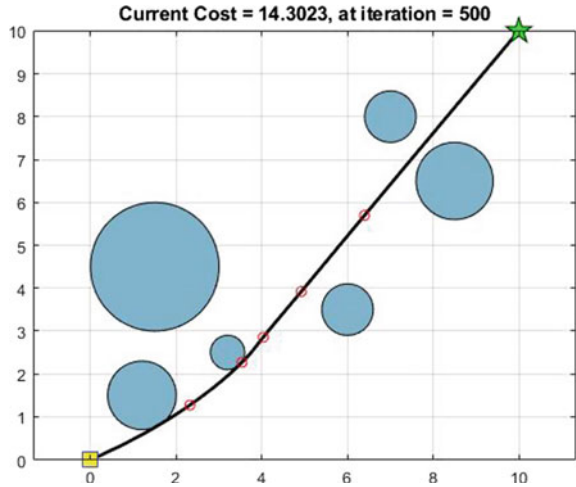
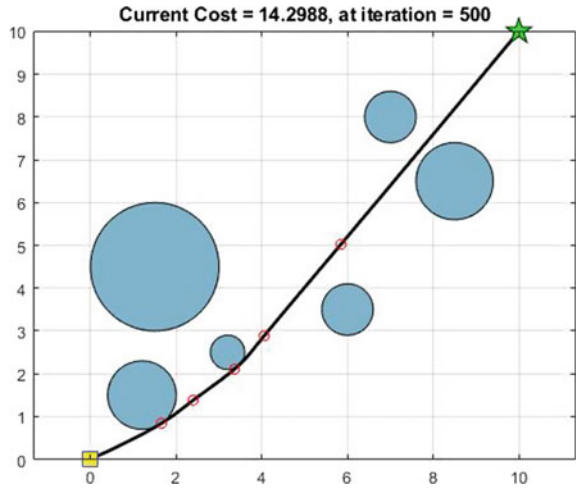


Fig. 2 TLBO map 1 path generated



Figures 1, 2, 3, 4, 5, 6, 7, and 8 show the best cost path given by TLBO and SFLA for each map among five tests conducted.

5 Conclusion and Future Scope

In this paper, the performance of SFLA and TLBO approach was simulated and evaluated based on the PPOA problem of a mobile robot in terms of the best cost (path length) and processing time. It can be inferred from Table 5 that TLBO is a very consistent and precise approach as value of best costs is closest to each other

Fig. 3 SFLA map 2 path generated

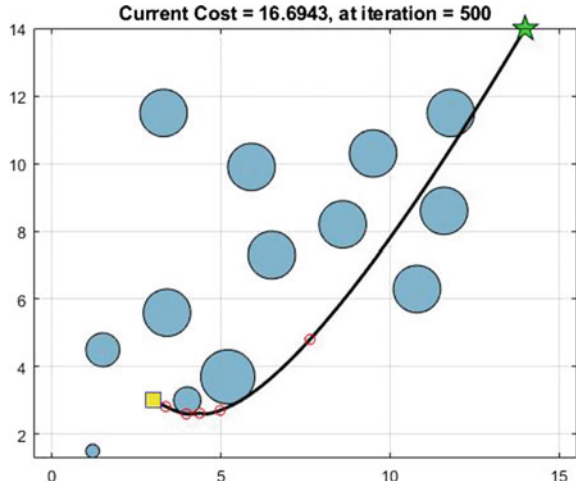
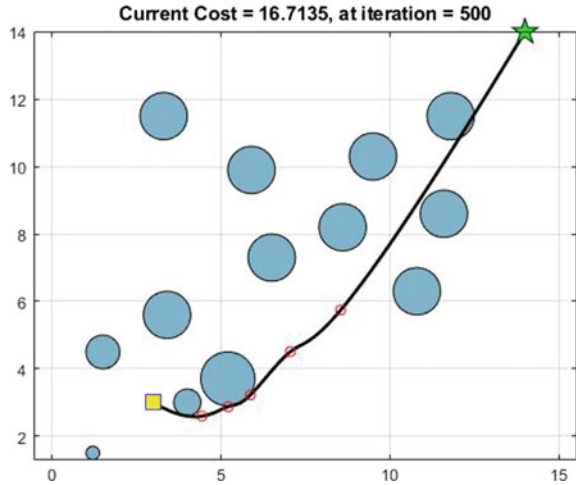


Fig. 4 TLBO map 2 path generated



for each map. So, it can be concluded that TLBO is a reliable approach for the PPOA problem. It can be seen from Table 5, and Figs. 1, 2, 3, 4, 5, and 6 that TLBO, despite being a specific parameter-less algorithm, performed better than SFLA for best, mean and worst solutions for different movements in all three maps. Moreover, TLBO is easy to implement and highly reliable because it is repeatable and precise in performance. For future work, tests would be conducted in real time on mobile robots, and their performance will be evaluated in comparison to simulation results.

Fig. 5 SFLA map 3 paths generated

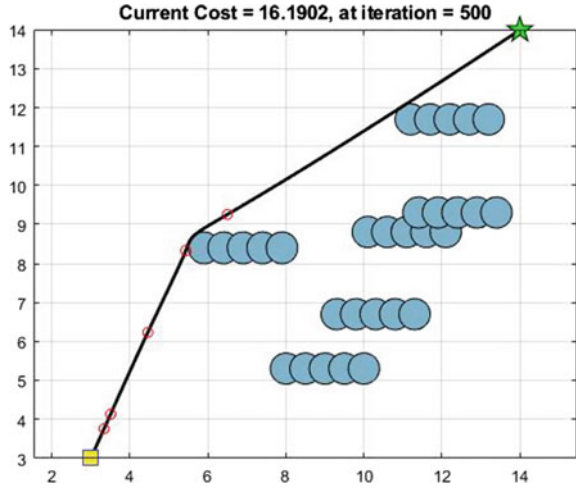
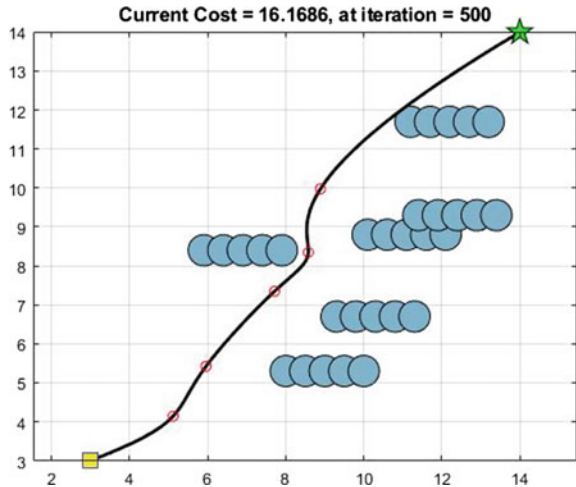


Fig. 6 TLBO map 3 paths generated



References

1. Kashyap AK, Pandey A (2020) Optimized path planning for three-wheeled autonomous robot using teaching-learning-based optimization technique. Lecture notes in mechanical engineering. Springer, Berlin, pp 49–57
2. Kundu S, Parhi DR (2013) Modified shuffled frog leaping algorithm based 6DOF motion for underwater mobile robot. In: International conference on computational intelligence: modeling, techniques and applications. Procedia Technol 10:295–303
3. Singh G, Sharma N, Sharma H (2020) Shuffled teaching-learning-based algorithms for solving robot path planning problems. Int J Metaheuristics 7(3):265–283
4. Paikray HK, Das PK, Panda S, Balabantaray BK (2019) Improved shuffled frog leaping algorithm for path planning of multiple mobile-robots. In: 2nd international conference on

- innovations in electronics, signal processing and communication (IESC), pp 132–137
5. Wu Z, Fu W, Xue R, Wang W (2016) A novel global path planning method for mobile robots based on teaching learning based optimization. *Information* 7(3):1–11
 6. Duan X, Niu T, Huang Q (2018) An improved shuffled frog leaping algorithm and its application in dynamic emergency vehicle dispatching. *Math Probl Eng* 2018, Article ID 7896926
 7. Savsani P, Jhala RL, Savsani VJ (2013) Optimized trajectory planning of a robotic arm using teaching-learning based optimization (TLBO) and artificial bee colony (ABC) optimization techniques. In: 2013 IEEE international systems conference, pp 381–386
 8. Ni J, Yin X, Chen J, Li X (2014) An improved shuffled frog leaping algorithm for robot path planning. In: 10th international conference on natural computation (ICNC), Xiamen, pp 545–549
 9. Aouf A, Boussaid L, Sakly A (2018) TLBO-based adaptive neuro-fuzzy controller for mobile robot navigation in a strange environment. *Comput Intell Neurosci* 2018, Article ID 3145436
 10. Eusuff M, Lansey K, Pasha F (2006) Shuffled frog-leaping algorithm: a memetic meta-heuristic for discrete optimization. *Eng Optim* 38(2):129–154
 11. Hassanzadeh I, Madani K, Badamchizadeh MA (2010) Mobile robot path planning based on shuffled frog leaping optimization algorithm. In: 6th Annual IEEE conference on automation science and engineering, pp 680–685
 12. Zhang Z, Yin J (2012) The study on mobile robot path planning based on frog leaping algorithm. *Adv Mater Res* 490–495:808–812
 13. Tao X, Li H, Mao C, Wang C, Yap JBH, Sepasgozar S, Shirowzhan S, Rose T (2019) Developing shuffled frog-leaping algorithm (SFLA) method to solve power load-constrained TCRTO problems in civil engineering. *Adv Civil Eng* 2019, Article ID 1404636
 14. Rao RV, Savsani VJ, Vakharia DP (2011) Teaching learning-based optimization: a novel method for constrained mechanical design optimization problems. *Comput Aided Des* 43(3):303–315
 15. Cheng YH, Chao PJ, Kuo CN (2019) Mobile robot path planning using a teaching learning-interactive learning-based optimization. *Int J Comput Sci* 46(2):1–9

New Locking Mechanism for Safe Landing



N. Rakshith

Abstract A study shows that 53% of all aviation accidents while landing occur because of human error. There is a high possibility that the orientation of the landing gear mechanism changing/moving from the position required for proper landing the aircraft (toggle/extreme position) because of loads along or opposite to the direction of motion of the landing gear. To avoid this, the pilot has to take extra precautions and follow a really complex procedure for landing, and this mitigates the risk but does not eliminate the possibility of motion completely as human error cannot be eliminated. In this paper, I aim to propose an approach of locking the landing gear mechanism in its extreme position and eliminate the risk of it changing its orientation while landing, by using an additional set of slider crank mechanisms which restricts the motion of the landing mechanism. By doing this, we eliminate the risk of motion of the landing gear during landing and thus reduce the risk of an accident during landing.

Keywords Landing gear mechanism · Slider crank · Orientation

1 Introduction

The landing gear also known as the under carriage is one of the critical subsystems of the aircraft and is often configured with the aircraft structure because of its substantial influence on the structural configuration. The purpose of landing gear is to provide suspension during taxi, take-off and landing. It is designed to absorb and dissipate the kinetic energy during landing, thereby reducing the impact loads transmitted to the air frame. It is often made retractable to minimise drag.

N. Rakshith (✉)
National Institute of Technology Karnataka, Mangalore, India

2 Literature Survey

The landing gear design is the integration of structures, kinematics, dynamics, etc. The design of the landing gear includes many stages of design, namely conceptual design and preliminary design, detailed design followed by stress, fatigue and reliability analysis [1]. Then, the manufacturability and maintenance are taken into consideration, and the required design changes are made to get the final product which is the best compromise between performance and cost and maintenance.

Section 3.1 gives brief description about the analysis of the existing model and its limitations. This paper comprises information about the conceptual and detailed design and the stress analysis.

3 Conceptual and Preliminary Design

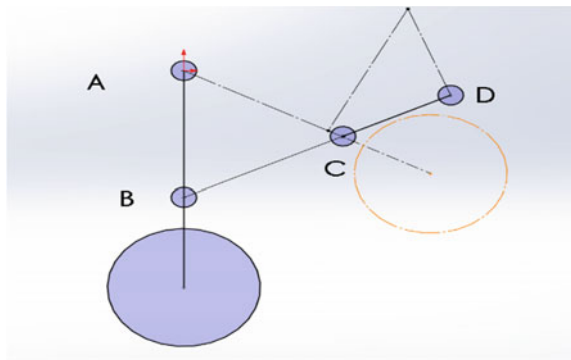
3.1 Analysing the Existing Model

The nose landing gear is the part that provides under carriage for the nose of the aircraft. The landing mechanism is a simple 4 bar mechanism with four revolute pairs, one link fixed to the aircraft frame.

In Fig. 1, link AD is the fixed link or the ground (the aircraft frame); link AB is the landing gear (it comprises all the structural components like shock absorbers, etc.); links CD and CB control the position of the landing gear [2].

The link CD is called crank. The crank is a powered link and is responsible for the actuation of the entire mechanism. The actuation (rotation) of the crank results in the rotation of the landing gear about A. The ratio of the angles rotated depends on the lengths of a mechanism and is fixed for a given mechanism [3, 4]. During take-off and landing, the crank actuates by a fixed angle which will result in the landing gear taking the required position, and this is the working principle of the landing gear [2].

Fig. 1 Kinematic diagram of the nose landing gear



The final configuration/orientation (the orientation of the landing gear during landing) shown in solid lines in the diagram is one of the extreme positions of the mechanism. A large force has to be applied on AB to change the orientation of the mechanism from this configuration. Such configurations are called toggle positions [3, 4].

If forces are applied in certain direction, the orientation of the mechanism can be changed; to prevent this from happening, the pilot pitches the aircraft up and first lands on the main landing gear and then lands the nose of the aeroplane. This does not eliminate the possibility of the landing gear's movement completely.

3.2 Conceptual Model of the Solution

The landing gear's configuration must be fixed during landing; to ensure this, the possibility of the landing gear's movement must be eliminated. It can be done by fixing the corresponding link temporarily (making the hinged support fixed support). This can be achieved by fixing one end of the link (landing gear) by introducing supports in the direction of motion. In this case 2, supports have to be introduced in the plane of rotation temporarily to restrict motion during landing. This can be done using a wide variety of mechanisms. But, the mechanism used should not change its orientation when forces from the landing gear act on it (i.e. the orientation should not be affected by the forces in the direction of the motion of the landing gear) so the supports must be introduced in the plane perpendicular to the plane of motion of the landing gear to satisfy the above conditions.

3.3 Preliminary Design

A mechanism has to be selected which satisfies all the conditions set/mentioned in the previous section. Many types of mechanisms like slider crank, rack and pinion, etc., can be used to ensure this [3, 4]. So, slider crank mechanism is selected. In slider crank mechanism, the direction of motion of the slider is not same as the landing gear, so the orientation of the mechanism will not change loads from the landing gear acting on it. Its implementation is easy, and it will be a lot lighter and more reliable than the rack and pinion mechanism. In this case two, slider crank mechanisms are used: one of the sliders is hollow (slider-1) and the second one is a solid slider (slider-2). The slider-1 acts a cylinder, and the slider-2 acts as a piston; as both the mechanisms reach the top dead centre configuration, the slider-2 (which acts like a piston) gets inserted into the cylinder completely and forms a thicker support. To lock the landing gear, a complex part, i.e. sliders with two cylinders and pistons have to be used. This is shown clearly in Fig. 3.

The components are designed to operate in the linear elastic region, any kind of nonlinearity that may occur because of the orientation of the forces, and the geometry

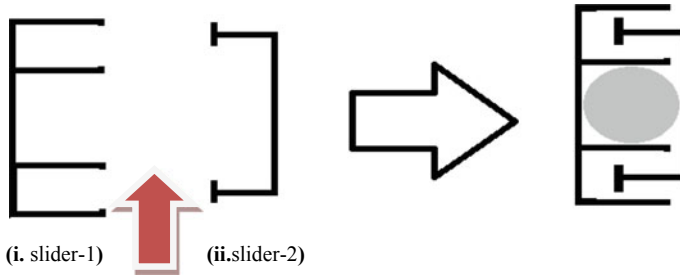
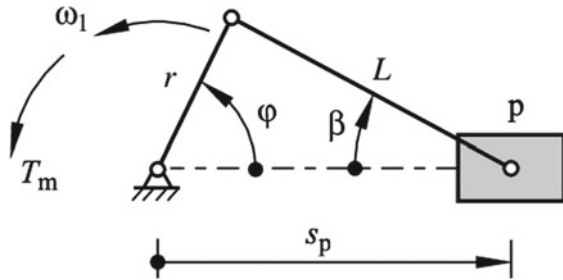


Fig. 2 Kinematic diagram of the piston cylinder locking mechanism. The arrow indicates the direction of motion of the landing gear and the direction of application of forces while landing, (i) the slider which acts as a cylinder (ii) the slider which acts as the piston

Fig. 3 Kinematic diagram of slider crank mechanism. [6] Source Adapted from



of the components will be taken into account when the entire system is broken down into small elements during finite element analysis [5].

A rack and pinion can be used, but there is a possibility that the teeth of the rack or the pinion can get damaged because of the huge amounts of load that will act on it. So, a really bulky rack and pinion with very large teeth will have to be used, and this will be heavier compared to the proposed slider crank. Therefore, slider crank is more suited than the rack and pinion (Fig. 2).

4 Detailed Design

The slider crank mechanism is made of four links and four kinematic pairs, namely three revolute and one prismatic. One link is fixed as ground, one of them can rotate about all the other links completely, this link is called crank, the slider is the link which can slide over the fixed link and form a prismatic pair, and the link which connects the slider and the rank is called connecting rod [3, 4].

There are two types of slider crank mechanism:

- (1) In line: The direction of motion of the slider and the pivot point lie on the same line.

- (2) Offset: The direction of motion of the slider and the pivot point do not lie on the same line.
- (3) This stage of design involves determining the lengths of the links and finalising the geometry of the mechanism and the links [3, 4].

4.1 Mechanism Definition:

The type of slider crank mechanism used has to be selected, and the factors kept in mind during selection are as follows:

- (1) Obtaining maximum retractability (stroke, distance covered by the slider).
- (2) The mechanism has to consume less space.
- (3) Quick return is not required.

So, by taking the above-mentioned points into consideration, in line slider crank mechanism is chosen.

First the length of the crank has to be fixed, it depends on the length of the stroke, and in this case the stroke has to be slightly greater than the width of the landing gear link (to ensure that there is no interference with the motion of the landing gear). We know that the stroke is twice the crank length, using this relation we can find the length given the width of the landing gear. This determines the depth of the cavity in the cylinder and length of the piston arms, thus the slider lengths can also be determined by keeping some allowance for the tabs. The length of the connecting depends on the pivot point of the crank and is equal to the shortest distance between the slider and crank when they are in one of their extreme positions. Thus, the dimensions of the mechanism can be fixed using the width and the pivot point of the crank (Fig. 3).

$$2R = S = W$$

R = crank length, S = stroke length, W = width of the landing gear link.

4.2 Designing

After finalising the lengths of the links, the geometry of the parts has to be finalised based on the ease of manufacturing, load bearing capacity, cost of production, etc. (Fig. 4)

A prismatic design was selected because the load acting on it will be distributed evenly all over the surface; if cylindrical designs were to be used, the entire load acting on it is to be concentrated on a single point or a line; this will result in large amounts of stresses in the point of application of force; this will cause large amount of deformation near the point of load application. To avoid this, prismatic sliders are used. The variation of cross section must be gradual to reduce stress concentration. The edges are filleted to minimise friction and to reduce stress concentration.

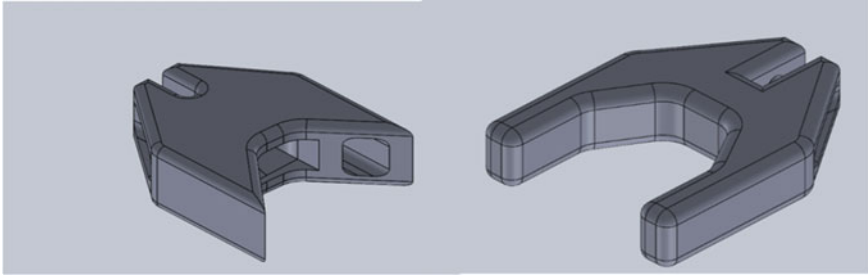


Fig. 4 Designs of the two types of sliders used developed with CAD software

5 Stress and Reliability Analysis

Analysis of the stresses is done to check if the part designed can withstand the force applied on it without failing and to find the stresses and deformation the part may undergo when it is loaded.

FEA is used to analyse the stresses and deformations. First step in this process is meshing, in this process part is divided into many small elements, and the stresses and deformations each and every element are calculated individually and then combined to get the final result. The elements are created for analysis tetrahedrons, and they are finer in corners and edges because stress concentration is higher in those regions so accurate reading is necessary for good analysis. Here more than one part is analysed, so identifying the contact surfaces is important because load is transferred through these surfaces. The surfaces in contact are highlighted in Fig. 5.

Next step is the problem definition, here the surfaces which will be fixed and the surfaces on which the forces act have to be indicated. The direction and magnitude of the forces have to be specified, and the type of stress and deformation required to be found is selected. After this, the computer starts to generate mathematical models to solve the problem and find the required stress and strains (Fig. 6).

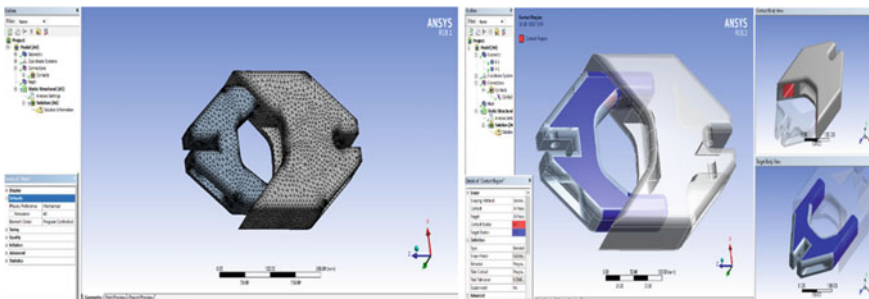


Fig. 5 Meshing and the contact surfaces identified during finite element analysis

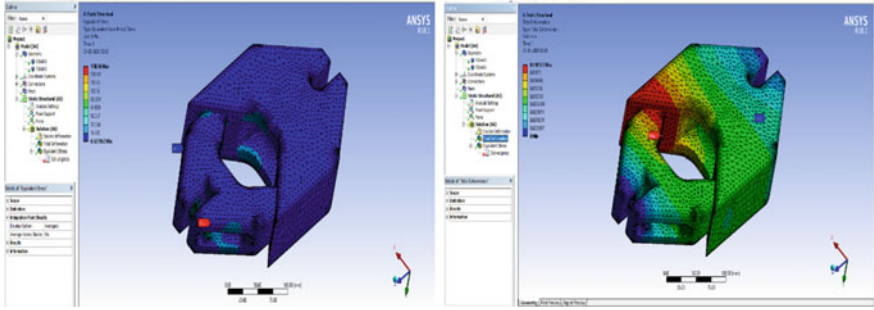


Fig. 6 Problem definition in the FEA software

In this model, the slots used to connect the sliders to the connecting rod are the surfaces that are fixed (indicated in blue). The force from the landing gear will act on the inner walls of the assembly (indicated in red). The arrow indicated the direction of the force applied (Fig. 7).

After the generation of mathematical model, the computer solves it and displays the results. The maximum stress and its concentration and the deformations are found, and required design changes are made and then analysed again till we obtain minimal stresses are obtained. Any part that is designed should have a factor of safety 1.5–3 to make sure that the part is reliable.

There will be regions in the component which will have large variations of stresses to get accurate values of stresses in those regions, and a process called convergence is carried out. The tetrahedrons elements in these regions are further broken down into smaller elements, and the stresses are calculated. This process is carried out till the values of stresses converge to a particular value, and this is done to obtain reliable results which are experimentally accurate. ANSYS a FEM software was used for the

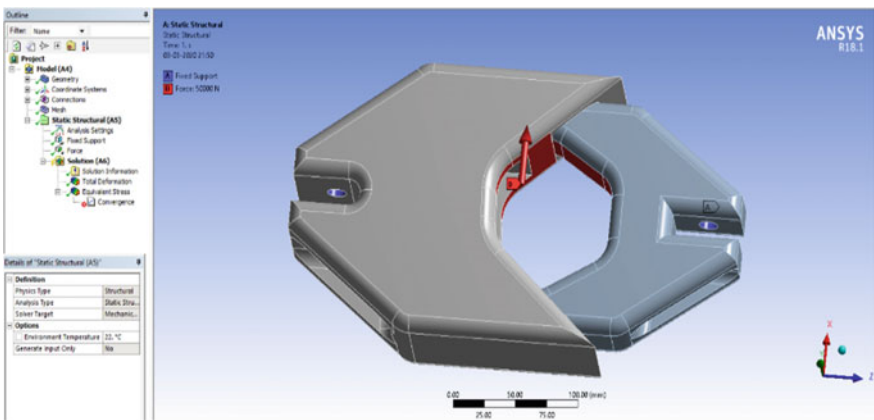


Fig. 7 Stress distribution and the deformations

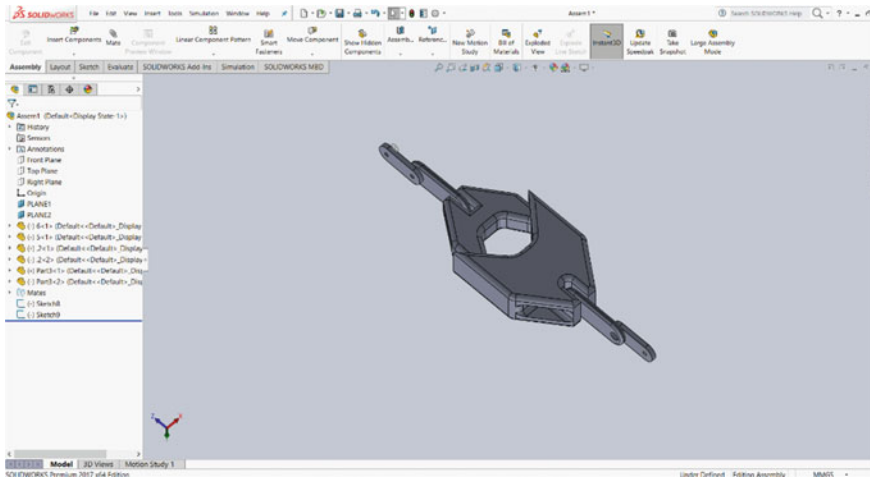


Fig. 8 Final assembly of the locking mechanism developed in CAD environment

analysis because it is a widely used software in industries and is well known for its accuracy [1, 5].

6 Conclusion

By locking the landing gear in the required position, we not only reduce the chances of an accident because of human error but also a lot of other factors like fast winds or pressure variations that might affect the landing of the aircraft.

This design can be made better by using smart materials, vibration dampeners, etc., which can help in smooth landing.

Thus, by locking the landing gear, we can make the safest mode of transportation safer (Fig. 8).

References

1. Daniels JN (2018) A method for landing gear modeling and simulation with experimental validation
2. Pritchard J (2001) Overview of landing gear dynamics. *J Aircr* 38(1):130–137
3. Myszka DH (2012) *Machines & mechanisms—applied kinematic analysis*, 4th edn. Pearson, New Jersey
4. Norton RL (2011) *Machine design—an integrated approach*, 4th edn. Pearson, New Jersey

5. Imran M, Ahmed RS, Haneef M (2015) FE analysis for landing gear of test air craft. Mater Today Proc 2(4-5):2170-2178
6. Quintero HF, Romero CA, Useche LV (2007) Thermodynamic and dynamic analysis of an internal combustion engine with a noncircular-gear based modified crank-slider mechanism

A Preliminary Assessment of Solar Industrial Process Heating for Cement Industry



Niranjan Sahoo , Anil Kumar , and Samsher 

Abstract Solar energy conversion technologies for supplying heat for many processes in various industries such as petroleum refining, textile, pulp and paper, cement, and food and beverage have become very encouraging in recent years. Industrial sectors can reduce their energy consumption by harnessing solar energy. Petroleum refining, pulp and paper, food and beverages, textile, chemical, cement, and automobile industries are some of the industrial sectors where solar energy has been utilized for their various processes successfully implemented. In this review article, a systematic review of the utilization of solar energy for various processes of cement industry was done. The temperature and energy requirement (thermal and electrical) for the various processes in the cement industries are identified. Finally, suitable solar collectors for process heating in the cement industry are also discussed.

Keywords Solar industrial process heating · Cement industry

1 Introduction

The cement industry consumes a huge amount of raw materials (limestone) and energy for the production of cement. The energy is utilized in the form of thermal energy and electrical energy. The production of one ton of clinker requires 1.7 tons of limestone and approximately 3.2–6.3 GJ of thermal and electrical energy. [1, 2]. The thermal energy utilized for the production of cement having a cost of around

N. Sahoo (✉)

Department of Mechanical Engineering, Galgotias College of Engineering and Technology, Greater Noida, New Delhi, India

e-mail: niranjan.sahoo@galgotiacollege.edu

N. Sahoo · A. Kumar · Samsher

Department of Mechanical Engineering, Delhi Technological University, New Delhi, India

A. Kumar · Samsher

Centre for Energy and Environment, Delhi Technological University, New Delhi, India

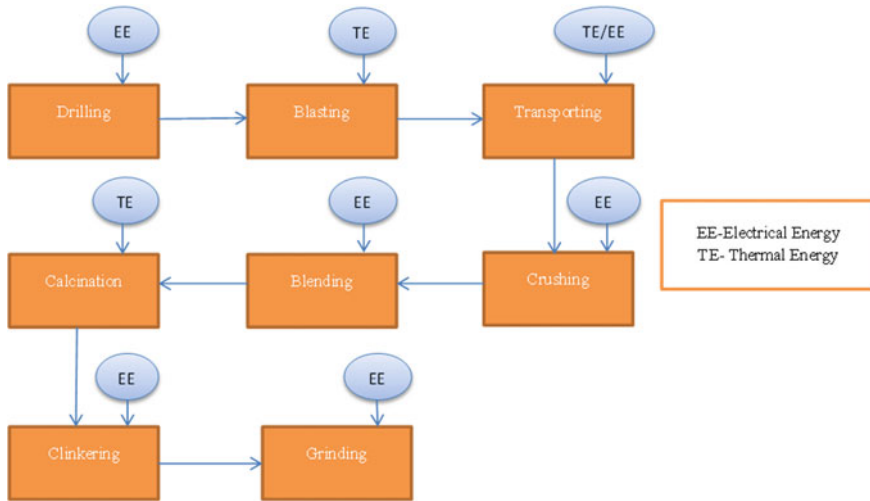


Fig. 1 Outline of cement manufacturing processes with nature of energy requirement

20–25% of the total production cost and a huge amount of electricity, i.e., 110–120 kWh is required per ton for the manufacturing of cement. Generally, the cement industries fulfilled the thermal energy requirement by burning of fossil fuels. The maximum percentage of electricity is utilized in grinding operations for producing cement powders [3]. Figure 1 shows the sequence of operations and the types of energy required for each process for the production of cement.

Consumption of cement is increasing at a fast rate globally. For meeting the demand for cement, a tremendous amount of fossil fuel is utilized. The commonly used fossil fuels are coal, natural gas, biomass and petro coke, etc., burning of a large amount of fossil fuel produces a lot of gases which have a very adverse effect on the environment. So it is necessary to reduce fossil fuel consumption without disturbing the thermal energy demand of the cement industry. The reduction of the use of fossil fuel ultimately reduces greenhouse gas emissions. This can be achieved by improving the efficiency of the system so that there will be a less consumption of fossil fuel and/or substituting fossil fuel by renewable sources of energy such as solar energy. Improving the efficiency of the system, no doubt a beneficial technique, but it is beneficial for the short run. But the implementation of the potential of renewable energy in the cement industry can give many benefits in the long run.

The main objective of this study is to review the potential of solar industrial process heating (SIPH) through the available research papers, books, and annual technical reports, etc. The article mainly emphasizes the scope of SIPH in the cement industry.

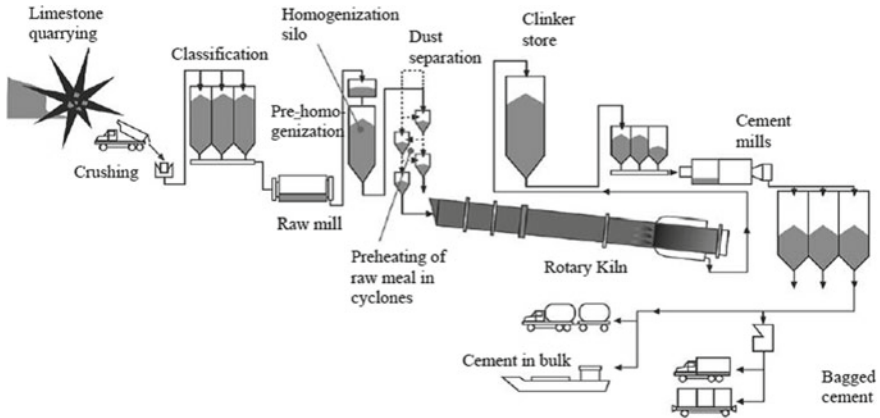


Fig. 2 Cement manufacturing process [6]

2 Cement Manufacturing Process

The sequence of operation/process for the production of cement mainly depends on the types of cement, which is to be produced, but the necessary process remains the same for any type of cement. For the production of cement, first limestone quarrying is done and then crushing to get the required size. After that, silica, iron, bauxite, and quartzite are added in the correct proportion, and then these are crushed, and then a raw meal is prepared. The raw meal is blended in blending silos and then heated in the pre-heating system. This process is known as calcination, in which the decomposition of calcium carbonate (CaCO_3) is done. It produces calcium oxide (CaO) and liberates carbon dioxide (CO_2). This is done at a temperature range of $900\text{ }^\circ\text{C}$. Then this calcium oxide (CaO) is passed through the kiln with silica, alumina, and ferrous oxide. This is known as clinkering process, which is done at a temperature range of $1400\text{--}1500\text{ }^\circ\text{C}$. This process produces clinker (silicates + aluminates + ferrites). Then this clinker is grounded with gypsum, limestone, and ashes to produce a fine product called cement [5]. Figure 2 shows the sequence of processes flows in a cement manufacturing plant.

3 Process Heating

It is generally defined as the transfer of thermal energy to a process during the production of any necessary items or goods. A typically process heating system includes three types of devices, namely as heating device for generation of heat, a heat transfer device for transfer of heat from the source to the required material, and a heat recovery device. There are generally four types of process heating systems [7, 8].

The first one is the fuel-based process heating system. This type of heating system liberates heat energy by burning of fuels. The fuels used may be in the form of solid, liquid, or gases. The heat energy is transferred directly or indirectly to the material to be produced. Ovens fired heaters and kilns are some of the examples of this type of system.

The second type is the electricity-based process heating system. This type of heating system uses electric current for generating heat, and it is transferred in a direct or indirect way. This technique is also referred to as electro technologies. Electric arc furnaces, induction heating, laser heating, and microwave processing are some of the examples of this type of system. The processes which include this type of heating system include heating, drying, curing, etc.

The third type is the steam-based process heating system. This type of heating system uses the application of steam for heating. It is similar to a fuel-based system. The application of steam can be applied directly or indirectly. This type of heating system is very significant for lower temperature industrial process heating, i.e., below 400 °C. Petrochemical industry, chemical manufacturing industry, paper and pulp industry, etc., are some of the industries where this type of heating system is used.

The fourth one is the hybrid process heating system. This type of heating system is used where the same energy source is used to optimize the energy use or to increase the overall thermal efficiency of the process. Example of this type of system includes when a conventional boiler is replaced by a boiler that can be operated by fuel and electricity both.

4 Solar Industrial Process Heating

Many researchers have done lots of researches about the potential of SIPH across the globe. The solar thermal systems are integrated with the processes of many industries to meet the thermal energy requirement. Some of these industries include dairy industry, food, and beverage industry, sheet metal industry, textile industry, and chemical industry, etc. A brief review of some of the research work has been focused here to evaluate the potential of SIPH in the case of cement industries. One of the researchers named Kalogirou investigated the potential of SIPH in Cyprus [9]. His work is suitable for the washing and drying processes for the food and beverage industries. The only disadvantage of this study is that it does not provide any quantitative estimates. This type of study is also done by many researchers in Australia and found that the potential of SIPH can be applied to many processes of mining, food processing, and textile industry without any quantitative estimates [10–12].

The heating and cooling technology with the help of solar energy was started by the International Energy Agency (IEA) in 1977. The main motive of this program was the maximum utilization of solar energy [13]. The members of IEA were from different countries and the European Union. An investigation was carried out under this plan, and the estimated potential of SIPH for the European Union was found

out to be 260PJ/ annum. This value was 3.8% of the total heat consumed by all the twenty-five countries of the European Union. As per another research report, Germany has a potential of 482.2 PJ annually [14].

There were many types of research about specific industries to check the potential of SIPH. One of the researchers in India calculated that there was a potential of 25 PJ for the paper industry [15]. Another researcher calculated the potential of SIPH for the dairy industry and estimated the value was 6.40PJ [16].

4.1 Solar Collectors Used for Process Heating

A solar collector mainly consists of an absorber plate and an appropriate heat transfer medium. Its primary function is to absorb the solar irradiation falling on its surface and transfer the heat to the fluid, which is working as a heat transfer medium. There are generally three categories of solar collector adapted for process heating operations [17]. The first category is the flat plate collector, which is lighter, durable, and cheaper. It is designed for the low-temperature process heating applications. The second type of collector is the evacuated tube collector. This is also adopted for low-temperature process heating applications or for water feeding to the boiler. The third type of solar collector is the concentrators. This is generally used for medium and high-temperature process heating. Some commercially available designs are the parabolic trough, parabolic dish, and linear Fresnel reflectors [18].

5 Discussion

The solar heat can be used for the fulfillment of the thermal energy requirement for many processes of different industrial sectors; due to the high potential of solar energy, the usability of this type of non-conventional energy for different industrial process heating increasing day by day across the globe. Figure 3 shows the installed capacity of the SIPH system in the last decades increases drastically. There is a lot of scope of SIPH system for different industrial sectors. The selection of solar collector design plays a vital role in achieving the required temperature for process heating. Figure 4 shows the different types of solar collectors with their range of operating temperatures. Higher temperatures can be achieved through the combination of different types of solar collectors.

Fig. 3 Installed capacity of SIPH system across the globe

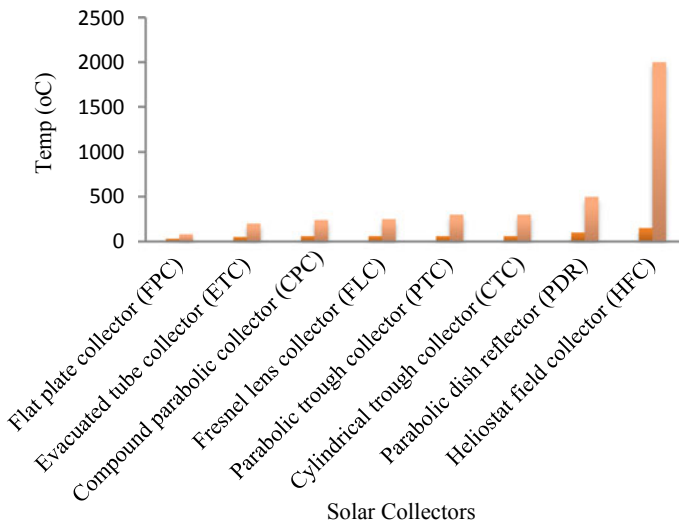
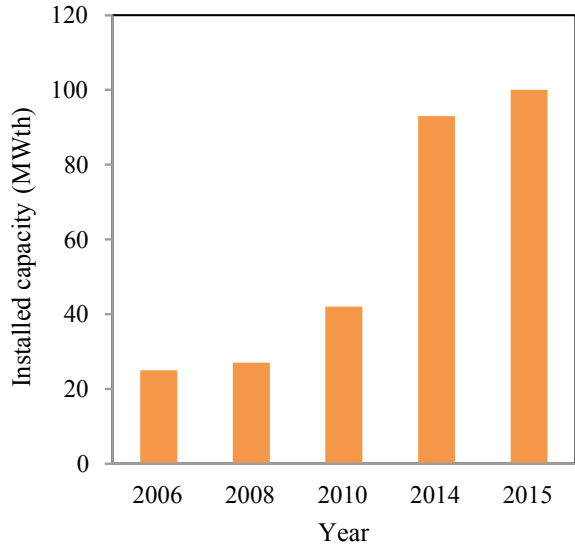


Fig. 4 Solar collectors with range of operating temperatures for industrial process heating

6 Conclusion

The review article focused on the potential of solar heat for many industrial processes and found that there were many industrial sectors around the globe that had successfully implemented the potential of SIPH system. It is found that there is a lot of

energy consumption of energy for converting raw materials to the final product, i.e., cement. Therefore, fuel substitution must be considered. This paper also identifies some solar collectors with their operating temperatures. Solar energy has a lot of potential for industrial process heating for the cement industry, and this is an area where lots of research is required in the future.

References

1. Van Oss HG, Padovani AC (2002) Cement manufacture and the environment: part I: chemistry and technology. *J Ind Ecol* 6(1):89–105
2. Van Oss HG, Padovani AC (2003) Cement manufacture and the environment part II: environmental challenges and opportunities. *J Ind Ecol* 7(1):93–126
3. Madlool NA, Saidur R, Hossain MS, Rahim NA (2011) A critical review on energy use and savings in the cement industries. *Renew Sustain Energy Rev* 15(4):2042–2060
4. Energy Efficiency Asia. <http://www.energyefficiencyasia.org/docs/IndustrySectors> Cement draft May 05.pdf, 20 Aug 2010.
5. European Commission (2011) Reference Document on the Best Available Techniques in the Cement and Lime Manufacturing Industries. BAT Reference Document (BREF), European IPPC Bureau, Seville, Spain
6. Kääntee U, Zevenhoven R, Backman R, Hupa M (2004) Cement manufacturing using alternative fuels and the advantages of process modelling. *Fuel Process Technol* 85(4):293–301
7. Department of Energy US. Improving process heating system performance: a sourcebook for industry. *Energy Effic Renew Energy US* 2008, <http://www.nrel.gov/docs/fy08osti/41589.pdf>. Accessed 15 May 2016
8. Energy Management Association (2011) Energy audit standard for process heat systems. A standard for the auditing of the energy efficiency of direct and indirect heating systems. See: http://emanz.org.nz/sites/default/files/data/Directory/Process_Heat_Systems_Audit_Std_V1.pdf
9. Kalogirou S (2003) The potential of solar industrial process heat applications. *Appl Energy* 76(4):337–361
10. Muller T (2004) PROMISE—production with solar energy potential study for solar thermal energy in Austrian industry—and industry within the factory of the future (BMVIT) subprogram, Final report
11. Fuller RJ (2011) Solar industrial process heating in Australia—Past and current status. *Renew Energy* 36(1):216–221
12. Beath AC (2012) Industrial energy usage in Australia and the potential for implementation of solar thermal heat and power. *Energy* 43(1):261–272
13. Solar Heating and Cooling Program. See: <https://www.iea-shc.org/programme-description>. Accessed 12 May 2016
14. Lauterbach C, Schmitt B, Jordan U, Vajen K (2012) The potential of solar heat for industrial processes in Germany. *Renew Sustain Energy Rev* 16(7):5121–5130
15. Sharma AK, Sharma C, Mullick SC, Kandpal TC (2015) Potential of solar energy utilization for process heating in paper industry in India: a preliminary assessment. *Energy Procedia* 79:284–289
16. Sharma AK, Sharma C, Mullick SC, Kandpal TC (2017) Potential of solar industrial process heating in dairy industry in India and consequent carbon mitigation. *J Clean Prod* 140:714–724
17. Mekhilef S, Saidur R, Safari A (2011) A review on solar energy use in industries. *Renew Sustain Energy Rev* 15(4):1777–1790
18. Kalogirou SA (2004) Solar thermal collectors and applications. *Prog Energy Combust Sci* 30(3):231–295

Experimental Investigation of Drying Tomato in a Double Slope Solar Dryer Under Natural Convection



E. Elavarasan, Yogesh kumar, R. Mouresh, and Sendhil Kumar Natarajan

Abstract In this study, thin layer drying of tomato slices under open sun drying and double slope solar dryer was conducted. The drying effect on exergy loss, exergetic efficiency, dryer efficiency, pickup efficiency, energy utilized, thermal and drying chamber efficiency has been obtained. It has been observed that the solar dryer with double slope had more efficiency than the open sun drying. The exergy loss range from 1196.82 to 11,758.18 kJ/kg having an average value of 6302.47 kJ/kg, the exergetic efficiency varied from 67.19% to 81.17% with an average value of 70.20%, respectively. The value of pickup efficiency varied from 10.89% to 14.33% with an average value of 12.22% with the dryer efficiency varying from 11.58% to 44.76% with an average value of 25.76%, respectively. The energy utilized ranged from 19.23 to 76.73 kJ/s with an average value of 55.2 kJ/s, the thermal efficiency is said to be varied from 5 to 14% and the drying chamber efficiency is said to be range from 9.70 to 77.52% with an average of 57.48% for the entire duration of the experiment. A comprehensive evaluation yielded that the double slope solar dryer was best suited for drying the samples.

Keywords Drying tomato slices · Solar energy · Activation energy · Exergy · Energy · Performance dryer

1 Introduction

Tomato plant (“*Solanum lycopersicum*”) has an edible berry that is commonly called as tomato and is consumed raw and cooked all around the world. Tomatoes are a major source of lycopene which is an antioxidant and is linked with various health benefits like reducing heart disease and cancer. Global exports for tomato cumulatively had a quantity of 7.3 million tonnes with an estimated value of \$9.7 Billion in 2018. The

E. Elavarasan · S. K. Natarajan (✉)
Department of Mechanical Engineering, NIT, Puducherry, Karaikal, India

Y. kumar · R. Mouresh
Department of Mechanical Engineering, Sri Ramakrishna Engineering College, Coimbatore, India

largest exporter of tomato is Mexico at 1.8 million tonnes followed by the Netherlands and Spain at 1.1 million and 797 thousand tonnes, respectively. Tomatoes grown in India are primarily consumed by the domestic market due to the large demand in the country. Arepally et al. [1] investigated the mixed-mode solar drying of tomato samples at 30°–60° air temperature. The moisture content of drying tomato samples decreased from 93.67–8% on a wet basis within 20, 23, and 30 h for three different load conditions. The experimental results were better in agreement with two-term drying model for 2, 4 kg m⁻² for load condition and having a Logarithmic drying model for 6 kgm⁻² load condition. They reported that energy utilization ratio of the dryer was varied from 24.2–58% and exergy efficiency varied from 50–59%. Pankaew et al. [2] used a equipped rice husk burning system on parabolic greenhouse dryer for producing dried banana. The highest efficiency of the burning was 87.7%. It was concluded that the drying efficiency increased by 12.6%. Murugavelh et al. [3] developed a mixed-mode solar tunnel dryer to dry tomato waste at 44–68 °C. The content of moisture of drying tomato paste reduced from 71.1–0.3% on a wet basis within 7 h in the tunnel dryer and 15 h in sun drying. It was concluded that the experimental results were better in agreement with Midilli et al. drying model and the exergetic efficiency of the tunnel dryer was varied from 38.5 to 67.5%. Ligayat et al. [4] conducted the experiment in an indirect solar dryer, which reduces the usage of fossil fuel. The mean thermal efficiency in the collector was 31.50% whereas the drying chamber efficiency was reported as 22.38%. They concluded that drying time was reduced in indirect solar drying method and more efficient than open drying process. Hamdi and Kooli [5] used mixed-mode greenhouse and solar dryer to dry tomato samples at 25–54 °C drying temperature. The moisture content of drying tomato decreased from 20.27 to 0.36 g water/g dry matter within 31 h under the greenhouse dryer and 48 h under open drying. experimental results were better in agreement with Midilli et al. drying model. They concluded that the exergetic efficiency of a dryer varied from 16.4–70.4% and average efficiency of energy of the system was 42%.

Johnson et al. [6] used a hot air dryer to determine the moisture diffusivity and shrinkage within the cylindrical piece of plantain were the thickness and the temperature will vary. They reported that the activation energy of the sample was estimated at 38.81 kJ, and Fick's diffusion equation identified the distribution of moisture. Kumar and Elavarasan [7] reviewed the application of computational fluid dynamics in natural and forced convection greenhouse dryer in different samples. Berinyuy et al. [8] developed a solar tunnel dryer to dry the vegetables containing very high moisture content. The dryer contains four trays and can dry 17 kg of cabbage moisture content reduced from 95 to 9% in five days. The mean efficiency of dryer was 17.86%, with airflow of 9.86 m³/h. It was reported that there was a reduction in dehydrating period by 30 and 50% based on the crop used and the dried product was acceptable visually. Hossain and Bala [9] studied mixed-mode type forced convection solar tunnel dryer to dry green and red chilies. The final moisture content of red chili 0.05% in 20 h in dryer and it took 32 h in open drying. In the case of green chili, 0.06% final moisture was obtained from 7.6% in 22 h in tunnel dryer and 35 h in sun drying. They concluded that the use of a solar tunnel leads to decrease the

dehydrating period. Vijayan et al. [10] studied the thermodynamic characteristics of the bitter melon by using indirect solar drying. They concluded that the mean value of moisture diffusivity was $12.95 \times 10^{-10} \text{ m}^2/\text{s}$, the mean value of pickup efficiency was 54.29%, and the mean value of exergy efficiency was 40.68%.

Midilli and Kucuk [11] studied indirect type of solar cabinet dryer to dry shelled and unshelled pistachios at 40–60 °C drying air temperature. The equilibrium moisture content of dried pistachios was observed within 6 h. They reported that exergy loss of solar cabinet dryer was varied from $0.5\text{--}3 \text{ kJ (kg)}^{-1}$. Kesaven et al. [12] made an indirect-type triple-pass forced convection dryer to analysis the exergy, thermal and pickup efficiency of drying potato slices. The flow rate was 0.062 kg s^{-1} , and the exit air temperature was 62 °C. The final moisture content of sample of potato was 13% after the drying process in 4.5 h. The thermal efficiency was 45%, the pickup efficiency was 29.9%, and the exergy efficiency was 53.57%. The Midilli and Kucuk model were best suited drying models for potato slices. Abbaspour-Gilandeh et al. [13] used a hot air dryer for drying quince sample at 50–70 °C drying air temperature with three different wind velocities used. The effective moisture diffusivity of drying quince sample was varied from $4.1\text{--}1.18 \times 10^{-9} \text{ m}^2 \text{ s}^{-1}$ and Midilli et al. drying model gave good agreement with experimental results. The energy utilization ratio, exergy efficiency and loss of hot air dryer were 0.882, 87.9% and 0.04 kJ s^{-1} . Nazghe-lichi et al. [14] analyzed exergy and energy of fluidized bed drying of carrot. Three inlet temperatures of 50, 60, 70 °C and 30, 60, 90 mm were used for the experiment. The size of the carrot cube was 4, 7 and 10 mm, respectively. The energy utilization range between 0.105 and 1.949 kJ/s and the energy utilization ratio (EUR) varied from 0.103 to 0.707. They concluded that the high air inlet temperatures, small particles and deep beds increased the energy utilization ratio (EUR). Tan et al. [15] conducted drying of cassava chips at temperatures of 30, 50 and 70 °C with different airflow rates. They concluded that the modified page model gave the best fit with the drying air temperature and rate of flow across the dryer. Based on the above-cited literature review, very few papers reported the drying parameters of tomato. Hence, in this paper, experimental studies were carried out to determine the pickup, dryer, thermal, drying chamber, exergy and energy efficiency of drying tomato slice of developed low-cost double slope solar dryer.

2 Experimental Setup

The experiment was conducted on February 11, 2020, in Karaikal District, Puducherry, India, to evaluate the drying characteristics of the tomato slices. The setup consists of a double slope dryer of a double trapezoid shape with a total length of 2.49 m, a breadth of 0.8 m and a height of 0.3 and 0.25 m on the longer and shorter sides of the dryer. The trapezoid shape of the dryer enabled the movement of moisture from a higher pressure to lower pressure region inside the dryer thus enabling faster drying of the samples. The inclination of the dryer was given at 10.2° on each sides matching the latitude of the experimental area which was covered with a pane glass

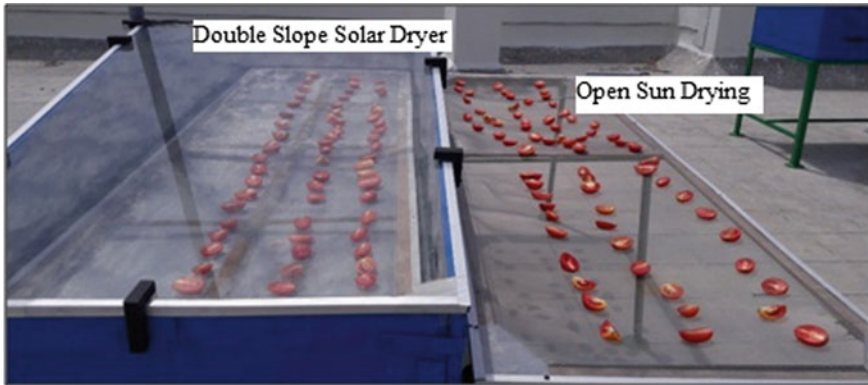


Fig. 1 Picture of double slope solar dryer and open sun drying for drying tomato

of thickness 0.04 m, the dryer was made out of galvanized Iron along with plywood of thickness 0.025 m to restrict heat transfer to and from the dryer. The samples were placed in an Aluminum mesh of 2.41 m \times 0.74 m inside the dryer to study wetness of the samples. One kg of samples was taken inside the dryer and open drying to compare and evaluate their drying capabilities. The entire drying setup was placed in the East–West direction for entire drying process [16, 17]. The highest temperature developed inside the dryer was recorded to be 70 °C, with a maximum RH value of 45%. Vents were employed to facilitate dehydration of the samples. The pictorial representation of the solar dryer was given in Fig. 1.

The acquired data via a data acquisition system (Agilent 34972A), which has a $\pm 0.25\%$ error correction. Eight K-type thermocouples were utilized to measure the various parameters within the system, within where five of them were used to measure the absorber plate temperature and three of them measured the drying air temperature at different locations. The ambient temperature was measured using a J-type thermocouple throughout the experiment. The average solar radiation was obtained using a Hukseflux Pyranometer with a sensitivity of 14.77×10^{-6} V/(W/m²). The photographs of the data acquisition system and Pyranometer used were shown in Fig. 2(a, b).

3 Analysis

The model presented by Midilli and Kucuk [11] for exergy and energy techniques of thin layer dehydrating operation is connected to this investigation. In the techniques of thermodynamics, a thin layer dehydrating operation is considered a constant steady flow method.



(i) Agilent Data Acquisition Unit



(ii) Hukseflux Pyranometer

Fig. 2 Picture of **a** Agilent data acquisition unit and **b** Hukseflux Pyranometer

3.1 Energy Technique

In extent of the first law of thermodynamics, the energy techniques of thin layer dehydrating operation of tomato was done to determine energy characteristic and dehydrating characteristic of drying air all through convective kind of chamber dryer. The air operation is modeled as a constant steady flow operation investigated by utilizing steady flow protection of mass and preservation of the energy standards [11].

The energy analysis of tray and dehydrating chamber can be calculated by following equations

$$\eta_t = \frac{\dot{m}_w h_f}{\dot{m}_d C_p (T_{ti} - T_h)} \tag{1}$$

$$\eta_d = \frac{\dot{m}_w h_f}{\dot{m}_d C_p (T_{di} - T_h)} \tag{2}$$

\dot{m}_w is denoted by the mass flow rate of removed moisture from tomato.

The required energy to transfer the wetness content during dehydrating operation was calculated by

$$Q_s = m_{ao}(h_i - h_o)$$

where Q_s = Mass flow rate of outlet, h_i = Enthalpy of the intake air, h_o = Enthalpy of exhaust air.

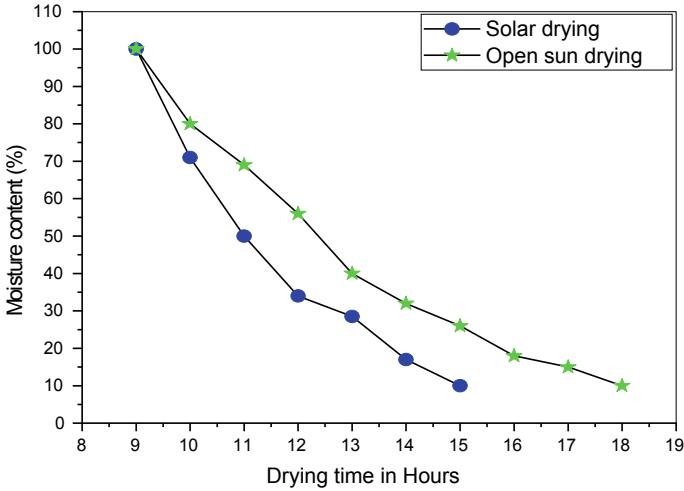


Fig. 3 Variation of moisture content reduction of tomato respective to drying time for solar dryer with double slope and open drying method

3.2 Exergy Analysis

In the extent of second law of thermodynamics, overall outflow of exergy, losses and inflow tray, and dehydrating chamber were evaluated. The essential technique for the exergy investigation of dehydrating chamber was to calculate the values of exergy at a constant steady flow and the exergy deviation for dehydrating operation [11].

The term exergetic efficiency was characterized as inflow to outflow ratio for dehydrating chamber. The generalized form of exergy efficiency was derived as

$$\text{Exergy Efficiency} = \frac{\text{Exergy (inflow-outflow)}}{\text{Exergy Inflow}} \tag{3}$$

$$\eta_{\text{exergetic}} = 1 - \frac{E_L}{E_i} \tag{4}$$

To calculate the exergy losses by the following equation.

$$\sum EX_{\text{LOSS}} = \sum EX_i - \sum EX_o \tag{5}$$

4 Results and Discussion

Figure 3 observes variation in content of moisture in tomato samples in a solar dryer with double slope and open drying process. The content of moisture in the samples decreased from an initial moisture from 94.42% to 10% (wb) in 7 h under solar dryer and 10 h under open drying process, respectively. The samples in the double slope solar dryer had faster drying rate than samples under open drying due to enclosed chamber and restricted inlet of air inside the drying chamber. The highest amount of moisture removal happened between 12:00 and 13:00 when peak solar radiation was recorded. The open sun drying required a second day of drying to achieve similar results to that of the double slope solar dryer.

The global solar radiation for the entire experiment peaked at 1031.82 W/m², having average value of 739.50 W/m². On observing Fig. 4, it was noted that there was a direct relation between the absorber plate temperature and the drying air temperature inside the dryer. The temperature of the absorber plate had a peak temperature of 59.25 °C at 13:00 with average of 42 °C, respectively. The temperature of drying air also followed the same pattern by obtaining a peak temperature of 54 °C and having a temperature of 42 °C on average, respectively. The inlet air had a maximum temperature of 44.67 and 38.23 °C on average. The ambient temperature hovered at 25.7 °C to 27.67 °C, with average of 26.86 °C, respectively. The drying pattern has been observed and has followed the usual path of drying.

On analyzing Fig. 5, the exergy loss varied from 1196.82 to 11,758.18 kJ/kg, having average value of 6302.47 kJ/kg. The exergy loss peaked during 13:00–14:00 when the incident solar radiation was also maximum. The exergy loss remains low if the exergy was properly utilized inside the dryer. Figure 6 shows the exergetic efficiency of the samples that was reported to peak around 12:00 noon due to the

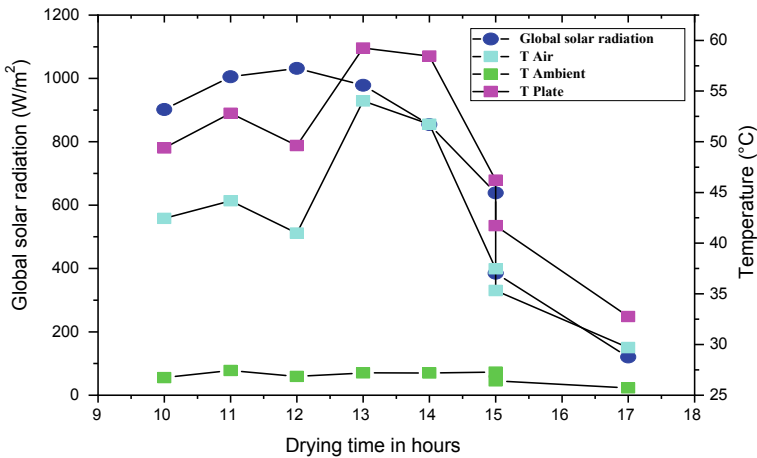


Fig. 4 Variance in global solar radiation, surface plate temperature, ambient temperature, and average air temperatures in double slope solar dryer

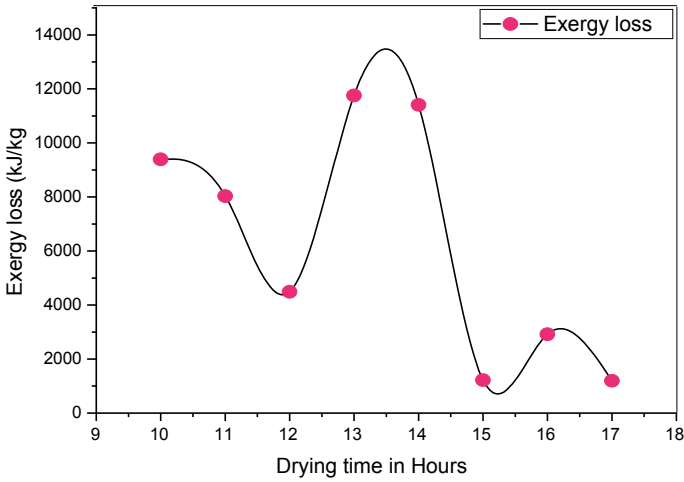


Fig. 5 Variance of exergy loss with a time of drying of the samples

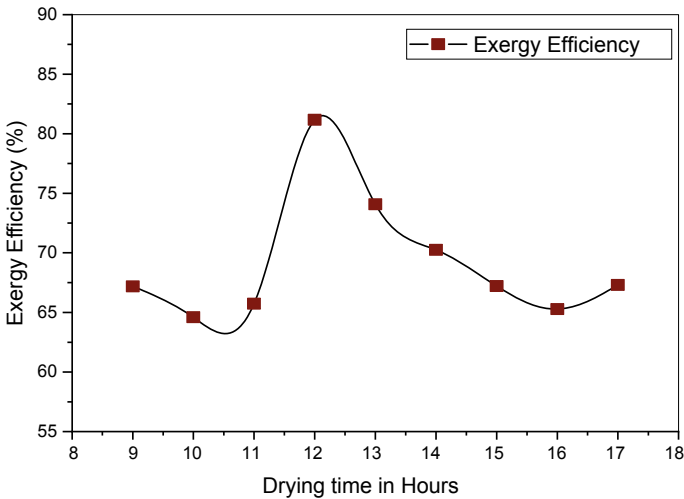


Fig. 6 Variance of exergy efficiency with the time of drying of the samples

maximum utilization of available exergy inside the drying chamber. The exergetic efficiency varied from 67.19 to 81.17% with an average value of 70.20% and it can also be observed that the exergetic efficiency kept decreasing after the peak value until the supply of exergy became low after 16:00 h after which a small increase was observed.

Figure 7 demonstrates the efficiency of pickup of solar drying. The value varies from 10.89 to 14.33%, with an average value of 12.22% for the entire duration of the

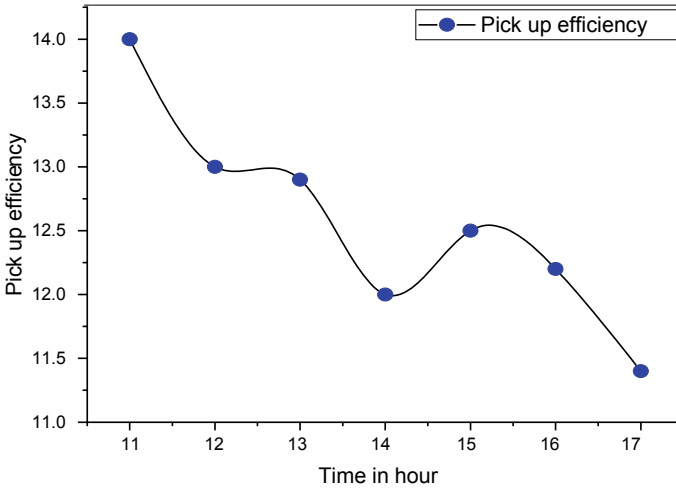


Fig. 7 Variance of efficiency of pickup with the time of drying of the samples

experiment. The pickup efficiency peaked at 11:00 and then proceeded to decrease till 14:00, after which it showed an increase till 15:00 before falling again for the remaining duration of the experiment. Figure 8 shows variance of dryer efficiency with the time of drying of the samples. The effectiveness of the dryer was varied from 11.58 to 44.76%, with an average value of 25.76%. The lower effectiveness of the dryer at 10.00 am due to the beginning of the experiment and that the arrangement had not yet been balanced out. At the point when insolation drops, the put-away heat was

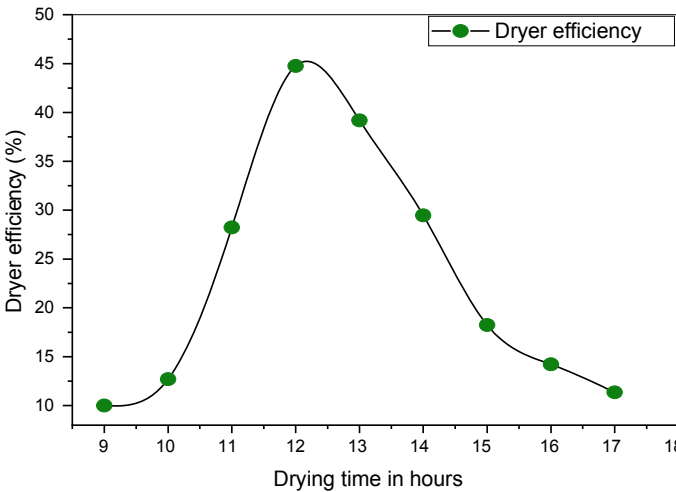


Fig. 8 Variance of efficiency of dryer with the time of drying of the samples

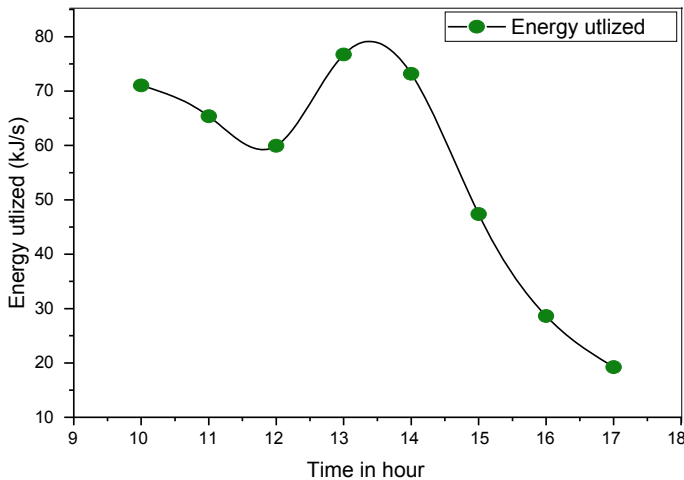


Fig. 9 Variation of Energy used with a drying time of samples

recovered while consequently keeping up greater air warmth and subsequently greater effectiveness. The effectiveness of the dryer was least during the peak incident solar radiation at 12:00 noon due to the rapid increase in surface temperature in the early afternoon with high incident solar radiation whereas the effectiveness of heat of air doesn't meet the extra load because of fixed speed causing it to lose its effectiveness.

Figure 9 shows variance of energy used with the time of drying of the samples. The values for energy utilized ranged from 19.23 to 76.73 kJ/s, with an average value of 55.2 kJ/s, respectively. The values peaked at 13:00–14:00 due to the high availability of energy caused by the peak in incident solar radiation where the energy used has been determined by utilizing the data of wetness expelled during analysis, as concluded by Emulue et al. [18]. The values of thermal efficiency were said to be varied from 5 to 14% peaking at 11:00–13:00 due to the high amount of solar radiation incident on the dryer. The drying chamber efficiency was said to be varying from 9.70% to 77.52%, having an average value of 57.48% increasing with the increase in chamber inlet temperature that facilitates the drying of the samples, respectively.

5 Conclusion

- Performances of a solar drying have been evaluated for tomato in double slope solar dryer.
- The drying was conducted from 9:30 to 16:30 on day 1 and 9:30 to 12:30 on day 2 to evaluate the drying properties of the samples. It is observed that the drying from 94.42 to 10% wet basis moisture took 7 h under solar drying and 10 h under open drying. The average solar radiation had a value of 739.5 W/m² and the airflow rate

had a value of 1.052 kg/s, the drying system, thermal, drying chamber and pickup efficiencies were found about 34.76%, 13%, 63% and 14.33%, respectively.

- The efficiency of exergy of the dryer is varied from 17.4 to 81.17%. The overall efficiency of energy of the dryer is reported as 77%.
- Thermal diffusivity of dried tomato sample minimum value of $1.891 \times 10^{-4} \text{ m}^2/\text{s}$ and maximum value of $4.823 \times 10^{-4} \text{ m}^2/\text{s}$.
- The rehydration ratio, density and porosity of dehydrated tomato slices is 10.26%, 1.57 g/cm² and 42%.
- The dried tomato samples also possessed excellent sensory characteristics while being hygienic and of a high quality due to shielding from pollutants and other quality hampering agents.
- It is concluded that double slope solar dryer is better and most suited for drying the samples than the open sun drying process.

References

1. Arepally D, Ravula S, Malik G, Kamidi V (2017) Mathematical modelling, energy and exergy analysis of tomato slices in a mixed mode natural convection solar Dryer. *Chem Sci Int J* 20(4):1–11
2. Pankaew P, Aumporn O, Janjai S, Mundpookhiew T, Bala BK (2019) Performance of parabolic greenhouse solar dryer equipped with rice husk burning system for banana drying. 14(1)
3. Murugavelh S, Anand B, Midhun Prasad K, Nagarajan R, Azariah Pravin Kumar S (2019) Exergy analysis and kinetic study of tomato waste drying in a mixed mode solar tunnel dryer. *Energy Sources Part A Recover Util Environ Eff* 1–17
4. Lingayat A, Chandramohan VP, Raju VRK (2016) Design, development and performance of indirect type solar dryer for banana drying. *Energy Procedia* 109:409–416
5. Hamdi A, Kooli S (2018) Exergy and energy analysis of the solar drying processes of tomatoes in Tunisia. In: 2018 9th International Renewable Energy Congress (IREC), pp 1–6
6. Johnson PNT, Brennan JG, Addo-Yobo FY (1998) Air-drying characteristics of plantain (Musa AAB). *J Food Eng* 37(2):233–242
7. Natarajan SK, Elavarasan E (2019) A review on computational fluid dynamics analysis on greenhouse dryer. *IOP Conf Ser Earth Environ Sci* 312(1)
8. Berinyuy E, Tangka JK, Weka Fotso GM (2012) Enhancing natural convection solar drying of high moisture vegetables with heat storage. *Agric Eng Int CIGR J* 141–148
9. Hossain MA, Bala BK (2007) Drying of hot chilli using solar tunnel drier. *Sol Energy* 85–92
10. Vijayan S, Arjunan TV, Kumar A (2020) Exergo-environmental analysis of an indirect forced convection solar dryer for drying bitter gourd slices. *Renew Energy* 146:2210–2223
11. Midilli A, Kucuk H (2003) Energy and exergy analyses of solar drying process of pistachio. *Energy* 28(6):539–556
12. Kesavan S, Arjunan TV, Vijayan S (2019) Thermodynamic analysis of a triple-pass solar dryer for drying potato slices. *J Therm Anal Calorim* 136(1):159–171
13. Abbaspour-Gilandeh Y, Jahanbakhshi A, Kaveh M (2020) Prediction kinetic, energy and exergy of quince under hot air dryer using ANNs and ANFIS. *Food Sci Nutr* 8(1):594–611
14. Nazghelichi T, Kianmehr MH, Aghbashlo M (2010) Thermodynamic analysis of fluidized bed drying of carrot cubes. *Energy* 35(12):4679–4684
15. Tan DLS, Perez JH, Diamante LM (2006) Thin-layer drying of cassava chips and grates. *Acta Hort* 703:233–240

16. Kumar Natarajan S et al (2019) Experimental comparative study on reduction in the moisture content of cucumber in a double slope solar dryer with open sun drying method. *J. Phys Conf Ser* 1276:1–6
17. Natarajan SK, Elavarasan E (2019) Experimental investigation of drying potato for Karaikal climatic condition. *IOP Conf Ser Earth Environ Sci* 312:012021
18. Toshniwal U, Karale SR (2013) A review paper on Solar Dryer. *Int J Eng Res Appl* 3(2):896–902

Design of Zig-Zag 1–3 Viscoelastic Composite Layer for the Improved Passive Damping Treatment of Beam



Abhay Gupta, Rajidi Shashidhar Reddy, and Satyajit Panda

Abstract A zig-zag 1–3 viscoelastic composite (VEC) layer is designed for improved passive damping treatment of the vibrating structural beam. A zig-zag 1–3 VEC comprises by incorporating graphite blocks in zig-zag manner within the conventional viscoelastic material (VEM) layer. For the estimation of its damping capacity in the passive damping treatment of a beam, the corresponding finite element (FE) model is formed. To investigate the effect of inclusions in their zig-zag form compared to regular form, primarily, the optimal dimensional properties of corresponding configurations are obtained for the maximum damping of the beam. Then, their optimal modal loss factors and the performance in controlling the forced vibration of beam are compared. The results reveal that VEC with a zig-zag form of inclusions improves damping significantly compared to their regular form and conventional VEM. Moreover, this enhancement in damping appears due to the improvement in both extensional and shear counterparts of modal loss factor.

Keywords Viscoelastic materials · Vibration control · Finite element method · Passive damping treatment

1 Introduction

Passive damping treatments are generally used to reduce the vibration in engineering structures. The unconstrained layer damping (UCLD) and passive constrained layer damping (PCLD) are the most popular passive damping treatments in engineering structures. In UCLD treatment, viscoelastic material (VEM) layer is attached to the surface of vibrating substrate structure, while in the case of PCLD treatment, VEM layer is constrained in between vibrating substrate structure and passive constraining layer. VEM is widely used in damping treatment because it has good energy absorption and dissipation capability under cyclic loading. The energy dissipation in UCLD and PCLD treatments is due to extension/compression and shear deformation in

A. Gupta (✉) · R. S. Reddy · S. Panda
Indian Institute of Technology Guwahati, Guwahati, India
e-mail: abhay.gupta@iitg.ac.in

© The Author(s), under exclusive license to Springer Nature Singapore Pte Ltd. 2022
K. Govindan et al. (eds.), *Advances in Mechanical and Materials Technology*,
Lecture Notes in Mechanical Engineering,
https://doi.org/10.1007/978-981-16-2794-1_17

191

VEM layer, respectively. However, energy dissipation or damping through PCLD treatment is much better than UCLD treatment [1]. Swallow [2] firstly introduced the PCLD treatment, and Kerwin [3] utilized it for the vibration reduction in engineering structures. Different design configurations were proposed for the enhancement of passive damping. Plunkett and Lee [4] utilized segmented constraining layers for the improving passive damping of a beam. However, the damping can also be increased by configuring segmented viscoelastic damping layer and metallic constraining layer in an alternate manner [5]. The damping can also be improved using multiple constrained damping layers [6]. The enhancement in damping occurs by adding stand-off layer so that the distance of damping layer from the natural axis increases and the damping of CLD (constrained layer damping) treated beam also increases [7]. Moreover, the optimal design of the laminated plate with CLD treatment for the maximum damping with minimum weight was also introduced [8]. Moita et al. [9] studied the damping performance of the sandwich plate made of functionally graded (FG) face layers and soft viscoelastic core.

Apart from these configurations, PCLD treatment can also be improved through different viscoelastic damping materials. In this queue, Rajoria and Jalili [10] utilized the carbon nanotube–epoxy composite core within sandwich beam for the enhancement of damping. It was observed that both stiffness and damping improve by adding the carbon nanotubes (CNT) in epoxy matrix. Attipou et al. [11] observed that damping of sandwich structures was also improved by the inclusion of viscoelastic particles. However, the damping was also improved significantly by using appropriate volume fraction of rubber particles and silica nanoparticles within epoxy matrix [12]. Kliem et al. [13] analysed the damping characteristics of cylindrical composite structures with improved VEM properties. However, recently some improved VECs were also proposed for the CLD treated vibrating structure [14–17].

It is observed from the aforesaid literature that in most of the design configurations, the damping enhancement was because of improvement in shear strain/deformation within viscoelastic layer. However, very few design configurations [14–16] are available where damping enhancement was due to increase in both shear and extension/compression deformation in VEM layer simultaneously. The present work is also influenced from aforesaid literature. A design of zig-zag 1–3 viscoelastic composite (VEC) layer is introduced to improve the CLD treated vibrating beam structure. A zig-zag 1–3 VEC is configured by the zig-zag inclusion of graphite blocks in conventional VEM layer instead of their regular form in existing 1–3 VEC (regular 1–3 VEC) [14]. It is expected from the present zig-zag 1–3 VEC that damping may be improved further through the enhancement of both shear and extension/compression deformation in VEM. Hence, in the present work, the influence of inclusions in their zig-zag form is investigated and compared to their regular form through the modal loss factor analysis. The shear and extensional/compression counterparts of the modal loss factor are also evaluated to show their effect on the improvement of overall modal loss factor. The earlier study on the damping capacity of 1–3 VEC with the regular form of inclusions [14] mainly states that the damping capacity significantly depends on the dimensional properties of 1–3 VEC, such as number of graphite blocks, VEM layer thickness and gap between two consequent

graphite blocks. Thus, in the present analysis, the optimal dimensional properties for the maximum damping of the vibrating beam are evaluated to show the effect of inclusions in a zig-zag form. The direct search method is used for evaluating the optimal dimensional properties of 1–3 VEC. A performance study in controlling the forced vibration of beam is also conducted for the enhancement of PCLD-treated beam.

2 Finite Element (FE) Modelling of the PCLD-treated Beam Structure

The beam with constrained conventional VEM layer, regular 1–3 VEC layer (three layered) and zig-zag 1–3 VEC layer are represented diagrammatically in Fig. 1. The length/width and thickness of substrate beam/constrained damping layer/passive constraining layer of PCLD-treated structural beam are designated by L/b and $h/h_d/h_c$, correspondingly. And, dimensional properties such as number of graphite blocks, VEM layer thickness and the gap between two consequent graphite blocks of zig-zag 1–3 VEC layer/regular 1–3 VEC layer are denoted by n , h_v and Δ , respectively (Fig. 1b–c). And transverse periodic point load (p_0) is applied at the centre of bottom surface of a fixed beam. With the assumption of plane stress in y -axis, the FE method is employed for the modelling of PCLD-treated structural beam in two-dimensional (2D) xz plane [18] (Fig. 1). So, the state of strain (ϵ) and stress (σ) at any point within xz plane can be expressed in Eq. (1).

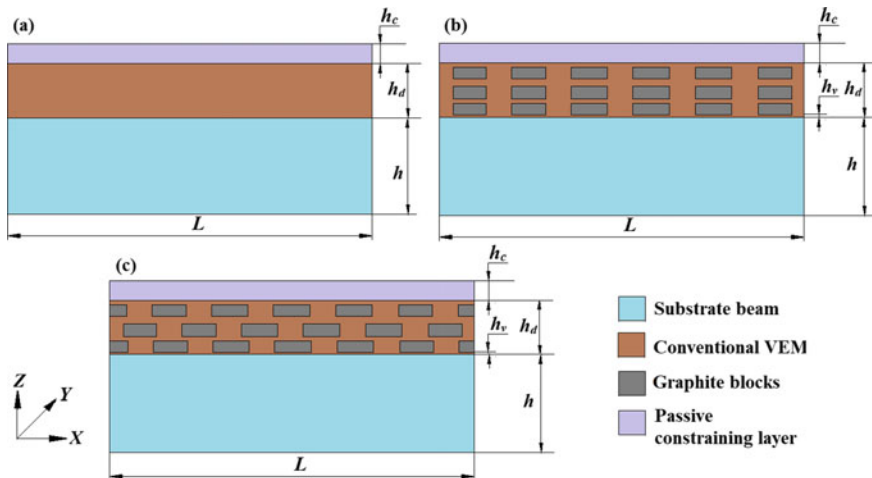


Fig. 1 Schematic diagram of the structural beam with constrained **a** conventional VEM layer, **b** regular 1–3 VEC layer, **c** zig-zag 1–3 VEC layer

$$\boldsymbol{\varepsilon}_b = \{ \varepsilon_{xx} \ \varepsilon_{zz} \}^T, \quad \boldsymbol{\varepsilon}_s = \gamma_{xz}, \quad \boldsymbol{\sigma}_b = \{ \sigma_{xx} \ \sigma_{zz} \}^T, \quad \boldsymbol{\sigma}_s = \tau_{xz} \quad (1)$$

where σ_{xx}/σ_{zz} and $\varepsilon_{xx}/\varepsilon_{zz}$ are bending stresses and strains in x/z axis, respectively; τ_{xz}/γ_{xz} is shear stress/strain in xz plane. For consideration of the linear deformations, the strain–displacement relation is

$$\boldsymbol{\varepsilon}_b = \mathbf{L}_b \mathbf{d}, \quad \boldsymbol{\varepsilon}_s = \mathbf{L}_s \mathbf{d}; \quad \mathbf{d} = \{ u \ w \}^T, \quad \mathbf{L}_b = \begin{bmatrix} \partial/\partial x & 0 \\ 0 & \partial/\partial z \end{bmatrix}^T, \quad \mathbf{L}_s = \begin{bmatrix} \partial/\partial z \\ \partial/\partial z \end{bmatrix}^T \quad (2)$$

where u/w are displacements in x/z direction. Equation (3) expresses the constitutive relation for k^{th} isotropic material within overall beam structure.

$$\boldsymbol{\sigma}_b^k = \mathbf{C}_b^k \boldsymbol{\varepsilon}_b^k; \quad \boldsymbol{\sigma}_s^k = \mathbf{C}_s^k \boldsymbol{\varepsilon}_s^k; \quad \text{where } \mathbf{C}_b^k = \frac{E^k}{1 - (\nu^k)^2} \begin{bmatrix} 1 & \nu^k \\ \nu^k & 1 \end{bmatrix}, \quad \mathbf{C}_s^k = E^k / (2(1 + \nu^k)) \quad (3)$$

where $k = 1$ and 4 are indicated for isotropic material of substrate beam and passive constraining layer, respectively, while $k = 2$ and 3 are indicated for graphite blocks and VEM, respectively. Here, material properties of VEM are taken as the frequency-dependent complex quantity at constant room temperature so it is modelled using complex stiffness method and expressed as $\mathbf{C}_b^k(\omega)$, $\mathbf{C}_s^k(\omega)$ (for $k = 3$).

The FE model of overall PCLD-treated beam structure is discretized into nine-node isoparametric elements in 2D xz plane (Fig. 1). Thus, displacement vector (\mathbf{d}) in Eq. (2) can also be expressed in form of shape function matrix (\mathbf{N}) and elemental displacement vector (\mathbf{d}^e) as given in Eq. (4).

$$\mathbf{d} = \mathbf{N} \mathbf{d}^e \quad (4)$$

The first variations of total potential (δT_P) and kinetic (δT_K) energy of an element can be expressed as

$$\delta T_P = \sum_{k=1}^4 \left[\int_{A_k} \left\{ (\delta \boldsymbol{\varepsilon}_b^k)^T \boldsymbol{\sigma}_b^k + (\delta \boldsymbol{\varepsilon}_s^k)^T \boldsymbol{\sigma}_s^k \right\} dA_k \right] - \langle (\delta w)(p_0/b) \rangle_{x=L/2, z=0} \quad (5a)$$

$$\delta T_K = \sum_{k=1}^4 \left[\int_{A_k} \left(\{ \delta \dot{u} \ \delta \dot{w} \} \rho^k \{ \dot{u} \ \dot{w} \}^T \right) dA_k \right] \quad (5b)$$

where ρ^k and A_k are the mass density and area corresponding to k^{th} material in xz plane, respectively. Equation (6) expresses the extended Hamilton's principle. Using this principle and Eqs. (3)–(5), the elemental FE governing equation of motion of

PCLD-treated beam structure is given in Eq. (7).

$$\int_{t_1}^{t_2} (\delta T_K - \delta T_P) dt = 0 \quad (6)$$

$$\mathbf{M}^e \ddot{\mathbf{d}}^e + (\mathbf{K}_b^e(\omega) + \mathbf{K}_s^e(\omega)) \mathbf{d}^e = \mathbf{P}_0^e$$

where

$$\mathbf{M}^e = \int_{A_k^e} (N^T \rho^k N) dA_k^e, \mathbf{K}_b^e = \int_{A_k^e} (N^T L_b^T C_b^k(\omega) L_b N) dA_k^e$$

$$\mathbf{K}_s^e = \int_{A_k^e} (N^T L_s^T C_s^k(\omega) L_s N) dA_k^e, \mathbf{P}_0^e = \left(\{0 \ 1\}^T (p_0/b) \right)_{x=L/2, z=0} \quad (7)$$

In Eq. (7), subscript s/b represents shear/bending counterparts; A_k^e denotes area of an element made of k th material. After the assembly of elemental matrices/vectors (Eq. (7)), the governing equation of motion of PCLD-treated beam structure can be obtained in the form of global matrices/vectors as given in Eq. (8).

$$\mathbf{M} \ddot{\mathbf{d}} + \mathbf{K}(\omega) \mathbf{d} = \mathbf{P}_0; \text{ where } \mathbf{K}(\omega) = \mathbf{K}_b(\omega) + \mathbf{K}_s(\omega) \quad (8)$$

In Eq. (8), \mathbf{M} and \mathbf{K} are mass and stiffness matrix, correspondingly; \mathbf{P}_0 and \mathbf{d} are mechanical load and displacement vector, correspondingly.

The procedure for the computation of fundamental frequency and its modal loss factor is given in [17, 19]. Moreover, in order to study the influence of shear and extension/compression deformation on the damping of beam with PCLD treatment, the shear and extensional counterparts of modal loss factor are evaluated. The assumptions $\mathbf{K}_b^I(\omega) = \mathbf{0}$ ($\mathbf{K}_s^I(\omega) \neq \mathbf{0}$) and $\mathbf{K}_s^I(\omega) = \mathbf{0}$ ($\mathbf{K}_b^I(\omega) \neq \mathbf{0}$) are considered in order to evaluate the shear (η_s) and extensional (η_e) counterparts of modal loss factor, respectively. However, overall damping or modal loss factor (η) can be evaluated without considering any assumptions ($\mathbf{K}_b^I(\omega) \neq \mathbf{0}, \mathbf{K}_s^I(\omega) \neq \mathbf{0}$).

3 Numerical Results and Discussions

The damping characteristics of PCLD-treated beam with zig-zag 1–3 VEC are compared to regular 1–3 VEC layer (three layered) and conventional VEM layer (Fig. 1) in the present section. The damping characteristics are mainly examined with the estimation of modal loss factors as well as corresponding frequency response under primary resonance due to forced periodic excitation. The dimensions of PCLD-treated structural beam are taken as $L = 0.4$ m, $b = 4$ mm, $h = 5$ mm, $h_d = 2.5$ mm

Table 1 Verification of FE model for the computation of modal loss factor of PCLD-treated beam structure

Modal loss factor	Conventional VEM layer	Regular 1–3 VEC (single layered)		
	η	η_s	η_e	η
Present results	0.00448	0.165	0.033	0.198
Reference	0.00448	0.165	0.033	0.198

and $h_c = 0.5$ mm (Fig. 1). The transverse periodic point load ($p_0 = 1$ N) is applied at the centre of bottom surface of a fixed beam. The substrate beam and passive constraining layer are fabricated with aluminium material ($\rho = 2740$ kg/m³, $E = 69$ GPa, $\nu = 0.3$), while 1–3 VEC consists of blocks in conventional VEM fabricated with graphite material ($\rho = 1400$ kg/m³, $E = 250$ GPa, $\nu = 0.3$). The frequency-dependent properties of conventional VEM are taken at 32 °C room temperature from [17, 20]. Initially, the FE modelling of the beam with constrained conventional VEM/regular 1–3 VEC is validated. Modal loss factor of the PCLD-treated structural beam using present FE model is computed for conventional VEM layer and regular 1–3 VEC (single layered) and collated it with similar results given in Table 1 for identical beam available in the reference [21] and [14], correspondingly. It may be noticed from Table 1 that present FE results are very close with the reference results.

In order to investigate the damping characteristics of PCLD-treated beam with zig-zag 1–3 VEC compared to regular 1–3 VEC layer (three layered) and conventional VEM layer, the modal loss factors corresponding to fundamental mode are evaluated using Eq. (8) by solving an eigen value problem. Through the study of modal loss factors of PCLD-treated beam with regular 1–3 VEC and zig-zag 1–3 VEC, it is observed that the damping properties mainly depend on the different dimensional properties [14] such as number of graphite blocks (n), VEM layer thickness (h_v) and the gap between two consequent graphite blocks (Δ). Hence, to show the corresponding dependency, the modal loss factors are evaluated at each and every point of a three-dimensional grid of dimensional properties (n, h_v, Δ). The limits of the three-dimensional grid are considered as $1 \leq n \leq 12$, $10 \mu\text{m} \leq h_v \leq 200 \mu\text{m}$, $10 \mu\text{m} \leq \Delta \leq 400 \mu\text{m}$. The corresponding variation of modal loss factor is represented in the form of 3D contour plots, as illustrated in Fig. 2a, b for zig-zag 1–3 VEC and regular 1–3 VEC (three layered), respectively. These contours in Fig. 2 are also useful to get the optimal dimensional properties via a direct search optimization method for the maximum damping of the PCLD-treated beam. The optimal dimensional properties (n, h_v, Δ) of these PCLD configurations are presented in Table 2. Using these dimensional properties (Table 2), the modal loss factor (η) of a PCLD-treated beam along with its shear (η_s) and extensional (η_e) counterparts is evaluated for regular and zig-zag 1–3 VEC configurations and presented in Table 3. Similarly, the results are calculated for PCLD-treated beam using conventional VEM and illustrated in same Table 3. The modal loss factor (η) of the beam with constrained conventional VEM layer has a major contribution of its shear counterpart (η_s) compared to its extensional counterpart (η_e) (Table 3). This demonstrates that its

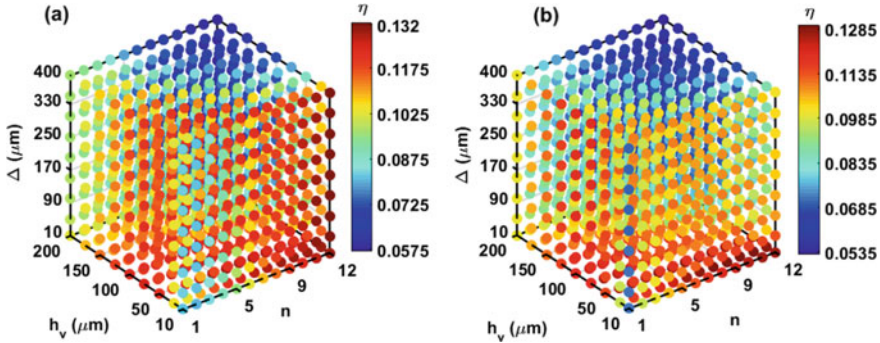


Fig. 2 Values of modal loss factor (η) of structural beam with constrained **a** zig-zag 1–3 VEC and **b** regular 1–3 VEC (three layered) at different dimensional properties (n, h_v, Δ) within three-dimensional contour

Table 2 Optimal dimensional properties (n, h_v, Δ) of PCLD configurations and corresponding modal loss factor (η) of the overall beam

PCLD configuration	n	h_v (μm)	Δ (μm)	η
Regular 1–3 VEC (three layered)	9	25	10	0.1296
Zig-zag 1–3 VEC	12	10	50	0.1324

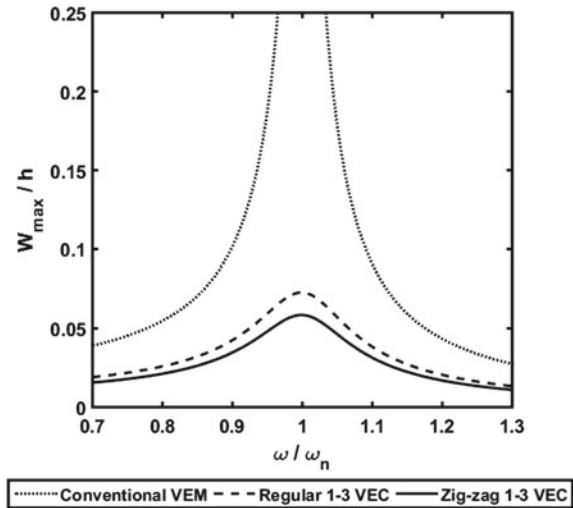
Table 3 Passive damping of different PCLD-treated beam configurations

PCLD configuration	η_e	η_s	η
Conventional VEM	9.268×10^{-5}	0.0374	0.0375
Regular 1–3 VEC (three layered)	0.0458	0.0827	0.1296
Zig-zag 1–3 VEC	0.0142	0.1194	0.1324

damping appears mainly through the energy dissipation through shear deformation of viscoelastic material. However, in case of a PCLD-treated beam using regular 1–3 VEC and zig-zag 1–3 VEC, there is significant contribution from its (modal loss factor) shear (η_s) as well as extensional (η_e) counterparts. The increase in shear (η_s) and extensional (η_e) counterparts of modal loss factor (η) occurs may be because of improvement in transverse shear strain and extensional/compression normal strain, respectively. However, extensional modal loss factor (η_e) is decreased due to zig-zag configuration compared to regular 1–3 VEC configuration, while shear counterpart (η_s) is enhanced. However, the overall damping of PCLD-treated beam using zig-zag 1–3 VEC becomes high compared to regular 1–3 VEC and conventional VEM.

To investigate the performance of PCLD-treated beam with zig-zag 1–3 VEC in reducing its resonant amplitude of vibration due to the transverse periodic force excitation, the frequency response (W_{max}/h) around the fundamental bending mode of vibration is evaluated and shown in Fig. 3. Similarly, the responses for regular 1–3

Fig. 3 Frequency response of different PCLD-treated beam configurations ($p_0 = 1$ N)



VEC and conventional VEM configurations are plotted in the same figure (Fig. 3). The improvement in the diminution of resonant vibrational displacement–amplitude (W_{\max}/h) of the beam with constrained zig-zag 1–3 VEC layer compared to regular 1–3 VEC and conventional VEM as shown in the same figure (Fig. 3). Thus, it may be noted from these results that the zig-zag 1–3 VEC layer can be useful for the improved PCLD-treated beam structures.

4 Conclusions

In this work, a zig-zag 1–3 VEC is introduced to improve the damping of PCLD-treated beam structure. The zig-zag 1–3 VEC comprises zig-zag inclusions of graphite blocks within the conventional viscoelastic material (VEM) layer. To investigate the effect of inclusions in their zig-zag form compared to regular form, the fundamental modal loss factors are evaluated along with corresponding the resonant frequency response of the PCLD-treated beam under periodic transverse force excitation. These results are evaluated by forming the explicit 2D FE model of the PCLD-treated beam structure. Initially, the effect of geometrical properties on the damping capacity of regular and zig-zag 1–3 VEC is analysed. Subsequently, the optimal dimensional properties for maximum damping are obtained for these PCLD configurations. At these optimal dimensional properties, the damping capacity of the different PCLD configurations is analysed. It is observed that in the case of conventional VEM, damping occurs mainly due to the shear deformations in VEM, whereas the shear deformation in VEM significantly improves with the inclusions in zig-zag/regular form along with the significant extensional/compressional deformations in VEM. Thus, the modal loss factor of a beam with 1–3 VEC is significantly

more than that of a beam with conventional VEM. The results also demonstrated that the zig-zag form of inclusions enhances the shear deformations in VEM but reduces the extensional/compressional deformations in VEM. However, the overall damping or attenuation in the vibrational amplitude is significantly higher in zig-zag 1–3 VEC than the regular 1–3 VEC layer. Thus, the zig-zag 1–3 VEC can be conceivable for the improved damping of PCLD-treated structural beam.

References

1. Kerwin EM (1965) Macromechanisms of damping in composite structures. In: Internal Friction, Damping, and Cyclic Plasticity
2. Swallow W (1939) An improved method of damping panel vibrations. Br Pat Specif 513:171
3. Kerwin JEM (1959) Damping of flexural waves by a constrained viscoelastic layer. J Acoust Soc Am 31:952–962
4. Plunkett R, Lee CT (1970) Length optimization for constrained viscoelastic layer damping. J Acoust Soc Am 48:150–161
5. Torvik PJ, Strickland DZ (1972) Damping additions for plates using constrained viscoelastic layers. J Acoust Soc Am 51:985–991
6. Alam N, Asnani NT (1984) Vibration and damping analysis of multilayered rectangular plates with constrained viscoelastic layers. J Sound Vib 97(4):597–614
7. Yellin JM, Shen IY (1998) Analytical model for a passive stand-off layer damping treatment applied to an Euler-Bernoulli beam. Smart Struct Mater 3327:349–357
8. Madeira JFA, Araujo AL, Mota Soares CM (2017) Multiobjective optimization of constrained layer damping treatments in composite plate structures. Mech Adv Mater Struct 24(5):427–436
9. Moita JS, Araujo AL, Soares CMM, Soares CAM (2018) Vibration analysis of functionally graded material sandwich structures with passive damping. Compos Struct 183:407–415
10. Rajoria H, Jalili N (2005) Passive vibration damping enhancement using carbon nanotube-epoxy reinforced composites. Compos Sci Technol 65(14):2079–2093
11. Attipou K, Nezamabadi S, Zahrouni H (2013) A multiscale approach for the vibration analysis of heterogeneous materials: application to passive damping. J Sound Vib 332(4):725–739
12. Huang CY, Tsai JL (2015) Characterizing vibration damping response of composite laminates containing silica nanoparticles and rubber particles. J Compos Mater 49(5):545–557
13. Kliem M, Hogsberg J, Vanwalleghem J, Filippatos A, Hoschutzky S, Fotsing ER, Berggreen C (2019) Damping analysis of cylindrical composite structures with enhanced viscoelastic properties. Applied Compos Mater 26(1):85–113
14. Kumar A, Panda S (2016) Design of a 1–3 viscoelastic composite layer for improved free/constrained layer passive damping treatment of structural vibration. Compos Part B Eng 96:204–214
15. Gupta A, Reddy RS, Panda S, Kumar N (2020) Damping treatment of beam with unconstrained/constrained 1–3 smart viscoelastic composite layer. Mater Today Proc 26:956–62
16. Gupta A, Rajidi SR, Panda S (2020) Design of a 1–3 smart viscoelastic composite layer for augmented constrained layer damping treatment of plates. IOP Conf Ser Mater Sci Eng 872(1):012067
17. Gupta A, Panda S, Reddy RS (2020) Improved damping in sandwich beams through the inclusion of dispersed graphite particles within the viscoelastic core. Compos Struct 112424
18. Popov EP (1990) Engineering mechanics of solids. Prentice Hall
19. Hu H, Belouettar S, Potier-Ferry M (2008) Review and assessment of various theories for modeling sandwich composites. Compos Struct 84(3):282–292

20. Jones DIG (2001) Handbook of viscoelastic vibration damping. Wiley (2001)
21. Lall AK, Asnani NT, Nakra BC (1988) Damping analysis of partially covered sandwich beams. J Sound Vib 123(2):247–259

Design and Simulation of Structural Components of Affordable, Automated Solar Panel Cleaning Mechanism



Shubham Jain and Rhythm Singh 

Abstract Efficiency of solar PV system decreases due to factors like dust accumulation and bird dropping which limit its performance by lowering the transmissivity. This decrement in efficiency is significant and can be observed in large arrays used for commercial purpose. In order to solve this problem of efficiency decrement, removal of these materials is necessary on regular basis. Many types of cleaning mechanisms are available to clean the solar panels in commercial applications; however, there is need for a more affordable system for residential applications. In this regard, work is taken up to design and simulate the structural components of an automatic solar PV panel cleaning mechanism which is structurally stable, durable and affordable for cleaning of residential PV panels. The system is designed in SOLIDWORKS to analyze its working process properly, and the components are designed and simulated in ANSYS workbench separately. The analysis mainly covers the threaded rod and rubber wiper, and the total torque requirement for the system has been estimated. This solar PV panel cleaning mechanism can be programmed with microcontroller and dust detecting sensor to make the system fully automatic.

Keywords PV panel cleaning mechanism · Dust cleaning mechanism · Structural components · Threaded rod · SOLIDWORKS · ANSYS

1 Introduction

Solar photovoltaic panel is a device which converts solar radiation received from the sun into the electricity directly. Number of solar cells are attached in series to provide the required current and a fixed voltage as the output of the solar PV panel. When the appropriate solar irradiation falls on these solar cells, a current is generated. If there is any shadow or any type of obstruction between solar cells and the solar rays, the output of the cell is decreased. These obstructions can be dust accumulation, bird dropping, water stain and garbage accumulation on the glass surface of PV panel which can

S. Jain · R. Singh (✉)

Indian Institute of Technology Roorkee, Roorkee, Uttarakhand 247667, India
e-mail: rhythm@hre.iitr.ac.in

© The Author(s), under exclusive license to Springer Nature Singapore Pte Ltd. 2022
K. Govindan et al. (eds.), *Advances in Mechanical and Materials Technology*,
Lecture Notes in Mechanical Engineering,
https://doi.org/10.1007/978-981-16-2794-1_18

201

block the incoming solar beam radiation. The amount of accumulated dust on the surface of the PV module affects the overall energy delivered from the PV module on a daily, monthly, seasonal and annual basis. Detailed studies have been conducted to study the effect of soiling on efficiency of panel [1]. Hammoud et al. [2] calculated the average increment of 32.27% in power generation by cleaning the dust with the help of designed robot. Haydar et al. [3] confirmed the degradation of performance of panel by 44% drop in power output in average, due to dust accumulation. Several attempts have also been made for developing automated cleaning mechanisms for PV panels, mainly for commercial applications. Halbavi et al. [4] and Abhilash and Panchal [14] have designed microcontroller-based automatic PV panel cleaning mechanisms. [5] discusses the design of a control system for self-cleaning mechanism for PV panels for street lighting system. Lu et al. [6] present a solar panel cleaning mechanism based on a linear piezoelectric actuator. Zhen and Yang [7] discuss the design of a robot for cleaning flat PV panel surfaces. Wable and Ganiger [8] discuss the design as well as manufacturing aspects of a solar PV panel cleaning mechanism. Tejwani and Solanki [9] present the implementation and working of 360° sun-tracking system with an automatic PV panel cleaning mechanism. Najeeb et al. [10] discuss the design of a PLC-based self-cleaning mechanism for PV panels, especially in the desert-like climatic conditions. Parrott et al. [11] also discuss a robot-based dry cleaning mechanism for PV panels with specially designed brush, making it more suitable for application in desert-like conditions. Al Baloushi et al. [12] and Aly et al. [13] have also presented self-cleaning mechanisms for PV panels in dry desert-like climatic conditions.

Manual cleaning is many times preferred to clean the solar PV panels used in residential applications as it is easy to clean few panels at rooftop but in commercial PV plant, regular cleaning by manpower is not an easy task. However, automatic dust cleaning robots used in commercial panels are not affordable to use at residential PV as it is costlier. To overcome these problems, a design of an affordable and structurally stable, automatic dust cleaning mechanism is proposed. This automatic panel cleaning mechanism consists of a wiper as cleaning component, threaded rod as prime mover, two DC motors to power the system and some other mechanical components to make the system simple and mechanically strong. Section 2 deals with the detailed design of the key structural components and the analytical study of the structural operation of the proposed mechanism. Section 3 discusses the simulations for analyzing the stability of major components, and the results and conclusions are presented in Sect. 4.

2 Proposed Design of Dust Cleaning Mechanism

This dust cleaning mechanism is basically designed for PV panel fixed on the rooftop at HRED, IIT Roorkee. The dimensions of the panel are as given in Table 1. To clean the surface, a wiper is used for mopping with repeated motion. Wiper is attached with the threaded rod by means of carriage block which converts the rotary motion

Table 1 Dimensions of PV panel

Length	Width	Thickness (glass included)
167 cm	100 cm	3.2 cm

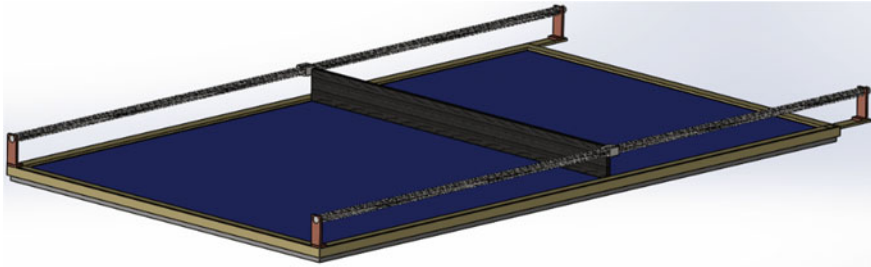


Fig. 1 Proposed design for dust cleaning mechanism

of threaded rod into linear motion just like the screw and nut assembly. This carriage block has internal teeth meeting with threads of rod. When the threaded rod rotates with the help of DC motors, the wiper moves linearly in contact with glass surface. Thus, the cleaning process completes and avoids the reduction of efficiency of panel. The proposed model, designed in SOLIDWORKS software, is given in Fig. 1.

2.1 Detailed Design

The dust cleaning mechanism shown in Fig. 1 majorly consists of two stainless steel rods of 12 mm diameter and 2 mm pitch, a rubber wiper attached with an iron rod to support at one end, two carriage blocks of 30 mm * 30 mm * 30 mm with internal diameter of 12 mm with same pitch. Both the threaded rods are supported in bearing at the ends and connected with DC motors. A programming unit is connected with DC motors to rotate the rod in clockwise and anti-clockwise direction alternatively. A separate water pipe can be attached at the top of panel for wet cleaning of PV panels.

The torque calculation for the system is done as follows:

$$\begin{aligned} \text{Rod diameter, } d &= 12 \text{ mm, Pitch, } p = 2 \text{ mm} \\ \text{Total rotation required : } L/p &= 1700/2 = 850 \end{aligned}$$

If motor with RPM of 500 is chosen to work, the time of one stroke will be $850/500 = 1.7$ min.

Torque required to raise the load against gravity in screw gage is given by Eq. (1)

$$T_1 = W \tan(\alpha + \varphi) \times (d/2) \tag{1}$$

where α is thread helix angle, φ is friction angle, d is diameter of threaded rod, μ is coefficient of friction between carriage block and threaded rod, and W is load to lift.

$$\tan \alpha = p/\pi \cdot d \quad (2)$$

$\tan \alpha = 2/\pi$ (12) = 0.053, $\alpha = 3.0367$ degree and $\varphi = \tan^{-1} \mu = \tan^{-1} (0.16) = 9.09$, where μ is the friction coefficient between the threaded rod and the carriage block mass of wiper $m_w = 1 * b * h * \text{density} + \text{mass of supporting rod} = 1 * 0.06 * 0.01 * 1100 + 1 \text{ kg} = 1.66 \text{ kg}$

$$F_s = \mu' \cdot m_w g \cos \theta \quad (3)$$

$$F_s = 0.5 * 1.66 * 9.81 \cos 30 = 7.051 \text{ N}$$

$$W = (m_e g \sin \theta + F_s)/2 \quad (4)$$

where θ is 30° (panel tilt for Roorkee), and μ' is the friction coefficient of glass and rubber interface with water as lubricant.

$$m_e = (\text{mass of wiper}) + 2 * \text{mass of carriage block} \quad (5)$$

$$m_e = (1.66) + 2 * 0.177 = 2.014 \text{ kg.}$$

$$\text{From Eq. (4), } W = (2.014 \times 9.81 \times 0.5 + 7.051)/2 = 8.464 \text{ N.}$$

By putting the value of W , α , φ and d in Eq. (1), we get $T_1 = 8.464 \times \tan (9.09 + 3.0367) \times (0.006) = 0.010957 \text{ N m.}$

The torque to overcome inertia is given by Eq. (6),

$$T_2 = I \cdot \alpha \quad (6)$$

where the moment of inertia (I) is given as, $I = mr^2/2 = 2.5662 * (0.006^2)/2 = 2.594\text{E}-05 \text{ kg m}^2$.

α required is 100 rad/s^2 .

$$\text{Thus, } T_2 = 2.594\text{E}-5 * 100 = 0.002594 \text{ N m.}$$

Thus, the total torque required is $0.010957 + 0.002594 = 0.0135069 \text{ N m.}$

Similar calculation is done for different material combination of threaded rod and carriage block, the results of which are shown in Table 2. The results shown in Table 2 have been further illustrated graphically in Fig. 2. It is clear from Fig. 2 that the minimum torque requirement is for a 12 mm diameter rod of stainless steel. Hence, the structural stability simulations for determining the deformation and fatigue life of this component were conducted in ANSYS, as detailed in the next section.

Table 2 Total torque calculation for different rod material

Wiper mass (kg)	Material of rod	Dia (mm)	Pitch (mm)	Density (kg/m ³)	Length of rod (mm)	Mass of rod (kg)	Mass of block (kg)	μ	T_1 (N m)	F_s (N)	I (kg m ²)	T_2 (N m)	$T = T_1 + T_2$
1.66	Steel	12	2	7500	1700	1.44	0.177	0.16	0.011	7.05	2.59E-05	0.0025	0.0135
1.66	Steel	16	2	7500	1700	2.56	0.157	0.16	0.013	7.05	8.2E-05	0.0081	0.0211
1.66	Steel	18	2.5	7500	1700	3.24	0.145	0.16	0.015	7.05	0.000131	0.0131	0.0281
1.66	Steel	20	2.5	7500	1700	4.00	0.131	0.16	0.016	7.05	0.0002	0.0200	0.036
1.66	Steel	22	2.5	7500	1700	4.84	0.116	0.16	0.017	7.05	0.000293	0.0293	0.0463
1.66	Steel	24	3	7500	1700	5.76	0.100	0.16	0.019	7.05	0.000415	0.0415	0.0605
1.66	Steel	27	3	7500	1700	7.29	0.073	0.16	0.021	7.05	0.000665	0.0664	0.0874
1.66	Cast iron	12	1.75	7874	1700	1.51	0.177	0.4	0.023	7.05	2.72E-05	0.0027	0.0257
1.66	Cast iron	16	2	7874	1700	2.69	0.157	0.4	0.029	7.05	8.61E-05	0.0086	0.0376
1.66	Cast iron	18	2.5	7874	1700	3.40	0.145	0.4	0.033	7.05	0.000138	0.0137	0.0467
1.66	Cast iron	20	2.5	7874	1700	4.20	0.131	0.4	0.036	7.05	0.00021	0.0210	0.057
1.66	Cast iron	22	2.5	7874	1700	5.08	0.116	0.4	0.039	7.05	0.000308	0.0307	0.0697
1.66	Cast iron	24	3	7874	1700	6.05	0.100	0.4	0.043	7.05	0.000436	0.0435	0.0865
1.66	Cast iron	27	3	7874	1700	7.66	0.073	0.4	0.047	7.05	0.000698	0.0698	0.1168
1.66	Al	12	1.75	2700	1700	0.51	0.177	0.45	0.025	7.05	9.34E-06	0.0009	0.0259
1.66	Al	16	2	2700	1700	0.92	0.157	0.45	0.033	7.05	2.95E-05	0.0029	0.0359
1.66	Al	18	2.5	2700	1700	1.16	0.145	0.45	0.037	7.05	4.73E-05	0.0047	0.0417
1.66	Al	20	2.5	2700	1700	1.44	0.131	0.45	0.041	7.05	7.21E-05	0.0072	0.0482
1.66	Al	22	2.5	2700	1700	1.74	0.116	0.45	0.044	7.05	0.000106	0.0105	0.0545
1.66	Al	24	3	2700	1700	2.07	0.100	0.45	0.048	7.05	0.000149	0.0149	0.0629

(continued)

Table 2 (continued)

Wiper mass (kg)	Material of rod	Dia (mm)	Pitch (mm)	Density (kg/m ³)	Length of rod (mm)	Mass of rod (kg)	Mass of block (kg)	μ	T_1 (N m)	F_s (N)	I (kg m ²)	T_2 (N m)	$T = T_1 + T_2$
1.66	Al	27	3	2700	1700	2.62	0.073	0.45	0.052	7.05	0.000239	0.0239	0.0759
1.66	Brass	12	1.75	8730	1700	1.67	0.177	0.35	0.020	7.05	3.02E-05	0.0030	0.023
1.66	Brass	16	2	8730	1700	2.98	0.157	0.35	0.026	7.05	9.54E-05	0.0095	0.0355
1.66	Brass	18	2.5	8730	1700	3.77	0.145	0.35	0.029	7.05	0.000153	0.0152	0.0442
1.66	Brass	20	2.5	8730	1700	4.66	0.131	0.35	0.032	7.05	0.000233	0.0233	0.0553
1.66	Brass	22	2.5	8730	1700	5.63	0.116	0.35	0.035	7.05	0.000341	0.0341	0.0691
1.66	Brass	24	3	8730	1700	6.71	0.100	0.35	0.038	7.05	0.000483	0.0483	0.0863
1.66	Brass	27	3	8730	1700	8.49	0.073	0.35	0.041	7.05	0.000774	0.0773	0.1183

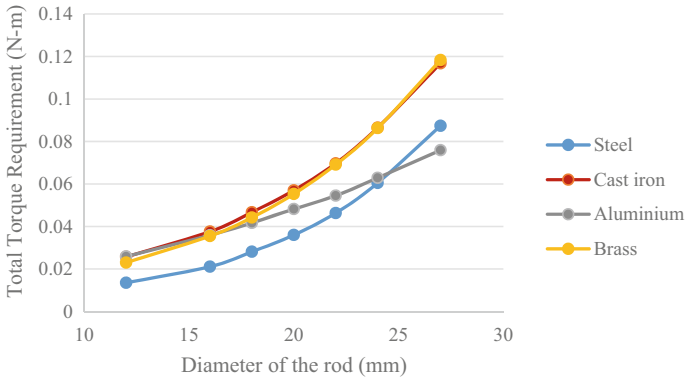


Fig. 2 Torque requirement results for different rod materials

3 Simulation Work

Threaded rod and wiper experience significant torque during the operation due to friction force. This friction can be assumed to be applied at mid-span of wiper which creates two couples at the threaded rod. These couple of moment can cause the deformation of threaded rod by fatigue loading. In order to check the stability of components, a small model, as shown in Fig. 3, is simulated in ANSYS software, and results in the terms of total deflection and life of component are calculated to check whether the component is stable or not for the load.

$$\text{Couple at threaded rod} = \text{friction force} * \text{width of panel}/2$$

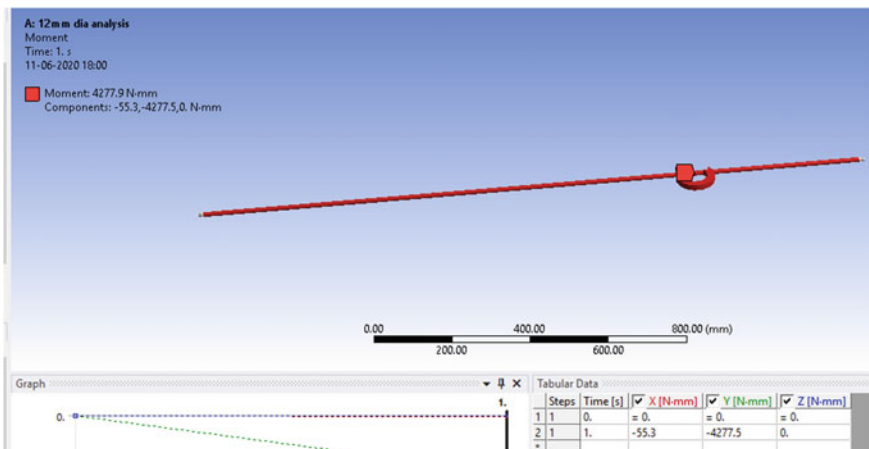


Fig. 3 Load at threaded rod cylindrically fixed at both ends

$$\begin{aligned}
 &= \mu' \cdot mwg \cos \theta * (1/2) = 0.5 * (1.66 + 0.177 * 2) \\
 &\quad * 9.81 * \cos 30 * (1/2) \\
 &= 8.555/2 = 4.775 \text{ N m} \tag{7}
 \end{aligned}$$

$$\begin{aligned}
 \text{Second couple on rod} &= \text{friction force} * d/2 \\
 &= 8.555 * (12/2) = 51.33 \text{ N mm} \\
 &= 0.051 \text{ N m} \tag{8}
 \end{aligned}$$

Wiper is also experiencing the torque due to friction force 8.555 N at the edge which is in contact with glass surface.

4 Results and Conclusion

For motor selection, required torque is calculated as 0.0135 N m at the end of rods. The simulation results of threaded rod show the maximum deflection (0.054 mm) and a life more than 10E6 number of cycles, when loaded with couples of (0.051 and 4.775 N m both are perpendicular) at mid-span as shown in Figs. 4 and 5.

As per the code of practice, typically, the maximum deflection is limited to the beam’s span length divided by 250. In this analysis, if the number L/250 is calculated, it comes equal to 1700 mm/250 = 6.8 mm, which is very high as compared to the deflection analyzed in ANSYS. Hence, the threaded rod of stainless steel material of 12 mm diameter is found safe to serve the purpose. Similarly, the simulation of wiper of 1000 mm * 60 mm * 10 mm, loaded with friction force at the lower surface, shows its maximum deflection of 5.38 mm (in Fig. 6) at the contact of wiper and glass. This deflection can be effectively utilized to suppress the wiper blade during fabrication.

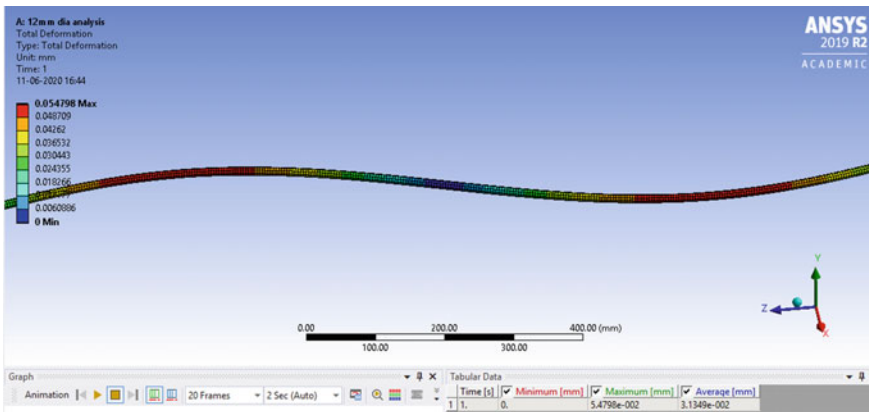


Fig. 4 Contour of total deformation of stainless steel rod

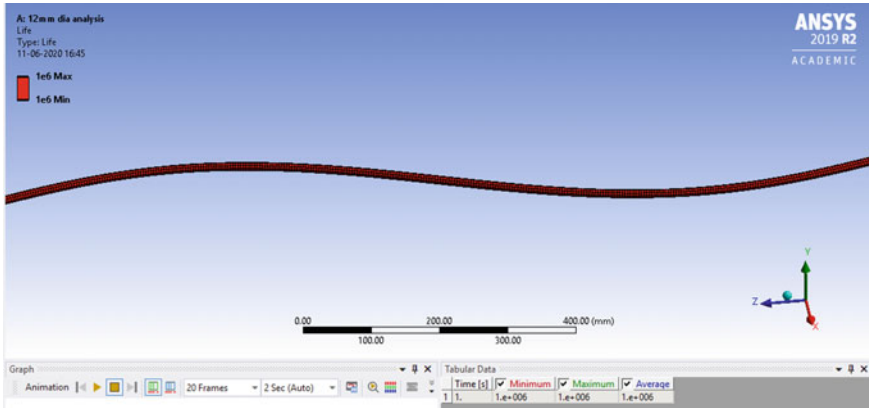


Fig. 5 Contour of fatigue life of stainless steel rod

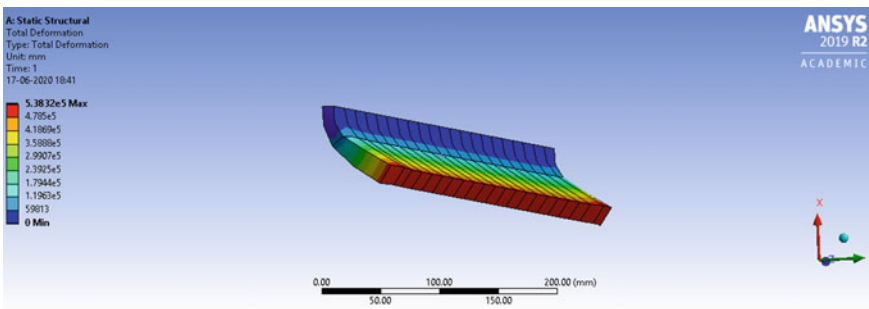


Fig. 6 Contour of total deformation of rubber wiper under frictional loading

In accordance with the analyzed data, this project has been fabricated and installed at HRED, IIT Roorkee. Thus, the paper presents a simple and affordable structural mechanism for a PV panel cleaning mechanism.

References

1. Maghami MR, Hizam H, Gomes C, Radzi MA, Rezadad MI, Hajighorbani S (2016) Power loss due to soiling on solar panel: a review. *Renew Sustain Energy Rev* 59:1307–1316
2. Hammoud M, Shokr B, Assi A, Hallal J, Khoury P (2019) Effect of dust cleaning on the enhancement of the power generation of a coastal PV-power plant at Zahrani Lebanon. *Sol Energy* 184:195–201
3. Haydar J, Nouraldean A, Fayad H, Fahs W, Al Haj Hassan H (2019) A low cost automated cleaning system for photovoltaic panels. In: *ACIT 2018—19th international Arab conference on information technology*

4. Halbhavi SB, Kulkarni SG, Kulkarni DB (2015) Microcontroller based automatic cleaning of solar panel. *Int J Latest Trends Eng Technol (IJLTET)* 5(4)
5. Mustafa F, Abd Sahb A, Al-Ammri AS, Ghazi A (2015) Self cleaning control system for PV solar panel street light. In: *The Sixth International Renewable Energy Congress (IREC2015)*. IEEE, pp 1–6
6. Lu X, Zhang Q, Hu J (2013) A linear piezoelectric actuator based solar panel cleaning system. *Energy* 60:401–406
7. Zhen JJ, Yang ZM (2012) Design and realization of a flat surface cleaning robot. *Adv Mater Res* 505:477–483
8. Wable SS, Ganiger S (2017) Design & manufacturing of solar panels cleaning system. *Int J Res Appl Sci Eng Technol (IJRASET)* 5(07):191–197
9. Tejwani R, Solanki CS (2010) 360 sun tracking with automated cleaning system for solar PV modules. In: *2010 35th IEEE photovoltaic specialists conference*. IEEE, pp 2895–2898
10. Najeeb NS, Soori PK, Kumar TR (2018) A low-cost and energy-efficient smart dust cleaning technique for solar panel system. In: *2018 International conference on smart grid and clean energy technologies (ICSGCE)*. IEEE, pp 125–129
11. Parrott B, Zanini PC, Shehri A, Kotsovos K, Gereige I (2018) Automated, robotic dry-cleaning of solar panels in Thuwal, Saudi Arabia using a silicone rubber brush. *Sol Energy* 171:526–533
12. Al Baloushi A, Saeed M, Marwan S, Al Gghafri S, Moumouni Y (2018) Portable robot for cleaning photovoltaic system: ensuring consistent and optimal year-round photovoltaic panel performance. In: *2018 advances in science and engineering technology international conferences (ASET)*. IEEE, pp 1–4
13. Aly SP, Gandhidasan P, Barth N, Ahzi S (2015) Novel dry cleaning machine for photovoltaic and solar panels. In: *2015 3rd international renewable and sustainable energy conference (IRSEC)*. IEEE, pp 1–6
14. Abhilash B, Panchal AK (2016) Self-cleaning and tracking solar photovoltaic panel for improving efficiency. In: *2016 2nd international conference on advances in electrical, electronics, information, communication and bio-informatics (AEEICB)*. IEEE, pp 1–4

Influence of Number of Lobe on Dynamic Performance of Hydrodynamic Journal Bearing



Vivek Kumar, Kush Shrivastava, Kuldeep Narwat, and Satish C. Sharma

Abstract This paper concerns with the numerical simulations of hydrodynamic journal bearing. Influence of number of lobes has been examined on the steady and dynamic performance parameters of bearing system. Finite Element (FE) formulation is carried out to perform numerical simulations of bearing system. The performance of circular and multi-lobe (2–4 lobe) journal bearings have been computed and compared for film pressure distribution, min. film thickness, rotor-dynamic coefficients, etc. These performance indices are obtained for a wider range of external load. It has been found that a two-lobe journal bearing offers better steady and dynamic performance as to circular and multi-lobe journal bearing configurations. It is observed that a two-lobe journal bearing vis-a-vis circular bearing significantly enhances the minimum film thickness and direct stiffness coefficients, and marginally reduces the threshold stability margin.

Keywords Journal bearing · Multi-lobe bearings · Rotor-dynamic coefficients · FEM

V. Kumar (✉) · K. Shrivastava
Department of Mechanical Engineering, School of Technology, PDPU, Gandhinagar 382007, India
e-mail: vivek.kumar@sot.pdpu.ac.in

K. Shrivastava
e-mail: Kush.smtmd19@sot.pdpu.ac.in

K. Narwat
School of Mechanical Engineering, Galgotias University, Greater Noida 203201, India
e-mail: Kuldeep.narwat@galgotiasuniversity.edu.in

S. C. Sharma
Mechanical and Industrial Engineering Department, IIT Roorkee, Roorkee 247667, India
e-mail: sshmefme@me.iitr.ac.in

1 Introduction

Hydrodynamic journal bearings found wide range of usage in machines such as turbines, pumps, turbo-generators, mechanical presses, and compressors [1, 2]. The hydrodynamic pressure is built up in such bearings by churning of lubricant in narrow converging passage between the runner and stationary surface. The bearing surface herein is separated by the thin film viscous fluid. The essential requirement for supporting external load is a converging passage, viscous medium and high/sufficient operating speed. These requirements ensure safe and reliable operation of hydrodynamic journal bearings [2].

Since, first reported application of journal bearing [3], many analytical, numerical and experimental investigations were reported dealing with performance improvement of these bearings. Basically, the operation of hydrodynamic journal bearing can be effectively managed by altering/adjusting the geometry of bearing and type of lubricant employed used during its operation/maintenance. Earlier design of these bearings is mainly concern with circular geometry of runner/shaft and bearing. With passage of time, the demand of higher productivity pushes the practicing engineers to operate machines under heavy load and high operating speed. Under such prevailing conditions, the earlier design circular bearings do not able to produce desirable or expected performance. Therefore, new design has been explored to improve the tribological performance of journal bearing system. With the availability of modern manufacturing technologies and computing facilities, non-circular bearings were more frequently analyzed, produced and employed in turbo-machine applications. These non-circular bearing such elliptical bearings [4], pressure dam bearing [5], tilting pads bearings [6], multi-lobe bearings [7], etc. were reported to provide better performance as compared to circular bearings.

Recently, Laser Surface Texturing (LST) /surface engineering [8, 9] is widely recognized as a new technique/sciences for enhancing the tribo-performance of hydrodynamic bearings. In LST, micro-dimple/grooves patterns, etc. are produced on bearing surface. Such patterns act as numerous micro-bearings [8] and provide substantial enhancement in the operation of tribo-pairs employed in different lubrication regimes. Theoretical and experimental investigations [8–13] were reported examining performance of textured surface bearing. In most of these studies, a marked improvement in load supporting ability [8, 11, 13] and significant in friction [8–10, 12] have been reported. These benefits of LST (in fluid film bearings) can be only achieved, when texture is provided with optimum attributes, dimension and shapes. The optimum values of texture attributes are reported to vary significantly with respect to operating conditions of the journal bearing system. After the manufacturing and installation of journal bearing in engineering applications, its tribological performance can be improved by selection of suitable/ formulation of appropriate type and quantity of lubricant. Commercial lubricant contains certain packages of additives such viscosity index improver, anti-friction and anti-wear agents, rust inhibitors, etc. [1, 2]. These agents are often mixed to the base/stock oil to impart specific characteristics. As a consequence, the lubricant during bearing operation, shows nonlinear

behavior. Experimental studies are reported investigating the effect of viscosity index improvers on coefficient of friction between tribo-pairs such as sliding surface [14], friction clutch [15] and journal bearings [16, 17]. Experimental and numerical study [16] suggested that the cubic shear stress fluid model better describes the nonlinear characters of lubricants containing viscosity index improvers. Afterward, many theoretical/analytical/numerical studies were reported [18–24] examining the influence of nonlinear nature of fluid on performance of different type of fluid film bearings. The studies used theories/law such as micropolar theory [18], power law [19], couple stress theory [18–22], and cubic shear stress law [16] to describe nonlinear behavior of fluids. The couple stress and micropolar theories are deals with influence chain length size of additives [20–24] on the operation of bearing systems, employing non-Newtonian lubricant. It is found that with an increase in chain length of additives/coupling number, load carrying capacity, min. film thickness gets enhance and fluid flow rate required through the journal bearing reduces. Theories such as power law fluid model and cubic shear stress law fluid model describe nonlinear nature of fluids in terms of shear stress vs. shear strain rate.

The available literature discussed above indicates that use of non-Newtonian fluids can enhance performance level of hydrodynamic journal bearing. Also, it was reported that using non-circular bearing geometry can substantially improve the performance of journal bearings. However, no comprehensive study was reported dealing with comparative analysis for dynamic performance of circular and multi-lobe (2–4) journal bearing operating in hydrodynamic regime. In view of this, this study has been planned to investigate the effect of number of lobe on rotor-dynamic coefficient and stability margin of hydrodynamic journal bearing.

2 Mathematical Formulation

Figure 1 presents geometric configurations of circular and multi-lobe hydrodynamic journal bearing. The lubricant in the bearing system is feed through a supply hole provided on the top bearing and housing. The lubricant is assumed to be behaving as a Newtonian fluid. The flow through the narrow space between runner (journal) and stationary surfaces (bearing) is assumed to be laminar, iso-viscous and incompressible. Under steady operation of the bearing, the flow of fluid could be described as follows [23]:

$$\frac{\partial}{\partial \bar{x}} \left(\bar{h}^3 \frac{\partial \bar{p}}{\partial \bar{x}} \right) + \frac{\partial}{\partial \bar{z}} \left(\bar{h}^3 \frac{\partial \bar{p}}{\partial \bar{z}} \right) = \Omega \frac{\partial \bar{h}}{\partial \bar{x}} + \frac{\partial \bar{h}}{\partial \bar{t}} \tag{1}$$

$$\bar{x} = \frac{x}{r_j}; \quad \bar{z} = \frac{z}{r_j}; \quad \bar{h} = \frac{h}{c_r}; \quad \bar{r} = \frac{r}{r_j};$$

$$\bar{p} = \frac{p - p_a}{p_r}; \quad \bar{\mu} = \frac{\mu}{\mu_r}; \quad p_r = \frac{\mu \omega r_j^2}{c_r^2}; \quad \bar{t} = t \omega$$

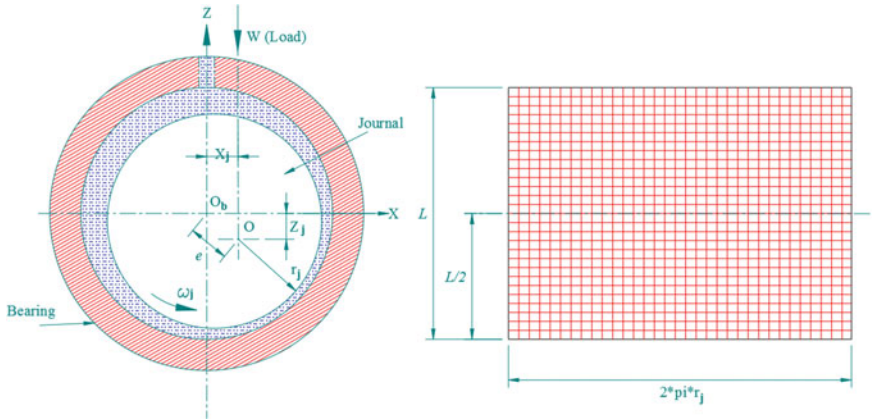


Fig. 1 Journal bearing system and unwrapped bearing flow domain

The film thickness expression for multi-lobe hydrodynamic journal bearings is as follows:

$$\bar{h} = \frac{1}{\delta} - (\bar{x}_j - \bar{x}_l^i) * \cos(\alpha) - (\bar{z}_j - \bar{z}_l^i) * \sin(\alpha) \tag{2}$$

where δ the offset factor and $[\bar{x}_j \bar{z}_j]$ are journal center and $[\bar{x}_l^i \bar{z}_l^i]$ are lobe center. The film thickness for circular journal bearing is obtained by substituting offset factor as one.

The solution of Eq. 1 is obtained by performing Finite Element (weak) formulation. The unwrapped bearing surface is divided into finite elements of 4-noded quadrilateral shape. The pressure is considered to be varying bi-linearly along within these elements.

$$\bar{p} = \sum_{j=1}^4 [N_j \bar{p}_j]; \quad N_j = \frac{1}{4} (1 + \xi_i \xi)(1 + \eta_i \eta) \tag{3}$$

Weighted residual method has been used to obtain weak form of Eq. 1. Galerkin approach is employed in which shape function of pressure is substituted as weights.

$$\iint_A \left(\frac{\partial}{\partial \bar{x}} \left(\bar{h}^3 \frac{\partial}{\partial \bar{x}} \left\{ \sum_{j=1}^4 (\bar{p}_j N_j) \right\} \right) + \frac{\partial}{\partial \bar{z}} \left(\bar{h}^3 \frac{\partial}{\partial \bar{z}} \left\{ \sum_{j=1}^4 (\bar{p}_j N_j) \right\} \right) - \Omega \frac{\partial \bar{h}}{\partial \bar{x}} - \frac{\partial \bar{h}}{\partial \bar{t}} \right) d\bar{x} d\bar{z} = 0 \tag{4}$$

Simplifying above Eq. 4 produces a set of linear algebraic equations, these equations are assembled to represent global flow equation in matrix-form.

$$[F]\{\bar{p}\} = [Q] + \Omega[H] + \bar{x}_j[\bar{S}_j] + \bar{z}_j[\bar{S}_j] \quad (5)$$

Starting from left, the terms in above equation represent fluidity, pressure, flow term, hydrodynamic and squeeze matrix, along x and z direction, respectively.

Following Boundary condition [23] is used to get the solution of Eq. 5.

- (a) At axial boundary: $z = \pm L/2$; $p = p_a$
- (b) At lubricant supply location: $x = 0$; $2\pi r_j$; $\bar{p} = p_a$
- (c) Lubricant film rupture: $x = x_c$; $\bar{p} = 0$; $\frac{\partial \bar{p}}{\partial x} = 0$.

The steady-state ($\bar{x}_j = \bar{z}_j = 0$) solution of Eq. 5 (0) yields pressure distribution over the bearing surface area. Integrating these values of film pressure values on bearing surface area provide film reaction force.

$$\text{Film reaction : } \bar{F} = [(\bar{F}_x)^2 + (\bar{F}_z)^2]^{1/2}; \quad (6)$$

$$\bar{F}_x = \int_{-1}^1 \int_0^{2\pi} \bar{p} \cos \alpha d\bar{x}d\bar{z}; \quad \bar{F}_z = \int_{-1}^1 \int_0^{2\pi} \bar{p} \sin \alpha d\bar{x}d\bar{z};$$

$$\text{Frictional Torque : } \bar{T}_f = \int_{-1}^1 \int_0^{2\pi} \left(\frac{\bar{h}}{2} \frac{\partial \bar{p}}{\partial \bar{x}} + \frac{\Omega}{\bar{h}} \right) d\bar{x}d\bar{z} \quad (7)$$

Newton Raphson method has been employed to compute obtain dynamic ($\bar{x}_j \neq 0$; $\bar{z}_j \neq 0$) performance parameters of bearing system. The direct and crossed-couple film stiffness and damping coefficient of bearing are numerically computed as follows:

$$\bar{k}_{ij} = -\frac{\partial \bar{F}_i}{\partial \bar{x}_j} \Rightarrow \bar{K} = -\begin{bmatrix} \bar{k}_{11} & \bar{k}_{12} \\ \bar{k}_{21} & \bar{k}_{22} \end{bmatrix} = -\begin{bmatrix} \frac{\partial \bar{F}_x}{\partial \bar{x}} & \frac{\partial \bar{F}_x}{\partial \bar{z}} \\ \frac{\partial \bar{F}_z}{\partial \bar{x}} & \frac{\partial \bar{F}_z}{\partial \bar{z}} \end{bmatrix} \quad (8)$$

$$D_{ij} = \frac{\partial \bar{F}_i}{\partial \dot{\bar{x}}_j} \Rightarrow \bar{D} = \begin{bmatrix} \bar{D}_{11} & \bar{D}_{12} \\ \bar{D}_{21} & \bar{D}_{22} \end{bmatrix} = \begin{bmatrix} \frac{\partial \bar{F}_x}{\partial \dot{\bar{x}}} & \frac{\partial \bar{F}_x}{\partial \dot{\bar{z}}} \\ \frac{\partial \bar{F}_z}{\partial \dot{\bar{x}}} & \frac{\partial \bar{F}_z}{\partial \dot{\bar{z}}} \end{bmatrix} \quad (9)$$

The abovementioned rotor-dynamic coefficients of bearing system are used to obtain the threshold speed (ω_t) margin of circular and multi-lobe journal bearings.

$$\omega_t = \left[\frac{\bar{m}_c}{\bar{F}} \right]^{1/2} \quad (10)$$

where \bar{m}_c is critical mass of journal. It has been computed using the film direct and crossed-couple stiffness and damping coefficients.

3 Solution Procedure

The analysis presented in Sect. 2 is employed to develop a source code which has been used to simulate circular and multi-lobe hydrodynamic journal bearings. As a direct solution of Reynold’s equation (Eq. 1) is a cumbersome process, hence Finite Element (FE) method had been employed to solve partial differential equations. The bearing input parameters are presented in Table 1. The bearing surface area is discretized regions using 2D (4-node) quad elements. The fluid pressure has been computed using Newton Raphson’s method.

An optimum mesh of 50 * 20 nodes along circumferential and axial direction is used to generate mesh independent numerical results. An optimum value of mesh is obtained when percentage difference between minimum film thicknesses falls below 1% on the continuous refinement of mesh size. Solution scheme/algorithm used in this work is depicted in Fig. 2. The numerical scheme has been converged on the basis of eccentricity in the bearing. A convergence (Eq. 11) of 10^{-05} is pre-defined on eccentricity to ensure reasonable accuracy of numerical results. Once the convergence criteria are satisfied, pressure and associated performance (indices as mentioned in previous section) has been computed.

Table 1 Bearing geometric and operating condition

Input parameters	Dimensional value	Input parameters	Dimensional value
Shaft radius (r_j)	50 mm	Radial clearance	0.05 mm
Axial length of bearing (L)	100 mm	Supply pressure	0.101325 MPa
Operating speed (N)	500 RPM	Lubricant viscosity	0.0345 Pa.s
External load (W)	6.77–9.94 kN	Lubricant density	860 kg/m ³

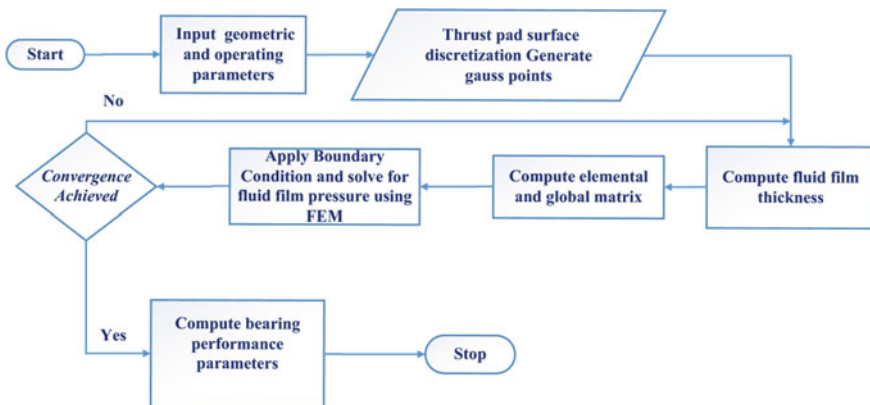


Fig. 2 Solution scheme

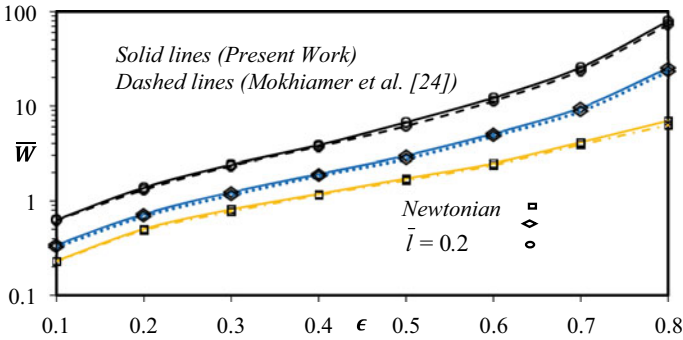


Fig. 3 Load carrying capacity vs. eccentricity ratio [24]

$$\left| \frac{\left[(\Delta \bar{x}_j^i)^2 + (\Delta \bar{z}_j^i)^2 \right]^{1/2}}{\left[(\bar{x}_j^i)^2 + (\bar{z}_j^i)^2 \right]^{1/2}} \right| \leq 10^{-05} \tag{11}$$

Figure 3 presents validation of proposed mathematical model (numerical solution scheme) with available published [24] results for hydrodynamic journal bearings. The developed MATLAB code is used to regenerate the numerical result of Mokhiamer et al. [24]. Figure 3 shows influence of eccentricity ratio on the load supporting capacity of hydrodynamic journal bearings. It could be clearly seen that result from two schemes closely follows one another. This proves the adequacy of developed source code to numerically simulate hydrodynamic journal bearing with good accuracy.

4 Results and Discussion

This section discusses in detail the simulation results of hydrodynamic circular and multi-lobe journal bearings. The influence of external load and number of lobes is investigated on performance of the journal bearing system. Performance of four different bearing configurations, namely circular, two-lobe, three-lobes and four-lobe, is compared in this section. The performance of bearing is evaluated and compared for film pressure, min. film thickness, rotor-dynamic coefficient, etc.

Figure 4 illustrates influence of number of lobes on fluid film pressure distribution for bearing operating under varying external load. There is considerable deviation in fluid film distribution with respect to an increase in external load imposed on bearing system. As the external load increase so does the peak film pressure in the bearing system. This peak film pressure is maximum for circular bearing configuration as compared to the multi-lobe bearings. Among multi-lobe bearings, the peak increases as lobes in the bearings increase from 2 to 4.

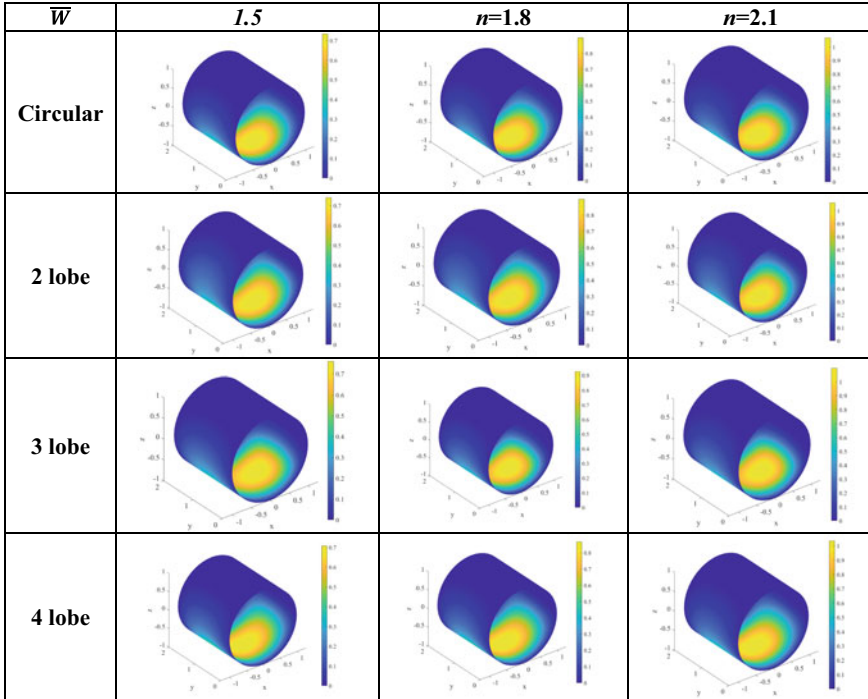


Fig. 4 Pressure distribution in circular and multi-lobe journal bearings as a function of external load

The influence of number of lobes and external load on minimum film thickness is illustrated in Fig. 5. A monotonous reduction in min. film thickness is noticed with an enhancement in external load acting on journal bearing system. The min. film thickness is seen minimum for circular journal bearing as to multi-lobe bearings. Two-lobe bearings are noticed to offer maximum value of min. film thickness as compared to the three-lobe and four-lobe bearing system. The higher value of min. film thickness reduces the chances of metal to metal contact between bearing and journal surfaces during transient operation of bearing. Use of two-lobe bearings as compared to the circular bearings enhances the min. film thickness by 6.2%. This effect is noticed to be increasing with a continuous increase in load imposed on bearing system.

Figure 6 depicts the effect of external load and lobe geometry of journal bearing on frictional torque. It has been found that with an increase the external load, the frictional torque of system increases gradually. Also, the use of multi-lobe bearing as compared to the circular bearing enhances frictional torque in system. Then enhancement in frictional torque is noticed to be marginal in three-lobe (2.15%) and four-lobe (2.93%) journal bearings, whereas it is significant (16.22%) in case of two-lobe journal bearings. The enhancement frictional torque owing to use of multi-lobe drops significantly with an increase in the external loads acting on bearing system.

Fig. 5 Min. film thickness versus Load

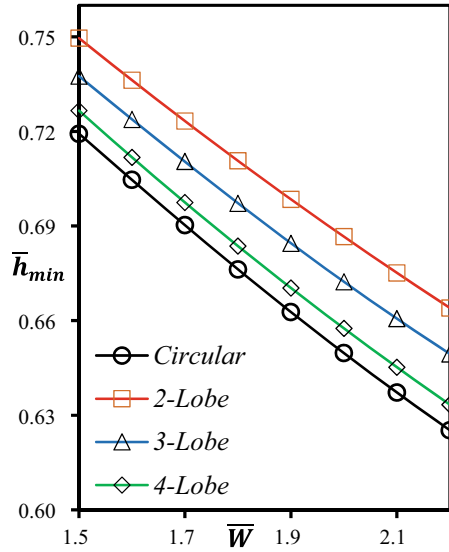
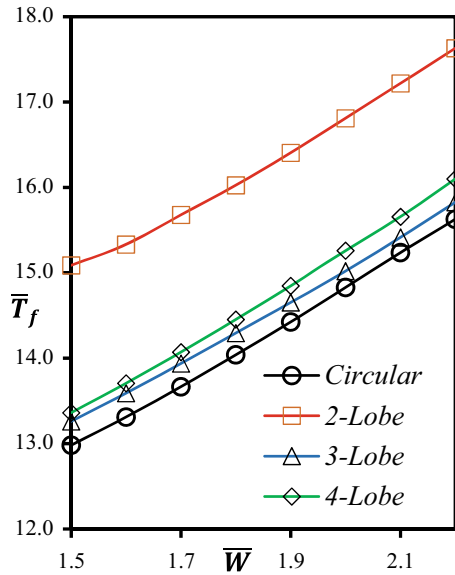


Fig. 6 Frictional torque (\bar{T}_f) versus Load



The numerical results for direct film stiffness coefficient (\bar{S}_{xx} and \bar{S}_{zz}) are illustrated in Figs. 7 and 8. It could be clearly seen an enhancement in external load, leads to a decrease in stiffness coefficient \bar{K}_{xx} of all journal bearing configuration. Over wider range of external load, 3 lobe and 4-lobe journal bearing provide minimum

Fig. 7 Stiffness coefficient (\bar{S}_{xx}) versus Load

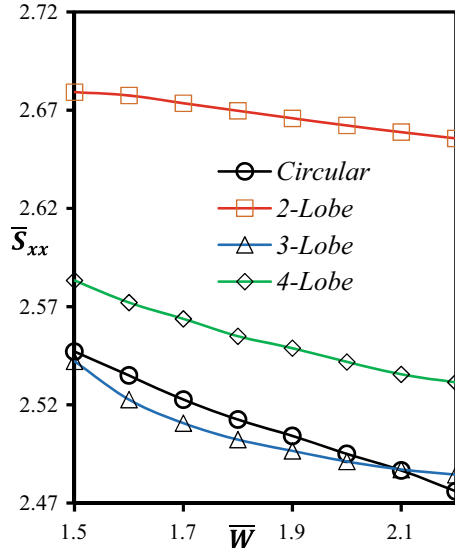
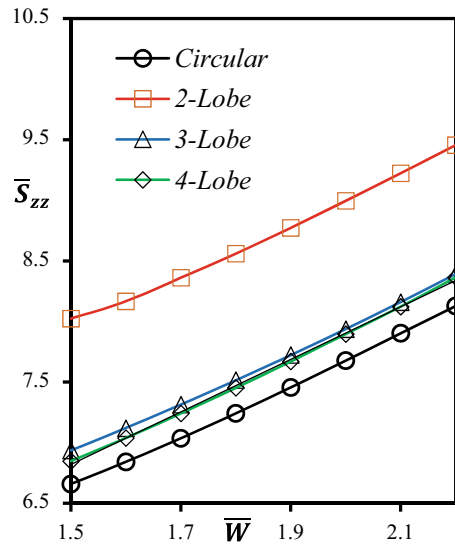


Fig. 8 Stiffness coefficient (\bar{S}_{zz}) versus Load



and maximum stiffness coefficient (\bar{S}_{xx}), respectively. Conversely, the direct stiffness coefficient (\bar{S}_{zz}) is seen to be increasing with respect to an increment in the load. The stiffness coefficient (\bar{S}_{zz}) is noticed to be maximum and minimum for two-lobe and circular journal bearing. The two-lobe bearings are noticed as an optimum lobe configuration which provides a 7.26% and 16.34% enhancement in \bar{S}_{xx} and \bar{S}_{zz} , respectively.

Figures 9 and 10 present effect of journal lobe configurations on the direct damping coefficient (\bar{C}_{xx} and \bar{C}_{zz}) of the bearing system under a wide range of external load. It can be noticed that increase in external load tends to enhance the damping coefficients of both circular and multi-lobe journal bearings. Three-lobe journal geometry is

Fig. 9 Damping coefficient (\bar{D}_{xx}) versus Load

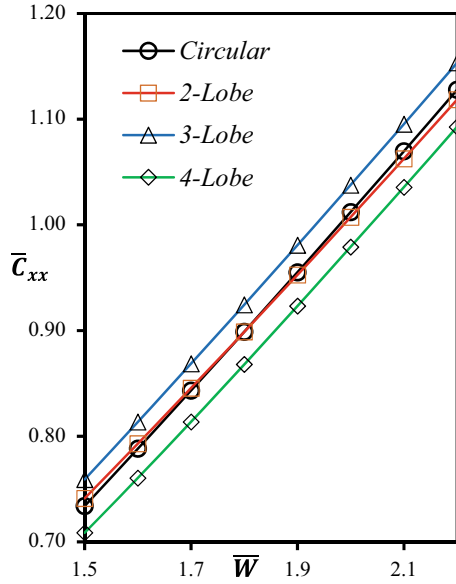
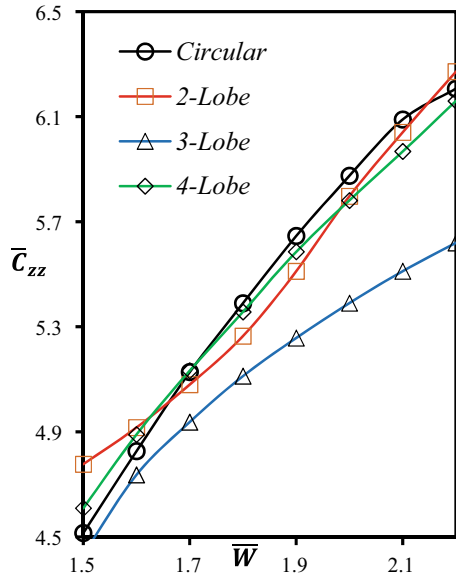


Fig. 10 Damping coefficient (\bar{D}_{zz}) versus Load



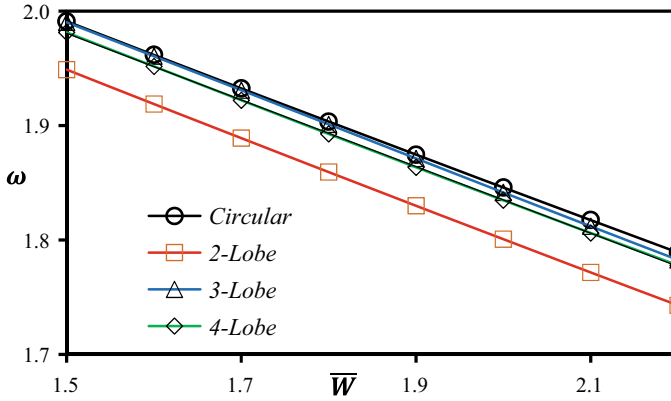


Fig. 11 Threshold speed margin (ω_t) versus Load

noticed to be beneficial in enhancing (3.43%) the (\bar{C}_{xx}) direct damping coefficient. No clear trends for \bar{C}_{zz} have been noticed w.r.t lobe geometry. However, circular journal bearing should be preferred for enhancing \bar{C}_{zz} over wide range of external loads.

Figure 11 presents trends for threshold speed of bearing with respect to load acting on the journal bearing. Threshold speed is dependent on direct and cross-coupled film stiffness and damping coefficients. It can be observed here that threshold speed margin of circular as well as multi-lobe bearings decreases linearly with a continuous enhancement in the external load. Further, it noticed that circular bearing vis-à-vis multi-lobe journal bearings offer maximum threshold speed margin. The maximum reduction ($- 2.65\%$) in ω_t has been noticed while use of 2-lobe journal bearings.

5 Conclusions

The results for numerical simulation of circular and multi-lobe journal bearing can be summarized as follows:

- The use of multi-lobe journal bearing is advantageous for enhancing the minimum film thickness. Among multi-lobe bearings, two-lobe bearing geometry should be preferred as it provides maximum enhancement (6.2%) in minimum film thickness.
- The film frictional torque enhanced significantly reduces (12.82%) owing to the use two-lobe journal bearing. Three-lobe and four-lobe journal bearing as compared to journal circular bearing marginally increases (1–3%) the frictional torque.

- Using multi-lobe bearing improves the direct stiffness coefficients of the bearings. Contrary to this, multi-lobe bearing geometry has adverse effect the direct damping coefficient of the bearing system.
- An increase in external load is noticed to have a marginal adverse effect on threshold speed margin of circular bearing and multi-lobe bearings. Also, use of multi-lobe (vis-à-vis circular journal bearings) marginally reduce (– 2.65% max.) the threshold speed margin.

References

1. Khonsari MM, Booser ER (2017) Applied tribology: bearing design and lubrication. Wiley, West Sussex
2. Bhushan B (2013) Introduction to tribology. Wiley, New York
3. Tower B (1883) First report on friction experiments. Proc Inst Mech Eng 34(1):632–659
4. Nair KP, Sinhasan R, Singh DV (1987) Elastohydrodynamic effects in elliptical bearings. Wear 118(2):129–145
5. Mehta NP, Singh A (1986) Stability analysis of finite offset-halves pressure dam bearing. J Tribol 108(2):270–274
6. Bing W, Chun-ge ZANG, Yu-hao SUN (2014) Experimental test of dynamic characteristics of tilting pad thrust bearing. Lubr Eng 39(4):55–60
7. Rahmatabadi AD, Rashidi MR, Nekoeimehr M (1987) Preload effects on the static performance of multi-lobe fixed profile journal bearings with micropolar fluids. Proc Inst Mech Eng Part J J Eng Tribol 225(8):718–730
8. Etsion I (2005) State of the art in laser surface texturing. J Tribol 127(1):248–253
9. Gropper D, Wang L, Harvey TJ (2016) Hydrodynamic lubrication of textured surfaces: a review of modeling techniques and key findings. Tribol Int 94:509–529
10. Tala-Ighil N, Fillon M, Maspeyrot P (2011) Effect of textured area on the performances of a hydrodynamic journal bearing. Tribol Int 44(3):211–219
11. Kumar V, Sharma SC (2020) Performance analysis of rough surface hybrid thrust bearing with elliptical dimples. Proc Inst Mech Eng Part J J Eng Tribol. <https://doi.org/10.1177/1350650120931981>
12. Cupillard S, Glavatskih S, Cervantes MJ (2008) Computational fluid dynamics analysis of a journal bearing with surface texturing. Proc Inst Mech Eng Part J J Eng Tribol 222(2):97–107
13. Kumar V, Sharma SC, Narwat K (2019) Influence of micro-groove attributes on frictional power loss and load-carrying capacity of hybrid thrust bearing. Ind Lubric Tribol 72(5):589–598
14. Spikes HA (1994) The behavior of lubricants in contacts: current understanding and future possibilities. Proc Inst Mech Eng Part J J Eng Tribol 28:3–15
15. Scott W, Suntiawattana P (1995) Effect of oil additives on the performance of a wet friction clutch material. Wear 181:850–855
16. Wada S, Hayashi H (1971) Hydrodynamic lubrication of journal bearings by pseudoplastic lubricants (part II, experimental studies). Bull JSME 14(69):279–286
17. Oliver DR (1988) Load enhancement effects due to polymer thickening in a short model journal bearing. J Nonnewton Fluid Mech 30:185–196
18. Khonsari MM, Brew DE (1989) On the performance of finite journal bearings lubricated with micropolar fluids. Tribol Trans 32(2):155–160
19. Kango S, Sharma RK (2010) Studies on the influence of surface texture on the performance of hydrodynamic journal bearing using power law model. Int J Surf Sci Eng 4(4–6):505–524
20. Lin JR (1997) Effects of couple stresses on the lubrication of finite journal bearings. Wear 206(1–2):171–178

21. Kumar V, Sharma SC (2018) Dynamic characteristics of compensated hydrostatic thrust pad bearing subjected to external transverse magnetic field. *Acta Mech* 229(3):1251–1274
22. Kumar V, Sharma SC (2017) Study of annular recess hydrostatic tilted thrust pad bearing under the influence of couple stress lubricant behaviour. *Int J Surf Sci Eng* 11(4):344–369
23. Kumar V, Sharma SC (2017) Combined influence of couple stress lubricant, recess geometry and method of compensation on the performance of hydrostatic circular thrust pad bearing. *Proc Inst Mech Eng Part J J Eng Tribol* 231(6):716–733
24. Mokhiamer U, Crosby W, El-Gamal H (1999) A study of a journal bearing lubricated by fluids with couple stress considering the elasticity of the liner. *Wear* 224(2):194–201

Performance Assessment of Parabolic Trough Collectors with Variable Mass Flow Rates



Anshul Tewari  and R. S. Mishra

Abstract This work deals with the assessment of a solar parabolic trough collector with variations in the mass flow rate of heat transfer fluid. A mathematical model based on engineering equation solver (EES) software was developed for carrying out this analysis. The values of flow rates considered for this study are 0.06, 0.08 and 0.10 kg/s. It is seen that flow rate of 0.10 kg/s provides the maximum collection efficiency of 58.47% at noon, and the values of efficiency decrease with a decrease in flow rate. Also, the maximum value of rate of useful heat gain is 1111 W for flow rate of 0.10 kg/s and decreases with decrease in flow rate. But, the highest fluid exit temperature is achieved for minimum flow rate of 0.06 kg/s.

Keywords Parabolic trough solar collector · Heat transfer fluid · Variable mass flow rate · Collection efficiency · Fluid exit temperature

1 Introduction

Solar concentrating collectors, unlike flat plate collectors, concentrate the solar radiation falling over it and thus producing high temperatures which cannot be achieved using a flat plate collector. It is a type of line-focusing solar collector that concentrates the incoming solar radiation over an absorber tube carrying heat transfer fluid. The high concentration ratios achievable in a PTC result in heat energy generation at the absorber tube. This heat energy may be used for power generation, refrigeration and process heating.

A. Tewari (✉) · R. S. Mishra
Delhi Technological University, New Delhi, India

© The Author(s), under exclusive license to Springer Nature Singapore Pte Ltd. 2022
K. Govindan et al. (eds.), *Advances in Mechanical and Materials Technology*,
Lecture Notes in Mechanical Engineering,
https://doi.org/10.1007/978-981-16-2794-1_20

225

1.1 Literature Review

Various previous research articles were analyzed during the course of this study. Murtuza et al. [1] analyzed the performance of a 5 m parabolic trough solar collector model. Year-round performance analysis was carried out, and it was inferred that the months of March, April and May resulted increased temperatures of outlet from 93 to 103 °C. This study also incorporated variations in mass flow rate, and it was simulated using ANSYS software. Maximum displacement, Von Mises stress and thermal strain were the parameters considered while designing the receiver tube, and the results were satisfactory. In another article, Behar et al. [2] proposed a new model for PTSC which was validated using the studies carried out at the laboratories of high eminence like SNL and NREL. The experiments conducted by SNL validate this model, especially for cermet-coated receivers. This model claims to have an uncertainty of 0.64% while predicting the thermal efficiency as compared with the 1.1% uncertainty of the NREL's engineering equation solver code for cermet coatings. However, this model suffered slide in accuracies while evaluating the heat losses at high temperatures. In different study, Jebasingh and Herbert [3] focused on performance of parabolic trough solar collector in the applications of refrigeration, process heating, desalination, air heating and power production. It concluded that the efficiency of PTC can be enhanced by working on materials of absorber tube its coating and efficient working fluids. It considered the thermal energy storage system as revolutionary for future energy crisis. In another research, Yilmaz et al. [4] showed that using inserts of wire coil in the observer tube enhances the performance of parabolic trough collectors by decreasing the associated temperature gradients and thereby reducing the irreversibilities in heat transfer. A parabolic trough collector with rim angle 80° and 9 m width was modeled. Profile of heat flux on the absorber was attained by employing Monte Carlo ray tracing which was later hinged with a CFD model. The inserts for triangular in cross section with 7.6 mm size. The increase in thermal efficiency ranges from 0.4 to 1.4% for various input parameters. It concluded that the effect of temperature gradient is significant at lower flow rates, and this is where the inserts are of higher importance.

1.2 Setup Description

The setup used for the development of this mathematical model comprises of a parabolic trough solar collector with continuous adjustment to minimize the incidence angle between the solar radiation and the plane of aperture. The concentrator of the parabolic trough has its focal axis horizontal and in the east-west direction. Figure 1 shows a cross-sectional view of the concentrator, absorber tube and the glass cover with their respective nomenclature of dimensions. The concentrator is incorporated with the aim to focus or concentrate the incident solar radiation to the absorber tube, where the heat transfer fluid flows. The absorber tube is hollow with respective

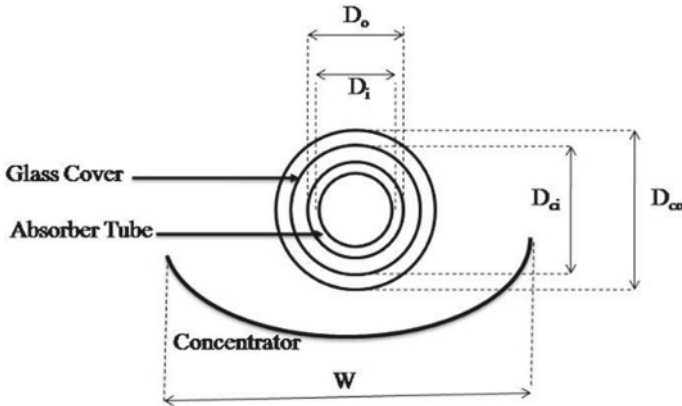


Fig. 1 Cross section of solar PTC with nomenclature

inside and outside diameters, and a twisted tape is also incorporated in the absorber to further increase the performance. It has a glass cover that fully surrounds it and prevents unnecessary heat loss due to high temperature. This glass cover too has its inside and outside diameters specified. The spacing between the outside diameter of the absorber tube and the inside diameter of the glass cover is filled with atmospheric

Table 1 Characteristics of the system

Parameters	Value
Location (New Delhi)	28° 35'N, 77° 12'E
Aperture of concentrator (W)	1.25 m
Length of concentrator (L)	3.657 m
Inner diameter of absorber tube (D_i)	0.0381 m
Outer diameter of absorber tube (D_o)	0.04135 m
Inner diameter of glass cover (D_{ci})	0.0560 m
Outer diameter of glass cover (D_{co})	0.0630 m
Tape twist ratio (x)	4
Reflectivity of concentrator (ρ)	0.85
Transmissivity of glass cover (τ)	0.85
Intercept factor (γ)	0.95
Emissivity/absorptivity of glass cover (ϵ_c)	0.88
Emissivity/absorptivity of absorber tube (ϵ_p)	0.95
Fluid inlet temperature (T_{fi})	50 °C/323.15 K
Concentration ratio (C)	9.304
Ambient pressure (P_{atm})	101.325 kPa

Table 2 Validation of the current model with results in [5]

Parameters	Models	Reference [5]
Useful heat gain (W)	1299	1289.8
Mean plate temperature (K)	441.3	441.13
Cover temperature (K)	334	333.39
Overall loss coefficient (W/m ² K)	13.13	13.27
Exit fluid temperature (K)	428.5	428.4
Instantaneous (%)	39.73	39.5

air. Table 1 shows the various characteristics of the system that is used as inputs to the mathematical model for this study.

1.3 Mathematical Modeling

The mathematical model developed to carry out this current analysis is outlined in this section. Engineering equation solver (EES) software was employed to program this model. The mathematical equations are derived from the thermal analysis of a PTC presented in [5]. The current model is validated by the results stated in [5], and also the variation trends follow those presented in [5]. Table 2 compares the results obtained with the current model and those presented in [5].

This model makes the following assumptions: The first one considers the complete system under steady state of heat transfer, and the second assumption is that the heat transfer fluid remains at atmospheric pressure at all times, neglecting the pressure variation inside the absorber tube, if any. Moreover, the effect of shading and dust deposition on the performance of the system is assumed negligible, and also, the properties of the construction material and heat transfer fluid are assumed constant.

The flux absorbed in absorber tube (S) is given as:

$$S = I_b r_b \rho \gamma (\tau\alpha)_b + I_b r_b (\tau\alpha)_b \left(\frac{D_o}{W - D_o} \right) \tag{1}$$

where I_b is the beam radiation, r_b being the tilt factor of concentrator, ρ is the reflectivity of the surface of the concentrator, γ is the intercept factor, $(\tau\alpha)_b$ is product of transmissivity and absorptivity for beam radiation, W is width or aperture of collector, and D_o is the outer diameter of absorber tube.

Now, the useful heat gain rate (Q_u) may be defined as:

$$Q_u = F_r (W - D_o) L [S - (T_f - T_a)] \tag{2}$$

Also

$$Q_u = \dot{m} C_p (T_{fo} - T_{fi}) \quad (3)$$

where F_r is the heat removal factor, L is the length of concentrator, U_1 is the overall loss coefficient, C is the concentration ratio, T_{fo} is the fluid exit temperature, T_{fi} is the fluid inlet temperature, and T_a is the ambient temperature. Heat removal factor is described as the ratio of heat gain rate actually to heat gain rate when the absorber tube is at temperature T_{fi} throughout. It is expressed in mathematical form as below

$$F_r = \frac{\dot{m} C_p}{\pi D_o L U_1} \left[1 - \exp \left\{ - \frac{F' \pi D_o U_1 L}{\dot{m} C_p} \right\} \right] \quad (4)$$

Here, F' denotes the efficiency factor of the collector, and it has similarities with the heat removal factor.

$$F' = \frac{1}{U_1 \left(\frac{1}{U_i} + \frac{D_o}{D_i h_f} \right)} \quad (5)$$

The coefficient of heat transfer of the thermic fluid is expressed as h_f and written as

$$h_f = \frac{Nu * K}{D_i} \quad (6)$$

Nusselt number calculations are conducted using empirical relations considering the characteristics of flow.

Concentration ratio (C) is ratio of effective area of aperture to the area of absorber tube and written as:

$$C = \frac{(W - D_o)}{\pi D_o} \quad (7)$$

U_1 being the overall loss coefficient is useful in defining the rate of heat loss as:

$$Q_1 = U_1 \pi D_o L (T_{pm} - T_a) \quad (8)$$

The instantaneous collection efficiency of the collector based on beam radiation alone is defined below:

$$\eta_i = \frac{Q_u}{I_b r_b W L} \quad (9)$$

2 Results and Discussion

The flow rate of heat transfer fluid (HTF) is varied, and the deviations in the performance of the collector are recorded. The results are studied in the form of a curve. The values of flow rate are 0.06, 0.08 and 0.10 kg/s. The results follow the trend stated in [5] for various parameters.

It is expressed in Fig. 2 that the temperature of receiver or absorber tube (T_{pm}) is maximum when the flow rate is least. The largest value of T_{pm} derived from this work is 344.3 K for flow rate 0.06 kg/s, at noon. This value is lowest at mornings and then increases to become largest at noon and further decreases from noon to evening. At noon, the lowest value of T_{pm} is derived for 0.10 kg/s flow rate, i.e., 338.5 K. A difference of 5.8 °C is expressed in T_{pm} for maximum and minimum flow rate at noon. Also, the value of T_{pm} is lowest in the morning for the whole day. The lowest value being 324.3 K for highest flow rate 0.10 kg/s. This nature of T_{pm} owes to increase in solar radiation during noon as more concentrated radiation results in temperature increase of absorber. Also, with the increase in flow rate, the heat capacity of the HTF also increases thereby requiring more heat to increase its temperature.

As can be derived from the aforementioned discussion, more temperature results higher losses. This statement is in compliance with the results expressed in Fig. 3. It is seen that the value of overall loss coefficient (U_l) is largest for the lowest flow

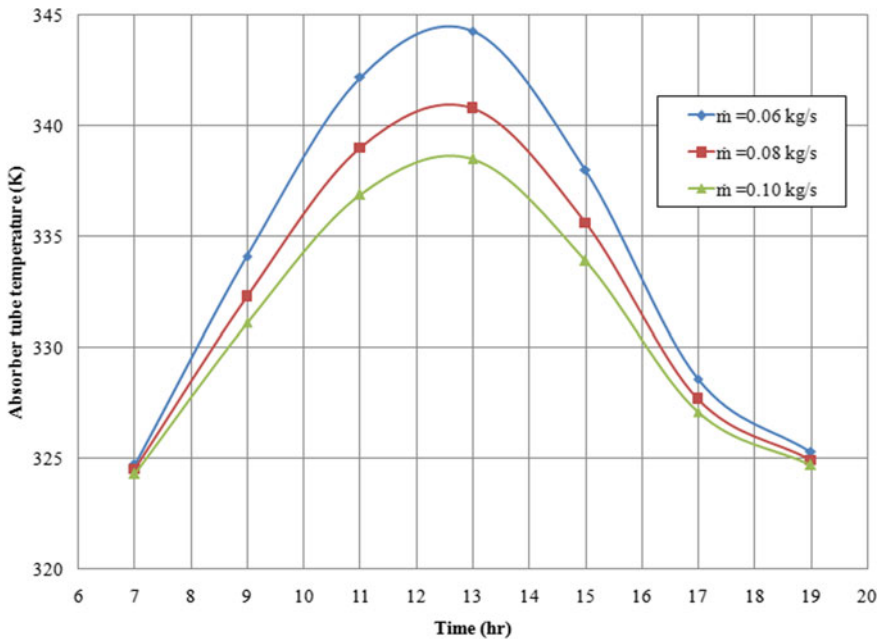


Fig. 2 Absorber tube temperature change over time for variable flow rate

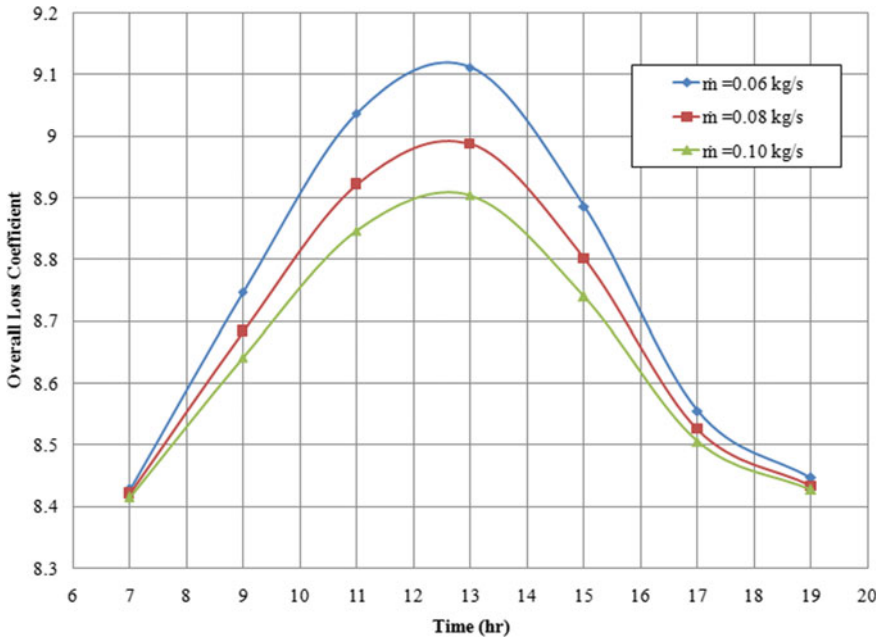


Fig. 3 Overall loss coefficient change over time for variable flow rate

rate of 0.06 kg/s for which T_{pm} is maximum. The highest losses are for lowest flow rate as T_{pm} is largest for this flow rate, whereas the loss coefficient is lowest when the flow rate is highest. Also, the heat removal factor for collector (F_r) is directly related to the flow rate; hence, this value is lowest for the least flow rate and goes on increasing by increasing the flow rate. Figure 4 shows that the value of F_r is lowest at noon and is higher both in the morning and evening.

The rate of useful heat gain (Q_u) is also related to the values of F_r and U_1 . For the lowest flow rate, the least value of F_r and the highest value of U_1 correspond to the lowest value of Q_u . As seen in Fig. 5, Q_u is lowest for the lowest flow rate, and it increases when flow rate is increased. 1111 W is the highest Q_u for highest flow rate at noon, and 81.94 W is the lowest for least flow rate in the morning.

Figure 6 shows the deviations in exit temperature of heat transfer fluid (HTF) by changing the flow rates. Though exit temperature is directly related to Q_u but its nature is opposite to Q_u because the increase in flow rate is much higher than the increase in Q_u by changing the flow rate. At noon, the percentage increase in Q_u for change in flow rate is 2.68%, whereas the same for flow rate is 66.67%. This higher increase in flow rate than Q_u is responsible for a decreased value in exit temperature for higher flow rate. With the increase in flow rate, the heat capacity of HTF increases; hence, it needs much higher heat to increase the exit temperature for higher flow rate. The highest value of exit temperature is 330.5 K for least flow rate.

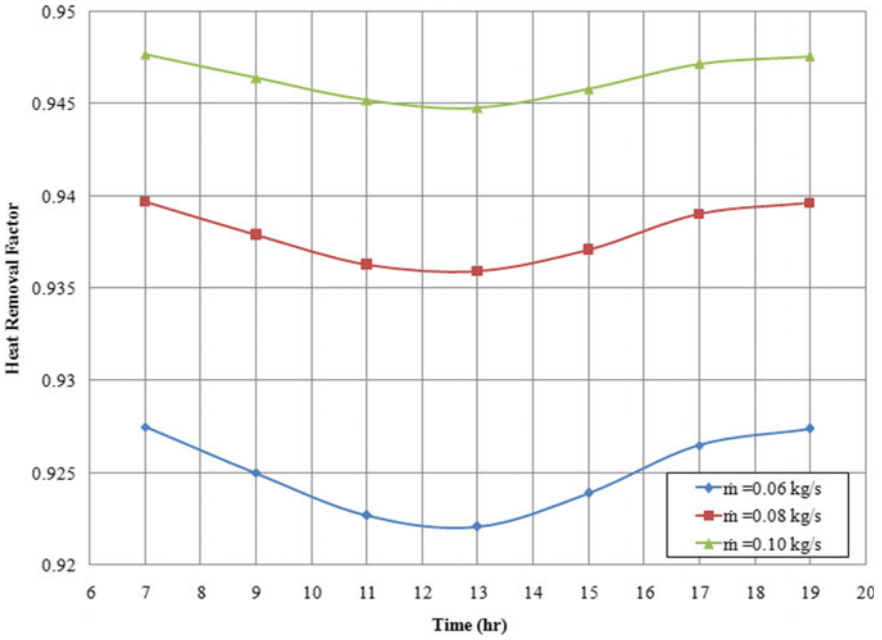


Fig. 4 Heat removal factor change over time for variable flow rate

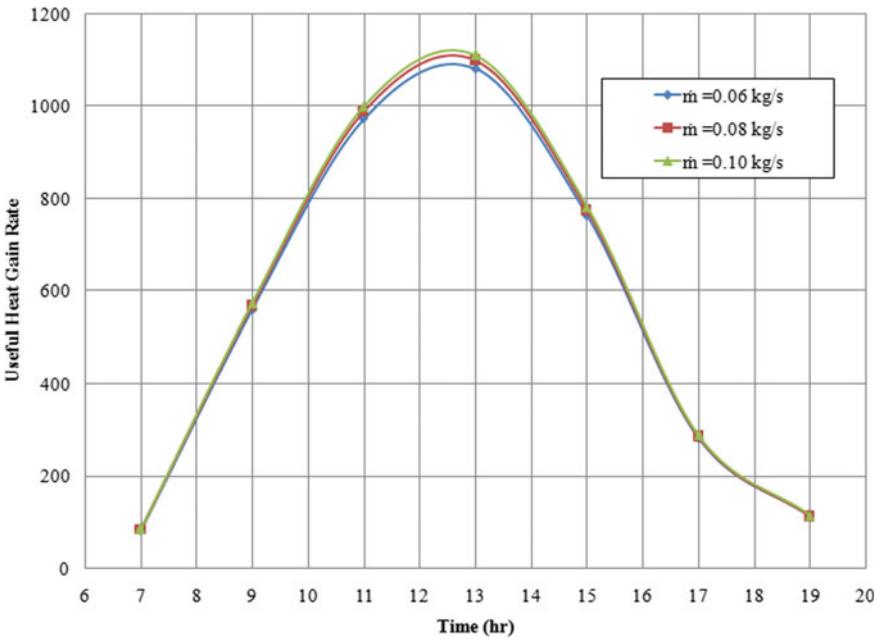


Fig. 5 Useful heat gain rate change over time for variable flow rate

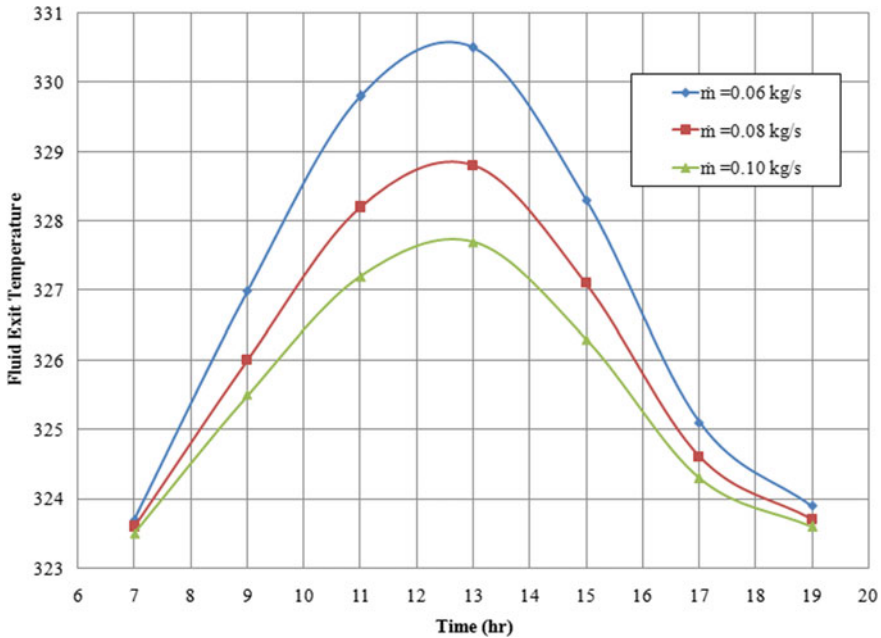


Fig. 6 Fluid exit temperature change over time for variable flow rate

At noon, the increase in exit temperature is 2.8 °C between highest and lowest flow rates.

Figure 7 is the deviation in instantaneous efficiency of collection with time for change in flow rate. The largest efficiency is 58.47% for highest flow rate at noon. It is expressed that the deviation in efficiency is larger for higher flow rate, and its value decreases for decrease in flow rate. This nature shows that although the conversion of solar radiation into heat and thereby into fluid exit temperature is higher for lower flow rate, but this conversion is not done efficiently in lower flow rates. The conversion of available solar radiation into useful heat is achieved with higher efficiency for larger flow rates. In other words, larger degradation of solar energy is done at lower flow rate of HTF. At noon, the difference in collection efficiency is 1.49% between the highest and least flow rate.

3 Conclusions

The performance of a PTC with variable flow rate is assessed using this mathematical model for steady-state situation. The results expressed through this study are examined to make the following conclusions:

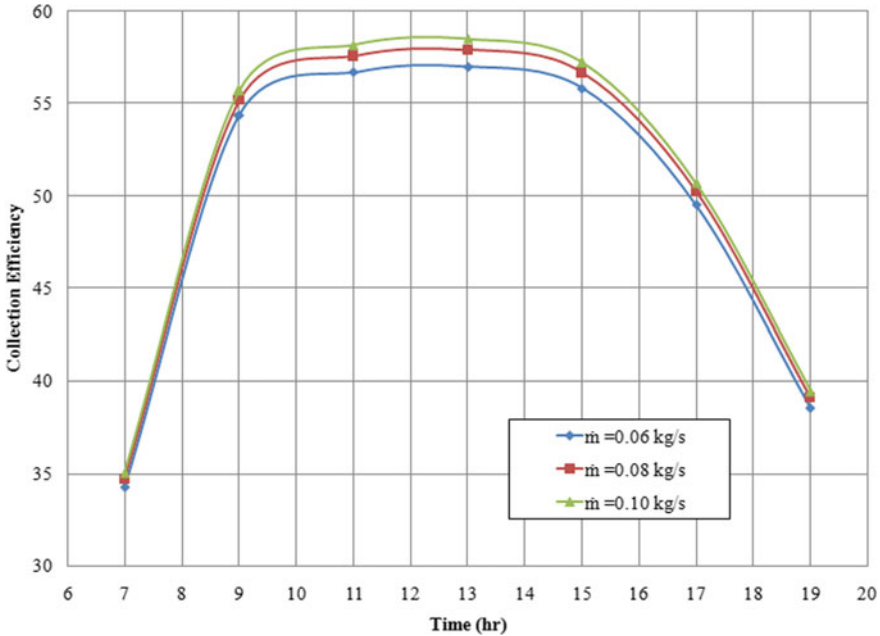


Fig. 7 Instantaneous collection efficiency change over time for variable flow rate

- The largest value of temperature of absorber tube expressed in this study is 344.3 K for least flow rate 0.06 kg/s. This value is largest at noon and minimum in the mornings. The magnitude of absorber temperature is reduced when the flow rate is increased. At noon, this difference in temperature is 5.8 °C.
- Due to higher absorber temperature, the convection, radiation and re-radiation losses are also higher. Therefore, the magnitude of loss coefficient is large for least flow rate and decreases by increasing the flow rate.
- Rate of useful heat gain is highest for maximum flow rate, and its value decreases when flow rate is reduced. 1111 W is the maximum rate derived from this study for highest flow rate 0.10 kg/s. At low flow rate, lower value of heat removal factor and higher value of loss lead to lower heat gain.
- The exit temperature of heat transfer fluid is highest for least flow rate, and its value is decreased by increasing the flow rate. At noon, the difference in temperature between lowest and highest flow rate is 2.8 °C.
- The maximum collection efficiency derived from this work is 58.47% for highest flow rate 0.10 kg/s. This value decreases when flow rate is decreased. The difference in efficiency between highest and lowest flow rate is 1.49%.
- Therefore, it can be derived that the maximum temperature is achieved with lower flow rate but degradation of energy is more in case of lower flow rate as compared with higher flow rate.

References

1. Murtuza SA, Byregowda HV, Ali-H MM, Imram M (2017) Experimental and simulation studies of parabolic trough collector design for obtaining solar energy. *Resour Eff Technol* 3(4):414–421
2. Behar O, Khellaf A, Mohammedi K (2015) A novel parabolic trough solar collector model—validation with experimental data and comparison to engineering equation Solver (EES). *Energy Convers Manage* 106:268–281
3. Jebasingh VK, Herbert GMJ (2016) A review of solar parabolic trough collector. *Renew Sustain Energy Rev* 54:1085–1091
4. Yilmaz IH, Mwesigye A, Goksu TT (2020) Enhancing the overall thermal performance of a large aperture parabolic trough solar collector using wire coil inserts. *Sustain Energy Technol Assess* 39:100696
5. Sukhatme JP, Nayak JK (2014) *Solar energy: principles of thermal collection and storage*, 3rd edn. McGraw Hill Education, New Delhi

Influence of Nanoparticles in Different Types of Cutting Fluids: A Literature Review



Anurag Sharma, R. C. Singh, Ranganath M. Singari, and S. L. Bhandarkar

Abstract The cutting fluids provide lubrication and cooling at the interface of work-piece and cutting tool. Nanoparticles of metals, metal oxides, non-metals, non-metal oxides, ceramics, etc. have been found to increase the lubrication, cooling and sometimes both lubrication and cooling with hybrid combinations on comparing with the base conventional cutting fluid. The nanoparticles are used with straight oils, lubricating oils and mineral oils have reduced the friction between contacting surfaces. This paper is focused toward the effects of nanoparticles found by researchers with different types of cutting fluids.

Keywords Nanoparticles · Nano-cutting fluids · Machining · Cooling · Lubrication

1 Introduction

Machining condition is the localized environment created in the proximity of the cutting tool and workpiece. Besides, machinability parameters like (i) speed, (ii) feed and (iii) depth of cut machining condition may be considered for the analysis of tool wear and surface morphology of workpiece. The machining condition may be dry, conventional cutting fluids, minimum quantity lubrication, and cryogenic cooling [1].

A. Sharma (✉) · R. C. Singh · R. M. Singari
Department of Mechanical Engineering, Delhi Technological University, New Delhi, Delhi
110042, India

S. L. Bhandarkar
Board of Technical Education, Pitampura, Muni Maya Ram Marg, Pitampura, Delhi 110088, India

1.1 Dry Machining

In this machining condition, cutting tool and workpiece may work in dry condition like without the use of any coolant or lubrication. This may increase the temperature at the interface of cutting tool and workpiece and deteriorated tool and surface of the workpiece. In the case of steel as workpiece, the chips were long, staggered at both sides with material outflow to both of the sides. This process may be considered as eco-friendly and economical but the manufacturing rate was slow due to machining at low machinability parameters for the optimum tool wear and surface roughness. Researchers have proposed some harder tool material with a coating of TiN, diamond powder, etc. [1, 2].

1.2 Conventional Cutting Fluid

In this machining condition, a conventional cutting fluid used at the interface of tool and workpiece. This may include natural oils, straight oils, vegetable oil and emulsions may vary with oil (1–20%) approximately in the remaining water. The supply rate could be from 500 to 20,000 ml per h. Researchers have found that tool wear and surface roughness were (20–31%) lower as compared with dry machining. This may vary further depending upon the type of workpiece material. But, environmental and health issues like skin infections, itching, nausea, etc. may emerge during the handling and recycling of debris and chips. The chips contaminated with the ingredients of cutting fluid may be difficult in separating and economically cost elevating. The fumes generated with conventional cutting fluids and contact with hands may increase skin infections, itching in eyes, sometimes nausea, etc. [2].

1.3 Minimum Quantity Lubrication (MQL)

The oil in small quantity generally 100–500 ml/h used during machining at the interface of cutting tool and workpiece. One method was continuous drop-wise flow and another method was mixing oil and compressed air in equal proportionate. The mist generated was supplied at the interface of the cutting tool and workpiece. This method may be environmentally friendly depending upon the type of oil. Vegetable and biocompatible oils could make this method eco-friendly and operator's health may be solved. The chips or debris created may be found clean and free from impurities and further recycled with almost negligible cost [2, 3].

1.4 Nano-cutting Fluids

Nanoparticles are in the range of 1–100 nm. Researchers have tried to mix nanoparticles in oils for lubrication and cooling purpose. The selection of nanoparticles was based on the type of base fluid like some nanoparticles were found easily mixing with oil but the same may not be mixing with water. Nanoparticles may increase the thermal conductivity of the base fluid and lowered the tool wear and surface roughness of workpiece during machining. Eco-friendly nano-cutting fluids could be made by selecting biodegradable oil and nanoparticles like nanoparticle of MoS₂ in sunflower or olive oil. The surfactant if used should be biocompatible. Water-based nano-cutting fluid could be economical. This may be easily availability of water and further conversion into distilled water. The heat transfer coefficient of water was found to be more than oil. This may improve the heat carrying capacity and further improvement in machinability properties. Besides, increasing cooling capacity of base fluids lubrication property may be imparted. The fluid may provide cooling and lubricating effect. Nanoparticles in water-based fluid with oil (1–10%) may be known as water emulsion. The percentage of oil may vary with the type of oil and the amount of lubrication needed [3, 4].

2 Literature Review

The research work is tabulated into four columns. The first column depicts serial number; second column shows author, year, and reference number; third and fourth column show work done and result/findings, respectively.

2.1 Cutting Fluids/High Pressure Fluids for Metal Cutting

Cutting fluids are used in machining processes for providing coolant and lubrication. Generally, cutting fluids are supplied by the in housed pump fitted in machine.

The speed of supply of cutting supply is almost fixed. The cutting fluid moves in a closed cycle and comes back to the pump after filtration.

Table 1 depicts the workdone by researchers during use of cutting fluids and high pressure fluids.

2.2 Effects of Nanoparticles in Cutting Fluids

Nanoparticles are very fine particles of magnitude of 10⁻⁹ m. These particles change various parameters during machining applications.

Table 1 Details of research papers regarding cutting/high pressure fluids at interface of cutting tool and workpiece

S. No.	Author, year, reference no.	Accomplishment of work	Outcome
1	Naves et al. 2013 [4]	The experimentation was done on lathe machine using AISI 316 as workpiece and coated carbide cutting insert with supply of high pressure cutting fluid at different levels of concentration and pressure	It was found that tool wear and tool chip length were declined on comparing with other concentration of cutting fluid. The amount of wear was lowest at higher concentration of cutting fluid and pressure
2	Mosleh et al. 2017 [5]	The experiments were performed on four-ball tester for checking and analyzing the wear properties of balls under prepared fluid with MoS ₂ at different concentrations varied from 2–4% and 0.5–1% for diamond	It has been found that wear scar length was shorter in prepared fluid of MoS ₂ for all concentration as compared with diamond particles
3	Paul et al. 2016 [6]	The experimentation was performed in different localized created environment like without any coolant (dry), wet and (MQL)	It was found the wear in tool declined and surface finish incremented during (MQL) minimum quantity lubrication as compared with dry and wet
4	Shokrani et al. 2012 [7]	The processes involved in machining of hard materials with different types of cooling techniques used by researchers have been discussed	It has been found that cooling technique was dependent on type of quality of machining, machining parameters and ease in availability
5	Jayal et al. 2009 [8]	The experiments were performed in different machining conditions. The nozzle was kept at overhead position of cutting chip during machining	The results showed that tool life was lower in dry condition as compared with other machining conditions
6	Verochaka et al. 2014 [9]	Investigated the effect of Filtered cathodic vacuum arc deposition (FCV AD) coatings on carbide inserts. Cutting parameters were selected in accordance with industrial applications	The results showed the cutting tool life of inserts in more than two times as compared to conventional coated carbide inserts

(continued)

Table 1 (continued)

S. No.	Author, year, reference no.	Accomplishment of work	Outcome
7	Bork et al. 2014 [10]	The experiments were performed by using new product jatropa vegetable base soluble cutting oil in relation to the canola oil (vegetable), synthetic (jatropa ester) and semi-synthetic (mineral) traditionally used in machining aluminum alloy	Jatropa cutting oil presented best result in relation to lubrication mean roughness index, life span of cutting tool increased by 30% as comparative to other oils
8	Sokovic et al. 2001 [11]	The properties of available cutting fluid were discussed and a newly cutting fluid was developed	It has been found that better results of machining characteristics with newly developed cutting fluid
9	Hermoso et al. 2014 [12]	The influence of additives on viscosity and different concentrations were analyzed for change in rheological properties at for oil base drilling fluids	It was found that organoclay and concentration highly effect the viscous flow of oil
10	Khan et al. 2009 [13]	The experimentation of turning was performed on under dry, wet and (MQL) for AISI 9310 as workpiece	It has been found that minimum quantity lubrication gave lower machining properties like tool wear, surface roughness, cutting temperature on comparing with other created localized environmental conditions with eco-friendly behavior
11	Lv et al. 2016[14]	The influence of oil mixed with LN ₂ in a mixing chamber and directly supplied at the contacting position of cutting tool and workpiece was compared with traditional cutting fluid for milling operation	It has been found that cooling strategy with LN ₂ gave lower tool wear and surface roughness
12	Baradie 1995 [15]	The study was done on the problems related to recycle of cutting fluids and disposal in environment which may not produce any toxic effects	Many pollution problems have been found to be solved on treating of cutting fluids with solvents that my reduced the toxic and other unwanted chemical effects as negligible. Then disposal problem was not an issue and became pollution free

(continued)

Table 1 (continued)

S. No.	Author, year, reference no.	Accomplishment of work	Outcome
13	Lotierzo et al. 2016 [16]	The properties of developed (MWF) with primary/tertiary amines in oil with water emulsions with brass was investigated	It has been found that corrosion to brass was influenced by number of carbon atoms in amines which was inversely proportionate
14	Rabic et al. 2002 [17]	The process of selection metal working fluids on the basis tribological property for milling machines were investigated	ISO-L-MAG (Synthetic concentrate) gave longer life as compared to ISO-L-MAE (Micro-emulsion)
15	Courbon et al. 2011 [18]	The cooling process with high pressure jet during turning was investigated with numerical model considering mechanical load and thermal effects	The numerical model was validated by FEM simulation using ALE approach
16	Xavior et al. 2009 [19]	The effects of different cooling methods were analyzed. The cooling was done individually by coconut oil, soluble oil and straight cutting oil with carbide tool	It has been found that wear in tool was declined but surface finish incremented with coconut oil as compared with other cooling methods

In accordance with the type of nanoparticles can give lubrication effect, cooling effects and abrasive effects.

Nanoparticles are water soluble and oil soluble. Generally, oil soluble nanoparticles cannot become soluble in water or vice versa. The nano-cutting fluids are supplied in very controlled way at the surface of tool.

Table 2 shows the research work done by using nanoparticles in cutting fluids.

2.3 Nanoparticles in Lubricants

Nanoparticles mixed with lubricants then lubricity of lubricants get increase many times. The hybrid use of more than one nanoparticles has increased the viscosity and film thickness.

The higher temperature has negligible effect on viscosity of nanolubricant as compared to base fluid (without nanoparticles).

Table 3 shows the research work done by developing nanolubricants.

Table 2 Details of research papers regarding nanoparticles in cutting fluids at the interface of cutting tool and workpiece

S. No.	Author, year, reference no.	Accomplishment of work	Outcome
1	Chan et al. 2013 [20]	The conventional cutting fluid was used for preparing for four samples of coolants. One sample was made with 5% cutting oil and 95% water (w/w), sample two was made with 2.5% cutting oil and 97.5 water (w/w). Sample three was made by treating composition by nanodroplets of 5% cutting oil, sample four was made by treating 2.5% nanodroplets and sample five was pure water. Each sample was characterized by contact angle and experiment was performed on lathe machine	In cutting experiments NDCF had high contact angles and gave better lubrication effect. The surface roughness was lower for sample of cutting fluid with 5% cutting oil remaining water with nanodroplets
2	Zong et al. 2008 [21]	An ultraprecision lathe machine was made with running accuracy of 550 nm and the range of moving guide way was 100 nm for grooving of monocrySTALLINE silicon (111) as workpiece	It has been found that the machined silicon surface depicted silicon carbide and diamond like carbon structure
3	Yin et al. 2003 [22]	The concentration of cobalt was varied from 0, 3, 5 and 8% for preparing a composite with alumina varied 59, 56, 54 and 51%. TIC remained constant on the basis of particle size. The samples were tested for mechanical properties	It was found that elastic modulus was declined with increase in temperature
4	Kumar et al. 2016 [23]	A nano-fluid was developed by using multiwalled nanocarbon tubes in sunflower oil as base fluid by 1% (w/w). The experiments were performed by using synthetic oil, sunflower oil and developed nanofluid on tribometer and grinding	Tribological properties got improved. The wheel worn out with lower rate. The surface finish of workpiece was improved by using nanofluid as compared of soluble oil cutting fluid

(continued)

Table 2 (continued)

S. No.	Author, year, reference no.	Accomplishment of work	Outcome
5	Zhang et al. 2015 [24]	First type of tool was made by creating nano-texturing and then depositing Ti55 Al45N as coating material. Second type of tool was created by depositing Ti55Al45N and surface was nano-textured	The first type of created tool performed better in reducing cutting forces, cutting temperature coefficient of friction and tool wear compared with firstly nano-scale textured and then coated tools (NCT)
6	Amrita et al. 2014 [25]	Four samples of nanofluids were prepared with nano-graphite, functionalized nano-graphite, nano-boric acid and nano-molybdenum sulfide with emulsion 0.3% (w/w). Emulsion was made from 20 parts of water and 1 part of conventional cutting oil. The experiments were performed on lathe machine by using different types of nanofluids at constant machining parameters	Functionalised nano-graphite (FNG) showed good stability in emulsifier oil-based cutting fluids than nano-graphite (NG). With respect to surface roughness, nano-MoS ₂ (Nano-molybdenum disulfide). Wear in tool and cutting force declined but surface finish incremented with nano-MoS ₂ as compared with other nanofluids
7	Sharma et al. 2016 [26]	The samples of nano-fluids were prepared by using Al ₂ O ₃ (0%, 0.25%, 0.5%, 1.0%, 1.5%, 2% and 3%) by volume with oil-water emulsion. The experiments were performed on lathe machine at constant machining parameters during dry, wet and minimum quantity lubrication	It has been found that Al ₂ O ₃ with 1% concentration had better thermal conductivity and viscosity (considering pressure drop relation with viscosity)
8	Sharma et al. 2016 [27]	A nano-fluid was developed by mixing TiO ₂ nanoparticle conventional cutting oil with water emulsion in different concentrations. 1% by volume of TiO ₂ was selected	It has been found that performance of TiO ₂ with 1% concentration was better as compared to other conditions

(continued)

Table 2 (continued)

S. No.	Author, year, reference no.	Accomplishment of work	Outcome
9	Padmini et al. 2016 [28]	The experiments were performed on lathe machine with dry, and samples of nano-fluids prepared by blending nano-MoS ₂ with (0, 0.25, 0.5, 0.75 and 1%) in conventional coconut oil, sesame oil and canola oil at constant machining parameters	It was found that composition with coconut oil with 0.5% nano-MoS ₂ particles gave better results as compared other compositions for machining characteristics
10	Uysal et al. 2015 [29]	The experiments were performed on milling machine in dry, conventional cutting oil and nano-fluid developed by using 1% MoS ₂ (w/w) with vegetable oil emulsion with water	It has been found that experimental result values with developed nano-fluid decreased
11	Wu et al. 2015 [30]	ALCrN coating and AlCrSiN Multilayer and nano-composite coatings were designed and deposited on the surface of HSS cutters	The service life of AlCrSiN nano-composite coating tool was increased 40% longer than AlCrN coated tool
12	Dobrzanski et al. 2005 [31]	The harden ability of cutting tool was increased by depositing many layers of nano-composites on high speed steel cutting tool	It has been found that silicon imparted higher hardness and more grain refinement in the coating. This incremented the cutting ability

Table 3 Details of research papers regarding nanoparticles in lubricants

S. No.	Author, year, reference no.	Accomplishment of work	Outcome
1	Esfe et al. 2017 [32]	The viscosity was investigated of nano-lubricants prepared by mixing multi-walled carbon tubes (90%) and zinc oxide (10%) by volume in engine oil of grade SAE 40 in different concentrations from (0–1%)	It has been found that nano-lubricants followed Newtons law of viscosity. The maximum ride in viscosity of nanolubricant was 33%
2	Ali et al. 2016 [33]	The experiments were performed on prepared nano-lubricants by mixing nano-alumina and titanium in different compositions for analyzing the tribological properties	It has been found that 0.25% concentration gave better results. Coefficient of friction and wear rate were declined
3	Asadi et al. 2016 [34]	The samples were prepared with nano-magnesium oxide and multi-walled carbon nano-tube in different compositions with lubricating oil SAE 50 and analyzed for change in viscosity at a particular range of temperature	It has been found that dynamic viscosity declined with increment in temperature. At room temperature the dynamic viscosity was lowest for all samples of nanolubricants
4	Ali et al. 2016 [35]	Investigated nano-additive for reducing frictional power automotive engine parts and gave a cleaner environment	It has been found that of composition of 0.05 wt% of nano-aluminina and titanium oxide gave better results in terms of frictional losses and wear rate as compared to other compositions of lubricants
5	Esfe et al. 2017 [36]	The samples of nanolubricants were prepared with different composition of Nanoparticles SiO ₂ in lubricating oil SAE 40 and investigated for change in rheological properties	It was found that all samples of nanolubricants followed Newtons law of viscosity

(continued)

Table 3 (continued)

S. No.	Author, year, reference no.	Accomplishment of work	Outcome
6	Maheswaran et al. 2016 [37]	The different samples were developed by varying the percentage of nano-garnet particles in the incrementing order of 0.25% (w/w) with SN500 lubricant	It was found all the developed samples were stable upto 500 °C The viscous behavior was influenced by the amount of concentration of nanoparticles
7	Callisti et al. 2014 [38]	A self lubricant W-S-C coating with different Ni-Ti-(CU) interlayers was fabricated by magnetron sputtering	The resistance to adhesion damage W-S-C coating was improved by using Ni-Ti (CU) interlayers
8	Afrand et al. 2016 [39]	The different samples of nanolubricants were developed with MWCNTs, SiO ₂ in SAE 40 lubricant	It has been found from optimal artificial neural network presented a deviation margin of 1.5%
9	Kumar et al. 2015 [40]	The thin layer of nanoparticles alumina was sprayed over the job piece of mild steel	It has been found that surface finish improved
10	Cho et al. 2013 [41]	Investigated the possible lubricating effects of aqueous dispersions of hexagonal boron nitride (h-BN) nanosheets	It was found that small amounts of h-BN nano-sheets enhanced wear resistance and reduced friction coefficient. The tribological properties were declined after the thirty days of preparation of nanofluid
11	Shahnazar et al. 2016 [42]	Nanolubricants were prepared by nanoparticles	Nanoparticles delivered excellent lubrication properties
12	Hu et al. 2015.[43]	The samples were prepared by using nanoparticle of copper in the base fluid of normal octane. Molecular dynamic and simulations models were formed for understanding mechanisms	It was found that nanolubricant could bear higher load without film breakage which was supported by both the models
13	Liv et al. 2017 [44]	Novel double hollow-sphere MoS ₂ (DHSM) nanoparticles with an average diameter of 90 nm were synthesized on sericite mic (SM)	The DHSM/SM composited was used an additive in polyalphaolefin oil friction and wear were decreased by 22.4% and 63.5%, respectively

(continued)

Table 3 (continued)

S. No.	Author, year, reference no.	Accomplishment of work	Outcome
14	Tao et al. 2014 [45]	The samples with different composition of treated and untreated nanoparticles AlN were mixed with lubricating oil and characterization was performed	It was found that nanoparticles improved the modified effect and enhanced dispersion stability in base oil. The composition of 0.3% concentration of nanoparticles performed better as compared to remaining samples
15	Zheng et al. 2017 [46]	Titanium nitride was treated with carbon nanohoops	It was found that hardness and flexibility incremented and tribological properties improved
16	Yang et al. 2016 [47]	Oleic acid surface—modified Lanthanum trifluoride graphene oxide (OA-LaF3-GO) nanohybrids were successfully prepared by surface modification technology	Tribological results showed that OA-LaF3 GO nanohybrids had excellent friction reduction and anti wear ability at the loading of 0.5 wt% of OA-LaF3-GO nano-hybrids compared to liquid paraffin alone
17	Xiang et al. 2014 [48]	The samples were prepared with magnetic nano-flakes with different composition with base lubricating oil and tested on four-ball tester for tribological properties	It was found that the composition of 1.5% magnetic ferric oxide performed better in delivery of results. The coefficient of friction and wear scar diameter were declined by 18.06% and 11.20%, respectively
18	Zovari et al. 2014 [49]	The polyester powder was applied on aluminum and investigated for change in properties	It was found that graphite or h-BN had influence on wear life
19	Tang et al. 2014 [50]	The properties of lubricants were improved by adding some additives which reduced friction of lubricants and wear rate of contacting surfaces. The modifications made by researchers have been discussed	It has been found that organomolybdenum compounds reduced friction and wear rate to higher extent as compared to other available compounds

3 Results and Discussion

The wear mechanism responsible for soft nanoparticles is the mending effect in which soft nanoparticles get embedded between the gaps or minor cracks developed during movement of contacting surfaces and create a smooth surface. The coefficient of friction get reduced.

The hard nanoparticles fill the gap like a roller bearing between contacting surface and reduce the coefficient of friction. This is known as rolling effect.

4 Conclusions

The work done by researchers is collected, deeply studied and broadly divided into three major categories of research papers related to cutting fluids/ high pressure fluids, nanoparticles in cutting fluids and nanoparticles in lubricants. The major conclusions are in the following ways:

- The mineral oil, straight oil and lubricating oil are used as cutting fluids in machining operations like turning, drilling, milling, etc.
- The conventional cutting fluids release fumes, itching to operators hands and sometimes eyes problems.
- The use of nanoparticles in different types of cutting fluids decreased the surface roughness, tool wear, cutting force and coefficient of friction by 15–25%, 25–30%, 32–35% and 40–45% as compared with dry machining condition found by previous researchers depending on type of workpiece material and machining parameters.
- The tool life increased by 40–65% using nanoparticles in cutting as compared to dry machining condition.
- The wear mechanism of rolling effect was found with hard nanoparticles.
- The wear mechanism of mending effect was found with soft nanoparticles.

References

1. Goindi GS, Sarkar P (2017) Dry machining: a step towards sustainable machining—challenges and future directions. *J Clean Prod.* <https://doi.org/10.1016/j.jclepro.2017.07.235>
2. Deshpande S, Deshpande Y (2019) A review on cooling systems used in machining processes. *Mater Today Proc* 18:5019–5031
3. Chetan BBC, Ghosh S, Rao PV (2016) Application of nanofluids during minimum quantity lubrication: a case study in turning process. *Tribol Int* 101:234–246
4. Naves VTG, Silva MBD, Silva FJD (2013) Evaluation of the effect of application of cutting fluid at high pressure on tool wear during turning operation of AISI 316 austenitic stainless steel. *Wear* 302:1201–1208

5. Mosleh M, Ghaderi M, Shirvani KA, Belk J, Grzina DJ (2017) Performance of cutting nanofluids in tribological testing and conventional drilling. *J Manuf Process* 25:70–76
6. Paul PS, Varadarajan AS, Cnandurai RR (2016) Study on the influence of fluid application parameters on tool vibration and cutting performance during turning of hardened steel. *Eng Sci Technol Int J* 19:241–253
7. Shokrani A, Dhokia V, Newman ST (2012) Environmentally conscious machining of difficult to machine materials with regard to cutting fluids. *Int J Mach Tools Manuf* 57:83–101
8. Jayal AD, Balaji AK (2014) Effects of cutting fluid application on tool wear in machining: interaction with tool surface features. *Wear* 267:1723–1730
9. Verschaka AA, Grigoriev SN, Vereschaka AS, Popov AY, Batako AD (2014) Nano-scale multi-layered composite coatings for cutting tools operating under heavy cutting conditions. *Proc CIRP* 14:239–244
10. Bork CAS, Goncalves JFDS, Gomes JDO, Gheller J (2014) Performance of the jatropha vegetable base soluble cutting oil as a renewable source in the aluminum alloy 7050-T7451 milling. *CIRP J Manuf Sci Technol* 7:210–221
11. Sokovic M, Mijanovic K (2011) Ecological aspects of the cutting fluids and its influence on quantifiable parameters of the cutting processes. *J Mater Process Technol* 190:181–189
12. Hermoso J, Boza FM, Gallegos C (2014) Influence of viscosity modifier and concentration on the viscous flow behaviour of oil based drilling fluids at high pressure. *Appl Clay Sci* 87:14–21
13. Khan MMA, Mithu MAH, Dhar NR (2009) Effects of minimum quantity lubrication on turning AISI 9310 alloy steel using vegetable oil-based cutting fluid. *J Mater Process Technol* 209:5573–5583
14. Xu DLJ, Ding W, Fu Y, Yang C (2016) Tool wear in milling Ti40 burn resistant titanium alloy using pneumatic mist jet impinging cooling. *J Mater Process Technol* 229:641–650
15. Baradie MAE (1996) Cutting fluids: part II, recycling and clean machining. *J Mater Process Technol* 56:798–806
16. Lotierzo A, Piffeir V, Artizzone S, Pasqualin P, Cappelletti G (2016) Insight into the role of amines in metal working fluids. *Corros Sci* 110:192–199
17. Rakic R, Rakic Z (2002) Tribological aspects of choice of metal working fluid in cutting processes. *J Mater Process Technol* 124:25–31
18. Courbon C, Sajin V, Kramar D, Rech J, Kosel F, Kopac J (2011) Investigation of machining performance in high pressure jet assisted turning of Inconel 718: a numerical model. *J Mater Process Technol* 211:1834–1851
19. Xavior MA, Adithan M (2009) Determining the influence of cutting fluids on tool wear and surface roughness during turning of AISI 304 austenitic stainless steel. *J Mater Process Technol* 209:900–909
20. Chan CY, Lee WB, Wang H (2013) Enhancement of surface finish using water-miscible nano cutting fluid in ultra precision turning. *Int J Mach Tools Manuf* 73:62–70
21. Zong WJ, Sun T, Cheng DLK, Liang YC (2008) XPS analysis of the groove wearing marks on flank face of diamond tool in nano metric cutting of silicon wafer. *Int J Mach Tools Manuf* 48:1678–1687
22. Yin Z, Huang C, Zou B, Liv H, Zhu H, Wang J (2013) High temperature mechanical properties of Al₂O₃/TiC micro nano-composite ceramic tool materials. *Ceram Int* 39:8877–8883
23. Kumar KM, Ghosh A (2016) Assessment of cooling lubrication and wettability characteristics of nano engineered sunflower oil as cutting fluid and its impact on SQCL grinding performance. *J Mater Process Technol* 237:55–64
24. Zhang K, Deng J, Meng R, Go P, Yue H (2015) Effect of nano scale textures on cutting performance of WC/Co-based Ti₅₅Al₄₅N coated tools in dry cutting. *Int J Refract Met Hard Mater* 51:35–49
25. Amrita M, Shariq SA, Manoj GC (2014) Experimental investigation on application of emulsifier oil based nano cutting fluid in metal cutting process. *Proc Eng* 97:1115–1124
26. Sharma AK, Singh RK, Dixit AR, Tiwari AK (2016) Characterization and experimental investigation of Al₂O₃ nanoparticle based cutting fluid in turning AISI 1040 steel under minimum quantity lubrication (MQL). *Mater Today Proc* 3:1899–1906

27. Sharma AK, Tiwari AK, Singh RK, Dixit AR (2016) Tribological investigation of TiO₂ nano particle based cutting fluid in machining under minimum quantity lubrication (MQL). *Mater Today Proc* 3:2155–2162
28. Padmini R, Krishna PV, Rao GKM (2016) Effectiveness of vegetable oil based nano fluids as potential cutting fluid in turning steel AISI 1040 Steel. *Tribol Int* 94:490–501
29. Uysal A, Demiren F, Atlan E (2015) Applying minimum quantity lubrication (MQL) method on milling of martensitic stainless steel by using Nano MoS₂ reinforced vegetable cutting fluid. *Proc Soc Behav Sci* 195:2742–2747
30. Wu W, Chen W, Yang S, Lin Y, Zhang S, Cho TY, Lee GH, Kwon SC (2015) Design of AlCrSiN multilayers and nanocomposites coating for HSS cutting tools. *Appl Surf Sci* 351:803–810
31. Dobrzanski LA, Golomek K (2005) Structure properties of cutting tools made from cemented carbides and cermet with TiN + mono -, gradient - or multi (Ti, Al, Si)N + TiN nano crystalline coatings. *J Mater Process Technol* 164–165:805–815
32. Esfe MH, Afrand M, Rostamian SH, Toghraie D (2017) Examination of rheological behavior of MWCNTs/ZnO-SAE40 hybrid nano-lubricants under various temperatures and solid volume fractions. *Exp Thermal Fluid Sci* 80:384–390
33. Ali MKA, Xianjun H, Mai L, Qingping C, Turkson RF, Bicheng C (2016) Improving the tribological characteristics of piston ring assembly in automotive engines using Al₂O₃ and TiO₂ nanomaterials as nano-lubricant additives. *Tribol Int* 103:540–554
34. Asadi A, Asadi M, Rezari M, Siahmargoi AF (2016) The effect of temperature and solid concentration on dynamic viscosity of MWCNT/MgO (20–80)-SAE50 hybrid nano-lubricant and proposing a new correlation: an experimental study. *Int Commun Heat Mass Transfer* 78:48–53
35. Ali MKA, Xianjun H, Mai L, Bicheng C, Turkson RF, Ping CQ (2016) Reducing frictional power losses and improving the scuffing resistance in automotive engines using hybrid nanomaterials as nano-lubricant additives. *Wear* 364–365:270–281
36. Esfe MH, Afrand M, Yan WM, Yarmand H, Toghraie D, Dahari M (2016) Effects of temperature and concentration on rheological behavior of MWCNTs, SiO₂(20–80)-SAE 40 hybrid nano-lubricant. *Int Commun Heat Mass Transfer* 76:133–138
37. Maheswaran R, Sunil J (2016) Effect of nano sized garnet particles dispersion on the viscous behaviour of extreme pressure lubricant. *J Mol Liq* 223:643–651
38. Callisti M, Polcar T (2014) The role of Ni-Ti (Cu) interlayer on the mechanical properties and nano scratch behaviour of solid lubricant W-S-C coatings. *Surf Coat Technol* 254:260–269
39. Afrand M, Najafabadi KN, Sina N, Safaei MR, Kherbeet AS, Wongwises S, Dahari M (2016) Prediction of dynamic viscosity of a hybrid of a hybrid nano-lubricant by an optimal artificial neural network. *Int Commun Heat Mass Transfer* 76:209–214
40. Kumar NS, Sammaiah P, Rao KV, Sneha M, Ashok C (2015) Influence of nano solid lubricant emulsions on surface roughness of mild steel when machining of lathe machine. *Mater Today Proc* 2:4413–4420
41. Cho DH, Kim JS, Kwon SH, Lee C, Lee YZ (2013) Evaluation of hexagonal boron nitride nano sheets as a lubricant additive in water. *Wear* 302:981–986
42. Shahnazar S, Begheri S, Hamid SBA (2016) Enhancing lubricant properties by nano particle additives. *Int J Hydrogen Energy* 41:3153–3170
43. Hu C, Bai M, Lv J, Li X (2015) Molecular dynamics simulation of mechanism of nano particle in improving load carrying capacity of lubricant film. *Comput Mater Sci* 109:97–103
44. Liu Y, Hu K, Hu E, Guo J, Han C, Hu X (2017) Double hollow MoS₂ nano-spheres: synthesis, tribological properties, and functional conversion from lubrication to photocatalysis. *Appl Surf Sci* 392:1144–1152
45. Tao Y, Tao Y, Wang B, Tai Y (2014) Preparation and investigation of nano—AlN lubricant with high performance. *Mater Chem Phys* 147:28–34
46. Zheng J, Ren X, Hao J, Li A, Liu W (2017) Carbon nanohoops as attractive toughening and lubricant agents in TiN porous films. *Appl Surf Sci* 393:60–66
47. Yang C, Hou X, Li Z, Li X, Yu L, Zhang Z (2016) Preparation of surface modified lanthanum fluoride—graphene oxide nanohybrids and evaluation of their tribological properties as lubricant additives in liquid paraffin. *Appl Surf Sci* 388:497–502

48. Xiang L, Gao C, Wang Y, Pan Z, Hu D (2014) Tribological and tribo chemical properties of magnetite nanoflakes as additives in oil lubricants. *Particuology* 17:136–144
49. Zovari M, Kharrat M, Dammak M, Barletta M (2014) A comparative investigation of the tribological behavior and scratch response of polyester powder coatings filled with different solid lubricants. *Prog Org Coat* 77:1408–1417
50. Tang Z, Li S (2014) A review of recent developments of friction modifiers for liquid lubricants (2007-present). *Curr Opin Solid State Mater Sci* 18:119–139

The High Energy Concentration of Heat Pipe for Enhanced Electronic Cooling



P. Senthil Kumar, Syed Abudhagir Umar, and R. Balaji

Abstract Availability and highly performed electronic devices there would be a more need of management in thermal properties of those electronic devices. The reciprocating or reciprocating heat pipe has more heat dissipation characteristics. In addition, it can be able to eliminate the higher heat flux. The thermal properties of those devices can transfer the excessive heat than the existing heat pipes. The usage of these heat pipes can be suitable for computers and latest electronic systems (satellites, etc.). In this work, the analysis made to understanding the working principles of a reciprocating heat pipe. The design as well as fabrication of heat pipe is done based on the uses like electronic system cooling, concept of green energy and the heat exchanger to allow fluid to circulate around it. Particularly, this research work is focused on the nanofluid technology for preparation of reciprocating heat pipe.

Keywords High energy · Nanofluid · Heat transfer rate

1 Introduction

Wang et al. [1] described in his article the understanding of innovative electronic devices for applying them to the thermal control in electronic devices and components. Senthil Kumar et al. [2] stated that a reciprocating heat pipe is subjected to elevated temperature, and the nanofluids circulate in the evaporator will increase the pressure. The interlinked bonding of the nanofluids in the tubes will allow flowing the

P. Senthil Kumar (✉)

Department of Mechanical Engineering, B. V. Raju Institute of Technology, Narsapur, Medak District, Telangana 502 313, India
e-mail: senthil.p@bvrit.ac.in

S. A. Umar · R. Balaji

Department of Electronics and Communication Engineering, B. V. Raju Institute of Technology, Narsapur, Medak District, Telangana 502 313, India
e-mail: syedabudhagir.u@bvrit.ac.in

R. Balaji

e-mail: balaji.r@bvrit.ac.in

liquid slug and vaporizing foams once in the first segment of the tunnel to the condenser portion, further leading to increase of slugs and foams in the next segment toward next temperature level in the evaporator portion. The heat pipes acting as an accelerating force and interplay as a restoring force, and thus, the restoring force allows the vapor and liquid in the vertical direction. The scenario of the operating condition in reciprocating heat pipes was the arrangement of heat tubes' single surging turned toward tunnel [3–5].

Compared with regular heat pipes, a reciprocating type had some common features, thus little drop in working fluid pressure. Though nanofluid has the wick-shaped structure, it is easier to fabricate [6, 7]. However, the wick-shaped reciprocating heat-pipe sections are inadequate to build. The pressure drops of the liquid caused by due to the frictional vapor flow were considerably decreased same as fluid flow [8]. These reciprocating flows of nanofluids inside the capillary tube produced vacuum surfaces by providing a thin-film region. The forced convection could distribute by the heat in the evaporating area that can overcome by the forced convection of the nanofluids. Due to this, a phase of heat transfer rate changes in the capillary-tube [9, 10] reciprocating motions.

The best and suitable applications for reciprocating heat pipe are in electronic cooling. For more effective cooling on this, an appropriate method should adopt to increase the performance of these electronic devices. In case of high-end of applications like CPU servers the cooling will be done through heat sinks. This work is mainly focusing to merge the technology of nanofluids with design of reciprocating heat pipe. It was observed that the change in dimensions of heat pipes is to make as compact.

1.1 Literature Survey

Tang et al. [11] extensively investigated the higher-end density packaging of electronic components that exhibit higher performance while used in mobile electronics. They stated that flattens thickness exerts significant influence on the thermal performance of UTHPs. In addition, they described that developing of UTHP process is crucial on fabricating UTHPs.

Xin et al. [12] studied and found wall temperature, pressure drop and velocity. The article consists of the facts that design of wick is put into a flat heat pipe, because of that the low thermal conductivity coefficient is with rate of heat transfer. Also, the changes in the tube and vapor chamber are found as more because of more heat dissipation. In addition, from the analytical calculations, they found that marginal effect is negligible on the parameters of thermal performance [13–15].

An integrated system was adopted for energy conversation by heat transfer values through samples. Based on the different parameters and scenario, a prototype is designed for cooling heat sink. They found that the range of cooling drastically increased to consumption of fuel with increasing ambient air temperature [16–20].

2 Experimental Setup

A prototype of the OHP is shown in Fig. 1. In the fabricated prototype, copper material is used for the heat pipe with conductivity of heat as 385.01 W/mk. Water is used as a working fluid with temperature range from 0 to 150 °C and 72.8×10^3 N/m as surface tension. The copper-made heat pipe is made with five spins. It contains the dimensions with specifications of 2.45 and 3 mm of external diameter as shown in Fig. 2. The specifications of plates with the 50-mm, 70 mm and 5 mm are taken as the evaporator and condensers in the heat pipes. The tubes were made bend by

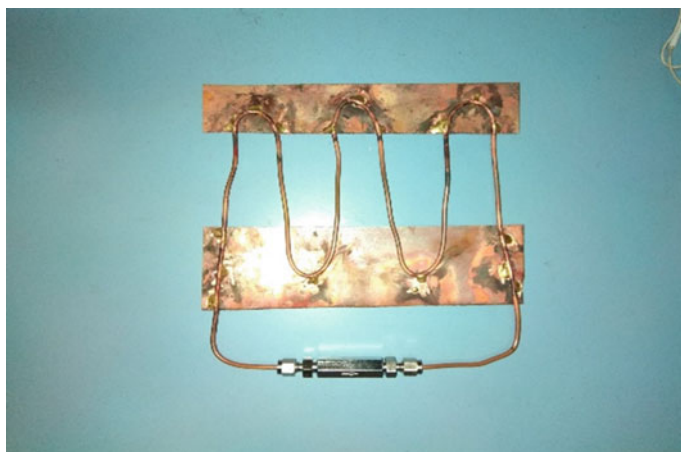


Fig. 1 Reciprocating heat pipe

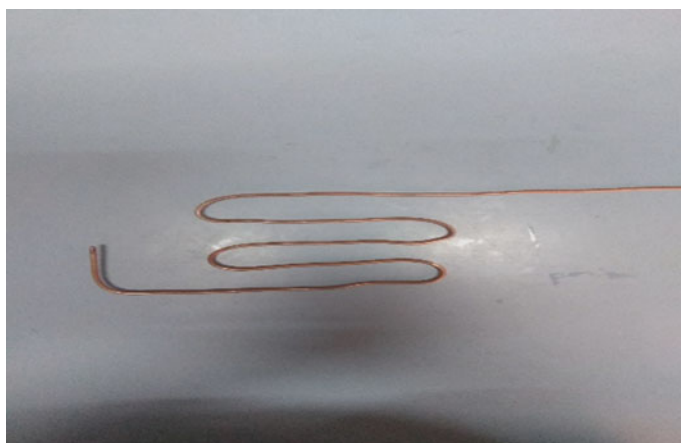


Fig. 2 Hand-made bend on tube

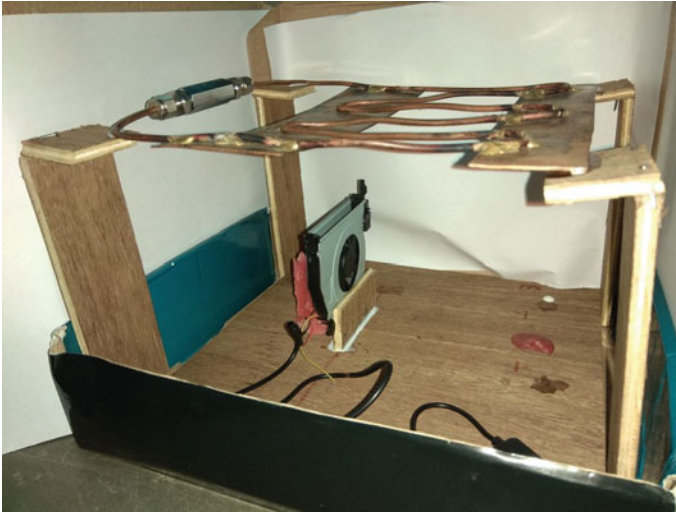


Fig. 3 Final setup for reciprocating heat pipe

hand with the arc radius of 12.5 mm each. Also 1060 mm is filled with 48% of water content.

The copper tubes and plates were treated with brazing to attain the uniform heat conductivity. A big-sized candle is used to heating the evaporator. A continuous temperature measurement was taken on the heat pipe using digital thermometer. The whole arrangement is mounted on a plywood frame for maintaining the ergonomics.

Initially, the evacuation and filling were done on the tube with vacuum. Further, the water is allowed to 48% on the tube. At the end of tubes, male connectors are provided with a size of 1/8 in. nonreturn valve. During the trials, the heating was done on evaporator for 1 min for reaching its mean temperature 70 °C. Later, the cooling fan is utilized for raising heat dissipation. Images of the investigational setup and its parameters are shown in Figs. 3 and 4.

3 Results and Discussion

From the study, the following observations were made:

1. The pressure in the evaporators of the oscillating pipe was available.
2. During the adiabatic fragment process of the heat pipe, a foam train flow was there.
3. The unsteady distribution of pressure is on heat pipe.

The heat pipe is purely dependent on the oscillating motions of the transfer in vapor–liquid mixture canal of heat pipe. The water particles in the reciprocating heat

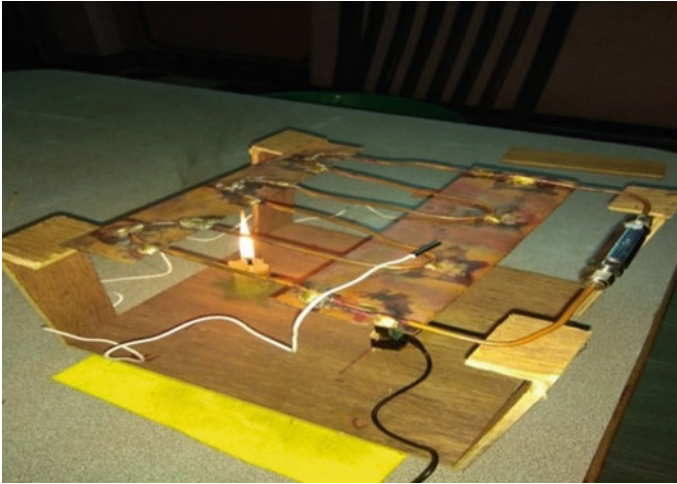


Fig. 4 Trail test on reciprocating setup

pipe are an important scenario for identifying the deviation in heat transfer rate of the heat pipes. The rate of heat transfer in the reciprocating pipe is observed that it is better than an existing used heat pipe. From the images, it can be observed that the period needs to reduce in the cooling load.

Characteristics of flow of vapor and nanofluid inside the capillary tubes were present including the effects in the capillary forces, constant of gas spring, specifications, gravitational forces and primary distributions of pressure on the working fluids.

Also, the analytical solution was indicating the generation of stronger reciprocations due the effect of isothermal bulk modulus. During the trail on the tubes, it is found that the bubble sizes and liquid plugs create the oscillation motions. And the forces like capillary and gravitational are the primary distributions of pressure in the working fluid.

Oscillation damp was occurring because of the force of gravitation, and it tends to steady the reciprocating motion of flow slug in the cell at few occasions. Hence, the slug flow in the reciprocating motion is orientation of tubes to the pipes. To maintain the sustainability of the slug flow, the required parameters in the tubes must reduce (Fig. 5).

During the positioning (orientation) process, the temperature changed from 90° to 60° . It shows better development in the thermal resistance of the heat pipes.

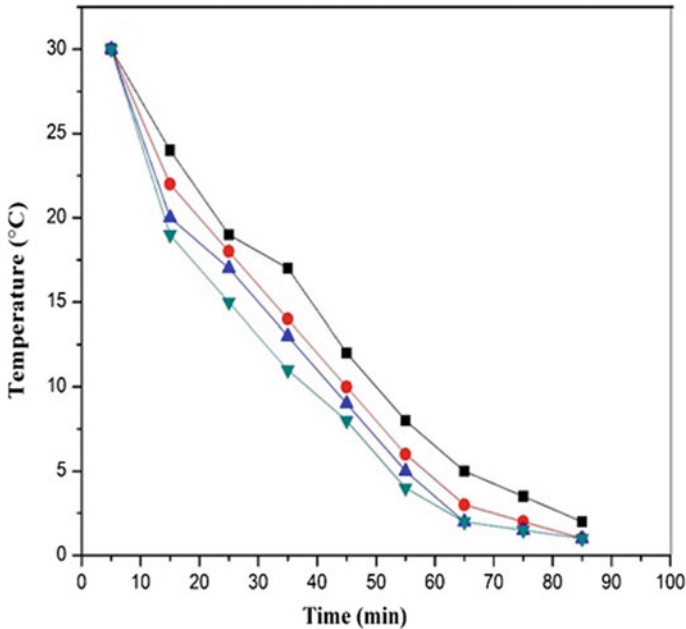


Fig. 5 Graph between time versus temperature

4 Conclusion

In this work, the heat pipe was fabricated then it investigated to the definite requirements of the heat pipe. Those findings are conducted and calculated from the simple experiments. From the experiments, it has been found that design is effective than existing heat pipes, and it will help to prevent the reciprocating heat pipe to reach its full potential. The evidence of performance from the trail is also up to mark. Due to its changeableness, it will have to keep for more research and development activity to expand as an excellent heat exchanger into our technology.

References

1. Wang Y, Peterson GP (2005) Investigation of a novel flat heat pipe. *J Heat Trans* 127(2):165–170
2. Senthil Kumar P, Kavimani V, Prakash KS, Krishna VM, Kumar GS (2020) Effect of TiB₂ on the corrosion resistance behavior of in situ Al composites. *Int J Metalcast* 14(1):84–91
3. Katoh T, Novotny S, Voge M, Xu G (2004) New attempt of forced-air cooling for high heat-flux applications. In: *Inter-society conference on thermal phenomena*, pp 34–39
4. Senthil Kumar P, Manimaran R, Krishna Reddy Y (2019) Evaluation of mechanical properties of hybrid Al7009 nanocomposite. *Energy Sources Part A Recov Utiliz Environ Eff* 1–9
5. Arulprakasajothi M, Elangovan K, Reddy KH, Suresh S (2015) Heat transfer study of water-based nanofluids containing titanium oxide nanoparticles. *Mater Today* 2(5):3648–3655

6. Avena Y, Schaeffer C, Schanen JL, Vassilev M (2007) Experimental study of a pulsating heat pipe with combined circular and square section channels. In: 42nd IAS annual meeting conference record of the industry applications conference. IEEE, pp 1419–1425
7. Kumar PS, Gurusami K, Rajaprasanna R, Puthilibai G, Chakaravarthi MA, Ramakrishnan G (2020) Characterizations on hybrid of caustic treated natural and glass fiber composites. *Mater Today: Proc* 33:4424–4427
8. Ma HB, Qu W (2007) Theoretical analysis of startup of a pulsating heat pipe. *Int J Heat Mass Transf* 50:2309–2316
9. Arulprakasajothi M, Elangovan K, Chandrasekhar U, Suresh S (2018) Experimental studies of water-based titanium oxide nanofluid in a circular pipe under transition flow with conical strip inserts. *Heat Transf Res* 49(5):439–456. <https://doi.org/10.1615/heattransres.2018015783>
10. Senthil Kumar P, Lakshminarayanan PR, Varahamoorthi R (2018) Effect of cooling rate and other factors on size and pattern of distribution of TiB₂ particles formed during solidification of the Al-TiB₂ melt for various pouring temperatures. *Int Res J Eng Technol* 3(6)
11. Tang H, Tang Y, Wan Z, Li J, Yuan W, Lu L, Li Y, Tang, K (2018) Review of applications and developments of ultra-thin micro heat pipes for electronic cooling. *Appl Energy* 223:383–400
12. Xin F, Ma T, Wang Q (2018) Thermal performance analysis of flat heat pipe with graded mini-grooves wick. *Appl Energy* 228:2129–2139
13. Xiao C, Liao H, Wang Y, Li J, Zhu W (2017) A novel automated heat-pipe cooling device for high-power LEDs. *Appl Therm Eng* 111:1320–1329
14. Sun X, Zhang L, Liao S (2017) Performance of a thermoelectric cooling system integrated with a gravity-assisted heat pipe for cooling electronics. *Appl Therm Eng* 116:433–444
15. Behi H, Ghanbarpour M, Behi M (2017) Investigation of PCM-assisted heat pipe for electronic cooling. *Appl Therm Eng* 127:1132–1142
16. Sun X, Yang Y, Zhang H, Si H, Huang L, Liao S, Gu X (2017) Experimental research of a thermoelectric cooling system integrated with gravity assistant heat pipe for cooling electronic devices. *Energy Proc* 105:4909–4914
17. Tiari S, Mahdavi M, Qiu S (2017) Experimental study of a latent heat thermal energy storage system assisted by a heat pipe network. *Energy Convers Manage* 153:362–373
18. Yang XH, Tan SC, He ZZ, Liu J (2018) Finned heat pipe assisted low melting point metal PCM heat sink against extremely high power thermal shock. *Energy Convers Manage* 160:467–476
19. Senthil Kumar P, Lakshminarayanan PR, Varahamoorthi R (2016) Effect of cooling rate and other factors on size and pattern of distribution of TiB₂ particles formed during solidification of the Al-TiB₂ melt for various pouring temperatures
20. Krishna J, Kishore PS, Solomon AB (2017) Heat pipe with nano enhanced-PCM for electronic cooling application. *Exp Thermal Fluid Sci* 81:84–92
21. Wang Y, Peterson GP (2005) Investigation of a novel flat heat pipe. *J Heat Transfer* 127(2):165–170

Effect of Block Location in a Suddenly Expanded Micro-combustor



Arees Qamareen , Shahood S. Alam , and Mubashshir A. Ansari

Abstract Premixed H₂/air combustion in a micro-combustor with backward facing step and axially located triangular block having variable blockage ratio (BR) was investigated numerically. Recirculation zones formed due to step and block insert help in better mixing and heat transfer. Simulations with inlet velocities varying from 4 to 48 m/s and BR = 0.4, 0.5 and 0.6 were done. The outer wall temperature distribution was found to be influenced by the axial location of block insert with the highest peaks observed for blocks farthest downstream for most of the inlet velocity regime due to enlargement of recirculation zone near the step wall.

Keywords Micro-combustor · Block · Axial location · Numerical simulation

1 Introduction

Cylindrical combustors with hydrocarbon fuels as heat releasing sources are widely researched using CFD modeling softwares such as ANSYS (Fluent & CFX), Comsol multiphysics, and opensource software OpenFOAM. These are often used along with the codes developed using various programming languages such as FORTRAN and C++.

The combustion devices find applications in macro- as well as micro-scaled devices such as IC engines, gas turbines, and direct power generating systems such as Micro-Thermo Electric (MTE) generators and Micro-Thermo Photo Voltaic (MTPV) units. Hydrocarbon fuels have a much higher energy densities (approximately 40 MJ/kg) as compared to the most efficient batteries (about 10 MJ/kg) [1]. Micro-combustors face several challenges due to their miniature-sized geometry which causes higher heat losses from the large outer surface area. Radical destruction at the gas-solid interfaces and reduced residence time also hinder the combustor performance. Still combustor-based micro-power generating devices have attracted a colossal increase in research lately [2]. CFD helps in the prediction of performance

A. Qamareen (✉) · S. S. Alam · M. A. Ansari

Department of Mechanical Engineering, Aligarh Muslim University, Aligarh 202002, India

of these devices and also the combustion characteristics of conventional as well as newly synthesized fuels.

Backward facing step has been found to enhance flame stability and outer wall temperature by inducing heat and flow recirculation [3]. Along with recirculation induced due to step, insertion of bluff bodies/blocks [4], wall fins/ribs [5, 6], cavities [7], porous media [8, 9], catalyst addition [10] have been explored with positive influence on the micro-combustor efficiency. While research on block inserted simple micro-combustors have been undertaken by various researchers, a detailed investigation of suddenly expanded micro-combustor with block inserts is still required.

In the present study, effectiveness of a triangular block insert in a suddenly expanded micro-combustor is reported in comparison with the case without any insertion. The varying parameters are inlet velocity and location of the block for different blockage ratios.

2 Mathematical Model

2.1 Geometric Model

Micro-combustors with combined backward facing step and a triangular block inserted along the centerline at varying axial locations are investigated and shown in Fig. 1. Case MC04L10 signifies micro-combustor with blockage ratio of 0.4 and block located at 1 mm from combustion chamber inlet and so on. The flame anchoring

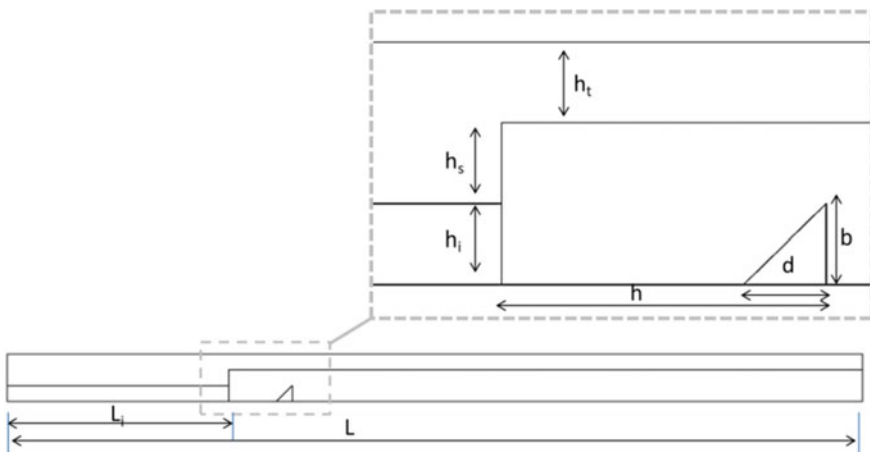


Fig. 1 Design features of micro-combustor with block insert

Table 1 Geometrical parameters of micro-combustors

Geometrical parameter	Parameter name	(mm)	Constant/variable
L	Combustor length	27	Constant
L_i	Inlet length	7	Constant
h	Block location	1, 2, 3	Variable
h_i	Inlet height	0.5	Constant
h_s	Step height	0.5	Constant
h_t	Combustor wall thickness	0.5	Constant
b	Block height	0.4, 0.5, 0.6	Variable
d	Block length	0.4, 0.5, 0.6	Variable
AR	Aspect ratio = d/b	1	Constant
BR	Blockage ratio = $d/(h_i + h_s)$	0.4, 0.5, 0.6	Variable

due to the step wall and block is expected to enhance combustion due to flow and heat recirculation. Table 1 summarizes the geometrical parameters considered.

2.2 Numerical Scheme

A global H_2 /air reaction mechanism was adopted for combustion modeling neglecting the surface reactions on the combustor wall. All the governing equations [11] including conservation of mass, momentum, energy and species along with pertinent boundary conditions were resolved by using the commercial finite volume solver ANSYS FLUENT 16.0. Second-order upwind discretization scheme and SIMPLE pressure–velocity coupling algorithm were employed. Turbulence-chemistry interaction was simulated using Finite Rate/Eddy Dissipation Model.

Reacting flows are difficult to solve numerically due to stability and convergence issues due to a strong coupling between the mass/momentum equations and species transport equation. Reactions occurring in combustion release excessive heat causing subsequent density fluctuations and large accelerations in flow (Table 2).

A reduced value of thermal conductivity (5 W/m–K) for stainless steel combustor wall and block was considered due to oxidation of steel at high temperatures [12]. Gas mixture density was attained from ideal gas equation and mixture specific heat, viscosity and thermal conductivity from mass fraction weighted average of the species properties. Specific heat for each species is calculated by piecewise polynomial fitting of temperature. Values of $k = 1 \times 10^{-3}$ for and $\varepsilon = 1 \times 10^{-3}$ for the k – ε turbulence model were defined.

Table 2 Boundary conditions

Boundary	Conditions applied
Fluid–solid interfaces	No-slip velocity condition Zero flux of all species Coupled heat transfer
Inlet	Uniform velocity inlet (4–48 m/s) Incoming H ₂ -air mixture temperature = 300 K Equivalence ratio of mixture, $\varphi = 0.8$
Outlet	Zero gauge pressure
Inlet/outlet walls	Adiabatic (zero heat flux)
Outer wall	Mixed boundary condition (radiation/convection) Wall Surface emissivity = 0.6 Heat transfer coefficient = 10 W/m ² -K Ambient temperature = 300 K

3 Results and Discussion

Premixed H₂/air combustion is extensively investigated for CFD applications. H₂ and various hydrocarbon fuels when numerically studied require large amount of computational time and power. Simulations are a great means to examine the experiment results and to obtain an in-depth insight of the combustion phenomenon occurring within the micro-scaled combustors which is otherwise difficult to visualize. The present numerical study has been carried out to comprehend the crucial factors that decree the wall temperature distribution rather than to obtain an extremely refined computational model having accurate estimation. Inherent stiffness of the equations makes it difficult to obtain numerical convergence. In numerical simulations, a structured quadrilateral multi-zone mesh is used with 1.26×10^5 numbers of nodes (see Fig. 2). Finer grids were also verified (not presented here), with no noticeable difference of T_{out} was witnessed.

The numerical result for the case with inlet velocity = 12 m/s, $\varphi = 0.8$ and $\varepsilon = 0.6$ was verified against the results (Fig. 3) that were obtained experimentally by Li et al. [13]. Difference in the temperature profiles may be due to various assumptions and problem simplifications in the numerical simulations. Consideration of global H₂-air reaction scheme which does not have several intermediate reactions [1] that are otherwise considered in the detailed mechanisms cause such differences in numerical and experimental results.

Figure 4 illustrates a comparative study of T_{out} (outer wall temperature) distribution of micro-combustors with varying block (BR = 0.4) locations along with the temperature contours for an overall view of temperature distribution throughout the combustor. The flame is located in the combustion chamber where the occurrence of maximum temperature gradient is witnessed. As inlet mixture velocity increases from 4 to 48 m/s, T_{out} increases dramatically. As observed from the figure, when the inlet velocity is increased, rise in T_{out} is observed with the location of peak temperature shifting downstream. The high temperature region behind the block

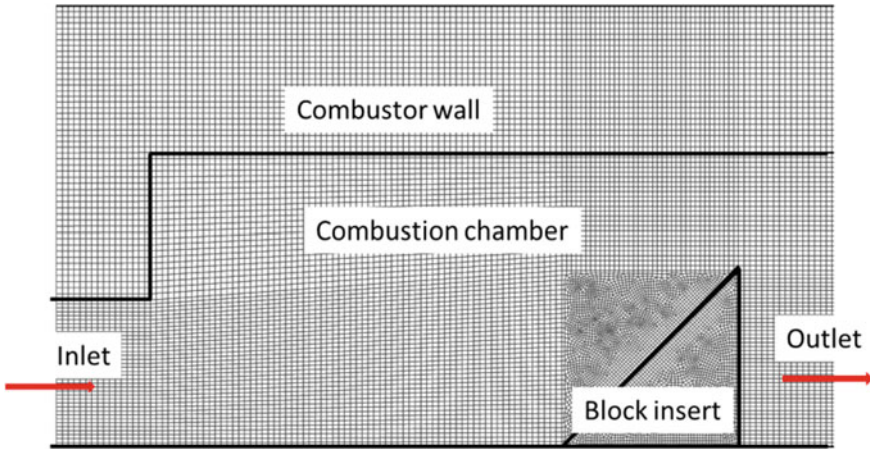
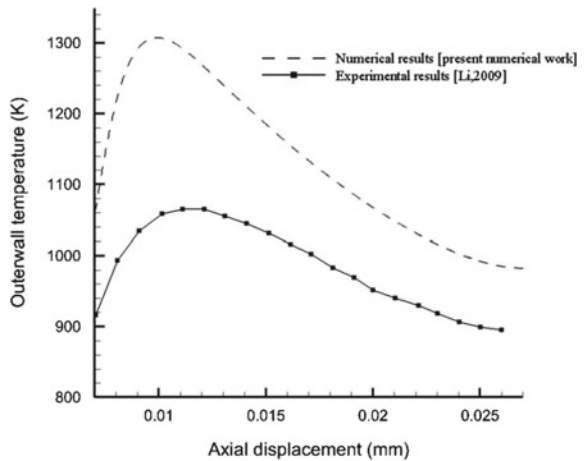


Fig. 2 Demonstration of mesh near the block inserted in the micro-combustor

Fig. 3 Validation of numerical results with Li et al. [13]



gets enlarged gradually as well as its position moves downstream. The increase in the inlet velocity lowers the temperature in the area before the block but a greater temperature is observed near the micro-combustor outlet. This takes place due to shifting of the flame toward the combustor exit.

Large amount of heat gets released in the combustion chamber due to an increased amount of incoming fuel. Upon further increasing the inlet velocity, sustenance of combustion in the combustion chamber is difficult due to greater amount of heat loss from the combustor.

Similar trends are observed for the micro-combustors with blocks having BR = 0.5 and 0.6 as are seen in Figs. 5 and 6. As the inlet velocity increases, the flame

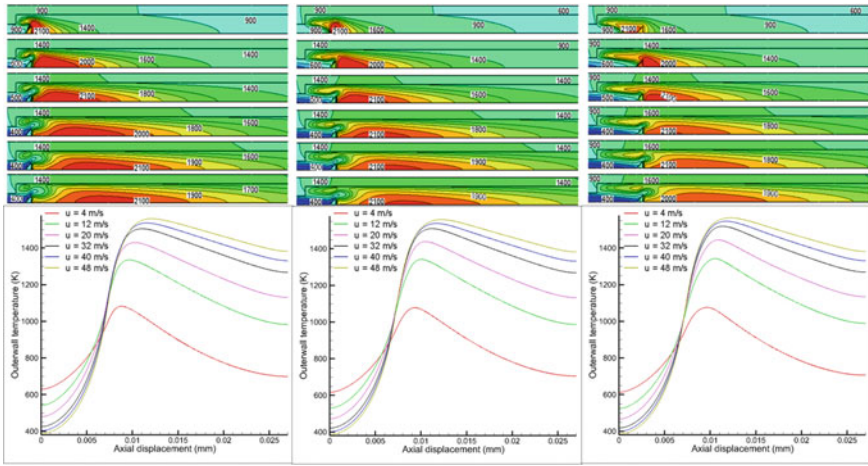


Fig. 4 Temperature contours and T_{out} distribution for MC04 with different block locations, $h = 1$ mm (left), $h = 2$ mm (center), $h = 3$ mm (right)

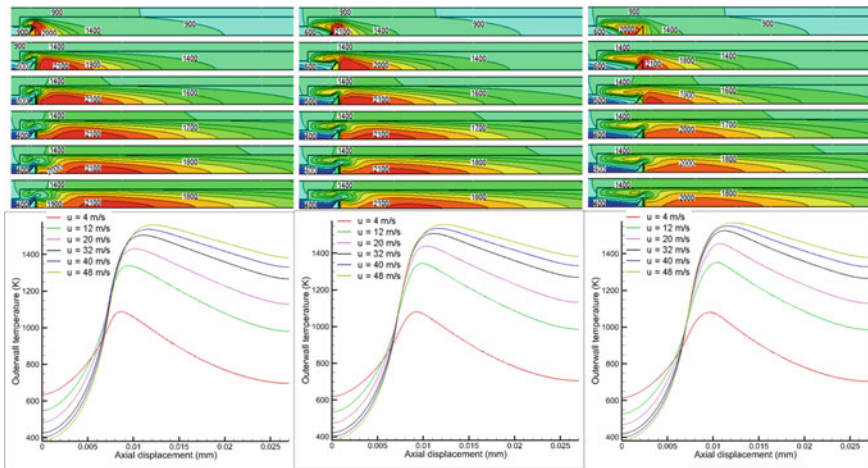


Fig. 5 Temperature contours and T_{out} distribution for MC05 with different block locations, $h = 1$ mm (left), $h = 2$ mm (center), $h = 3$ mm (right)

moves behind the obstruction and two recirculation zones are formed—one near the step and other behind the block.

Figure 7 shows the effect of block location on the maximum T_{out} attained at a particular inlet velocity. For lower velocity of 4 m/s, it is observed that for blocks nearest to the inlet, higher peak temperatures are attained for all blockage ratios. This phenomenon can be explained from the streamline plots shown in Figs. 8, 9 and 10 where the recirculation zones formed behind the blocks for a particular blockage ratio

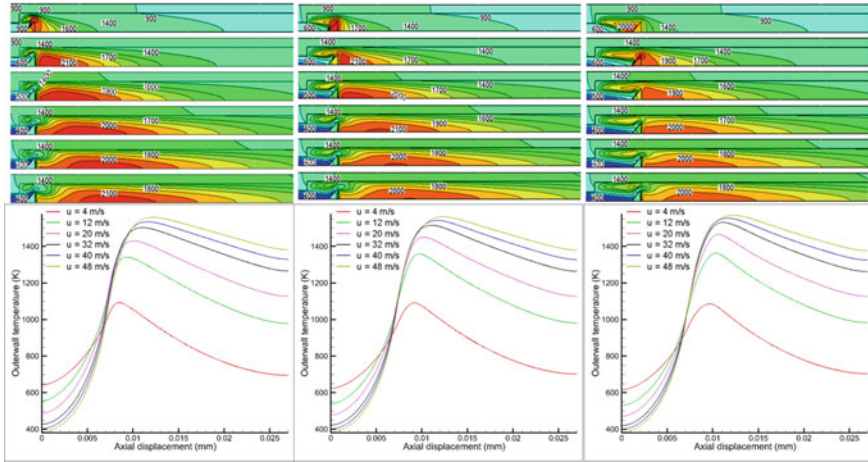


Fig. 6 Temperature contours and T_{out} distribution for MC06 with different block locations, $h = 1$ mm (left), $h = 2$ mm (center), $h = 3$ mm (right)

and $u = 4$ m/s keep shrinking in size as the block moves downstream. On increasing the velocity, micro-combustors with blocks farthest downstream seem to dominate and perform better for all blockage ratios.

Figures 8, 9 and 10, help in the explanation of heat transfer and flow recirculation phenomenon occurring within the combustion chamber. For a particular case, an increase in velocity causes strengthening and enlargement of vortices formed near the step as well as behind the block. As the block is moved downstream, the recirculation zone near the step gets enlarged causing more heat transfer. For $BR = 0.6$, one can clearly see an enlargement of the recirculation zone near the step as well as behind the block. This causes an enhanced heat recirculation in the combustion chamber, leading to additional heat transfer to the combustor wall. Overall performance of the micro-combustors with block insertion farthest from the inlet is better and a higher T_{out} is observed.

4 Conclusions

The effect of axial location of triangular block insert in a suddenly expanded micro-combustor on the outer wall temperature was numerically investigated. From the results, it can be concluded that the block which is placed farthest from the combustion chamber inlet showed best performance due to enlargement of recirculation zones formed near the step and behind the block. The recirculation zones help in better heat transfer from the combustion zone to the combustor wall causing higher wall temperatures.

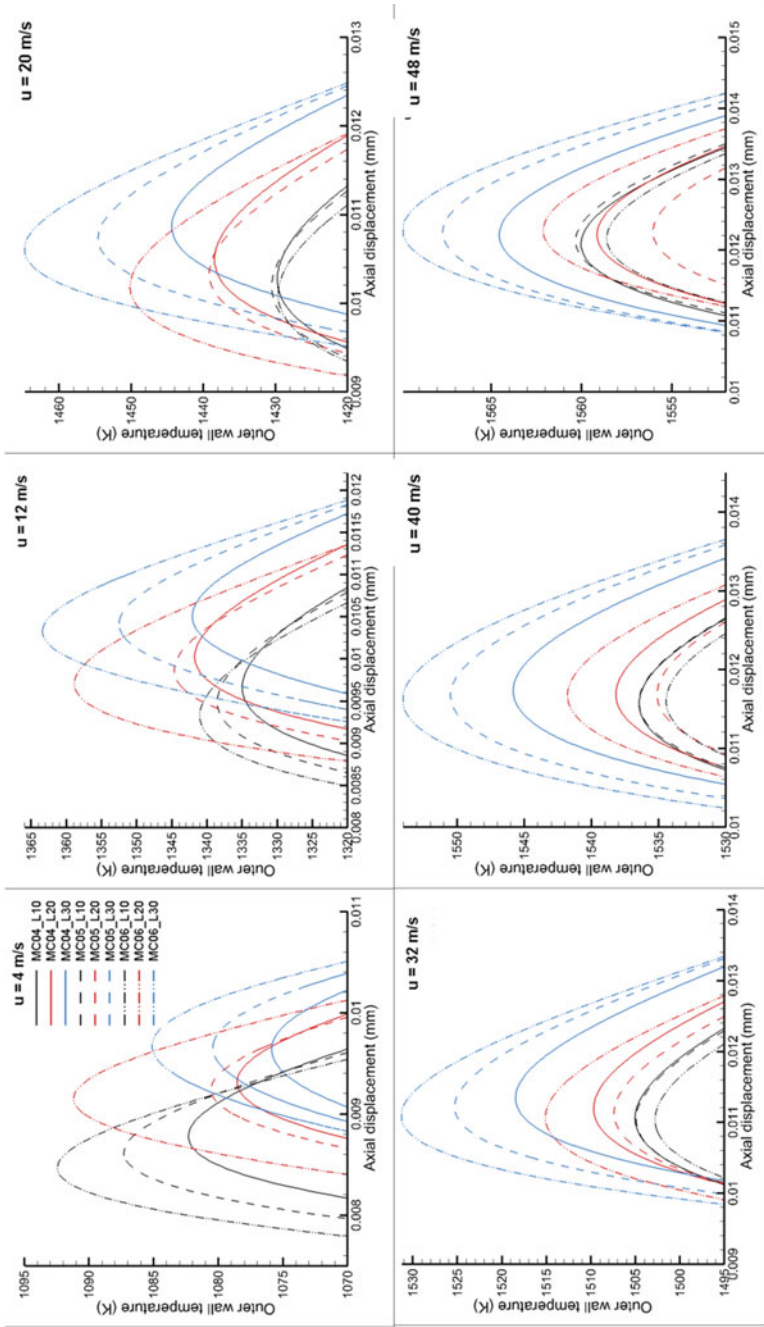


Fig. 7 Comparison of T_{out} for different micro-combustors at various inlet velocities

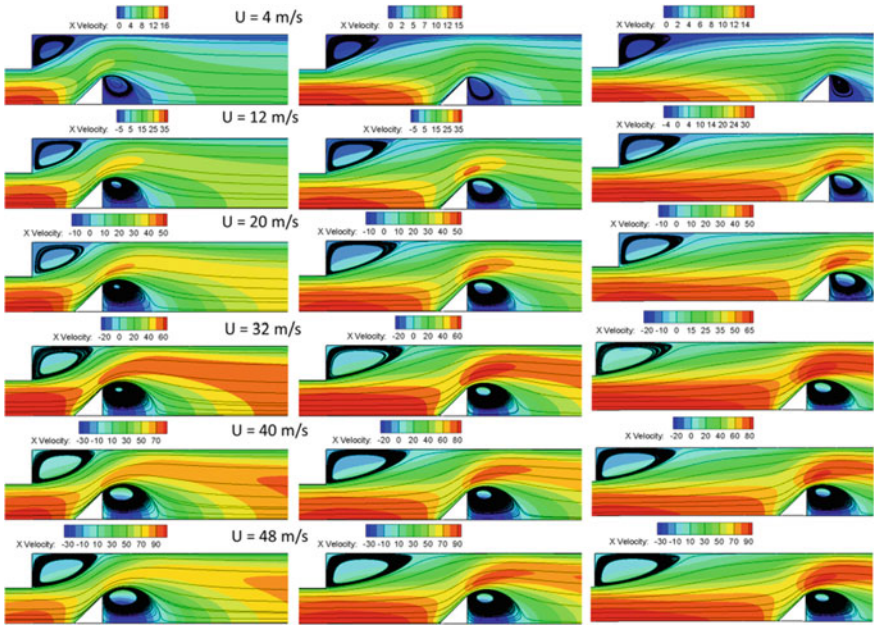


Fig. 8 Axial velocity contours overlaid with streamlines for MC04 for varying block locations

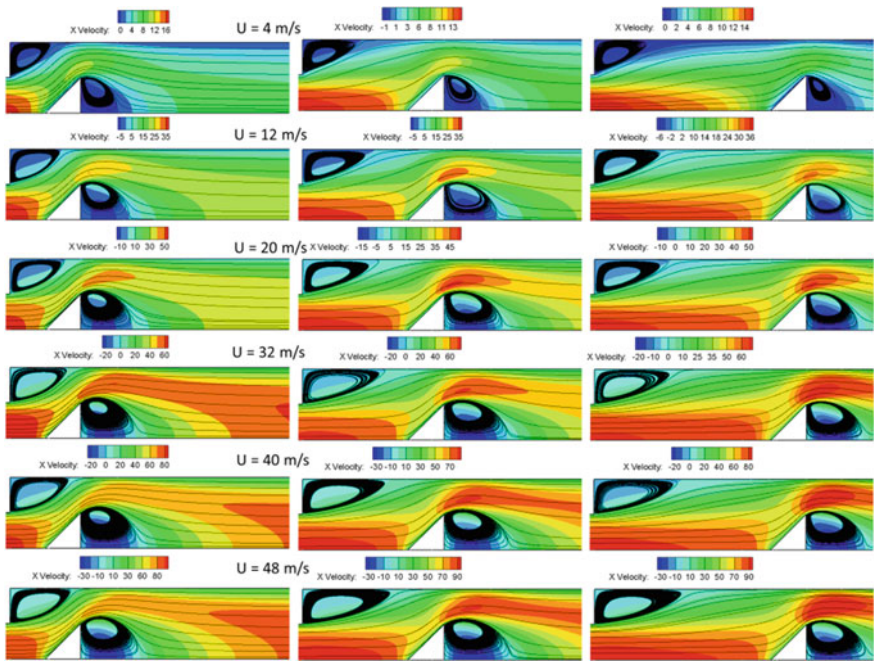


Fig. 9 Axial velocity contours overlaid with streamlines for MC05 for varying block locations

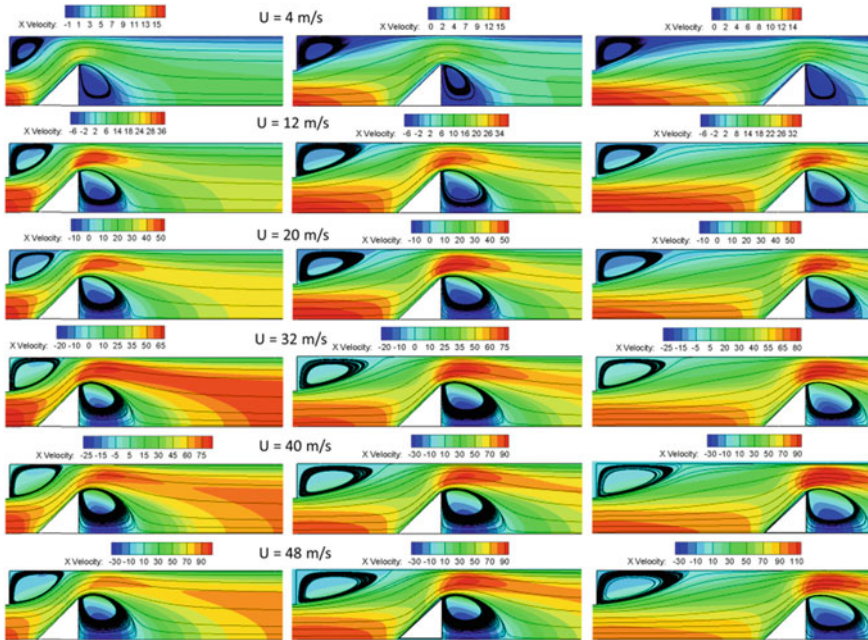


Fig. 10 Axial velocity contours overlaid with streamlines for MC06 for varying block locations

References

1. Mansouri Z (2018) Combustion in wavy micro-channels for thermo-photovoltaic applications—part I: effects of wavy wall geometry, wall temperature profile and reaction mechanism. *Energy Convers Manag* 198:0–1
2. Pan J, Zhang C, Pan Z, Wu D, Zhu Y, Lu Q, Zhang Y, (2020) Investigation on the effect of bluff body ball on the combustion characteristics for methane/oxygen in micro combustor. *Energy*, 190:116465
3. Akhtar S, Khan MN, Kurnia JC, Shamim T (2017) Investigation of energy conversion and flame stability in a curved micro-combustor for thermo-photovoltaic (TPV) applications. *Appl Energy* 192:134–145
4. Zhang Z, Wu K, Yuen R, Yao W, Wang J (2020) Numerical investigation on the performance of bluff body augmented micro cavity-combustor. *Int J Hydrogen Energy* 45(7):4932–4945
5. Chen H, Liu W (2019) Numerical investigation of the combustion in an improved microcombustion chamber with rib. *J Chem* 1–12
6. Wang H, Fang H, Lou B, Abubakar S, Li Y., Meng L (2020) Exploring the benefits of annular rectangular rib for enhancing thermal efficiency of nonpremixed micro-combustor. *J Chem* 2020:1–13.
7. Li L, Yang W, Fan A (2018) ScienceDirect effect of the cavity aft ramp angle on combustion efficiency of lean hydrogen / air flames in a micro. *Int J Hydrogen Energy*, 1–10
8. Pan JF, Wu D, Liu YX, Zhang HF, Tang AK, Xue H (2015) Hydrogen/oxygen premixed combustion characteristics in micro porous media combustor. *Appl Energy* 160:802–807
9. Bani S, Pan J, Tang A, Lu Q, Zhang Y (2017) Micro combustion in a porous media for thermophotovoltaic power generation. *Appl Therm Eng* 129:596–605

10. Yan Y, Liu Y, Li L, Cui Y, Zhang L, Yang Z (2019) Numerical comparison of H₂/air catalytic combustion characteristic of micro-combustors with a conventional, slotted or controllable slotted bluff body. *Energy* 189:116242
11. Bazooyar B, Darabkhani HG (2019) Analysis of flame stabilization to a thermo-photovoltaic micro-combustor step in turbulent premixed hydrogen flame. *Fuel* 257:115989
12. Akhtar S, Kurnia JC, Shamim T (2015) A three-dimensional computational model of H₂-air premixed combustion in non-circular micro-channels for a thermo-photovoltaic (TPV) application. *Appl Energy* 152:47–57
13. Li J, Chou SK, Yang WM, Li ZW (2009) Experimental and numerical study of the wall temperature of cylindrical micro combustors. *J Micromech Microeng* 19(1):015019

An Analysis of the Effect of E-mobility Trend on the Traditional Suppliers in the Global Automotive Industry



Akshay Suhas Narkar  and Tejas Pramod Naik 

Abstract The automobile is undoubtedly one of the best inventions in human lives. Since a decade, the automotive industry is on the verge of transformation due to certain technological megatrends. To combat global issues such as depleting oil reserves, rising fuel prices, and ever-increasing greenhouse gas and carbon footprint, all countries in the world have started considering the option of E-mobility. Although electrification is a sustainable solution for urban mobility, it is highly disrupting the business of major stakeholders within the automotive industry. This study aims at presenting a status quo of the E-mobility trend in the automotive industry. It also covers the risks associated with the trend for traditional automotive suppliers. For this purpose, a mixed approach consisting of both qualitative and quantitative methods have been used. Using a risk management approach, the major business risks due to E-mobility have been identified, and the level of impact has been evaluated. It was found that the E-mobility trend presents the suppliers with certain medium-to-high risks and various opportunities at the same time. At the end of this work, a set of strategies have been proposed on how the suppliers can position themselves in future automotive industry, which is more uncertain than ever. Crucial for business success would be the adoption of modern technology by anticipating market trends with the development of innovative business models.

Keywords E-mobility · Automotive industry · Suppliers · Business risks · Business opportunities · Business strategies

A. S. Narkar (✉)

SRH Hochschule Heidelberg, Ludwig-Guttman-Straße 6, 69123 Heidelberg, Germany

T. P. Naik

Mechanical and Industrial Engineering Department, IIT Roorkee, Roorkee 247667, India

1 Introduction

Today's world is dramatically changing. Certain megatrends are emerging in the global market that has been revolutionizing the industrial sector. They have always managed to help the economies of the countries flourish at a rapid pace.

When it comes to the automobile sector, an unprecedented transformation has already begun. The global automotive industry has found itself amid a disruption for several years now. The shift to driverless, electric vehicles (EVs), change of ownership, and a whole new digitized driving experience are directing these developments forward. Moreover, forces like globalization, entry of fresh players, supply chain digitization, and rise in cost pressure are shaping the face of the future auto industry. The last century was all about fine tuning of the production of automobiles to make them more efficient for mass scale. There is a more fundamental force for change from now on: Digital channeling along with safe and ecological drives to redefine the role that the automobiles play in human lives. To summarize, connected cars, autonomous driving, shared mobility, and E-mobility are the top four megatrends present in the current automotive industry [1].

The current climate change, in particular, is driving original equipment manufacturers (OEMs) and the suppliers to continually improve the environmental compatibility and carbon dioxide (CO₂) and particulate matter (PM) efficiency of their products. E-mobility is arguably one of the best solutions to tackle this problem and promote sustainability. Although it seems to be highly eco-friendly on the consumers' side, it has significant impact on the business of established stakeholders within the industry. The effect of this wave of transformation is not only limited to auto manufacturers. However, it will also affect the other participants in the automotive sector, including automotive component suppliers. There are certain highly specialized suppliers in the market that have been running their core business model on a single product group and are therefore dependent on a single source of revenue since their establishment. Due to the transition from internal combustion engines to electric motors, a large number of traditional suppliers are expected to be affected by this trend [2].

This study aims to address the status quo of E-mobility trend along with the risks involved for the traditional automotive suppliers in accordance with the rate of development of the trend. This study also intends to provide recommendations of certain strategies for the traditional suppliers, thus helping them to take precautionary measures against the imminent changes in future.

2 Methodology

Qualitative and quantitative research has been used to acquire relevant data for this study. Both primary and secondary data have been used for this purpose.

The qualitative approach has been conducted using semi-structured interviews with 7 different individuals employed in the automotive industry in Germany and India, two countries with entirely different scenarios regarding E-mobility trend.

The following interviews were conducted to acquire the required data:

- Interview 1: Development Engineer at OEM, Stuttgart, Germany
- Interview 2: Strategic Buyer at Tier-1 supplier, Stuttgart, Germany
- Interview 3: Development Engineer at Tier-1 supplier, Sailauf, Germany
- Interview 4: Product Development Manager at Tier-1 supplier, Pune, India
- Interview 5: Project Engineer at OEM, Chennai, India
- Interview 6: Purchase Engineer at Tier-1 supplier, Pune, India
- Interview 7: Senior Manager [Retd.] at OEM, Pune, India.

The responses recorded in the interviews helped to gain insights about the trend. The participants were given a choice to stay anonymous, considering their identity protection. Each interview took about 20–30 min. The interviews were based on a semi-structured method, i.e., subsequent questions were derived as per the responses.

The quantitative method in the form of the questionnaire provided statistical data about the expectations about E-mobility of 50 different individuals.

3 E-mobility

E-mobility is not a hyped topic anymore. It has clearly shown tremendous development potential in the past few years. Ability to cut substantial carbon footprint, reduction in operational and maintenance costs, the gradual development of charging infrastructure, a significant reduction in battery costs, and government incentives have made the EVs a perfect choice for future mobility.

Norway, China, Japan, USA, Germany, France, South Korea, and the Netherlands have been leading the race of E-mobility for a while. In contrast, developing nations like India, Brazil, and Eastern European countries somehow lack behind [3].

Currently, variants such as ICEs, Fuel Cell EVs (FCEV), Hybrid EVs (HEV), Plug-in Hybrid EVs (PHEV), and Battery EVs (BEV) are available in the market [4] (Table 1; Fig. 1).

Table 1 Powertrain variants and characteristics

Type	Power source	Range	Infrastructure	Sustainability
ICEV	Petrol or diesel	High	High	Low
FCEV	Hydrogen + Oxygen	High	Low	Average
HEV	ICE + Battery (internal charging)	High	High	Average
PHEV	ICE + Battery (external charging)	High	High	Average
BEV	Only battery pack	Average	Average	High

Fig. 1 Global forecast of powertrain variants [5]

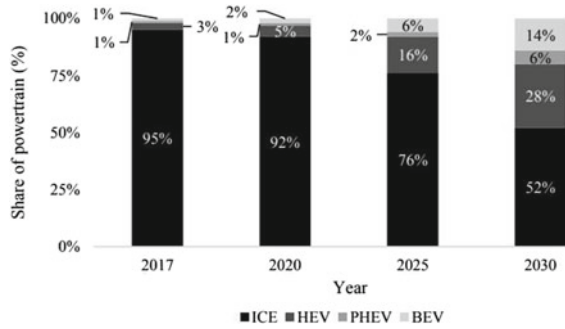


Table 2 Effect of E-mobility trend on individual parts [6]

#	Part(s)	Vulnerability
1	Transmission, engine, fuel, and exhaust system	High
2	Axles, brakes, climate control, and cooling system	Medium
3	Exterior, interior, steering, infotainment system	Low

Owing to the distinct powertrains, the future beholds production of all of them. It can be seen in the above forecast that the ICE powertrains are gradually losing their share after 2020, whereas HEVs are showing immense potential. BEVs, after a slow start, advance for a larger share after 2025.

In the E-mobility age, apart from powertrain components, some of the other major auto components are subjected to change, due to inter-linkage.

Table 2 represents the effect of electrification on major parts of a vehicle. It can be clearly seen that the powertrain components including transmission systems, engine components (pistons, cylinders, crankshafts, camshafts), fuel supply systems (tank, injection, filler, line), and exhaust systems (mufflers, resonators, catalytic converters, pipes) are at risk at the highest level than any other parts due to the E-mobility trend.

4 Risk Analysis

Using brainstorming and checklist methods, the following risks were identified. The risks have been further classified into two scenarios: Business risks with the current product portfolio and business risks, while entering the E-mobility sector. For convenience, the risks are marked as R1, R2, R3, ..., R16.

4.1 Business Risks for Current Product Portfolio

R1: Compliance risks: The introduction of certain emission norms such as Euro 6 in Europe, Bharat Stage VI in India, China 6 in China and other such norms worldwide have put the exhaust system developers under relentless pressure to develop systems with zero emissions [7]. Thus, they are subjected to compliance risks country wise.

R2: Strategic market: The automotive market is currently developing much slower than in the past due to changes in buying patterns, fuel prices, interest rate levels, and uncertainty in the powertrain forecast, while exhibiting increasing instability and ambiguity [8]. A shift in forecasted sales could have a severe impact on the business.

R3: Technology and innovation: Powertrain electrification in automobiles is progressing, and thus, the optimization of ICE powertrains is being pressurized. The rapid pace of development in battery technology and cost reduction can lead to early adoption of BEVs, thus jeopardizing the business of ICE powertrain suppliers. The transition ICEVs to BEVs will result in the increasing value of new products, thus affecting suppliers' return on sales (ROS) and return on investment (ROI) on their products.

R4: Obsolescence of products: An ICE drivetrain is built out of around 2000 + parts, whereas a BEV drivetrain comprises of only 20 parts [9]. The parts are already becoming less relevant and are getting replaced with new ones. The decline of the ICE will result in gradual obsolescence of their core products, thus resulting in diminishing relationships with the current suppliers, as their services will not be required anymore.

R5: Shutting down of plants: The suppliers possess a prominent risk of shutting down, downsizing production lines, and selling some of the operating divisions in the E-mobility age in certain regions, which can incur unavoidable costs. This could adversely affect the profitability margin and reduction in market share.

R6: Intense Competition/New Entrants: The suppliers are subjected to risks of being surpassed by existing competitors or new entrants and their products being substituted by new products. The availability of new high-tech substitutes to core products directly affects the aftermarket business. Moreover, new entrants like Tesla have been using their all force to target the key markets all over the world. Although they will need time achieve the required expertise concerning the dynamics and other mechanics, it still creates a risk for the experienced suppliers.

R7: Change in OEMs' External Sourcing Strategy: The OEMs have increased the external sourcing of engineering services as a reaction to the uncertainty of different powertrain technologies, thus boosting the models' diversity and ever shorter model lifecycles [10]. However, it is plausible that OEMs will utilize their own engineering services for cost reduction in future. This will significantly reduce the demand for projects, and thus, contraction in future business volume.

R8: Pricing risks: There are high chances that OEMs will attempt to negotiate the price of products and services with their suppliers in order to compensate for the cost of production lines for new powertrain technology on their side. Moreover, there is always immense pricing pressure from procuring bodies and leaner competitors, particularly in the rising markets.

4.2 Business Risks for Future Product Portfolio (E-mobility)

R9: Project risks: Many inherent risks, including unforeseen technical hurdles, may arise during the development and production stage of new E-mobility projects, and this could lead to higher series initial costs or higher capital spending than they were initially proposed. The range and complications of projects can entail risks in planning, calculating, implementing, and processing.

R10: Personnel risks: The development of future E-mobility systems will require employees with individual-specific skillsets, especially in the Research and Development (R&D), product management and sales [11]. Moreover, the reduction in demand for traditional components due to E-mobility will result in laying-off the current staff.

R11: Procurement risks: New E-mobility products will demand a group of entirely new Tier-2 suppliers. It will take time for the company to gain trust and form strong business relationships with the new suppliers.

R12: Production risks: E-mobility production will demand a new set of tools and machinery and thus, new manufacturing methods. This means the investment of time and money in new production processes.

R13: Product piracy risks: E-mobility systems are supposed to be developed with high-quality standards and a high degree of innovation, and thus, it makes them vulnerable to product piracy to a great extent. Alternate average-quality products are generally available, especially in the third-world country markets like India and China, with significantly reduced prices, which disrupts product demand and thus results in a request for price reductions.

R14: Product Launch: The launch or development of a new product in the E-mobility era can be a challenging task for traditional suppliers. The underlying success factors for a new product launch include the timely design optimization by the OEMs before start of production (SOP), the readiness of production facilities, efficient manufacturing processes, precise number on targeted volumes, and quality of the product. The failure-to-success to any of these factors will result in incurring the risk of new product launch.

R15: Liquidity risks: Every company has the pressure of not meeting its payment obligations before deadlines. Due to increasing cost pressure in the investment of

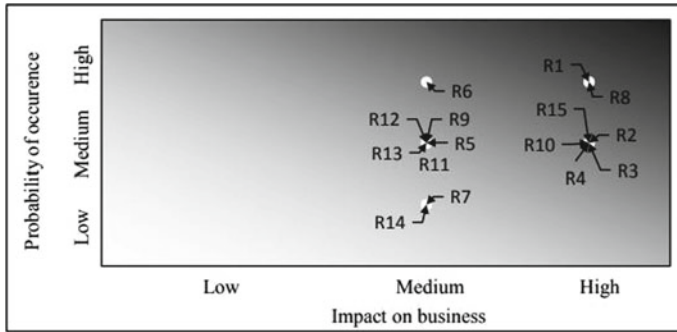


Fig. 2 Risk severity

E-mobility products, liquidity risks may occur if current equity or debt financing schemes cannot meet the funding needs. The loan and bond agreements include certain limitations with an obligation to meeting financial bonds. Under some instances, the investors are entitled to call the debt before maturity, even if promises are not fulfilled, which would increase the debt amount being due instantly (Fig. 2).

5 Strategy Development

Opportunities come hand-in-hand with risks. Although the challenges are substantial for traditional suppliers, they offer excellent opportunities to grab new markets and further minimize their expenses.

For developing strategies, scenario analysis has been used considering the timeframe of the E-mobility trend and high vulnerability for the powertrain suppliers.

5.1 SCENARIO 1: High Vulnerability and Slow Electrification

STRATEGY 1: Diversification Through Consolidation

Several components will be used in both HEVs and BEVs simultaneously. One of the most common parts includes a traction battery pack, which is used to store energy generated during the braking mechanism for HEVs and from externally sourced power for PHEVs. Today, battery constitutes one-third of BEV’s total cost, making it overly expensive [12].

However, building EV components has not been the core proficiencies of most traditional suppliers. Since battery pack is a brand-new product to them, it would cost the company much pressure in terms of R&D investment and time to develop the product on their own.

OEMs have been following the concept of consolidation for a long time. It seems that they have realized that grouping up with industry peers, mainly to keep pace with non-core technological challengers instead of managing impending risks alone, will be fundamental to future success strategies [13]. Therefore, the suppliers should consider developing “strategic alliances” or “vertical partnerships” with battery technology specialists. Forming alliances could be in terms of joint ventures or acquisition of startups, who are already developing batteries and looking for a platform to establish themselves in the automotive industry. There are always smaller companies that manufacture auxiliary auto parts, such as batteries, alternators, and inverters.

The further improvement of energy storage systems could be in the form of increasing the battery density, optimizing the battery life intelligently, downsizing the outer covering, increasing durability, reducing charging time, reliability, and safety. Also, investing in a charging infrastructure might be a promising idea, thus optimizing the charging performance and reducing the charging time.

This strategy would allow the suppliers to cut down R&D expenditures along with the development of new products even faster in the market. The exchange would be in the form of expertise and market share for both.

STRATEGY 2: Product Development

The government agencies will continue to put pressure on the OEMs and suppliers to reduce CO₂ emissions. To tackle the challenge of complying with intensifying environmental regulations, traditional auto suppliers, especially the engine and exhaust system manufacturers, need to develop efficient products over the next few years. It means that cars with conventional engines must be fitted with special devices such as engine control systems and improved exhaust after-treatment technologies.

This creates an opportunity for the exhaust system suppliers to transform themselves into a more efficient supplier for a low-emissions and zero-emissions age. Zero-emission systems and air quality systems are the latest technologies that the future sustainable market needs.

This will expand their business and improve their market position simultaneously. Using the expertise developed over the years and recruiting additional experts would help them to achieve this goal.

STRATEGY 3: Market Development

The pace of electrification is lower than expected in the developing Arabic and Asian countries. For example, five out of the top ten most abundant oil reserves are located in the Gulf countries. When it comes to E-mobility, they lack charging infrastructure and the charging stations are built at a slow pace [14]. Also, coal constitutes for 48.7% of the total electricity production in India, which is highly non-sustainable source [15]. This leads to the conclusion that the nations in the Middle East and Asia will continue the usage of ICEs with a parallel growth of hybrids. BEVs have a long way to go.

Consequently, this provides powertrain players with a chance to establish themselves in such markets and thus expand their business. This could aid the companies

in terms of extending their footprint, and thus grabbing a new market share and increasing earnings.

5.2 SCENARIO 2: High Vulnerability and Fast Electrification

STRATEGY 4: Cashing Out

If a supplier located in a developed country has a little technological leeway or not enough financial resources to invest in a new portfolio of E-mobility products or enter new markets from scratch with a limited span left, it may be reasonable to consider cashing out as soon as possible.

6 Discussion

E-mobility will definitely reshape the auto industry. The automotive industry has managed to master an impressive range of challenges over the last century. However, the level of challenges is elevated than it used to be, and the upcoming disruptions will be on a much bigger scale.

Although it is highly impossible to estimate the nature of powertrains after a decade from now, the suppliers should get themselves ready to play a role in the car industry's profoundly diverse prospect. Powertrain suppliers need to prepare themselves for considerable declines in their market share and sales volumes. They will be obliged to pay high production costs, primarily because of the excessive R&D to design and manufacture different powertrains.

Suppliers will have the choice to adapt to the E-mobility trend by being the first movers or followers. In the latter, the risks are higher as it will be not easy to catch up with the other players. Moreover, the competitors may develop their expertise and become the market leaders within that period.

For suppliers that grasp the new realities, there are opportunities to adapt to the new world and position themselves innovatively through diversification, including sectors beyond the core competencies so that they prosper in the broader mobility ecosystem. They should also expand their technological expertise about the critical components required in EVs and thus be among the leaders of the future mobility. Finally, they should increase the depth and breadth of added value in the production of their core product in the internal combustion engines.

7 Conclusions

- The transition from ICEs to hybrids and finally to BEVs will be a long-term roadmap, thus providing enough time for suppliers to revise their business model.
- The powertrain suppliers possess medium-to-high risks, including country wise compliance risks, obsolescence of products, high pricing, R&D costs, and threats from new entrants. To tackle these challenges, diversifying products through consolidation with battery manufacturers, developing air quality and zero emission systems along with sustainable after-exhaust treatment systems, and expanding markets with current products in the unexplored regions are some of the strategies that can be implemented to increase profitability margin and market share.
- To conclude, adaptability to the new era of E-mobility by transforming its core product portfolio can help the suppliers to survive the technological and financial pressure that this trend is about to bring upon their business.

Acknowledgements The author, Akshay Narkar, gratefully acknowledges the interview participants for their valuable time during the process. He expresses sincere gratitude toward all the individuals who helped him to accomplish the goal of completing this research paper.

References

1. Ataii E et al (2019) Mobility 2030: transforming the mobility landscape
2. Betatti A et al (2018) The future of mobility 3.0
3. Busse A et al (2019) E-mobility index 2019
4. Andre F et al (2017) From CO₂ neutral fuels to emission-free driving
5. Andersen M et al (2018) The electric car tipping point: the future of powertrains for owned and shared mobility. Boston Consulting Group, p 18
6. Borowski A et al (2019) Staying in the driving seat: how automotive suppliers should deal with electromobility
7. CPT Group GmbH (2019) Worldwide emission standards and related regulations
8. Fulthorpe M (2014) Five critical challenges facing the automotive industry
9. Forbes webpage. <https://www.forbes.com/sites/sap/2018/09/06/seven-reasons-why-the-internal-combustion-engine-is-a-dead-man-walking-updated/#4e3bfae1603f>. Last accessed 02 June 2020
10. Bertrandt AG (2019) Bertrandt annual report 2019
11. Seider C (2015) Automotive 4.0: sensing the road ahead for tier 1 suppliers. NTT Data Deutschland GmbH, p 56
12. Lutsey N, Nicholas M (2019) Update on electric vehicle costs in the United States through 2030
13. Becker D (2019) Global automotive executive survey 2019
14. Europe Autonews webpage. <https://europe.autonews.com/automakers/bmw-rd-chief-sees-rising-demand-diverse-multifunctional-powertrains>. Last accessed 05 June 2020
15. International Energy Agency (2020) India 2020: energy policy review

Faster RCNN for Face Detection on a FACENET Model



U. Syed Abudhagir, Karne Anuja, and Jigar Patel

Abstract In this work, an individual face detection process is involved and outcomes which are more exact are gained within a short amount of spell through less amount of intricacy on a face detection yardstick that is well-thought-out as a podium by using FACENET. Enhancement is added to the performance by using a Faster Regional Convolutional Neural Networks (RCNN) process entailing diverse number of stratagems named as hard negative mining that separates positive and negative examples, multi-scale training to train different scales images, model pre-training and concatenation of characteristics on one shot learned images with loss functions with the support of region of interest (ROI) and regional proposed networks (RPN). As a consequence, this scheme comprises of one of the best face detection performance, as the images in dataset are one shot learned. It has the triplet loss which helps to avoid more unrelated example of pictures while passing through the convolutional sheets.

Keywords Regional convolutional neural network · Region of interests · Face detection · Hard negative mining · Feature concatenation

1 Introduction

Nowadays, use of unconventional apparatus in every field became popular. Artificial intelligence is the cutting-edge technology which is making the anthropoid work to get demounted and helping us in every possible occasion. A lot of biometrical security systems are being developed. These are using physical contact for face detection and also there are voluminous problems in the existing systems. Computer vision can be helpful for various aspects if some extra assets or functions are added to the current

U. S. Abudhagir (✉) · K. Anuja · J. Patel
Department of Electronics and Communication Engineering, B. V. Raju Institute of Technology,
Narsapur, Medak District, Telengana, India
e-mail: syedabudhagir.u@bvrit.ac.in

J. Patel
e-mail: jigar.patel@bvrit.ac.in

© The Author(s), under exclusive license to Springer Nature Singapore Pte Ltd. 2022
K. Govindan et al. (eds.), *Advances in Mechanical and Materials Technology*,
Lecture Notes in Mechanical Engineering,
https://doi.org/10.1007/978-981-16-2794-1_25

283

procedures. Detection of face is considered as key in order to access many face regarding bids. These applications may be face classification, face recognition, face bunching, face dissection, etc. In topical years usage of biometric claims is too often, so computer vision is mentioned as the emerging tool to handle all the profligate technology nonetheless people need bright entities with hand-crafted features in computer vision field and each personage can only accomplish individual tasks at an optimal level. To complete a progression, these optimal tasks should be combined and the results may not be a full magnitude here. In order to avoid, Convolutional Neural Network (CNN) is concealed to overcome the difficulties in computer vision field. In this paper, the unrehearsed CNN framework called Faster Regional Convolutional Neural Networks (RCNN) on a FACENET model is used.

Machine learning is taking the prime and many applications dispute solving skills using trending methods. There are different encroachments in this field that will campaign us to have a closer idea to any problem while processing. This area has a genre involving machine work to larger extent. Face recognition is a sensitive field that has to be fingered carefully. It has been arising out from various ways that are considered as backward comparing to the present methods. Newfangled implementations are added to the prevailing works. Some inventiveness is made based on the previous predictions. Faster RCNN is emerged out from past face detection problems with the content that may solve the issues humans came up with. Computer vision is considered as the mostly used application, keeping in mind the use it has with the many projects. Before coming up with faster RCNN, there is already an idea on convolutional networks which are the most resourceful detection schemes unlike OpenCV. Convolutional neural networks are used for dealing out with a preexisting dataset and applying different techniques on it leads to better results which make our project dissimilar from the existing.

2 Related Work

Viola and Jones [1] have proposed rectangular HAAR-like features in a cascaded AdaBoost classifier for triumphing real-time face detection in 2001. Characteristic size was too large and also it could not properly handle non-anterior faces and aspects consisting in the wild.

Zhu et al. [2] proposed a methodology to derive the more intricate features like HOG that tops to the occurrence of inclinational positioning of circumscribed portions of an image.

Later SIFT, SURF [3] have been proposed in 2013 by Li, J., and Zhang, Y., which pleats the internal feature points of the iris and then limit the scale indifferent key points in the iris image to express later the key points using the local patterns that are present around the key points.

Yang et al. [4] have proposed a novel aggregate channel features, which was premeditated as the ratio of two factors.

Liao et al. [5] introduced a retrieval-based manner that gains back the images and diversified with differentiate learning. But this type of training and testing are more time-consuming methods. In this approach, performance increment was relatively limited.

Davis E. King proposed Dlib-m which is a well-known Dlib C++ Library [6] took Support Vector Machine (SVM) classifier in aspect detector. Increasing the process in order to cope with the errors of detection was another emerging topic.

Zhu [7] came up with a method to seizure faces that involve different views and expressions in a deformable method.

Chen et al. [8] have proposed a model to ensure the detection of faces with face position. In their model, they have achieved best performance through accuracy and less time. In recent years, the advancement in the area of face detection using deep learning approach significantly dominates the traditional computer vision processes.

Girshick [9] and others worked on object detection and combined regions with convolutional neural networks.

Girshick [10] came up with fast RCNN for detection by training with the help of a deep network and boosted the existing methods in accuracy.

Li et al. [11] presented a method for wild faces detection, which integrates a convolutional network and a 3D face model in a multi-task discriminative agenda.

Recently, Jiang and Learned-Miller [12] have proposed the faster RCNN for nonspecific object detector and accomplished better results. In addition to this, numerous efforts have been done to rectify the faster RCNN architecture.

3 Model

FACENET model is a prototype which is fulfilled by one shot learning. It can be used to cluster faces and has embedded images with triplet losses. Once a planetary of vector is formed, applications such as recognition, corroboration and clustering can be implemented. Here the new imageries have been auxiliariated without the use of repeated training. At initial stage, the picture goes through sophisticated layers. Feature maps are extracted. A coasting window has used in RPN for each location over the feature map. For each location, to bring out regional proposals anchor packets are used. A cataloguing layer predicts and outputs whether there is object or not for k chests. A regression layer outputs 1 k for the coordinates of k boxes. RPN using CNN will be swapped instead with Selective Search (SS) for RPN. At later stages, Region of Interests (ROI) pooling has performed. The pooled area goes through CNN and two Fully Connected (FC) branches for Softmax and hop box regression.

Since the convolutional layers are shared to citate the feature maps with various yields at the end, training process is different. Train RPN with FACENET model. Separate detection network can be trained with FACENET. Use the detector network to prime the RPN training, fix the shared convolutional layers and fine-tune only the unique layers of RPN. Having the convolutional layers fixed, fine-tuning is done on the inimitable layers of detector network. This proposition is tested with feature

extractors of FACENET having output strides for the extractor. Training set along with testing set is split from the dataset as 70% and 30%, respectively. Then a pre-trained model is loaded and used to engender features for the selected images of firm resolutions.

Faster RCNN is applied over the dataset trained over FACENET. Faster RCNN implementation is better than other slants in matching strategy, bounding box ratio, data augmentation and in the feature map used for object detection. As there is no need to conduct 2000 proposals for one single image and the dataset is one shot learned, the exactitude is increased and time is fewer for detection process. This work is developed by applying faster RCNN which is a deep learning charter to FACENET, as it gives the precise results. This context consists of a proposed network with regions called as RPN to develop a section proposals list which embraces objects pain staked as ROIs and faster RCNN network that refines the boundaries of previously developed ROIs after classifying each region of interest. In this work, some more layers are added to the existing faster RCNN. First, train the model with the set and then use this on test set. Initially, the CNN model of faster RCNN is taken and drilled using the wider face dataset. Same dataset is used to examine the pre-trained model in order to generate hard negative mining's as shown in Fig. 1.

Fig. 1 Procedure in the form of flowchart



In the successive step, feed the images to develop hard or solid negative mining's into the network. The model generated will be fine-tuned on the face detection standard dataset. End process includes the multi-scale training and feature concatenation to rally this model. This whole training procedure has the similar training method as that of faster RCNN. Final stage usually converts the rectangular boxes presenting detection to ellipses as human faces are elliptical in shape. Functional procedure of each part of faster RCNN is explained in the ensuing section which encompasses the major part of the project.

3.1 Hard Negative Mining

The first is the Hard Negative (HN) Mining which is for upgrading the recital of the model for object detection tasks in deep learning. These are the areas of ROIs named as the hard negative. The network nosedives in involving a correct prediction in these parts. So, iterate the process by resending these negatives so as to improve the performance of proposed model and have a better classification by having the fewer positives in false.

A hard negative is the region whose Jacquard index, i.e., area of intersection and area of union ratio is less than 0.5. It involves in construction of both positive ROIs and a subset of negative ROIs would be given to the region of interests so as to improve the act of the model. Here this will go through this stage to make the foreground and background ratio to 1:3.

3.2 Multi-scale Training

In multi-scale training, immovable size of images is maintained. The way of training process can be seen in Fig. 2. The detector can cram the image having features made with similar magnitude. This scale invariance may be helpful for efficient work later on. Usually, three or more values are consigned in order to pass onto the network.

3.3 Feature Concatenation

Faster RCNN uses Feature Concatenation in Fig. 3 which is nothing but summation of several input layers to rundown to one output layer. ROI pooling is done in order to use a single map of features for all RPN's. This approach can't be used for all the images, because sometimes this may leave some important features off. This results in many important parts loss and that leads to less performance. Feature maps of multiple convolutional layers are combined and to improve the ROI pooling higher and lower features are also included. This bid combines all the ROI pooled features

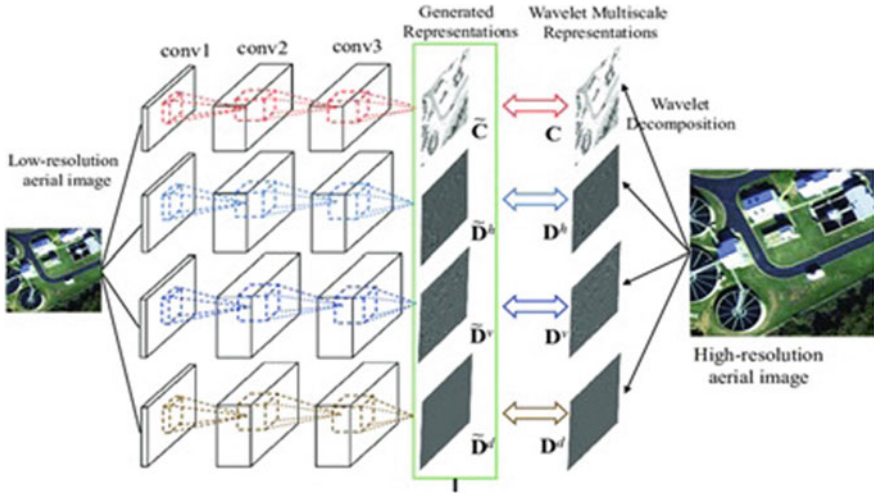


Fig. 2 Showing multi-scale training

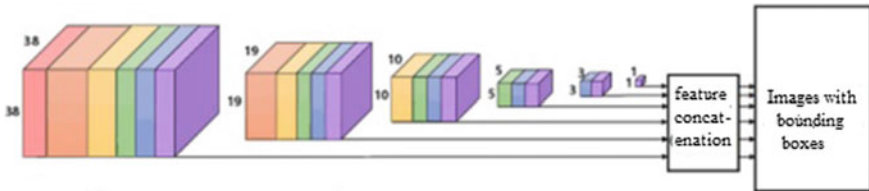


Fig. 3 Picture showing feature concatenation scheme

in every convolutional layer to match the unique features. Mostly these features are L2 pooled. One layered CNN will be passed to the original network in order to match with any one of the channels.

4 Implementation

This process is appraised on a face detection benchmark using a pre-trained model, that has a total of nearly 10,000 images used for testing and called as nn4_small2 dataset whereas trained set is from Labelled Faces in the Wild (LFW) with 30,000 images which generates triple loss each time when they are passed into convolution layers and these images are already one shot learned and has 128 embeddings with trio loss functions. This dataset has chosen and compared with the FACENET images. This procedure is started after giving the imageries some initial values. Every factor picked is started with zero and ignores the picture or image that has the values which

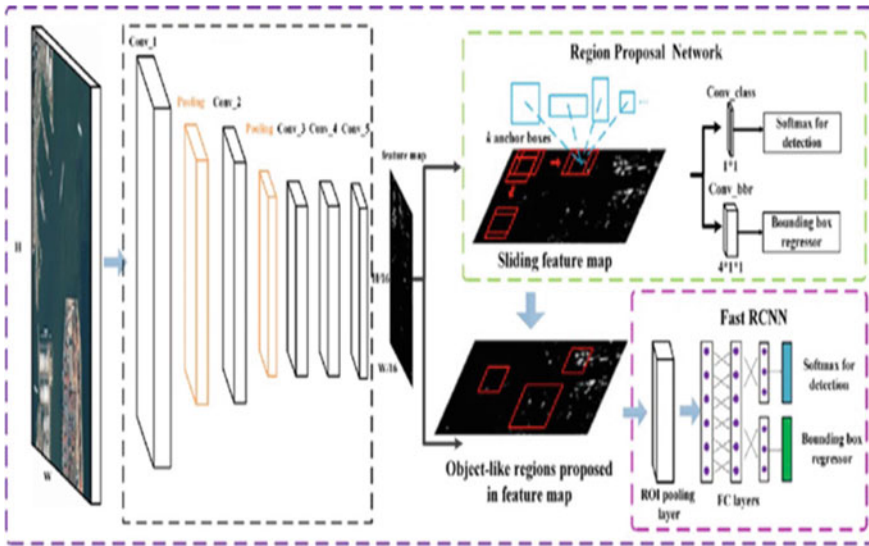


Fig. 4 Faster RCNN architecture

are greater than the near alike values. At this stage, many images are deleted. The detailed faster RCNN architecture is shown in Fig. 4.

A pre-trained model is used to get into the networks for some hundred times with the rate of learning rate to some 0.001. Assumption of any of the original ratio of size helps the pre-trained images to get compared. Short and long sides are rescaled. Horizontal flipping is done for data augmentation. During the time of training images with pixel size 160 and ratio 1:1 are used. Then the background values and foreground values are compared and checked if the comparison is more than 0.6. In order to have the equivalence well, ratio between background and foreground is fixed as 1:2 ratios. Now the dataset is passed to CNN. The images that are more comparative than the fixed are moved to next step whereas the images having the harmonizing less than 0.6 are discarded. These are considered as hard negatives. This procedure of finding hard negatives is repeated up to some iteration until all the images having this 0.6 value are deleted. This is finally used for our detection task. This model is also verified by changing the dimensions and aspect ratios to different values. Even if new images are added to this dataset, retraining the model is not required. Both increments and decrements in images have been tried. But some limitations are given while increasing the size of copy.

Same procedure is repeated here as previous. All the outputs from each convolutional layer are joined. The scales after changing, may give different or fixed results. Here combining all the iterations per image, nearly 30,000 iterations are done with learning rate 0.01. In each step of generating the region proposals, a total of 90 proposals are generated. One among this is regarded as face if its match is greater than 0.6. One shot learned and embedded images are used in this work. And also,

Table 1 Value assignment

Blur		Expressions	Illuminations	Occlusion		Pose
Normal	High			Normal	High	
0.6	1	1	1	0.6	1	1

generated triplet loss at each stage and applying faster RCNN increases the accuracy and performance and decreases complexity compared to existing models (Table 1).

5 Results and Discussion

Below are the two tables, one is representing the datasets along with features and another one shows comparison between the different approaches present along with the specifications of this model. The tables show the process approach in this method and in various existing methods regarding batch sizes, resolutions, anchor boxes, speed and accuracy (Tables 2 and 3).

Table 2 Ablation studies of the proposal along with previous works

S. No.	Dataset	Triplet loss	Length	Scale
1	Kaggle	No	Small	Fixed
2	ImageNet	No	Long	Unfixed
3	Google	No	Long	Unfixed
4	FACENET	Yes	Long	Unfixed

Table 3 Different neural networks

Approach	Reference papers	Batch size	Resolution	Anchor boxes	Speed	mAP (%)
RCNN	Rich feature hierarchies for accurate object detection and semantic segmentation	1	224×224	Around 50	120	50–60
Fast RCNN	Fast R-CNN	1	500×500	Around 100	2000	60–70
Faster RCNN	Face detection with the faster R-CNN	1	1000×600	Around 4800	125	86–90
Faster RCNN with FACENET	Proposed Model	2	1000×800	Around 5000	2250	96

CNN is an interdisciplinary field of computer vision achieving enormous amounts of attention in the past years. Since CNNs are introduced, self-driving vehicles took the center stage. The major reason in having no proceedings with this issue by structuring a standard CNN tracked by a Fully Connected (FC) layer. Length of the productive layer is variable, because of the number of incidences of the objects of notice is not stable.

RCNN is to face this incident of choosing a greater number of regions in selective and extracting 2 k regions from these images to use them as region proposals. It takes more amount of time to train the system to classify 2000 region proposals per image. It is not possible to execute in real time because it took nearly 47 s for each test image. Static search algorithm has been used in this work. As there is no trending in that stage which leads to the generation of bad candidate region proposals, RCNN is used.

An improvised object detection procedure is familiarized and named it as fast RCNN. This way is similar to R-CNN algorithm. The difference is that, instead giving the RPN to the CNN. Train and Test image is fed to produce a convolutional feature map. Region of proposals are found from the convolutional feature maps and bended to squares using a RoI pooling layer and also redesigning them to an immobile size has done so that it can be given to the FC layer. A Softmax layer is used from the RoI feature vector.

Fast R-CNN has more speed than R-CNN because of that it does not require prior 2 k region process to the neural network every time. In replacement, the convolution operation per image is fixed and generation of feature maps is involved. The CNN is present in fast R-CNN generally pre-trained on the classification task of ImageNet using its final pooling layer called as “RoI pooling” layer and its final FC layer will be replaced by two divisions $\times(K + 1)$ category Softmax layer division and a category-specific bounding box regression division. Into the backbone CNN, the entire image is given and features from the previous convolution layer are taken. According to CNN used, the characteristic output maps are much smaller compared to the original image size. This relies to pace the CNN backbone, comprising of 15 numbers in the VGG backbone. The object proposal windows are found from a region proposal method like selective search. The exceptional case of RoI pooling is spatial pyramid pooling (SPP) layer with unbiased one pyramid level. The layer chiefly splits the structures from the selected proposal windows which come from the region proposal algorithm and goes into sub-windows of size height/Height by width/Width and makes a pooling operation in each of these sub-windows. A fixed-size output features of size irrespective of the input size is given. The output is compatible with the network’s first FC layer. The Softmax classification division gives probability values of each ROI fitting to K categories and catching one from all background categories. The bounding box regression division output is to make these bounding boxes from the RPN procedures more accurate.

Some images in Fig. 5 of well-known people with faces from the dataset bounded by a rectangular box if the image needed is recognized. The images are indicating the faces, with the rectangular box bounded around the face image implying that they are detected. Images of dataset may have similar classes taken in different conditions



Fig. 5 Examples with rectangular bounding box

and also different poses, i.e., the same person images will be under same class but considered as non-similar picture.

6 Conclusion

This proposition is a dissimilar method in order to detect faces with the help of deep learning techniques. It came up with addition of techniques to make the application more advanced. Most importantly it achieved the increment in accuracy using faster RCNN framework which has more impact on the images in dataset. It used one shot learned, hard negative mining, feature concatenation and multi-scale training as the extra boostings to the framework. This made the training procedure less complex and the results have taken with less time. It ranked as the best compared to the erstwhile methods.

References

1. Viola P, Jones M (2001) Rapid object detection using a boosted cascade of simple features. In: 2001 IEEE computer society conference on computer vision and pattern recognition. CVPR 2001, vol 1. IEEE, p 1
2. Zhu Q, Yeh MC, Cheng KT, Avidan S (2006) Fast human detection using a cascade of histograms of oriented gradients. In: 2006 IEEE computer society conference on computer vision and pattern recognition (CVPR'06), vol 2. IEEE, pp 1491–1498
3. Li J, Zhang Y (2013) Learning surf cascade for fast and accurate object detection. In: Proceedings of the IEEE conference on computer vision and pattern recognition, pp 3468–3475
4. Yang B, Yan J, Lei Z, Li SZ (2014) Aggregate channel features for multi-view face detection. In: IEEE international joint conference on biometrics. IEEE, pp 1–8
5. Liao S, Jain AK, Li SZ (2015) A fast and accurate unconstrained face detector. IEEE Trans Pattern Anal Mach Intell 38(2):211–223

6. King DE (2009) Dlib-ml: a machine learning toolkit. *J Mach Learn Res* 10:1755–1758
7. Zhu X, Ramanan D (2012) Face detection, pose estimation, and landmark localization in the wild. In: 2012 IEEE conference on computer vision and pattern recognition. IEEE, pp 2879–2886
8. Chen D, Ren S, Wei Y, Cao X, Sun J (2014) Joint cascade face detection and alignment. In: European conference on computer vision. Springer, Cham, pp 109–122
9. Girshick R, Donahue J, Darrell T, Malik J (2014) Rich feature hierarchies for accurate object detection and semantic segmentation. In: Proceedings of the IEEE conference on computer vision and pattern recognition, pp 580–587
10. Girshick R (2015) Fast R-CNN. In: Proceedings of the IEEE international conference on computer vision, pp 1440–1448
11. Li Y, Sun B, Wu T, Wang Y (2016) Face detection with end-to-end integration of a ConvNet and a 3d model. In: European conference on computer vision. Springer, Cham, pp 420–436
12. Jiang H, Learned-Miller E (2016) Face detection with the faster R-CNN. ArXiv preprint arXiv:1606.03473

Study of the Degradation in a Unitized Regenerative Fuel Cell



Amit C. Bhosale, Reeshab Goenka, and Prakash C. Ghosh

Abstract The study details out the various causes of ageing of a unitized regenerative fuel cell operated in its respective modes, viz. fuel cell and electrolysis mode. The study is carried out when electrolysis mode is carried out at higher temperature of supplied water, i.e., 45 °C. The durability of the cells is examined with respect to the membrane, catalysts used (Pt/C and IrO₂) and the bipolar plates. The results analyzed using scanning electron microscopy, transmission electron microscopy and inductively coupled plasma technique reveal electrolysis mode to be the primary cause of URFC ageing. Furthermore, oxidation base of the catalyst, i.e., carbon leading to the catalyst agglomeration and its further loss over time is primary result of the high temperature electrolysis. Results also reveal the electrode getting delaminated from the solid electrolyte, i.e., membrane. The surfaces of bipolar plates are observed to have been oxidized.

Keywords Bipolar plate degradation · Agglomeration of catalyst · Delamination of electrode · Membrane thinning · Regenerative fuel cell

1 Introduction

A Unitized regenerative fuel cell (URFC) is an extension of conventional fuel cell with an additional functionality to work in electrolysis (EL) mode [1]. It therefore, works in both fuel cell (FC) mode as well as EL mode. Since, URFC's power

A. C. Bhosale (✉)

Department of Hydro and Renewable Energy, Indian Institute of Technology Roorkee, Roorkee 247667, India

e-mail: achbhosale@hre.iitr.ac.in

R. Goenka

Advanced Biofuels Division, The Energy and Resources Institute (TERI), Darbari Seth Block, Core 6C, India Habitat Centre, Lodhi Road, New Delhi 110003, India

P. C. Ghosh

Department of Energy Science and Engineering, Indian Institute of Technology Bombay, Mumbai 400076, India

© The Author(s), under exclusive license to Springer Nature Singapore Pte Ltd. 2022

295

K. Govindan et al. (eds.), *Advances in Mechanical and Materials Technology*,

Lecture Notes in Mechanical Engineering,

https://doi.org/10.1007/978-981-16-2794-1_26

and energy can be decoupled, it can potentially mitigate the mismatch in energy required in stand-alone renewable energy systems [2, 3]. Despite efforts to use URFCs commercially, several factors have hindered them from being used on a large scale, including component costs, cell durability, the quality of fuel supplied and even some operating parameters [4].

Degradation in individual fuel cells and electrolyzers has been studied by several authors [5–8] and membrane cracking and thinning, corrosion, catalyst oxidation and dissolution, operating conditions of temperature, water formation, etc. are only some of the factors which have been identified. An accelerated degradation study of a water electrolyzer based on polymer electrolyte membrane revealed catalyst precipitation within the membrane in conjunction with membrane thinning [9]. In order to improve the stability and durability of a polybenzimidazole (PBI) based polymer electrolyte membrane (PEM) electrolyzer, various combinations of RuO₂ and Ta₂O₅ catalyst have been used [10]. Of these, a 90:10 ratio by wt of RuO₂:Ta₂O₅ offered better stability than just RuO₂ for ~5 h at ~150 °C. Besides the catalysts and the membranes; even bipolar plates (BPPs) and diffusion layers [11], have been studied for degradation and the application of anticorrosive coatings on base plates [12] have been found to be preventive.

Long term exposure to the fuel (hydrogen) and oxidant (air/oxygen) gases, i.e., prolonged operation at open circuit, have been reported [13–15] to cause catalyst oxidation, leading to a loss in durability. The formation of water does not only reduce a fuel cell performance due to flooding but in depth studies [7, 16, 17], with a focus on degradation, have revealed it to cause morphological changes in the membrane electrode assembly (MEA) and gas diffusion layer (GDL), ionomer dissolution, corrosion, loss of the catalyst in terms of active surface area, thereby diminishing the cell durability [18].

Among the other causes for fuel cell degradation, the ionomer (Nafion[®]) that is used in electrodes have been found to play a dominant role [19]. An accelerated test investigating the catalyst base for PEMFC degradation [20], did not yield a definite relation between the electrochemical surface area (ECSA) and ratio of the Pt doped Carbon (Pt/C), however, pinhole formation emerged as a major factor [6, 21]. It was confirmed that the MEA failed during the PEMFC degradation due to dissolution of the microporous layer (MPL) and the polytetrafluoroethylene (PTFE) over time. Such phenomenon consequently led to the agglomeration of Pt, which increased from inlet of reactant flow to its outlet because of the large pores produced. Pinholes near inlet caused more decrements in the open circuit voltage (OCV) of the cell and also more hydrogen crossover.

Authors, in their previous work, underlined the importance of temperature of water on the degradation of URFC where catalyst agglomeration, membrane thinning, etc. were studied in detail [22]. In this work, an attempt has been made to extend the results particularly on bipolar plate (BPP) degradation over fixed cycles of both modes of operation.

2 Experimental Method

2.1 Preparation of the Single Cell

The electrolyte, i.e., Nafion[®] membrane (NRE-212, DuPont), was used after the pretreatment. MEA was prepared as per the protocol given in [22]. In brief, a uniform suspension of activated carbon (VulcanXC-72) and hydrophobic agent (PTFE, ~15 wt%) in an appropriate solvent (isopropyl alcohol, IPA) was coated on gas diffusion backing layer, viz. carbon paper. The coating process was repeated until the activated carbon in appropriate quantity ($\sim 1.5 \text{ mg cm}^{-2}$) was loaded and later sintered at $350 \text{ }^\circ\text{C}$ to form the gas diffusion layers (GDLs). It was then followed by electrode preparation, by coating the catalysts, i.e., Pt/C (40 wt%) and IrO₂, both mixed in IPA along with Nafion[®] solution (5 wt%) as an ionomer on the GDL. Catalyst loading for hydrogen electrode was maintained at 0.1 mg cm^{-2} of Pt while that for the oxygen electrode was 0.5 mg cm^{-2} of both Pt and IrO₂. The electrodes (apparent area = $4.5 \text{ cm} \times 5 \text{ cm}$) and the pretreated membrane were then hot pressed at $\sim 60 \text{ kg cm}^{-2}$ with platens maintained at $\sim 130 \text{ }^\circ\text{C}$. The entire assembly was cushioned appropriately and was pressed for $\sim 3 \text{ min}$ to form MEA. A pair of SS bipolar plates, coated with titanium nitride (TiN, Oerlikon Balzers) to avoid corrosion at the interfaces, was used with the MEA placed in between. The entire assembly was then clamped with nuts and bolts using a torque wrench to form the complete single cell. The same torque of 2.8 Nm was applied to each of the 4 bolts, to ensure uniform contact pressure at the interface of electrode and bipolar plate and consequently decrease the contact resistance [23] and ensuring the leak-proof cell as well.

2.2 Identification of Degradation

In order to diagnose the degradation, the cell was characterized in terms of its current and power outputs. Further visual and chemical analyses were performed on the MEA, both before and after the tests. Scanning electron microscopy (SEM) was used to visualize the impact on membrane as well as catalyst layer positioning and their physical appearances. Transmission electron microscopy (TEM) was found helpful in comparing the catalyst agglomeration before and after the study. Also, inductively coupled plasma-atomic emission spectroscopy (ICP-AES) was used for quantifying the catalyst that was washed away during electrolysis mode in the view of cell degradation.

2.2.1 Electrochemical Characterization

The URFC performance was studied throughout 3 days in both modes, alternatively FC mode and EL mode as illustrated in Fig. 1a, at an operating temperature of $45 \text{ }^\circ\text{C}$

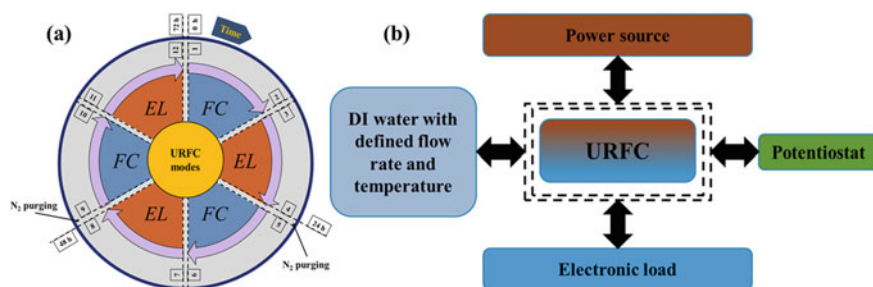


Fig. 1 **a** Plan for the experimental investigation and **b** graphic outline of the set up

(temperature of the deionized (DI) water in the electrolysis mode). The procedure was initiated in FC mode with the conditioning of the MEA (1–2 in Fig. 1a), followed by a switch to the electrolysis mode wherein deionized (DI) water was supplied at the operating temperature of the cell. The cell was run in this mode for 8 h (3–4 in Fig. 1a), using the chronopotentiometry at 100 mA in a programmable DC power source, followed by an idle duration for 4 h (4–5 in Fig. 1a), thus completing one cycle. The same cycle was then repeated on days 2 and 3, as per the nomenclature in Fig. 1a. The cell was characterized at 2, 6, 10, 3, 4, 8, and, 12, in the respective fuel cell and electrolysis modes.

Different combinations of equipments were adopted to handle the intricacies of the experiments in the different modes, as presented in Fig. 1b. A fuel cell test station (FCATS-G050, Green Light Innovation, Canada) was used in the FC mode for conditioning as well as to study the polarization behaviors of the cells, whereas, a programmable DC power source (2651A source meter, Keithley, USA) was used to study the URFC in electrolysis mode. An arrangement of DI water, at definite temperature and flow rate was made for a comfortable operation in electrolysis mode.

2.2.2 Visual Analysis

SEM (Ultra 55, Zeiss, Germany), together with elemental mapping, was used to visualize the MEA cross-sections, before and after subjecting those to the cycles of electrochemical tests mentioned earlier. The relative distribution of the catalysts, i.e., Pt and Ir were respectively compared. TEM (CM200, Philips, Netherlands) was also performed on these MEAs, to study the catalyst degradation.

2.2.3 Chemical Analysis

Inductively coupled plasma-atomic emission spectroscopy (ICP-AES) was performed on the MEAs to measure the catalyst concentrations (Pt and Ir) before and after the electrochemical testing cycles were completed. Samples of the MEAs

were cut out (2 cm^2) which were then dissolved in a blend of 2 mL HNO_3 (45 wt%), 10 mL HF (40 wt%) and 2 mL HCl (60 wt%) in a microwave maintained at $\sim 250 \text{ }^\circ\text{C}$ for ~ 30 min. The acid digested MEA was filtered and this filtered solution was collected in a beaker to which DI water was added later to make the total volume to 25 mL. The solution was later inspected by a ICP spectrometry (SPECTRO Analytical Instruments GmbH, Germany) to quantify the catalyst concentrations.

3 Results and Discussion

Multiple MEAs for the cell were fabricated for examination at $45 \text{ }^\circ\text{C}$. The results thus obtained were averaged and reported.

3.1 I–V Characteristics

Figure 2a shows the current–voltage behavior of the URFC in FC mode and EL mode, respectively, on the various days. This is one of the initial steps toward the understanding of the degradation. The performance decrease was quite rapid at $45 \text{ }^\circ\text{C}$, as is evident in the figure. This rapid degradation could be attributed to catalyst oxidation and its agglomeration, which may have been facilitated by the oxidation of carbon during the EL mode. Furthermore, degradation (thermal, mechanical and chemical) of the membrane was also considered, and later confirmed by further studies. The temperature, coupled with the high voltages in the EL mode, makes the various parts of the cell more prone to corrosion, especially, the ones that come in contact with active oxygen.

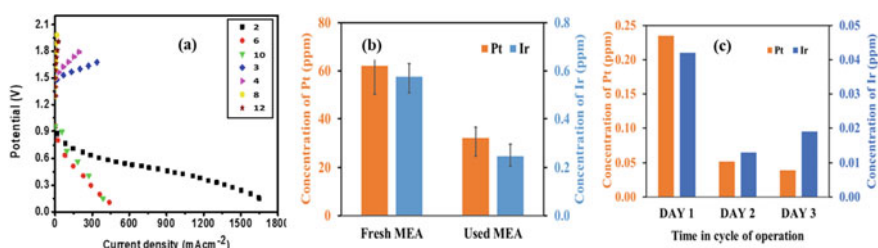


Fig. 2 **a** Performance comparison of the cell operated in both FC and EL modes, **b** comparison of catalysts present in fresh and used MEA and **c** measures of catalysts found in DI water samples over time

3.2 ICP-AES

The catalyst present in the MEA and its loss was quantified using inductively coupled plasma—atomic emission spectroscopy (ICP-AES) to appreciate the amounts of Pt and Ir present in the samples. Figure 2b showcases the comparison between the catalyst concentrations in a fresh MEA and the one after it was used during the investigation. The difference clearly indicates the loss of catalyst which could be attributed to oxidation of catalyst base, i.e., carbon.

Figure 2c quantifies the Pt and Ir concentrations found in the effluent DI water that was supplied to the cell during the EL mode. For each successive day, the water was replaced with fresh DI water before commencement of each EL mode of operation. The quantity of catalyst on day 1 was the highest to the rest, indicating that most of the catalyst got washed away at end of the day 1. These values further corroborate the earlier inferences of the EL mode operation causing the most degradation. This was due to the oxidation of the catalyst base, leaving the catalyst (Pt and Ir) to be washed away with water. On day 2 and 3, the catalyst remaining within the MEA was already quite low, and hence lower amounts of catalyst were washed away with the DI water supplied.

3.3 Microscopy Study

The cross-sections of fresh MEA were compared with that of used one to reveal the delamination observed between electrodes and the membrane (Fig. 3a, b). Furthermore, membrane thinning was also seen underlining the heavy loss in mechanical (structural) as well as chemical strength of the membrane. Consequently, uneven surfaces were produced on a microscopic scale thereby separating out the electrodes (delamination of the MEA).

Figure 3c, d revealed the particle size as well as distribution of catalyst before and after the study respectively using TEM analysis. The degraded MEA was observed to have more agglomerated catalyst particles compared to fresh one. This provides compelling evidence of the oxidation of the catalyst base, hypothesized with the earlier tests and confirms the cause of the low performance of the URFC over time.

3.4 Chronopotentiometry

The potential of cells during EL mode was recorded against 100 mA of supply current and plotted to observe its variation. Figure 4c reveals the variation of potential over time when cell is operated during EL mode. It was observed that on day 1, the performance in EL mode was relatively stable and the cell impedance did not vary much; however, on day 2, with time, the cell impedance increased. This implies that

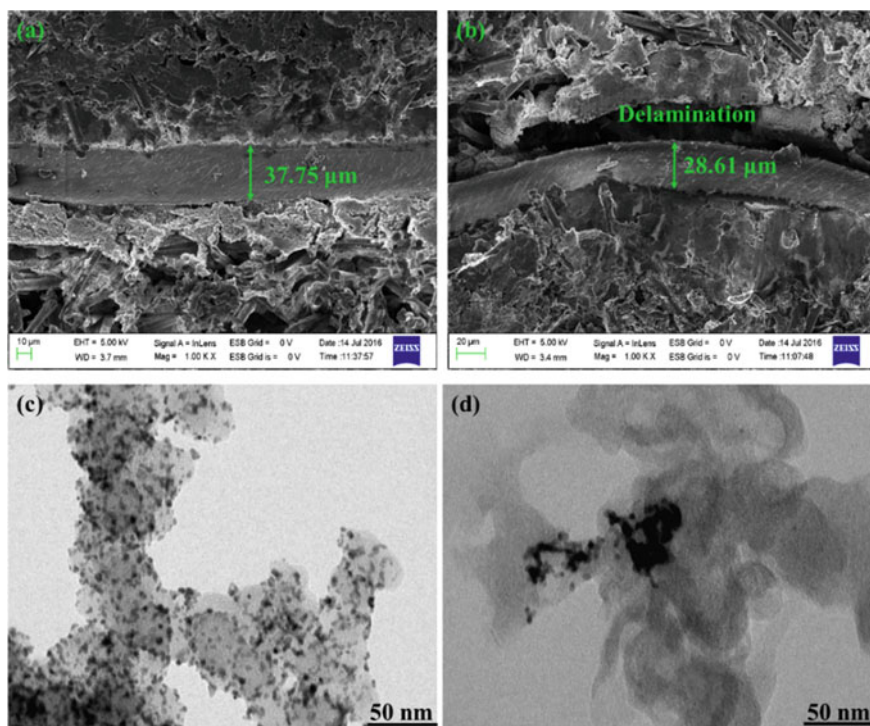


Fig. 3 SEM images of cross-section of **a** fresh MEA and **b** used MEA; TEM analysis of catalyst distribution before **c** and after **d** the investigation

there was degradation in the catalyst, membrane or bipolar plate (BPP) (Fig. 4a, b) or in all of them and that the degradation likely took place right after the operations on day 1.

3.4.1 X Ray Diffraction

The fresh and used BPPs were further analyzed for X ray diffraction (XRD) to evaluate the presence of oxidized layer over the surface of the coated plates. Figure 4a, b shows the pictorial view of BPP before and after the analysis. The presence of an oxide layer was detected confirming the loss in conductivity of the surface. XRD analysis (Fig. 4d) of the plates revealed the presence of various oxides and other oxidation products of TiN, such as Ti_2CN and Ti_5O_5 . The fresh BPP, as expected, was seen to predominantly have TiN over entire surface as confirmed from the XRD peaks.

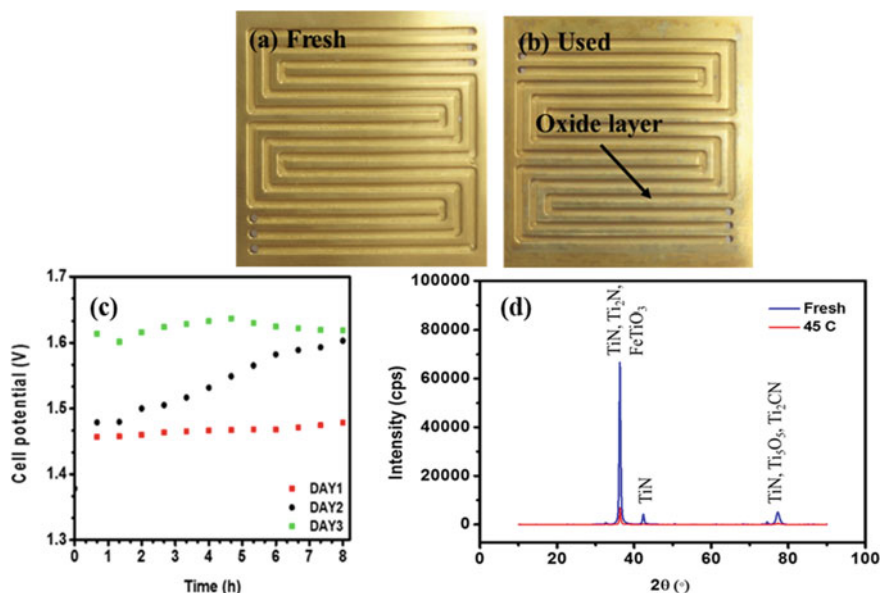


Fig. 4 Surface imaging of BPPs **a** before and **b** after the analysis, **c** chronopotentiometry at a constant current of 100 mA and **d** XRD patterns of fresh and used BPP surfaces

4 Conclusions

In this study, URFC degradation is studied at 45 °C. The results, clearly indicate that the degradation is prominent, especially in the EL mode operation, where the degradation process is enhanced. Loss in mechanical and chemical strength of the solid electrolyte is brought about, leading to its thinning over time and consequently, its delamination. However, the clamping pressure applied during assembly tends to mask the consequences of this delamination, when the cell is in the assembled condition. Catalyst agglomeration and its washout over time, however, severely degrades the URFC due to the loss of catalyst support (oxidation), carbon, at the inflated operating potentials of the cell, especially in the EL mode. The severely diminished solidity and longevity of the bipolar plate surface in the view of electrical conductivity is due to the oxidation at the high potentials in the EL mode. Therefore, in order to mitigate these problems for the future, the material of the catalyst base and the bipolar plates, need to be studied more deeply, and accordingly, suitable modifications need to be made.

References

1. Verma A, Basu S (2004) Feasibility study of a simple unitized regenerative fuel cell. *J Power Sources* 135:62–65. <https://doi.org/10.1016/j.jpowsour.2004.03.077>
2. Chavez-Ramirez AU, Cruz JC, Espinosa-Lumbreras R, Ledesma-García J, Durón-Torres SM, Arriaga LG (2013) Design and setup of a hybrid power system (PV-WT-URFC) for a stand-alone application in Mexico. *Int J Hydrogen Energy* 38:12623–12633
3. Raj AS, Ghosh PC (2012) Standalone PV-diesel system vs. PV-H₂ system: an economic analysis. *Energy* 42, 270–280. <https://doi.org/10.1016/j.energy.2012.03.059>
4. Wang Y, Leung DYC, Xuan J, Wang H (2016) A review on unitized regenerative fuel cell technologies, part-A: unitized regenerative proton exchange membrane fuel cells. *Renew Sustain Energy Rev* 65:961–977. <https://doi.org/10.1016/j.rser.2016.07.046>
5. Seo J-S, Kim D-Y, Hwang S-M, Seo MH, Seo D-J, Yang SY, Han CH, Jung Y-M, Guim H, Nahm KS, Yoon Y-G, Kim T-Y (2016) Degradation of polymer electrolyte membrane fuel cell by siloxane in biogas. *J Power Sources* 316:44–52. <https://doi.org/10.1016/j.jpowsour.2016.03.063>
6. Wang C, Zhang J, Wang S, Hao S, Li J, Mao Z, Mao Z, Quyang M, Liu Z (2016) Degradation study of membrane electrode assembly with PTFE/Nafion composite membrane utilizing accelerated stress technique. *Int J Hydrogen Energy* 1–8
7. Ous T, Arcoumanis C (2013) Degradation aspects of water formation and transport in proton exchange membrane fuel cell: a review. *J Power Sources* 240:558–582
8. Millet P, Ranjbari A, De Guglielmo F, Grigoriev SA, Auprêtre F (2012) Cell failure mechanisms in PEM water electrolyzers. *Int J Hydrogen Energy* 37:17478–17487. <https://doi.org/10.1016/j.ijhydene.2012.06.017>
9. Grigoriev SA, Dzhus KA, Bessarabov DG, Millet P (2014) Failure of PEM water electrolysis cells: case study involving anode dissolution and membrane thinning. *Int J Hydrogen Energy* 39:20440–20446. <https://doi.org/10.1016/j.ijhydene.2014.05.043>
10. Natarajan V, Basu S (2015) Performance and degradation studies of RuO₂-Ta₂O₅ anode electrocatalyst for high temperature PBI based proton exchange membrane water electrolyser. *Int J Hydrogen Energy* 40:16702–16713. <https://doi.org/10.1016/j.ijhydene.2015.07.041>
11. Liu CY, Hu LH, Sung CC (2012) Micro-protective layer for lifetime extension of solid polymer electrolyte water electrolysis. *J Power Sources* 207:81–85. <https://doi.org/10.1016/j.jpowsour.2012.01.045>
12. Gago AS, Ansar SA, Saruhan B, Schulz U, Lettenmeier P, Cañas NA, Gazdzicki P, Morawietz T, Hiesgen R, Arnold J, Friedrich KA (2016) Protective coatings on stainless steel bipolar plates for proton exchange membrane (PEM) electrolyzers. *J Power Sources* 307:815–825. <https://doi.org/10.1016/j.jpowsour.2015.12.071>
13. Zhang S, Yuan X-Z, Hiesgen R, Friedrich KA, Wang H, Schulze M, Haug A, Li H (2012) Effect of open circuit voltage on degradation of a short proton exchange membrane fuel cell stack with bilayer membrane configurations. *J Power Sources* 205:290–300. <https://doi.org/10.1016/j.jpowsour.2012.01.031>
14. Oyarce A, Zakrisson E, Ivity M, Lagergren C, Ofstad AB, Boden A, Lindbergh G (2014) Comparing shut-down strategies for proton exchange membrane fuel cells. *J Power Sources* 254:232–240
15. Tokarz W, Piela P (2016) Mitigation of catalysts degradation upon stopping work of polymer electrolyte membrane fuel cells for longer time. *Int J Hydrogen Energy* 41:15002–15006
16. Kim M, Jung N, Eom K, Yoo SJ, Kim JY, Jang JH, Kim HJ, Hong BK, Cho E (2014) Effects of anode flooding on the performance degradation of polymer electrolyte membrane fuel cells. *J Power Sources* 266:332–340. <https://doi.org/10.1016/j.jpowsour.2014.04.092>
17. Nandjou F, Poirot-Crouvezier J-P, Chandesaris M, Blachot J-F, Bonnaud C, Bultel Y (2016) Impact of heat and water management on proton exchange membrane fuel cells degradation in automotive application. *J Power Sources* 326:182–192. <https://doi.org/10.1016/j.jpowsour.2016.07.004>

18. Shan J, Lin R, Xia S, Liu D, Zhang Q (2016) Local resolved investigation of PEMFC performance degradation mechanism during dynamic driving cycle. *Int J Hydrogen Energy* 41:4239–4250. <https://doi.org/10.1016/j.ijhydene.2016.01.048>
19. Zheng Q, Cheng X, Jao T-C, Weng F-B, Su A, Chiang Y-C (2012) Degradation analyses of Ru85Se15 catalyst layer in proton exchange membrane fuel cells. *J Power Sources* 218:79–87. <https://doi.org/10.1016/j.jpowsour.2012.06.076>
20. Speder J, Zana A, Spanos I, Kirkensgaard JJK, Mortensen K, Hanzlik M, Arenz M (2014) Comparative degradation study of carbon supported proton exchange membrane fuel cell electrocatalysts—the influence of the platinum to carbon ratio on the degradation rate. *J Power Sources* 261:14–22. <https://doi.org/10.1016/j.jpowsour.2014.03.039>
21. Bodner M, Hochenauer C, Hacker V (2015) Effect of pinhole location on degradation in polymer electrolyte fuel cells. *J Power Sources* 295:336–348. <https://doi.org/10.1016/j.jpowsour.2015.07.021>
22. Bhosale AC, Meenakshi S, Ghosh PC (2017) Root cause analysis of the degradation in a unitized regenerative fuel cell. *J Power Sources* 343:275–283. <https://doi.org/10.1016/j.jpowsour.2017.01.060>
23. Bhosale AC, Rengaswamy R (2019) Interfacial contact resistance in polymer electrolyte membrane fuel cells: recent developments and challenges. *Renew Sustain Energy Rev* 115, 109351. <https://doi.org/10.1016/j.rser.2019.109351>

Crashworthiness of Bird Inspired Fuselage of Small UAV



Rohit Naryal and Pankaj Dorlikar

Abstract With the increasing demand for advanced UAVs in the market, high sustainability, reliability, and better workability are the most critical priorities. During UAV operations, accidents are common, leading to severe damage to expensive and vital equipment. A crashworthy UAV structure would help reduce equipment loss, which would lead to safer conditions while flying. The growing requirement for surveillance through onboard cameras dictates stable flying. Hence, we are adopting a hummingbird body, having the best hovering capabilities available within nature. Our research explores the simulations of crash scenarios to understand the collision resistance and crash-energy absorption capability of the hummingbird inspired CAD model. We have identified the sections in a UAV's fuselage, which carries mission-critical components and found the maximum acceleration at those sections. RADIOSS™ module of Altair HyperWorks™ Software is used to simulate the crashes and to examine the maximum acceleration responses at the vital locations. The 3D printed multi-material composite UAV's fuselage with strengthening at critical locations made the notable difference in energy absorption of structure and transfer of acceleration on the payload. We found that the specific energy absorption maximized and transferred acceleration on the critical locations reduced up to 8.88% when compared with the initial ABS material. This design methodology is proposed to be used in small UAVs to minimize the crash loads in avian flight-based vehicles.

Keywords Crashworthiness · UAV (unmanned aerial vehicle) · Fuselage · Energy absorption · Hummingbird

R. Naryal (✉) · P. Dorlikar
Department of Mechanical Engineering, Army Institute of Technology, Pune 411015, India
e-mail: rohitnaryal_18985@aitpune.edu.in

P. Dorlikar
e-mail: pvdorlikar@aitpune.edu.in

© The Author(s), under exclusive license to Springer Nature Singapore Pte Ltd. 2022
K. Govindan et al. (eds.), *Advances in Mechanical and Materials Technology*,
Lecture Notes in Mechanical Engineering,
https://doi.org/10.1007/978-981-16-2794-1_27

305

1 Introduction

UAVs carry expensive onboard modules like cameras, RCs, and battery, which gets damaged when UAVs crash. We must design UAVs for crashworthiness, as studies prove their accident rates are considerably higher than crewed airplanes. To extract vital information collected during UAV's operations, our prime concern is to minimize transferred acceleration at the expensive payload during crashing. Few researchers have already worked on solving the same problem. Troiani and Falaschetti [1] have proposed a crashworthiness improvement with a new carbon-fiber-reinforced polymer (CFRP) crash absorber. It reduces the resistance forces in the avionic and payload bay of a small UAV. They have conducted experiments to analyze the characteristics of energy absorption by the material. They had investigated the outcomes of energy dissipation at specific locations where the crash absorber has been installed in the UAV's fuselage. The study concludes that this new light crash absorber helps in minimizing the reaction forces and the stresses at the vital module locations.

Hiremath and Somashekar [2] studied the crash behavior of UAV during two separate landing impacts (bill down accident and belly landing collision). They found the maximum amount of crushing force at the specific locations where some of the crucial modules were installed, like surveillance cameras, servomotors, the fuel tank, payload, and receiver. They developed a finite element model of UAV using LS-DYNA. The necessary components in the UAV modeled as mass elements. By assigning the nodal forces to capture the resultant forces, the crashing force–time histories were investigated for each part individually. Their research concludes that the design of critical modules and supporting structures must overcome these maximum crashing forces at these locations of the UAV structure. They also suggested two solutions to minimize peak forces. The first is to reduce the elevation or terminal velocity of the UAV to minimize resultant collision force. And the second one is to use a crash absorber as a supporting structure.

Some studies used a different way to reach the target of enhancing the crashworthiness. Leomar et al. [3], has been successful in doing the same. They have strengthened the structure components using composite materials. In their study, the fuselage is reinforced by choosing appropriate fiber orientations and stacking sequence as design variables. They have used E-Glass/Epoxy and High modulus (HM) carbon/Epoxy composites to manufacture the designed UAV fuselage.

From our literature review [1–9], we found that understanding the material response used in the manufacturing of the UAV after the crash is vital, and it can be improved using numerous techniques. Different methods to enhance the crashing response are, installing a crash absorber with new configuration or new material [6], varying the structural stiffness of the skin [5], or strengthening the main assembly using a new composite material configuration [7, 8]. In this research, for implementing the learnings, we have used the RADIOSS™ module of HyperWorks™ Software to develop an FE model of the Hummingbird based UAV fuselage. We analyzed for the crashworthiness of the UAV's fuselage using the same material configuration.

Then, we have further optimized maximum stress regions using different materials to minimize the generated stresses. We have focused only on 3D printing rapid prototyping techniques because of the availability and freedom of manufacturing, even the complex shapes. The results show the locations of maximum stresses during different crashing situations. Hence, the fuselage design could be enhanced with the help of the FE techniques by varying the material configurations.

2 Finite Element Modeling and Simulation

The basis of our UAV is adopted from nature's best hovering capable hummingbird body. Hence it is necessary to incorporate the natural attributes like shape and size of Hummingbird inside our FEA model. We first modeled a CAD geometry using the exterior form data of Hummingbird. As maximum materials exhibit non-linear behaviors in the real world, therefore, it is crucial to possess a basic understanding of non-linear behavior of materials to construct an FE model. The FEA modeling of the designed UAV fuselage created considering the non-linear response of the material. The plastic material data and stress–strain curves reviewed from the research papers [10]. Altair RADIOSS™ module of Altair HyperWorks™ Software is used to simulate the crashes and to examine the maximum acceleration responses at the vital locations surrounding the payload of the modeled UAV fuselage. Furthermore, it contains a complete library of various material models to simulate the non-linear behavior of materials. The FEA modeling of the modeled UAV's fuselage is carried out using the steps described in detail in the following subsections. Vital components, like the camera and flapping mechanisms, are adopted as concentrated mass elements.

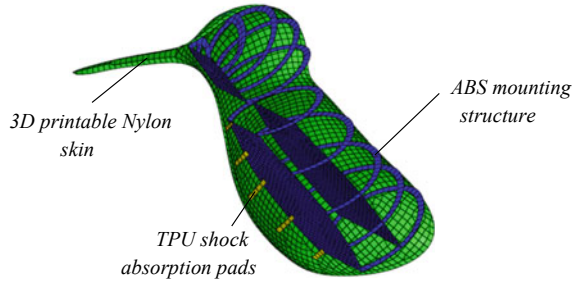
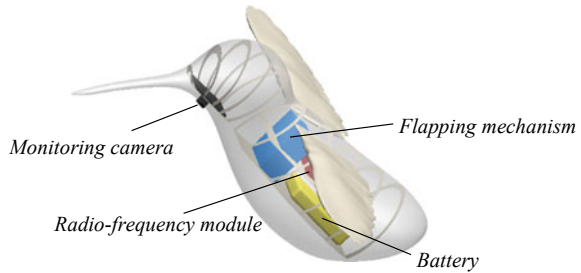
The basic equation of motion equation for the structural impact of the fuselage can be expressed as:

$$[M] \left\{ \frac{d^2 u}{dt^2} \right\} + C \left\{ \frac{du}{dt} \right\} + K \{u\} = \{F_{\text{ext}}(t)\}$$

where M is the mass matrix, C is damping matrix, K is stiffness matrix, u is displacement vector, and F_{ext} is an external force vector [9, 11]. We can notice that for our proposed small UAV fuselage, since the fuselage is light, hence the acceleration can be much higher in intensity for the same amount of external force acting on it while crashing. The final FEA mesh model with selected material can be seen in Fig. 1.

2.1 CAD Modeling

Hummingbirds are one of a few species having the outstanding capability to hover. Because of their different bone structure, they can quickly fly in any direction. Their outer body shape also plays a vital role in providing them with a better lift. Inspired

Fig. 1 FEM mesh**Fig. 2** UAV internal layout

by hummingbirds, we have designed a fuselage model using the available image data at different profiles. Then, we have opted for the approach of strengthening the biomimetic structure at specific locations to reduce the transfer of acceleration to the payloads. Mounting locations added to place equipment like monitoring camera, flapping mechanism, and battery, as shown in Fig. 2. These locations then stiffened using circular rings. 3D printable TPU pads incorporated to have better shock absorption capability.

2.2 Initial Landing Conditions

The material model MAT/LAW 36 “PLAS_TAB” in RADIOSS™ is adapted to model ABS and Nylon components such as fuselage skin, stiffeners. The material model MAT/LAW 65 “ELASTOMER” in RADIOSS adopted to model TPU components, i.e., shock absorber pads. Crash behavior has been investigated using different materials and applied impact forces. To model crashing conditions, the FE model UAV fuselage strikes a hard floor. The rigid base restrained in all degrees of freedom. Crash analysis carried out on the UAV fuselage model for two different impact landing conditions, and post-processing of the results are investigated for these impact conditions to determine the maximum force at the payload. Four different material configurations were tested for two separate impact conditions based on the angle of impact, the first one is a vertical impact (bill down), and the second one is an inclined

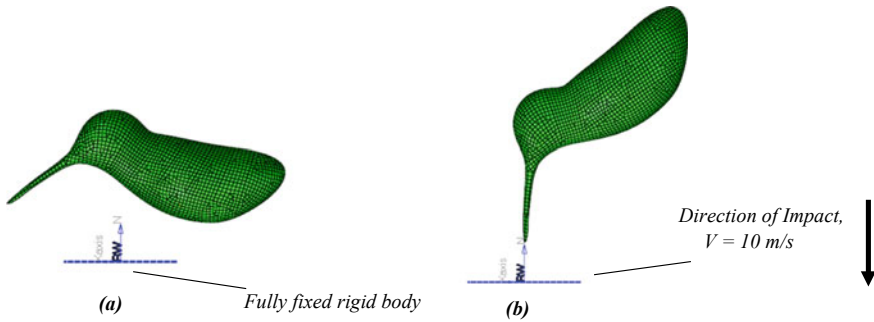


Fig. 3 Different impact conditions. **a** Inclined impact at an angle of 50° . **b** Vertical impact

impact (belly landing) with a 50° angle, as shown in Fig. 3. The FE UAV fuselage model impacts the floor with an initial velocity of 10 m/s for these impact conditions. Besides, standard earth gravity (g) is applied to all components as acceleration due to gravity is considered as the leading force for all design considerations.

3 Results and Discussions

This work concentrates on the study of the crashing response of the critical system inside the UAV fuselage. Due to its high cost and valuable information, we want the resultant acceleration to be minimum. The payload in the UAV is necessary and unavoidable to complete different operations to accomplish the mission. To achieve the minimization of acceleration, we have opted for strengthening the fuselage structure by varying the appropriate 3D printable material. The response of the proposed fuselage was investigated through the acceleration-time histories on the critical system, i.e., payload and compared with the initially referenced fuselage.

The crashing acceleration parameter is a crucial factor during the crashing process because it causes severe damage to the fuselage structural components. Therefore the acceleration-time histories of the critical system have been captured to know the maximum crashing acceleration during the different impacts. This paper exhibits the acceleration-time accounts of the vital equipment during the two distinct collision situations.

After knowing the maximum accelerations on the payload while crashing, it was essential to formulate a technique to lessen it, like strengthening or increasing the stiffness of the fuselage structure surrounding the payload to sustain the maximum crushing acceleration. Looking at the results, as shown in Fig. 4, the maximum crushing accelerations on the payload/critical system of the composite fuselage in comparison with reference fuselage reduces up to 8.88% in the case of vertical collision. The other case, as shown in Fig. 5, the collision was at an impact angle of 50° . It was found that maximum acceleration on the payload of the proposed fuselage in

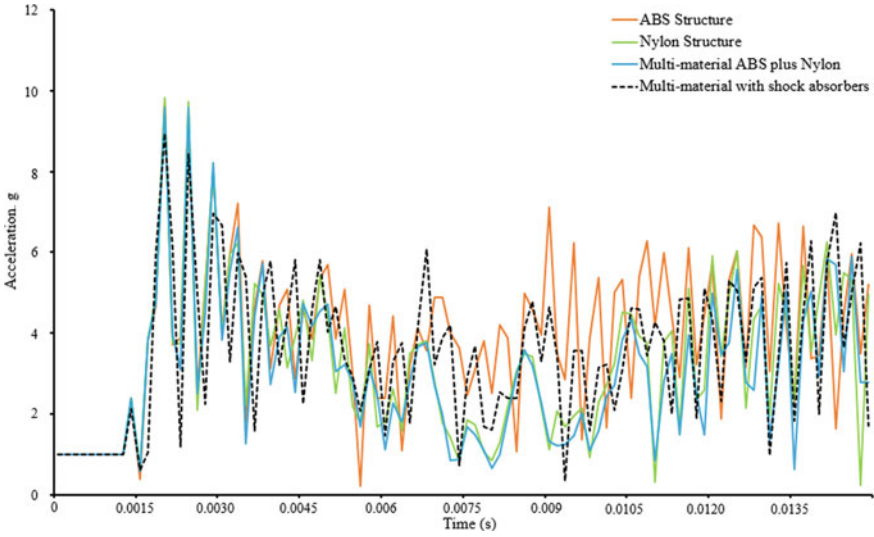


Fig. 4 Acceleration-time graph of the payload during a vertical collision

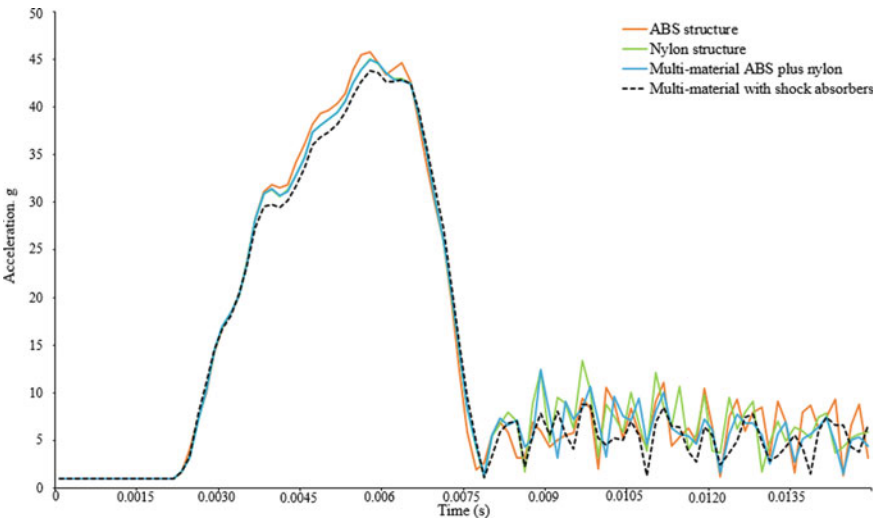


Fig. 5 Acceleration-time graph of the payload during an inclined collision at 50°

comparison with the reference fuselage was reduced to 4.45%. The crashing acceleration can be reduced by reducing the altitude at which the UAV is flying, or by reducing the propelling velocity.

Table 1 Comparison in terms of % variation of local acceleration concerning reference configuration

Structure	Vertical impact acceleration $\Delta\%$	Inclined impact acceleration $\Delta\%$
Nylon structure	-0.1727	-1.62
Composite ABS plus Nylon	-2.467	-1.77
Composite structure with shock absorbers	-8.88	-4.45

The following Table 1 compares the variation in the maximum acceleration of varieties of the fuselage structure. It can be seen that one could easily safeguard the fuselage choosing the right configuration of the material.

4 Conclusions

The rapid evolution of unmanned aerial vehicles leads to an increased concentration on their huge accident rates. More attention to improving the protection and safety levels is required. Hence, the prime motive of the present study is to investigate the crashworthiness of Hummingbird based UAV fuselage to protect the critical system. The methodology followed to achieve the aim of the present study was, first, generate the UAV fuselage from available data. Second, the development of its FE (finite element) model using RADIOSS software. Third, study the crash analysis of the fuselage under different impact conditions. Then, establish a multi-material model fuselage based on the crash analysis study and analysis of its crashworthiness. Finally, comparing the crashworthiness results concerning the payload among the designed and improved UAV fuselage. Results show that increasing the strength of UAV fuselage with the help of a multi-material model plays a vital role in absorbing energy effectively. This fuselage structure was efficient in reducing the transferred acceleration by 8.88% on the payload when compared with ABS fuselage. The results can be further refined to reduce the crashing acceleration by reducing the altitude at which the UAV is flying. Another way to achieve this can be by reducing the propelling velocity.

References

1. Troiani E, Falaschetti M, Taddia S, Ceruti A (2015) CFRP crash absorbers in small UAV: design and optimization. SAE technical paper. <https://doi.org/10.4271/2015-01-2461>
2. Hiremath MK, Somashekar V (2016) Crash analysis of unmanned aerial vehicle using FEA. Int J Innov Res Sci Eng Technol 5. <https://doi.org/10.15680/IJRSET.2015.0506032>

3. Leomar P, Tamre M, Riibe T, Vaher T, Haggi T (2006) Optimal design and analysis of UAV swan fuselage. *Solid State Phenom* 113:91–96. <https://doi.org/10.4028/www.scientific.net/ssp.113.91>
4. Zahran M, Abdelwahab M (2019) Crash analysis of UAV hybrid composite fuselage structure under different impact conditions. *Mater Sci Forum* 953:88–94. <https://doi.org/10.4028/www.scientific.net/MSF.953.88>
5. Yiru R, Jinwu X, Jianqiang Z, Zhangping L (2016) Crashworthiness analysis of aircraft fuselage with sine-wave beam structure. *Chin J Aeronaut* 29, pp 403–410. <https://doi.org/10.1016/j.cja.2016.02.002>
6. Liang P, Xiaopeng W, Meiyang Z (2013) Improved fuselage design for crashworthiness. *Appl Mech Mater* 246:777–781. <https://doi.org/10.4028/www.scientific.net/AMM.246-247.777>
7. Yu ZL, Xue P (2017) Crashworthiness study of composite fuselage section. *Key Eng Mater* 725:94–98. <https://doi.org/10.4028/www.scientific.net/KEM.725.94>
8. Maia L, de Oliveira P (2005) Crashworthy composite fuselage section concept for next generation general aviation. SAE technical paper. <https://doi.org/10.4271/2005-01-4011>
9. Tian-chun Z, Xiao-min Z, Hao-lei M, Zhen-yu F (2012) The influences of complex impact conditions on aircraft fuselage crashworthiness. *Appl Mech Mater* 184:546–552. <https://doi.org/10.4028/www.scientific.net/AMM.184-185.546>
10. Aliheidari N, Tripuraneni R, Ameli A, Nadimpalli S (2017) Fracture resistance measurement of fused deposition modeling 3D printed polymers. *Polym Test* 60:94–101. <https://doi.org/10.1016/j.polymertesting.2017.03.016>
11. Gokhale NS, Deshpande SS, Bedekar SV, Thite AN (2008) Practical finite element analysis. *Finite to Infinite*, Pune, India, ISBN-13: 978-0-07-060092-8

An Experimental Study to Determine the Optimum Order of Design Review Parameters for Designing Review in Immersive Virtual Environment



D. Shukla, A. Patil, P. Dholiya, S. J. Singh , and V. Vakharia 

Abstract This paper studies the experiential learning in a virtual environment using HMD-based immersive virtual reality technologies. This digital technology is mostly beneficial in product design and development. However, usability of virtual reality in the area of the design is still explorative for reviewing a 3D model. Several factors having an impact on the design review of 3D models in the virtual environment. In experiment, design review score is calculated for different working conditions with different parameter ranges. The significant order of the parameters is determined using Taguchi method, and the outcomes are compared with ANOVA method. Experimental results indicate that the effect of factor-1 (grooves) is more contributing than factor-3 (blocks), and factor-2 (sidewall) is least significant on design review process in simulated 3D state.

Keywords Design review · Virtual reality · Taguchi method · ANOVA

Nomenclature

ANOVA	Analysis of variance
CAD	Computer-aided design
CI	Confidence interval
DOF	Degree of freedom
IVE	Immersive virtual environment
IVR	Immersive virtual reality
OA	Orthogonal array
S/N	Signal-to-noise ratio
SD	Standard deviation

D. Shukla · S. J. Singh · V. Vakharia (✉)
Pandit Deendayal Petroleum University, Gandhinagar 382008, India
e-mail: vinay.vakharia@sot.pdpu.ac.in

A. Patil · P. Dholiya
CEAT Ltd., Halol 389350, India

© The Author(s), under exclusive license to Springer Nature Singapore Pte Ltd. 2022
K. Govindan et al. (eds.), *Advances in Mechanical and Materials Technology*,
Lecture Notes in Mechanical Engineering,
https://doi.org/10.1007/978-981-16-2794-1_28

VE	Virtual environment
VR	Virtual reality

1 Introduction

Virtual reality is a digitally created non-real environment which gives operators the impression of being someplace other than where they are. The principal features that separate it from different means that of displaying info are the ideas of immersion and presence. Reviewing in virtual reality system was more evident than the desktop-based interface when reviewing product models at a higher level of difficulty [1]. VR gives a secure, immersive and realistic feel for users. One of the principles focuses on Industry 4.0 is to connect the simulated system and physical system, which are referred to as cyberphysical systems. This environment gives exceptional potential to support this endeavor. Kovar et al. [2] sum up the numerous applications in the Industry 4.0 and state that this digital platform can successfully deduct cost as well as time at some point in the design of new machines. Mujber et al. [3] categorize this digital systems based on immersion into three sets: non-immersive systems, partially immersive system and completely immersive systems. Fully IVR systems yield quality by picking up the human gesture and interface with models and replicating the same in the digital state. Non-immersive system conjointly places the user during a 3D setting and permits manipulations, but only utilizing a conventional hardware. Improvements in new gadgets and high-end connectivity have made VR progressively attractive and reasonable. This expanded trend is qualified for an extensive range of user areas for this digital technology outside of the gaming world. Today, these digital technologies are used in a broad range of fields such as teaching, military, medical science, engineering, sports and many more. Initial applicable areas can be found in entertainment, promotion and publicity. Use of prototyping and design review in virtual environment permits participants to observe models in a realistic way in the earlier design stages. This process is conducted by many corporates to detect faults in their newly developed products before the actual one is manufactured. Today, the process of classic design review is achieved directly on CAD modeling software. The 3D models are observed on the screen and find the possible errors. The issue here is that the user is not familiar with modeling software and may not complete this process. The simple consideration of difficult 3D models on a 2D interface forms the undesirable impressions of the measurements, and scales are lost. Previous study tells that the users observed two categories of 3D models for predefined errors. The outcomes of those studies specify that this activity in virtual environment permits operators to see a little more errors than in a traditional 3D CAD-created method on a system.

Kwon [4] conducted experiments, and results show that the vividness and interactivity on digital platform permit the participants to closely distinguish virtual capabilities as direct involvements and learning outcome are enhanced. Lanzotti et al. [5]

analyze simulated prototype and real prototypes using fuzzy methodology toward the estimation of the optimal design. Additive manufactured physical model is used for this case study. In their methodology, they tested on the Neapolitan coffee-maker, for the optimal design [5]. Wolfartsberger [6] developed VR-based tool named as “VRSmart” to check the experience of users. Design review based on digital platform permits manipulators to determine slightly further faults throughout a 3D model than desktop-based approach [6]. Gao et al. [7] developed a VR-based module to simulate different assembly tasks, and visibility of assembling parts and postures of a user are quantified in presence of human factors. The new methods of calculations based on final positions and forces during assembly are presented to perform additional realistic assembly operations [7]. Linn et al. [8] generate an idea for digital visual remote assessments of manufacturing equipment.

VR is a useful tool to assist maintaining activities with remote inspections that allow you to optimize the maintenance process. By comparing desktop interface and virtual interface, Satter et al. [9] stated that user with digital surroundings required substantially less time to finish the given assignment. Author conveyed that some activities like path tracking take additional time on this platform [10]. They stated that comment on greater capabilities in this non-real surrounding results in a longer span of design reviews. Hou et al. [11] claimed that VR tool has greater capability for analyzing 3D models since they preserve realistic features of a given model, offer a natural sensation when manipulating with the model, allow participants to develop precise optimistic visualization and create a better sense of presence. In the case study, members specified that virtual environment assists them in keeping attention on the engineering design review since no visual interruptions from external world could disturb the process [12]. Users were trained to identify faults in given models, and the results propose the same error finding performance in VR and DI [13]. Authors experimented and observed VR with basic manipulation functions and advanced functions to improve the understanding of designs in respect of counting the parts. Use of the advanced functions boosted the confidence of the users in terms of answering related to visualization of design [14]. Abidi et al. [15] experimented in digital platform and gain better result on completing the assembly task within limits. VR-based assembly training is beneficial in terms of economically and time. In design review, the final prototype of any physical system leads to high cost and manufacturing of the individual product [15]. In comparison with the use of VR has demonstrated a more effective result. This offers an opportunity for a more realistic virtual prototype with comparatively low cost and minimum time to produce. As compared to traditional method simulation and visualization with CAD software, VR gives a more realistic experience each time participant senses in space of the virtual environment. Current virtual reality technology gives a quantitative and qualitative result in terms of visualization. Interaction with the virtual model increases due to immersion and high-quality resolution. Computer-generated reality will not substitute the customary design review process; however, it is a significant expansion for any research organization that performs design reviews on 3D models of their respective products.

2 Experimental Design

2.1 Hardware Setup

Two hardware setups were used in this experiment. For 3D review portions of the experiment, the interface consisted of a regular PC screen, a keyboard and a mouse. For the VR portion of the experiment, the hardware setup includes an HMD as an output display (HTC VIVE) and a gamepad controller for input. The HMD resolution per eye is 1080 * 1200 pixels, with a 165° field of view, internal tracking via gyroscope, accelerometer and magnetometer updating at 1000 Hz and positional tracking via near-infrared sensor and CMOS sensor updating at 90 Hz. The infrared positional tracking was placed above the computer monitor approximately 20 in. in front of the participant. It requires 12–15 ft space for full setup.

2.2 Taguchi Method

Many researchers have focused on how different parameters are affected on the design review process, but the significant order and impact of the factors in the virtual environment have not been determined by using classical techniques. Genichi Taguchi gives a method for process or parameter optimization. Key advantages are reduction in time, low development cost and less effort for more number of experiments. This method has orthogonal array tables to offer a comprehensive performance. In design review process, three different parameters as in Table 1 are considered, such as grooves, block with sipes and sidewall.

In Taguchi methodology, the outcomes of the objective functions are changed to the S/N quantity. “Higher is better” is chosen for this case. This approach is applied to VR design review to maximize data from each experiment of the system. Initially, the degree of freedom was calculated, and after that, orthogonal array was decided. There are three factors associated with all three levels; overall DOF is 7. As indicated by the Taguchi technique, an orthogonal array ought to be higher than DOF, and nine cases are adequate to check the order with optimum condition of working. Thus, L9 OA is indorsed by this technique.

Table 1 Factor classifications

Factor no.	Factor name		
Factor-1	Lateral grooves	Circumferential grooves	Grooves angle
Factor-2	Tread blocks	Sipes	Rib
Factor-3	Sidewall	Rim	

2.3 Analysis of Variance (ANOVA)

This method is used to analyze the contribution of the individual factor on the performance. This approach is used to demonstrate the significant order of influencing factors on the output and used to endorse the outcomes found from the Taguchi method. The significance of individual parameter on the design review of the tire in VR is determined by calculating SS of individual factors and determines the contribution of each factor on target functions. The significance level of this method is 0.05 (95% CI).

3 Results and Discussion

Taguchi’s approach may be finished with a lesser range of experimentations in comparison to different analysis. This experiment contains three factors and three levels. Taguchi method reduced the experiments with L9 orthogonal array from 27 experiments to nine experiments. This experimental design has been applied to set the best order of the design factors of tires in VR for design review with L9 orthogonal array. In results, Taguchi method gives an optimum order based on rank (difference in S/N ratio) as shown in Table 2.

The difference between the uppermost and lowermost S/N ratio is less, and at that point, the impact of the factor on the objective function is moderately small. Highest difference is with rank 1 and then rank 2 and rank 3. From results, factor-1 contribution is more significant than factor 3, and factor 2 is least significant and less effect of noise factor on this experimentation. The contribution for each parameter on tire design review task is calculated, and the results of Taguchi methodology (rank of factors) are endorsed with ANOVA technique (% contribution of SS of individual factor).

The contribution of factors found on basis of the Taguchi technique is shown in Table 2. An impact ratio of factor-1, factor-2 and factor-3 is 52.40%, 19.87% and 27.71%, respectively. The influence quantity acquired based on the ANOVA is presented in Table 3. An impact ratio of factor-1, factor-2 and factor-3 is 51.37%, 17.12% and 27.80%, accordingly. Match the two outcomes as shown in Fig. 1, and the optimum order of the factors for tire design review is determined based on (%) contribution: factor-1 > factor-3 > factor-2.

Table 2 Factorial effect for tire design review in VR (Taguchi)

No.	Factor-1	Factor-2	Factor-3
Delta	0.87	0.33	0.46
% contribution	52.40	19.87	27.71
Rank	1	3	2

Table 3 Factorial effect for tire design review in VR (ANOVA)

Source	DOF	Adj. sum of square (%)	Rank
Factor-1	2	51.37	1
Factor-2	2	17.12	3
Factor-3	2	27.80	2
Error	2	3.71	
Total	8		

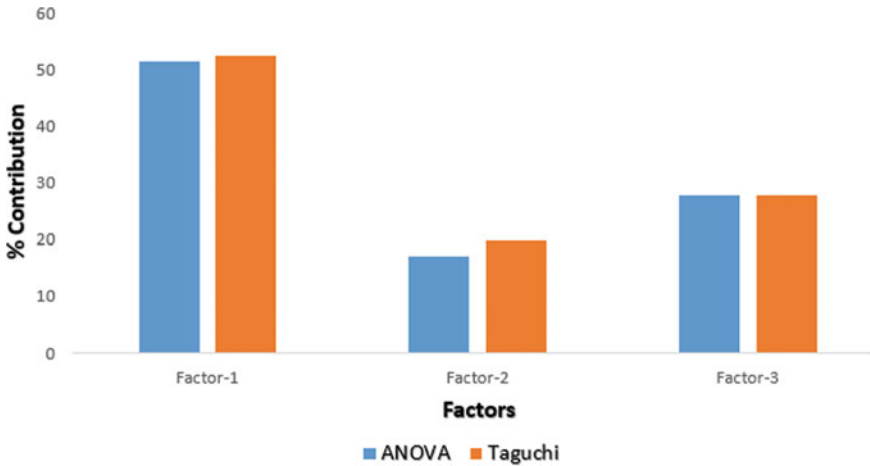


Fig. 1 Results' comparison

4 Conclusions

This present study describes the use of Taguchi procedure to decide the optimum order of design parameters of tire for a design review in virtual product (tire) room. Taguchi method is used, and results are compared with ANOVA. Results show that optimum order for design review of the tire as a result of the Taguchi experiment is nearer to ANOVA. For design review of tire, effect of factor 1 is more significant than factor 3, and factor 2 is least significant. The general investigation tells that virtual reality is a valuable expansion, but not a substitution, to existing design review activity.

In the above work, less number of experiments have been conducted because of fewer factors. Factors are classified into three groups. For optimization, conventional methods are used like Taguchi and ANOVA. But in case of more factors, analysis of those factors may be difficult with the use of these conventional techniques. For more reliable solution, the use of non-conventional techniques like fuzzy logic, multi-criteria decision making (MCDM) analysis and machine learning techniques may be opted. For more accurate results, more number of data are required for these non-conventional techniques [5].

Acknowledgements The project “Design Review through Virtual Reality” is funded by the CEAT Ltd., Vadodara. The authors would like to acknowledge and thank CEAT Ltd., Vadodara and Pandit Deendayal Petroleum University, Gandhinagar.

References

1. Horvat N, Škec S, Martinec T, Lukačević F, Perišić MM (2019) Comparing virtual reality and desktop interface for reviewing 3D CAD models. *Proc Des Soc Int Conf Eng Des* 1(1):1923–1932. <https://doi.org/10.1017/dsi.2019.198>
2. Kovar J, Mouralova K, Ksica F, Kroupa J, Andrs O, Hadas Z (2016) Virtual reality in context of Industry 4.0 proposed projects at Brno University of Technology. In: 2016 17th international conference on mechatronics-mechatronika (ME), pp 1–7
3. Mujber TS, Szecsi T, Hashmi MSJ (2004) Virtual reality applications in manufacturing process simulation. *J Mater Process Technol* 155–156(1–3):1834–1838. <https://doi.org/10.1016/j.jma.2004.04.401>
4. Kwon C (2018) Verification of the possibility and effectiveness of experiential learning using HMD-based immersive VR technologies. *Virtual Real* 0123456789. <https://doi.org/10.1007/s10055-018-0364-1>
5. Lanzotti A, Carbone F, Grazioso S, Renno F, Staiano M (2018) A new interactive design approach for concept selection based on expert opinion. *Int J Interact Des Manuf* 12(4):1189–1199. <https://doi.org/10.1007/s12008-018-0482-8>
6. Wolfartsberger J (2019) Analyzing the potential of virtual reality for engineering design review. *Autom Constr* 104:27–37. <https://doi.org/10.1016/j.autcon.2019.03.018>
7. Gao W, Shao X, Liu H (2016) Enhancing fidelity of virtual assembly by considering human factors, pp 873–886. <https://doi.org/10.1007/s00170-015-7628-7>
8. Linn C, Bender S, Prosser J, Schmitt K, Werth D (2018) Virtual remote inspection—a new concept for virtual reality enhanced real-time maintenance. In: Proceedings of the 2017 23rd international conference on virtual system and multimedia (VSMM 2017), vol 2018, pp 1–6. <https://doi.org/10.1109/VSM2017.8346304>
9. Satter K, Butler A (2015) Competitive usability analysis of immersive virtual environments in engineering design review. *J Comput Inf Sci Eng* 15(3)
10. de Casenave L, Lugo JE (2017) Design review using virtual reality enabled CAD, 06 Aug 2017. <https://doi.org/10.1115/DETC2017-67878>
11. Hou M, Hollands JG, Scipione A, Magee L, Greenley M (2009) Comparative evaluation of display technologies for collaborative design review. *PRESENCE Teleoperators Virtual Environ* 18(2):125–138
12. Berg LP, Vance JM (2017) An industry case study: investigating early design decision making in virtual reality. *J Comput Inf Sci Eng* 17(1)
13. De Casenave L, Lugo JE (2018) Effects of immersion on virtual reality prototype design reviews of mechanical assemblies. *Proc ASME Des Eng Tech Conf* 7:1–11. <https://doi.org/10.1115/DETC2018-85542>
14. Freeman IJ, Salmon JL, Coburn JQ (2016) CAD integration in virtual reality design reviews for improved engineering model interaction. *ASME Int Mech Eng Congr Expo Proc* 11:1–10. <https://doi.org/10.1115/IMECE201666948>
15. Abidi MH, Ahmad A, El-Tamimi AM, Al-Ahmari AM (2012) Development and evaluation of a virtual assembly trainer. *Proc Hum Fact Ergon Soc Annu Meet* 56(1):2560–2564

Energy and Exergy Analysis of Poovan Banana Under Single Slope Forced and Natural Convection Solar Drying



E. Elavarasan, Anagh S. Bhanu, Yogesh Kumar, R. Mouresh,
and Sendhil Kumar Natarajan

Abstract The presence of moisture in the food particles can be reduced up to a certain level through the process of drying. This allows to stretch out the expiry period of the products and storage safety by inhibiting the growth of bacteria. Poovan banana is extensively grown in tropical region which is one of the most consumed varieties of banana all over the world. Hence it is necessary to preserve banana to avoid the post-harvest losses. Sun drying is the conventional mode, practised in many countries. But this method has several issues which arises due to the accumulation of dust, soil, sand particles, insects, etc. Several methods of drying came into existence to overcome this drawback. Solar dryer utilises the energy from the insolation and collector to dry the food products. A single slope solar dryer is fabricated with both forced and natural mode of convection to conduct the analysis of energy and exergy of drying of poovan banana. One kilogram of uniform size poovan banana samples were placed on the rectangular mesh of both the drying units. The equilibrium moisture content was achieved within 7 h in forced convection solar drying, whereas it took 10 h using natural convection solar drying. The analysis was conducted using the first and second law of thermodynamic to determine the ratio of utilisation of energy, exergy losses and efficiency. The obtained results are explained with the help of graphs.

Keywords Banana drying · Forced convection solar dryer · Natural convection solar dryer · Energy and exergy analysis

E. Elavarasan · A. S. Bhanu · S. K. Natarajan (✉)
Department of Mechanical Engineering, NIT Puducherry, Karaikal, Union Territory of
Puducherry, India
e-mail: sendhil80@nitpy.ac.in

Y. Kumar · R. Mouresh
Sri Ramakrishna Engineering College, Coimbatore, India

© The Author(s), under exclusive license to Springer Nature Singapore Pte Ltd. 2022
K. Govindan et al. (eds.), *Advances in Mechanical and Materials Technology*,
Lecture Notes in Mechanical Engineering,
https://doi.org/10.1007/978-981-16-2794-1_29

321

1 Introduction

Bananas are one of the most consumed and cheapest fruits in the world which mainly grown for its fruit. It is the most traded fruit and the fifth most traded agricultural product. There are over 1000 different varieties of banana available around the globe, which is subdivided into 50 groups. Poovan banana is one of the most consumed varieties of banana across the world [1]. The banana is extensively cultivated in tropical climate and they have a wetness of 74% by wet basis [2]. For minimising the post-production losses and the difficulty in storage and transport, drying is used as preservation method. Moisture present in the food crops can be minimised by performing, so that the growth of bacteria present in the product will be inhibited and the expiry of the product will increase. It is used for preserving agricultural products because the quality of the products is least affected due to drying [3]. Sun drying is the convectional mode of drying practised all over the world. But this method has a lot of demerits which arise due to the accumulation of dust, soil, sand particles insects, etc. However, several types of fryers came into existence to overcome this drawback such as infrared dryer, microwave dryer, and vacuum dryer. Solar dryer is the best and cheapest mode of drying because it uses solar energy which is renewable, inexhaustible, abundant and non-pollutant. Food samples placed inside the drying unit will receive energy from the collector and insolation. This analysis is an important tool to determine the design, analysis and optimisation of any drying unit [4]. The maximum amount of useful work that can be extracted from a thermodynamic system when it is brought to dead state is known as exergy [5]. The objective of the drying process is to utilise minimum amount of energy to remove maximum amount of wetness from the food sample for the preferred final condition of the product.

Natarajan and Elavarasan [6] elaborately reviewed the application of computational fluid dynamics analysis on different types of greenhouse dryer for dehydrating various agricultural crops in forced and natural mode of convections. Maia et al. [7] designed a prototype solar updraft tower to conduct thermodynamic analysis banana dried in it. They concluded that exergetic efficiency would be higher if incident solar radiation is higher. They observed an increase in exergetic efficiency with the load. Bennamoun [8] conducted an all-round review about the different mathematical methods to calculate energy and exergy efficiency of a drying unit. Energy balance and mass balance were established to obtain the result. After calculating input, output and exergy loss exergy balance is established to obtain the exergy efficiency. Rabha et al. [9] designed a tunnel dryer using solar energy with active mode of convection having a heat exchanger to dehumidify ghost chilli and slice ginger. The analysis of exergy shows that the exergetic efficiency when ghost chilli was dried was in the range of 21–98% having a mean of 63% and for the ginger slices it was 4–96% with an average of 47%. They also noted an increase in exergetic efficiency increases according to the duration of drying hours. Corzo et al. [10] conducted exergy analysis of corobo samples at different temperature and velocities in a heat exchanger. The values of exergy losses vary from 0.005 to 0.010 kJ and the exergetic efficiency is in between 97 and 80%. Akpınar [11] conducted a detailed investigation of sliced

red pepper dried in a convective drier. He conducted the experiment by varying both the inlet temperature and air velocity. The exergy losses vary from 0.06 kJ/kg to 1.48 kJ/kg whereas the exergetic efficiency is obtained as 67.28–97.92%. Lingayat et al. [12] fabricated an indirect type passive solar dryer to study the energy and exergy analysis on drying of banana. The loss of exergy ranges from 3.36 to 25.21 kJ/kg and the exergetic efficiency values vary from 7.4 to 45.32%. Akbulut and Durmus [13] designed a solar dryer of active mode of convection to analyse the exergy of drying of mulberry samples. The experiments were performed in different mass flow rates of drying air and they have observed that the loss in exergy dipped with the increase in the mass flow rate. Tiwari et al. [14] developed a greenhouse dryer to analyse energy exergy on drying of fish. They observed that the exergetic efficiency is lower than its corresponding energy efficiency of the active and passive mode of drying.

The detailed literature review for this study shows that there is no much research conducted by comparing the energy and exergy efficiency of the poovan banana dried under forced and natural convection solar dryer. Hence, this paper majorly focuses on the energy and exergy analysis of the poovan banana dried in a single slope forced and natural convection solar drying unit which is located in the geographical condition of Karaikal (11° N, 80° E), India.

2 Material and Methods

2.1 Solar Drier Setup

The experiments were conducted in a single sloped forced and natural convection solar dryer which is 125 cm long, 82 cm wide and 45 cm high. Galvanised iron sheet is used to laminate the interior of the both drying units. The walls of the drying units were insulated with coconut husk and thermocol to prevent the escape of hot air gases to the environment. Glass plane was fixed at the top of the plane with an inclination of 11° facing south. Correctly measured banana samples were placed inside the drying units by keeping them on the wire mesh tray. The photograph of the drying units is given in Fig. 1.

2.2 Devices Used

Hukseflux pyranometer (SR20-TI, secondary standard (ISO 9060)) having a sensitivity of 14.77×10^{-6} V/W/m² is used to measure the Global solar radiation. Each drying unit was connected with 8 K-type thermocouple. Out of 8 thermocouples, three thermocouples were used to measure drying air temperature, two thermocouples for absorber plate and one thermocouple each to measure inlet, outlet and glass



Fig. 1 Single slope forced convection and natural convection solar dryer

temperature [15]. To display the data from the thermocouples, the output of the thermocouples were interlinked with a data acquisition system of type Agilent 34972A having an error correction of $\pm 0.25\%$ [16].

2.3 Sample Preparation

Fresh poovan bananas were bought from the market in Karaikal, India. The bananas were cut into slices having uniform thickness and shape. 1 kg of bananas were accurately measured with weighing balance and were placed on the rectangular-shaped wire mesh tray of both the drying unit and open sun drying.

3 Calculation

3.1 Energy Analysis

The energy analysis was conducted by using the data obtained during the experiment. First law of thermodynamics is used to do the analysis by considering open steady flow [11].

Mass balance equation of the drying system is,

$$\sum (\dot{m}_i s_i + \dot{m}_p) = \sum \dot{m}_o \quad (1)$$

Energy conservation of the system is,

$$\dot{Q} - \dot{W} = \sum \dot{m}_o \left[h_o + \frac{v_o^2}{2} \right] - \sum \dot{m}_i \left[h_i + \frac{v_i^2}{2} \right] \quad (2)$$

where, \dot{Q} and \dot{W} are the heat energy flow and the rate of mechanical work respectively in Watts. \dot{m} is the mass flow rate of air in kg/s. h_i and h_o are the enthalpy of drying air at inlet and outlet air, respectively. v_i and v_o are the velocity of air at inlet and outlet respectively in m/s. By eliminating the terms which have no effect the process, Eq. (3) becomes,

$$EU = \dot{m}(h_i - h_o) \quad (3)$$

The energy utilisation ratio (EUR) can be calculated by applying following Eq. (4).

$$EUR = \frac{\dot{m}(h_i - h_o)}{\dot{m}(h_i - h_\infty)} \quad (4)$$

3.2 Exergy Analysis

Second law of thermodynamics which tells about the grade, quantity and direction of decrease of the energy is used to do the exergy analysis. The law states that the part of energy entering the dryer will be destroyed due to the irreversibilities. According to these postulates, the total inflow, outflow and the losses of exergy of the processes were determined. This analysis is a significant tool that can be utilised to design the thermal system. The basic formula of exergy for a steady state system is given by [11],

$$\text{Exergy} = \text{Work} + \text{Internal Energy} + \text{Chemical Energy} + \text{Gravity} - \text{Entropy} \quad (5)$$

By simplifying and eliminating the unwanted terms, Eq. (5) can be reduced to the form a shown below,

$$Ex = C_p \left[(T - T_\infty) - T_\infty \ln \frac{T}{T_\infty} \right] \quad (6)$$

where, C_p is specific heat in J/kg. By using the above equation the exergy inflow and outflow at the outlet and inlet temperature of the drying unit were calculated (7) and (8). The loss in exergy can be determined by using the formula given below (10),

$$Ex_i = C_{pi} \left[(T_i - T_\infty) - T_\infty \ln \frac{T_i}{T_\infty} \right] \quad (7)$$

$$Ex_o = C_{po} \left[(T_o - T_\infty) - T_\infty \ln \frac{T_o}{T_\infty} \right] \quad (8)$$

$$\text{Exergy loss} = \text{Exergy inflow} - \text{Exergy outflow} \quad (9)$$

$$\sum Ex_{\text{loss}} = \sum Ex_i - \sum Ex_o \quad (10)$$

The exergetic efficiency can be described as the fraction of exergy used for dehydrating the banana sample to the exergy of the drying air supplied to the system. The expression for calculating exergetic efficiency is shown Eq. (11)

$$\text{Exergy efficiency} = \frac{\text{Exergy inflow} - \text{Exergy loss}}{\text{Exergy inflow}} \quad (11)$$

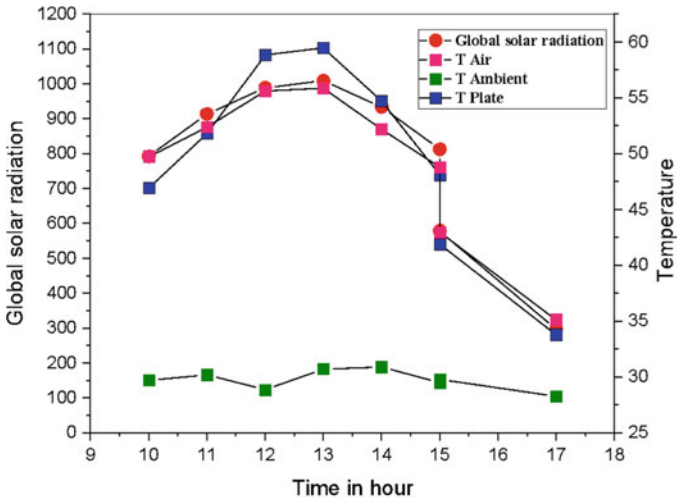
Equation (12) can also be stated as,

$$\eta_{EX} = 1 - \frac{EX_{\text{loss}}}{EX_i} \quad (12)$$

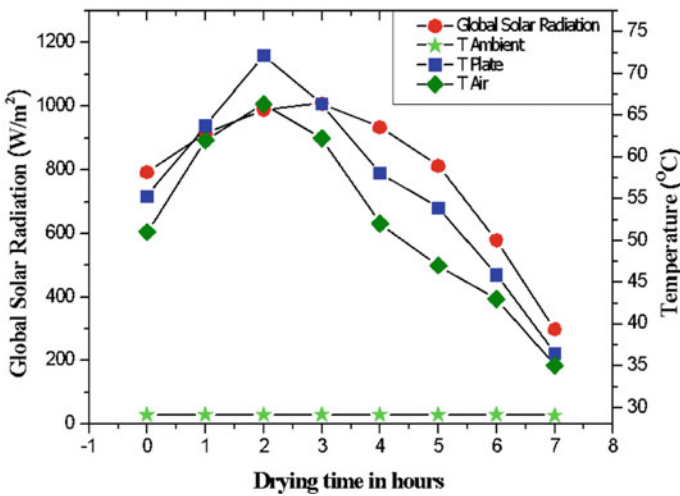
4 Results and Discussions

4.1 Drying Characteristics and Environmental Conditions

Dehumidification process by solar dryers is affected by several environmental conditions like the insolation, the surrounding temperature, relative humidity and velocity of wind inside the dryer. Figure 2a, b shows the change in some of these parameters with respect to drying in both types of solar dryers. The incident global solar radiation varied from 297 to 1008 W/m². At the beginning of the experiment, the recorded ambient temperature was 29 °C, after a while, maximised to a temperature of 31 °C at the 3rd hour of drying. At the termination of the experiment the ambient temperature was reported to be 28 °C. The drying temperature of natural convection dryer varied from 35 to 56 °C and for forced convection solar dryer, the temperature varied from 38 °C to 68 °C. The temperature of the collector plate of the natural convection dryer varied from 33 to 60 °C and that of forced convection solar dryer varied from 36 to 72 °C. The temperature variation in the solar dryer is showing the same trend of variation of the incident solar radiation.



(a) Natural convection



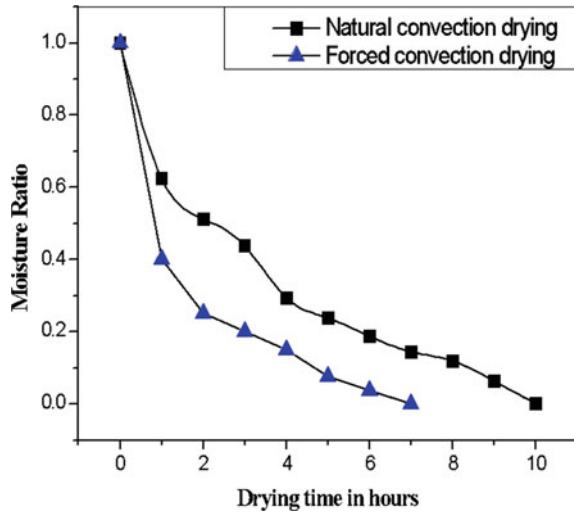
(b) Forced convection

Fig. 2 a and b Effect of solar radiation inlet, drying air, absorber plate and ambient temperature on natural and forced convection solar dryer, respectively

4.2 Moisture Ratio

Comparison of variation of moisture ratio of poovan banana samples dried under the natural and forced convection solar dryer is shown in Fig. 3. In both the curves we can notice that at the beginning of the experiment the moisture ratio decreases rapidly and gradually the rate of decrease of moisture. The poovan banana samples were dried

Fig. 3 Comparison of moisture ratio between forced and natural convection solar dryer with respect to drying hours



to 20% wet basis wetness content from an initial moisture content of 74% within 7 h when dried using forced convection solar dryer, while the same moisture content was achieved within 10 h when the samples were dried using the natural convection solar dryer. From the graph, it is observed that the period of drying required is shorter for forced convection than the natural convection solar drying process. This shorter time period occurred in forced convection process due to the high air velocity created inside along with energy received from the incident solar radiation, while the natural convection had a lower air velocity and lower energy received via the incident solar radiation.

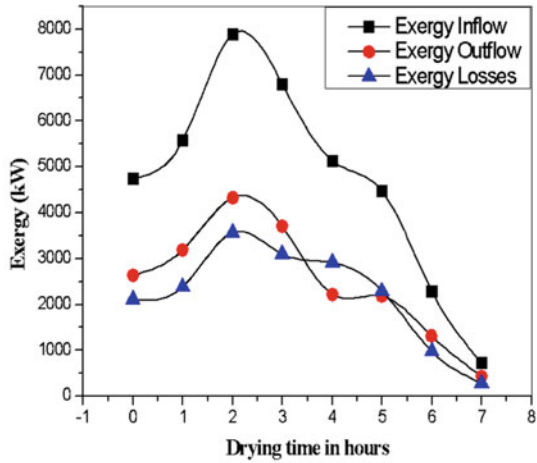
4.3 Energy and Exergy Analysis

The energy and exergy analysis is vital to determine the performance of the dryer since it analyses the energy and available energy associated with the dryer and their utilisation. Figure 4a, b shows the deviation of exergy at inlet, outlet and losses of the single slope natural and forced convection solar dryers. The results show that the exergy of inflow and outflow varied corresponding to the variations in the incident solar radiation.

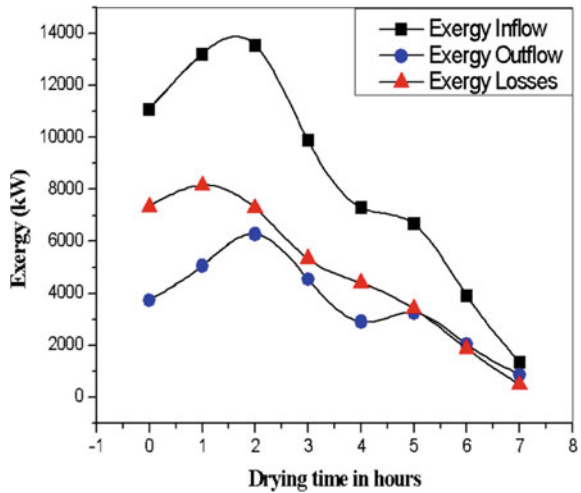
A comparative study of variation in energy utilisation ratio of natural solar dryer and forced solar dryer is mentioned in Fig. 5. The energy utilisation ratio of natural convection dryer varies from 38 to 59% with an average of 46% whereas in the case of forced convection dryer it varies from 14 to 30% with an average of 23%.

Figure 6 represents the change in exergetic efficiency with respect to drying time of forced convection and natural convection solar dryer. The exergetic efficiency of the forced convection solar dryer varies from 36 to 66% with an average of 53%. In

Fig. 4 Variation of exergy during inflow, outflow and losses in natural convection drying and forced convection drying, respectively



(a) Natural Convection



(b) Forced Convection

the natural convection solar dryer, the value varies from 39 to 56% with an average of 46%.

5 Conclusion

The energy and exergy analysis of poovan banana dried in single slope solar dryer with natural and forced mode of convection were done in this study. The wet basis

Fig. 5 Variation of energy utilisation ratio under forced and natural convection solar dryer

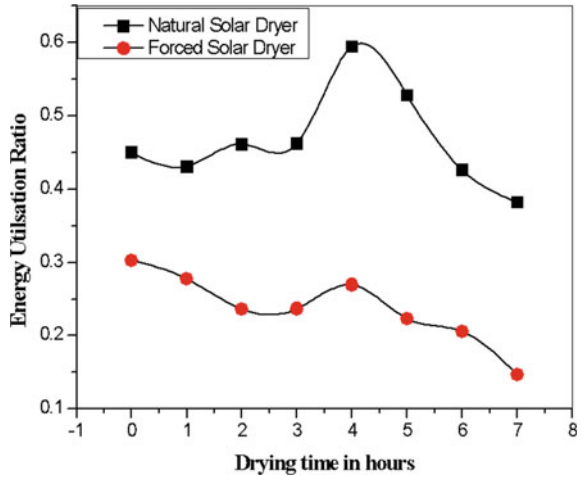
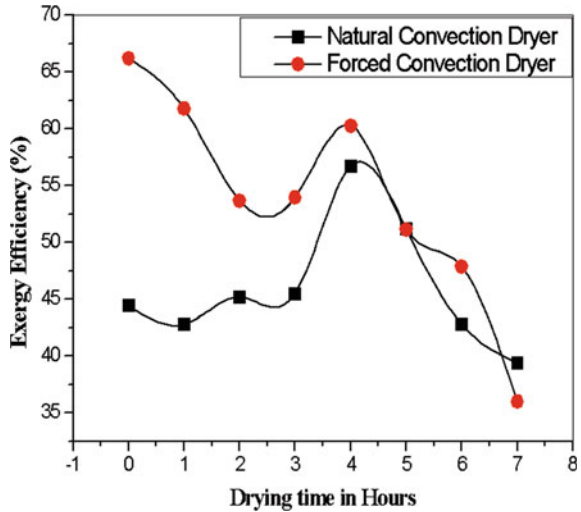


Fig. 6 Variation of exergy efficiency with time in forced convection and natural convection solar dryer



wetness present in the bananas were minimised to 20% from an initial wetness content of 74%. The equilibrium moisture content was achieved in the forced convection solar dryer within 7 h with the temperatures ranging from 37 to 68 °C. However, the natural convection solar dryer took 10 h of drying to achieve equilibrium moisture content with the temperatures ranging from 35 °C to 56 °C, respectively. The insolation was observed to be from 297 to 1008 W/m². The exergetic efficiency of the forced convection dryer was about 53% whereas in natural convection solar dryer it is 46%. The highest value of exergy was obtained when the exergy losses were minimum. At higher temperatures, the exergy losses were minimum and higher value of exergetic efficiency was obtained. The energy utilisation ratio of natural convection solar

dryer varies from 38 to 59% with an average of 46% whereas in the case of forced convection dryer it varies from 14 to 30% with an average of 23%.

References

1. Banana Link (2020) Working towards a fair & sustainable banana trade. Retrieved 30 June 2020, from <https://www.bananalink.org.uk/>
2. Doymaz İ (2010) Evaluation of mathematical models for prediction of thin-layer drying of banana slices. *Int J Food Prop* 13(3):486–497
3. Janjai S, Lamler N, Intawee P, Mahayothee B, Bala B, Nagle M, Müller J (2009) Experimental and simulated performance of a PV-ventilated solar greenhouse dryer for drying of peeled longan and banana. *Sol Energy* 83(9):1550–1565
4. Dincer I, Sahin A (2004) A new model for thermodynamic analysis of a drying process. *Int J Heat Mass Transf* 47(4):645–652
5. Dincer I (2002) On energetic, exergetic and environmental aspects of drying systems. *Int J Energy Res* 26(8):717–727
6. Natarajan SK, Elavarasan E (2019) A review on computational fluid dynamics analysis on greenhouse dryer. *IOP Conf Ser Earth Environ Sci* 312:012033
7. Maia C, Ferreira A, Cabezas-Gómez L, de Oliveira Castro Silva J, de Morais Hanriot S (2017) Thermodynamic analysis of the drying process of bananas in a small-scale solar updraft tower in Brazil. *Renew Energy* 114, pp 1005–1012
8. Bennamoun L (2012) An overview on application of exergy and energy for determination of solar drying efficiency. *Int J Energy Eng* 2(5):184–194
9. Rabha D, Muthukumar P (2017) Performance studies on a forced convection solar dryer integrated with a paraffin wax-based latent heat storage system. *Sol Energy* 149:214–226
10. Corzo O, Bracho N, Vásquez A, Pereira A (2008) Energy and exergy analyses of thin layer drying of coroba slices. *J Food Eng* 86(2):151–161
11. Akpınar EK (2004) Energy and exergy analyses of drying of red pepper slices in a convective type dryer. *Int Commun Heat Mass Transfer* 31(8):1165–1176
12. Lingayat A, Chandramohan VP, Raju VRK (2019) Energy and exergy analysis on drying of banana using indirect type natural convection solar dryer. *Heat Transfer Eng* 1–11
13. Akbulut A, Durmuş A (2010) Energy and exergy analyses of thin layer drying of mulberry in a forced solar dryer. *Energy* 35(4):1754–1763
14. Tiwari GN, Das T, Chen CR, Barnwal P (2009) Energy and exergy analyses of greenhouse fish drying. *Int J Exergy* 6(5):620
15. Kumar Natarajan S, Sankaranarayanan K, Ponnusamy S, Kavya Chowdary V, Kumar J, Rahul D, Agarwal S, Elavarasan E (2019) Experimental comparative study on reduction in the moisture content of cucumber in a double slope solar dryer with open sun drying method. *J Phys Conf Ser* 1276:012054
16. Natarajan SK, Elavarasan E (2019) Experimental investigation of drying potato for karaikal climatic condition. *IOP Conf Ser Earth Environ Sci* 312:012021

Experimental Investigation of Surface Roughness in Electric Discharge Machining of Hybrid Metal Matrix Composite



Gurpreet Singh Matharou and B. K. Bhuyan

Abstract This study is an attempt to investigate the influence of selected input variables on very essential response parameters surface roughness (R_a) during die-sinking electrode discharge machining (EDM) of aluminum-based hybrid metal matrix composite (HMMC) using a copper electrode. The HMMC was developed through stir casting route with the parent metal (Aluminum 6063), reinforcement materials (silicon carbide (SiC) and boron carbide (B_4C)), and magnesium (Mg). The trend of the graph suggests that R_a increases with an increase in voltage, current, and pulse on time but decreases with an increase in pulse off time. Moreover, the lowest value of R_a observed at spark gap at 5 mm, current at 5 A, and voltage at 25-V settings, and the highest R_a was obtained at pulse of time at 8 μ m with spark gap at 7 mm and current at 10 A parameter settings.

Keywords Electric discharge machining · Material removal rate · Aluminum composite · Current · Voltage · HMMC

Abbreviations

R_a	Surface roughness
MRR	Material removal rate
EWR	Electrode wear rate
V	Voltage
I_p	Current
T_{on}	Pulse on time
T_{off}	Pulse off time
S_g	Spark gap
Al	Aluminum
10SiC	10% wt of Silicon carbide

G. S. Matharou (✉) · B. K. Bhuyan
Mechanical Engineering Department, Faculty of Engineering and Technology, Manav Rachna
International Institute of Research and Studies, Faridabad, Haryana, India

5B₄C 5% wt of boron carbide
Mg Magnesium

1 Introduction

Advanced engineering materials are known for their improved temperature and corrosion resistance with extreme strength and hardness properties. Composite materials are one such material that is in exponential demand from different fields of automobiles, space research, nuclear energy, aeronautics, missile technology, electronics, and biomedical engineering, etc. [1] Composites materials are developed from two or more additive material or elements with differentiating chemical composition and physical properties that, when combined, produce a new substance with characteristics different from base materials. Aluminum-based metal matrix composite has emerged as an advance engineering material due to high stiffness, high strength, less density, better resistance against wear, and high thermal properties. The new novel HMMC is Al-SiC-B₄C-Mg, which has got lots of demand in elaborative applications in automobiles, mineral processing industries, aerospace, etc. [2] Traditional processes have machining difficulties in machining and finishing these novel materials due to extremely high machining costs, low processing speed, and poor cut quality. Non-conventional machining processes like, electro-chemical machining (ECM), laser beam machining (LBM), water jet machining (WJM), etc., are an alternative to overcome the stated problems. Still, these processes generally carry limitations of their own regarding processing cost, workpiece material, shapes, method, etc. To cope up with such problems, the die-sinking EDM has now being developed for a competent and cost-effective machining process. In die-sinking EDM, the shape of the electrode is mirrored on the workpiece. The electrode of complex shape requires considerable time for development. Still, once it has been developed, a large number of workpieces can be mirrored by the electrode shape using die-sinking EDM. In EDM process, the input variables such as current (A), gap voltage (V), pulse on time (T_{on}), Spark gap (S_g), and duty factor (T) have more influence on output variables like MRR, EWR, and R_a [3]. The input process parameters thus need to be optimized to meet the industry requirements. In the past, much research had performed to conduct the experiments using EDM of different composites, alloys, steels, tungsten materials, etc.

Dikshit et al. [4] had conducted an investigation on Inconel 625 superalloy by forming an empirical model for R_a and MRR as output variables. They concluded that MRR got influenced by I_p and then by T_{on} , and R_a got greatly influenced by T_{on} then T_{off} . Sahu et al. [5] had attempted EDM of Nimonic alloy using the copper electrode to ascertain the effect of I_p and T_{on} on MRR, EWR, and R_a . They reported that with a variation of I_p and T_{on} , MRR and EWR increases. Goyal [6] had experimentally observed that the T_{on} , cryogenically treated tool electrode and current directly affects MRR and R_a while working on Inconel 625 with zinc-coated wire in EDM. It

was reported after every T_{on} cycle, a considerable amount of debris was ejected on workpiece causing higher R_a . Luis et al. [7] have framed a mathematical model while studying the effect of T_{on} and I_p on R_a , EWR, and MRR during EDM of siliconized silicon carbide (SiSiC). They had concluded that current proportionally affects both MRR and EWR, whereas the pulse duration increases and reduces MRR and EWR, respectively. Jithin et al. [8] had proposed two spark models to predict the R_a for electro-discharge texturing had predicted the arithmetic mean deviation of R_a with the experimental values of other authors and had reported prediction error of around 18% and 110%, respectively, for low and high values of T_{on} and I_p .

Gopalakannan and Senthilvelan [9] had investigated on EDM machining of aluminum with boron carbide and had concluded I_p and T_{on} as factors influencing the MRR. Yang et al. [10] and Yilmaz et al. [11] have found that the addition of rigid ceramic part to a soft matrix alloy (aluminum) improves the wear resistance, performance of creep, and has enhanced the strength of the material. Vijaya et al. [12] had experimentally proved that aluminum matrix could be strengthened by reinforcing with ceramic particles such as silicon carbide (SiC), boron carbide (B_4C), and alumina (Al_2O_3). Uvuraja et al. [13] had varied the reinforced material (SiC, B_4C) volume fraction from 2 to 11 wt% with base metal Aluminum 6061 they concluded that with increase in reinforced volume fraction, the friction coefficient and electrode wear rate decrease, and the presence of SiC improves the microhardness value. Satyaraj et al. [2] had used B_4C and Al_2O_3 separately as a reinforcement material in Al-MMC. They compared the 3 and 6% addition of B_4C and Al_2O_3 in Al-MMC and had concluded that with an increase in SiC, the hardness value had increased, and with a rise in Al_2O_3 , the impact value and wear resistance increases. Patel et al. [14] had used an aluminum ceramic composite with a regression model of the second order for prediction of R_a through response surface methodology (RSM).

From the available literature review, the HMMC Al 6063-10SiC-5 B_4C -Mg is found to be in the experimental stage as very little work has been reported. The EDM input parameters role in affecting R_a of the said composite workpiece has attempted.

2 Experimental Work

2.1 Fabrication of Hybrid Metal Matrix Composite

The HMMC Al 6063-10SiC-5 B_4C -Mg was prepared using the conventional stir casting method since it is known for its low cost, most straight forward operation, and mass production suitability. Kalaiselvan et al. [15] Table 1 shows the composition of the composite. The reinforcement material SiC is known to withstand extreme temperatures and has got high hardness with low density, and B_4C has got good mechanical strength with properties relating to neutron absorption Shorowordi et al. [16].

Table 1 Composition of hybrid composite materials

Element	Aluminum 6063	SiC of micron size 45 μm	B ₄ C of micron size 52 μm	Mg
% (wt)	84	10	5	1

Firstly, the elements of the composites were measured using an electronic balancer to ascertain the % wt of the constituents Fig. 1a. The reinforced materials SiC and B₄C were preheated at about 900–1050 °C for about 1 h in a furnace Fig. 1b to remove any moisture in them and to oxidize their surfaces. The Aluminum 6063 pieces were taken in a new crucible and heated to 480–500 °C for around 2 h before melting. After that the aluminum is heated beyond its melting temperature at 700–750 °C, so that it completely melts. Now for about 15–20 min, SiC and B₄C are being added manually, and stirrer motor is operated in between at 400 and 500 rpm to mix the contents and to achieve the best consistency possible. After stirring operation, the melt was poured in the rectangular mold Fig. 1c to give a brick of size length 140 mm, breadth 60 mm, and height 30 mm.

The brick is further cut into a smaller size of 20 mm \times 30 mm \times 5 mm for experimentation on die-sinking EDM Fig. 2, and the pure copper with 15 mm cutting diameter has been used as an electrode. The composition of Al-6063 is shown in

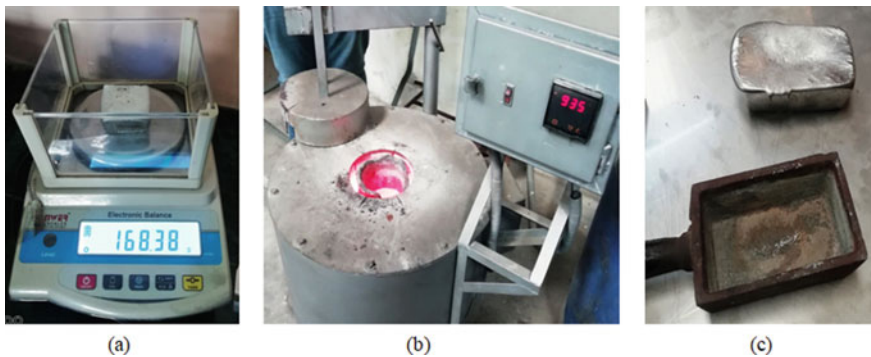


Fig. 1 Composite development through stir casting. **a** Electronic balancer. **b** Electric furnace. **c** Mold with composite brick



Fig. 2 HMMC samples

Table 2 Composition of Al-6063

Al-6063 composition	Wt%	Al-6063 composition	Wt%
Al	Max 97.5	Mn	Max 0.1
Cr	Max 0.1	Si	0.2–0.6
Cu	Max 0.1	Ti	Max 0.1
Fe	Max 0.35	Zn	Max 0.1
Mg	0.45–0.9		

Table 3 Thermal and mechanical properties of the individual constituents

Material	Tensile strength	Density	Thermal conductivity	Modulus of elasticity
	(MPa)	(g/cm ²)	(W/m–K)	(GPa)
Al alloy 6063	300	2.7	167	68.9
Silicon carbide	137.9	3.1	120	450
Boron carbide	261	2.3	30–42	362

Table 4 Mechanical properties of hybrid composite materials Kalaiselvan et al. [15]

Hybrid metal matrix composite material	Tensile strength	Yield strength	Density	Brinell hardness	Break load
	(N/mm ²)	(N/mm ²)	(Kg/m ³)	(HB)	(kN)
84 wt% Al–10 wt% SiC–5 wt% B ₄ C	120.32	98.75	2537.5	71.58	9.45
	Maximum displacement	Elongation	Flexural break load	Flexural maximum deflection	Flexural strength
	(mm)	%	(kN)	(mm)	(MPa)
	9.7	7.53	3.68	5.6	214.12

Table 2. The thermal and mechanical properties of the individual constituents of the composite are depicted in Table 3. Table 4 shows the mechanical properties of hybrid composite materials.

2.2 Experimentation on an EDM

The die-sinking EDM machine used was a JOEMARS EDM AZ50 series Taiwan make with three-phase power input with a maximum current of 50 A. With direct polarity, a pure copper electrode was used for experimentation. Figure 3 shows the JOEMARS EDM. Table 5 shows the experimental facility used.



Fig. 3 JOEMARS EDM AZ50 series

Table 5 Experimental facility used

Facility	Specifications
EDM machine	JOEMARS EDM AZ50 series Taiwan make
Surface roughness tester	Mitutoyo SJ-201 Sr. No. 500829 surface finish meter ($-200\ \mu\text{m}$ to $+150\ \mu\text{m}$)
Digital weigh balancer	Generic Digital Pocket Scale 0.001–200 gm
Electrode	Pure copper rod of dia 15 mm and height 100 mm
Flushing speed	Flow rate of $1.2\ \text{kg}/\text{cm}^2$ kept constant through all experiments
Dielectric medium	Kerosene-based EDM oil

The ranges of selected input variables were voltage “V” (25, 50, 75 V), current “ I_p ” (5, 10, 15 A), pulse on time “ T_{on} ” (50, 75, 100 μs), pulse off time “ T_{off} ” (8, 12, 16 μs), and spark gap “ S_g ” (3, 5, 7 mm); a most predominant output parameter like R_a (μm) is selected based on literature review and pilot experiments. Machining time is kept constant at 15 min per sample.

2.3 Calculation of R_a

The samples were cut into equal sizes of $20 \times 30 \times 4\ \text{mm}$ Fig. 1d. The copper electrode of 15 mm diameter and an initial sample weight was measured using the Generic Digital Pocket Scale (0.001–200 gm). The workpiece and electrode were mounted on the workbench and chuck, respectively, and alignment and leveling performed.

As per the design of experiment, the input parameters were feed in the EDM. Before starting the EDM machine, the input voltage was being checked for any faults in terms of fluctuations, etc. The side flushing method is used by manually setting the flow of flushing pressure directly on the top of the surface of the workpiece for maximum cleaning action and thus better R_a . The electrode placed near the workpiece, and the lift was adjusted accordingly. The machine was allowed to run for 15 min. During this period, the electrode approaches near to the surface of the workpiece, creating a spark, and then lifts off. During liftoff, the flushing mechanism flushes the debris of the workpiece from its surface. After 15 min of EDM action, the machine switched off, the workpiece and electrode were removed and weighed again with the digital scale. Mitutoyo SJ-201 Sr.No., 500829 surface finish meter, has been used to find R_a .

3 Results and Discussion

The consequence of various input parameters like voltage (V), current (I_p), pulse on time (T_{on}), pulse off time (T_{off}), and spark gap (S_g) on output parameter R_a was studied using EDM process during the machining of Al6063-10SiC-5B₄C-Mg with an electrode made from pure copper. The experiments had been carried out with varying one input parameter while keeping other parameters to remain constant. The following trends of graph have been illustrated and elaborated in different sections.

3.1 Effect of V on R_a

Effect of applied voltage on R_a in the EDM process, keeping other parameters constant is illustrated in (Fig. 4). It can be observed in the figure that the R_a increases proportionally with an increase in applied voltage for three different values of spark gap (3, 5 and 7) mm. This phenomenon is because as V increases, the spark energy increases, causing more material removal rate leading to a rise in R_a . However, due

Fig. 4 Effect of voltage on R_a

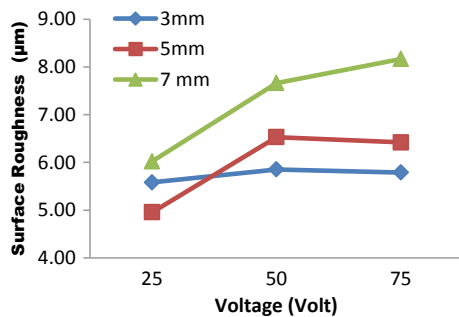
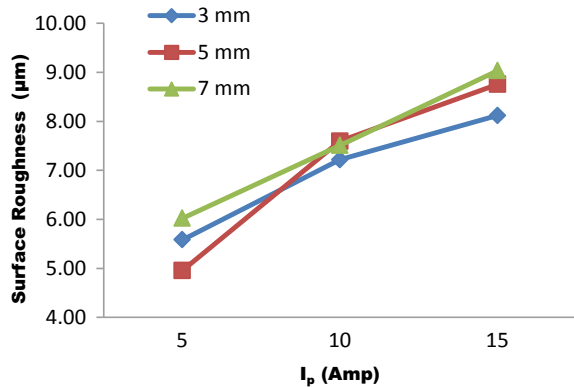


Fig. 5 Effect of current on R_a



to the carbide particle availability in the HMMC, it brings down the material removal rate. It does not give ample energy to melt and aerate the carbide material when a voltage increases beyond 50 V, decrease in R_a was observed.

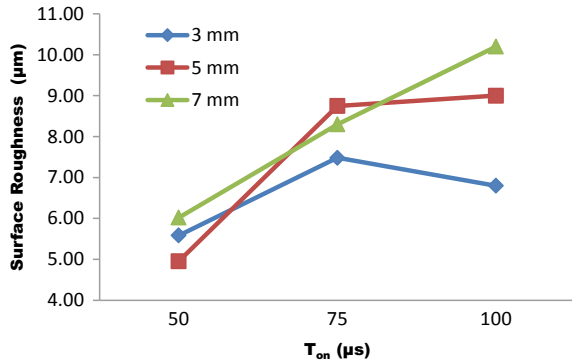
3.2 Effect of I_p on R_a

The R_a rises with an increase in current. The occurrence could be because, as current increases, more will be the spark energy content. Due to high energy content in the spark, more will be the MRR due to the high rate of erosion, causing more deep craters on the surface of the workpiece, thereby increase in R_a . The lowest value of R_a is observed at $I_p = 5$ A with S_g 5 mm (Fig. 5).

3.3 Effect of T_{on} on R_a

The R_a has increasing patten concerning T_{on} increase, keeping other parameters constant. As T_{on} increases, more heat energy liberated per cycle of operation. (Fig. 6) That increases the localized heat causes clusters formation on the workpiece surface, leading to a deteriorated surface finish. Besides, the melted materials from the work-piece might also get re-solidified back onto the surface crest in uneven form, thereby increasing R_a . A significant observation made that beyond T_{on} (75 μs) at 3 and 5 mm spark gap, the decline in R_a was observed because of the deposition of molten metal back into the cavities and pores. At a 7 mm spark gap, no such decrease in R_a can be observed. The lowest value of R_a is visible at T_{on} (50 μs) with a 5 mm spark gap.

Fig. 6 Effect of pulse on time on R_a



3.4 Effect of T_{off} on R_a

The general trend shows a decline in R_a with an increase in T_{off} . (Fig. 7) The phenomenon could be because of better flushing action. As T_{off} increases, better flushing is possible since the time for workpiece surface cleaning improves, thereby removal of molten metal formed during T_{on} action flushed out from the workpiece surface in a better way. Moreover, more T_{off} time will reduce the temperature of the surface; some of the molten metal gets re-solidified back onto the surface, thereby filling the gaps caused during machining. At high T_{off} , less R_a observed.

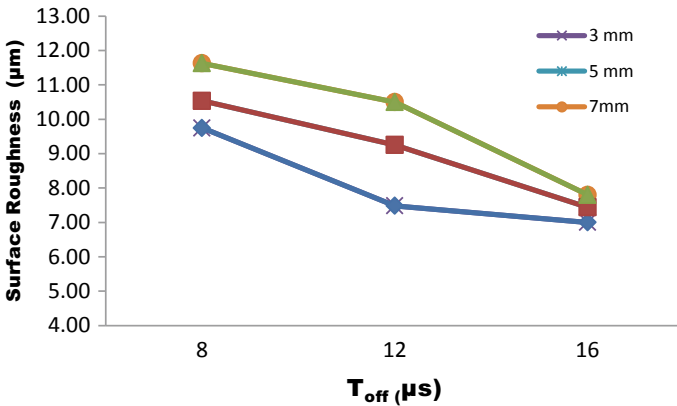


Fig. 7 Effect of pulse off time on R_a

4 Conclusion

The hybrid metal matrix composite with Al 6063 as matrix material and B₄C, SiC as reinforced material, has been successfully prepared using a stir casting route. The key observations noted while EDM of the HMMC is as follows.

- With an increase in V , I_p , and T_{on} , the R_a increases because of excessive spark energy discharge from the electrode, causing significant material removal from the workpiece surface, causing uneven surface topology. A decrease in surface roughness is observed when the V increases beyond 50 V. Almost constant R_a values at a S_g of 3 mm.
- The R_a observed to decrease with an increase in T_{off} . The I_p and T_{on} are the most influential input parameters on which the R_a depends directly. R_a decreases beyond T_{on} (75 μ s) at a S_g of 3 and 5 mm.
- The trends of the graphs demonstrate that S_g of 5 mm, depicted with the higher MRR as compared to the S_g at 3 mm and 7 mm. The lowest value of R_a is observed during S_g at 5 mm, I_p at 5 A, and V at 25 V, and the highest R_a was obtained at T_{off} at 8 μ m with S_g at 7 mm and I_p at 10 A.

References

1. Narayana KJ, Gupta BR (2018) A review of recent research on multifunctional composite materials and structures with their applications. *Mater Today Proc* 5(2):5580–5590
2. Sathyaraj S, Venkatesan K, Srikanth J (2018) Fabrication of aluminium 6061-SiC-Al₂O₃ MMC and HMMC by stir casting technique and comparing the mechanical properties. *Int J Mech Product Eng Res Dev* 8(1):635–642
3. Qudeiri JE, Mourad AH, Ziout A, Abidi MH, Elkaseer A (2018) Electric discharge machining of titanium and its alloys: review. *Int J Adv Manuf Technol* 96(4):1319–1339
4. Dikshit MK, Anand J, Narayan D, Jindal S (2019) Machining characteristics and optimization of process parameters in die-sinking EDM of Inconel 625. *J Braz Soc Mech Sci Eng* 41(7):412–419
5. Sahu D, Sahu SK, Jadam T, Datta S (2019) Electro-discharge machining performance of Nimonic 80A. An experimental observation. *Arab J Sci Eng* 44, 10155–10167
6. Goyal A (2017) Investigation of material removal rate and surface roughness during electrical discharge machining (EDM) of Inconel 625 super alloy by cryogenic treated tool electrode. *J King Saud Univ* 29(4):528–535
7. Luis CJ, Puertas I, Villa G (2005) Material removal rate and electrode wear study on the EDM of silicon carbide. *J Mater Process Technol* 164:889–896
8. Jithin S, Bhandarkar UV, Joshi SS (2020) Multi-spark model for predicting surface roughness of electrical discharge textured surfaces. *Int J Adv Manufact Technol*. <https://doi.org/10.1007/s00170-019-04841-5>
9. Gopalakannan S, Senthilvelan T (2013) A parametric study of electrical discharge machining process parameters on machining of cast Al = B₄C metal matrix nanocomposites. *Proc Inst Mech Eng Part B J Eng Manufact* 227:993–1004
10. Yang JB, Lin CB, Wang TC, Chu HJ (2004) The tribological characteristics of A356.2 alloy/Gr(ρ) composites. *Wear* 257:941–952
11. Yilmaz O, Butoz S (2001) Abrasive wear of AlO₃-reinforcement aluminum-based MMCs. *Compos Sci Technol* 61:2381–2392

12. Vijaya Ramnath B (2014) Evaluation of mechanical properties of aluminium alloy–alumina–boron carbide metal matrix composites. *Mater Des* 58:332–338
13. Uvaraja VC, Natarajan N (2012) Tribological characterization of stir cast hybrid composite aluminium 6061 reinforced with SiC and B₄C Particulates. *Eur J Sci Res* 76(4):539–552
14. Patel KM, Pandey PM, Venkateswara RP (2009) Determination of an optimum parametric combination using a surface roughness prediction model for EDM of Al₂O₃ = SiCw = TiC ceramic composite. *Mater Manufact Process* 24:675–682
15. Kalaiselvan K, Muruganand N, Siva P (2011) Production and characterization of AA6061-B₄C stir cast composite. *Mater Des* 32:4004–4009
16. Shorowordi KM, Haseeb ASMA, Celis JP (2006) Tribo-surface characteristics of Al–B₄C and Al–SiC composites worn under different contact pressures. *Wear* 261(5–6):634–641

Modeling and Simulation of Mechanical System for Power Generation Using Footsteps



Anmol Singh, Anshul Singh, and Arunesh Chandra 

Abstract Energy needs have been majorly met by fossil fuels like coal, natural gas, and petroleum, and its fulfillment has become an issue that has deteriorated the surrounding environment in many ways. Into the growing world of a massive population, the needs of humans have increased drastically. This is due to a significant change in the lifestyle and social status of the people in the past 2–3 decades, and these needs result in the requirement of the enormous amount of energy in the modern era. As a result, there is an urgent need for an alternative source to meet the energy crises, and renewable sources like solar, wind, thermal, ocean, etc., have shown good results to meet the needs, but its economics, efficiency, and effectiveness are still a matter of concern. The work presented in this study is an approach to find a feasible solution to the problem by harnessing the enormous amount of footstep energy which can be generated by a massive population using the principle of electromagnetic induction. In this method, change in the magnetic field is obtained with the help of a special generator that converts the vertical displacement of the foot by the use of a special double grooved shaft that fits in a freely moving dual ratchet mechanism. This unidirectional rotation is possible with the help of bearings that utilize the momentum and increase the rotation speed of the outer wheel with magnets which induces electricity into the windings, providing an approximate 2.5 V per footstep. The method provided in this study is green, economical and if installed effectively at workplaces having large population or gathering will deliver huge energy which can be used and stored for further use.

Keywords Footsteps · Energy generation · Simulation · Electromagnetic induction

A. Singh · A. Singh (✉) · A. Chandra
KIET Group OF Institutions, Ghaziabad, India

A. Chandra
e-mail: arunesh.chandra@kiet.edu

1 Introduction

All organisms need the energy to exist. Energy is connected to any or all life activities: Whenever we predict or move, we tend to utilize the energy that is held in our body, and every one of the objects that we tend to use or that surround us want energy to figure or require energy once they were engineered. Energy illuminates and warms our homes, aids the vehicles to maneuver, feeds the tools we tend to use to harvest food, and so on. All that produces energy is “an energy source”. The Sun is the main supply of energy for the planet [1, 2].

The way into the future is based on the alternative fuel and systems which not only help fulfill the energy needs but also can promise good eco-friendly results. These come up with very not so promising results till date as mankind rushing toward a replaceable source, the current productivity of these alternative systems is still low but if these can be managed to integrate into a connected system that can help utilize the bits of these outputs and transform it to a larger one [3].

The development of several green (clean) energy system is a major strategy to achieve environment balance [4–7]. We know that most people spend most of their lifetime in walking. During walking, human feet exert force on the ground, and this force can be used to generate electrical energy with the help of footstep power generator.

Several types of footstep power generations methods are available, and majority of these devices use piezoelectric transducer to generate power. Major problem in designing with piezoelectric transducer is the selection of suitable ferroelectric material because it governs the efficiency of energy conversion, i.e., from kinetic to electrical energy [8].

In this paper, we are talking about a proposal toward a newer thought of generating electricity, by taking the human footsteps as the primary source of the supply of fuel. The growing population leaves a larger footfall which rejects the energy down toward the earth, and this not so large energy yet can be utilized in a way through the system designed and connected in order to harness the footfall’s exerted force.

2 Literature Review

Innovative technology always gives the latest and versatile trend in every field. In the past few years, we have perceived that every task was difficult due to less evolved technologies, but today’s technology provides many more new directions in every field of electronics, agriculture, business, medical, etc. This project portrays the evolution of technology in the field of alternate sources of energy. The new development that our project offers is that we composed the design of the device which converts human kinetic energy into electrical energy. In previously published papers on footsteps arrangement, we found that there were used rack and pinion mechanisms and piezoelectric materials for power generation through human footsteps.

Our arrangement consists of a shaft, pin, nut, and ratchet mechanism which has simpler construction than rack and pinion arrangement and is more economical than the one with piezoelectric sensors.

The paper [9] presents a mechanism that harvests energy from human walking efficiently. A power generation arrangement is consisting of a permanent magnetic motor, racks and pinions gears, and a one-way clutch unit. The up-and-down motion of the paver's high panel to the unidirectional rotational motion is achieved by one-way clutch unit. A regulator is connected to the electrical generator to gain the full advantage of the available potential energy during human walking. Their experimental results show that, during typical human walking, the arrangement is capable of producing an average electric power of 3.6 W, with a peak value of 12 W.

In the paper [10], authors present an idea to harvest non-conventional energy from just walking into electrical energy. They used a simple drive mechanism, i.e., rack and pinion assembly for power generation. The management mechanism carries the rack and pinion and D.C generator to output. In this project, they used to generate electrical power as a non-conventional method by simply walking or running. A battery is used to store the generated power and also for activating the connected loads. Power generation by this type of method uses compact and efficient systems that can easily be installed in many regions.

In the paper [11], the idea is the same for power generation, i.e., using piezoelectric materials, but they also used a GPS tracking system with their arrangement to trace the number of footsteps. Their working is based on the principle of the piezoelectric effect. The piezoelectric sensors are used to produce output energy in the form of AC voltage. With GPS tracking, streetlights switching techniques are also added as compared with the existing model.

Most of the footsteps generators are based on piezoelectric transducer which increase the cost of power generation. To counter this problem, Ang et al. [12] proposed a simple and economical mechanism of power generation.

According to this paper [13], the maximum output generated by tile during both downward and upward motion is 15 W. A synchronous generator is used for its better output and its suitability. A flywheel is used to store required potential energy and to get maximum inertia as much as possible. For smooth power generation with less damping, two one-way clutches units are used. To generate different output, different flywheels with different inertia can be used.

In the context [14], authors developed a system based on two square-sized tile structure pavers in which two fluid bags are connected through flow control mechanisms including unidirectional valves and a mini-hydro generator that convert human motion like walking and running into electrical energy. Their working is based on a fluid mechanics mechanism, and the arrangement can produce an average output of 1.4 W per step during typical human walking and can power up a DC load of 390 Ω LED.

3 Methodology

3.1 Material Selection

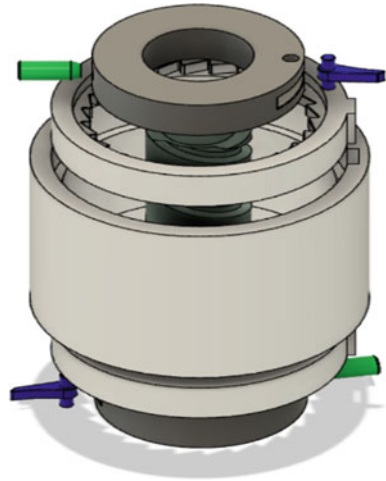
The design has to be taking the to and fro loads during a longer period time, so the tensile strength of the material and also their fatigue strength shall be high so that they can withstand such type of repeated loading without having any problem. The material that would be preferred for the actual prototype is S45C steel, this steel is used heavily and most commonly in the gear making industry, we will make the shaft, ratchets, pins, pawls, and nut out of this steel, and for the outer wheel and caging purpose, we would use the S40C steel [15]. The outermost case for all the material will be of black steel. With the use of stainless steel eventually, the weight of the device can be reduced and at the same time will not have to negotiate with the strength of the device.

3.2 Components Used

- Generator
- Shaft
- Nut
- Pin
- Pawl
- Ratchet
- Outer wheel
- Casing
- Magnets
- Winding coil
- Tile (1 × 1 sq. ft)
- Bearings (Fig. 1).

3.3 Design and Simulation

After seeing the low productivity of the piezoelectric systems and the low reliability of the rack and pinion mechanism, there arose a need to design a new type of device. Based on the principle of electromagnetism a new method of power generation has been developed to harness the human footsteps energy. This also led to the development of unidirectional motion (uniform output) whether the shaft goes down or comes up. For this designing of a double helical grooved shaft that has a separation slot, was done. Then, these grooves are locked into the pins which are mounted on the nut, this nut also has a pawl on the opposite end which is in contact with one of the two

Fig. 1 CAD exploded view

ratchets, and these ratchets are then keyed into the outer wheel with a slotted key joint. At last, the outer wheel gives the uninterrupted unidirectional motion out of the vertical to and fro because of the footstep. The simulation of the major parts taken with average weight as 65 kg has shown that our design is safe at all points and can be feasible too.

3.4 3D Printed Prototype

After the simulation of our model using Fusion 360 software, the next step was to get some hands-on the actual conditional working of the device, so printing a 3D model of a smaller scaled device to check off some flaws or the improvements that can be suggested on the existing model. This was done using the IDEA MAKER software. This process helped to understand and look deeper into the design problems that could emerge in the actual fabrication of the full-scale model (Figs. 2, 3 and 4).

3.5 Design Modification

After testing the individual elements into the software, it was then the time to check that the mechanism worked out on the actual turf, so checking this with the help of the 3D model through additive manufacturing. It was also noticed there were a few flaws that needed improvements and had to be changed so that during actual manufacturing they do not pose a problem.

These flaws were as follows:



Fig. 2 Shaft

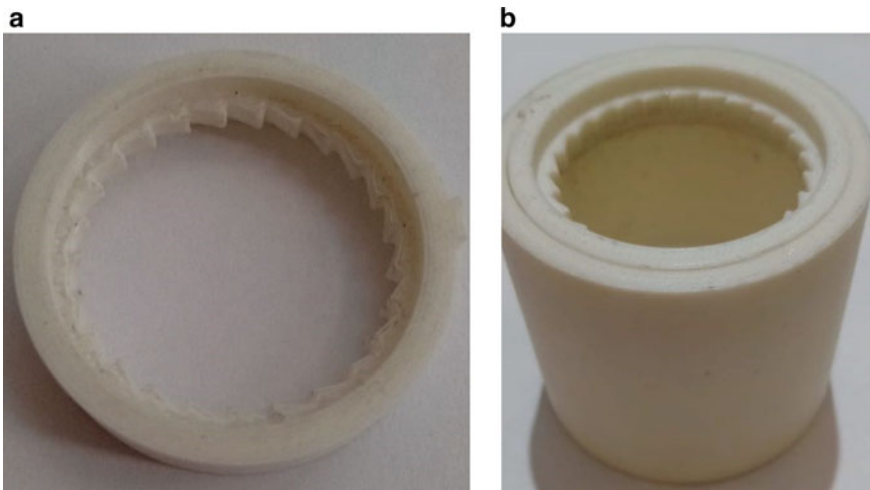


Fig. 3 a Ratchet b Outer wheel with ratchet

1. The incorporation of pawl into the nut as manufacturing it individually was creating a problem of integrating it inside the nut at that time. So, redesigning of pawl into two parts and providing threads to both the parts are done to solve this problem.
2. It then was also seen that the pin was somewhat thrown out of its cavity by the forces of the shaft's rotation, so here comes up the solution to give threads to

Fig. 4 Nut



the pin as well as the internal cavity of the nut. This helped to maintain the pin in the position and oppose the force.

3. It was also noticed some slippage of the nut in the vertical direction because of gravity therefore giving some ring-like extensions to the ratchet to lock the nut and the pawl in the right place (Fig. 5).

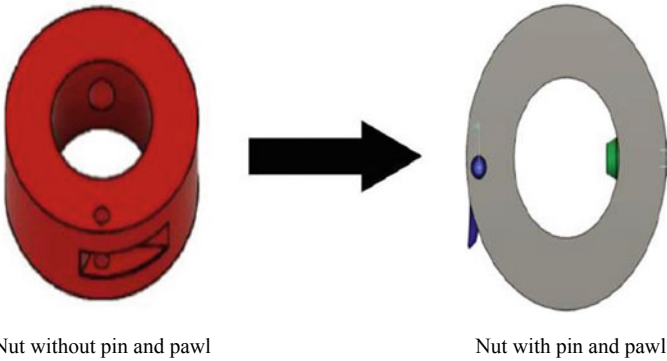


Fig. 5 Nut design upgradation

3.6 Final 3D Print Prototype

The final and actual-sized prototype shows that the mechanism would work properly and can be used for the testing and trials for the next phase of increasing output and making it more reliable by using the actual materials to test it on the real turf.

4 Working

Working is based on both mechanical and electrical phenomenon. Mechanically, footfall force is required to rotate the shaft, and electrically, the mechanism is based on Faraday’s law of electromagnetic induction. This electrical mechanism is coupled with mechanical arrangement to generate electricity.

With the help of a block diagram, the working procedure is explained in step-by-step manner (Fig. 6.)

- Step 1: When the force is applied on the tile by virtue stamping of the tile, the shaft starts rotating downward.
- Step 2: Pin slides in the shaft groove and is also attached to the nut through the screwed joint, so when the shaft starts rotating, the nut also starts rotating.
- Step 3: The rotating shaft produces a torque which is the product of the force applied on the tile and shaft radius.
- Step 4: Pawl attached to the nut also rotates with the nut and gets engaged with ratchet teeth, and therefore, ratchet starts rotating.

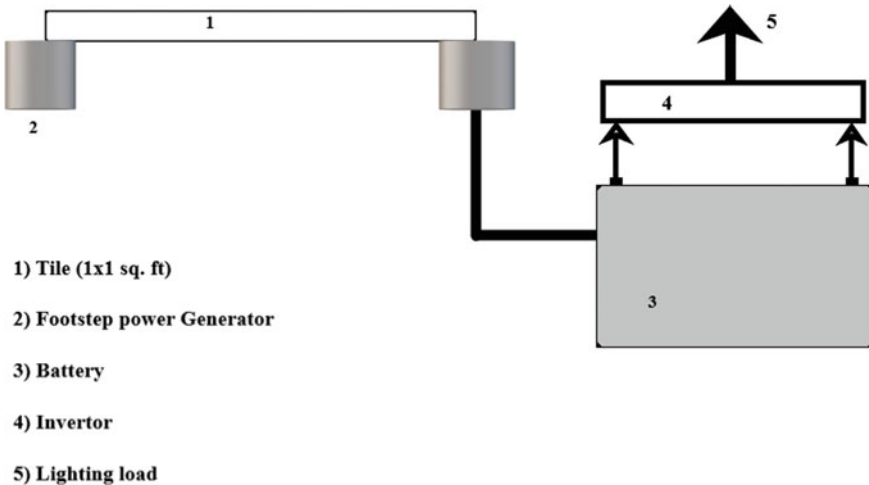


Fig. 6 Footsteps arrangement block diagram

Step 5: Ratchet is connected to an outer wheel, and therefore, the outer wheel also rotates with the shaft’s downward and upward motion.

Step 6: Number of rotations of the shaft is fixed in both upward and downward motion which is equal to the number of helical types grooved on it.

Step 7: This outer wheel is fixed into a simple ball bearing, and magnets are also attached to the bearing. The winding wheel is fixed with a casing inside which magnets on the bearing rotate to induce EMF into the coil.

Step 8: Induced EMF produces electricity that can be used for practical application directly or through an energy storage system like a battery.

5 Simulation

Simulation is carried out in the Autodesk fusion 360 software to check the impact of the load on the moving parts like shaft, pin, and ratchet wheel (Table 1).

The simulation analysis of the components is done by taking load, i.e., taking three times the average human weight (2000 N approx.). The blue region shows that parts are within the safety limits.

$$\text{Load, } P = 65 \times 3 \times 9.81 = 1912.95$$

$$\text{Yield Strength of Steel} = 207 \text{ MPa}$$

$$\therefore \text{Maximum Permissible Force} = 207 \times \text{area of shaft} = 4062.375 \text{ N}$$

The force by footfall on one tile is distributed over four tiles attached underneath of the tile in an ideal condition.

$$\therefore \text{Actual Force on shaft} = 1912.95 \div 4 = 478.23 \text{ N}$$

Table 1 Generator dimensions used for 3D print

Parts	Material used	Yield strength (MPa)	Dimensions (mm)		
			Length diameter	Inner diameter	Outer
Shaft	Steel	207	45	05	
Outer Wheel	Steel	207	28	28	32
Ratchet	Steel	207		24	28
Nut	Steel	207		10.50	20
Pin	Steel	207	05.80	01.86	02.716
Pawl	Steel	207	04.767	02	

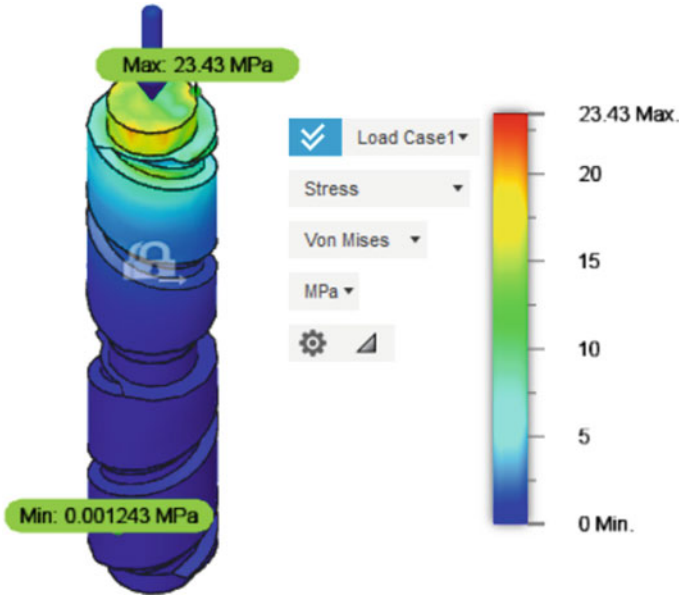


Fig. 7 Shear stresses induce on the shaft

Actual force is less than the maximum permissible force, and hence, we can say that shaft is safe under practical loading conditions.

$$\text{Factor of safety} = 4062.375 \div 478.23 = 8.49$$

Blue region in Fig. 7 shows that shear stresses induced on the shaft under loading are within a limit and eight FOS show that external load can be exceeded by the factor of 8.

Pin simulation is also carried out in a similar manner which is shown in Fig. 8. The red region is under deformation due to shear stresses induced on it, but this will only happen if the factor of safety in this region is less than 2. The rest part of the pin is safe which is shown by the blue region.

6 Conclusion

After looking into many new technologies, likewise solar, wind, geothermal, there is one thing that comes common to all of them. All these have one or more very drastically unfavorable reasons for not giving their full potential of use. Although it can also not be said that the footstep technology is the only future, there is a new alternative available now which can be used in almost any weather condition, ideally, zero paid raw input for continuous generation and only requires a minimal workforce



Fig. 8 Pin simulation

to handle the maintenance factor of the project. The money invested would also turn up to give future profits in a very short duration.

Furthermore, the technology is also beneficial in those highly populated target zones where the generated output can be utilized for street lightings, Wi-Fi routers, and even lighting up the shopping malls, etc., at a very minimal cost and no loss to nature. Mankind is not changing all the things, nor we can afford to, it is rather our turn and time to upgrade the old possibilities.

References

1. Ipsos M (2011) Global support poll shift towards alternative source energy resource
2. Global Wind Power Cumulative Capacity, Global Wind Energy Council (2018)
3. IRENA (2017), Renewable Energy Prospects for India, a working paper based on REmap. The International Renewable Energy Agency (IRENA), Abu Dhabi. www.irena.org/remap
4. Thakur J, Rauner S, Chakraborty B (2017) Int J Smart Grid Clean Energy 6:3
5. Stefanov Y, Ivanov K, Petrov P (2017) Int J Smart Grid Clean Energy 6:3
6. Zhang J, Daniela A, Fang Y, Desmonda A, Antwi EO (2018) Int J Smart Grid Clean Energy 7:3
7. Chang EC, Liu YC (2018) Int J Smart Grid Clean Energy 7:1
8. Nyan HR (2015) J Mater Sci Eng 4:3
9. Liu M, Lin R, Zhou S, Yu Y, Ishida A, McGrath M, Kennedy B, Hajj M, Zuo L (2018) Design, simulation and experiment of a novel high efficiency energy harvesting paver. Appl Energy 212(15):966–975. ISSN 0306-2619
10. Nandan S, Trivedi R (2019) Design and Fabrication of mechanical footstep power generator. Int J Eng Appl Sci Technol 4(5):214–222. ISSN No. 2455-2143
11. Prasad PR, Bhanuja A, Bhavani L, Bhoomika N, Srinivas B (2019) Power generation through footsteps using piezoelectric sensors along with GPS tracking. In: 2019 4th international conference on recent trends on electronics, information, communication & technology (RTEICT), Bangalore, India, pp 1499–1504. <https://doi.org/10.1109/RTEICT46194.2019.9016865>
12. Ang CK, Al-Talib AA, Tai SM, Lim WH (25019) Development of a footstep power generator in converting kinetic energy to electricity. E3S Web of Conferences 80:02001

13. Somalaraju K, Singh JG (2020) Enhancement of power generation from electromagnetic scavenging tile. In: International conference on power electronics & IoT applications in renewable energy and its control (PARC), Issue: 28–29, February 2020
14. Chand AA, Shamsul Arefin ASM, Islam FR, Prasad KA, Singh S, Cirrincione M, Mamun KA (2020) Design simulation of a novel fluid based footstep energy harvesting system. *Sustain Energy Technol Assess* 39. ISSN 2213-1388
15. <https://theswitch.co.uk/technology/guides/energy/energy-harvesting-tiles>

Case Study on Bearing Fault Diagnosis in Liquid Rocket Engine Using Envelope Detection Technique



Debanjan Das, P. Padmanabhan, V. Kumaresan, and D. P. Sudhakar

Abstract The case study undertaken in the paper briefs the analysis of turbopump vibration parameters for prognostic health monitoring of a pump fed liquid rocket engine (LRE). Real-time vibration data acquired during ground testing of LRE is highly composite since all disturbances occurring during engine operation get transmitted to the sensor via structure. The resulting signal is a convolution of multiple forcing functions with transfer function of their concerned transmission path. Identifying weak impulses from bearing faults hence becomes a challenging task. The paper presents an application of envelope-based demodulation using high-frequency resonant technique (HFRT) to analyze a ground test vibration signal facilitating detection of bearing inner race fault at early stages of fault development. Comparison of the short-time Fourier transform spectra of raw data for the case discussed with an earlier test (used as reference signal with same deterministic frequencies) was found to distinguish carrier resonant frequency excited by the fault. The same was used as central frequency for a band-pass filter design for pre-processing of raw data with bandwidth set to nearly twice the fault frequency. The filtered signal was demodulated using Hilbert transform. Computation of power spectral density (PSD) for the demodulated waveform could distinctly detect the fault frequency with its first harmonic.

Keywords Liquid rocket engine · Rolling element bearing fault · Hilbert transform

1 Introduction

Signals of rolling element bearings are generally non-stationary in nature. Analysis of these signals in time domain involves estimation of factors like root mean square acceleration and kurtosis [1]. The constituent frequencies in the time waveform can be identified by employing analytical tools in frequency domain such as fast Fourier transform (FFT), auto and cross-power spectrum, and cepstrum techniques

D. Das (✉) · P. Padmanabhan · V. Kumaresan · D. P. Sudhakar
ISRO Propulsion Complex, Mahendragiri, Tamil Nadu 627133, India

© The Author(s), under exclusive license to Springer Nature Singapore Pte Ltd. 2022
K. Govindan et al. (eds.), *Advances in Mechanical and Materials Technology*,
Lecture Notes in Mechanical Engineering,
https://doi.org/10.1007/978-981-16-2794-1_32

357

[2, 3]. These methods intend to detect distinct frequencies arising due to bearing fault since impulses created in such systems occur after certain definite intervals as the imperfection, in course of its movement, hits other contacting surfaces (races and/or rolling elements).

Fault frequency of the bearings (in Hz) can be calculated using kinematic relationships as follows (Eqs. 1–4) [4].

$$\text{BPFO (Ball Pass Frequency Outer race)} = \frac{n_r N}{2} \left(1 - \frac{d_r}{D_p} \cos \emptyset \right) \quad (1)$$

$$\text{BPFI (Ball Pass Frequency Inner race)} = \frac{n_r N}{2} \left(1 + \frac{d_r}{D_p} \cos \emptyset \right) \quad (2)$$

$$\text{FTF (Fundamental Train Frequency)} = \frac{N}{2} \left(1 - \frac{d_r}{D_p} \cos \emptyset \right) \quad (3)$$

$$\text{BSF (Ball Spin Frequency)} = \frac{N D_p}{2 d_r} \left\{ 1 - \left(\frac{d_r}{D_p} \cos \emptyset \right)^2 \right\} \quad (4)$$

Here, n_r denotes number of rolling elements, N represents shaft rotational speed in revolutions per second, D_p is the bearing pitch diameter (in mm), d_r is the rolling element diameter (in mm), and \emptyset is the contact angle.

The presence of any such frequency signature in the LRE vibration signal hampers the reliability of the engine operation, and their detection is of utmost importance during operational testing of the engine on ground before flight induction. However, for such complex real-time systems involving rolling element bearing vibration, direct detection of such frequencies becomes difficult, the signals being generated by multiple input multiple outputs (MIMO) systems coupled with high background noise. This case study presents a systematic approach for extraction of fault features in such systems using envelope-based fault detection technique [5, 6].

The LRE discussed in the paper uses a bi-propellant gas generator cycle with hypergolic earth-storable propellant combination. The propellants are fed into the combustion chamber by a turbopump which consists of fuel, oxidizer, and coolant pumps (coolant is used to bring down temperature of combustion products from gas generator) driven by a turbine. The study highlights an instance of crack development in inner raceway of coolant pump bearing during one of the engine ground tests. Engine was operated at a chamber pressure of 64 bar for a test duration of 150 s with turbopump operating at a rated speed of 178 revolutions per second.

2 Vibration Data Acquisition Set up for Ground Test

Figure 1 shows the rotating system configuration in this LRE mounted on three bearings. Three vibration sensors are mounted, one on each pump housing for acquiring

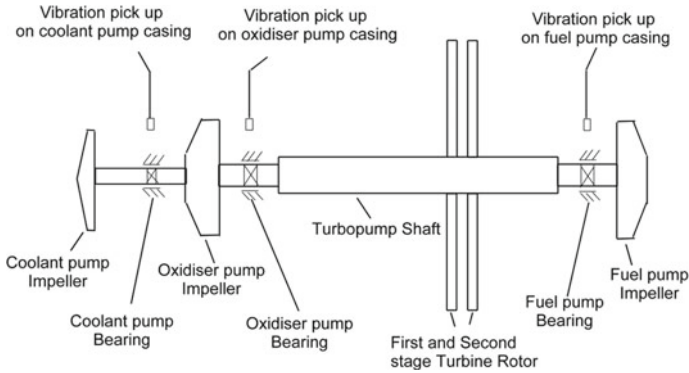


Fig. 1 Position of vibration sensors in ground test setup

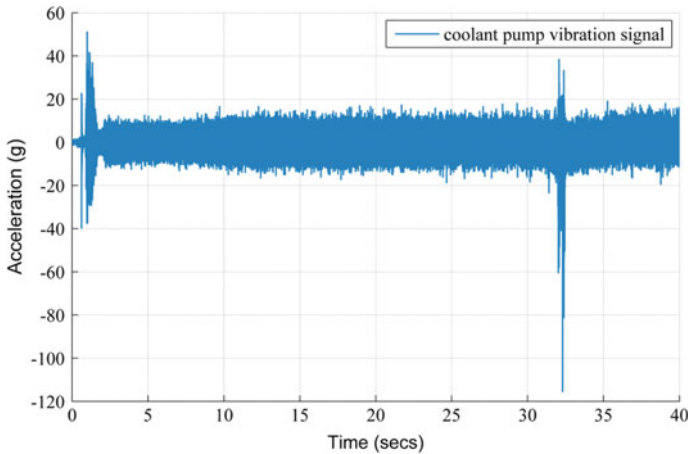


Fig. 2 Time waveform for coolant pump vibration signal

real-time data during engine hot test. In the case discussed, high-amplitude vibrations were noted in the raw data acquired from the vibration sensor mounted on coolant pump housing at 32 s depicting an anomaly (Fig. 2). Subsequently, the signals obtained were analyzed for the presence of any fault signature using envelope-based demodulation as detailed in subsequent sections.

3 Methods for Processing Acquired Waveform from Sensor

A comparison of the raw data spectrum of the obtained signal is made with that of a reference signal to distinguish the anomalies since all other deterministic frequencies,

being a system characteristic, remain unchanged in all tests. The spectrum is obtained by solving the discrete Fourier transform equations (Eq. 5) implementing the fast Fourier transform algorithm [7].

$$Q(k) = \left(\frac{1}{N_L} \right) \sum_{n=0}^{N_L-1} q(n) \exp(-j2\pi kn/N_L) \quad (5)$$

where $Q(k)$ is in frequency domain and is the Fourier transform of $q(n)$, the waveform in time domain. N_L denotes waveform length considered for computation.

Power spectral density is another way of presenting the spectrum. First, the auto co-relation function is calculated for the waveform, and subsequently, FFT is done on the same to obtain the PSD. Also, time–frequency plots generated by applying Short-time Fourier transform has been implemented in this study to confirm the repeated appearance of any anomalous feature over time which facilitates to distinguish it from any random noise effect.

Since impulses from bearing faults generally modulate the amplitude of vibrations at the carrier resonant frequency of the structure which it excites, the fault frequencies therefore do not often appear directly in the raw data spectrum. Instead, they are manifested as modulated sideband spacing of the carrier. However, detection of sidebands becomes difficult due to higher background noise in rocket engine systems. Hence, the waveform is filtered and demodulated to obtain the envelope in which the defect frequency can be noted directly. It is to be noted that the central frequency for designing the band-pass Butterworth filter (as used in the case study) should be close to the carrier frequency with a design bandwidth equal to or slightly more than twice the fault/modulation frequency to facilitate its detection in the envelope spectrum.

The envelope analysis has been carried out by using Hilbert transform [7]. For a waveform $s_i(t)$, the Hilbert transform, denoted as $H_i[s_i(t)]$, is given as (Eq. 6)

$$H_i[s_i(t)] = \frac{1}{\pi} \int_{-\infty}^{\infty} \frac{s_i(\tau)}{t - \tau} d\tau \quad (6)$$

The analytic waveform $p_i(t)$ is then given as (Eq. 7)

$$p_i(t) = s_i(t) + jH_i[s_i(t)] \quad (7)$$

The amplitude of $p_i(t)$ gives the required demodulated waveform envelope (Eq. 8)

$$a_i(t) = \sqrt{s_i^2(t) + H_i^2[s_i(t)]} \quad (8)$$

The above-mentioned computations were carried out for this study using MATLAB R2018a software.

4 Results and Discussion

During the LRE ground test, the vibration sensor mounted on coolant pump cover read high amplitude vibrations at 32 s. The time–frequency visualization of the time waveform in Fig. 2 is shown in Fig. 3. The distinct frequencies recorded in frequency domain are 178 Hz (1 N), 712.9 Hz (4 N), 1426 Hz (8 N), 2139 Hz (12 N), 2852 Hz (16 N), 4277 Hz (24 N), and 4364 Hz.

1 N frequency is corresponding to pump’s rotational speed and comparison of the amplitude, when made with spectrum of earlier test with similar operating conditions depicted that the residual unbalance was within acceptable range, and there was no anomaly. The appearance of 4 N, 8 N and their harmonics were also as observed in earlier test data, with comparable amplitudes, and they correspond to the blade pass frequencies of the impellers. This is attributed to the fact that the impellers used for the engine have 4 half vanes and 4 full vanes where the initial half of the full vanes (effectively 4 half vanes) act as inducer for maintaining the required net positive suction head at suction, and the latter half of the full vanes (effectively 4 half vanes) with the other 4 half vanes (altogether 8 half vanes) act in series with the inducer generating the required pumping action. 4364 Hz is an acoustic mode frequency appearing due to standing pressure wave formation in the combustion chamber due to interaction of incident fluctuating pressure waves generated at the flame and the reflected wave from the sonic throat where a steep gradient in change of hot gas density usually occurs.

The spectrum of the interval before 32 s for anomalous test (Fig. 4a) was compared with that of an earlier good test (Fig. 4b). It was observed that frequency of 2.69 kHz came in the anomalous test which did not appear in spectrum of similar earlier tests.

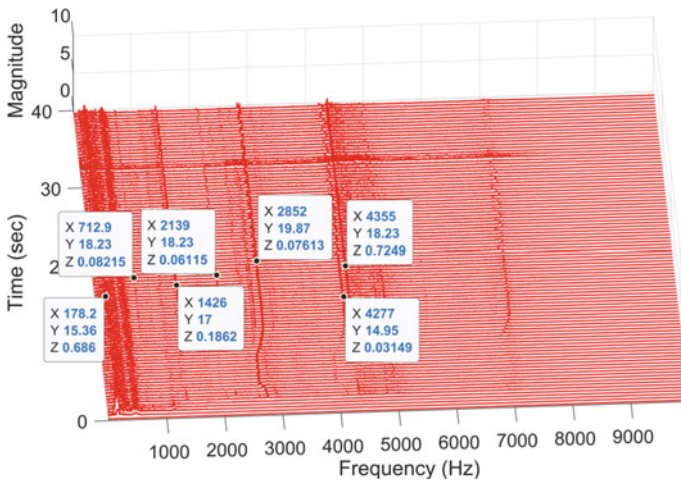


Fig. 3 Waterfall plot for coolant pump vibration signal

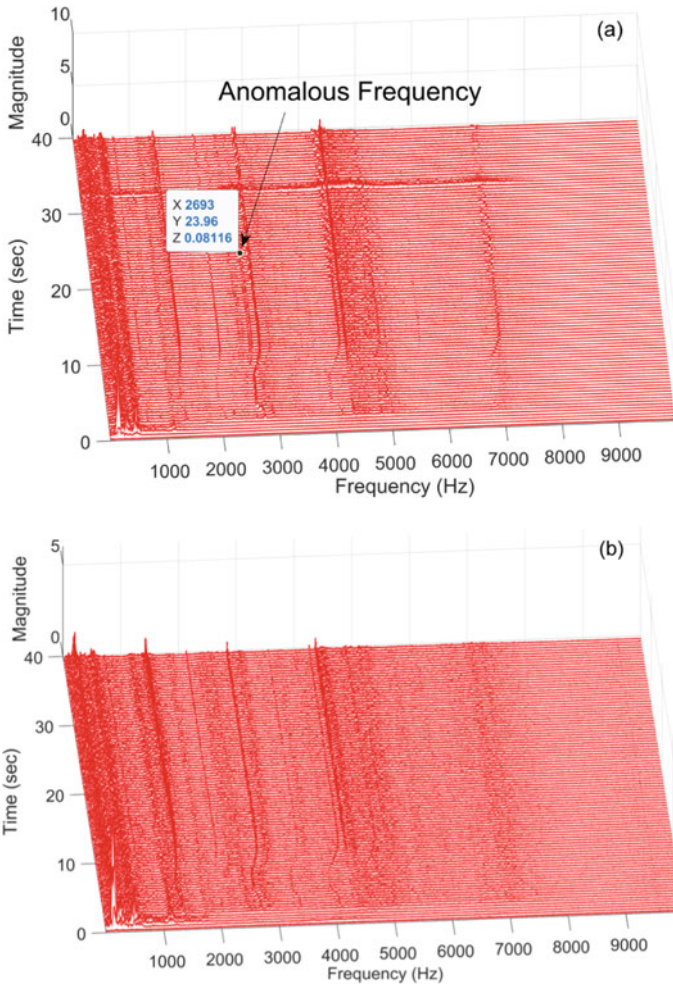


Fig. 4 **a** Waterfall plot for anomalous test. **b** Waterfall plot for good test

Also, the said frequency was observed only till 32 s after which it could not be distinctly detected in rest of the waterfall spectrum.

Based on the frequency of 2.69 kHz seen in anomalous test, extracted segments from both tests were filtered with a sixth-order band-pass Butterworth filter. Filter central frequency was varied in the range of 2.45–2.95 kHz, and bandwidth was set to slightly more than twice the value of each of the fault frequencies. When the bandwidth was set to 2600 Hz, BPF started appearing in the envelope spectrum obtained by Hilbert transform. The detection became prominent in the envelope spectrum of the signal filtered with 2.5 kHz as central frequency and a bandwidth of 3 kHz. Filtered signals for anomalous test and good test are shown in Fig. 5a, c, respectively, and their corresponding envelopes in Fig. 5b, d in that order.

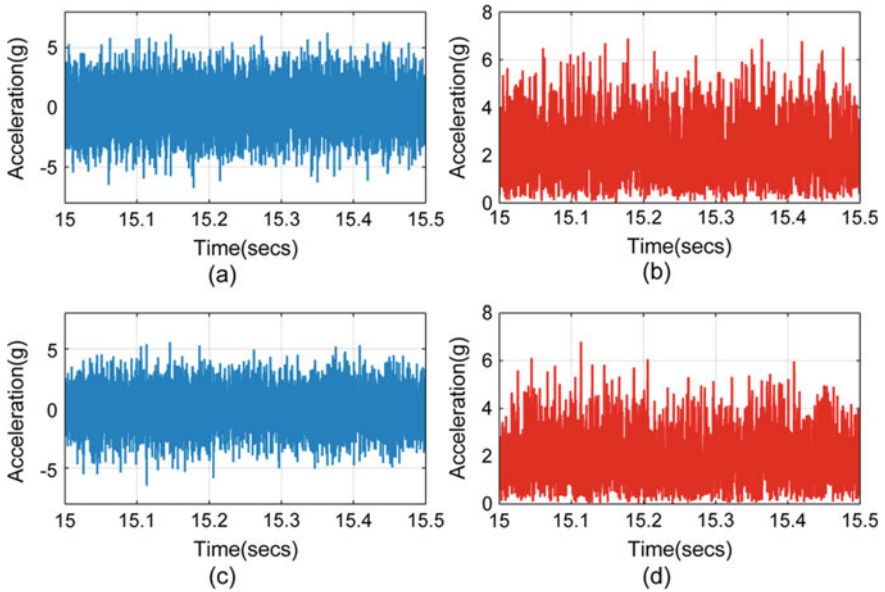


Fig. 5 **a** Extracted segment for analysis from anomalous test data filtered. **b** Envelope of time waveform for anomalous test. **c** Extracted segment for analysis from good test data filtered. **d** Envelope of time waveform for good test

PSD of the envelope for the anomalous test detected a distinct frequency of 1289 Hz and its first harmonic (Fig. 6). The same could not be noted in the frequency spectrum of the good test as seen in comparison of PSD for good and anomalous test

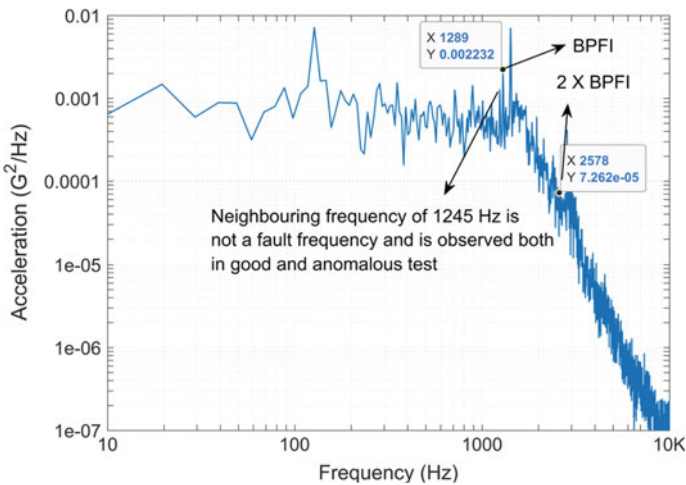


Fig. 6 Power spectral density of anomalous test data envelope

(Fig. 7). The fact that the frequency of 1289 Hz is a distinct frequency and can be differentiated from random noise which is evident from the waterfall plot computed for the envelope waveform (Fig. 8) where the fault frequency is seen to repeat for

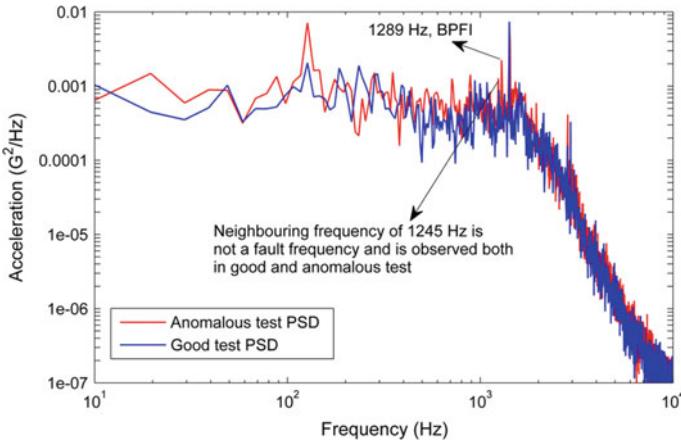


Fig. 7 Comparison of test data envelope PSD for anomalous test and good test

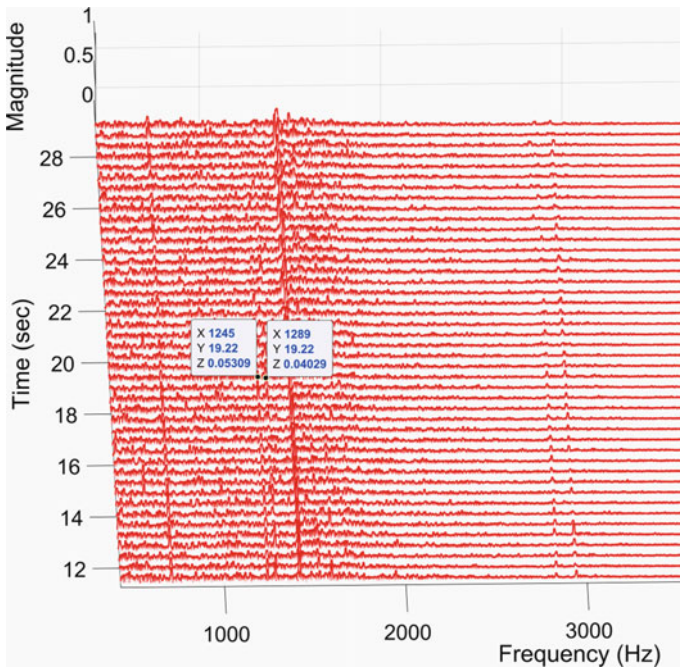


Fig. 8 Zoomed part of waterfall plot of anomalous test data showing distinct appearance of 1289 Hz

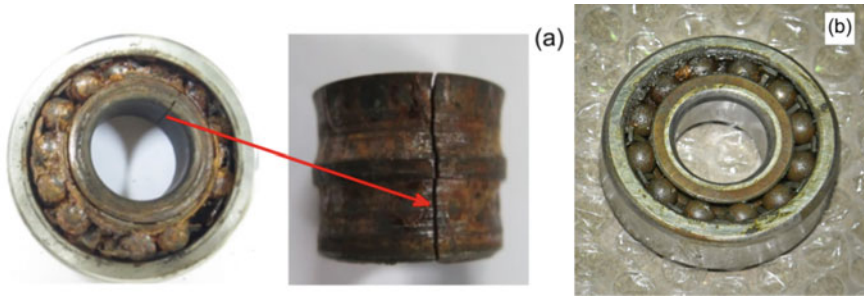


Fig. 9 **a** Post-test observations showing thermal cracking of bearing inner race in anomalous test. **b** Healthy bearing after good test

successive time instants. Also, the frequency cannot be detected after 32 s. It may be noted that another neighboring frequency of 1245 Hz is also detected in the envelope spectrum. However, it is not a fault frequency and has been noted in good test PSD as well (Fig. 7).

The appearance of the fault frequency of the inner race was confirmed upon post-test disassembly of the bearing (Fig. 9a). A healthy bearing after good test is also shown for comparison (Fig. 9b). The crack was studied to have occurred due to anomaly in material composition resulting in lesser hot strength and thermal cracking of inner race.

5 Conclusion

The bearing used for coolant pump in the hot test is a self-aligning double row ball bearing with 12 nos. of ball per row, nominal bore diameter of 20 mm, and outside diameter of 52 mm. The calculated value of BPF_I (from Eq. 2) for this bearing corresponds to 7.17 N, i.e., 1276 Hz. Hence, the detected frequency was found close to BPF_I, i.e., frequency corresponding to imperfection on inner race. The deviation of the observed frequency from calculated frequency is around 0.87% which is due to the existence of some amount of random slip in real-time bearing systems in contrary to the supposition of the model without slip for the calculated frequency.

The appearance of harmonic in the spectrum depends on the nature of impact. Harmonics signify the deviation of the impact waveform nature from a pure sine wave.

Also, the appearance of BPF_I before 32 s shows that the generated crack edges are sharp during initial stages generating strong impulses but eventually smoothen out due to deformation resulting from repeated impacts with rolling elements rotating at a very high operating speed. Hence, the method helps in fault detection at early stages of its development.

References

1. Heng RBW, Nor MJM (1998) Statistical analysis of sound and vibration signals for monitoring rolling element bearing condition. *Appl Acoust* 53(1–3):211–226
2. Tandon N, Choudhury A (1999) Review of vibration and acoustic measurement methods for the detection of defects in rolling element bearings. *Tribol Int* 32(8):469–480
3. Smith JD, McFadden PD (1984) Vibration monitoring of rolling element bearings by the high frequency resonance technique: a review. *Tribol Int* 17(1):3–10
4. Tiwari R (2018) *Rotor systems: analysis and identification*, 1st edn. CRC Press, Taylor and Francis
5. Prashad H, Ghosh M, Biswas S (1985) Diagnostic monitoring of rolling-element bearings by high-frequency resonance technique. *ASLE Trans* 28(4):439–448
6. Junsheng C, Dejie Y, Yu Y (2007) The application of energy operator demodulation approach based on EMD in machinery fault diagnosis. *Mech Syst Signal Process* 21(2):668–677
7. Randall RB, Antoni J (2011) Rolling element bearing diagnostics—a tutorial. *Mech Syst Signal Process* 25(2):485–520

A Study on Machining Behaviour of Metal Matrix Composite: A Review



Nikhil Bharat  and P. S. C. Bose

Abstract Machining of metal matrix composite is extreme when analysed with inflexible materials like steel and aluminium due to the presence of abrasive in the reinforcement which causes damage to the workpiece. Metal matrix composite has replaced most of the conventionally used metal components because of the high strength and low weight of the material. Metal matrix composites find wide modern applications in the different areas of aviation just as automobile enterprises because of good mechanical and actual properties. This paper attempts to audit the outcomes of different information boundaries and strategies embraced to get an enhanced outcome.

Keywords MMC · Machining · Cutting tool · Fabrication

1 Introduction

Composites are those materials in which two or more constituents are combined to obtain the desired product having better physical and mechanical properties. Composites usually consist of a matrix that is in continuous phase and reinforcement which are in the discontinuous phase in the form of particles, fibres. The reinforcement must be non-reactive and stable at high temperatures. Aluminium oxide (Al_2O_3) as well as silicon carbide (SiC) are regularly utilized reinforcements because of their better strength, hardness, accessibility, and having great wear opposing properties. Composite materials have replaced conventional materials and are widely accepted by the various sectors because of their characteristic behaviour of high strength and low weight of the material. Aluminium and its alloy metal matrix composite are extensively used in aerospace industries, automobile industries, etc. However, products made from MMC required machining operation to achieve the required demand, i.e. dimensional exactness and surface completion. Machinability is expressed in terms of some factors like cutting powers, tool wear, and surface completion. Better

N. Bharat (✉) · P. S. C. Bose

Mechanical Engineering Department, National Institute of Technology, Warangal 506004, India
e-mail: nikhilbharat@student.nitw.ac.in

© The Author(s), under exclusive license to Springer Nature Singapore Pte Ltd. 2022
K. Govindan et al. (eds.), *Advances in Mechanical and Materials Technology*,
Lecture Notes in Mechanical Engineering,
https://doi.org/10.1007/978-981-16-2794-1_33

367

machining consumes low power, less friction, low tool wear, and good surface finish. In this paper, a review has been done regarding the consequences of experimental parameters, i.e. speed, feed, profundity of cut, and cutting tool during machining of metal matrix composite.

2 Literature Review

Ozben et al. [1] concluded that hardness and tensile strength of $AlSi_7Mg_2$ metal matrix composite increase with an increase in the reinforcement ratio but impact toughness decreased, and it was found that surface quality was better when cutting speed decreased. Lin et al. [2] used A359/SiC/20p metal matrix composite for the experiment purpose and observed that the main reason for wear formation was abrasion wear. Surface quality was affected by increasing feed rates at a constant speed. Ding et al. [3] selected Al-SiC metal matrix composite as a working material and utilized PCBN and PCD apparatuses at different cutting rates. PCD tool performs in a way that is better than the PCBN tool as it possesses better abrasion and fracture resistance. Vineeth Kumar et al. [4] selected Al6063 as a working material fortified with 5.0 as well as 10.0 wt% of steel chips with a normal size of 50–100 μ . The stir casting method was used for the production of work material. The addition of steel dust improved the mechanical properties of the workpiece and concluded that the maximum hardness value of 84HRC was achieved compared to the control sample of 70HRC. Sahoo et al. [5] conducted an investigation utilizing Taguchi orthogonal array and turned Al/SiCp utilizing uncoated tungsten carbide tool, and it was seen that the flank wear was mostly impacted by the cutting pace, not with the profundity of cut. Rahman et al. [6] analysed the wear properties as well as surface irregularities of two different tool inserts and examined that CBN inserts performed better in contrast with tungsten carbide and ceramic insert. Manna and Bhattacharya [7] investigated the machining behaviour of Al/SiCp composite using a rhombic uncoated carbide tool during turning operation. From the test outcomes and diverse SEM micrographs, the satisfactory scope of speed, feed, and profundity of cut was chosen for better machining execution. EI-Gallab [8] analysed the machining behaviour of Al/SiC (20%SiC) particulate metal matrix composite using PCD tools, alumina, and coated carbide tool and found that PCD tool provides better tool life than others, and abrasion was discovered to be the essential wear system for flank wear. Puhan et al. [9] analysed on machining behaviour qualities of Al/SiCp utilizing EDM. A hybrid procedure was utilized coordinating principal component analysis (PCA) and fuzzy deduction framework with the Taguchi strategy to redo the multi-reaction. Miller and Monghan [10] investigated the machining behaviour of SiCp strengthened with Al metal matrix composite using various non-conventional machining cycle, for example, EDM, laser cutting, AWJ and presumed that laser and AWJ machining offers amazing efficiency compensation for harsh cut-off application but EDM is more applicable for machining ‘particle-reinforced metal matrix composite (PRMMC)’. Manna and Bhattacharya [7] investigated on machinability of Al/SiCp

composite utilizing the fixed rhombic tool and examined that feed showed less resistance to flank wear in contrast with cutting speed. Dhulipalla et al. [11] researched on blend and machining attributes of novel TiC ceramics and MOS_2 p strengthened Al compound 7075 metal matrix composite and used stir casting method for synthesis and found that AMCs have enhanced machining behaviour in contrast with base alloy. Nataraj et al. [12] used RSM way to deal with advance the machining boundaries for CNC turning of Al/ Al_2O_3 metal matrix composite. It was seen that surface unpleasantness was affected by cutting pace just as feed rate, and best surface quality was acquired at speed = 175.20 mm/min, feed rate = 0.052 mm/rev., and profundity of cut = 0.256 mm. Srinivasan et al. [13] investigated on hybrid aluminium metal matrix composite manufactured using ‘stir cum squeeze casting’ using zirconium dioxide and graphite and found that the value of tensile strength got enhanced with increasing in weight percentage of zirconium dioxide and hardener also. Gurupavan et al. [14] selected Al6061 as a working material and performed the experiment on CONCORD four-axis CNC WEDM using molybdenum wire for machining of and embraced L27 orthogonal exhibit strategy to direct the examinations and found that neural network prepared with 70% of the information in preparing gives better anticipate results. Przystacki et al. [15] conducted the experiment using the laser-assisted method for turning A359/20SiCp composite and found that selected depth of cut as well as the tool’s angular distance from laser beam decreases the surface irregularities and also improves the wear resistance of the composite. Wei et al. [16] selected Al2124 matrix reinforced with SiCp as a working material and utilized laser-aided turning (LAT) machine for machining and reasoned that heat influenced zones were deficient to 20–30 μm Ra while utilizing rapid laser-aided turning and also found that smaller the beam diameter, better the surface of the composite.

3 Fabrication Method

The most common liquid state method adopted is the stir casting method for the production of metal matrix composite. It is a cost-effective and simple process used for the manufacturing of particle-reinforced metal matrix composite. The steps to be followed for the casting of the composite are as shown in Figs. 1 and 2.

3.1 *Melting of Metal Matrix Composite Material*

There is a range of furnaces for dissolving purposes yet the base pouring heater is generally fitting for the manufacture of metal matrix composite. In this technique, the metal framework material is liquefied and kept up at a firm temperature for 2–4 h in the heater, and simultaneously, reinforcements are preheated in different furnaces [18].

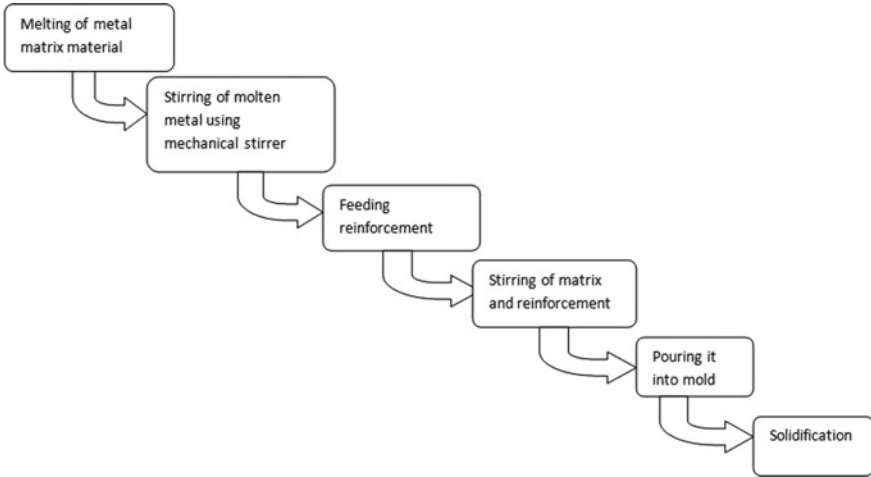
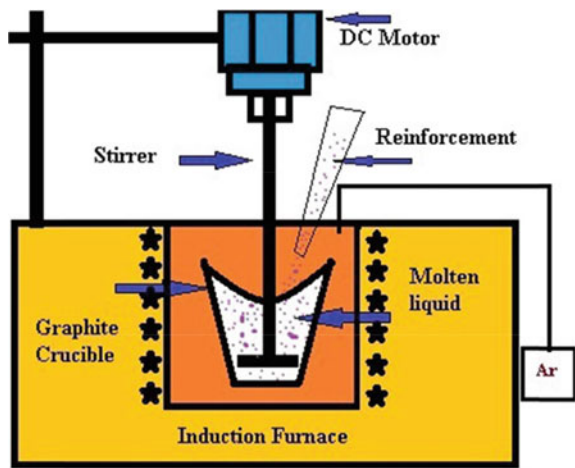


Fig.1 Process of stir casting

Fig. 2 Stir casting process [17]



3.2 Mechanical Stirring

The mechanical stirrer is associated with the going pace engine to control the speed. There are for the most part three phases of blending the combination, for example, single-stage mixing, twofold stage blending, and multistage mixing. The single-stage blending technique is essentially utilized because of its flexibility and furthermore to limit the extraordinary vortex flow. Stirring assumes the main part in the examination of mechanical properties and microstructure of the composites as it keeps up the circulation of reinforcement in the matrix material. The mixing cycle can be advanced

by streamlining the mixing speed, mixing time, feed rate, impeller's cutting edge size, and blade angle [18].

4 Effect of Process Parameters Speed, Feed, Depth of Cut, Temperature, and Cutting Tool

Kannan and Kishawy [19] concluded that the level of imperfections expanded with speeding up as the strain, strain rate, and temperature corresponds to cutting speed while machining of 'Al6061 metal matrix composite'. Anthony and Ajith Kumar [20] in their research work observed that surface irregularity was mainly affected by the feed rate as well as cutting speed and also concluded that the presence of graphite as a lubricating property provides a better surface finish. Kim et al. [21] compared the machining of Al/SiCp using ultrasonically aided turning (UAT) and conventional turning machine and found that ultrasonically assisted turning was more effective while using WC tool. Kumar et al. [4] concluded that while machining of formed Al alloy LM06 MRR enhanced with enhancing in cutting pace, feed, and depth of cut in all the experiments. Das et al. [22] seen that PCD inserts performed superior in contrast with carbide inserts because of wear behaviour and better surface irregularity. El Gallab and Sklad [8] examined that cutting forces were got enhanced while using Al_2O_3/TiC tool in contrast with TiN coated carbide tool while machining Al/SiC particulate metal matrix composite and develop edge (BUE) was seen in all devices under every single cutting condition. Manna and Bhattacharya [7] in their research inferred that cutting rate zone between 65 and 145 m/min is adequate for machining of Al/SiC metal matrix composite and furthermore saw that feed rate having less effect on flank wear when contrasted with cutting rate. Miiller and Monaghan [10] experimented and concluded that laser machining is pertinent for a high pace of 3100 mm/min, and AWJ is reasonable for a pace up to 150 mm/min and for machining of particulate reinforced metal matrix composite (AA2618/SiC/20p). Puhan et al. [9] utilized the Taguchi strategy for getting the improved outcome and discovered that ideal value for $MRR = 14.376 \text{ mm}^3/\text{min}$ also, surface irregularity = $3.043 \mu\text{m}$ during machining on AlSiCp. Przystacki [23] compared the machining of A359/20 SiCp material with laser-assisted machining (LAM) and conventional turning process and concluded that less tool wear and improved tool life were found in laser-assisted method. Shoba et al. [24] observed that the cutting forces are much lower for hybrid composites as compared to unreinforced alloy and concluded that depth of cut plays a vital role for increasing the force component due to increase in contact area. Errico and Calzvarini [25] performed the turning experiment of the work material Al.359/SiC/20p using two different types of tools, i.e. PCD and CVD tool, and found that PCD performs better. Roy [26] performed the experiment by designing an expert system using fuzzy logic and genetic algorithm for machining of Al6061/SiCp metal matrix composite and found that genetical algorithm-trained fuzzy expert system (GAFES) performed better than a genetic algorithm. Niknam

Table 1 Turning parameters and tool effect [30]

S. No.	Tool	Matrix	SiC fraction	Comment
1	PCD	Al 356	5% (mass fraction)	Good surface irregularities were obtained as 2.86 μm , and rMRR = 36.80 cm^3/min
2	HSS	Al 7075	10% (mass fraction)	Cutting powers are free of cutting pace
3	Carbide insert	Al 7075	10% (mass fraction)	Optimum surface roughness was achieved
4	PCD	Al 7075	10% (mass fraction)	The best surface finish
5	Carbide insert	Al 7075	15% (mass fraction)	Better tool life was obtained and having a tool life of 6.67 min
6	K20 series	Al 6025	20% (mass fraction)	Good surface quality with enhanced tool life

et al. [27] in his experiment investigated the dry and semi-dry turning of titanium metal matrix composite (Ti-6Al-4V) using SECO uncoated carbide tool and found that more cutting forces as well as high surface roughness were observed in semi-dry cutting conditions. Davim et al. [28] analysed the experimental and numerical procedures for drilling of A356/20%SiCp-T6 and found that the main reason for wear was abrasion, whereas torque was not sensitive to the tool wear. Kwak and Kim [29] investigated the mechanical properties as well as grinding behaviour on aluminium matrix composite and observed that the (i) table speed and (ii) profundity of cut has remarkable impact on the grinding forces (Table 1).

5 Conclusion

From the detailed literature survey, it is reasoned that:

- Very few machining works have been done using hybrid machining since most of the work has been done either using the conventional or non-conventional machine.
- PCD tool gives better results with regards to wearing resistance as well as tool life compared to other tools while machining metal matrix composite.
- Abrasion wear was the main wear that has been observed during the machining operations of the composite.
- Feed rate plays a key role in the quality of the surface irregularities.

References

1. Ozben T, Kilickap E, Orhan C (2007) Investigation of mechanical and machinability properties of SiC particle reinforced Al-MMC. *J Mater Process Technol* 8:220–225. <https://doi.org/10.1016/j.jmatprotec.2007.06.082>
2. Wu Q, Si Y, Wang GS, Wang L (2016) Machinability of a silicon carbide particle-reinforced metal matrix composite. *RSC Adv* 6(26):21765–21775. <https://doi.org/10.1039/c6ra00340k>
3. Ding X, Liew WYH, Liu XD (2005) Evaluation of machining performance of MMC with PCBN and PCD tools. *Wear* 259(7–12):1225–1234. <https://doi.org/10.1016/j.wear.2005.02.094>
4. Vineeth Kumar K, Jayahari L (2018) Study of mechanical properties and wear behaviour of aluminium 6063 matrix composites reinforced with steel machining chips. *Mater Today Proc* 5(9):20285–20291. <https://doi.org/10.1016/j.matpr.2018.06.400>
5. Sahoo AK, Pradhan S (2013) Modeling and optimization of Al/SiCp MMC machining using Taguchi approach. *Meas J Int Meas Confed* 46(9):3064–3072. <https://doi.org/10.1016/j.measurement.2013.06.001>
6. Rahman M, Ramakrishna S, Prakash JRS, Tan DCG (1999) Machinability study of carbon fiber reinforced composite. *J Mater Process Technol* 89–90:292–297. [https://doi.org/10.1016/S0924-0136\(99\)00040-0](https://doi.org/10.1016/S0924-0136(99)00040-0)
7. Manna A, Bhattacharayya B (2003) A study on machinability of Al/SiC-MMC. *J Mater Process Technol* 140(1–3):711–716. [https://doi.org/10.1016/S0924-0136\(03\)00905-1](https://doi.org/10.1016/S0924-0136(03)00905-1)
8. El-Gallab M, Sklad M (1998) Machining of Al/SiC particulate metal-matrix composites part I: tool performance. *J Mater Process Technol* 83(1–3):151–158. [https://doi.org/10.1016/S0924-0136\(98\)00054-5](https://doi.org/10.1016/S0924-0136(98)00054-5)
9. Puhan D, Mahapatra SS, Sahu J, Das L (2013) A hybrid approach for multi-response optimization of non-conventional machining on AlSiCp MMC. *Meas J Int Meas Confed* 46(9):3581–3592. <https://doi.org/10.1016/j.measurement.2013.06.007>
10. Müller F, Monaghan J (1998) Electro discharge machining of a particle reinforced metal matrix composite. *VDI Berichte* 40(1405):513–522. https://doi.org/10.1007/978-1-349-14620-8_67
11. Dhulipalla A et al (2020) Synthesis and machining characteristics of novel TiC ceramic and MoS₂ soft particulate reinforced aluminium alloy 7075 matrix composites. *Manuf Lett* 24:82–86. <https://doi.org/10.1016/j.mfglet.2020.04.001>
12. Nataraj M, Balasubramanian K, Palanisamy D (2018) Optimization of machining parameters for CNC turning of Al/Al₂O₃ MMC using RSM approach. *Mater Today Proc* 5(6):14265–14272. <https://doi.org/10.1016/j.matpr.2018.03.008>
13. Srinivasan R, Hemanth Shrinivasan B, Jeevan Prasath K, Johnson Saleth R, Anandhan RD (2020) Experimental investigation of aluminium hybrid metal matrix composites processed through squeeze casting process. *Mater Today Proc* 27:3–8. <https://doi.org/10.1016/j.matpr.2020.03.786>
14. Gurupavan HR, Devegowda TM, Ravindra HV, Ugrasen G (2017) Estimation of machining performances in WEDM of aluminium based metal matrix composite material using ANN. *Mater. Today Proc* 4(9):10035–10038. <https://doi.org/10.1016/j.matpr.2017.06.316>
15. Przystacki D, Szymanski P, Wojciechowski S (2016) Composites: part a formation of surface layer in metal matrix composite A359/20SiCP during laser assisted turning. *Compos Part A* 91:370–379. <https://doi.org/10.1016/j.compositesa.2016.10.026>
16. Wei C et al (2020) High speed, high power density laser-assisted machining of Al-SiC metal matrix composite with significant increase in productivity and surface quality. *J Mater Process Tech* 285:116784. <https://doi.org/10.1016/j.jmatprotec.2020.116784>
17. Madhukar P, Selvaraj N, Gujjala R, Surya C, Rao P (2019) Ultrasonics—sonochemistry production of high performance AA7150-1 % SiC nanocomposite by novel fabrication process of ultrasonication assisted stir casting. *J Ultrason Sonochem* 58:104665. <https://doi.org/10.1016/j.ultrasonch.2019.104665>
18. Open Access, We are IntechOpen, the world's leading publisher of Open Access books built by scientists, for scientists TOP 1 %

19. Kannan S, Kishawy HA (2006) Surface characteristics of machined aluminium metal matrix composites. *Int J Mach Tools Manuf* 46(15):2017–2025. <https://doi.org/10.1016/j.ijmactools.2006.01.003>
20. Xavier MA, Kumar JPA (2017) Machinability of hybrid metal matrix composite—a review. *Proc Eng* 174:1110–1118. <https://doi.org/10.1016/j.proeng.2017.01.264>
21. Kim J, Bai W, Roy A, Jones LCR, Ayvar-Soberanis S, Silberschmidt VV (2019) Hybrid machining of metal-matrix composite. *Proc CIRP* 82:184–189. <https://doi.org/10.1016/j.procir.2019.04.162>
22. Das M, Mishra D, Mahapatra TR (2019) Machinability of metal matrix composites: a review. *Mater Today Proc* 18:5373–5381. <https://doi.org/10.1016/j.matpr.2019.07.564>
23. Przystacki D (2014) Conventional and laser assisted machining of composite A359/20SiCp. *Proc CIRP* 14:229–233. <https://doi.org/10.1016/j.procir.2014.03.029>
24. Shoba C, Ramanaiah N, Rao DN (2015) Effect of reinforcement on the cutting forces while machining metal matrix composites—an experimental approach. *Eng Sci Technol Int J* 18(4):658–663. <https://doi.org/10.1016/j.jestch.2015.03.013>
25. Errico GED, Calzavarini R (2001) Turning of metal matrix composites. *J Mater Process Technol* 119:257–260
26. Roy SS (2006) Design of genetic-fuzzy expert system for predicting surface finish in ultra-precision diamond turning of metal matrix composite. *J Mater Process Technol* 173:337–344. <https://doi.org/10.1016/j.jmatprotec.2005.12.003>
27. Cirp P et al (2018) (2018) A new methodology to analyze the functional and physical architecture of existing products for an assembly oriented product family identification. *Proc CIRP* 77:62–65. <https://doi.org/10.1016/j.procir.2018.08.215>
28. Davim JP (2001) Optimal drilling of particulate metal matrix composites based on experimental and numerical procedures. *Int J Mach Tools Manuf* 41:21–31
29. Kwak JS, Kim YS (2007) Mechanical properties and grinding performance on aluminum-based metal matrix composites. *J Mater Process Technol* 1:596–600. <https://doi.org/10.1016/j.jmatprotec.2007.11.139>
30. Chen J (2020) A review on conventional and nonconventional machining of SiC particle-reinforced aluminium matrix composites. *Adv Manuf*. <https://doi.org/10.1007/s40436-020-00313-2>

Optimisation of E-Shell Heat Exchanger Using Multi-objective Evolutionary Algorithm NSGA-II



Abhisekh Kumar Maurya, Anubhav Agrawal, Robert Singh, Owais Ali Khan, and Brahma Nand Agrawal

Abstract The wide applications of shell and tube heat exchanger in several industries are forced to decrease the capital and operational cost of it. In this direction, this paper presents the multi-objective entropy-based optimization of a stainless-steel E-Shell heat exchanger by using the genetic algorithm. A modified NSGA-II algorithm has been used to optimize heat exchanger. The objective functions under consideration are the operating cost, capital cost and entropy generation number. The design parameters have been used as the number of tubes, baffle spacing and tube outer diameter. Kern method has been used for the modelling of the heat exchanger with some modifications. The relation between the hand-off of optimizing one objective to another has been established. A relationship has been developed between the total cost of E-Shell heat exchanger and EGN. A Pareto-optimal front has been obtained for all four cases. The results reveal that the overall cost of heat exchanger reduced. Increment in the capital investment of STHE has been found on reducing the entropy generation number of the shell and tube heat exchanger. The robustness of the algorithm increases by decreasing the number of objectives.

Keywords Genetic algorithm · Entropy generation number · Optimization · Shell tube heat exchanger

Nomenclature

A	Heat exchanger surface area (m^2)
B	Baffle spacing (m)
C_i	Capital investment (\$)
C_o	Annual operating cost (\$)
C_{op}	Discounted operating cost
C_{tot}	Total cost (\$)

A. K. Maurya (✉) · A. Agrawal · R. Singh · O. A. Khan · B. N. Agrawal
Department of Mechanical Engineering, Galgotias University, Greater Noida, Uttar Pradesh
203201, India

d_e	Equivalent shell diameter (m)
d_o	Tube outer diameter (m)
D_s	Shell inside diameter (m)
L	Tube length (m)
N_s	Entropy generation number (EGN)
P	Pumping power (W)
S_t	Tube pitch (m)
U	Overall heat transfer coefficient ($\text{W}/\text{m}^2\text{K}$)
ΔP	Pressure drop (Pa)
$\Delta \dot{S}$	Entropy generation rate

1 Introduction

Shell and tube heat exchanger (STHE) is the most commonly used type of heat exchanger. It is used in a broad range of industries like petrochemical, agriculture, other chemical processes. STHE is commonly used because they can operate for a wide domain of flow, pressure and temperature. In a standard STHE, there are multiple design parameters tube diameter, baffles, number of tubes, tube layout, etc. In the industrial process, there is a need to reduce the global cost (including both the material and operational costs). NSGA-II has been used to optimize a standard STHE model. Non-dominated sorting genetic algorithm-II (NSGA-II) presented [1] attenuates all three difficulties of multi-objective evolutionary algorithm (EAs): non-elitism approach, computational complexity and the requirement of defining a sharing parameter.

The multi-objective based on exergy optimization via a genetic algorithm (GA) is implemented to study and enhance the operations based on STHE. Exergy efficiency and cost were used as two key parameters. ε -NTU and Bell–Delaware method were followed to converge on the optimal design, heat transfer coefficient and pressure drop in a STHE. The results were reported as maximized efficiency of exergy and minimized the investment [2]. The particle swarm algorithm (PSO) has a higher rate of convergence in comparison with the GA. However, the GA helps in providing a better precision in locating the search space. When a comparative study for thermal and economic optimization of a STHE was carried out, the result showed an increase in the tubes leading to a reduction in the objective function is accompanied by to a substantial percentage increase in the function values [3]. A multi-objective solver was utilized as a genetic algorithm to optimize four different design variations. It was indicated that baffle space to be approximated to 0.5 m for lower annual cost values. While for smaller length, baffle spacing and diameter to approximately to 0.05–1.5 m [4]. The Pareto archived evolution strategy (PAES) algorithm represents an uncomplicated non-trivial algorithm which has the ability of generating solutions in the Pareto-optimal set. The study shows PAES can be viewed as a simple approach for multi-objective optimization [5]. To compare the PSO and the GA of the heater

design, the Bell–Delaware method was used. It has been reported that the PSO attain a stronger set of Pareto-optimal population [6]. Thermal modelling for a new design of a STHE was carried out by using the logarithmic mean method. It was reported that operating cost of the derived design went down by 17–18% as compared to previous studies and the initial cost went up by 1.76%. The study on multiple objective optimization of STHE with helical baffles was carried out. The objective function comprises of LMTD and pressure drop across the STHE while compared to the original data the optimum configurations increased [7, 8]. To navigate to the optimal values, a multi-objective optimization procedure was implemented. The material cost and minimization of energy consumption were the two main objectives. It was reported that the solutions for both cost of energy and material were more efficient when compared to baseline designs. After 50th generation optimization was stopped after that no other improvements were observed [9]. The genetic algorithm for optimal designs of STHE's was presented from an economic point of view. The result provided improved geometries and coefficients. In two case studies out of three, reduced value of cost obtained while compared to the previous studies [10].

Many researchers have used different techniques like particle swarm, Pareto-archived evolution strategy and genetic algorithms. In this paper, fast and elitist multi-objective genetic algorithm NSGA-II has been used to present a standard STHE model. This paper has been also modified NSGA-II which includes inverse generalized distance (IGD) to provide the next generation of candidates with each iteration of the algorithm.

2 Mathematical Modelling

2.1 Proposed Method

The pumping power and heat transfer area are the two functions considered to control the pressure drop. It is desired to compute the optimization of annual cost by using LMTD and a set of design variable values [11]. The theoretical process layout is given below:

- Selection of fluid on shell and tube side.
- Determine stream temperature.
- Determine the exchanger pressure drop.
- Determine velocity limits for exchanger.
- Calculate fouling coefficients and heat transfer models for heat exchanger.

2.2 Thermal Model of the Heat Exchanger

The mathematical approach for the design of STHE is as follows:

2.2.1 The Heat Transfer Coefficient

' Q ' is given in Eq. (1). The heat transfer coefficient of exchanger (h_t) and h_s is given by Eqs. (2) and (3), respectively. The shell diameter (D_s) is given by Eq. (4).

$$Q = (m_t c_{pt}) * (T_{co} - T_{ci}) \quad (1)$$

$$h_t = (k_t/d_i)0.024\text{Re}_t^{0.8}\text{Pr}_t^{0.4} \quad (2)$$

$$h_s = \frac{0.36 * k_s}{d_e} * \text{Re}_s^{0.55} * \text{Pr}_s^{0.33} * \left(\frac{\mu_s}{\mu_{wt_s}}\right)^{0.14} \quad (3)$$

$$D_s = 0.637st \sqrt{\pi Nt \left(\frac{\text{CL}}{\text{CTP}}\right)} \quad (4)$$

where st , CL and CTP are tube pitch, tube layout constant and tube count calculation constant, respectively, for 45° and 90° tube arrangement the value of CL is 1, and for 30° and 60°, CL = 0.87. The values of CTP are 0.93, 0.90 and 0.85 for one, two and three tubes pass, respectively. d_e (m) the equivalent shell diameter is given by Eq. (5) [12]. While U is given by Eq. (6) [13],

$$d_e = 4 * \frac{0.43S_t^2 - (\Pi * 0.25 * d_o^2)}{0.5(\Pi * d_o)} \quad (5)$$

$$U = \frac{1}{\left(\frac{1}{h_s}\right) + R_{fs} + \left(\frac{d_o}{d_i}\right)\left(R_{ft} + \left(\frac{1}{h_t}\right)\right) + \frac{d_o \ln\left(\frac{d_o}{d_i}\right)}{2k_t}} \quad (6)$$

In the design part, to determine the true temperature difference a correction factor (F) is used. The heat exchanger surface area is given by Eq. (7).

$$A = \frac{Q}{U * F * \text{LMTD}} \quad (7)$$

2.2.2 Pressure Drops

The tube and shell side pressure drop are calculated by Eqs. (8) and (9), respectively. where Darcy friction coefficient is given by f_t

$$\Delta P_t = \frac{\rho_t v_t^2}{2} * \left(\left(\frac{L}{d_i}\right) f_t + p\right) n \quad (8)$$

Table 1 Standard values for stainless-steel E-Shell heat exchangers

Parameters	Values
Constant a_1 (\$)	8000
Constant a_2 (\$/m ²)	259.2
Constant a_3	0.93
Energy cost C_e (\$/kWh)	0.12
Operating time H (h/year)	8000
Discount rate per annum i (%)	10
Number of years of operation n_1	5
Pump efficiency η	0.7

$$\Delta P_s = f_s \left(\frac{\rho_s v_s^2}{2} \right) \left(\frac{L}{B} \right) \left(\frac{D_s}{D_e} \right) \quad (9)$$

2.2.3 Objective Function

The total cost is the sum of material cost and discounted operating cost, which is given by Eq. (10). The material cost C_i for the STHE is given by Eq. (11), and the discounted operating cost is given by Eq. (12) while the pumping power is given by Eq. (13). Table 1 shows standard value to calculate the costs

$$C_{\text{tot}} = C_i + C_{\text{op}} \quad (10)$$

$$C_i = a_1 + a_2 A^{a_3} \quad (11)$$

$$C_{\text{op}} = \sum_{x=1}^{n_y} \frac{C_o}{(1+i)^x} = P C_e H \quad (12)$$

$$P = \frac{1}{\eta} \left(\frac{m_t}{\rho_t} \Delta P_t + \frac{m_s}{\rho_s} \Delta P_s \right) \quad (13)$$

2.2.4 Entropy Generation Number (EGN)

The entropy generation rate is a parameter used to reduce the thermodynamic irreversibility that reduces the performance of the STHE. The total rate of entropy generation in STHE is given by Eq. (14). The Hessel greaves EGN are shown by Eq. (15), which is a modification of Bejan's EGN. It is used due to Bejan's EGN produces an entropy generation paradox [14].

$$\Delta \dot{S} = \Delta \dot{S}_{\Delta t} + \Delta \dot{S}_{\Delta s} \tag{14}$$

$$N_s = \frac{\Delta \dot{S} T_{c,i}}{Q} \tag{15}$$

2.3 Genetic Algorithm

GAs is a traditional method for optimization. GAs use a direct analogy of the natural phenomenon of evolution like crossover and mutation. The parameter values are represented as strings in the algorithm. The GAs work with strings instead of the parameters themselves. A randomly generated population within the sample space is taken, then with the underlying objective function and constraints it is evaluated accordingly. Fitness function is used to assign values to individual stings in population in absence of constraints. Mutation operators and crossover are applied to pairs of individuals from the parent generation. Both operators usually ensure that the values can escape from the local minima. The samples with the best fitness value have a higher possibility to be comprised in the next generation. Then the selected population from the previous generation goes to the beginning of the entire process. After multiple generations, the solution starts to converge on the global minimum [15]. The multiple stopping parameters can be chosen to end the iterative process like the number of generations, time, duplicity of n and $n + 1$ population (Fig. 1).

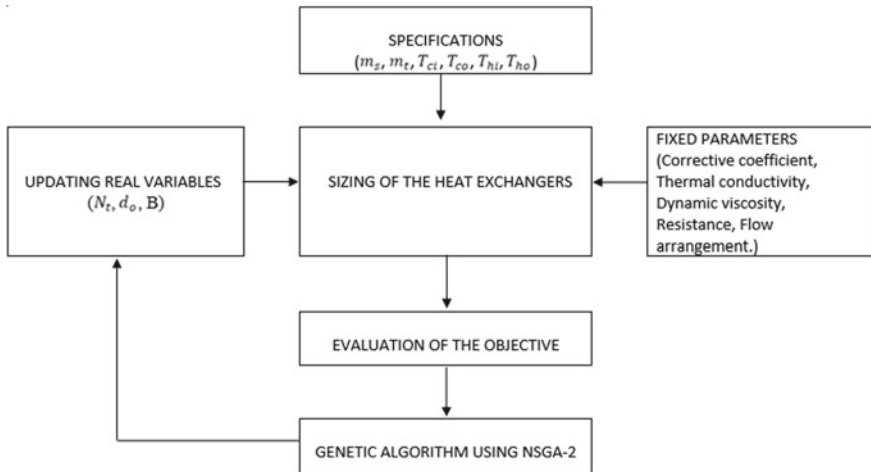


Fig. 1 Algorithm flowchart

2.3.1 Non-dominated Sorting Genetic Algorithm-II

A solution $X(b)$ is dominated by another solution $X(a)$ in non-dominated sorting, if any condition is true as follows:

- i. rank of $X(b) >$ rank of $X(a)$
- ii. if rank of $X(b) =$ rank of $X(a)$ then, distance of $X(a) >$ distance of $X(b)$.

In GA selection of suitable individuals form, the population takes place by tournament selection method. Two strings randomly selected from the population compete against each other; this takes place in a knockout tournament format. The process imitates the survival of the fittest. Random mutation and uniform crossover are run to obtain the $(n + 1)$ th population. The density of solutions surrounding a solution is calculated by crowding distance. It is used, where an individual’s crowding is the rectangle perimeter with its closest neighbour at the other end corner. Therefore, if two individuals (b) and (a) have an equal rank, the individual with bigger crowding distance is more suitable [16].

2.3.2 Inverse Generalized Distance (IGD) Ratio

The IGD ratio was defined to compare the IGD value of current generation to past q generations. The user-defined δ was used to decide when to execute the local search. In this paper, the number of generations is determined by observing 0.001 or less change in the δ ratio as shown in Eq. (16) which is also given in the modified NSGA [15].

$$\frac{IGD_{\max} - IGD_{\min}}{q} \leq \delta \tag{16}$$

3 Results and Discussion

The standard values for a stainless-steel E-Shell heat exchanger have been defined in Table 2. Limits for the number of tubes have been given from 50 to 300 and the outer diameter of the tubes 0.015–0.051 m for all the iterations.

The input parameters for the NSGA-II algorithm have been compiled in Table 3. All combinations of the three objectives were executed against each other except the EGN versus the discounted operations cost because both are obtained from the same parameter of tube and shell pressure drop. The four cases are explained as follows;

Case 1. The graph is plotted between discounted operating cost and capital cost shown in Fig. 2. It has been observed that a Pareto-optimal front is being formed. The graph showed a decrease in the operating cost with increasing capital investment. One of the optimal solutions, $C_{op} = 3124.855\$$ and $C_i = 9096.19\$$, obtained from

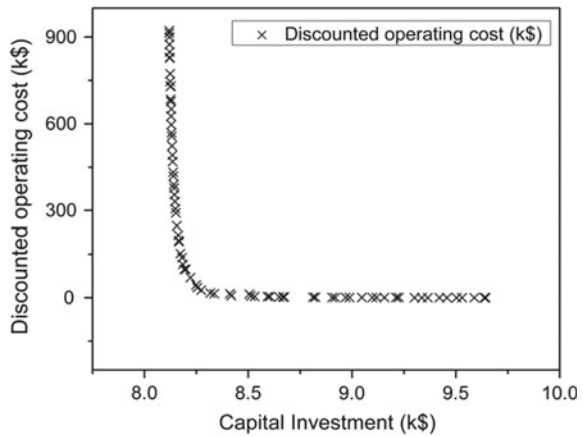
Table 2 Standard data of STHE

Parameters	Tube side	Shell side
Inlet temperature T_i (K)	76.7	199
Outlet temperature T_o (K)	37.8	–
Mass flow rate m (kg/s)	18.80	5.52
Density ρ (kg/m ³)	995	850
Specific heat C_p (J/Kg K)	2.05	2.47
Kinematic viscosity μ (Pa-s)	0.00358	0.0004
Fouling resistance R_f	0.0061	0.0061
Prandtl number Pr	0.05645	0.0076

Table 3 Constant parameters for NSGA-II

Parameter	Value
Population	40
Max. no. of generations	500
Probability of crossover	0.9
Probability of mutation	0.25
Index of crossover operator	15
Index of mutation operator	20

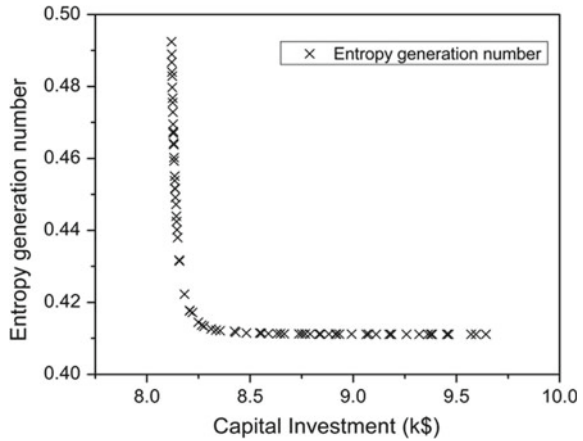
Fig. 2 Variation of DOC to CI



the set of non-dominated population after the algorithm was terminated. It has been found that the total cost obtained in this case study was significantly lower when compared to the total cost given by [17].

Case 2. The graph was plotted between the capital cost and the EGN as shown in Fig. 3. It has been deduced from the graph that EGN decreases with higher the capital cost which is due to increase the volume of material required. The optimum solution

Fig. 3 Variation of EGN to capital investment



obtained, by decreasing the irreversible losses of the STHE at the cost of increasing the capital investment.

Case 3. To examine the entropy generation number and total operating cost, the graph has been plotted as shown in Fig. 4. Figure 4 from observation shows that the values of EGN are from 0.41 to 0.42, so it can be concluded that the set of population have converged to the global optimum in the same number of generation and also an inverse relation between EGN and total operating cost is being observed. The decrease in EGN is achieved on the expense of sacrificing total operating cost.

Case 4. In this case, all three objectives have been executed simultaneously. In Fig. 1, it has been deduced that the population has been converged towards a solution of Pareto-optimal set. The efficiency of the algorithm decrease with an increase in number of objectives [18]. A similar trend can be seen in Fig. 7 where some solution sets have not converged to the Pareto front, unlike the other cases where an optimal

Fig. 4 EGN versus total operating cost (\$)

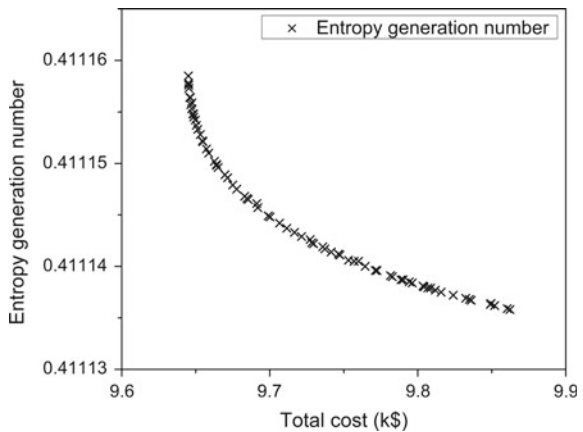


Fig. 5 EGN versus DOC

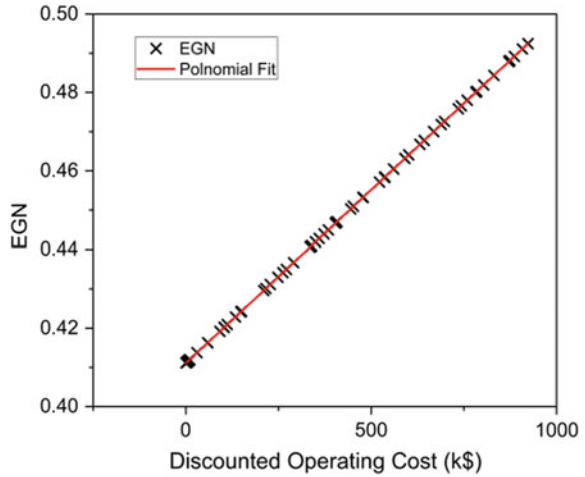
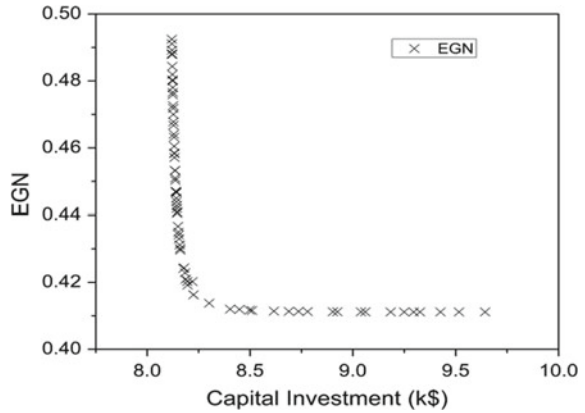


Fig. 6 EGN versus capital investment



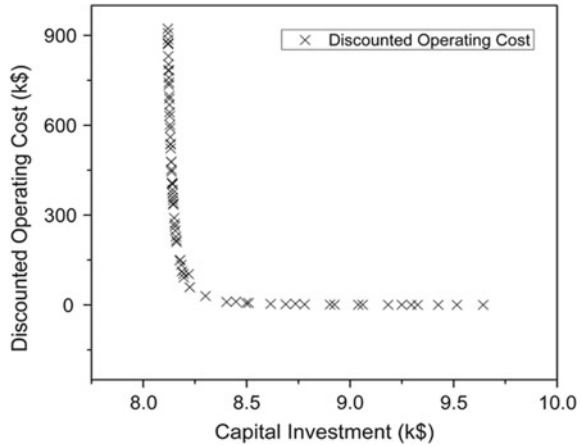
Pareto front is obtained. Contrary to both the graphs, the obtained result is shown in Fig. 5. The linear proportionality noticed; it is because these both objectives are derived from the same parameters (Figs. 6 and 7).

4 Conclusion

This study shows an entropy used optimization through a GA which has been conducted to optimize the both the cost of materials and operation in the STHE. The following points can be concluded from the study:

- The optimal design has been developed for heat exchanger by reducing the overall cost of the STHE while compared with previous research results.

Fig. 7 DOC versus capital investment



- While decreasing the EGN of the STHE, the capital investment of STHE increased.
- The EGN found reduced at the cost of sacrificing the total operating cost.
- By decreasing the number of objectives, the robustness of the algorithm increases.

References

1. Deb K, Pratap A, Agarwal S, Meyarivan T (2002) A fast and elitist multiobjective genetic algorithm: NSGA-II. *IEEE Trans Evol Comput* 6(2):182–197. <https://doi.org/10.1109/4235.996017>
2. Hajabdollahi H, Ahmadi P, Dincer I (2012) Exergetic optimization of shell-and-tube heat exchangers using NSGA-II. *Heat Transf Eng* 33(7):618–628. <https://doi.org/10.1080/01457632.2012.630266>
3. Hajabdollahi H, Ahmadi P, Dincer I (2011) Thermoeconomic optimization of a shell and tube condenser using both genetic algorithm and particle swarm. *Int J Refrig* 34(4):1066–1076. <https://doi.org/10.1016/j.ijrefrig.2011.02.014>
4. Jena S, Patro P, Behera SS (2013) Multi-objective optimization of design parameters of a shell & tube type heat exchanger using genetic algorithm. *Int J Curr Eng Technol* 3(4):1379–1386
5. Knowles J, Corne D (1999) The Pareto archived evolution strategy: a new baseline algorithm for Pareto multiobjective optimisation. In: *Proceedings of the 1999 congress on evolutionary computation (CEC 1999)*, vol 1, pp 98–105. <https://doi.org/10.1109/CEC.1999.781913>
6. Ghanei A, Assareh E, Biglari M, Ghanbarzadeh A, Noghrehabadi AR (2014) Thermal-economic multi-objective optimization of shell and tube heat exchanger using particle swarm optimization (PSO). *Heat Mass Transf Stoffuebertragung* 50(10):1375–1384. <https://doi.org/10.1007/s00231-014-1340-2>
7. Baadache K, Bougriou C (2015) Optimisation of the design of shell and double concentric tubes heat exchanger using the genetic algorithm. *Heat Mass Transf Stoffuebertragung* 51(10):1371–1381. <https://doi.org/10.1007/s00231-015-1501-y>
8. Wang S, Xiao J, Wang J, Jian G, Wen J, Zhang Z (2017) Configuration optimization of shell-and-tube heat exchangers with helical baffles using multi-objective genetic algorithm based on

- fluid-structure interaction. *Int Commun Heat Mass Transf* 85:62–69. <https://doi.org/10.1016/j.icheatmasstransfer.2017.04.016>
9. Gholap AK, Khan JA (2007) Design and multi-objective optimization of heat exchangers for refrigerators. *Appl Energy* 84(12):1226–1239. <https://doi.org/10.1016/j.apenergy.2007.02.014>
 10. Ponce-Ortega JM, Serna-González M, Jiménez-Gutiérrez A (2009) Use of genetic algorithms for the optimal design of shell-and-tube heat exchangers. *Appl Therm Eng* 29(2–3):203–209. <https://doi.org/10.1016/j.applthermaleng.2007.06.040>
 11. Edwards BJE, Design and rating shell and tube heat exchangers
 12. Amini M, Bazargan M (2014) Two objective optimization in shell-and-tube heat exchangers using genetic algorithm. *Appl Therm Eng* 69(1–2):278–285. <https://doi.org/10.1016/j.applthermaleng.2013.11.034>
 13. Kakaç S, Liu H (2002) Heat exchangers: selection, rating, and thermal design, 2nd edn
 14. Guo J, Cheng L, Xu M (2009) Optimization design of shell-and-tube heat exchanger by entropy generation minimization and genetic algorithm. *Appl Therm Eng* 29(14–15):2954–2960. <https://doi.org/10.1016/j.applthermaleng.2009.03.011>
 15. Barakat N, Sharma D (2019) Evolutionary multi-objective optimization for bulldozer and its blade in soil cutting. *Int J Manag Sci Eng Manag* 14(2):102–112. <https://doi.org/10.1080/17509653.2018.1500953>
 16. Deb K, Goel T (2001) Controlled elitist non-dominated sorting genetic algorithms for better convergence. In: *Lecture notes computer science (including subseries Lecture notes in artificial intelligence and lecture notes in bioinformatics)*, vol 1993, pp 67–81. https://doi.org/10.1007/3-540-44719-9_5s
 17. Kumar HK, Nagaraj P, Uday RH (2014) MAE 598 design optimization design optimization of a shell and tube heat exchanger [Online]. Available: http://designinformatics.github.io/teaching/designopt/projects/2016/desopt_2016_02.pdf
 18. Elarbi M, Bechikh S, Gupta A, Ben Said L, Ong Y (2017) A new decomposition-based NSGA-II for many-objective optimization, pp 1–20

Integrated Approach for Flexible Job Shop Scheduling Using Multi-objective Genetic Algorithm



Sunita Nayak, Anoop Kumar Sood, and Abhishek Pandey

Abstract The study proposes a genetic algorithm-based integrated approach where the selection of suitable machine and sequencing of operations in machines are performed simultaneously in a flexible job shop-based environment. For this, chromosome representation chosen is simple to code and decode and always results in a feasible solution on the application of genetic operators. In true sense to real production problems, multiple objectives are considered which will reduce the total production time of the entire batch with efficient machine utilization. The proposed solution is evaluated on test data, and it was shown that the algorithm is giving equivalent and in some cases better results in comparison with existing methodologies.

Keywords FJSP · GA · Pareto front · Makespan · Maximum machine workload · Total machine workload

S. Nayak

Department of Mechanical Engineering, Bhubanananda Odisha School of Engineering, Cuttack, Odisha 753007, India

A. K. Sood (✉)

Department of Manufacturing Engineering, National Institute of Foundry and Forge Technology, Ranchi 834003, India

A. Pandey

Department of Mechanical Engineering, ABES Engineering College, Ghaziabad, Uttar Pradesh 201009, India

e-mail: abhishek.pandey@abes.ac.in

1 Introduction

Flexible job shop scheduling (FJS) problem arises in a job shop-based production environment where multiple machines are available for performing a particular operation. This additional flexibility demands two types of decisions to be made, namely selection of appropriate machine from the available machines for performing an operation on a job and then finding an appropriate sequence of operations of same or different jobs to be performed in a particular machine to achieve some desired objectives. The first type of decision comes under the routing subproblems, and the second type of decision falls under the scheduling subproblems of production planning domain. In line with its predecessor job shop scheduling problem (JSP), which only concerns the scheduling of operations, it is a combinatorial NP-hard problem, but the presence of routing makes it more difficult to solve in comparison with JSP.

Several alternative approaches have been suggested in the literature to tackle FJS problems (FJSP) which can be characterized as heuristic and meta-heuristic solution methodologies. Heuristic approaches may guarantee the optimal solution but that may not be true if large size problem instances are considered. Whereas high-level strategies known as meta-heuristics have produced optimal solutions within a reasonable computational time for a different size of problem instances [1]. These meta-heuristics use either a hierarchical or a combination approach to solve FJSP. The hierarchical approach decomposes the FJSP into routing and sequencing subproblems. Routing can be done using simple dispatching rules or a combination of them, and then some other higher-order heuristic can be used to solve the sequencing subproblem. In a combination approach, both types of subproblems are combined and solved simultaneously [2]. Although integration is difficult to implement, the quality of solutions is better than the hierarchical approach. In this direction, GA [2], PSO [3, 4], and ACO [5] are effective meta-heuristics which can exploit a lot of domain knowledge and implemented to solve the FJSP. GA is the most popular meta-heuristics technique as it explores solution space more diversely by using the population of solutions and provides resistance to premature convergence on local minima. Recently, more and more papers are concentrating on GA [6] or hybrid GA [7] with different population representation and generation strategies.

Most of these approaches concentrated on determining an optimum schedule which satisfies a single objective [4, 7]. The real-world production scenario demands production of a complete batch in minimum time and proper utilization of all the available machines so that no single machine is under-utilized or over-utilized. The presence of these multiple objectives put additional difficulty in FJSP solution methodology [8–10].

In this regard, the present study proposes the use of simple GA to solve multi-objective FJSP. As per the combinatorial nature of FJSP, solution coding and encoding are incorporated using problem-specific knowledge to obtain feasible solutions. In the true sense of many-objective behaviour of the problem, no artificial fix up is used. Instead, the Pareto-optimal approach [9] is used. In this approach, superiority of one

solution over others is not established for all the objectives considered simultaneously. Through this algorithm will try to find out a diverse set of solutions close to Pareto front. The main aim of developed GA is to obtain a diverse set of solutions as close as possible to the actual Pareto-optimal front.

2 Problem Formulation

Multi-objective FJSP addressed in this study consider n jobs (indexed by i) and M machines (indexed by k). Each job has a total of Q_i operations, and operation sequence is given by O_{ij} for $j = 1, 2, \dots, Q_i$. Machines for each O_{ij} are represented by M_{ijk} . If $M_{ijk} \subset M$, it is a case of partial flexibility, and if $M_{ijk} = M$, it is a case of full flexibility. Processing time of M_{ijk} is predefined and given by p_{ijk} . The goal is to determine schedule which results in the minimization of makespan (F_1); maximal workload (F_2), and the total workload of the machines (F_3).

It is assumed that all machines and jobs are available and ready to start at time $t = 0$. Jobs are independent of each other, and machines never breakdown and process single operation at a time with a non-preemption condition. Precedence constraint between the operations of the same job is known and maintained. Each job could visit the machine more than once. The setup time and job transportation time are included in the corresponding processing time.

3 Solution Procedure

3.1 Coding and Decoding

In FJSP, potential solutions known as individuals or chromosome consist of two genes representing scheduling and routing subproblems, respectively. Hence, chromosome representation consists of two parts, namely operation sequence (OP) and machine assignment (MS), as shown in Fig. 1. In OP, integer i indicates job number and its j th repetition indicates O_{ij} operation. In MS, machines are indicated by integer values and arranged in order of jobs. That is first we arrange the machines for first job operations, then for second job operations and so on.

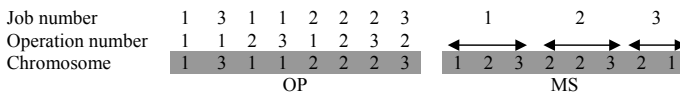


Fig. 1 Structure of proposed chromosome

To reduce the large feasible search space resulting chromosome is mapped to the corresponding phenotype using an active schedule. In an active schedule, an operation is scheduled at the earliest available time in a machine.

3.2 *Non-domination Sorting*

In this step, the population is sorted in ranks according to an ascending level of non-domination [10]. The non-dominating solutions from the entire population are assigned rank 1, followed by assigning rank 2 to those solutions which are only dominated by rank 1 solutions and so on. For determining the diversity among individuals of the same front crowding distance is calculated. It is a Euclidian distance between the members of the same rank calculated using their function value in the m dimensional hyperspace. The crowding distance of members at the extreme is taken equal to infinity.

3.3 *Initial Population*

The efficiency of the present approach is increased by selecting suitable chromosomes located at a proper region in search space so that algorithm reaches the Pareto front in the least possible time and without endanger of trapping in local optima. To achieve this, 50% of the initial population is generated randomly and the remaining 50% population is generated using a problem-specific approach. For random population generation, alleles of OP gene are generated randomly with the restriction that each i appear Q_i times. For MS sub-string, each i in OP is decoded to corresponding job and operation, then for i th job j th operation set of available machines M_{ijk} is identified and one machine is assigned randomly. The second part of the initial population is generated using a problem-specific heuristic. For this, OP is generated randomly as in random population generation, but for elements of MS, the machine which has the minimum processing time for performing selected operation from OP is selected.

3.4 *Selection*

Selection of individual chromosomes for generating next-generation children is an important criterion to balance exploitation and exploration capability of an algorithm. For this tournament-selection procedure is adopted. In this method, two distinct individual solutions are selected randomly and compare. The comparison is done on the bases of rank, and the solution with the least rank is selected. If ranks are same, then individual with maximum crowding distance is selected. Between individuals of the

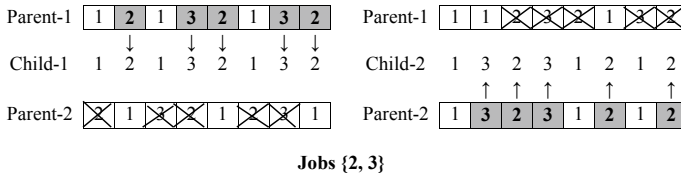
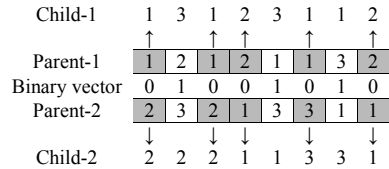


Fig. 2 POX crossover for OS part

Fig. 3 MPX crossover for MS sub-string



same rank, the one with maximum crowding distance is selected else random selection is done. The selected individual is added to the mating pool for the generation of next-generation individuals.

3.5 Crossover

Pair of distinct individuals are selected randomly from the mating pool for crossover operation. For crossover of OP, sub-string of chromosome precedence preserving order-based crossover (POX) is used, and for MS sub-string multi-point preservative (MPX) crossover is used. In POX, as shown in Fig. 2, two jobs are selected randomly from a set of available jobs and where it occurs in parent-1; at the same position, it is added in child-1 and deleted from parent-2. Remaining entries in parent-2 are added in child-1 empty positions in a sequence as in a parent-2. Then roles of two parents are reversed, and child-2 is formed as explained for child-1. In MPX crossover, as shown in Fig. 3, a binary vector of length equals to MS length is generated with the element as 0 or 1. At a particular position of this vector if 0 is present then for child-1, allele value at that position in parent-1 is added and for child-2 allele value at that position of parent-2 is added; otherwise, parent-1 and parent-2 are reversed.

3.6 Mutation

The generated children will replace their parents in population, and then the entire population is subjected to mutation. The individual for mutation is selected randomly. For an OP part of selected individual two positions are selected at random and sub-string is inverted between these two positions. For MS sub-string of the same

selected individual, any job is selected randomly and the machines associated with each operation of the respective job are replaced randomly from the set of available machines.

3.7 *Elitism*

Better solutions of the previous generation known as elites of the population are merged with the solutions of the current generation to find the elites of the present generation. Non-domination sorting is performed on this merged population, and solutions having rank one are preserved as an elite of present generation. Out of these generated elites, only those which are not present in the current generation are added in the population and worst solutions are removed to keep population size constant. Complete steps followed in this algorithm are represented in Fig. 4.

4 Results

To illustrate the efficiency and effectiveness of the proposed GA for optimization of multi-objective FJSP, five Kacem instances, namely 4×5 , 8×8 , 10×7 , 10×10 and 15×10 , are used. An algorithm is coded in MATLAB and run in Intel™ core7 computer having 8 GB RAM. Algorithm parameters are given in Table 1.

For comparison purpose, results given in [1, 3, 5, 11] are combined and non-dominating sorting is performed to find out the optimal solutions. Results from the proposed methodology are compared with those from the literature and are shown in Table 2. From the obtained result, it is seen that for 4×5 , 8×8 and 10×10 problem our algorithm gives the same result as discovered by other researchers. But for the case of 10×7 and 15×10 problems, proposed algorithm can locate better Pareto front as shown in Fig. 5.

5 Conclusions

In this study, a simple genetic algorithm is proposed to solve the multi-objective flexible job shop scheduling problems. The main highlight of the work and associated advantages are as follows.

- Solutions known as chromosomes are represented using an integrated approach.
- In this, single chromosome consists of two parts known as operation sequence and machine sequence. Operation sequence represents the routing subproblem, and machine sequence represents the scheduling subproblem of FJSP.

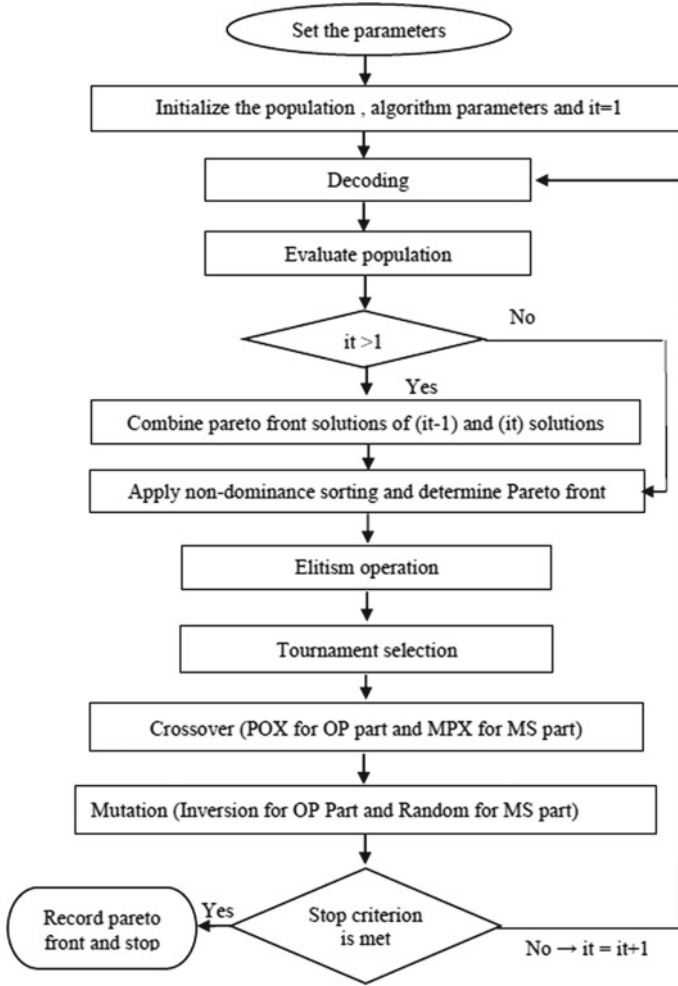


Fig. 4 Flowchart of multi-objective genetic algorithm for FJSP (it = iteration number)

Table 1 Algorithm parameters

Parameters	Value
Generations	200
Total population	10 × length of chromosome
Percentage of population generated randomly	10%
Crossover probability	90%
Mutation probability	1%

Table 2 Comparison of results of proposed algorithm with those from literature

Problem	Length of chromosome	Pareto front from literature			Obtained Pareto front		
		F_1	F_2	F_3	F_1	F_2	F_3
4×5	24	11	9	34	11	9	34
		11	10	32	11	10	32
		12	8	32	12	8	32
		13	7	33	13	7	33
8×8	54	14	12	77	14	12	77
		15	12	75	15	12	75
		16	11	77	16	11	77
		16	13	73	16	13	73
10×7	58	11	10	62	11	10	62
		12	12	60	11	11	60
		11	11	61	12	10	61
					12	11	59
					12	12	58
10×10	60	7	5	43	7	5	43
		7	6	42	7	6	42
		8	5	42	8	5	42
		8	7	41	8	7	41
15×10	112	11	10	93	11	10	93
		11	11	91	11	11	91
					13	10	90

- Efficient chromosome representation adopted in this work simplifies the generation of active schedule and requires no repair mechanism during genetic alteration and hence always results in a feasible schedule.
- Chromosome coding and decoding mechanism adopted is suitable for both full and partial flexible problems.
- The performance of the approach is evaluated with the results obtained from other authors' algorithms, and it was shown that the algorithm is giving equivalent and in some cases better results.
- In future, work will be extended to incorporate the uncertainty in scheduling like machine breakdown or fuzziness in the planning horizon.

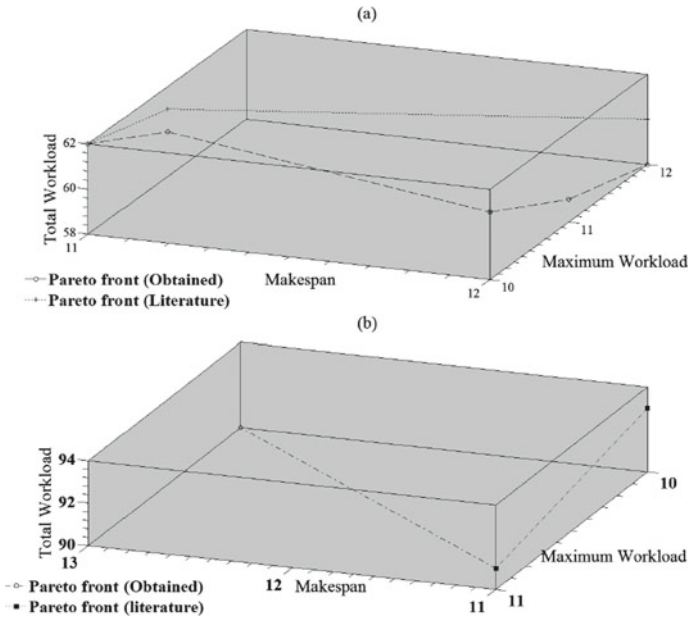


Fig. 5 Comparison of obtained Pareto fronts **a** 10 × 7 problem; **b** 15 × 10 problem

References

1. Shahsavari-Pour N, Ghasemishabankareh B (2013) A novel hybrid meta-heuristic algorithm for solving multi objective flexible job shop scheduling. *J Manuf Syst* 32(4):771–780
2. Amin-Naseri MR, Afshari AJ (2012) A hybrid genetic algorithm for integrated process planning and scheduling problem with precedence constraints. *Int J Adv Manuf Technol* 59(1–4):273–287
3. Zhang G, Shao X, Li P, Gao L (2009) An effective hybrid particle swarm optimization algorithm for multi-objective flexible job-shop scheduling problem. *Comput Ind Eng* 56:1309–1318
4. Nouri M, Bekrar A, Jemai A, Niar S, Ammari AC (2018) An effective and distributed particle swarm optimization algorithm for flexible job-shop scheduling problem. *J Intell Manuf* 29:603–615
5. Wang L, Zhou G, Xu Y, Liu M (2012) An enhanced pareto-based artificial bee colony algorithm for the multi-objective flexible job-shop scheduling. *Int J Adv Manuf Technol* 60(9):1111–1123
6. Rooyani D, Defersha FM (2019) An efficient two-stage genetic algorithm for flexible job-shop scheduling. *IFAC Pap Online* 52–13:2519–2524
7. Li X, Gao L (2016) An effective hybrid genetic algorithm and tabu search for flexible job shop scheduling problem. *Int J Prod Econ* 174:93–110
8. Beheshtinia M, Ghazivakili N (2018) Reference group genetic algorithm for flexible job shop scheduling problem with multiple objective functions. *J Ind Syst Eng* 11(4):153–169
9. García-León AA, Dauxère-Pérès S, Mati Y (2019) An efficient Pareto approach for solving the multi-objective flexible job-shop scheduling problem with regular criteria. *Comput Oper Res* 108:187–200
10. Deb K (2010) *Multi-objective optimization using evolutionary algorithms*. Wiley India (P.) Ltd., New Delhi
11. Chiang T, Lin H (2013) A simple and effective evolutionary algorithm for multi objective flexible job shop scheduling. *Int J Prod Econ* 141(1):87–98

Mathematical Analysis of Angular Distortion in GTAW of Stainless Steel 304 Sheets



Ayush Kumar, Udit Saini, Vivek Yadav, and Pradeep Khanna

Abstract Gas tungsten arc welding is an electric arc welding process. In GTAW, an arc is developed in mid of the work which is to be welded and an inexhaustible tungsten electrode. Its vast and protean usage allows it to be used in various industries like automotive, chemical, rail-car manufacturing with potential to weld any metal with exceptional weld character. TIG happens to be an arc-based welding process, and as a consequence of it, brisk cycles of cooling and heating are detected in this process, rendering the weldment to irregular thermal expansions and contractions giving rise to stresses and ultimately leading to distortions. Weld distortions cause quality-related issues and undesirable deformation of the weld which creates assembly problems. These distortions are of various types like longitudinal and transverse distortions, bowing, dishing, buckling, twisting, etc. Careful study over the years through various surveys and reports found that most pronouncing of these distortions happens to be angular distortion. In angular distortion, the distortion is transverse to the welding direction which is induced by shrinkage near the fusion zone causing a change in the angle of the parts. The present investigative work aims to analyze and report the effects of certain parameters on angular distortion. Torch angle, welding current, and welding speed are those parameters. The work material has been chosen as grade 304. This steel contains chromium (15–20%) and nickel (2–10.5%) as the main non-ferrous constituents. The material has exceptionally good corrosion resistance and finds extensive usage in food processing and chemical industry. The present work is carried out on thin sheets of this material which are used in food processing industry, and it is expected that the outcomes of this work shall be of use to industrial applications. Statistical technique of experiments design has been adopted to generate a mathematical equation between the input parameters and the output response. Response surface methodology is adopted to analyze graphical results.

Keywords GTAW · Design of experiments · Angular distortion · Input parameters · Mathematical equation

A. Kumar · U. Saini (✉) · V. Yadav · P. Khanna
MPA Engineering Division, Netaji Subhas University of Technology, New Delhi, India

1 Introduction

Gas tungsten arc welding is also called tungsten inert gas welding (TIG). In GTAW, an electric arc is developed in mid of the work metal and tungsten electrode. Inert shielding gas does not allow the surrounding air to react with the arc and the weld pool while welding by the help of a gas nozzle which replaces the atmospheric air with the shielding gas. Unlike other welding processes, the electrode is not consumed in GTAW [1]. Input parameters like torch angle, nozzle to plate distance, welding speed and current directly affect angular distortion observed [2, 3]. To get maximum yields out of joint efficiency and mechanical properties, the above-discussed parameters are to be optimized. As GTAW generates exquisite weld quality and is used to coalesce thin and medium sheets, it is widely applied in aircraft and spacecraft industry, automotive and food industry. Heating and cooling cycles occur in non-uniform manner in any welding process. This leads to uneven and rapid thermal expansions and contractions which render the weldment to certain stresses ultimately giving rise to certain types of distortions such as longitudinal, transverse, angular distortion, bowing/dishing, buckling and twisting [4]. Dimensional deviations and the spooliation of the joint are to be prevented by keeping the distortions minimum. These distortions are inevitable but can be minimized. Literature review has affirmed that angular distortion is the most captious distortion among these variants. It is the out of plane distortion [5] and plummets the performance of the welded structure as well as majorly destroys the physical appearance. The schematic for angular distortion is shown in Fig. 1. Thin sheets of austenite stainless steel of grade 304 are used as the work material in the present study. The material has exceptionally good inter-granular corrosion resistance and finds extensive usage in food processing and chemical industry. Approximate chemical composition for the material is shown in Table 1 [6]. Table 2 shows the mechanical characteristics of the material. Studying the effect of welding input features torch angle, welding current and speed is carried out in the current experimentation. A mathematical model has been refined through the statistical technique of central composite face-centered method, and the graphical results showing the individual and interaction effects were analyzed using response surface methodology. Since this stainless steel is majorly used in the food industry, present work can be of significant value to the food and chemical industry.

Fig. 1 Angular distortion



Table 1 Chemical content of 304 stainless steel [6]

Fe	Cr	Ni	Mn	N	S	C	Si	P
66.44%	18%	8%	2%	0.10%	0.03%	0.08%	0.75%	0.04%

Table 2 Mechanical properties of 304 stainless steel [7]

Tensile strength ultimate (MPa)	Tensile strength yield (MPa)	Elongation (%)	Hardness (Rockwell-B)
621	290	55	82

Fig. 2 Welding setup

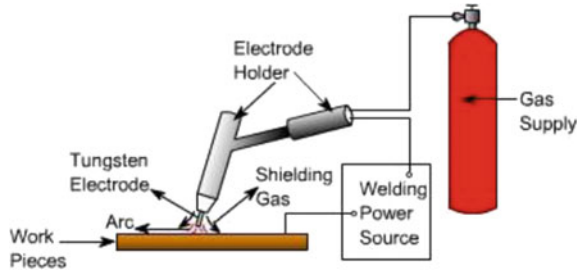
2 The Welding Setup

In the performed experiment, a constant current power with a rated capacity of 200 A was applied. A mechanized carriage unit was provided with varying welding speeds demanded in the experiment. Constant welding speed is provided by this mechanized unit and manages a reproducible weld character. Varying linear speed of the weld table was achieved using a variable frequency drive which gives a range between 0 and 50 cm/min. On the radial arm of the mentioned unit, the welding torch was fastened allowing movement in up and down directions to facilitate varying heights of the works. To get different arc lengths, fine vertical movement is also arranged. Furnishing the tilting of the torch to obtain the angle between -45° and 45° along the vertical. Pure argon gas was adopted. The flow rate was kept at approximately 15 L/min. The actual weld site is shown in Fig. 2, and the schematic diagram of complete welding setup is shown in Fig. 3.

3 Plan of Investigation

Investigation presented here was done in the following steps.

Fig. 3 Schematics of TIG welding setup



3.1 Selection of Weld Input Parameters

For the analysis, input welding boundaries like the welding current, the welding speed, the torch inclination, the nozzle tip gap and the gas stream rate were analyzed. Given the writing review, previous knowledge and the quantity of preliminaries performed, it was discovered that lone the initial three had critical impact on the response boundary which is angular distortion. Consequently, these were chosen.

3.2 Determining the Working Limits of the Input Parameters

The working of upper and lower limits of controllable variables (independent) was concluded via several trial runs. The observations made were

- Uniform bead appearance is observed.
- No over penetration
- Plates do not overlap.

The input variables were planned to be set at three levels with minimum represented as (-1), maximum as (+1) and the intermediate by (0), respectively, as shown in Table 3.

Table 3 Input parameters and their limits

Input variables	Units	-1	0	1
Welding current	Ampere	110	125	140
Welding Speed	cm/min	25	30	35
Torch Angle	Degrees	0	22.5	45

Table 4 Design matrix

Run	Welding speed (cm/min)	Current (A)	Torch angle (°)	Angular distortion (°)
1	0	0	-1	0.15
2	1	-1	-1	2.62
3	0	0	0	0.45
4	0	0	0	0.49
5	-1	-1	1	-3.88
6	1	-1	1	-1.03
7	-1	0	0	0.85
8	-1	1	1	-4.15
9	0	1	0	-2.05
10	1	1	-1	1.80
11	1	0	0	4.01
12	0	0	0	1.48
13	-1	1	-1	0.02
14	0	0	1	-1.79
15	1	1	1	0.84
16	-1	-1	-1	2.05
17	0	-1	0	0.58
18	0	0	0	0.46
19	0	0	0	0.47
20	0	0	0	0.46

3.3 Developing the Design Matrix

A design matrix has been developed with 20 experimental runs while using composite face-centered technique as shown in Table 4. The details of these numbers are

$$2^3 = 8(\text{factorial points}) + 2 * 3(\text{star points}) + 6(\text{center points}) = 20$$

3.4 Experimentation

Twenty number of welds were made on the experimental setup shown in Fig. 2. The experiments were conducted by taking the combinations of input parameters as shown in the design matrix in Table 4. The trial runs were randomized so as to keep away from any precise error of the framework. Once the specimens were welded, they were numbered according to their welding parameter combinations.

Fig. 4 Angular distortion measuring setup



3.5 Measuring the Angular Distortion

Using the setup shown in Fig. 4, angular distortion on the work specimens was quoted. It consisted of Vernier height gauge, a surface plate and the counter weight. Readings were taken to measure the raised height of one plate against the other, and the relation $\text{Sin } \theta = \text{height}/L$ was used to calculate angular distortion, where L is the plate width. Repetition of the aforesaid procedure was carried out for the other side of the joint as well, and the mean of the two was taken as the angular distortion. In a similar manner, all the remaining weld specimens were checked for angular distortion.

3.6 Developing the Mathematical Model

The functional relation between response and selected parameters is

$$f(\theta) = (A, B, C)$$

where

θ = angular distortion

A = welding current

B = welding speed

C = torch angle.

The general mathematical model is described as follows:

$$\theta = \beta_0 + \beta_1 A + \beta_2 B + \beta_3 C + \beta_{12} AB + \beta_{13} AC + \beta_{23} BC$$

$$+ \beta_{11}A^2 + \beta_{22}B^2 + \beta_{33}C^2$$

where

β_0 = Modal constant

$\beta_1, \beta_2, \beta_3$ = Coefficients of linear terms

$\beta_{12}, \beta_{13}, \beta_{23}$ = Coefficients of interactive terms

$\beta_{11}, \beta_{22}, \beta_{33}$ = Coefficients of quadratic terms.

The actual mathematical equation generated by the software is given as follows.

$$\theta = 0.60 + 1.34A - 0.38B - 1.67C + 0.42AB + 0.68AC + 0.55BC + 1.86A^2 - 1.30B^2 - 1.39C^2$$

3.7 Results and Their Analysis

The ANOVA table obtained from the software is shown in Table 5. The *R* square value of 94% as per Table 6 indicates the goodness of fit. The scatter diagram shown at Fig. 5 indicates a close clustering of the points around the line of fit again validating the adequacy of the developed model.

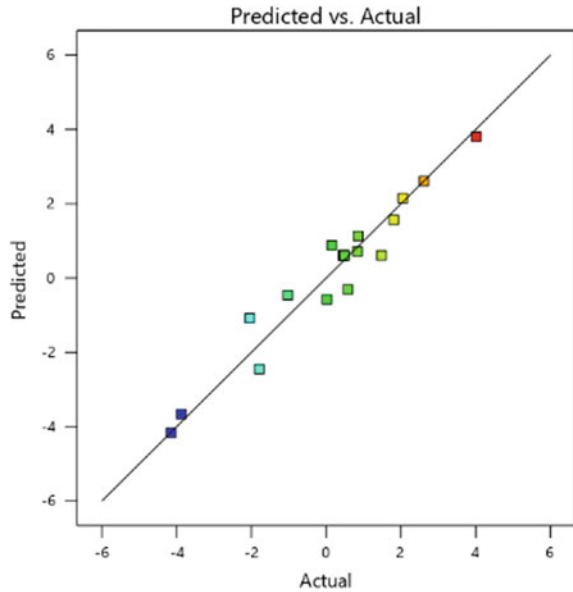
Table 5 ANOVA analysis

Source	Sum of squares	df	Mean square	F-value	p-value	
Model	70.98	9	7.89	17.63	<0.0001	Significant
Welding speed (A)	17.82	1	17.82	39.84	<0.0001	
Current (B)	1.50	1	1.50	3.35	0.0971	
Torch angle (C)	27.74	1	27.74	62.00	<0.0001	
AB	1.41	1	1.41	3.15	0.1064	
AC	3.76	1	3.76	8.40	0.0159	
BC	2.46	1	2.46	5.50	0.0410	
A ²	9.51	1	9.51	21.27	0.0010	
B ²	4.68	1	4.68	10.45	0.0090	
C ²	5.33	1	5.33	11.92	0.0062	
Residual	4.47	10	0.4474			
Lack of fit	3.62	5	0.7232	4.22	0.0702	
Pure error	0.8578	5	0.1716			
Cor total	75.46	19				

Table 6 Fit statistic

Std. dev.	0.6688	R^2	0.9407
Mean	0.1914	Adjusted R^2	0.8874
C.V.%	349.40	Predicted R^2	0.5924

Fig. 5 Scatter diagram between actual and predicted values



The graphical results obtained from response surface methodology are shown in Figs. 6, 7 and 8.

Interactive Effects of Welding Current and Speed on Angular Distortion

It is clear from Fig. 6 that angular distortion is under interactive influence from welding current and welding speed. Also, distortion increases initially and later decreases as welding current increases. The reason could be that the input heat elevated with the hike in welding current that proceeded extra distortion and later the effect of welding speed became more pronounced and reduced it.

Interactive Torch Inclination and Welding Speed Effects on Angular Distortion

Figure 7 depicts that rise in torch angle fluctuates angular distortion which first increases and then decreases. The reason for the initial increase is due to increase in torch angle and dissemination of the arc ahead of the weld bead increased, which infused heat in more area causing more distortion. But at a later stage, the negative effects of welding speed became more pronounced and reduced the angular distortion.

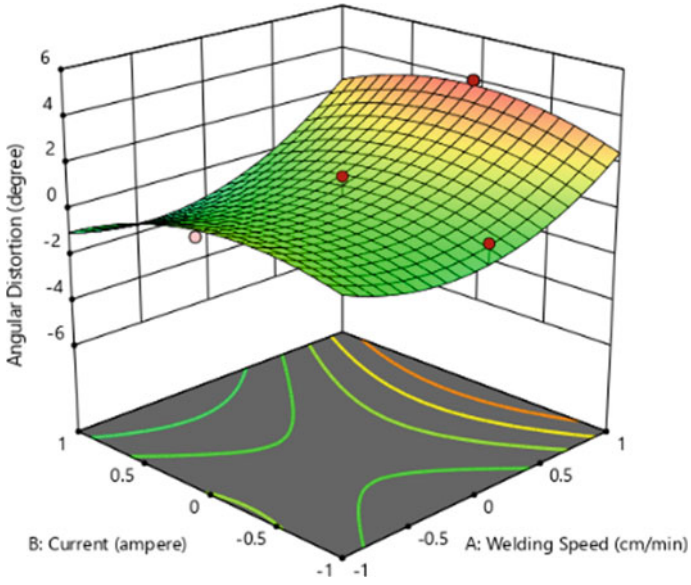


Fig. 6 Interactive welding current and speed effects

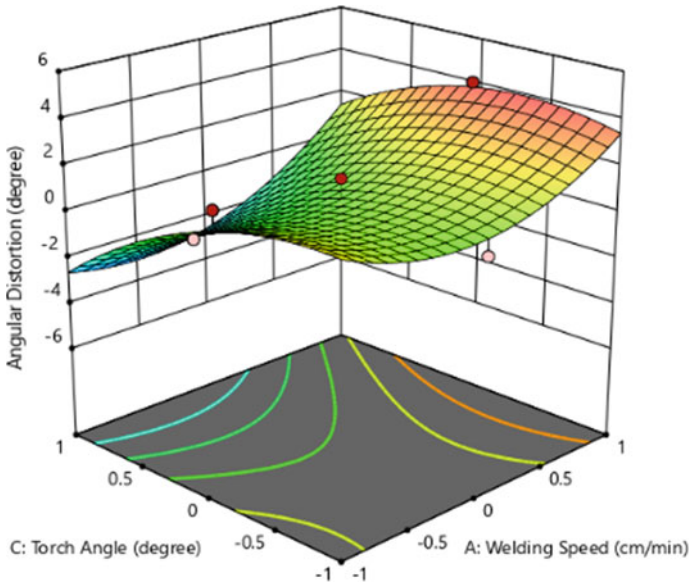


Fig. 7 Interactive torch angle and welding speed effects

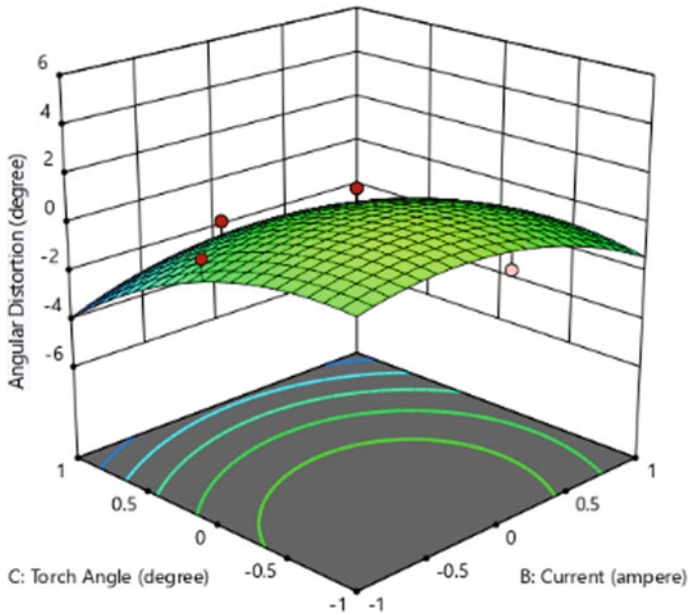


Fig. 8 Interactive torch angle and welding current effects

Interactive Torch Inclination and Welding Current Effects on Angular Distortion

Figure 8 shows the interactive effects of torch angle and welding current on angular distortion. It is seen that angular distortion escalates with the initial hike in welding current because of more heat going into the joint. Later, the trend seems to reverse probably because of the pronounced negative effect of the torch angle.

4 Conclusions

The study of work has extrapolated the following:

- The optimal condition for angular distortion 0.02° is achieved with input parameters, namely welding current, welding speed and torch angle at 122.93 A, 32.77 cm/min, and 31.66, respectively.
- Maximum angular distortions observed were of 4.01 and -4.15° in positive and negative sides, respectively.
- At 125 A welding current, welding speed of magnitude 35 cm/min and torch angle of 22.5, maximum angular distortion was achieved.
- The input parameter welding speed affects the response parameter angular distortion negatively, whereas the welding current and torch angle affect positively.

References

1. Devkumar D, Jabaraj DB (2014) Research on gas Tungsten arc welding of stainless steel—an overview. *Int J Sci Eng Res* 5(1):1612–1618
2. Malik D, Kumar S, Saini M (2014) Effect of process parameters on angular distortion of gas tungsten arc welded SS 302 & MS plate. *Int J Enhanc Res Sci Technol Eng* 3(8):18–24
3. Ramani S, Velmurugan V (2014) Effect of process parameters on angular distortion of MIG welded AI6061 plates. In: All India manufacturing technology, design and research conference, 12–14 Dec 2014, pp 401.1–401.6
4. Duhan S, Mor A, Malik D (2015) Study of angular distortion of SS 302 and MS plate with GTAW. *Int J Rec Res Aspects* 2(2):159–163
5. Sudhakaran R, Murugan VV, Sivasakthivel PS (2012) Optimization of process parameters to minimize angular distortion in gas tungsten arc welded stainless steel 202 grade plates using particle swarm optimization. *J Eng Sci Technol* 7(2):195–208
6. Mubarak N, Notonegoro H, Thosin K (2018) Comparative mechanical improvement of stainless steel 304 through three methods. *IOP Conf Ser Mater Sci Eng* 367:012023. <https://doi.org/10.1088/1757-899X/367/1/012023>
7. Steel A (2018). AK Steel 304/304L product data bulletin. Retrieved from AK Steel. https://www.aksteel.com/sites/default/files/2018-01/304304L201706_1.pdf

Development of a Programmable Contour Following Unit for TIG Welding



Palash Hazra, Ashish Kumar, Sanyam Jain, Sourabh Naskar,
and Pradeep Khanna

Abstract Welding is an extensively used joining process in the fabrication industry owing to its ability to make monolithic structures, vast range of materials joining, portability and durable joints. Conventionally, TIG welding of different contour is done manually and hence consumes time, and the weld finish depends on the skill of the labour. The system designed and developed is an effort to provide a basic and economic solution to such requirement. It is made up of a robust frame, which provides stability to the whole set-up. The torch is clamped and follows the profile of the weldment maintaining a constant arc length throughout the job. An AC motor dispenses the power to the system which further is reduced with the help of a single transmission gearbox. The whole arrangement is synchronized and was tested several times on different profiles and gave satisfactory result on each run.

Keywords Automation · TIG welding · Weld finish · Contour welding · Microcontroller

1 Introduction

GTA welding is basically a slow process as it requires eye and hand coordination significantly more than other welding processes, and when it comes to weld the contours, the effective speed gets even more reduced. Automation is a key technology necessary for improving the quality and speed of the process with fairly good reproducibility [1]. Gas tungsten arc welding is known for its high-quality weld and could promote its development in the industry [2]. TIG welding is known for its high weld quality and is highly used in practices such as vessel and pipe welding [3]. Increase in competition has formed the need for innovation [4]. Conventionally, contours are welded manually and hence is time consuming and requires high skill and manoeuvrability on the part of the welder. The present work is an effort to design and build a system so that contours can be welded automatically with fairly good

P. Hazra (✉) · A. Kumar · S. Jain · S. Naskar · P. Khanna
MPAE Division, NSUT, New Delhi 110078, India

degree of repeatability and dependence on the welder’s skills can be done away with. To remain competitive, there is a need to produce products at lower prices and higher quality [5]. The system developed can be operated easily to weld contours with the ability to keep the arc length constant throughout irrespective of the shape and size of the contour and maintains a constant arc length throughout. To ensure the stability of the system, the structure made is sturdy to absorb vibrations. The torch is held firmly and is clamped tightly by C-clamps, and hence, it can easily trace the profile of the weldment maintaining a constant arc length throughout the job. A 1440 rpm rated AC motor delivers the power to the system which further intentionally reduced to 360 rpm through a single transmission gearbox of transmission ratio of 1/4, to get the desired translatory speed of the torch. Arduino UNO microcontroller has been used to control the pulses for two stepper motors with four start lead screw, which facilitates the vertical motion of the torch. Different current load and speed are used for different materials and thickness. Since it is an automated system, speed and current can be altered as needed.

2 The Design Set-Up

The actual depiction of the developed system is shown in Figs. 1 and 2:

The whole set-up can be explained and categorized as follows.

2.1 Actuation

It consists of two segments:

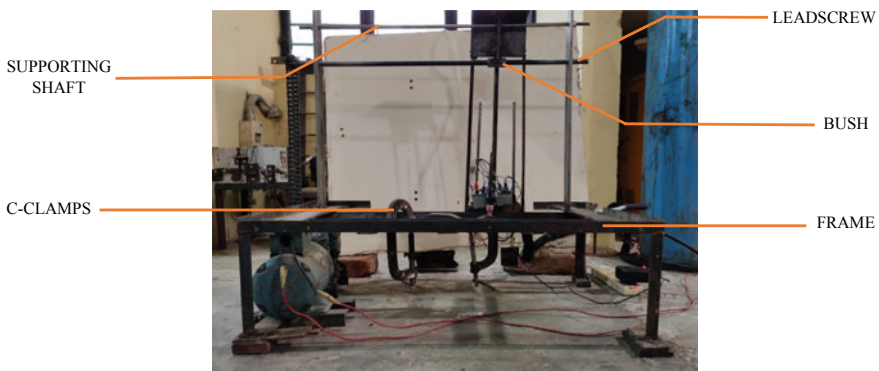


Fig. 1 Front view of the system

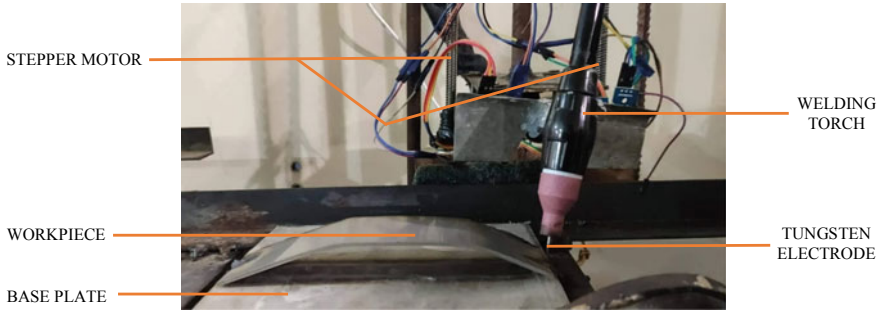


Fig. 2 Welding torch holding unit

- An AC motor coupled with a single transmission gearbox is used to drive the welding torch in horizontal direction.
- Two stepper motors with four start lead screw are used for the vertical motion of the welding torch holding unit.

In this manner, the welding torch can smoothly and easily trace the profile of the workpiece to be welded.

2.2 Control Unit

The Arduino UNO microcontroller is used to command the stepper motors in a prescribed manner in order to weld the given contour of the job whose program (set of codes) is provided in the later segment of this work.

2.3 Torch Holding Mechanism

The GTAW torch is held in an indigenously designed holding unit with the provisions for precise vertical movement. It is ensured that the smoothness and accuracy of the movement are of highest possible level, because the same has to follow the profile of the workpiece to be welded.

3 Working

The developed system is shown in Fig. 3. The working of the same can be described as follows:

- The workpiece is clamped securely on to the base plate in a required manner.

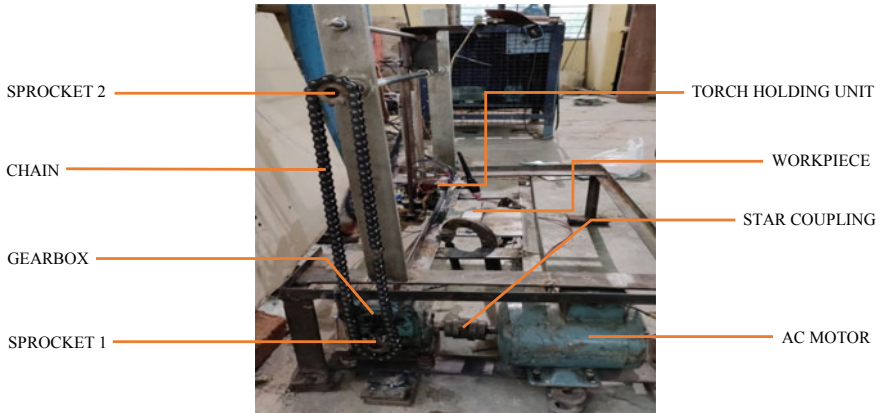


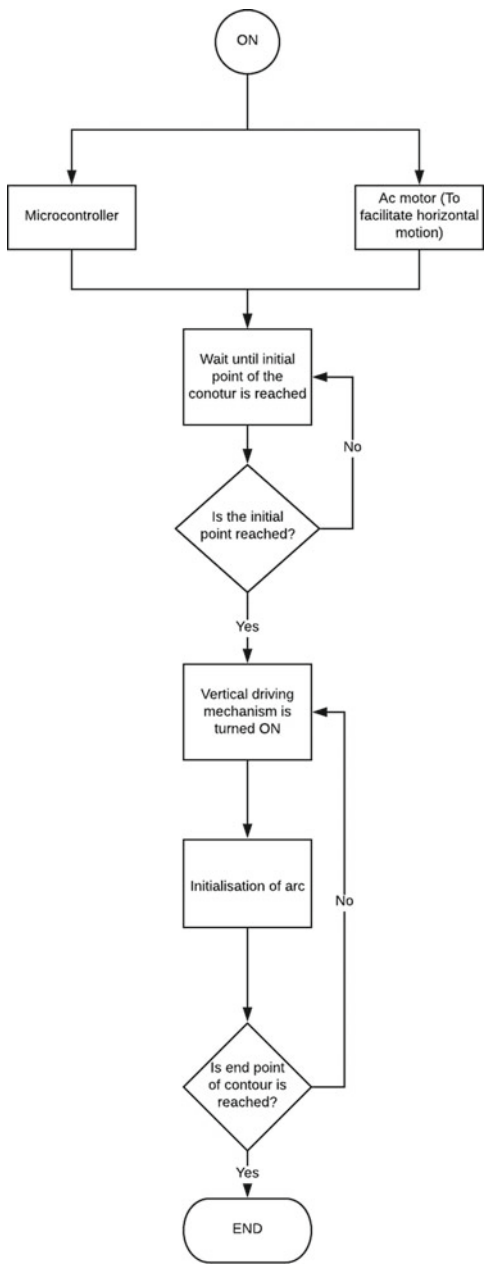
Fig. 3 Side view of the system

- After ensuring the correct positioning of the torch on to a specially developed torch holder and setting the welding power source at desired input parameters, the system is turned on.
- This energizes the horizontal traverse of the weld torch unit.
- The moment welding torch reaches the weld start point on the clamped workpiece; the welding arc is triggered.
- The contour of the workpiece is followed by the welding torch according to the already selected programme accessed from the library.
- During the movement of the torch over the contour, it is ensured that a constant arc gap is maintained throughout the traversing movement of the torch, otherwise the weld quality may get adversely affected.
- Once the torch reaches the end point of the contour weld line, the power supply is turned off.

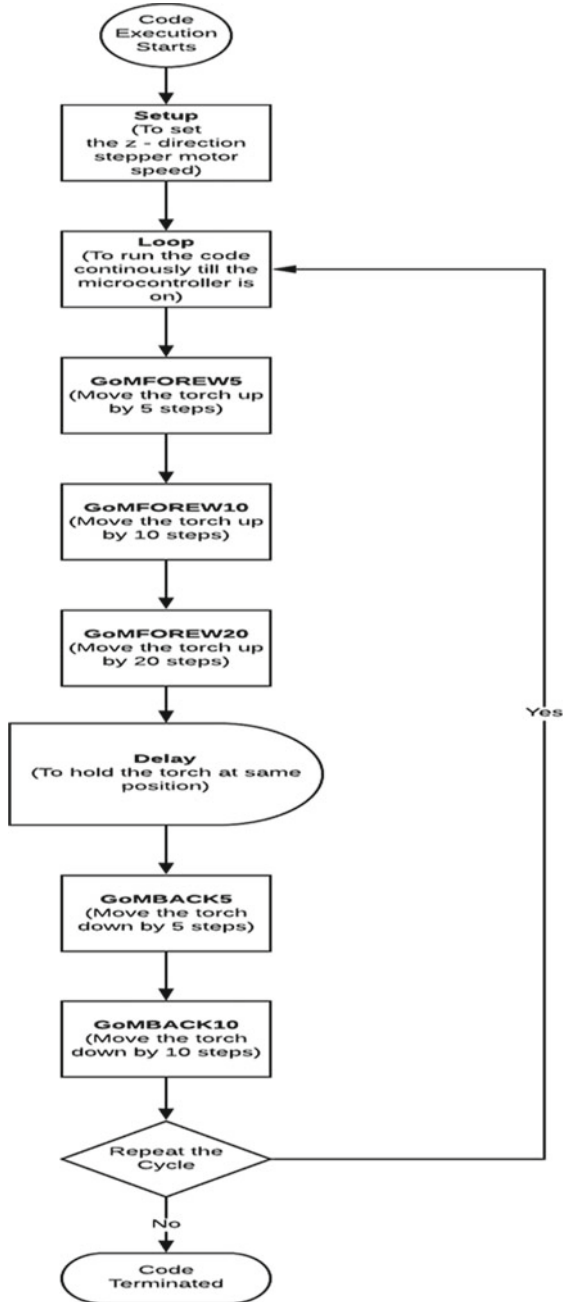
Upon inspecting the weldment, it has been found that it is free from any visible irregularity. The result has been validated by running torch several times on the weld profile with almost the same results every time.

3.1 Flow Chart of Working

The schematic functioning of the set-up can be summarized and easily interpreted by the following flow chart.



4.1 Flow Chart for the Code



5 Cost Analysis

S. No.	Item	Quantity	Price/unit (Rs.)	Cost (Rs.)
1.	Shaft (\varnothing 10 mm)	1	110/-	110/-
2.	Lead screw (\varnothing 16 mm)	1	450/-	450/-
3.	Ball bearing (6202)	2	100/-	200/-
4.	Roller chain (12.5 mm)	2 m	100/-	200/-
5.	Sprocket (12.5 mm)	2	100/-	200/-
6.	Mild steel flat (10 mm \times 50 mm \times 1220 mm)	4 ft	225/-	1100/-
7.	Angle bar (30 mm \times 30 mm)	6 ft	30/-	180/-
8.	Stepper motor (12 V, 1 A)	2	800/-	1600/-
9.	Microcontroller (Arduino UNO)	1	900/-	900/-
10.	C-clamps (100 mm)	2	30/-	60/-
11.	Star coupling (12.5 mm)	1	100/-	100/-
12.	AC motor (220 V, 1440 rpm)	1	1700/-	1700/-
13.	Reduction gearbox (gear ratio—1/4)	1	3000/-	3000/-
	Total cost			10,000/-

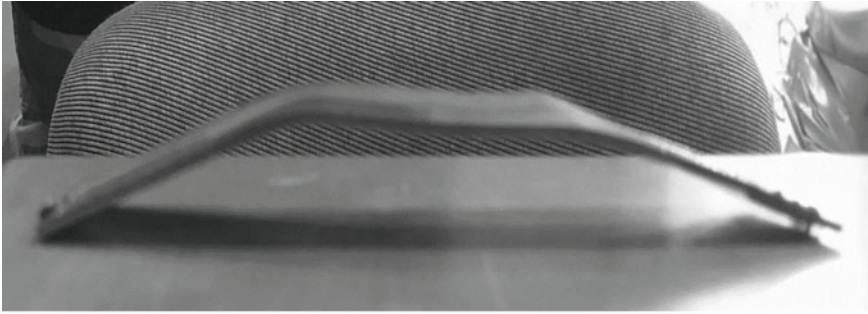
6 Importance of the Proposed Model

The industrial systems available in the market to perform profile welding are very costly, sophisticated and high-end products, with complex and highly specialized software and control systems. It may therefore not possible for the small- and medium-sized industries engaged in profile welding jobs to afford such elaborated systems.

The present developed system however conceptualizes a very cheap and robust alternative to the above-mentioned industrial systems and has successfully been tested. The authors believe that if the same concept is commercialized, the system can cost effectively produce profile welds with reasonable accuracy.

7 Result

The developed system has been run and tested several times on different work profiles with different input parameters by feeding the corresponding program to the micro-processor from the library, and it is giving satisfactory performance with good quality of welds.



(a)



(b)

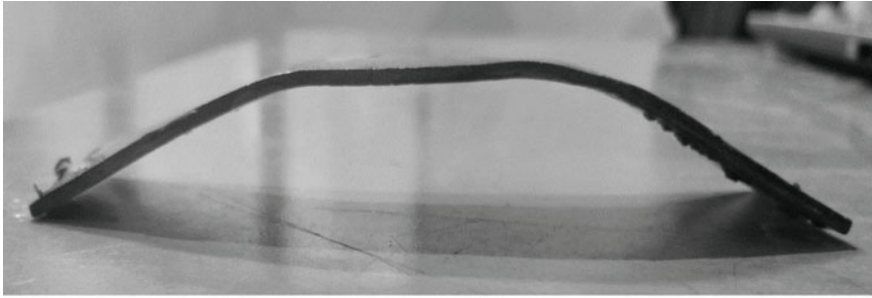
Fig. 4 Welding at 55 A **a** Work profile, **b** Weldment

Figures 4a and 5a reveal the weld profile, whereas Figs. 4b and 5b indicate the weld bead appearance without any major weld defects. It can also be observed that the width of the weld bead is constant throughout the length of the weld profile.

8 Future Scope

The authors believe, though the system developed has many useful features from the industrial application view point but still following additions may be made in future:

- Provision of different welding speeds.
- Provision of three-dimensional movements.
- Ability to accommodate wide variety of profiles to be welded.
- Provision can also be made for self-assessment of the profile to be welded so as to avoid prefeeding of the given profile details into the system each time the profile changes.



(a)



(b)

Fig. 5 Welding at 45 A **a** Work profile, **b** Weldment

9 Conclusions

The following conclusions can be drawn from the carried-out work:

1. The microcontroller Arduino UNO has been found to give adequate competence to perform such tasks.
2. The speed of the system can be changed as per the requirements.
3. The developed system is simple to handle and less complicated.
4. The present set-up provides only two-dimensional motion.
5. Cost and space requirement of the whole set-up is less.
6. If commercialized, the system with minute changes, and modification can successfully be used in assembly lines effectively.
7. The present system does not offer range of speeds.

References

1. Beigi H (1995) Automation in manufacturing. In: Proceedings of 1st annual conference on technological advancements in developing countries. Columbia University, New York, 24–25 July 1993, pp 85–92
2. Li YC, Ushio M, Tanaka M (2000) Effect of surface active flux on welding-pool depth and arc phenomena in TIG welding. *Chin J Mech Eng* 36(12):43–44
3. Karafi MR, Narimani R, Hojjat Y, Gheybi M (2010) Study on automatic control of arc gap in robotic TIG welding. *Int J Adv Manufact Technol* 50(9):953–960
4. Vyshnavi TS, Chetan N (2016) A review on implementation of agile in manufacturing industries using key enablers. *Int Res J Eng Technol* 3(3):1929–1933
5. Yusuf YY, Sarhadi M, Gunasekaran A (1999) Agile manufacturing: the drivers, concepts and attributes. *Int J Prod Econ* 62:33–43

Modal Analysis of a Pre-stressed Quadcopter Propeller Using Finite Element Analysis



Faraz Ahmad, Pushendra Kumar, and Pravin P. Patil

Abstract A quadcopter is a multi-rotor-type helicopter that is lifted and propelled by four propellers. These propellers were driven by four DC motors. The difference in angular speeds of propellers is responsible for roll, pitch, and yaw motions. Nowadays, research in the field of unmanned aerial vehicles (UAV) is increasing because of their interesting applications. During the flight of a quadcopter, the propellers are subjected to thrust forces and vibrations. The main objective of this study is to find out the natural failure frequency of a propeller and the best-suited material which can sustain the loading and vibration during the flight. The CAD model of a propeller is designed in Creo 2.0 design software, and ANSYS 16.2 is used to analyze the vibration frequency. In this paper, the propeller is subjected to a thrust force of 50 N. Furthermore, modal analysis has been performed to find out the resonance frequency under pre-stressed condition. The obtained simulation results are validated with the previous works in the existing literature.

Keywords Quadcopter · Propeller · Vibration frequency · Resonance · Pre-stress

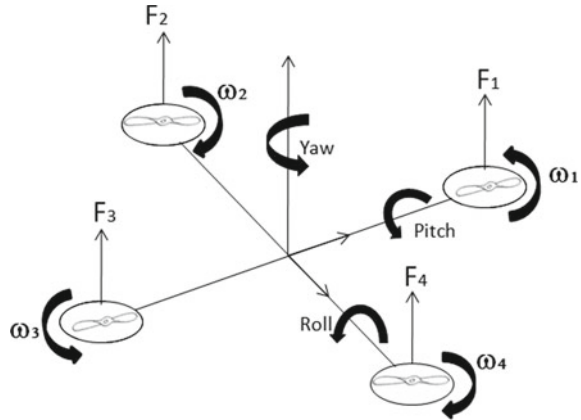
1 Introduction

A quadcopter UAV is a demanding mechatronics device because of its interesting applications in many areas such as industries, transportation, surveillance, military operations, and many more. It provides robustness in flight with vertical take-off and landing capability. A quadcopter consists of four propellers mounted at the end of each arm. Three-dimensional (3D) motion of a quadcopter is governed by the rotary combination of these propellers. Figure 1 shows the schematic diagram of a quadcopter, where F_1 , F_2 , F_3 , and F_4 show the thrust forces of all four propellers generated by the angular speeds ω_1 , ω_2 , ω_3 and ω_4 , respectively. These propellers generate more thrust force compared to a classical helicopter. That is why it can carry more payload and can fly safely with better flight control [1]. The difference in

F. Ahmad (✉) · P. Kumar · P. P. Patil

Department of Mechanical Engineering, Graphic Era Deemed to be University, Dehradun, India

Fig. 1 Quadcopter schematic representation



F_1 and F_3 governs the left–right motions using roll, and the difference in F_2 and F_4 governs the forward–backward motions using pitch. When all four propellers rotate with the same angular speed, it will result in the vertical motion of the quadcopter [2].

The structural strength of the quadcopter frame also plays an important role in working performance. Many researchers are working on quadcopter flight improvement considering the structural strength. Kuantama et al. [1] calculated the air pressure around the propeller. Ahmed et al. [3] presented the aerodynamic and structural analysis of the quadcopter frame. F450 quadcopter frame was analyzed for total deformation, and the obtained result was under considerable limits. Penkov et al. [4] calculated the shroud influence on the lift force using the CFD analysis. The result of the lift force was compared with and without the shroud. Kumar et al. [5] designed the multi-mode vehicle type quadcopter, which can drive on the ground and fly as well. Furthermore, the finite element analysis was performed to check the performance of different components for the structural strength. In [6], modal analysis of the quadcopter propeller was performed to calculate the natural frequencies but the propeller was not subjected to pre-loading conditions. In [7, 8], aerodynamic performance was analyzed by a quadcopter propeller.

The main objective of this study is to find out the resonance frequency with the application of applied thrust force (this thrust force generate stress in the propeller and make the propeller pre-stressed). Hence, in this paper, a quadcopter’s propeller is analyzed with pre-stressed conditions due to the effect of the thrust force acting on the propeller. The modal analysis has been performed on a quadcopter’s propeller with the pre-stressed condition, and the natural frequencies of vibration are calculated. Three different materials are used for the analysis and compared for their respective performances. The present paper is arranged in five sections; (1) presents the introduction with literature; (2) demonstrates the CAD modeling and material properties; (3) explains the FEA simulation results with material comparison; and (4) concludes the paper.

2 CAD Modeling and Material Properties

The computer-aided design (CAD) software Creo 2.0 is used for the designing of a quadcopter’s propeller. Figures 2 and 3 show the CAD solid model and mesh model of the propeller, respectively. The CAD model of the propeller has been imported to ANSYS 16.2 workbench to calculate the natural vibration frequency. ANSYS is the most widely used software, whose result can be used for the evaluation of a product’s performance. It can be used in many engineering applications like fluid–solid interaction, vibration, harmonic response, explicit dynamics, magnetic, thermal, static loading, dynamic loading, etc. The model is analyzed for three different materials, namely G-10 (phenolic epoxy fiber), aluminum (Alloy 6061-T6), and carbon fiber reinforced polymer (CFRP). The mechanical properties of these materials are given in Table 1.

Fig. 2 Solid CAD model

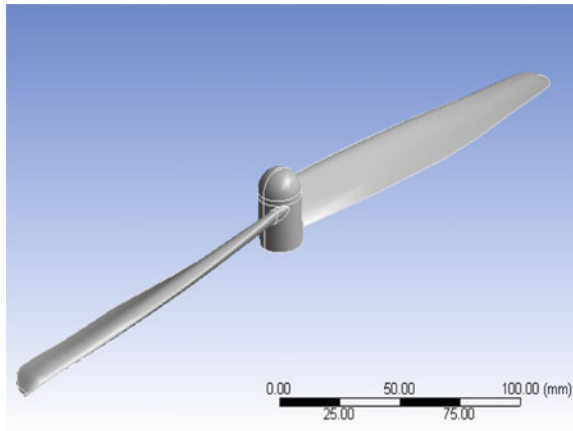


Fig. 3 Mesh model of a propeller

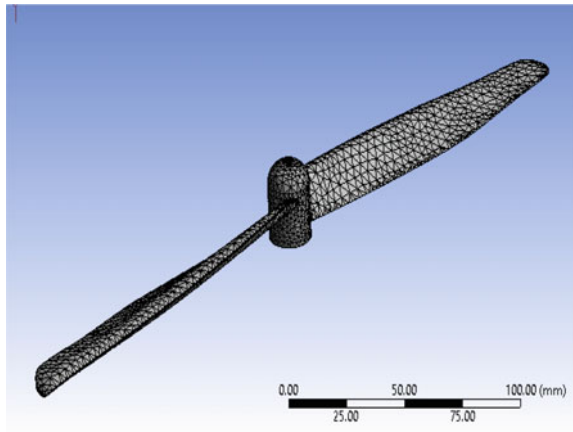


Table 1 Material properties [6]

Materials	Density (kg/m ³)	Young's modulus (MPa)	Poisson ratio	Bulk modulus (Mpa)
G-10	2100	14,000	0.3	11,667
Alloy 6061-T6	2712	68,900	0.3	66,559
CFRP	1600	70,000	0.3	58,333

3 FEA Simulation and Result

First, the CAD model of a propeller has been imported from Creo 2.0 to ANSYS workbench, and then the boundary conditions are applied. The propeller has been fixed around the rotational axis, where it is connected to the motor shaft. Figure 4 shows the fixed position (blue color) boundary condition. Figure 5 shows the applied thrust force F , because of which stress is being generated in the propeller (pre-stress

Fig. 4 Fixed boundary condition

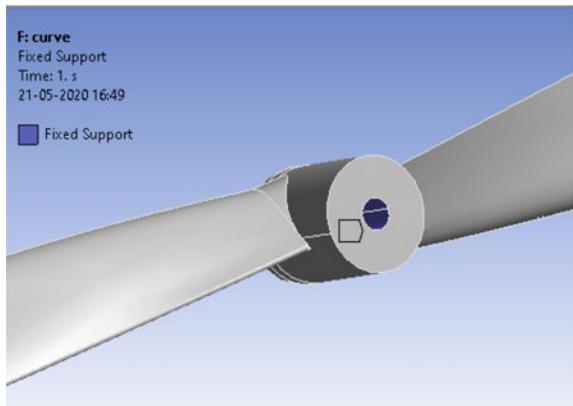
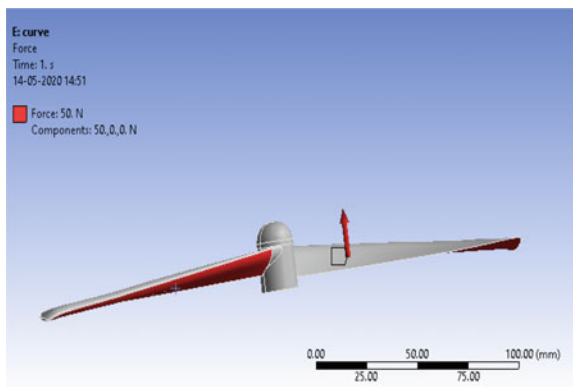


Fig. 5 Applied 50 N thrust force



condition).

$$F = F_1 + F_2 + F_3 + F_4 \quad (1)$$

$$F_i = K_i \omega_i^2 \quad (2)$$

where K_i is the coefficient, which depends upon the propeller's geometry and air density. If the quadcopter lifts a payload of 20 kg, then the value of the total thrust force is calculated as follows.

$$\text{Total Thrust force } (F) = m * g = 20 * 9.81 = 196.2 \text{ N.}$$

where m is the total mass and g is the acceleration due to gravity.

$$\text{Thrust force required per properller} = \frac{F}{4} = \frac{196.2}{4} = 49.05 \text{ N.}$$

The value of thrust force is 50 N approximately to lift a payload of 20 kg. Therefore, 50 N thrust force has been applied to the propeller as shown in Fig. 5. The thrust force generates the stress, strain, and deformation in the propeller. This pre-stressed propeller is analyzed based on the modal analysis in order to find out the resonance frequency. Fixed support and material property, these two boundary conditions have been selected for the modal analysis. First, six frequency variation modes have been calculated against the deformation, where red color shows the maximum and blue color shows the minimum deformation under that frequency (Figs. 6, 7 and 8).

Figures 6, 7, and 8 show the first six modes of deformation with frequency variation. The frequency varies from 71.78 to 529.2 Hz, 140.52 to 1034.8 Hz, and 184.1 to 1355.9 Hz for G-10, aluminum alloy, and CFRP materials, respectively. From Table 2, it can be observed that CFRP material shows the maximum value of natural failure frequency and can sustain deformation better than the other two materials. In all the mode shape results, the red color is at the tip of the propeller which shows the maximum deformation and more chances to fail at that point. This red color zone deformation is because of the spiked point tip of the propeller.

Table 3 shows the previously published frequency variation without pre-loading condition (propeller only subjected to vibration), and Fig. 9 demonstrates a comparison between frequencies of CFRP made propeller based on the present and previously published results. From the comparison, it is observed that the frequency range reduces for the pre-stressed propeller.

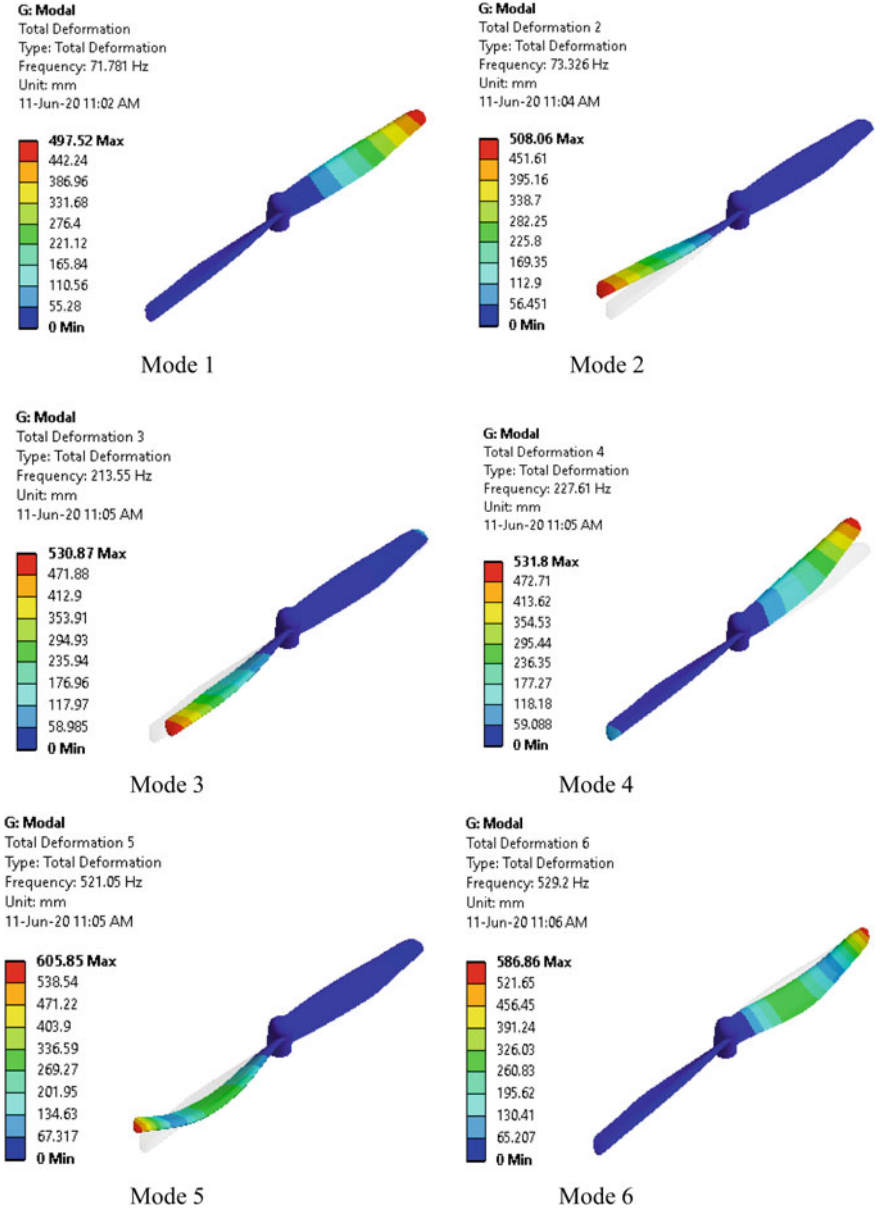


Fig. 6 G-10 material-based frequency variation in six modes

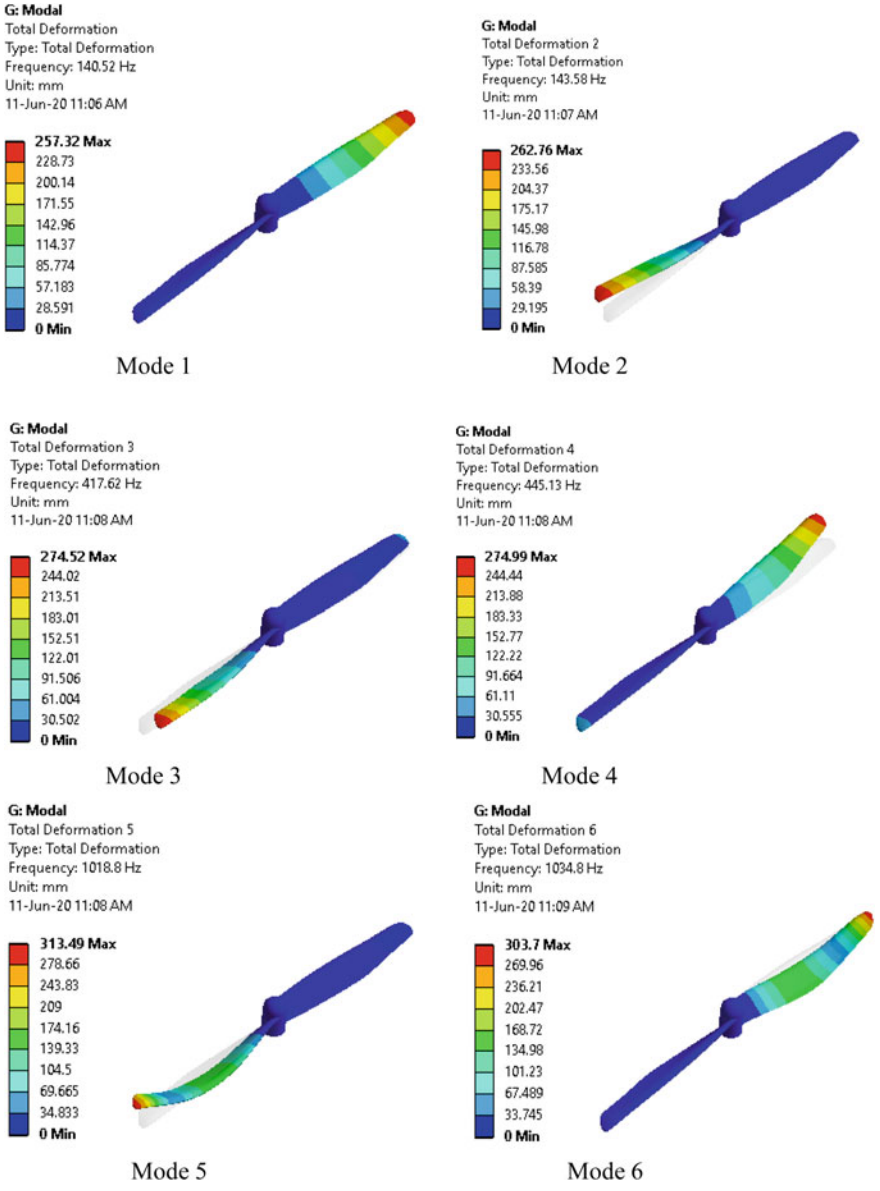


Fig. 7 Aluminum alloy material-based frequency variation in six modes

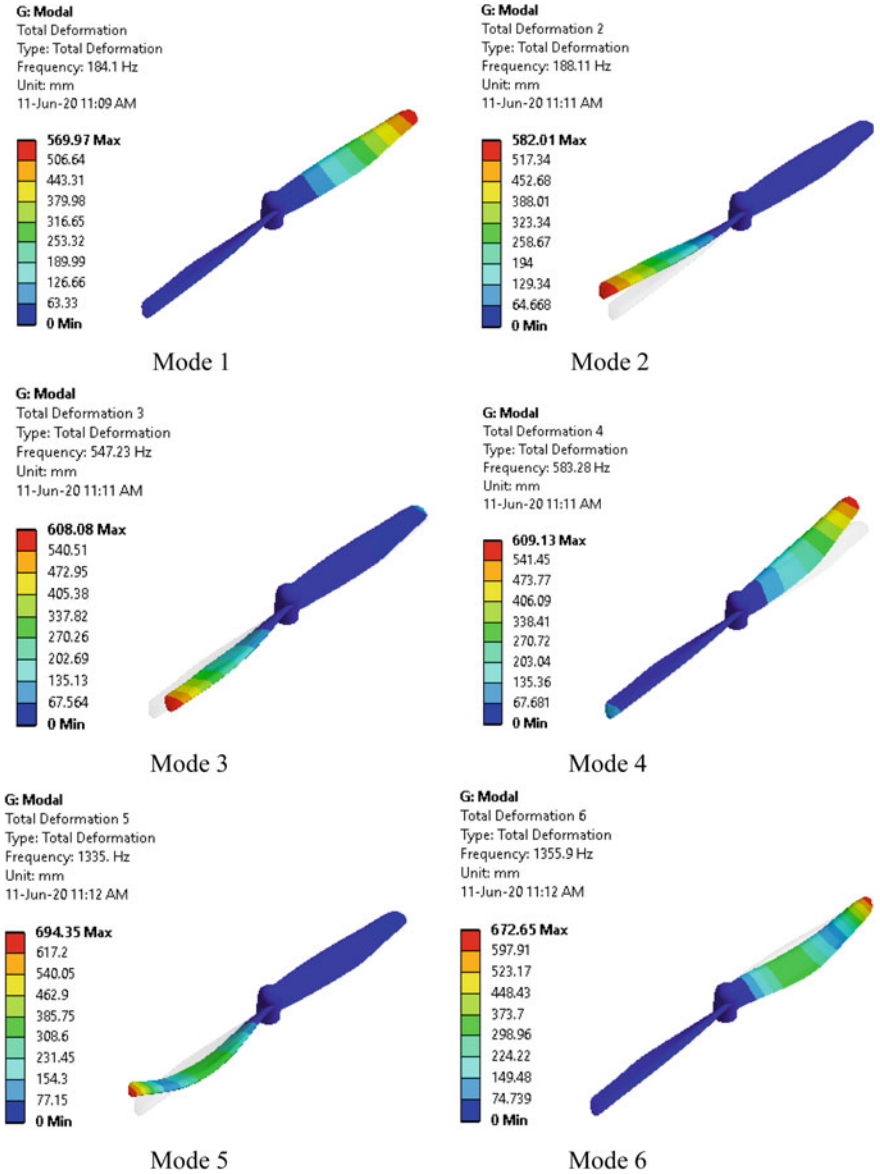


Fig. 8 CFRP material-based frequency variation in six modes

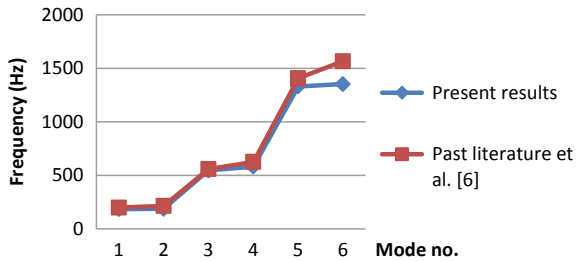
Table 2 Frequency values of used materials

Mode No.	G-10	Aluminum	CFRP
1	71.781	140.52	184.1
2	73.326	143.58	188.11
3	213.55	417.62	547.23
4	227.61	445.13	583.28
5	521.05	1018.8	1335.
6	529.2	1034.8	1355.9

Table 3 Propeller frequency result of past literature without pre-loading condition [6]

Mode No.	G-10	Alloy 6061-T6	CFRP
1	77.873	152.24	199.49
2	83.565	163.36	214.07
3	218.06	426.28	558.6
4	244.55	478.07	626.47
5	549.32	1073.9	1407.2
6	611.58	1195.6	1566.7

Fig. 9 CFRP made propeller result comparison with the previous work



4 Conclusion

This paper presents the modal analysis of a quadcopter’s propeller which is subjected to initial loading condition. The natural frequencies of vibration are calculated with the pre-stressed condition due to the thrust force of the propeller. The obtained results are compared with the past literature [6], in terms of CFRP made propeller’s natural frequency. In the past work [6], the same analysis was conducted without any external loading condition and the obtained frequency range was 199.49–1566.7 Hz for the CFRP propeller, which is greater than the present CFRP propeller’s frequency. It concludes that the external loading of 50 N decreases the failure frequency. Referring to Tables 2 and 3, the lastingness of CFRP material-based propeller is higher than the other two materials without and with external loading condition. Therefore, the propeller made of CFRP material can be used for the heavy payload applications.

References

1. Kuantama E, Craciun D, Tarca I, Tarca R (2017) Quadcopter propeller design and performance analysis. *New advances in mechanisms, mechanical transmissions and robotics*. Springer, Cham, pp 269–277
2. Ahmad F, Kumar P, Bhandari A, Patil PP (2020) Simulation of the quadcopter dynamics with LQR based control. *Mater Today: Proc* 24:326–332
3. Ahmed MF, Zafar MN, Mohanta JC (2020) Modeling and analysis of Quadcopter F450 frame. In: *2020 international conference on contemporary computing and applications (IC3A)*. IEEE, pp 196–201
4. Penkov I, Aleksandrov D (2017) Propeller shrouding influence on lift force of mini unmanned Quadcopter. *Int J Automot Mech Eng* 14:4486–4495
5. Kumar S, Mishra PC (2016) Finite element modeling for structural strength of Quadcopter type multi-mode vehicle. *Aerosp Sci Technol* 53:252–266
6. Ahmad F, Bhandari A, Kumar P, Patil PP (2019) Modeling and mechanical vibration characteristics analysis of a Quadcopter propeller using FEA. In: *IOP conference series: materials science and engineering*, vol 577, no 1. IOP Publishing, p 012022
7. Christodoulou K, Vozinidis M, Karanatsios A, Karipidis E, Katsanevakis F, Vlahostergios Z (2019) Aerodynamic analysis of a Quadcopter drone propeller with the use of computational fluid dynamics. *Chem Eng Trans* 76:181–186
8. Céspedes JF, Lopez OD (2019) Simulation and validation of the aerodynamic performance of a Quadcopter in hover condition using overset mesh. In: *AIAA Aviation Forum* p 2824

Development of Mathematical Model for Prediction and Control of Weld Dilution in MIG Welded Stainless Steel 202 Plates



Prithu Mishra, Mayank Pandit, Shruti Sood, and Pradeep Khanna

Abstract The attributes of the weld joint are determined by its microstructural composition. Therefore, it is imperative to have an appropriate combination of welding input process variables which result in the desired weld composition that governs mechanical and chemical attributes of the weld joint during its service life. The degree of mixing of base metal and deposited metal is expressed by dilution, which is defined as the fraction of the weight of base metal melted in the weld bead to the total weld bead weight represented in percentage. Sometimes special filler material is used to achieve desirable properties in the weld for which the composition of the filler and base metal can differ significantly. In such cases, it becomes very important to evaluate the dilution caused by the base metal in the resulting weld. The extent of dilution is governed by input welding variables such as welding speed, wire feed rate, torch angle, standoff distance and voltage. In order to control the extent of dilution, it calls for wisely selecting the input parameters and to analyze the possibility of relating these variables with resulting dilution. Such a model was developed to relate the above-mentioned input parameters with the resulting dilution using statistical technique. The experiment under investigation was conducted on the Stainless Steel 202 plate on which AISI 308L filler wire was deposited by metal inert gas welding, and graphical results of direct and combined effects of two input process variables were scrutinized using response surface methodology (RSM). Parametric optimization of weld dilution was also done using RSM, and the appropriacy of the established mathematical model was verified by analysis of variance (ANOVA) technique.

Keywords Stainless steel · Dilution · Mathematical modeling · MIG · RSM · ANOVA

P. Mishra (✉) · M. Pandit · S. Sood · P. Khanna
Division of Manufacturing Processes and Automation Engineering, Netaji Subhas University of Technology, New Delhi 110078, India

© The Author(s), under exclusive license to Springer Nature Singapore Pte Ltd. 2022
K. Govindan et al. (eds.), *Advances in Mechanical and Materials Technology*,
Lecture Notes in Mechanical Engineering,
https://doi.org/10.1007/978-981-16-2794-1_39

431

1 Introduction

One of the most extensively utilized arc welding procedures is the metal inert gas welding, in which a continuous arc is maintained between the workpiece and a consumable wire, acting as an electrode, in a protective gas atmosphere provided by one or a mixture of inert gases like helium, argon or carbon dioxide. High reliability, capability to ensure continuous weld joints in a wide variety of available metals and alloys for commercial use, capability to weld in all positions, potential to get fully automated and high productivity are some of the leading factors, which contribute to its widespread industrial applications. Welding of austenitic stainless steels has become possible and convenient at high production rates with the MIG welding process.

SS 202 is a non-magnetic, manganese-alloyed austenitic stainless steel, which possesses excellent toughness at lower temperatures. In comparison to SS 304, it has low nickel content (substituted by manganese) which leads to a significant difference in performance and price. SS 202 has similar oxidation resistance at high temperatures, but it has lower toughness and anti-corrosion properties over 700 °C as compared to SS 304 [1]. SS 202 possesses good strength-to-weight ratio, and as compared to SS 304, its sheets require greater forming forces [2]. Owing to its potential to be drawn into plates, coils and sheets, it finds widespread application in cooking utensils, restaurant equipment and architectural utilities such as doors and windows, hose clamps, trailers and railway cars. The choice of the consumable wire is made so as to match the physical and mechanical characteristics of base metal. The consumable wire employed was SS 308L, which is preferred for austenitic stainless steels. It improves the strength of the welded joint, and its lower carbon proportion makes it viable for applications subjected to inter-granular corrosion [2].

Dilution is defined as the fraction of the weight of the melted base metal to the total weight of the weld bead represented in percentage, and its geometric estimation is obtained by the division of the penetration area by the overall weld bead area. In Fig. 1, A_p represents the area covered under penetration, and A_r represents the area covered under reinforcement. Mathematically, dilution can be expressed as:

$$\text{Dilution (\%)} = \left[\frac{A_p}{A_p + A_r} \right] 100$$

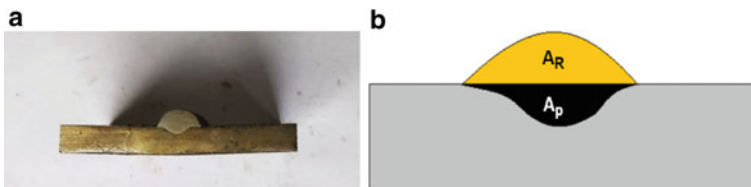


Fig. 1 a Weld bead obtained and b diagram of respective areas

Hence, dilution essentially becomes an extension of the study of the dependence of the geometry of the weld bead on the welding variables. Weld bead geometry includes the extent of penetration, weld width and reinforcement height, and from past literature survey, it has been established that mechanical attributes of the weldment are governed by the bead geometry and the chemical composition [3]. The direct dependence of the obtained bead geometry and hence dilution on the welding variables demands correlating bead geometry with process inputs like arc voltage, travel speed, standoff distance, wire feed rate, etc. Using the information obtained from experimental data, several attempts in the past have been made for achieving this correlation using models developed by various statistical techniques [4, 5]. The above findings verify the significant impact of the welding variables such as wire feed rate (A), welding speed (B), arc voltage (C), standoff distance (D) and torch angle (E) on the bead geometry parameters relevant to dilution, and the success of these attempts certifies the accuracy of the developed mathematical models.

Dilution chiefly affects the properties and composition of clad metals and plays a crucial role in multipass arc welding. At higher values of dilution, a rise in the carbon content of the clad layer is noted, resulting in reduced corrosion resistance of the layer and concurrently contributing to several other metallurgical problems [6].

It has been found that the extent of dilution depends upon the weld-surfacing process employed in the cladding operation. Higher dilution levels (15–30%) are achieved in oxy-acetylene welding (OAW), gas metal arc welding (GMAW), submerged arc welding (SAW), manual metal arc welding (MMAW) and flux-cored arc welding (FCAW). OAW is more commonly used for lighter sections with smaller areas of deposits. Both MMAW and SAW are preferred for heavier sections; however, MMAW is employed for multilayer cladding operation, whereas SAW is used where high deposit quality is desired. GMAW is a faster alternative to MMAW and does not suffer from stub-end losses unlike MMAW. FCAW is similar to GMAW and is primarily employed for iron-base alloys to ensure good abrasion resistance. Lower dilution levels (2–10%) are obtained from the plasma transferred arc welding (PTAW) and tungsten inert gas welding (TIGW). These weld-surfacing processes are found more suitable for high-quality deposits [7].

In this investigative research, the endeavor is to construct a mathematical model to determine the relation between the input welding variables that are wire feed rate (A), welding speed (B), voltage (C), standoff distance (D) and torch angle (E) and the response parameter dilution. The generated quadratic model may be used to predict the extent of dilution and may also be used to automate the welding process by feeding this model in the computer program. The selection of the welding input parameters that are under investigation was done on the basis of the previous literature review as highlighted above.

Several researchers in the past have demonstrated the efficient implementation of statistical design of experiment method for inclusion of empirical approach in welding procedure [8]. Response surface methodology (RSM) has been previously reported to prove useful in the analysis of problems where a response or dependent variable is governed by numerous independent variables. This technique has been adopted by various scholars in the recent past for development of quadratic models

from the data obtained from experiments to analyze the impact of the input welding factors on the obtained bead geometry [9]. Central rotatable composite design is widely employed experimental design for fitting a developed quadratic model. Rotatable signifies that the variance of the response projected at any point is a function of only its distance from the center of the design and not its direction [10].

A five-level, five-factor rotatable design matrix was generated using the statistical technique of design of experiment for conducting the experiments in a structured manner. The mathematical model was constructed using RSM. Appropriacy of the quadratic model developed was verified by the ANOVA technique which determines data variability rather than its direct analysis, and direct and interactive outcomes of two input process variables are graphically represented.

2 Experimental Investigation

2.1 Experimental Setup and Materials

SS 202 plates of thickness of 6 mm were cut in size 100×100 mm, and their surface was cleaned using emery paper to prepare them for MIG welding. The experimental runs were carried out on a welding power source rated 400 Amps, having 100% duty cycle and invariably flat V-I characteristic which are preferred for semi- and fully automatic welding procedures. The welding was carried out on a motor-driven mechanized carriage unit to ensure uniform weld quality at different preset welding speed values. Industrially pure argon gas with a flow rate of 16 L/min was employed for shielding purpose. SS 308L was used as the filler wire with 1.2 mm diameter. The chemical constitution of SS 202 and SS 308L is given below in Table 1. While the experimental setup used in this investigation is shown below in Fig. 2.

Table 1 Composition (wt. %) of SS 202 [11] and SS 308L [12]

Element	SS 202 (wt. %)	SS 308L (wt. %)
Ni	5.0	10.1
Mn	9.0	1.90
Cr	17.0	0.32
C	0.15	0.02
Si	1.0	0.32
S	0.03	0.01
P	0.06	0.02
N	0.25	–

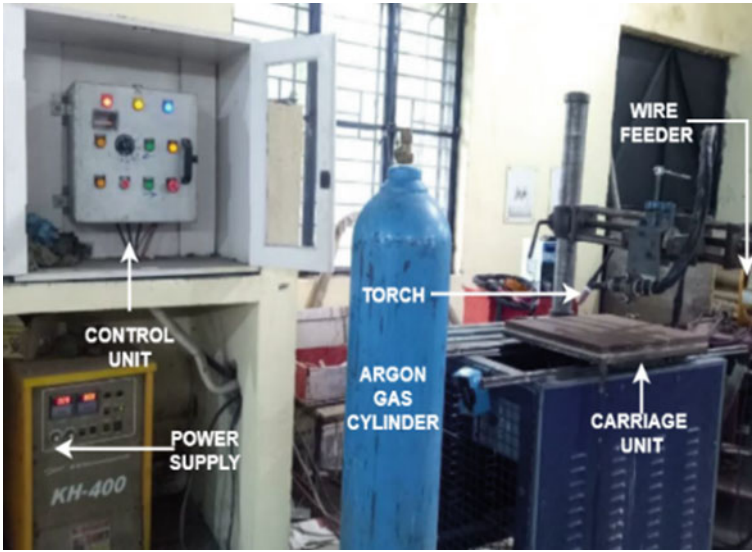


Fig. 2 Experimental setup

2.2 Estimation of Working Limits of the Input Factors

Twenty trial experiments were carried out in which one of the input variables was varied, keeping the others fixed for deciding the working limits of the input welding variables. The upper and lower working limits were decided on the basis of weld quality obtained between them, keeping in view the uniformity of the bead, continuity of the bead and no spatters (Table 2).

Table 2 Working levels of input factors

S. No.	Input factors	Units	Coded levels of input factors				
			-2	-1	0	+1	+2
1	Wire feed rate (<i>A</i>)	m/min	0.3	0.6	0.9	1.2	1.5
2	Welding speed (<i>B</i>)	cm/min	25	30	35	40	45
3	Voltage (<i>C</i>)	Volts	14	16	18	20	22
4	Standoff distance (<i>D</i>)	mm	10	12.5	15	17.5	20
5	Torch angle (<i>E</i>)	Degrees	70	80	90	100	110

2.3 Construction of Design Matrix

On the basis of the input variables and their working limits, design of experiment (DOE) methodology was employed to construct a design matrix. The experimental runs were conducted in accordance with the developed matrix. Central composite technique of rotatable configuration was employed to construct the models comprising of total 32 runs. These 32 runs comprised of $2^4 = 16$ runs using half factorial, 6 runs representing center points and $2 \times 5 = 10$ runs representing star points. Table 3 shows the developed design matrix.

2.4 Conduction of the Experiment as Per the Matrix Designed and Development of Mathematical Model

The 32 experimental runs were performed in a randomized manner so as to avoid systematic error if any. Single bead was laid at the center of the plate lengthwise as shown in Fig. 3a. Following this, to study the bead profile, a specimen of dimension $50 \times 50 \times 6$ mm was cut from the middle of the welded plate to extract best weld bead obtained in the run, and the cut specimens were polished using emery paper. Disk polishing machine was used for further fine polishing. The polished specimens were then etched. The etchant was prepared by mixing 120 ml HCL and 50 g FeCl_3 in 480 ml H_2O . The bead features were measured using shadowgraphs.

Let Z denotes the response factor dependent on the five input variables (A, B, C, D, E), where A, B, C, D and E are the selected input variables as discussed above. Then, Z can be written as $Z = f(A, B, C, D, E)$.

The mathematical equation furnished by the design expert software is

$$\begin{aligned} \text{Dilution (\%)} = & 23.28 + 0.50 * A - 1.24 * B + 3.55 * C \\ & - 0.89 * D - 0.61 * E + 1.56 * AB + 1.03 * AC - 0.77 \\ & * AD + 0.91 * AE - 1.77 * BC + 1.36 * BD \\ & + 1.36 * BD - 1.52 * BE - 0.6 * CD - 0.03 * CE \\ & - 0.8 * DE - 1.91 * A^2 + 0.41 * B^2 \\ & + 1.04 * C^2 + 0.33 * D^2 - 1.27 * E^2 \end{aligned}$$

2.5 Testing the Appropriacy of the Model Developed

The attained values of dilution along with the corresponding experimental runs were supplied in the design expert software for analysis. The appropriacy of the model developed was confirmed using the ANOVA method, and the values returned are

Table 3 Developed design matrix

Std. order	Run order	Variables in coded values					Dilution (%)
		Wire feed rate (m/min)	Welding speed (cm/min)	Voltage (V)	Standoff distance (mm)	Torch angle (degrees)	
13	1	-1	-1	1	1	1	26.22
8	2	1	1	1	-1	-1	26.21
24	3	0	0	0	2	0	22.14
5	4	-1	-1	1	-1	-1	29.19
14	5	1	-1	1	1	-1	23.17
10	6	1	-1	-1	1	1	14.21
29	7	0	0	0	0	0	24.71
28	8	0	0	0	0	0	25.07
9	9	-1	-1	-1	1	-1	19.37
27	10	0	0	0	0	0	23.78
21	11	0	0	-2	0	0	21.16
3	12	-1	1	-1	-1	-1	17.79
26	13	0	0	0	0	2	15.65
23	14	0	0	0	-2	0	27.53
18	15	2	0	0	0	0	17.87
32	16	0	0	0	0	0	15.7
25	17	0	0	0	0	-2	21.26
12	18	1	1	-1	1	-1	21.74
30	19	0	0	0	0	0	25.07
31	20	0	0	0	0	0	24.88
17	21	-2	0	0	0	0	13.91
6	22	1	-1	1	-1	1	34.32
15	23	-1	1	1	1	-1	24.18
4	24	1	1	-1	-1	1	19.09
19	25	0	-2	0	0	0	28.56
1	26	-1	-1	-1	-1	1	21.5
11	27	-1	1	-1	1	1	16.71
16	28	1	1	1	1	1	23.18
7	29	-1	1	1	-1	1	17.06
20	30	0	2	0	0	0	21.75
22	31	0	0	2	0	0	34.25
2	32	1	-1	-1	-1	-1	14.12

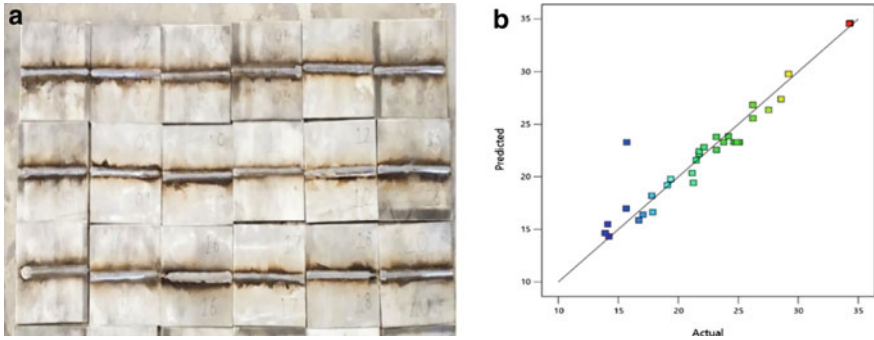


Fig. 3 a Welded specimens and b predicted versus actual scatter diagram

Table 4 ANOVA and fit statistics for the developed quadratic model

<i>p</i> -value	<i>F</i> -value	<i>R</i> ²	Adeq precision	Adjusted <i>R</i> ²	Predicted <i>R</i> ²
0.0042	5.07	0.9021	8.9583	0.7241	0.3642

computed in Table 4. The *p*-value of the whole model is found to be 0.0042 (<0.05), which validates the model adequacy. The terms with *p*-value lower than 0.05 are considered significant, and for the developed quadratic model, the terms *C*, *AB*, *BC*, *A*² and *E*² are significant terms. The *F*-value of the model is 5.07 which further validates its significance and highlights a mere 0.42% chance that the obtained *F*-value could have occurred due to external noise.

The high value of *R*² is desirable, and the Adeq precision, which indicates the signal-to-noise ratio for the developed model, is 8.96 which is higher than the desired value of 4, and hence, the signal adequacy is verified. Scatter diagram in Fig. 3b shows the connection between the actual and the predicted values, and the close proximity of these values as observed in the diagram further authenticates the model validity.

3 Result Analysis

The mathematical model developed and described in Sect. 2.4 can be employed for the prediction of the dilution levels by replacing the appropriate input variable values. The measured values of dilution as obtained from the constructed model for each series of the coded input variable levels are graphically depicted and analyzed in the direct trends. While attempting to explain the two-factor combined effect, the rest of the input parameters were fixed at their 0 level. The importance of accessing the integrity and sensitivity of the process behavior with regard to the selected input variables makes combined interactions an important aspect to study.

3.1 Direct Effect of Input Welding Parameters on the Extent of Dilution

The direct effects of the variations in the selected input welding parameters on dilution have been graphically represented in Fig. 4. The trends and variations of dilution under the effect of referred parameters are discussed below.

A rise in the wire feed rate (WFR) values leads to a heightened energy input per unit length, and as a consequence, more melting of base plate occurs leading to higher penetration values. An increase in the area of penetration also results due to the increased momentum of the filler material droplets striking the base plate at higher WFR values [10]. With a rise in WFR, a corresponding increase in the reinforcement levels is also observed which can be ascribed to higher consumable filler wire melting. The rise in the value of dilution with the increase in WFR can be explained on the account of greater initial rise in the penetration. However, with further rise in WFR, the filler material has an increased tendency of piling up rather than spreading and broadening the bead width resulting in consequent reduction in dilution.

A consistent decline in the dilution values is detected with the rise in welding speed (WS) values. With an increase in WS values, the input heat per unit weld length reduces, which corresponds to low penetrating effects and smaller weld pool. Similarly, a decrease in the reinforcement also occurs owing to a decrease in the rate of deposition of the consumable filler wire per unit length. Yet, a decline in the degree of dilution is noticed as the percentage decrease in the melted base metal area is higher than the percentage decrease in the filler material deposited.

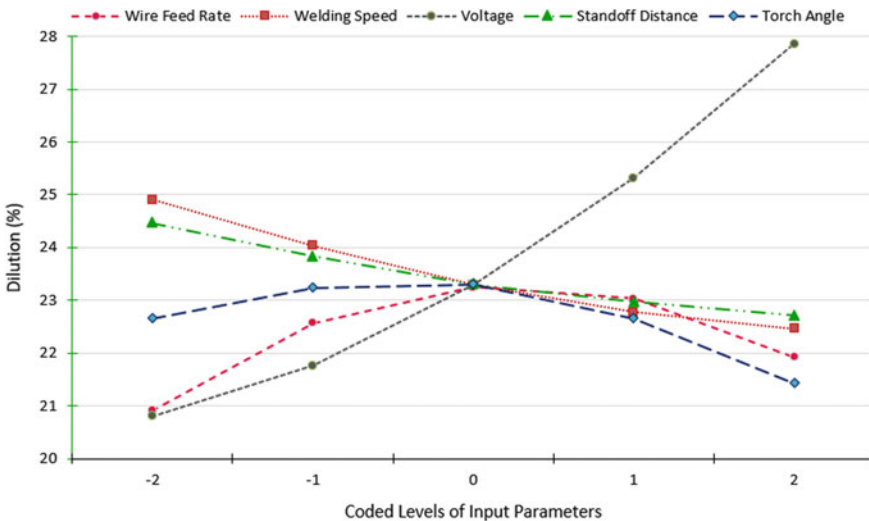


Fig. 4 Direct effect of input parameters on dilution (%)

At higher arc voltages, more heat is delivered to the weldment due to the formation of a larger arc cone, leading to heightened values of penetration. Moreover, with an increase in the voltage, the tendency of spreading of the arc increases leading to a higher bead width at the expense of decreased reinforcement. Thus, the area of the molten metal increases, whereas a decrease in the area of the melted filler material is reported, leading to a rise in the dilution levels.

It can be inferred from the figure that dilution decreases with a rise in the standoff distance. At higher values of standoff distance, the distance traveled by the filler material and hence the time spent in the arc during the metal transfer are greater, leading to an increase in the filler material temperature or the pre-melting of the filler material. This pre-melting of the filler material occurs at the expense of heat that is to be supplied to the plate and is called resistive heating. This leads to a lower amount of heat remaining for penetration of the workpiece and results in lesser penetration and greater reinforcement. Mass of the filler metal that penetrated is less than mass of the filler metal which is reinforced for a constant width of the bead resulting in a corresponding decrease in the extent of dilution.

Due to the trailing nature of the arc at lower torch angles, additional heat is supplied to the weldment as the arc is always directed toward the welded part leading to higher penetration. With the rise in the torch angle, a component of the arc force in the direction of welding is exerted on the molten metal which contributes in an increased tendency of spreading of the arc, resulting in an increased weld width at the expense of reduced reinforcement. Thus, at lower torch angles, dilution increases owing to a growth in the penetration area and a reduction in the reinforcement area. However, at increased torch angles, the percentage reduction in the area of the molten metal is higher than decrease in the area of the deposited molten filler metal, leading to lower dilution values as shown in the figure.

3.2 Combined Effects of Input Parameters on the Extent of Dilution

Combined effects of WFR (A) and voltage (C). In the surface plot in Fig. 5a, for all values of arc voltage, dilution is observed to first rise to a maximum value and then fall as the wire feed rate (WFR) is increased. With a rise in WFR, the input heat per unit weld length is higher which contributes in higher melting of the consumable filler wire and the base plate. However, owing to a greater rise in the penetration area as compared to the area of the melted filler material, a rise in dilution is observed. With still a greater increase in the WFR and consequently the heat input, the area under reinforcement increases due to the enhanced tendency of piling up of the molten metal rather than contributing to the bead width leading to fall in the extent of dilution. At higher arc voltages, owing to the formation of larger arc cone and increased tendency of spreading of the arc, the extent of penetration increases while a sharp fall in the reinforcement at the expense of increased width is observed.

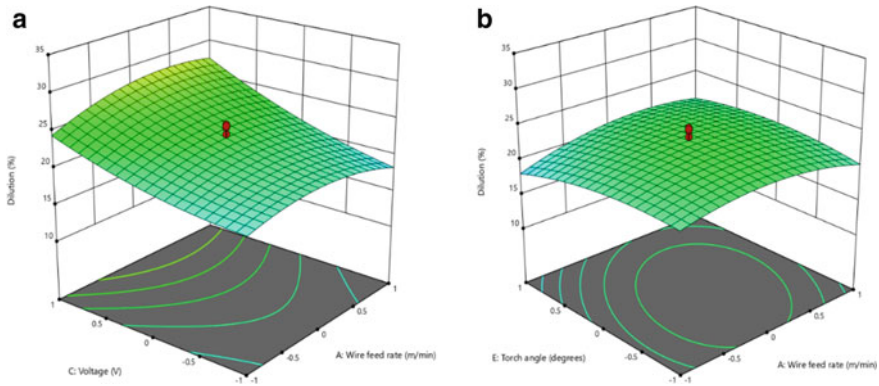


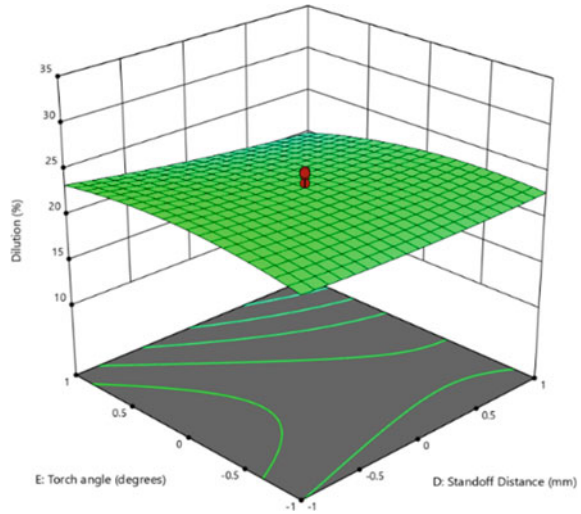
Fig. 5 Combined effect of **a** WFR and voltage and **b** WFR and torch angle on extent of dilution

Hence, a steep rise in dilution levels is observed with increasing voltage levels for all values of wire feed rate.

Combined effects of WFR (A) and torch angle (E). Additional heat supply at lower torch angles causes a greater rise in the extent of penetration as compared to the reinforcement area. In contrast, at higher torch angles, an arc force component in the direction of welding speed is exerted on the molten metal which is responsible for spreading of the arc over a wider area, resulting in a consequent decrease in reinforcement. Owing to higher decrease in the area of penetration against the reinforcement area, dilution is found to first rise and then decrease with a rise in torch angles at all values of wire feed rate (WFR) as shown in Fig. 5b. A greater rise in the area of penetration as compared to the reinforcement area is observed resulting in an increase in the dilution with rise in WFR due to lower heat input. With further increase in WFR, the melted filler material has increased tendency of piling up rather than spreading and broadening the weld width, resulting in reduced dilution levels for all values of torch angle.

Combined effects of standoff distance (D) and torch angle (E). From the graph in Fig. 6, it can be inferred that dilution level depreciates with a rise in the standoff distance for all values of torch angle. At higher values of standoff distance due to the increased time spent by the filler material in the arc during metal transfer, the phenomenon of pre-melting of filler material, referred to as resistive heating, occurs which reduces the heat input available for penetration of the workpiece. Thus, owing to the lower penetration and greater reinforcement due to more filler material melting, a fall in the extent of dilution is observed as the standoff distance increases. At lower torch angles, additional heat is supplied to the welded part, which leads to a greater rise in the extent of penetration as compared to the reinforcement area. However, at higher torch angle due to the increased tendency of spreading of the arc, the percentage decrease in the area of penetration is higher than the reinforcement area.

Fig. 6 Interactive effect of standoff distance and torch angle on extent of dilution



Thus, with an increase in torch angle, dilution is first found to rise and then fall for all values of welding speed.

4 Conclusions

In the present study, a mathematical model based on rotatable central composite technique was constructed using a five-factor, five-level half-factorial design matrix, for establishing a relationship between the user-controllable inputs and resulting dilution. Welding speed and standoff distance were found to have a negative effect on the extent of dilution due to fall in the heat input per unit weld length and resistive heating. Both the torch angle and wire feed rate were found to have a similar effect on the dilution levels, an initial rise in dilution levels due to higher heat input and the trailing nature of arc at lower torch angles. However, as the WFR and torch angles are increased after a certain value, a decrement in dilution is observed due to increased tendency of piling up of the molten filler material and higher spreading of the arc. Voltage was found to be the most dominating input parameter, and a rise in voltage led to a rise in the extent of dilution. The optimum process parameters for minimum dilution as recommended by the study are: wire feed rate (A) = 0.50 m/min, welding speed (B) = 42.78 cm/min, voltage (C) = 22 V, standoff distance (D) = 10 mm and torch angle (E) = 104.55°.

References

1. Mulimbayan F, Mena MG (2016) Comparative study of the corrosion behavior of low-nickel AISI 202 and conventional AISI 304 stainless steels in citric acid using electrochemical techniques. *Appl Mech Mater*
2. Vignesh G, Narayanan CS, Pandivelan C, Shanmugapriya K, Tejavath BN, Tirupathi L (2019) Forming, fracture and corrosion behaviour of stainless steel 202 sheet formed by single point incremental forming process. *Mater Res Express*
3. Rao PS, Gupta OP, Murty SSN, Rao ABK (2009) Effect of process parameters and mathematical model for the prediction of bead geometry in pulsed GMA welding. *Int J Adv Manuf Technol*
4. Jha MN, Pratihari DK, Dey V, Saha TK, Bapat AV (2011) Study on electron beam butt welding of austenitic stainless steel 304 plates and its input-output modelling using neural networks. *Proc Inst Mech Eng Part B: J Eng Manuf*
5. Kim D, Rhee S (2004) Optimization of a gas metal arc welding process using the desirability function and the genetic algorithm. *Proc Inst Mech Eng Part B: J Eng Manuf*
6. Shahi AS, Pandey S (2008) Modelling of the effects of welding conditions on dilution of stainless steel claddings produced by gas metal arc welding procedures. *J Mater Process Technol*
7. Shahi AS, Pandey S (2008) Effect of auxiliary preheating of the filler wire on quality of gas metal arc stainless steel claddings. *J Mater Eng Perform*
8. Murugan N, Parmar RS (1997) Stainless steel cladding deposited by automatic gas metal arc welding. *Weld J (Miami, Fla)*
9. Benyounis KY, Olabi AG, Hashmi MSJ (2005) Effect of laser welding parameters on the heat input and weld-bead profile. *J Mater Process Technol*
10. Shahi AS, Pandey S (2006) Prediction of dilution in GMA and UGMA stainless steel single layer cladding using response surface methodology. *Sci Technol Weld Join*
11. Bharwal S, Vyas C (2014) Weldability issue of AISI 202 SS (stainless steel) grade with GTAW process compared to AISI 304 SS grade. *Int J Adv Mech Eng* 4:695–700
12. Hsu CH, Chen TC, Huang RT, Tsay LW (2017) Stress corrosion cracking susceptibility of 304L Substrate and 308L weld metal exposed to a salt spray. *Materials (Basel)*

Artificial Neural Network-Based Classifier for Fault Detection in Photovoltaic Modules



Kritika Anuragi, Mohak Gaba, Ashir Raza Malik, Ritwik Gambhir, and Bhavnesh Kumar

Abstract The widespread use of solar energy today highlights the importance of maintaining the performance characteristics as well as optimizing the efficiency of photovoltaic (PV) system installations. PV system performances are often lost due to several factors such as shading (uniform or partial), breakage or cracks and creation of hot spots. Such faults can also sometimes result in glass breakage, cell degradation and permanent damage to the PV module. Numerous parameters must be constantly monitored to ensure that any abnormal losses and faults ensuing on the PV module are detected timely. Many monitoring systems in the industry are based on the monitoring of temperature, solar irradiance, variable resistance, direct current and voltage. In this paper, a fault detection method for PV modules has been described. It consists of using a classifier based on artificial neural network (ANN) that estimates the generated output (photovoltaic current and photovoltaic voltage) under variable input conditions. The input (solar irradiation, temperature and variable load) and output (current and voltage) data measured over a period of six weeks has been used for the development of the ANN-based classifier. The differences between the estimated values of current and voltage generated by the ANN and the measured values generated from the physical setup are used to predict the operating state of the photovoltaic module. The results showed that this method, which uses only two meteorological conditions, accurately detects the operating state as normal (un-shaded condition) or faulty (shaded condition) of the photovoltaic module.

Keywords Fault classifier · Photovoltaic module · Artificial neural network · Partial shading

K. Anuragi (✉) · M. Gaba · A. R. Malik · R. Gambhir · B. Kumar
Netaji Subhas University of Technology, New Delhi, India

© The Author(s), under exclusive license to Springer Nature Singapore Pte Ltd. 2022
K. Govindan et al. (eds.), *Advances in Mechanical and Materials Technology*,
Lecture Notes in Mechanical Engineering,
https://doi.org/10.1007/978-981-16-2794-1_40

445

1 Introduction

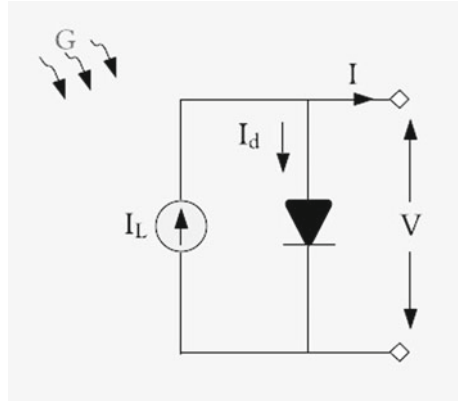
A photovoltaic (PV) system consists of one or more solar panels that utilize sunlight as an energy source to generate electricity. Today, such photovoltaic systems play a crucial role in electrical power applications and are being widely used for commercial and residential purposes. The widespread use of solar energy in the present day underlines the requirement for optimizing the efficiency of PV installations and developing effective monitoring systems for maintaining the performance of PV systems [1]. Monitoring systems should be equipped to continuously follow the PV system's operating state. This is essential for early detection of errors and failures that trigger performance losses. Shading, hot spotting [2] and cell shunting [3] are few major factors that severely affect PV performances. To mitigate the aforementioned problems, monitoring systems use meteorological parameters such as temperature and solar irradiance as well as output parameters like current and voltage.

Many existing methods of fault detection use plant function data collected over a period of time to monitor the operating state and detect abnormalities and faults, i.e., they operate offline only [4]. Some other techniques that were developed required complex mathematical calculations to predict faulty parameters [5]. Most of these methods did not estimate the system's real operating state and were mostly based upon analysis of system performances and I-V curve measurements [6]. These techniques fail to give real operation state in peculiar cases such as that of partial shading. All these methods involve tedious calculations and complex analysis for determination of the operating state of PV installations.

Artificial intelligence techniques are slowly penetrating every field of research, and the same is true for the photovoltaic field where ANNs are being successfully employed in multiple ways such as health monitoring [7, 8], maximum power point tracking [9–11], solar forecasting [12] and modeling and simulation.

In this paper, a fault detection method for PV modules has been described that employs ANN algorithms in the developed classifier. ANN generated estimated values of output current and voltage under variable input conditions (temperature, solar irradiance and variable resistive load). This method enables real-time fault detection. The introduced method is independent of PV module performances. The difference between the predicted values of voltage and current generated by the ANN and the measured values generated from the physical setup is used to detect the operation state. This method allows us to avoid complex calculations and intensive analysis of system performances. Thus, the method is autonomous and will always be able to conclude the operation state of the module as normal (un-shaded condition) or faulty (shaded condition).

Fig. 1 Equivalent circuit of a PN junction PV cell



2 System Description

2.1 Equivalent Model of a PV Cell

An ideal PV cell can be visualized to be a current source, wherein the current produced by the cell is directly proportional to the light intensity being received by the cell. An equivalent model of the PV cell can be obtained by adding appropriate components, which will show the electrical and optical losses of the PV cell with an ideal current source.

$$I = I_L - I_d \tag{1}$$

$$I_d = I_o \left(e^{\frac{qV}{nkT}} - 1 \right) \tag{2}$$

Figure 1 illustrates the single-diode model for a PV cell. I_L is the light-generated current, I_D is the current that passes through the diode, whereas I and V are the PV cell current and voltage, respectively. Optical losses are represented by the current source as illustrated in the electrical circuit shown in Fig. 1. In this single-diode model, the diode represents the loss which results from recombination in base and emitter region.

2.2 I-V Characteristics of a PV Cell

PV cells are characterized and compared with each other using short-circuit current, open-circuit voltage and fill factor. The aforementioned parameters are represented in the I-V curve of PV cell shown in Fig. 2.

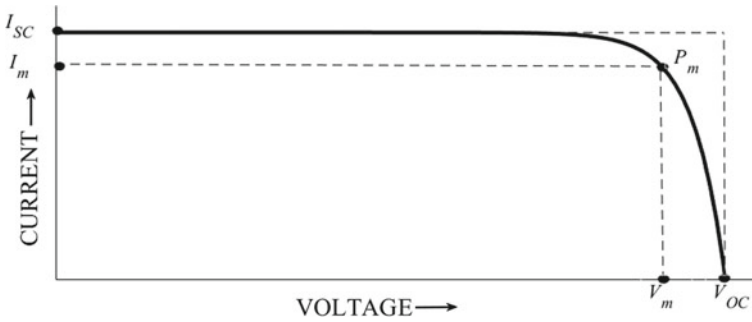


Fig. 2 Typical I-V characteristics of a PV cell

Short-circuit current, I_{SC} , is nothing but the maximum current that flows in a solar cell when both the P-terminal and N-terminal are short-circuited with each other, and hence, V is zero. Putting $V = 0$ in given equation, we will get $I_{SC} = I_L$. Thus, the short circuit is nothing else but the light-generated current, I_L . Open-circuit voltage, V_{OC} , is defined as the maximum voltage that is produced across the terminals of a solar cell when the circuit is kept open that is $I = 0$. Putting the above conditions in the equation of current, we will get the following expression for open-circuit voltage:

$$V_{OC} = \frac{nkT}{q} \ln\left(\frac{I_L}{I_0} + 1\right) \quad (3)$$

Thus, V_{OC} depends on the reverse saturation current and light-generated current.

3 Materials and Methodology

The proposed solution for fault detection of PV module involved the use of artificial neural network. The ANN was trained using actual data collected by a physical setup using a solar panel. This trained neural network further gives estimated values of the output current and voltage for the given input parameters. The difference between the estimated and the measured values is the basis of classification.

3.1 Database Generation Using PV Panel

The data was measured using a Loom Solar 20 W–12 V PV module at Netaji Subhas University of Technology.

A dataset of 4000 + vectors was generated over a period of six weeks. The datasets were then divided into two subsets—70% of the samples were used for training of

Table 1 Specifications for Loom Solar 20 W–12 V solar panel at STC

Maximum Power, P_m	20 W
Maximum Power Voltage, V_m	19.25 V
Maximum Power Current, I_m	1.04 A
Short-circuit Current, I_{SC}	1.11 A
Open-circuit Voltage, V_{OC}	22.50 V

the neural network, and 30% of samples were used for testing and validation. Table 1 gives the specifications of the PV module used for generating the training data.

3.2 Experimental Setup

The physical setup for data collection basically involved a PV panel being connected to a variable load. Different sets of readings were taken at variable timings to incorporate a wide range of input temperatures (T) and irradiance (G). The output values of photovoltaic current (I_{PV}) and photovoltaic voltage (V_{PV}) were measured across a rheostat with resistance values ranging from 1 to 5000 Ω . The data generated for training was measured under temperatures ranging from 20 to 40 $^{\circ}\text{C}$ and irradiance ranging from 70 to 1200 W/m^2 . Figure 3 illustrates the process of data generation using experimental setup.

Multiple sets of readings were generated at varying input conditions of temperature and irradiance. The data points for each set were plotted to obtain a trend line.

All these graphs closely resembled the characteristic I-V curve of a PV cell, which reiterated the accuracy of the readings. The trend lines were used to obtain the equations for each reading. These equations were further used to obtain more

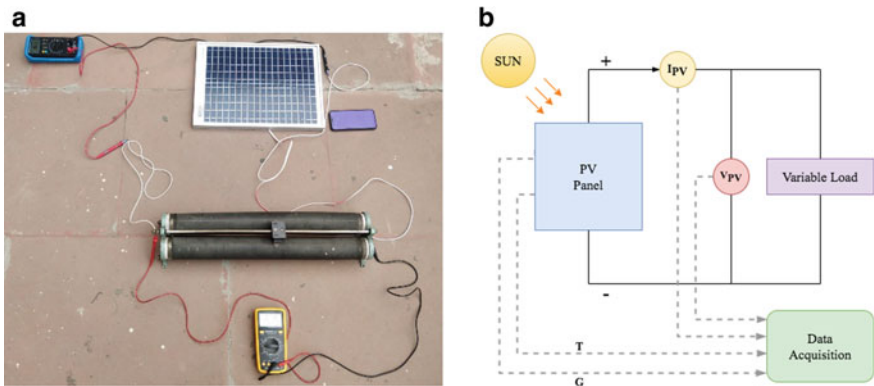


Fig. 3 Data generation: **a** Experimental setup. **b** Block diagram representation

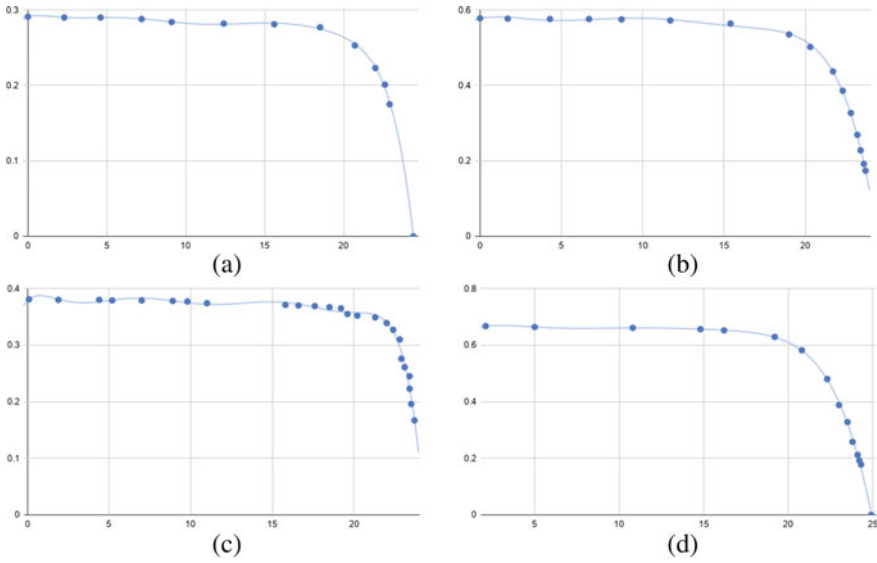


Fig. 4 Current–voltage curves for **a** $T = 29^\circ\text{C}$ and $G = 72.68\text{ W/m}^2$. **b** $T = 26^\circ\text{C}$ and $G = 143.78\text{ W/m}^2$. **c** $T = 28^\circ\text{C}$ and $G = 148.52\text{ W/m}^2$. **d** $T = 29^\circ\text{C}$ and $G = 289.14\text{ W/m}^2$ (X-axis: Voltage (V), Y-axis: Current (A))

datasets for a given value of temperature and irradiance for varying load values. Some of the graphs obtained have been shown in Fig. 4 (voltage across X-axis and current across Y-axis).

4 Proposed ANN Classifier

Temperature, irradiance and load values were fed to the input layer for training the network as shown in Fig. 5. Every input into the network is further fed to the nodes in hidden layer. ANN uses input values, modification is done by multiplying the input values with the weight value, these new values are added and sent to the activation

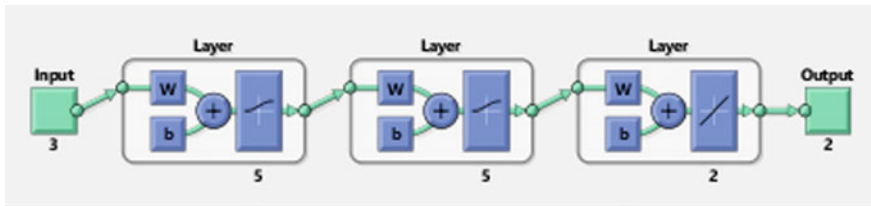
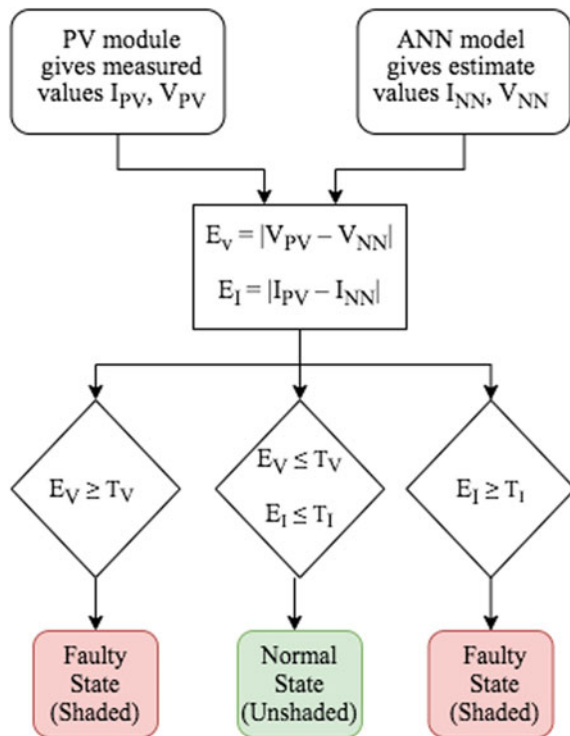


Fig. 5 Proposed multilayer perceptron structure

function in the hidden layers, and the output from the hidden layers now becomes the input for the next hidden layer (if present), otherwise for the output layer. Different activation functions along with varying combinations of number of hidden layers as well as number of neurons in hidden layers were used to obtain best results. Primarily, resilient back propagation (RPPROP) algorithm and Levenberg–Marquardt (LM) algorithm were used.

Figure 6 illustrates the working of the classifier. The trained neural network generates estimate values of output current and voltage when input values of temperature, irradiance and resistance are fed to the neural network. Further, output measurements are also obtained for the same input from the physical system. If the error between the measured and estimated values, E_V and E_I , both falls under acceptable error threshold values, T_V and T_I , then the operation of PV module is classified as normal (un-shaded condition). In all other cases, the operation state of PV module is classified as faulty (shaded condition).

Fig. 6 Classifier flowchart



5 Results and Discussion

It was observed that different training algorithms provided different results as described in Table 2 and the training performance is illustrated in Figs. 7 and 8. It was also observed that varying the number of hidden layers or the number of neurons also altered the training results.

The panel was manually shaded to obtain results from the classifier under varying conditions of faulty operations. The values were measured at input conditions of irradiance (G) = 130 W/m², temperature (T) = 20 °C and resistance load (R) = 80 Ω. The obtained classifier results are recorded in Table 3.

It was observed that the classifier produces satisfactory results. This comparison-based classifier model has multifaceted applications in daily life. It is necessary to study the real-time operation states of the PV module. This fault detection classifier aims to avoid critical damage to the PV module by timely detection of faulty operation under shaded conditions.

Table 2 Training results from different algorithms

Algorithm	Best training performance
Resilient back propagation	0.46017
Levenberg–Marquardt	0.013631

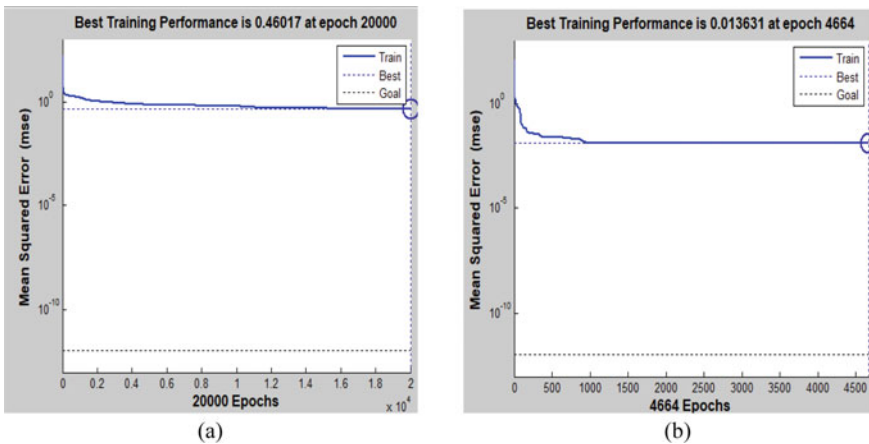


Fig. 7 Performance and MSE curve for: **a** RPROP, **b** LM

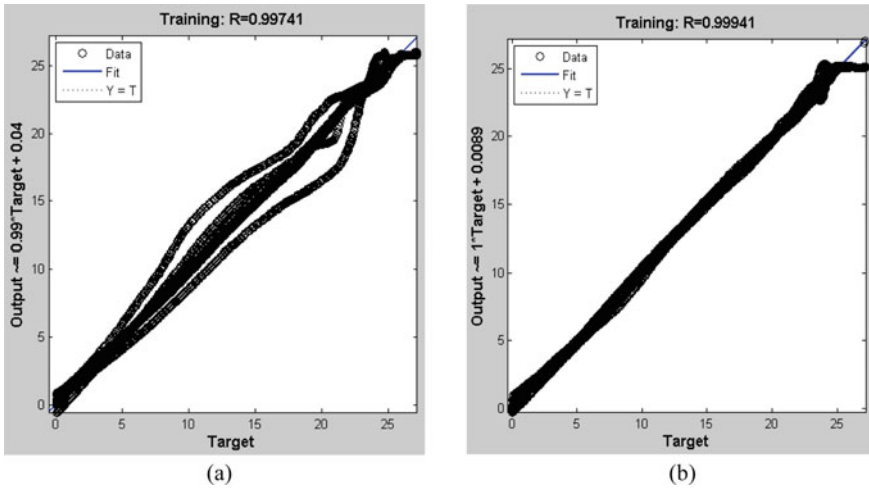


Fig. 8 Regression curve for: **a** RPROP, **b** LM

Table 3 Classifier outputs for different shading conditions

Parameter	Values		
	During no-shading	During 25% shading	During 50% shading
V_{PV} (V)	24.124	10.63	5.12
I_{PV} (A)	0.3102	0.1265	0.0621
V_{NN} (V)	23.0456	23.0456	23.0456
I_{NN} (A)	0.2981	0.2981	0.2981
E_V (V)	1.074	12.4156	17.92
E_I (A)	0.0121	0.1716	0.236
T_V (V)	2.3	2.3	2.3
T_I (A)	0.02981	0.02981	0.02981
$E_V \leq T_V$	Yes	No	No
$E_I \leq T_I$	Yes	No	No
Result	Normal (Un-shaded)	Faulty (Shaded)	Faulty (Shaded)

6 Conclusion

It can be concluded that after gathering physical data split over several readings, a neural network based on a Levenberg–Marquardt learning paradigm is more suitable for approximating the I-V characteristics of a solar panel, when compared to a resilient back propagation network and other training paradigms. This trained artificial neural network is a key aspect of the developed classifier which can be used

to identify if a solar panel is working in faulty state (shaded condition) or normal state (un-shaded condition). Real-time detection of the PV module's operating state is crucial in order to prevent damages and losses due to faults. Once the operating state of the panel has been identified by the classifier, this information can be further used to determine the nature and extent of the fault as well as develop appropriate mitigation and prevention strategies.

References

1. Ciani L, Cristaldi L, Faifer M, Lazzaroni M, Rossi M (2013) Design and implementation of a on-board device for photovoltaic panels monitoring. In: Proceedings of the 2013 IEEE international instrumentation and measurement technology conference, pp 1599–1604
2. Simon M, Meyer E (2010) Detection and analysis of hot-spot formation in solar cells. *Sol Energy Mater Sol Cells* 94(2):106–113
3. Spataru S, Sera D, Kerekes T, Teodorescu R (2013) Photovoltaic array condition monitoring based on online regression of performance model. In: Proceedings of the 2013 IEEE thirty-ninth photovoltaic specialists conference (PVSC), pp 0815–0820
4. Ducange P, Fazzolari M, Lazzarini B, Marcelloni F (2011) An intelligent system for detecting faults in photovoltaic fields. In: Proceedings of the 2011 eleventh international conference on intelligent systems design and applications (ISDA). IEEE, pp 1341–1346
5. Sera D, Teodorescu R, Rodriguez P (2008) Photovoltaic module diagnostics by series resistance monitoring and temperature and rated power estimation. In: Proceedings of the thirty fourth annual conference of on industrial electronics, IECON 2008, pp 2195–2199
6. Kim K, Seo G, Cho B, Krein P (2016) Photovoltaic hot-spot detection for solar panel substrings using AC parameter characterization. *IEEE Trans Power Electron* 31(2):1121–1130
7. Mekki H, Mellit A, Salhi H (2016) Artificial neural network-based modelling and fault detection of partial shaded photovoltaic modules. *Simul Model Pract Theory* 67:1–13
8. Velilla E, Valencia J, Jaramillo F (2014) Performance evaluation of two solar photovoltaic technologies under atmospheric exposure using artificial neural network models. *Sol Energy* 107:260–271
9. Liu Y, Liu C, Huang J, Chen J (2013) Neural-network-based maximum power point tracking methods for photovoltaic systems operating under fast changing environments. *Sol Energy* 89:42–53
10. Kumar B, Chauhan Y, Shrivastava V (2014) A comparative study of maximum power point tracking methods for a photovoltaic-based water pumping system. *Int J Sustain Energy* 33(4):797–810. <https://doi.org/10.1080/14786451.2013.769990>
11. Syafaruddin EK, Hiyama T (2009) Artificial neural network-polar coordinated fuzzy controller based maximum power point tracking control under partially shaded conditions. *IET Renew Power Gener* 3(2):239
12. Abuella M, Chowdhury B (2019) Forecasting of solar power ramp events: a post-processing approach. *Renewable Energy* 133:1380–1392

Improvement in Overall Equipment Effectiveness in Manufacturing Industry Using Autonomous Maintenance



S. Gurpreet Singh Bali, Gurvinder Singh, Balbir Singh, and Sanjay Mohan

Abstract To maximize the production at minimum cost, the maintenance of the equipment is to be carried out on a routine basis, and with this, the equipment becomes more reliable. Regular maintenance keeps the machine in good working condition and prevents the degradation of the machine components. Maintenance is broadly classified as planned and unplanned maintenance. Preventive maintenance and predictive maintenance are planned maintenance, whereas corrective or breakdown maintenance is the unplanned maintenance. Proper maintenance reduces the downtime of machines/equipment and improves the mean time between failures (MTBF). Overall equipment effectiveness (OEE) is an indicator to measure equipment effectiveness. Higher OEE is desirable in today's highly competitive environment. Autonomous maintenance—a pillar of total productive maintenance—is the latest trend across manufacturing industries to improve the OEE. Autonomous maintenance is a planned maintenance program that involves operators' responsibility to take care of the equipment, i.e., the operator of the machine is responsible for the overall health of the equipment. Autonomous maintenance helps to achieve higher OEE by reducing breakdown time. The present work is a part of a project undertaken to improve OEE using autonomous maintenance, in the automotive oil filter manufacturing unit. The machines of the plant were studied, and required data was collected. Based on data collected, the most critical machine was selected and autonomous maintenance was implemented. The findings have shown improvement of 14–15% in OEE after implementing autonomous maintenance.

Keywords Autonomous maintenance · Availability · Breakdown · Maintenance · Overall equipment effectiveness · Total productive maintenance

S. Gurpreet Singh Bali (✉) · G. Singh · B. Singh · S. Mohan
School of Mechanical Engineering, Shri Mata Vaishno Devi University Katra, Katra, Jammu & Kashmir, India

B. Singh
e-mail: Balbirlsst@smvdu.ac.in

S. Mohan
e-mail: sanjay.mohan@smvdu.ac.in

1 Introduction

1.1 Overall Equipment Effectiveness

Overall equipment effectiveness (OEE) describes the overall operational efficiency of the plant. Seiichi Nikajima coined the term overall equipment effectiveness. OEE is calculated to measure the effectiveness of a single machine or multiple (integrated) set of machines. Due to breakdown and quality losses, it is not easy for any manufacturing unit to have an OEE of 100%. OEE is a roadmap that helps to eliminate the different types of associated losses [1]. The difference between the actual OEE and the targeted or expected OEE of a plant acts as a driving force to improve the maintenance policies. OEE with 85% is considered to be better. For obtaining world-class OEE, the target for availability, performance, and quality of the machine is 90%, 95%, and 85%, respectively. Thus, we can conclude that there is scope for improvement in OEE in many manufacturing industries [2]. Raut S, stated that OEE is a function of three components—availability (uptime), performance, and quality. The literature reveals that there is no standard available for calculation of OEE. The components of OEE are calculated separately, and their product gives the OEE value [1].

$$\text{OEE} = \text{Availability} \times \text{Performance} \times \text{Quality} \quad (1)$$

Availability

The parameter “Availability” of OEE indicates the performance of the maintenance department of an organization [3]. It is the time for which an equipment can produce components out of the total time. The difference is due to breakdowns, adjustment, setup losses, etc. The “Availability” of any equipment could be computed using the following formula as given by Eqs. 2 and 3.

$$\text{Availability} = \frac{\text{Actual Runtime}}{\text{Planned production}} \quad (2)$$

where actual runtime can be calculated as

$$\text{Actual Runtime} = \frac{\text{Planned production time} - \text{Idle time (stop time)}}{\text{Planned production}} \quad (3)$$

Planned production time is the available time of equipment excluding all other schedule’s stoppages, e.g., lunch break and meetings [4].

Performance

Performance helps to identify the hidden losses of equipment [4], e.g., speed losses of equipment. Speed losses may include any factor that makes the machine operate at a low speed than the maximum possible speed. These losses can be due to the operator

(operator inefficiency), component wear, etc. The performance of equipment can be computed using the following formula as mentioned in Eqs. 4 and 5.

$$\text{Performance} = \frac{\text{Idea cycle time} \times \text{Total count}}{\text{Actual runtime}} \quad (4)$$

$$\text{Performance} = \frac{\text{Idea cycle time} \times \text{Total count}}{\text{Planned production} - \text{Stop time}} \quad (5)$$

Quality

Quality is simply a measure of good products to the total products produced. Nicholas [5] defined quality rate as a percentage of goods produced by equipment that has zero defects. Rework and scrap, along with yield and start-up losses, affect the quality. The quality of equipment can be computed using the following formula as mentioned in Eqs. 4 and 5.

$$\text{Quality} = \frac{\text{Good count produced}}{\text{Total count produced}} \quad (6)$$

$$\text{Quality} = \frac{\text{Total count produced} - \text{Defected count}}{\text{Total count produced}} \quad (7)$$

1.2 Total Productive Maintenance (TPM)

TPM is a maintenance strategy that focuses on improving the design and function of the existing or older equipment in the plant [6]. Hartman has defined TPM as a permanent method of a maintenance program to improve OEE with the active participation of the operators [7]. Swapnil Raut defined TPM as a continuous improvement program that aims to reduce wastage and minimize downtime. It involves newly defined procedures that are used in the maintenance of the plant [4]. TPM aims to improve availability (by decreasing downtime), performance, and quality by implementing seven different TPM pillars as shown in Fig. 1 [7].

1.2.1 History of TPM

TPM—an innovative Japanese approach (1951)—was primarily based on preventive maintenance (PM) procedures. The concept of preventive maintenance was adopted by Japanese from the USA. In 1960, Nippondenso—supplier of Tata Motors company, Japan—became the first unit/plant to introduce PM approach in the entire plant. With the passage of time, the plant was automated by the said company. Hence,

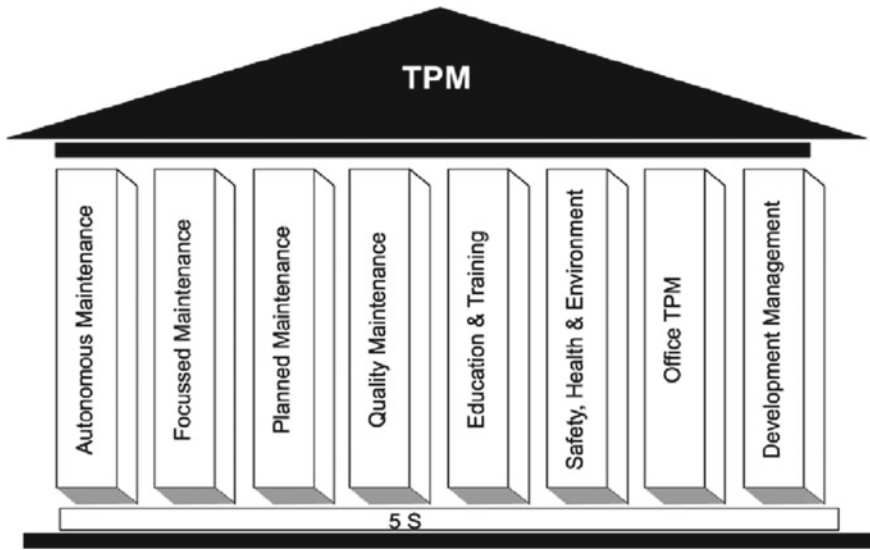


Fig. 1 Pillars of TPM [7]

maintenance became quite challenging task demanding more working hands. Thereafter, the management came with another innovative idea of routine maintenance to be carried out by the operator. This maintenance approach was called autonomous maintenance which is one of the pillars of TPM. Thus, Nippondenso added PM with AM for basic maintenance strategy [8].

1.3 Autonomous Maintenance

Autonomous maintenance (AM) is one of the pillars of TPM. AM is a maintenance strategy, wherein the operator operating the machine is responsible for the health and the performance of machine/equipment. Hence, operators are responsible to keep their equipment in good working condition and to prevent the deterioration of equipment. AM includes daily maintenance tasks like cleaning, lubricating, tightening, inspection (by sense), adjustment, retightening, etc. AM aims to eliminate all forms of downtimes (due to machine breakdown) of the production system which causes a direct impact on process performance [9, 10]. AM program helps an organization to reduce the cost associated with maintenance, operation, and repair [11]. Ribson and Ginder defined AM as a process in which an equipment/machine operator accepts and shares the responsibility for the health and the performance of machine/equipment.

Table 1 Autonomous maintenance implementation steps

Steps	Nature of activities
01	Initial cleaning
02	Eliminating source of contamination
03	Establish cleaning and inspection standards
04	Conduct general equipment inspection and training
05	Conduct general process inspection
06	Systematize autonomous maintenance
07	Continue improvement by autonomous maintenance

1.3.1 Benefits of AM

The benefits of autonomous maintenance can be summarized as follows:

- Sense of pride as well as ownership of machines is experienced by the operator.
- Machines and work areas are safer and easier to work around.
- Losses like breakdown, defects, etc., are reduced.
- Approach for zero defect and zero breakdown.
- Lowers maintenance and production costs and reduced equipment downtime.

1.3.2 Steps of Autonomous Maintenance

For the successful implementation of autonomous maintenance, Nikajima’s seven steps are followed as shown in Table 1 [12, 13].

2 Literature Review

Gupta (2012) implemented TPM program in the automobile industry to reduce the losses associated with OEE. They implemented 5S, Kaizen, and autonomous maintenance in the manufacturing sector to increase the OEE. This resulted in OEE improvement from 58.7 to 70% with a reduction of breakdown frequency [14]. Kumbi (2013) focused on enhancing procedures in the maintenance sector to achieve good availability by activities like cleaning, lubrication, inspection, and tightening. This helped to prevent the forced deterioration of the equipment. The authors also discussed challenges like strong resistance to change and operator’s challenges faced in implementing AM [13]. Guariente (2017) implemented AM on air-conditioning tube manufacturing unit in an automotive plant, aiming to reduce unplanned downtime. AM resulted in a decreased breakdown and also helped to decrease the number of interventions/backlogs on the production line. There was an increase in the monthly indicator of equipment availability on the line, thus resulting in a 10% increase in OEE. Moreover, due to the implementation of visual management like one-point

lesson, MTBF increased resulted in reduced MTTR [15]. Chen (2011) reported that out of eight pillars of TPM, effective and successful implementation of autonomous maintenance is a key success to TPM [16]. Vijay (2015) stated OEE as a roadmap to boost the effectiveness of industrial processes and the equipment. OEE helps to explain the reason for job delay it not only measures inefficiency, also categorizes these inefficiencies into three categories [17]. Nikajima (1988) reported that total productive maintenance as a maintenance strategy that helps to eliminate waste, minimize breakdown, and optimize the effectiveness of equipment. It also promoted autonomous maintenance activities in day-to-day activities that involve total work force [18]. Mainea (2010) laid focus on hidden wastes like operating machine below desired/normal speed, start-up time, bottlenecks, etc. Early management techniques helped to create reliable and safe equipment and processes. After implementing the TPM technique (autonomous maintenance), the indicator OEE increased to 90% and even 100% in some cases [19]. Ashwin (2016) improved OEE by TPM approach and stated that TPM helps an organization to improve overall performance if implemented properly. With TPM, an industry can gain maximum benefits with very less investment as it helps to decrease various associated costs [20].

3 Case Study

3.1 About the Company

The present study was performed in one of the leading oil filter manufacturing industry, XYZ. The company manufactures oil filters used in automotive industries. It has been manufacturing oil filter for premier automotive brands in India. The following machines shown in Table 2 are presented in sequential order as used in the fabrication of oil filter.

Table 2 Machines used for fabrication of filter (sequence wise as per process)

Process	Machine	Description/function of machine
1	Marathon	This is used to make pleats to the filter paper
2	Precuring oven	This helps to cure these pleated filter paper
3	Clip cinching	This helps to join the ends of the filter paper after pleated
4	Adhesive dispenser	Releases adhesive that is used to join top and bottom caps to cured filter paper
5	Induction	Induction heat is used to quickly join top cap and filter paper
6	Final cure oven	Used to finally cure filter and also to join bottom cap and filter paper
7	Seaming machine	Used to seam the filter bowl and the cover assembly
8	Leak testing	Used to check the leakage of the manufactured bowls

3.2 Methodology

The data for three months was collected for all the machines using Pareto technique. From the analysis of the data, it was known that among all the machines, the seaming machine on both line-I and line-II was responsible for lower OEE (Figs. 2 and 3).

On the basis of the collected data, the breakdown and defect data are shown in Table 3. OEE and its associated parameters are also shown in Table 4.

After data collection, brainstorming sessions were carried out with management and technical staff. From the discussions, it was finalized that autonomous maintenance should be implemented to improve OEE which will further help to eliminate the above-discussed problems. The most critical machines, i.e., seaming machine I and seaming machine II, were finalized for implementing autonomous maintenance using Pareto tool.

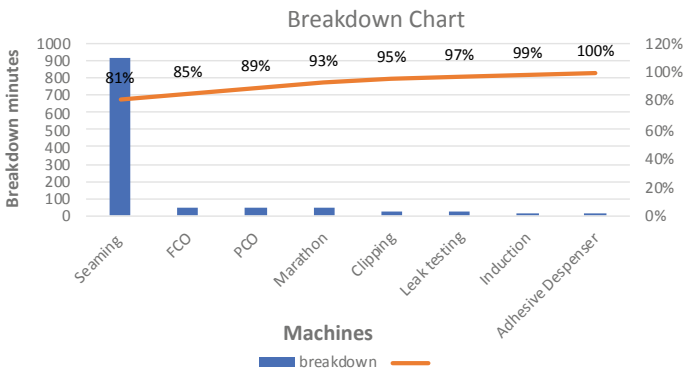


Fig. 2 Machine breakdown Pareto analysis

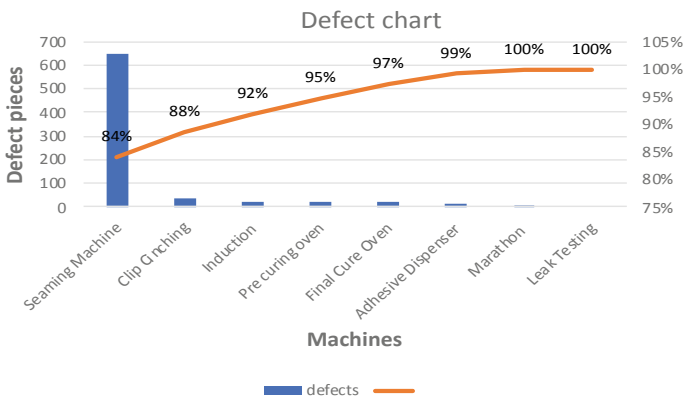


Fig. 3 Machine defect Pareto analysis

Table 3 Seaming machines' three-month data before implementation of AM

Machine	Make/model	Breakdown (minutes)	Defects (Pcs)
Seaming I	Bubber/07	473	290
Seaming II	Ramgarhia/12	440	333

Table 4 Seaming machines' three-month OEE parameter data before implementation of AM

Machine	Availability (%)	Performance (%)	Quality (%)	OEE (%)
Seaming I	95	74	98	69
Seaming II	96	76	98	71

Seaming Machine

The seaming machines installed at the industry are manual and 02 in number. The bowl of the oil filter and cover assembly are seamed with the help of the seaming process. Oil filter is assembled in two parts: One is the preparatory process in which spring and cured filter paper with an inner retainer are placed inside the filter bowl. The other is the seaming process in which cover assembly and filter bowl are seamed (joined and sealed). The filter bowl (with spring, cured filter paper, and inner retainer) and cover assembly are kept on the lifter plate by the operator. As the pedal is pushed by the operator, it lifts the lifter plate (along with unseamed filter) to the seaming chuck where seaming rollers seam the filter. When the operator lifts the foot from the foot pedal, the lifter plate with a seamed filter comes down and completes the seaming operation.

3.3 Steps of Implementing Autonomous Maintenance

The autonomous maintenance is implemented in seven different steps as mentioned below.

Step I: Initial cleaning

An individual machine or line is identified on which AM is to be implemented. The identified machine is cleaned, and hidden abnormalities are identified. Tagging of these abnormalities is done using red tag and white tag. Figure 4 shows the tagging of the seaming machine.

Step II: Eliminating the source of contamination

Contamination sources that degrade the machine or affect its performance are identified. Also, in this step, the action is taken against unsafe contamination sources and unsafe places. The following pictures show pre- and post-pictures of AM (Fig. 5).



Fig. 4 Initial cleaning and tagging



Fig. 5 Pre- and post-AM (stopping source of contamination)

Step III: Establish cleaning and inspection standards

This step includes the identification and documentation of critical cleaning, inspection, and lubrication points. Based on these identified critical points, the format in Table 5 has been prepared and all the critical lubricating points are mentioned with plan, i.e., whether to lubricate daily, weekly, or on a monthly basis.

Step IV: Conduct general equipment inspection and training

In this step, detection and identification of malfunctioning through four senses (smell, hearing, seeing, and feeling) are carried out. The development of one-point lessons is also done in this step of autonomous maintenance.

Table 5 Critical lubrication points of seaming machine

Machine : Seaming		AUTONOMOUS MAINTENANCE PLAN																												FORMATE NO:			
																														Month : Jan 2020			
I.No.	Check points	Period	1	2	3	4	5	6	7	8	9	10	11	12	13	14	15	16	17	18	19	20	21	22	23	24	25	26	27	28	29	30	SIGNATURE
1 Seaming Machine 01																																	
A	Belt tension and belt health	D																															
B	Check overall health (nut bolt)	D																															
C	Oiling of moving parts	D																															
D	Greasing Gear, rollers etc	W																															
E	Cleaning of moving parts	D																															
F	Roller setting with proper torque and tightening	D																															
G	Clean extra deposit from Chuck , Roller , bottom bowl holder	D																															
H	Tighten Lifter plate Nut Bolt	D																															
I	Cleaning machine in general	W																															
2 Seaming Machine 02																																	
A	Belt tension and belt health	D																															
B	Check overall health (nut bolt)	D																															
C	Oiling of moving parts	D																															
D	Greasing Gear, rollers etc	W																															
E	Cleaning of moving parts	D																															
F	Roller setting with proper torque and tightening	D																															
G	Clean extra deposit from Chuck , Roller , bottom bowl holder	D																															
H	Tighten Lifter plate Nut Bolt	D																															
I	Cleaning machine in general	W																															

शब्द-संक्षेप: OK (✓), NOT OK (✗), D= Daily W= weekly M= Monthly

Step V: Conduct general process inspection

In this step, general process inspection of AM standards is developed for routine internal check-up, i.e., cleaning, lubrication, inspection, tightening (CLIT). The main CLIT points are drawn on CLIT sheet format as shown in Table 6.

Table 6 CLIT sheet for seaming machine

शुद्धता		सफाई		ग्रीसिंग		बजावट		दोष		कारण		काम		दिनांक		वर्ष		दिनांक		वर्ष		दिनांक		वर्ष		दिनांक		वर्ष		दिनांक		वर्ष			
क्र. सं.	वर्ष	क्र. सं.	वर्ष	क्र. सं.	वर्ष	क्र. सं.	वर्ष	क्र. सं.	वर्ष	क्र. सं.	वर्ष	क्र. सं.	वर्ष	क्र. सं.	वर्ष	क्र. सं.	वर्ष	क्र. सं.	वर्ष	क्र. सं.	वर्ष	क्र. सं.	वर्ष	क्र. सं.	वर्ष	क्र. सं.	वर्ष	क्र. सं.	वर्ष	क्र. सं.	वर्ष				
1	Seaming machine	सफाई	सफाई	Cleanliness	दोष	कारण	दोष	कारण	दोष	कारण	D																								
				Lubrication	दोष	कारण	दोष	कारण	दोष	कारण	दोष	कारण	W																						
				Inspection	दोष	कारण	दोष	कारण	दोष	कारण	दोष	कारण	D																						
				Tightening	दोष	कारण	दोष	कारण	दोष	कारण	दोष	कारण	D																						

शुद्धता

शब्द-संक्षेप: OK (✓), NOT OK (✗), C - CLEANING, L - LUBRICATING, I - INSPECTION, T - TIGHTNING G - GREASING D - DAILY ; W - WEEKLY ; M - MONTHLY



Fig. 6 One-point lessons (on seaming machine)

Step VI: Systematize autonomous maintenance

It includes display of visual management prepared in step V of AM, like one-point lessons (OPLs). OPL is a five-minute lesson in the form of visuals like drawing or photos so that operator can easily understand the message conveyed through one-point lesson. OPLs can be used for improving basic knowledge like lubrication, cleaning, safety, improvement, etc. The various OPLs displayed on the seaming line are shown in Fig. 6.

Step VII: Continue improvement by autonomous maintenance

In this step, the results of each process are compared with the actual goal—zero accident, zero defect, zero breakdown.

4 Results and Discussion

After implementing autonomous maintenance on the machine, i.e., seaming machines I & II, OEE is calculated again. The results of OEE after implementation of AM are shown in Tables 7 and 8 for both the seaming machines, and their corresponding bar graph is also shown in Figs. 7 and 8.

From the computed results as shown in Tables 7 and 8, it is observed that all the three parameters of OEE are marginally improved in seaming machine I with OEE improvement from 69 to 84%. Similarly, all three parameters of OEE are improved in seaming II, with OEE improvement from 71 to 85%. The visual display graphs in Figs. 7 and 8 also show the improvement in each of these parameters. These graphs

Table 7 OEE parameters' comparison seaming I

S. No.	Parameter	Before AM phase I (%)	After AM phase II (%)
1	Availability	95	99
2	Performance	74	85
3	Quality	98	100
4	OEE	69	84

Table 8 OEE parameters' comparison seaming I

S. No.	Parameter	Before AM Phase I (%)	After AM Phase II (%)
1	Availability	96	99
2	Performance	76	86
3	Quality	98	100
4	OEE	71	85

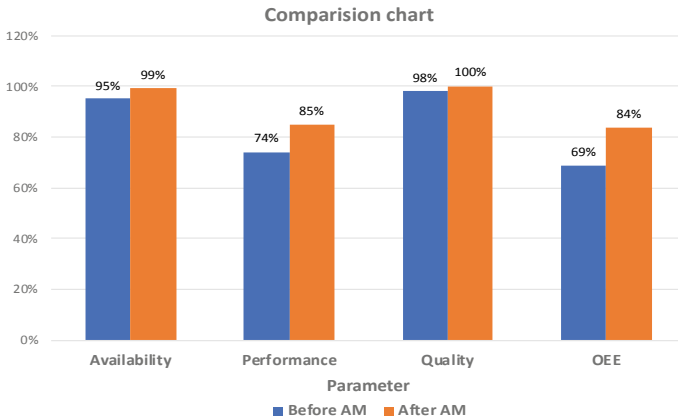


Fig. 7 OEE comparison chart seaming I

also show a visual comparison between each of these parameters and OEE, before and after implementing AM. Thus, after implementing autonomous maintenance, OEE has improved.

5 Conclusion

To compete in today's era of globalization and highly changing market trends, every industry tries to be competitive in the market incorporating new and latest trends for improvement. AM is an effective trend for improvement in OEE of individual

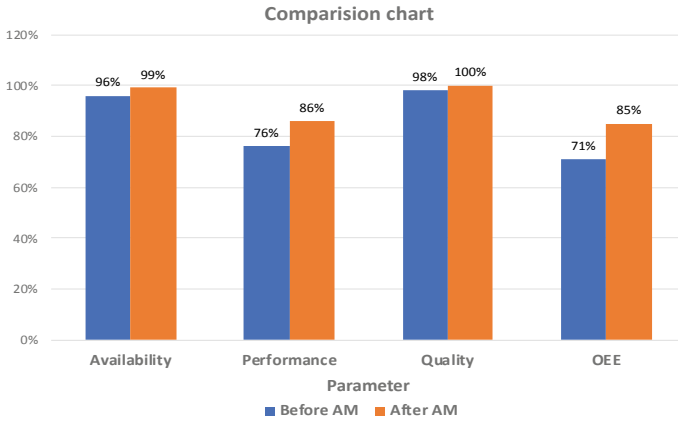


Fig. 8 OEE comparison chart seaming

machines or an integrated set of machines as it increases availability by reducing downtime. This study was done in the automotive oil filter manufacturing industry to improve OEE and improve maintenance policy as well. It was observed that the OEE of the industry was around 70%, and after implementing AM, there was a noticeable improvement in OEE by 14–15%. As the availability and quality components of OEE are close to 100%, therefore, more focus should be laid on improving performance component which may improve OEE significantly. For improving the basic knowledge and skills of an operator, the focus should be laid on visual managements like OPLs and training sessions.

Acknowledgements The current paper is related to our project work taken at the oil filter manufacturing industry. I am thankful to the industry for allowing us to take this project at the industry. I am also thankful for sharing the data related to the industry.

References

1. Raut S, Raut N (2017) Implementation of TPM to enhance OEE in medium scale industries. *IJISSET* 4(3)
2. Leflar (1999) TPM at Hewlett-Packard. In: 10th total productive maintenance conference, Las Vegas, NV, Productivity, Inc
3. Hartman E (1992) Successfully installing TPM in a Non- Japanese plant. TPM Press Inc., Pittsburgh, PA
4. Kunio S, Seiichi N (1992) TPM for supervisors. CRC Press, Boca Raton, FL
5. Nicholas JM (1998) Competitive manufacturing management: “continuous improvement, lean production, and customer-focused quality”. McGraw-Hill, US. 103 Roland Berger Strategy Consultants
6. Swanson (2001) Linking maintenance strategies to performance. *Int J Prod Econ* 70(3):237–244

7. Bamber CJ, Sharp JM, Hides MT (1999) Factors affecting successful implementation of total productive maintenance. A UK manufacturing case study perspective. *J Qual Maintenance Eng* 5(3):162–181
8. An introduction to Total Productive Maintenance (TPM); plant maintenance resource centre accessed on 26 June 2020 (http://www.plant-maintenance.com/articles/tpm_intro.shtml)
9. Wakjira MW, Ananth I (014) Bonfring *Int J Ind Eng Manag Sci*
10. Ahmad R, Kamaruddin S, Azid (2011) Development of autonomous maintenance implementation framework for semiconductor industries. *Int J Ind Syst Eng* 9(3):268
11. Shahanaghi K, Yazdian SA (2009) Analyzing the effects of implementation of Total Productive Maintenance (TPM) in the manufacturing companies: a system dynamics approach. *World J Model Simul* 5(2):120–129
12. Nakajima S (1988) TPM development program. Productivity Press, Cambridge, UK
13. Mugwindiri K, Mbohwa C (2013) Availability performance improvement by using autonomous maintenance—the case of a developing country. Zimbabwe, *World Congr Eng*
14. Gupta AK, Garg RK (2012) OEE improvement by TPM implementation: a case study. *IJISAER* 1
15. Guariente P, Antonioli I, Ferreira LP, Pereira T (2017) Implementing autonomous maintenance in an automotive manufacturing components manufacturer. *MESIC*
16. Min CS, Ahmad R, Kamaruddin S, Azid IA (2011) Development of autonomous maintenance implementation framework for semiconductor industries. *Int J Ind Syst Eng* 9(3):268–297
17. Lahri V, Pathak P (2015) A case study of implementation of overall equipment effectiveness on CNC table type boring & milling machine of a heavy machinery manufacturing industry. *IOSR J Mech Civil Eng* 12(05):63–70
18. Seiichi N (1989) *Introduction to TPM*. Mass Productivity Press, Cambridge
19. Mainea M (2010) A method to optimize the overall equipment effectiveness. *IFAC* 33(17):237–241
20. Virupakshar AB, Badiger A (2016) Enhancing productivity through TPM concepts: a case study. *Int J Adv Prod Mech Eng* 2(2):23–26

Design and Selection of Hydraulic Components for the Rotary Head System of Blasthole Drill Machine



Alok Vardhan and Ajay Pratap Singh

Abstract Blasthole drilling is one of the drilling methods used in surface mining activities. By this method, a hole is produced into surface of rock called as ‘Blast hole’ and the machine used for producing that hole is called blasthole drill machine. In blasthole drill machine, rotation of rotary head, feed mechanism, levelling and drill pipe addition all depend on hydraulic systems. In this paper, an attempt has been made to find out the methodology for design and selection of hydraulic components for the rotary head system of blasthole drill machine used in open cast coal mines. The proposed methodology may be helpful for the designers to propose the guidelines for design and development of the hydraulic system of a HEMM.

Keywords Blasthole drilling · Blasthole drill machine · Open cast coal mines · Heavy earth moving machinery (HEMM)

1 Introduction

Blasthole drilling is one of the primary drilling techniques employed in surface mining operations. By this technique, a hole is drilled into the rock surface, packed with explosive material and detonated. Such a hole made by the machine is known as the “blast hole” and the machine used for drilling is called blasthole drill machine. Hydraulic system plays a vital and significant role in blasthole drill machines. Whether the machine’s move, rotation of rotary head, feed mechanism, levelling, drill pipe addition all depend on hydraulic systems [1–3].

In blasthole drill machine, the rotation of drill bit is done with help of an open-circuit high-torque low-speed primary controlled hydraulic drive system. A hydraulic drive configuration is provided for that. This drive consists of a variable displacement pump and two identical hydraulic motors with a gear reducer unit [4]. Figure 1 shows a layout representing them, where the swash plate angle of the pump is varied

A. Vardhan (✉) · A. P. Singh
Department of Mechanical Engineering, AKGEC, Ghaziabad, Uttar Pradesh, India

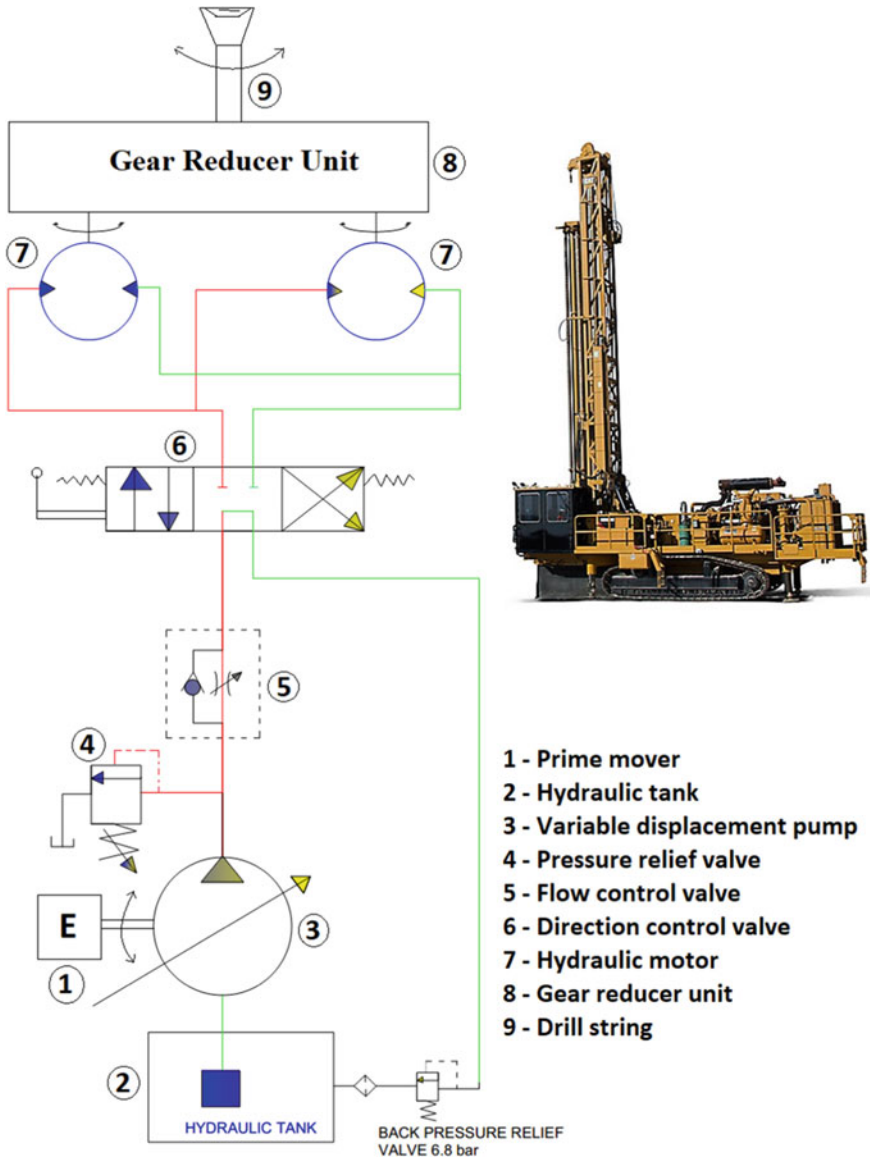


Fig. 1 Hydraulic drive for rotary head system of blasthole drill machine

to control the speed of hydraulic motors. Aim of this article is to find out the methodology for design and selection of hydraulic components for the rotary head system of blasthole drill machine used in open cast coal mines. Such a study has not yet been performed.

2 Physical System

The suggested hydraulic drive for the blasthole drill machine rotary head system is shown in Fig. 1.

Referring to Fig. 1, proposed hydraulic drive consists of a variable displacement axial piston pump (3) driven by the prime mover (1) which operates at the rotatory speed of 2000 rpm. The pump supplies the pressurized fluid to the two identical fixed displacement hydraulic motors (7) through the directional control valve (6). The hydraulic tank (2) provides the oil supply for the entire system. A pressure relief valve (4) is used to set the maximum pressure in the hydraulic system. A flow control valve (5) is used to provide a required flow to the hydraulic motors.

3 Required Torque at Drill Head for Drilling Blast Hole

In this regard, field observations and research have developed various empirical formulas for calculating the required torque at drill head for drilling blast hole.

According to Nelmark’s empirical formula [3], the required torque at drill head for drilling blast hole is

$$T = 5252 \times K \times D^{2.5} \times W^{1.5} \tag{1}$$

where T (ftlb), K , D (inches) and W (thousands of lbs/inch bit diameter) are the required torque at drill head, rock properties constant, blast hole diameter and weight on the bit, respectively.

The value of K is between 14×10^{-5} and 4×10^{-5} and depends mainly on the drillability of the rock. For the softer rocks, higher values are to be used, and for harder rocks, lower values are to be used. Whereas, the value of W is obtained by dividing maximum bit load with diameter of hole [3].

Based on the mention data in Table 1, the calculation for the torque requirement at drill head for drilling blast hole of size 6.25 inch is made and is given in Table 2.

According to Fedorov’s empirical formula [3], the required torque at drill head for drilling blast hole is

Table 1 Operating parameters for blasthole drilling [3, 4]

Rock description	Uniaxial compressive strength of the rock (MPa)	Rock properties constant, K	Blast hole diameter, D (inches)	Weight on the bit, W (lbs)	Drill speed, N (rpm)
Soft	34–69	13×10^{-5}	6.25	19,000	75–100
Medium	69–103	8×10^{-5}	6.25	25,000	50–75
Hard	103–207	6×10^{-5}	6.25	30,000	40–50

Table 2 Required torque at the drill head for drilling blast hole according to Nelmark’s formula

Rock description	Blast hole diameter, D (inches)	K value	W value (thousand of lbs per inch of bit diameter)	Torque (lbft)	Torque (Nm)
Soft	6.25	13×10^{-5}	3.04	353.41	479.16
Medium	6.25	8×10^{-5}	4	328.25	445.05
Hard	6.25	6×10^{-5}	4.8	323.62	438.77

$$P = \alpha \times \gamma \times L \times D^2 \times N^{1.7} + 0.7854 \times N_0 \times D^2 + 8 \times 10^{-7} W \times N \quad (2)$$

where P (kW), D (cm), N (rpm), γ (kg/m³), L (m), N_0 (kW/cm²) and W (N) are the rotary power for drilling, hole diameter, drill speed, flushing medium density, hole depth, the power used in cutting the lower cross-sectional area of blast hole and weight on the drill bit, respectively.

Inclination of mast is depending on α . Its value can be established using Fig. 2. Factor N_0 has a value of 0.1 to 0.15 kW/cm² depending on hardness formation. Little value is applied to soft structures, and high value is applied to rigid formations [3]. From above empirical equation discussed in (2), the rotational power for drilling can be calculated, and the torque can be determined for a particular rotational speed.

The required torque at the drill head for $L = 53$ m, $\alpha = 4.7 \times 10^{-8}$, $N_0 = 0.135$, $\gamma = 1.2252$ and $D = 6.25$ inch is calculated and given in Table 3.

By comparing the torque required when drilling for the different types of rock shown in Tables 2 and 3, it can be observed that Fedorov’s empirical method provides

Fig. 2 Value of α for the different angle of inclination of the mast

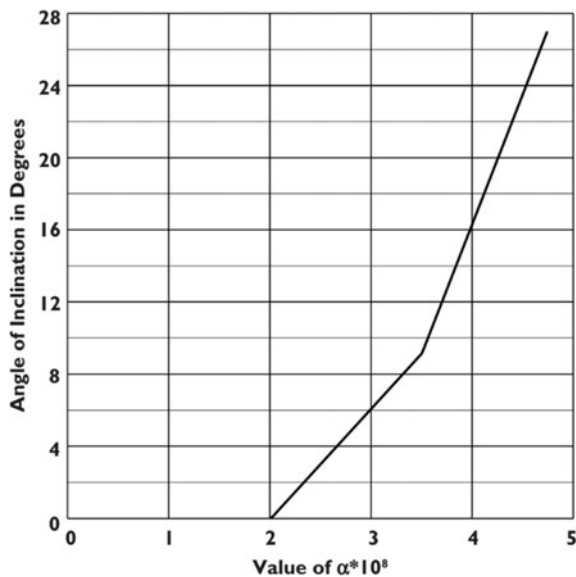


Table 3 Required torque at the drill head for drilling blast hole according to Fedorov’s formula

Rock description	Blast hole diameter		Bit load		Drill rotary speed (rpm)	Rotary power for drilling (kW)	Torque (lbft)	Torque (Nm)
	inches	cm	lbs	Newton				
Soft	6.25	15.875	19,000	84,516	100	35.41	2493.29	3380.45
Medium	6.25	15.875	25,000	111,206	60	32.87	3856.90	5229.25
Hard	6.25	15.875	30,000	133,447	40	31.40	5526.37	7492.75

the highest required torque when compared to Nelmark’s empirical formula. Because, Nelmark’s empirical formula does not consider many important factors, i.e. hole inclination, hole depth and flushing medium density. Therefore, it is suggested that the required torque values calculated by Fedorov’s empirical method can be used for the genuine design [3].

4 Selection of Hydraulic Components

The hydraulic system mainly consists of a hydraulic pump driven by the prime mover, directional control valve, flow control valve, hydraulic motors and the gear reducer unit. The selection criteria of such components play vital role in the design and development of the system. As an example, in order to design the hydraulic system used in the rotary head of drill machine for hole diameter of 6.25 inch which can be used for wide variation of rock strength (34–207 MPa), the following assumptions are made:

- Maximum rotary speed of the drill string (Nd) is = 100 rpm
- Maximum working pressure for the system (Pm) is = 205 bar
- System has used two identical low-speed high-torque hydraulic motors.
- System has a gear reducer unit of 7:1 gear ratio and having efficiency of 95% [5].

4.1 Selection of Hydraulic Motors

From Table 3, the maximum required torque at drill head for drilling blast hole is

$$T = 7492.75 \text{ Nm}$$

Assuming 10% factor of safety for safe design of the system [3], the maximum required torque at drill head for drilling blast hole is

$$T_d = 7492.75 \times 1.10 \text{ Nm}$$

$$T_d = 8242.03 \text{ Nm}$$

The required torque (T_d) to drive the drill string is provided by the two identical motors along with the gear reducer unit of 7:1 gear ratio having 95% efficiency [5]. Therefore, the load torque on each hydraulic motor (T_m) is (Fig. 3)

$$T_m = \frac{T_d}{2 \times GR \times \eta_g} \tag{3}$$

where

T_d required torque at drill head for drilling blast hole.

GR gear ratio of gear reducer unit.

η_g efficiency of gear reducer unit.

From Eq. (3),

$$T_m = 619.70 \text{ Nm}$$

The maximum speed of the drill string (N_d) is

$$N_d = 100 \text{ rpm}$$

Therefore, the maximum rotary speed of each hydraulic motor (N_m) is

$$N_m = N_d \times GR \tag{4}$$

From Eq. (4),

$$N_m = 700 \text{ rpm}$$

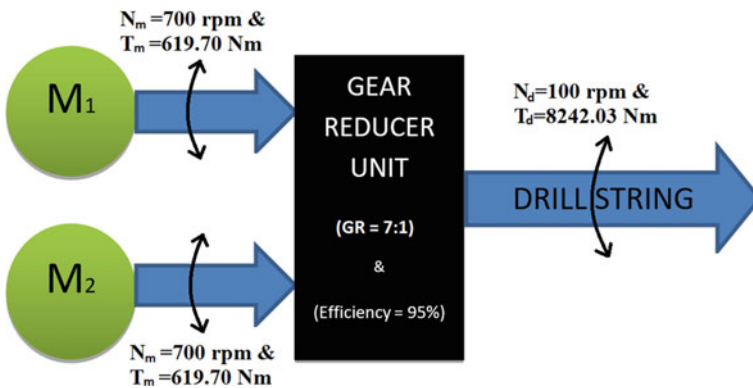


Fig. 3 Load torque and speed distribution

Mechanical efficiency (η_{m_m}) for hydraulic motor is

$$\eta_{m_m} = \frac{2\pi T_m}{P_m D_m} \quad (5)$$

where

D_m displacement of the hydraulic motor.

P_m pressure drop across the hydraulic motor.

η_{m_m} mechanical efficiency for hydraulic motor (assume, $\eta_{m_m} = 0.85$).

From Eq. (5), it is found that

$$D_m = 223.45 \text{ cc/rev}$$

We can select standard hydraulic motor available in the market, i.e. 225 cc/rev. The specifications of the selected hydraulic motor suitable for the rotary head of drill machine are obtained from its product catalogue [6].

4.2 Selection of Pump

The size of hydraulic pump considered for rotary head system of the drill machine is obtained from required flow to drive hydraulic motors.

The flow required to drive both the hydraulic motors as its maximum speed (700 rpm) is

$$Q_p = 2 \times Q_m \quad (6)$$

Volumetric efficiency for hydraulic motor (η_{m_v}) is

$$\eta_{m_v} = \frac{D_m N_m}{Q_m} \quad (7)$$

where

Q_m flow required to each hydraulic motor.

N_m maximum speed for hydraulic motor.

η_{m_v} volumetric efficiency for hydraulic motor (assume, $\eta_{m_v} = 0.95$).

From Eq. (7),

$$Q_m = 165.79 \text{ lpm}$$

Considering both the hydraulic motors, from Eq. (6), total flow required is

$$Q_p = 331.58 \text{ lpm}$$

Assuming the flow-losses occur in the valves and accessories of the hydraulic system due to leakage is 10% [7], then the maximum required flow is:

$$Q_p = 331.58 \times 1.10 \text{ lpm}$$

$$Q_p = 364.74 \text{ lpm}$$

The displacement of the pump to be selected for the drill machine is obtained by

$$\eta_{p_v} = \frac{Q_p}{D_p N} \quad (8)$$

where

D_p displacement of the pump.

N prime mover speed (2000 rpm).

η_{p_v} volumetric efficiency of the pump (assume, $\eta_{p_v} = 0.95$).

From Eq. (8), the displacement of the pump is

$$D_p = 191.97 \text{ cc/rev}$$

Thus, the hydraulic pump suitable for the rotary head system of drill machine should have the following relevant properties:

- Considering 15 bar pressure loss across the control valves and the connecting hoses [7], the maximum required operating pressure for the pump (P_p) is = 205 + 15 = 220 bar
- Maximum required displacement of the pump is = 191.97 cc/rev
- Maximum required speed = 2000 rpm

Therefore, we can select standard pump available in the market, i.e. 193 cc/rev. The specifications of the selected pump suitable for the rotary head of drill machine are obtained from its product catalogue [8]. This pump provides actual flow rate of 386 lpm at 2000 rpm speed.

The required torque for driving the pump (T_p) is obtained by the following equation:

$$\eta_{p_m} = \frac{D_p P_p}{2\pi T_p} \quad (9)$$

where

P_p pressure across the pump.

η_{p_m} mechanical efficiency of the pump (assume, $\eta_{p_m} = 0.85$).

From Eq. (9),

$$T_p = 795.03 \text{ Nm}$$

4.3 Selection of Directional Control Valve (DCV)

For the flow rate of 386 lpm and the system pressure of 220 bar, we can select standard 4/3 way lever-operated spring-returned directional control valve of size NG25 available in the market. The detailed specifications of the selected directional control valve are obtained from its product catalogue [9]. The pressure drops in this valve for different spool positions corresponding to flow rate are given in Fig. 4. For the flow rate of 386 lpm and the system pressure of 220 bar, we can select standard 4/3 way lever-operated spring-returned directional control valve of size NG25 available in the market. The detailed specifications of the selected directional control valve are obtained from its product catalogue [9]. The pressure drops in this valve for different spool positions corresponding to flow rate are given in Fig. 4.

4.4 Selection of Flow Control Valve (FCV)

For the flow rate of 386 lpm and the system pressure of 220 bar, we can select standard flow control valve of size NG30 available in the market. The detailed specifications of the selected flow control valve are obtained from its product catalogue [10]. The pressure drop in this valve corresponding to flow rate is given in Fig. 5.

4.5 Selection of Pressure Relief Valve (PRV)

The pressure relief valve is set at the pressure 10% higher than system's working pressure [7]. Thus, required setting pressure of pressure relief valve is 242 bar. For the flow rate of 386 lpm and the required pressure, we can select standard pressure relief valve of size NG25 available in the market. The detailed specifications of the selected pressure relief valve are obtained from its product catalogue [11]. The setting pressure of the standard pressure relief valve is 250 bar (254.93 kg/cm²).

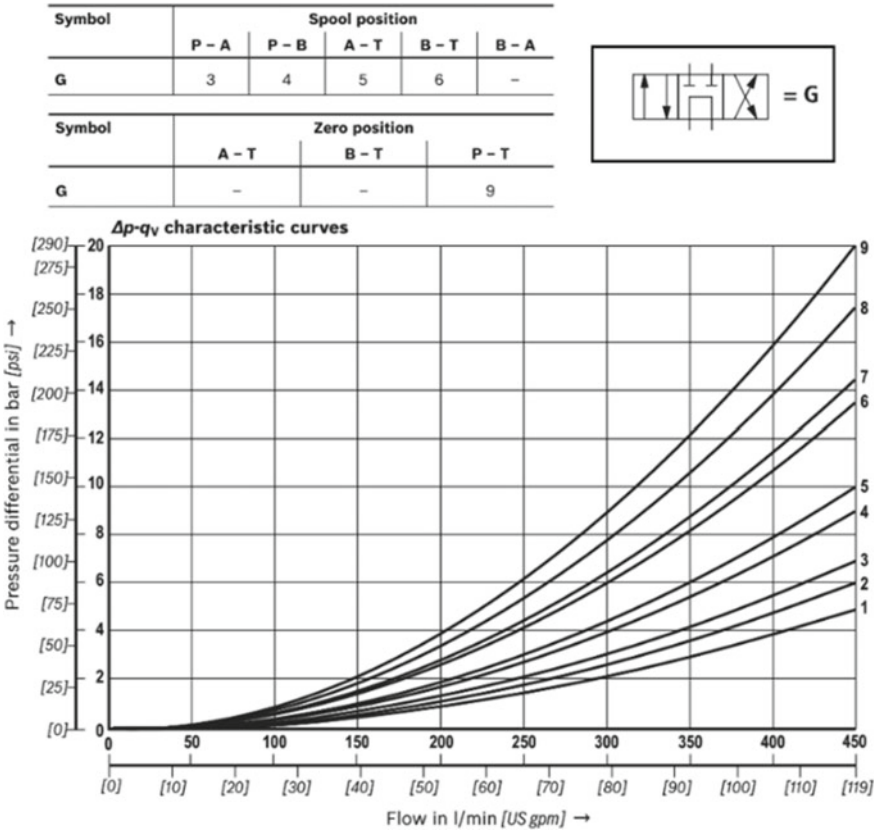


Fig. 4 Characteristics curve for the directional control valve

4.6 Selection of Prime Mover

Required power to drive the pump is

$$kW = \frac{P_{rv} Q_p}{612 \eta_{p_o}} \tag{10}$$

where

- P_{rv} setting pressure of the relief valve in kg/cm².
- Q_p pump flow in lpm.
- η_{p_o} overall efficiency of pump ($\eta_{p_o} = 0.95 \times 0.85 = 0.81$).

From Eq. (10),

$$kW = \frac{254.93 \times 386}{612 \times 0.81}$$

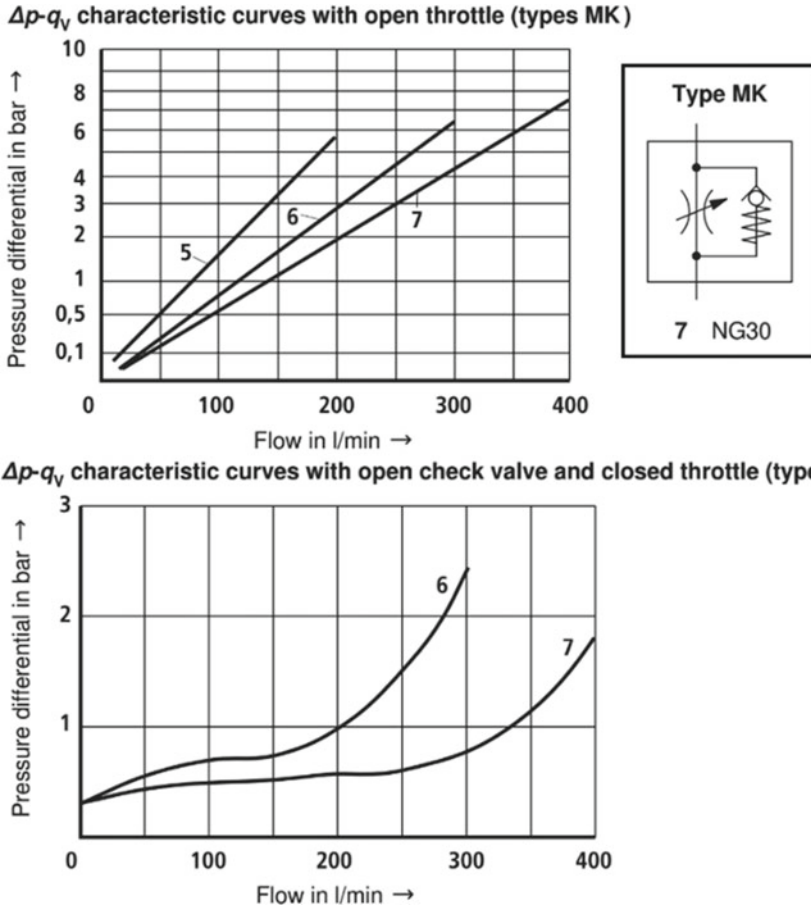


Fig. 5 Characteristics curve for the flow control valve

$$kW = 198.51 \text{ kW} = 266.10 \text{ HP.}$$

We can select standard prime mover available in the market, i.e. 280 HP. The detailed specifications of the selected prime mover are obtained from its product catalogue [12], and the characteristics curve for the prime mover is given in Fig. 6. This prime mover provides 1000 Nm torque at 2000 rpm speed.

5 Conclusion

In this paper, an attempt has been made to find out the methodology for design and selection of hydraulic components for the rotary head system of blasthole drill machine used in open cast coal mines. Depending on the maximum flow rate in

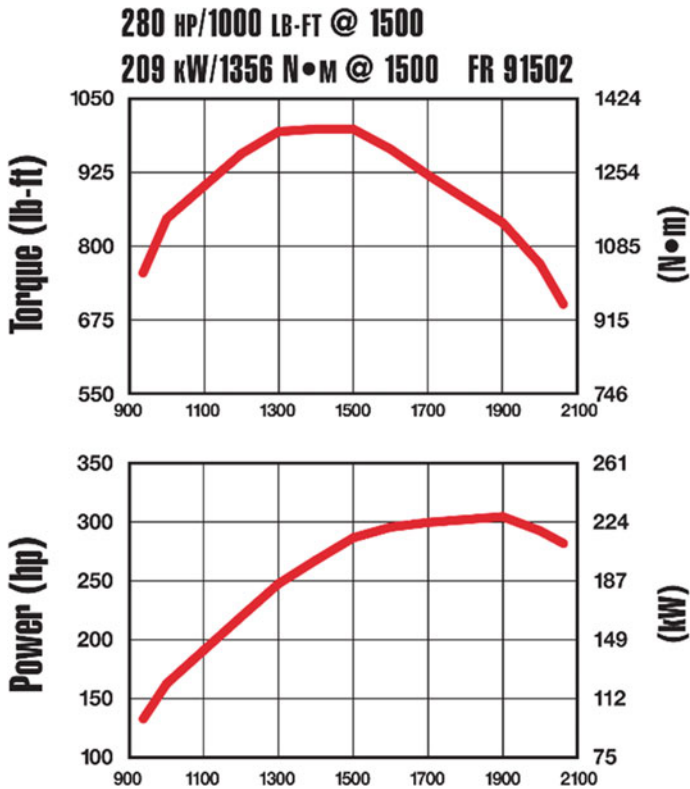


Fig. 6 Characteristics curve for the prime mover

the hydraulic system and the system pressure, the other components like directional control valve (DCV), flow control valve (FCV) and the pressure relief valve (PRV) are selected. The proposed methodology used for the design and selection of the hydraulic components may be helpful for the designers to propose the guidelines for the development of the hydraulic system of a HEMM.

Acknowledgements The authors express their sincere gratitude to Dr. R. K. Aggarwal, Director General, Dr. Devendra Singh, Head of Mechanical Engineering Department and Professor Ashiva Shah, Head of CORE, AKGEC, Ghaziabad, for all kinds of help and support.

References

1. Jimeno EL, Jimino CL, Carcedo A (1995) Drilling and blasting of rocks. CRC Press
2. Misra GB (1979) Surface mining. Dhanbad Publishers
3. Gokhale BV (2010) Rotary drilling and blasting in large surface mines. CRC Press

4. Operation and maintenance manual of C-650 drill. Revathi Equipment Limited Coimbatore, India
5. Product catalogue of standard gear unit modular system CSB140. New Allenberry Works, India
6. Product catalogue of the radial piston motor for wheel drives MCR-F, RE 15198/12.2013. Bosch Rexroth India Ltd.
7. Pinches MJ, Ashby JG (1989) Power hydraulics. Prentice Hall
8. Product catalogue of the axial piston variable pump RE 92500/10.09. Bosch Rexroth India Ltd.
9. Product catalogue of the directional control valve RE 24751/2016-06. Bosch Rexroth India Ltd.
10. Product catalogue of the throttle and throttle check valve RE 27219/01.09. Bosch Rexroth India Ltd.
11. Product catalogue of the pressure relief valve, direct operated RE 25402/2016-07. Bosch Rexroth India Ltd.
12. Product catalogue of the prime mover QSC 4087067, Rev 6/06. Cummins Engine Company Ltd UK

A Simulation Method for the Behavior of Hybrid Mg-Based Composite Brake Caliper in Automobile Application



Sakshi Singh and Kamal Kant Singh

Abstract Generally, heavy-weight brake caliper is made of gray iron (GI) which affects the overall weight of the vehicle performance and leads to high fuel consumption. The key problem in GI caliper is deflection during bending, i.e., clamping action which causes brake pedal travel. This study demonstrates the simulation analysis of the Mg-based brake caliper as an alternative. This investigation reflects the capability of Mg-based brake caliper because of its light-weight and high strength as well as high elastic modulus properties. The results reveal that hybrid Mg-based composite brake caliper has excellent (improved) performance by the reduction in weight and deformation with enduring ability to elastic stress–strain as compared to GI brake caliper.

Keywords Gray iron · Hybrid Mg composite · Brake caliper · Ansys · Mesh analysis · Von Mises

1 Introduction

The U-shaped housing of brake caliper enclosed around the disk brake and commonly composed of gray iron [1]. Floating GI caliper is placed on a pin to provide cylindrical support and gives the linear movement [2]. The existing challenges for this caliper are its heavy-weight, high consumption of brake fluid, corrosion and overheating. However, if high structural rigidity is provided, the caliper could attain the different positive aspects such as short pedal travel, least wearing of braking pads, and providing safe driving [3]. Another issue of GI brake caliper is bending because of the hydraulic pressure applied to the caliper housing and the piston. This will cause brake pedal travel which means extra fluid is required to fix the bending problem [4].

S. Singh (✉)

MAE Department, Indira Gandhi Delhi Technical University for Women, Delhi, India

K. K. Singh

ME Department, Gautam Buddha University, Greater Noida, Uttar Pradesh, India

Table 1 Mechanical properties of GI and Mg-based composite brake caliper

S. No.	Properties	Gray iron brake caliper	Mg-based composite brake caliper
1	Density, Kg/m ³	7200–7400	1891
2	Elastic modulus, GPa	95–100	102

Thus for designing, the prime consideration is to reducing the mass and enhancing the stiffness value.

In recent years, computer simulation analysis became an essential part to solve the deformation problem of a brake caliper. The mesh analysis helps to analyze the strengthening properties according to the optimized results. Many literature studies demonstrate the stress analysis of composite-based brake caliper by optimizing the data values [5]. Ajibola et al. [6] simulate a structural model of Mg-based composite brake caliper as a substitution for iron- and Al-based alloys. According to Heinrich et al. [7] FEM model, advanced Mg-based carbide-reinforced composites can efficiently reduce mass and improve the efficiency with less fuel consumption in the automobile sector. Khatkar et al. [8] have illustrated a review study on Mg-based hybrid composites with graphite (Gr) to enhance the ductility of composites and to revive the microstructural and hardness characteristics related to the given applications.

This paper focused on the modeling analysis of brake caliper by a modular approach. In this study, model (GI brake caliper) is compared with the simulated mesh model (made of hybrid Mg-based composite).

$$\text{Force(N)} = \frac{4 \times \text{Oil Pressure} \left(\text{N/mm}^2 \right) \times \text{Section area of Piston} \left(\text{mm}^2 \right) \times \text{Fiction coefficient}}{\text{Efficiency Coefficient} \times \text{Radius of Wheel Cylinder}(\text{mm}) \times \text{Rolling Radius of Wheel}(\text{mm})}$$

The analyzed mechanical data values of GI brake caliper are as shown in Table 1 [9] (Fig. 1).

2 FE Modeling Analysis

Figure 2 represents the different processing stages such as type of analysis as pre-processing steps, properties of materials, selection of mesh analysis by element size, and determination of boundary and load condition. The desired results of the processing stages are computed, and the evaluated results have been summarized in the final processing step. Table 1 represents the involved mechanical properties having both gray iron and hybrid Mg-based composite brake caliper (AZ91/7SiC/7Gr), respectively.

To enhance the mesh quality, additional features have been added as default mesh setting. Different parameters of mesh have been considered such as orthogonal and

Fig. 1 Structural mesh model of Mg-based composite brake caliper



element quality with skewness values. An average mesh element value (0.6) is evaluated and accepted. To attain a high quality of the mesh, different techniques of meshing have been used (Figs. 2, 3 and 4). There are three functions employed at different size functions, i.e., fixed, proximity, and curvature. Both curvature and proximity are counted as better having different cross sections and curve regions as compared to fixed-size function. “Tetrahedron” patch meshed is the most appropriate as it considered curvature regions more prominently as compared to other mesh zones such as sweep, multi-zone, and hexagonal dominant. Figures 3 and 4 investigate the standard mesh metrics’ spectrums having orthogonal and skewness quality. However, the meshing technique having appropriate mesh parameters has been achieved as optimum results, i.e., 0.86 is the average orthogonal quality, 0.85 is the average element quality, and 0.15 is the average skewness quality (Figs. 2, 3, and 4). These elements state that high meshing qualities have been involved in this work (Table 2).

The boundary and load conditions have been applied according to the brake fluid pressure. The loads have been determined at the severe condition when the alarming braking condition has come across. In this situation, brake fluid pressure is established at 8 MPa [9]. Simultaneously, load values are the same due to its equable force induces because of fluid pressure.

3 Result and Discussion

In this section, results of finite element analysis have been discussed. Figures 5 and 6 represent the results of the gray iron caliper and hybrid Mg-based composite caliper, respectively. The analysis of hybrid Mg-based caliper revealed that it attains maximum elastic strain value with smaller deformation dispersion as compared to the

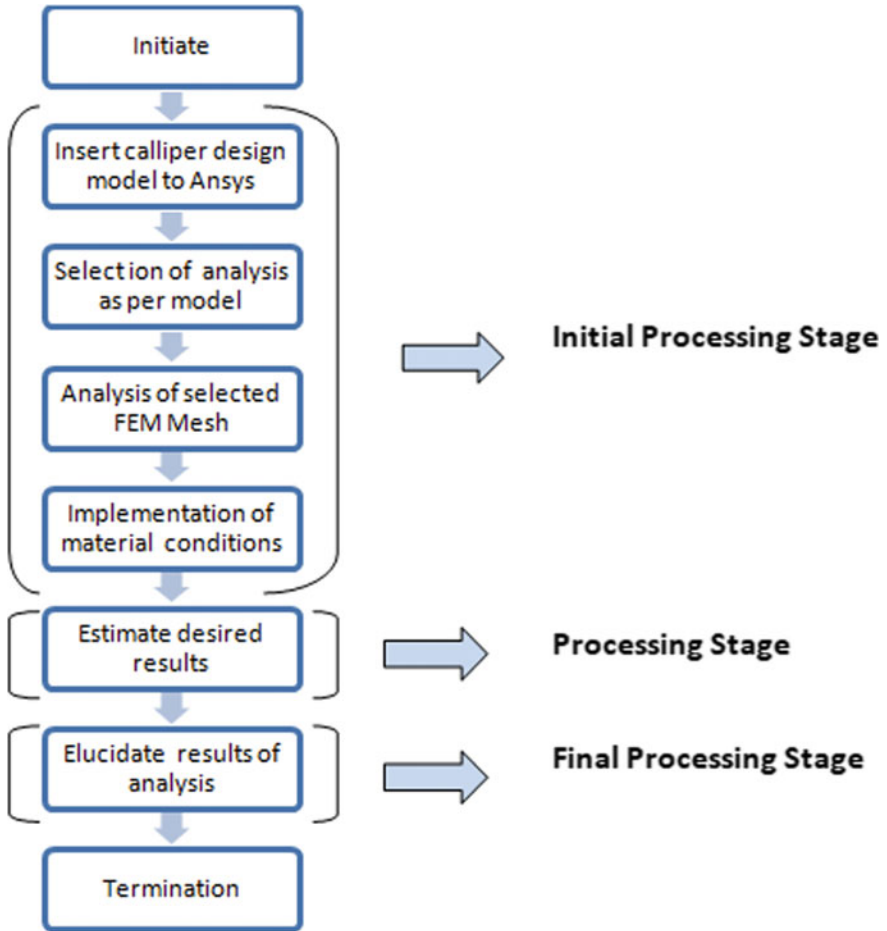


Fig. 2 Flowchart for finite element analysis of brake caliper

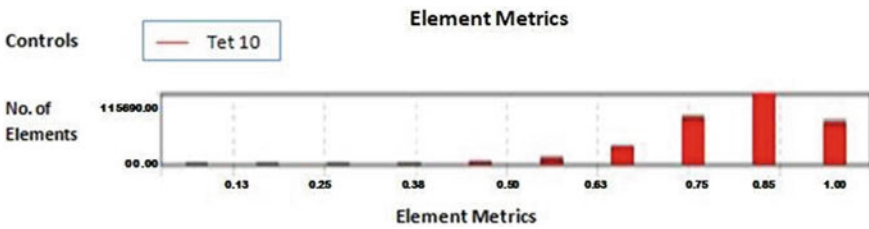


Fig. 3 Mesh average element quality

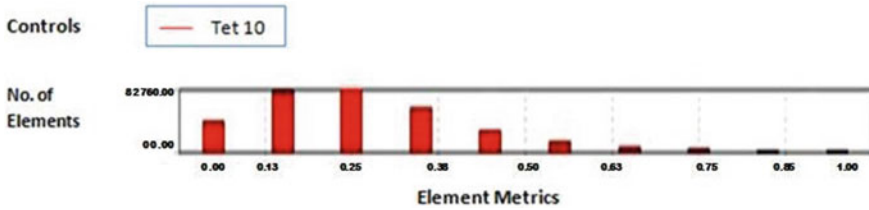


Fig. 4 Skewness quality values (mesh average)

Table 2 Spectrum mesh metrics' values of skewness and orthogonal quality

Spectrum analysis of skewness mesh metrics					
Unacceptable	Bad	Acceptable	Good	Very good	Excellent
0.95–1.00	0.94–0.98	0.78–0.96	0.50–0.78	0.24–0.52	0–0.26
Spectrum analysis of orthogonal quality mesh metrics					
Excellent	Very good	Good	Acceptable	Bad	Unacceptable
0.98–1.00	0.68–0.96	0.20–0.68	0.14–0.22	0.002–0.16	0.0–0.002

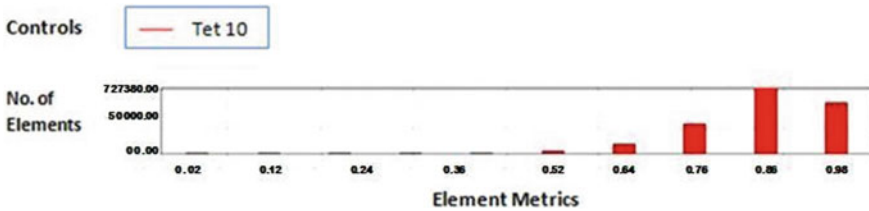


Fig. 5 Orthogonal quality values (mesh average)

gray iron caliper. 3.48% and 5.31% of variations have been observed, respectively. This is possible due to hybrid Mg-based composite caliper is stiffer than gray caliper, because it possesses high elastic modulus than gray iron caliper. However, literature study reports that deflection of the brake caliper is the critical problem during its performance. This problem can be recovered by significant features of bridge design. However, Fatchurrohman et al. [10] suggested that bridge design characteristics are the most significant factor to control the structural stiffness. Summarized finite element analysis (Table 3) results indicate that hybrid Mg-based composites obtain the desired results. As these desired results include low elastic strain values, varied von Mises stress results, and small (total) deformation. In comparison to gray iron model, hybrid Mg-based composite brake caliper weight is 57.36% reduced. About 0.44% of increment has been observed in von Mises stress dissipation value of hybrid Mg-based composite caliper as compared to the gray iron caliper. Large von Mises structural stress value indicates that composite is approximately near to yielding point value. However, if von Mises stress value is greater than yield point

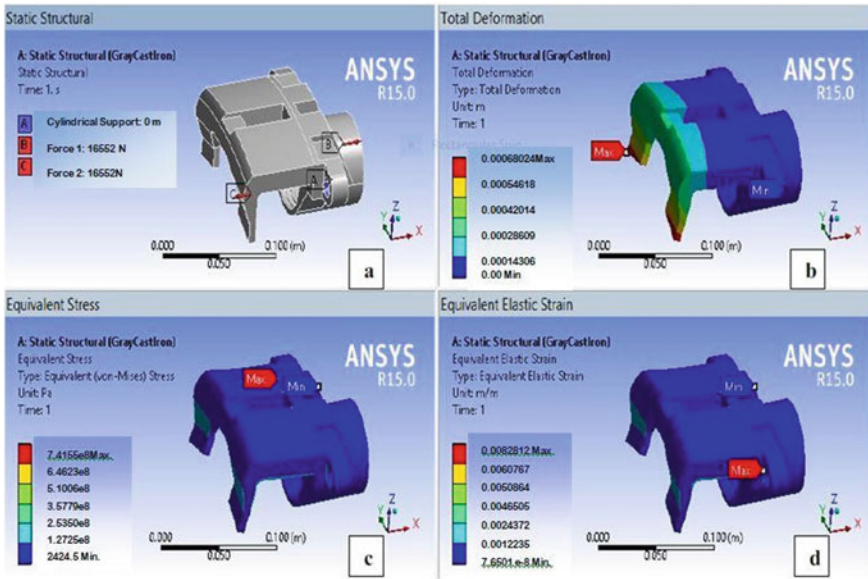


Fig. 6 Gray iron caliper Ansys result analysis: **a** static structural loading, **b** deformation, **c** Eq. stresses, and **d** Eq. elastic strain

Table 3 Concluded analyzed results of gray iron and hybrid Mg-based composite brake caliper

Properties	Improvement percentage	Gray iron brake caliper	Hybrid Mg-based composite brake caliper
Total mass, Kg	57.36	2.2517	0.9601
Total deformation (max.), m	5.31	0.0008240	0.0007802
Equivalent stress (max.), Pa	-0.44	$7.155e^8$	$7.187e^8$
Equivalent elastic Strain (max.), m/m	3.48	0.008211	0.007925

value, then composite/material can endure some permanent dispersion which means composite does not sustain its standard shape [11]. Von Mises’ structural stress signifies the stress value which distorts the original shape of the composite. Besides, new investigations have been performed by the engineers to weaken of the distorted material and minimize the peak stress values by different simulation methods [12]. Besides, hardly very few studies have been reported by the authors to customize a standard hybrid Mg-based composite brake caliper as similar structures. Lastly, this study is only focused to influence of hybrid Mg-based caliper through average mesh analysis method (Fig. 7).

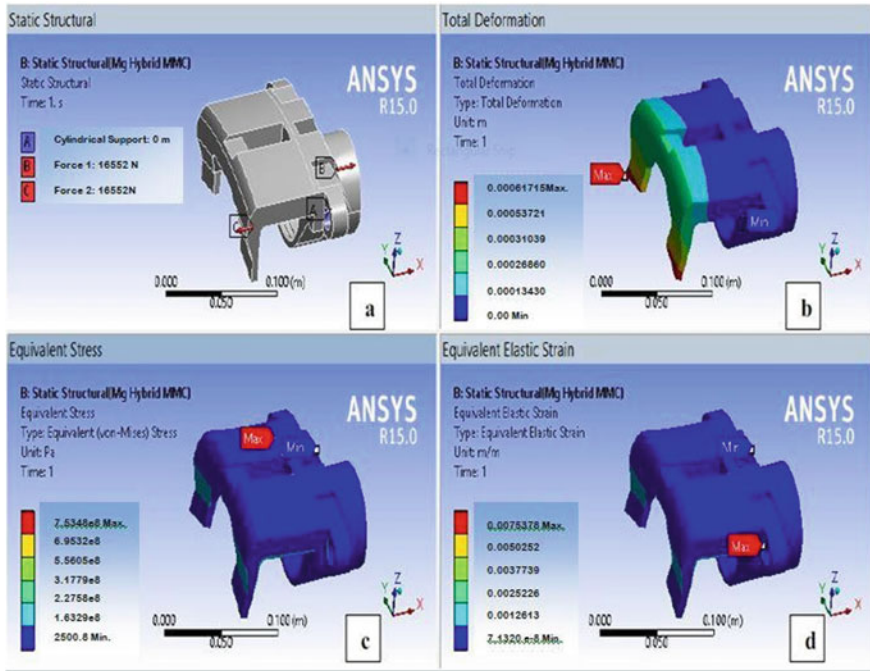


Fig. 7 Hybrid Mg-based composite caliper Ansys result analysis: **a** static structural loading, **b** deformation, **c** Eq. stresses, and **d** Eq. elastic strain

4 Conclusions

From this study, the following conclusions have been drawn:

1. The hybrid Mg-based brake caliper can sustain rigidity with a low deflection value as well as a reduction in final weight as compared to the gray iron brake caliper.
2. Proposed hybrid Mg-based composite brake caliper having AZ91/7SiC/7Gr can be a good substitute to replace gray iron brake caliper.
3. Hybrid Mg-based composite brake caliper potentially favorable under the extreme deflection condition of the brake caliper.
4. As compared to gray iron caliper, this study suggested that hybrid Mg-based brake caliper has a better ability to resist equivalent elastic strain value with low deformation.

References

1. Habeeb HA, Mohan AE, Abdullah MA, Abdul MH, Tunggal D (2020) Performance analysis of brake discs in trains. *Jurnal Tribologi* 25:1–15
2. Kharate NK, Chaudhari SS (2018) Effect of material properties on disc brake squeal and performance using FEM and EMA approach. *Mater Today Proc* 5(2):4986–4994
3. Shanker PS (2018) A review on properties of conventional and metal matrix composite materials in manufacturing of disc brake. *Mater Today Proc* 5(2):5864–5869
4. Pan H, Guo X, Pei X, Dong X (2017) Modeling, simulation and experimental analysis of brake pedal feel for passenger car. SAE. <https://doi.org/10.4271/2017-01-1371>
5. Ting CS (2016) Design selection of floating brake calliper magnesium hybrid composites. Doctoral Dissertation, University Malaysia Pahang
6. Ajibola OO, Aribi S, Ige OO, Akinribide OJ, Akinwamide SO, Olubambi PA (2019) Wear behaviour of cast aluminium silicon (Al–Si) alloy in dot 4 brake fluid. In: IOP conference series: materials science and engineering. IOP Publishing, vol 628, no 1, p 012012
7. Heinrich Möller GG, Stumpf W (2016) Factors influencing tensile mechanical properties of Al–7Si–Mg casting. *Light Metals* 467–470
8. Khatkar SK, Suri NM, Kant S (2018) A review on mechanical and tribological properties of graphite reinforced self lubricating hybrid metal matrix composites. *Rev Adv Mater Sci* 56(1):1–20
9. Chen Z, Wu J, Zhao J, He R, Yang C, Zhang Y (2018) ABS control algorithm based on direct slip rate for hybrid brake system. SAE Technical Paper (No. 2018-01-0830)
10. Fatchurrohman N, Chia ST (2017) Performance of hybrid nano-micro reinforced Mg metal matrix composites brake calliper: simulation approach. *MS&E* 257(1):012060
11. Johnnary TN, Ebitei FW (2020) Von misses pure shear in Kirchhoff's plate buckling. *Open J Civil Eng* 10(2):105–116
12. Borawski A (2019) Common methods in analysing the tribological properties of brake pads and discs—a review. *Acta Mechanica et Automatic* 13(3):189–199

Prediction of Tensile Strength of Hybrid Natural Fiber Reinforced Composites Using Machine Learning Approach



Murugappan Elango , V. Naveen Krishna , Adithyan Annamalai ,
and P. Harish

Abstract In the presence of engineering, the trend of investing in an alternative material for the metal is emerging. In the meanwhile, focusing on the high-end applications, the composite materials can sustain in all economic and ambient working conditions. Currently, there is a trend of developing the natural fiber composites which has similar mechanical properties compared to the synthetic fibers and also biodegradable (Gholampour and Ozbakkaloglu in *J Mater Sci* 1–64, 2020 [1]). The present investigation is conducted to study the hybrid (madar and bamboo) fiber's tensile strength values. The execution of hand layup approach is chosen here to prepare the composite material plates. After this, experimental result for the tensile test of the composite plates was obtained. After that, FEA model is developed and validated using ANSYS to emulate the experimental conditions. In the validated FEA model, tensile strength of the hybrid multilayered composite laminates was determined. From the simulation results, a generalized regression equation was generated for the tensile property of any given composite ply angles.

Keywords Bamboo fiber · Madar fiber · Hand layup · FEA · Regression analysis · R-tool

1 Introduction

In this decade, due to the widely risen awareness on the depletion of non-renewable materials, there is essential to track down the natural materials. Natural fibers such as jute, flax, hemp and sisal are used because of their low density, good thermal insulation and also low price. Natural fibers are used as a suitable alternative for the un-natural fibers like carbon and glass fiber [2]. The series of experimental work conducted on the hybrid composite laminates by changing each layer of ply with different materials. These results displaced that the blended composite plates had better properties than individual composite plates [3]. Bamboo fibers are high

M. Elango (✉) · V. Naveen Krishna · A. Annamalai · P. Harish
Thiagarajar College of Engineering, Tamil Nadu, Madurai 625015, India

strength natural fibers which are used for reinforcing hybrid composite materials and also have the good wetting of the fiber with the matrix for achieving the superior mechanical properties [4]. The method of soaking the fiber into NaOH solution is used for enhancing the mechanical strength [5]. Bamboo fiber can further be used for construction purposes as they possess good dynamic properties [6]. Madar fiber, a novel natural material, is extracted manually from the stem portion of the madar plant. These fibers are combined with *Bauhinia Racemosa* and goat hair to produce a composite plate through hand layup approach. The composite plate was then put through a series of tests in order to evaluate its mechanical properties [7]. In recent days, a number of researchers are concentrating on hybrid natural fibers. Largely, hybrid natural fibers exhibited superior static mechanical properties than the single natural fibers and are fairly equal to the man-made fibers [8]. The blending of coir with hemp or flax hybrid natural composites enhances the mechanical properties, and it exposed good surface consolidation properties [9]. The regression equation models revealed the bond between the two variables and also helped in predicting one variable from another [10]. Till now, most researchers had concentrated on experimental approach for determining the properties of natural fibers. It was observed that the study on hybrid fibers and machine learning approach for the forecast of mechanical properties was less addressed. So, the current work, the hybrid composite laminate with the materials of madar and bamboo fiber is fabricated with the three-ply angle 0° , 45° and 60° using hand layup technique and tested for tensile strength and also compared with the FEM results to create the regression equation.

2 Materials and Methodology

2.1 *Bamboo Fiber*

Bamboo fiber is an eco-friendly fiber belonging to the Poaceae family. The researchers focused on these fibers because of their advantageous properties such as lightweight, eminent specific strength and non-hazardous which have immense potential in automotive industry by replacing synthetic fibers [11]. The fibers are extracted by crushing and treating them with enzymes.

2.2 *Madar Fiber*

Madar fiber belongs to Asclepiadaceae family. The fibers are obtained from the stem part. It can be utilized in lightweight applications such as textile and automobile industries. Madar fiber has superior properties like lower elongation and high tensile



Fig. 1 Photographic image of madar fiber and bamboo fiber

Table 1 Composition of madar and bamboo fiber

S. No.	Contents	Madar	Bamboo
1	Cellulose	71.55	60.8
2	Hemi-cellulose	24.35	23.5
3	Lignin	10.8	32.2
4	Moisture content	7.2	11.7

strength, thus standing as a perfect replacement to synthetic fibers [12]. The photographic image and composition of madar and bamboo fibers are shown in Fig. 1 and Table 1, respectively.

2.3 Polyester Resin

Polyester resin is utilized here to obtain good finish. It needs a catalyst and accelerator, which starts up the chemical reaction. The catalyst and accelerator ratio used here is 1:2. Water obtained as the derivative product during the reaction, and it is continuously removed in order to proceed the reaction [13]. The photographic image of the polyester resin is shown in Fig. 2.

2.4 Catalyst and Accelerator

Catalysts are invariably organic peroxides. Methyl ethyl ketone peroxide (MEKP) is used here as the catalyst along with the unsaturated polyester resin of grade (0051). The catalyst and polyester resin were mixed together and chemically interacted, causing the resin to set up for curing. Accelerator plays a major role in most chemical reactions [14]. Cobalt octoate is the accelerator used for speeding up the chemical

Fig. 2 Photographic image of polyester resin



Table 2 Properties of catalyst and accelerator

S. No.	Properties	Catalyst	Accelerator
1	Composition	MEKP in phthalate plasticizer	Cobalt octoate in 1:2 ratio with MEKP
2	Appearance	Slightly viscous liquid	Blue violet liquid

reactions between the polyester and the catalyst. It is suited for surface coatings [15]. The properties of catalyst and accelerator are shown in Table 2.

2.5 Hand Layup Technique

It is the traditional method for preparing the composite plate specimens. Mild steel material is used for making the mold, and the dimensions of the mold are $300 \times 270 \times 10 \text{ mm}^3$. The resin is applied at the bottom of the mold. Above this, the hybrid layer of bamboo and madar fiber is kept at an orientation angle of 45° . Again, the resin is applied above the hybrid fiber layer. The OHP sheets are placed above and below the mold to avoid sticking [16]. The photographic image of mold and 45° composite laminate is shown in Fig. 3.

3 Results and Discussion

3.1 Experimental Determination of Tensile Strength

The tensile testing is carried out by universal testing machine. The sample for tensile testing is prepared based on the ASTM standard D638 for the ply angle 45° . The

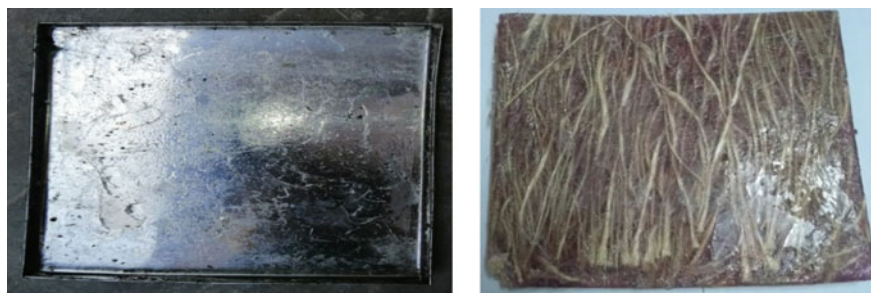


Fig. 3 Photographic image of mold and 45° composite laminate

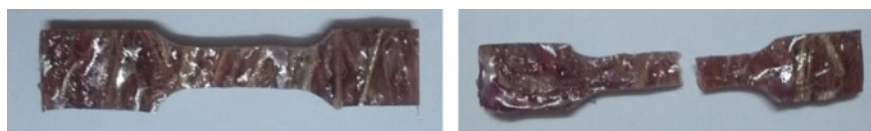


Fig. 4 Photographic image of 45° tensile specimen before and after testing

dimension of the sample is $165 \times 25 \times 3 \text{ mm}^3$ [17]. The tensile strength of the specimen is found to be 15.95 MPa. The photographic image of 45° tensile specimen before testing and after testing is shown in Fig. 4.

3.2 Determination of Tensile Strength by Analysis

The analysis of the tensile specimen is done using ANSYS Workbench software. The values of the hybrid composites are entered in the new engineering data table with the known values of Young's modulus, Poisson's ratio and density. For meshing, the body sizing option is selected in the mesh control [18]. The whole body is selected, and the size is given about 2 mm. In this FEA model, 4704 nodes and 3180 elements are presented, respectively. So, the fixed support is given to the crown edge of the model, and tensile load of about 1220 N is given in the bottom edge of the model in the X direction. Then, the single ply model is created for the orientation angle of 45° with the thickness of about 3 mm. By analysis, the tensile strength of the model is found to be 15.67 MPa. Since the experimental and analysis results are found to be near, the same analysis model can be extended to determine the tensile strength of the hybrid multilayered composite laminates. The photographic image of 45° orientation of single composite laminate and the photographic image of fixed support and tensile load on the end of the tensile specimen are shown in Figs. 5 and 6, respectively.

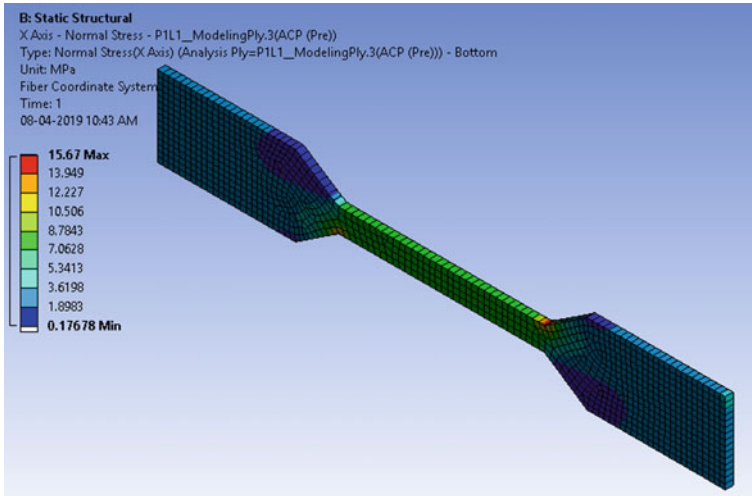


Fig. 5 Photographic image of 45° orientation of single composite laminate

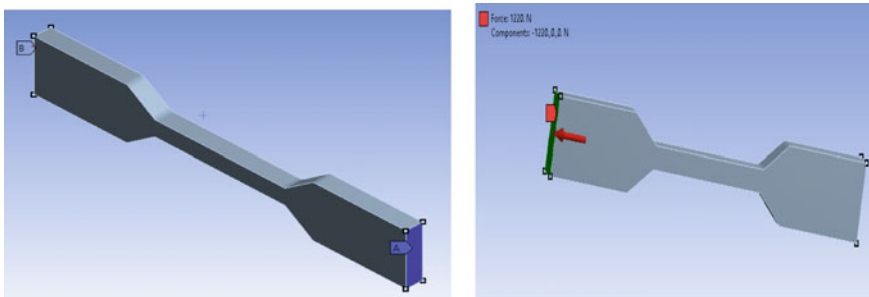


Fig. 6 Photographic image of fixed support and tensile load on the end of the tensile specimen

3.3 Behavior Modeling Through Regression Analysis

It is a machine learning technique which creates a relationship model between two or more variables. Here, we can find out the relationship between the hybrid composite ply angles and the tensile strength of the composite laminates [19]. Here, the regression analysis is done by using R-tool software. R programming is used for developers to train and evaluate an algorithm and predict the future events. Thus, R makes machine learning easier and more approachable. Regression analysis is one of the methods for recognizing the variables which enables us to determine the factor that matters the most and the one that can be ignored. This allows us to examine the bond between the used variables [20]. In this, the regression equation for the forecasting values of tensile property for the different orientation of composite laminates was

Table 3 Comparison table of ANSYS results and predicted results

Fiber orientation angle			Tensile strength (MPa)	
θ_1	θ_2	θ_3	ANSYS results	Predicted results
0°	0°	0°	19.44	19.94
0°	45°	60°	15.33	15.89
0°	45°	45°	16.86	16.67
45°	45°	45°	15.57	14.47
45°	0°	0°	18.15	17.74
45°	60°	60°	15.37	13.38
60°	60°	60°	11.04	12.65
60°	0°	60°	13.79	13.88
60°	60°	45°	12.51	13.43

generated. The regression equation for determination of tensile strength is given as follows

$$\text{Tensile strength} = 19.94058 - 0.04889 \theta_1 - 0.02051 \theta_2 - 0.05212 \theta_3.$$

The comparison table of ANSYS results and predicted results is shown in Table 3.

3.4 Correlation Plots

Correlation plot is used to examine the dependence between multiple variables and the outcome of correlation coefficients. It includes individual variable and others [21]. The function corrplot() is the package used that creates a graphical display of a correlation matrix, highlighting the most correlated variables in a data table. Positive correlations are showed in blue, and negative correlations are displayed in red color. The intensity of color and the circle size are in proportional to the correlation coefficients.

The photographic image of correlation plot obtained is shown in Fig. 7. It clearly explains the interdependency of the variables. The tensile strength is negatively correlated to first angle laminate θ_1 (-0.67), negatively correlated to second angle laminate θ_2 (-0.61) and also negatively correlated to third angle laminate θ_3 (-0.76).

3.5 Residual Histogram and Residual Plot

The histogram of the residual and residual box plot is checked here for the normal distribution of variance. A bell-shaped histogram is evenly distributed around zero.

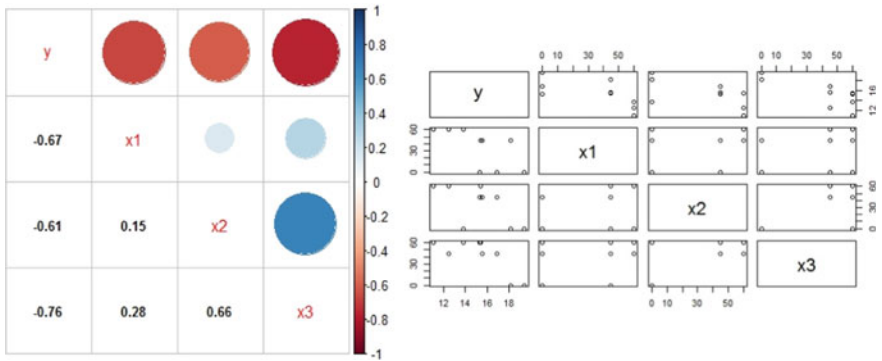


Fig. 7 Photographic image of correlated plots

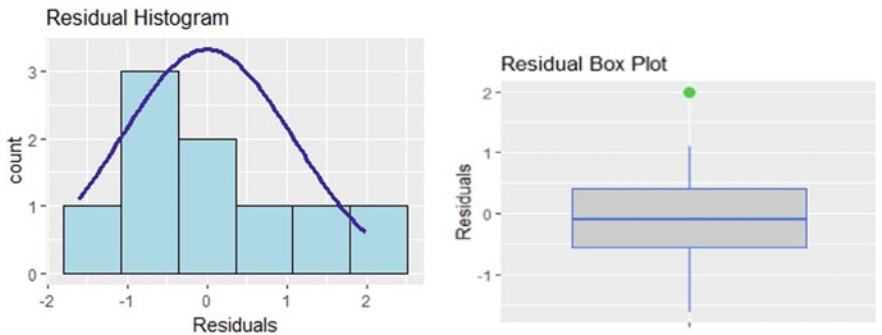


Fig. 8 Photographic images of residual histogram and residual box plot

Boxplots are a data distribution measurement and divide the data set in three equal shares. From the above boxplot, it is found that residue varies from -0.55 to 0.49 and it is found to be acceptable. The photographic images of residual histogram and residual box plot are shown in Fig. 8.

3.6 Q-Q Chart

Quantile–Quantile (Q-Q) plots are used to determine if data can be approximated by statistical distribution. They are used to compare the different data sets to determine if their distributions are comparable. The Q-Q plot is a graphical tool that can be used to determine whether a collection of data came from a theoretical distribution such as a Normal, Exponential, or Uniform distribution. The photographic image of Q-Q Chart is shown in Fig. 9.

Fig. 9 Photographic image of normal Q-Q plot

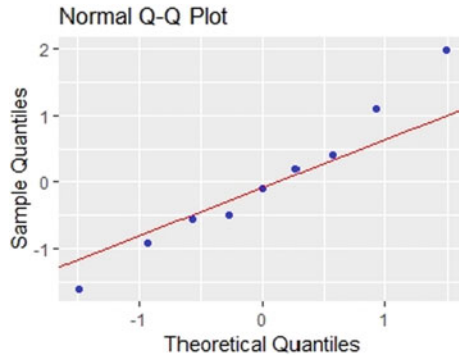
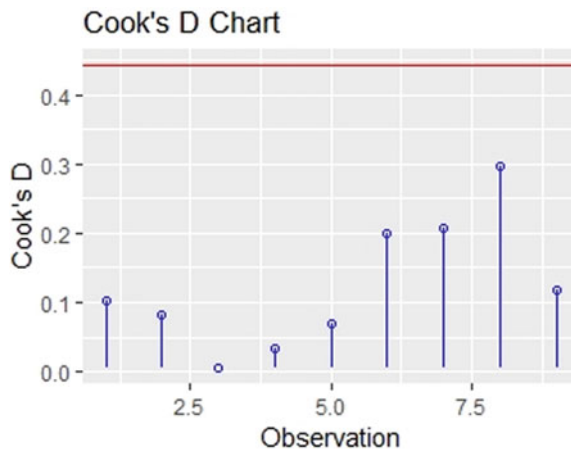


Fig. 10 Photographic image of Cook's D chart



3.7 Cook's D Chart

In Cook's D chart, D_i is the distance used in analysis of regression to find the influential set of predicted variables. If more, the leverage and residuals, higher is the Cook's distance. By theoretically, Cook's D is calculated by erasing the i th data from the model and refinding the regression. It summaries the change in the model of regression when the i th data is removed. The photographic image of Cook's D chart is shown in Fig. 10.

3.8 Coefficient of Determination for Regression Analysis

The industrial world is a constant state of change. Machine learning is an essential tool in modernizing mechanical streams. It brings new and exciting approaches, and it is

used to optimize the product characteristics. The quality, flexibility and efficiency of the system can be improved with the help of available data. We train on multiple data that are generated via simulations or experiments, and we make a predictive model like *R*-tool, ANN, etc. If the value of R^2 is more, the successful rate for simple linear regression model in explaining y variation is easier. When the analysis of regression analysis is done by a statistical package, either R^2 or $100R^2$ (the variation percentage explained by the tool) is a vital part of the outcomes. If R^2 is low, there is a search for a replaceable model that could be more factual explained in deviation. $100R^2$ Value of the model is 80.8% implying that it is an acceptable range. The generalized regression equation for finding tensile strength = $19.94058 - 0.04889 \theta_1 - 0.02051 \theta_2 - 0.05212 \theta_3$.

4 Conclusion

The hybrid madar–bamboo fiber composites are fabricated, and tensile strength of the specimen is determined by experimental approach with ply angle of 45° . Then, the FEA model is validated by comparing the experimental results with ANSYS results. The FEA model is extended to multilayered hybrid composites with different ply angle combinations. For each ply angle combination, the tensile strength of the multilayered hybrid composites is obtained by ANSYS. Then, the regression equation is developed by *R*-tool software to create a relationship with the ply angles and tensile strength. The importance of creating the regression equation is to avoid the need for different specimen preparation for different ply angle combinations and also to avoid the experimental testing of tensile specimen using UTM for the different ply angles combinations of the same material. Thus, it can reduce specimen preparation cost and tensile testing time. In future, this regression equations can be developed to determine the various mechanical properties of the hybrid composite materials. It is also helpful for the designers to select the proper composite combination for the specific applications.

References

1. Gholampour A, Ozbakkaloglu T (2020) A review of natural fiber composites: properties, modification and processing techniques, characterization, applications. *J Mater Sci* 1–64
2. Yashas Gowda TG, Sanjay MR, Subrahmanya Bhat K, Madhu P, Senthamaraikannan P, Yogesha B (2018) Polymer matrix-natural fiber composites: an overview. *Cogent Eng* 5(1):1446667
3. Ashik KP, Sharma RS (2015) A review on mechanical properties of natural fiber reinforced hybrid polymer composites. *J Min Mater Charact Eng* 3:420
4. Zhang K, Wang F, Liang W, Wang Z, Duan Z, Yang B (2018) Thermal and mechanical properties of bamboo fiber reinforced epoxy composites. *Polymers* 10(6):608
5. Sukmawan R, Takagi H, Nakagaito AN (2016) Strength evaluation of cross-ply green composite laminates reinforced by bamboo fiber. *Compos Part B: Eng J* 84:9–16

6. Perremans D, Trujillo E, Ivens J et al (2018) Effect of discontinuities in bamboo fibre reinforced epoxy composites. *Compos Sci Technol J* 155:50–57
7. Ganeshan P, Ramshankar P, Raja K et al (2018) Mechanical properties of madar/bauhinia racemosa hybrid composites. *Taga J* 14:1369–1375
8. Premnath AA (2018) Impact of surface treatment on the mechanical properties of sisal and jute reinforced with epoxy resin natural fiber hybrid composites. *J Nat Fibers*
9. Ciccarelli L, Cloppenburg F, Ramaswamy S et al (2019) Sustainable composites: Processing of coir fibres and application in hybrid-fibre composites. *Compos Mater J* 1–14
10. Ganeshan P, Raja K (2016) Improvement on the mechanical properties of madar fiber reinforced polyester composites. *Int J Adv Engg Tech* 7:261–264
11. Lokesh P, TSA Surya Kumari, Gopi R, Loganathan GB (2020) A study on mechanical properties of bamboo fiber reinforced polymer composite. *Mater Today Proc* 22:897–903
12. Ganeshan P, Nagaraja Ganesh B, Ramshankar P et al (2018) *Calotropis gigantea* fibers: a potential reinforcement for polymer matrices. *Int J Polym Anal Charact* 23(3):271–277
13. Das S (2017) Mechanical properties of waste paper/jute fabric reinforced polyester resin matrix hybrid composites. *Carbohydr Polym* 172:60–67
14. Weatherhead RG (1980) Catalysts, accelerators and inhibitors for unsaturated polyester resins. *FRP Technol J* 204–239
15. Easwara Prasad GL, Keerthi Gowda BS, Velmurugan R (2020) Study on mechanical properties of basalt rock fiber reinforced polyester composites. *Mech Compos Multi-funct Mater* 5:63–68
16. Prasad V, Muhammed Hunize CV, Abhiraj RI, Joseph MA, Sekar K, Ali M (2019) Mechanical properties of flax fiber reinforced composites manufactured using hand layup and compression molding—a comparison. *Adv Ind Prod Eng* 781–789
17. Repon R, Abdul Motaleb KZM, Tauhidul Islam M, Al Mamun R, Mithu MR (2017) Tensile and water absorption properties of jute and pineapple fabric reinforced polyester composite. *Int J Compos Mater* 7(2):72–76
18. Barbero EJ, Shahbazi M (2017) Determination of material properties for ANSYS progressive damage analysis of laminated composites. *Compos Struct* 176:768–779
19. Karthiyaini S, Senthamarikannan K, Priyadarshini J, Gupta K, Shanmugasundaram M (2019) Prediction of mechanical strength of fiber admixed concrete using multiple regression analysis and artificial neural network. *Adv Mater Sci Eng*
20. Bello SA, Agunsoye JO, Adebisi JA, Adeyemo RG, Hassan SB (2020) Optimization of tensile properties of epoxy aluminum particulate composites using regression models. *J King Saud Univ Sci* 32(1):402–411
21. Mangalaraja RV, Manvel Raj T, Rama Prabha D (2019) Statistical features of epoxy resin based hybrid composites reinforced with jute, banana and flax natural fibers. *J Chem Technol Metall* 54(1)

Simulation Analysis for Minimizing Waiting Time of Patients in an Outpatient Department



Murugappan Elango , S. Sivalingam, Adithyan Annamalai , and Abinav Karthikeyan

Abstract This paper puts forward a methodology to study the patient flow in a typical Indian hospital's outpatient department. In this study, a discrete event simulation model replicating the outpatient department was modeled, and a suitable doctor schedule and nurse schedule are drafted by putting together the simulation model into an optimization tool prospectively minimizing the waiting time of the patients ultimately avoiding investment in additional infrastructure.

Keywords Discrete event simulation · Outpatient department · Optimization tool · Arena model

1 Introduction

Of late, with the service sector being the largest economic sector in many considered societies, the quality levels alongside the productivity of the considered service have transformed to be a growing concern in judging the livelihood of the particular service firm. Generally speaking, the contemporary service economy has grown in size but has endured a roadblock in terms of productivity. With this being prevalent in the healthcare sector, a vital cog in the wheel called service sector. In several outpatient departments in hospitals, the long waiting time meant for treatments has been a long-time issue and one to ponder upon. Such complaints are often phrased as “Waiting for two hours to get a treatment with a duration less than three minutes”. This long waiting time has been on the radar for quite some time, with researchers, physicians and academicians, striving to find a remedy. According to most researchers, the reason for the prolonged waiting time is the inappropriate scheduling of doctors in the outpatient department [1]. Researchers had found that a proper scheduling of

M. Elango · A. Annamalai (✉) · A. Karthikeyan
Thiagarajar College of Engineering, Tamil Nadu, Madurai 625015, India

S. Sivalingam
Kurinji College of Engineering and Technology, Tamil Nadu, Manapparai, Tiruchirapalli 621307, India

doctors and nurses in the outpatient department will inflict a reduction in the patients waiting time. In this study, the discrete simulation model replicating the outpatient department is modeled. This study analyzes the effect of the doctor schedule and nurse schedule of the outpatient department in reducing the waiting time of the patient. The prime reasons surging the importance of modeling methods across healthcare sectors are the pressure ensuing from the goals not to refrain from the prime patient care and in tandem, reducing costs.

2 Literature Survey

Most studies concerning with scheduling and attributing simulations with regards to healthcare institutions have been focused toward patient scheduling [2]. Significant number of studies have catered to the requirement of scheduling staff while accommodating the patient demand and maintaining the patient arrivals unaltered. Other studies proposed another approach which significantly minimized average patient waiting time replicating the nurse's tasks in an emergency section [3]. Reference [4] studied several nurse-scheduling alternatives and deduced a method that offered maximum nurse utilization. But most of the authors had concentrated on scheduling the patients which is an unprecedented and daunting task. Reference [5] formulated the simulation model for varied patient mix, analyzed the model based on the patient sequences and identified the best patient sequence that reduced the patient waiting time. References [6–10] have formulated model for optimizing the doctor schedule, and [11] summarized prime issues in managing patient appointment systems. Reference [12] had developed a two-stage heuristic algorithm based on simulation for optimizing outpatient appointment draft.

From the literature review, the following points are evident:

- Many studies did not consider the supporting sections like x-ray, lab, etc.
- Most studies assumed an absence of secondary consultation.
- Many studies out forward the problem as a single-server system, with assumptions that a single physician was only present to cater to consultations.
- Many studies consider scheduling of either doctor or nurse resources.

Hence, this study will consider the supporting sections also for analyzing the patient flow, and here, the secondary consultation after testing was also considered. Also, this thesis considered the scheduling of both doctors and nurse resources.

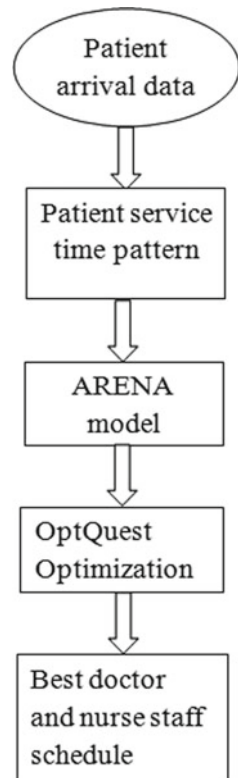
3 Methodology

In this paper, the discrete simulation model of an outpatient section was created. The real-time data of the patient arrival was collected from the outpatient department of the Government Rajaji Hospital, Madurai. The percentage of patient's visiting each

section was calculated from the collected patient arrival data in each section, and it will be given as the input to the simulation model. The service time for the patients in each section was collected from the patients, and the way in which it was varying is identified by using the input analyzer which is a tool in the ARENA package. The equation framed by the input analyzer will be given as the delay time of the process in the simulation model.

Then, the simulation model was simulated a number of times integrated with the OptQuest software for finding the suitable doctor and nurse schedule that will minimize the patient delay. The proposed methodology is explained in the flow diagram as shown in Fig. 1.

Fig. 1 Flowchart of proposed method



Best Solutions																		
Select	Simulation	Objective Value	Status	Doctor1	Doctor10	Doctor2	Doctor3	Doctor4	Doctor5	Doctor6	Doctor7	Doctor9	Staff	staff 4	Staff1	Staff2	Staff3	
<input type="checkbox"/>	119	7.157148	Feasible	2	2	3	2	2	2	2	2	2	2	2	2	3	1	2
<input type="checkbox"/>	16	7.591162	Feasible	2	2	3	2	2	2	2	2	2	2	2	2	3	2	2
<input type="checkbox"/>	131	8.084631	Feasible	2	2	3	2	2	2	2	2	2	2	1	4	2	2	2
<input type="checkbox"/>	125	8.614531	Feasible	2	2	3	2	2	2	2	2	2	2	1	1	3	2	2
<input type="checkbox"/>	73	9.140894	Feasible	2	2	3	2	2	2	2	2	2	2	1	2	3	2	2
<input type="checkbox"/>	135	10.526958	Feasible	2	2	3	2	2	2	2	2	2	2	2	2	2	2	2
<input type="checkbox"/>	93	10.685340	Feasible	2	2	3	2	2	2	2	2	2	2	3	2	2	2	2
<input type="checkbox"/>	137	11.258097	Feasible	2	2	3	3	2	2	2	2	2	1	2	1	3	2	2
<input type="checkbox"/>	72	12.185899	Feasible	2	2	3	3	2	2	2	2	1	2	2	3	2	2	2
<input type="checkbox"/>	124	12.797332	Feasible	3	2	3	2	2	2	2	1	2	1	3	3	2	2	2

Fig. 2 Optimum doctor schedule framed by the OptQuest software. *Doctor1—Neurology, Doctor2—General, Doctor3—Gallbladder, Doctor4—Paralysis, Doctor5—Recheckup, Doctor6—Siddha, Doctor7—Heart, Doctor9—Brain nerve, Doctor10—Urology, Staff-Tablet distribution, Staff1—Lab, Staff2—Xr-ray registration, Staff3—Biometric lab

4 Simulation Model

4.1 Description of Outpatient Department

There are ten different types of departments where the patients visit based on the required consultation service. They are nerve disorder, general, paralysis, heart, recheckup, Siddha, gallbladder, brain nerve, urology and X-ray section. During the consultation, the doctor decides the tests to be undertaken: blood, urinary, X-ray or endoscopy tests or the patient needs to be sent to the treatment room or needed to be admitted in bed. Patients must consult the same doctor before they get discharged from the hospital. Following the second consultation, patients can get discharged. Before the consultation starts or after the consultation, the patients will undergo basic analysis like weight checking, blood pressure measurement, etc., by nurse staff in their corresponding consultation sections. In this hospital, the specialist doctors can also give consultation to the patients in the general section. Likewise, the doctors in the general section can give consultation to the patients in other special sections. Here, the ARENA model with and without the nurse staff resources is shown in Figs. 2, 3, 4, 5, 6 and 7. The patient arrivals of each section are given in Tables 1 and 2.

4.2 Doctor and Nurse Schedule

The simulation model alone is not enough to find the optimum doctor schedule. The simulation model can only be used to find the performance measures of the model by analyzing the waiting time of the patient. Hence, our study integrated the simulation with the optimizing tool in ARENA named OptQuest. Here, the motive of the optimization tool is to reduce the average waiting time of patients for all

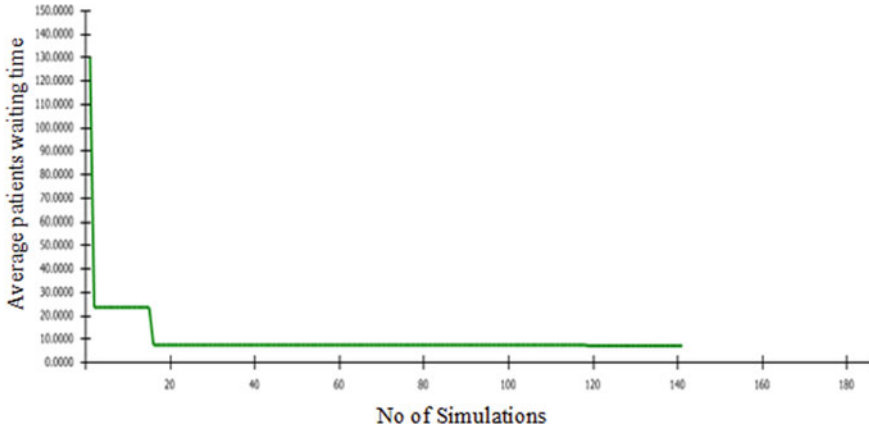


Fig. 3 Simulations done to obtain the optimum value

Simulation	Objective Value	Status	Doctor1	Doctor2	Doctor3	Doctor4	Doctor5	Doctor6	Doctor7	Doctor9	Nurse B	Nurse G	Nurse H	Nurse N	Nurse O	Nurse U	Staff	staff 4	Staff1	Staff2	Staff3	Staff4	
111	7.899485	Feasible	2	2	3	2	2	2	2	2	3	3	2	2	1	2	2	2	3	2	1	2	2
185	7.899485	Feasible	2	2	3	2	2	2	2	2	2	3	2	2	1	2	2	2	3	2	1	2	2
176	8.251659	Feasible	2	1	3	3	2	2	2	2	2	4	2	2	1	2	2	2	3	2	1	2	2
161	8.613144	Feasible	2	2	3	2	2	2	2	2	2	4	2	2	1	2	2	2	3	2	2	2	2
198	8.663463	Feasible	2	2	3	2	2	2	2	2	3	3	2	2	1	2	2	2	2	2	2	3	2
116	8.872077	Feasible	2	2	3	2	2	2	2	2	3	3	2	2	1	2	2	2	3	2	2	2	2
204	8.967680	Feasible	2	1	3	3	2	2	2	2	2	3	2	2	1	2	2	2	3	2	2	2	2
125	8.967680	Feasible	2	1	3	3	2	2	2	2	3	3	2	2	1	2	2	2	3	2	2	2	2
208	9.183287	Feasible	2	1	3	3	2	2	2	2	3	2	2	2	1	2	2	2	3	2	1	2	2
176	9.201278	Feasible	2	2	3	2	2	2	2	2	2	3	2	2	1	2	2	2	3	2	2	2	2
187	9.254324	Feasible	2	1	3	3	2	2	2	2	3	2	2	2	1	2	2	2	4	2	1	2	2
76	9.454026	Feasible	2	1	3	3	2	2	2	2	3	3	2	2	1	2	2	2	3	2	1	2	2
196	9.551403	Feasible	2	2	3	2	2	2	2	2	3	2	2	2	1	2	2	3	2	3	2	2	2
122	9.988698	Feasible	2	1	3	3	2	2	2	2	2	4	2	2	1	2	2	2	3	2	2	2	2
185	10.158526	Feasible	2	1	3	3	2	2	2	2	1	4	2	2	1	2	2	2	3	2	2	2	2
127	10.231927	Feasible	2	1	3	3	2	2	2	2	3	2	3	2	1	2	2	2	4	2	1	2	2
209	10.232127	Feasible	2	1	3	3	2	2	2	2	3	2	3	2	1	2	2	2	3	2	1	2	2
84	10.444378	Feasible	2	1	3	2	2	2	2	3	2	2	2	2	1	2	2	2	3	2	2	2	2
115	10.444378	Feasible	2	1	3	2	2	2	2	3	2	2	2	2	1	2	2	3	2	3	2	2	2
195	10.444378	Feasible	2	1	3	2	2	2	2	3	2	2	2	2	1	2	2	2	3	2	2	2	2

Fig. 4 Optimum doctor and nurse staff schedule framed by the OptQuest software. *Doctor1—Neurology, Doctor2—General, Doctor3—Gallbladder, Doctor4—Paralysis, Doctor5—Recheckup, Doctor6—Siddha, Doctor7—Heart, Doctor9—Brain nerve, Doctor10—Urology, Staff-Tablet distribution, Staff1—Lab, Staff2—X-ray registration, Staff3—Biometric lab, NurseG—General, NurseN—Neurology, NurseGa—Gallbladder, NurseH—Heart, NurseO—Recheckup, NurseP—Paralysis, NurseU—Urology, NurseB—Brain nerve

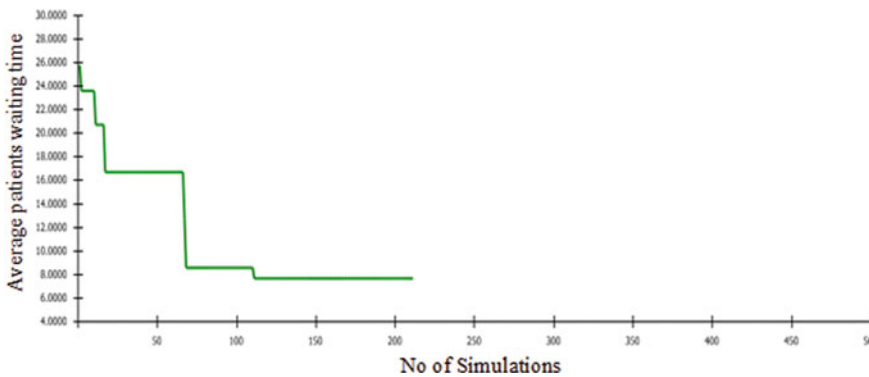


Fig. 5 Simulations done to obtain the optimum value

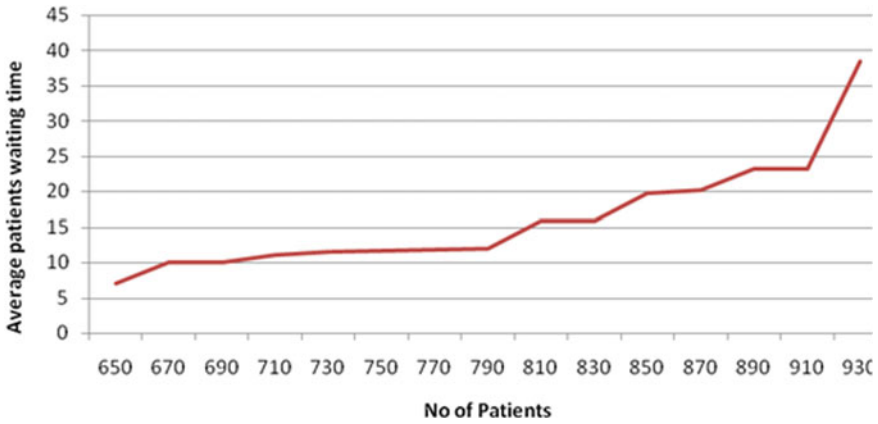


Fig. 6 Sensitivity analysis—optimum doctor schedule

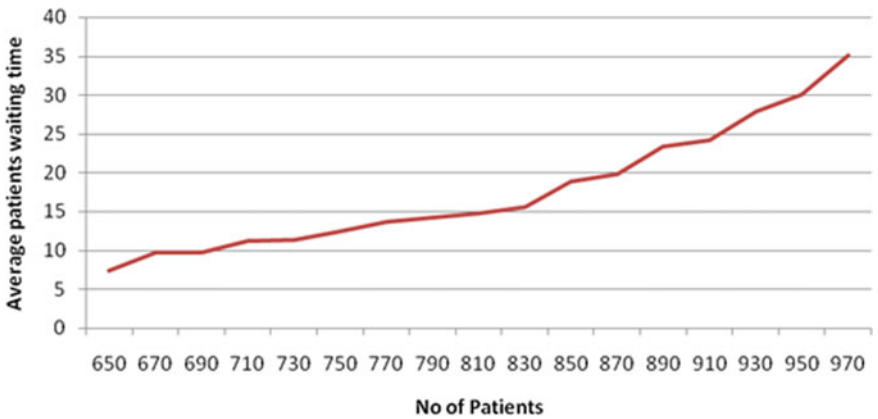


Fig. 7 Sensitivity analysis—optimum doctor and nurse staff schedule

sections. The currently existing total doctors in our case are twenty-two, the existing total number of staff is eleven, and the existing total number of the nurse staff is fifteen. The OptQuest will allocate the number of doctors and nurse staff for each section from the existing resources without adding any new resources to the total resources.

4.3 Model Formulation

The major performance measure taken in this study is the waiting time of each patient. Here, the performance measure is the patient waiting time. The objective

Table 1 Patient arrival data for each section

Sections	08-Sep	09-Oct	10-Nov	11-Dec	%
Neurology	13	12	38	14	11.34
General	21	48	62	45	27.07
Paralysis	12	19	28	18	11.84
Gallbladder	6	16	36	18	11.69
X-ray	4	9	7	9	4.46
Heart	17	25	34	11	13.38
Brain nerve	–	–	30	12	6.45
Siddha	3	3	5	4	2.76
Recheckup after operation	–	–	29	4	5.07
Urology	–	–	26	22	7.38
X-ray registration	3	4	2	2	3.72
Lab	8	13	12	10	14.57
Biometric lab	8	15	10	7	13.56
Tablet Distribution	20	57	72	52	68.14

Table 2 Distribution patterns of the service time in each section

Sections	Expression of the service time
Nerve	4.5 + 16 * BETA(0.269, 0.184)
General	4.5 + 16 * BETA(0.451, 0.511)
Gallbladder	9.5 + 11 * BETA(0.397, 0.275)
Heart	9.5 + 6 * BETA(0.0694, 0.0972)
Brain nerve	9.5 + 21 * BETA(0.213, 0.0994)
Siddha	9.5 + 6 * BETA(0.0875, 0.262)
Paralysis	9.5 + 11 * BETA(0.397, 0.275)
Tablet distribution	NORM(2, 0.632)
X-ray department	19.5 + 11 * BETA(0.0994, 0.213)
Urology	9.5 + 11 * BETA(0.275, 0.397)
Recheck	4.5 + 16 * BETA(0.511, 0.451)
Biometric lab	9.5 + 16 * BETA(0.511, 0.451)
Lab	14.5 + 6 * BETA(0.0972, 0.0694)
X-ray registration	TRIA(0.5, 1.8, 2.5)

is to minimize the patient idle time which is given in the below equation, and the resource constraints for the model are given in the Eqs. 1–4.

Minimize

$$WT = \frac{1}{N} \sum_{i=0}^N WT_i$$

Subject to

$$x_1 + x_2 + x_3 + \dots + x_{10} \leq 19 \quad (1)$$

$$y_1 + y_2 + y_3 + y_4 \leq 11 \quad (2)$$

$$n_1 + n_2 + \dots + n_{10} \leq 15 \quad (3)$$

$$x_i, y_i \geq 1 \quad (4)$$

where

- WT Weighted average patient waiting time.
 WT_{*i*} Time difference between consultation start time and actual arrival time.
 N Number of patients.
 x_{*i*} Number of doctors allocated for *i*th consulting sections.
 y_{*i*} Number of staffs allocated for *i*th supporting sections.
 n_{*i*} Number of nurse staffs allocated for *i*th consulting section.

5 Results and Discussion

5.1 Simulation Results

The model had simulated in integration with the optimization software OptQuest. Simulation was done for 200 times. The doctor resource location is shown in Table 3. From the analysis, it is clear that the waiting time of patients is lesser with the new doctor schedule and nurse staff schedule. The comparison of the average waiting time, patients arrived, patients attended is shown in Table 4 for the schedule with doctor resource and in Table 5 for the schedule with nurse schedule. By analyzing the outcomes, it is known that the doctors and nurses are contributing to the patients waiting times but the scheduling of the doctoral resources is contributing more in reducing the waiting time as shown in Figs. 2, 3, 4 and 5.

5.2 Sensitivity Analysis

Sensitivity analysis is a methodology, used to estimate outcomes of a decision, in case the resulting scenario turns out to be contrasting, when compared to the key predictions. Sensitivity analysis also holds good in determining the impact of a particular variable on the actual outcome if the value for the variable is altered from

Table 3 Doctor resource allocation

Sections	Current Number of resources	Proposed Number of resources
Nerve disorder	2	2
General	2	3
Paralysis	2	2
Gallbladder	3	2
X-ray department	3	2
Heart	2	2
Brain nerve	2	2
Siddha	2	2
Recheckup	2	2
Urology	2	2
X-ray registration	2	1
Lab	2	3
Biometric lab	2	2
Tablet distribution	2	2

Table 4 Comparison between the present and proposed schedule

	Present schedule	Proposed schedule
Average waiting time (min)	19	7
Patients arrived	675	659
Patients attended	641	648
Patients waiting	34	11

Table 5 Comparison between the present and proposed schedule with nurse resource

	Present schedule	Proposed schedule
Average waiting time (min)	24	7
Patients arrived	682	611
Patients attended	654	585
Patients waiting	28	26

the actual one. By the creation of a given scenario set, the analyst is able to determine how alterations of a particular variable could impact the target variable. In this thesis, the impact of various patient arrivals for the proposed schedule is analyzed. The graph for the various patient arrivals is given in Figs. 6 and 7.

By doing the sensitivity analysis on the optimal schedule, the effect due to the various patient arrivals on the optimal schedule is found. From a study, released by the Royal College of Physicians, it is known that the tolerable maximum delay time for getting consultation in an outpatient department of a hospital is 30 min. By

keeping the 30 min waiting time as the upper limit, the optimal schedule may be best used up to the patient arrival of 910. The optimal schedule along with the nurse staff may be best used up to the patient arrival of 940. By keeping the waiting time as 15 min, the optimal schedule of the doctor schedule may work best up to the patient arrival of 810. The optimal schedule along with the nurse resource will work best up to the patient arrival of 830.

6 Conclusion

The most affected section due to the patient idle time in the hospital is the outpatient department. This idle time of the patients is due to the improper scheduling of the available resources. This thesis reduced the patient waiting time by finding the optimal doctor and nurse staff schedule using the OptQuest software. By implementing the proposed doctor schedule, the waiting time is reduced up to 63%. By implementing the proposed optimal schedule with the doctor and nurse staff, the waiting time is reduced up to 70.83%. The sensitivity analysis is done to find the effect on the optimal schedule due to the variations in the patient arrival. By fixing maximum allowable waiting time as 30 min, the optimal schedule with doctor resource alone may be best up to the patient arrival of 910. The optimal schedule along with nurse staff schedule may be best up to the patient arrival of 940.

References

1. Wijeckrama AKA, Takakuwa S (2006) Simulation analysis of an outpatient department of internal medicine in a university hospital. In: Proceedings of the winter simulation conference, pp 425–432
2. Wijeckrama AKA, Takakuwa S (2008) Outpatient appointment scheduling in a multi facility system. In: Proceedings of the winter simulation conference, pp 1563–1571
3. Draeger MA (1992) An emergency department simulation model used to evaluate alternative nurse staffing and patient population scenarios. In: Proceedings of the winter simulation conference, pp 1057–1064
4. Kumar AP, Kapur R (1989) Discrete simulation application—scheduling staff for the emergency room. In: Proceedings of the winter simulation conference, pp 1112–1120
5. SyiSu C-L (2003) Managing a mixed-registration-type appointment system in outpatient clinics. *Int J Med Inform* 70:31–40
6. Erhard M, Schoenfelder J, Fügener A, Brunner JO (2018) State of the art in physician scheduling. *Eur J Oper Res* 265(1):1–18
7. Mansini R, Zanotti R (2020) Optimizing the physician scheduling problem in a large hospital ward. *J Sched* 23:337–361
8. Schoenfelder J, Pfefferlen C (2018) Decision support for the physician scheduling process at a German hospital. *Serv Sci* 10(3):215–229
9. Niroumandrad N, Lahrichi N (2018) A stochastic tabu search algorithm to align physician schedule with patient flow. *Health Care Manag Sci* 21(2):244–258
10. Bowers MR, Noon CE, Wu W, Bass JK (2016) Neonatal physician scheduling at the University of Tennessee Medical Center. *Interfaces* 46(2):168–182

11. Gupta D, Denton B (2008) Appointment scheduling in health care: challenges and opportunities. *IIE Trans* 40:800–819
12. Lin CKY, Ling TWC, Yeung WK (2017) Resource allocation and outpatient appointment scheduling using simulation optimization. *J Healthc Eng* 2017(9034737)

Material Removal Rate and Surface Roughness Prediction in Turning and Milling Operations Using Taguchi Analysis, Support Vector Machine and Gaussian Process Regression



V. Vakharia , J. Sanghvi, and H. Thakker

Abstract In the present methodology, the influence of operating parameters on surface roughness and material removal rate for the specimen manufactured through turning and milling is evaluated using the Design of Experiment, and optimization was done with Taguchi analysis. The operating parameters investigated were speed, feed, and depth of cut with three levels. Further two machine learning models were used and results are compared to predict surface roughness and material removal rate. Training with 70% of experimental data and testing with 30% of experimental data from DOE was done for both the models. It is observed that the lowest error of 0.20% and the highest correlation of 0.96 using testing was observed when the material removal rate is predicted using SVM for the specimen manufactured through turning operation. Also, proximity observed between predicted and experimental measured value.

Keywords Design of experiment · Taguchi · Surface roughness · Material removal rate · SVM · GPR

1 Introduction

In a manufacturing industry, surface roughness is a significant parameter which affects the machining accuracy, and higher material removal rate (MRR) is also desirable for high production rate without compromising the quality of machined component [1]. Roughness of machined component represents texture of a surface and is examined by profilometer. Surface roughness and MRR depend on machining parameters, the material of tool and workpiece, tool geometry, etc. Higher MRR can be accomplished through optimizing the process parameters like cutting velocity, feed, and depth of cut [2, 3]. Thus, the determination and selection of process parameters are crucial for the manufacturing of good quality products with a higher production rate. Better surface finish and high MRR can be obtained by selecting the suitable

V. Vakharia (✉) · J. Sanghvi · H. Thakker
Pandit Deendayal Petroleum University, Gandhinagar, Gujarat 382007, India
e-mail: vinay.vakharia@sot.pdpu.ac.in

level of optimal parameters [4, 5]. Design of Experiment (DOE) is a statistical technique in which orthogonal arrays are utilized to take in to account the inclusion of variations of all the machining parameters. It is also used to determine the underlying relationship between the varying machining parameters and output [6]. Regression analysis is a mathematical modeling technique that allows determining the relationship between the varying operating parameters and the measured experimental value. Machine learning-based regression modeling effectively maps the association between the input and the target value based on historical data. Machine learning models have been used by various authors for the Prediction of machined surfaces [7, 8], Prediction of compressive strength [9], and Roughness (Ra) Prediction in additive manufacturing of Titanium alloy [10], etc. Shakeri et al. [11] examined the influence of variation of machined parameters on MRR and surface roughness using linear regression and ANN. Experiments were conducted with variation in input parameters like pulse current, pulse frequency, wire speed etc. in electro-discharge machining for alloy steel. After comparing the results, ANN gives better accuracy for prediction. In another study, RSM based approach was developed by Shandley et al. [12], to predict the MRR in the Electric discharge diamond grinding process. A second-order quadratic polynomial regression model was developed to investigate the relationship between input and predicted parameter. Results are compared and validated with ANN and it was found that the predicted results were close to the experimental results.

In the present study, the authors conducted an experimental study using milling and turning operations using the design of experiments and Taguchi analysis. Twenty-seven experiments for each operation were conducted with varying operating parameters and MRR, surface roughness was experimentally determined. A machine learning model was developed and results are validated using SVM and Gaussian Process Regression (GPR). Figure 1 shows the methodology used by the authors.

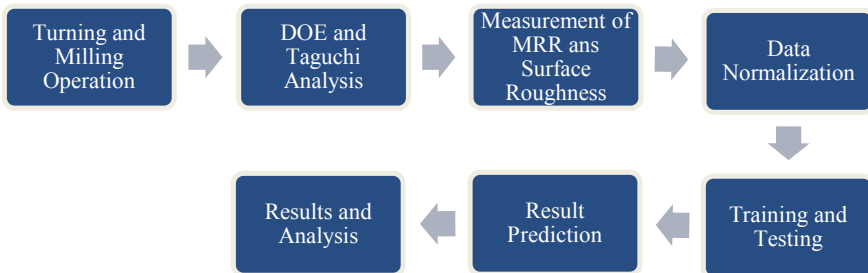


Fig. 1 Flowchart of methodology for prediction of MRR and surface roughness

2 Regression Model Using Machine Learning Techniques

Machine learning techniques can be used for classification and prediction. Since the objective of the presented work is to predict MRR and surface roughness, therefore authors have used the regression model of SVM and GPR. Support Vector Regression (SVR) extends the combined concept of the kernel, hyperplane, and decision boundary from the basic formulation of SVM to create a regression model to make predictions for the experimental data. Structural risk minimization is implemented in SVR to achieve generalization capability. As compared to linear regression or Ridge regression, SVR is much more flexible in defining the acceptable limit of the error to find the hyperplane. In the present study, a nonlinear quadratic kernel was considered. GPR is a nonparametric kernel-based probabilistic model, which uses the Bayesian approach for implementing regression modelling. The probability distribution is calculated on all admissible functions, rather than the specific function which fits the data. In this method, a prior distribution $p(z)$ is specified and probabilities are relocated based on the training data. The Prior distribution is updated using Bayes' Rule to get a new distribution known as Posterior distribution which is finally used for prediction.

3 Experiment Details and Taguchi Analysis

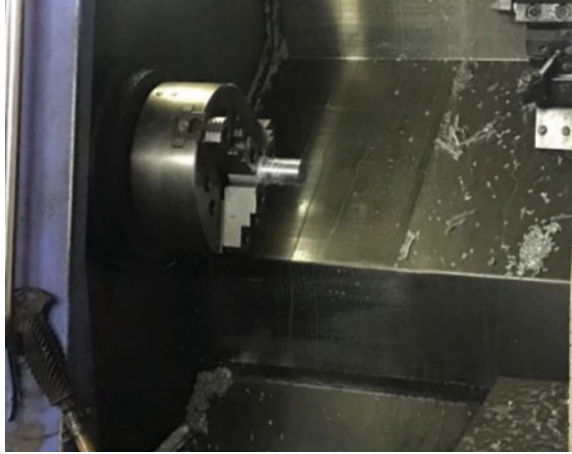
In the study, 27 experiments each on CNC milling and turning was performed with variations in operating parameters like Cutting Speed, Feed, and Depth of Cut (DOC). For the conduction of the experiment multilevel factorial designed carried out using Design of Experiments (DOE). The experiment for turning was carried out on an Aluminium rod of diameter 25 and 500 mm length on 'VX-135 Junior' CNC Lathe as shown in Fig. 2. Milling operation is carried out on an Aluminium plate of 12 mm thickness using a conventional milling machine having an automatic feed as shown in Fig. 3. Surface Roughness R_a is measured through Surface Roughness profilometer, for all the samples Fig. 4. Surface roughness for all the 54 cases is measured at three different locations and the average R_a value is recorded. MRR represents the volume of material removed in per unit time from the surface of the workpiece and is calculated using the formula:

$$\text{MRR} = (\text{Initial Weight} - \text{Final Weight}) / \text{Turning operation time} \quad (1)$$

Table 1 shows the summary of R_a and MRR. S/N ratio for R_a and MRR is mathematically expressed as:

$$S/N = -10 * \log(\Sigma(Y^2)/n) \quad (2)$$

$$S/N = -10 * \log(\Sigma(1/Z^2)/n) \quad (3)$$

Fig. 2 CNC turning setup**Fig. 3** Milling experiment setup

here Y and Z , represents R_a and MRR.

Mean S/N for R_a for turning and milling specimen are shown in Tables 2 and 3 respectively. Similarly, the mean S/N graph for surface roughness for turning and milling is shown in Figs. 5 and 6 respectively. As seen from Table 2, the delta value for feed is very high as compared to speed and DOC, so it can be concluded that R_a value depends mostly on feed which can be observed from Fig. 6. Similarly, the effect of DOC and speed is found to be comparatively less from main effect plot. Optimal results corresponding to the highest S/N ratio values are reflected in the main effect plot. Thus, the optimal values for R_a in Milling are as follows: cutting speed at level 3 (380), feed at level 1 (20), and DOC at level 2 (1 mm) respectively.

Similarly, response for MRR of turning and milling experiments is shown in Tables 4 and 5 respectively and the mean S/N graph are represented in Figs. 7 and



Fig. 4 Surface roughness measurement

Table 1 Summary of R_a and MRR

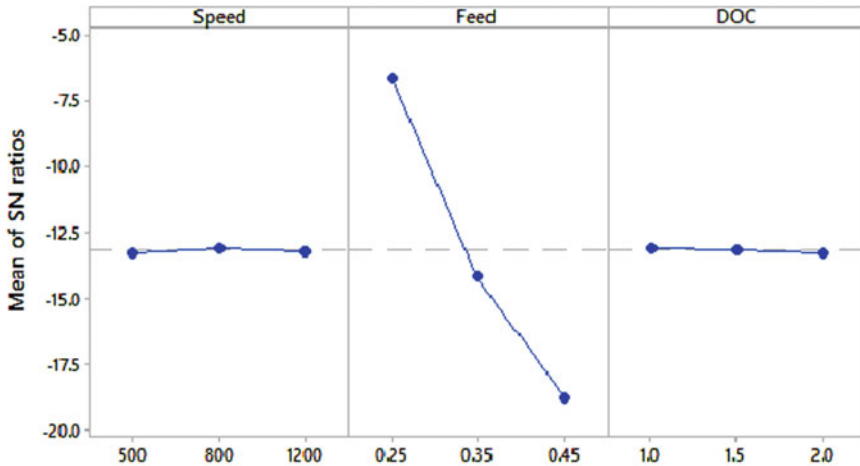
Response	Minimum	Maximum	Mean
R_a (Turning) μm	2.03	9.02	5.32
MRR (Turning) mm^3/s	0.64	5.05	2.13
R_a (Milling) μm	0.47	1.59	1.04
MRR (Milling) mm^3/s	0.24	2.45	0.96

Table 2 Mean S/N ratio response for R_a in turning

Level	Speed	Feed	DOC
1	-13.291	-6.623	-13.113
2	-13.1	-14.172	-13.171
3	-13.213	-18.808	-13.32
Delta	0.191	12.184	0.207
Rank	3	1	2

Table 3 Mean S/N ratio response for R_a in milling

Level	Speed	Feed	DOC
1	-0.573	2.469	-0.05026
2	0.329	-0.74673	0.432
3	0.341	-1.6244	-0.28406
Delta	0.9147	4.093	0.715
Rank	2	1	3



Signal-to-noise: Smaller is better

Fig. 5 Main effect plot for R_a in turning

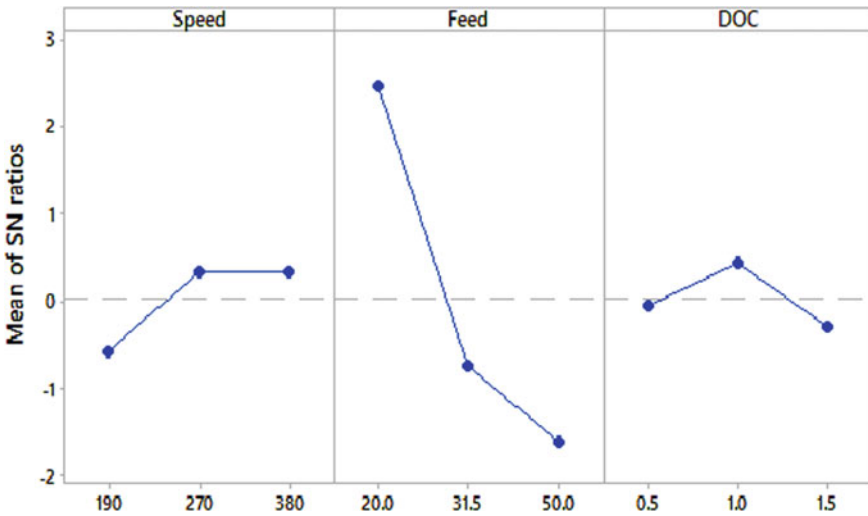


Fig. 6 Main effect plot for R_a in milling

Table 4 Mean S/N ratio response for MRR in turning

Level	Speed	Feed	DOC
1	1.704	2.764	2.831
2	5.623	5.652	5.975
3	9.274	8.193	7.805
Delta	7.57	5.429	4.973
Rank	1	2	3

Table 5 Mean S/N ratio response for MRR in milling

Level	Speed	Feed	DOC
1	-0.7915	-5.147	-5.019
2	-0.8728	-3.004	-1.512
3	-3.3413	3.1466	1.525
Delta	2.549	8.2952	6.5432
Rank	3	1	2

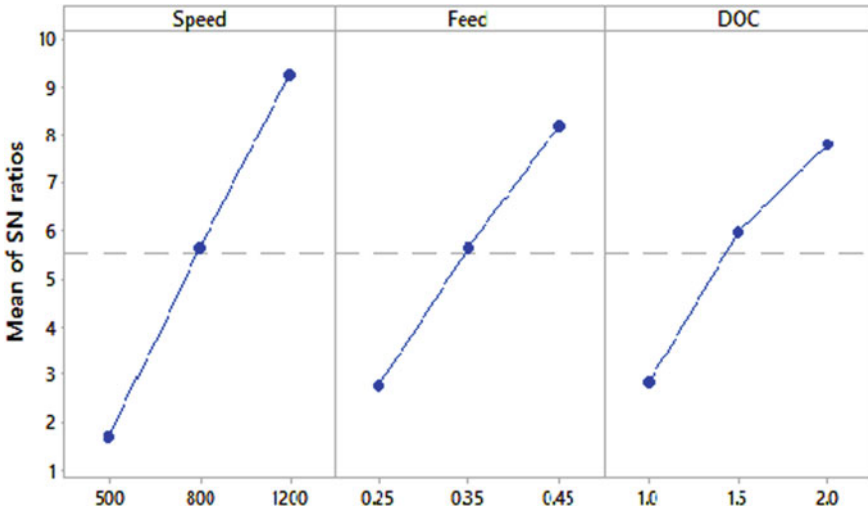


Fig. 7 Main effect plot for MRR in turning

8 respectively. Based on the main effect plot, the effects of variation of all the three varying process parameters can be analyzed. It is observed from Fig. 7, in the case of a specimen prepared from turning there is no specific contribution of single operating parameters on MRR is observed. From Table 5, an increase in speed governs higher MRR followed by feed and DOC. The optimal process parameters for MRR in turning are as follows: cutting speed at level 3 (1200), feed at level 3 (0.45) and DOC at level 3 (2 mm) and cutting speed at level 1 (190), feed at level 3 (50) and DOC at level 3 (1.5 mm) for milling respectively, as seen from Table 5 and Fig. 8 respectively.

4 Prediction Using Machine Learning Techniques

The predicted results from SVM and GPR machine learning models are reflected in Tables 6 and 7. The DOE data is split into training and testing in which 70% of experimental readings are used for training of model and rest 30% for testing. To consider nonlinearity in the model quadratic and exponential kernel functions are

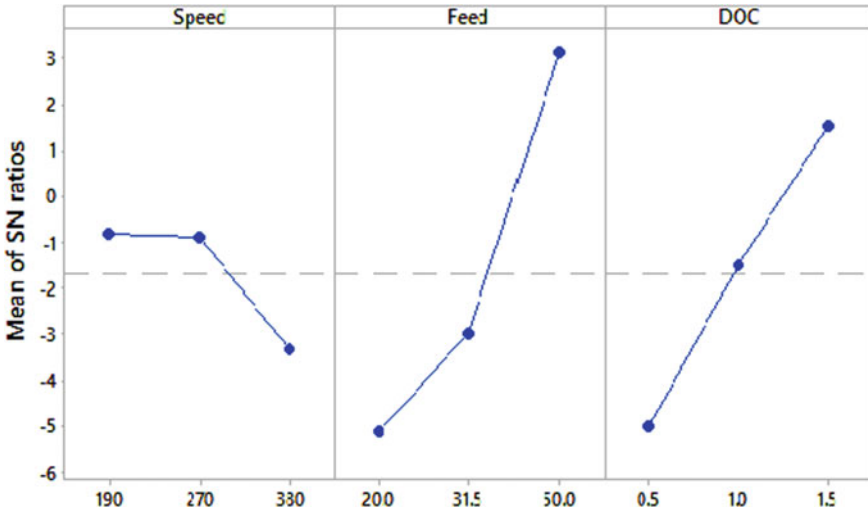


Fig. 8 Main effect plot for MRR in milling

Table 6 Prediction results based on statistical parameters and SVM

Parameter	Method	RMSE	R ²	Process
Turning MRR	Training	0.09	0.99	Exponential GPR
	Testing (30% held out)	0.27	0.96	
Turning R _a	Training	0.38	0.98	
	Testing (30% held out)	0.44	0.97	
Milling MRR	Training	0.21	0.83	
	Testing (30% held out)	0.24	0.83	
Milling R _a	Training	0.22	0.49	
	Testing (30% held out)	0.24	0.36	

Table 7 Prediction results based on statistical parameters and exponential GPR

Parameter	Method	RMSE	R ²	Process
Turning MRR	Training	0.0	1	Quadratic SVM process
	Testing (30% held out)	0.38	0.92	
Turning R _a	Training	0.0	1	
	Testing (30% held out)	0.50	0.86	
Milling MRR	Training	0.0	1	
	Testing (30% held out)	0.21	0.86	
Milling R _a	Training	0.0	0.99	
	Testing (30% held out)	0.26	0.85	

used in SVM and GPR respectively. After observing Tables 6 and 7, better prediction result for R_a is observed for turning specimens through Exponential GPR as compared to Quadratic SVM. Similarly, better prediction result for R_a is observed for milling specimen through Exponential GPR as compared to Quadratic SVM, since it gives a lower RMSE value and higher R^2 value. To predict MRR for turning specimen, SVM gives better results as compared to GPR whereas in the case of milling; GPR gives better prediction results as compared to SVM which can be observed from the respective tables.

5 Conclusion

The effect of operating parameters like speed, feed and DOC on the specimen manufactured from Turning and Milling operations on MRR and Surface roughness has been investigated in detail in present study. Machining operations carried out according to DOE and optimize process parameters were obtained using Taguchi analysis considering S/N ratio. To predict the output like MRR and Surface roughness, machine learning models such as SVM and GPR applied. Following observations can be made:

- In case of turning operation, to predict both MRR and R_a , SVM gives better prediction results as compared to GPR.
- In case of milling operation, to predict both MRR and R_a , GPR gives better prediction results as compared to SVM.
- Considering both training and testing, GPR prediction results are better than SVM.

Better accuracy can be obtained with a greater number of experiments and detailed investigation can be carried out in future with applications of more machine learning algorithms.

Acknowledgements Authors acknowledge the financial support provided by ORSP PDPU Gandhinagar to conduct experimental study.

References

1. Touggui Y, Belhadi S, Mechraoui SE et al (2020) Multi objective optimization of turning parameters for targeting surface roughness and maximizing material removal rate in dry turning of AISI316L with PVD coated cermet insert. S N Appl Sci 2:1360
2. Sahoo AK, Baral AN, Rout AK, Routra BC (2012) Multi-objective optimization and predictive modelling of surface roughness and material removal rate in turning using grey relational and regression analysis. Procedia Eng 38:1606–1627
3. Singh NK, Pandey PM, Singh KK (2019) A semi-empirical model to predict material removal rate during air-assisted electrical discharge machining. J Braz Soc Mech Sci Eng 41:122

4. Patel M, Lokare D, Chate GR et al (2019) Analysis and optimization of surface quality while machining high strength aluminium alloy. *Measurement* 153(1):107337
5. Devarajaiah D (2019) Muthumari C: Fuzzy logic-integrated PSO methodology for parameters optimization in end milling of Al/SiC_p MMC. *J Braz Soc Mech Sci Eng* 41:222
6. Karim MR, Siddique RA, Dilwar F (2020) Study of surface roughness and MRR in turning of SiC reinforced Al alloy composite using Taguchi design method, ANN and PCA approach under MQL cutting condition. *Adv Mater Res* 1158:115–131
7. Vakharia V, Kiran MB, Dave NJ, Kagathara U (2017) Feature extraction and classification of machined component texture images using wavelet and artificial intelligence techniques. In: 8th International conference on mechanical and aerospace engineering 2017 ICMAE. IEEE Xplore, pp 140–144
8. Patel DR, Thakker H, Vakharia V, Kiran MB (2020) Surface roughness prediction of machined components using gray level co-occurrence matrix and bagging tree. *FME Trans* 48:468–475
9. Vakharia V, Gujar R (2019) Prediction of compressive strength and portland cement composition using cross-validation and feature ranking techniques. *Constr Build Mater* 225:292–301
10. Li Z, Zhang Z, Shi J, Wu D (2019) Prediction of surface roughness in extrusion-based additive manufacturing with machine learning. *Robot Comput-Integr Manuf* 57:488–495
11. Shakeri S, Ghassemi A, Hassani M (2016) Investigation of material removal rate and surface roughness in wire electrical discharge machining process for cementation alloy steel using artificial neural network. *Int J Adv Manuf Technol* 82:549–557
12. Shandley R, Choudhary S, Jha SK (2019) Material removal rate prediction of EDDG of PCBN cutting tool inserts based on experimental design and artificial neural networks. *Appl Artif Intell Tech Eng* 689:481–489

Prediction of Angular Distortion in MIG Welding of Stainless Steel 202 Plates



Laksha, Preksha Bharti, and Pradeep Khanna

Abstract Metal inert gas (MIG) welding is a popularly used arc welding process for the joining of materials. The process can weld successfully all the materials for which suitable filler material is available. The process is preferred by the fabrication, automotive, food processing and chemical industries owing to its versatility, all-position welding capability, portability and adaptability to fully automatic and robotic welding. The present study is carried out to understand a very important characteristic of arc welding processes with MIG welding being no exception. During arc welding processes, the weld metal experiences non-uniform and rapid heating and cooling cycles. Moreover, the top surface of the weld receives more heat as compared to the bottom surface of the weld, thereby creating a thermal gradient across the thickness. The high heat content of the top surface results in its greater contraction as compared to its bottom-most layer. The distortion thus occurred in the cross-direction of the weld is known as angular distortion. Angular distortion once occurred may result in poor aesthetics, difficulty in the fitment of welded plates into the parent structure and sometimes rejection altogether. This distortion is very difficult and sometimes economically infeasible to remove during post-weld treatments. It is therefore the endeavour of the weld engineer to keep it to the lowest possible extent. An attempt has been made to relate this distortion with the input welding parameters via a mathematical model so that for any given setting of weld parameters the resulting angular distortion can be predicted and suitable preventive measures can be taken. The experiments have been designed using the statistical approach of central composite rotatable design. The sufficiency of the generated model was verified using analysis of variance (ANOVA) technique. Further, the results were graphically analysed using response surface methodology (RSM).

Keywords Angular distortion · MIG welding · Stainless steel · ANOVA · Mathematical modelling

Laksha · P. Bharti (✉) · P. Khanna (✉)
MPAE Division, NSUT, Dwarka, Delhi 110078, India

© The Author(s), under exclusive license to Springer Nature Singapore Pte Ltd. 2022
K. Govindan et al. (eds.), *Advances in Mechanical and Materials Technology*,
Lecture Notes in Mechanical Engineering,
https://doi.org/10.1007/978-981-16-2794-1_47

525



Fig. 1 Transverse section of angular distortion in a plate [6]

1 Introduction

MIG welding, a fusion joining procedure, is extensively used to weld a wide variety of materials in a good range of thickness. In this process, the arc is established between the workpiece and a continuously fed consumable wire electrode. The arc is being maintained between the workpiece and consumable electrode in the presence of inert gas atmosphere. Like other arc welding processes, the generation of intense heat in a localized area in the workpieces results in rapid heating and cooling cycles causing non-uniform expansion and contraction across the thickness of the weldment. It can be seen that the topmost layer of weldment has a tendency to contract more than the bottom-most layer, thereby causing transverse angular distortion of the weldment. Angular distortion turned out to be critical as far as performance, productivity and quality are concerned [1]. Post-welding heat treatment is required to control this kind of distortion [2]. Stainless steel 202 has been selected for the present investigation. It is an austenitic stainless steel with manganese as the alloying element, stainless steel 302 grade has similar properties as 202 grade, but the latter is much cheaper and a great substitute for 302 grade [3]. Welding of stainless steel turned out to be feasible by metal inert gas (MIG) welding [4]. Stainless steel has vast application in the aviation industry, food and catering industry and the automotive industry [5]. The statistical technique of face-centred composite (FCC) was used to analyse input parameters for angular distortion. A mathematical model was developed, and sufficiency of the generated model was verified using ANOVA. The generation of mathematical equation and surface plots, as well as ANOVA, was done using design of expert software (Fig. 1).

2 Equipment and Set-Up for Experimental Runs

For the experiment, a DC power source of current rating 200 A with drooping $V-I$ characteristics was used. To facilitate welding at different speeds, a mechanized carriage was used for welding. The mechanized carriage unit consisted of a welding table, a gearbox and driving motor. The movement of the welding table was facilitated by the gearbox arrangement with a variable frequency. Pure argon was used as the shielding gas. The consistency in the runs was achieved by using a rotating



Fig. 2 Experimental set-up

arm where the torch was attached and was capable of moving across the table. The set-up is shown in Fig. 2.

3 Summary of Research

The steps involved in the research can be sequentially arranged as given below:

- Identifying relevant input parameters
- Selecting working limits for input parameters
- Generating design matrix
- Performing experiments
- Recording results
- Generation of mathematical equation
- Examining model sufficiency
- Results and analysis
- Conclusions.

Table 1 Working limits of input parameters

Factor	Name	Units	(− 2)	(− 1)	(0)	(+ 1)	(+ 2)
A	WFR	m/min	0.3	0.6	0.9	1.2	1.5
B	WS	cm/min	30	35	40	45	50
C	Voltage	volts	14	16	18	20	22
D	NPD	mm	10	12.5	15	17.5	20
E	Torch angle	degrees	70	80	90	100	110

3.1 Identifying Relevant Input Parameters

Several trial experiments were conducted by taking different possible input variables to check their effect. It was established that voltage, wire feed rate (WFR), welding speed (WS), torch angle, nozzle–plate distance (NPD) and gas flow rate are the input variables affecting the angular distortion. A further close examination revealed that the effect of gas flow rate on angular distortion is insignificant and hence can be conveniently dropped from the list of selected input variables.

3.2 Selecting Working Limits for Input Parameters

The working limits of the short-listed variables were estimated by carrying out another series of experiments in which each variable was varied to see its effect on the weld quality. In this manner, the peripheral conditions of the parameters were estimated by taking into consideration a reasonably good quality of the weld. The lower limits were coded as (− 2) and the upper limit as (+ 2) with intermediate levels as (− 1) and (+ 1) while the mid-level as (0). The lower and upper limits with their coded values are shown in Table 1.

3.3 Generating Design Matrix

Statistical technique was used to create the design matrix for the present investigation. The approach of central composite rotatable design (CCRD) was found suitable for the present number of variables and their levels. CCRD is a hybrid approach that is a combination of fractional factorial points, centre points and star points. The design matrix was developed by using design of expert software and is given in Table 2. A total of 32 experimental runs were suggested by the design matrix.

Table 2 Design matrix

Std	Run	Factor 1 A: wire feed rate m/min	Factor 2 B: welding speed cm/mi n	Factor 3 C: voltage V	Factor 4 D: NPD mm	Factor 5 E: torch angle degree	Response 1 Angular distortion degrees
9	1	- 1	- 1	- 1	1	- 1	4.68
26	2	0	0	0	0	2	4.02
11	3	- 1	1	- 1	1	1	5.68
2	4	1	- 1	- 1	- 1	- 1	0.96
12	5	1	1	- 1	1	- 1	6.38
23	6	0	0	0	- 2	0	3.28
17	7	- 2	0	0	0	0	5.06
21	8	0	0	- 2	0	0	3.04
28	9	0	0	0	0	0	2
16	10	1	1	1	1	1	1.92
20	11	0	2	0	0	0	5.76
32	12	0	0	0	0	0	1
13	13	- 1	- 1	1	1	1	6.16
24	14	0	0	0	2	0	4.54
30	15	0	0	0	0	0	1.5
14	16	1	- 1	1	1	- 1	1.5
3	17	- 1	1	- 1	- 1	- 1	4.98
1	18	- 1	- 1	- 1	- 1	1	2.44
18	19	2	0	0	0	0	2.32
15	20	- 1	1	1	1	- 1	5.78
29	21	0	0	0	0	0	1
27	22	0	0	0	0	0	1.5
8	23	1	1	1	- 1	- 1	2.26
31	24	0	0	0	0	0	1
10	25	1	- 1	- 1	1	1	1.38
6	26	1	- 1	1	- 1	1	2.1
5	27	- 1	- 1	1	- 1	- 1	3.52
25	28	0	0	0	0	- 2	4.08
19	29	0	- 2	0	0	0	2.42
4	30	1	1	- 1	- 1	1	4.38
7	31	- 1	1	1	- 1	1	5.94
22	32	0	0	2	0	0	1.18

3.4 Performing Experiments

Experimental runs were carried out at the combination suggested in Table 2. For systematic error to be eliminated, the runs were carried out in a non-specific manner. The experimental runs were conducted by carefully setting each input parameter as suggested by the design matrix. All the prepared specimens were marked with a number to ensure that there is no confusion whatsoever later on.

3.5 Recording Results

The response parameter in the present case is angular distortion. It can be measured with the help of a set-up consisting of a properly levelled surface plate, a vernier height gauge and a dial test indicator. The dial test indicator was attached to the vernier height gauge such that the stylus of the same was used to ensure constant measuring pressure each time to ascertain consistency of the readings. The welded specimen was positioned on the surface plate and one side of the plates forced against the surface plate. The stylus of the dial test indicator was pressed against the edge of the pressed plate of the weld, and the dial was set to 0. This sets measuring pressure. The reading of height gauge at this instance was taken as R_1 . The height gauge was now moved towards the raised plate of the weld, and the stylus was pressed against the edge of the raised plate to an extent that the dial test indicator reads 0. The reading of the height gauge at this instance was taken as R_2 . The angular distortion can now be calculated by using the relation $\text{Sin } \theta = (R_2 - R_1)/W$, where θ is the angular distortion and w is the width of each plate. The same procedure was repeated on all the welded pieces, and values of all measured angular distortions were put in the relevant column of Table 2. The angular measurement set-up is shown in Fig. 3.

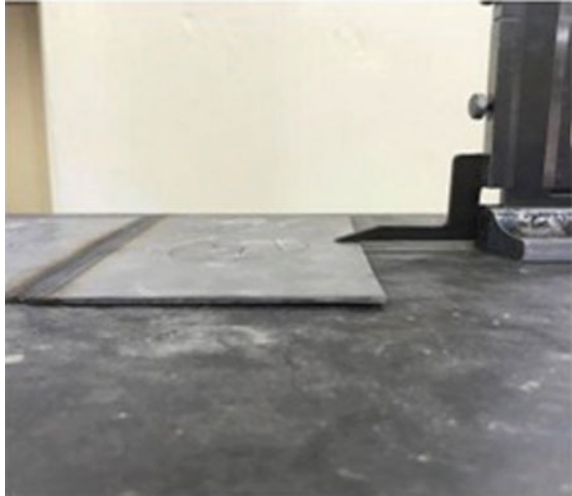
3.6 Generation of Mathematical Equation

The mathematical equation generated is as follows:

$$\begin{aligned} \text{Angular distortion} = & + 1.40 - 0.9908 * A + 0.8858 * B - 0.2258 * C + \\ & 0.3925 * D - 0.0075 * E + 0.2138 * AB - 0.5587 * AC - 0.2462 * AD - \\ & 0.1613 * AE - 0.5838 * BC - 0.1562 * BD - 0.1813 * BE - 0.2387 * CD + \\ & 0.3862 * CE - 0.3963 * DE + 0.5209 * A^2 + 0.6209 * B^2 + 0.1259 * C^2 + \\ & 0.5759 * D^2 + 0.6109 * E^2. \end{aligned}$$

This is a second-degree polynomial equation where direct effects and interaction effects of the input parameters are expressed. The square terms indicate the curvature of the surface plots given in the later sections. The higher-order terms and the interaction of three-parameter terms have been ignored as they are of little industrial consequence.

Fig. 3 Angle measuring set-up [7]



3.7 Examining Model Sufficiency

The sufficiency of the model that was developed was examined by using the technique of analysis of variance (ANOVA), where the values of F -ratio and R -ratio are calculated and analysed with their tabulated values for the relevant degrees of freedom. In case the calculated value of F -ratio and R -ratio comes out to be less than and greater than their respective tabulated values, the model is said to be appropriate. The results of the ANOVA as generated by the software are shown in Table 3, and it is apparent that the model that was developed is appropriate for the range of input parameter set for carrying out the investigations. The higher values of R^2 and adjusted R^2 as shown in Table 3 clearly suggest that the model is adequate. Further, the scatter diagram as given in Fig. 4 also confirms this claim as the predicted and actual values are plotted quite near to the central line (Table 4).

3.8 Results and Analysis

Effect of Wire Feed Rate and Welding Speed: It is predictable from Fig. 5 that there is a negative effect of WFR and a positive effect of WS on the angular distortion. That means, angular distortion decreases with increase in WFR and increases with increase in WS. The explanation could be that as the WS was increased the time for which the heat could spread into the joint was reduced, resulting in fast cooling. Rapid cooling of the joint was responsible for the greater amounts of distortion. With the increase in WFR, the heat could uniformly spread across the material and resulted

Table 3 ANOVA table

Source	Sum of squares	df	Mean square	F-value	p-value	
Model	98.64	20	4.93	16.14	< 0.0001	Significant
A: wire feed rate	23.56	1	23.56	77.12	< 0.0001	
B: welding speed	18.83	1	18.83	61.64	< 0.0001	
C: voltage	1.22	1	1.22	4.01	0.0706	
D: NPD	3.70	1	3.70	12.10	0.0052	
E: torch angle	0.0014	1	0.0014	0.0044	0.9482	
AB	0.7310	1	0.7310	2.39	0.1502	
AC	5.00	1	5.00	16.35	0.0019	
AD	0.9702	1	0.9702	3.18	0.1023	
AE	0.4160	1	0.4160	1.36	0.2679	
BC	5.45	1	5.45	17.84	0.0014	
BD	0.3906	1	0.3906	1.28	0.2822	
BE	0.5256	1	0.5256	1.72	0.2164	
CD	0.9120	1	0.9120	2.98	0.1120	
CE	2.39	1	2.39	7.81	0.0174	
DE	2.51	1	2.51	8.22	0.0153	
A ²	7.96	1	7.96	26.05	0.0003	
B ²	11.31	1	11.31	37.01	< 0.0001	
C ²	0.4650	1	0.4650	1.52	0.2430	
D ²	9.73	1	9.73	31.84	0.0002	
E ²	10.95	1	10.95	35.83	< 0.0001	
Residual	3.36	11	0.3055			
Lack of fit	2.53	6	0.4213	2.53	0.1639	Not significant
Pure error	0.8333	5	0.1667			
Cor total	102.00	31				

in slower cooling rates causing the stresses to relieve uniformly, thereby resulting in lesser distortion.

Effect of Welding Speed and Voltage: As evident from Fig. 6, the WS has a positive influence on angular distortion for the reason already explained in the previous paragraph. However, the effect of voltage is slightly negative on the angular distortion. The anticipated reason could be that increase in voltage has a more widening impact on the arc, rather than weld penetration, thereby causing a lesser impact on angular distortion.

Effect of Nozzle–Plate Distance and Voltage: The interaction effects of NPD and voltage are shown in Fig. 7. Voltage has a negative effect on angular distortion, the probable cause of which has already been explained earlier. However, the distortion

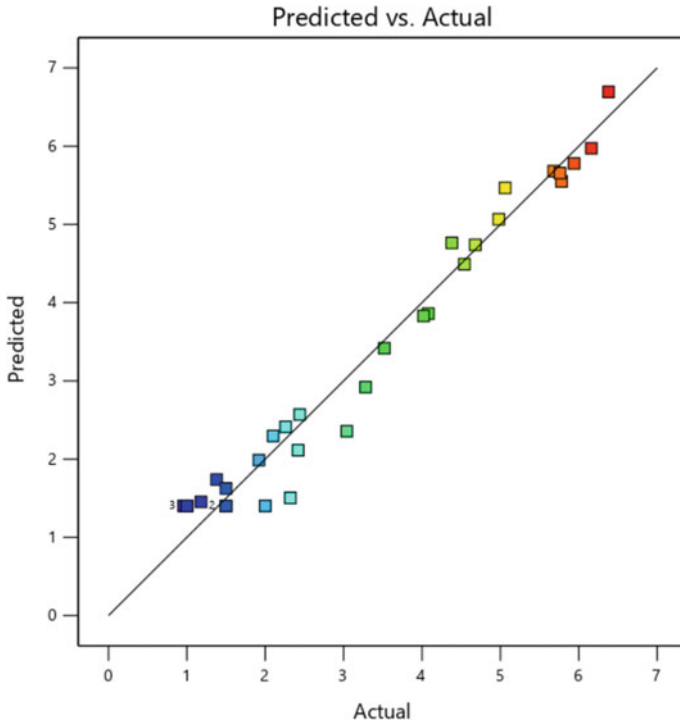


Fig. 4 Predicted versus actual values

Table 4 R² table

Std. dev	0.5528	R ²	0.9671
Mean	3.24	Adjusted R ²	0.9071
C.V. %	17.05	Predicted R ²	0.3477
		Adeq precision	11.8202

is found to have been increasing slightly with NPD. The reason for this could be that with the increase in NPD, the length of un-melted wire increases before the arc. This causes resistive heating of the wire causing more molten wire to deposit on the workpiece surface resulting in a steep thermal gradient between the top and the bottom faces of the workpiece.

Effect of Nozzle–Plate Distance and Welding Speed: Figure 8 shows the effects of WS and NPD on angular distortion. It is visible that the effect of both these parameters is positive on angular distortion; i.e. angular distortion increases with an increase in WS and NPD. The probable explanations have been explained in the preceding paragraphs.

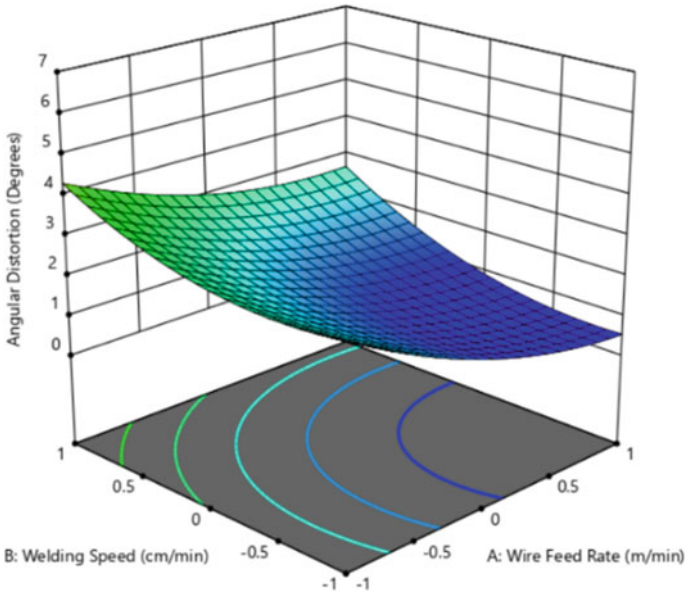


Fig. 5 Effect of WFR and welding WS

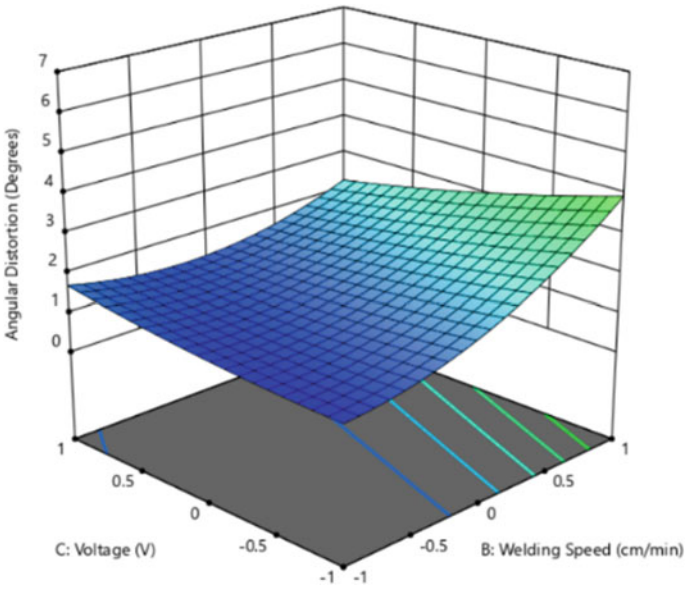


Fig. 6 Effect of WS and voltage

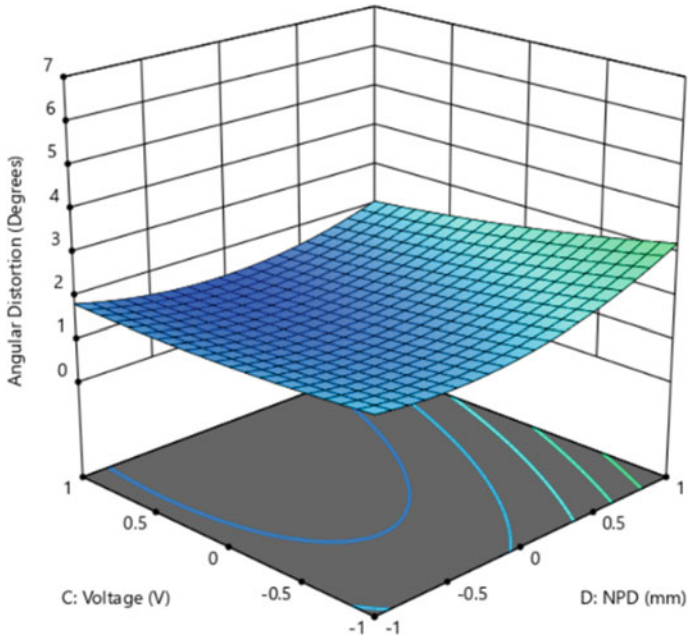


Fig. 7 Effect of NPD and voltage

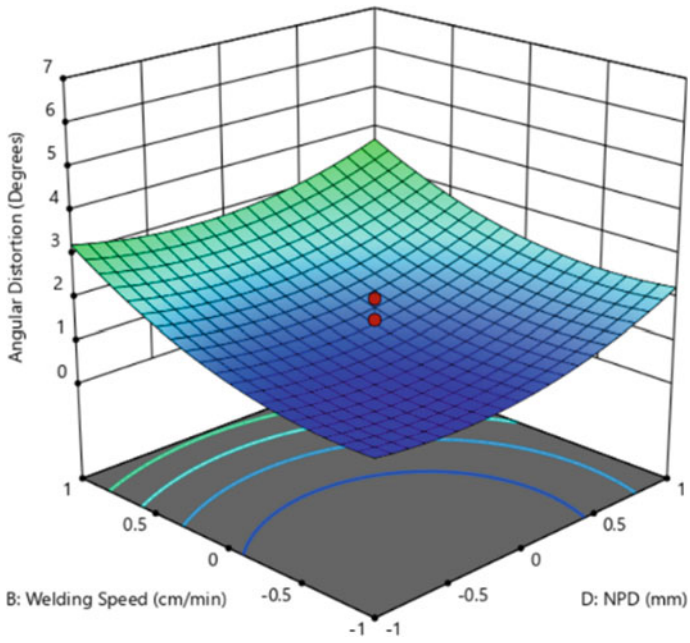


Fig. 8 Effect of NPD and WS

4 Conclusions

On the basis of the experiments and their respective analysis, it is concluded that:

- WS has a positive effect on angular distortion, whereas WFR has a negative effect. Maximum angular distortion was observed at maximum speed and minimum WFR.
- The effect of voltage on angular distortion is negative, with maximum distortion occurring at minimum voltage.
- NPD has a slightly positive effect with maximum distortion at maximum value of NPD.
- Torch angle showed to have a slightly negative effect on angular distortion with maximum distortion at minimum torch angle.

References

1. Jung GH, Tsai CL (2004) Fundamental studies on the effect of distortion control plans on angular distortion in fillet welded T-joints. *Weld J New York* 83(7):213S–223S
2. Khanna P, Maheshwari S (2018) Development of mathematical models for prediction and control of weld bead dimensions in MIG welding of stainless steel 409M. *Mater Today: Proc* 5(2):4475–4488
3. Jindal Steels Website, <https://www.jindalstainless.com/pdfs/200series.pdf>
4. Parmar RS (2010) *Welding processes and technology*, 10th edn. Khanna Publishers, New Delhi
5. Sudhakaran R, Murugan V, Sivasakthivel P (2012) Optimization of process parameters to minimize angular distortion in gas tungsten Arc welded stainless steel 202 grade plates using particle swarm optimization. *J Eng Sci Technol* 7(2):195–208
6. Baruah M, Bag S (2016) Influence of heat input in microwelding of titanium alloy by micro plasma arc. *J Mater Process Technol* 231:100–112
7. Pandit M, Sood S, Mishra P, Khanna P (2021) Mathematical analysis of the effect of process parameters on angular distortion of MIG welded stainless steel 202 plates by using the technique of response surface methodology. *Mater Today: Proc* 41(50):1045–1054

Modeling and Simulation of Steering and Front Wheel Assembly for FSAE Vehicle



Katya Sah, Rashmi Kaushal, Parnika Chauhan, and Vivek K. Chawla

Abstract This paper addresses the designing and analysis of the wheel assembly and steering system for a formula student race vehicle. The study follows three phases. The first phase involves research and creating the CAD model of the front suspension and steering system to check and determine the pickup points and other variable parameters like caster, camber, kingpin, rack position, and its alignment concerning the upright. The second phase involves calculating forces acting on the uprights, hub, and the steering system along with material selection. The third phase includes creating a CAD model of the upright, hub, Ackerman bracket, upper ball joint tab, and steering wheel. This phase also deals with the optimization of these parts for weight reduction and re-analysis using Ansys-Workbench for ensuring strength and durability before final manufacturing.

Keywords Wheel assembly · Steering system · FEA

1 Introduction

The steering and wheel assembly is an integral part of a vehicle. A responsive steering assembly along with a lightweight wheel assembly which efficiently handles the load under dynamic conditions makes it an important subject for research among engineers worldwide. The idea of the paper is the modeling and optimization of steering and wheel assembly. It also aims at improving the reliability of the components, weight reduction, and increase in performance. FOS and total deformation results were used for finalizing the design. Compared to the previous vehicle, the current front wheel assembly is 15 kg lighter. This was made possible by optimizing uprights and making hubs hollow. To provide variable Ackerman percentage, we have designed Ackerman bracket which was earlier absent. The steering wheel is also half the weight than the previous vehicle.

K. Sah (✉) · R. Kaushal · P. Chauhan · V. K. Chawla
Indira Gandhi Delhi Technical University, Kashmere Gate, Delhi 110009, India

© The Author(s), under exclusive license to Springer Nature Singapore Pte Ltd. 2022
K. Govindan et al. (eds.), *Advances in Mechanical and Materials Technology*,
Lecture Notes in Mechanical Engineering,
https://doi.org/10.1007/978-981-16-2794-1_48

537

Caster Angle—In the side view of the vehicle, it is the angle made by the line passing through the upper ball joint and lower ball joint with the vertical axis [1]. **Kingpin Inclusion Angle**—In the front view of the vehicle, it is the angle made by a line passing through the upper ball joint and lower ball joint with the vertical axis [1]. **Camber**—In the front view of the vehicle, it is the angle made by the tire with the vertical axis [1]. **Instantaneous Center (IC)**—In the front view of the vehicle, it is the point where the inclination of the upper and lower wishbone meets [5]. **Roll center (RC)**—In the front view of the vehicle, when the IC is extended backward to join the tire bottommost position, then the point where it cuts the center of the car (since it's symmetric) is termed as RC of the car [5]. **Rack position**—The position of the rack is important for steering geometry and driver's ergonomics. The rack can be placed between driver and tire center, tire center, or between pedal assembly and tire center [4]. Steering geometry and techniques of joining different components should be chosen after researching all the alternatives available. The components should be designed to withstand all the forces and torques acting on it while steering [6]. The wheel assembly contributes to the unsprung mass whose behavior cannot be predicted, and thus, it should be designed lighter to reduce forces acting on it at the time of load transfer. Also many forces act on the components simultaneously, so proper calculation and analysis are required to prevent failure of these components [8].

2 Main Procedure

2.1 Initial Phase

A basic geometrical model of the front suspension pickup point was made after taking into account the different suspension and steering angles.

Criteria for the Basic Geometry. Based on the constraints, the following criteria was referred (i) The front roll center was kept lower than the rear to generate sufficient rolling moment and keep the desired load transfer in the front [1]. (ii) Positive kingpin was selected to improve downwards thrust to all the tires while cornering. (iii) Positive caster was selected in front as it loads the inner tire while cornering and allows the diagonal tires to behave in a similar manner which ultimately unloads the inner rear tire. (iv) Initially, the camber was set to zero. (v) The rack was placed to give anti-Ackerman steering geometry. (vi) The track width (TW) in front was kept more than the rear to get the desired load transfer and prevent understeer [1].

Designing of a CAD and Lotus Model. A geometrical CAD model was made for the wheel assembly as shown in Fig. 1. The model acted as a base for modifying and fixing final points in Lotus software and modified to get desired results.

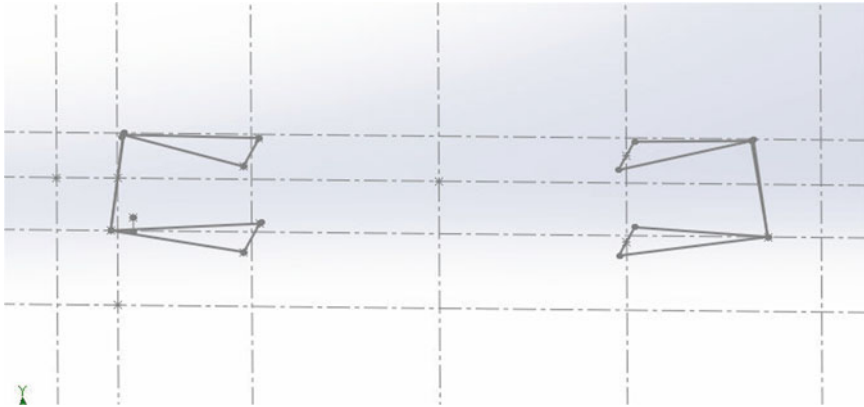


Fig. 1 CAD model

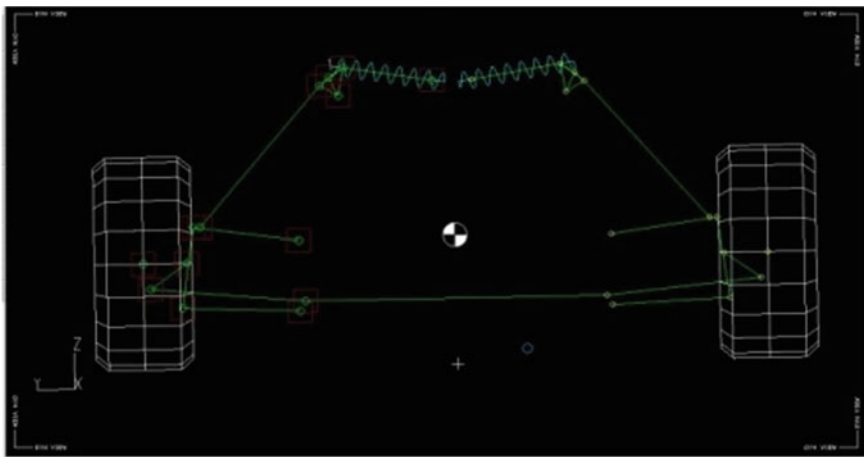


Fig. 2 Lotus model

As the value of kingpin was increasing to get the desired instantaneous and roll center, the downward thrust to the tire was also increasing, so we need to increase the value of caster to unload the innermost rear tire in the turns, which will make steering harder [1]. The position of the rack was selected between the tire center and pedal assembly to get the desired Ackerman percentage. In the top view, the steering tie rod and rack should be in the same line for efficient transfer of torque generated from the steering wheel to the tire and to reduce compliance (Fig. 2; Table 1).

Table 1 Basic parameters

Parameters	Value
Kingpin inclination	8°
Caster angle	6°
Roll center position	13.9954 mm
Toe	0°
Track width	53"

2.2 Steering

The steering system helps to steer/turn the vehicle in the desired direction. The rack position was already decided. We have chosen double Universal joint, and while designing different steering components and its connection, we have considered

(i) Universal joint phasing- The phasing between the universal joint was checked as shown in Fig. 3 [2], which was chosen to make the steering wheel position comfortable for the driver, and while steering at its maximum position, driver's hand should not go beyond the front roll hoop [3]. (ii). Cockpit internal cross-sectional template rule—According to the rule, the template should pass from the cockpit opening [4].

Steering Force Calculation. Mass at the time of cornering in each tire = 75 kg

$$F = \mu gm \quad (1)$$

$$\text{Torque}_{\text{tie rod}} = \text{Force on tie rod} \times \text{dist between tire centre and tie rod} \quad (2)$$

$$\text{Force on rack} = 2 \times \text{Force on tie rod} = 1300.5625 \text{ N}$$

$$\begin{aligned} \text{Torque}_{\text{pinion}} &= \text{Force on rack} \times \text{radius of pinion} \\ &= 1300.5625 \times 0.008 \\ &= 10.40 \text{ Nm} \end{aligned} \quad (3)$$

Turn Angle and Steering Wheel Size Calculations. Using basic Geometry—Refer Fig. 5 and below mentioned equations (Fig. 4) [4, 7]

$$R = ((\text{Turning Radius})^2 - (\text{Rear axle to COG distance})^2)^{1/2} \quad (4)$$

$$\tan \theta_o = \text{WB}/(\text{R} + (\text{TW} \div 2)) \quad (5)$$

$$\tan \theta_i = \text{WB}/(\text{R} - (\text{TW} \div 2)) \quad (6)$$

$$SR = \text{Max steering wheel turn angle} / ((\theta_o + \theta_i) \div 2) \tag{7}$$

$$= 6.42(\text{Angles were } 28^\circ \text{ and } 26^\circ)$$

$$SR = 2\pi r \div (\text{Rack Travel}) \tag{8}$$

The radius ‘r’ of the steering wheel to get the desired steering ratio = 110.35 mm.

Connection of the Steering System. The different components in steering assembly are steering wheel, quick release unit, universal joint, steering column, rack, rack extension, tie rod, and clevis.

For horizontal connections, steering rack is placed in its position. The rack extension is connected on both sides of the rack and has rod end on its other end. Tie rod on one side is connected to the clevis and on the other side to rod end. The clevis part is connected to rack extension, and the rod end part of tie rod is connected to Ackermann bracket. This completes the horizontal connection.

For vertical connections, the steering column is connected to Universal joints. One end is connected to pinion via splines. To vertically fix the steering column at the desired angle, the support plate was welded to chassis and then the bearing sleeve surface to support plate. The quick release (QR) shaft is connected to Universal joint. One part of QR hub is bolted to steering wheel and the other to QR shaft via splines (Figs. 6 and 7).

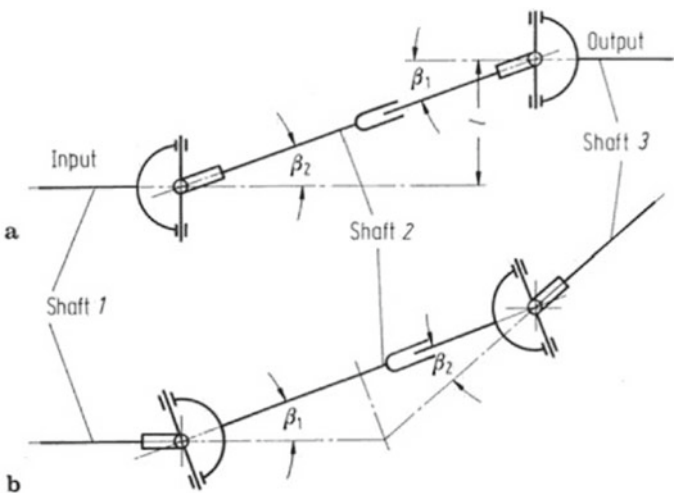


Fig. 3 Universal joint phasing [2]

Fig. 4 Internal cross-sectional template [3]

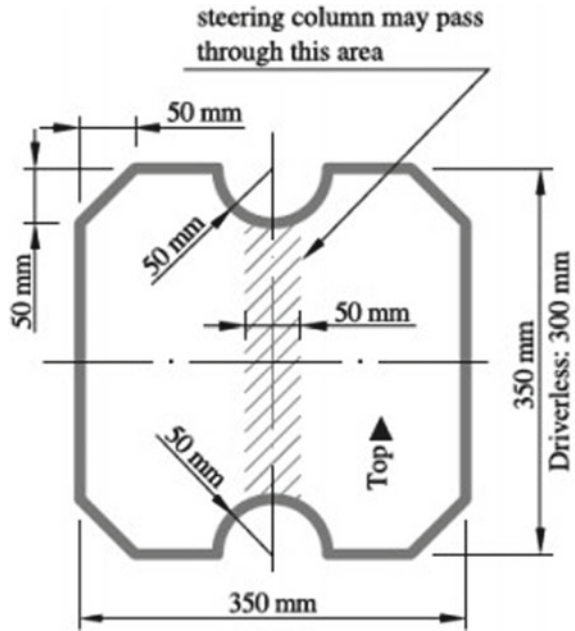
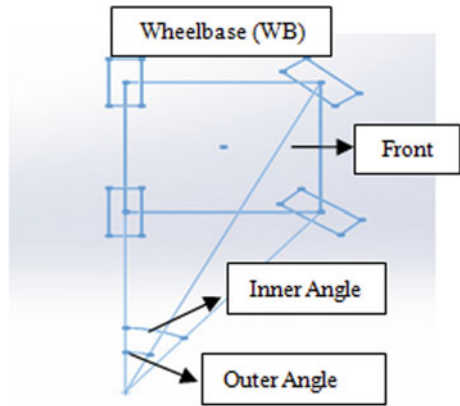


Fig. 5 Tire angles while taking a right turn



2.3 Wheel Assembly

The wheel assembly includes the upright, hub, rotor carrier, and rotor. Here we will cover the upright and hub. Before calculating forces, we determined the bearing position. We had planned of making an integrated hub, so we opted for live spindle in the front. First the bearing was press-fitted into the upright along with the spacer. The integrated hub spindle portion was then press-fitted into the upright bearing. The assembly was secured using castle nut along with a split pin [10].

Fig. 6 Steering system

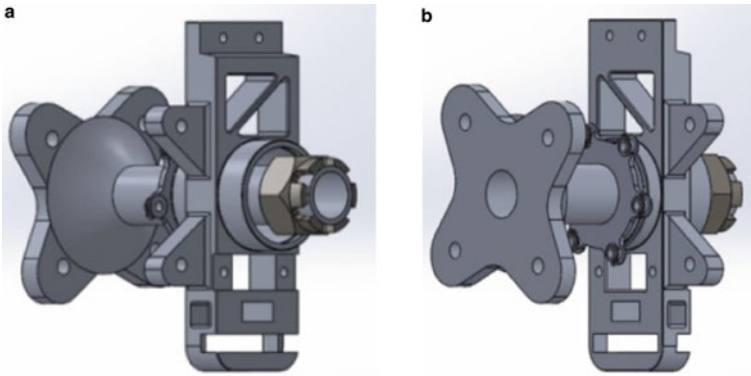


Fig. 7 a Inner side of wheel assembly. b Outer side of wheel assembly

Force Calculation in Wheel Assembly. The height of COG was to be determined before proceeding with the calculation. To determine it, we have used Pythagoras theorem along with tangent laws. It was calculated by first weighing the previous vehicle under normal static condition and then by raising it to 10 inches at the rear and weighing the front part of the vehicle.

COG height (in inches) = 11.

Sprung mass on each tire = 58 kg.

Unsprung mass on each tire = 17 kg.

Bump was considered 3 g as our vehicle has moderate speed and no aerodynamics (Table 2).

Considering load transfer equations when the driver is applying brakes on a bumpy corner [5]

$$\text{Longitudinal load transfer} = (\text{Braking Acceleration} * \text{Weight} * h_{CG})/WB \quad (9)$$

Table 2 Acceleration in various conditions

Load transfer conditions	Acceleration value (g)
Braking	1.3
Lateral	2
Bump	3

$$\text{Lateral Load Transfer} = (\text{Lateral Acceleration} * \text{Weight} * h_{CG})/TW \quad (10)$$

$$\text{Bump Load Transfer} = \text{Unsprung mass} * \text{Bump Acceleration} \quad (11)$$

$$\text{Total mass on each tire(Extreme case)} = 198.46 + 51 = 250 \text{ kg}$$

Force Components on Each Tire. The components of force acting on each tire are calculated using the total mass on each tire and the acceleration values previously mentioned. These values were used in the analysis of hub and uprights (Table 3).

Calculation of Bolt Dimensions. The dimensions of different types of bolts are calculated using the below mentioned equations [6].

Calculation of Bolt Dimensions for UBJ and Ackerman Bracket.

$$\begin{aligned} \text{Max. shear force acting on bolt} &= \left((F_{\text{longitudinal}})^2 + (F_{\text{bump}})^2 \right)^{1/2} \\ &= \left((1595)^2 + (1480)^2 \right)^{1/2} = 2175 \text{ N approx} \end{aligned} \quad (12)$$

For Grade 8.8 bolt Yield Strength = 580 N/mm² and bolt in double shear

$$\text{Allowable Shear Stress} = \text{Shear force/Shear Area} \quad (13)$$

Diameter of Bolt = 3.09 mm (Taking FOS = 2).

The value is too small. So, the bolt decided for UBJ and Ackerman bracket is M6.

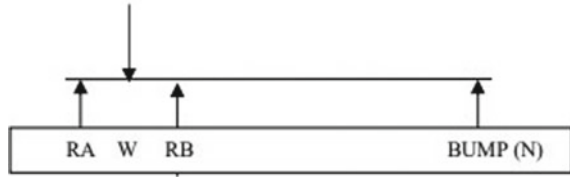
Calculation of Bolt Dimensions for A-arms Mounting.

$$\begin{aligned} \text{Max. shear force acting on bolt} &= \left((F_{\text{longitudinal}})^2 + (F_{\text{lateral}})^2 \right)^{1/2} \\ &= \left((1595)^2 + (2455)^2 \right)^{1/2} = 2930 \text{ N approx} \end{aligned} \quad (14)$$

Table 3 Force components under various conditions

Loading conditions	Force component (N)
Longitudinal	3190
Lateral	4905
Vertical (Bump + mass)	2955

Fig. 8 Forces acting on the bearing of upright (FBD)



For Grade 8.8 bolt Yield Strength = 580 N/mm^2 and bolt in double shear

$$\text{Allowable Shear Stress} = \text{Shear force/Shear Area} \tag{15}$$

Diameter of Bolt = 3.59 mm (Taking FOS = 2).

The value is too small, M6 bolt was selected for A-arms, and M8 for Tie rod mounting.

Calculation of Bearing Dimensions in Upright. We have selected single row taper roller bearing as it can withstand both axial and radial forces. We planned to use it in pairs for better load handling.

As we have used live spindle, so RA and RB are the reaction forces acting on the bearing, W is the weight of the car acting at the center of upright (spacer center), and N will be the bump force acting at the tire center as shown in Fig. 8. Here, the total spacer length is 20 mm. Distance between different bearings concerning the hub is calculated from a rough wheel assembly design.

On balancing forces and applying the law of moments [6].

RA = 1781.66 N and RB = -1546.66 N.

Bending moment is calculated at different position, and the maximum bending moment was at Mb = 57425Nmm [6].

$$D^3 = \left(16 * (Mt^2 + Mb^2)^{\frac{1}{2}}\right) \div (\pi * \text{Allowable shear stress}) \tag{16}$$

$$\text{Torque } Mt = m * g * r \tag{17}$$

where Mt = 313100Nmm, Shear stress = 207 MPa, FOS = 3.

D = 28.649 mm (Substituting these values in the above equations). The bearing should be selected that has ID \geq 3 cm. The bearing selected has OD as 59.975 mm, ID as 34.987 mm, and thickness as 15.875 mm.

2.4 Material Selection for Different Components

A lightweight vehicle attains more acceleration compared to a heavy vehicle at same engine torque. Keeping this in mind, the considered options are listed in Table 4.

Table 4 Material comparison table

Properties	M. Steel	Al-6061T6	Al-7075T6
Weight	Heavy	Light	Light
Strength	Great	Good	Great
Cost	Least	Costly	High

Material Selection for Steering. (i) Steering Wheel—The steering wheel should be lightweight and sustain torque acting on it. So, Al-6061T6 was selected. (ii) Other Components- Large components of forces act on components like QR shaft, steering column, and tie rod; also due to budget constraints, we have selected mild steel.

Material Selection for Wheel Assembly. (i) Upright- Our main aim was to make it lightweight and strong at a decent price. So, Al-6061T6 was selected. (ii) Hub— Since it connects the wheels to the vehicle, it should be the most durable to withstand the unknown forces acting upon it. We selected mild steel.

2.5 Design and Optimization

Upright Design. Based on calculated values, a model of the upright was made and then tested on Ansys—Workbench.

Upright Analysis and Optimization. The different forces, torque acting on the upright includes lateral force, longitudinal force, bump force, and braking torque.

For analyzing upright, we divided the total forces acting on the upright into two parts, i.e., UBJ and LBJ force components. Then the respective forces were applied on UBJ and LBJ holes. Steering forces were applied on Ackerman bracket holes which include load transfer and force applied by tie rod to turn the tire. Braking torque was applied on the caliper mounting position, whereas the central bearing portion will act as cylindrical support. Initially, the FOS was very high. So, it was optimized further [9] (Figs. 9, 10, 11, and 12).

Upper Ball Joint Tab Design, Analysis and Optimization. The upper ball joint tab (UBJ) was designed based on the mounting position of A-arms. It was designed to be accommodated in upright without interference.

For analyzing the UBJ tab—Part of lateral, longitudinal, and bump forces acting on UBJ was applied on the mounting point of A-arms, and it was fixed from the positions of the holes where it will be connected to the upright. After analysis, thickness was optimized (Figs. 13, 14 and 15).

Ackerman Bracket Design, Analysis and Optimization. The Ackerman bracket was designed based on the bolt dimensions and position of the tie rod, such that the tie rod movement is not obstructed by the Ackerman bracket. For analyzing Ackerman bracket, steering forces and part of load transfer were applied on the tie rod mounting

Fig. 9 Upright basic model

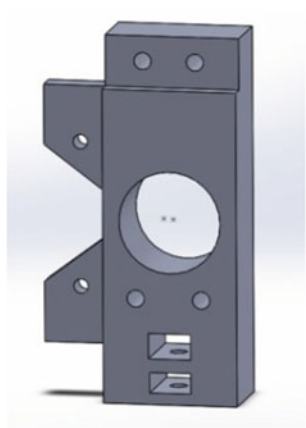


Fig. 10 Upright optimized model

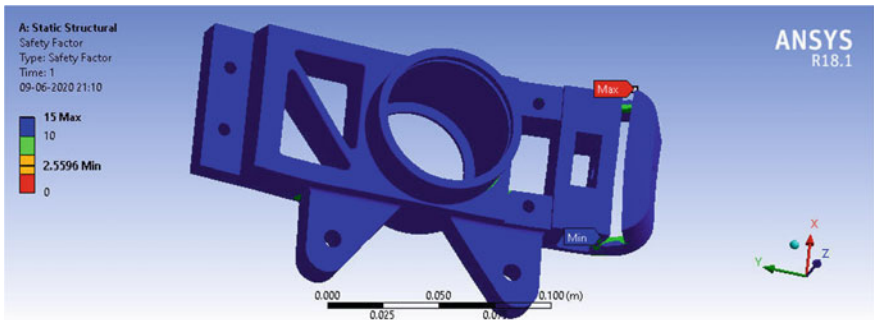
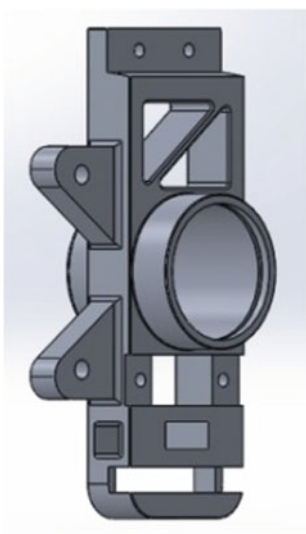


Fig. 11 Upright FOS

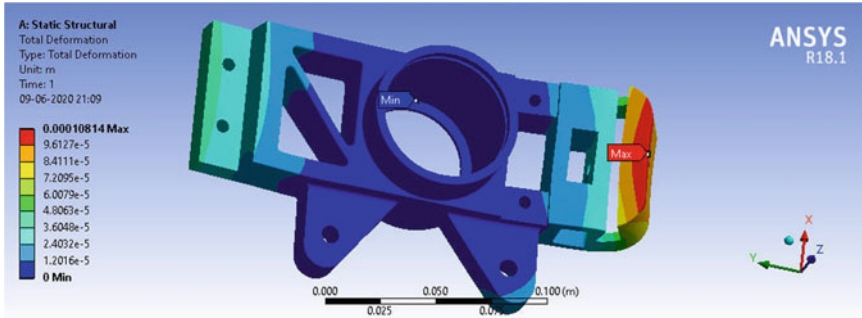


Fig. 12 Upright total deformation

Fig. 13 Upper ball joint tab

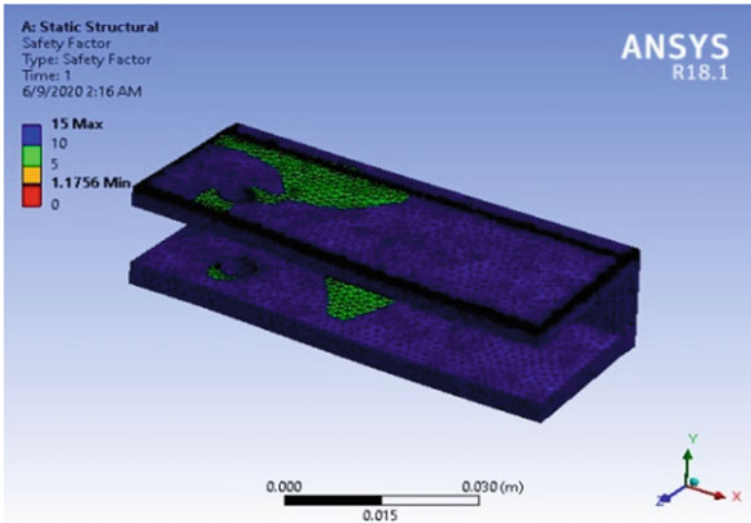
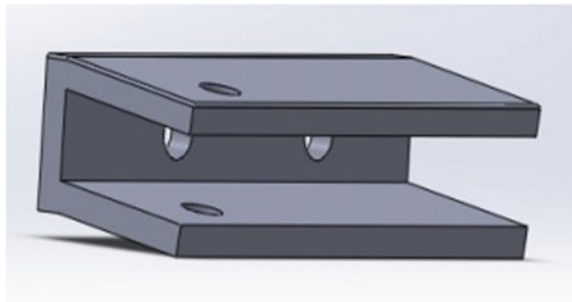


Fig. 14 Upper ball joint tab FOS

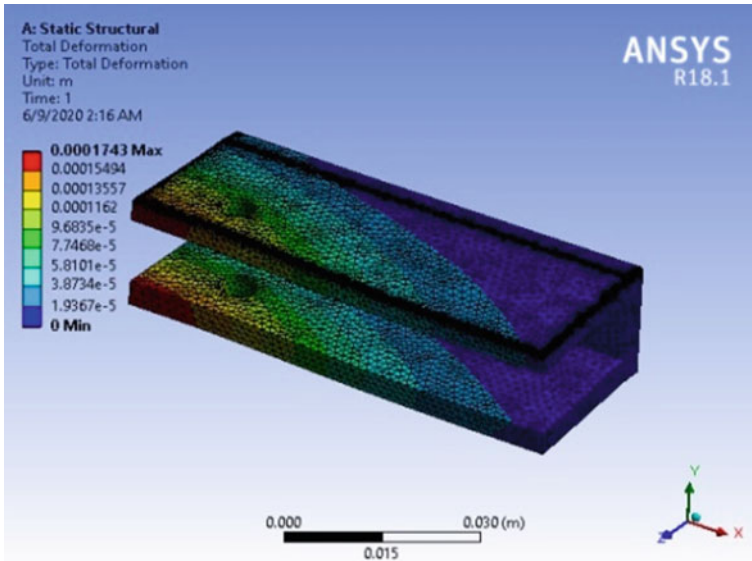


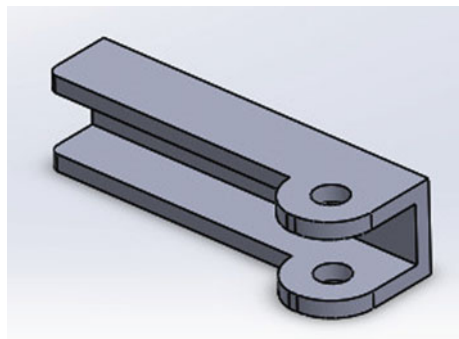
Fig. 15 Upper ball joint tab total deformation

position, and the bracket was fixed from the points where it will be connected. After analysis, optimization was made in its thickness (Figs. 16, 17 and 18).

Hub Design. The hub was designed with an integrated rotor carrier, based on the mounting points to tire, the internal diameter of upright's bearing, position of rotor carrier, and the stress concentration factor. A step was made on the hub to constrain the upright to its original position.

Hub Analysis and Optimization. The different forces/torques acting on the hub are braking torque, anti-braking torque, and load transfer forces. The forces due to the load transfer are lateral, longitudinal, and bump forces. For analyzing hub, braking torque is applied on rotor carrier and anti-braking on hub petal. The part where it is

Fig. 16 Ackerman bracket



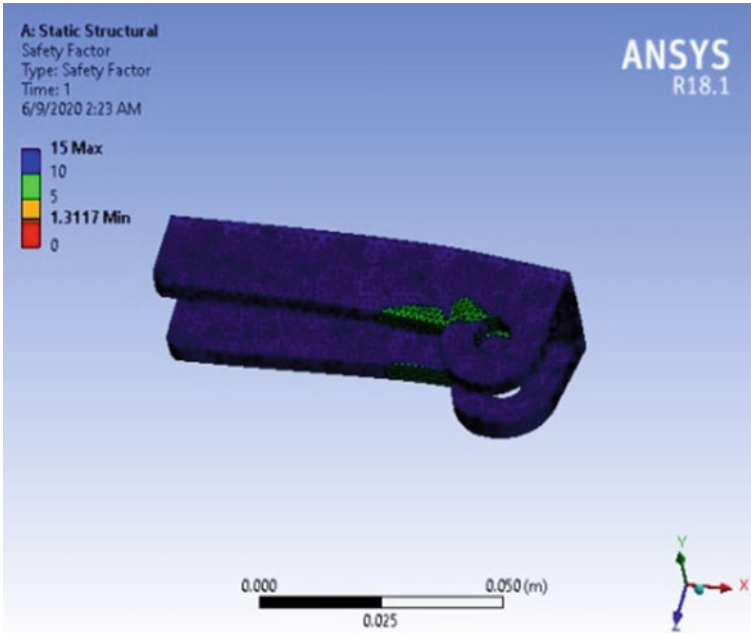


Fig. 17 Ackerman bracket FOS

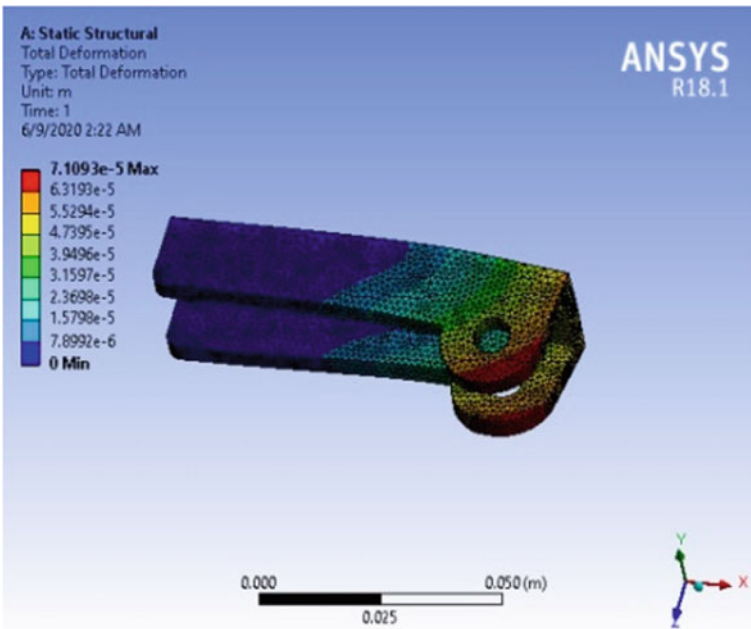


Fig. 18 Ackerman bracket total deformation

connected to the rim is the place where load transfer forces will act along, i.e., transfer of force from the tire to the hub. Also those mounting points will be fixed. After the analysis, the hub was made hollow which helped in weight reduction. We have given internal steps in the hub to increase its strength [11] (Figs. 19, 20, 21, 22, and 23; Table 5).

Steering Design. The steering wheel was designed in a manner that it should not have sharp edges. It should have a continuous perimeter with near-circular or near oval shape [3]. The calculations performed earlier gave us the radius of the steering wheel.

Fig. 19 Hub basic model

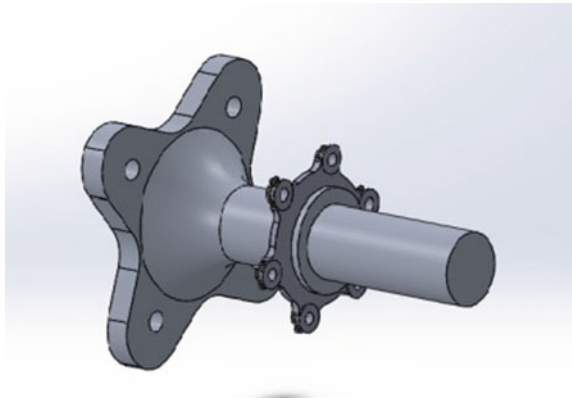
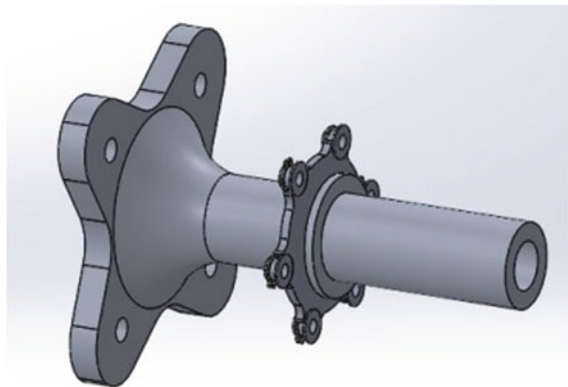


Fig. 20 Hub optimized model



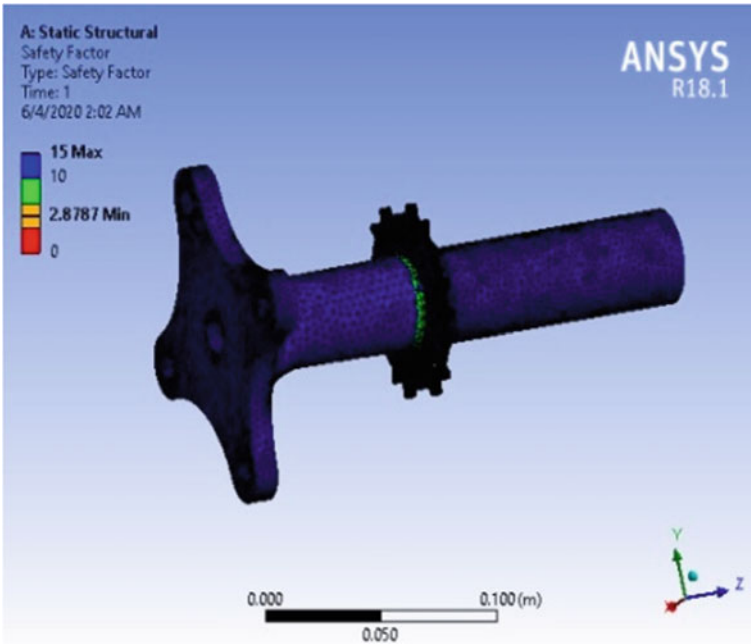


Fig. 21 Hub FOS

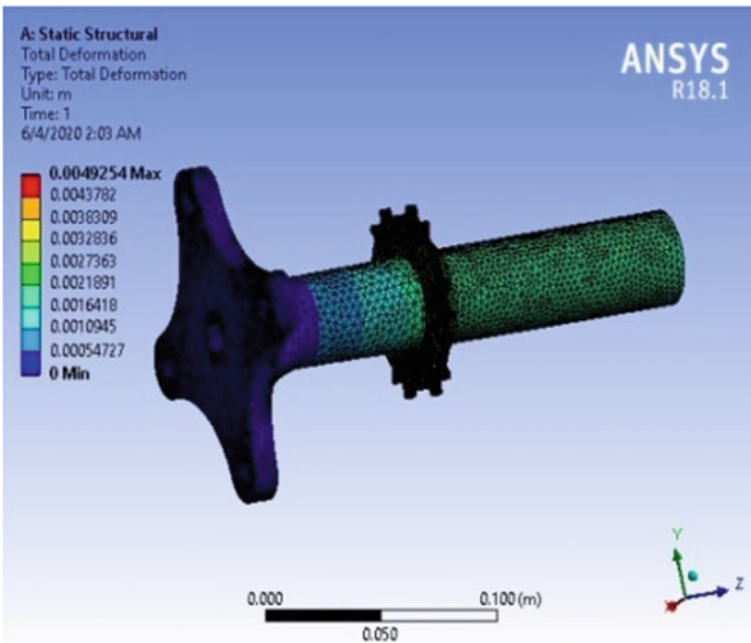
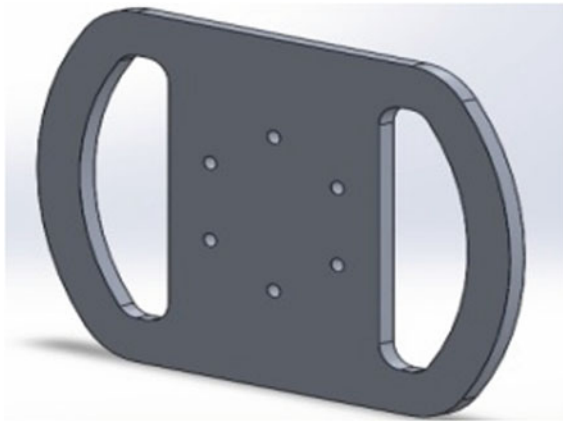


Fig. 22 Hub total deformation

Table 5 Comparison between analytical and computational values

	Upright		Hub	
	Analytical	Computational	Analytical	Computational
Max stress (Pa)	1.09×10^8	2.4×10^8	1.52×10^8	3.7×10^8
FOS	2.5596	2	2.8787	2

Fig. 23 Steering wheel



Steering Wheel Analysis and Optimization. For analysis—the steering wheel was applied with the maximum torque that will be acting on its surface and fixed it from the holes where it will be bolted to the quick release hub. After doing iteration, the desired thickness of the steering wheel was selected, thus optimizing its thickness (Figs. 24 and 25).

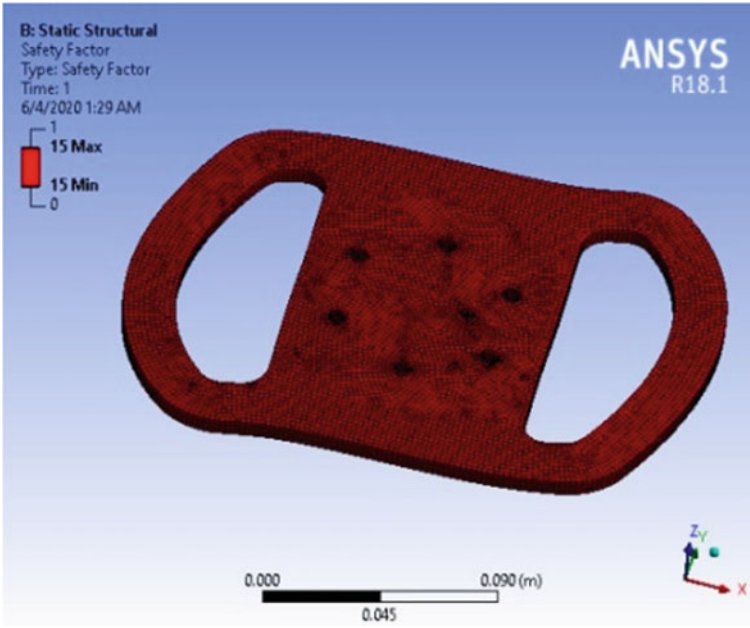


Fig. 24 Steering wheel FOS

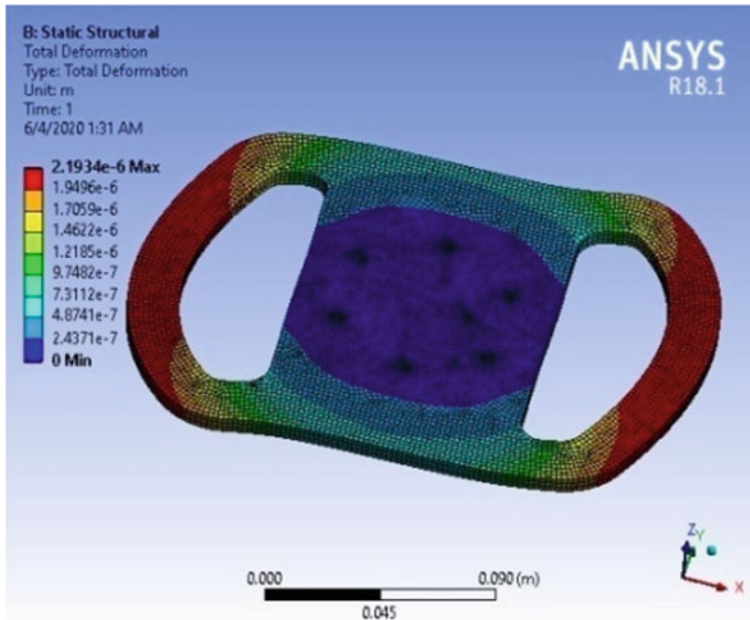


Fig. 25 Steering wheel total deformation

3 Conclusion

A CAD model of steering and wheel assembly was successfully made based on the calculations and design constraints. After analyzing the components in Ansys-Workbench for stress and durability, necessary modifications in the CAD model lead to a reduction in stress concentration, an increase in durability, reduction in the weight of the components, and made it cost-efficient. The factor of safety analysis of all the components is greater than 1 under extreme load condition, and the total deformation is also negligible. So the parts are safe under dynamic conditions. Since the parts were already analyzed and assembled beforehand by making CAD assembly, interferences in the assembly were detected and removed. This reduced after manufacturing errors.

References

1. Smith C (1978) Tune to Win. Aero Publishers, CA, USA
2. Schmelz F, Christoph H, Thoss S (2006) Universal joints and driveshafts: analysis, design, applications, 2nd edn. Springer Science & Business Media, Germany, PA
3. Society of Automotive Engineer (2018) Formula Bharat 2020 Rules booklet Adaptation of FS-Rules_2019_V1.1. SAE, Brooklyn, MI
4. Reimpell J, Stoll H, Betzler JW (2001) The automotive Chassis: engineering principles, 2nd edn. Society of Automotive Engineers, Warrandale, PA
5. Milliken WF, Milliken DL (1995) Race car vehicle dynamics. SAE International, Warrandale, PA
6. Bhandari VB (2010) Design of machine elements, 2nd edn. TMH Tata McGraw-Hill Education, New Delhi, India
7. Biswal S, Prasanth A, Dheeraj MS, Sehli S (2016) Design and optimization of the steering system of a formula SAE car using solidworks and Lotus Shark. In: Proceedings of the world congress on engineering, II, London, UK
8. Mahadik SS (2018) Design and ANSYS analysis of components of wheel assembly of SAE car. Int J Curr Eng Technol, VIII(2) (Maharashtra, India)
9. Bharadwaj S, Ashok B, Lath U, Aggarwal A (2018) Design And Optimization of steering upright to reduce the weight using FEA. In: SAE Technical Paper, Vellore, India
10. Wable PV, Shah SS (2017) Design analysis and optimization of hub used in FSAE cars. Int J Innov Res Sci Eng Technol (Pune, India)
11. Sajjan B, Parthasarathy A, Kiran SP, Kumar VKN (2016) Product design and development of wheel hub for an All Terrain Vehicle (ATV). Int J Res Technol (Karnataka, India)

Design and Analysis of Pedal Assembly for an FSAE Vehicle



Deepanshi Gupta, Pragya Mahajan, and Vivek K. Chawla

Abstract The pedal assembly of an FSAE vehicle should be able to provide the driver with optimal and consistent control over pedals without compromising on ergonomic adjustments. The purpose of the study is to develop a pedal assembly that is compact and efficient. An FSAE vehicle should be light in weight in order to achieve optimum performance. For performance optimization, it is requisite to design a lightweight pedal box assembly as the overall weight of the vehicle influences the position of center of gravity and weight transfer. It is necessary to devise such geometry which shows robustness to failure yet reliable, easy to manufacture, and less complex, while maintaining structural integrity. A balance bar is also incorporated in the pedal assembly to adjust the front rear biasing according to the driving conditions.

Keyword Pedal box · FSAE · Braking system · Brake pedal · Lightweight · Compact

1 Introduction

Braking system is one of the most significant systems of the vehicle. This system must be designed with utmost caution considering the driver's safety and comfort. The driver must have proper control over the pedals to operate the brakes efficiently and stop the vehicle with minimum stopping distance. The pedal assembly directly affects the reliability and performance of the vehicle. The intent of this study is to develop a pedal assembly that is strong and capable of locking all four wheels of the vehicle simultaneously with minimum compliance. This study deals with the designing and manufacturing of compact and lightweight pedal assembly using angled master cylinders geometry. The parts of assembly focused in this study are brake pedal, throttle pedal, clutch pedal, and mounting plate that must function collectively and effectively to slow down or stop the vehicle. In order to achieve desirable results, parameters of

D. Gupta (✉) · P. Mahajan · V. K. Chawla
Department of Mechanical and Automation Engineering, Indira Gandhi Delhi Technical University for Women, Madrasa Road, Opposite St. James Church, Kashmere Gate, Delhi 110006, India

pedal assembly but not limited to pedal length, pedal ratio, pedal travel, brake biasing, inclination of master cylinders, and required and available braking torque are determined and calculated to have an optimized geometry. These values are determined on the basis of vehicle parameters such as overall weight of the vehicle, static and dynamic weight distribution, height of center of gravity of vehicle, wheelbase, wheel diameter, and coefficient of friction of tires. CAE tools like SolidWorks and Ansys are used to develop the CAD model of the assembly and to perform structural simulations to validate the strength of the assembly, respectively. Multiple simulations and topology optimizations are performed to work out the dimensions and material so as to make assembly reliable and cost-effective without negotiating on strength and driver's ergonomics. Various iterations of designs and simulations resulted in a distinct pedal assembly which is lightweight, less susceptible to stresses, easy to manufacture, and gives satisfactory results on a running vehicle.

2 Literature Review

2.1 Braking System

Brakes must safely operate under all highly probable loading situations, which includes damp, wet, dry, smooth, and rough tracks; when the vehicle is lightly or fully loaded; when braking while cornering or in a straight line; with new or faded brakes; when applied by an amateur or a skilled driver. The core functions of a brake system must be provided under foreseeable circumstances, at a reasonable cost and brake wear life, while providing directional stability and acceptable tire-road friction utilization [1].

2.2 Hydraulic Actuation and Brake Balance

The brake-actuating system can be mechanical, hydraulic, pneumatic, electromagnetic, or a combination of these. In a hydraulic braking system, the input piston is in the master cylinder. Each piston operates two brakes in dual input-piston master cylinders. Usually, front brakes form one circuit and rear brakes form the other circuit. But some dual systems operate a diagonal pair of brakes with each piston, such as the right-front and left-rear, and vice versa. Output pistons are located inside the brakes. Disc-brake calipers use one or more output pistons to move the pads, clamping the rotor [2]. Appropriate brake balance is highly crucial. The vehicle will not reach its maximum braking deceleration until all four wheels are brought to rest simultaneously. The common way to adjust the brake balance is to use a dual master cylinder setup with an adjustable balance beam splitting the pedal force between the two cylinders [3].

2.3 Design Considerations

The ease with which the driver can satisfactorily use the braking functionalities of the vehicle falls under ergonomics which plays a critical role in the design of a brake system. Apart from the orientation of brake pedal, the most prominent design variables acknowledged are driver's force and deflection characteristics during braking [4]. A braking system must be competent in producing sufficient braking force to surpass the deceleration capability of the tires, at whatever speed of the vehicle, again and again, for the entire span of the drive. The exerted force by the driver must be in direct and linear proportionality with the generated braking effort. The optimum balance between the rear and front wheels must be developed by the braking system just so under panic braking the driver can keep the steering control and all the decelerative capacities of all four tires are utilized. The brake pedal as well as its attachment to the chassis must be rigid and strong to withstand high forces [5].

3 Objective

The pedal assembly design of the preceding year's vehicle is bulky and acquires large space because of the horizontal arrangement of master cylinders. This assembly is to be replaced by a lightweight and compact assembly with master cylinders mounted at an inclination. This geometry results in stiffer brake pedal and reduced pedal travel which offers a better pedal feel to the driver.

4 Methodology

The primary goal is to lock all four wheels of the vehicle simultaneously. A low value of the center of gravity is favorable in an FSAE vehicle for it to perform better. Considering driver's ergonomics, floor-mounted pedals are incorporated in the car which facilitates in reducing the car height and hence gives a low value of center of gravity. To optimize the braking power, adjustments in the relative amount of hydraulic pressure applied in front and rear are to be made. A dual hydraulic braking system in conjugation with a balance bar to adjust the force distribution in front and rear is opted to serve this purpose. The biasing of 50–50 is decided upon for front-rear pressure distribution. The master cylinders are mounted at an angle with an explicit purpose of weight reduction, stiffer brake pedal, and less pedal travel. After considering varied choices available, master cylinders are sourced from AP Racing [6] and brake calipers from Brembo [7] and Wilwood [8]. Clutch and throttle pedals are cable-actuated. To bring the pedal to its initial position, return springs are used. For brake pedal, there is no need for return spring as returning of the pedal to its initial position is facilitated by master cylinders. As per FSAE rule requirements, a

Table 1 Vehicle parameters

STATIC		
Overall weight (kg)	275	
Wheelbase (inches)	65	
COG height (inches)	11	
Front weight (kg)	137.5	50%
Rear weight (kg)	137.5	50%
Deceleration (g)	1.01	
Wheel diameter (inches)	18	
Coefficient of friction	0.85	

brake over travel switch (BOTS) must be installed so that in the event of a failure in at least one of the brake circuits the brake pedal over travel will result in the shutdown circuit being open. The position of BOTS and pedal stops is determined from the pedal travel calculations.

5 Braking Torque Calculations

5.1 Vehicle Parameters Under Static Conditions

The vehicle parameters like overall weight, wheelbase, and wheel diameter shown in Table 1 are inputted to evaluate longitudinal weight transfer while braking.

5.2 Weight Transfer

The calculated longitudinal weight transfer while braking is shown in Table 2.

Table 2 Weight transfer values

DYNAMIC (Dry conditions)	
Weight on front tires (kg)	184.5038
Weight on rear tires (kg)	90.49615
Weight on front tires (%)	67.09231
Weight on rear tires (%)	32.90769

Table 3 Required braking torque

Required torque	Front	Rear
Axle force (N)	1823.823	900.905
Force required on tire (N)	911.9115	450.452
Braking force (N)	775.1247	382.884
Braking torque (Nm)	177.1935	87.5274
Torque ratio	2.024435	

5.3 Required Braking Torque

The data obtained from weight transfer calculations is used to calculate the required braking force and torque on each tire. The estimated required braking torque is shown in Table 3.

5.4 Available Braking Torque

Table 4 lists the specifications of the opted master cylinders. The available torque, shown in Table 5 is calculated which is to be in accordance with the required braking torque values such that the braking occurs properly and vehicle does not lose control in panic braking conditions. The maximum pedal force applied by the driver is 36 kg.

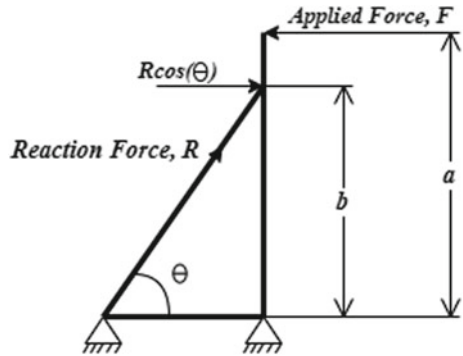
Table 4 Master cylinder specifications

Master cylinder	Front	Rear
Diameter of piston (mm)	14	15
Area (mm ²)	153.86	176.625

Table 5 Available braking torque

Available torque	Front	Rear
Force on master cylinder (N)	603.9036	603.9036
Pressure in brake lines (N/m ²)	3925.02	3419.129
Clamping force on Caliper (N)	7123.598	3463.24
Braking force (N)	2849.439	1385.296
Braking torque (Nm)	182.3641	93.23041
Torque distribution (%)	66.171	33.282
Torque ratio	1.956058	

Fig. 1 Force diagram of brake pedal



5.5 Force Calculations

Fundamental force calculations are performed to estimate the pedal ratio. Force diagram of the brake pedal is shown in Fig. 1.

On balancing the moments,

$$F \times a = R \cos(\theta) \times b$$

Thus,

$$\frac{R}{F} = \frac{a}{b \cos(\theta)} \tag{1}$$

The pedal ratio or mechanical advantage is determined from Eq. (1). From braking torque calculations, $R = 1207.8072 \text{ N}$ and $F = 353.16 \text{ N}$.

Thus,

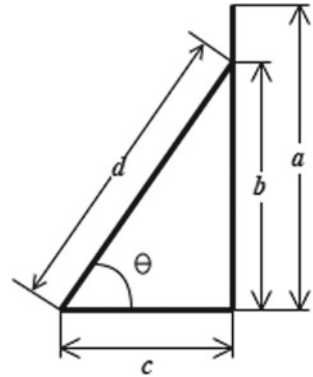
$$\text{Pedal Ratio} = 3.42$$

In order for the cosine value to be lower, the angle θ must be large. This is carried out with the intention of providing a larger pedal ratio to amplify the applied force, while maintaining an optimum height of the brake pedal.

5.6 Pedal Box Dimension Calculations

As shown in Fig. 2, the length of the brake pedal, 'a' is decided according to driver's ergonomics and comfort. Multiple iterations are performed to determine the master cylinder inclination. The final and optimum inclination, θ comes out to be 67° from the horizontal. The distance 'd' between the master cylinder & balance bar position

Fig. 2 Pedal box dimensions



' b ' is determined from available length of master cylinder and by applying trigonometric relations. Similarly, the distance ' c ' between master cylinder and brake pedal is obtained.

6 Material Selection

The elements of pedal assembly brake pedal, clutch pedal, throttle pedal, mounting plate, and BOTS mount are machined from aluminum alloy 6061 T6. This material is selected based on its good strength, machinability characteristics, and excellent resistance to corrosion. The selection is done considering cost constraints and easy availability of the material.

7 Brake Pedal

7.1 Modeling and FEA Analysis

The basic CAD model of brake pedal is developed using 3D modeling software, Solid-Works. After developing the CAD model, static structural simulations are performed in Ansys for finite element analysis. The boundary conditions are applied. The input parameters are force applied by the driver and reaction forces of master cylinders. Figure 3 shows the modeled design and FEA result.

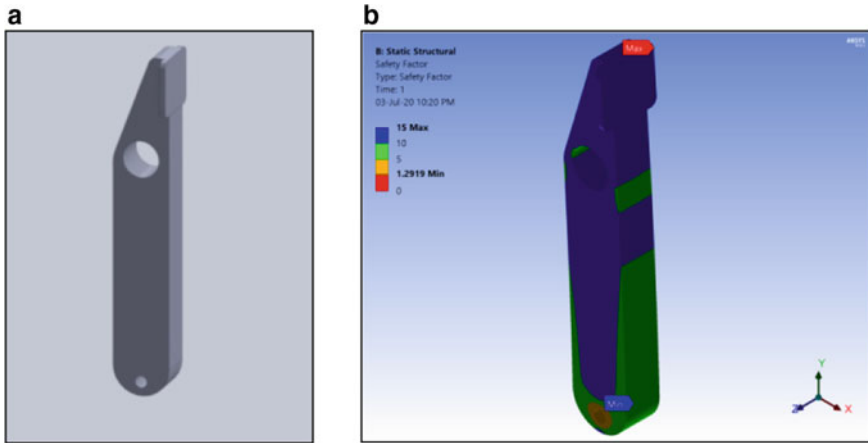


Fig. 3 a Brake pedal CAD model; b Static structural analysis

7.2 Topology Optimization

The topology optimization of the brake pedal is performed to achieve the objective of weight reduction. The design is modified as per the results of finite element analysis. Figure 4a shows the optimized model of the brake pedal. Further, static structural simulations are performed for the optimized model to validate its strength (Fig. 5).

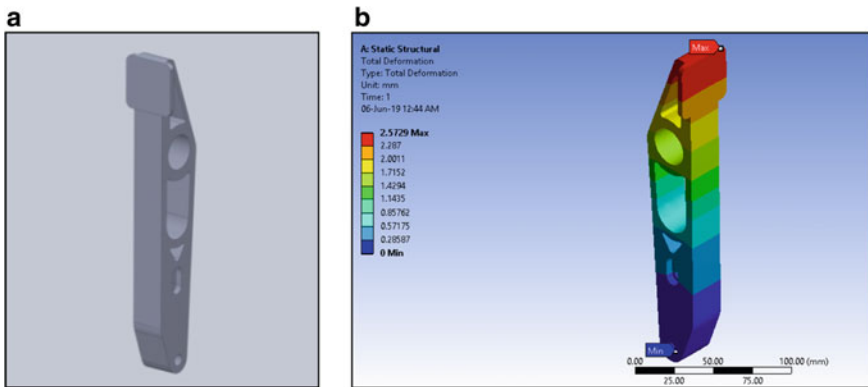


Fig. 4 a Optimized brake pedal design; b Total deformation

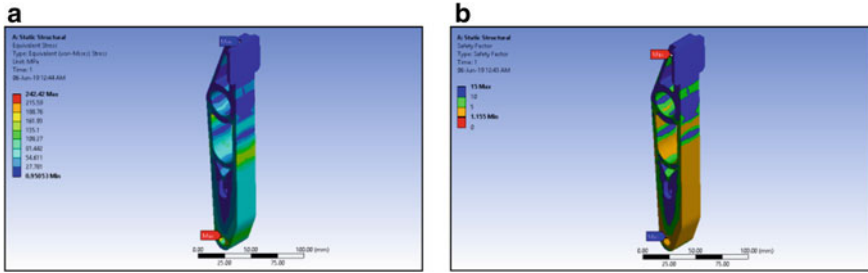


Fig. 5 a Equivalent stress; b Factor of safety

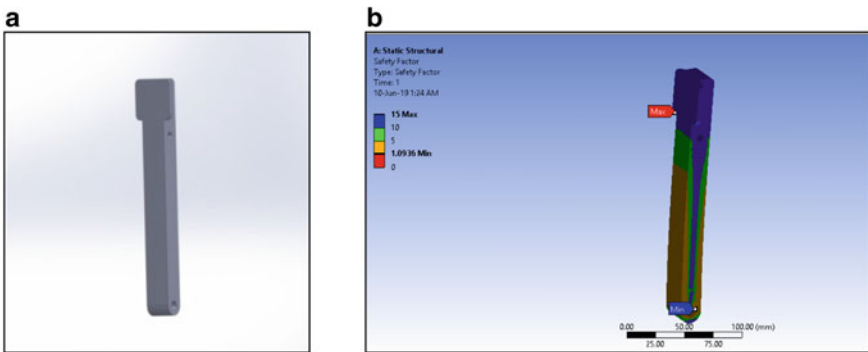


Fig. 6 a Pedal CAD model; b Static structural analysis

8 Clutch and Throttle Pedal

8.1 Modeling and FEA Analysis

The geometry of the clutch pedal and the throttle pedal is kept same to enable the driver to operate pedals with ease and less effort. Both pedals are cable-actuated. The CAD model of the pedal is developed in SolidWorks. Static structural simulations are performed in Ansys for FEA. The boundary conditions and force exerted by the driver are inputted to generate results. Figure 6 shows the pedal design and FEA result.

8.2 Topology Optimization

The pedal design is optimized to reduce weight. Figure 7a shows the optimized design of the pedal. Static structural simulations for finite element analysis are performed for the optimized design on Ansys (Fig. 8).

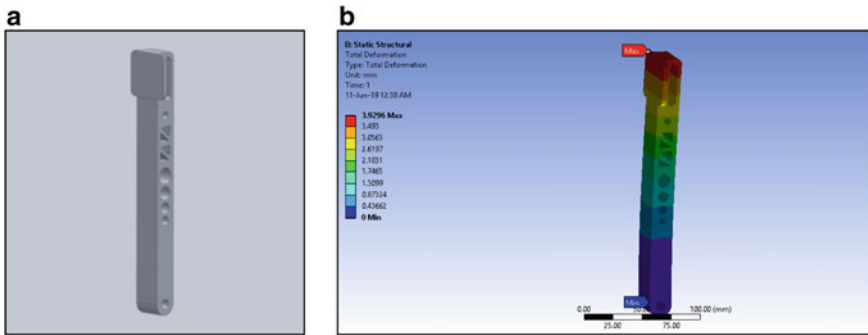


Fig. 7 a Optimized pedal design; b Total deformation

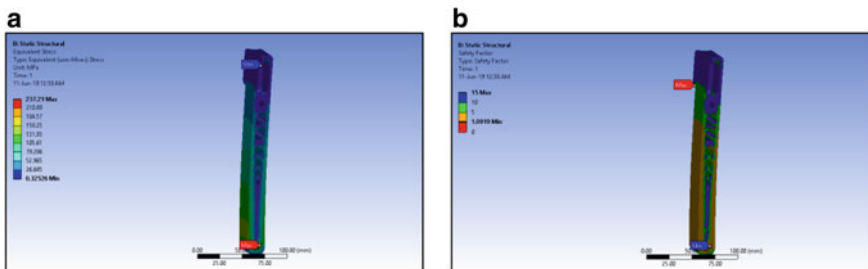


Fig. 8 a Equivalent stress; b Factor of safety

9 Other Components

9.1 Mounting Plate

The dimensions of the mounting plate are determined from the pedal box dimensions calculations. The mounting plate is intended to accommodate brake pedal, clutch pedal, throttle pedal, brake over travel switch (BOTS) mount and pedal stops for throttle and clutch pedals. Figure 9a shows the design of the mounting plate modeled in SolidWorks. For finite element analysis, boundary conditions and input forces are applied to perform static structural simulations in Ansys. Figure 10 shows FEA results.

9.2 Brake Over Travel Switch Mount

The BOTS mount is bolted to the mounting plate. The position of switch is worked out with the help of pedal travel calculations. The mount is designed according to the

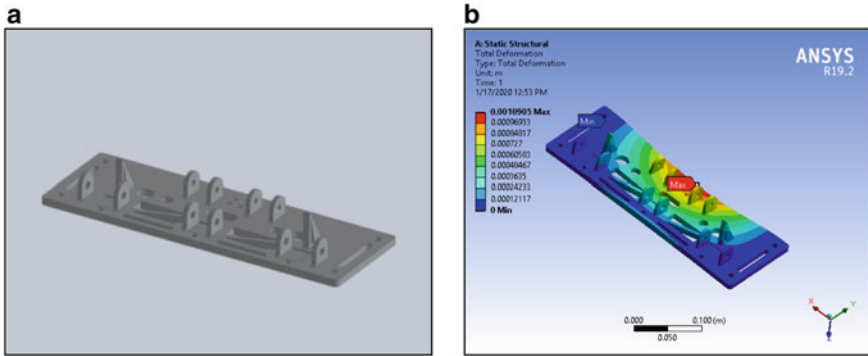


Fig. 9 a Mounting plate CAD model; b Total deformation

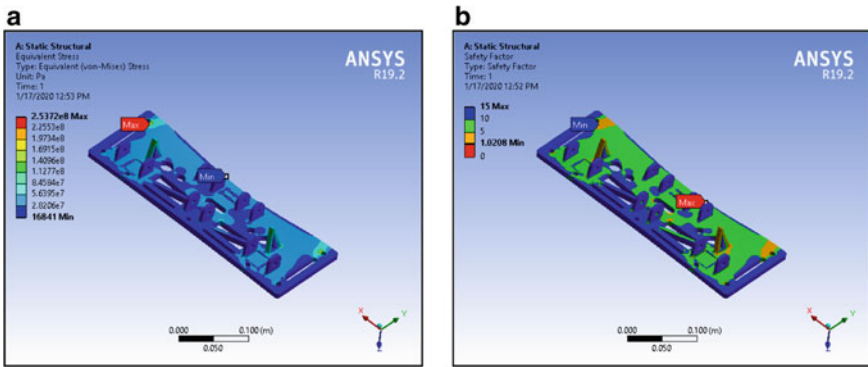


Fig. 10 a Equivalent stress; b Factor of safety

dimensions of an available switch. Figure 11a shows the design of the mount modeled using SolidWorks. Further, FEA analysis is performed by applying boundary and loading conditions and results are shown in Fig. 12.

10 Results

The results obtained from the finite element analysis performed on Ansys are shown in Table 6.

The results imply that the brake pedal after topology optimization can withstand forces even in panic braking conditions. The other parts of the pedal assembly designed are able to withstand high forces applied in driving conditions. The manufacturing process is decided with the aim of less welded joints and high accuracy in dimensions. CNC machining process is taken into account to serve this purpose as

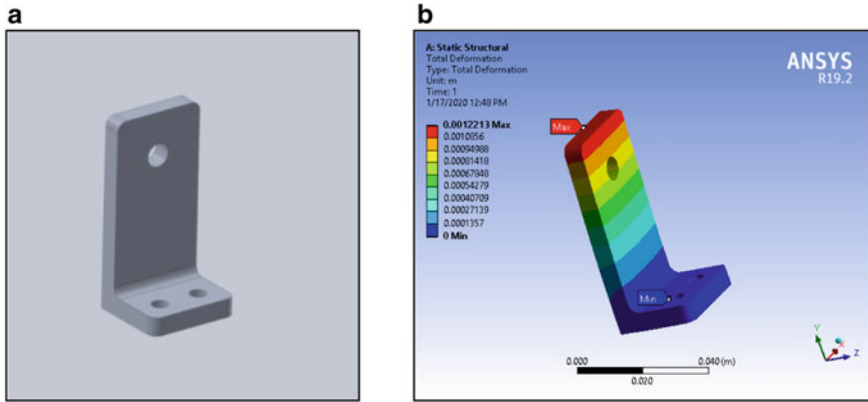


Fig. 11 a BOTS mount; b Total deformation

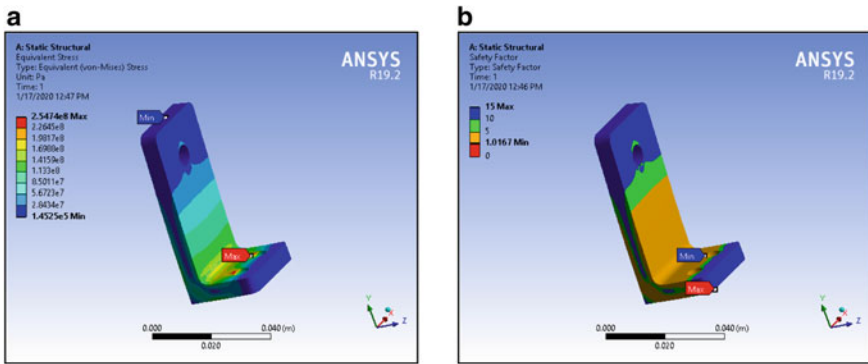
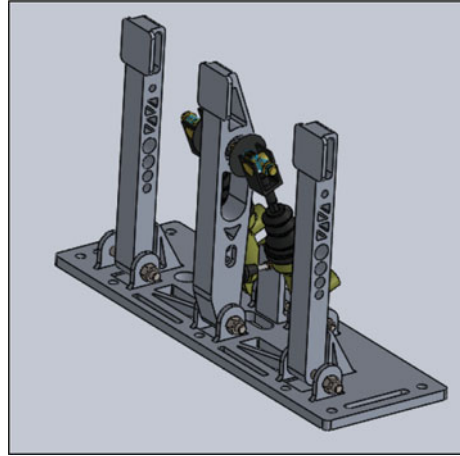


Fig. 12 a Equivalent stress; b Factor of safety

Table 6 Finite element analysis results

Component	Total deformation (mm)	Maximum stress (MPa)	Factor Of safety
Brake pedal	–	–	1.29
Optimized brake pedal	2.57	242.42	1.15
Clutch and throttle pedal	–	–	1.09
Optimized clutch and throttle pedal	3.93	237.21	1.09
Mounting plate	1.09	253.72	1.02
BOTS mount	1.22	254.74	1.02

Fig. 13 Final pedal assembly



this technique provides the freedom to design any possible geometry which further helps in weight reduction. The pedal assembly shown in Fig. 13 is the final assembly which weighs 2.5 kg, weighing approximately 53.6% less than the previous year's pedal assembly.

11 Conclusion

The primary goal was to lock all four wheels of the vehicle simultaneously and to develop a pedal assembly that is lightweight, compact, and robust to withstand braking forces in all conditions. Various resources were researched thoroughly and knowledge was applied to design the assembly whose characteristics resonate with the objective and is in compliance with the FSAE rules. The final pedal assembly is lightweight and compact. Weight as well as space optimization were carried out successfully with a weight reduction of approximately 53.6%. The assembly was manufactured with exquisite ease and at a low cost. The several testing sessions concluded that the driver had optimum control over pedals and better pedal feel. The assembly is reliable, efficient, and provides satisfactory performance results.

References

1. Limpert R (2011) Brake design and safety. Published by SAE International, Warrendale
2. Puhn F (1985) Brake handbook. Published by HP Books, New York
3. Milliken WF, Milliken DL (1994) Race car vehicle dynamics. Published by SAE International, Warrendale
4. Gillespie TD (1992) Fundamentals of vehicle dynamics. Published by SAE International, Warrendale

5. Smith C (1978) Tune to win. Aero Publishers, Fallbrook
6. AP Racing Catalogue Issue 3. <https://catalogue.apracing.com/64/>
7. Brembo Formula Student/SAE Catalogue. https://www.bremsen-center.de/brembo/downloads/racing/brembo-formula-student-katalog-2014_1.pdf
8. Wilwood Disc Brakes Technical and Parts Guide. <https://www.wilwood.com/Pdf/Catalogs/TechnicalCatalog.pdf>

Design and Analysis of Drivetrain Assembly for FSAE Vehicle



Sukriti Dhauni, Vanshita Sharma, and Vivek K. Chawla

Abstract This work emphasizes the method for designing, modelling, and stimulation of the drivetrain system for a formula student car. The objective of the project was to maximize torque transmission and reduce the complexities of the drivetrain assembly. Therefore, a spool is designed that cuts down the cost and overall weight of the vehicle. It holds the half shaft and transmits the torque efficiently to the tyres. Eccentric disc mounts are used for mounting the spool assembly. It also reduces the chain adjustment time and provides robust support for the spool. Eccentric discs can accommodate elongation or compression of approximately 4 cm. Aluminium 6061-T6 was selected for the manufacturing of the assembly as it has high strength and machinability. Moreover, it is lightweight and offers high-corrosion resistance. The assembly was CNC machined for better precision and high accuracy.

Keywords Drivetrain assembly · Spool · Eccentric disc · Formula student

1 Introduction

In design, simulation and fabrication of a formula student vehicle, the drivetrain assembly plays the most crucial role. It deals with the transmission of power delivered by the engine to the driving wheels. The objective of this paper is to develop an efficient drivetrain system that transfers maximum power and has an effective chain tensioning mechanism. The design should be simple, reliable and the cost of manufacturing should be low. The study deals with the designing and analysis of differential and its mounts. Keeping in mind the goal of simplicity and low cost while remaining efficient, all solutions available for each component were explored to get the best approach.

The purpose of a differential is to shift the torque to each rear-axle, while still enabling them to rotate at separate speeds. Considering all the factors locked differential or spool is chosen for the formula student vehicle. A spool overcomes the

S. Dhauni (✉) · V. Sharma · V. K. Chawla
Indira Gandhi Delhi Technical University for Women, Kashmere Gate, Delhi 110006, India

limitation of an open differential by coupling the rear tyres such that they spin at the same rate. Compared to other differentials, it is exceptionally lightweight, which reduces the rotating mass of the assembly. Due to its mechanical simplicity, it is highly reliable. The torque distribution depends on the amount of traction of each rear tyre. It can transfer up to 100% of the torque to a tyre if the other tyre is unloaded. It reduces the weight of the car, the cost of the car, and the part count of the car [1].

The differential mount holds the spool in place, while it is free to rotate about its axis. The chain tensioning mechanism used will drive the drivetrain mount design. It should be lightweight and should comply with the chain tensioning mechanism. The eccentric disc chain mechanism is the most favourable and effective chain tensioning mechanism. It is a simple, robust design that allows for easy adjustment of the chain [2].

Designing of the CAD model was preceded by the calculation of forces acting on the spool in the horizontal and vertical direction and the net torsional moment generated due to engine torque. Its basic design is to hold the half shafts and transmit the torque efficiently. The length of the spool is kept as short as possible to minimize the driveshaft angles. Eccentric discs have an inbuilt feature of chain tensioning and offer elongation or compression of up to an approximate length of 4 cm. The entire mounting assembly consists of two components, namely an eccentric disc and an eccentric disc mount. The mount holds the eccentric disc with the help of a clamping bolt that applies radial pressure on the disc. Both the disc and the mount consist of several small holes which help to vary the length of the chain by rotating the disc. The CAD model of the component was made using SolidWorks and the finite element analysis was done using Ansys. The manufacturing of the entire drivetrain assembly was done using Aluminium-6061 T6 as it provided the required strength and was economical. The outcome of the project was a completed and functioning drivetrain for 2020 team's vehicle. The car went through a series of testing phases and the drivetrain has worked efficiently so far. This ensured the design was fail-proof and helped improve the performance of the vehicle.

2 Problem Statement

This study is conducted to develop an efficient drivetrain system that transfers maximum power from the engine to driving tyres and has an effective chain tensioning mechanism. The design should be simple, lightweight, reliable, and the cost of manufacturing should be low. The study deals with the designing and analysis of differential and differential mounts.

Earlier the team used an open differential system that was heavy and had the traction difference problem. In open differential, when one tyre has a lower grip, it significantly limits the amount of power received by the vehicle. This is because the torque distribution is always 50–50, if one wheel cannot put down much power, the other will receive an equally low amount of torque. Most of the power is transmitted to the wheel with lower traction. Therefore, spool is used in this year's vehicle. The spool

locks the two driving wheels together on the axle and the wheels rotate at the same rate. Both the wheels receive the same power at all times. It is a simple design and is highly reliable. Compared to the open differential, the spool is extremely lightweight, and non-uniform torque distribution solves the traction difference problem. If one of the rear tyres is unloaded, almost all the torque received by the spool is transferred to the other tyre.

The chain tensioning mechanism in the previous car was inefficient and the tensioner kept on wearing off. Hence, the eccentric disc mount solves the issue of chain tensioning. By rotating the eccentric disc the whole spool assembly is shifted by some distance which allows the adjustment of the chain length.

3 Methodology

The spool was chosen as the differential system for the FSAE vehicle. The following constraints were kept in mind before designing the spool; (i) it should have housing for C.V. cups (axle end); (ii) length should be less for better half shaft angle; (iii) it should provide mounting for the sprocket. The inner diameter of the spool was fixed to accommodate C.V. cups and the outer diameter was decided by making different cad models and testing. The length of the spool was kept as low as possible so that the angle of inclination of half shaft is close to zero for better torque transmission. The sprocket is bolted to the spool. The rotational energy received by the driven sprocket is transferred to the spool and makes it rotate about its axis. The C.V. cups are press-fitted into the spool, thus C.V. joints rotate with the spool to turn the half shaft, and consequently the wheels of the vehicle.

After the design of the spool is finalized, the spool mount is designed. The mount holds the spool and allows it to rotate at its place. It should be lightweight and should comply with the chain tensioning mechanism. The chain tensioning mechanism chosen for the vehicle is the eccentric disc chain tensioning mechanism. It mainly consists of two parts; eccentric disc and eccentric disc mount. The eccentric discs hold the spool using bearing which allows the rotation of spool about its axis. The inner diameter of the eccentric disc is fixed as it is equal to the outer diameter of the bearing. A hole is made at the tip of the mount, through which a bolt is passed. On tightening the bolt, clamping force is applied on the eccentric disc. Before the bolt is tightened, the eccentric disc is free to rotate inside it. On rotating the eccentric disc, the whole assembly is shifted by some distance, which allows the slack to be removed from the chain. When initially installed, its alignment is maintained through the rotation.

All the parts have been designed using SolidWorks. Designing or modelling is an iterative process. Concepts are accomplished in CAD, parts are combined to generate assemblies, interferences are checked and resolved, elements are tested with FEA that is completed on Ansys, and strength problems are self-addressed within the CAD model. The original CAD design may need to be modified at any point, and the process starts over again.

4 Modelling

4.1 Spool Design 1

This idea allows the use of a single-body configuration that provides CV cup accommodation. The CV cups are press-fitted into the spool. The design has grooves on the outer surface for the use of circlips to secure the bearing. A disc/mount is made for mounting the sprocket. The sprocket is bolted to the mount. A constant outer diameter of 80 mm was chosen to accommodate the CV cup. The constant outer diameter makes it simple and easy to manufacture. The grooves for circlip and boring of the middle make this a lightweight solution. It provides good support to CV cups. The downside of the design is that the stress concentration will be high at the circlip grooves and the bearing size would be larger (Fig. 1).

Fig. 1 Isometric view of first spool design

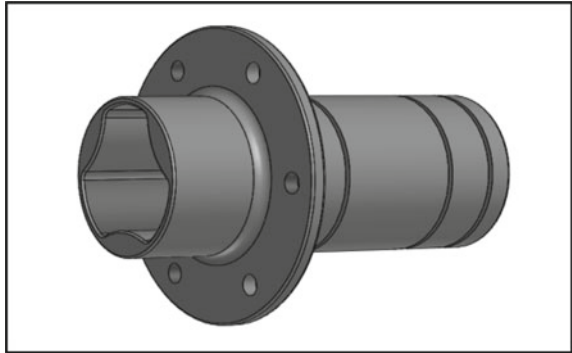


Fig. 2 Isometric view of second spool design

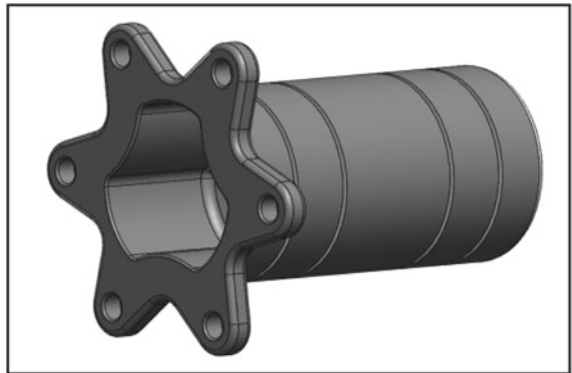
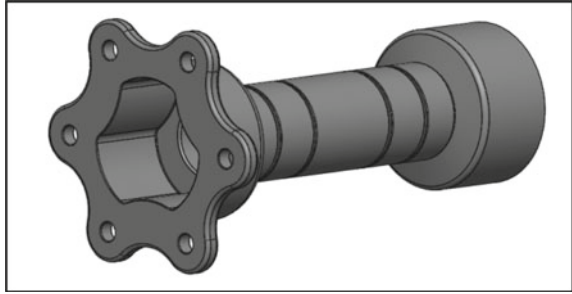


Fig. 3 Isometric view of third spool design



4.2 Spool Design 2

This design is identical to concept one except the sprocket mount is shifted to the left end, and the length is increased. This concept also uses circlip grooves and circlips for the bearing housing. The sprocket mount is moved to the left end to make its mounting easier. Excess material from the mount is removed, which reduces its weight. The length of the spool is increased to support a significant part of the CV cup, which provides more rigidity and strength. It is a simple, single-body design. The strength of the design is more because of increased length. There is more room for the material to be removed to make it lightweight. Stress concentration will be there at circlip grooves and bearing size would be larger (Fig. 2).

4.3 Spool Design 3 (Selected Design)

This design is different from the rest of the designs. The concept utilizes a two-body design with graduated diameter. The diameter at ends is 80 mm and is reduced to 50 mm in the middle. All the excess material is removed from the body, which makes it lightweight. The ends have a larger diameter to accommodate CV cups, and it is reduced in the middle to hold its splined portion. Sprocket mount is at the left end of the design. This concept also uses circlip grooves and circlips for the bearing housing. Since the size of the spool is reduced, smaller and lighter bearings are used. Excess metal is removed, which makes it lightweight (Fig. 3).

4.4 Spool Final Design

Concept 3 is selected as the best spool design because it has a low moment of inertia and is lightweight. It is a two-body design with one part press-fitted into another. Key is cut on the part to be press-fitted, and a slot is made on the other part for the keyway. This prevents relative motion between the parts and enables torque transmission. The

Fig. 4 Assembled view of final spool design

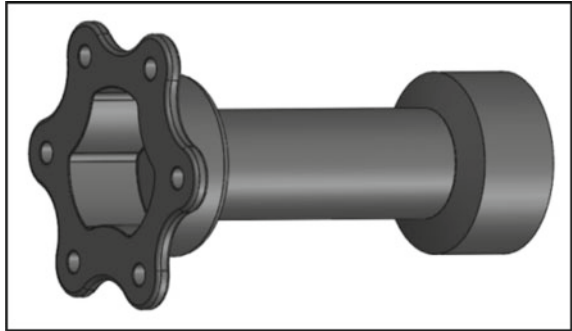
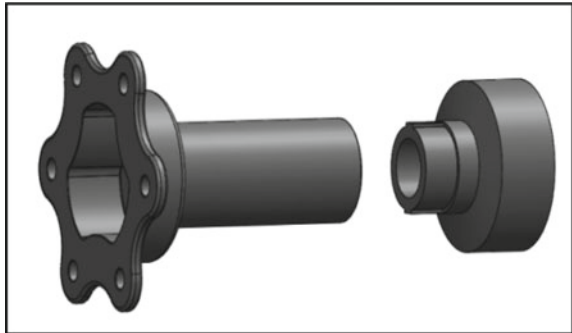


Fig. 5 Exploded view of spool design



diameter at ends is 80 mm to accommodate CV cups and is reduced to 50 mm in the middle. This allows the usage of small diameter bearing, which reduces the weight of the assembly. Housing is made for the CV cup to provide proper support. Splines are cut inside the spool for appropriate engagement of CV cup and torque transmission. When considering packaging, it was discovered that the half shaft angle has reduced, which in turn has improved the efficiency of the drivetrain. Aluminium 6061-T6 was selected for manufacturing of spool as it has high machinability and lightweight. Moreover, it offers good corrosion resistance. The part was CNC machined for better precision and high accuracy (Figs. 4 and 5).

4.5 Eccentric Disc Mounts

The design is simple and allows exact adjustment of the chain. The differential mount consists of two components, namely, eccentric disc and eccentric disc mount. This mount utilizes an eccentric disc to adjust the tension in the chain. The mount holds the eccentric disc with the help of a clamping bolt that prevents the rotation of the eccentric disc. The desired chain tension can be achieved by rotating the eccentric disc. The disc and the mount consist of several small holes, which help to vary the

length of the chain by rotating the disc and locking it using two M4 bolts. It can accommodate elongation or compression of up to an approximate range of 4 cm (approximate length of about 2 chain links). The shoulder is made on the mount to secure the eccentric disc, and it also provides an additional frictional surface to keep the eccentric disc in place. The shoulder on the disc secures the bearing from slipping, and a groove is cut on the other side to secure the bearing using a circlip. However, the issue with this design is that it is difficult to machine such a complicated design.

Aluminium 6061-T6 was selected for the manufacturing of eccentric mount as it has high strength and machinability. Moreover, it is lightweight and offers high corrosion resistance. The assembly was CNC machined for better precision and high accuracy. Figure 6 shows the final design of eccentric disc and eccentric disc mount and Fig. 7 shows the assembled eccentric mount.

Fig. 6 a Eccentric disc
b eccentric disc mount

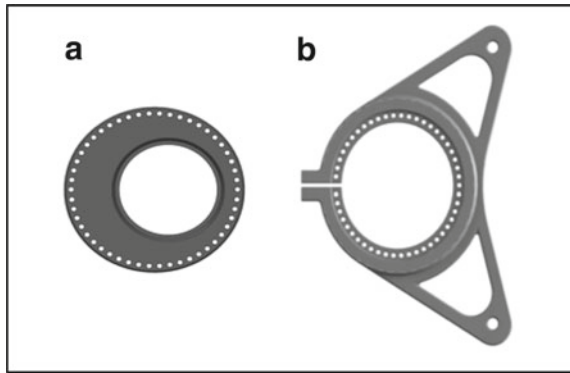
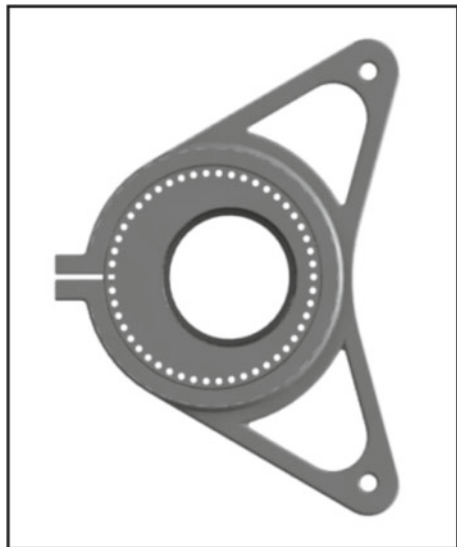


Fig. 7 Assembled eccentric mount



5 Calculations and Analysis

5.1 Spool

FEA analysis was conducted on the spool to ensure the strength of the spool is sufficient to withstand the loads generated while driving. Using the following equations, a cumulative load required at spool was identified for carrying out this study. The final drive reduction is the ratio between driven and driver sprocket and there are two other reductions; the primary reduction and secondary reduction. The primary reduction is the ratio between the clutch input shaft idle gear and the idle gear on the layshaft. The secondary reduction is in the main gearbox which changes according to every gear as the driver demands more torque for more speed. It is the ratio between the drive gears of the layshaft and output shaft [3].

$$T_{\text{output}} = T_{\text{engine}}(R_p \times R_s \times R_d) \quad (1)$$

$$\begin{aligned} T_{\text{engine}} &= \text{Torque delivered by the engine (KTM Duke 390)} \\ &= 35 \text{ N-m (at 7250 rpm)} \end{aligned}$$

$$\begin{aligned} R_p &= \text{Primary reduction} \\ &= 2.66 \end{aligned}$$

$$\begin{aligned} R_s &= \text{Secondary reduction} \\ &= 2.667 \end{aligned}$$

$$\begin{aligned} R_d &= \text{Final drive reduction} \\ &= 2.8 \end{aligned}$$

$$\begin{aligned} T_{\text{output}} &= 35(2.66 \times 2.667 \times 2.8) \\ &= 695.233 \text{ N-m} \end{aligned}$$

For the FEA analysis, the load was applied at the spool sprocket interface while the CV cup housing was made fixed. A worst-case scenario was analyzed to understand the loading case. The worst-case scenario was while taking a turn the outer wheel is fully unloaded and all the torque is transmitted to the other side of the spool [4].

The results shown in Figs. 8, 9, and 10 are from when the entire load is transferred to right side, and Figs. 11, 12, and 13 are from when the entire load is transferred to left side.

The highest stresses on both the spool ends arise directly adjacent to fixed faces. The stresses produced in the spool are spread uniformly and are significantly less than the material's yield stress. The minimum safety factor is attained. The result of the FEA analysis indicates that the spool can withstand the loads to which it is expected to be subjected to.

Fig. 8 Spool equivalent stresses (right side)

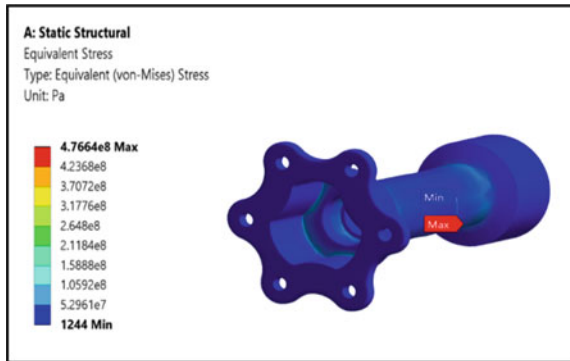


Fig. 9 Spool total deformation (right side)

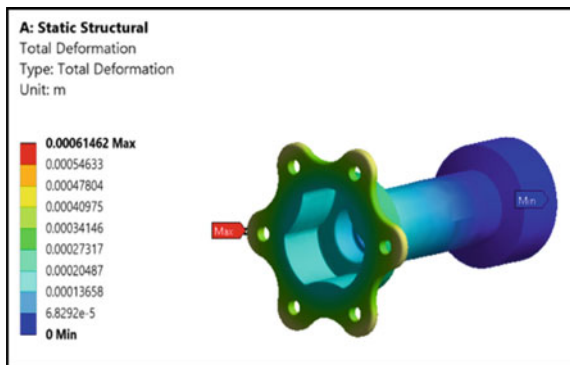


Fig. 10 Spool safety factor (right side)

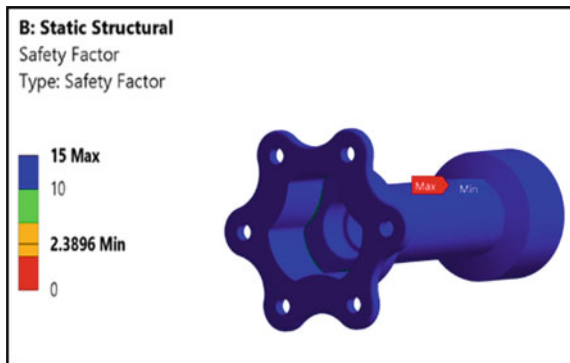


Fig. 11 Spool equivalent stress (left side)

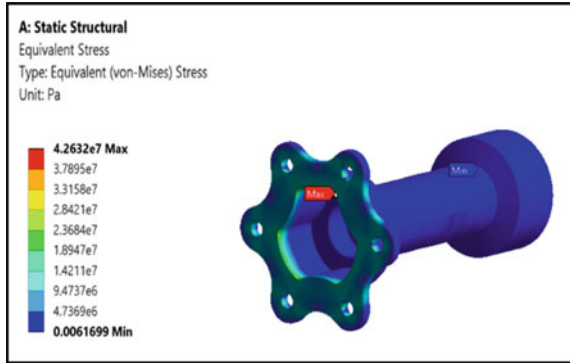


Fig. 12 Spool total deformation (left side)

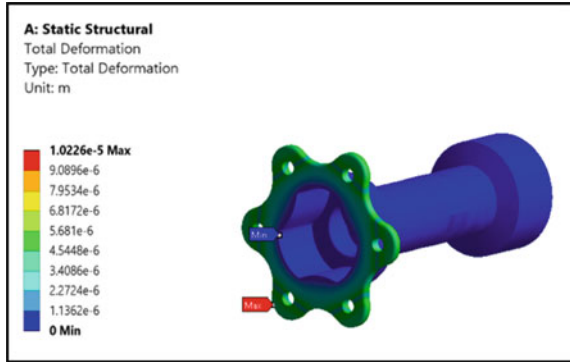
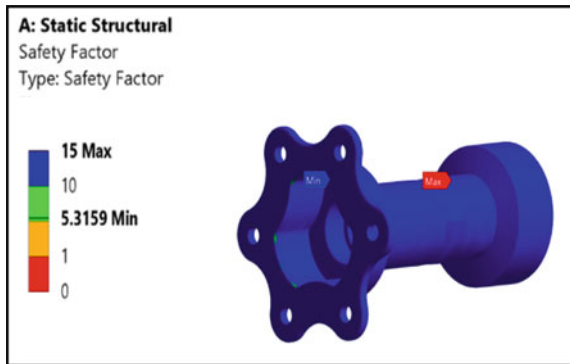


Fig. 13 Spool safety factor (left side)



5.2 Eccentric Disc Mounts

To ensure that the strength of the eccentric disc mount is adequate to withstand the load, FEA analysis was performed. Following calculations were done to find the load.

Maximum Force Generated

For calculating the maximum forces generated at the differential mount, maximum chain tension is calculated using maximum torque produced by the engine.

Pitch radius of rear sprocket (R_r) = 0.110 m.

Pitch radius of front sprocket (R_f) = 0.035 m.

Wrap Angle = 256; $\Phi = 37$.

Torque produced by engine (T) = 35 Nm.

Tension in chain (T_t),

$$T_t = T/R_f \tag{2}$$

$T_t = 1000$ N.

Solving for components of T_t (refer to Fig. 14),

$$T_x = T_t \times \cos(\Phi) \tag{3}$$

$$T_y = T_t \times \sin(\Phi) \tag{4}$$

$T_x = 800$ N; $T_y = 602$ N (Figs. 14 and 15).

Following components are shown in Fig. 15.

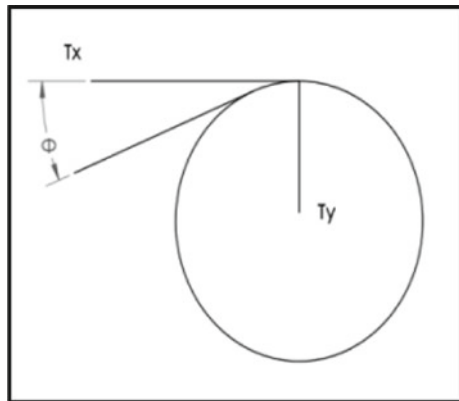
- A—Sprocket B—Eccentric disc + mount + bearing (left)
- C—Spool centre D—Eccentric disc + mount + bearing (right)

Since the system is in equilibrium,

$$\Sigma F_y = 0 \tag{5}$$

$$B_y + D_y = -635.35 \tag{6}$$

Fig. 14 Components of T_t



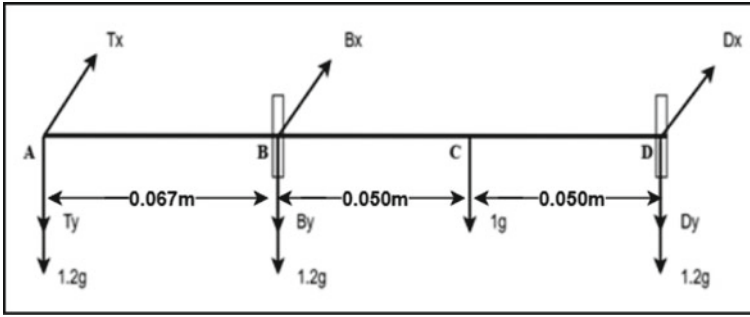


Fig. 15 Free body diagram

$$\Sigma F_x = 0 \tag{7}$$

$$B_x + D_x = -800 \tag{8}$$

Taking moment zero about point D,

$$\Sigma M_y = 0 \tag{9}$$

$$\Sigma M_x = 0 \tag{10}$$

$$B_x = -1360 \text{ N}; D_x = +560 \text{ N}.$$

$$B_y = -1060.089 \text{ N}; D_y = +413.089 \text{ N}.$$

Resultant of reaction forces,

$$F_B = 1724 \text{ N} \quad F_D = 695.87 \text{ N}$$

The reactions are higher on the left differential mount. Therefore, forces at B are considered for calculations.

$$F_x = -1360 \text{ N} \quad M_x = 0 \text{ N-m}$$

$$F_y = -1060.089 \text{ N} \quad M_y = 0 \text{ N-m}$$

$$F_z = 0 \text{ N} \quad M_z = 0 \text{ N-m}$$

Clamping Force

To find the clamping force required to keep the eccentric plate from spinning during operation, following calculations were done.

Centre distance between bearing and eccentric disc (L_1) = 0.010 m.

Centre distance between Eccentric Disc and bolt hole (L_2) = 0.085 m.

Torque required by bolt (T_B) is given by the product of resultant force on the bearing and the distance between the centres of the eccentric disc and the bearing.

$$T_B = F_B \times L_1 \tag{11}$$

$$T_B = 17.24 \text{ N-m.}$$

For the calculation of clamping force on the bolt, the coefficient of friction was taken as 0.12 [5] and a safety factor coefficient of 1.5 was taken to amplify the forces in the system [6].

$$\text{Safety factor } (f) = 1.5$$

$$\text{Coefficient of friction } (\mu) = 0.12.$$

$$\text{Clamping force } (F),$$

$$F = \frac{f \times T}{L_2 \times \mu} \tag{12}$$

$$F = 2535.29 \text{ N.}$$

For finite element analysis, static structural simulations are performed in Ansys. The boundary conditions and input forces are applied. Since both the mounts are identical, testing was performed on one mount. On applying the load on the eccentric disc mount, the following results were achieved.

The results of the analysis show that this design can uphold the stress with a safety factor of approximately 10 and the stresses generated within the mount are equally distributed. After performing the FEA analysis of the differential mounts it was observed that the maximum stress generated in the mount is within the permissible limit of the material. Hence, the mounts will withstand the loads that it is expected to be subjected to (Figs. 16, 17 and 18).

The final spool and eccentric mount assembly are shown in Fig. 19. All the parts were CNC machined for high accuracy and precision. It gives the freedom to build any possible design that further helps to minimize weight.

Fig. 16 Equivalent stress generated in mount

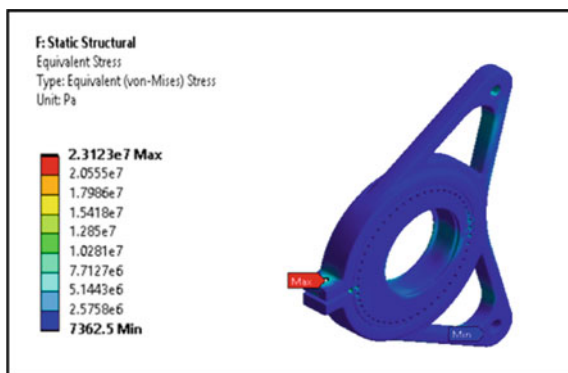


Fig. 17 Total deformation in mount

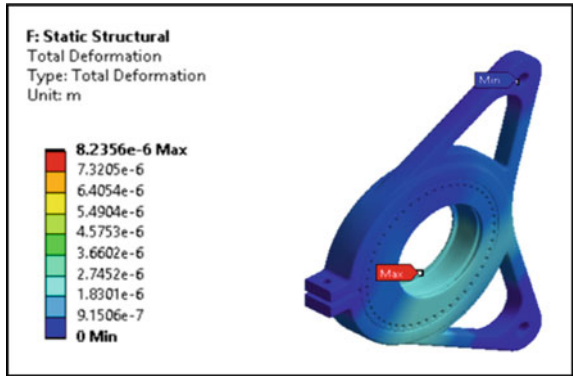
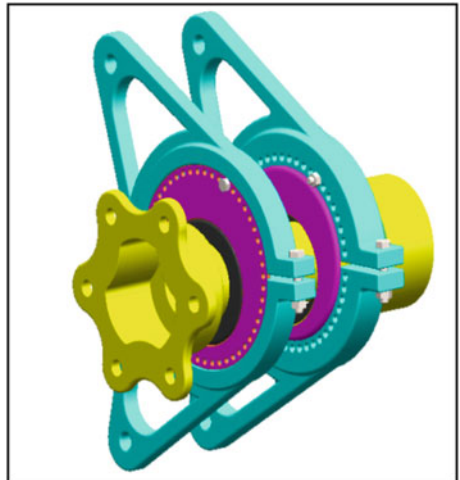


Fig. 18 Factor of safety of mount



Fig. 19 Spool and spool mount assembly



6 Conclusion

Considering all the factors spool is chosen for the formula student vehicle. The spool locks the two driving wheels together on the axle and the wheels rotate at the same rate. Both the wheels receive the same power at all times. It is a simple design and is highly reliable. Compared to all other differentials, the spool is extremely lightweight. The torque is transferred from the wheels to the road which pushes the car in the forward direction. The distribution of torque is not uniform. The torque distribution is dependent on the traction amount of each rear wheel. If one of the rear tyres is unloaded, almost all the torque received by the spool is transferred to the other tyre. Furthermore, spools make inboard brakes a possible packaging-wise for FSAE cars because of their compact nature. It reduces the outboard mass, as well as the car's overall weight.

For the next design, the length of the spool can be reduced by making housing for C.V. joint and not using C.V. cups. By reducing the diameter of the spool, bearing size can be reduced which will in turn reduce the size of the eccentric disc and the mount. This will cut down a significant amount of weight from the assembly.

The eccentric disc chain tensioning mechanism is the most favourable mechanism for chain tensioning. By rotating the eccentric disc the whole spool assembly is shifted by some distance which allows the adjustment of the chain length. It can accommodate elongation or compression of up to an approximate range of 4 cm. This design is not solely sturdy however permits for the highest level of adjustability. The count of components has also reduced by using eccentric disc mount. The manufacturing could complex still it is the most effective possible chain tensioning and differential aligning experience.

For the next design, the weight of the mounts can be reduced since the factor of safety is high. Smaller eccentric discs could be used which would severely reduce the mass of the system.

References

1. Giang B. <https://murmotorsports.eng.unimelb.edu.au/>. Last accessed 2019
2. Dewade AV, Mayuresh SJ, Shubham RA, Mohit DA (2011) Design of chain tensioner for FSAE car. IRJET 4(07):2017
3. Nimbalkar A, Pranav P, Abhishek R, Raj D (2018) Design and development of solid axle system for FS car. IJREAM. ISSN: 2454-9150
4. Ayres TJ (2013) Design and manufacture of a formula SAE Engine. Edith Cowan University
5. Mohan K (2011) Frictional analysis of aerospace alloys and composite materials. University of New South Wales, Sydney
6. Lebowsky J (2016) Drivetrain design for the 2016 global formula racing combustion car. Oregon State University Honors College

Emission Analysis of Compression Ignition Engine with Induced Chemical Reaction Between Engine Exhaust and Slaked Calcium Hydroxide Solution



Vadivel Ayyakkannu, Periyasamy Sivanandi,
and Arivazhagan Sampathkumar

Abstract In the current scenario, one of the primary challenges is global warming and the primitive task is to curtail the emission of CO₂ which is a mainspring for global warming. Climate change as a consequence of global warming is the additional worryment. The human being and all other living organisms are seriously affecting by global warming in straight or diffusely. This paper analyzes the emission level parameters of a four-stroke diesel engine with the induced chemical reaction between slaked calcium hydroxide solution and exhaust emission have been studied experimentally. The calcium hydroxide solution setup was fabricated and exercised on a single-cylinder, four-stroke compression ignition engine with variable loads of zero, 2, 4, 6, and 8 kg. This setup was placed in between the engine exhaust manifold and exhaust gas line. Using the AVL gas analyzer, the emissions like as HC, CO, CO₂, and NO_x were measured outwardly. The test results demonstrated that the emissions of contaminants decreased significantly after the calcium hydroxide solution has been used. The installation of the slaked calcium hydroxide solution setup results in reducing unburned HC, CO₂, and CO by 13, 11.3, and 35%, respectively. The slight increase of the NO_x emissions appears as a negative factor. There was no fuel penalty by using the calcium hydroxide solution setup.

Keywords CI engine · Calcium hydroxide solution · Exhaust line

V. Ayyakkannu (✉)

Department of Mechanical Engineering, Sri Ramakrishna Engineering College, Coimbatore, Tamil Nadu 641022, India

P. Sivanandi

Department of Mechanical Engineering, Government College of Technology, Coimbatore, Tamil Nadu 641013, India

A. Sampathkumar

Department of Mechanical Engineering, National Institute of Technology Puducherry, Karaikal, U.T. of Puducherry, India

1 Introduction

The emissions from CI engines cause severe air pollution which can cause serious health and well-being effects. These emissions also cause significant harm, like heart disease, headache, fatigue; decrease the capacity of the lungs to work, and cause coughing and chest pain. The emission of noxious gases flying exponentially in the last decade which results raise in temperature of the earth close to 1 °C [1]. Linda S. Bafver et al. investigated the effect of adding limestone with the fuel in the residential combustion of the oat grain. The results show that the emission mass of the particle can be decreased by adding kaolin to the fuel. On the other hand, there was no effect on particle mass by the addition of limestone to the fuel [2]. Alahmer et al. by an experimentally investigated that the quantity of water content added to diesel fuel in a diesel engine can increase the thermal efficiency and decreased the nitrogen oxide emission significantly. It was also found that the carbon dioxide emission level increased in the diesel emulsion fuel [3]. Dhanalakshmi et al. design and fabricated eco-friendly silencer and tested in a diesel engine. This silencer is created by applying a layer of activated carbon pellets, aluminum balls, and soda-lime. From the experimental result, it was found that the emission and smoke level from the diesel engine is reduced a lot [4]. Daniel Chatterjee et al. proposed the model with creating a combined system that consists of NO_x storage and NH₃-SCR catalytic system, predicted that this combined system provides higher nitrogen oxide conversions in comparison with stand-alone NO_x storage and reduction catalyst [5].

Juan Chen et al. were carried out a coal combustion experimental analysis with adding kaolin or limestone to coal in a drop tube furnace. From the experimental result, it was concluded that particulate matter (PM) emissions are effectively reduced by the addition of limestone to coal [6]. Vinodbabu Chintada et al. conducted an emission test in a diesel engine with reducing toxic particle silencer (RTP) by varying the speed and different quantities of limestone content. The test results show that while increasing the limestone content in RTP from 25 to 150 g, the hydrocarbon emission reduced by 38.5% and CO emissions reduced by 44.1% [7]. Qadir Bakhsh Jamali et al. investigated the engine emission characteristics with an engine emission control system like an aqua silencer. Through the use of lime water in the silencer, the toxic NO_x gas concentrations are decreased along with the final exhaust gas temperature which also has a positive environmental effect [8]. Jay M. Parmar et al. were carried out an emission test in a diesel engine with a perforated limestone plate catalytic converter. It was concluded that the limestone plate catalytic converter was feasible as it produced a satisfying performance for the provided operational conditions and the reduction of CO₂, HC, and CO emissions [9]. R. Bharath et al. design and fabricated eco-friendly silencer and tested in a four-stroke petrol engine. This green silencer was made with adding layer form of an activated charcoal layer and soda-lime water. From the experimental result, it was found that the emission and smoke level from the petrol engine is reduced a lot [10]. Wail Adaileh and Ali Alahmer investigated the emission characteristics on Nissan Sunny sedan engine using limestone filter in silencer. The test showed that the average reduction in unreacted HC, CO, CO₂, and

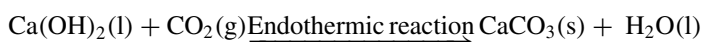
NO_x after use of the limestone filter was 26.8, 44.4, 4.6, and 40.2%, respectively [11]. Murari Mohon Roy et al. developed an exhaust gas treatment system and it is tested in a stationary direct injection diesel engine. Through this system, the engine exhaust gas was passed into the silica gel absorbing material. From the experimental result, it was found that the exhaust odor and smoke reduced to almost nil level, and the emissions like HC, CO, CO_2 , and NO_x were significantly reduced [12]. Ahmad Sakhrieh developed a simple low-cost limestone filter and experimented on a four-cylinder diesel engine with performance and emission characteristics. The carbon dioxide and nitrogen oxide emission concentrations were found to have decreased considerably without raising the fuel usage rate [13].

Mylaudy S. Rajadurai et al. investigated the characteristics of emission gases on four-cylinder four-stroke diesel engine with pre-heated ZSM-5 zeolite in silencer. It was concluded that the average reduction of carbon dioxide was 5.89% and 9.44 ppm for unburnt hydrocarbon reduction [14]. Norman T. Huff studied the variety of fibrous materials for use in an absorptive silencer system. He concluded that the durability of chemical and thermal of the materials has a significant role in absorptive silencer system. Furthermore, the size of the fibers and the number of fibers per cubic meter has a significant influence on the acoustic performance of the materials [15]. Across the world, scientists and researchers endeavoring different methods, setup, and design modification of mechanical systems to exploit the maximal fossil fuel usage and reducing in the ejection of unsafe gases.

However, to the author's best knowledge, very few publications can be found available in the literature that discusses the effect of using slaked calcium hydroxide solution setup to reduce the emission. The main aim of this paper is to study the effect of slaked calcium hydroxide solution setup in the compression ignition engine to reduce the emission.

2 Chemical Reaction Induced

Conversion of CO_2 to baking soda, calcium hydroxide stone compounds by inducing the reaction between exhaust gas, and slaked calcium hydroxide solution by passing through CO_2 . Accomplishing the trapping of gaseous carbon dioxide and monoxide which is emitted from the automobile completely eco-friendly in the precipitated form of calcium hydroxide stone, meanwhile, the cooling of outlet exhaust gases adds as side merit thus lowering the NO_x and HC levels as well. Moreover, the compensation package is the production of calcium hydroxide stone from CO_2 through endothermic reaction as well as cooling the exhaust gas before releasing it to the atmospheric gases [16].



3 Experimental Setup

The slacking unit, which was introduced adjacent to the conventional three-way catalytic converter, consists of a completely sealed tank with a filter opening mechanism, concealed inlet–outlet openings, a conventional 0.1 HP/12V liquid pump, and a current supply from the battery. When kept vertically inside the bumper, the bottom of the setup acts as a storage tank/sump while the top provides ample space for the reaction to take place. The inner section of the upper segment lays a special spraying mechanism that ensures that all the incoming CO₂ gets trapped within the sprayed solution. This segment could be larger and roomier than the storage section beneath. The only layer which separates these two segments is the detachable filter mechanism which collects the trapped carbon precipitate. The slacking unit made by PU material of dimension confined to total working space of two liters with 500 ml storage capacity where the inlet of exhaust gas. The spraying section composes of two sprayers each of 60 L/h discharge, this was to ensure that no cognition damage occurs to the sprayers. These two sprayers were mounted in such a way that the spray-reach all the nook and corners of both vertical and horizontal sections of the spraying unit to provide maximum reaction feasibility. The slaked calcium hydroxide solution filter setup was constructed and tested on a diesel engine. The engine details were listed out in Table 1. The exhaust discharge was analyzed using an AVL gas analyzer. The description of the gas analyzer was provided in Table 2. Figure 1 shows the test rig employed at Sri Ramakrishna Engineering College Thermal Engineering

Table 1 Technical specification for the testing apparatus

Make and model	Kirloskar TV1
Type	Four-stroke, DI, diesel engine
Bore × Stroke	87.5 mm × 110 mm
Rated power	5.2 kW
Compression ratio	17.5:1
Type of cooling	Water

Table 2 Specification of AVL gas analyzer

Make and model	AVL 444 di-gas analyzer
Measures	CO, HC, NO _x
Measurement frequency	About 1 Hz
Sensor	O ₂ : Electrochemical CO ₂ : NDIR (infrared)
Accuracy	O ₂ : 5% of measured value ± 1digit CO ₂ : 5% of measured value ± 1digit
The diameter of gas pipe	6 mm
Air flow	0.51/min



Fig. 1 Single-cylinder four-stroke CI engine with slaked calcium hydroxide solution setup

laboratory. The complete experiment and its function are seen in Fig. 2. Figure 3 represents the slaking calcium hydroxide solution unit used for the experiment.

The exhaust gases of the engine were measured using an AVL five gas analysis tool. Engine pollutants such as CO, CO₂, HC, and NO_x were analyzed [17]. The emission concentration was measured with and without calcium hydroxide solution filter setup. A single-cylinder engine combined with a dynamometer was used for data collection. Figure 4 shows the solution of slaked Ca(OH)₂ in a measuring beaker and calcium hydroxide stone deposit in a semi-soil form after conducting an endurance test in the diesel engine. The solution of slaked Ca(OH)₂ was reacted with engine exhaust emission and converted into calcium hydroxide stone.

4 Error Analysis

Error analysis has usually been conducted to investigate inconsistencies in the tests. Some uncertainties are considered for the experiment as described below: (a) calibration of equipment, (b) ambient and laboratory conditions, (c) observations during an experiment, and (d) instruments used for the experiment. Complete uncertainty was calculated during the experiment using the propagation of error techniques following Holman's technique. Holman [18]. Table 3 displays the uncertainty from the experiment. The overall uncertainty was found to be $\pm 2.29\%$ during the experiment.

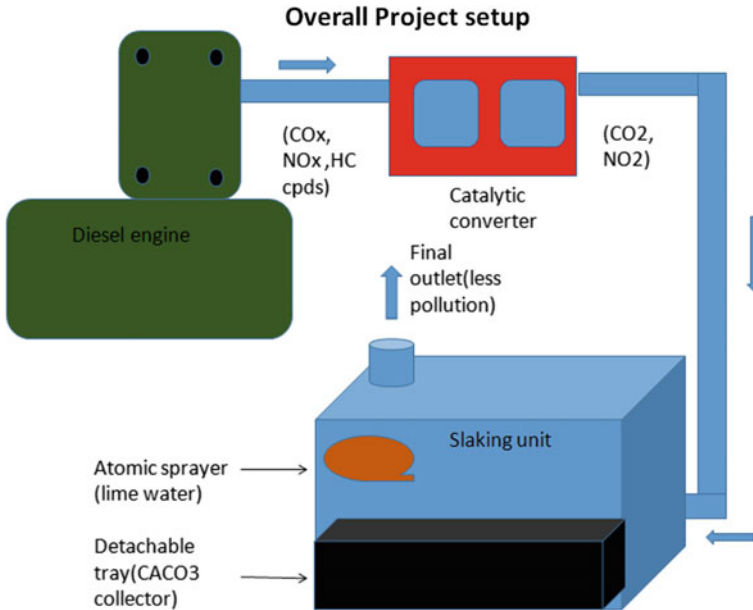


Fig. 2 Overall experimental setup

5 Results and Discussion

Experimental investigations were performed under various loading conditions ranging from zero loads to maximum load and that each reading was carried out under stable conditions. The slaked calcium hydroxide solution setup in the compression ignition engine with various load conditions was tested for the emission characteristics.

5.1 Emission Characteristics

5.1.1 Carbon Dioxide (CO₂) Emission

Figure 5 indicates the CO₂ emission with and without the use of a slaked calcium hydroxide solution. At peak load, the concentrations of CO₂ with and without using slaked calcium hydroxide solution are 2.75 and 3.1%, respectively. The significant decrease in CO₂ after the use of calcium hydroxide solution was 11.3%. Carbon dioxide (CO₂) is a non-combustion and colorless gas released when carbon-fueled fuels burn completely. Besides, CO₂ is an important exhaust parameter for engine emissions. Calcium carbonate can precipitate when the CO₂ present in the engine



Fig. 3 Slaking calcium hydroxide solution unit with sprayer capacity of 60 L/h



Fig. 4 Slaked $\text{Ca}(\text{OH})_2$ solution and calcium hydroxide stone deposit after conducting an endurance experiment in the diesel engine

Table 3 Experiment uncertainties

Parameters	Systematic errors (\pm)
Load	± 0.1 N
NO _x	± 10 ppm
CO	$\pm 0.03\%$
CO ₂	$\pm 0.03\%$
HC	± 12 ppm

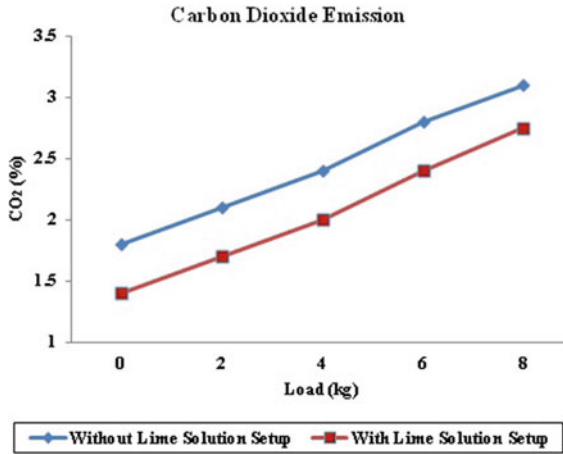
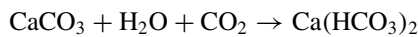
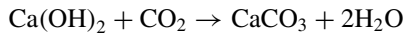
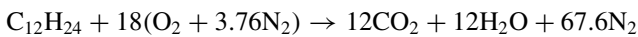


Fig. 5 CO₂ concentration variation with and without using slaked calcium hydroxide solution as a result of engine load

exhaust interacts with the slaked calcium hydroxide solution. Finally, carbon bicarbonate will be precipitated when calcium carbonate further revealed to carbon dioxide.



The chemical process of diesel fuel to total combustion was



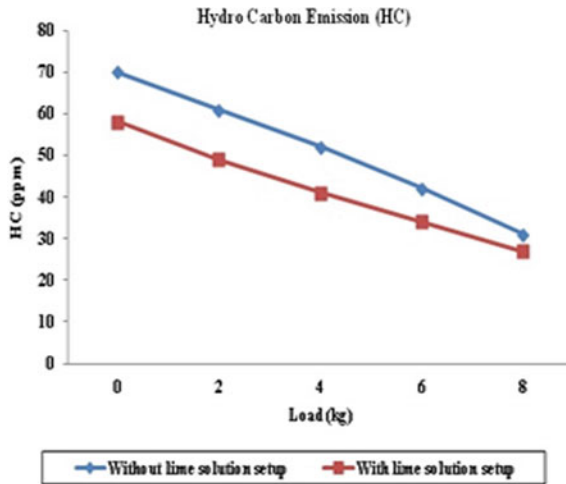


Fig. 6 HC concentration variance with and without using slaked calcium hydroxide solution as a result of engine load

5.1.2 Hydrocarbon (HC) Emission

The hydrocarbon (HC) is produced by six main ways and they are (a) crankcase blow-by gases; (b) leakage in exhaust valve; (c) in-cylinder liquid fuel; (d) flame extinguishing on cylinder walls; (e) absorption and desorption in oil film on cylinder walls; and (f) misfired combustion occurring in a highly rich or lean situation. The hydrocarbon is typically emitted in the engine exhaust if the combustion processes are not fully completed. The total hydrocarbon concentration is measured in parts per million. The concentration of HC emission for different loads with and without using slaked calcium hydroxide solution is represented in Fig. 6. After using slaked calcium hydroxide solution setup in the engine, the amount of HC has been gradually decreasing. And the average reduction of HC after using calcium hydroxide solution setup was 13%.

5.1.3 Nitrogen Oxide (NO_x) Emission

Generally, the NO_x level heavily depends on the oxygen content of the engine intake air and the temperature sustained during combustion. Under high temperatures and pressures, nitrogen and oxygen react to form NO_x and NO₂ during combustion. The rate of NO_x formation is temperature-related. Figure 7 indicates the formation of NO_x with and without slaked calcium hydroxide solution. It is shown that the NO_x emission was raised on average by 11.75% after experimenting with the use of a slaked calcium hydroxide solution. It appears as a negative factor as a result. Water can soak up the nitrogen oxides to a greater extent. The preceding reaction

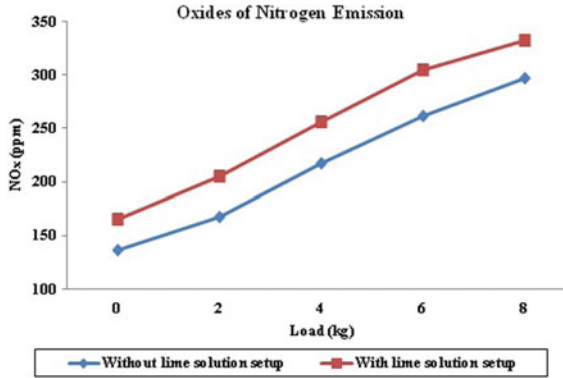
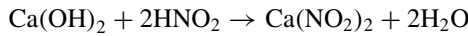
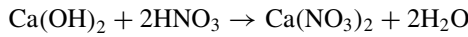


Fig. 7 NO_x concentration variance with and without using slaked calcium hydroxide solution as a result of engine load

mechanism provides evidence for the above-mentioned argument.



Another result is that the maximum temperature of combustion resulting in an increase in engine load during chemical reactions is directly influenced by NO_x formation.

5.1.4 Carbon Monoxide (CO) Emission

From Fig. 8, it is noted that the carbon monoxide emission is reduced with the effect of slaked calcium hydroxide solution when compared with the no setup condition. Usually, CO has been produced at combustion, as the engine operates in rich mixtures. Exhaust gases can produce a significant amount of CO because all carbon atoms of fuel cannot be oxidized to CO₂. Therefore, a key element in producing CO emissions would be the air–fuel equivalence ratio. Sources of CO formation are the effects of wall and crevice and partial oxidation of HC and slow expansion kinetics. But in this experiment, using the slaked calcium hydroxide solution setup CO concentration reduced at an average of 35%.

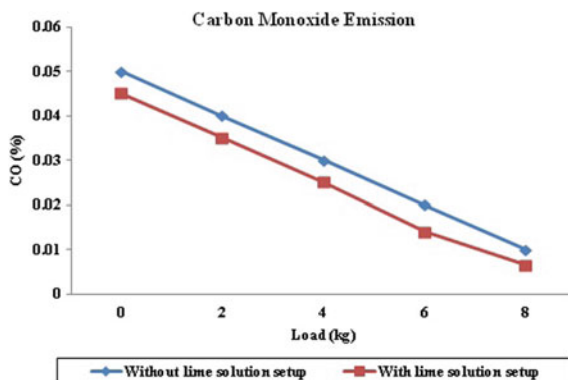


Fig. 8 CO concentration variance with and without using slaked calcium hydroxide solution due to engine load

6 Conclusion

A slaked calcium hydroxide solution setup was developed and evaluated on a diesel engine. The following emission characteristics have been found with the use of this emission control system in the compression ignition engine. The study concluded that the unit should be used in combination with or in place of a catalytic converter. With this unit, emission levels at the tailpipe of the exhaust system can easily be reduced below the specified levels. From the conducted experiment, it is possible to conclude that the installation of the slaked calcium hydroxide solution filter results in reducing unburned HC, CO₂, and CO by 13, 11.3, and 35%, respectively. At the same time, NO_x emission was increased by 11.75% and no fuel penalty by using the calcium hydroxide solution filter. This concept can also be applied to CO₂ release sources, such as automobiles and generators. The main result of this concept is cost-efficient, carbonic acid neutralization and turns CO₂ into something useful and environmentally friendly way. This experimental study implemented a technique to reduce the flue gases from the diesel engine.

Acknowledgements The author thanks the Sri Ramakrishna Engineering College, India for providing complete support in conducting research work in the Variable Compression Ratio IC Engine.

References

1. Ganeshan V (2003) Internal combustion of engines, 2nd edn. Tata McGraw Hill, New Delhi
2. Båfver LS, Rönmbäck M, Leckner B, Claesson F, Tullin C (2009) Particle emission from combustion of oat grain and its potential reduction by addition of limestone or kaolin. *Fuel Process Technol* 90:353–359

3. Alahmer A, Yamin J, Sakhrieh A, Hamdan MA (2010) Engine performance using emulsified diesel fuel. *Energy Convers Manag* 51:1708–1713
4. Dhanalakshmi A, Suresh M, Ravinthiran A, Pradeep P, Saleem A (2019) Experimentation of emission control on a four stroke diesel engine using an eco-friendly silencer with excess air. *Int J Recent Technol Eng* 8:620–625
5. Chatterjee D, Kočí P, Schmeißer V, Marek M, Weibel M, Krutzsch B (2010) Modelling of a combined NO_x storage and NH_3 -SCR catalytic system for diesel exhaust gas aftertreatment. *Catal Today* 151:395–409
6. Chen J, Yao H, Zhang P, Xiao L, Luo G, Xu M (2011) Control of PM_{10} by kaolin or limestone during O_2/CO_2 pulverized coal combustion. *Proc Combust Inst* 33:2837–2843
7. Chintada V, Uppada S, Seela CRAO (2016) Design and fabrication of reducing toxic particle silencer. *Int J Chem Sci* 14:2012–2020
8. Jamali QB (2019) Analysis of CO_2 , CO, NO, NO_2 and PM particulates of a diesel engine exhaust. *Eng Technol Appl Sci Res* 9:4912–4916
9. Parmar JM, Keyur P (2014) Performance analysis of limestone coated wiremesh catalytic converter for emission control of C. I. engine. *Int J Sci Res* 1:2377–2380
10. Bharath MR, Gokulakrishnan S, Infant Y, Janarthan K, Jayakanthan P (2018) Design and reduction of carbon monoxide and NO_x in petrol engine aqua silencer. *Int Res J Eng Technol* 5:1443–1449
11. Adaleh W, Alahmer A (2014) Reduction of the spark ignition engine emissions. *Senra Acad Publ Br Columbia* 8:2761–2767
12. Roy MM, Parvez R, Sarker RI (2011) Exhaust odour and smoke reduction of stationary DI diesel engines to an acceptable level by water-scrubbing and air-dilution system. *Appl Energy* 88:2391–2399
13. Sakhrieh A (2013) Experimental study on exhaust gas after treatment using limestone. *Therm Sci* 17:49–56
14. Rajadurai MS, Kamalakkanan K, M MSA (2016) Research Article validation and optimization of exhaust gas flow control parameters to control CO_2 emission with the aid of preheated ZSM-5 zeolite supported by lime water testing. *J Chem Pharm Res* 8:265–272
15. Huff NT (2001) Materials for absorptive silencer systems. SAE Technical Paper
16. Jain PC, Jain M (2004) Engineering chemistry, 15th edn. Dhanpatrai Publications, New Delhi
17. Khopkar SM (2015) Environmental pollution analysis, 2nd edn. New Age International, India
18. Holman JP (2007) Experimental techniques for engineers. Tata McGraw Hill, New Delhi

Modeling and Analysis of Sustainability Practices in Indian Apparel Industries Using Fuzzy Analytic Hierarchy Process (FAHP)



Amit Vishwakarma, M. L. Meena, G. S. Dangayach, and Sumit Gupta

Abstract India is one of the leading apparel manufacturing countries. Various industries are working in the apparel sector so there is a very competitive market in this sector. Those industries which adopt sustainability practice to get advantages in this in this competitive market. Thus, sustainable manufacturing plays a crucial role in industries' development. Consequently, every industry tries to adopt sustainability practice in all the aspect of manufacturing. Some of the common sustainable manufacturing practices are eco-design, non-polluting process, lean manufacturing, and easy disposal of clothing. In this paper, weightage is assigned to the above-discussed sustainable manufacturing practices and use of the fuzzy analytic hierarchy process (FAHP) to the sequence the sustainable manufacturing practices.

Keywords ED · EDC · NPP · LM · FAHP

1 Introduction

Sustainable manufacturing is used to describe the manufacturing practice that does not produce any negative impact to the environment. Sustainability plays a major role in environmental protection as well as a better way to use their source. But apparel industries have so many challenges. Environmental challenges consist of use die and toxic chemicals, emission of greenhouse gases, etc. Social challenges consist of involvement of child labor, overtime working, gender inequality [1], etc. Economic challenges consist of low wages paid to workers, lack of implementation of corporate social responsibility (CSR) policy [2]. All these challenges come under sustainability practices. Sustainability plays an important role to face all these challenges. So every firm is treating sustainability as one of the objectives to increase its growth and

A. Vishwakarma · M. L. Meena · G. S. Dangayach
Department of Mechanical Engineering, Malaviya National Institute of Technology Jaipur, Jaipur, India

S. Gupta (✉)
Department of Mechanical Engineering, Amity School of Engineering and Technology, Amity University Noida, Noida, India

competitiveness [3]. To become sustainable firms work on certain parameters, and it is required to maintain them. For the apparel sector, these are the common parameters eco-design of product, non-polluting process, lean manufacturing, and easy disposal of clothing [4], etc. This study focuses on some common sustainability practices in the Indian apparel sector and their interrelationship. Moreover, it also applies multi-criteria decision modeling through the fuzzy analytic hierarchy process (FAHP) to sequence the sustainability practices.

2 Literature Review

The concept of sustainable manufacturing comes into the light during 1980s. Some of the connotations are given in Table 1. Initially, it was with a different name which is related to environmental protection. This becomes crucial and important because of the disaster and contamination of the resources [5]. Some industries

Table 1 Literature review

Author	Year	Connotations
[9]	2015	It used different criteria for sustainable manufacturing related to electrical panel industries. To sequence, these electrical panel industries based on their adoption of sustainable manufacturing practices are taken. For this, it uses the AHP method to find out the rank of these electrical panel industries
[10]	2016	Textile consumption and its effect on environment were investigated by using the life cycle assessment (LCA) method. The industry sector approach is used for the assessment of different interventions. It contributes to environmental and social sustainability in the textile sector
[11]	2016	It utilized a social constructionist approach to address the gap between sustainable fashion consumption and understanding of sustainable fashion
[12]	2017	The apparel and textile firm's performances are increased after the adoption of the environmental management system. Performance increase in terms of sales, profitability, and operational efficiency
[13]	2017	Integration of lean practice (LP) to environmental sustainability in the apparel sector. Moreover, it also identified various barriers that arise due to this and how to tackle them effectively
[14]	2018	14 barriers related to apparel and textile sustainability were identified. Further, it identifies critical barriers among them with the use of the DEMATEL method. Lack of effective government policies and poor infrastructure came out to be significant barriers
[15]	2019	Various challenges were identified for incorporating sustainability in the design process and categorized it as internal and external challenges. Internal challenges include lack of consensus and knowledge regarding sustainable design, perceived insufficient consumer demand, attitudes and behavior gaps in consumer purchasing decisions
[16]	2020	Some eco-friendly approaches followed for sustainable garment manufacturing from raw materials selection to the final stage of garment manufacturing

Table 2 Sustainability practices

S. No.	Code	Sustainability practices	Source
1	ED	Eco-design	[10, 18]
2	EDC	Easy disposal of clothing	[12, 19]
3	NPP	Non-polluting process	[15, 20]
4	LM	Lean manufacturing	[13, 21]

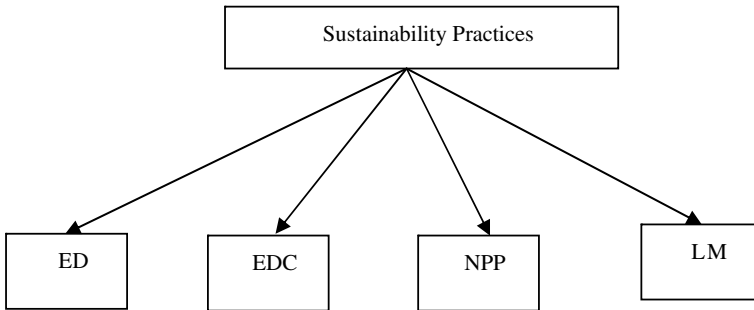


Fig 1 Sustainability parameter

like textile and apparel which pollute the natural resource on a vast level [6]. For sustainability in the apparel industry, some authors suggested the triple top-line model [7]. This model focuses on three pillars of sustainability that is economy, equity, and ecology. Furthermore, for sustainability at design and production level, cradle-to-cradle apparel design model is there. This model helps apparel designers and manufacturers to solve sustainability problems related to design and production [8]. However, the Indian apparel sector needs more work to bring out sustainability.

Adoption of sustainable manufacturing practices in the organizations leads to better organizational performance. The firm manager aware of his workforce toward environmental sustainability and also properly use manpower [17]. Four sustainability practices related to the apparel sector used in this paper for sequencing are shown in Table 2 and Fig. 1.

3 Research Methodology

In this paper, a hypothetical firm is taken that is practicing sustainable manufacturing. For analyzing four parameters eco-design [22], easy disposal of clothing, non-polluting process [23], lean manufacturing [24] are taken. These parameters are model into FAHP. The purpose of this is to whether there is consistency or inconsistency in sustainability.

3.1 Fuzzy Analytic Hierarchy Process (FAHP)

This segment provides a brief introduction to the FAHP process. This process is used for formulating the multi-criteria problem and logical decision making based on the various parameters [25]. It can be defined as an approach to decision making that involves structuring criteria into a hierarchy.

4 Result and Discussion

Based on the parameter, pair-wise comparison matrix is obtained. In this problem, four variables are taken so the matrix is of order 4×4 , and based on the manufacturing practice, weightage is assigned to each variable (Table 3).

Matrix is obtained by the following logical relation

$$C = \begin{bmatrix} c_{11} & \cdots & c_{1N} \\ \vdots & \vdots & \vdots \\ c_{N1} & \cdots & c_{NN} \end{bmatrix}, \quad c_{ii} = 1, c_{ji} = \frac{1}{c_{ij}}, c_{ij} \neq 0$$

By using Table 4, it calculates the best non-fuzzy performance (BNP) as shown in Table 5.

Table 3 Comparison of parameters

	ED	EDC	NPP	LM
ED	1	4	6	6
EDC	0.25	1	3	2
NPP	0.16	0.33	1	5
LM	0.16	0.5	0.2	1

Table 4 Weightage assign among different parameter

	ED	EDC	NPP	LM	$\tilde{c}_{i1} \times \tilde{c}_{i2} \times \cdots \times \tilde{c}_{iN}$
ED	(1, 1, 1)	(3, 4, 5)	(5, 6, 7)	(5, 6, 7)	(75, 144, 245)
EDC	(0.2, 0.25, 0.33)	(1, 1, 1)	(1, 2, 3)	(2, 3, 4)	(0.4, 1.5, 3.96)
NPP	(0.14, 0.17, 0.2)	(0.33, 0.5, 1)	(1, 1, 1)	(5, 6, 7)	(0.23, 0.51, 1.4)
LM	(0.14, 0.17, 0.2)	(0.25, 0.33, 0.5)	(0.14, 0.17, 0.2)	(1, 1, 1)	(0.005, 0.008, 0.02)

Table 5 Eigenvalues

	$\tilde{c}_{i1} \times \tilde{c}_{i2} \times \dots \times \tilde{c}_{iN}$	Fuzzy geometric mean	Fuzzy weight	BNP	Eigenvalues
ED	(75, 144, 245)	(2.9, 3.4, 3.9)	(0.42, 0.6, 0.84)	0.48	5.16
EDC	(0.4, 1.5, 3.96)	(0.79, 1.1, 1.4)	(0.11, 0.19, 0.3)	0.19	4.5
NPP	(0.23, 0.51, 1.4)	(0.69, 0.84, 1.23)	(0.1, 0.14, 0.26)	0.15	3.6
LM	(0.005, 0.008, 0.02)	(0.26, 0.29, 0.37)	(0.03, 0.05, 0.08)	0.05	5.2
		(4.64, 5.63, 6.9)			Sum (18.46)

$$\begin{aligned} \text{Average of Eigen values} &= 4.615 \\ \text{Consistency index} &= 0.205 \quad \text{CR} = \frac{\text{CI}}{\text{RI}} \\ \text{Consistency ratio (CR)} &= 0.23 \end{aligned}$$

For a consistent matrix, the consistency ratio is zero if the value of CR is coming out to be more than 0.1. Then, it indicates inconsistency. In case of inconsistency, the decision maker has to think again to get a better result. For the above matrix, the value of CR is larger than 0.1; then, it shows the inconsistent result.

4.1 Advantages and Practice for Adopting Sustainability

This paper discusses the sustainability practices of the apparel industry. It is the need of every apparel industry to incorporate them.

Eco-design—It is the design of the product which does not provide any harm to the environment. The use of adaptable apparel [26] and design for disassembly [27] are some of the examples of it.

Easy disposal of clothing—Every firm try to use natural fiber or biodegradable material so that the problem of disposable can be eliminated. However, the problem of disposal can be solved by awareness of consumer and reuse, recycle of material [28].

Non-polluting process—Use of natural die for coloration purpose did not pollute the water source.

Lean manufacturing—It minimizes the waste so the cost of production gets reduced so it is beneficial for economic as well as environmental sustainability.

5 Conclusion

- This paper discussed challenges that the Indian apparel industry is facing also discussed some of the sustainability practices.
- Application of fuzzy analytic hierarchy process (FAHP) on sustainability practices to sequence them.
- It discusses some advantages and practices for adopting sustainability in the apparel firm.

5.1 Future Work

- This work can be extended by proper weight analysis assign to fuzzy numbers and develop a software-based tool for sustainable manufacturing evaluation.
- More sustainability parameters can be accommodated to find a better result.

References

1. Asif AKMAH (2017) An overview of sustainability on apparel manufacturing industry in Bangladesh. *Sci J Energy Eng* 5(1):1–12
2. White CL, Nielsen AE, Valentini C (2017) CSR research in the apparel industry: a quantitative and qualitative review of existing literature. *Corp Soc Responsib Environ Manag* 24(5):382–394
3. Zhu Q, Sarkis J, Geng Y (2006) Green supply chain management in China: drivers, practices and performance. *Int J Oper Prod Manag* 25(5):449–468
4. Pedersen ERG, Andersen KR (2015) Sustainability innovators and anchor draggers: a global expert study on sustainable fashion. *J Fashion Market Manage* 19(3):315–327. <https://doi.org/10.1108/JFMM-08-2014-0059>
5. OECD (2001) Extended producer responsibility: a guidance manual for governments. <http://www.oecd.org/publications/ebook9701041E.pdf>
6. Wong CWY, Lai K-H, Shang K-C, Lu C-S, Leung TKP (2012) Green operations and the moderating role of environmental management capability of suppliers on manufacturing firm performance. *Int J Prod Econ* 140:283–294
7. Cao H, Scudder C, Dickson MA (2017) Sustainability of apparel supply chain in South Africa: application of the triple top line model. *Cloth Text Res J* 35(2):81–97
8. Jin GH, Cao H, Farr C, Heine L (2009) C2CAD: a sustainable apparel design and production model. *Int J Cloth Sci Technol* 21(4) 166–179. <https://doi.org/10.1108/09556220910959954>
9. Gupta S, Dangayach GS, Singh AK (2015) Analytic hierarchy process (AHP) model for evaluating sustainable manufacturing practices in Indian electrical panel. In: *International conference of the society of operations management 2015*, pp 208–216
10. Roos S, Zamani B, Sandin G, Peters GM, Svanström M (2016) A life cycle assessment (LCA)-based approach to guiding an industry sector towards sustainability: the case of the Swedish apparel sector. *J Clean Prod* 133:691–700
11. Henninger CE, Alevizou PJ, Oates CJ (2016) What is sustainable fashion? *J Fashion Market Manage* 20(4):400–416. <https://doi.org/10.1108/JFMM-07-2015-0052>
12. Li B, Wu K (2017) Environmental management system adoption and the operational performance of firm in the textile and apparel industry of China. *Sustainability* 9(6):992

13. Raj D, Ma YJ, Gam HJ, Banning J (2017) Implementation of lean production and environmental sustainability in the Indian apparel manufacturing industry: a way to reach the triple bottom line. *Int J Fashion Des Technol Educ* 10(3):254–264
14. Gardas BB, Raut RD, Narkhede B (2018) Modelling the challenges to sustainability in the textile and apparel (T&A) sector: a Delphi-DEMATEL approach. *Sustain Prod Consumption* 15:96–108
15. Hur E, Cassidy T (2019) Perceptions and attitudes towards sustainable fashion design: challenges and opportunities for implementing sustainability in fashion. *Int J Fashion Des Technol Educ* 12(2):208–217
16. Nayak R, Panwar T, Nguyen LVT (2020) Sustainability in fashion and textiles: a survey from developing country. In: *Sustainable technologies for fashion and textiles*. Woodhead Publishing, Cambridge, pp 3–30
17. Aziz FF, Yasmin F, Sultana T (2020) The impact of green human resources managerial practices on environmental sustainability: evidence from garments industry of Bangladesh. *Asian J Empirical Res* 10(3):81–96
18. Gupta S, Dangayach GS, Singh AK, Meena ML, Rao PN (2018b) Implementation of sustainable manufacturing practices in Indian manufacturing companies. *Benchmarking Int J* 25(7):2441–2459
19. Gupta S, Dangayach GS, Singh AK, Meena ML, Rao PN (2018) Adoption of sustainable supply operation quality practices and their impact on stake-holder's performance and sustainable performance for sustainable competitiveness in Indian manufacturing companies. *Int J Intell Enterp* 5(1–2):108–124
20. Gupta S (2016) Some issues in sustainable manufacturing: a select study of Indian manufacturing companies. Doctoral dissertation, MNIT Jaipur
21. Jaiswal P, Kumar A, Gupta S (2018) Prioritization of green manufacturing drivers in Indian SMEs through If-Topsis approach. *U.P.B. Sci Bull Ser D* 80(2):277–292
22. Akermark AM (1999) Design for the environment from the designers perspective. In: *Environmentally conscious design and inverse manufacturing, proceedings, first international symposium on ecodesign, vol 99*, pp 47–50
23. Fresner J (1998) Starting continuous improvement with a cleaner production assessment in an Austrian textile mill. *J Clean Prod* 6:85–91
24. Simpson DF, Power DJ (2005) Use the supply relationship to develop lean and green suppliers. *Supply Chain Manag Int J* 10(1):60–68
25. Mikhailov L, Tsvetnikov P (2004) Evaluation of services using a fuzzy analytic hierarchy process. *Appl Soft Comput* 5:23–33
26. Cao H, Chang R, Kallal J, Manalo G, McCord J, Shaw J, Starner H (2014) Adaptable apparel: a sustainable design solution for excess apparel consumption problem. *J Fashion Market Manage* 18(1):52–69. <https://doi.org/10.1108/JFMM-08-2012-0046>
27. Jin Gam H, Cao H, Bennett J, Helmkamp C, Farr C (2011) Application of design for disassembly in men's jacket: a study on sustainable apparel design. *Int J Cloth Sci Technol* 23(2/3):83–94. <https://doi.org/10.1108/09556221111107289>
28. Morgan LR, Birtwistle G (2009) An investigation of young fashion consumers' disposal habits. *Int J Consum Stud* 33(2):190–198

Numerical Comparison of Elliptical and Conical Cavity Receiver of Solar Parabolic Dish Collector System



M. Tharun, S. R. Navin, K. Arjun Singh, Arivazhagan Sampathkumar, and Sendhil Kumar Natarajan

Abstract The solar parabolic dish collector system is one of the concentrated solar power technologies. It attracts researchers all around the globe because of its higher thermal conversion efficiency. The cavity receivers play a major role in bettering the overall solar collector efficiency by reducing the heat losses. With minimum heat losses, the employment of the concentrated power increases. This current study compares two types of cavity receivers such as elliptical and conical through numerical simulations and determines the heat loss coefficient. The combinations of various parameters such as temperature (673 K, 773 K, 873 K, 973 K, and 1073 K), orientation (0° , 30° , 45° , 60° , and 90°), and aspect ratio (1.5, 1.75, 2.0, 2.25, 2.5) of the cavity receivers were considered for the simulation. The conical cavity receiver has less heat loss coefficient than the elliptical cavity receiver. Among the different combinations of parameters, the heat loss at 0° inclination of conical cavity receiver is 31% less than at 90° for 673 K and others.

Keywords Elliptical · Conical · Cavity receiver

1 Introduction

The energy with environmentally friendly is solar, hydro, wind, geothermal, and so on, as for solar it can be utilized mainly in two ways, that is, photovoltaic (PV) and solar thermal energy conversion technology. In solar thermal, concentrating solar power (CSP) is a technology in which solar radiation is concentrated to generate high temperature for process heating applications or electricity production. The recent advances of concentrated solar power (CSP) systems have contributed to an

M. Tharun · S. R. Navin

Department of Mechanical Engineering, Sri Ramakrishna Engineering College, Coimbatore, Tamil Nadu, India

K. Arjun Singh · A. Sampathkumar · S. K. Natarajan (✉)

Solar Energy Laboratory, Department of Mechanical Engineering, National Institute of Technology Puducherry, Karaikal, U.T. of Puducherry, India

e-mail: sendhil80@nitpy.ac.in

improvement in the potential to concentrate and harness solar energy for electricity generation, heat and power applications, space heating, and others. The parabolic dish concentrator system is a point focus type that follows the sun in both azimuth and altitude angles and concentrates solar energy on the receiver located at the focal point of the dish. The receiver absorbs and converts the concentrated rays into thermal energy and transfers it to the working fluid. This energy may be converted into electricity or can be used as thermal power by means of suitable power conversion technique. A temperature of more than 1500 °C can be achieved by using dish concentrators [1].

Initially, Harris et al. suggest an idea of utilizing solar energy through cavity receivers. The results conclude variation in cavity configuration have a lesser effect on the total efficiency. But rim angle alongside the cavity geometry influences the overall efficiency to a greater extent [2]. A. Steinfeld et al. projected a semi-empirical technique to calculate an optimum aperture dimensions for a cavity receiver for which the efficiency is maximum for energy conversion [3]. The optimum operating temperature of the receiver is also determined through the same method and a particular range is defined. One of the very first examples of convective heat loss in a cavity receiver [4]. K. S. Reddy et al. investigated the effect of working temperature, the emissivity of the surface, alignment, and geometry on the overall heat loss on the receiver. The Nusselt number correlation was derived and the convective and radiative heat losses decreased eventually for increasing angles up to 90° [5]. The same results are discussed by N. Sendhil Kumar et al., but for three different receiver configurations, namely cavity receiver, semi-cavity receiver, and modified cavity receiver. All the numerical results are compared and the modified cavity receivers are concluded to be optimum [6]. Mawire et al. experimentally investigated the performance of an SK-14 parabolic dish receiver with a cylindrical cavity receiver using energy and exergy analyses. And has found that exergy values spike under high solar radiations and high operating temperature. The main aim of this setup is to teach people the knowledge of solar parabolic dishes [7]. Wang et al. propose a new inverse design method to quickly calculate the cavity receiver designs with relative uniform wall cavity surface temperature. In this design, a heat transfer model is utilized to analyze the foremost heat transfer between the wall cavity, other surfaces and the working fluid and a ray-tracing method are used to obtain the boundary conditions [8]. The solar parabolic dish is the most reliable CSP technology as it has 31.25% efficiency in converting solar radiation to electricity. Affandi et al. emphasizes on the impact of direct solar irradiance (DNI), receiver and collector on the receiver losses. MATLAB and Simulink are used for studying and simulation purposes. It is further concluded that factors like solar irradiation, material reflectivity influence the value of heat transfer coefficient [9].

A receiver unit for a gas turbine is developed with a cylindrical absorber wall and semi-spherical bottom for low heat loss, and an optimum design configuration was obtained for a peak flux temperature to 1200° and exit temperature at 840° [10]. Xu et al. proposed a new tapered tube bundle receiver (TTBR) system for high temperature operating receivers (>1000 K) to combat cracking, melting, and flow instability problems due to non-uniform solar flux distribution. The performance analysis of the proposed model was conformed through the theory of energy balance, CFX

simulation and ray-tracing simulation, and the efficiency was recorded 80% which is comparatively more than the existing counterparts [11]. The energy and exergy performance of a coiled tube solar receiver is found experimentally at steady-state conditions with solar irradiance maintained at (650 W/m^2) and the solar flux during the test was 1000 kW/m^2 (approx.) at the aperture. The experimental results prove evidence that the efficiency of the receiver ranges 70–80% while the highest energy efficiency is 82% and the maximum exergy rate reached up to 38.3% (approx.) [12]. Not much of optical efficiency works have been discussed earlier. One of the first examples of optical efficiency comparison between the existing geometries has been discussed by A. M. Daabo et al. The very primitive conical, cylindrical, and spherical geometries with defined dimensions are subjected to ray tracing and CFD analysis method, and certain conclusions are arrived on the optical, thermal, and heat flux distribution. Among the three shapes, the conical receiver proved to have a lower heat loss and a higher optical efficiency of about 75–85% with varying focal length [13]. Ahmed M. Daabo et al. establishes a new relationship between the heat flux distribution on the internal surface and the optical efficiency. The conical shape again proved to exhibit high efficiency (75.35%) followed by cylindrical (71.5%) and spherical (70.1%) shapes. The theory concluded that the focal point location depends on the shape of the cavity receiver and the absorptivity in [14]. R. Loni et al. thermodynamically analyzed an organic Rankine cycle with a square prismatic tubular cavity receiver. Thermodynamic performance of several working fluid was analyzed among which methanol proved to perform better in terms of thermal efficiency, net power output, and availability ratio of turbine inlet temperature [15]. S. Yang et al. extend his work on reducing the convective heat losses from the cavity receiver for forced convection. A modified cylindrical cavity receiver approved by Australian National University (ANU) was selected for the experiment and the CFD tool was used. A 3-D CFD simulation in Fluent 17.0 for calculating the convective heat loss was preferred to get more accurate results. Different inclination angles and the temperature were given input to run simulations. The forced air circulation system showed 58% less convective heat loss than the natural air circulation conditions [16]. M. Abuseada et al. modeled a cavity receiver to perform heat transfer analysis based on heat flux measurements using the Monte Carlo ray-tracing method. For the peak power, total power, half-width, half power, the absolute percentage error was 0.8, 0.5, 1.1, and 3.2% (approx.), respectively. By this, it can be concluded that the variable aperture is a better performer in all applications and the optimum radius was observed to be 57.5 mm. But it is stated that with the implementation of the variable aperture, a certain concern should be shown in the thickness of the mechanism, as the saved can be blocked by the same [17].

A cavity receiver in the solar dish is a very important part of the collector system. Any modification applied to the cavity receiver widely influences the system efficiency to a greater extent. Loss of heat during the heat transfer to the fluids is one of the major issues and this should be addressed with much priority. Among all, the convective heat loss accounts for most of the heat loss percentage.

In the current work, a new geometry was developed for the elliptical and conical cavity receiver of the solar parabolic dish, a little different from the existing geometries to determine the convective heat loss coefficient. Several new geometries are introduced for the cavity receiver in order to minimize the heat losses and eventually maximize the corresponding efficiencies. The cavity receiver's model was selected depending upon many factors such as the mathematical suitability and its tendency to perform calculation on both 2D and 3D geometries. For elliptical and conical model, five different cavity geometries of each are modeled in order to run and test simulations on all the different models and to choose the model based on the less heat loss coefficient.

2 Methodology

2.1 Mathematical Model

Convective heat loss is one of the major heat losses in cavity receivers of solar parabolic dish collector system which is difficult to settle because of its structural complexity. The parameters like shape of the receiver, orientation, wind velocity, and wind direction influence the convective heat loss. In natural convection, the effect of the wind speed and wind direction is negligible. Employing the following equations, the heat loss of a cavity receiver can be determined [2].

$$\text{Nu}_{\text{cavity}} = \frac{hL}{k} = 0.52P(\varnothing)I_c^{1.75}(\text{Gr}_L\text{Pr})^{1/4}$$

$$\dot{q}_{\text{cavity}} = hA_T(T_{\text{Cavity}} - T_{\text{ambient}})$$

where

$$\text{Gr}_L = L^3 g\beta(T_{\text{Cavity}} - T_{\text{ambient}})/v^2$$

$$P(\varnothing) = \begin{cases} \cos^{3.2} \varnothing & 0 \leq \varnothing \leq 45^\circ \\ 0.707 \cos^{2.2} \varnothing & 45^\circ \leq \varnothing \leq 90^\circ \end{cases}$$

$$L = \sqrt{2}R_{\text{cavity},i}$$

$$I_c = \begin{cases} R_{\text{aperture}}/R_{\text{cavity},i} & R_{\text{aperture}} \leq R_{\text{cavity},i} \\ I & R_{\text{aperture}} = R_{\text{cavity},i} \end{cases}$$

$$\beta = 1/T$$

2.2 Modeling of Elliptical and Conical Receiver

Among all the heat losses, the bulk of the solar parabolic dish collector’s receiver efficiency is greatly affected by convective heat loss. In this current study, natural convection loss for the elliptical and conical receiver was considered for the simulation. The schematic of the elliptical and cavity receivers was shown in Figs. 1 and 2, respectively, below. A 2D analysis was done using ANSYS 2019 R1 for both the cavity receivers for different geometrical parameters and angular orientations.

For elliptical cavity receiver, the ratio of the major axis (b) to minor axis (a) was varied from 1.5 to 2.5 with an increment of 0.25 and for the conical cavity receiver, and the ratio of height (h) to radius (r) was changed from 1.5 to 2.5 with

Fig. 1 Schematic diagram of elliptical cavity receiver at 0° with b/a ratio 2

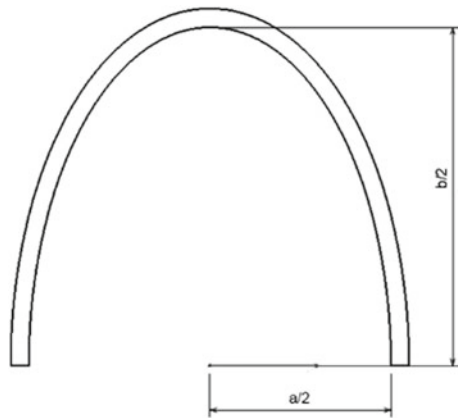
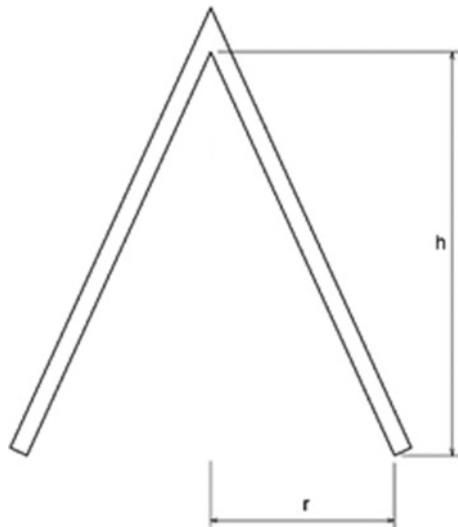


Fig. 2 Schematic diagram of conical cavity receiver at 0° with b/a ratio 2



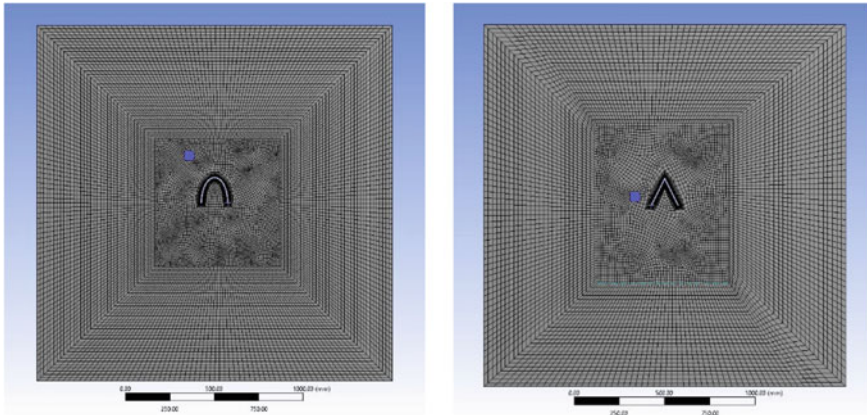


Fig. 3 Meshed models of elliptical and conical receivers

an increment of 0.25. The various inclinations such as 0° , 30° , 45° , 60° , and 90° were also considered for the simulation of cavity receivers. The cavity receiver was assumed to be inside an infinite air domain for the analysis. A cubical-shaped air domain is considered and designed as it was the cavity receiver lies exactly in the midriff of the cubical domain. Adaptive sizing with a resolution of 5 was preferred in meshing for both the domain and the receiver. The meshed models of both the receivers are shown in Fig. 3.

2.3 Simulation of Elliptical and Conical Receiver

Isothermal boundary conditions were applied to the inner walls of the cavity receiver and the temperature was varied between (673–1073 K) with an increment of 100 K for each geometry. The receiver outside wall was considered adiabatic, as there was no heat transfer due to the fact that it was covered by a well-insulated material. The thickness between the inner walls (concentrated area) and the outer walls (insulated area) was considered as 10 mm. The air domain was treated to maintain the temperature as the ambient temperature (303 K). The laminar model was preferred and the effect of gravity was also considered for the simulation. On account of buoyancy effect, a Boussinesq model was adopted for air as the fluid is stationary and weakly compressible. The air domain was set as pressure inlet type with the ambient temperature, and the inner walls and the outer walls were subjected to temperature boundary condition. The SIMPLE scheme was used, for pressure velocity coupling and first-order upwind type follow for the density and momentum equation, and the energy equation follows a second-order upwind. The criteria for the convergence of continuity equation and energy equation were set as $25e-03$ and $1e-04$, respectively, and finally, the simulation results were obtained.

3 Results and Discussions

Totally, 125 sets of combination were simulated using parametric sweep of the parameters such as temperature (673 K, 773 K, 873 K, 973 K, and 1073 K), orientation angle (0° , 30° , 45° , 60° , and 90°), and b/a (for elliptical) or h/r (for conical) (1.5, 1.75, 2.0, 2.25, 2.5) ratio of the cavity receivers. The convective heat loss pattern for the elliptical and conical cavity receiver at 873 K and b/a (for elliptical) or h/r (for conical) ratio of 2.5 with all orientations are shown in Figs. 4 and 5, respectively.

The contours of the velocity profile are presented in Figs. 4 and 5 for all the orientations considered for analysis. From the observation, the cavity receiver at 0° orientation has a less convective zone than the other orientations. More the heat, available in the receiver leads to increase in the performance of the solar thermal system. The convective heat loss coefficients were proportional to the size of convective zones. From the obtained results, the heat loss coefficients were computed based on the mathematical relations given and graphically presented below.

The simulation results for the elliptical and cavity receiver shows that the convective heat loss is higher at ($\theta = 90^\circ$) than for the inclination facing sideways ($\theta = 0^\circ$). Technically, the convective heat loss is highest at 90° than any other inclination. The conical receiver exhibits less convective heat loss than semi-elliptical cavity receiver. Contours of temperature of the $h = 2.5r$ conical cavity receiver at 873 K is showed, and it is clearly evident that the stated conclusion copes well with the discussion than

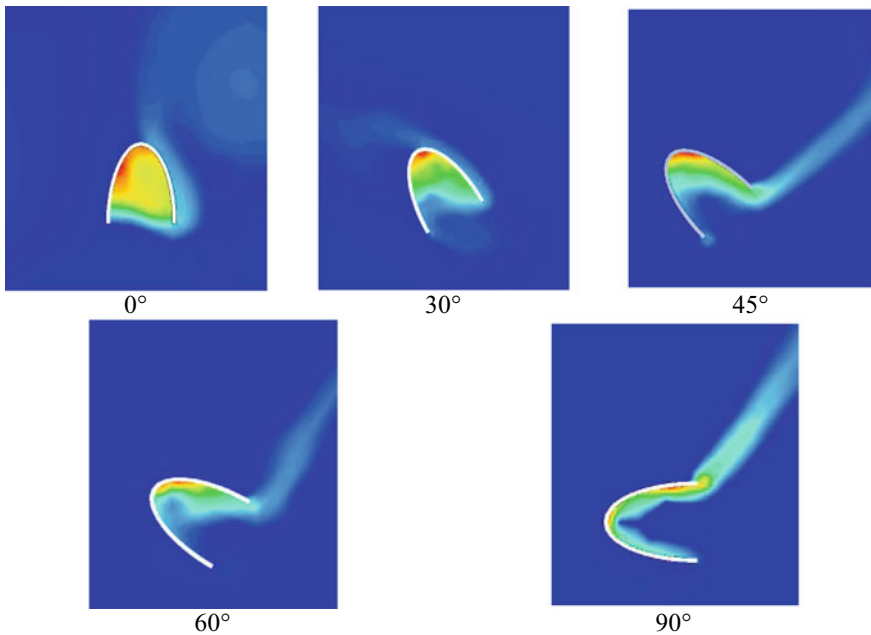


Fig. 4 Schematic diagram of conical cavity receiver with b/a ratio 2

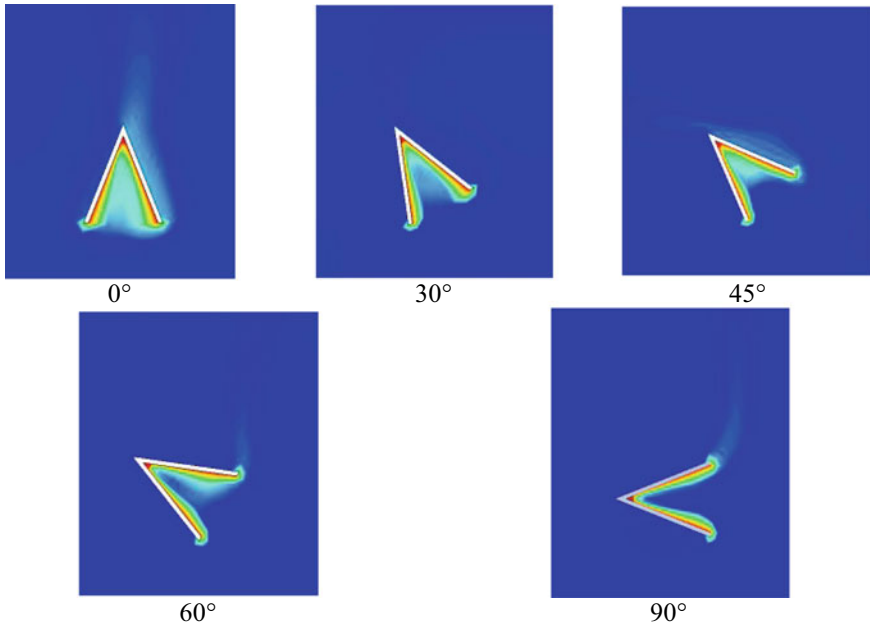


Fig. 5 Schematic diagram of conical cavity receiver with b/a ratio 2

other set of combinations. When the receiver is at ($\theta = 0^\circ$) inclination, the convective heat loss is at the lowest and increases gradually with increase in the inclination. The heat loss at 30° is lesser than the heat loss at 60° for all temperatures and for all geometries as well. The results discussed apply to all geometries of the elliptical and conical cavity receiver. In this case, the magnitude of change in the heat loss at each consecutive inclination is very less because of natural convection. In case of forced convection (considering wind speed), the magnitude of change may be higher. From the results, it can be observed that the stagnation of heat is very much high at 0° , and eventually, it becomes lesser with increase in temperature. More stagnation means lesser heat is lost due to natural convection and the above-stated argument goes well with this statement.

The graphs are plotted for each of the geometry to analyze the effect of convective heat loss coefficient for all orientations of receiver and above-mentioned temperatures at Figs. 6 and 7.

When the receiver is at 0° inclination (opening facing downwards), the convective heat loss is at the lowest. Meanwhile, the receiver at 90° inclination has increased heat loss. When absorbed closely, at some conditions, the heat loss seems to vary, but as per the real-time situations, the heat loss is maximum at 90° inclination. Thus, it can be concluded that the heat loss increases as the receiver inclination changes from 0° to 90° in all temperatures ranging between 673 and 1073 K. This is due to the fact that at 90° inclination, the receiver is uncovered to the air domain and it makes easier for the air to escape at the tilt. For all temperatures, the same condition follows and

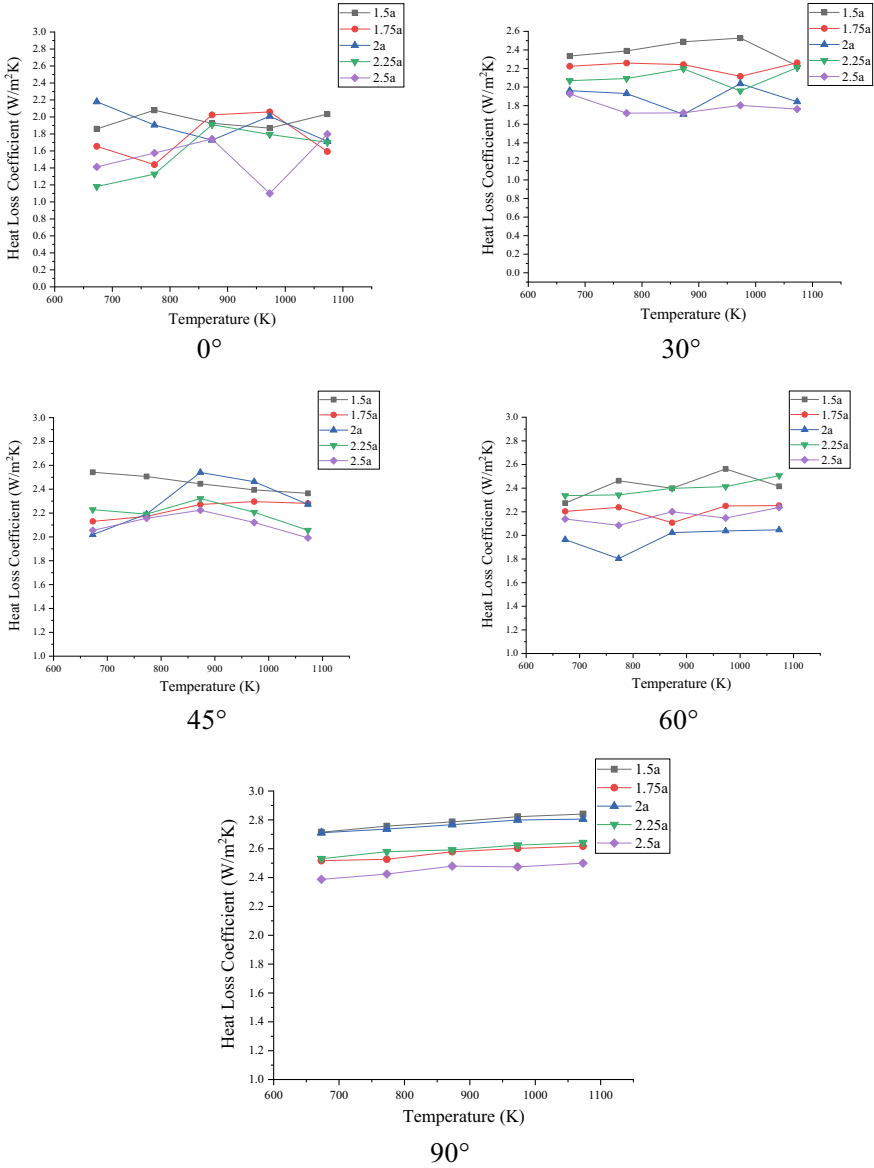


Fig. 6 Graphical representation of heat loss coefficient at corresponding angles of elliptical cavity receiver

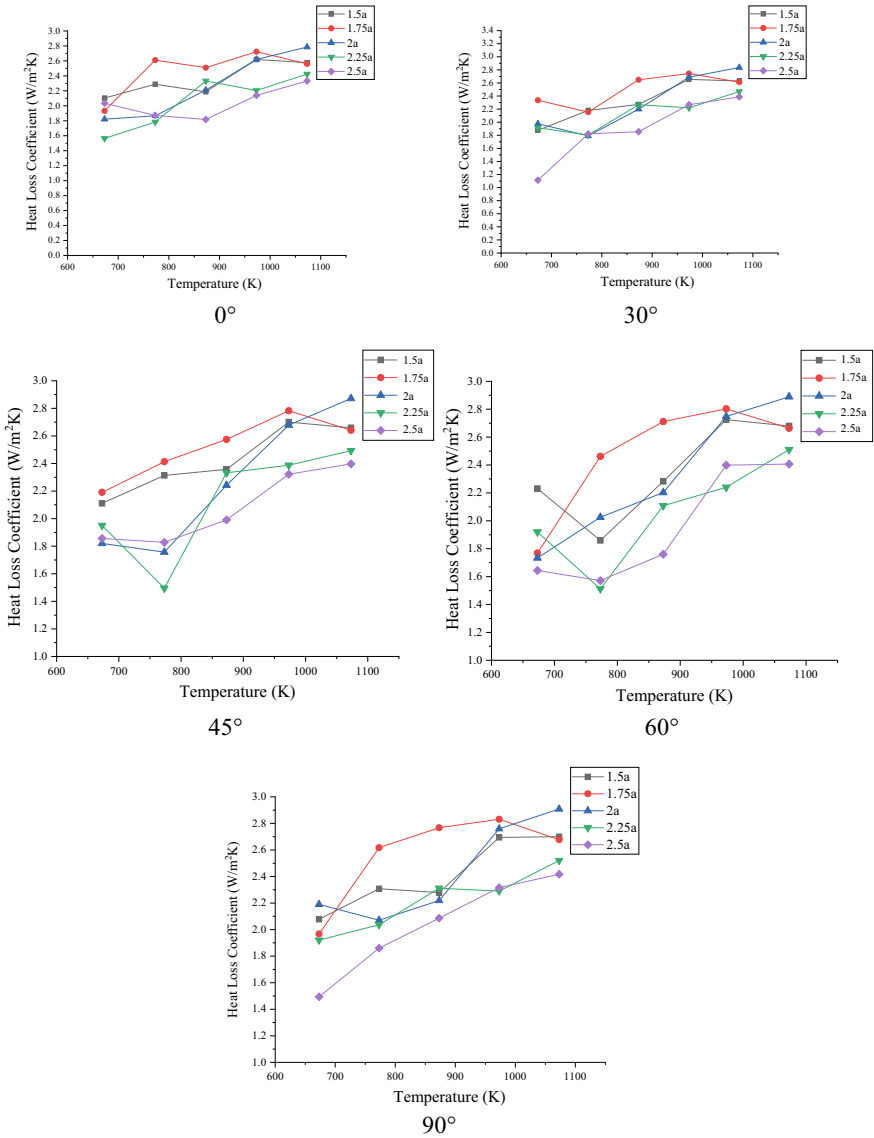


Fig. 7 Graphical representation of heat loss coefficient at corresponding angles of conical cavity receiver

no exception can be stated. It is likewise to be noted at the heat loss at 90° is very much different than at 0° for any particular geometry. Besides, the heat loss change at 0° inclination is 31% less than at 90° for 673 K and applies for all geometry.

4 Conclusion

The simulations were performed for the elliptical and conical cavity receivers with different parameters such as temperature, tilt, and aspect ratio. The convective heat loss coefficient was determined for each 125 sets separately by using ANSYS. From the simulation results, it can be reasoned that the cavity receiver of conical geometry with 2.5 aspect ratio has less heat loss coefficient compared to all other combination sets. This work can be further stretched to different geometries to find the best geometry by estimating the heat loss coefficient. Moreover, the optimization techniques can be carried out to predict the effective cavity receiver model in order to enhance the efficiency of the solar dish concentrator system.

References

1. Sukhatme SP, Nayak JK (2017) Solar energy, 4th edn., vol 38. McGraw Hill, New York (2017)
2. Harris JA, Lenz TG (1985) Thermal performance of solar concentrator/cavity receiver systems. *Sol Energy* 34(2):135–142
3. Steinfeld A, Schubnell M (1993) Optimum aperture size and operating temperature of a solar cavity-receiver. *Sol Energy* 50(1):19–25
4. Taumofolau T, Paitoonsurikarn S, Hughes G, Lovegrove K (2004) Experimental investigation of natural convection heat loss from a model solar concentrator cavity receiver. *J Sol Energy Eng* 126(2):801
5. Reddy KS, Sendhil Kumar N (2008) Combined laminar natural convection and surface radiation heat transfer in a modified cavity receiver of solar parabolic dish. *Int J Therm Sci* 47(12):1647–1657
6. Sendhil Kumar N, Reddy KS (2008) Comparison of receivers for solar dish collector system. *Energy Convers Manag* 49(4):812–819
7. Mawire A, Taole SH (2014) Experimental energy and exergy performance of a solar receiver for a domestic parabolic dish concentrator for teaching purposes. *Energy Sustain Dev* 19(1):162–169
8. Wang W, Xu H, Laumert B, Strand T (2014) An inverse design method for a cavity receiver used in solar dish Brayton system. *Sol Energy* 110:745–755
9. Affandi R, Ghani MRA, Ghan CK, Pheng LG (2015) The impact of the solar irradiation, collector and the receiver to the receiver losses in parabolic dish system. *Procedia Soc Behav Sci* 195:2382–2390
10. Wang W, Ragnolo G, Aichmayer L, Strand T, Laumert B (2015) Integrated design of a hybrid gas turbine-receiver unit for a solar dish system. *Energy Procedia* 69:583–592
11. Xu G et al (2015) Design and characteristics of a novel tapered tube bundle receiver for high-temperature solar dish system. *Appl Therm Eng* 91:791–799
12. Zhu J, Wang K, Wu H, Wang D, Du J, Olabi AG (2015) Experimental investigation on the energy and exergy performance of a coiled tube solar receiver. *Appl Energy* 156:519–527
13. Daabo AM, Mahmoud S, Al-Dadah RK (2016) The optical efficiency of three different geometries of a small scale cavity receiver for concentrated solar applications. *Appl Energy* 179
14. Daabo AM, Mahmoud S, Al-Dadah RK (2016) The effect of receiver geometry on the optical performance of a small-scale solar cavity receiver for parabolic dish applications. *Energy* 114:513–525
15. Loni R, Kasaieian AB, Mahian O, Sahin AZ (2016) Thermodynamic analysis of an organic rankine cycle using a tubular solar cavity receiver. *Energy Convers Manag* 127:494–503

16. Yang S, Wang J, Lund PD, Wang S, Jiang C (2018) Reducing convective heat losses in solar dish cavity receivers through a modified air-curtain system. *Sol Energy* 166:50–58
17. Abuseada M, Ozalp N, Ophoff C (2019) Numerical and experimental investigation of heat transfer in a solar receiver with a variable aperture. *Int J Heat Mass Transf* 128:125–135

Optimization of Weld Parameters for Cladding Using Box–Behnken Design Method



Amit Kumar Singh, Vivek Singh, Som Ashutosh, Abhishek Gupta, and Ajay Pratap Singh

Abstract Cladding is a method of depositing a layer (more than 3 mm) of a corrosion resistant material over corrosion prone material to boost the corrosion resistance properties. It enhances production economies by enabling the utilization of less costly, easy to fabricate parent material coated with better metals (generally more corrosion resistive) and alloys for achieving desired properties in specific areas of components. The cladding material is usually an austenitic stainless steel or a nickel alloy, though certain copper-based alloys are also used. In the present work, low carbon steel (LCS) plates were cladded with stainless steel (ER309L) electrode wire. Experimental design as per Box–Behnken design (BBD) was used for weld parameters optimization. Design matrix was prepared using MINITAB software and then bead samples were prepared according to the designed matrix. The optimum values of affecting parameters were recommended to minimize the dilution level.

Keywords Cladding · Gas metal arc welding · Stainless steel · Box–Behnken design method

1 Introduction

Cladding is a surfacing technique in which a layer of resistance material to corrosion commonly stainless steel (SS) is coated over LCS to increase its resistance to corrosion property. The main purpose of cladding is to increase the life on component in corrosive environment economically. The LCS meets the requirements of the industrial applications but lacks on corrosion resistance [1]. Stainless steel cladding offers corrosion and abrasion resistance while the base metal provides mechanical strength and thermal conductivity [2]. The corrosion property of SS is enhanced by getting low dilution by which the deposited metal is nearly matching with the composition of filler wire [3]. The cladded bead geometry and chemical composition affect the mechanical property of cladding [4]. The higher dilution leads to migration of

A. K. Singh · V. Singh · S. Ashutosh · A. Gupta · A. P. Singh (✉)
Department of Mechanical Engineering, AKGEC, Ghaziabad, Uttar Pradesh, India

carbon from base metal to deposited clad layer which leads to decrease the resistance to corrosion property [5].

The deposited weld shape characteristics such as low penetration (P), higher bead width (W), high reinforcement (R), and lower dilution are required in cladding process. This bead shape is necessary for the method that permits to cover the possible space with lesser number of weld passes, which helps in saving filler wire and time [6]. A value between 10 and 15% is usually considered optimum. But less than 10% raises the question of bond integrity, and more than 15% will increase the cost of the filler metal. Unfortunately, most welding processes have significantly higher dilution.

After investigating researches in this field, it was found that there are very few researches available that investigate the influence of weld parameters on clad bead geometry using response surface methodology (RSM). The objective of present work was set as follows:

- To study the influence of weld parameters on clad bead geometry
- Optimization of cladding parameters using Box–Behnken design.

2 Identification of Factors and Responses

In previous studies, factors such as wire feed rate (F), voltage (V), nozzle to plate distance (NTD), and welding speed (S) were found to be affecting the output responses such as penetration, width, reinforcement, and dilution [7]. The responses were chosen based on the impact of parameters on clad bead geometry. When dilution is under a limit, the final deposited metal composition is being similar to the filler wire and hence increases the resistance to corrosion properties of cladding [2]. The favourable parameters were selected to obtain lesser dilution and wider and thicker clad bead geometry.

3 Design of Experiment

For the optimization of input parameters, the RSM was used. In this method, the objective is to optimize the response surface which is influenced by input process parameters. RSM is widely used to predict the weld bead geometry and mechanical properties in many welding processes. Box–Behnken design is one of the ways of RSM for fitting response surfaces. BBD is effective than the central composite design (CCD) and three-level full factorial designs. The BBD does not combine the factors simultaneously at their maximum or lowermost levels. These designs are helpful in performing minimum experiments under extreme conditions, for which unacceptable results might occur [8].

The process parameters F , V , S , NTD affecting cladding process could be optimized with a minimum experimental runs. For design of experiment and statistical

Table 1 Parameters and selected levels

S. No.	Factors	Level (1)	Level (2)	Level (3)
1	Wire feed rate (m/min)	8	11	14
2	Voltage (V)	23	25	27
3	Nozzle to plate distance (mm)	10	15	20
4	Welding speed (mm/min)	220	260	300

analysis, MINITAB software was used. Before conducting experiment, random trials were performed to select the range of parameters. The range of welding parameters was decided by examining the cladded bead for acceptable bead profile [9]. The selected range is depicted in Table 1.

4 Experimental Procedure

A constant voltage gas metal arc welding machine as shown in Fig. 1 (Make: Fronius; Model: TransPuls Synergic 3200) was used for carrying out the experiment. GMAW deposits the filler metal by continuous feeding of electrode which overcome the restriction of weld achieved by SMAW process and also overcome the incapability of the SAW process to weld in all position [10] which makes it suitable for cladding. The filler wire of dia. 1 mm (ER309L) was used as filler material. A composition of 98% Ar + 2% of O₂ was used as shielding gas. Test plates having dimension of 150 × 150 × 8 mm were extracted from LCS plate of grade AISI 1018, and the rust of base plate was removed by grinding before cladding. Chemical composition of consumables is mentioned in Table 2.



Fig. 1 Mechanization of GMAW process

Table 2 Chemical composition of consumables

Materials	C	Si	Mn	P	S	Mo	Cr	Ni
LCS(AISI 1018)	0.14–0.15	0.24–0.25	0.53	0.08	0.03	0.003	0.025	0.004
SS(ER309L)	0.03	1.0	2.0	0.045	0.03	–	19.0	10.0

5 Conducting Experiment as Per Design Matrix

As per experimental design matrix by BBD, factors were arranged as shown in Table 3.

Table 3 BBD design matrix with selected parameters

Bead	<i>F</i> (m/min)	<i>V</i> (V)	NTD (mm)	<i>S</i> (mm/min)	Current (A)
1	11	25	20	220	161
2	11	23	15	300	173
3	11	25	15	260	175
4	14	27	15	260	207
5	14	25	20	260	181
6	14	23	15	260	201
7	11	23	20	260	157
8	14	25	10	260	228
9	14	25	15	300	202
10	11	25	15	260	177
11	11	23	15	220	175
12	11	25	15	260	177
13	11	25	10	300	200
14	14	27	10	260	222
15	11	27	15	300	175
16	8	25	15	300	145
17	11	27	15	220	183
18	8	25	10	260	164
19	11	23	10	260	194
20	8	27	15	260	153
21	11	25	10	220	198
22	8	25	20	260	132
23	14	25	15	220	198
24	8	23	15	260	145
25	11	25	20	300	156
26	8	25	15	220	146
27	11	27	20	260	158

6 Results and Discussion

All the bead profiles (Fig. 3) were analysed using vision measurement machine. With the help of area measurement tool, both the penetration area (A_P) and the reinforcement area (A_R) as shown in Fig. 2 were measured and corresponding dilution level was calculated [5] using Eq. (1). Results obtained after calculation are shown in Table 4.

$$\text{Dilution (\%)} \left[\frac{A_P}{A_P + A_R} \right] 100 \tag{1}$$

From ANOVA (Table 5), it can be observed that nozzle to plate distance (NTD) plays the most significant role in controlling the dilution level followed by voltage, welding speed, and wire feed. Terms with P -value < 0.05 were considered significant. It is clear from main effects plot (Fig. 4) that with an increase in the NTD , resistance increases which decreases the current resulting in low penetration [4]. The low level of penetration helps in reducing the dilution level. While increasing voltage and travelling speed, voltage being the higher contributor as shown in Table 5 increased the dilution level due to higher heat input overturning the impact of increase in travelling speed for selected range. Dilution took a slight dip and then increased with increase in wire feed rate. Obtained equation after analysis is shown as Eq. (2) which can be used to predict dilution level in the investigated range of parameters.

$$\begin{aligned} \text{Dilution} = & 223 - 5.45 \text{ Feed} - 11.3 \text{ Voltage} - 2.72 \text{ NTD} - 0.234 \text{ Speed} \\ & + 0.2071 \text{ Feed} * \text{Feed} + 0.193 \text{ Voltage} * \text{Voltage} \\ & + 0.0786 \text{ NTD} * \text{NTD} + 0.000283 \text{ Speed} * \text{Speed} \\ & + 0.130 \text{ Feed} * \text{Voltage} + 0.0137 \text{ Feed} * \text{NTD} \\ & - 0.01185 \text{ Feed} * \text{Speed} - 0.0468 \text{ Voltage} * \text{NTD} \\ & + 0.0095 \text{ Voltage} * \text{Speed} + 0.00252 \text{ NTD} * \text{Speed} \end{aligned} \tag{2}$$

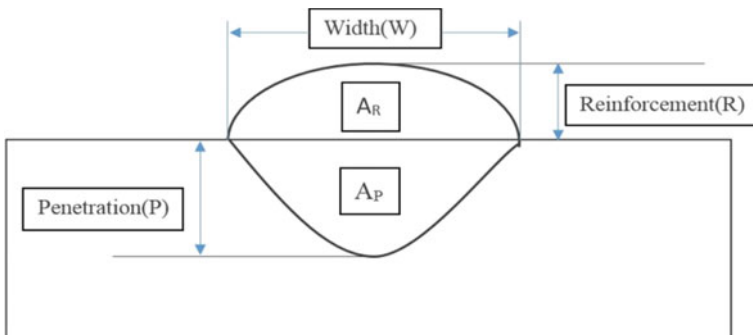


Fig. 2 Clad bead profile



Fig. 3 Prepared samples using design matrix

6.1 Response Optimization: Dilution

While using BBD approach, dilution (D) was considered as the only response for optimization, because it plays the most significant role in cladding. For cladding, the dilution level should be minimized so while using MINITAB for optimization, and the goal for the process was set to minimum. Since no other response was considered for optimization, a weightage of 1 was given to the dilution. Optimum values are obtained (Table 6) and optimization plot is shown in Fig. 5.

7 Conclusion

The present work used Box–Behnken design for the optimization of cladding process parameters to obtain desirable clad bead geometry. Below mentioned are some of the conclusions drawn from the experimental investigation:

Table 4 Dilution level in prepared samples

Std order	Weld bead	Feed (m/min)	Voltage (V)	NTD (mm)	Speed (mm/min)	Dilution (%)
4	4	14	27	15	260	26.43
10	23	14	25	15	220	16.84
25	10	11	25	15	260	19.87
11	16	8	25	15	300	28.07
22	17	11	27	15	220	21.61
18	8	14	25	10	260	23.43
8	25	11	25	20	300	22.23
3	20	8	27	15	260	25.18
26	12	11	25	15	260	19.40
17	18	8	25	10	260	28.73
7	13	11	25	10	300	27.94
6	1	11	25	20	220	15.85
12	9	14	25	15	300	21.01
19	22	8	25	20	260	21.74
27	3	11	25	15	260	18.39
21	11	11	23	15	220	17.43
16	27	11	27	20	260	19.88
20	5	14	25	20	260	17.26
15	7	11	23	20	260	14.44
23	2	11	23	15	300	17.25
5	21	11	25	10	220	23.58
14	14	11	27	10	260	29.40
2	6	14	23	15	260	18.50
13	19	11	23	10	260	22.09
24	15	11	27	15	300	24.46
1	24	8	23	15	260	20.37
9	26	8	25	15	220	18.21

- To obtain the optimum level of dilution in the range, BBD method recommends 11.57 m/min wire feed rate, 23 V voltage, 19.6 mm nozzle to plate distance and 220 mm/min travelling speed. This set of parameters is capable of producing a minimum dilution level of approximately 14%.
- It was found that all the four parameters, i.e. *F*, *V*, *NTD*, and *S*, play significant roles in determining the dilution level. The interaction effects have a significant effect over the clad bead profile and their effects cannot be ignored.
- Among various welding parameters, *NTD* having the most significant variable which affects dilution followed by *V*, *S*, and *F*.

Table 5 Analysis of variance (ANOVA)

Source	Contribution (%)	Adj SS	Adj MS	F-value	P-value
Model	91.04	411.200	29.371	8.70	0.000
Linear	80.87	365.289	91.322	27.06	0.000
<i>F</i> (m/min)	6.54	29.547	29.547	8.76	0.012
<i>V</i> (V)	25.09	113.345	113.345	33.59	0.000
<i>NTD</i> (mm)	35.35	159.651	159.651	47.31	0.000
<i>S</i> (mm/min)	13.89	62.746	62.746	18.59	0.001
Square	6.87	31.025	7.756	2.30	0.119
<i>F</i> * <i>F</i>	2.22	18.534	18.534	5.49	0.037
<i>NTD</i> * <i>NTD</i>	4.37	20.576	20.576	6.10	0.030
Error	8.96	40.493	3.374		
Lack-of-fit	8.71	39.349	3.935	6.88	0.133
Pure error	0.25	1.144	0.572		

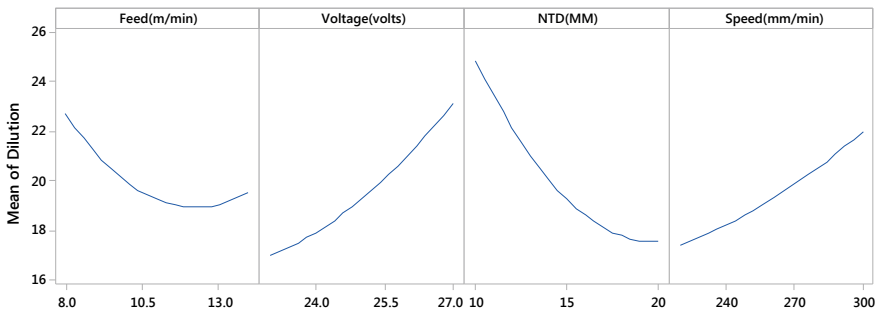


Fig. 4 Main effects plot for dilution

Table 6 Optimization table

Feed (m/min)	Voltage (V)	NTD (mm)	Speed (mm/min)	Dilution fit	Composite desirability
11.5758	23	19.5960	220	14.0426	1

- Dilution level decreased with the increase of *NTD* because of low penetration while it increased with the increase of *V* and *S* overturning the impact of increase in *S*.
- For the range of parameters investigated, optimum dilution conditions were obtained at low levels of *V* and *S*, medium level of current, and higher level of *NTD*.

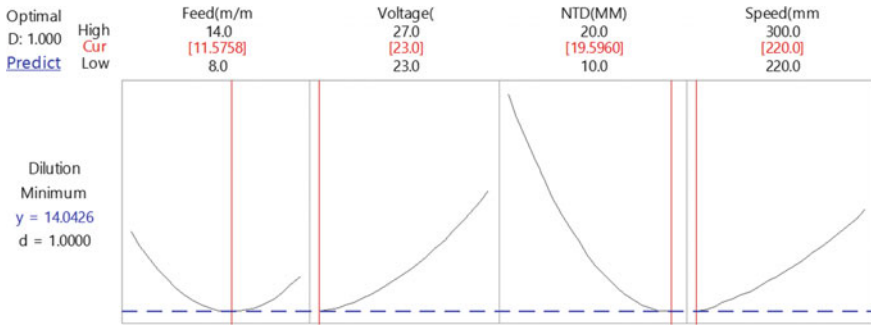


Fig. 5 Optimization plot

References

1. Senthilkumar B, Birundha P, Kannan T (2014) Modelling and simulation of austenitic stainless steel claddings deposited by GMAW. *Int J Sci Eng Res* 5(5)
2. Welding, brazing, and soldering. In: ASM handbook, vol 6 (1993)
3. Sreeraj P, Kannan T, Maji S. Estimation of optimum dilution in the GMAW process using integrated ANN-GA. *J Eng* 2013. <http://doi.org/10.1155/2013/285030>
4. Kannan T, Murugan N (2006) Prediction of ferrite number of duplex stainless steel clad metals using RSM. *Weld J* 91–99
5. Murugan N, Parmar RS (1994) Effects of MIG process parameters on the geometry of the bead in the automatic surfacing of stainless steel. *J Mater Process Technol* 41:381–398
6. Palani PK, Murugan N (2007) Optimization of weld bead geometry for stainless steel claddings deposited by FCAW. *J Mater Process Technol* 190:291–299
7. Shahi AS, Pandey S (2008) Modelling of the effects of welding conditions on dilution of stainless steel claddings produced by gas metal arc welding procedures. *J Mater Process Technol* 196:339–344
8. Ferreira SLC, Bruns RE, Ferreira HS, Matos GD, David JM, Brandão GC, da Silva EGP, Portugal LA, dos Reisc PS, Souza AS, dos Santos WNL (2007) Box-Behnken design: an alternative for the optimization of analytical methods. *Anal Chim Acta* 597:179–186
9. Kannan T, Yoganandh J (2010) Effect of process parameters on clad bead geometry and its shape of stainless steel claddings deposited by GMAW. *Int J Adv Manuf Technol* 47:1083–1095
10. Singla M, Singh D, Deepak D (2010) Parametric optimization of gas metal arc welding processes by using factorial design approach. *J Miner Mater Charact Eng* 9(4):353–363

A New Approach for Sustainability-Based Material Selection Model of Toxic Chemicals in Manufacturing Domain



Ankush Anand, Amit Kumar Sinha, Falak Idrees Tak, Aafaq Amin Tak,
and Raof Ahmad Khan

Abstract The issue of material selection though sustainability is something which needs a critical analysis of various factors that are vital for selection of materials based on several important characteristic features. There are greater challenges, which the material scientists, product designers, manufacturers, and environmentalists are facing in terms of sustainability of various systems. The role of designers and decision makers in selection process involving toxic chemical-related materials is something, which needs to be addressed very critically. This paper deals with the development of a system which systematically addresses the sustainability issues in materials selection for toxic chemical industry. The system features are first of all identified and are referred as sustainability parameters. These factors are then used to find the interrelationships among various design attributes. The existing relationships are highlighted by means of sustainability attribute structure, which is further represented by a matrix for its analysis. A function is then developed for analysis of various sustainability design attributes. A step-by-step framework is developed to evaluate and rank various toxic chemical materials from sustainability perspective. The proposed approach will guide decision makers, manufacturers, engineers, designer, and environmentalists in decision making while addressing the issue of sustainability in systems. An example has been considered to illustrate the developed approach.

Keywords Material selection · Toxicology · Sustainability · Multi-criteria decision making · Manufacturing

A. Anand (✉) · A. K. Sinha · F. I. Tak · A. A. Tak
School of Mechanical Engineering, SMVD University, Katra, Jammu and Kashmir 182320, India

R. A. Khan
Government College of Engineering and Technology, Safapora, Ganderbal, Jammu and Kashmir,
India

1 Introduction

In the industries where toxic chemical is involved whether in production processes or during the process of product design, for example, petrochemical industry, the factors like economy, environment, society, and legal factors are very critical from design point of view. The sustainability is therefore to a large extent involved in such industrial scenarios where toxicology of materials or products is a matter of paramount concern for a designer.

During the design phase of product development, [1] has developed a safety index which is quite useful for decision makers. In the safety area, an another development has been noted by Tugnoli et al. [2] who proposed a domino hazard index for assessing the layout of product development.

An environmentally decision-making model at early design stage has been developed by Santos-Reyes and Lawlor-Wright [3] which is quite useful for decision maker for selecting alternatives from a pool of alternatives. Kuo et al. [4] used fuzzy logic for evaluating the eco-friendly alternatives for product design. Based on the fuzzy logic, an important scaling system has been developed which is useful for selecting best alternative. Selection of best materials on the basis of risk assessment has been developed by Godwin et al. [5]. The researchers opined that the classification helps in better decision-making process which consequently minimizes the risk. The researchers have concluded that the 80% of the cost of the product/system to be manufactured is determined in conceptual design phase itself [6, 7].

The effect of toxic on air, water, and soil can be minimized by proper selection of chemical materials at early design stage of product life cycle. In fact, the selection of appropriate materials in the design process itself reduces the overall toxic impact in today global warming world [8, 9]. A large number of materials selection-based design methodologies were previously developed by material scientists which integrates sustainable material selection to help address the environmental performance of products [10, 11]. This paper is based after analyzing various material selection methodologies developed by researchers during the past few decades [12–14].

1.1 Material Selection Attributes Relationship Digraph of a Product

Material selection model based on graph theory is developed using the careful selection of attributes and their degree of relationship. Materials selection attributes and their degree of relationship are illustrated in Tables 1 and 2 correspondingly. Materials selection attribute digraph ($M_{at}S_{el}A^g$) has been constructed, where $G^t = (N^t, E^t)$ has been defined with the help of a set of nodes $N^t = \{N^t_1, N^t_2, \dots, N^t_5\}$, and the set of edges $E^t = \{e^t_{12}, e^t_{13}, \dots\}$. $M_{at}S_{el}A^g$ has been constructed (see Fig. 1) with the help of five attributes, namely technology (T), environment (Env.), energy

Table 1 Materials selection attributes

S. No.	Material selection requirements	Factors facilitating material selection of a product	$M_{at}S_{el}$
1	Biocompatible and energy-efficient technologies, longevity materials, minimum power/energy consumption, high heat dissipation, minimum environmental hazards, minimum wastage, enhanced dimensional stability, etc	Green materials, self-lubrication, easy to machine, formability and weldability characteristics, compatibility, minimum toxic harm rate, surface coatings, bio-friendly, etc	Technology (T)
2	Minimum environmental impact, minimum cost, material conservation characteristics, minimum contamination, minimum hazardous emission, environmentally friendly product, biodegradable materials, environmentally friendly physical and chemical properties	Sustainable or biocompatible materials, coefficient of friction, energy-efficient materials, high heat dissipation, environmentally adapted lubrication characteristics, biodegradability, etc	Environment (E)
3	Lightweight, low environmental impact, operational and hazard analysis, friction, low energy requirements, ease of production/processing, low energy consumption during disposal/recycling, etc	Low density, sustainability characteristics, manufacturing/production technologies, minimum environmental degradation, compliance to government regulations, ISO, etc	Energy conservation (EC)
4	Low cost materials, less emission of gases during manufacturing processes, zero-waste policy, least energy requirement, easy inventory, and environmentally friendly logistics	Increased use of naturally available materials, availability of manufacturing processes/technologies, environmental consciousness, sustainable approach, compatible and convenient disposal or recycling strategies, etc	Economy (Eco.)

(continued)

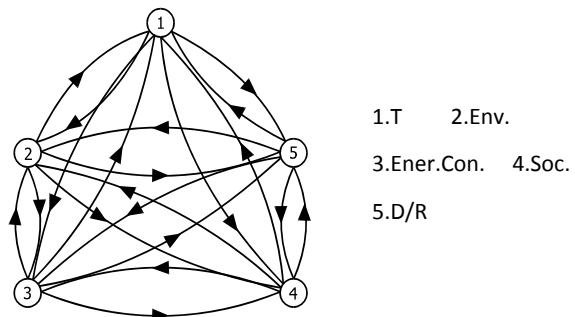
Table 1 (continued)

S. No.	Material selection requirements	Factors facilitating material selection of a product	$M_{atS_{el}}$
5	Availability of compatible technologies for disposal/recycling, ease of recycle/disposal, environmental impact assessment, retention of virginity, etc	Technology readiness and acceptability, sustainability-based thinking, increased conservation of materials, etc	Disposability and recycling (D/R)

Table 2 Material selection attributes and degree of relationship among attributes

S. No.	Material selection attribute	Abbr.	Degree of interrelationship among various attributes			
			Strong ($t_{ij} = 3$)	Medium ($t_{ij} = 2$)	Weak ($t_{ij} = 1$)	None ($t_{ij} = 0$)
1	Technology	T	2, 3, 4, 5	–	–	–
2	Environment	Env	1	3, 4, 5	–	–
3	Energy conservation	EC	1	2, 4, 5	–	–
4	Economy	Eco	1, 5	2, 3	–	–
5	Disposability/Recycling	D/R	1, 4	2, 3	–	–

Fig. 1 $M_{atS_{el}}$ attributes relationship digraph



conservation (EC), economy (Eco.), and disposability/recycling (D/R). The direction of any edge is clearly defined from the joining of their corresponding nodes. The direction of the edge directly indicated the degree of relationship between the attributes [15].

For carrying out evaluation in terms of some quantifiable value, the $M_{atS_{el}}A^g$ is expressed in a matrix form which is illustrated in next section.

1.2 Matrix Representation of a $M_{atS_{el}}A^g$ Attributes Digraph

Material selection attribute digraph ($M_{atS_{el}}A^g$) which is based on the above five suggested attributes and their degree of relationship can be converted into matrix form. These attributes help in developing the life cycle assessment of the product. During the conversion from $M_{atS_{el}}A^g$ to matrix form, the basic fundamental which is necessary to follow is as follows: (i) z th nodes is converted into z th order binary matrix $[t_{ij}]$, and Eq. (1.1) illustrates the t_{ij}

$$(ii) t_{ij} = \begin{cases} 1; & \text{if the attributes } i, \text{ and } j \text{ have some degree of relationship} \\ 0; & \text{Otherwise} \end{cases} \quad (1.1)$$

Based on above-suggested steps, $M_{atS_{el}}A^g$ has been converted into matrix form which is shown in Eq. (1.2)

$$R^t = \begin{bmatrix} 0 & 1 & 1 & 1 & 1 \\ 1 & 0 & 1 & 1 & 1 \\ 1 & 1 & 0 & 1 & 1 \\ 1 & 1 & 1 & 0 & 1 \\ 1 & 1 & 1 & 1 & 1 \end{bmatrix} \quad (1.2)$$

The matrix which is expressed in Eq. (1.2) content all the diagonal elements zero and the rest of the elements are 1. It means that the relationship among the attributes has not been considered which is necessary for evaluating the degree of the interrelationship among attributes. Therefore, a new matrix known as material selection attributes relationship permanent matrix has been defined where the degree of the interrelationship has been taken into account. Material selection attributes relationship permanent matrix is expressed in Eq. (1.3)

$$Q^t = [AI^t + R^t] = \begin{bmatrix} T & 1 & 1 & 1 & 1 \\ 1 & T & 1 & 1 & 1 \\ 1 & 1 & T & 1 & 1 \\ 1 & 1 & 1 & T & 1 \\ 1 & 1 & 1 & 1 & T \end{bmatrix} \quad (1.3)$$

- I^t Identity matrix.
- T Attribute value.

From Eq. (1.3), two most observation has been observed. The first observation is each attribute has been assigned an equal value which is not possible in a real-life situation. The second observation is the degree of relationship among each attribute (i.e., t_{ij}) which may vary between zero to one. Therefore, a generalized material selection attributes relationship permanent matrix should be formulated where diagonal elements (T_i), and off diagonal element (t_{ij}) should contain general attribute

value and degree of relationship among attributes, respectively, from a selection of sustainable materials point of view. In this regard, a variable material selection attributes relationship permanent matrix ($V M_{atS_{el}^{per}}$) has been defined, and in this matrix, the off diagonal and diagonal elements are expressed in terms of Q' , and H' matrix, respectively. The excellent and weak attribute of the product has been assigned maximum and minimum value, respectively. In between the excellent and weak performance of the attributes, an intermediate value has been assigned during material selection processes. It means a scaling system is required for assessing the contribution of attributes during the selection of a sustainable material model. The assigned value of attributes may be assigned either in terms of qualitatively or quantitatively. The $V M_{atS_{el}^{per}}$ matrix for the suggested $M_{atS_{el}A^g}$ has been developed in Eq. (1.4).

$$Q' = [H' + F'] = \begin{bmatrix} T_1 & t_{12} & t_{13} & t_{14} & t_{15} \\ t_{21} & T_2 & t_{23} & t_{24} & t_{25} \\ t_{31} & t_{32} & T_3 & t_{34} & t_{35} \\ t_{41} & t_{42} & t_{43} & T_4 & t_{45} \\ t_{51} & t_{52} & t_{53} & t_{54} & T_5 \end{bmatrix} \tag{1.4}$$

The $V M_{atS_{el}^{per}}$ matrix which is illustrated in Eq. (1.4) has diagonal, and off diagonal values are assigned as value of attributes (T_i 's) and their interrelationship among the attributes (t_{ij} 's) for the sustainable material selection model. Permanent of the matrix can be defined as [16]:

$$VPF - t : \text{Permanent of the matrix(or Per}(T)) = VM_{atS_{el}A^{per}}$$

Sigma expression of the permanent matrix (VPF-t) is expressed in Eq. (1.5). In the sigma expression, it has been observed that there is no negative expression which concludes that there is no information loss which occurs during development of sustainable material selection model.

$$\begin{aligned} \text{Per}(T) = & \prod_{i=1}^5 T_i + \sum_i \sum_j \sum_k \sum_l \sum_m (t_{ij} \cdot t_{ji}) T_k \cdot T_l \cdot T_m \\ & + \sum_i \sum_j \sum_k \sum_l \sum_m (t_{ij} \cdot t_{jk} \cdot t_{ki} + t_{ik} \cdot t_{kj} \cdot t_{ji}) T_l \cdot T_m \\ & + \left(\sum_i \sum_j \sum_k \sum_l \sum_m (t_{ij} \cdot t_{ji}) (t_{kl} \cdot t_{lk}) T_m \right. \\ & \left. + \sum_i \sum_j \sum_k \sum_l \sum_m (t_{ij} \cdot t_{jk} \cdot t_{kl} \cdot t_{li} + t_{il} \cdot t_{lk} \cdot t_{kj} \cdot t_{ji}) T_m \right) \\ & + \left(\sum_i \sum_j \sum_k \sum_l \sum_m (t_{ij} \cdot t_{ji}) (t_{kl} \cdot t_{lm} \cdot t_{mk} + t_{km} \cdot t_{ml} \cdot t_{lk}) \right. \\ & \left. + \sum_i \sum_j \sum_k \sum_l \sum_m (t_{ij} \cdot t_{jk} \cdot t_{kl} \cdot t_{lm} \cdot t_{mi} + t_{im} \cdot t_{ml} \cdot t_{lk} \cdot t_{kj} \cdot t_{ji}) \right) \end{aligned} \tag{1.5}$$

The developed sigma expression is based on five identified attributes. Therefore, all together addition of six products is expressed in sigma expression whose descriptions are as follows: (i) First term: It has a multiplication of five attributes (i.e., $T_i T_j T_k T_l T_m$); (ii) Second term: It is not applicable because the concept of self-looping is not available in the proposed digraph; (iii) Third term: It has a multiplication of three attribute ($T_k T_m T_l$) plus two attribute relationship loop ($t_{ij} t_{ji}$); (iv) Fourth term: It has a multiplication of two attribute (i.e., $T_l T_m$) plus three attribute relationship loop ($t_{ij} t_{jk} t_{ki}$); (v) Fifth term: It has a multiplication of one attribute (i.e., T_m) and two attribute relationship loops ($t_{ij} t_{ji}$ and $t_{kl} t_{lk}$) plus multiplication of one attribute (i.e., T_m) and four attributes relationship loop ($t_{ij} t_{jk} t_{kl} t_{li}$); (vi) Sixth term: It has a multiplication of two attribute relationship loop ($t_{ij} t_{ji}$) and three attributes relationship loop ($t_{kl} t_{lm} t_{mk}$) plus five attribute relationship loop ($t_{ij} t_{jk} t_{kl} t_{lm} t_{mi}$). In this way, the proposed sigma expression is a strong development of degree of interrelationship among attributes for sustainable material selection model.

1.3 Material Selection Index

A material selection index is necessary tool for decision maker during sustainable material selection model. Therefore, a material selection index (I_i^t) has been developed. A higher value of I_i^t indicates better sustainable material selection and vice versa. In this, both the contributions of attributes and their degree of relationship have been accommodated during development of material selection index value. This index is nothing more than VPF-t which is a permanent of matrix, and it cannot be calculated as negative value because it has no negative expression. In nutshell, the calculated value of permanent matrix is expressed in terms of material selection index value.

For calculating I_i^t , numerical value must be assigned in the matrix expression. Therefore, diagonal elements (T_i 's) and off diagonal elements (t_{ij}) should be assigned during evaluation of I_i^t . In this context, a scaling system should be developed during evaluation of material selection index. Table 3 illustrates the scoring value which should be assigned during material selection processes.

Table 3 Value (T_i) of material attributes

S. No.	Effect of attribute on material selection	Score (T_i)
1	Exceptionally favorable	5
2	Most favorable	4
3	Highly favorable	3
4	Favorable	2
5	Least favorable	1
6	Not favorable	0

The higher calculated value of material selection index shows better alternative material from sustainable point of view. The ideal value of material selection index (I^t_{ideal}) can be calculated from permanent matrix by putting score value of the diagonal element to five (exceptionally favorable condition). The calculated I^t_{ideal} is observed as 3.98×10^4 . Now, rest of the material selection index can be easily compared from I^t_{ideal} . In this way, relative value of I_i^t is calculated, and lastly, a ranking of different available materials can be developed. The relative material selection index is expressed in Eq. (1.6)

$$I_r^t = \frac{I_i^t}{I^t_{ideal}} \times 100\% \tag{1.6}$$

where

- I_r^t Relative material selection index
- I_i^t Material selection index
- I^t_{ideal} Ideal material selection index.

The relative material selection index helps for designer during early stage of design for selection of sustainable material from a pool of different available materials. Although, different researchers and practitioners may assign different score value and get the different value of material selection index but the overall ranking of the material will remain unchanged [17–19]. Although, any value of scoring can be assigned during decision making but lower scale value is advisable for reducing the subjectivity problem. However, the overall ranking will remain unchanged, or ranking is independent from the assigning value of scaling system.

1.4 Steps—Material Selection Index Evaluation

The flowchart of proposed methodology for evaluating material selection index I^t_i is shown in Fig. 2 [20]. The readers are advised to follow the steps for index evaluation.

The proposed flowchart is useful for converting life cycle assessment into $M_{at}S_{el}As$. In this example, $M_{at}S_{el}As$ remains same, as shown in Fig. 1. The $V M_{at}S_{el}A^{per}$ for $M_{at}S_{el}As$ is obtained in Eq. (1.7)

$$Q^t = \begin{bmatrix} T_1 & t_{12} & t_{13} & t_{14} & t_{15} \\ t_{21} & T_2 & t_{23} & t_{24} & t_{25} \\ t_{31} & t_{32} & T_3 & t_{34} & t_{35} \\ t_{41} & t_{42} & t_{43} & T_4 & t_{45} \\ t_{51} & t_{52} & t_{53} & t_{54} & T_5 \end{bmatrix} \tag{1.7}$$

Out of six different alternative toxic materials, higher values of material selection index are the best choice from toxicity point of view and vice versa (see Table 4).

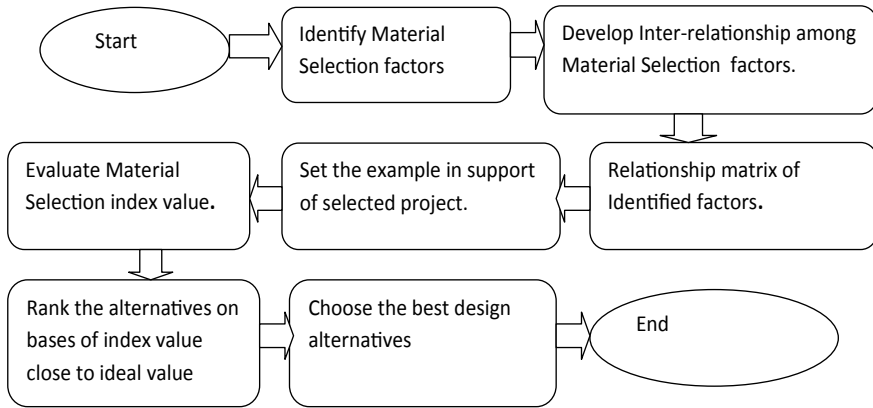


Fig. 2 Flowchart for evaluating material selection index

Table 4 Ranking of alternatives for various toxic materials

S. No.	Alternative	I'_i	Rank
1	1,1,2-trichloroethane	2.19	4th
2	Carbon tetrachloride	1.03	6th
3	Methylene chloride	1.76	5th
4	Tetrachloroethylene	3.03	2nd
5	Carbon disulfide	2.75	3rd
6	1,1,1,2-tetrachloroethane	3.29	1st

The simple example of six alternative toxic material is demonstrated based on the suggested sustainable material selection model. A computer-based programming should be developed for evaluating such type of material selection index value.

2 Example

For demonstrating the proposed sustainable material selection model, a case study has been taken from Yuan and Dornfeld [21]. In this case study, selection of toxic material from sustainable point of view has been taken from six different toxic materials.

In this example, ranking of 1,1,1,2-tetrachloroethane, tetrachloroethylene, carbon disulfide, 1,1,2-trichloroethane, methylene chloride, and carbon tetrachloride has been observed as ranking 1, 2, 3, 4, 5, and 6, respectively.

The necessary characteristics of every candidate material from sustainable prospective have been clearly analyzed, and their characteristics are elaborated which has great overall environmental effects. Based on the methodology proposed above

and the characteristics of various candidate materials, all the six materials were subjected to index evaluation by assigning different score values (0–5) as shown above in the table, and finally, the ranking is obtained (see Table 4).

3 Conclusions

Some of the major conclusions are as follows:

- Toxic behavior of materials from sustainability consideration in design and development process has been analyzed.
- Importance of selection of materials from the perspective of release of toxic waste has been analyzed.
- A methodology for toxic sustainable material selection is proposed here using a multi-criteria decision-making approach.
- The proposed methodology enables researchers and practitioners in evaluation and ranking of various toxic materials in a logical manner.

References

1. Leong CT, Sharriff AM (2008) Inherent safety index module (ISIM) to assess inherent safety level during preliminary design stage. *Process Saf Environ Prot* 86:113–119
2. Tugnoli A, Khan F, Amyotte P, Cozzani V (2008) Safety assessment in plant layout design using indexing approach: implementing inherent safety perspective. Part 1—guideword applicability and method description. *J Hazard Mater* 160:100–109
3. Santos-Reyes DE, Lawlor-Wright T (2001) A design for the environment methodology to support an environmental management system. *Integr Manuf Syst* 12(5):323–332
4. Kuo TC, Chang SH, Huang SH (2006) Environmentally conscious design by using fuzzy multi-attribute decision-making. *Int J Adv Manuf Technol* 29(5):419–425
5. Godwin H, Nameth C, Avery D, Bergeson LL, Bernard D, Beryt E, Boyes W, Brown S, Clippinger AJ, Cohen Y, Doa M (2015) Nanomaterial categorization for assessing risk potential to facilitate regulatory decision-making. *ACS Nano* 9(4):3409–3417
6. Li H, Li LX (2000) Integrating systems concepts into manufacturing information systems. *Syst Res Behav Sci* 17(2):135
7. Cooper G, Thompson G (2001) Concept design and reliability. *Advanced engineering design. Cost engineering for manufacturing: current and future research. Int J Comput Integr Manuf* 25(4–5):300–314
8. Holloway L (1998) Materials selection for optimal environmental impact in mechanical design. *Mater Des* 19:133–143
9. Matos MJ, Simplicio MH (2006) Innovation and sustainability in mechanical design through materials selection. *Mater Des* 27:74–78
10. Wegst UGK, Ashby MF (1998) The development and use of a methodology for the environmentally conscious selection of materials. In: *Proceedings of the third biennial world conference on integrated design and process technology*, vol 5, Berlin, Germany, July 6–9, pp 88–93
11. Tong TKL, Chan JWK (2007) Multi-criteria material selections and end-of-life product strategy: grey relational analysis approach. *Mater Des* 28:1539–1546

12. Jee DH, Kang KJ (2000) A method for optimal material selection aided with decision making theory. *Mater Des* 21:199–206
13. Yuan C, Dornfeld D (2009) Sustainable material selection of toxic chemicals in design and manufacturing from human health impact perspective. ASME Paper No. DETC 2009-87145
14. Liao TW (1996) A fuzzy multicriteria decision-making method for material selection. *J Manuf Syst* 15(1):1–12
15. Deo N (2016) *Graph theory with applications to engineering and computer science*. Courier Dover Publications, USA
16. Jurkat WB, Ryser HJ (1966) Matrix factorizations of determinants and permanents. *J Algebra* 3(1):1–27
17. Khan RA, Anand A, Wani MF (2018) A holistic framework for environment conscious based product risk modeling and assessment using multi criteria decision making. *J Clean Prod* 174:954–965
18. Sinha AK, Anand A (2018) Development of sustainable supplier selection index for new product development using multi criteria decision making. *J Clean Prod* 197:1587–1596
19. Anand A, Wani MF (2010) Product life-cycle modeling and evaluation at the conceptual design stage: a digraph and matrix approach. *Trans ASME J Mech Des* 132(9):091010
20. Anand A, Khan RA, Wani MF (2016) Development of a sustainability risk assessment index of a mechanical system at conceptual design stage. *J Clean prod* 139:258–266
21. Risitano A, Rosa GL, Giudice F (2005) Materials selection in the life cycle design process: a method to integrate mechanical and environmental performances in optimal choice. *Mater Des* 26:9–20

Zero Waste Concept: Recycling of Slag to Use as Flux in Submerged Arc Welding



Deepanjali Nimker and Reeta Wattal

Abstract The present work has been aimed to recycle slag with a process called agglomeration. The purpose of carrying out this research was to reduce the harmful effects posed by large amount of slag generated after flux consumed in submerged arc welding (SAW). This slag can be reused if it is replenished with correct percentage of additives and binders. The weld pad generated using different composition of slag and fresh flux helps in finding the right composition required to develop recycled slag equivalent to fresh flux. It was observed that 87.5% slag when mixed with 5.5% CaCO_3 and Al powder along with 7% of K_2TiO_3 and Mn powder in addition of K_2SiO_3 to wet the mixture was suitable composition to recycle slag and use it as equivalent to flux.

Keywords Agglomeration · Submerged arc welding · Recycled slag

1 Introduction

SAW is a shielded arc welding process which uses an arc struck between the electrode and workpiece to melt weld metal under a blanket of flux. This flux blanket prevents weld metal from atmospheric contamination and converts into slag. This slag then treated as waste and discarded. Submerged arc welding due to high deposition rate, invisible arc, minimum spatters and less skilled labour requirement, it is commonly used in the construction of pipelines, pressure vessels, etc. With the use of submerged arc welding in various applications, large quantity of flux is consumed and thus slag is dumped as waste.

$$\text{Flux consumed} = \text{slag produced}$$

D. Nimker (✉) · R. Wattal
Mechanical Engineering Department, Delhi Technological University, Delhi, India

© The Author(s), under exclusive license to Springer Nature Singapore Pte Ltd. 2022
K. Govindan et al. (eds.), *Advances in Mechanical and Materials Technology*,
Lecture Notes in Mechanical Engineering,
https://doi.org/10.1007/978-981-16-2794-1_56

641

Research related to the process of slag reclamation has not been interesting for the researchers so far. But the concept of this process and its future scope is very vast and bright. This slag reclamation is a step towards decreasing the damage caused by the waste generated, i.e. slag and thus saving the environment from its hazardous effects. It was found that by carrying out proper experimental procedure, slag can be used as fresh flux without generating any harmful effect on the weld metal characteristics, then this technique can be applied practically to the field thus leads to 'zero waste concept' [1, 2]. To maximise the effectiveness of the slag used, it is necessary to recycle it in accordance with American Welding Society (AWS) standards. Once reclaimed it was found reliable and provide economic benefits to the companies [3]. Few researchers reclaimed slag by mixing it with varying percentage of fresh flux and found that the mixture up to 60% slag was within AWS specifications and cleared the weld qualification tests such as visual inspection, dye penetrant test and radiography. Slag when replenished by the process of agglomeration and used in combination with EL-8 wire then results in satisfactory performance when tested for mechanical properties and chemical composition [4, 5]. This slag flux mixture % was also used as a process parameter to evaluate its influence on bead geometry and heat affected zone (HAZ) through analysis of variance (ANOVA) technique [6–9]. Another researcher evaluated slag by performing weld qualification tests, mechanical property, weld metal integrity, metallurgical studies and cost analysis. Results revealed that it is feasible to use slag as an alternative for fresh flux which is efficient by 70.73% [10].

The literature review mentioned has been found to be very useful for further research in this field. The research and results carried out by the researchers are described in this introduction. It has been observed that some of the work related to the replenishment of slag has been reviewed. Therefore, it can be concluded that very few researchers have worked on the concept of recycling of slag in SAW.

2 Material and Methods

To recycle slag, it was first collected from the scrap yard of boiler industry. The slag was first cleaned in tap water, and then it was air dried, powdered and sieved to approx. 12 mesh size which is equivalent to size of fresh flux. Once slag was prepared, pad (4 layers high with 3 passes per layer) was developed on mild steel plate using flux and pure slag according to American Society of Mechanical Engineers (ASME) SFA 5.17. To estimate the chemical composition, Spectro analysis was implemented. The composition of electrode and base metal has been described in Table 1. The chemical configuration of the welded metal attained using pure flux and replenished slag was investigated carefully and compared. During this process, it was revealed that slag was deficient in various elements which lead to its poor performance during welding. Figure 1 shows submerged arc welding setup. In order to replenish slag, the method of replenishment was defined to achieve the similar characteristics as that of virgin flux. Different composition through hit and trial was tried to achieve desired

Table 1 Composition of electrode and base metal

	C%	Mn%	Si%	S%	P%
Electrode	0.10	1.70	0.10	0.030	0.030
Base metal	0.197	0.412	0.152	0.028	0.029

Fig. 1 Submerged arc welding machine

composition. Figure 2 shows recycled slag prepared after reclamation. Welding input factors were presented in Table 2. In order to replenish slag, pulverised form (100 mesh size) slag was added with deoxidisers, i.e. CaCO_3 ; Al powder; Mn powder with K_2TiO_3 which act as arc stabiliser, and K_2SiO_3 added as binder to bind the mixture. Table 3 shows different combinations of slag mixture. Then, this mixture was filtered through sieve to form pellets which were air dried for 24 hours. Later, these pellets were overheated at $850\text{ }^\circ\text{C}$ for 2 hours [10]. These baked mass pellets were then used

Fig. 2 Recycled slag prepared after reclamation

Table 2 Welding input factors

S. No.	Factors	Unit	Value
1	Welding speed	cm/min	35
2	Wire feed rate	cm/min	140
3	Nozzle tip to plate distance	mm	25
4	Arc Voltage	V	30

Table 3 Different combinations of slag mixture

S. No.		Slag %	CaCO ₃ + Al powder (%)	K ₂ TiO ₃ + Mn powder (%)	K ₂ SiO ₃
1	Slag composition 1	87.5	5.5	7	Enough to wet the mixture
2	Slag composition 2	80.7	8.25	11	Enough to wet the mixture
3	Slag composition 3	74	11	15	Enough to wet the mixture

as replenished slag. Now, this replenished slag was used to prepare weld pad, which was examined by the spectroscope for weld metal composition. If the composition obtained did not qualify the AWS standards, then the process was repeated again and again by adding deoxidisers and binders in varying percentage till the desired composition was attained. Different combinations of slag mixture were shown in Table 3. This recycled slag was used in combination with EH14 wire in submerged arc welding process. The welding characteristics and conditions are in accordance with ASME SFA 5.17 [11]. Figure 3 shows weld pad as per ASME SFA 5.17 standard [11]. Figure 4 shows weld pad prepared using recycled slag.

3 Results and Discussion

Chemical configuration of weld pad with different combinations of slag, fresh flux and pure slag compared with AWS standard is shown in Table 4. It was found that virgin slag presents varying percentage of Mn and Si which is not suitable as per AWS specifications. Whereas when we compare the composition of three types of slag with AWS standard, it was found that slag composition 1 has better composition and it lies within the standard range. It may be due to the addition of additives such as CaCO₃; Al powder; Mn powder along with K₂TiO₃ as arc stabiliser, and K₂SiO₃ as binder to the pure slag. Therefore, it was observed that 87.5% slag when mixed with 5.5% CaCO₃ and Al powder along with 7% of K₂TiO₃ and Mn powder in addition of K₂SiO₃ solution to wet the mixture are the most suitable composition of slag to use it as equivalent to virgin flux. This recycled slag (slag composition 1) was

Fig. 3 Weld pad as per ASME SFA 5.17 standard

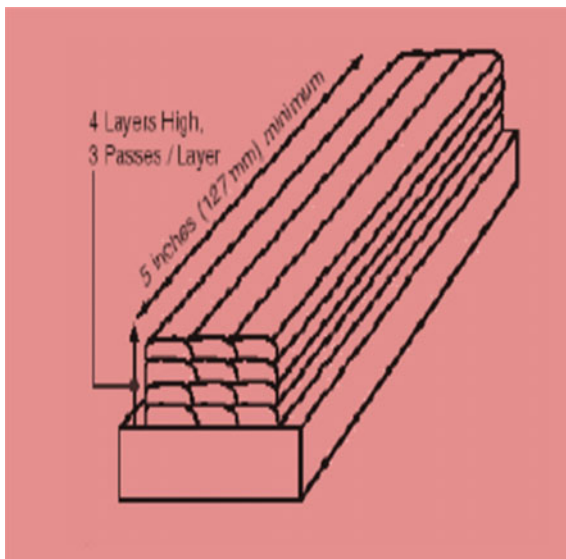


Fig. 4 Weld pad prepared using recycled slag



used in combination with EH14 wire which confirms to ASME SFA 5.17. Figure 5 elaborates the graphical presentation of different combinations of slag, pure flux and virgin slag. Figure 6 shows comparison chart between recycled slag and fresh flux.

Table 4 Chemical configuration of weld pad with different combinations of slag, fresh flux and pure slag compared with AWS standard

S. No.		C%	Mn%	Si%	S%	P%
1	AWS	0.05–0.15	0.80–1.25	0.1–0.35	0.03 max	0.03max
2	Fresh flux	0.092	1.901	0.463	0.012	0.025
3	Pure slag	0.108	1.567	0.364	0.016	0.025
4	Slag composition 1	0.089	1.101	0.123	0.019	0.020
5	Slag composition 2	0.086	1.277	0.078	0.015	0.020
6	Slag composition 3	0.092	1.257	0.064	0.016	0.020

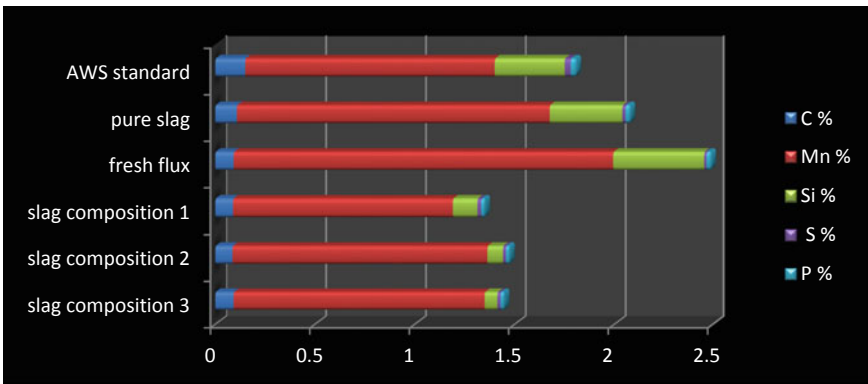


Fig. 5 Graphical presentation of different combinations of slag, pure flux and virgin slag

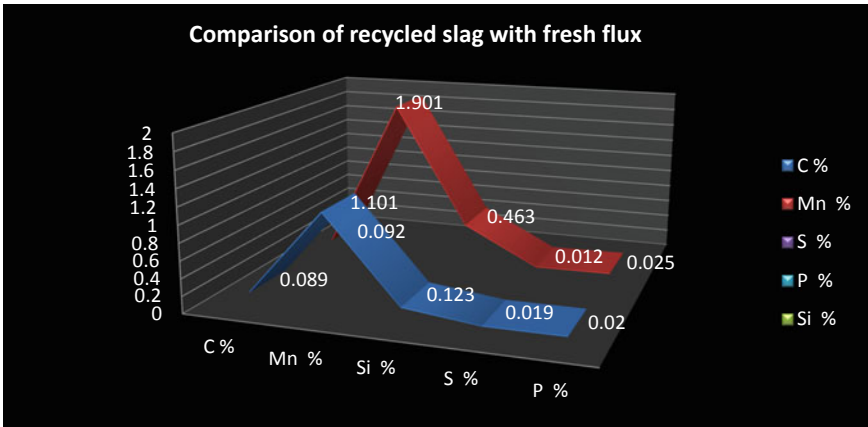


Fig. 6 Comparison chart between recycled slag and fresh flux

4 Conclusions

The process of slag reclamation proves to be beneficial from the environmental aspect. The addition of binders as well as additives enhances the characteristics of recycled slag and thus gives chemical composition nearly similar to that of fresh flux. Both flux and recycled slag have composition within the acceptable range of AWS standards. The weld pad produced using slag shows negligible detrimental effects on weld quality. Visual inspection as well as slag detachability and arc stability shows satisfactory results. In the future, it is recommended to recycle slag with this process of agglomeration, and therefore, results in producing good quality slag.

References

1. Singh K, Singh J (2010) Influence of slag flux mixture on mechanical properties of welds in submerged arc welding. In: National conference on advancements and futuristic trends in mechanical Engineering, 19–20 Feb
2. Garg J, Singh K (2010) Recycling of submerged arc welding slag for economy and environment. In: National conference on advancements and futuristic trends in mechanical and materials engineering, 19–20 Feb
3. Beck HP, Jackson AR (1996) Recycling SAW slag proves reliable and repeatable. *Weld J* 6:75
4. Singh K, Pandey S (2009) Recycling of slag to act as a flux in submerged arc welding. *Res Conserv Recycl* 53:552–558. <https://doi.org/10.1016/j.resconrec.2009.04.006>
5. Singh K, Pandey S, Mani RA (2006) Recycling of submerged welding slag. *Australas Weld J* 51(2):34–38
6. Datta S (2008) Slag recycling in submerged arc welding and its influence on weld quality leading to parametric optimization. *Int J Adv Manuf Technol* 39:229–238. <https://doi.org/10.1007/s00170-007-1224-4>
7. Moi SC, Bandyopadhyay A, Pal PK (2001) Submerged arc welding with a mixture of fresh flux and fused slag. In: Proceedings of national seminar on advances in material and processing, IIT, Roorkee, India. <https://doi.org/10.1007/s00170-006-0776-z>
8. Pal PK, Bandyopadhyay A (2001) Some aspects of submerged arc welding with mixture of fresh flux and fused slag. In: Proceedings of international conference BUET, Dhaka, Bangladesh
9. Datta S, Bandyopadhyay A, Pal PK (2008) Solving multi-criteria optimization problem in submerged arc welding consuming a mixture of fresh flux and fused slag. *Int J Adv Manuf Technol* 35(9):935–942. <https://doi.org/10.1007/s00170-006-0776-z>
10. Mahto D, Kumar A (2010) Novel method of productivity improvement and waste reduction through recycling of submerged arc welding slag. *Jordan J Mech Ind Eng* 4:451–466
11. ASME, Sec-II (2010) Specifications for carbon steel electrodes and fluxes for submerged arc welding. *Pressure Vessels Boiler Codes*, pp 427–443

Study of High-Velocity Oxy-fuel Coating Technique and Fe-Based High-Velocity Oxy-fuel Coatings



Subrat Sharma, Paras Mahajan, and Sanjay Mohan

Abstract Many industrial components have been developed using different fabrication techniques. The evolution of different fabrication techniques is due to the requirement of desired properties in the materials. Materials in bulk and coatings have been developed by researchers. Coatings provide safety to the substrate from corrosion, friction, wear, etc., and the effectiveness of the coating depends upon the coating technique being used. Recently, thermal spray techniques have been devised for producing effective coatings. This paper elaborates on the thermal spraying process, namely the high-velocity oxygen-fuel (HVOF), and addresses its evolution. Literature about iron-based composite coatings has been intensely reviewed, and the composite coatings fabricated through the HVOF process have been discussed in this paper. The article also elaborates on the properties of these coatings. This article will bring forth the usefulness of this process and researchers will be getting more insight into the application of the HVOF technique in developing new coatings.

Keywords High-velocity oxygen-fuel (HVOF) · Iron (Fe) · Molybdenum (Mo) · Wear · Friction · Coatings

1 Introduction

The thermal spraying method is among the most effective methods of all advanced coating techniques due to the fabrication of a large variety of protective and preventive coatings on different substrates. Surface treatment coatings are used to shield parts against various forms of wear and corrosion. The materials are layered with low thermally conductive matters to increase their heat resistance and absorption capacities [1]. These coating techniques help in solving various engineering problems in several industries including automobile, aerospace, petroleum, petrochemical, etc. Kumar and Kumar found that the historic and widely used metal protection method is

S. Sharma · P. Mahajan · S. Mohan (✉)
School of Mechanical Engineering, Shri Mata Vaishno Devi University, Katra, India

© The Author(s), under exclusive license to Springer Nature Singapore Pte Ltd. 2022
K. Govindan et al. (eds.), *Advances in Mechanical and Materials Technology*,
Lecture Notes in Mechanical Engineering,
https://doi.org/10.1007/978-981-16-2794-1_57

649

base metal coating as it is more durable, more decorative, and provides better excellent corrosion resistance [2]. Many corrosion-resistant coatings must be categorized based on their essential properties and basic fundamental characteristics. The fundamental characteristics required by every coating material are adhesion resistance, abrasion resistance, high-temperature resistance, and frictional resistance [3]. Many processes have been used for the fabrication of coatings in the past, and each one has its merits and demerits. The limitations of these processes have made researchers and scientists explore more in this area, and thus the evolution of these processes has taken place. Some of the very common methods being used are electroplating, electroforming, electroless plating, hot dipping, metal spraying, wire spraying, etc. These techniques have been used to provide coatings that have been used in various applications. High efficiency and fill factor of 1.40% and 0.37% were obtained from a solar cell which was coated by using spraying and electroplating techniques. Low-cost solar cells based on $\text{TiO}_2/\text{CuO}/\text{Cu}$ using the above techniques have been produced by researchers. Improved light-capturing ability and electron transportability were seen as results due to the combination of CuO and Cu [4]. On the same lines, Rokhmat et al. also developed the coating using fix current electroplating, and the results have shown better results than the coating developed through ordinary electroplating. The authors recorded that the performance and fill factor was 1.62% and 0.42% [5]. The low cost and ability to obtain close tolerances in the manufacturing of complex components has made electroforming to emerge as a manufacturing technique commonly used in macro manufacturing and modern micro-manufacturing fields. These include the fabrication using electroforming, tooling, molding, and the combination of lithography, and plastic molding process [6]. Schiefler et al. have reported less corrosion resistance and high corrosion current in thermally sprayed cathodic coatings as compared to bulk materials. The poor corrosion resistance was attributed to low porosity. Thus, a need to develop coating with high density and corrosion resistance has led to the development of high-velocity processes, such as HVOF and HVCW spraying techniques, which are required for improved corrosion protection [7].

This paper presents an overview of thermal spray processes being used for developing various coatings. A detailed discussion on the high-velocity oxygen-fuel coating technique and its importance has been carried out in this article. A comparison has also been drawn between various thermal spray processes. The paper also presents a review of the past research work carried out in developing different Fe-based coatings using the high-velocity oxy-fuel thermal spray technique.

2 Thermal Spray Processes

The melting of the material at high temperature by a heat gun or a similar device is usually carried out in thermal processes. The material in the molten state is atomized into tiny particles which are sprayed onto the prepared substrate surface [2]. The spraying is carried out for those materials only which can be brought to a molten

state. The formation of platelets or splats has been observed on the surface of the substrate. Chandra and Fauchais found that these splats/platelets get interlocked and thus build up and form a coating [8]. There is more mechanical interaction between the thermally sprayed coating and the substrate. Thermal spray processes have been mainly classified into thermal spray process are (i) detonation gun (D-Gun) process, (ii) plasma spray, (iii) wire arc spray process, (iv) flame spraying, and (v) high-velocity oxygen-fuel (HVOF) process.

Gan and Berndt found that the thermal spraying methods have been commonly used for preventing the product from any deterioration. The coatings can also be reapplied depending upon the deterioration of the existing coatings, thus, keeping the product (substrate) safe. Due to this very fact, there had been a massive use of coatings in industries [9]. Researchers and scientists have been on the continuous lookout for advancement in the application of thermally sprayed coatings. Thermal spraying has played a significant role in enhancing the longevity of products along with restoring and re-engineering outdated or defective products.

2.1 High-Velocity Oxygen-Fuel Thermal Spray Process

The high-velocity oxygen-fuel process involves the transmission of kinetic and thermal energy. Thermal energy is used to bring the coating material to a molten state and kinetic energy is used to accelerate the intensity of the feeder with powder. The powder through the feedstock is fed into the spraying system axially or radially that rushes through the barrel to deposit on the substrate.

High-Velocity Oxygen-Fuel Process: Working principle

High-velocity oxygen-fuel gun (Figs. 1 and 2) consists of an internal combustion chamber in which gases such as propylene, propane, hydrogen, or liquid fuel such as K-1 kerosene and oxygen is infused at high pressures and high flow rates [3]. The powder is heated, ignited, and speeded up by the flames, in the combustion chamber. Oksa et al. have reported that the combustion chamber produces a high-velocity stream that combines fuel gasses and sprays powder to reach greater particle accelerations and velocities. The higher combustion pressures ensure efficient heat transfer due to which the injected material is completely melted. The powder is accrued on the surface of the substrate along with a stream of hot gas with high velocity, thus, form the contact bond and get densely deposited [10]. The components of the high-velocity oxygen-fuel spray system are mentioned below with brief details:

HVOF powder spray gun: Oxy-fuel spray gun with suitable X–Y mount to employ its movement in the desired direction easily.

Control Console: This console comprises oxygen and fuel flow meters with a control valve and FlashBack Arrester.

Powder Feeder: The rotary type powder feeder is capable of feeding a full range of HVOF powder at the desired speed regardless of morphology.

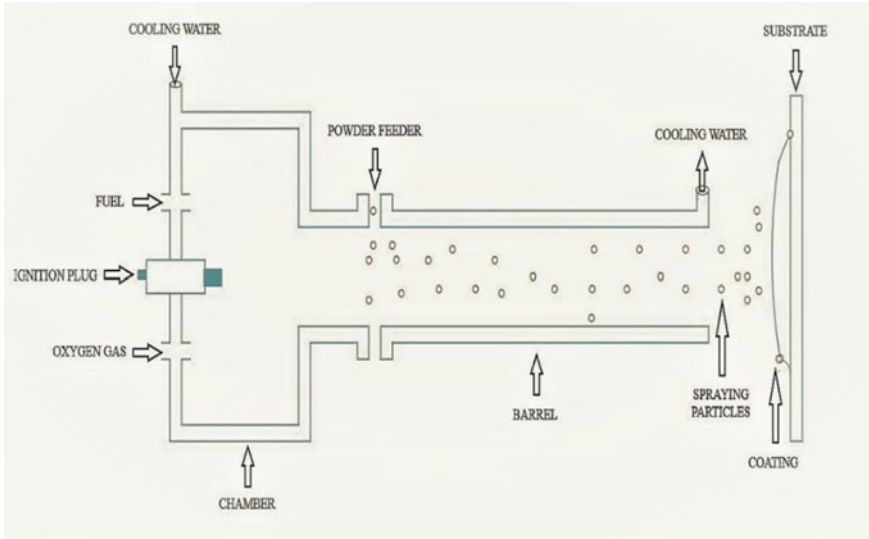


Fig. 1 High-velocity oxygen-fuel process

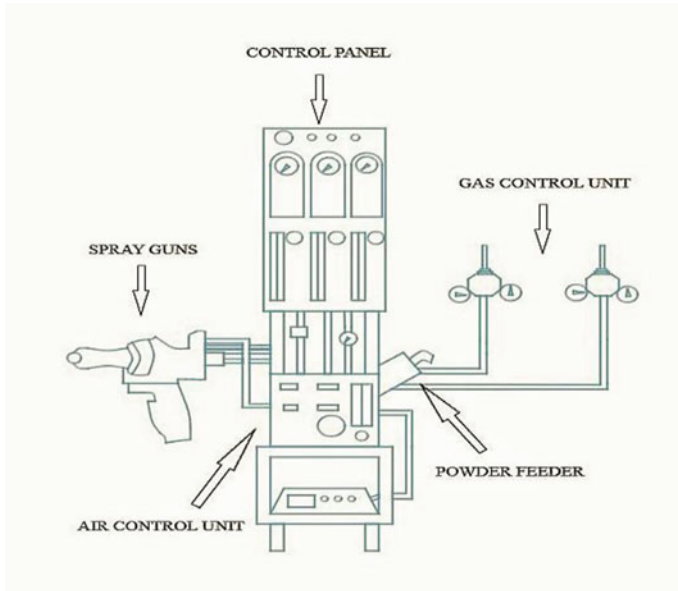


Fig. 2 High-velocity oxygen-fuel spray system

Air Control Unit: It comprises of automatic drain and air filter. The diaphragm operated air filter and pressure compensated by balanced poppet maintain flow and regulate pressure.

Gas Control Unit: This unit ensures a regular supply instrument. It consists of two-stage regulators pressure of the oxygen, nitrogen, and LPG gas supplied of gas from the cylinder to the that regulate the inlet the by the cylinder.

2.2 Importance of HVOF Process

The high-velocity oxygen-fuel spraying process is an emerging technology used to improve the materials durability, reliability, and efficiency in a wide variety of industrial applications, including spacecraft, jet aircraft, land-based gas turbines, metalworking forges, mills and rollers, paper, pumps, compressors, and even household products such as cookware [3]. The minimal change in the phase composition of the material makes HVOF spraying technique a better and competitive process. The velocity with which particle accelerates toward the surface of the substrate results in decreased porosities and raised densities of the coatings. The decrease in porosity level leads to increased cohesive forces on the substrate resulting in higher bond strength and better resistance against abrasion and erosion.

Kuroda et al. found that the chief advantages of HVOF processes are their ability to spray carbide coatings, superior in terms of density, adhesion, and reduced changes in the phase composition, to those sprayed by other techniques [11].

2.3 Comparison of Thermal Spray Methods

HVOF has been compared with other coating techniques and the comparison has been presented in the below-mentioned points.

Electroplating may or may not give uniform coating and can lead to the low-standard appearance of the plated content, whereas HVOF provides very strong, clean, smooth surface finish, dense, and homogeneous coatings.

In the case of electroplating, the fluid after the completion of the process must be disposed of carefully and thus is a matter of environmental concern [4], whereas the HVOF process is more environmentally friendly because of the absence of any fluid or solution. HVOF process can also be fully automated utilizing robotic equipment.

McGeough et al. found that the electroforming components are not always strong or large and are more susceptible to damages [6], whereas HVOF coatings have a higher substrate-binding efficiency within the adhesive coating and even low coating element distortion due to high density and lower porosity.

The main problem in hot-dip galvanizing was the deformation of thin structures due to heating, whereas with HVOF, a thicker and a strong is formed and no deformation due to heating as there are low heat-affected zones.

In hot-dip galvanizing, the degraded coating cannot be repaired, whereas HVOF has the highest toughness due to lower oxidation of the carbide coat and better corrosion resistance to protect the coating from any damage.

HVOF processes result in coating densities, oxide contents, and adhesion far better than plasma-sprayed coatings.

Bolelli et al. have found that the HVOF coatings are also significantly denser than wire-arc and flame-sprayed coatings, a direct consequence of HVOF's higher particle velocities [12].

The lower jet temperatures of HVOF as compared to plasma spraying can result in reduced oxidation.

HVOF combustion spray is a relatively new, thermal spray technology and is capable of depositing cermets, mainly carbide, and denser metal coatings, have lower oxide contents, and higher bond strengths than similar coatings deposited by thermal spraying, wire-arc, or air plasma spray processes.

HVOF does not differ from other thermal spray methods in that the use of 'optimized' spray parameters produces the desired results. Judicious variation of spray parameters may have a huge influence on the microstructures of the coating.

3 Coatings Developed Through HVOF Process

This section of the paper discusses the wear and friction behavior of the various Fe-based coatings developed through HVOF.

Researchers have been developing various novel coatings on different substrates using the HVOF technique. The microstructure, sliding wear, and corrosion resistance of HVOF sprayed Fe–V–Cr–C coatings have been studied by researchers and compared with other HVOF sprayed Ni–Cr–B–Si and Stellite-6 coatings. At room temperature, the coating was observed to exhibit strong wear resistance. The rate of wear of Fe-based coating relative to the rate of wear of Ni-based coating indicated a much lower rate of wear of the former coating [13]. Koga et al. reported the corrosion and wear performance of iron-based coating Fe–Cr–Mn–Co–Si (also known as CaviTec alloy) developed by HVOF and deposited the same on 304 stainless steel. The findings had revealed that both uncoated and HVOF coated stainless steel exhibited almost the same wear and friction results [14]. Fe-based Fe–15Cr–14Mo–15C–6B–2Y amorphous coatings have been effectively coated on mild steel substrate using HVOF. From the results, it was known that the finer powders developed dense coating, but the coarser powders improved corrosion resistance due to varying oxygen content in the coatings [15]. Stellite-6 coating having composition 28 wt% Co, 4.9 wt% Cr, 2.7 wt% W, 2.3 wt% Fe, 1.2 wt% Ni, 1.1 wt% C, 0.4 wt% Si, 0.13 wt% Mn, Mo in wt% efficiently and effectively deposited via high-velocity oxy-fuel thermal spray technique. Nickel and iron-based superalloy

substrates with a porosity of less than 2% were applied to coatings with a thickness of 250–300 μm . The hardness value of the coatings was found to be between 800 and 900 HV. In comparison, the coating hardness (800–900 HV) was very high in value relative to the substrates alloys. The microhardness of the coatings is balanced by the distance from the coating-the ground interface. In the cross-section of the coatings, microstructural variations are mostly due to porosity, oxidized, molten, and semi-molten crystals [16]. Milanti et al. studied the tribological efficiency using the HVOF method of Fe–Cr–Ni–B–C and Fe–Cr–Ni–B–Mo–C Fe-based coatings. The Fe-based coating efficiency was compared to WC–CoCr hard metal and traditional Ni-based Ni–Cr–Fe–Si–B–C coatings. The results concluded that Fe coatings displayed a good microstructure with almost zero porosity, moderate anti-slip properties, high wear properties, and almost double wear resistance relative to other Ni-based and hard metal coatings [17]. The mechanical behavior of Fe–10Cr–4P–4B–2C, Fe-based coating on mild steel substrates with grit-blasting has been studied. In Fe-based coatings, high micro- and nano-hardness has been found and all-composite coatings have a low wear rate due to improved hardness [18]. The Fe₃Al–TiC coating was developed using HVOF and it was discovered that with significantly increasing TiC content from 30 to 50 mol%, and the coating hardness increased and the rate of wear decreased by 75%. Further, the wear process changes from adhesive to abrasive wear with the increase in sliding speed from 0.04 to 0.8 m/s, respectively [19]. Amiriyani et al. examined the effects of TiC on the wear rate of Fe–TiC coatings on Alumina coatings. The results revealed that numerous coating properties such as Vickers hardness and wear resistance also showed a gradual increase in the increase in TiC content in the Fe matrix [20]. Fe-based amorphous coatings (Fe–Nb–B, Fe–Cr–Mo–C–B–Y, Fe–Co–Ni–Zr–Si–B, Fe–Ni–P–B) had been developed using HVOF coatings and tested for various properties. The authors suggested that corrosive wear resistance is decreased by the presence of fractures, voids, and non-bonded surfaces on the coatings. As indicated by the authors, the reduction of these defects can be achieved through optimization of spraying parameters, the inclusion of the alloy element, and post-treatment [21]. The authors the effect of the BN/Ti content on the tribological properties of Fe₃Al-prepared high-velocity oxygen-fuel coatings. The authors reported that when BN and Ti were applied, and the rate of wear of the Fe₃Al coating was increased. The mechanical characteristics were also influenced by the porosity and also affected the coating's surface elasticity [22]. Ceschini et al. carried out their investigation on tribological characteristics of Fe–C–Mo and Fe–C–Cr Fe-based coatings. Results have shown that Fe–C–Mo steels are more wear-resistant than Fe–C–Cr steels with 1.5 wt% Mo. Due to the high resistance to plastic flow, the materials showed high friction coefficient values [23]. The study on Fe₃Si and FeNb alloy coatings fabricated using the HVOF method was carried out. Upon the modification of the spraying conditions, an amorphous coating from the FeNb powder was acquired. It has been stated that a significant decrease in structural stability has occurred with the integration of boron into the alloy matrix [24]. Colferoloy (Fe–Cr–Ni–Si–B–C) alloy coatings were developed as an alternative to the conventional Ni-based Ni–Cr–Fe–Si–B–C alloy coatings for wear protection. It was observed that the sliding wear resistance of Fe-based coatings is considerably

superior to that of HVOF thermally sprayed Ni coating. Both coatings were softened at 400 °C and their sliding wear behavior was dominated by more extreme abrasive grooving. However, the Colferloy coatings were performing better than the Ni-based Ni–Cr–Fe–Si–B–C coatings [25]. The cavitation erosion of HVOF sprayed Fe–Cr–Ni–B–C coatings was studied in distilled water. The author observed that, relative to long-established Ni-based and WC–CoCr coatings, Fe-based coatings are more resistant to cavitation erosion. The erosion resistance of coatings based on Fe was twice as high as that of coatings based on WC–CoCr and Ni [26]. The researchers have analyzed two independent thermal spraying methods (HVOF and HVAF) for the depositing two Fe-based powders having composition Cr-31, Ni-12 B-3.6, C-0.6, and Fe bal. (in wt%) and Cr-31, Ni-12, Mo-2, B-3.6, C-0.6, and Fe bal. (in wt%) They found that HVOF sprayed coatings showed microstructural enhancements than sprayed high-velocity air–fuel coatings, resulting in improved nano-hardness and high elasticity of the surface. Due to the high-velocity effects of the molten or semi-molten droplets and choosing the appropriate set of process parameters, oxidation was prevented. The HVAF Fe (Mo) coating's low surface elasticity and microhardness is due to a potentially faulty particle boundary [27]. The author tested the microstructural properties of W–C–Co–Mo composite coatings deposited using the thermal spraying technique of high-velocity oxy-fuel on a steel substrate. The addition of Mo was carried out at 10, 20, 30, and 40 weight percentages. With the increase in Mo content, the authors observed an improvement in the hardness [28]. Pauleau et al., in their study, focused on tribological test conditions and film thicknesses. The author observed the calcium fluoride films had relatively low friction coefficients between room temperature and 500 °C and were found to be between 0.3 and 0.15. The results show that sputtering films exhibit outstanding tribological properties and strong, favorable lubricant coatings for mechanical components. Moreover, the tribological properties of thin CaF₂ films and found out that these films have better tribological properties as compared to chromium–carbon (Cr₃C₂) and can be used as a favorable lubricant coating for mechanical components because of their high precision tolerance capability [29]. It has also been reported by researchers that the CaF₂ composite coating shows favorable anti-wear properties at a raised temperature which may be related to the formation of the transfer films on the substrate surface at high temperatures [30]. Several scholars have investigated effective sealing techniques for high-speed oxy-fuel-sprayed coatings to increase corrosion and wear resistance. They found that the inorganic binder (AlPO₄ sealant) had penetrated the pores of the coated surface and passed through the amorphous metal coating thermally sprayed by the HVOF at a depth of 50.0 μm, while the coating surface had just been coated by the Na₃SiO₄ and cerium salt sealants. On the exterior, the cerium salt sealant developed a micro-cracked layer. The inorganic binder (AlPO₄-sealed) coating's microhardness has been shown to improve from 800 to 1000 HV. This development has shown us that it is possible to increase the wear resistance of the coatings effectively and can be used under abrasive or corrosive conditions [31]. Koga et al. investigated the effect of different sliding speeds on 60 at.% Fe, 8 at.% Cr, 8 at.% Nb, 24 at.% B, amorphous coating developed using HVOF process. The coating thickness was 280.0 μm and processed via HVOF spray process on the steel

substrate API 5L X80. It was noted that with the rise in sliding speed, the loss of wear of the substrate decreased, while HVOF coatings displayed an increase in the rate of erosion or wear [32]. The sliding behavior of two distinct coatings was studied by the authors. Coatings exhibit hardness value 235 HV10 were produced on the external of standard perlitic CI disks via HVOF process. The first coating was formulated with powder of WC–Co–Cr comprising 86 wt% of WC particles coated in a 10 wt% Co and 4 wt% Cr metal matrix. The secondary coating was made with a 25 wt% NiCr matrix of Cr₃C₂–NiCr. These coatings control the temperature of the sliding bodies as they enable various friction mechanisms. The coefficient of heat partition (HPC) measured in the sliding of these coatings is ‘1,’ and the temperature of the disk starts to increase as a consequence of the sliding, contributing to a decline in HPC [33]. Simard et al., from their study, concluded that the HVOF technique can allow some cermet-based materials such as tungsten carbide to form a protective coating onto different surfaces. They also observed that (i) the output of the coatings has been impaired by corrosion reactions and (ii) the metal matrix content plays a very significant and important in the stability of the coatings as well as deterioration rate [34]. The author compared the performance of the Fe–Cr–Ni–Si–B–(W, Ti)C coating processed by the electric arc spray technique with the WC-based WC–12Co coating formed by HVOF technique. They observed that with the increase in the hardness, the compactness, and high fracture toughness also increased. HVOF coating found superior microhardness than EAS coatings [35]. Analysis involving three types of HVOF sprayed NiCr/Cr₃C₂–BaF₂.CaF₂ coatings were produced by Huang et al. The authors observed that the three coatings had less porosity and substantially higher bond strength relative to plasma spray coatings, and their coefficient of friction decreased when temperature increased [36]. An investigation on the tribological behavior of Fe_{49.5}Cr_{18.3}Mo_{7.7}W_{1.6}Mn_{1.8}B_{14.9}C_{3.6}Si_{2.6} (Co) alloy coating was carried out. The study revealed that the optimal anti-wear properties were achieved when Co was introduced to the above coating and annealed at an elevated temperature of 700 °C. When the cobalt element is added to the Fe-based alloy, the author found out that it formed coatings with enhanced corrosion and tribo properties [37]. Ramesh et al. analyzed the impact of HVOF composite molybdenum and molybdenum-silicon carbide coatings on mild steel. Studies have shown that there is outstanding bonding at the substrate and coating interface. Produced Mo coatings reported an improvement in microhardness of 7.50% and 10 Mo wt% of SiC composite coatings reported an enhancement of 23% in microhardness and porosity below 2% [38]. HVOF technique has been considered a good alternative to the plasma spraying process. Researchers have observed that the high speed of the jet causes the shearing of the droplets into many tiny droplets, resulting in improved healing of the droplets in the HVOF jet [39]. Fe-based amorphous coatings microstructure evolution and thermal stability were examined by the author. Fe-based coating (composition: 18.9 Fe at.%, 16.1 Cr at.%, 4.0 B at.%, 2.8 C at.%, 2.4 Si at.%, 1.9 Mo at.%, 1.7 Mn at.% W alloy) was produced by HVOF. The study showed that variations in the microhardness of the coatings were dependent on various factors such as annealing time and temperature. The report says that annealing above 550 °C may improve the hardness of the coatings; however, the improvement of coating is reliable on the various conditions like

temperature and the heat treatment time. Over a set interval of time which is 60 min, the authors found the two temperature on which the 9.20 GPa hardness value is substantially improved. At first, it improved at 650 °C on which peak hardness value was found to be 12.50 GPa and after that it improved at 750 °C where peak hardness value found to be 11.80 GPa, by annealing for several intervals, respectively, although a small improvement was observed at 925 °C. However, at annealing periods of longer duration, the value of hardness is declined steadily from the peak value [40]. Masoumi et al. had stated that in the microhardness value of the WC–10Co–4Cr HVOF sprayed coatings on low carbon steel there was a progressive increment which is caused by increase in residual compressive stresses. They observed that the microhardness depends more on the residual stress than the coating porosity. The indenter from penetrating gets restricted by the compressive stress coating and thereby displays a microhardness greater than the inherent microhardness [41]. In two HVOF sprayed coatings, which are WC–Co coating and Cr₃C₂–NiCr coating, carbide particles were spotted by many authors which are stayed in the solid phase after passing through the blaze. Tiny carbide particles can adopt the flattening process of the liquid binder and deposit can be embedded quickly, whereas two-phase droplet of large carbide particles gets recover simply via HVOF spraying as the droplets touch the outside of the substrate [42]. Masuku et al., in their study, reported that the chemical structure of the metallic binder carries out an important and notable role during HVOF spray coatings. HVOF was collected on 312L of the austenitic stainless steel substrate by WC-based powders such as WC–12Co, WC–7Co–2Co, WC–10Co–4Cr, and WC–12Co (60NiCr) (in wt. percent). The binder also played a crucial function in impacting the corrosion and wear actions of the coating. The introduction of Cr in the binder during wet sliding increases the hard-wearing opposition of the WC-based coating. WC-based WC–10Co–4Cr wt% coating displayed the prominent hard-wearing opposition during the wet sliding situation as well as exhibits the finest corrosive actions due to the passive film-forming of Cr₂O₃ oxides in tested coatings [43]. Researchers have also researched the porosity of Hastelloy C HVOF spray coatings. Hastelloy C feedstock chemical composition was found to be 16.95 wt% Mo, 16.57 wt% Cr, 6.21 wt% Fe, 4.52 wt% W, 0.72 wt% Mn, 0.31 wt% Co, 0.73 wt% Si, and Ni balance, respectively. This study showed that porosity depends on two factors, i.e., the stacking arrangement and coating's thickness of the sprayed particle. The paper also reports that the coating which was prepared under high combustion pressure showed zero porosity [44]. The efficiency of the HVOF method for the production of thick coatings for hard-wearing opposition applications was investigated by Rajasekaran et al. The results suggested that fabrication of thick cold work steel coatings can be done via appropriate HVOF criterion.

The thick coating presented a higher level of abrasive wear resistance. The abrasive opposition of cold work tool steel encrusted fastener proved to be more advanced than the normal high-speed steel when rubbed against the soft and fine garnet paper. In addition, the output of coated pins in opposition to hard and thick granite paper was observed in comparison with previous high-speed steel coatings [45].

The four HVOF coatings (i) Fe-based FeNi01 (composition: 20 Ni wt%, 19 Cr wt%, 15 Mo wt%, 6 Si wt%, 3 W wt%, 3 Cu wt%, 2 B wt%, 0.3 C wt%, and

Fe-balance wt%), (ii) Co-based CoCr01 (composition: 29Cr wt%, 8.5Mo wt%, 3Ni wt%, 3Fe wt%, 2C wt%, 1.5Si wt%, and Co-balance wt%), (iii) Cr-based CrNi01 (composition: 39Ni wt%, 3Mo wt%, 1Si wt%, 1B wt% and Cr-balance wt%), and (iv) Ni-based NiCr02 (composition: 16Cr wt%, 15Mo wt%, 6Fe wt%, 3 W wt%, and Ni-balance wt%) were studied and the findings revealed that these coatings showed lower porosity. Also, their density increased when the porosity decreased and vice-versa [46].

4 Conclusion

The importance of thermal spray processes had led many researchers to adopt these techniques. The present work deals with the HVOF thermal spray process and other thermal sprayed process. Apart from this, the work also mentions the comparisons drawn between HVOF and other thermal spray processes. In this work, the significance of the HVOF method has been expanded. The authors have thoroughly studied literature about the Fe-based coatings developed through the HVOF technique and have elaborated the work carried out by the authors in the recent past. The work brings forth the shortcomings of other processes that had been taken care of by the HVOF process.

References

1. Mehta J, Mittal VK, Gupta P (2017) Role of thermal spray coatings on wear. *J Appl Sci Eng* 20(4):445–452
2. Kumar R, Kumar S (2018) Thermal spray coating: a study. *Int J Eng Sci Res Technol* 7(3):610–617
3. Irving B, Knight R, Smith RW (1993) The HVOF process—the hottest topic in the thermal spray industry. *Weld J* 72(7):25–30
4. Rokhmat M, Wibowo E, Sutisna, Khairurrijal, Abdullah M (2017) Performance improvement of TiO₂/CuO solar cell by growing copper particle using fix current electroplating method. *Procedia Eng* 170:72–77
5. Rokhmat M, Wibowo E, Sutisna, Khairurrijal, Abdullah M (2018) Development of a low-cost TiO₂/CuO/Cu solar cell by using combined spraying and electroplating method. *J Math Fundam Sci* 50(1):92–101
6. McGeough JA, Leu MC, Rajurkar KP, De Silva AKM, Liu Q (2001) Electroforming process and application to micro/macro manufacturing. *CIRP Ann* 50(2):499–514
7. Schieffler Filho MFO, Buschinelli AJA, Gartner F, Kirsten A, Voyer J, Kreye H (2004) Influence of process parameters on the quality of thermally sprayed X46Cr13 stainless steel coatings. *J Braz Soc Mech Sci Eng* 26(1):98–106
8. Chandra S, Fauchais P (2009) Formation of solid splats during thermal spray deposition. *J Therm Spray Technol* 18(2):148–180
9. Gan JA, Berndt CC (2013) Review on the oxidation of metallic thermal sprayed coatings: a case study with reference to rare-earth permanent magnetic coatings. *J Therm Spray Technol* 22(7):1069–1091

10. Oksa M, Turunen E, Suhonen T, Varis T, Hannula S-P (2011) Optimization and characterization of high velocity oxy-fuel sprayed coatings: techniques, materials, and applications. *Coatings* 1(1):17–52
11. Kuroda S, Kawakita J, Fukushima T, Tobe S (2003) Importance of the adhesion of HVOF sprayed coatings for aqueous corrosion resistance. *Mater Trans* 44(3):381–388
12. Bolelli G, Lusvardi L, Manfredini T, Mantini FP, Polini R, Turunen E, Varis T, Hannula SP (2007) Comparison between plasma and HVOF-sprayed ceramic coatings. Part I: microstructure and mechanical properties. *Int J Surf Sci Eng* 1(1):38–61
13. Sassatelli P, Bolelli G, Lusvardi L, Manfredini T, Rigon R (2016) Manufacturing and properties of high-velocity oxygen fuel (HVOF)-sprayed FeVCrC coatings. *J Therm Spray Technol* 25:1302–1321
14. Koga GY, Wolf W, Schulz R, Savoie S, Bolfarini C, Kiminami CS, Botta WJ (2018) Corrosion and wear properties of FeCrMnCoSi HVOF coatings. *Surf Coat Technol* 1–42
15. Zhang C, Guo RQ, Yang Y, Wu Y, Liu L (2011) Influence of the size of spraying powders on the microstructure and corrosion resistance of Fe-based amorphous coating. *Electrochim Acta* 56(18):6380–6388
16. Sidhu TS, Prakash S, Agrawal RD (2006) Studies of the metallurgical and mechanical properties of high velocity oxy-fuel sprayed stellite-6 coatings on Ni and Fe-based superalloys. *Surf Coat Technol* 201(1–2):273–281
17. Milanti A, Koivuluoto H, Vuoristo P, Bolelli G, Bozza F, Lusvardi L (2014) Microstructural characteristics and tribological behavior of HVOF-sprayed novel Fe-based alloy coatings. *Coatings* 4(1):98–120
18. Nayak SK, Kumar A, Pathak A, Banerjee A, Laha T (2020) Multi-scale mechanical properties of Fe-based amorphous/nanocrystalline composite coating synthesized by HVOF spraying. *J Alloy Compd* 825:154120
19. Ghazanfari H, Blais C, Alamdari H, Garipey M, Savoie S, Schulz R (2019) Characterization of dry-sliding wear of HVOF coatings made of Fe₃Al powders reinforced with sub-micrometer TiC particles produced by combustion synthesis. *Surf Coat Technol* 260:29–38
20. Amiriyan M, Alamdari HD, Blais C, Savoie S, Schulz R, Garipey M (2015) Dry sliding wear behavior of Fe₃Al and Fe₃Al/TiC coatings prepared by HVOF. *Wear* 342–343:154–162
21. Huang B, Zhang C, Zhang G, Liao H (2019) Wear and corrosion resistant performance of thermal-sprayed Fe-based amorphous coatings: a review. *Surf Coat Technol* 377:124896
22. Pougoum F, Schmitt T, Martinu L, Klemberg-Sapieha J-E, Savoie S, Schulz R (2017) Wear behavior of Fe₃Al-TiN-TiB₂ HVOF coatings: a comparative study between in situ and ex situ powder processing routes. *Ceram Int* 43(11):8040–8050
23. Ceschini L, Palombarini G, Sambogna G, Firrao D, Scavino G, Ubertalli G (2006) Friction and wear behaviour of sintered steels submitted to sliding and abrasion tests. *Tribol Int* 39(8):748–755
24. Cherigui M, Feraoun H, Feninehe N, Aourag H, Coddet C (2004) Structure of amorphous iron-based coatings processed by HVOF and APS thermally spraying. *Mater Chem Phys* 85(1):113–119
25. Bolelli G, Bonferroni B, Laurila J, Lusvardi L, Milanti A, Niemi K, Vuoristo P (2012) Micromechanical properties and sliding wear behaviour of HVOF-sprayed Fe-based alloy coatings. *Wear* 276–277:29–47
26. Milanti A, Koivuluoto H, Vuoristo P, Bolelli G, Bozza F, Lusvardi L (2013) Wear and corrosion resistance of high-velocity oxygen-fuel sprayed iron-based composite coatings. In: ASME international mechanical engineering congress and exposition (IMECE) proceedings, vol 11, p 63397. IMECE Publishing, USA
27. Milanti A, Matikainen V, Bolelli G, Koivuluoto H, Lusvardi L, Vuoristo P (2016) Microstructure and sliding wear behavior of Fe-based coatings manufactured with HVOF and HVAF thermal spray processes. *J Therm Spray Technol* 25(5):1040–1055
28. Islak S, Kir D, Buytoz S, Ozorak C, Akkas M, Caligulu U (2015) Microstructure characterization of WCCo-Mo based coating produced using high-velocity oxygen fuel. *Pamukkale Univ J Eng Sci* 21(8):344–347

29. Pauleau Y, Juliet P, Gras R (1998) Tribological properties of calcium fluoride-based solid lubricant coatings at high temperatures. *Thin Solid Films* 317(1–2):481–485
30. Wang C, Zhang C, Zhang SJ, Guo LJ (2015) The effect of CaF₂ on the magnesium production with silicothermal process. *Int J Miner Process* 142:147–153
31. Wang Y, Jiang SL, Zheng YG, Ke W, Sun WH, Wang JQ (2011) Effect of porosity sealing treatments on the corrosion resistance of high-velocity oxy-fuel (HVOF)-sprayed Fe-based amorphous metallic coatings. *Surf Coat Technol* 206(6):1307–1318
32. Koga GY, Schulz R, Savoie S, Nascimento ARC, Drolet Y, Bolfarini C, Kiminami CS, Botta WJ (2017) Microstructure and wear behavior of Fe-based amorphous HVOF coatings produced from commercial precursors. *Surf Coat Technol* 309:938–944
33. Federici M, Straffelini G, Gialanella S (2017) Pin-on-disc testing of low-metallic friction material sliding against HVOF coated cast iron: modelling of the contact temperature evolution. *Tribol Lett* 65(4):121
34. Simards S, Arsenault B, Legoux JG, Hawthorne HM (1999) Performance of HVOF carbide coatings under erosion/corrosion. In: *International nuclear information system (INIS)*, vol 32, issue no 28. INIS Publishing, Canada, pp 357–369
35. Lakhdari R, Fernandes F, Antunes P, Mebdoua Y, Cavaleiro A, Legouera M (2019) Fe-based (W,Ti)C EAS and WC–12Co HVOF sprayed coatings: microstructure, mechanical properties and micro-scale abrasion performance. *Mater Res Express* 6:096580
36. Huang CB, Du LZ, Zhang WG (2011) Microstructure, mechanical and tribological characteristics of plasma, detonation gun and HVOF sprayed NiCr/Cr₃C₂–BaF₂.CaF₂ coatings. *Surf Eng* 27(10):762–769
37. Liu WH, Shieu FS, Hsiao WT (2014) Enhancement of wear and corrosion resistance of iron-based hard coatings deposited by high-velocity oxygen-fuel (HVOF) thermal spraying. *Surf Coat Technol* 249:24–41
38. Ramesh CS, Adarsha H, Chaturvedi A, Nair N (2018) Investigations on the effect of molybdenum (Mo) and molybdenum silicon carbide (Mo-10% Sic) composite coatings on mild steel substrate using HVOF technique. *Mater Today Proc* 5(11):24422–24427
39. Cetegen BM, Basu S (2009) Review of modeling of liquid precursor droplets and particles injected into plasmas and high-velocity oxy-fuel (HVOF) flame jets for thermal spray deposition applications. *J Therm Spray Technol* 18(5–6):769–793
40. Chokethawai K, McCartney DG, Shipway PH (2009) Microstructure evolution and thermal stability of Fe-based amorphous alloy powder and thermally sprayed coatings. *J Alloy Compd* 480(2):351–359
41. Masoumi H, Safavi SM, Salehi M, Nahvi SM (2014) Effect of grinding on the residual stress and adhesion strength of HVOF thermally sprayed WC–10Co–4Cr coating. *Mater Manuf Process* 29(9):1139–1151
42. Li C-J, Wang Y-Y, Yang G-J, Ohmori A, Khor KA (2004) Effect of solid carbide particle size on deposition behavior, microstructure and wear performance of HVOF cermet coatings. *Mater Sci Technol* 20(9):1087–1096
43. Masuku ZH, Olubambi PA, Potgieter JH, Obadele BA (2015) Tribological and corrosion behavior of HVOF-sprayed WC–Co-based composite coatings in simulated mine water environments. *Tribol Trans* 58(2):337–348
44. Kawakita J, Kuroda S, Kodama T (2003) Evaluation of through-porosity of HVOF sprayed coating. *Surf Coat Technol* 166:17–23
45. Rajasekaran B, Mauer G, Vaben R, Rottger A, Weber S, Theisen W (2010) Thick tool steel coatings using HVOF spraying for wear resistance applications. *Surf Coat Technol* 205(7):2449–2454
46. Chidambaram D, Clayton CR, Dorfman MR (2004) Evaluation of the electrochemical behavior of HVOF-sprayed alloy coatings. *Surf Coat Technol* 176(3):307–317

Automation in Conventional Drilling Machine to Multi-spindle Drilling SPM



Vinay D. Patel, Mahendra Choudhary, Rushikesh Bhosale, Sarvesh Wapikar, Pranav Bhamare, and Ashish J. Chaudhari

Abstract The current scenario for small-scale industries is the production of use box component workpiece of 14 mm and 10 mm square rod that takes two workers to operate the conventional pillar drilling machine (Model-SKP 20 mm capacity) to drill three holes of various diameters at various center distance. The time required to complete the process for one workpiece is about 2–3 min. The production target of 14 mm square rod is 6000 pieces, and 10 mm square rod is 10000 pieces in 26 days. The aim of this paper is to automate the entire process with minimum human intervention and thereby increasing production rate and minimizing the process time. The entire theoretical design calculation, manufacturing, and experimental work are carried out in industries as it demands to reduce the process time and increase the production rate. Therefore, the conventional pillar drilling machine setup is to be automated. Now, to fulfill the above purpose, the modification in conventional machine needs to be done and is to incorporate a separate motor for both z -axis and x -axis travel and that is controlled by using a microcontroller, new designed multi-spindle head, and helical gears. Production rate measured for different feed rate for drilling operation on multi-spindle and measured reduction cycle time to fulfill the process requirements. Jig plate provision is made to improve the accuracy and reduce the workpiece rejection rate. Finally, power consumption calculation is made in which the automated multi-spindle reduced 78.85% than conventional drilling machine.

Keywords Multi-spindle · Drilling machine · Microcontroller · Production rate · Jig plate · Automation

V. D. Patel (✉) · M. Choudhary · R. Bhosale · S. Wapikar · P. Bhamare · A. J. Chaudhari
Department of Mechanical Engineering, Vidyavardhini's College of Engineering and Technology,
Vasai (W), Maharashtra 401202, India
e-mail: vinay.patel@vcet.edu.in

© The Author(s), under exclusive license to Springer Nature Singapore Pte Ltd. 2022
K. Govindan et al. (eds.), *Advances in Mechanical and Materials Technology*,
Lecture Notes in Mechanical Engineering,
https://doi.org/10.1007/978-981-16-2794-1_58

663

1 Introduction

Manufacturing industries have evolved a lot throughout the years in terms of technology. Large-scale industries have already started using automation for production. Nevertheless, large-scale industries rely on smaller industries to produce components that are to be used in their assemblies. However, small-scale and mini-scale industries still prefer conventional machining operations. This leads to low production rate and long working hours. To maximize productivity and obtain accuracy, these industries need to opt for the automated process. Gears are the most important components for power transmission at high speeds. If not selected properly, it can cause problems such as vibrations, heating due to friction, and high-frequency noise intolerable to human ears and jamming of gears. For this, the factors affecting are center distance between gears, gear material and their hardness, helix angle, pressure angle, bearing type, and lubrication. Gearbox is specially designed for such special purpose machine (SPM). This includes gear selection and its material to be used. Types of gear failures and their causes are considered while design of gearbox. The main objectives of this paper are to design a multi-spindle gearbox for maximum 2800 rpm drilling speed. The overall complete design of setup in SolidWorks including manufacturing drawings. Testing the multi-spindle and linear x -axis and z -axis travel of setup. Testing the drilling operation for hole diameter of 2.5mm for cycle time at optimum feed and speed condition.

The vertical pillar drilling machine is used to generate a hole [1]. In today's industrialization scenario, demand is increasing for special purpose machine as it performs multi-operation to increase its productivity in single cycle. The multi-spindle attachment is advantageous over the conventional machine as it performs a single operations at a time [2]. However, many industries are now realized the importance of automation [3]. In flexible manufacturing system (FMS), versatile machining centers handle high machining flexibility in variety of jobs. Examples like in multi-spindle machine tools and head changers are used in FMS [4]. Intelligent sensor system used FMS for monitoring the spindle system with microcontroller [5]. It is problematic to find out the performance parameters due to probabilistic drills tool life to operate multi-tool assembly. With the help of computer program, an optimum operation can be achieved [6]. In mass production, large quantity is to be produced in less job variety and at a faster rate; hence, planetary gear system arrangement is to be performed to get more accurate function in multi-spindle drilling machine [2].

The design of gear box plays a crucial role in the multispindle drilling machine [7]. The fixtures have locators and clamps sets on them which can be replaced with hydraulic fixtures in present design. Function concept and formalized method IDEF0 and UML diagram is used in fixture design process [8]. Dual driven spindle system (DSSS) is used for quality machining and tool life [9]. Gear transmits power between prime movers and driven units [10]. The author is more focused in reducing total machining operations in organization and growth of Indian manufacturing sector and industrial to increase the production target [11]. There are various parameters over which the performance of the spindle depends. Based on the FEM, the static and

dynamic analysis has been performed. In the static analysis, it considers parameters such as material of the spindle, bearing span, Morse taper. The dynamic analysis has been performed corresponding to the optimized static model, and modal shapes are obtained. With the help of Campbell diagram, critical velocity has been found out. The harmonic response is performed to check the design, and with the required speed, transient analysis is performed [12]. The effective approach of Taguchi optimization is used to minimize the problem in drilling [13].

2 Theoretical Calculation

The initial step in design is the calculation of the power transmitting elements. This includes the types of gears used, number of spindles, force and thrust exerted, drill sizes and type of material to be drilled. The initial step in design is the calculation of the power transmitting elements. The necessary design parameters are calculated like helical gear design power, virtual number of teeth, Z_{v1} and Z_{v2} , shear strength of tooth, dynamic load, wear load calculation F_w , shaft design: torsion, bolt calculation: shear strength S_{sv} , bearing calculation like cutting speed and axial thrust P , and equivalent load P_e are carried out. Table 1 shows the summary of calculated parameter values obtained after calculations of power transmission elements.

Table 1 Summary of parameters needs to be designed for power transmission elements and multi-spindle gearbox

S. No.	Power transmission elements	Theoretical calculated values
1	Power	0.14 kW
2	Helical gear design power	1.3 kW
3	Virtual number of teeth, Z_{v1}	35.94
4	Virtual number of teeth, Z_{v2}	21.56
5	Shear strength of tooth	1904 N
6	Dynamic load	469.08 N
7	Wear load calculation (F_w)	1236.96 N
8	Shaft design: torsion	7.72 N/mm ²
9	Bolt calculation: shear strength (S_{sy})	200 N/mm ²
10	Bearing calculation: (i) cutting speed	19 m/min
11	Axial thrust (P)	385.4 N
12	Equivalent load (P_e)	0.793 kN

3 Experimental Work

A conventional pillar drilling machine as shown in Fig. 1 consists of a manual arm that is used to lower the drill head and is retracted by the spring mechanism. To reduce worker fatigue and errors due to human intervention, the process of drill head travel (lowering and raising) is automated. Motor selected for this application is NEMA 46 considering the weight of the multi-spindle to be transmitted. The feed and depth changes as per the changes in workpiece sizes. The calculated feed and depth for various workpiece sizes are fed accordingly into the code that can be uploaded to Arduino for stepper motor controlling. The values for depth and feed are set using the keypad given on the control panel. Keypad is provided for easier machine operating by workers. A controller that consists of start, stop, kill switch, and manual two-way switch is used to control z -axis. (a) Calculation of z -axis motor: steps per revolution

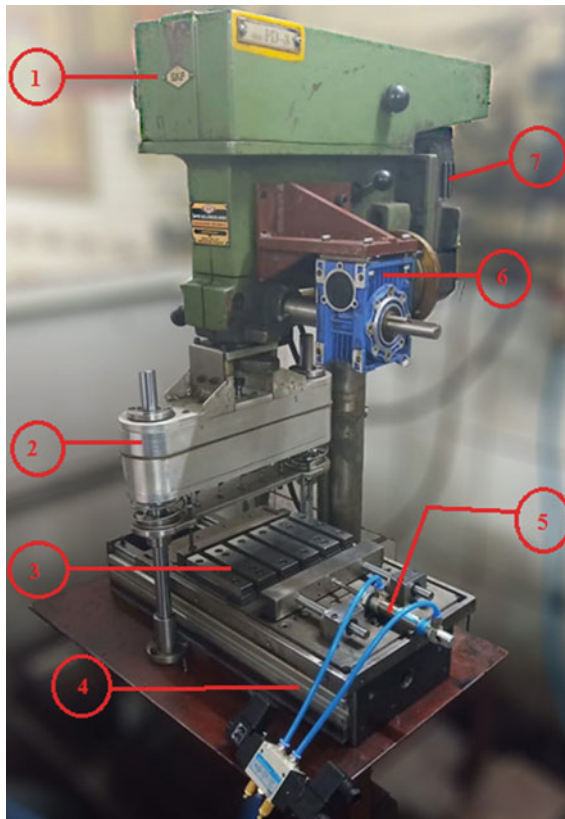


Fig. 1 Conventional pillar drilling machine arrangement view with multi-spindle gearbox. 1—pillar-type drilling machine, 2—multi-spindle drilling head, 3—drilling fixture, 4— x -axis travel lead screw table, 5—pneumatic clamping, 6—worm gearbox, 7—0.75 HP motor

= 200, at full stepping, i.e., one step of 1.8° . If lead = 1 in. per revolution, therefore, the resolution of lead screw = 0.005 in./step. The desired hole location 400 step/rev at 1.8° step, 50 step/rev at 0.225° step, motor selected NEMA 46–46 kg cm (b) X-axis automation: A bottom plate specially designed to house fixture pallet, where workpiece is to be fixed, located, and operated. A lead screw, block nut and stepper motor are used to attain linear travel along x-axis. Aluminum extrusions are used to support the guide rails on which guide blocks move linearly that carry the bottom plate. Stepper motor selected for this application is NEMA 34 considering the overall weight of the fixture pallet and bottom plate.

Coupling is used to connect lead screw to stepper motor. A bracket designed to house stepper motor is assembled to the side structure of bottom plate. (c) Lead screw selection: lead screw material: EN1, Type-M24 \times 5.0 2 Start. Like z-axis automation, the stepper motor of x-axis is controlled using the microcontroller, for precise required travel in microns or millimeters. (d) Manufacturing of the gearbox: Gearbox fabrication is done using part drawings based on the 3D CAD model. Ergonomic factors are considered which leads to ease in machine operation, human's safety, and greater productivity. Bearing holes, gear-shaft, bolts, bush holes, and other assembly features are indicated with appropriate tolerances. The method of manufacturing used is machining, and the material preferred is of aluminum series. (e) Manufacturing of fixture: Fixture size and shape depend on the workpiece dimensions. The fixture is specifically made up of hardened steel that gives strength and toughness to withstand forces due to metal contact further resisting wear and tear. Two different fixture pallets are manufactured depending upon sizes of workpiece. Fabrication is done based on manufacturing 3D CAD model drawing provided.

4 Results and Discussion

Improvement in cycle time for single-spindle z-axis automation: (i) cycle time 1: feed 0.07 mm/rev, (ii) cycle time 2: feed 0.09 mm/rev, (iii) cycle time 3: manual feed. The results obtained from the z-axis travel automation showed reduction in cycle time for drilling operation with an increase in production rate as shown in Fig. 2.

The cycle time varies depending on the feed and depth of workpiece. The results obtained from the overall automation show reduction by 79.5% in cycle time for feed rate of 0.07 mm/rev and reduction of 80.27% in cycle time for feed rate of 0.09 mm/rev compared to cycle time of manual drilling operation for performing drilling operation on five workpieces.

Figure 3 shows the comparison for total cycle time for 3 different conditions for 30 number of readings. From the above graph, when the operator used to drill 15 number of holes (i.e., 5 workpieces consisting of 3 holes on each) at an average time consumption of 380 s. But after introduction of automation of the machine, the cycle time reduced drastically. At feed rate of 0.07 mm/rev on an automated drilling setup, the cycle time for 15 number of holes (i.e., 5 workpieces consisting of 3 holes on

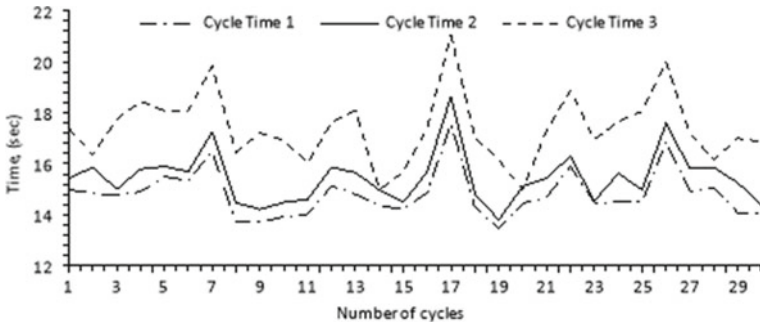


Fig. 2 Cycle time operation of multi-spindle gearbox

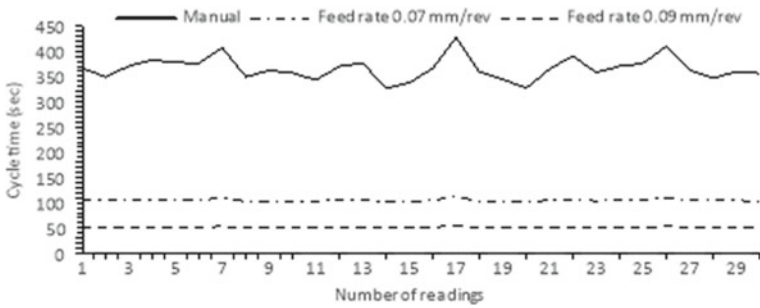


Fig. 3 Cycle time comparison between two feeds

each) was observed to be 100 s, whereas at feed rate of 0.09 mm/rev, it was observed to be 53 s.

Figure 4 shows the variation in the center distance in mm between five spindles for five number of readings without jig plate. It can be seen from the graph that without using jig plate, there is a considerable variation in center distance (around 0.5–1 mm). Hence, it can affect the accuracy of the hole that is drilled on workpiece and

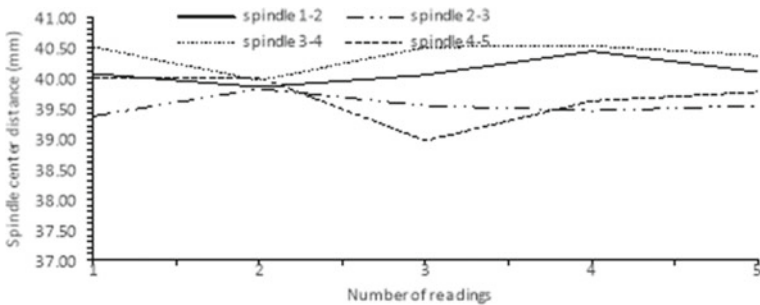


Fig. 4 Center distance variation without jig plate

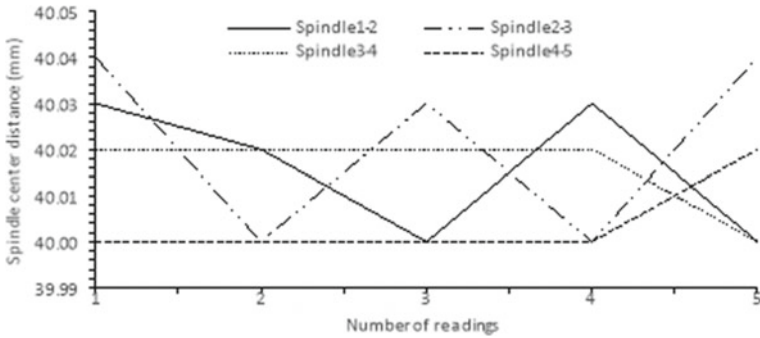


Fig. 5 Center distance variation reduced by using jig plate

could also lead to the rejection of workpiece. This creates the requirement to use jig plate while drilling.

Figure 5 shows the variation in the center distance in mm between the spindles for five number of readings with jig plate. Now, from the above graph, it shows that the variation between center distances is comparatively less (around 0.02–0.04 mm) by using jig plate in drilling operation. Hence, it can be seen from the reading that using jig plate can lead to reduce the center distance variation eventually improve the accuracy of the workpiece and reduce the rejection rate of the workpieces. Figure 6 shows the variation in spindle deflection in mm between five numbers of spindles for ten number of readings with jig plate. From the graph, it can be observed that the third spindle has zero mm deflection as it is the main transmitting spindle. The deflection increases as it moves toward outside from center, i.e., from third spindle to first and fifth spindle.

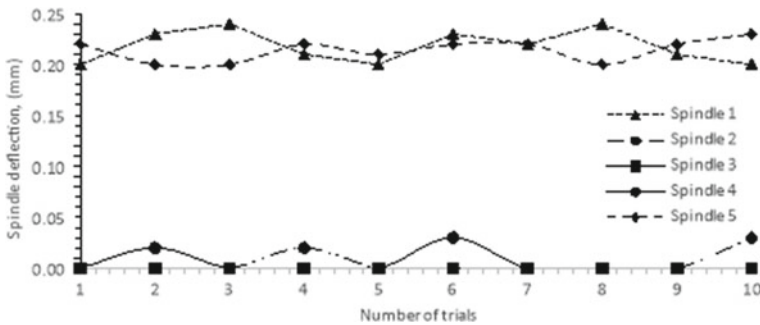


Fig. 6 Variation in spindle deflection

Table 2 Without gearbox for five machine in kW hours

Power consumption, W	2500.00
Average usage per day (in hours)	12.00
Number of days used	365.00
Cost per kWh	5.21
<i>Output</i>	
kWh (per year)	10,950.00
Cost (per year)	57,049.50

Table 3 Automated drilling machine with multi-spindle gearbox (single setup)

Power consumption, W	800.00
Average usage per day (in hours)	12.00
Number of days used	365.00
Cost per kWh	5.21
<i>Output</i>	
kWh (per year)	3504.00
Cost (per year)	18,255.84

5 Power Consumption

Table 2 shows power consumption without gearbox for five machine in kWh. To achieve this condition with conventional drilling machine, there is a requirement of five separate drilling machine. Hence, the above consumption data is compared between five conventional drilling machines without multi-spindle gearbox and one conventional drilling machine with multi-spindle gearbox. Below data shows annual power consumption for five conventional machines without multi-spindle gearbox. Table 3 shows annual power consumption for automated drilling machine with multi-spindle gearbox (single setup). The power consumption between with and without multi-spindle gearbox by the machine for 20 number of readings is shown in Fig. 7. With the five spindle gearbox, the machine is now capable to perform drilling operations on five individual workpieces. If we use conventional drilling machine with automated multi-spindle gearbox, then there will be 78.85% reduction in the power consumption as compared to five conventional drilling machines.

6 Conclusion

The results after fabrication and implementation of this special purpose machine automation show increase in production resulting in improved product quality and net profit to the industry. Following points are achieved due to multi-spindle gearbox and

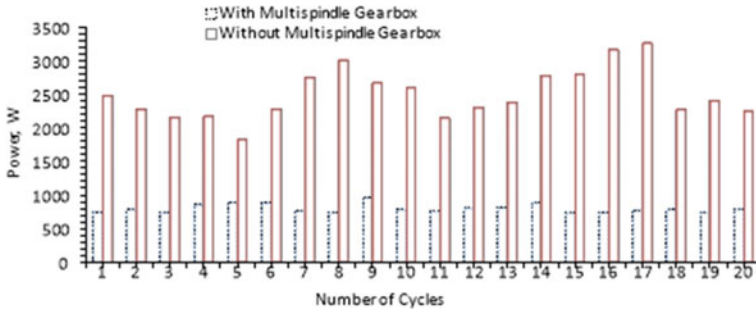


Fig. 7 Power consumption with and without multi-spindle gearbox

automation of the setup: (i) Improved product quality with lesser human intervention. (ii) Increase in production rate since five workpieces are drilled at a time. (iii) Reduced cycle time of operation with increased net profits. (iv) Reduction in labor and possible human errors. (v) Higher accuracy and precision with appropriate tolerances have been achieved. (vi) Power consumption reduction 78.85% observed in automated multi-spindle drilling machine.

Acknowledgements Authors are thankful to Vidyavardhini's Trust, Vasai and Mr. Ramnik Panchal and Mr. Virat Panchal, Proprietor of Soham Industries, Vasai for their support in Automation in Conventional Drilling Machine to Multi-spindle Drilling SPM experimental setup.

References

1. Sawant PR, Barawade RA (2012) Design and development of SPM—a case study in multi drilling and tapping machine. *IJAERS I(II)*:55–57
2. Gawande SR, Trikal SP (2016) Design of special purpose multi spindle drilling machine. *Int J Innovative Emerg Res Eng* 3(1):6–10
3. Sakate PR, Jadhav AS, Bamankar PB, Miss Jagadale AA, Miss Bhosale PS (2015) A review on multi spindle purpose machine with respect to productivity. *Int J Sci Res Dev* 3(08):560–562. ISSN (online):2321-0613
4. EIMaraghy HA (1982) Simulation and graphical animation of advanced manufacturing systems. *J Manuf Syst* 1(1):53–63
5. Husen H (1991) Sensor system for monitoring of multispindle drilling. *IFAC Proceedings* 24(6):565–570
6. Batra JL, Barash MM (1974) Automatic computerized optimization of multi-spindle drilling with probabilistic tool life. In: Koenigsberger F et al (eds) *Proceedings of the fourteenth international machine tool design and research conference*. Macmillan Publishers Limited, New York, pp 125–126
7. Nangare Patil BH, Sawant PR (2013) Design and development of gearbox for multi-spindle drilling machine (SPM). *Int J Eng Res Technol (IJERT)* 2(5):1414–1423. ISSN: 22780181
8. Hunter R, Rios J, Perez JM, Vizan A (2006) A functional approach for the formalization of the fixture design process. *Int J Mach Tools Manuf* 46:683–697
9. Soshi M, Ishiguro H, Yamazaki K (2009) A study on the development of a multi-purpose spindle system for quality productive machining. *CIRP Ann Manuf Technol* 58:327–330

10. Bhandari VB (2007) Design of machine elements, 2nd edn., vol 1. Tata McGraw-Hill Publishing Company Limited, New Delhi, pp 706–712
11. Deepak U, Tharun Prabhakar C, Prasanth PM, Manikandan S (2017) Multispindle drilling machine. In: International conference on latest innovations in applied science, engineering and technology (ICLIASET 2017), pp 143–149
12. Central Machine Tool Institute—Bangalore (1982) Machine tool design handbook. Tata McGraw-Hill, New Delhi, p 995
13. Gaitonde VN, Karnik SR, Achyutha BT, Siddeswarappa B (2008) Taguchi optimization in drilling of AISI 316L stainless steel to minimize burr size using multi-performance objective based on membership function. *J Mater Process Technol* 202:374–379

Mechanical Behavior of 3D Printed Polymeric Materials: Impact of Process Parameters



Aman Agrawal, Sunil Bhawnani, Anmol Sharma, Ankush Raina, and Mir Irfan Ul Haq

Abstract Additive manufacturing (AM) is a technology to develop different types of products with a wide range of applications. Fused deposition modeling (FDM) is preferred owing to its capabilities to convert low-cost material into high-strength parts. In this work, a systematic study of research papers is conducted, which is related to the effect of different parameters of 3D printer on the various mechanical properties of 3D printed material. From the different studies carried out in the past, it can be observed that in creep testing, orientation of material plays a significant role along with the cross-sectional area of printed object and in fatigue testing, infill density aided in increasing the fatigue life of material. Due to interrelation between mechanical properties of printed material and process parameters of printing, it is challenging to find best combination of process parameters. However, there are a limited studies related to the mechanical properties such as creep, fatigue and thermal stability which are affected by different process parameters of 3D printer. This work is aimed at summarizing the effect of various process parameters on fatigue, creep, compressive strength and impact strength of 3D printed materials.

Keywords 3D printing · Fatigue · Creep · Tensile strength · Flexural strength · Composites · Polymers

1 Introduction

Additive manufacturing (AM) or 3D printing is a technology through which we can print intricate parts without special tools which are required for different manufacturing processes [1, 2]. Due to simplicity, it is used in different industries such as food, electronic, machinery, aerospace, automobiles, medical and dental applications, textile, construction, education and architecture [3–5], particularly in automotive sector [6]. Additive manufacturing emphasizes on creating basic models quickly from which other products or final products can be derived. Additive manufacturing

A. Agrawal · S. Bhawnani · A. Sharma · A. Raina · M. Irfan Ul Haq (✉)
School of Mechanical Engineering, Shri Mata Vaishno University, Katra 182320, India

© The Author(s), under exclusive license to Springer Nature Singapore Pte Ltd. 2022
K. Govindan et al. (eds.), *Advances in Mechanical and Materials Technology*,
Lecture Notes in Mechanical Engineering,
https://doi.org/10.1007/978-981-16-2794-1_59

673

simplifies the process of manufacturing by complex objects directly from the CAD file thereby removing the necessity of detailed process plan which takes time and effort [7]. The ways to identify different AM technologies include material that can be used, way of layer creation and bonding of layers. Such differences will determine different factors like the accuracy and properties of created parts. Along with this, they can also determine cost, time and size of machine which were involved in the process of manufacturing [8].

The most widely used AM technology is fused deposition modeling (FDM). In FDM, polymers such as PLA are melted at higher temperature and then extruded from extruder which releases the continuous layers and is used for making the design [9]. Polymers find variety of applications in engineering products due to ease in manufacturing, recyclability and less weight [10, 11]. The main advantage of this process is that no post-processing is required. But, it also takes a lot of time for printing of large and complex objects. It has also low resolution along z-axis compared to the other AM technologies [12]. The design can be prepared in any modeling software but should be in the relevant and compatible formats.

The process of extrusion is capable to manufacture different products made up of different materials at cheaper rates; therefore, it is not only used in industries but also in institutions. Additive manufacturing involves different steps to generate a 3D printed object which is given in Fig. 1. These steps involve from designing of the part on software to the post-processing of the printed object by the printer [8]. Briefly, the process of printing starts from virtual design; then, the designed part gets sliced by software, and after that, sliced part is converted into a code which further instructs the machine to print the required geometry.

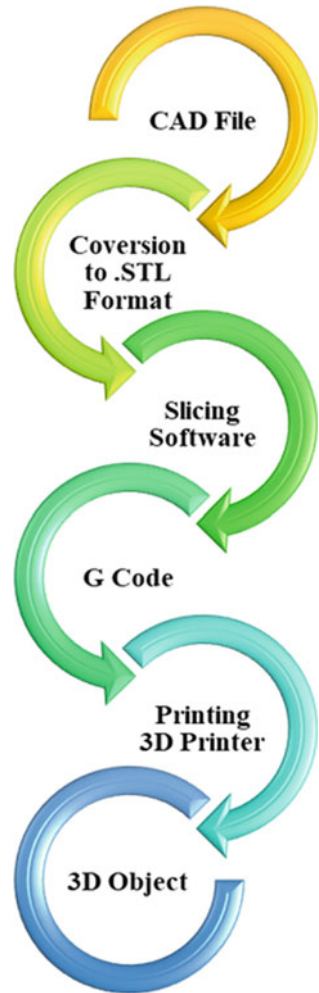
2 Types of 3D Printing

Based on the technology and the material compatibility, various 3D printing technologies [13] are briefly discussed as follows:

2.1 *Stereolithography—SLA*

This process of 3D printing is accurate and precise. In this process, machine converts liquid type of photopolymers into solid layer by layer. The plastic firstly heated so that its solid form converts into semi-liquid form, and when comes in contact with the surface, it gets hard. Printer uses the UV laser, directed by scanning mirrors mainly in *X* and *Y* direction.

Fig. 1 Schematic diagram showing the various steps involved in 3D printing



2.2 Digital Light Processing—DLP

This type of printing also uses the photo polymer which makes it similar to SLA. In this type of printing plastic resin is used in liquid form which moves into a container. This is the major cause that differentiate SLA and DLP and while SLA uses UV rays DLP uses the arc lamps.

2.3 Fused Deposition Modeling—FDM

This type of printing uses the thermoplastics. The bundle of thermoplastics passes through hot nozzle which instantly turns it into semi-liquid, and then, that layer solidifies and printer prints next layer [14]. In this type of 3D printing, printing is done layer by layer. Before printing the sample, the CAD drawing of sample is sliced by means of some special software.

2.4 Selective Laser Melting—SLM

This printing process utilizes high-power laser beams to print required desired sample. In this process, the laser beam liquefies and fuses various metallic powders together. Firstly, the laser beam hits a thin layer of the material which results in joining of the particles together. After one layer printing, the other layer gets printed on previous layer.

2.5 Selective Laser Sintering—SLS

In this process, the printer uses the high-powered CO₂ laser to fuse particles of printing material together. The laser sinters the particles of powdered metal printing materials. The bed of printer lowers incrementally with each added layer.

2.6 Electronic Beam Melting—EBM

This printing process is very much similar to SLM, and the working principle is similar to powder bed fusion technique. The thing that differentiate these two is power source. The SLM approach uses the high-power laser inside an inert atmosphere, while EBM uses a powerful beam of electron in complete vacuum.

2.7 Laminated Object Manufacturing Technology—LOM

This process of printing is a rapid prototyping technology in this printer that applies both heat and pressure to join two laminating paper or sheets together. This arrangement of printer has one roll of sheet in which the sheet of lamination is coiled.

2.8 Binder Jetting Technology—BJ

In this process, printer uses two materials for printing one as a base material which is in powder form and other as a binder agent. Binder agent used as a joining agent or adhesive to the base powder material. After printing of each layer, bed goes down automatically to provide space for further layers.

2.9 Material Jetting (MJ)

This process has been carried out from several centuries mostly by jewelers. In this process, once the CAD file is uploaded to system, then after that everything is automatic. The printer adds molten wax layer to the platform layer by layer until the build gets finished.

3 Slicing Software and Process Parameters in FDM

3.1 Slicing Software

Slicing software is the most essential part of 3D printer. It is used to convert or simplify a CAD design into G code, which is basically the path that is to be followed by 3D printer. G code is the set of instructions which are followed by 3D printer to make the particular design. The slicing software first splits the object as pile of plane layers and then describes these layers as linear movements of the 3D printer extruder.

3.2 Process Parameters

The different process parameters [15] that are detrimental to the performance of 3D printed parts are shown in Fig. 2. The most influencing parameter is the infill density. It signifies the amount of valuable material that has to be added in the model. Infill density varies from 0 to 100%. This parameter helps to provide strength as well as it saves time and costs by converting solid object to the hollow ones. Bed temperature refers to the temperature of the bottom glass on which model has to be printed. It is important to set bed temperature at the desirable level such that lowest layer can stick properly with the glass and printing can be done easily. The other important parameter is the infill pattern. Infill patterns are mostly classified into rectilinear, honeycomb and triangular pattern. It decides the different mechanical properties of the model as well as the amount of material to be used.

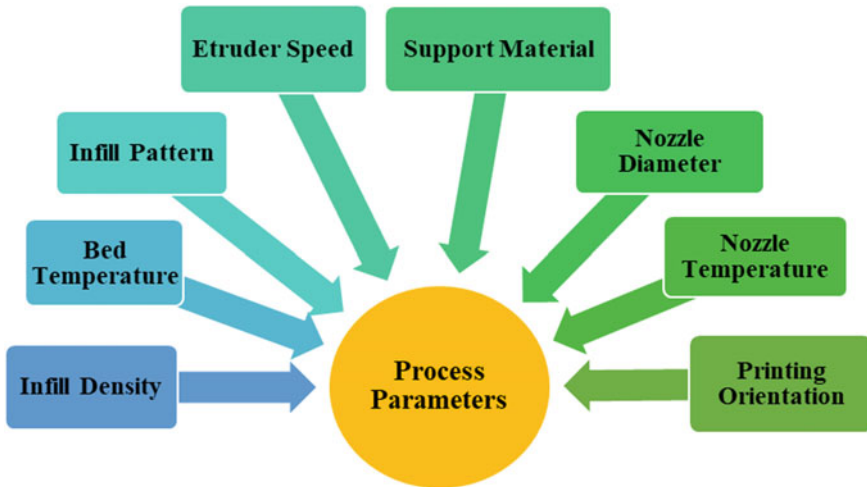


Fig. 2 Different process parameters of 3D printing

4 Research Studies Concerning the Mechanical Characteristics of 3D Printed Polymers

In this section, research carried out to evaluate the mechanical behavior of 3D printed polymeric materials has been summarized. The effect of different process parameters on the mechanical characteristics such as creep, fatigue strength, compressive and impact strength has been presented. Jacob et al. [15], in their work on fatigue related to 3D printed elastomer material, have reported that changing of material or using of composites does not have a significant effect on the specimen fatigue life. Also the authors have observed that the fatigue life gets reduced significantly if the specimen cross section area reduces. Hossain et al. [16] focused on increasing the tensile strength of 3D printed parts by varying different process parameters such as raster angle, orientation and infill density. The authors have observed an improvement of around 19% in tensile strength after changing parameters from the default set of parameters [16].

Wu et al. [17] in their work focused on the impact of layer thickness and raster angle on the mechanical behavior of 3D-Printed PEEK. The optimal mechanical properties were observed at a layer thickness of 300 μm and a raster angle of 0° [17]. Torres et al. [18] researched on the influence of different process parameters on torsion of 3D printed material. Variation in shear stress was found by changing layer thickness. The layer thickness and infill density had a significant impact [18]. Wittbrodt and Pearce [19] studied the color effect on mechanical properties. The various colors which were checked include white, black, blue, gray and natural. While there was not a momentous variation in Young's modulus of parts printed in different colors, there was a significant variation of the crystallization of differently colored printed

parts, with white PLA producing the largest percent crystallinity, followed by blue, gray, black and finally natural PLA [19]. Weng et al. [20] researched on the thermal and mechanical characteristics of nano-composites based on ABS with montmorillonite as additive. Thermal and mechanical properties improve considerably with the introduction of OMMT in ABS [20]. Szykiedans and Credo [21] in their research observed that other than strength tensile, a material which is produced from a low-cost 3D printer behaves good under compressive loading. Different 3D printers used were Zortrax Z-ABS, Z-Ultra, Z-glass-PETG [21]. Fernandez-Vicente et al. [22] in their work have documented that an increase in the infill density led to an increase in the tensile strength, since increasing density resulted in the decrease in volume of voids [22].

Christiyan et al. [23] did analysis of mechanical properties of ABS with reinforcement of hydrous magnesium silicate based on ASTM D638 and ASTM D760 standard for the bending test. Here, a variety of samples were made with different printing speed and layer thickness. The authors have recommended that low speed of printing and a lower layer thickness yield better tensile and flexural characteristics, among the other printing parameters [23]. Yang [24] studied that the crystallinity of the material changes with the change in temperature for 3D printed PEEK [24]. Carroll [25] investigated the properties of a Ti-6Al-4V component developed by directed energy deposition process. Also, the effect of oxygen on strength and ductility was measured [25]. Ahn et al. [26] reported that parameters like raster orientation and air gap influence the tensile strength when related to model temperature, raster width and color. Further, the authors have recommended a variety of build parameters for better tensile strength [26]. From the above research studies, it was observed that like other mechanical properties, fatigue and creep behavior performance of 3D printed parts is also a strong function of varying process parameters. Also, it came to the fore that very less work has been done in this direction. Therefore, it is clear that fatigue and creep behavior is an important engineering consideration as these are the critical properties and result in failure without giving any prior indication.

5 Challenges in 3D Printing

Despite being simple, geometrically accurate, ability to build complex shapes and commercial success the products made from 3D printer does not acquire the required mechanical properties which results in improper functioning of the developed product. Major research carried out using FDM is focused on improving these mechanical properties. Since technology is widely used, so it is important to remove shortcomings related to the technology. Research has been carried out for improving the properties by changing material or using different process parameters. The issue of cost and skilled labor to handle 3D printing machines, compatibility of materials with various technologies, etc. still limit the widespread use of 3D printing technologies for developing engineering components.

6 Conclusions and Future Scope

The study summarizes the effect of process parameters on the mechanical behavior of 3D printed polymeric materials. In order to achieve a better strength of 3D printed parts, the optimal process parameters are important, and the process parameters vary for different materials. The creep and fatigue behavior also depends strongly on the various 3D printing parameters similar to the behavior in case of tensile, flexural and compression behavior. Further, it came to the fore comparatively less work has been carried out thus far in the area of thermal characterization, creep and fatigue behavior of 3D printed parts. Future studies could be carried out in studying the effect on process parameters on the thermal properties, creep and fatigue behavior of 3D printed parts. Also a wider range of materials and advanced materials such as 3D printed nanocomposites could also be studied so as to widen the applications of these materials. Also studies related to optimizing the process parameters, studying the underlying mechanisms, fracture behavior at macro as well as microscopic level. The paper shall stimulate future studies related to the field.

References

1. Chadha A, Haq MIU, Raina A, Singh RR, Penumarti NB, Bishnoi MS (2019) Effect of fused deposition modelling process parameters on mechanical properties of 3D printed parts. *World J Eng* 16(4):550–559. <https://doi.org/10.1108/WJE-09-2018-0329>
2. Javaid M, Haleem A (2018) Additive manufacturing applications in medical cases: a literature based review. *Alexandria J Med* 54:411–422
3. Haq MIU, Khuroo S, Raina A, Khajuria S, Javaid M, Haq MFU, Haleem A (2020) 3D printing for development of medical equipment amidst coronavirus (COVID-19) pandemic—review and advancements. *Res Biomed Eng* 1–11
4. Gebhardt A (2012) Understanding additive manufacturing. Carl Hanser Verlag GmbH & Co. KG, Munich
5. Haleem A, Javaid M (2020) 3D printed medical parts with different materials using additive manufacturing. *Clin Epidemiol Glob Health* 8:215–223
6. Baba ZU, Shafi WK, Haq MIU, Raina A (2019) Towards sustainable automobiles—advancements and challenges. *Prog Ind Ecol Int J* 13:315–331
7. Kruth J-P, Leu M-C, Nakagawa T (1998) Progress in additive manufacturing and rapid prototyping. *CIRP Ann Technol* 47:525–540
8. Gibson I, Rosen DW, Stucker B et al (2014) Additive manufacturing technologies. Springer, Berlin
9. Aziz R, Haq MIU, Raina A (2020) Effect of surface texturing on friction behaviour of 3D printed polylactic acid (PLA). *Polym Test* 85:106434
10. Kumar R, Ul Haq MI, Ankush RAA (2018) Industrial applications of natural fiber reinforced polymer composites—challenges and opportunities. *J Sustain Eng*. <http://doi.org/10.1080/19397038.2018.1538267>
11. Gulzar S, Underwood S (2019) Use of polymer nanocomposites in asphalt binder modification. In: Salam S, Butola BS (eds) *Advanced functional textiles and polymers*. Wiley, USA, pp 405–431
12. Wong KV, Hernandez A (2012) A review of additive manufacturing. *Int Sch Res Not* 2012
13. Wang X, Jiang M, Zhou Z, Gou J, Hui D (2017) 3D printing of polymer matrix composites: a review and prospective. *Compos Part B Eng* 110:442–458

14. Hofmann M (2014) 3D printing gets a boost and opportunities with polymer materials, pp 382–386. <https://doi.org/10.1021/mz4006556>
15. Moore JP, Williams CB (2012) Fatigue characterization of 3D printed elastomer material. In: International solid freeform fabrication symposium, pp 641–655
16. Hossain MS, Ramos J, Espalin D, Perez M, Wicker R (2013) Improving tensile mechanical properties of FDM-manufactured specimens via modifying build parameters. In: International solid freeform fabrication symposium: an additive manufacturing conference, Austin, TX, pp 380–392
17. Wu W, Geng P, Li G, Zhao D, Zhang H, Zhao J (2015) Influence of layer thickness and raster angle on the mechanical properties of 3D-printed PEEK and a comparative mechanical study between PEEK and ABS. *Materials (Basel)* 8:5834–5846
18. Torres J, Cotelo J, Karl J, Gordon AP (2015) Mechanical property optimization of FDM PLA in shear with multiple objectives. *Jom* 67:1183–1193
19. Wittbrodt B, Pearce JM (2015) The effects of PLA color on material properties of 3-D printed components. *Addit Manuf* 8:110–116
20. Weng Z, Wang J, Senthil T, Wu L (2016) Mechanical and thermal properties of ABS/montmorillonite nanocomposites for fused deposition modeling 3D printing. *Mater Des* 102:276–283
21. Szykiedans K, Credo W (2016) Mechanical properties of FDM and SLA low-cost 3-D prints. *Procedia Eng* 136:257–262
22. Fernandez-Vicente M, Calle W, Ferrandiz S, Conejero A (2016) Effect of infill parameters on tensile mechanical behavior in desktop 3D printing. *3D Print Addit Manuf* 3:183–192
23. Christiyani KGJ, Chandrasekhar U, Venkateswarlu K (2016) A study on the influence of process parameters on the mechanical properties of 3D printed ABS composite. In: IOP conference series: materials science and engineering, p 12109
24. Yang C, Tian X, Li D, Cao Y, Zhao F, Shi C (2017) Influence of thermal processing conditions in 3D printing on the crystallinity and mechanical properties of PEEK material. *J Mater Process Technol* 248:1–7
25. Carroll BE, Palmer TA, Beese AM (2015) Anisotropic tensile behavior of Ti–6Al–4V components fabricated with directed energy deposition additive manufacturing. *Acta Mater* 87:309–320
26. Ahn S-H, Montero M, Odell D, Roundy S, Wright PK (2002) Anisotropic material properties of fused deposition modeling ABS. *Rapid Prototyping J* 8:248–257

Deformation Behaviours of Magnesium Alloy AZ41 Beyond Necking Using Extrapolation Method



Manish Kumar Gupta and N. K. Singh

Abstract In the present work, finite element analysis (FEA) is applied to study the behaviour of magnesium alloy AZ41 after necking using extrapolation method. Suitability of Hollomon, Swift, Ludwik, Ghosh, Voce and Hockett-Sherby models is examined for the above estimation. Material constants of these models are determined using regression analysis. It is found that the results predicted by these models in before and after necking are different. The Swift curve is anticipated very well in whole regions of the deforming alloy.

Keywords Necking phenomenon · FEA · Constitutive models · Regression analysis

1 Introduction

Magnesium alloys are important for automotive, aerospace, marine and electronics industries due to their high strength to density ratio, vibration damping capacity, good corrosion resistance and electrical conductivity. Behaviour of the alloys beyond necking is required for its detail information in design engineering. Necking is an instability during deformation of a ductile material under tensile loads. The study of necking phenomena in the material can be broadly classified into two methods: First one is experimental methods, and the other one is numerical methods. Stress and strain of flow curves are directly measured during experimentation process for example DIC [1–3]. In numerical methods [4–6], the discrepancies between the experimental and numerical results are minimized. Bridgman [7] derived the models for flow behaviour of round bar about necking based on experimental measurement of necking region. Zhang [8] developed the Bridgman work for rectangular specimens. Mirone [9] recommended a model for round specimen's necking behaviour. Effect of strain rate on necking phenomena under dynamic conditions had been studied by Mirone et al. [10]; results revealed that the necking position was dependent to

M. K. Gupta (✉) · N. K. Singh

Department of Mechanical Engineering, National Institute of Technology Patna, Patna 800005, India

the strain rate. Zhang and Li [11] presented a new numerical approach to get the post-necking characterization of materials and verified with the experimental result performed on round smooth specimens made up of steel. It was similar to Bridgman's method in precision and more convenient as it was free from measurement of radial necked area. Necking behaviour of sheet metals was studied by Hogstro et al. [12]. Abbassi et al. [13] used the Swift hardening law and GTN model to predict the material behaviour. Extrapolation method based on power law and linear function was used by Ling [14] to investigate the post-necking behaviour in Abaqus software by trial-and-error method. Coppiters et al. [15] observed the flow behaviour of steel beyond necking by extrapolation of material models. Here, six important models are used to predict the flow behaviour of AZ41 magnesium alloy after necking. The constants of each models are determined through least square method by keeping the minimum error between experimental and model data.

2 Methodology

This paper presents the numerical analysis of magnesium alloy AZ41 at crosshead speed 0.025 mm/s beyond necking. Applicability of six material models is used. True stress and true strain of a tensile specimen can be found by the commonly used formula given in Refs. [16–18]. However, these formula are effective up to ultimate stress and do not provide exact values after this point as their stress triaxiality develops in the material. Extrapolation method is applied to investigate the material characteristics after necking.

2.1 Finite Element Analysis

Numerical simulation of tensile test of magnesium AZ41 is carried out in Abaqus 6.14 [19]. Here, tensile specimen having gauge area $25 \times 6 \text{ mm}^2$ with 4 mm thick is modelled in Abaqus as shown in Fig. 1a. C3D8R elements are used to mesh the model. Mesh convergence analysis is used to select mesh size. Experimental data of magnesium alloy AZ41 at quasi-static strain rate 0.025 mm/s having true stress at necking is 246.40 MPa and is used for numerical simulation [20].

2.2 Hardening Behaviour

Here, the flow behaviour of magnesium alloy AZ41 at 0.025 mm/s found by experimental test is close-fitting with models listed in Table 1. Regression method is used to find the model parameters.

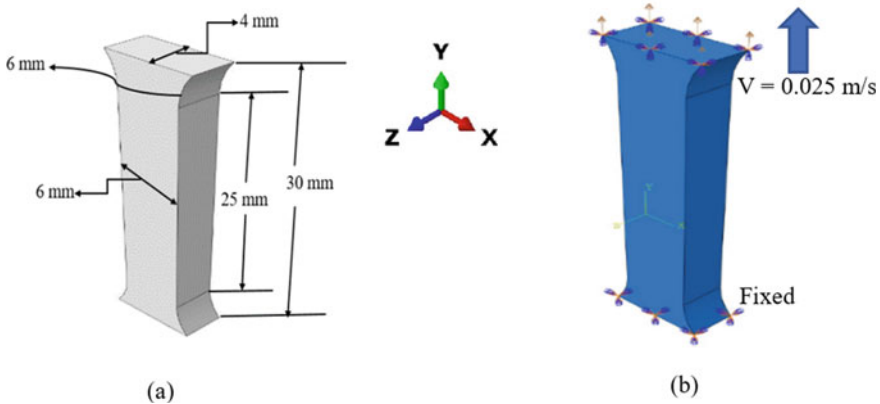


Fig. 1 Geometrical model with boundary conditions

Table 1 Constitutive models

Model	Expression
Hollomon [21]	$\sigma = K \epsilon_p^n$
Swift [22]	$\sigma = K(\epsilon_0 + \epsilon_p)^n$
Ludwik [23]	$\sigma = \sigma_0 + K \epsilon_p^n$
Ghosh [24]	$\sigma = K(\epsilon_0 + \epsilon_p)^n - C$
Voce [25]	$\sigma = \sigma_0 + K[1 - \text{EXP}(-A\epsilon_p)]$
Hockett-Sherby [26]	$\sigma = \sigma_0 + K[1 - \text{EXP}(-A\epsilon_p^n)]$

Where σ is the equivalent stress, ϵ_p is the plastic strain and others are the fitting parameters

3 Results and Discussion

Strain gradient became large just after the UTS in a region known as necking and the stress triaxiality developed as the necking begins. The ABAQUS 6.14 is used to explain the behaviour under quasi-static condition. Model applicability is also checked around necking.

3.1 Numerical Simulation

In finite element analysis, the element size plays an important role to find the accurate results. In order to see the mesh (element) size effect, tensile simulations are performed by changing the size of the element from 0.5 to 0.1. Better stress concentrations in the necking area are observed for the element size 0.2 and 0.1 as compared to others (Fig. 2).

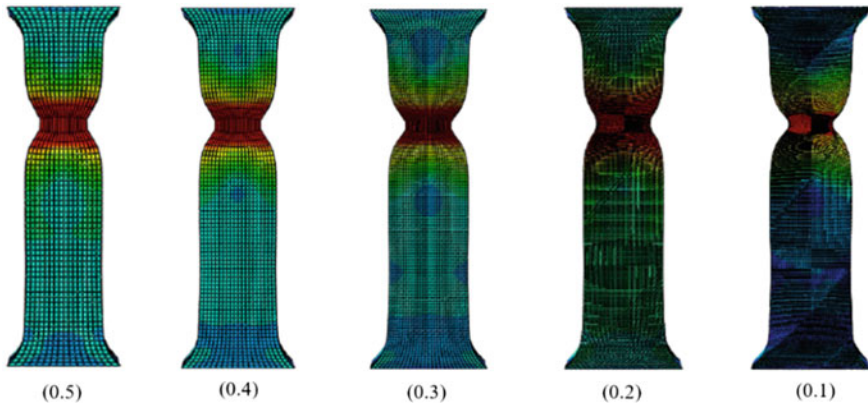


Fig. 2 Stress concentration at necking for different mesh size

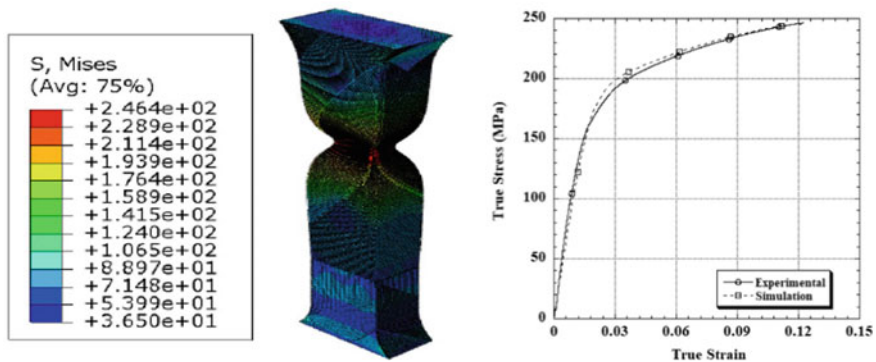


Fig. 3 Numerical simulation for deformation of a tensile specimen

After convergence analysis of mesh, 0.1 element size is selected for whole specimen, and the solution is achieved with 500 step time. The number of elements and nodes is 1,102,080 and 1,146,565, respectively. Figure 3 shows the comparison between simulation results with the experimental results. The experimental and simulated stresses at necking are 246.40 MPa and 246.45 MPa, respectively.

3.2 Flow Behaviour Before and After Necking

To study the flow behaviour of magnesium AZ41 before necking, regression method is used. The material constants are summarised in Table 2. Extrapolated curves are used to identify the behaviour of the alloy after necking [27]. Suitability of these models is compared in Figs. 4 and 5 for before and after necking, respectively.

Table 2 Parameter values for each constitutive model

Model	Hollomon	Swift	Ludwik	Ghosh	Voce	Hockett-sherby
Parameters	$K = 361.8$	$K = 342.83$	$\sigma_0 = 124.81$	$K = 249.88$	$\sigma_0 = 148.03$	$\sigma_0 = 105.04$
	$n = 0.17986$	$\epsilon_0 = 0.0092308$	$K = 300.62$	$\epsilon_0 = 0.89762$	$K = 113.68$	$K = 179.64$
	$R = 0.99892$	$n = 0.1505$	$n = 0.42745$	$n = 2.4498$	$A = 16.202$	$A = 5.4303$
		$R = 0.9998$	$R = 0.98819$	$C = 9.4648$	$R = 0.99906$	$n = 0.60557$
				$R = 0.97601$		$R = 0.99779$

All the models predict the flow stress well before necking. After finding of models parameters, simulation of tensile specimen of magnesium AZ41 is done by using each material model as input for Abaqus. The true stress at necking point is 247.182 MPa for Hollomon, 244.884 MPa for Swift, 247.376 MPa for Ludwik, 253.843 MPa for Ghosh, 244.308 MPa for Voce and 243.436 MPa for Hocett-Sherby.

All hardening laws used in this paper show very decent agreement with experimental outcomes for the region before necking. However, for region after necking, each extrapolated curve shows discrepancy with experimental extrapolated curve. Swift hardening law shows accurate results.

4 Conclusions

The extrapolation technique is utilized in the fitted curves of the models to explain the post-necking phenomenon. The numerical simulation of the alloy’s stress–strain behaviour in Abaqus demonstrates near compliance with the experimental curve. In pre-necking region, Voce and Swift models show better accuracy than the other models. In post-necking region, the predicted results of the models deviate from the experimental results. However, the Swift model can predict the flow behaviour of the alloy very well.

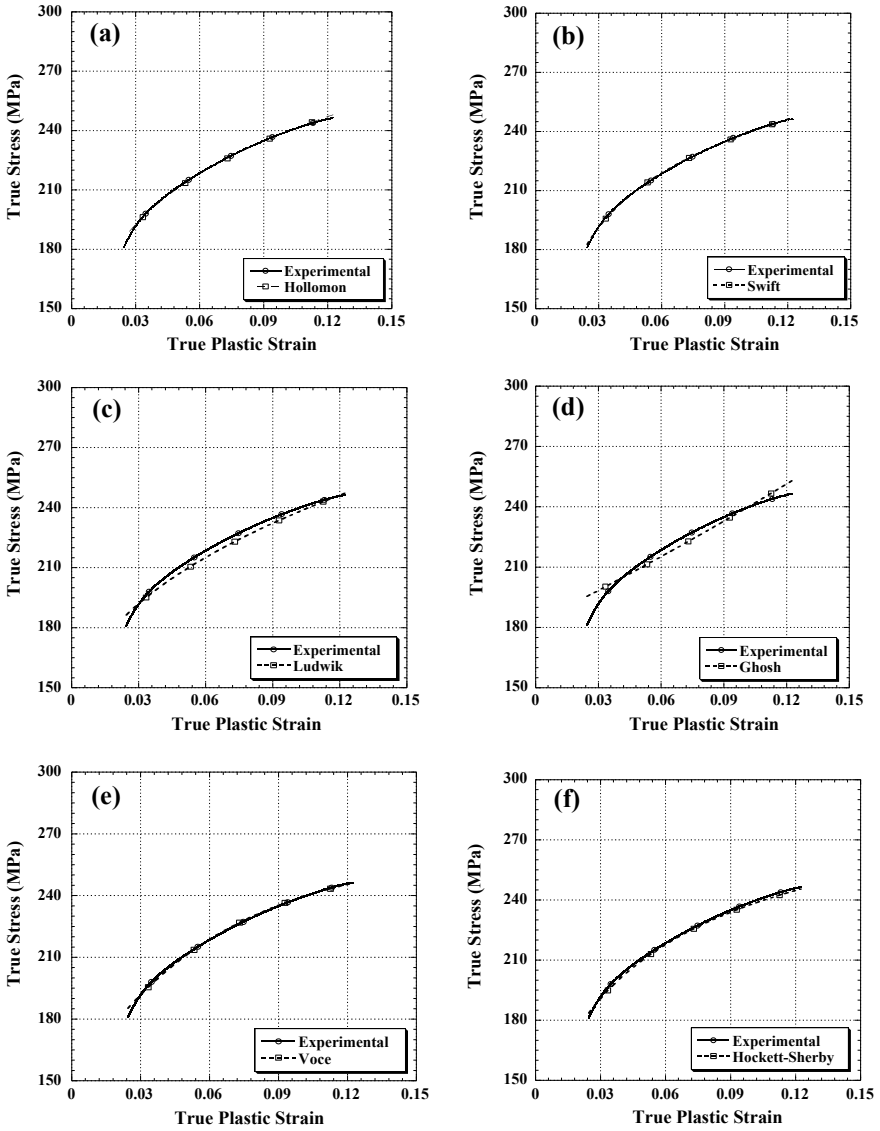
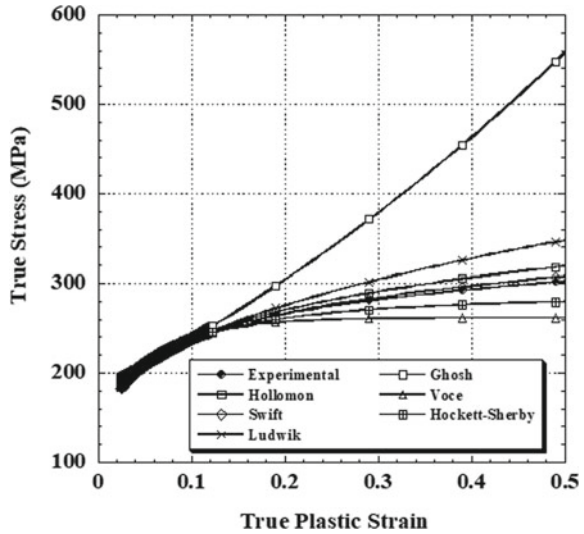


Fig. 4 Prediction by models before necking

Fig. 5 Predicted curves by extrapolated models in post-necking region



References

- Vacher P, Haddad A, Arrieux R (1999) Determination of the forming limit diagrams using image analysis by the correlation method. *CIRP Ann Manuf Technol* 48(1):227–230. [https://doi.org/10.1016/S0007-8506\(07\)63171-0](https://doi.org/10.1016/S0007-8506(07)63171-0)
- Wang K, Carsley JE, He B, Li J, Zhang L (2014) Measuring forming limit strains with digital image correlation analysis. *J Mater Process Technol* 214(5):1120–1130. <https://doi.org/10.1016/j.jmatprotec.2014.01.001>
- Li H (2013) Benchmark 1–nonlinear strain path forming limit of a reverse draw. In: American institute of physics conference proceedings, vol 15, p 1567
- Cabezas EE, Celentano DJ (2004) Experimental and numerical analysis of the tensile test using sheet specimens. In: *Finite elements in analysis and design*, vol 40, no 5–6, pp 555–575. [http://doi.org/10.1016/S0168-874X\(03\)00096-9](http://doi.org/10.1016/S0168-874X(03)00096-9)
- Saje M (1979) Necking of a cylindrical bar in tension. *Int J Solids Struct* 15(9):731–742. [https://doi.org/10.1016/0020-7683\(79\)90070-2](https://doi.org/10.1016/0020-7683(79)90070-2)
- Joun M, Choi I, Eom J, Lee M (2007) Finite element analysis of tensile testing with emphasis on necking. *Comput Mater Sci* 41(1):63–69. <http://doi.org/10.1016/j.commatsci.2007.03.002>
- Bridgman PW (1952) *Studies in large plastic flow and fracture*. McGraw Hill, New York. <http://doi.org/10.1126/science.115.2990.424>
- Zhang KS (1995) Fracture prediction and necking analysis. *Eng Fract Mech* 52:575–582. [https://doi.org/10.1016/0013-7944\(95\)00032-Q](https://doi.org/10.1016/0013-7944(95)00032-Q)
- Mirone G (2004) A new model for the elastoplastic characterization and the stress–strain determination on the necking section of a tensile specimen. *Int J Solids Struct* 41:3545–3564. <https://doi.org/10.1016/j.ijsolstr.2004.02.011>
- Mirone G, Corallo D, Barbagallo R (2016) Interaction of strain rate and necking on the stress-strain response of uniaxial tension tests by Hopkinson bar. *Procedia Struct Integrity* 2:974–985. <https://doi.org/10.1016/j.prostr.2016.06.125>
- Zhang KS, Li ZH (1994) Numerical analysis of the stress-strain curve and fracture initiation for ductile material. *Eng Fract Mech* 49(2):235–241. [https://doi.org/10.1016/0013-7944\(94\)90006-X](https://doi.org/10.1016/0013-7944(94)90006-X)

12. Hogstro P, Ringsberg JW, Johnson E (2009) An experimental and numerical study of the effects of length scale and strain state on the necking and fracture behaviours in sheet metals. *Int J Impact Eng* 36:1194–1203. <https://doi.org/10.1016/j.ijimpeng.2009.05.005>
13. Abbassi F, Mistou S, Pantale O, Zghal A (2015) FE simulation and full-field strain measurements to evaluate the necking phenomena. *Procedia Manuf* 2:500–504. <https://doi.org/10.1016/j.promfg.2015.07.086>
14. Ling Y (1996) Uniaxial true stress-strain after necking. *AMP J Technol* 5:37–48
15. Coppieters S, Cooreman S, Sol H, Houtte PV, Debruyne D (2011) Identification of the post-necking hardening behaviour of sheet metal by comparison of the internal and external work in the necking zone. *J Mater Process Technol* 211:545–552. <https://doi.org/10.1016/j.matprotec.2010.11.015>
16. Prakash G, Singh NK, Gupta NK (2021) Flow stress behavior of AZ81 magnesium alloy under dynamic loads. *J Mater Civ Eng* 33(3):04020486. [https://doi.org/10.1061/\(ASCE\)MT.1943-5533.0003607](https://doi.org/10.1061/(ASCE)MT.1943-5533.0003607)
17. Prakash G, Singh NK, Gupta NK (2020) Mechanical behavior of magnesium alloy AZ61 at different strain rates and temperatures under tensile, compressive, and flexural loads. *J Mater Civ Eng* 32(11):04020336. [http://doi.org/10.1061/\(ASCE\)MT.1943-5533.0003436](http://doi.org/10.1061/(ASCE)MT.1943-5533.0003436)
18. Prakash G, Singh NK, Sharma P, Gupta NK (2020) Tensile, compressive, and flexural behaviors of Al5052-H32 in a wide range of strain rates and temperatures. *J Mater Civ Eng* 32(5):04020090. [http://doi.org/10.1061/\(ASCE\)MT.1943-5533.0003154](http://doi.org/10.1061/(ASCE)MT.1943-5533.0003154)
19. Abaqus (2014) Abaqus user's manual. Version 6.14. Dassault Systemes Simulia Corp., Providence, RI, USA
20. Prakash G, Singh NK, Kumar D, Chandel P (2020) Dynamic tensile behaviour of magnesium alloy az41 at different strain rates and temperatures. *U.P.B. Sci Bull Ser D* 82(1):1454–2358
21. Hollomon JH (1945) Tensile deformation. *Trans Metall Soc AIME* 162:268–290
22. Swift HW (1952) Plastic instability under plane stress. *J Mech Phys Solids* 1:1–18. [https://doi.org/10.1016/0022-5096\(52\)90002-1](https://doi.org/10.1016/0022-5096(52)90002-1)
23. Ludwik P (1909) *Elemente der technologischen mechanik*. Springer, Berlin, p 32
24. Ghosh AK (1980) A physically-based constitutive model for metal deformation. *Acta Metall* 28:1443–1465. [https://doi.org/10.1016/0001-6160\(80\)90046-2](https://doi.org/10.1016/0001-6160(80)90046-2)
25. Voce E (1978) The relationship between stress and strain for homogeneous deformation. *J Inst Met* 74:537–562
26. Hockett JE, Sherby OD (1975) Large strain deformation of polycrystalline metals at low homologous temperatures. *J Mech Phys Solids* 23(2):87–98. [https://doi.org/10.1016/0022-5096\(75\)90018-6](https://doi.org/10.1016/0022-5096(75)90018-6)
27. Gupta MK, Singh NK (2020) Modelling and simulation on deformation behaviour of Al2014-T6 alloy beyond necking. *Mater Today Proc* <http://doi.org/10.1016/j.matpr.2020.10.533>

Thermal Analysis of Tank Gun Barrel



Nirav Shah, Aadish Meghani, Dhruvi Panchal, Dhruvit Patel,
and Vinayak H. Khatawate

Abstract In the present study, an analytical method was used to compute heat transfer rate and maximum temperature of a tank gun barrel by rapid expansion of gas within a barrel. For the analysis, heat flux was assumed to be exponential decaying for given ammunition parameters. A finite element analysis (FEA) was employed to model the gun barrel temperature history (temperature variation over time). The barrel was subjected to two modes of transient heat transfer, namely conduction and convection with heat conducting through the barrel material and subsequently to the air via convection. The tank used for the study is the German made Rheinmetall-120 which is a smoothbore 120 mm calibre tank. Simulations were performed for single shot fired, and the results of FEA were found to be in close agreement with the corresponding analytical result.

Keywords Transient heat transfer · Convective heat transfer · Bore temperature

1 Introduction

Tanks are heavy combat vehicles that provide firepower and protective armour against explosives and detonations. A tank has numerous armaments, and the main one being the tank gun is mounted on the turret. The gun barrel varies in sizes that depend on its firing capacity. Modern-day tank gun barrels are capable of firing multiple rounds of armour piercing projectiles at a high velocity. Due to this, the gun barrel is subjected to several mechanical and thermal stresses, of which, thermal stresses are prevalent. On an average, if the maximum bore surface temperature increases by about 10%, i.e. from 900 to 1000 K, then the wear per cycle increases 2.5 times [1]. The barrel material is chosen appropriately to withstand the extreme changes in temperature. The phenomenon of gun barrel wear has been studied and observed

N. Shah (✉) · A. Meghani · D. Panchal · D. Patel · V. H. Khatawate
Dwarkadas J. Sanghvi College of Engineering, Vile Parle, Mumbai 400056, India

V. H. Khatawate
e-mail: vinayak.khatawate@djsce.ac.in

© The Author(s), under exclusive license to Springer Nature Singapore Pte Ltd. 2022
K. Govindan et al. (eds.), *Advances in Mechanical and Materials Technology*,
Lecture Notes in Mechanical Engineering,
https://doi.org/10.1007/978-981-16-2794-1_61

691

Fig. 1 Typical field heavy gun [1]

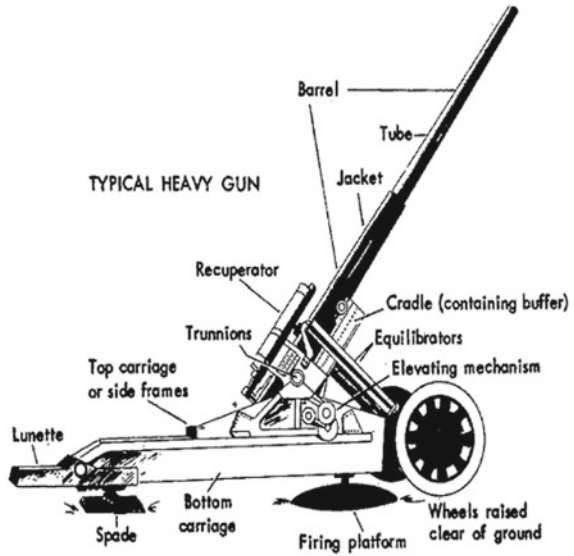
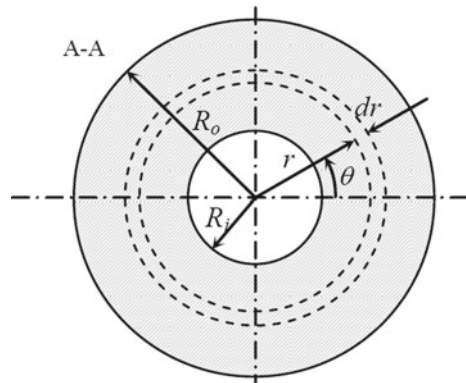


Fig. 2 Cross-sectional area of cylinder [1]



by many researchers [2–6]. Volatile changes in pressure and temperature may result in undesirable variations in the bore dimensions and material properties. Hence, the thermal study of the barrel is important. Typical field heavy gun is shown in Figs. 1 and 2.

2 Maximum Bore Temperature Calculation

Since the barrel is cylindrical in geometry and heat transfer mainly occurs through conduction, the one-dimensional Fourier equation in cylindrical coordinates system

is used:

$$\frac{\delta T}{\delta t} = \alpha(T) \left[\frac{\delta^2 T}{\delta r^2} + \frac{1}{r} \frac{\delta T}{\delta r} + \frac{1}{k(T)} \frac{\delta k(T)}{\delta T} \left(\frac{\delta T}{\delta r} \right)^2 \right] \tag{1}$$

During the internal ballistic cycle, the axial temperature gradient $\frac{\delta T}{\delta z}$ is much smaller than that of the radial temperature gradient $\frac{\delta T}{\delta r}$. Heat generated due to friction between the projectile and the barrel was neglected for the barrel under study which is relatively large [7].

$\alpha(T)$ is the thermal diffusivity:

$$\alpha(T) = \frac{k(T)}{\rho_b C_p(T)} \tag{2}$$

Initial conditions are as follows:

$$T(r, t) \text{ at } (t = 0) \text{ is } T_\infty \text{ for } R_i < r < R_o$$

The boundary conditions for inside as well as the outside faces of the barrel are as follows:

$$\text{At } r = R_1 \text{ and } t > 0, \quad h_g(T_g - T_i) = -k \frac{\delta T}{\delta r} |_{r = R_i}$$

$$\text{At } r = R_0 \text{ and } t > 0, \quad h_{air}(T_\infty - T_0) = -k \frac{\delta T}{\delta r} |_{r = R_o}$$

where T_i and T_0 are the temperatures at the inside and outside faces of the gun barrel, respectively; k is the coefficient of heat conduction of the material of the barrel; h_g is the heat convection coefficient of combustion gases; h_{air} is the surrounding air's coefficient of heat convection, and T_g is the combustion gases temperature.

Temperature Distribution Equation

$$T_j^{n+1} = \frac{T_{j-1}^n + (M_j^n - 2)T_j^n + T_{j+1}^n}{M_j^n} + \left(\frac{C_j^n}{2r_j} + \frac{k_{j+1}^n - k_{j-1}^n}{4M_j^n k_j^n} \right) (T_{j+1}^n - T_{j-1}^n) \tag{3}$$

where

$$M_n^j = \frac{(\Delta r)^2}{\alpha_n^j \Delta t}$$

$$C_n^j = \frac{\alpha_n^j \Delta t}{\Delta r}$$

where j denotes radial position and n indicates the time step. This equation gives the temperature distribution at the inner points of the barrel.

The temperature distribution of the products of combustion at different levels of cross section is given by the following equations:

$$T_g = \frac{P \left[V_B - m_B \left(z\eta + \frac{1-z}{\rho} \right) + \frac{\pi D^2 x}{4} \right]}{(A_{\text{mol}} m_B z R)} \quad (4)$$

In order to calculate the maximum temperature of the barrel [1],

$$\frac{T_f - 1.8T_i}{T_{\text{max}} - T_i} = 1.8 + \frac{288 * k}{\text{Re}^{0.866} * K_g} * \sqrt{\frac{K_g}{\alpha}} \quad (5)$$

where $\text{Re} = \frac{m \times V_m}{d^2 \times \mu}$ $K_g = V_m \times d$.

Substituting the values and re-arranging the above equation:

$$T_{\text{max}} = T_i + \frac{T_f - 1.8T_i}{1.8 + \frac{7130 * d^{2.22}}{m^{0.86} v^{0.36}}} \quad (6)$$

This equation gives an average ± 30 °C when compared to the measured value and all the calculations are within ± 50 °C of observed value [8].

2.1 Heat Input Per Round

In case of heat transfer by conduction in the gun barrel, the majority of the heat is transferred to the barrel surface instantaneously, and the heat flux increases rapidly to a maximum value and then reduces much slowly.

Therefore, heat transfer modelling can be simplified by assuming heat flux as exponential decaying. Based on this assumption, the following relation between heat transfer per round and maximum bore temperature is given in, and this relation was found out as follows:

$$q = q_0^{\frac{-t}{t_0}} \quad (7)$$

The total heat input is then calculated by integrating Eq. (7) from time '0' to time interval 't' as follows:

$$H = \int_0^t q dt = \int_0^t q_0 \frac{-t}{t_0} dt = q_0 t_0 \left(1 - \exp\left(\frac{-t}{t_0}\right) \right) \tag{8}$$

The quantity q_0, t_0 is the total heat input as $t \rightarrow \infty$ and so Eq. (5) can be rewritten as follows:

$$\frac{H}{H_\infty} = 1 - \exp\left(\frac{-t}{t_0}\right) \tag{9}$$

where time constant t_0 is

$$t_0 = \frac{0.8(m_r V_m)}{(d^2 P_{\max})}$$

Therefore,

$$H_\infty = \frac{K \times (T_{\max} - T_i)}{1.082} \times \sqrt{\frac{\pi \times t_0}{K}}$$

$$\text{Heat Flux} = \frac{656833.61}{60} = 10947.2268 \text{ W/m}^2$$

The maximum bore temperature was calculated analytically by using Eq. (6). The input parameters for calculating maximum bore temperature are shown in Table 1.

On putting the values in Eq. (6):

$$T_{\max} = 293 + \frac{3000 - 1.8 * 293}{1.8 + \frac{7130 * 0.12^{2.22}}{8.0^{0.86} * 1606^{0.36}}} = 1260.23 \text{ K} \tag{10}$$

Table 1 Input parameters for calculating maximum bore temperature

Notation	Parameter	Value
T_f	Flame temperature of propellant	3000 K
d	Bore diameter	0.120 m
m_c	Mass of propellant	8.0 kg
V_m	Muzzle velocity	1600 m/s
T_i	Initial temperature	293 K

Table 2 Properties of steel and thermal parameters

Thermal diffusivity (K)	$9e-6 \text{ m}^2/\text{s}$
Thermal conductivity of the barrel material (k)	35 W/m K
Mass of the shot (m_f)	6.8 kg
Maximum bore pressure (P_{max})	510 MPa
Time constant (t_o)	0.001123 s
Heat input per round ($H\infty$)	$656,833.6138 \text{ J/m}^2$

3 Material Properties

Stainless steel is used as a material for tank gun barrel.

Properties of stainless steel which is used in this experiment are shown in Table 2.

4 Finite Element Model

To calculate the maximum bore temperature, a 1D, transient, thermal analysis was performed for a single shot fired by using FEA. ANSYS Workbench 19.0 software was used for the analysis [9]. Due to symmetry, chamber of only 10 mm length was modelled in ANSYS to reduce the calculation time. The heat load was given as a heat flux equivalent to $10,947.22 \text{ W/m}^2$ at the inner surface. Due to high muzzle velocity and rapid expansion of the products of combustion, heat transfer to the barrel usually takes place in the order of a few milliseconds, and completion of heat input takes place in a very short period of time. Empirically, the time for heat input is calculated as $t = 5 \times t_o$ [10], where t_o is the time constant (Table 2). In this case, ‘ t ’ was about 5 ms, so heat input was applied for a period of 5 ms, and the analysis was run for six seconds with a time step of 0.01 s. The mesh used was of multi-zone type with hexahedral elements instead of tetrahedron to maintain a uniform and accurate mesh model. Edge sizing was provided to set the number of elements.

At the outer surface, there is convection between the barrel and the atmosphere. Hence, convection boundary condition was used at the outer surface. Initial barrel temperature was considered to be at $20 \text{ }^\circ\text{C}$ (293 K), and ‘coefficient of convective heat transfer’ (h_{air}) between gun steel and atmospheric air was taken to be 6.5 W/m K and air temperature is $20 \text{ }^\circ\text{C}$. The other two surfaces are perfectly insulated to restrict the heat transfer in only one direction, i.e. radial. And by using these boundary conditions, the maximum bore temperature was computed, and it was observed that the results are in good agreement with the calculated maximum temperature.

Slice of meshed barrel is shown in Fig. 3 on which analysis has been done. Thickness of barrel is 10 mm. Figure 4 shows cross-sectional view of meshed barrel. Also, boundary conditions are specified for the calculation purpose. Figure 5 shows boundary conditions for thermal analysis of gun barrel.

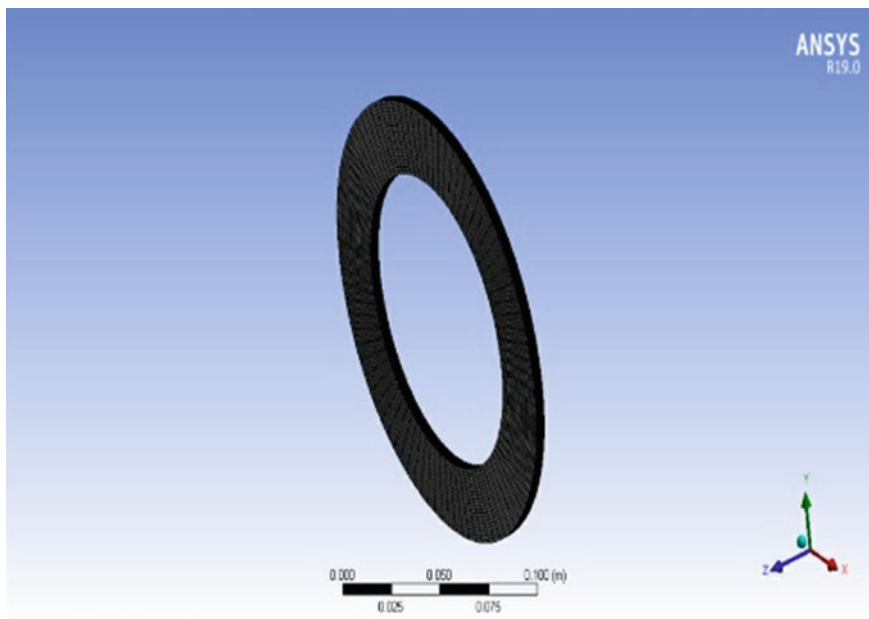


Fig. 3 Slice of barrel (10 mm thick)

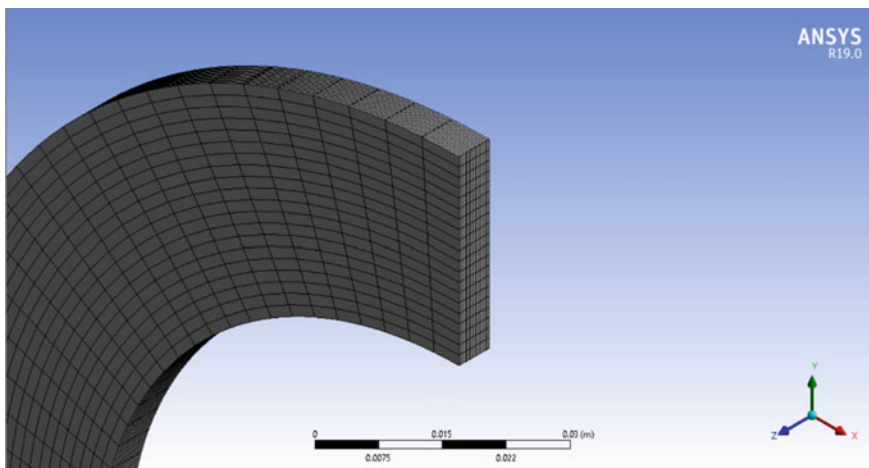


Fig. 4 Sectional view of meshed barrel

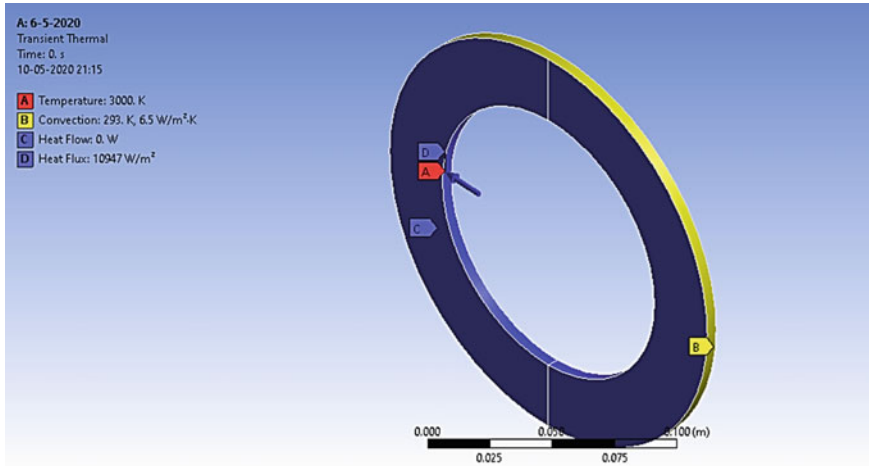


Fig. 5 Boundary conditions for thermal analysis gun barrel

4.1 Step Controls for Simulation

1. Number of steps = 6
2. Time step = $1e-002$ s
3. Step end time = 1 s.

5 Results and Discussions

Theoretically, final temperature obtained from Eq. (10) is 1260.23 K. With FEA transient thermal analysis, two iterations were performed.

Iteration 1:

In this case, number of nodes = 22,638 and number of elements = 4900.

Figure 6 shows meshed gun barrel with a smaller number of nodes for calculation.

The final temperature in this case is 1270.7 K which is close to the calculated value but still there is a difference. Calculation of final temperature is shown in Fig. 7.

Iteration 2:

In this case, number of nodes = 116,323 and number of elements = 26,700. Figure 8 shows meshed gun barrel with high number of nodes for calculation.

The final temperature in this case is 1267.8 K which is in a very close agreement with the calculated value. FEA result of final temperature is shown in Fig. 9. The time step table for maximum bore temperature and heat flux is given below. Different bore temperatures values from ANSYS are shown stepwise in Table 3 as well as different heat flux values from ANSYS are shown stepwise in Table 4.

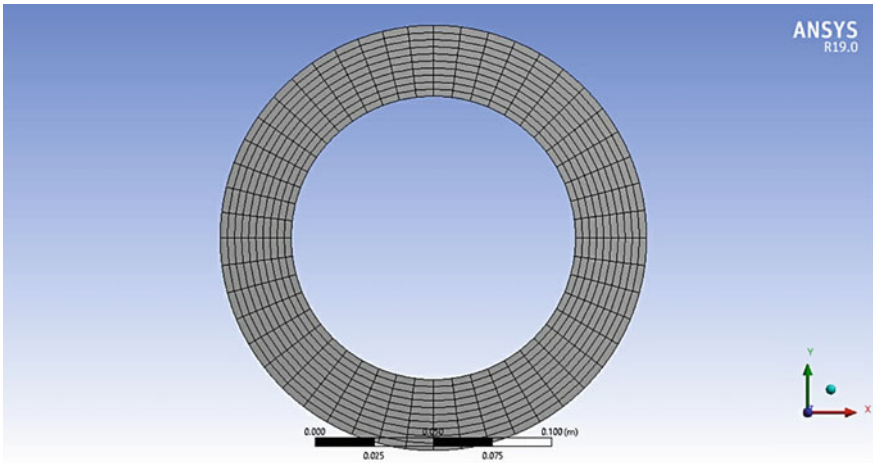


Fig. 6 Meshed gun barrel with less number of nodes (22,638)

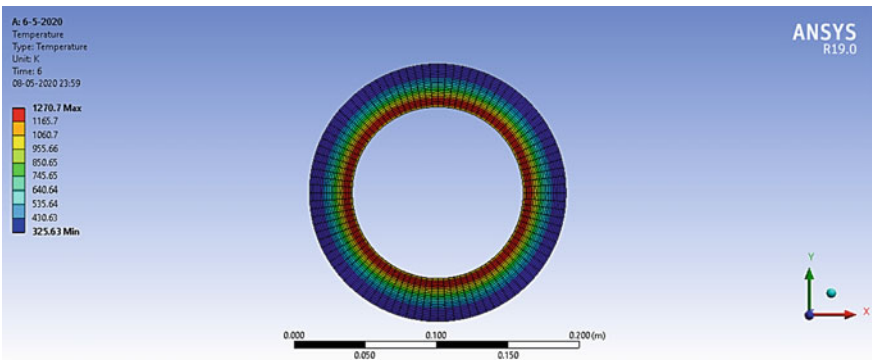


Fig. 7 Calculation of the final temperature

6 Conclusion

In this report, the temperatures of gun barrel obtained from analytical calculations and that obtained from finite element analysis are in close agreement with each other. The maximum bore temperatures obtained by analytical method and FEA is 1260.23 K and 1267.8 K, respectively. Total difference of 0.818% is there between the temperature obtained from the finite element method and temperature obtained from Eq. (10) because FEM is an approximate method. However, it should also be noted that analytical calculations were performed by taking into account several assumptions (such as neglecting friction between the ammunition and the barrel surface, the value of heat convection coefficient), and therefore, actual values may vary.

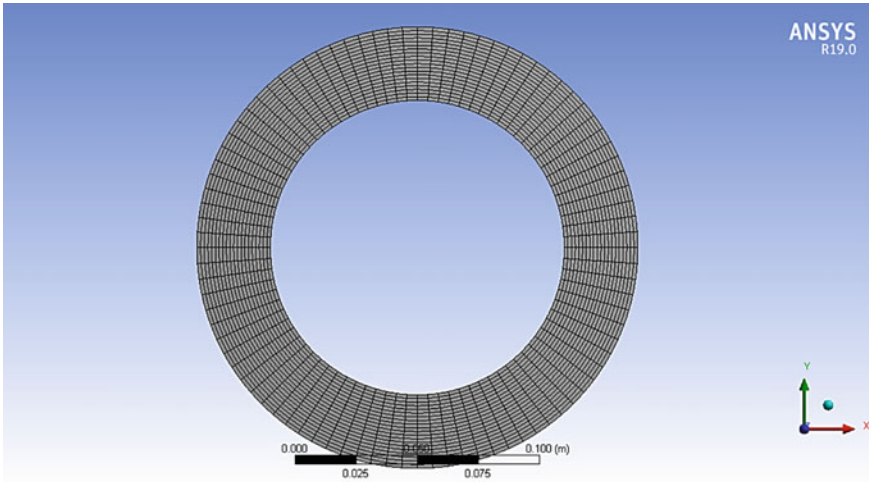


Fig. 8 Meshed gun barrel with higher number of nodes (116,323)

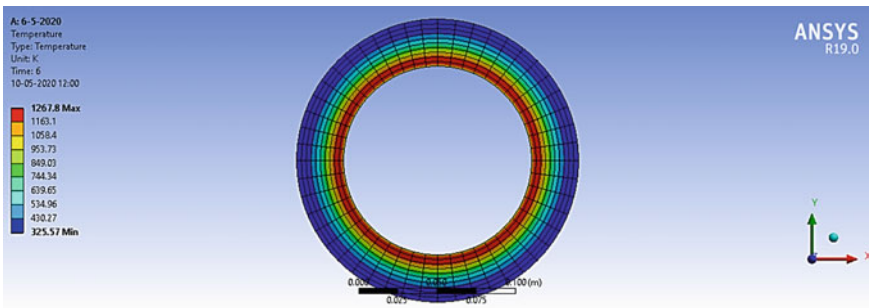


Fig. 9 Calculation of the final temperature

Table 3 Bore temperature observed at different steps

Steps	Time (s)	Temperature (K)
1	0	3000
	5.e-003	3000
	1	2700
2	2	2460
3	3	2120
4	4	1946
5	5	1743
6	6	1000

Table 4 Heat flux observed at different step

Steps	Time (s)	Heat flux (W/m ²)
1	0	10,947
	5.e-003	
	1	9130.3
2	2	7304.2
3	3	5478.2
4	4	3652.1
5	5	1826.1
6	6	0

The bore temperature reduces to around 1000 K (from around 3000 K) in about 6 s, and therefore, passive cooling is enough considering a convective heat transfer coefficient of 6.5 W/m K. An example of a 120 mm diameter gun barrel was used in this study. However, any bore diameter with different wall thickness can be studied, and their maximum bore temperature analysed by the above method.

Appendix

- A_{mol}* Number of moles of the propellant
- C_p* Barrel material's specific heat capacity
- C_v* Propellant gases' specific heat coefficient
- D* Barrel's inner diameter
- k* Barrel material's thermal conductivity
- m_B* Propellant's initial mass
- r* Radius of the bore
- P* Pressure of propellant gases
- R* Universal gas constant
- R_i* Barrel's inner radius
- R_o* Barrel's outer radius
- t* Time
- T* Temperature
- T_∞* Temperature of surrounding air
- U* Projectile velocity at time *t*
- V_B* Combustion chamber volume
- x* Distance which the projectile moved at time *t*
- z* Burned propellant's percentage

Greek Symbols

α	Barrel material's thermal diffusivity
ρ	Density of the propellant gases
γ	Specific heat ratio of propellant gases
ρ_b	Barrel material's density
η	Co-volume of the propellant gases

Subscript

j Spatial position

References

1. Lawton B, Klingenberg G (1995) Transient temperature in engineering and science. Oxford Science Publication, pp 452–453, 461–462, 455–456, 450
2. Heo J-H, Chung B-J (2012) Natural convection heat transfer on the outer surface of inclined cylinders. Chem Eng Sci 73:366–372
3. Parker AP (1999) Stability of arrays of multiple edge cracks. Eng Fract Mech 62:577–591
4. Cote PJ, Rickard C (2000) Gas-metal reaction products in the erosion of chromium-plated gun bores. Wear 241:17–25
5. Francol P, Peter H (2001) Gun barrel erosion: study of thermally insulating layers. In: 19th international symposium of ballistics, Interlaken, Switzerland
6. Lawton B (2001) Thermo-chemical erosion in gun barrels. Wear 251:827–838
7. Gerber N, Bundy M (1992) Effect of variable thermal properties on gun tube heating. Army Ballistic Research Laboratory Report No. BRLMR- 3984
8. Longbridge JA (2008) Internal ballistics. Bibilobazar Publications
9. ANSYS Workbench, Version 19.0, ANSYS Inc., 1970
10. Lawton BB (2010) Transient thermal analyses of midwall cooling and external cooling methods for a gun barrel
11. Lawton B (1992) Quasi steady heat transfer in gun barrel. In: 17th international symposium on ballistics South Africa

Modelling and Simulation on Behaviours of Aluminium Alloys



Ravi Kumar and N. K. Singh

Abstract Aluminium alloys are commonly used structural materials for civil and mechanical engineering applications due to high strength to density ratio, corrosion resistance, vibrational stability, recyclability and good formability. The knowledge of mechanical behaviours of these alloys at different strain rates is necessary for safe and optimum design of a crashworthy structure. In this paper, numerical analysis on the deformation behaviours of two aluminium alloys (AA6063-T6 and Al5052-H32) is presented under tension, compression and flexure/three-point bending using ANSYS. The tensile ($5\text{--}780\text{ s}^{-1}$) and compressive ($110\text{--}850\text{ s}^{-1}$) behaviour of AA6063-T6 alloy and the flexural behaviour (at crosshead velocity 100 mm/s) of Al5052-H32 alloy are simulated using explicit dynamics approach in ANSYS. Johnson–Cook model is used in the numerical simulations to define the nonlinear characteristics of the alloys. The above finite element analysis can help the design engineer to detect the system response (stress, strain, etc.) during the design process and incorporate the design changes before construction of possible prototypes. The simulation results are in good agreement with the analytical results of J–C model and also with the experimental results available in literature.

Keywords Aluminium alloys · Strain rates · Johnson–Cook model · Numerical simulation · ANSYS explicit dynamics

1 Introduction

Aluminium alloys are extensively used materials in transportation and aviation industries because of their low specific gravity and high strength [1–5]. Hence, better understanding about dynamic behaviour of aluminium alloys under different strain rates is essential for safety of mechanical components against impact, crash or blast

R. Kumar (✉) · N. K. Singh

Department of Mechanical Engineering, National Institute of Technology Patna, Patna, India

N. K. Singh

e-mail: nilambersingh@nitp.ac.in

loads. Numerical simulation of the deformation behaviour of the alloys helps the design engineer in understanding the system responses under various loading conditions. The material models are important when actual experimental apparatus is unavailable, expensive or consuming more time in performing experiments. Therefore, accuracy of material models is important in predicting the real behaviour of the materials. Singh et al. [6–8] presented the experimental analysis on dynamic behaviour of aluminium alloys at different loading conditions and determined the material model parameters of J–C and C–S model for AA6063-T6 and A15052-H32 alloys. Several authors carried out the numerical simulation on mechanical behaviour of different metallic materials under various loading conditions. Scholl et al. [9] investigated the strain hardening behaviour of mild steel under tension using a semi-empirical model. Elguedj et al. [10] presented the finite element analysis of 3D crack propagation under transient loading condition. Wang et al. [11] investigated the compressive behaviour of square metallic tube reinforced with rivets and influence of local stiffness during deformation. Gupta et al. [12] presented the J–C model parameters of cast aluminium alloys at different strain rates and temperatures under tension and compression. Khaire et al. [13] studied the behaviour of thin hemispherical shell of aluminium alloy against the impact of give nose projectile at very high velocity and conducted the numerical analysis of the problem on ABAQUS software with Johnson–Cook model. Szumigala and Polus [14] investigated the mechanical behaviour on aluminium–concrete beam under transverse loading through numerical simulation in ABAQUS software and compared the results with the experimental results. Yamashita et al. [15] developed an apparatus of high-speed biaxial stretching and determined the loading rate effect on the forming limit strain of thin aluminium sheets. It observed that multiple cracks were formed in A5052 sheet at strain rate 100 s^{-1} , and strain rate sensitivity changes to positive as strain rate increases from 0.1 s^{-1} to 100 s^{-1} . Bueno et al. [16] studied the effects of strain rate on fracture and formability behaviour of AA5754 aluminium alloy. Numerical studies on the tensile and compressive behaviours of mild steel and high strength steels are presented by Kumar and Singh [17, 18] using ANSYS. In this paper, the mechanical characteristics of the aluminium alloys, AA6063-T6 and A15052-H32 are simulated in ANSYS explicit dynamics under tension, compression and flexure at different loading rates based on the experimental studies presented by Singh et al. [6–8].

2 Methodology

2.1 Materials and Specimen

Stress–strain behaviours of AA6063-T6 and A15052-H32 alloys are simulated in ANSYS at different loading rates. The tensile, compressive and flexural test specimen's 3D models are first generated in CATIA, and then, it is brought to ANSYS in suitable file format (.igs format) for finite element analysis. Information regarding

mechanical properties of the aluminium alloys (AA6063-T6 and Al5052-H32) and the model parameters of Johnson–Cook are needed to specify in engineering data section of ANSYS explicit dynamics. Specimen dimensions: flat specimens of gauge length = 10 mm, width = 4 mm and thickness = 2 mm are used for tensile tests; cylindrical specimens of diameter = 16 mm and height = 16 mm are used for compression tests; and flat specimens having thickness = 6 mm, width = 10 mm, total length = 250 mm are used in three-point bending/flexure tests. The bending specimens of span length 120 mm are supported by two hemispherical supports of 25 mm radius each, and the nose radius of used indenter is 10 mm.

2.2 Johnson–Cook (J-C) Constitutive Model

This model is widely used for predicting the flow stress of the material under large strain, high strain rates and high temperature. It is also available in many computational code and used for defining the nonlinearity of the materials/alloys. This model has seven material parameters as follows: A (quasi-static true yield stress), B (hardening constant), C (strain rate constant), n (hardening exponent), m (thermal softening, taken as 1), melting point temperature (610–650 °C) and reference strain rate ($\dot{\epsilon}_0$ taken as 0.001 s⁻¹). In the standard expression of Johnson–Cook (J–C) model, it consists of three sets (bracket) representing strain hardening effect, strain rate effect and temperature effect. In the present investigation, temperature set is neglected because all analyses were done for room temperature condition. The modified equation of the model can be written as follows:

$$\sigma = [A + B\varepsilon_{pl}^n][1 + C \ln \dot{\epsilon}^*] \quad (1)$$

where $\dot{\epsilon}^* = \dot{\epsilon}/\dot{\epsilon}_0 =$ dimensionless plastic strain rate and $\varepsilon_{pl} =$ equivalent plastic strain. For calculation of analytical results, i.e. true stress value (dynamic stress), we need to substitute the model parameters on Eq. (1). Here, the parameters for aluminium alloys are taken from published literature [6–8].

2.3 Finite Element Simulation in ANSYS

The FEA simulation of the behaviours of the aluminium alloys (AA6063-T6 and Al5052-H32) is done on explicit dynamics of ANSYS workbench. Mesh size selected for tensile and compressive specimen is medium while for rectangular flexural specimen, it is of 2 mm. After meshing, tensile test specimen has 1356 nodes and 846 elements, compressive test specimen has 15,575 nodes and 14,040 elements, and rectangular flexural test specimen has 3024 nodes and 1875 elements. The element type is of Hex 8, i.e. hexahedron with eight nodes (brick type) for all specimens. Here, for simulation of problem at different strain rates, different velocity is applied

to the specimen as input parameter which is obtained by multiplying strain rate with gauge length of specimen. In tension test, the flat geometrical model is fixed on one end surface, and a velocity for specific strain rate is applied at other end surface at outward direction (i.e. positive velocity). In compression test, the cylindrical geometrical model is fixed on one end surface, and a velocity is applied at other end surface at inward direction (i.e. negative velocity). In flexure test, the crosshead velocity of 100 mm/s is applied in the downward direction to get deformation at mid span while other two outer supports are fixed at the base. Support structures are specified with materials of very high modulus of elasticity to get negligible or no deformation. The 3D model of specimen with their boundary conditions against tension, compression and flexure is shown in Fig. 1. End time of the simulation is defined based on hit and trial method to get the results up to fracture or failure limit point. The output parameters (system responses) such as von Mises stress and plastic strain are specified in the solution tab. Thereafter solving the problem in ANSYS explicit dynamics, the simulated results (stress–strain data) with the corresponding deformed specimen FE model under tension, compression and flexure load are shown in Fig. 2.

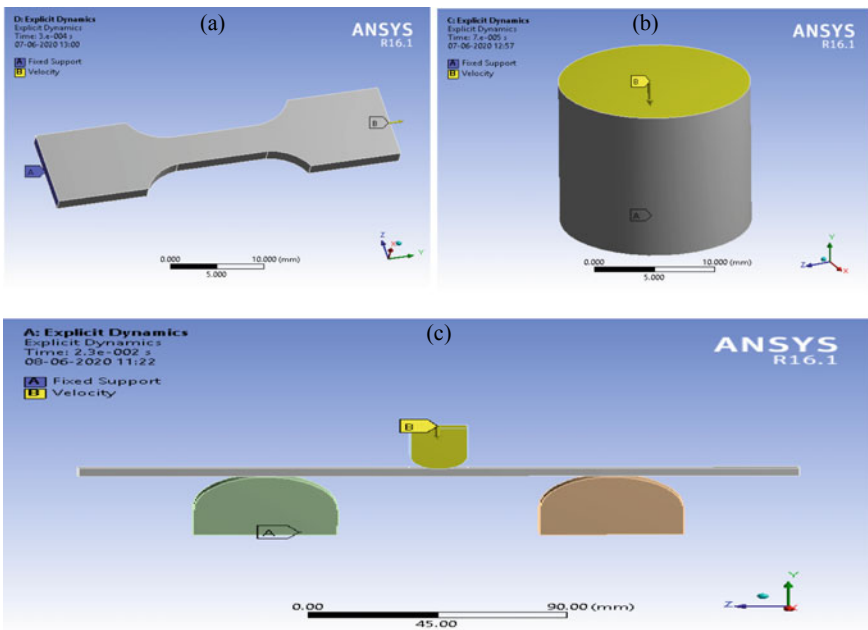


Fig. 1 Aluminium alloy specimens 3D model with their boundary conditions under **a** tension, **b** compression and **c** three-point bending/flexure

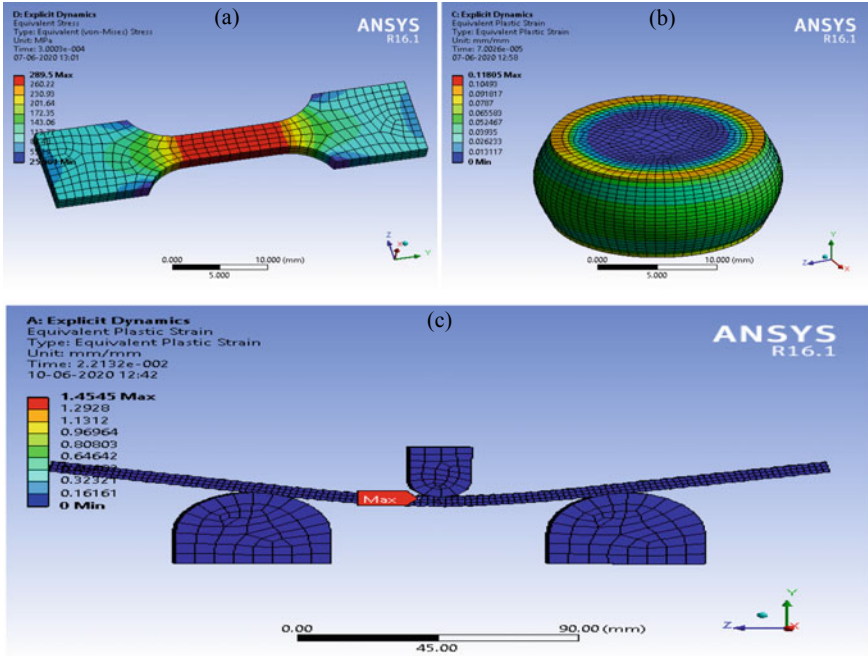


Fig. 2 Deformed finite element models of aluminium alloy specimens under **a** tension (780 s^{-1}), **b** compression (850 s^{-1}) and **c** flexure (100 mm/s)

3 Results and Discussion

The tensile ($5\text{--}780\text{ s}^{-1}$) and compressive ($110\text{--}850\text{ s}^{-1}$) behaviours of the AA6063-T6 aluminium alloy are simulated in ANSYS. The computational time for simulation at low strain rate ($\leq 5\text{ s}^{-1}$) requires more time ($\geq 24\text{ h}$), whereas high strain rate ($\geq 5\text{ s}^{-1}$) simulation requires comparatively less time ($\leq 24\text{ h}$) with higher accuracy. The analytical (predicted) results are calculated for each strain rate by the Johnson–Cook model. The comparison of true yield stress value of AA6063-T6 alloy at different strain rates under tension and compression test is given in Tables 1 and 2. Here, ANSYS and analytical (J–C model) results are individually compared with the experimental results [6, 7], and the percentage deviations between them are presented for both tension and compression. The graphical comparison of stress–strain behaviour of AA6063-T6 alloy at different strain rates under tension and compression is shown in Figs. 3 and 4, respectively.

The behaviour of A15052-H32 alloy under flexure/bending loads at crosshead velocity 100 mm/s is simulated in ANSYS. The comparison of simulated results with analytical results of Johnson–Cook model and percentage deviation between them are shown in Table 3. Authors have not found the experimental results at this velocity (100 mm/s) in literature; however, Singh et al. [8] presented the experimental

Table 1 Comparison of ANSYS simulation and analytical results with the experimental results of AA6063-T6 alloy under tension

Strain rate (s^{-1})	True yield stress, MPa (experimental) 'A'	True yield stress, MPa (ANSYS) 'B'	% deviation of ANSYS results, $\left(\frac{B-A}{A}\right) \times 100\%$	True yield stress, MPa (analytical) 'C'	% Deviation of Analytical results, $\left(\frac{C-A}{A}\right) \times 100\%$
5	162	169	+ 4.32	169	+ 4.32
25	160	167.3	+ 4.56	168.48	+ 5.3
400	176	180	+ 2.27	181.12	+ 2.9
660	180	183	+ 1.67	183.88	+ 2.15
780	171	175.75	+ 2.77	175.9	+ 2.86

Table 2 Comparison of ANSYS simulation and analytical results with the experimental results of AA6063-T6 alloy under compression

Strain rate (s^{-1})	True yield stress, MPa (experimental) 'A'	True yield stress, MPa (ANSYS) 'B'	% deviation of ANSYS results, $\left(\frac{B-A}{A}\right) \times 100\%$	True yield stress, MPa (analytical) 'C'	% deviation of analytical results, $\left(\frac{C-A}{A}\right) \times 100\%$
110	204	222	+ 8.82	219	+ 7.35
400	207	222.22	+ 7.35	223	+ 7.73
550	228	231.12	+ 1.36	231	+ 1.31
700	230	233	+ 1.3	235	+ 2.17
850	240	237	-1.25	236	-1.67

results of this alloy at different crosshead velocities in the range 100-200 mm/min with Johnson–Cook model. For numerical simulation of the problem at velocity 100 mm/s, the value of strain rate constant ($C = 0.01$) is assumed while the other model parameters are taken same as given in the published results. The simulation time at low velocity requires more time (≥ 500 h) in ANSYS. The reason for taking the positive strain rate constant for A15052-H32 is explained by Yamashita et al. [15] and stated that the value of strain rate constant changes to positive when strain rate increases from $0.1 s^{-1}$ to $100 s^{-1}$. The computational time for simulation of flexural behaviour of the alloy is very large as it takes almost 500 h to generate the data up to 0.1% of equivalent plastic strain.

4 Conclusions

The behaviours of aluminium alloys (AA6063-T6 and A15052-H32) at different strain rates under tension, compression and three-point bending/flexure are successfully simulated in ANSYS explicit dynamics by using Johnson–Cook model. The results of

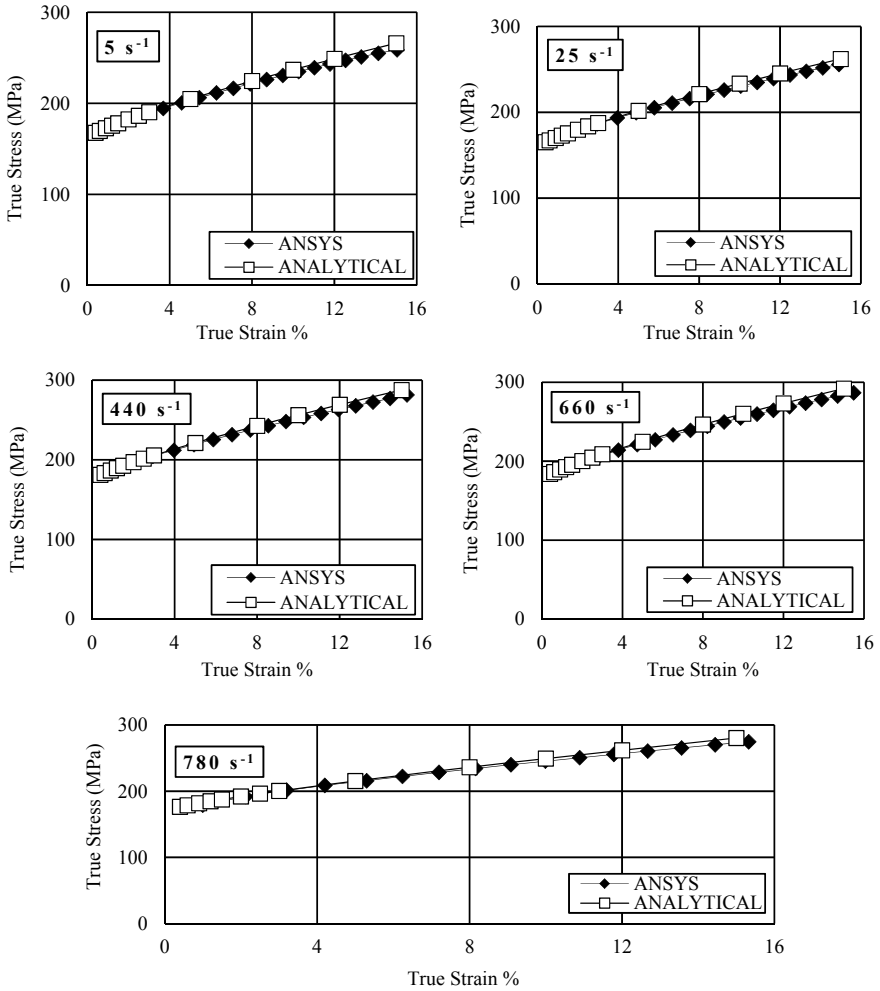


Fig. 3 Comparison of flow stress behaviour of AA6063-T6 alloy obtained by ANSYS simulation with analytical results of J-C model at different strain rates under tension

modelling and numerical simulation of the alloys can enrich the structural mechanics. The model helps in predicting the stress-strain value at different strain rates for safe and optimum design of mechanical components. The following conclusions are drawn from the present investigation:

- Strain rate sensitivity of aluminium alloys is very poor/ irregular, i.e. the mechanical properties increase/decrease slightly with increase in strain rate.
- The percentage deviations of simulated results and analytical (predicted) results with respect to the experimental results are within $\pm 8\%$. At low strain rates, the

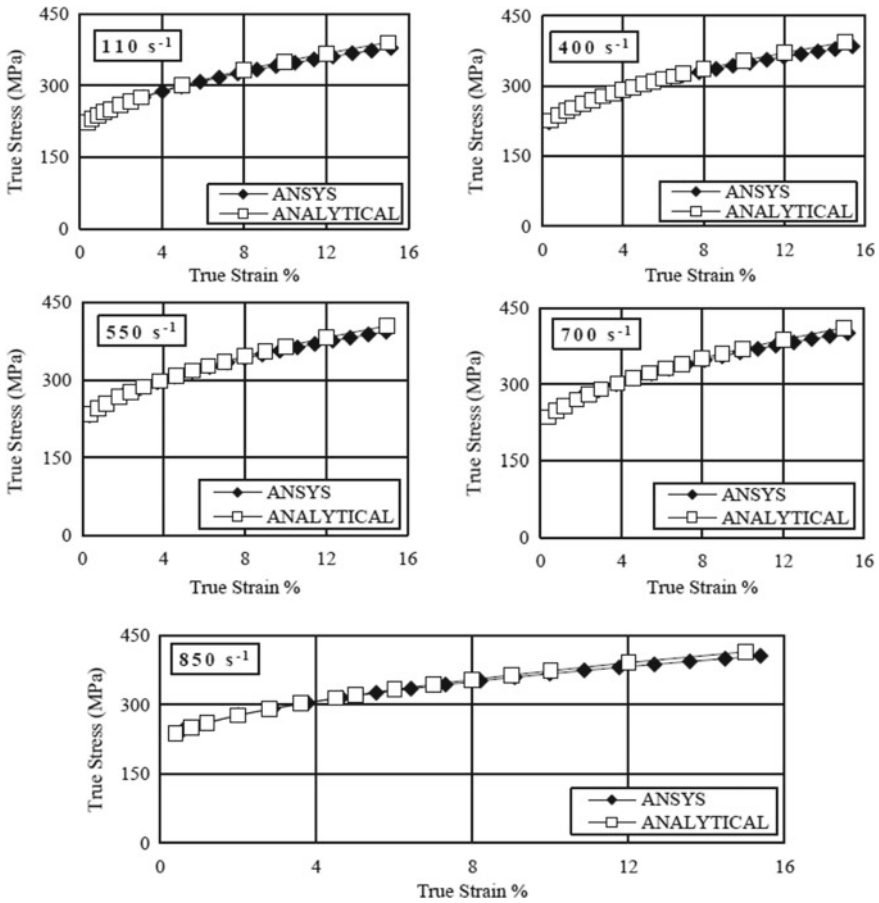


Fig. 4 Comparison of flow stress behaviour of AA6063-T6 alloy obtained by ANSYS simulation with analytical results of J-C model at different strain rates under compression

Table 3 Comparison of ANSYS simulation results with the analytical (J-C model) results of Al5052-H32 alloy under flexure

Simulated results (ANSYS)		Predicted results (analytical)		% Deviation in true yield stress, $\left(\frac{A-B}{A}\right) \times 100\%$
Eq. plastic strain %	True stress, A (MPa)	Eq. plastic strain %	True stress, B (MPa)	
0.011	280	0.01	281.6	-0.57
0.023598	288.4	0.02	290	-0.55
0.032888	295.1	0.03	294.7	0.13
0.041299	301.1	0.04	296.2	1.65
0.051381	308.4	0.05	300	2.8
0.064547	317	0.06	303.4	4.48
0.071665	323	0.08	310	4.19

deviation is slightly higher (i.e. $\pm 5\%$ under tension and $\pm 8\%$ under compression), whereas at high strain rates, it reduces to $\pm 3\%$ for both tension and compression.

- For flexural test, the percentage deviation of simulated results with respect to analytical (predicted) results is within $\pm 5\%$.
- The ANSYS simulated results are in good agreement with analytical results of Johnson–Cook model and also with experimental results of published literature.

References

1. Bobbili R, Madhu V, Gogia AK (2016) Tensile behaviour of aluminium 7017 alloy at various temperatures and strain rates. *J Market Res* 5(2):190–197
2. Zhu D, Mobasher B, Rajan SD, Peralta P (2011) Characterization of dynamic tensile testing using aluminum alloy 6061-T6 at intermediate strain rates. *J Eng Mech* 669–679. [https://doi.org/10.1061/\(ASCE\)EM.1943-7889.0000264](https://doi.org/10.1061/(ASCE)EM.1943-7889.0000264)
3. Vikas P, Sudhakar I, Dilkush MG, Srinivas B (2020) Aging behaviour of hot deformed AA7075 aluminium alloy. *Mater Today: Proc.* <https://doi.org/10.1016/j.matpr.2020.06.117>
4. Mudrock RN, Lebyodkin MA, Kurath P, Beaudoin AJ, Lebedkina TA (2011) Strain-rate fluctuations during macroscopically uniform deformation of a solution-strengthened alloy. *Scripta Mater* 65:1093–1096
5. Bozkurt Y, Toptas E, Ersoy S (2018) Comparison of the vibration properties of materials AA2124/SiC/25p and aluminum 6061-T6. *Online J Sci Technol* 8(2):44–47
6. Singh NK, Singha MK, Cadoni E, Gupta NK (2013) Dynamic characteristics of aluminium alloys at wide range of strain rates. *Proc Indian Natn Sci Acad* 79(4) (Spl. Issue, Part A):587–595. <https://doi.org/10.16943/ptinsa/2013/v79i4/47998>
7. Singh NK, Singha MK, Cadoni E, Gupta NK (2012) Strain rate sensitivity of an aluminium alloy under compressive loads. *Adv Mater Res* 548:169–173
8. Prakash G, Singh NK, Sharma P, Gupta NK (2020) Tensile, compressive, and flexural behaviors of Al5052-H32 in a wide range of strain rates and temperatures. *ASCE J Mater Civ Eng* 32(5):04020090. [https://doi.org/10.1061/\(ASCE\)MT.1943-5533.0003154](https://doi.org/10.1061/(ASCE)MT.1943-5533.0003154)
9. Scholl N, Minuth-Hadi F, Thiele K (2018) Modelling the strain rate dependent hardening of constructional steel using semi-empirical models. *J Construct Steel Res* 145:414–424
10. Elguedj T, Maurice RPS, Combescure A, Faucher V, Prabel B (2018) Extended finite element modeling of 3D dynamic crack growth under impact loading. *Finite Elem Anal Des* 151:1–17
11. Wang Z, Wang X, Shi C, Li Z, Zhou W (2019) Mechanical behaviors of square metallic tube reinforced with rivets-experiment and simulation. *Int J Mech Sci* 163:105118
12. Gupta S, Abotula S, Shukla A (2014) Determination of Johnson-cook parameters for cast aluminum alloys. *J Eng Mater Technol.* <https://doi.org/10.1115/1.4027793>
13. Khaire N, Tiwari G, Gurusankar A (2020) Numerical study of energy absorption behaviour of thin aluminium hemispherical shell against projectile impact. *Mater Today: Proc* 21:1958–1963
14. Szumigala M, Polus Ł (2017) An numerical simulation of an aluminium-concrete beam. *Procedia Eng* 172:1086–1092
15. Yamashita M, Nikawa M, Kuroda T (2018) Effect of strain-rate on forming limit in biaxial stretching of aluminum sheet. *Procedia Manuf* 15:877–883
16. Bueno M, Galdos L, Sáenz de Argandona E, Weiss M, Rolfe B, Lou Y, Mendiguren J (2020) Strain rate effect on the fracture behavior of the AA5754 aluminum alloy. *Procedia Manuf* 47:1264–1269
17. Kumar R, Singh NK (2019) Modelling and simulation on behaviours of mild steel. *Vibroeng Procedia* 29:266–269
18. Kumar R, Singh NK (2020) Modelling and simulation on behaviours of high strength steels. *Mater Today: Proc* 28:2345–2352

Accelerometer Mass Effects on Vibration Frequencies of Magnesium Alloy Fixed–Fixed Beam



Anuj Yadav and N. K. Singh

Abstract The purpose of this article is to investigate the impact of accelerometer mass on natural frequencies of a magnesium alloy (AZ61) fixed–fixed beam using experimental, numerical, and analytical methods. The FFT analyzer (OROS-34) is used to evaluate the beam’s natural frequency at multiple accelerometer positions in the impact hammer test setup. For analytical calculations, the Euler–Bernoulli fixed–fixed beam with the accelerometer’s concentrated point mass is considered and the finite element solution is done in ANSYS Workbench 16.1. Effects of accelerometer mass are found to be dependent on its positions, mode of vibration, and mass magnitude. A strong consensus is reached in theoretical, computational, and laboratory tests.

Keywords Fixed–fixed beam · FFT analyzer · Accelerometer and ANSYS

1 Introduction

The information of physical nature of vibration phenomenon has continually been essential for researchers and engineers in industry. Nowadays, structure is becoming lighter and flexible due to high demands for speed, comfort, and safety. Vibration of any structure creates major problems like early breakdown or failure of structure, noise, and reduced performance. The vibration problems can be prevented by two ways: first cure through perfect design and second by modification in structure. In any condition, knowledge of dynamic behavior of structure is essential; hence, best models are required to describe the nature of vibration. Two methods are used to model the dynamic behavior of structures, namely experimental modal testing analysis and finite element numerical method. In experimental modal analysis of structure, various types of errors (mass loading effect of accelerometer, mounting

A. Yadav (✉) · N. K. Singh

Department of Mechanical Engineering, National Institute of Technology, Patna 800005, India

N. K. Singh

e-mail: nilambersingh@nitp.ac.in

effects, noise, and nonlinearity of structure) are induced during experiment. Therefore, it is necessary to examine the effects of errors on modal parameters to avoid accident. The mass loading of transducer induced major error in modal parameters, but during the heavy structure analysis, it is neglected. For the analysis of lighter structure like microelectromechanical system, it should be considered. The models made by modal testing generally have poor quality due to source of a lack of precision in experimental testing. The lack of precision in testing is the reason of poor data acquisition process, signal processing error, and modal analysis error. The major effects in experimental results occur due to mechanical errors like mass loading effect of accelerometer. Several researchers have investigated the mass loading effects on natural frequency of different structures with different approaches. Özkaya et al. [1] explained the vibration frequency of a beam mass system. The beam is supported by conditions of immovable end, resulting in stretching during the vibration. Low [2] explained experimental and analytical frequency analysis of centrally loaded beam. Forecasts of analytical frequencies are verified by experimental approaches on fixed-free beams holding masses at their centers. Rosa et al. [3, 4] studied vibration frequency of mass loaded beam with alternative approach of dual-frame reference. Low [5] presented an eigenfrequency analysis using single frame of reference technique of mass carrying beam with multiple boundary conditions. The modal analysis of mass carrying beams for ten basic beams is performed with guided, cantilever, and pin ends. Low [6] presented the comparative study of frequency analysis method of signal and dual-frame reference. Mermertas and Erol [7] have investigated the eigenfrequency of cracked cantilever beam with attached mass. Kotambkar [8, 9] investigated the effects on frequency of cracked free-free beam due to accelerometer mass with analytical, numerical, and experimental methods. Kumar et al. [10] investigated the vibration analysis of fixed-free beam done by ANSYS Workbench and the MATLAB programming performed for finite element analysis. Yadav and Singh [11] investigated similar problem of fixed-free beam with analytical, numerical, and experimental approaches. Sharma [12] performed theoretical, experimental, and numerical beam modal analysis in a free-free and simply supported boundary state. Yadav and Singh [13] studied the mass impacts on natural frequencies of Mg alloy pinned and roller-supported beam with analytical, numerical, and experimental approaches. In this article, the accelerometer impacts on the natural frequency of Mg alloy fixed-fixed beam are studied.

2 Laboratory Test Setup

The test setup (Fig. 1) has an FFT analyzer (OROS-34), a computer, an Mg alloy (AZ61) beam, and a sensor hammer. Elasticity modulus (E) and mass density (ρ) of the beam ($250 \times 10 \times 4$ in mm) material are considered as 45 GPa and 1800 kg/m^3 , respectively. Both ends of the beam are fixed with the help of wooden supports, and the span of the beam is 230 mm (L) long. The accelerometer (mass: 12.95 g) is placed on the beam at the desired location to record the vibration signal. This OROS

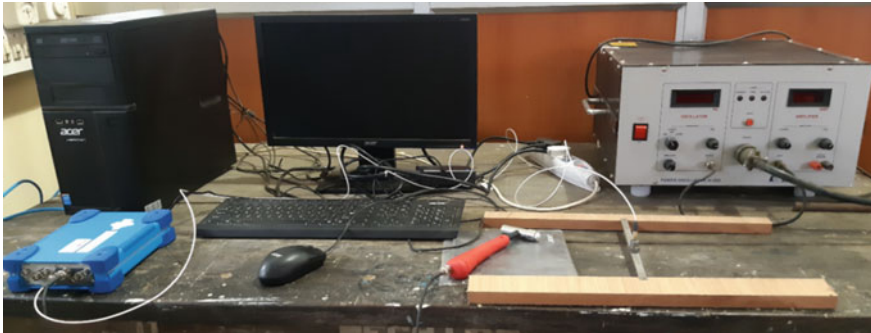


Fig. 1 Experimental setup

analyzer converts input time domain data in to frequency domain. The frequency domain data is appeared in to monitor with the help of NVGate software. This procedure is repeated for multiple beam positions, and its fundamental frequency is obtained in Mode I corresponding to each position.

3 Analytical Solution

An Euler–Bernoulli fixed–fixed beam (Fig. 2) with accelerometer mass (m) and span length (L) of 230 mm is considered for analytical solution. In a dual-frame reference, the problem is solved, and the beam model is split into two components from the accelerometer location. Each portion has 4 constants, and thus, these are added up to 8 constants ($A_j, j = 1-8$) for the beam in solution, but only four end conditions (the slope and the deflection at both ends of the beam are zero) are available. The four additional conditions [3] are used to solve the problem.

The free vibration equation for the Euler–Bernoulli beam is given as

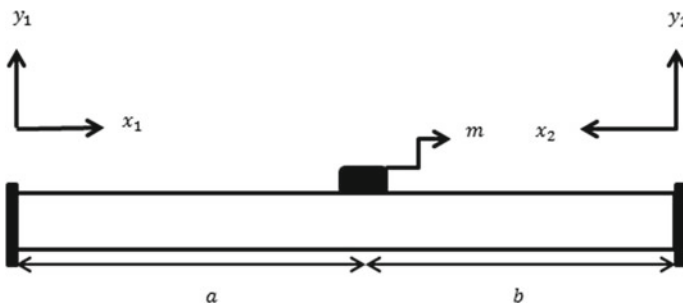


Fig. 2 Analytical model

$$EI \frac{\partial^4 y}{\partial x^4} + \rho A \frac{\partial^2 y}{\partial t^2} = 0 \quad (1)$$

The solution is written as (variable separable method)

$$y(x, t) = Y(x) \cdot T(t) \quad (2)$$

The displacement function $Y(x)$ is defined as

$$Y(x) = A_1 \cosh \beta x + A_2 \sin \beta x + A_3 \cos \beta x + A_4 \sin \beta x \quad (3)$$

where $\beta^4 = \left(\omega^2 \frac{\rho A}{EI} \right)$

where ω is expressed as natural frequency.

$$\omega = \beta^2 \sqrt{\frac{EI}{\rho A}} \quad (4)$$

The two frames of references are taken at each end of beam, and the beam is split into two components at the mass position.

$$Y_1(x_1) = A_1 \cosh \beta x_1 + A_2 \sin \beta x_1 + A_3 \cos \beta x_1 + A_4 \sin \beta x_1 \quad (5)$$

$$Y_2(x_2) = A_5 \cosh \beta x_2 + A_6 \sin \beta x_2 + A_7 \cos \beta x_2 + A_8 \sin \beta x_2 \quad (6)$$

At left end, ($x_1 = 0_{\text{at } x=0}$), ($x_2 = 0_{\text{at } x=L}$), $y_1 = 0$, and $y_1' = 0$, and $y_1(x, t)$ can be define as:

$$Y_1(x_1) = (\cosh \beta x_1 - \cos \beta x_1) A_1 + (\sinh \beta x_1 - \sin \beta x_1) A_2 \quad (7)$$

At right end, $y_2 = 0$ and $y_2' = 0$, and $y_2(x, t)$ can be define as:

$$Y_2(x_2) = (\cosh \beta x_2 - \cos \beta x_2) A_5 - (\sinh \beta x_2 - \sin \beta x_2) A_6 \quad (8)$$

Displacement field equation at the position of attached point mass is

$$y_1(x_1)_{\text{at } x_1=a} = y_2(x_2)_{\text{at } x_2=b} \quad (9)$$

$$\begin{aligned} &(\cosh \beta a - \cos \beta a) A_1 + (\sinh \beta a - \sin \beta a) A_2 \\ &- (\cosh \beta b - \cos \beta b) A_5 + (\sinh \beta b - \sin \beta b) A_6 = 0 \end{aligned} \quad (10)$$

Slope equation at the position of attached point mass is

$$y_1'(x_1)_{\text{at } x_1=a} = -y_2'(x_2)_{\text{at } x_2=b} \quad (11)$$

$$\begin{aligned}
& (\sinh \beta a + \sin \beta a)A_1 + (\cosh \beta a - \cos \beta a)A_2 \\
& + (\sinh \beta b + \sin \beta b)A_5 - (\cosh \beta b - \cos \beta b)A_6 = 0
\end{aligned} \tag{12}$$

Moment equation at the position of attached point mass is

$$y_1''(x_1)_{\text{at } x_1=a} = y_2''(x_2)_{\text{at } x_2=b} \tag{13}$$

$$\begin{aligned}
& (\cosh \beta a + \cos \beta a)A_1 + (\sinh \beta a + \sin \beta a)A_2 \\
& - (\cosh \beta b + \cos \beta b)A_5 + (\sinh \beta b + \sin \beta b)A_6 = 0
\end{aligned} \tag{14}$$

Shear force at the position of attached point mass is

$$y_1'''(x_1)_{\text{at } x_1=a} + y_2'''(x_2)_{\text{at } x_2=b} + m \cdot \ddot{y}_1(x_1)_{\text{at } x_1=a} = 0 \tag{15}$$

$$\begin{aligned}
& (\sinh \beta a - \sin \beta a)A_1 + (\cosh \beta a + \cos \beta a)A_2 \\
& + (\sinh \beta b - \sin \beta b)A_5 - (\cosh \beta b + \cos \beta b)A_6 \\
& + \left(\frac{m\beta}{\rho A} \right) \{ (\cosh \beta a - \cos \beta a)A_1 + (\sinh \beta a - \sin \beta a)A_2 \} = 0
\end{aligned} \tag{16}$$

Non-dimensional parameter of mass location is $(\alpha) = \frac{a}{L}$.

$$R_a = \cosh \beta L\alpha - \cos \beta L\alpha$$

$$S_a = \sinh \beta L\alpha - \sin \beta L\alpha$$

$$P_a = \cosh \beta L\alpha + \cos \beta L\alpha$$

$$Q_a = \sinh \beta L\alpha + \sin \beta L\alpha$$

$$R_b = \cosh \beta L(1 - \alpha) - \cos \beta L(1 - \alpha)$$

$$S_b = \sinh \beta L(1 - \alpha) - \sin \beta L(1 - \alpha)$$

$$P_b = \cosh \beta L(1 - \alpha) + \cos \beta L(1 - \alpha)$$

$$Q_b = \sinh \beta L(1 - \alpha) + \sin \beta L(1 - \alpha)$$

$$\gamma = \frac{m\beta}{\rho A}$$

Adding Eqs. (10), (12), (14), and (16), the final non-dimensional characteristic equation is obtained in the form of determinant,

$$\begin{vmatrix}
R_a & S_a & -R_b & S_b \\
Q_a & R_a & Q_b & -R_b \\
P_a & Q_a & -P_b & Q_b \\
S_a + R_a \cdot \gamma & P_a + S_a \cdot \gamma & S_b & -P_b
\end{vmatrix} = 0 \tag{17}$$

The βL values (Table 1) in first, second, and third mode for multiple locations (α) on the beam are calculated after solving Eq. (17) with the aid of MATLAB. Thus, Eq. (4) is used to obtain corresponding natural frequencies. For measurement, only half span of the beam is taken because the beam is symmetric. The deviations of βL

Table 1 Impacts of mass attachment positions on first three bending modes

S. no.	$\alpha = \frac{a}{L}$	βL		
		First mode	Second mode	Third mode
1	0.1	4.6951	7.4614	9.6952
2	0.2	4.3737	6.5486	9.7196
3	0.3	3.9349	6.7319	10.6276
4	0.4	3.6717	7.3498	10.7241
5	0.5	3.5889	7.8532	9.8537

values with regard to parameters of mass location (α) are shown for different modes in Figs. 3, 4, and 5.

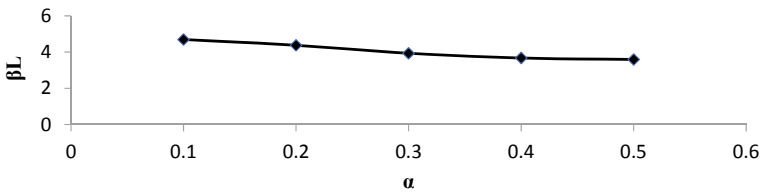


Fig. 3 Impacts of mass loading on the first mode of natural frequency

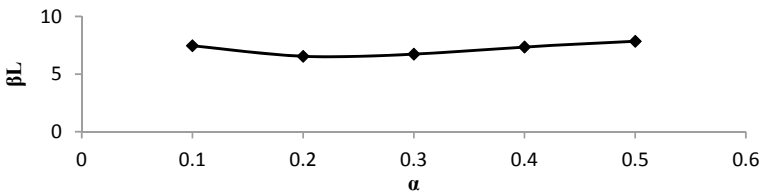


Fig. 4 Impacts of mass loading on the second mode of natural frequency

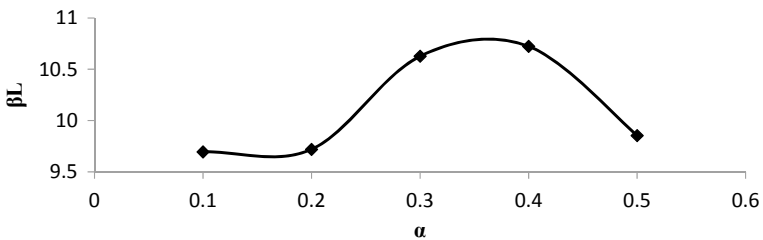


Fig. 5 Impacts of mass loading on the third mode of natural frequency

4 Numerical Simulation

The numerical modal analysis is performed in ANSYS Workbench 16.1. At first, the design modeler of the ANSYS program generates a three-dimensional rectangular cross-sectional beam model (Fig. 6a) with dimensions $230 \times 10 \times 4$ (mm) with concentrated point mass at the desired position and that point mass acts as the mass of the accelerometer. This beam model is now fixed at both ends to act as a fixed–fixed beam, and the model is meshed (Fig. 6b) with Hex20 element. The total elements are 1000, and nodes are 6345. The program gets the natural frequencies of the three-dimensional model.

The comparison is done in between the natural frequencies (Hz) retrieved from the analytical and numerical methods for the bending modes I, II, and III in Table 2 at different mass locations. Table 3 presents natural frequencies retrieved from analytical, numerical, and experimental studies for Mode I. The results obtained from different methods are similar.

5 Conclusions

Mass attachment reduces the beam's natural frequencies and influences the mode shapes but the form of the first mode not changed. In first and second mode, nodes are located at locations ($\alpha = 0.5$) and at locations ($\alpha = 0.359, 0.641$), respectively. When the accelerometer is mounted on the peak point (antinode), the frequency variation is observed more, and if it is mounted on the node location, the frequency remains insensitive. The accelerometer mass-to-the beam mass ratio ($m / \rho aL$) also influenced the beam's natural frequency. For neglecting the impacts of mass, this ratio should be minimum.

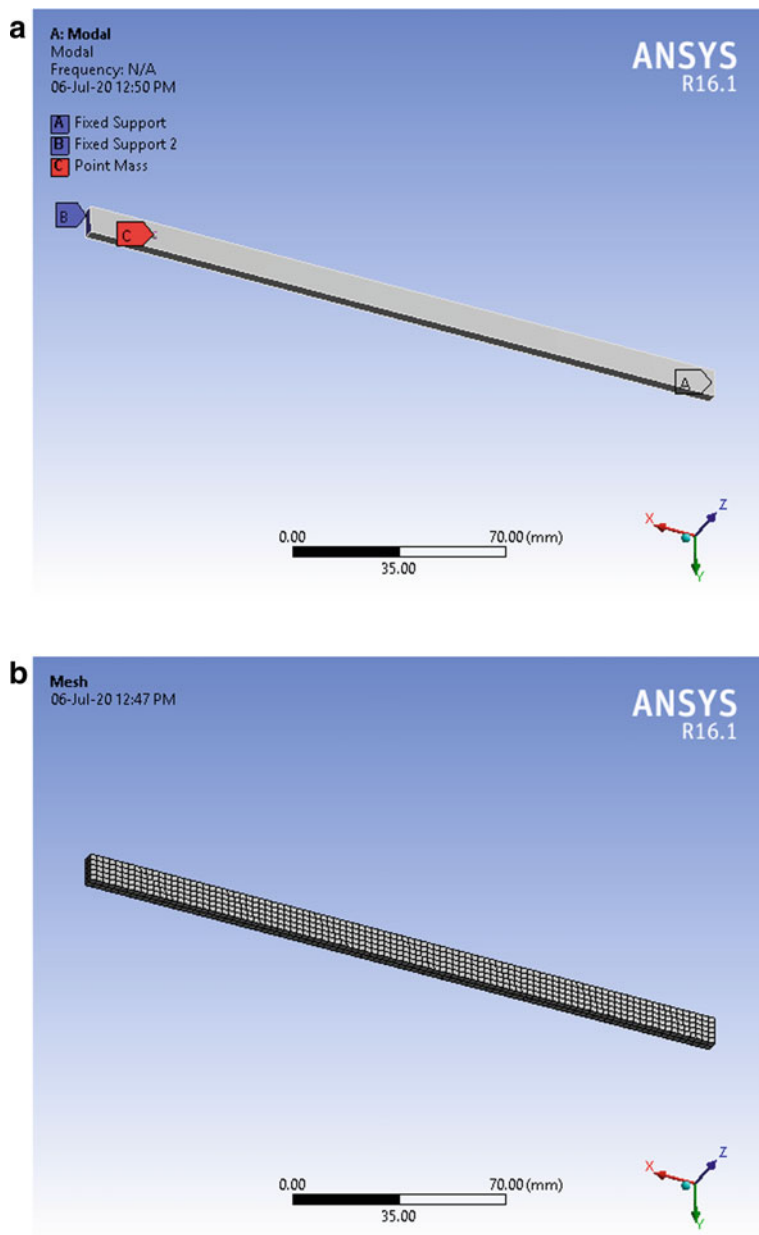


Fig. 6 a 3D geometrical model. b 3D mesh model

Table 2 Fixed-fixed beam mass system natural frequencies in three different bending modes

S. no.	α	First mode		Second Mode		Third mode	
		Numerical	Analytical	Numerical	Analytical	Numerical	Analytical
1	0.1	384.54	380.265	967.15	960.339	1622.3	1621.428
2	0.2	333.84	329.975	746.08	739.743	1635.5	1629.600
3	0.3	270.13	267.086	788.03	781.735	1948.4	1948.294
4	0.4	235.12	232.551	938.02	931.827	1982.6	1983.837
5	0.5	224.60	222.180	1068.40	1063.843	1684.4	1674.877

Table 3 Natural frequencies of bending Mode I obtained from theoretical, computational, and laboratory tests

S. no.	α	Natural frequencies (Hz)		
		Analytical	Numerical simulation	Experimental
1	0.1	380.265	384.54	372
2	0.2	329.98	333.83	319
3	0.3	267.086	270.13	254
4	0.4	232.550	235.12	223
5	0.5	222.180	224.60	199

References

- Özkaya E, Pakdemirli M, Öz HR (1977) Non-linear vibrations of a beam mass system under different boundary conditions. *J Sound Vib* 199(4):679–696
- Low KH, Lim TM, Chai GB (1993) Experimental and analytical investigations of vibration frequencies for centre-loaded beams. *Comput Struct* 48(6):1157–1165
- De Rosa MA, Ascoli S, Nicastro S (1996) Exact dynamic analysis of beam mass systems. *J Sound Vib* 196(4):529–533
- De Rosa MA, Franciosi C, Maurizi MJ (1996) on the dynamic behaviour of slender beams with elastic ends carrying a concentrated mass. *Comput Struct* 58:1145–1159
- Low KH (1998) On the eigenfrequencies for mass loaded beams under classical boundary conditions. *J Sound Vib* 215:381–409
- Low KH (2001) A comparative study of the eigenvalue solutions for mass-loaded beams under classical boundary conditions. *Int J Mech Sci* 43:237–244
- Mermertas V, Erol H (2001) Effect of mass attachment on the free vibration of cracked beam. In: 8th international congress on sound and vibration, Hong Kong, China, pp 2803–2810
- Kotambkar MS (2014) Mass loading effect on natural frequency of cracked beam in free-free condition. *Int J Eng Res Tech (IJERT)* 3(9):113–120
- Kotambkar MS (2014) Effect of mass attachment on natural frequency of free-free beam. *Int J Eng Res Tech (IJERT)* 102–105
- Kumar P, Bhaduri S, Kumar A (2016) Vibration analysis of cantilever beam: an experimental study. *IJRASET* 4(II):361–369
- Yadav A, Singh NK (2019) Effects of accelerometer mass on natural frequency of a magnesium alloy cantilever beam. *Vibroeng. Procedia* 29:207–212

12. Sharma JK (2019) Theoretical and experimental modal analysis of beam. *Eng Vib Commun Inf Process* 478:177–185
13. Yadav A, Singh NK (2020) Investigation for accelerometer mass effects on natural frequency of magnesium alloy simply supported beam. *Mater Today Proc* 28:2561–2565

Prediction and Optimization of Weld Bead Geometry of MIG Welded Stainless Steel 202 Plates



Shruti Sood, Prithu Mishra, Mayank Pandit, and Pradeep Khanna

Abstract Stainless steels are being used extensively in fabrication applications due to their unique engineering properties. Metal inert gas (MIG) welding, one of the popular joining processes, is vastly used for the purpose. Weld bead geometry parameters largely decide the strength and performance of the joint in service and are affected by input parameters. The present investigation deals with MIG welding of austenitic grade stainless steel plates in order to develop mathematical models to predict and optimize the weld bead geometry. The experiments were conducted using central composite face-centered design technique. Results were graphically analyzed by response surface methodology (RSM), and model appropriacy was verified by the ANOVA technique. The developed models could predict the two-factor interactive effects of welding parameters on bead width, depth of penetration, and height of reinforcement.

Keywords Stainless steel 202 · MIG · Bead geometry · Mathematical modeling · ANOVA · RSM

1 Introduction

SS 202 is a non-magnetic, manganese-alloyed austenitic stainless steel having widespread applications owing to its good ductility. It has lesser nickel content as compared to its SS 302 counterpart. Thus, it acts as a cost-effective alternative with comparable mechanical properties and corrosion resistance under a certain range of lower temperatures [1]. Welding of austenitic stainless steels has become easier and possible at high production rates with the MIG welding process in the industry [2]. High reliability, capability to weld in all positions, and high productivity are some of the primary factors due to which it is widely used for various industrial applications [3]. SS 308L is a commonly used filler material for MIG welding of austenitic stainless steels. Literature survey reports that the mechanical attributes of

S. Sood (✉) · P. Mishra · M. Pandit · P. Khanna
Division of Manufacturing Processes and Automation Engineering, Netaji Subhas University of Technology, New Delhi 110078, India

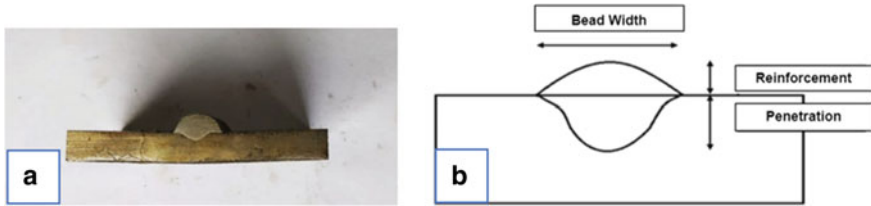


Fig. 1 a Bead profile obtained, b schematic diagram of bead profile

a weldment are governed by factors like bead geometry and chemical composition [4, 5]. Thus, to achieve the required mechanical properties, obtaining an optimum weld bead geometry is essential [6]. However, the bead profile is itself dependent on the input welding variables (like travel speed, stand-off distance, wire feed rate, etc.) selected, thereby making the correlation of the bead geometry with welding parameters the task of prime importance [7]. The correlation can be achieved by the development of mathematical models from the data collected through experimental investigations. The establishment of quadratic models is essential for the efficient application of automated arc welding processes [8, 9]. Figure 1a shows the bead profile obtained, while Fig. 1b shows the schematic diagram of it.

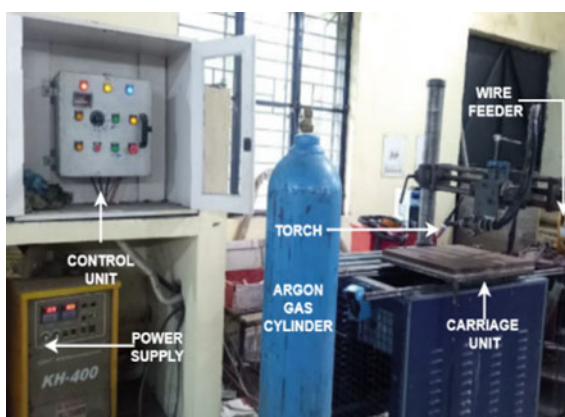
Previous studies have attempted to develop models in order to establish a relationship between the bead profile parameters and the welding variables [10, 11]. Kim et al. employed the method of multiple regression analysis to correlate the process input variables with bead penetration for automated GMAW [12]. Xu et al. used RSM for developing mathematical models to correlate bead profile with input variables in oscillating narrow gap MIG [8]. Cruz et. al devised a methodology for optimization of bead width of GMAW through the use of artificial neural networks [13]. Pandey et al established a statistical model for determining shape relationships and bead profile for GMAW of aluminum alloys [14]. The above findings show that bead profile is significantly influenced by welding variables like wire feed rate, travel speed, arc voltage, stand-off distance, and torch angle. Thus, the present investigation aims at studying the correlation of these welding variables with bead profile parameters like reinforcement height (R), bead width (W), and depth of penetration (P). The welding parameters have also been optimized to attain the desired bead profile. The tools used for verifying the appropriacy of the developed models and graphically analyzing the results obtained were ANOVA and RSM, respectively [15, 16].

2 Experimental Investigation

SS202 plates of thickness of 6 mm were cut in size 100×100 mm, and their surface was cleaned using emery paper to prepare them for MIG welding. The experimental runs were carried out on a welding power source rated 400 A, having 60% duty cycle with flat VI characteristic. The workpiece was placed on a motor-operated carriage

Table 1 Composition (wt. %) of SS 202 [1] and SS 308L [17]

Element	SS 202 (wt. %)	SS 308L (wt. %)
Ni	5.0	10.1
Mn	9.0	1.90
Cr	17.0	0.32
C	0.15	0.02
Si	1.0	0.32
S	0.03	0.01
P	0.06	0.02
N	0.25	–

Fig. 2 Experimental setup

unit to ensure that at different values of travel speed, the weld quality remains uniform. Industrially pure argon with 16 L/minute flow rate was used as the shielding gas. SS 308L having a diameter of 1.2 mm was employed as the filler wire. Table 1 gives the composition of SS 202 and SS 308L, while the setup used in this investigation is given in Fig. 2.

2.1 Estimation of Working Ranges of Input Parameters

The working range of the welding variables was estimated by conducting around 20 trial experiments. The trials were conducted in such a manner that only one of the welding variables was varied keeping the rest of them fixed. The upper and lower limits were decided based on weld quality obtained between them keeping in view the uniformity of the bead, continuity of the bead, and no spatters. Table 2 depicts the input parameters with their working limits divided into five levels.

Table 2 Working ranges of input parameters

S. No	Input parameters	Units	Coded levels of Input Parameters				
			- 2	- 1	0	+ 1	+ 2
1	Wire feed rate (<i>A</i>)	m/min	0.3	0.6	0.9	1.2	1.5
2	Welding speed (<i>B</i>)	cm/min	25	30	35	40	45
3	Voltage (<i>C</i>)	Volts	14	16	18	20	22
4	Stand-off distance (<i>D</i>)	mm	10	12.5	15	17.5	20
5	Torch angle (<i>E</i>)	°	70	80	90	100	110

2.2 Construction of Design Matrix

Based on the input variables and their working limits, design of experiments (DOE) technique was employed to generate a design matrix. The developed matrix was then used to conduct the experiments. Central composite technique of rotatable configuration was employed to construct the models of a total of 32 runs, comprising of $2^4 = 16$ runs using half factorial, 6 runs representing center points, and $2 \times 5 = 10$ runs representing star points [18] (Table 3).

2.3 Conduction of the Experiment on the Basis of the Matrix Designed

To avoid systematic error, if any, the 32 experimental runs were conducted in a random order. The welded specimens are shown in Fig. 3. Following this, to study the bead profile, a specimen of dimension $50 \times 50 \times 6$ mm was cut from each plate and polished using emery paper. Disk polishing machine was used for further fine polishing followed by etching. 480 mL H_2O , 50 g $FeCl_3$, and 120 mL HCL were added in order to prepare the etchant. At last, the bead dimensions were measured using shadowgraphs.

2.4 Mathematical Model Development

Let Z denote the response factor dependent on the five input factors (A, B, C, D, E). Then, Z can be written as $Z = f(A, B, C, D, E)$.

The mathematical equations including the significant factors as suggested by the design expert software are given below

$$\begin{aligned} \text{Width} = & 9.05 + 0.97 * A - 0.33 * B + 0.88 * C - 0.22 * AC \\ & - 0.46 * AE - 0.01 * BC - 0.33 * A2 \end{aligned} \quad (1)$$

Table 3 Developed design matrix

Std.	Run	A (mm/min)	B (cm/min)	C (V)	D (mm)	E (°)	W (mm)	P (mm)	R (mm)
13	1	- 1	- 1	1	1	1	8.79	1.06	2.64
8	2	1	1	1	- 1	- 1	10.25	1.63	2.77
24	3	0	0	0	2	0	8.46	1.37	2.58
5	4	- 1	- 1	1	- 1	- 1	9.06	1.72	2.28
14	5	1	- 1	1	1	- 1	10.74	1.95	3.22
10	6	1	- 1	- 1	1	1	7.71	1.53	2.75
29	7	0	0	0	0	0	9.17	1.68	2.56
28	8	0	0	0	0	0	9.31	1.16	2.65
9	9	- 1	- 1	- 1	1	- 1	6.82	1.37	3.24
27	10	0	0	0	0	0	8.89	1.3	2.56
21	11	0	0	- 2	0	0	7.24	1.11	3.16
3	12	- 1	1	- 1	- 1	-1	5.53	1.3	4.08
26	13	0	0	0	0	2	8.86	1.04	3.116
23	14	0	0	0	- 2	0	10.31	1.45	2.89
18	15	2	0	0	0	0	9.7	1.62	3.09
32	16	0	0	0	0	0	9.31	1.16	2.37
25	17	0	0	0	0	- 2	8.59	0.85	3.21
12	18	1	1	- 1	1	- 1	9.72	1.57	2.75
30	19	0	0	0	0	0	9.31	1.16	2.65
31	20	0	0	0	0	0	8.4	1.45	2.81
17	21	- 2	0	0	0	0	5.66	0.78	2.22
6	22	1	- 1	1	- 1	1	11.07	2.53	3.07
15	23	- 1	1	1	1	-1	8.1	1.01	1.748
4	24	1	1	- 1	- 1	1	7.65	1.53	2.59
19	25	0	- 2	0	0	0	10.54	2	3.15
1	26	- 1	- 1	-1	- 1	1	6.54	1.67	2.7
11	27	- 1	1	- 1	1	1	6.93	1.34	2.82
16	28	1	1	1	1	1	9.77	2.15	2.8
7	29	- 1	1	1	- 1	1	9.99	0.62	2.17
20	30	0	2	0	0	0	8.08	1.33	2.54
22	31	0	0	2	0	0	9.41	2.23	3.03
2	32	1	- 1	- 1	- 1	- 1	10.13	1.32	2.91

Fig. 3 Welded specimens

$$\begin{aligned} \text{Penetration} = & 1.30 + 0.24 * A - 0.14 * B + 0.136 * C + 0.07 \\ & * AB + 0.22 * AC + 0.14 * BD + 0.11 * C2 \end{aligned} \quad (2)$$

$$\begin{aligned} \text{Reinforcement} = & 2.78 + 0.12 * A - 0.09 * B - 0.14 * C - 0.06 * AB \\ & + 0.30 * AC + 0.15 * BC + 0.17 * CE. \end{aligned} \quad (3)$$

2.5 Testing of the Model Adequacy

To test the appropriacy of the developed models, the tabulated and calculated F -values were contrasted. A model is considered to be appropriate if the tabulated F -value is greater than the calculated F -value. For all the models developed in this investigation, the F -value obtained was less than 4.95, which is the tabulated F -value. The p -values obtained were also observed to be less than 0.05, as shown in Table 4, thus confirming the appropriacy of the developed models.

3 Analysis of Achieved Results

This section involves a detailed graphical analysis of direct as well as two-factor combined effects on the bead profile. Analysis of the two-factor combined effects was carried out keeping the rest of the input variables fixed at their 0 levels. The study of two-factor combined effects is essential so as to access the integrity and sensitivity of the process behavior with respect to input variables [19].

Table 4 Analysis of variance for the quadratic models developed

Bead parameter	F -value	p -value	R^2	Adequacy of the model
Width	4.11	0.0005	0.9372	Adequate
Penetration	1.26	0.0049	0.8989	Adequate
Reinforcement	4.55	0.0051	0.7857	Adequate

3.1 Direct Effects of Welding Variables on Bead Profile

Figure 4a illustrates that an increment in wire feed rate leads to an increase in reinforcement, width, and penetration. At high current density, the filler wire deposited increases and the area of the base covered by the bead becomes wider, leading to an increment in width and reinforcement, respectively. Moreover, with a rise in welding current, greater heat content is supplied leading to more melting of the base plate, resulting in higher penetration. Another factor causing higher penetration is the greater arc force due to an increased wire feed rate.

With an increment in travel speed, all three bead dimensions are observed to decrease as seen in Fig. 4b. At higher travel speed, a smaller melt pool is formed as a lower amount of heat is supplied to the base plate. Due to a lower heat content, a lesser amount of base metal melts causing lesser penetration. Both width and reinforcement are found to decrease with a rise in welding speed owing to a decrease in the amount of filler material that melts and gets deposited on the base plate.

The arc's tendency to spread increases leading to a greater width, due to an increased voltage. However, reinforcement reduces at higher voltage as the width of the melting zone rises at the expense of it. In Fig. 5a, penetration is observed to gradually increase as more heat is delivered to the weld pool due to a larger arc cone at higher voltage.

Figure 5b shows that as the stand-off distance increases, reinforcement decreases, width first falls and then rises, and penetration remains nearly constant. The reason for this can be attributed to the interactive effect of other factors affecting bead geometry.

From Fig. 6, it is evident that a rise in torch angle leads to lower penetration which is justified as the arc force leads the arc resulting in lower heat input. A similar variation in penetration is observed when the torch angle is decreased. The reason for this trend can be attributed to the interactive effect of other factors affecting bead geometry. Moreover, as at higher torch angles, the tendency of spreading of the arc

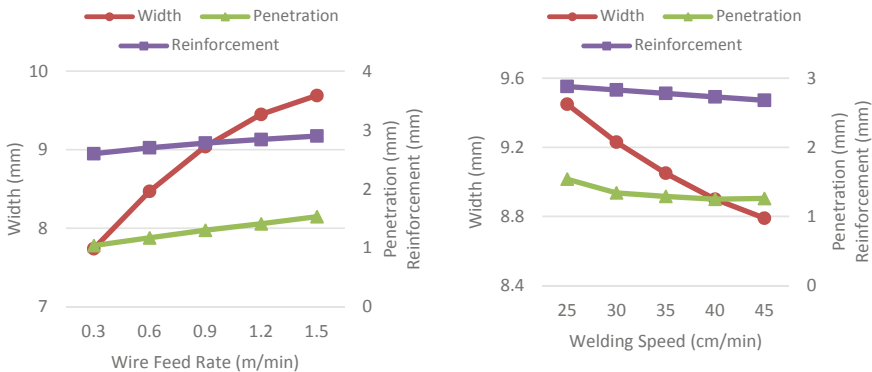


Fig. 4 Effect of variation in a wire feed rate, b welding speed

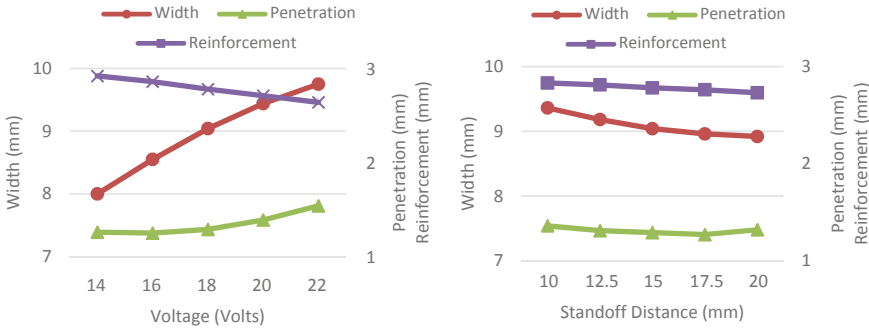
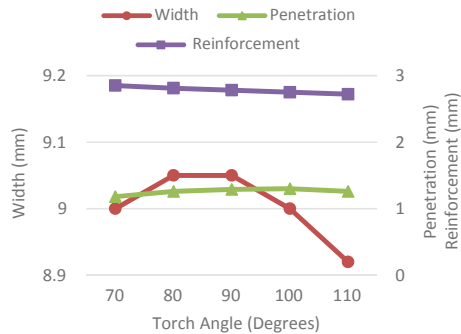


Fig. 5 Effect of variation in **a** voltage, **b** stand-off distance

Fig. 6 Effect of variation in torch angle



increases leading to greater width at the expense of reinforcement. However, due to the interactive effect of other factors affecting bead geometry, a drop in both width and reinforcement is observed.

3.2 Combined Effect of Welding Variables on Bead Width (W)

The surface graph in Fig. 7a illustrates that with a rise in wire feed rate, the bead width increased for the complete working range of arc voltage. At high welding current, greater quantity of filler wire melts leading to increased width. Similarly, at high values of voltage, a high arc spread leads to an increased width. In Sect. 2.4, mathematical equation (1) confirms the same as the coefficient of A as well as C is positive.

Figure 7b demonstrates that the bead width increased with a rise in voltage at all values of travel speed. However, weld width decreased at higher values of speed even for higher voltages. This is because at higher speed, heat input per unit weld length was lower, reducing the maximum value of width even at maximum voltage.

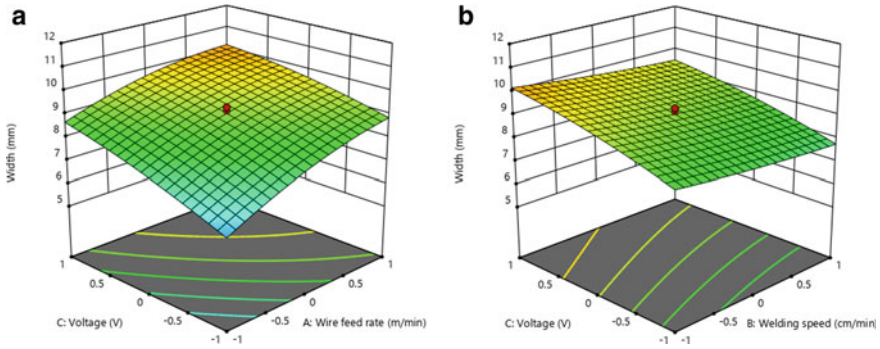


Fig. 7 Combined effect of **a** voltage and wire feed rate, **b** voltage and welding speed on width

These trends can be verified from Sect. 2.4, mathematical equation (1) where the coefficient of C is positive while that of B is negative.

3.3 Combined Effect of Welding Variables on Penetration (P)

Figure 8a shows a fall in the penetration with increasing values of welding speed for complete working range of wire feed rate. While a contrasting trend is seen when the wire feed rate increased at all values of travel speed, a possible reason for this could be the greater or lesser amount of heat supplied to the weldment with a rise in wire feed rate or travel speed, respectively. The mathematical equation (2), given in Sect. 2.4, validates the above observation as the coefficient of A is positive and that of B is negative.

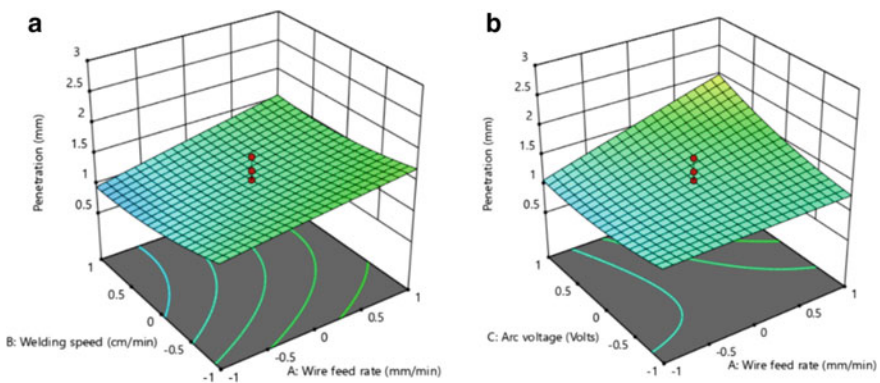


Fig. 8 Combined effect of **a** welding speed and wire feed rate, **b** voltage and wire feed rate on penetration

In Fig. 8b, rise in penetration is observed with an increment in wire feed rate at all values of voltage owing to more input heat content resulting in more melting of the base plate. A similar increase in penetration is seen with a rise in the arc voltage due to the formation of a higher arc cone leading to greater heat supply to the weldment. The same can be confirmed from mathematical equation (2) in Sect. 2.4, where the coefficients of A , C , and AC are positive.

3.4 Combined Effect of Welding Variables on Reinforcement (R)

Figure 9a demonstrates that with a rise in wire feed rate a greater reinforcement height is observed at all values of travel speed. However, a contrasting trend is observed with respect to travel speed. A possible explanation for this observation could be the change in the amount of filler wire melted. The trend observed from the below surface plot can be confirmed from the mathematical equation (3) given in Sect. 2.4, where the coefficient of A is positive and that of B is negative.

For all values of voltage, a rise in reinforcement is observed with an increment in wire feed rate as shown in Fig. 9b. This increase in reinforcement can be attributed to higher filler wire melting. On the other hand, with a rise in arc voltage, the input heat content increases leading to more arc spread at the expense of reduced reinforcement.

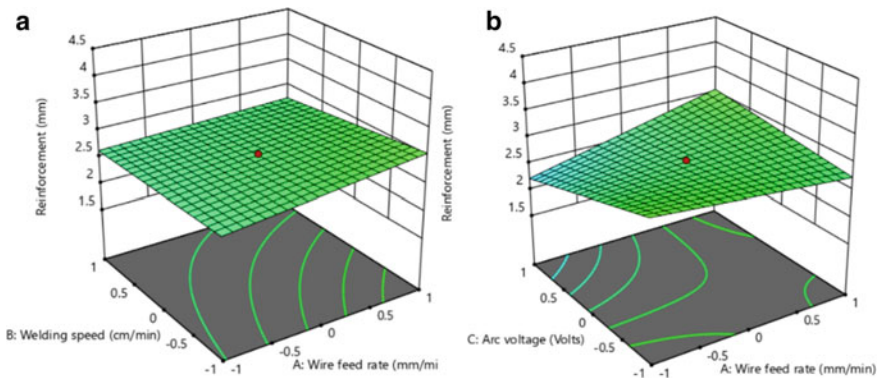


Fig. 9 Combined effect of **a** welding speed and wire feed rate on reinforcement, **b** voltage and wire feed rate

Table 5 Result of single-objective optimization

Response parameter	Objective	Value (mm)	Optimum welding parameters				
			A (m/min)	B (cm/min)	C (Volts)	D (mm)	E (°)
Width (<i>W</i>)	Maximize	11.07	1.50	29.16	20.30	14.72	110
Penetration (<i>P</i>)	Maximize	2.53	0.3	25.89	21.87	11.00	110
Reinforcement (<i>R</i>)	Minimize	1.748	0.50	42.37	19.25	20	110

4 Optimization of Welding Variables

The vital part of this research was to optimize the input variables for attaining the required bead profile. For this, the response optimizer feature in Minitab® was employed. Table 5 gives the result of single-objective optimization, while multi-objective optimization furnished the values of $A = 0.33$ m/min, $B = 27.41$ cm/min, $C = 22$ V, $D = 11.36$ mm, and $E = 93.72^\circ$, at which maximum penetration, minimum height of reinforcement, and maximum width were obtained.

5 Conclusions

In the present study, central composite rotatable design was employed for studying the variation of weld bead dimensions with the selected welding parameters through the development of mathematical models. It can be concluded that in contrast to travel speed, wire feed rate showed a positive effect on all the three bead dimensions. On the other hand, penetration remained nearly constant with an increment in stand-off distance, while, width decreased. Reinforcement showed an inverse relation with arc voltage, stand-off distance, and torch angle. Both bead width and penetration showed a positive trend with respect to arc voltage and a negative trend with respect to torch angle. Among the interaction effects, the combined effect of arc voltage and wire feed rate was observed to have maximum effect on the all response parameters. The peak of penetration (2.53 mm) was attained when the arc voltage neared its maximum value and the wire feed rate was at its lowest working limit. The peak of width (11.07 mm) was achieved at maximum values of torch angle and wire feed rate, while minimum reinforcement was observed to be 1.748 mm when both torch angle and stand-off distance were maximum. The optimal values of input variables suggested are as follows: wire feed rate (A) = 0.33 m/min, welding speed (B) = 27.41 cm/min, voltage (C) = 22 V, stand-off distance (D) = 11.36 mm, and torch angle (E) = 93.72°.

References

1. Bharwal S, Vyas C (2014) Weldability issue of AISI 202 SS (stainless steel) grade with GTAW process compared to AISI 304 SS grade. *Int J Adv Mech Eng* 4
2. Parmar RS (2015) *Welding engineering and technology*
3. Kannan T, Yoganandh J (2010) Effect of process parameters on clad bead geometry and its shape relationships of stainless steel claddings deposited by GMAW. *Int J Adv Manuf Technol*
4. Rao PS, Gupta OP, Murty SSN, Rao ABK (2009) Effect of process parameters and mathematical model for the prediction of bead geometry in pulsed GMA welding. *Int J Adv Manuf Technol*
5. Palani PK, Murugan N (2006) Development of mathematical models for prediction of weld bead geometry in cladding by flux cored arc welding. *Int J Adv Manuf Technol*
6. Murugan N, Parmar RS (1995) Mathematical models for bead geometry prediction in automatic stainless steel surfacing by MIG welding. *Int J Join Mater*
7. Narang HK, Mahapatra MM, Jha PK, Mukherjee I (2012) Modelling and predicting the effects of submerged arc weldment process parameters on weldment characteristics and shape profiles. *Proc Inst Mech Eng Part B J Eng Manuf*
8. Xu WH, Lin SB, Fan CL, Yang CL (2015) Prediction and optimization of weld bead geometry in oscillating arc narrow gap all-position GMA welding. *Int J Adv Manuf Technol*
9. Kim I (1995) Numerical and experimental analysis for the GMAW process
10. Jha MN, Pratihari DK, Dey V, Saha TK, Bapat AV (2011) Study on electron beam butt welding of austenitic stainless steel 304 plates and its input-output modelling using neural networks. *Proc Inst Mech Eng Part B: J Eng Manuf*
11. Kim D, Rhee S (2004) Optimization of a gas metal arc welding process using the desirability function and the genetic algorithm. *Proc Inst Mech Eng Part B: J Eng Manuf*
12. Kim IS, Son JS, Kim IG, Kim JY, Kim OS (2003) A study on relationship between process variables and bead penetration for robotic CO₂ arc welding. *J Mater Process Technol*
13. Cruz JG, Torres EM, Absi Alfaro SC (2015) A methodology for modeling and control of weld bead width in the GMAW process. *J Brazil Soc Mech Sci Eng*
14. Pandey S, Parmar RS (1990) Mathematical models for predicting bead geometry and shape relationships for MIG welding of aluminum alloy 5083. In: *Proceedings of the 2nd international conference on recent trends in welding science and technology, USA*
15. Gunaraj V, Murugan N (1999) Application of response surface methodology for predicting weld bead quality in submerged arc welding of pipes. *J Mater Process Technol*
16. Datta S, Bandyopadhyay A, Kumar Pal P (2009) Modeling and optimization of features of bead geometry including percentage dilution in submerged arc welding using mixture of fresh flux and fused slag. *Int J Adv Manuf Technol*
17. Hsu CH, Chen TC, Huang RT, Tsay LW (2017) Stress corrosion cracking susceptibility of 304L substrate and 308L weld metal exposed to a salt spray. *Mater (Basel)*
18. Benyounis KY, Olabi AG (2008) Optimization of different welding processes using statistical and numerical approaches—a reference guide. *Adv Eng Softw*
19. Khanna P, Maheshwari S (2018) Development of mathematical models for prediction and control of weld bead dimensions in MIG welding of stainless steel 409M. *Mater Today: Proc*

Ultrasonic Metal Welding: A Novel Joining Technique for Phosphor Bronze Sheets



Bharat Sanga, Reeta Wattal, and D. S. Nagesh

Abstract Thin sheets of phosphor bronze are utilized for the manufacturing of a number of small components used in electrical and electronics products. The prevailing joining methods pose restrictions on their applicability and are less supportive of the environment due to the formation of the by-products. Ultrasonic metal welding can bridge this gap owing to its numerous unique features. The present study is executed to explore the ultrasonic weldability of thin phosphor bronze sheets. The experiments are performed according to the Box–Behnken design of the response surface method to investigate the effect of major parameters on the responses such as tensile–shear load, weld area, and interface temperature. The weightage of the parameters and their mutual interaction is analyzed by ANOVA and response surfaces. Two different approaches have been employed to calculate the weld area, and a fairly good correlation of weld area is observed with the weld strength. A regression model has been developed to predict the weld strength, and the parameters are optimized using the simulated annealing algorithm. Further, a study related to the mechanical, thermal, and microstructural characterization of the joint has revealed some more interesting findings of the process and its utility for the applications. Finally, it is concluded that phosphor bronze is a perfect candidate for ultrasonic metal welding. The process can produce sound, flawless, and sufficiently strong joints within the prescribed range of the parameters.

Keyword Ultrasonic welding · Phosphor bronze · Box–Behnken · ANOVA · Response surface method · Simulated annealing optimization · Microstructure

B. Sanga (✉) · R. Wattal · D. S. Nagesh
Department of Mechanical Engineering, Delhi Technological University, Delhi, India

B. Sanga
Department of Mechanical Engineering, Guru Nanak Dev Institute of Technology, Delhi, India

1 Introduction

The emerging interest in the ultrasonic spot metal welding (USMW) vouches for its versatility as a unique metal joining technique. The method was patented about 60 years back [1] but still evolving and striving for its place among other welding techniques. The USMW is capable of joining a large number of similar and dissimilar combinations of materials [2–5], with varying thicknesses in a remarkably short duration. In this process, the workpieces are held together in an overlapping position under moderate pressure and are rubbed locally against each other at low amplitude ultrasonic frequency resulting in the dispersal of the oxide and other contaminants. Instantaneous temperature rise promotes the progressive deformation and shearing at the weld interface and strong micro-bonds form between the pure metallic surfaces of the workpieces [6]. Unlike fusion welding, the temperature rise at the interface is quite lower than the melting temperature of the weld metals (usually in the range of 30% to 50% of the melting temperature) that is why the USMW is treated as a cold welding technique [7]. The process consumes very little energy, spreads no air pollution, and requires no consumables or inert environment. The capability of USMW to join sheets of varying thickness and range of metals makes it stand in a strong contest with other existing joining methods [8]. The thickness, hardness, and orientation (only overlapping) of the weld components pose a limitation on its applications [9]. Considering the above features and limitations, USMW finds its applications in automotive, electronics, and electrical connections as shown in Fig. 1.

Recently, the demand for hybrid vehicles has posed a challenge to the existing auto parts manufacturers to explore new product designs owing to the global shift from the IC engine to electrical vehicles. That is why it is the need of the hour, to look for some efficient, economic, and eco-friendly joining method for highly conductive metals and their alloys such as phosphor bronze (PB). Phosphor bronze provides strong

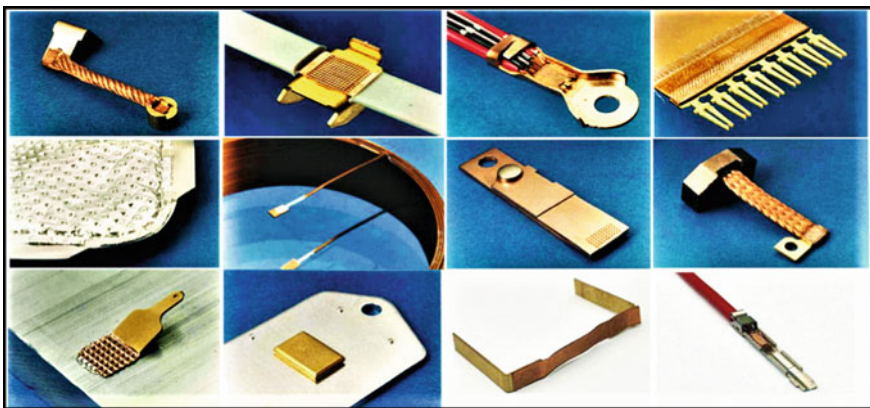


Fig. 1 Applications of ultrasonic metal welding in automotive, electrical, and electronics connections. *Source* TELESONIC Ultrasonics Inc., USA

and flexible connections without sacrificing its conductivity in numerous applications, e.g., battery terminals, electrodes, current collectors, bus bars, etc. [10]. The conventional method like resistance spot welding faces many challenges regarding the quality of the joints due to high thermal conductivity and a low melting point of the weld metals in comparison with other alloys. Even modified forms of the conventional methods such as laser droplet joining [11], duo-thermal soldering [12] and resistance micro-welding [13] face many difficulties when used for the manufacturing of these parts with varied designs of the products. In the present scenario, USMW overcomes these challenges and provides the opportunity to explore the weldability of a wider range of materials and their combinations.

The weldability of the material is evaluated by analyzing the responses at different levels of the process parameters. It is necessary to perform the basic investigation pertaining to the influence of the process parameters on the responses in corroboration with the microstructural evolution in USMW with similar and dissimilar joints. The studies conducted by Elangovan et al. [14], DeVries [7], Kirkpatrick et al. [15], De Leon et al. [16], Bakavos and Pragnell [17] and Yang et al. [18] are important in context to the current work. The current work explores the weldability and feasibility of USMW of standard weld coupons of phosphor bronze sheet. This paper presents the analysis and optimization of the results using different statistical methods. The further investigation includes the influence of the weld energy on the weld area and the weld strength and their correlation. The results are supported by the microstructural evolution.

2 Experimental Details

A 3 kW, 20 kHz Telesonic® make M-4000 ultrasonic metal welder with flat rectangular serrated sonotrode tip of size 13 mm × 10 mm was employed to carry out the experiments. The standard specimens of 100 mm × 25 mm × 0.36 mm were prepared as per ASTM code D1002-05. Preliminary screening experiments resulted in three major parameters, namely weld time (W_t), vibration amplitude (V_a), and weld pressure (W_p) with the specified range shown in Table 1. Three values of each parameter were taken for experiments. The tensile–shear load, weld area, and weld interface temperature were assigned as the response parameters. The design matrix was prepared as per Box–Behnken design of response surface method (RSM)

Table 1 Process parameters and their range

Parameter	Symbol	Parameter levels		
		Low	Middle	High
Weld time (s)	W_t	0.50	0.85	1.20
Weld pressure (MPa)	W_p	0.20	0.28	0.36
Vibration amplitude (μm)	V_a	28.0	31.5	35.0

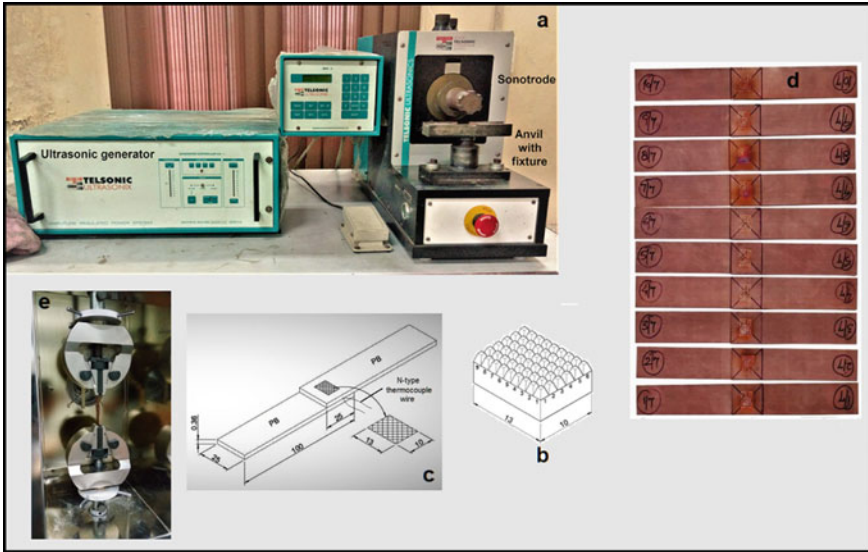


Fig. 2 a Experimental setup, b sonotrode tip serrations, c schematic view of weld coupon, d welded coupons, e tensile–shear load testing of weld coupon

consisting of 15 randomized runs with three replicates each. The joint strength was measured using a computerized universal testing machine. N-type thermocouple wire attached with the data acquisition module was used to measure the real-time interface temperature. The weld area which is the aggregate of a number of tiny weld nuggets in the weld zone was measured employing two different methods using ImageJ software. The analysis of the results was performed using Design Expert 10.0.1 software. Lastly, the microstructural analysis of the interface substantiated the results in support of USMW of PB sheets. The experimental setup, welded coupons, sonotrode tip, and tensile testing are shown in Fig. 2.

3 Methodology

The methodology adopted for this work includes ANOVA analysis of the data obtained from tensile–shear tests. A regression model was developed from the curved response surface created from the experimental data. Further, the process parameters were optimized using the simulated annealing optimization (SAO) algorithm [19] through *simulannealbnd* function of MATLAB optimization toolbox with the initial temperature set at 100 and rate of cooling as 5% reduction in each run.

The strength of the joint is proportional to the weld area. But unlike resistance spot welding, the joint of USMW is an agglomeration of a number of tiny nuggets that collectively provide the strength to the joint. It is comparatively difficult to measure

the accurate weld area; therefore, two different methods were adopted to compute it. In the first method, the average cross-sectional area of one of the teeth on sonotrode tip was calculated and multiplied by the number of teeth present on the surface of the tip. During the tensile–shear load testing, the weld joint was stretched to such an extent that it finally got separated. The second method includes the measurement of the weld area of the scanned and enlarged images of the separated surfaces by ImageJ Ver. 1.52a software.

The third performance characteristic—interface temperature—was measured in real time by a sacrificial thermocouple wire (N-type) having a diameter equal to 0.2 mm. It was attached at the center of the overlap of the weld coupons during welding. The cold junction of the thermocouple was attached with the Data Translation® make DT 9828 data acquisition module which was interfaced with the QuickDAQ software. The QuickDAQ software is capable of converting the temperature values obtained during welding into the graphical form.

Lastly, the effect of weld energy was investigated on three responses—weld strength, interface temperature, and microstructural evolution. Further, the gradual transformation of failure mode with varying energy levels was also established.

4 Results and Discussions

4.1 ANOVA Analysis

The critical F -value (for $\alpha = 0.05$) obtained is $F_{0.95;1,5} = 6.607$, whereas the F -values for W_p , W_t , and V_a are 222.96, 116.99, and 50.25, respectively. As the F -values of all the parameters exceed the critical value, it indicates that all the parameters affect the weld strength significantly. Weld pressure is the most influential parameter, followed by weld time and vibration amplitude. The main effect plots shown in Fig. 3 reveal that W_p affects the weld strength the most (almost 1000 N increment in its range) followed by W_t which increases almost 750 N in its range and the V_a affects least (only 475 N in its range). This is in agreement with the ANOVA results. It is also observed

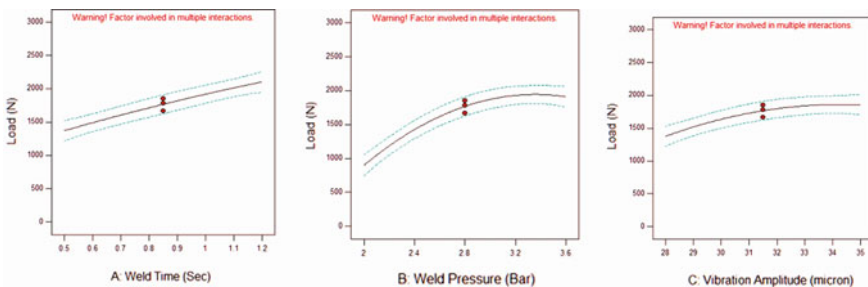


Fig. 3 Main effect plots showing mean weld strength

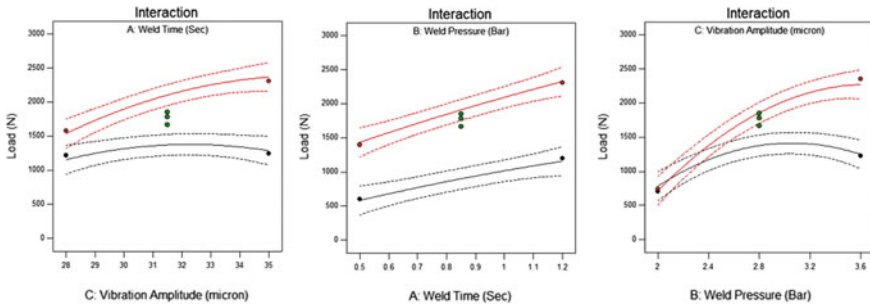


Fig. 4 Interaction effect plots for mean weld strength

that neither weaker nor stronger joints are affected by V_a ; however, W_p affects both weaker as well as stronger joints and W_t affects only stronger joints. The combined effect of parameters is evaluated by F -values during ANOVA analysis. The W_p/V_a combination was found most significant, followed by W_t/V_a combination. But, the effect of W_t/W_p combination was almost negligible. The above facts are also clear from the interaction plots as shown in Fig. 4.

The present study reveals that the individual parameters influence more than their various combinations. However, the outcome is in contrast to some other cases [20]. Different combinations of similar and dissimilar materials have diverse approaches for joint formation. The weld pressure was found as the most prominent parameter which helped in the removal of the surfacial asperities and brought the contacting surfaces closer to each other. It resulted in an increase in the weld area and thus stronger joints.

4.2 Response Surface Analysis

The response surfaces and contour plots between different parameters were developed and shown in Fig. 5. The response surfaces of all the combinations of the parameters have convex curvature with respect to the weld strength. The optimal ranges for the weld strength (more than 2000 N) shown in corresponding contour plots are $W_p > 0.32$ MPa and $W_t > 0.9$ s. (for W_p/W_t combination), $W_t > 1.1$ s. and $V_a > 32$ μm (for W_t/V_a combination), and $W_p > 0.30$ MPa and $V_a > 32$ μm (for W_p/V_a combination). The response surfaces and contour plots drawn with the interacting parameters revealed that all the three parameters needed to be closer to their upper bound to get the maximum value of the weld strength. By increasing the weld time, the process got more time available to remove the contaminants, and mixing of the material at the interface was better. The contacting area increased with enhanced vibration amplitude, whereas higher pressure helped in removing the surface asperities. The cumulative effect was to increase the effective surface area where micro-bonds formed. Thus, higher values of all the three parameters enhanced

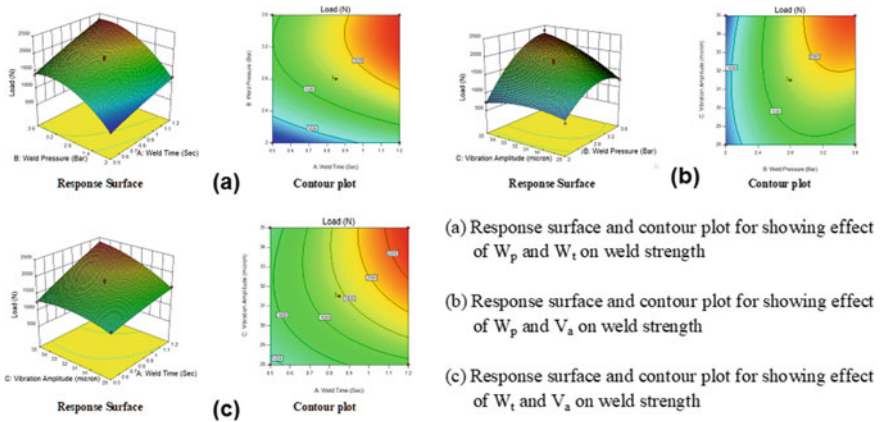


Fig. 5 Response surface and contour plots for different combination of parameters

the possibility of formation of a large number of micro-bonds, and as a result, the weld strength grew further.

A second-order regression model is developed from RSM to predict the weld strength as follows:

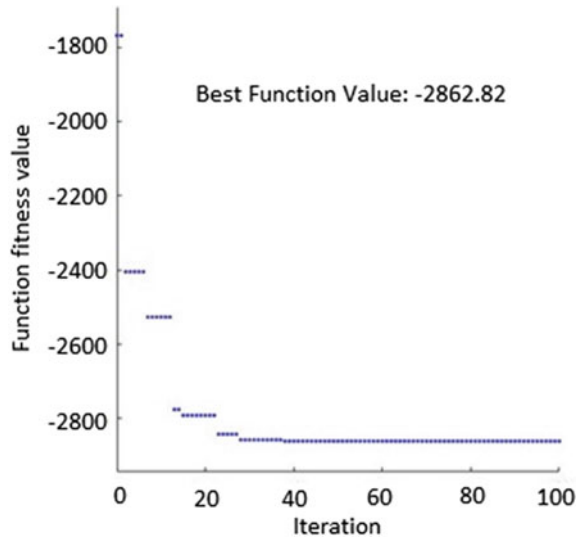
$$\begin{aligned}
 W_p = & -6735.23 + 484.65 * W_p - 3805.71 * W_t + 446.58 * V_a \\
 & + 282.44 * W_t * W_p + 142.04 * W_t * V_a + 97.50 * W_p * V_a \\
 & - 565.08 * W_p^2 - 243.41 * W_t^2 - 12.25 * V_a^2
 \end{aligned}
 \tag{1}$$

where W_p is the predicted weld strength. The coefficient of determination was calculated to estimate the closeness and significance of the regression model. The predicted results obtained by the regression model are very well fitted with the experimental results with the coefficient of determination (R^2) equal to 0.99. Therefore, regression model can be used for predicting the weld strength within the given range of the parameters. The regression model was further implanted with a metaheuristic technique (simulated annealing optimization) to optimize the parameters.

4.3 Optimization by Simulated Annealing Algorithm

After conducting a number of trials with various combinations of the parameters, the optimum values of all the three parameters were obtained. It was observed that the values were at the upper bound for all the three parameters in the given range and the chosen material. The convergence plot of SAO shown in Fig. 6 indicates the load at optimal parameters. To corroborate the findings of the optimization, five confirmatory weld coupons were prepared and tested for the tensile–shear load. The mean value

Fig. 6 Convergence plot of SAO



obtained from the confirmatory tests was found very close to the estimated value with a small error (almost 5%).

4.4 Calculation of Weld Area

Figure 7 shows the separated interface with a number of broken macro-bonds. The cumulative weld area of all the macro-bonds was calculated by employing two

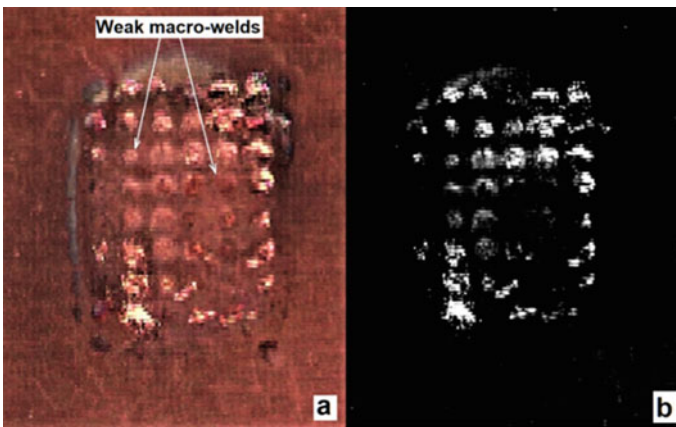


Fig. 7 a) Weld interface showing weak bonds, b) ImageJ threshold view of the bonds

different methods and correlated with the strength of the joint. The coefficient of correlation calculated was 0.77 which indicates a sufficiently strong relation between the joint area and the joint strength. The analysis of the weld area revealed that some of the spots at the separated interface looked like weld nuggets but actually they were not strong enough to contribute to the strength of the weld joint. That is why some of the joints had a larger weld area in comparison with other weld coupons but still had a lesser value of the tensile–shear load. The reason for this anomaly is that more material flow in the convoluted and spiral form at the weld interface made it thinner and hotter which resulted in breaking of the weaker joints, whereas properly built-up joints became stronger upon cooling at the end of the weld cycle.

4.5 Effect of Weld Energy

To investigate the effect of weld energy on the weld strength, the weld specimens were prepared in energy mode, and the temperature at the weld interface was measured by an N-type thermocouple in real time with the help of a DAQ module. The temperature profiles were drawn and analyzed with respect to the weld energy. The temperature rose instantly to its peak value and dropped gradually after the formation of the joint as shown in Fig. 8. There is a remarkable difference in the rate to temperature rise and temperature fall. The maximum temperature value is achieved in the time duration equal to the weld time, whereas it takes about 100 s to reach the room temperature. The instant temperature rise promotes the micro-bond formation due to enhanced dislocation integration. A slower rate of cooling at a later stage helps in achieving a uniform grain structure at the joint interface. It is observed that the peak temperature is almost 1/3rd of the melting temperature of phosphor bronze; hence, the possibility of melting is ruled out.

The tensile–shear load starts increasing at a slow pace initially (stage A) but starts increasing rapidly with increasing weld energy (stage B) till the load value becomes almost stable (stage C) in the end as shown in Fig. 9. The peak value of the tensile–

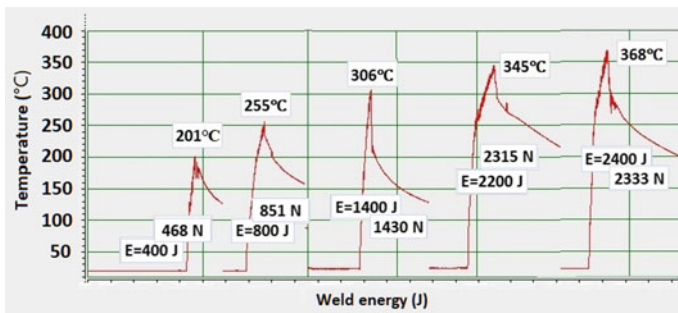


Fig. 8 Temperature profile of weld interface with respect to weld energy

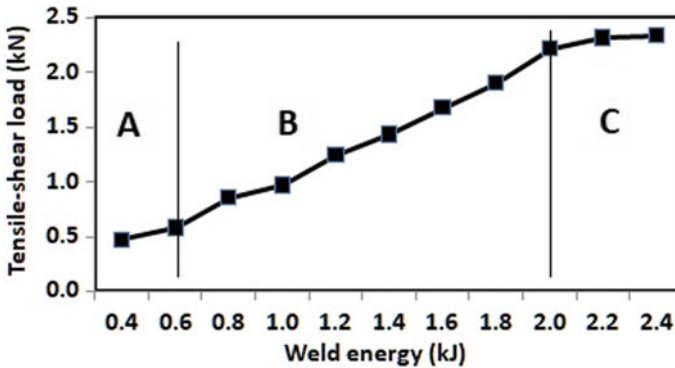


Fig. 9 Graph between tensile–shear load and weld energy showing different stages

shear load was achieved at 2.4 kJ of weld energy. A minimum value of weld energy initiated the micro-bond formation at the interface (stage A) and as more energy is dissipated at the weld interface, the interfacial temperature increased resulted in a rise in the number and size of the micro-bonds, and therefore higher value of the weld strength was recorded (stage B). The micro-bonds propagated at a faster rate at higher-energy levels and finally got saturated at some higher value of the weld energy, thus no remarkable change in the tensile–shear load was observed after a particular value of the weld energy (stage C). A minimum value of temperature rise is necessary to initiate the joint formation at the weld interface that goes up with the input of more weld energy. At lower weld energy, the joint is failed by the detachment of the overlapped surfaces. But at higher-energy values, the joint was stronger and failed by partial nugget pull-out. The joint surface starts burning due to excessive heat formation at the weld interface once stage C is passed.

The failure mode of the weld joint changed continuously when weld energy was varied. At lower values of the weld energy, the mode was debonding of the interface, which eventually changed to partial nugget pull-out mode at a higher-energy level as shown in Fig. 10.

4.6 Microstructural Analysis

The microscopic examination of the weld joint section at lower and higher-energy levels revealed that the parting line vanishes at higher-energy levels due to uniformly merged grains in the bonding region. The flow of material is visible in Fig. 11 in the bonding region which demonstrates that interlocking takes place at a higher-energy level. This observation justifies the increased weld strength at higher-energy levels. The present study suggests that the joint formation may be due to the combined effect of the micro-bonding and mechanical interlocking. The value of interface temperature was very less than the melting temperature of PB, and the welding time

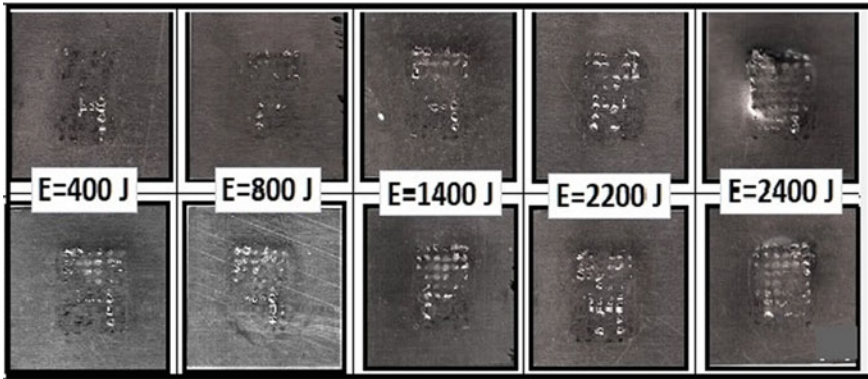


Fig. 10 Fractured specimens in the tensile–shear strength test showing increasing weld area with increasing weld energy

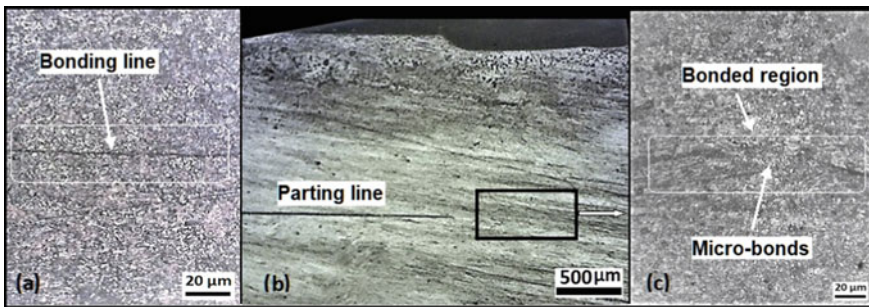


Fig. 11 Micrographs of weld interface cross section **a** bonding line is visible at low-energy value, **b** bonding at high weld energy at low resolution, **c** enlarged view of bonding region at high weld energy

was also very small so the possibility of melting and inter-atomic diffusion at the interface is nil. There was no change in the size of the grains, so re-crystallization did not take place. As the friction force dispersed the oxide layer from the interface and the pure metallic surfaces got exposed, the micro-bonding joined the contacting surfaces through metallurgical adhesion, and the strength of the joint is enhanced due to mechanical interlocking of the material.

5 Conclusions

The current study conducted as USMW of 0.36–mm-thick phosphor bronze sheets investigates the effect of influential parameters on the weld strength which is the major quality parameter for spot joints in electrical connectors in many applications.

The weld joints formed by USMW in phosphor bronze sheets incorporate many inherent advantages. The conclusions drawn on the basis of the findings clearly show that USMW proves to be a promising joining method for the manufacturing of many electrical and electronics components. Following outcomes are concluded in this study:

- USMW of phosphor bronze sheets produces strong, sound, and flawless spot joints in a remarkably short duration and with low-energy consumption. Weld pressure (W_p) and its combination with vibration amplitude (W_p/V_a interaction) are the most influencing parameters for weld strength.
- The parametric optimization using simulated annealing algorithm resulted in the following values of the parameters: 0.36 MPa of weld pressure, 1.2 s. of weld time, and 35 μm of vibration amplitude. The estimated weld strength is 2862.8 N.
- The weld area calculated using two different methods reveals that a strong correlation exists between the weld area and the weld strength. If weld energy is increased in substantial amount, it results in the threefold increase in the weld area and the weld strength. It shows that weld area and weld strength are closely connected.
- The thermal profiles of interfacial temperature clarify that there are no chances of joining by melting of the weld metals. The weld strength increases almost four times with increasing weld energy. The joint failure mode changed from sheet detached mode at low-energy value to partial pull-out mode at higher-energy values.
- The bond formation is characterized by the uniform structure in and around the bonding region. The joining line appears at a low-energy level but eventually vanishes at higher-energy levels. The convoluted wavy shape of the flow of the grains verifies the mechanical interlocking of the material at a higher-energy level showing more weld strength.

References

1. Jones JB, Elmore WC, De Prisco CF (1960) Method and apparatus employing vibratory energy for bonding metal
2. Zhu Z, Lee KY, Wang X (2012) Ultrasonic welding of dissimilar metals, AA6061 and Ti6Al4V. *Int J Adv Manuf Technol* 59(5–8):569–574. <https://doi.org/10.1007/s00170-011-3534-9>
3. Pop-Calimanu M (2013) Optimization of ultrasonic welding parameters and temperature. In: Conference on Proceeding—Metal. Brno, Czech Republic, EU, no 1, pp 1–7
4. Matsuoka SI (1998) Ultrasonic welding of ceramics/metals using inserts. *J Mater Process Technol* 75(1–3):259–265. <https://doi.org/10.2472/jsms.54.1191>
5. Lu P, Zhi L, Gao Q, Liu YH, Wang ZH (2017) Repairing ultrasonic welded carbon fiber—reinforced nylon 66. *Compos Suppl Weld J* 439–450
6. Kim W, Argento A, Grima A, Scholl D, Ward S (2011) Thermo-mechanical analysis of frictional heating in ultrasonic spot welding of aluminium plates. *Proc Inst Mech Eng Part B J Eng Manuf* 225(7):1093–1103. <https://doi.org/10.1177/2041297510393664>
7. De Vries E (2004) Mechanics and mechanisms of ultrasonic metal welding. Ph.D. Thesis, The Ohio State University

8. Neppiras EA (1965) Ultrasonic welding of metals. *Ultrasonics* 3(3):128–135. [https://doi.org/10.1016/S0041-624X\(65\)80003-8](https://doi.org/10.1016/S0041-624X(65)80003-8)
9. Matheny MP, Graff KF (2014), Ultrasonic welding of metals. Elsevier Ltd.
10. Weight BL, Magleby SP, Howell LL (2007) Configuration selection, modeling, and preliminary testing in support of constant force electrical connectors. *Trans ASME* 129:236–246. <https://doi.org/10.1115/1.2721080>
11. Weigl M, Schmidt M, Govekar E, Jeric A (2009) Laser droplet generation: application to droplet joining. *CIRP Ann Manuf Technol* 58:205–208. <https://doi.org/10.1016/j.cirp.2009.03.005>
12. Consiglio S, Fleschutz T, Seliger G, Seutemann J (2006) Development of a duothermal soldering process. *Ann CIRP* 55(1):1–4. [https://doi.org/10.1016/S0007-8506\(07\)60360-6](https://doi.org/10.1016/S0007-8506(07)60360-6)
13. Mo B, Guo Z, Li Y, Huang Z, Wang G (2011) Mechanism of resistance microwelding of insulated copper wire to phosphor bronze sheet. *Mater Trans* 52(6):1252–1258. <https://doi.org/10.2320/matertrans.M2011013>
14. Elangovan S, Prakasan K, Jaiganesh V (2010) Optimization of ultrasonic welding parameters for copper to copper joints using design of experiments. *Int J Adv Manuf Technol* 51(1–4):163–171. <https://doi.org/10.1007/s00170-010-2627-1>
15. Kirkpatrick MP, Gelatt S, Vecchi CD (1983) Optimization by simulated annealing. *Science* 220(4598):671–680. <https://doi.org/10.1017/CBO9781107415324.004>
16. Shin HS, De Leon M (2015) Parametric study in similar ultrasonic spot welding of A5052–H32 alloy sheets. *J Mater Process Technol* 224:222–232. <https://doi.org/10.1016/j.jmatprotec.2015.05.013>
17. Bakavos D, Prangnell PB (2010) Mechanisms of joint and microstructure formation in high power ultrasonic spot welding 6111 aluminium automotive sheet. *Mater Sci Eng A* 527(23):6320–6334. <https://doi.org/10.1016/j.msea.2010.06.038>
18. Yang JW, Cao B, He XC, Luo HS (2014) Microstructure evolution and mechanical properties of Cu—Al joints by ultrasonic welding. *Sci Technol Weld Join* 19(6):500–504. <https://doi.org/10.1179/1362171814Y.0000000218>
19. Yang SH, Srinivas J, Mohan S, Lee DM, Balaji S (2009) Optimization of electric discharge machining using simulated annealing. *J Mater Process Technol* 209(9):4471–4475. <https://doi.org/10.1016/j.jmatprotec.2008.10.053>
20. Zhao D, Ren D, Zhao K, Pan S, Guo X (2017) Effect of welding parameters on tensile strength of ultrasonic spot welded joints of aluminum to steel—by experimentation and artificial neural network. *J Manuf Process* 30:63–74. <https://doi.org/10.1016/j.jmapro.2017.08.009>

An Investigation to Different Methods of Health Assessment in Power Transformers



Anuj Banshwar, Naveen Kumar Sharma, Mohit Pathak,
Bharat Bhushan Sharma, and Sujit Kumar

Abstract Power transformer is the critical device of the power system. As essential equipment, its operation plays a vital place in reliability of electrical power system. Important methodologies for accessing transformer health have been discussed in the present work.

Keywords Duval triangle · Health assessment · Ratio method

1 Introduction

Power transformer is the critical device of the power system. As essential equipment, its operation plays a vital place in reliability of electrical power system. It has an ability to change V–I levels to facilitate electrical power system in economic manner. Figure 1 shows the fault categorization as per IEC (std. 60599) and IEEE (std. C.57.104) standards [1].

A. Banshwar (✉)
Government Polytechnic Puranpur, Pilibhit, Uttar Pradesh, India

N. Kumar Sharma
IKGPTU Main Campus, Jalandhar, Punjab, India

M. Pathak
Noida Institute of Engineering & Technology, Greater Noida, Uttar Pradesh, India

B. B. Sharma
School of Automation, Banasthali Vidyapith, Rajasthan, India

S. Kumar
Jain (Deemed to be University), Bangalore, Karnataka, India

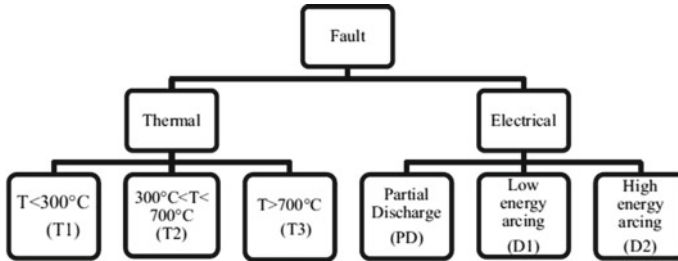


Fig. 1 Categorization of faults in power transformer

Flashover with power follow through can destroy the transformer, in which case the fault and evidence of damage will confirm, or indicate the cause of failure. In the latter case, if the flashover has taken place inside the tank, DGA results after failure indicate the severity of the fault. Broken or loose connections in winding, lead to a small arc, which burns the surrounding solid insulation and can result in transformer sudden failure. Deteriorated conductor insulation paper, i.e., as a result of a previous short of the transformer two adjacent turns and forming a closed loop around the main magnetic flux. This loop will melt down in seconds due to excessive high induced current flow. A broken, loose, or damaged draw rod in a bushing can cause sparking and arcing within the bushing tube and cause melt down of adjoining copper, producing gas. The buchholz relay may activate and disconnect the transformer from the system. In extreme cases, the bushing may explode and lead to fire.

In this paper, the key methodologies of combined DGA method (see block diagram in Fig. 2) for accessing transformer health have been discussed.

2 Ratio Methods

The ratio methods use gas ratios to find possible fault in the sample. The base of such methods depends upon the experience of the investigator by correlating the gaseous analyses with the fault type. The typical methods that comes under this category are as follows.

2.1 Doerneburg Ratio Method

It employs gas concentrations from which Ratios R_1 , R_2 , R_3 , and R_4 are calculated. In this method, the values for these gases are first compared to special concentrations L_1 given in Fig. 3 [2].

The ratios R_1 , R_2 , R_3 , and R_4 are compared to restrictive limits, providing a fault diagnosis methodology as suggested in flowchart (see Fig. 4). This gives the

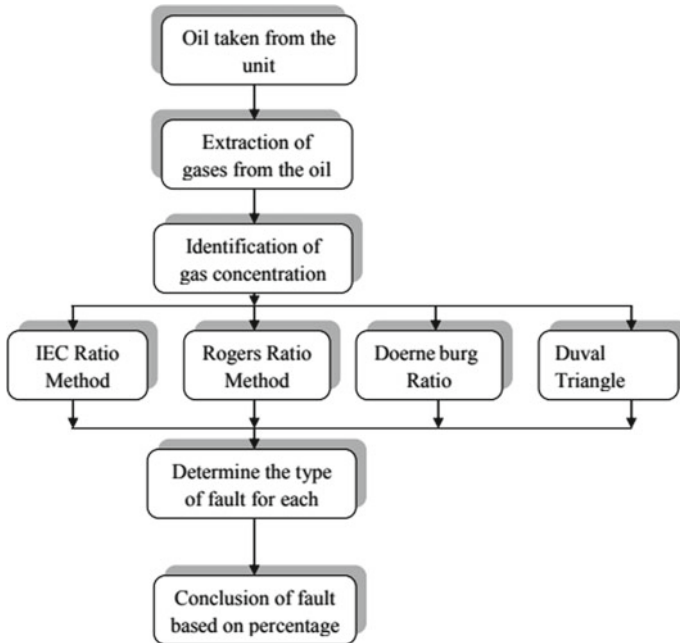


Fig. 2 Block diagram of combined DGA

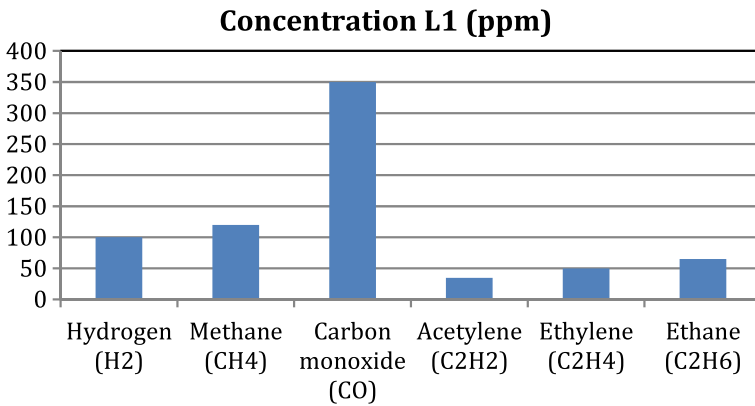


Fig. 3 Concentration limits of dissolved gases

restrictive values for ratios of gases dissolved in the oil and gases obtained from the transformer gas space or gas relay [3].

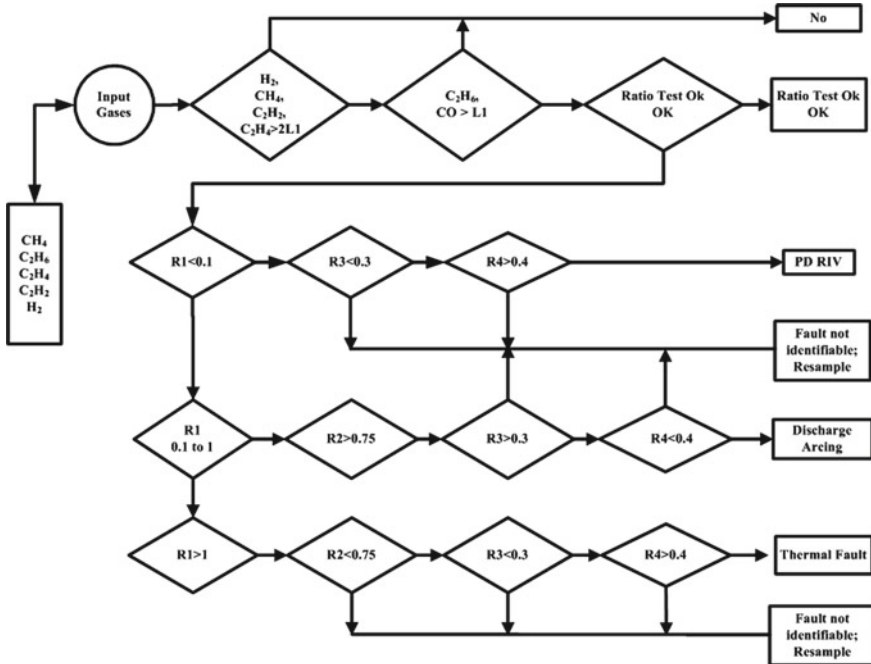


Fig. 4 Flowchart for Doerneburg ratio method

2.2 Roger Ratio Method

Herein, four gas ratios $R_1 = (CH_4/H_2)$; $R_6 = (C_2H_6/CH_4)$; $R_5 = (C_2H_4/C_2H_6)$; $R_2 = (C_2H_2/C_2H_4)$ are calculated, and faults are diagnosed based on a coding scheme and a methodology given in flowchart (see Fig. 5) [3].

2.3 IEC Ratio Method

Since the ratio R_6 is a temperature indicator in RR method, it has been dropped here. Herein, the ratio codes have different ranges as illustrated in flowchart given in Fig. 6 [4].

3 Duval Triangle Method

This method is employed with transformers insulated with the help of oil and is considered to be one of the most accurate fault diagnosis tool that comes under DGA

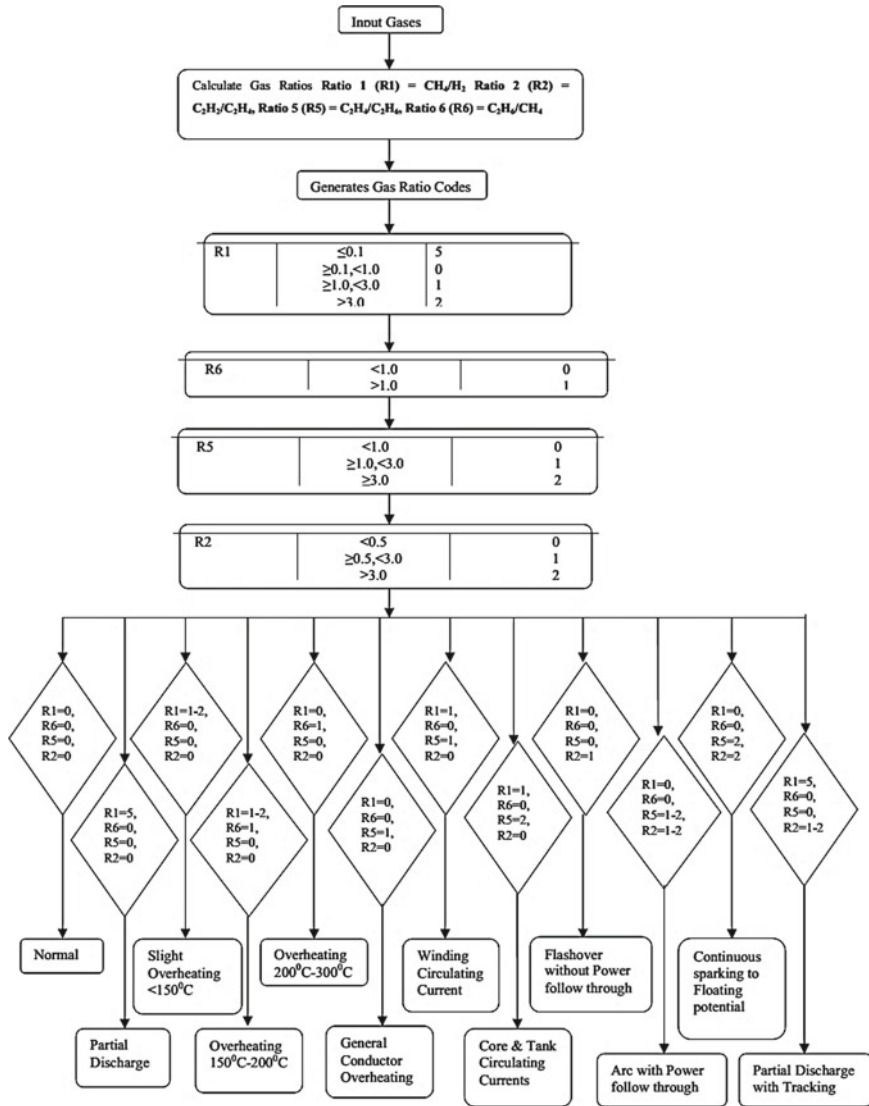


Fig. 5 Flowchart for Roger ratio method

[5]. This method uses methane, ethylene and acetylene as hydrocarbon gases only. The duval triangle is shown in Fig. 7.

where coordinates [6]:

$$\%C_2H_2 = \frac{100C_2H_2}{C_2H_2 + C_2H_4 + CH_4}$$

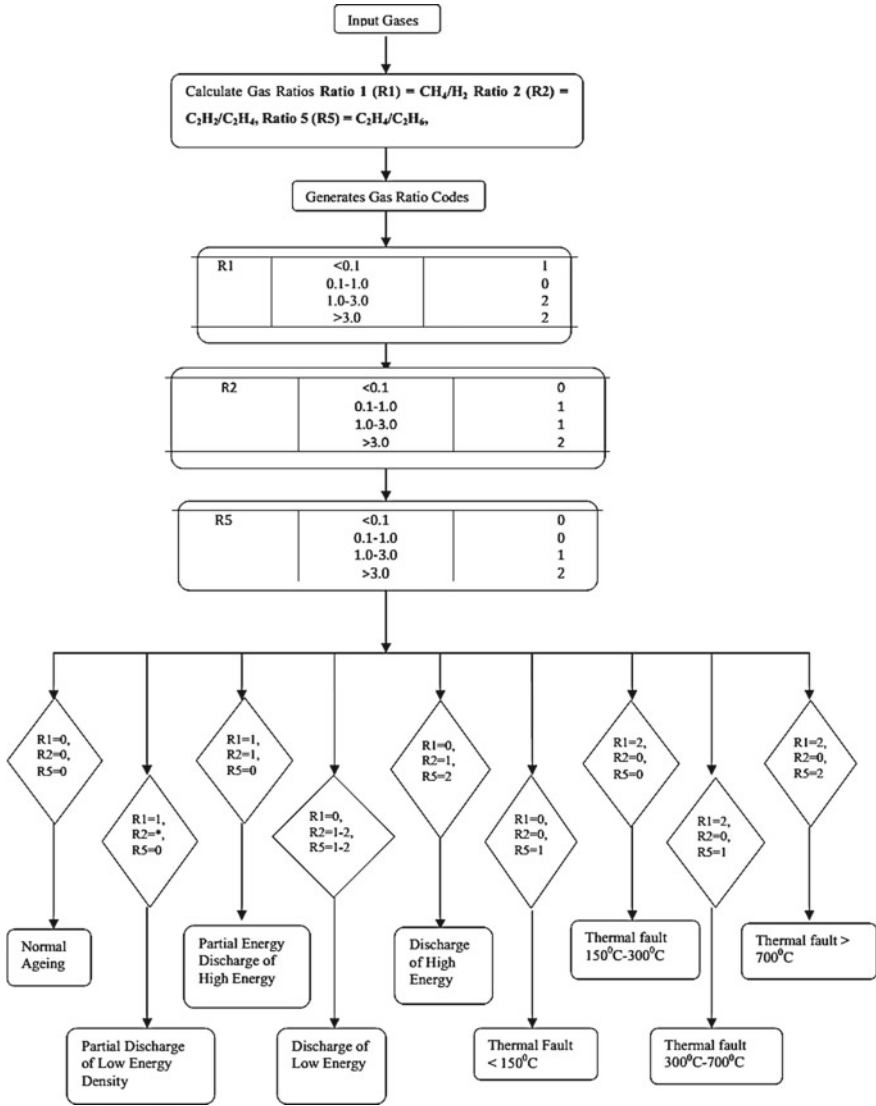


Fig. 6 Flowchart for IEC ratio method

$$\%C_2H_4 = \frac{100C_2H_4}{C_2H_2 + C_2H_4 + CH_4}$$

$$\%CH_4 = \frac{100CH_4}{C_2H_2 + C_2H_4 + CH_4}$$

The flowchart for this method is illustrated in Fig. 8.

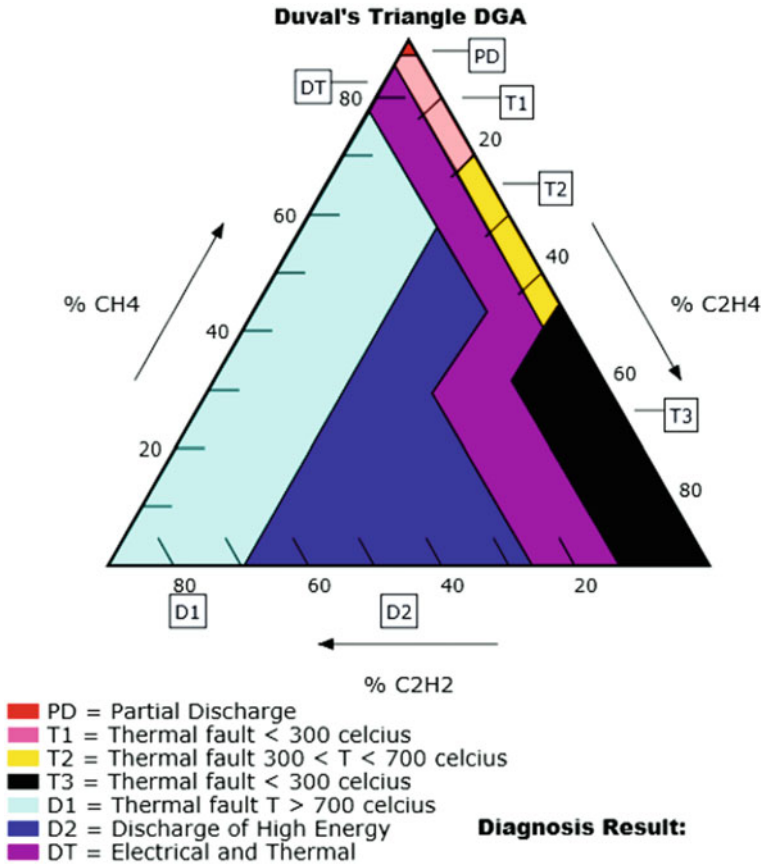


Fig. 7 Duval triangle

4 Conclusion

In this paper, a brief study has been carried out related to commonly used methodologies for power transformer health assessment. These techniques include a methodology-based monitoring system to take health tests of power transformers.

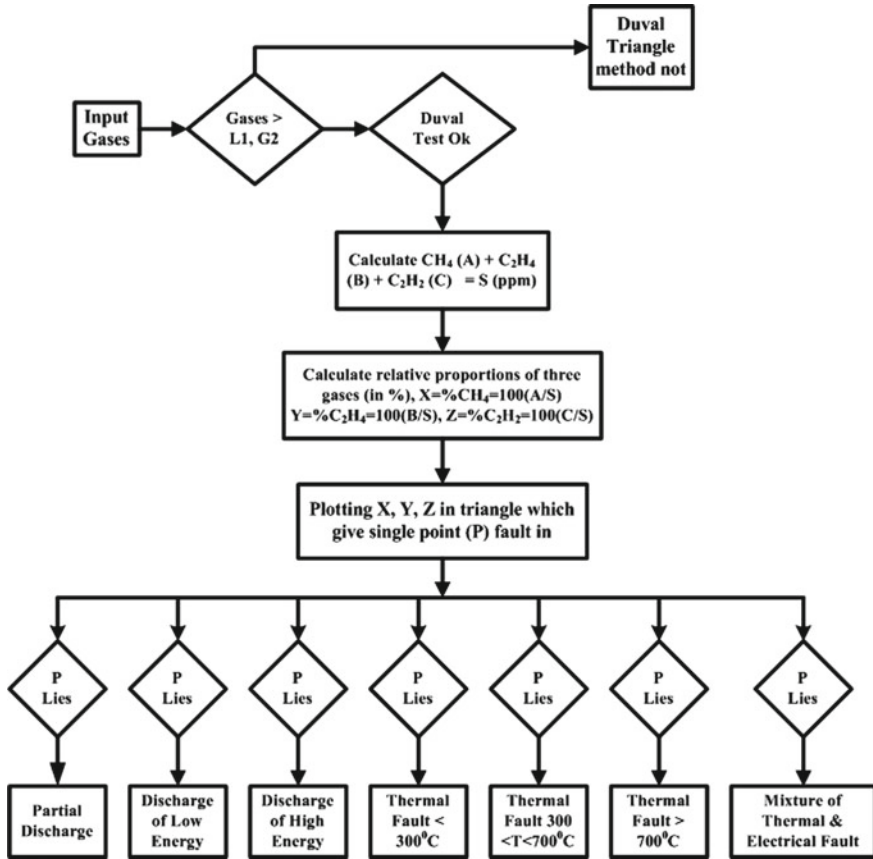


Fig. 8 Flowchart for duval triangle method

References

1. Gupta A, Jain K, Sood YR., Sharma NK (2018) Comparative study of duval triangle with the new DGA interpretation scheme. In: Advances in system optimization and control. Lecture notes in electrical engineering, vol 509. Springer, Singapore, pp 261–268
2. Febriyanto A, Saha TK (2008) Oil-immersed power transformers condition diagnosis with limited dissolved gas analysis (DGA) data. In: Australasian Universities power engineering conference (AUPEC), pp 073
3. ANSI/IEEE Std C57.104-1991 (1992) IEEE guide for the interpretation of gases generated in oil-immersed transformers. IEEE Power Engineering Society
4. Roger RR (1978) IEEE and IEC codes to interpret incipient faults in transformers, using gas in oil analysis. IEEE Trans Electr Insulation 13(5):349–354
5. Bakar NA, Abu-Siada A, Islam S (2014) A review of dissolved gas analysis measurement and interpretation techniques. IEEE Electr Insulation Mag 30(3):39–49
6. Patel A, Sharma NK, Banshwar A, Sharma BB, Pathak M (2020) An evaluation of different health assessment methods on 50 MVA power transformer: a case study. In: 2020 IEEE students conference on engineering and systems (SCES), Prayagraj, India, pp 1–5

Effect of MgO Powder Addition in Synthesis of Recycled Waste Bagasse Reinforced Green Composite Materials



Nitin Srivastava, Shashi Prakash Dwivedi, V. K. Dwivedi, and Rajat Yadav

Abstract Bagasse waste comes out from the sugar mill. This waste often causes pollution in many ways outside the sugar mill. Also, when bagasse waste rots, it gives rise to various viruses. This virus causes great harm to the health of people. This study attempts to make composite materials using bagasse waste. Composite made using stir casting apparatus. Microstructure outcome showed uniform spread of carbonized bagasse ash and magnesium oxide powder in Al-base matrix material. Maximum tensile strength and ductility were found to be 103 MPa and 20.83%, respectively, for composition Al/2.5 wt.% carbonized bagasse ash/12.5 wt.% magnesium oxide powder composite. Highest hardness has been found 78 HRB for composition Al/0% carbonized bagasse/15% magnesium oxide powder composite. However, toughness and expenditure of bagasse ash reinforced composite decrease by enhancing percentage of reinforcing agent.

Keywords Solid waste bagasse · Clean technology · Environment pollution · MgO powder · Mechanical properties

1 Introduction

For the betterment of materials in terms of physical, chemical and mechanical properties, the composite is useful. Combination or mixing of two or more than two things is called composite. All the materials have different physical, chemical and mechanical properties. Matrix and reinforcement are the two advantageous things to increase the mechanical, physical and chemical property [1]. Compare of bulk materials with

N. Srivastava

Dr. A.P.J. Abdul Kalam Technical University, Lucknow, Uttar Pradesh 226031, India

S. P. Dwivedi (✉)

G. L. Bajaj Institute of Technology and Management, Gautam Buddha Nagar, Greater Noida, Uttar Pradesh 201310, India

V. K. Dwivedi · R. Yadav

Department of Mechanical Engg, IET, GLA University, Mathura, Uttar Pradesh 281406, India

© The Author(s), under exclusive license to Springer Nature Singapore Pte Ltd. 2022

757

K. Govindan et al. (eds.), *Advances in Mechanical and Materials Technology*,

Lecture Notes in Mechanical Engineering,

https://doi.org/10.1007/978-981-16-2794-1_67

composite materials shows, and composite materials is better because composite material has high stiffness and strength. Stiffness and strength are developing by the reinforcing phase. Mostly matrix is less hard and less strong than the reinforcement. Either particulate or fibre type reinforcement is there. Particulate composite has regular or irregular shape but its dimension is circa to all directions. Continuous fibre composite is much stiff and stronger than the particulate composite; due to this, it is costly also. Processing is the snag of the particulate composite due to which reinforcement is utilized less [2–4]. This pure aluminium is used with bagasse and MgO. Combination of aluminium and bagasse is called composite, and a combination of aluminium, bagasse and MgO is called hybrid [5].

Aluminium is very common in our earth, and it is utilized everywhere but mostly in engineering field. It has major qualities like it is very durable, light and very important it is functional [6–8]. Due to all this, it is the most important material all the time. It is used in fridge, automobiles, mobiles, aircraft, trains and many more [9]. Magnesium oxide is also utilized in this work. It is a white powder tasteless substance which has a melting point 2800 °C, and it is used in various factors like pharmaceuticals and food packaging. MgO is the combustion of MgCO_3 and $\text{Mg}(\text{OH})_2$. For improving the mechanical properties of composite, MgO is considered as secondary reinforcement. MgO is utilized in the aluminium matrix for enlarging the strength, thermal stability and abrasive wear [10, 11].

Bagasse is a waste of material from sugarcane. It affects the environment very much due to which environment condition is become traumatized. But nowadays, it is useful for various factors like production of electricity and to enhance mechanical and physical properties of substance [12]. The environment becomes eco-friendly by the use of bagasse. While using all together like MgO, bagasse and aluminium, a hybrid is formed, and while forming hybrid, mechanical properties as toughness, hardness and tensile strength are calculated.

2 Materials and Methods

2.1 Matrix Material

Pure aluminium is used whose have 99% alumina. Today aluminium is used in most of the material like planes, automobiles, toys, building structure and many more. Aluminium has there owned mechanical properties which describe in Table 1. The main purpose is to increase the mechanical properties while using reinforcement. Aluminium is a matrix material in this and to enhance mechanical and physical properties of aluminium is main purpose.

Table 1 Mechanical properties [11, 12]

S. No.	Properties	Values
1	Yield strength	93 MPa
2	Hardness	30 HRB
3	Toughness (Charpy test)	50 J
4	Ductility (per cent elongation)	19.44%
5	Melting temperature	660 °C

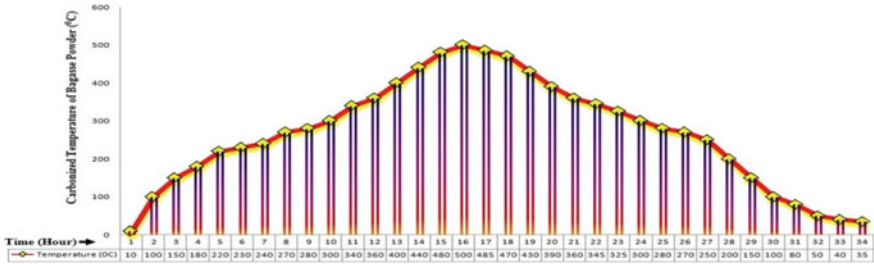


Fig. 1 Carbonized temperature of bagasse powder with in time (hour)

2.2 Reinforcement Materials

2.2.1 Primary Reinforcement Material (Agricultural Sugarcane Waste (Bagasse))

Bagasse particles are the primary reinforcement material, and it consists of ceramic materials. The liquid is completely removed from sugarcane under the sun. Sugarcane powder is produced when dried sugarcane was grinding. For carbonized, the sugarcane powder is heated at 500 °C for removing the carbonaceous material. Consider the sugarcane particle whose particle size is examined. The pattern of un-carbonized sugarcane powder and carbonized sugarcane powder was considered as reinforcement particles. 15% is the highest amount of sugarcane powder with zero amount of MgO is considered (Fig. 1).

The dried sugarcane bagasse, which has carbonaceous material, has different chemical properties which shown in Table 2, and the burned dried sugarcane bagasse, which does not have carbonaceous material, has different chemical properties which shown in Table 3.

2.2.2 Magnesium Oxide (MgO) as Secondary Reinforcement

MgO is secondary reinforcement material whose properties are shown in Table 4. For improving the mechanical properties of composite, MgO is considered as secondary

Table 2 Experimental with chemical of dried and washed bagasse powder [11, 12]

S. No.	Composition of substance	Wt. per cent (%)
1	Ash	1–4
2	Hemi-cellulose	20–25
3	Lignin	18–24
4	Cellulose	45–55
5	Waxes	< 1

Table 3 Comparison chemical properties between carbonized bagasse ash and cement [11, 12]

S. No.	Characteristic (%)	Carbonized bagasse ash	Cement
1	SiO ₂	72.8	19.4
2	Al ₂ O ₃	6.4	4.0
3	Fe ₂ O ₃	5.5	3.6
4	CaO	3.8	64.5
5	MgO	2.3	1.5
6	K ₂ O	2.7	0.4
7	Na ₂ O	1.2	0.5

Table 4 Chemical properties of magnesium oxide powder

S.No	Properties	Values
1	Density	3.58 g/cm ³
2	Appearance	White powder
3	Boiling point	3600 °C
4	Molecular weight	40.3 g
5	Melting point	2852 °C

reinforcement. Enlarging the strength, thermal stability and abrasive wear introduces MgO in the aluminium matrix. The density of aluminium alloy (2.7 g/cm³) is very near to MgO (3.58 g/cm³) which consider MgO as a secondary reinforcement for aluminium metal matrix composite. MgO has good resistance for acid, molten salts up to 8000 °C and alkalis. The main reason to consider MgO is it has good measurement with Al-alloys while adding it and it is easily available.

2.2.3 Development of Composite Materials

Electric furnace casting setup is utilized to fabricate metal matrix composite which shows in Fig. 2. Electric furnace technique was used for the preparation of metal matrix composite and hybrid metal matrix composite. In electric furnace, matrix

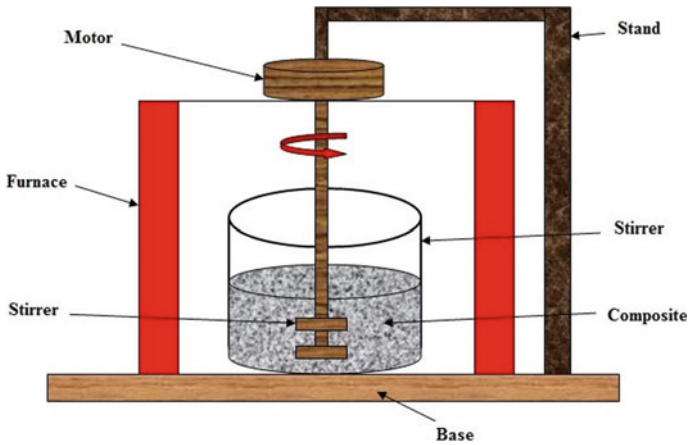


Fig. 2 Schematic diagram of stir casting rout [11]

material was heated above its liquid temperature. Now aluminium and bagasse are mixed together in electric furnace and preheated, and the reinforcement particles, which mean bagasse, are helped to remove the testability problem. The liquid aluminium alloy was drizzle into sugarcane (bagasse). MgO powder is a secondary reinforcement which was mixed in melt alloy. While taking out the metal matrix composite and hybrid metal matrix composite from electric furnace, melted composite was completely converted into a solid composite. From the middle regions of the composites, the samples were taken out for the study and are shown in Fig. 2.

2.2.4 Sample Preparation and Material Testing

There are two types of reinforcement is used for the preparation of composite, sugarcane waste powder (bagasse) and MgO powder. Stir casting technique was utilized for preparation of metal matrix composite. Mixing of aluminium and sugarcane powder helps to form metal matrix composite, and mixing of aluminium, sugarcane powder and MgO powder utilized for making hybrid metal matrix composite. After preparation of metal matrix composite, testing sample was prepared from this reinforcing agent. The impact of sample is utilized in several experimental analyses as thermal expansion and corrosion (Table 5).

2.2.5 Microstructure Sample

It is difficult to prepare reinforced particle metal matrix composite because sugarcane particle has a lower density. While mixing higher and lower density material, it is very tough to avoid losses like cracks, relief, etc. Power hacksaw was utilized for cutting the cast samples. It was used for cutting the uneven surfaces and taken

Table 5 Composition of prepared sample

S. No.	Sample Designation	Composition	Wt. % of Un-carbonized Bagasse Powder	Wt. % of Carbonized Bagasse Powder	Wt. % of MgO Powder
1	G1	Al + 2.5 % Uncarbo. Bagasse	2.5%	-	-
2	G2	Al+ 5 % Uncarbo. Bagasse	5%	-	-
3	G3	Al+ 7.5 % Uncarbo. Bagasse	7.5%	-	-
4	G4	Al+ 10 % Uncarbo. Bagasse	10%	-	-
5	G5	Al+ 12.5 % Uncarbo. Bagasse	12.5%	-	-
6	G6	Al+ 2.5 % Carbo. Bagasse	-	2.5%	-
7	G7	Al+ 5 % Carbo. Bagasse	-	5%	-
8	G8	Al+ 7.5 % Carbo. Bagasse	-	7.5%	-
9	G9	Al+ 10% Carbo. Bagasse	-	10%	-
10	G10	Al+ 12.5 % Carbo. Bagasse	-	12.5%	-
11	G11	Al+ 0% Carbo. Bagasse + 15 % MgO	-	0	15%
12	G12	Al+ 2.5 % Carbo. Bagasse + 12.5 % MgO	-	2.5%	12.5%
13	G13	Al+ 5 % Carbo. Bagasse + 10 % MgO	-	5%	10%
14	G14	Al+ 7.5 % Carbo. Bagasse + 7.5 % MgO	-	7.5%	7.5%
15	G15	Al+ 10 % Carbo. Bagasse + 5 % MgO	-	10%	5%
16	G16	Al+ 12.5 % Carbo. Bagasse + 2.5 % MgO	-	12.5%	2.5%
17	G17	Al+ 15 % Carbo. Bagasse	-	15%	0
18	G18	Al+ 2.5 % MgO	-	-	2.5%
19	G19	Al+ 5 % MgO	-	-	5%
20	G20	Al+ 7.5 % MgO	-	-	7.5%
21	G21	Al+ 10 % MgO	-	-	10%
22	G22	Al+ 12.5 % MgO	-	-	12.5%

for grinding/polishing operation. Grinding machine was used first for obtaining the smooth sample surface. All the scratches were removed from the grinding machine and surface become smooth and flat. Emery paper with different grit is utilized, after polishing the samples for making the surface smooth and flat. Two types of emery paper are utilized to make the test surface sample smooth. It starts with emery paper grit no. 400 for rubbing on test sample for preparing the test surface flat and smooth and its end on emery paper grit no. 600. The test samples were polished with a fine polishing machine using alumina/diamond polish. The whole process is done for preparing the surface smooth and considered for further characterization. Similarly, prepare the entire test sample flat and smooth under this process, for further analysis.

2.2.6 Tensile, Impact, Hardness Sample

Toughness, hardness, and tensile samples were prepared to test the mechanical properties. Tensile specimen dimension is standard as ASTM E8, and toughness specimen dimension is (“10 mm × 10 mm × 55 mm with 45° of V-notch at centre of 2 mm depth”) and hardness specimen dimension (10 mm × 10 mm × 10 mm). Lathe machine was utilized to prepare the tensile sample for testing the tensile strength. ASTM E8 standard is followed to prepare the tensile specimens. 36 mm is a gauge length, and 6 mm is a diameter of tensile sample. As per the standard, all the hardness and impact (Toughness) specimens were prepared.

3 Results and Discussion

3.1 Microstructure Analysis

Microstructural image of composite is shown Fig. 3. It is done to check uniform spread of reinforcing particle in composite. The microstructure is done on that sample which has high tensile strength. The sample, which has high tensile strength, shows the low value of toughness. Microstructure helps to get to know the proper spread of reinforcement during the preparation of composite. Microstructure structure images showed the proper spread of reinforcement particles.

3.2 Yield Strength

Highest yield strength has been found 103 MPa for sample designation G12 (Al + 2.5% carbonized bagasse ash + 12.5% MgO powder). Yield strength of pure aluminium was observed 93 MPa (Table 1). Tensile strength of composite improved

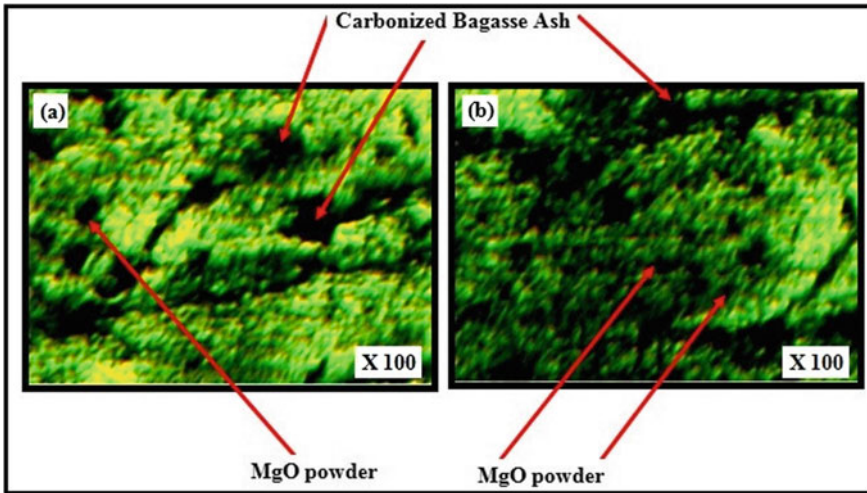


Fig. 3 Microstructure of Al/MgO powder/bagasse ash hybrid metal matrix composite

by 10.75% by adding bagasse as reinforcement particle (Fig. 4). Result also indicates that waste bagasse can be used as reinforcement material with aluminium in development of metal matrix composite or hybrid metal matrix composite. Sugar-cane bagasse has presence of hemicelluloses and cellulose which having the property to increase tensile strength because it has the high interfacial bonding on building composite. If interfacial bonding is decreased, then tensile strength is also decreased.

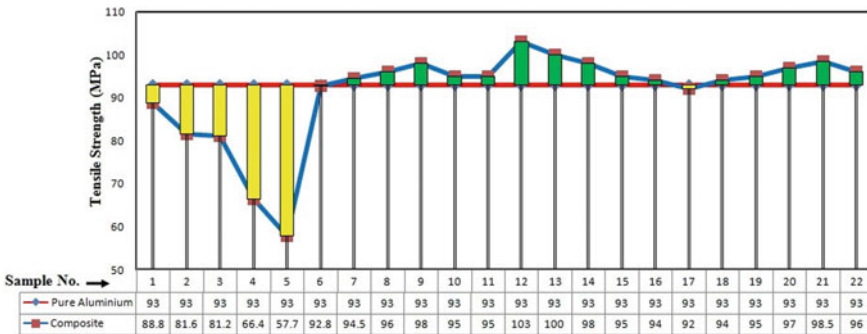


Fig. 4 Tensile strength of various sample designation

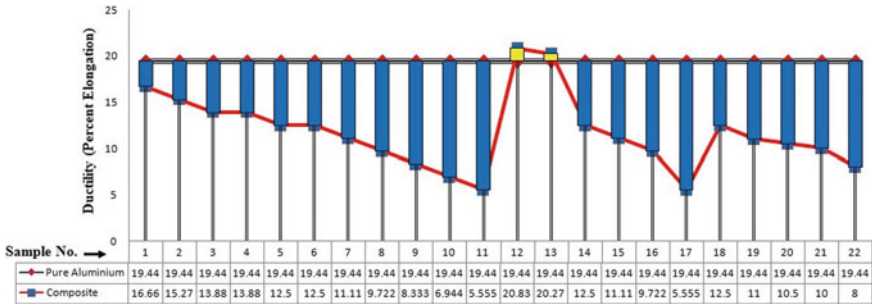


Fig. 5 Ductility of various sample designation

3.3 Ductility (Percent Elongation)

Figure 5 shows ductility behaviour of composite material. Ductility was found to be 20.83% for sample designation G12 (Al + 2.5 wt.% carbonized bagasse ash + 12.5 wt.% Magnesium oxide particles). Ductility of sample designation G12 is shown by yellow deviation bar. It was observed that by adding 2.5 wt.% bagasse ash and 12.5 wt.% MgO particles in Al, about 7.15% ductility improved concerning base aluminium alloy.

3.4 Hardness Analysis

Figure 6 displays the hardness of composite material. Sample designation G11 shows the maximum hardness. 78 HRB is a maximum hardness which shows in sample designation G11. But sample designation G12 shows the maximum tensile strength

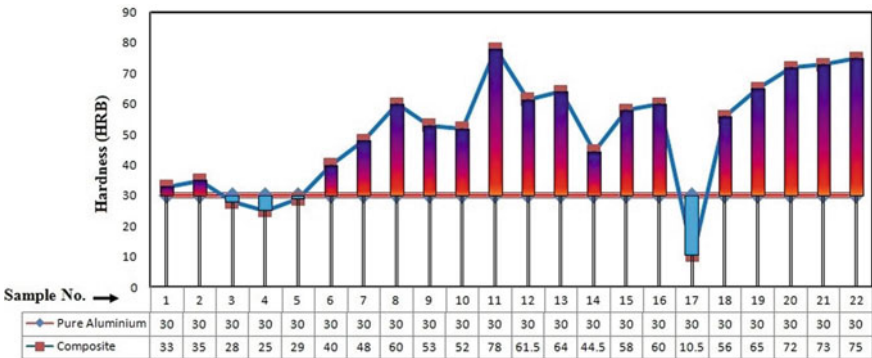


Fig. 6 Hardness of various sample designations

and ductility. Hardness for sample designation G12 was found to be 61.5 HRB. Hardness result of sample designation G11 shows about 160% improvement concerning base metal, while sample designation G12 also shows about 105% improvement in hardness. Replacement of ceramic particles may be bagasse ash which shows in this result. When the composite develops, sometimes due to the stirring process, some air interrupt inside the composite. These air form porosity. During the hardness test, the surface is very important because this test is done on the surface. Two readings were considered of each sample because during the test if one reading is taken from that point where porosity is found, then reading is come low. So, due to that second reading is also taken where the presence of reinforcement is present. Proper distribution of reinforcement particles improved the hardness. The hardness value is increased while increasing the quantity of MgO and decreasing the quantity of bagasse. MgO is helping to improve the hardness because its particles have high stiffness in the polystyrene matrix leads to a high indentation resistance due to which G11 composite has high hardness in comparison to other composites.

3.5 Toughness Analysis

From this analysis, it was observed that maximum toughness was gotten to be 45 J for sample designation G1 (Al + 2.5% Uncarbo. Bagasse) as shown in Fig. 7. It was notified that about 10% toughness reduced concerning base material. The small grain size of bagasse helps to increase the toughness. Due to the decrease in tensile strength, toughness is increased. G1 shows a low value of tensile strength due to which toughness value is increased. The low quantity of small grain size helps to increase the toughness. G1 have a crack which is deflected repeatedly at matrix interface because composite is brittle constituents which have high toughness.

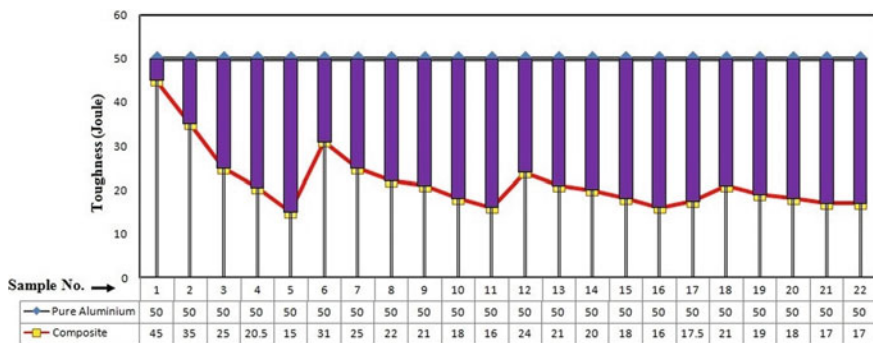


Fig. 7 Toughness of various sample designations in joule

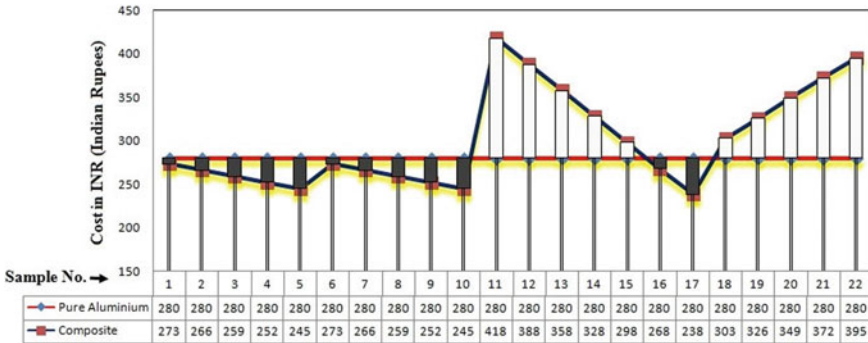


Fig. 8 Cost estimation of various sample designations in Indian rupees (INR)

3.6 Cost Estimation

Cost of material selection is a very important factor. The study of overall cost of the composite is a very important factor which studied in this. Cost of pure aluminium (matrix material) is 280 Rs./kg (Indian Rupees) which is purchase directly from the market. Bagasse is a waste material which is easily available from juice shop at free of cost that's why its cost was almost zero. Secondary reinforcement was MgO powder which was purchase directly from market at 600 Rs./kg (Indian Rupees). Cost of the composite decreases by increasing Wt. % of bagasse ash which is shown in Fig. 8. In place of ceramic particles, use of bagasse ash is good partial replacement which shows in the result.

4 Conclusions

An aluminium-based composite material made using bagasse waste and MgO as reinforcement. When MgO was added as second reinforcement, it was observed that wettability of bagasse ash enhanced with aluminium. A good enhancement in both tensile strength and hardness value was observed. When bagasse waste and MgO were added together, tensile strength increased by 10.75%, while the value of hardness increased very well. The value of hardness is increased by about 160%. However, toughness and ductility decrease. The overall cost of composite also decreased when it was mixed with aluminium due to bagasse being a waste product.

References

1. Sepúlveda-Cervantes Cynthia V, Soto-Regalado E, Rivas-García P, Loredó-Cancino M, Cerino-Córdova FDJ, García Reyes Refugio B (2018) Technical-environmental optimization of the activated carbon production of an agro industrial waste by means response surface and life cycle assessment. *Waste Manag Res* 36:121–130
2. Arsène M-A, Bilba K, Onésippe C, Rodier L (2015) Thermal and flexural properties of bagasse/cement composites. *Green Mater* 3:132–143
3. Camarini G, dos Santos Lima KD, Pinheiro SMM (2015) Investigation on gypsum plaster waste recycling: an eco-friendly material. *Green Mater* 3:104–112
4. Ezio R, Gabriela I, Arcangela F, Eleonora P, Cristina RA, Vincenzo C (2017) Sampling, characterisation and processing of solid recovered fuel production from municipal solid waste: an Italian plant case study. *Waste Manag Res* 35:890–898
5. Kuniko M, Hidekazu N (2016) Requirement analysis to promote small-sized E-waste collection from consumers. *Waste Manag Res* 34:122–128
6. Cao Q, Yu Q, Connell DW, Yu G (2013) Titania/carbon nanotube composite (TiO₂/CNT) and its application for removal of organic pollutants. *Clean Technol Environ Policy* 15:871–880
7. Saikia P, Goswami T, Dutta D, Dutta NK, Sengupta P, Neog D (2017) Development of a flexible composite from leather industry waste and evaluation of their physico-chemical properties. *Clean Technol Environ Policy* 19:2171–2178
8. Sands JM, Fink BK, McKnight SH, Newton CH, Gillespie JW, Palmese GR (2001) Environmental issues for polymer matrix composites and structural adhesives. *Clean Technol Environ Policy* 2:228–235
9. Prasad DS, Shoba C, Ramanaiah N (2013) Investigations on mechanical properties of aluminum hybrid composites. *J Mater Res Technol* 3:79–85
10. Dhanashekar M, Senthil Kumar VS (2014) Squeeze casting of aluminium metal matrix composites—an overview. In: 12th global congress on manufacturing and management, vol 97, pp 412–420
11. Dwivedi SP, Dwivedi G (2020) Utilization of recycled hazardous waste bagasse as reinforcement to develop green composite material. *World J Eng.* <https://doi.org/10.1108/WJE-03-2019-0069>
12. Srivastava N, Dwivedi SP (2019) Development of green hybrid metal matrix composite using agricultural waste bagasse as reinforcement—a review. In: IOP conference series: materials science and engineering, vol 691, pp 012051

Low-Amplitude and High-Frequency Loading Influences Interstitial Fluid Flow in Osteogenesis Imperfecta Osteon



Nikhil Vivek Shrivastava, Abhishek Kumar Tiwari, Dharmendra Tripathi, and Santosh Patil

Abstract Osteogenesis Imperfecta (OI) is a brittle bone disorder caused due to mutation in genes encoding collagen Type-1 (col-1). Symptomatic treatments such as surgery, physiotherapy, and bisphosphonate treatments are available for OI patients. It is observed that bone is sensitive to external dynamic loading as it stimulates bone adaptation. Therefore, external mechanical stimulation may be an alternative to strengthen the OI bone. Low-amplitude, high-frequency treatment may offer a favorable path for noninvasive stimulation of bone formation in OI patients. Fluid flow is assumed as mechanobiological stimulus for osteocyte cells in bone which initiates new bone formation at micro-scale level, however, it is important to understand how loading parameters affect fluid flow in OI bone in comparison with normal healthy bone. The present study aims to probe the effects of low-amplitude, high-frequency loading on the behavior of interstitial fluid flow in osteogenesis imperfecta bone osteon and its comparison with the flow behavior in normal bone subjected to similar loading condition. A mathematical model of osteon is developed considering two boundary conditions with material properties of normal and OI bones. It has been observed that the fluid velocity at high frequency and low magnitude in OI case is nearly matching the range of fluid velocity found in the normal case at low frequency. The preliminary findings present here may be useful in the design of better biomechanical pathways to enhance the strength of OI bone.

N. V. Shrivastava · S. Patil

Department of Mechanical Engineering, Manipal University Jaipur, Jaipur, Rajasthan 303007, India

N. V. Shrivastava

Department of Mechatronics Engineering, Manipal University Jaipur, Jaipur, Rajasthan 303007, India

A. K. Tiwari (✉)

Department of Applied Mechanics, Motilal Nehru National Institute of Technology Allahabad, Prayagraj, Uttar Pradesh 211004, India
e-mail: aktiwari@mnnit.ac.in

D. Tripathi

Department of Mathematics, National Institute of Technology Uttarakhand, Srinagar, Uttarakhand 246174, India

Keywords Osteogenesis imperfecta · Osteon · Low amplitude · High frequency · Fluid flow

1 Introduction

Osteogenesis imperfecta (OI) is also recognized as brittle bone disorder. It makes bone more sensitive to fractures which may range from minimal trauma to multiple fractures. Surgery and pharmaceutical management methods are used to treat OI patients. It has been observed that antalgic posture may also induce bone loss in OI patient which is similar to disuse bone loss and therefore increases the levels of bone fragility. Bisphosphonates treatment in OI children enhances bone density and microscopic structure over two–three years of treatment as reported in some literature [1]. This much long duration treatment of bisphosphonates may impact on bone remodeling activities resulting in poor bone quality with high mineral content.

Bone responds to cyclic loading in the form of new development at the elevated strain magnitude sites. It is observed that bone remodeling is highly affected with strain rate, strain magnitude, [2] and loading frequency [3, 4]. For example, higher bone formation is observed with increase in strain amplitude strain [5, 6], whereas similar characteristics is observed at low-strain and high-frequency loading [7, 8]. OI patients cannot be treated with high physiotherapy loads/strain due to brittleness. Low-amplitude and high-frequency loading can be potential alternative method to stimulate bone remodeling and strengthen the bone. Several in-vivo studies have examined the effect of high-frequency vibration on bone formation using animal models of different age groups and vibration frequency [7, 9]. Investigations observed that low-magnitude and high-frequency loading presents a positive anabolic response with high upsurge in bone mass [10, 11]. A similar observation is found for both cortical and trabecular bones [4, 10]. Low-magnitude, high-frequency loading is equally important to induce a mechanobiological stimulus in bone tissue similar to high-amplitude and low-frequency loading This is because the rate at which a physiological signal is experienced by the bone is usually a function of amplitude and the frequency of loading [12, 13]. This concept is validated in a few in-vivo studies which stated that low-amplitude high-frequency promotes new bone formation sufficiently as compared to low-frequency high-amplitude loading [14].

Lau et al. have explained that the osteocyte activates in response to external stimulus and also differentiates mechanical stimuli induced at different frequencies [11]. One may consider that mechanical stimuli of fluctuating frequency and magnitude may control discrete signaling pathways [15]. Chen et al. [16] concluded that pore-pressure fluctuates in magnitude and also influences the activities of the osteonal fluid with change in loading frequency. Wu et al. [12] mathematically presented an osteon to illustrate the effect of physiological loading circumstances and material parameters on the fluid flow distribution. They also have demonstrated that the interstitial fluid pressure and fluid flow are largely affected by loading frequency [12]. This means that small mechanical stimuli may provoke a cellular response if applied at

higher frequency. Most of these studies computed the stimuli in healthy normal bone, whereas it is equally important how loading frequency influences the mechanical environment in bone subject to disease such as OI. Accordingly, the present focuses on the study of interstitial fluid, a mechanobiological stimulus of bone remodeling, as a function of loading frequency in OI bone and compared it with healthy bone. Interstitial fluid flow behavior in healthy osteon and osteon of patients suffering a severe form of osteogenesis imperfecta (type III) is computed. The outcomes may be useful to suitably design the therapies to enhance the mechanobiological stimulus in OI bone to strengthen it.

2 Methodology

The current study intends to comprehend how low-amplitude and high-frequency loading influences interstitial fluid flows within the fundamental unit of compact bone, i.e., osteon of healthy versus OI (type III) bone. Osteon is assumed cylindrical, and a cylindrical coordinate system is employed for the modeling. The height of osteon is 'h' with outer radius r_o and inner radius r_i as shown in Fig. 1 [12, 17]. Osteon is assumed axisymmetric. The model computes fluid distribution along the radius of osteon as a function of loading frequency. The pressure (p) and the radial displacement (u_r) are the function of radius (r) and time (t), and compatibility equations have been used to relate pore-pressure (p) and radial displacement (u_r) subjected to assumed solutions $p = p_o e^{i\omega t}$ and $u_r = u_o e^{i\omega t}$ as

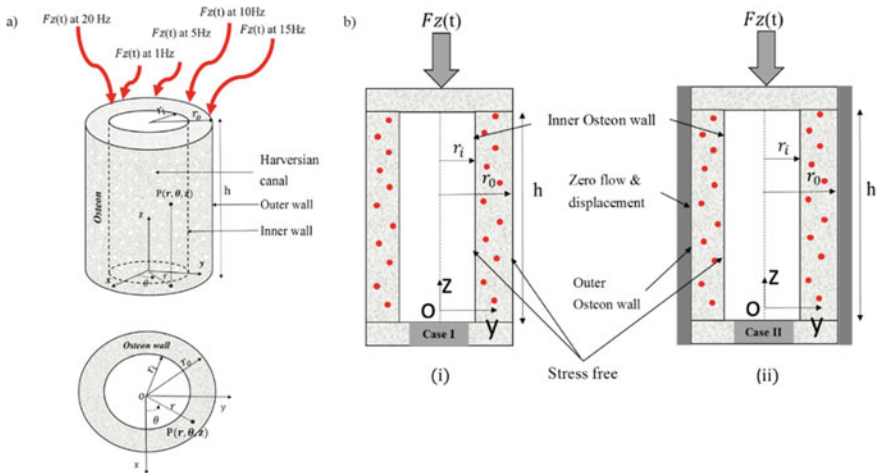


Fig. 1 a Schematic of osteon loaded with varying frequency $F_z(t)$, b schematic illustration of assumed boundary conditions: (i) both boundaries permeable and (ii) inner boundary permeable [12]

Table 1 Material and geometrical properties used in the mathematical modeling

Parameters	Definition	Normal [12, 17, 18]	OI (Type III) [19, 20]
E_t (GPa)	Young’s modulus in transverse direction	15.9	13.92
E_l (GPa)	Young’s modulus in longitudinal direction	20.3	15.22
ν_t	Poisson’s ratio in transverse direction	0.328	0.25
ν_l	Poisson’s ratio in longitudinal direction	0.25	0.35
B (GPa)	Biot’s modulus	38	0.587
r_i (mm)	Inner radius of osteon	50	25
r_o (μm)	Outer radius of osteon	150	112
α_0	Biot’s coefficients in $(r - \theta)$ plane	0.132	0.53
α_1	Biot’s coefficients in longitudinal plane (z direction)	0.092	0.042
k (m^2)	Intrinsic permeability	10–18	10–18
μ (Pa.s)	Pore fluid dynamic viscosity	10–3	10–3

$$\frac{d^2 p}{dr^2} + \frac{1}{r} \frac{dp}{dr} - \frac{i\omega\mu(C_{11} + B\alpha^2)}{kBC_{11}} p = \frac{i\omega\mu(\alpha_0 c + \alpha_1 \varepsilon_{z0})}{k} \tag{1}$$

where $C_{11} = \frac{E_r(E_l - E_r\nu_l^2)}{(1 + \nu_r)(E_l - E_l\nu_r - 2E_r\nu_r^2)}$ is the elastic constants tensor. Other parameters used in the study are listed in Table 1.

Shrivas et al. [17] and Wu et al. [12] presented two possible boundary conditions which are used in the present study. In first case, both the surfaces are considered to be permeable and stress-free. Tol et al. [21] described this condition as the osteon is enclosed in one more osteon or the outer wall of the osteon found to be in contact with neighboring osteon and can be called as *osteon in osteon*. Therefore, the outer boundary may be considered as impermeable, whereas the inner surface will act as a permeable surface. Thus, boundary conditions can be defined as

Case I:

$$\sigma_{rr} = 0 \text{ and } p = 0 \text{ at } r = r_i \tag{2}$$

$$\sigma_{rr} = 0 \text{ and } p = 0 \text{ at } r = r_o \tag{3}$$

Case II:

$$\sigma_{rr} = 0 \text{ and } p = 0 \text{ at } r = r_i \tag{4}$$

$$u_r = 0 \text{ and } \frac{\partial p}{\partial r} = 0 \text{ at } r = r_o \tag{5}$$

The pore-pressure in the osteon can be estimated as

Case I:

$$p(r, t) = \frac{BC_{11}(\alpha_1 c_1 + \alpha_o \varepsilon_{z0})}{C_{11} + M\alpha_o^2} \left\{ \frac{[K_0(Cr_o) - K_0(Cr_i)]I_0(Cr) - [I_0(Cr_o) - I_0(Cr_i)]K_0(Cr)}{I_0(Cr_i)K_0(Cr_o) - I_0(Cr_o)K_0(Cr_i)} - 1 \right\} e^{i\omega t} \tag{6}$$

Case II:

$$p(r, t) = \frac{BC_{11}(\alpha_o c_2 + \alpha_1 \varepsilon_{z0})}{C_{11} + B\alpha_o^2} \left\{ \frac{I_0(Cr)K_1(Cr_o) + K_0(Cr)I_1(Cr_o)}{I_0(Cr_i)K_1(Cr_o) + I_1(Cr_o)K_0(Cr_i)} - 1 \right\} e^{i\omega t} \tag{7}$$

where $C = \sqrt{\frac{i\omega\mu(C_{11} + B\alpha_o^2)}{kBC_{11}}}$ and c_1, c_2 are calculated from the boundary conditions (8).

The osteonal fluid velocity is obtained by means of Darcy’s law which is defined as

$$V_r = -\frac{k}{\mu} \frac{\partial p}{\partial r} \tag{9}$$

Thus, radial velocity V_r can be defined for each case as

Case I

$$V_r(r, t) = -\frac{k}{\mu} \frac{BC_{11}C(\alpha_o c_1 + \alpha_1 \varepsilon_{z0})}{C_{11} + B\alpha_o^2} \left\{ \frac{[K_0(Cr_o) - K_0(Cr_i)]I_1(Cr) + [I_0(Cr_o) - I_0(Cr_i)]K_1(Cr)}{I_0(Cr_i)K_0(Cr_o) - I_0(Cr_o)K_0(Cr_i)} - 1 \right\} e^{i\omega t} \tag{10}$$

Case II

$$V_r(r, t) = -\frac{k}{\mu} \frac{BC_{11}C(\alpha_o c_2 + \alpha_1 \varepsilon_{z0})}{C_{11} + B\alpha_o^2} \left\{ \frac{I_0(Cr)K_1(Cr_o) + K_0(Cr)I_1(Cr_o)}{I_0(Cr_i)K_1(Cr_o) + I_1(Cr_o)K_0(Cr_i)} \right\} e^{i\omega t} \tag{11}$$

In order to probe the influence of the low-amplitude, high-frequency loading on pore-pressure and fluid transport behavior, the osteon is loaded with a strain amplitude of $\varepsilon_{z0} = 1000$ microstrain and 500 microstrain with a varying frequency of 1–20 Hz

[22] was selected. The load is applied a varying frequency of 1, 5, 10, 15, and 20 Hz keeping the strain rate fixed for the normal and OI conditions. Finally, the model was simulated to obtain the pressure and velocity distribution along with the radial direction by considering the boundary conditions.

3 Result and Discussion

The model was simulated using the material properties of normal or healthy and OI osteon for both the boundary conditions. In case I, the inner and outer boundary of the osteon are considered as permeable assuming the canaliculi crosses the boundaries. Curtis et al. [23] also reported that canaliculi may cross the cement line and thus fluid motion may occur from this surface as well. In the second case, the outer boundary is considered as impermeable since in some case the canaliculi may not cross the cement line or it may be surrounded by other osteon forming an osteon in osteon structure [21].

The model was tested for 1000 microstrain and 500 microstrain which also represent the strain induced during physiological loading. Osteon is exposed to loading frequency of 1 Hz, 5 Hz, 10 Hz, 15 Hz, and 20 Hz, respectively. High-amplitude loading treatment had a significant effect on the interstitial flow parameters. The result indicates a surge in the pore-pressure in OI as well as normal case is observed when loaded at 1000 microstrain. A linear increase is visible in both the velocity and pore-pressure magnitude when the frequency is increased from 1 to 20 Hz (Fig. 2). In addition, Fig. 2a–d reflects the pressure magnitude for case I and case II at 1000 microstrain and 500 microstrain, respectively. The pressure distribution observed in case I to be almost zero at the inner surface of osteon ($r_1 = 50 \mu\text{m}$) and the outer surface of osteon ($r_4 = 150 \mu\text{m}$). It can be noticed that pore-pressure is maximum near the mid-osteon wall thickness and is equal to 1331 Pa when the osteon is loaded with 1000 microstrain at 20 Hz loading frequency (Fig. 2a). For case II, the maximum pore-pressure is observed at the outer boundary and is almost equal to 11,555 Pa at 1000 microstrain and 20 Hz loading frequency. It has been observed that the pore-pressure achieves the physiological range as of healthy osteon in OI case when osteon is loaded at high frequency.

The fluid velocity also increases linearly in case I and case II for healthy and OI osteon. For case I, the velocity magnitude is almost zero near the mid-osteon wall, and the maximum velocity is observed in the healthy case when loaded with 20 Hz frequency and 1000 microstrain. The peak velocity is found to be $575 \mu\text{m/s}$ (Fig. 3c) in case II at 20 Hz. In OI osteon, the fluid velocity is also showing similar changes at loading amplitude of 1000 microstrain and 500 microstrain. The fluid velocity enhances at higher frequency, and its value is almost matching with the magnitude of fluid velocity at low frequency in the normal case. The maximum fluid velocity in OI subjects is equal to $56 \mu\text{m/s}$ at 20 Hz and 1000 microstrain loading. This fluid is within the physiologic range observed in normal subjects. The pore-pressure and

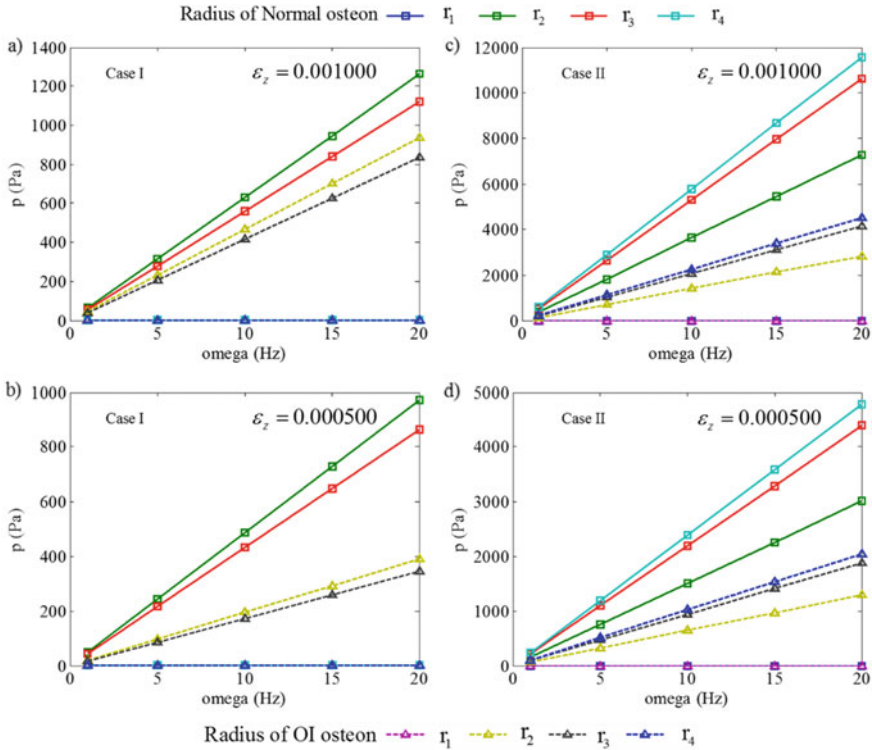


Fig. 2 a Distribution of pore-pressure at 1000 microstrain with varying frequency for *case I*; b distribution of pore-pressure at 500 microstrain with varying frequency for *case I*; c distribution of pore-pressure at 1000 microstrain with varying frequency for *case II*; d distribution of pore-pressure at 500 microstrain with varying frequency for *case II*. ($r_1 = 50 \mu\text{m}$, $r_2 = 83 \mu\text{m}$, $r_3 = 116 \mu\text{m}$, and $r_4 = 150 \mu\text{m}$ are the radius from the center of normal osteon, and $r_1 = 25 \mu\text{m}$, $r_2 = 55 \mu\text{m}$, $r_3 = 84 \mu\text{m}$, and $r_4 = 112 \mu\text{m}$ are the radius from the center of OI osteon)

velocity values almost become half of that of the normal/healthy osteon when loaded at 500 microstrain.

The current study validates the osteogenic effect of a low-amplitude high-frequency therapy in osteogenesis imperfecta osteon. An increase in both pore-pressure and fluid velocity with increase in loading frequency is observed. This may help in improving the mechanical properties of OI bone. Vanleene et al. have observed similar kind of response in the cortical and the trabecular bone structure when the young OI mouse bone limb was exposed to low-amplitude and high-frequency loading [4].

The fluid transport in the lacunar-canalicular network of bone occurs due to dynamic loading, which in turn generates shear stresses on bone cells. This fluid shear is assumed responsible for mechanotransduction and osteogenesis. The present research also adds the proelastic behavior of osteon subjected to a varying range

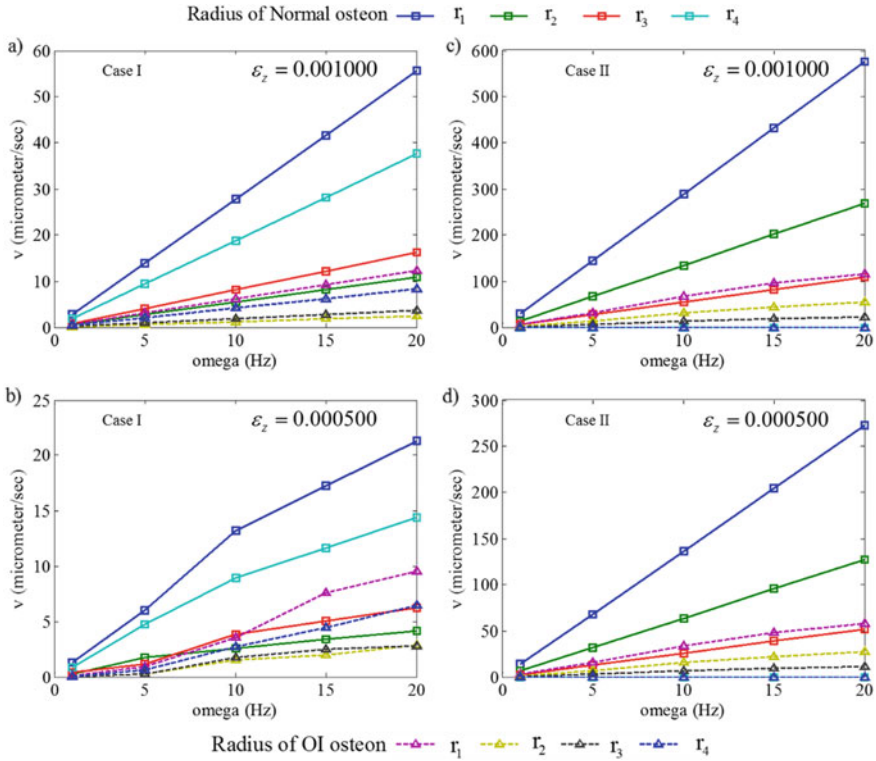


Fig. 3 **a** Distribution of fluid velocity at 1000 microstrain with varying frequency for *case I*; **b** distribution of fluid velocity at 500 microstrain with varying frequency for *case I*; **c** distribution of fluid velocity at 1000 microstrain with varying frequency for *case II*; **d** distribution of fluid velocity at 500 microstrain with varying frequency for *case II*. ($r_1 = 50 \mu\text{m}$, $r_2 = 83 \mu\text{m}$, $r_3 = 116 \mu\text{m}$, and $r_4 = 150 \mu\text{m}$ are the radius from the center of normal osteon, and $r_1 = 25 \mu\text{m}$, $r_2 = 55 \mu\text{m}$, $r_3 = 84 \mu\text{m}$, and $r_4 = 112 \mu\text{m}$ are the radius from the center of OI osteon)

of low- to high-frequency (1–20 Hz) cyclic loading generated due to physiological exercises such as locomotion and maintenance of posture [24].

The model does not incorporate the porosities available at different length scales, e.g., vascular and lacunar porosity which is a limitation of the model. The effect of intermittent dynamic loading on bone remodeling has not been considered in the present study. The results of the current study suggest that the pore-pressure of fluid flow is affected by low-amplitude high-frequency physiological loading in OI bone as well. Therefore, the bone cell may experience constant fluid shear in case of normal loading [17]. In such a case, bone cell will not relax, and it may adversely affect the mechano-sensitivity. This may eventually cause hindered remodeling activities [25]. This also shows that osteogenesis activities in OI bones can be enhanced through low-amplitude mechanical strain at high frequency with rest in between loading cycles. Further, experimental investigations are required in order to see the anabolic

and catabolic effect in the OI bone due to low-amplitude and high-frequency cyclic loading.

4 Conclusions

The outcome of the present study can be summarized as follows:

- i. Fluid velocity and pore-pressure vary linearly with strain and frequency in both normal and OI osteon.
- ii. Maximum pore-pressure and fluid motion in OI achieve the normal physiological range when the osteon is loaded at a higher frequency, i.e., 20 Hz.
- iii. Mechanobiological stimulus required for bone remodeling may be induced in OI bone while loading osteon at higher frequency.

The outcomes may be useful in the design of biomechanical therapeutics to address bone loss.

References

1. Rauch, F, Glorieux, FH (2006) Treatment of children with osteogenesis imperfecta. *Current osteoporosis reports*, 4(4), 159–164.
2. LaMothe JM, Hamilton NH, Zernicke RF (2005) Strain rate influences periosteal adaptation in mature bone. *Med Eng Phys* 27:277–284. <https://doi.org/10.1016/j.medengphy.2004.04.012>
3. Hsieh YF, Turner CH (2001) Effects of loading frequency on mechanically induced bone formation. *J Bone Miner Res* 16:918–924. <https://doi.org/10.1359/jbmr.2001.16.5.918>
4. Vanleene M, Shefelbine SJ (2013) Therapeutic impact of low amplitude high frequency whole body vibrations on the osteogenesis imperfecta mouse bone. *Bone* 53:507–514. <https://doi.org/10.1016/j.bone.2013.01.023>
5. Robling AG, Burr DB, Turner CH (2001) Recovery periods restore mechanosensitivity to dynamically loaded bone. *J Exp Biol* 204:3389–3399
6. Sugiyama T (2018) Physical activity and bone health: understanding mechanical strain-related stimuli. *Int J Epidemiol* 47:669–670. <https://doi.org/10.1093/ije/dyy037>
7. Judex S, Rubin C (2003) Mechanical influences on bone mass and morphology. In: Orwoll ES, Blizotes M (eds) *Osteoporosis: pathophysiology and clinical management*. Humana Press, Totowa, NJ, pp 199–220. https://doi.org/10.1007/978-1-59259-278-4_10
8. Torcasio A, Jähn K, Van Guyse M, Spaepen P, Tami AE, Vander Sloten J, Stoddart MJ, van Lenthe GH (2014) Trabecular bone adaptation to low-magnitude high-frequency loading in microgravity. *PLoS ONE* 9:e93527. <https://doi.org/10.1371/journal.pone.0093527>
9. Zhang R, Gong H, Zhu D, Gao J, Fang J, Fan Y (2014) Seven day insertion rest in whole body vibration improves multi-level bone quality in tail suspension rats. *PLoS ONE* 9:e92312. <https://doi.org/10.1371/journal.pone.0092312>
10. Rubinacci A, Marenzana M, Cavani F, Colasante F, Villa I, Willnecker J, Moro GL, Spreafico LP, Ferretti M, Guidobono F, Marotti G (2008) Ovariectomy sensitizes rat cortical bone to whole-body vibration. *Calcif Tissue Int* 82:316–326. <https://doi.org/10.1007/s00223-008-9115-8>

11. Lau E, Al-Dujaili S, Guenther A, Liu D, Wang L, You L (2010) Effect of low-magnitude, high-frequency vibration on osteocytes in the regulation of osteoclasts. *Bone* 46:1508–1515. <https://doi.org/10.1016/j.bone.2010.02.031>
12. Wu X-G, Chen W-Y (2013) A hollow osteon model for examining its poroelastic behaviors: mathematically modeling an osteon with different boundary cases. *Eur J Mech A/Solids* 40:34–49
13. Uzan MO, Baskan Ö, Karadaş Ö, Özçivici E (2016) Application of low intensity mechanical vibrations for bone tissue maintenance and regeneration. *Turk J Biol* 40:300–307
14. Yanagihara GR, Paiva AG, Gasparini GA, Macedo AP, Frighetto PD, Volpon JB, Shimano AC (2016) High-impact exercise in rats prior to and during suspension can prevent bone loss. *Braz J Med Biol Res* 49. <https://doi.org/10.1590/1414-431X20155086>
15. Hoffman BD, Grashoff C, Schwartz MA (2011) Dynamic molecular processes mediate cellular mechanotransduction. *Nature* 475:316–323. <https://doi.org/10.1038/nature10316>
16. Chen Y, Wang W, Ding S, Wang X, Chen Q, Li X (2018) A multi-layered poroelastic slab model under cyclic loading for a single osteon. *Biomed Eng Online* 17:97
17. Shrivastava NV, Tiwari AK, Kumar R, Tripathi D, Sharma VR (2018) Investigation on loading-induced fluid flow in osteogenesis imperfecta bone. In: ASME 2018 5th joint US-European fluids engineering division summer meeting. American Society of Mechanical Engineers Digital Collection
18. Nguyen V-H, Lemaire T, Naili S (2009) Numerical study of deformation-induced fluid flows in periodic osteonal matrix under harmonic axial loading. *CR Mec* 337:268–276
19. Jameson JR (2014) Characterization of bone material properties and microstructure in osteogenesis Imperfecta/Brittle bone disease
20. Pazzaglia UE, Congiu T, Brunelli PC, Magnano L, Benetti A (2013) The long bone deformity of osteogenesis imperfecta III: analysis of structural changes carried out with scanning electron microscopic morphometry. *Calcif Tissue Int* 93:453–461
21. van Tol AF, Roschger A, Repp F, Chen J, Roschger P, Berzlanovich A, Gruber GM, Fratzl P, Weinkamer R (2020) Network architecture strongly influences the fluid flow pattern through the lacunocanalicular network in human osteons. *Biomech Model Mechanobiol* 19:823–840. <https://doi.org/10.1007/s10237-019-01250-1>
22. Cowin SC (2002) Mechanosensation and fluid transport in living bone. *J Musculoskeletal Neuronal Interact* 2:256–260
23. Curtis TA, Ashrafi SH, Weber DF (1985) Canalicular communication in the cortices of human long bones. *Anat Rec* 212:336–344. <https://doi.org/10.1002/ar.1092120403>
24. Weinbaum S, Cowin SC, Zeng Y (1994) A model for the excitation of osteocytes by mechanical loading-induced bone fluid shear stresses. *J Biomech* 27:339–360. [https://doi.org/10.1016/0021-9290\(94\)90010-8](https://doi.org/10.1016/0021-9290(94)90010-8)
25. Lanyon LE, Rubin CT (1984) Static vs dynamic loads as an influence on bone remodelling. *J Biomech* 17:897–905. [https://doi.org/10.1016/0021-9290\(84\)90003-4](https://doi.org/10.1016/0021-9290(84)90003-4)

DGA-Based Health Assessment of a 20 MVA Power Transformer



Naveen Kumar Sharma, Anuj Banshwar, Bharat Bhushan Sharma,
Mohit Pathak, and Sujit Kumar

Abstract Power transformer is the pivotal device of the power system. Dissolved gas analysis (DGA) is widely used for assessment of incipient faults in oil-filled equipment and the most important tool in determining the condition of a transformer. In this paper, DGA method has been used to assess health of 20 MVA power transformer in terms of details of gas and fault existence in the oil sample.

Keywords DGA · Health assessment · Duval triangle

1 Introduction

The power transformer is the pivotal device of the power system. DGA is the most important tool in determining their health condition [1, 2]. Flashover with power follow through can destroy the transformer, in which case the fault and evidence of damage will confirm, or indicate the cause of failure. In the latter case, if the flashover has taken place inside the tank, DGA results after failure indicate the severity of the fault. Broken or loose connections in winding, lead to a small arc, which burns the surrounding solid insulation and can result in transformer sudden failure. Deteriorated conductor insulation paper, i.e. as a result of a previous short of the transformer, two adjacent turns and forming a closed loop around the main magnetic flux. This loop will melt down in seconds due to excessive high-induced current flow.

N. K. Sharma (✉)
IKGPTU Main Campus, Jalandhar, Punjab, India

A. Banshwar
Government Polytechnic Puranpur, Pilibhit, Uttar Pradesh, India

B. B. Sharma
Noida Institute of Engineering & Technology, Greater Noida, Uttar Pradesh, India

M. Pathak
School of Automation, Banasthali Vidyapith, Rajasthan, India

S. Kumar
Jain (Deemed To Be University), Bangalore, Karnataka, India

A broken, loose or damaged draw rod in a bushing can cause sparking and arcing within the bushing tube and cause melt down of adjoining copper, producing gas. The Buchholz relay may activate and disconnect the transformer from the system. In extreme cases, the bushing may explode and lead to fire.

Instantaneous faults and faults developing within seconds to minutes are possibly not detected by DGA.

2 Duval Triangle Method

This method is employed with transformers insulated with the help of oil and is considered to be one of the most accurate fault diagnosis tools that comes under DGA [3, 4]. This triangle based on this method is indicated in Fig. 1 [5].

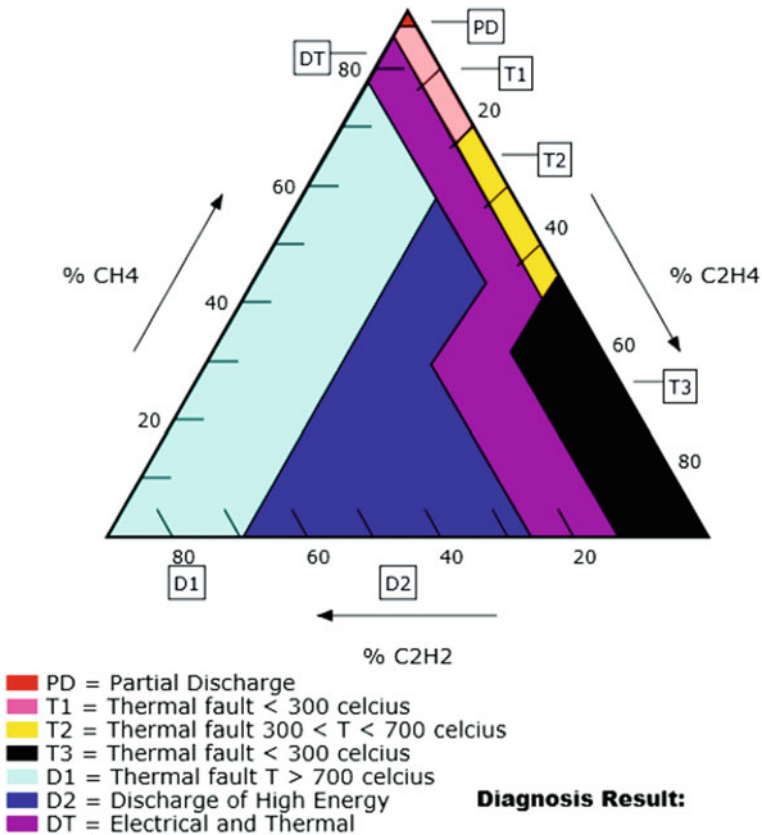


Fig. 1 Duval triangle

where coordinates:

$$\%C_2H_2 = \frac{100C_2H_2}{C_2H_2 + C_2H_4 + CH_4}$$

$$\%C_2H_4 = \frac{100C_2H_4}{C_2H_2 + C_2H_4 + CH_4}$$

$$\%CH_4 = \frac{100CH_4}{C_2H_2 + C_2H_4 + CH_4}$$

This method uses methane, ethylene and acetylene as hydrocarbon gases only. The flowchart for this method is illustrated in Fig. 2.



Fig. 2 Flowchart for Duval triangle method

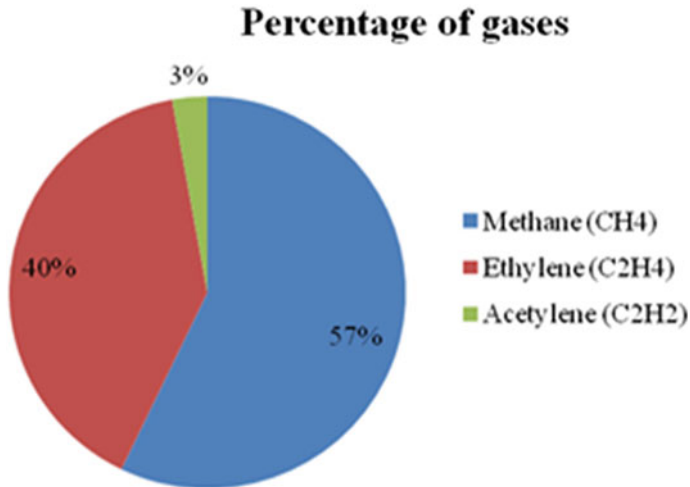


Fig. 3 Percentage of methane, ethylene and acetylene gases

3 Experimental Set-Up and Obtained Results

DGA method has been performed on a 20 MVA transformer, 132 kV substation at Barotiwala located at Solan (H.P.) for finding health assessment of insulation oil sample. The details of methane, ethylene, acetylene gases and type of fault present in sample oil are given in Figs. 3 and 4, respectively.

4 Conclusion

In this work, Duval triangle-based DGA method has been performed on a 20 MVA power transformer for finding the health assessment of oil sample. The details of methane, ethylene and acetylene gases and type of fault present in sample oil are obtained using DGA.

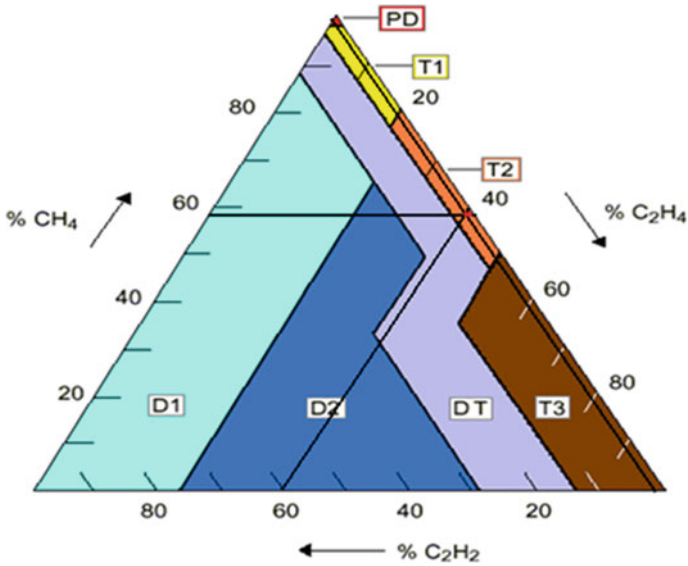


Fig. 4 Thermal fault from Duval triangle

References

1. Bandyopadhyay MN, Singh S (2010) Dissolved gas analysis technique for incipient fault diagnosis in power transformers: a bibliographic survey. *IEEE Electr Insulation Mag* 26(6):41–46
2. Wang M, Vandermaar AJ, Srivastava KD (2002) Review of condition assessment of power transformers in service. *IEEE Electr Insulation Mag* 18(6):12–25
3. Bakar NA, Abu-Siada A, Islam S (2014) A review of dissolved gas analysis measurement and interpretation techniques. *IEEE Electr Insulation Mag* 30(3):39–49
4. Duval M (1989) Dissolved gas analysis: it can save your transformer. *IEEE Electr Insulation Mag* 5(6):22–27
5. Patel A, Sharma NK, Banshwar A, Sharma BB, Pathak M (2020) An evaluation of different health assessment methods on 50 MVA power transformer: a case study. In: 2020 IEEE students conference on engineering and systems (SCES), Prayagraj, India, pp 1–5

Study of Fabrication Methods, Mechanical Features and Applications of Natural Fiber Composites



R. Muthalagu, V. Srinivasan, S. Sathees Kumar, and V. Murali Krishna

Abstract Normal fiber-strengthened composites are a developing territory in polymer discipline. These regular fibers are ease fibers with quiet density and elevated explicit attributes. These are decomposable and non-coarse. The trademark fiber composites proposition express credits for all intents and purposes indistinguishable from those of ordinary fiber blends. Due to their low rate, similarly incredible mechanical properties, outrageous express quality, non-grating, eco-accommodating and natural ascribes. The ductile characters of natural fiber-reinforced polymers are essentially impacted by the hookup attachment among the matrix and the fibers. This report presents the detailed effort on characteristic of fiber-reinforced mixtures with exceptional testimonial to the types of strands, fabrication method, mechanical attributes and numerous applications of fibers.

Keywords Composites · Fibers · Jute · Mechanical · Sisal · Tensile

1 Introduction

In the course of recent spans, we invention that polymers have supplanted huge numbers of the traditional materials in different purposes. This is conceivable in light of the points of interest polymers offered across regular materials. The best significant points of interest of utilizing polymers are the simplicity of handling, profitability and amount of decrease. In a large portion of these functions, the attributes of polymers are changed utilizing fillers and filaments to suit the extreme quality/peak

R. Muthalagu (✉) · V. Srinivasan

Department of Manufacturing Engineering, Annamalai University, Chidambaram, Tamil Nadu, India

S. S. Kumar

Department of Mechanical Engineering, CMR Institute of Technology, Hyderabad, Telangana, India

V. M. Krishna

Department of Mechanical Engineering, B.V. Raju Institute of Technology, Narsapur, Medak District, Telangana, India

modulus necessities. Fiber-strengthened polymers propose points of interest upon other customary materials after explicit attributes are thought about. These composites are discovering usages in differing domains from machines to rockets. Trademark filaments have starting late pulled in the thought of analysts and technologists by virtue of the positive conditions that these fibers give over normal stronghold materials, and the headway of regular strand blends has been an investigation of energy as far back as barely any years [1–4]. These trademark fibers are negligible exertion strands with low thickness and high unequivocal qualities. Recyclability or biological of regular fiber composite things a while later a supportive life makes it to them more huge and approve the vehicle producers to fabricate the utilization of trademark strands. On the off chance that biodegradable strands were picked to substitute a significant number of the current composite parts, one may lessen extraordinary troubles of discarding these products [5]. Lucintel's [6] report estimates that the regular strand mixture substances market will develop to 532 million \$ in 2016. Solicitation from vehicle associations for materials with clatter decline limits similarly as extended eco-cordiality by reducing the weight has expanded [7] in view of the way that standard fiber composites have splendid sound-immersing capacities, are more break safe and have more capable imperatives the board credits than glass and the premium for typical fiber combinations has extended in the market [8]. Solicitation for basic strands in plastic combinations are figure to create at a 15–20% in vehicle use and half or further in picked structural designing reason [9]. Normal strand-based car segments, for example, different boards, and shoes of brakes are appealing to the car business since they have diminished the heaviness of elements by over 10% and have additionally carried the expense somewhere near as much as 5% [10, 11]. In any case, specific drawbacks, for example, mismatch with the hydrophobic polymer substance, the slant to shape totalizes through making, and weak opposition to wetness significantly decrease the capability of characteristic filaments to be utilized as support in polymers. In this report, the uncovered go after various pieces of trademark fiber fortified composites and allude a segment of the principal matters being created of such composites.

2 Categories of Fibers

Common filaments are classified into three kinds: leaf strands, seed hair and bast strands, reliant on the source. A few plants are cotton, ramie, jute, and flax, and sisal and abaca (leaf strands) of these filaments, jute, ramie, flax, and sisal are the most extreme habitually go through strands for polymer composites. Characteristic strands in the method of wood dust have additionally been consistently utilized for the plan of regular strand mixtures. Figure 1 shows the classification of natural fiber. Plants and its fibers are shown in the following images from Figs. 2, 3, 4, 5, 6, 7, 8 and 9 (*Source: <https://www.google.com/fibers>*).

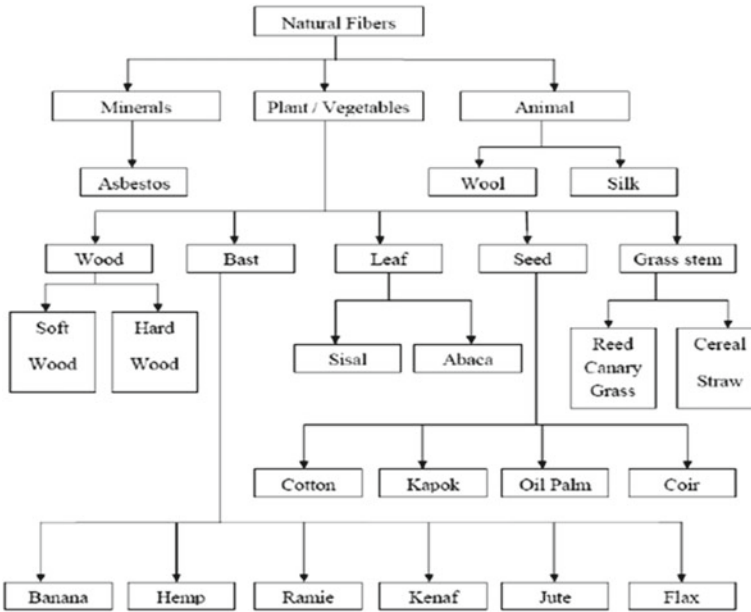


Fig. 1 Classification of natural fibers

Fig. 2 Sisal plant and its fiber



Fig. 3 Hemp plant and its fiber



Fig. 4 Ramie plant and its fiber



Fig. 5 Cotton plant and its fiber



Fig. 6 Flax plant and its fiber



Fig. 7 Coconut tree and its fibers



Fig. 8 Jute plant and its fiber



Fig. 9 Stalk plant and its fiber



2.1 Plant Fibers

Sisal: Sisal plant has a spot with the agave family (Agavaceae). The plant looks like goliath pineapples. The fragile tissue is scratched from the strands truly or mama chine. It is essentially used for mats, floor covers, and various other stronghold materials.

Hemp: Hemp filaments have for a long while been regarded for their extraordinary quality and broad fiber length, and have been used generally in the formation of ropes and sails, similarly with respect to paper and materials. It is an extreme plant and grows well in a decently chilly air. Hemp strands are basically made out of cellulose, hemicellulose, and lignin, and gelatin.

2.2 Leaf Fiber

Ramie: Ramie is a costly and strong fiber. The ramie plant can without much of a stretch develop in textures. It is broadly utilized in creation of furniture covers and backdrop and so on.

Cotton: Cotton is the most significant fiber utilized in the material business. Cotton is commonly gathered by choosing which is for the most part conveyed by hand. Correlating with other normal filaments, cotton is for the most part utilized in the manufacturing of garments, covers and carpets.

Flax: Flax fiber is one of the most grounded fibers among common fiber. Flax has great warmth directing attributes. Nevertheless, predictable wrinkling in a comparative spot in sharp cover will in general break the fiber. Flax is used for the making of material, canvas, ropes and sacks.

Table 1 Formation of chemical for various fibers

Fiber type	Cellulose (wt%)	Hemicellulose (wt%)	Pectin (wt%)	Lignin (wt%)	Moisture content (wt%)	References
Abaca	56–63	–	1	12–13	5–10	[12]
Banana	63–64	10	–	5	10–12	[12, 14]
Cotton	85–90	5.7	0–1	–	7.85–8.5	[14]
Coir	32–43	0.15–0.25	3–4	40–45	8	[14]
Flax	71	18.6–20.6	2.3	2.2	8–12	[12, 13]
Hemp	70–74	17.9–22.4	0.9	3.7–5.7	6.2–12	[14, 15]
Jute	61.1–71.5	13.6–20.4	0.2	12–13	12.5–13.7	[14, 15]
Kenaf	45–57	21.5	3–5	8–13	–	[15]
PALF	70–82	–	–	5–12.7	11.8	[16]
Ramie	68.6–76.2	13.1–16.7	1.9	0.6–0.7	7.5–17	[15]
Sisal	66–78	10–14	10	10–14	10–22	[15]

2.3 Fruit Fibers

Coir: For the most part, coconut filaments are procured from the husk of the result of the coconut palm. These coconut strands are strong and light and adequately withstand warmth and salt water.

2.4 Stem Fiber

Jute fiber: Generally, jute filaments are extricated from the strip of the stem. It is utilized as bundling material (sacks), cover sponsorship, ropes and yarns and in numerous other improving things. Table 1 displays the classification and uses of plant fibers, and Table 1 illustrates the composition of chemical for various fibers.

2.5 Stalk Fiber

These strands are really separated from the stalks of the plant, for instance, rice, grain, straws of wheat, bamboo and grass.

Table 1 represents the chemical formation of numerous fibers.

3 Methods of Fabrication of Natural Fiber Composites

Manufactures of composites are finished by specific techniques, which are explained below. These cycles are redone for the express substances that are presence taken care of. For the determination of the suitable resin, polymer interactions assume a significant part in it. The accompanying strategies are broadly utilized strategy by various specialists.

3.1 *Hand Layup*

This is the most un-problematic pattern of dealing with the thermoset amassed strands. Close by lay-up strategy, right off the bat a delivering specialist is applied outwardly of structure to keep up a key good ways from the holding fast of polymer to the outside. To get the remarkable surface summit of things, slim plastic layers are utilized at the most noteworthy and base of shape. Strands as a fortress also in sort of woven knot or in the cut structure are set at the outside of the shape. By then, a blend of thermosetting pitch and reasonable hardener are exhausted apparently of tangle as of late arranged in the shape. The polymer is dependably scattering with the assistance of contact. Another layer of the fortress is then arranged on the polymer outside, and a roller is utilized to clear air correspondingly as wealth framework existing. The practice is continuous for each layer of help and grid, till the important solidness is cultivated. In this technique, epoxy gum is used by different investigators [17–21] and polyester pitch is used by scientists [22–25] for production of cross-breed composites by using this system.

3.2 *Compression Molding*

Compression molding is a fastened molding progression with extreme weight usage. In this technique, both coordinated metal molds are utilized to create composite item. The bottom plate is fixed, while top plate is mobile in pressure decay. Fortification and lattice are put in the metallic shape, and the entire gathering is maintained in the middle of the pressure decay [26]. The necessary measure of warmth and weight relies on geometry and size of composites. The support and grid are put between the decay overlays, which streams owing to use of weight and warmth. The relieving of composites happens at atmospheric temperature. In the wake of restoring of composite, shape is unbolted and mixture item is taken out for additional preparing. This technique is reasonable for thermosets just as thermoplasts-built strands (manufactured just as normal) composites. Strand-strengthened thermoset composite is set up by various scientists [27–32], and thermoplasts-built fiber composite is set up by [33].

3.3 Injection Molding

This system is utilized for the progression of plastic segments with uncommon measurement precision. The things, for example, home things, play things, vehicle parts, furnishings, packaging things, contraptions and clinical departure needles, are passed on by the implantation shaping cycle. Implantation molding is a method of circling things by persuading liquid plastic substances under strain into a structure where it is chilled, set and thusly passed on by opening up the 2 pieces of the structure [34]. This framework is reasonable for thermosets comparatively to thermoplastic-based strand (made similarly as ordinary) fortified composite. The thermoplastic-based fiber composite is set up by [34–36] utilizing this strategy.

3.4 Pultrusion

This is a predictable framework for accumulating things having a predictable cross-piece, e.g., tubing, basic shapes, bars pipe, channels, bar stock and anticipating posts. In this system, the consistent wandering of the stronghold is impregnated with tar bypassing through the tar shower and here and there later crossed steel bombs hopelessly. The steel bombs horribly fortifies the sprinkled help, puts the condition of the stock, and controls the fiber/gum degree. The give is warmed to basically fix the gum [36]. The pultrusion technique is proper for thermoset polymer composites sustained by either made or normal fibers. This technique is utilized by [37] to make the creamer composites.

4 Mechanical Attributes

Elasticity and modulus of rigidity of fibers increase by expanding cellulose [37]. The small-scale fibrillar point resolves the stiffness of the strands. Strands are additional tensile if the smaller-scale fibrils have a winding direction to the strand pivot. On the off possibility that the smaller-scale fibrils are printed corresponding to the strand pivot, the strands will be unbending and solid, and have peak elasticity. The attributes of natural fiber-strengthened composites depend upon various boundaries, for example, volume portion of the fibers, fiber viewpoint proportion, fiber framework bond, stress move at the interlink, furthermore, direction. The majority of the examinations on regular fiber composites include investigation of mechanical attributes as an element of fiber contented, impact of different medicines of strands and the utilization of outside connection agents [38–42]. Further angles incorporate the expectation of modulus and quality utilizing some settled models for both stage frameworks and correlation with test data [43]. Both the lattice and strand attributes are significant in enhancing mechanical characters of the mixtures. The unbending

nature is more sensible to the framework attributes; however, the moduli are reliant on the fiber attributes. To develop the versatility, a solid interface and low-pressure focus, strand direction is needed; however, strand obsession, strand moistening in the grid stage and high strand point of view extent choose elastic modulus.

4.1 *Tensile Attributes*

The ductile attributes of common fiber composites are for the most part influenced by the interlink bond among the resin and fibers [44]. Substantial and substance alteration of the fiber and tar upgrades the ductile attributes of composites. The ductile attributes of common fiber composites are profoundly reliant on the strand volume division in the grid sap. Though different scientists demonstrated flighty examples for flexible properties of blends as a part of strand volume parcel, it is commonly evident that by an expansion in the strand amount under an ideal worth, the load is conveyed to other filaments and the grid can convey the operated burden later strands crack. This can indicate an extreme elasticity for the composite. The opposite and unpredictable patterns for the pliable attributes can be a direct result of numerous components, including contrariness among the fibers and medium, fiber deprivation and improper manufacturing processes [45]. With further increments in the fiber volume part after the ideal sum, weak break happens in the filaments and the framework cannot bolster the extra burden from the fibers. Under these conditions, the low elasticity in the long run prompts disappointment of the entire composite [46]. Sathees Kumar [47] developed hybrid composites by using three dissimilar natural fibers (sisal fiber (SF), jute fiber (JF) and sorghum bicolor fiber (SBF))-reinforced polyester composites. In this experiment, the specimens were fabricated through hand layup method and the composition (wt%) of three different fibers is specimen A—SF 50, JF 45 and SBF 5; specimen B—SF 40, JF 50 and SBF 10; specimen C—SF 50, JF 35 and SBF 15; specimen D—SF 40, JF 40 and SBF 20; specimen E—SF 50, JF 25 and SBF 25; and specimen F—SF 40, JF 30 and SBF 30. From the experimental work, the ductile properties of above compositions are illustrated in Fig. 10. From Fig. 10, sample D achieved the maximum ductile strength. Because sisal and jute fibers are equally shared, the maximum weight % (40 and 40) and sorghum fiber composition have very less % (20). This result exhibits the individual characteristics of fibers. The maximum contents of individual fiber have few unique characters. Figure 11 demonstrates the prolongation of crossover composites, and the stretching character of composites likewise expanded ahead to the degree of 14.4 mm (D). The elastic component of mixtures extended steadily from A, B, C and D examples. Out of the blue, it has decreased on E and F sample. Extending the sorghum fiber substance may diminish the yielding attribute and extend the shortcoming of the examples. By and large, higher fiber content is needed with the ultimate objective of achieving first class of short fiber-invigorated polymer composites (SFPCs). It is frequently seen that the nearness of strand or other support in the polymeric substance promotes the mixture quality and ductile moduli [48]. In this manner, the impact of

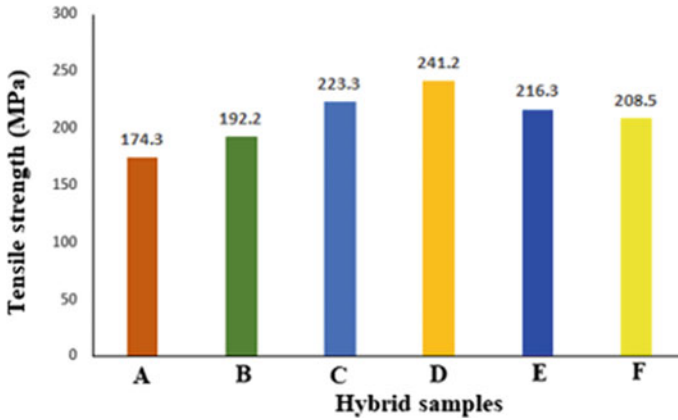


Fig. 10 Tensile strength of composites [47]

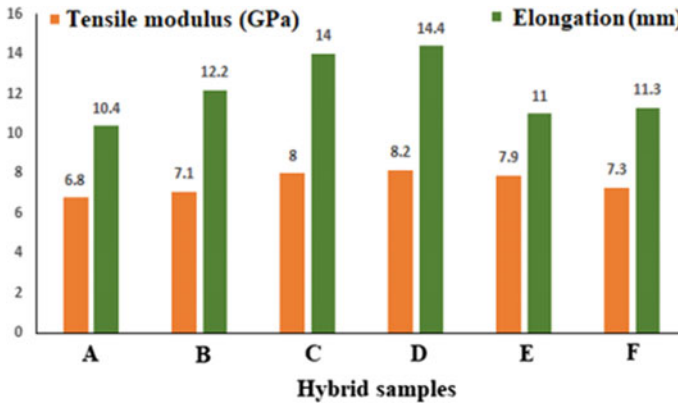


Fig. 11 Tensile modulus and elongation of composites [47]

fiber contented on the ductile attributes of strand-strengthened mixtures is of exact attention and importance for some investigators [49]. Sathees Kumar [50] studied the effect of mechanical attributes on three dissimilar natural fibers. In this study, different combinations of compositions of fibers (sisal fiber (SF), jute fiber (JF) and banana fiber (BF)) were utilized to prepare the samples as follows: sample A—SF 90, JF 5 and BF 5; sample B—SF 80, JF 10 and BF 10; sample C—SF 70, JF 15 and BF 15; sample D—SF 60, JF 20 and BF 20; and specimen E—SF 50, JF 25 and BF 25. From the experimental work, the ductile properties of above compositions are illustrated in Fig. 12. In this study, sisal as base fiber and remaining two fibers are fillers. Half of the weight % (50) of sisal and remaining two halves of each fiber % (25 and 25) attained the higher tensile values. Figure 12 because of legitimate

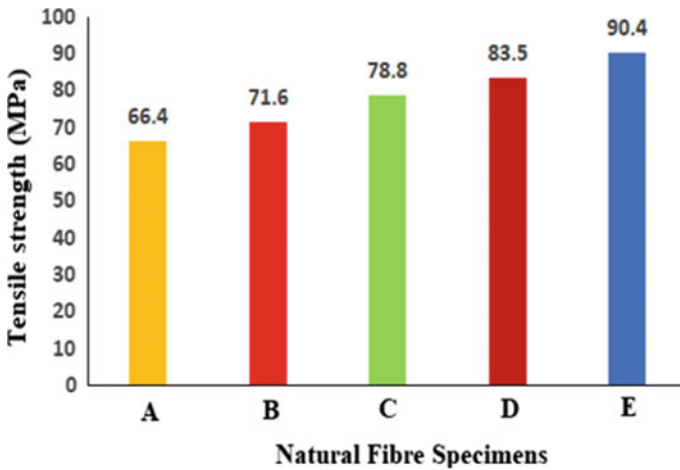


Fig. 12 Tensile strength of natural fiber composites [50]

scattering of base fiber and equivalent sharing of high fillers attained better flexible property.

4.2 Applications of Natural Fiber Composites

As of late, common strands alike hemp, jute, sisal and flax have been a part of cutting point development and initiated to expel their negligence. The use of common strand mixtures has enlarged and is collecting up proclivity across glass and carbon fiber for the reason that of their comfort and weightless attributes. Europe-based common strand mixture disintegrates, e.g., Dräxlmaier Group and Faurecia, flexibly car inside parts, for example, main events, side also, seats, back dividers and floor cover to Audi, Volvo and GM [51–53]. This kind of composite material can be helpful for bundling, shipping industry and interior decoration for civil engineering domains [54–58].

5 Conclusion

- In the most recent decade, the utilization of regular strands has been essentially expanded for industrial and automotive applications.
- Natural fiber composites as of late had an incredible recharged enthusiasm for an assortment of reasons, for example, diminished the price, simplicity of creation, less thickness and weightiness, and an expanded mindfulness regarding the matter of reusing and the effect of substances on the earth have likewise assumed a significant job in the reception of common strand mixtures.

- For a decent combination, it is expected to have incomprehensible interface characteristics among strand and cross-territory for the trading of the weight percent interfaces.
- Natural strand mixtures are consumed in a grouping of inside and outside bits of vehicles, bundling in ventures and development fields.
- Current research for a more observable comprehension of fundamental fiber compo-objections will comparably add to a more obvious interest take-up in these standard fiber-based composite grid by an industry that will continue instigating a steadily developing number of things entering the business later on.

References

1. Schneider JP, Myers GE, Clemons CM, English BW (1995) Biofibres as reinforcing fillers in thermoplastic composites. *Eng Plast (UK)* 8(3):207–222
2. Pothan LA, Thomas S, Neelakantan NR (1997) Short banana fiber reinforced polyester composites: mechanical, failure and aging characteristics. *J Rein Plast Comp* 16(8):744–765
3. Francis R (2016) *Recycling of polymers: methods, characterization and applications*. Wiley (2016)
4. Saheb DN, Jog JP (1999) Natural fiber polymer composites: a review. *Adv Polym Technol J Poly Proc Inst* 18(4):351–363
5. Mohanty AK, Misra M, Hinrichsen G (2000) *Macromol. Mater Eng* 276/277
6. Lucintel NFCMT (2011) Forecast 2011, trend. In: *Forecast and opportunity analysis (2016)*
7. Wambua P, Ivens J, Verpoest I (2003) Natural fibres: can they replace glass in fibre reinforced plastics? *Compos Sci Technol* 63(9):1259–1264
8. Wegst UG (1996) *The mechanical performance of natural materials* (Doctoral dissertation, University of Cambridge)
9. Ticoalu A, Aravinthan T, Cardona F (2010) A review of current development in natural fiber composites for structural and infrastructure applications. In: *Proceedings of the southern region engineering conference (SREC 2010)*, pp 113–117. Engineers Australia
10. Karus M, Kamp M, Lohmeyer D (2000) Study of markets and price situation of natural fibres. (Germany and EU) Nova Institute, Germany
11. Kozłowski R, Mieleniak B, Muzyczek M, Mańkowski J (2008) Development of insulation composite based on FR bast fibers and wool. In: *International conference on flax and other bast plants*, pp 176–182
12. Armentano I, Dottori M, Fortunati E, Mattioli S, Kenny JM (2010) Biodegradable polymer matrix nanocomposites for tissue engineering: a review. *Polym Degrad Stab* 95(11):2126–2146
13. Summerscales J, Dissanayake NP, Virk AS, Hall W (2010) A review of bast fibres and their composites. Part 1–Fibres as reinforcements. *Compos Part A Appl Sci Manuf* 41(10):1329–1335
14. Rowell RM, Sanadi AR, Caulfield DF, Jacobson RE (1997) Utilization of natural fibers in plastic composites: problems and opportunities. *Lignocellulosic-Plast Comp* 13:23–51
15. Delicano JA (2018) A review on abaca fiber reinforced composites. *Compos Interfaces* 25(12):1039–1066
16. Motaung TE, Anandjiwala RD (2015) Effect of alkali and acid treatment on thermal degradation kinetics of sugar cane bagasse. *Ind Crops Prod* 74:472–477
17. Ramnath BV, Kokan SJ, Raja RN, Sathyanarayanan R, Elanchezhian C, Prasad AR, Manickavasagam VM (2013) Evaluation of mechanical properties of abaca–jute–glass fibre reinforced epoxy composite. *Mater Des* 51:357–366

18. Ahmed KS, Vijayarangan S (2008) Tensile, flexural and interlaminar shear properties of woven jute and jute-glass fabric reinforced polyester composites. *J Mater Process Technol* 207(1–3):330–335
19. Mishra S, Mohanty AK, Drzal LT, Misra M, Parija S, Nayak SK, Tripathy SS (2003) Studies on mechanical performance of biofibre/glass reinforced polyester hybrid composites. *Compos Sci Technol* 63(10):1377–1385
20. Da Silva LJ, Panzera TH, Velloso VR, Christoforo AL, Scarpa F (2012) Hybrid polymeric composites reinforced with sisal fibres and silica microparticles. *Compos B Eng* 43(8):3436–3444
21. Shinoj S, Visvanathan R, Panigrahi S, Kochubabu M (2011) Oil palm fiber (OPF) and its composites: a review. *Ind Crops Prod* 33(1):7–22
22. Athijayamani A, Thiruchitrabalam M, Manikandan V, Pazhanivel B (2019) Mechanical properties of natural fibers reinforced polyester hybrid composite. *IJ Plast Tech* 14(1):104–116
23. Pavithran C, Mukherjee PS, Brahmakumar M, Damodaran AD (1991) Impact properties of sisal-glass hybrid laminates. *J Mater Sci* 26(2):455–459
24. Khanam PN, Khalil HA, Reddy GR, Naidu SV (2011) Tensile, flexural and chemical resistance properties of sisal fibre reinforced polymer composites: effect of fiber surface treatment. *J Poly Environ* 19(1):115–119
25. Sarasini F, Tirillò J, Valente M, Valente T, Cioffi S, Iannace S, Sorrentino L (2013) Effect of basalt fiber hybridization on the impact behavior under low impact velocity of glass/basalt woven fabric/epoxy resin composites. *Compos Part A Appl Sci Manuf* 47:109–123
26. Huda MS, Drzal LT, Mohanty AK, Misra M (2006) Chopped glass and recycled newspaper as reinforcement fibers in injection molded poly (lactic acid)(PLA) composites: a comparative study. *Comp Sci Tech* 66(11–12):1813–1824
27. Shanmugam D, Thiruchitrabalam M (2013) Static and dynamic mechanical properties of alkali treated unidirectional continuous Palmyra Palm Leaf Stalk Fiber/jute fiber reinforced hybrid polyester composites. *Mater Des* 50:533–542
28. Akil HM, Santulli C, Sarasini F, Tirillò J, Valente T (2014) Environmental effects on the mechanical behaviour of pultruded jute/glass fibre-reinforced polyester hybrid composites. *Comp Sci Tech* 94:62–70
29. Pérez-Fonseca AA, Robledo-Ortíz JR, Ramirez-Arreola DE, Ortega-Gudiño P, Rodrigue D, González-Núñez R (2014) Effect of hybridization on the physical and mechanical properties of high density polyethylene–(pine/agave) composites. *Mater Des* 64:35–43
30. Zhong LX, Fu SY, Zhou XS, Zhan HY (2011) Effect of surface microfibrillation of sisal fibre on the mechanical properties of sisal/aramid fibre hybrid composites. *Comp Part A Appl Sci Manuf* 42(3):244–252
31. Huda MS, Drzal LT, Mohanty AK, Misra M (2007) The effect of silane treated-and untreated-talc on the mechanical and physico-mechanical properties of poly (lactic acid)/newspaper fibers/talc hybrid composites. *Comp Part B: Eng* 38(3):367–379
32. Graupner N, Herrmann AS, Müssig J (2009) Natural and man-made cellulose fibre-reinforced poly (lactic acid)(PLA) composites: an overview about mechanical characteristics and application areas. *Comp Part A App Sci Manuf* 40(6–7):810–821
33. Narendar R, Dasan KP, Nair M (2014) Development of coir pith/nylon fabric/epoxy hybrid composites: mechanical and ageing studies. *Mater Des* 54:644–651
34. Venkateshwaran N, ElayaPerumal A (2014) Mechanical and water absorption properties of woven jute/banana hybrid composites. *Fib Poly* 13(7):907–914
35. Singh B, Gupta M, Verma A (1995) Mechanical behaviour of particulate hybrid composite laminates as potential building materials. *Const Build Mater* 9(1):39–44
36. Tzounis L, Debnath S, Rooj S, Fischer D, Mäder E, Das A, Heinrich G (2014) High performance natural rubber composites with a hierarchical reinforcement structure of carbon nanotube modified natural fibers. *Mater Des* 58:1–11
37. Athijayamani A, Thiruchitrabalam M, Natarajan U, Pazhanivel B (2009) Effect of moisture absorption on the mechanical properties of randomly oriented natural fibers/polyester hybrid composite. *Mater Sci Eng A* 517(1–2):344–353

38. Gassan J, Dietz T, Bledzki AK (2000) Effect of silicone interphase on the mechanical properties of flax-polyurethane composites. *Comp Inter* 7(2):103–115
39. Wright JR, Mathias LJ (1993) New lightweight materials: Balsa wood-polymer composites based on ethyl α -(hydroxymethyl) acrylate. *J Appl Poly Sci* 48(12):2241–2247
40. Belgacem MN, Bataille P, Sapieha S (1994) Effect of corona modification on the mechanical properties of polypropylene/cellulose composites. *J Appl Poly Sci* 53(4):379–385
41. Sain MM, Kokta BV (1994) Polyolefin-wood filler composite, performance of m-phenylene bismaleimide-modified wood fiber in polypropylene composite. *J Appl Poly Sci* 54(10):1545–1559
42. Sain MM, Kokta BV, Imbert C (1994) Structure-property relationships of wood fiber-filled polypropylene composite. *Poly Plast Tech Eng* 33(1):89–104
43. Ota T, Takahashi M, Hibi T, Ozawa M, Suzuki S, Hikichi Y, Suzuki H (1995) Biomimetic process for producing SiC-wood. *J Amer Ceram Soc* 78(12):3409–3411
44. Campilho RD (ed) (2015) Natural fiber composites. CRC Press
45. Ku H, Wang H, Pattarachaiyakop N, Trada M (2011) A review on the tensile properties of natural fiber reinforced polymer composites. *Compos Part B Eng* 42(4):856–873
46. Bowen CR, Dent AC, Stevens R, Cain M, Stewart M (2005) Determination of critical and minimum volume fraction for composite sensors and actuators. In: 4M2005 conference on multi-material micro manufacture
47. Sathees Kumar S (2020) Effect of natural fiber loading on mechanical properties and thermal characteristics of hybrid polyester composites for industrial and construction fields. *Fib Poly* 21(7):1508–1514
48. Ahmad I, Baharum A, Abdullah I (2006) Effect of extrusion rate and fiber loading on mechanical properties of Twaron fiber-thermoplastic natural rubber (TPNR) composites. *J Rein Plast Comp* 25(9):957–965
49. Li X, Tabil LG, Panigrahi S, Crerar WJ (2006) The influence of fiber content on properties of injection molded flax fiber-HDPE biocomposites. In: 2006 ASAE annual meeting. American Society of Agricultural and Biological Engineers, p 1
50. Sathees Kumar S, Vardhan TV, Babu BS, Chakravarthy CN, Prabhakar N, Rao KV, Tirupathi K (2020) Dataset on tribological, characterization and thermal properties of Silicon carbide reinforced polyamide composites for industrial applications. Data in Brief 105662
51. Boberg J, Fasihi F, Forkman M, Martinsson H, Sturesson P, Varosy J (2015) *Cellulosafiber-förstärkta plastbåtar*
52. Hill K, Swiecki B, Cregger J (2012) The bio-based materials automotive value chain. Center for Auto Res 112
53. Mugesh Raja V, Sathees Kumar S (2019) Determination of static and fatigue characteristics of carbon fiber reinforced polyester composites for automobile applications. *Mater Res* 22(6)
54. Sudhagar S, Raja VM, Sathees Kumar S, Samuel AJ (2019) The wear behaviour and service life of Madar and Bauhinia Racemosa reinforced polyester hybrid composites for gear applications. *Mater Today Proc* 19:589–593
55. Sathees Kumar S, Mugesh Raja V, Sridhar Babu B, Tirupathi K (2020) Comparison of ductile, flexural, impact and hardness attributes of sisal fiber-reinforced polyester composites. *Intel Manuf Ener Sustain* 645–654
56. Sathees Kumar S (2018) Evaluation of tensile, flexural, hardness and impact characteristics of polymer composites. *Int J Mech Eng Tech* 9:575–581
57. Sathees Kumar S (2010) Tribological characteristics of natural fiber reinforced polyester hybrid composites. *Int J Innov Tech Explo Eng* 8(10):947–952
58. Sathees Kumar S (2019) Mechanical and water absorption properties of Madar and Bauhinia Racemosa natural fiber composites. *Int J Rec Tech Eng* 8(2):2338–2342.

Elastic Instability of the Functionally Graded Porous Cylindrical Panel



Abhay Gupta, Amit Kumar Mangoliwala, Rajidi Shashidhar Reddy,
and Satyajit Panda

Abstract In present work, the transverse deflection characteristics of a functionally graded porous (FGP) cylindrical panel are analyzed. The FGP cylindrical panel is fabricated by varying the material properties along the thickness direction corresponding to different porosity distributions such as symmetric center-enhanced porosity distribution (SCPD), top-enhanced porosity distribution (TPD) and bottom-enhanced porosity distribution (BPD). The geometrically nonlinear incremental finite element (FE) model of the FGP cylindrical panel is developed. Further, FE governing equation of motion is solved using Newton–Raphson method. Initially, the present model is validated. Substantially, the present results are focused on the influence of various distributions of porous material, value of porosity index and radius of curvature on critical load for the elastic instability of FGP cylindrical panel. It is concluded from the results that critical loads of FGP cylindrical panel occur in ascending order for TPD, BPD and SCPD distributions, respectively.

Keywords Functionally graded materials · Porous materials · Finite element method · Elastic instability

1 Introduction

Porous materials are utilized in many advanced structural application owing to several properties such as light weight with high strength, magnificent energy-absorbing capability and low value of electrical/thermal conductivity [1]. Due to the very low density of porous materials, it can also be used as part of composite structures in many industrial applications such as in automotive/aerospace/marine/civil engineering and biomedical components [2]. These porous materials are in the form of various gradings of porous distributions. However, porosity distribution within the domain of a structure can also be tailored to meet with a specific structural design requirement leading to the functionally graded porous materials (FGPMs). Because of its

A. Gupta (✉) · A. K. Mangoliwala · R. S. Reddy · S. Panda
Indian Institute of Technology Guwahati, Guwahati, India
e-mail: abhay.gupta@iitg.ac.in

© The Author(s), under exclusive license to Springer Nature Singapore Pte Ltd. 2022
K. Govindan et al. (eds.), *Advances in Mechanical and Materials Technology*,
Lecture Notes in Mechanical Engineering,
https://doi.org/10.1007/978-981-16-2794-1_71

799

advantageous mechanical properties, these FGPMs are fetching for the utilization in structural applications. A lot of research work has been done based on the influence of FGPMs [3–10].

Besides, Wang et al. [11] analyzed the structural vibration of the functionally graded porous (FGP) plate. The result predicted that dynamic response and resonance region improve and decrease, correspondingly, because of incorporating porosity. Rezaei et al. [12] investigated the effects of various parameters such as distribution of porous and value of porosity index on natural frequency of FG plate. It was found that the natural frequency was more sensitive for the evenly distributed pores. Thang et al. [13] examined the buckling and vibration analysis of porous cellular plates with symmetric/uniform and non-symmetric/non-uniform distributions of the porous material. Similar investigations for the FG beam fabricated with symmetric and asymmetric distribution of porous material were done by Heshmati and Daneshmand [14]. In parallel, these studies have also been done for doubly curved panels/shells [15]. Kumar et al. [16] studied the influence of various porosity gradings and loadings on transverse deflection/stress of an FG porous plate.

It may be concluded from aforesaid literature that the FGPMs are extensively utilized in the design of advanced structures. However, a limited number of studies have been done, and most of the investigations are done for linear structural behavior of porous beams and plates. Besides these basic structural elements like beams and plates, the cylindrical panel is also useful for thin-walled structural element owing to its various structural utilizations. The specific advantage of the cylindrical panel lies in its high bending rigidity in comparison to that of plate structures, and it leads to wider application of panel structures. But, an associated discrepancy is the elastic instability of panel structures against the bending load, where the static equilibrium of a panel shifts to a new equilibrium position at a certain value of the applied load. This kind of elastic instability is commonly known as a snap-through phenomenon. In the present work, the finite element (FE) geometrically nonlinear incremental formulation of FGP cylindrical panel is obtained. The influence of different types of porosity distribution such as symmetric center-enhanced porosity distribution (SCPD), top-enhanced porosity distribution (TPD) and bottom-enhanced porosity distribution (BPD) in a cylindrical panel on its elastic instability is studied. Detailed investigations are reported in the following sections.

2 Finite Element Formulation of the FGP Cylindrical Panel

The FGP cylindrical panel in the curvilinear system is represented diagrammatically in Fig. 1a. The x - and y -axis are along the circumferential and longitudinal directions, respectively. The middle plane of cylindrical panel is taken as reference plane. The subtended angle and radius of curvature of cylindrical panel are indicated by θ and R , respectively. The thickness of cylindrical panel is denoted by h , while the length of cylindrical panel along the longitudinal and circumferential directions is denoted by a and b ($b = \theta R$), respectively. The material properties of cylindrical panel are

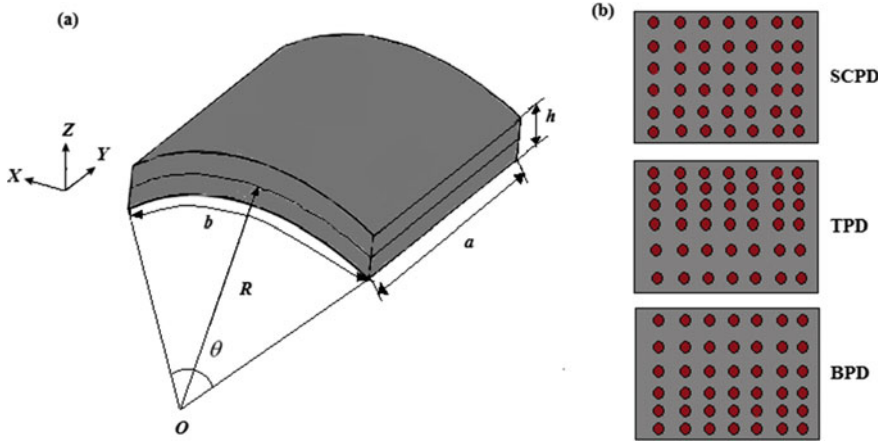


Fig. 1 Schematic diagram of the **a** FGP cylindrical panel in the curvilinear coordinate system and with **b** various porosity distribution

considered as the FGPM distributed along the thickness direction. Mainly, symmetric center-enhanced porosity distribution (SCPD), top-enhanced porosity distribution (TPD) and bottom-enhanced porosity distribution (BPD) are considered in the present analysis (Fig. 1b). This FGP cylindrical panel is subjected to transverse uniformly distributed load (UDL) (p_0) at its top ($z = h/2$) surface, while the edges of cylindrical panel are clamped edges.

By using first-order shear deformation theory (FSDT), the displacement components $u/v/w$ at any point along $x/y/z$ directions can be expressed as,

$$u = u_0 + z\theta_x, \quad v = v_0 + z\theta_y, \quad w = w_0 \tag{1}$$

With the plane stress assumptions, the state of strains (ϵ_b, ϵ_s) and stresses (σ_b, σ_s) at any point is obtained as in Eq. (2).

$$\begin{aligned} \epsilon_b &= \{ \epsilon_x \ \epsilon_y \ \epsilon_{xy} \}^T, & \epsilon_s &= \{ \epsilon_{xz} \ \epsilon_{yz} \}^T \\ \sigma_b &= \{ \sigma_x \ \sigma_y \ \sigma_{xy} \}^T, & \sigma_s &= \{ \sigma_{xz} \ \sigma_{yz} \}^T \end{aligned} \tag{2}$$

The strains (ϵ_b, ϵ_s) are obtained in Eq. (3), based on nonlinear strain–displacement correlation.

$$\epsilon_b = \epsilon_{bL} + \epsilon_{bN} + z\kappa, \quad \epsilon_s = \left\{ \left(\frac{\partial w_0}{\partial x} + \theta_x \right) \left(\frac{\partial w_0}{\partial y} + \theta_y \right) \right\}^T$$

where

$$\epsilon_{bL} = \left\{ \left(\frac{\partial u_0}{\partial x} + \frac{w_0}{R} \right) \frac{\partial v_0}{\partial y} \left(\frac{\partial u_0}{\partial y} + \frac{\partial v_0}{\partial x} \right) \right\}^T,$$

$$\boldsymbol{\varepsilon}_{bN} = \left\{ \frac{1}{2} \left(\frac{\partial w_0}{\partial x} \right)^2 \frac{1}{2} \left(\frac{\partial w_0}{\partial y} \right)^2 \left(\frac{\partial w_0}{\partial y} \frac{\partial w_0}{\partial x} \right) \right\}^T, \quad \boldsymbol{\kappa} = \left\{ \frac{\partial \theta_x}{\partial x} \frac{\partial \theta_y}{\partial y} \left(\frac{\partial \theta_x}{\partial y} + \frac{\partial \theta_y}{\partial x} \right) \right\}^T \quad (3)$$

The constitutive relations for the FGP cylindrical panel can be written as

$$\boldsymbol{\sigma}_b = \mathbf{C}_b \boldsymbol{\varepsilon}_b, \quad \boldsymbol{\sigma}_s = \mathbf{C}_s \boldsymbol{\varepsilon}_s; \quad \mathbf{C}_b = \frac{E(z)}{1-\nu^2} \begin{bmatrix} 1 & \nu & 0 \\ \nu & 1 & 0 \\ 0 & 0 & (1-\nu)/2 \end{bmatrix},$$

$$\mathbf{C}_s = \frac{E(z)}{1+\nu} \begin{bmatrix} 1/2 & 0 \\ 0 & 1/2 \end{bmatrix} \quad (4)$$

where $\mathbf{C}_b/\mathbf{C}_s$ and $E(z)/\nu$ are the stiffness matrices and Young’s modulus/Poisson’s ratio, correspondingly. Since the cylindrical panel is made of FGPM, it is graded along the thickness (z -axis). Thus, the distribution/value of $E(z)$ is dependent on the type of porosity distribution (Fig. 1b) as given in Eq. (5) [16].

- SCPD:

$$E(z) = \left[(E_t - E_b) \left(\frac{z}{h} + \frac{1}{2} \right)^k + E_b \right] \left[1 - X_p \cos\left(\frac{\pi z}{h} \right) \right] \quad (5a)$$

- TPD:

$$E(z) = \left[(E_t - E_b) \left(\frac{z}{h} + \frac{1}{2} \right)^k + E_b \right] \left[1 - X_p \cos\left(\frac{\pi}{2} \left(\frac{z}{h} - 0.5 \right) \right) \right] \quad (5b)$$

- BPD:

$$E(z) = \left[(E_t - E_b) \left(\frac{z}{h} + \frac{1}{2} \right)^k + E_b \right] \left[1 - X_p \cos\left(\frac{\pi}{2} \left(\frac{z}{h} + 0.5 \right) \right) \right] \quad (5c)$$

where subscript t/b denotes top/bottom surface of FGP cylindrical panel; k is the grading index, and it is taken as $k = 0.5$ in the present analysis; X_p denotes porosity index, and its value varies from 0 to 1 ($0 < X_p < 1$). First variation of total potential energy (δT_p) of the cylindrical panel is obtained in Eq. (6).

$$\delta T_p = \int_0^a \int_0^b \left[\int_{-h/2}^{h/2} \langle (\delta \varepsilon_b)^T \boldsymbol{\sigma}_b + (\delta \varepsilon_s)^T \boldsymbol{\sigma}_s \rangle dz - (\delta w) p_0 \right] dx dy \quad (6)$$

The state of deformation is expressed in terms of incremental form in Eq. (7), and the generalized strain ($\varepsilon_b, \varepsilon_s$) given in Eq. (3) can be obtained in incremental form as expressed in Eq. (8).

$$\mathbf{d} = \{u_0 \ v_0 \ w_0 \ \theta_x \ \theta_y\}^T = (\mathbf{d}^i + \Delta\mathbf{d}),$$

$$\mathbf{d}^i = \{u_0^i \ v_0^i \ w_0^i \ \theta_x^i \ \theta_y^i\}^T, \quad \Delta\mathbf{d} = \{\Delta u_0 \ \Delta v_0 \ \Delta w_0 \ \Delta\theta_x \ \Delta\theta_y\}^T \quad (7)$$

$$\boldsymbol{\varepsilon}_b = (\boldsymbol{\varepsilon}_b^i + \Delta\boldsymbol{\varepsilon}_b), \quad \boldsymbol{\varepsilon}_s = (\boldsymbol{\varepsilon}_s^i + \Delta\boldsymbol{\varepsilon}_s),$$

where

$$\boldsymbol{\varepsilon}_b^i = (\boldsymbol{\varepsilon}_{bL}^i + \boldsymbol{\varepsilon}_{bN}^i + z\boldsymbol{\kappa}^i), \quad \Delta\boldsymbol{\varepsilon}_b = (\Delta\boldsymbol{\varepsilon}_{bL} + \Delta\boldsymbol{\varepsilon}_{bN} + z\Delta\boldsymbol{\kappa}) \quad (8)$$

where $\boldsymbol{\varepsilon}_{bL}^i/\boldsymbol{\varepsilon}_{bN}^i/\boldsymbol{\kappa}^i/\boldsymbol{\varepsilon}_s^i$ and $\Delta\boldsymbol{\varepsilon}_{bL}/\Delta\boldsymbol{\varepsilon}_{bN}/\Delta\boldsymbol{\kappa}/\Delta\boldsymbol{\varepsilon}_s$ represent generalized strain vectors and its increments, correspondingly.

The FE model of overall cylindrical panel is discretized into nine-node isoparametric elements in 2D xy -plane. Thus, displacement vector (\mathbf{d}) and its increment ($\Delta\mathbf{d}$) can be expressed in form of shape function matrix (N) and elemental displacement vectors (\mathbf{d}^e , $\Delta\mathbf{d}^e$) as given in Eq. (9).

$$\mathbf{d} = N\mathbf{d}^e, \quad \Delta\mathbf{d} = N\Delta\mathbf{d}^e \quad (9)$$

By substituting Eqs. (4), (7), (8) and (9) in Eq. (6), δT_p can be expressed as,

$$\delta T_p^e = \left[\{\delta\Delta\mathbf{d}^e\}^T (\mathbf{K}_L^e + \mathbf{K}_N^{ie} + \mathbf{K}_{NN}^{ie}) \mathbf{d}^{ie} + \{\delta\Delta\mathbf{d}^e\}^T (\mathbf{K}_L^e + \mathbf{K}_N^e + \mathbf{K}_{NN}^e) \Delta\mathbf{d}^e - \{\delta\mathbf{d}^e\}^T \mathbf{F}^e \right] \quad (10)$$

where \mathbf{K}_L^e , \mathbf{K}_N^{ie} , \mathbf{K}_{NN}^{ie} , \mathbf{K}_N^e , \mathbf{K}_{NN}^e are the elemental stiffness matrices; \mathbf{F}^e denotes load vector; A_e designates area of an element in xy -plane. Since $\delta T_p^e = 0$, the elemental equations of equilibrium are expressed in Eq. (11).

$$(\mathbf{K}_L^e + \mathbf{K}_N^{ie} + \mathbf{K}_{NN}^{ie}) \mathbf{d}^{ie} + (\mathbf{K}_L^e + \mathbf{K}_N^e + \mathbf{K}_{NN}^e) \Delta\mathbf{d}^e = \mathbf{F}^e \quad (11)$$

After the assembly of elemental matrices/vectors (Eq. (11)), the governing equation of motion of the overall cylindrical panel can be obtained in the form of global matrices/vectors as given in Eq. (12).

$$\begin{aligned} (\mathbf{K}_L + \mathbf{K}_N^i + \mathbf{K}_{NN}^i) \mathbf{d}^i + (\mathbf{K}_L + \mathbf{K}_N + \mathbf{K}_{NN}) \Delta\mathbf{d} &= \mathbf{F} \\ (\mathbf{K}_L + \mathbf{K}_N + \mathbf{K}_{NN}) \Delta\mathbf{d} &= (\mathbf{F} - (\mathbf{K}_L + \mathbf{K}_N^i + \mathbf{K}_{NN}^i) \mathbf{d}^i) \end{aligned} \quad (12)$$

where \mathbf{d}/P_0 and \mathbf{K} represent global mechanical load/displacement vector and stiffness matrix, correspondingly.

Solution Methodology

Newton–Raphson method [17] is utilized to estimate the solution of Eq. (12). In this method, the value of \mathbf{d}^i is set to be zero in the first step of the first iteration, and

then, the increment of the solution is computed in each iteration from the equilibrium Eq. (12) as

$$\Delta \mathbf{d} = (\mathbf{K}_L + \mathbf{K}_N + \mathbf{K}_{NN})^{-1} (\mathbf{F} - (\mathbf{K}_L + \mathbf{K}_N^i + \mathbf{K}_{NN}^i) \mathbf{d}^i) \quad (13)$$

The solution in every step is updated for n^{th} iteration as $\mathbf{d}^{(n)} = \mathbf{d}^{i(n-1)} + \Delta \mathbf{d}^{(n)}$.

At the same time, the nonlinear stiffness matrix ($\mathbf{K}_N^i, \mathbf{K}_{NN}^i, \mathbf{K}_N, \mathbf{K}_{NN}$) is also updated after each iteration, and the convergence of the iterative solution is checked. If the convergence criteria are satisfied, the converged solution is taken as the equilibrium solution corresponding to that load. Then, the load is incremented, the iteration counter is initialized, and the steps are repeated for calculating the increment in the displacement.

3 Numerical Results and Discussion

The numerical results are presented in this section to investigate the influence of various porosity distributions, porosity index and radius of curvature on the critical load for elastic instability of the FGP cylindrical panel. The thickness $h = 0.001$ m and length $a = 1.01$ m and $b = 1.01$ m are taken in the longitudinal and circumferential directions of the cylindrical panel. The top and bottom surfaces of the FGP cylindrical panel are made of ceramic ($\text{Al}_2\text{O}_3: E_t = 380$ GPa, $\nu = 0.3$) and metal ($\text{Al}: E_b = 70$ GPa, $\nu = 0.3$), respectively. These materials are functionally graded along the thickness direction and distributed in the three ways, SCPD, TPD and BPD (Fig. 1b). The material properties for various porosity distributions are taken from [16]. The transverse UDL (p_0) is applied at the FGP cylindrical panel with clamped edges.

Initially, the FE model is validated for an isotropic cylindrical panel. Figure 2a illustrates the variation of central deflection with uniformly distributed load for the

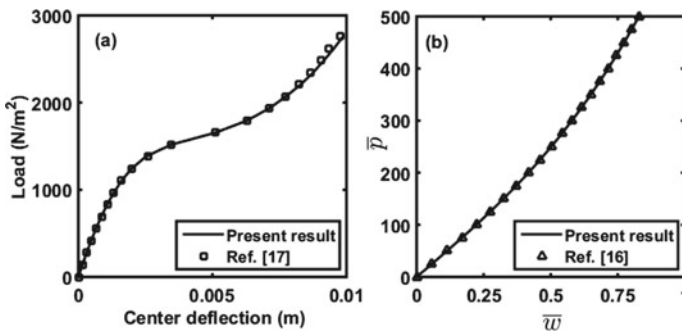


Fig. 2 Validation for the variation of a load with central deflection for isotropic cylindrical panel and b deflection parameter (\bar{w}) with load parameter (\bar{p}) for the FGP flat plate

isotropic cylindrical panel using present FE formulation and solution methodology, as expressed in Sect. 2. The similar result for identical cylindrical panel [17] is also illustrated in the same figure (Fig. 2a). The present FE results illustrated in Fig. 2a are very close with the reference result available in [17]. However, the results for the validation of the modeling of FGP cylindrical panel are not available in the literature. The modeling of FGP material is validated by considering the FGP flat plate (radius of curvature $R = \infty$). Figure 2b illustrates the variation of deflection parameter ($\bar{w} = w/h$) with load parameter ($\bar{p} = 12(1 - \nu^2)p_0a^4/E_t h^4$) for the FGP flat plate. The similar result for identical FGP flat plate [16] is also illustrated in the same figure (Fig. 2b). The present FE results illustrated in Fig. 2b are very close with the reference result available in [16]. These results verify the modeling of the present FGP cylindrical panel as well as the accuracy of the developed MATLAB code for the computation of static deflection.

For investigating the effect of radius of curvature (R) as well as porosity index (X_p) of SCPD, TPD and BPD of the FGP cylindrical panel, the variation of deflection parameter ($\bar{w} = w/h$) with load parameter ($\bar{p} = 12(1 - \nu^2)p_0a^4/E_t h^4$) is analyzed (Figs. 3, 4, 5 and 6). Figures 3a, 4a and 5a illustrate the variation of deflection parameter (\bar{w}) with load parameter (\bar{p}) at different radius of curvature (R) with a constant porosity index ($X_p = 0.35$) for SCPD, TPD and BPD, respectively. It may be observed from these figures that at lower values of radius of curvature, the elastic instability or snap-through phenomenon arises, whereas it disappears for the higher radii of curvature. However, the critical load for elastic instability or snap-through phenomenon decreases with an increase in the radius of curvature. Thus, it can be seen that the elastic instability clearly appears for the radius of curvature $R = 2$ m of the FGP cylindrical panel.

However, the elastic instability of the FGP cylindrical panel clearly appears at the radius of curvature $R = 2$ m. For elastic instability of the FGP cylindrical panel, the consequence of the value of porosity index (X_p) on critical load is studied at the same radius of curvature. Figures 3b, 4b and 5b illustrate the variation of deflection

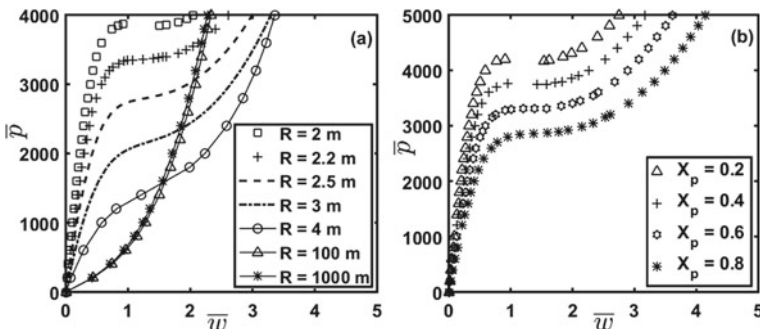


Fig. 3 Variation of deflection parameter (\bar{w}) with load parameter (\bar{p}) at **a** different radius of curvature (R) with a constant porosity index ($X_p = 0.35$) and **b** different porosity index (X_p) with a constant radius of curvature ($R = 2$ m) for SCPD of the FGP cylindrical panel

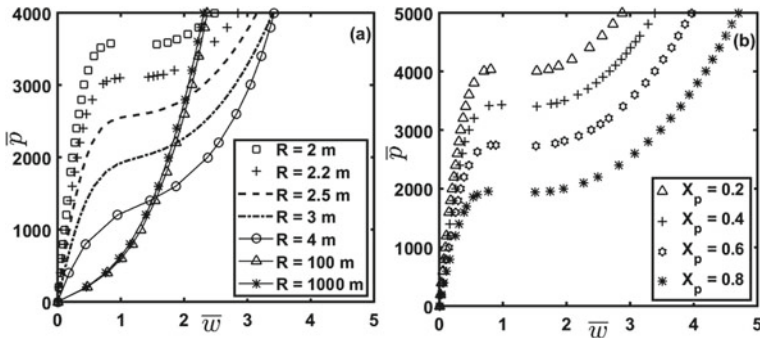


Fig. 4 Variation of deflection parameter (\bar{w}) with load parameter (\bar{p}) at a different radius of curvature (R) with a constant porosity index ($X_p = 0.35$) and b different porosity index (X_p) with a constant radius of curvature ($R = 2$ m) for TDP of the FGP cylindrical panel

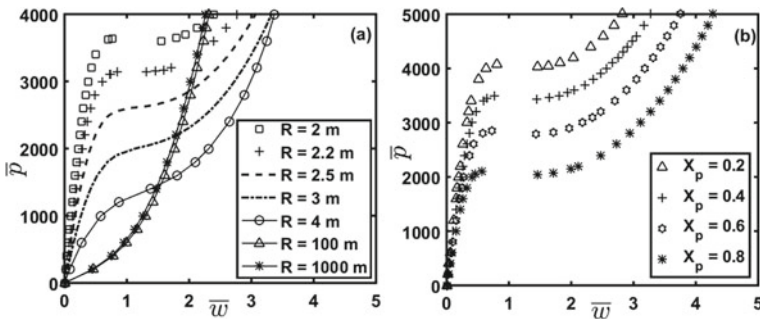


Fig. 5 Variation of deflection parameter (\bar{w}) with load parameter (\bar{p}) at a different radius of curvature (R) with a constant porosity index ($X_p = 0.35$) and b different porosity index (X_p) with a constant radius of curvature ($R = 2$ m) for BPD of the FGP cylindrical panel

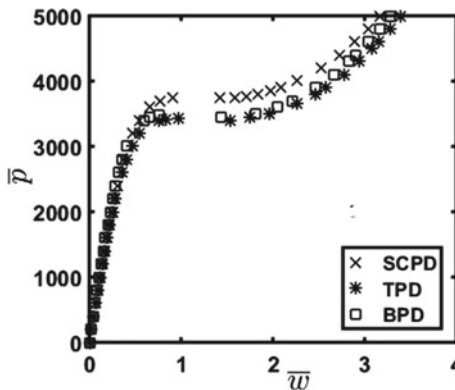


Fig. 6 Variation of deflection parameter (\bar{w}) with load parameter (\bar{p}) for different porosity distribution of the FGP cylindrical panel (at $R = 2$ m, $X_p = 0.35$)

Table 1 Variation of non-dimensional critical load value at different porosity index (X_p) with a constant radius of curvature ($R = 2$ m) for different porosity distribution of the FGP cylindrical panel

Porosity index (X_p)	Non-dimensional critical load		
	SCPD	TPD	BPD
0.2	4203	4046	4084
0.35	3870	3584	3644
0.4	3758	3442	3491
0.6	3314	2755	2853
0.8	2857	1963	2111

parameter (\bar{w}) with load parameter (\bar{p}) at different porosity index ($0 < X_p < 1$) with a constant radius of curvature ($R = 2$ m) for SCPD, TPD and BPD, respectively. With the rise in porosity index (X_p), critical load of FGP cylindrical panel reduces. However, decrease in deflection elevates near the critical load for different values of porosity index (X_p), while it changes drastically after the critical load. To analyze the change in instability characteristics for various porosity distributions, SCPD, TPD and BPD, load–deflection curves at a constant radius of curvature ($R = 2$ m) and porosity index ($X_p = 0.35$) are evaluated and presented in figure (Fig. 6). The value of critical loads of FGP cylindrical panel occurs in ascending order for TPD, BPD and SCPD distributions, respectively. Thus, the minimum and maximum critical loads for elastic instability are obtained for TPD and SCPD, respectively.

The non-dimensional critical load values at different porosity index (X_p) with a constant radius of curvature ($R = 2$ m) for different porosity distribution of the FGP cylindrical panel are presented in tabular form (Table 1). The results in Table 1 reveal that the critical load for elastic instability decreases with the increase of porosity index value (X_p). The minimum critical load occurs for TPD, and maximum critical load occurs for SCPD of the FGP cylindrical panel.

4 Conclusions

In this work, the elastic instability of FGP cylindrical panel is investigated. Moreover, the influence of radius of curvature, porosity distribution and the value of porosity index on the critical load is also investigated. Initially, the geometrically nonlinear incremental finite element formulation of the FGP cylindrical panel is formed. Then, corresponding FE governing equations of motion are solved by applying the procedure Newton–Raphson method. The material properties of the FGP cylindrical panel are varying along the thickness direction based on different types of porosity distributions such as SCPD, TPD and BPD. The variations of load–deflection characteristic are studied. The results reveal that the critical load reduces with the rise in radius of curvature. However, for the lower values of radius of curvature, the elastic instability

or snap-through phenomenon arises, whereas it disappears for the higher radii of curvature. It is also found that the critical load reduces with the rise in the value of porosity index. However, decrease in deflection elevates near the critical load for different values of porosity index, while it changes drastically after the critical load. The critical loads of the FGP cylindrical panel occur in ascending order for TPD, BPD and SCPD distributions, respectively.

References

1. Lefebvre LP, Banhart J, Dunand DC (2008) Porous metals and metallic foams: current status and recent developments. *Adv Eng Mater* 10(9):775–787
2. Pompe W, Worch H, Epple M, Friess W, Gelinsky M, Greil P, Hempel U, Scharnweber D, Schulte K (2003) Functionally graded materials for biomedical applications. *Mater Sci Eng A* 362(1–2):40–60
3. Magnucka-Blandzi E (2008) Axi-symmetrical deflection and buckling of circular porous-cellular plate. *Thin-Wall Struct* 46(3):333–337
4. Chen D, Yang J, Kitipornchai S (2015) Elastic buckling and static bending of shear deformable functionally graded porous beam. *Compos Struct* 133:54–61
5. Ebrahimi F, Zia M (2015) Large amplitude nonlinear vibration analysis of functionally graded Timoshenko beams with porosities. *Acta Astro* 116:117–125
6. Akbas SD (2017) Vibration and static analysis of functionally graded porous plates. *J Appl Comput Mech* 3(3):199–207
7. Tang H, Li L, Hu Y (2018) Buckling analysis of two-directionally porous beam. *Aero Sci Tech* 78:471–479
8. Kitipornchai S, Chen D, Yang J (2017) Free vibration and elastic buckling of functionally graded porous beams reinforced by graphene platelets. *Mater Des* 116:656–665
9. Gupta A, Panda S, Rajidi SR (2020) Design of graded laminated composite beam under moving load. *Mater Today Proc* 26:1572–1579
10. Wu D, Liu A, Huang Y, Huang Y, Pi Y, Gao W (2018) Dynamic analysis of functionally graded porous structures through finite element analysis. *Eng Struct* 165:287–301
11. Wang YQ, Wan YH, Zhang YF (2017) Vibrations of longitudinally traveling functionally graded material plates with porosities. *Eur J Mech-A/Sol* 66:55–68
12. Rezaei AS, Saidi AR, Abrishamdari M, Mohammadi MP (2017) Natural frequencies of functionally graded plates with porosities via a simple four variable plate theory: an analytical approach. *Thin Wall Struct* 120:366–377
13. Thang PT, Nguyen-Thoi T, Lee D, Kang J, Lee J (2018) Elastic buckling and free vibration analyses of porous-cellular plates with uniform and non-uniform porosity distributions. *Aero Sci Tech* 79:278–287
14. Heshmati M, Daneshmand F (2019) Vibration analysis of non-uniform porous beams with functionally graded porosity distribution. *Proc Inst Mech Eng Part L J Mater Des Appl* 233(8):1678–1697
15. Zhao J, Xie F, Wang A, Shuai C, Tang J, Wang Q (2019) Vibration behavior of the functionally graded porous (FGP) doubly-curved panels and shells of revolution by using a semi-analytical method. *Compos Part B Eng* 157:219–238
16. Kumar R, Lal A, Singh BN, Singh J (2020) Non-linear analysis of porous elastically supported FGM plate under various loading. *Compos Struct* 233:111721
17. Reddy JN (2014) An introduction to nonlinear finite element analysis: with applications to heat transfer, fluid mechanics, and solid mechanics. Oxford University Press, Oxford

Design and Development of Industry 4.0-Enabled Monitoring System



Abhimanyu Sharma, Parth Gahalot, Sharjil Talib, Sumit Gupta, Nipun Gautam, Atul Singh, Umananda Goswami, and Shubham

Abstract Current scenario of industrialization allows for the higher levels of automation, but as a result affecting the natural environment negatively. Pollution in the era of industrialization is a major concern. The releasing of unwanted wastes in the environment especially in industrial areas is hazardous to workers' health. A robust system was built to measure various industrial parameters such as temperature, humidity, and air particles. This automated system would reduce the need for human interference in monitoring processes at the workshop level. On monitoring various parameters, the automated system would be able to inform authorities of any variations from standards through a platform. A Wi-Fi module is introduced to facilitate live monitoring of pre-defined parameters and alerts the authorities in the case of disturbances such as smoke, temperature and carbon content of machinery affecting the system.

Keywords IoT · Industry 4.0 · Sensors

1 Introduction

In the current era, emerging technologies like big data analytics, industrial robots and interaction between machines and robots are producing opportunities for future factories: Factory 4.0 [1]. Automation has to be implemented in production for the benefit of emerging competitive markets so that a flexible, adaptive and more integrated approach can be implemented by using IoT by different companies of the world [2]. The new mechanism of transmitting information is radically changing the nature of things. Product functionality is embedded with sensors and microprocessors to product cloud space, designed to store and analyze data. The objective of this research work is to develop a module to minimize human involvement in monitoring operations in industries. To facilitate this automation technology, the tool of Industry 4.0 “Internet of Things (IoT)” is used for efficient monitoring. The

A. Sharma · P. Gahalot · S. Talib · S. Gupta (✉) · N. Gautam · A. Singh · U. Goswami · Shubham
Department of Mechanical Engineering, Amity School of Engineering and Technology, Amity
University, Noida 201313, India

developed module uses the Web as an IoT enabler so that the user may screen and mechanize the workspace remotely.

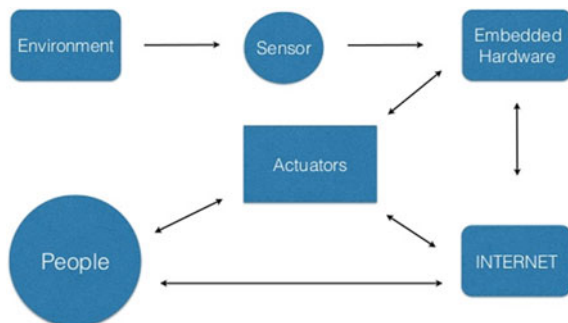
2 Literature Review

The Industry 4.0 (I 4.0) concept is such that it seeks to change factories of today into smart factories by creating a system of production where human interference is very less as compared to normal factories this will be done by using smart machines which are all linked to each other and can sense their surroundings and learn from it and using smart products which can communicate as well as perform some other functions [3]. Artificial intelligence (AI) coupled with IoT technologies provides a bright answer for automation of the various industry sectors. IoT enables vertical and horizontal integration of businesses through packages such as enterprise resource planning (ERP). Such packages are instrumental in monitoring and controlling various business operations not only in manufacturing but also in the service industry. In manufacturing industries, IoT enables the operators to monitor and control their workstations through an IoT module. This would ensure the safety of the operator from exposure to dangerous environments [4, 5].

2.1 Internet of Things (IoT)

IoT makes use of programming to coordinate with sensors and other electronic components and form a network that can enhance performing various tasks. This network of components constantly trades information to facilitate making user decision making easier [6]. IoT frameworks consist of physical entities or components that are identified by their own IP address in the system. These entities form a network between them and with other gadgets that belong to a separate network (Fig. 1).

Fig. 1 IoT framework



This research work is divided into four parts, each having its significance. The concepts of automation and IoT are used to carry out this work.

2.2 Industrial Internet of Things (IIoT) with Industry 4.0

IoT is a major component of Industry 4.0 that enables various industries develop formative enterprises to enter the Industry 4.0 age [7]. Also, Industry 4.0 improves the manufacturing operations and monitors the different parameters [8]. The Industry 4.0 industrial formations are flexible in progress volume, mass customization, with harmonization between suppliers and clientele [9, 10].

3 Methodology

The module was made to demonstrate a framework to inspect and monitor various factors and to warn operators/users when any of these factors deviate from the pre-defined standard. This module consists of four articles, viz. power supply unit, an input device, an output device and a controller. A Wi-Fi module is installed which would screen any variations from the standard that affect standard operating procedures such as smoke, temperature anomalies and pressure.

4 Design Scheme and Fabrication

The design schematic was done using MS Paint. Figure 2 illustrates the schematic arrangement of the components that were used in the module. The design includes an Arduino microprocessor, an LCD for display, a relay to facilitate control, a Wi-Fi module for seamless data transmission and sensors for data collection.

4.1 CAD Model Development

The model was developed using the eagle software (illustrated in Fig. 3). The software is an automated script design (EDA) application. The software is capable of schematic acquisition, designing printed circuit boards (PCBs) and enables production enablers such as computer-aided manufacturing (CAM). The design (Fig. 3) is the blueprint of the project. The design accommodates all the components that were used to make the monitoring system.

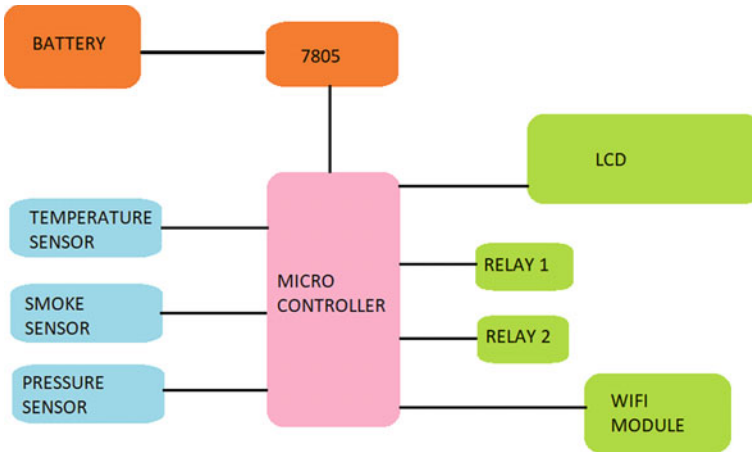


Fig. 2 Blue print of hardware design

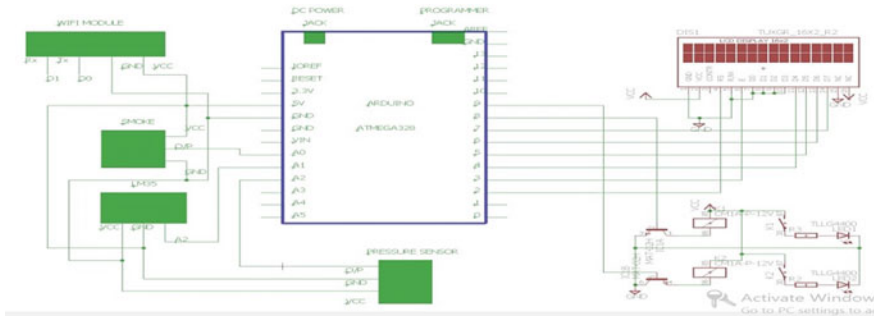


Fig. 3 Developed CAD model

4.2 Integration of Components

Figure 4 illustrates all the hardware assembled to make the monitoring system. A circuit board forms the basis of the module consisting of the Arduino board, connecting four relay boards. The LCD for display of information and the sensors used are connected in the circuit. The Wi-Fi module ensures wireless data transmission, and to power all these modules, a power supply is provided. Four load devices are connected as a means of collecting data. These include a bulb, a heater, a pump and a motor.

The circuit connection forms the basis of the device, making it capable of detecting any variations that may be hazardous in a manufacturing environment (Fig. 5).

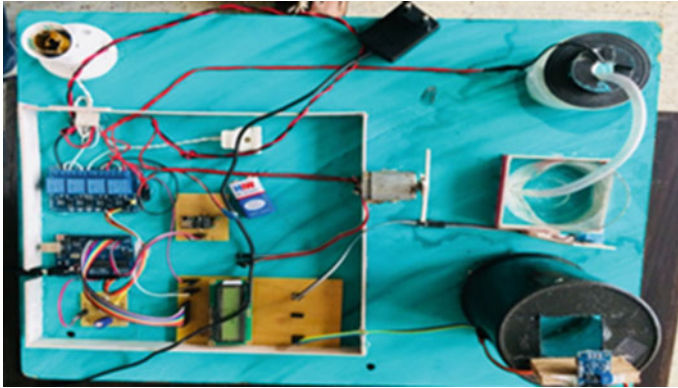


Fig. 4 Intermediate setup

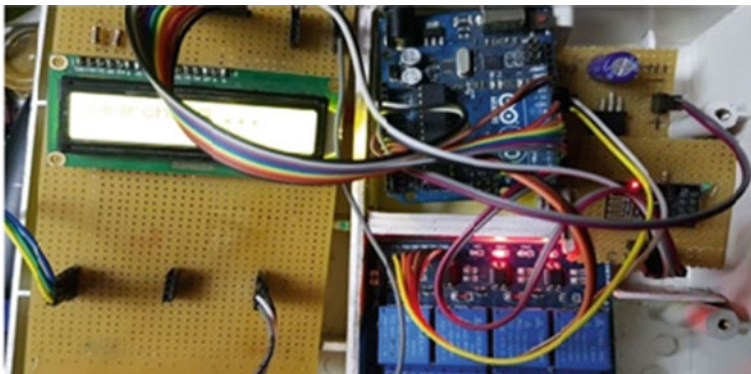


Fig. 5 Circuit connections and components

4.3 Soft Wares Used and Their Implication

4.3.1 C Program

The C programming language was developed in 1969 by Dennis Ritchie. It can be used to code more than one function, where each function performs a particular undertaking. The C programming bolsters both high- and low-level applications.

4.3.2 Coding the Arduino

The coding of the Arduino UNO was developed in the C programming language. C is a middle-level programming language. It is necessary to know about RAM affiliation before starting off with the unobtrusive components.

Fig. 6 Relays OFF



Fig. 7 Relays ON



4.4 Website Development

To design the Website, Html and PHP were used. PHP admin was used to creating the database. This includes data like temperature, humidity, etc. Bootstrap Maxcdn plugin was used to make the page responsive and enable the buttons to function.

4.4.1 Website Layout

See Figs. 6 and 7.

5 Conclusion

In a world where technology is constantly being upgraded, we face the issue of high cost in implementing new technologies. With I 4.0 implemented, people who otherwise would have to work in vulnerable conditions are made safe. The system developed in this project work is cost-effective. It can monitor as well as control

variables that control various processes. This enables operators to control workstations from a remote location. In a dangerous environment where there is exposure to high temperatures and pressure, this remote access ensures that the operators and the machinery are safe. The system developed enables automation with IoT-enabled technologies, allowing the operator to monitor and resolve the issue remotely in the comfort of a safe environment. Consider an instance when the smoke level increases from the standard set level, the sensor detects and returns a value to the server. The user can then control these levels by turning the relays in the ON/OFF condition as favorable to the situation. Accordingly, through this system, temperature and entity weights may also be monitored on the Web and subsequently controlled.

References

1. Aggarwal A, Gupta S, Ojha MK (2019) Evaluation of key challenges to Industry 4.0 in Indian context: a DEMATEL approach. In: *Advances in industrial and production engineering*. Springer, Singapore, pp 387–396
2. Pavithra D, Balakrishnan R (2015) IoT based monitoring and control system for home automation. In: *2015 global conference on communication technologies (GCCT)*. IEEE, pp 169–173
3. Qin J, Liu Y, Grosvenor R (2016) A categorical framework of manufacturing for industry 4.0 and beyond. *Proc Cirp* 52:173–178
4. Bagheri B, Yang S, Kao HA, Lee J (2015) Cyber-physical systems architecture for self-aware machines in industry 4.0 environment. *IFAC Pap Online* 48(3):1622–1627
5. Weyer S, Schmitt M, Ohmer M, Gorecky D (2015) Towards Industry 4.0-standardization as the crucial challenge for highly modular, multi-vendor production systems. *IFAC Pap Online*, 48(3):579–584
6. Palattella MR, Accettura N, Grieco LA, Boggia G, Dohler M, Engel T (2013) On optimal scheduling in duty-cycled industrial IoT applications using IEEE802.15.4e TSCH. *IEEE Sens J* 13(10):3655–3666
7. Shrouf F, Ordieres J, Miragliotta G (2014) Smart factories in Industry 4.0: a review of the concept and of energy management approached in production based on the Internet of Things paradigm. In: *2014 IEEE international conference on industrial engineering and engineering management*. IEEE, pp 697–701
8. Jamwal A, Agrawal R, Sharma M, Dangayach GS, Gupta S (2021) Application of optimization techniques in metal cutting operations: A bibliometric analysis. *Materials Today: Proc.* 38, 365–370
9. Gubbi J, Buyya R, Marusic S, Palaniswami M (2013) Internet of Things (IoT): a vision, architectural elements, and future directions. *Futur Gener Comput Syst* 29(7):1645–1660
10. Janik K, Thompson I, Walley G, Land P, Suwala A (2019) Leading edge assembly real time process monitoring using industrial Internet of Things (IIoT) (No. 2019-01-1367). SAE technical paper

Theoretical Modelling of Thin Air Film Thickness in Miscible Liquids



Vijayakumar Mathaiyan, R. Vijayanandh, and Dong Won Jung

Abstract Current available theories about thickness of air film trapped in between droplet and bath of miscible liquids can also be explained in terms of conservation of energy. Though the authors proved the governing equation can be derived from energy equation, the detailed explanation is not available in any source. Detailed derivation of the thin air film thickness in miscible liquids and stages of coalescence are presented in the paper.

Keywords Miscible liquids · Thin air film thickness · Conservation of energy

1 Introduction

Hele-Shaw's work on the fluid flow in thin geometry [1] gained interest for its applicability in wide range of fluids. The thin geometry is later called as Hele-Shaw cell [2]. In recent researches, thin air film in between the liquids was considered as thin fluid flow inside the cell. The cell can be natural or artificially produced, and their theories were applied in the field of microfluidics and so on.

From the literature review [3–6], thin air film cushioning the droplet prevents coalescence of miscible liquids for a certain period. The vibration of liquid bath can extend the time taken to coalesce the miscible liquids. The research on levitating droplet under vibrations wither to new pathway in the field [7]. The lubrication theory, Marangoni stress, and scaling laws explain the phenomena. Moreover, the temperature difference creates a thermo capillary action inside the droplet and liquid bath surface. Pressure is the dominant factor in non-coalescence of liquid, and its dependency on viscosity is researched in Ref. [8].

V. Mathaiyan · D. W. Jung (✉)
Jeju National University, Jeju si 63243, South Korea
e-mail: jungdw77@naver.com

R. Vijayanandh
Kumaraguru College of Technology, Coimbatore 641049, India

Gao et al. [9] calculated the force between liquid droplet and material surface using the Reynolds lubrication approximation. Referred works suggested a relation between pressure and film thickness rate which covers the physics involved in the phenomena. But, Geri et al. derived a pressure relation with an additional term, i.e. sum of velocities.

Temperature difference in droplet and atmosphere is studied in detail. There is a change in penetration depth of droplets at various temperatures [10]. Approach of employing Marangoni flow theory to the miscible liquids resulted in an equation which holds good with experimental results [11]. The study of droplet in a viscous gas details the phenomena in a different perspective [12].

Eggers et al.'s [13] numerical and analytical analysis for the coalescence of droplet gives out the relation between radius of droplet and time. Duchemin et al. [14] studied the coalescence of two droplets with air film and found that the film is responsible for the toroidal enclosure. The relation found from the study follows Couder et al. equation [6]. The modified version of the equation is obtained for the viscous fluids in coalescence of two droplets [15]. Since the energy is transferred from a system to an another, we believed that the conservation of energy can also explain the phenomena of coalescence. The detailed explanation with derivation which validated the Couder's equation for thin air film thickness is presented below.

2 Vijay's Governing Equation for Thin Air Film Thickness in Non-coalescence of Miscible Liquids

Let us consider the droplet of radius R floating on the surface of liquid bath. The thin air film thickness h of density ρ with viscosity μ is trapped between the droplet and bath. Let t be the time taken for a droplet to create the thin air film which cushions it against acceleration due to gravity g .

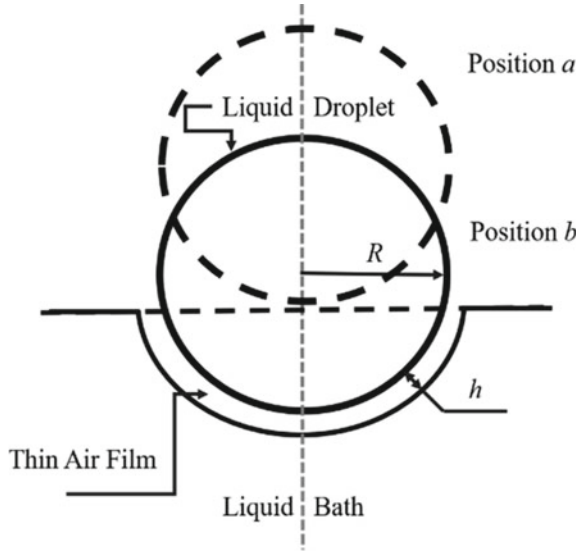
Figure 1 shows the different positions of the droplet and the change in bath surface. As mentioned above, when the droplet moves from position a to b in a certain time t , a crater forms on bath surface in which the thin air film is trapped between them. Over a certain period, the droplet coalesces with the bath surface in approximately six to seven stages depending on the liquid [3].

Since this phenomena transfers energy from one source to an another, let us consider the energy equation for a unit volume. Pressure p acts on the surface because of the potential energy of droplet.

$$\rho g dh + dp + \rho v dv = 0 \quad (1)$$

The droplet is almost stagnant; hence, the velocity is very small. Neglecting the velocity v of the droplet in the equation, we can write the energy equation as given below.

Fig. 1 Depiction of droplet from position *a* to *b* which creates the crater in liquid bath. The thin air film is cushioning or levitating the droplet



$$\rho g dh + dp = 0 \tag{2}$$

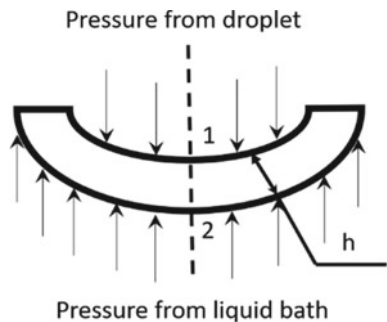
Figure 2 shows the pressures acting on the thin air film on its surfaces, and the pressure difference is equal to the potential energy as per Eq. (2).

$$\rho g dh = -dp \tag{3}$$

Substituting Eq. (3) for the change in *h* from 1 to 2 as shown in Fig. 2, we will get the following terms.

$$\rho gh = dp \tag{4}$$

Fig. 2 Pressure from droplet acting on the upper surface of thin air film due to the potential energy of droplet. Resistant pressure from liquid bath acts on bottom surface of air film



Geri et al. [3] derived the pressure relation from the Navier's Stokes equation in terms of average velocity Δv . Rewriting the equation for our case without the radius of air film in the bottom surface r , we will get Eq. (5). The pressure acting on the bottom surface of film is not predominantly based on the dimension r , but R acting on the top surface has considerable effect on the film.

$$\frac{3\mu R^2 v_z}{h^3} + \frac{6\mu R \Delta v}{h^2} = dp \quad (5)$$

Equate (4) and (5), we call this resultant Eq. (6) as Vijay's governing equation for thin air film thickness in miscible liquid.

$$\frac{3\mu R^2 v_z}{h^3} + \frac{6\mu R \Delta v}{h^2} = \rho gh \quad (6)$$

If we have considered that the velocity in z direction as 0, then above equation will be deduced to Eq. (7).

$$\frac{6\mu R \Delta v}{h^2} = \rho gh \quad (7)$$

Let us consider that the velocity u of air in the film from the top surface because of potential energy of the droplet. Whereas v is velocity of air in the film from the bottom surface, then the average velocity acting on the surfaces is $(u + v)/2$. We have assumed that the velocity of the droplet u is 0; hence, the average velocity is $v/2$. Velocity of air from the bottom surface $v = \text{change in displacement (dx)}/\text{change in time (dt)}$.

The droplet at time $t = 0$ s has the displacement $x(0) = 0$ on the bath surface and at time t sec, the displacement $x(t) = h$. Thus, $v = h/t$. Applying the value in average velocity, we will get the following equation.

$$\frac{h}{2t} = \Delta v \quad (8)$$

Substitute Eq. (8) in (7), we get the Couder's [16] approximate governing equation for the thin air film thickness (9).

$$\frac{3\mu R}{ht} = \rho gh \quad (9)$$

Figure 3 is the plot for thin film thickness variation with time t and radius of the droplet R . Constant from Eq. (9) is not accounted to plot the graph as it is just a scaling factor. Equation (9) validates the Vijay's governing equation for the thin air film thickness in non-coalescence of miscible liquids. It is notable that radius of the droplet is proportional to the thin air film thickness. The time taken t for the coalescence of the liquids depends on the R and h .

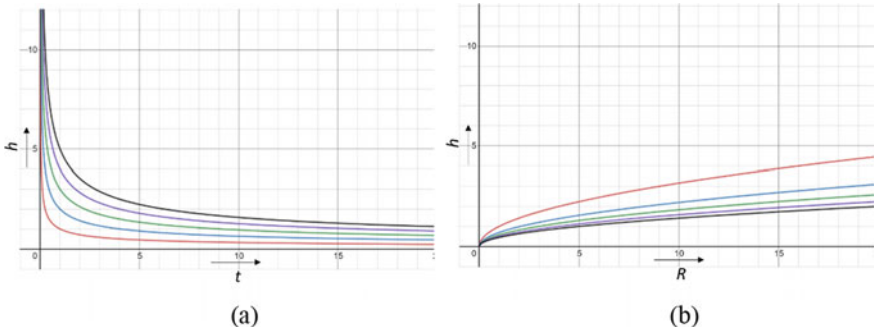


Fig. 3 Graph representing the thin film thickness variation with time and radius of the droplet. **a** Variation of h with t by increasing \sqrt{R} from 1, 2, 3... up to n . **b** Variation of h with R by increasing \sqrt{t} from 1, 2, 3... up to n .

From the approximation of Couder et al., it is mentioned that $c(\theta)$, a term which is a function of sine and cosine remains almost same. The difference in the value of $c(\theta)$ from 0 to 45° is 0.06. If Vijay’s governing equation is equated with Couder et al.’s equation, 0.06 times of $\frac{6\mu R \Delta v}{h^2}$ is equal to $\frac{3\mu R^2 v_z}{h^3}$ in Eq. (6). It is understood that term Rv_z/h is the value changes from 0 to 0.06.

Roberto et al. [17] experiments clarify the relationship between the coalescence of a bubble and surface tension. The same may be applicable for the coalescence of droplet. References [18, 19] provide valuable information required for better understanding of droplet when impacts on a solid surface. Presence or absence of air affects the droplets coalescence [20].

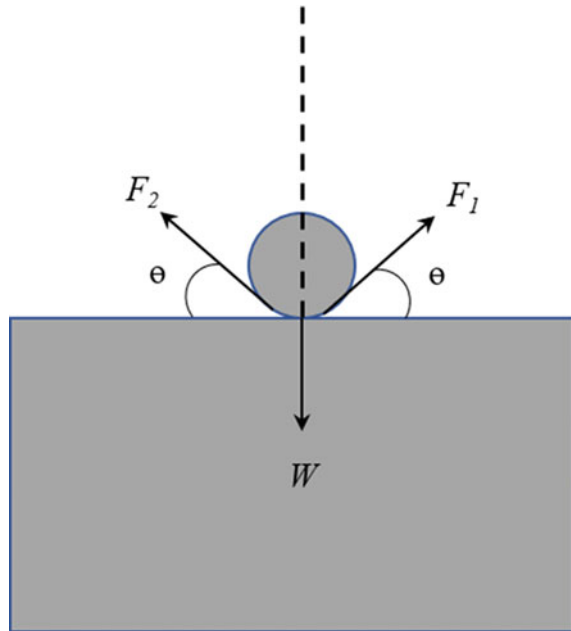
3 Water Droplet on the Surface Without Any Air Gap

Let us consider the circular cross section as the droplet on the water surface without the thin air film as shown in Fig. 4. It is observed that the droplet does not diminish suddenly, and it happens only after a gradual reduction in size of the droplet. We have assumed the same to derive the equation. From Ref. [16], the relation between the object and bath is found from the force equilibrium. Thus, we are resolving the forces to derive at the equation of equilibrium.

Consider a droplet of diameter D on the bath surface. If droplet of mass m with density ρ and volume V under acceleration due to gravity g on the surface of the bath, then penetration depth depends on the weight of object. When forces are a function of surface tension γ , then force equilibrium will provide the weight of droplet $W = 2\gamma L \cos \theta$. We know that weight of spherical droplet can be given as in Eq. (10).

$$W = mg = \frac{\rho g}{V} = \frac{6\rho g}{\pi D^3} \tag{10}$$

Fig. 4 Droplet on the surface of liquid. The contact makes an angle θ and the forces (F_1 , F_2 , and W) acting on the droplet is mentioned in the figure



Equation (11) is obtained by equating the values of weight,

$$\frac{6\rho g}{\pi D^3} = 2L\gamma \cos \theta \tag{11}$$

If length L is equal to the diameter of spherical droplet on bath, then Eq. (11) can be written as,

$$\frac{3\rho g}{\pi \gamma \cos \theta} = D^4 \tag{12}$$

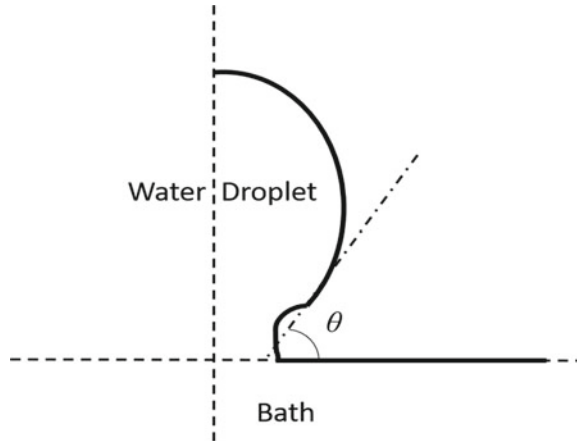
Figure 5 shows the variation in shape of droplet when there is a change in diameter. The diameter of droplet changes over a period and slowly diminish in a certain number of stages. Adding the small change of diameter dD and assuming the change in angle is too small, then the equation is,

$$\frac{3\rho g}{\pi \gamma \cos \theta} = (D + dD)^4 \tag{13}$$

If the droplet is completely diminished, then sum of diameter and change in diameter of the sphere is equal to zero. This in turn will give the value of contact angle $\theta = 90^\circ$.

Neglecting the higher order terms and rewriting the above equation with the constant $\frac{3\rho g}{\pi \gamma} = k$, we will get,

Fig. 5 Droplet with change in diameter at a point of time which creates the angle θ with surface of the bath



$$\frac{k - D^4 \cos \theta}{4D^3 \cos \theta} = dD \tag{14}$$

If the dD is zero, then the droplet will be spherical in nature. The condition for water droplet to be spherical in shape is $k - D^4 \cos \theta = 0$. In other terms, the liquid droplet will be spherical in nature, when $\cos \theta = \frac{D^4}{k}$ (Fig. 6).

The validation of the derivation is yet to be carried out, and its comparison with experimental results may give a better understanding. Note that there are six or seven stages in the coalescence of a liquid as mentioned in Geri et al. The diameter of droplet reduces in every stage to an extent with respect to surface tension. The authors believe that there is a relation between number of sides of snowflake and stages of coalescence in water. This is because the number of sides in a snowflake are almost equal to the number of stages in coalescence of droplet.

Most of the cell in living things is hexagonal in shape. The shape of snowflake is because of molecular structure of water; hence, the molecular structure should

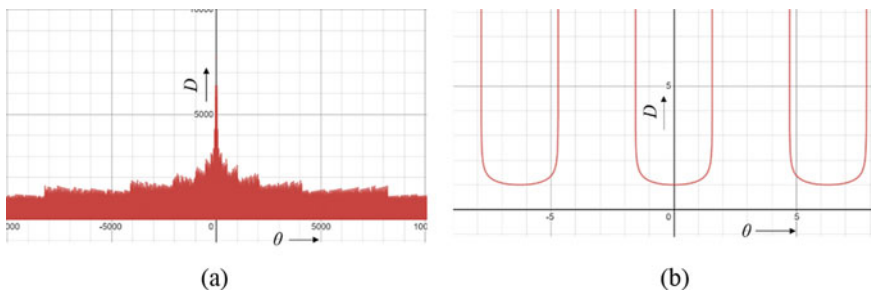


Fig. 6 Graph represents relation of diameter of droplet D and contact angle θ without the scaling constant k . **a** Shows the relation in large scale whereas **b** is in small scale. *Note* Function used in graphs **(a)** and **(b)** are same which is the condition for droplet to be spherical in shape

decide coalescence stages and shape of cells. It is found that cell division and wall formation happen in a certain paradigm to resemble the dynamic behaviour of fluid at certain conditions. For example, shape of mammary gland of human beings has the shape of droplet on a smooth vertical wall. The cellular division inside glands should follow a certain paradigm to provide the overall shape [21].

Acknowledgements We would like to thank Professor Sunghwan Jung, Cornell University, USA for his suggestions and support. Special thanks to Professor Sunghwan Jung, Dankook University, South Korea for his extended help.

References

1. Shaw H (1898) The flow of water. *Nature* 34–36
2. Batchelor GK (2000) An introduction to fluid dynamics. Cambridge University Press, pp 222–225
3. Geri M et al (2017) Thermal delay of drop coalescence. *J Fluid Mech* 1–12
4. Yahashi M et al (2016) Scaling crossover in thin-film drag dynamics of fluid drops in the Hele-Shaw cell. *Nature* 1–8
5. Klyuzhin IS et al (2011) Persisting water droplets on water surfaces. *J Phys Chem B* 14020–14027
6. Couder Y et al (2005) From bouncing to floating: noncoalescence of drops on a fluid bath. *Phys Rev Lett* 177801-1–4
7. Thomson SJ et al (2020) Collective vibrations of confined levitating droplets. *Phys Rev Fluids* 5:083601-1–6
8. Schmelzer JWP et al (2005) Pressure dependence of viscosity. *J Chem Phys* 1–8
9. Gao Y et al (2019) Interaction forces between water droplets and solid surfaces across air films. *Am Chem Soc* 1–9
10. Saifi AH et al (2020) Distinct coalescence behaviors of hot and cold drops in the presence of a surrounding viscous liquid. *Phys Liq* 32:082101-1–10
11. Kim H et al (2017) Solutal Marangoni flows of miscible liquids drive. *Nat Phys Lett* 1105–1110
12. Sprittles JE et al (2014) A parametric study of the coalescence of liquid drops in a viscous gas. *J Fluid Mech* 276–306 (Cambridge University Press)
13. Eggers J et al (1999) Coalescence of liquid drops. *J Fluid Mech* 293–310 (Cambridge University Press).
14. Duchemin L et al (2003) Inviscid coalescence of drops. *J Fluid Mech* 167–178 (Cambridge University Press)
15. Xia X et al (2019) Universality in the viscous-to-inertial coalescence of liquid droplets. *PNAS* 1–6
16. White FM (2011) Fluid mechanics, 7th edn. McGraw-Hills Series, pp 68–71
17. Roberto P-G et al (2020) Coalescence of air bubbles: effect of the electrical double layer. *Miner Eng* 150:1–7
18. Langley KR et al (2019) Gliding on a layer of air: impact of a large-viscosity drop on a liquid film. *J Fluid Mech* 878 R2-1–16
19. Chen L et al (2017) Submillimeter-sized bubble entrapment and a high-speed jet emission during droplet impact on solid surfaces. *Am Chem Soc* 1–6
20. Joseph D (2013) Paulsen: approach and coalescence of liquid drops in air. *Phys Rev E* 88(6):1–15
21. Mathaiyan V et al (2020) Theory of shape for living and non-living things based on thin fluid flows in Hele-Shaw cell, submitted work

Analysis of Output Parameters of EDM: A Review



Akash Gupta and V. K. Dwivedi

Abstract Electrical discharge machining (EDM) is the non-traditional machining choice, aimed at making of complicated profiles of all electrically conductive material which is hard to machine by a traditional method. EDM machine hard material with minimum forces is its greatest strength. There is no contact between the electrode and the job that is why cutting force is very low in EDM, which indicates research interests in the field of EDM. Many new and marvellous techniques are explored by the researches that are apart from the old traditional sparking technique, and these new concepts help in increasing sparking efficiency. The main focus of the researcher is obtaining maximum metal removal rate and minimizing the tool wear with better surface quality. This paper identifies major academic study done on improvising process performance, optimizing process parameters, and the growth of die-sinking EDM. A glance at upcoming future research on EDM is also including in this paper.

Keywords EDM · Development of EDM · Ultrasonic vibration EDM · Dry EDM · Powder additives

1 Introduction

In the twenty-first century, there is a requirement of fast machining with better accuracy for fulfilling these many unconventional machines, and robotics is used by industries. EDM is a vastly familiar manufacturing process for machining of complicated shapes and designs on hard material (as well as on soft material) but the materials should be electrically conducted. EDM is a process where electrode and material are not in mechanical contact, so there is no vibration, chatter and mechanical stresses, throughout machining [1]. EDM uses electric discharge for material removal from the job to produce a required shape product [2]. When the electricity starts passing

A. Gupta (✉) · V. K. Dwivedi
Department of Mechanical Engineering, GLA University, Mathura, Uttar Pradesh 281406, India

V. K. Dwivedi
e-mail: Vijay.dwivedi@gla.ac.in

through the electrode (tool) to the workpiece, a spark generated and removes material from the surface of raw material in dielectric fluid. The electrode and the job both are fully dipped in a dielectric medium like petroleum-based synthetic and vegetable-based oils. EDM was firstly discovered by the English Scientist Joseph Priestly far back in 1770s. However, it was not completely useful prior to 1943 when Russian scientists learned how erosive effects of technique could be controlled and are used for machining objectives [3]. After a couple of decades, this technique was transferred into a machine tool for industrial uses. In the mid-twentieth century, the progress on the EDM phenomenon had been started and many scientists took interest in this new technique. The first patent on the EDM machine was granted to a British scientist named Rudoff in 1950. In the early years of the 1950s, Switzerland, Japan, and the USA developed their first machine. In 1952 when the Korean War was going on, the USA patents first sparking machine. The development of the semiconductor industry in 1960 improves the research on EDM machines and makes it more reliable. When the numerical position control system comes into the market in the early 70s, the electrodes moved more precisely. In the mid of 1970s and early 1980s, computer numerical control (CNC) system carried further developments in the process effectiveness of the EDM technique. Many more changes and improvements came during 1980–90 like servo motor for better control, robotics, process atomization. In small-hole making industries, micro-EDM slowly started its growth. While some little decision was taken to redeveloping the drill machine, a big decision was considered to improvise the micro-EDM as an industrial process after coming of wire electro-discharge grinding.

In the mid-'80s, when the development of the EDM was going on, the researcher worries about the environmental losses, shortage of petroleum base oils, fire hazards, generation of toxic gases, and all others problems that are associated with the EDM. To overcome all these problems, dry EDM is introduced. In dry EDM, inert gases are used instead of dielectric fluid. In 1985, Ramani et al. use dry EDM to make small holes and explain the advantages of using inert gases in the EDM [4].

This migration increases the demand for EDM and also made it more appealing over conventional machining processes in the manufacturing market. After 2000, industrial and academic show their interest in the development of hybrid machining, i.e. using the advantages of both conventional and unconventional materials removing process and limiting the drawbacks of both when applied individually.

When industrial and academic researchers start their interest to developed hybrid machining, they introduced many such techniques based on EDM principal like electrical discharge drilling (EDD), electrical discharge grinding (EDG), rotary tool near-dry electrical discharge machining (RT-ND-EDM) and electrical discharge texturing (EDTx) in the mid of 2000s.

In the last decade (the 2010s), a lot of studies conducted in the field of EDM to fulfil the research gap. In these studies, some are about the development of material and modelling techniques of EDM. Researchers also find a new scope of EDM by conducting or studying the EDM process on ceramic and composite materials [5]. Other than this, the use of optimization techniques like neural network, genetic algorithm, finite element analysis is increased to determine the best arrangement of

process parameters of EDM to obtain maximum output. Today, EDM is used vastly globally with its all unique techniques.

For cold-rolled and Al, further new specialized alternatives include electrical discharge texture (EDT) used for texturing of cold-rolled sheets and Al sheets [6] and electrical discharge grinding is aimed at manufacturing of polycrystalline diamond cutting tool, and pair die fitting [7]. A book published by Rajurkar in 1994 suggests some future trends of EDM, i.e. better surface finish, better accuracy, machining of advanced material and composites, control, and automation [8].

This review paper provides a brief study of various researches conducted on the EDM process over the past 75 years, involving the first discovery of material removal through electricity. Figure 1 shows the evolution of EDM with their corresponding years. Even after a long time and research, the technique of EDM material removal, i.e. erosion, is still arguable. Some recent improvements MRR, TWR, surface finishing and accuracy come after improvements in the control system, robotics and automation, dielectric and flushing system.

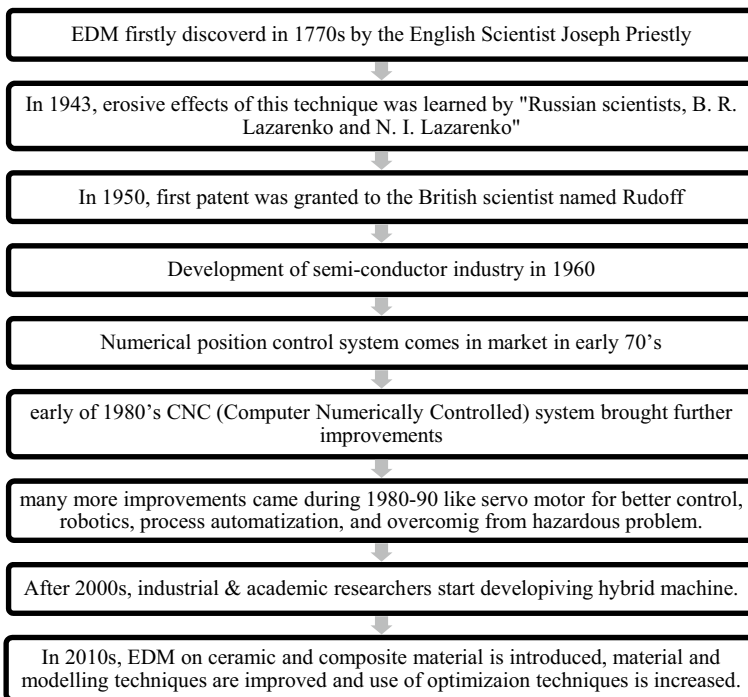


Fig. 1 How the development of EDM technique was done over the past decades since it was discovered in the 1770s

2 Principle of EDM

The basic principle of the electrical discharge machine depends upon the thermo-electric energy. The thermoelectric energy is produced b/w job and the electrode that is submerged in dielectric fluid/medium. There is a small gap that separated the job and the tool. Firstly, current is supplied to electrode and then it moves towards the job and reduces the spark gap in such a manner that the dielectric fluid is ionized by the applied voltage. When this gap is filled by an insulating fluid, arc discharged occurred. Herein process, the metal particles are taken out from the job in controlled wearing action under rapid spark ejection occurring in spark gap of range 10–125 μm . If average voltage gap is exceeding reference voltage, system increases feed speed. The electric path of the power supply and the electric and mechanical systems are shown in Fig. 2.

The job is fixed with anode end, and the electrode is fixed with the cathode end of the power circuit. Voltage travels through the spark gap and develops appropriately high electric-discharge via a small-break in incarnation of spark in pause of 10 μs . After this, electron-ion moves in the direction of the positive ions which brings a discharge passageway which will be conductive. It happens exclusively for a short time while the potential difference is proper to set up across electrode and job, and accelerated electron ions may ultimately collisions with dielectric fluid molecules causing the creation of a passage of plasma. This makes a very high magnetic field which causes a very high temperature on the tool and specimen of range 10,000–12,000 $^{\circ}\text{C}$. This high-temperature spark liquefied or eroded the material of the electrode and the job. Hence, the material is removed due to locale vaporization of metal particles.

EDM consists of different parts for its precise operation. Components of the electric discharge machine are briefly discussed in Table 1.

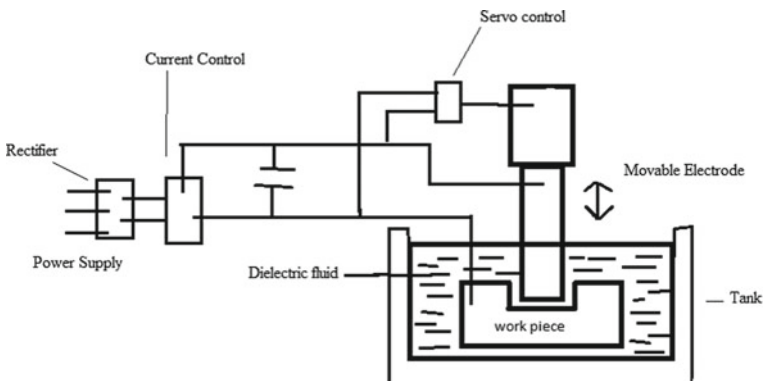


Fig. 2 Setup diagram of EDM

Table 1 Terms of EDM

S. No.	Components	Brief explanation
1	The servo mechanism	The servo mechanism is used to provide feed to the electrode and maintains the spark gap in a controlled manner. It plays important role in EDM
2	Working area	Working area means the area in which the machining is running. Up to some extent, the specimen is dipped in the oil. This oil is re-circulated in the machine with the help of a pump
3	The working table	Firstly, the tool is set to mid of the workpiece, then coordinates are set to zero on the monitor and then tighten the screw. The least count of the handle is 0.05 mm. In other words, we can say that we give the moment to the job piece in X- and Y-directions
4	The tool holder and electrode	Tool holder holds the electrode for machining. It is mounted on Z-axis. The tool electrode must be fabricated from the material of an electrically conductive. The form or shape of the tool electrode is a replica of the completed desired shape in the workpiece, with its dimension measurements is used to take into account the quantity of overcut (OC) that happens
5	Dielectric reservoir, pump and circulation system	Dielectric reservoir stores the EDM oil and filter at each passes because when material removes, some debris particles are mixed with the EDM oil; then dielectric reservoir and circulation system keep the facility to filter the EDM oil. Function of pump is to provide EDM oil to working tank and flushing tubes whenever required
6	Power generator and control unit	It consists of power which is directly related to voltage and current, so control unit can control the amount of energy which is to be consumed in the removal of material. Too much current can harm the job as well as the tool. All the machining parameters (like T_{on} , T_{off} , duty cycle) are controlled by the control unit and maintain the spark gap [9]

There are few parameters, characteristics, factors, and technical terms that have an important role to understand the experimental study of the EDM machine. These are briefly discussed in Table 2.

EDM processes classified as:

Die-Sinking EDM

In Die-sink electrical discharge machine, workpiece and tool both are submerged in dielectric fluid/medium and parted by spark gap. After inputting the machining parameters in the machine, controllers process is started. As the process starts, an electric arc between the tool and workpiece has generated that melts and vaporizes the surface of the workpiece in a controlled environment. Current can vary from 0.5 to 400 A, the voltage range is 40–300 V, and the duration of the pulse is between 2 to 200 μ s. Flushing of different types is used to smooth the process and removed the unwanted particles from the gap. These types of machines are used for the making of dies, mould cavities because they only generate the replica or the mirror image of the tool on the job. Some commonly used dielectric fluids are kerosene, organic oils, EDM oil or transformer oil.

Wire Cut EDM

Wire EDM or electrically discharge wire cut machining uses an electrically conductive metal wire to cut the workpiece for the manufacturing of complex shapes with 2D or 3D profiles. The whole process is done under de-ionized water which acts as dielectric fluid or as coolant. The wire is fixed b/w two rollers in such a way that the used part of the wire changed constantly. Brass or copper is commonly used as the electrode wire. The diameter range of the wire is between 0.5 and 0.25 mm. It is a very slow process because of wire movement speed, i.e. 3 m/min. Guo et al. [13] suggested that with the support of ultrasonic, cutting efficiency of wire-cut EDM could be enhanced by 30% and surface roughness is also minimized from 1.95 to 1.7 Ra.

3 Advancement of EDM

EDM new trends and advancement are done by many scientists on the EDM techniques like ultrasonic vibration, dry electrical discharge machine, powder additives in EDM, water EDM, and modelling approaches to enhance the overall performance of the EDM are discussed below. Figure 3 chart represents the percentage of studies carried out on the various types of EDM techniques [5].

Table 2 Terms of EDM

S. No.	Terms	Brief explanation
1	Thermal conductivity	It is temperature difference between two surfaces on any side of material. It is an energy of heat transferred per unit time and per unit surface area, divided by temperature difference [10]. Its unit is watts per metre Kelvin
2	Liquefying point	It is a temperature at which a hard material becomes a liquid at atmospheric pressure. Higher the liquefying point of the electrode material will have enhanced the wear ratio between a tool and the specimen [11]
3	Overcut	A cavity that is produced by an EDM machine is always bigger than the electrode employed to machine it. The difference in the size of the tool and the cavity is called the overcut. When calculating overcut, be assured to identify whether one is referring to complete overcut (diametric OC) or overcut per side
4	Discharge current (C)	It is the current flowing through the circuit to remove the material. It has the energy to melt the material. Its unit is ampere (A)
5	Sparking gap	While sparking there is a small gap, b/w job, and the tool, this gap is called sparking gap. It is b/w 10–125 μm
6	Duty cycle (τ)	Ratio between pulse on-time and total cycle time called duty cycle. It is shown in percentage
7	Pulse off time (T_{off})	It is time duration when voltage is absent b/w job and electrode. Its unit is microseconds (μs)
8	Pulse on-time (T_{on})	It is the time duration when current is flowing b/w the job and electrode. Its unit is microseconds (μs)
9	Voltage (V)	It is the potential difference between two points. It plays an important role that affects MRR in the EDM
10	Heat-affected zone (HAZ)	An area below the re-form or recast the layer. This area has been lay open to elevated temperatures that have changed the properties of the workpiece
11	Material removal rate (MRR)	It is the ratio of change in weight of job to the density of the material and per unit time. It is measured in mm^3/min . It is directly proportional to " T_{on} ", "C and V" and inversely proportional to " T_{off} "

(continued)

Table 2 (continued)

S. No.	Terms	Brief explanation
12	Tool wear rate (TWR)	When current flows, the electron emitted from the tool surface means some material is removed from the surfaces and when this strikes with some high velocity to dielectric fluid and then strikes with workpiece material and erosion of more material on the workpiece will take place [12]. We can calculate TWR in terms of change in the weight of tool divided by the density of material \times time (mm^3/min). Or otherwise, change in weight is divided by time (g/min)

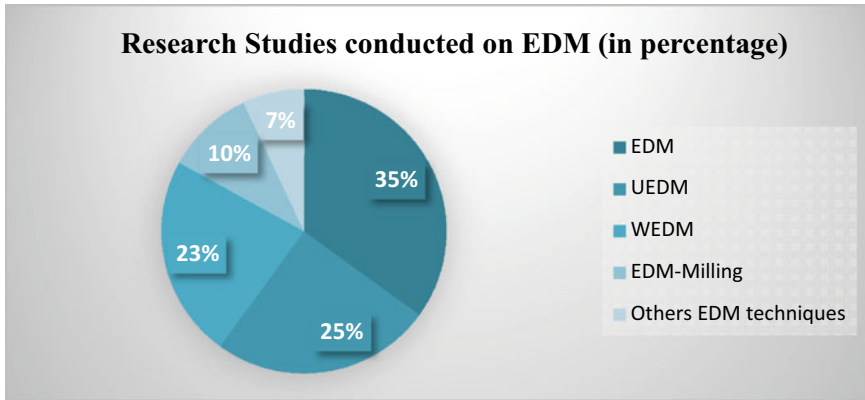


Fig. 3 Research studies conducted on EDM (in percentage)

3.1 Ultrasonic Vibration

By introducing ultrasonic vibration in the tool, machining performance is increased of hard to machine materials and application are expanded of the EDM. Since the mid-'80 s, there is a study is going to understand the properties of ultrasonic vibration on the vibration of the EDM. By employing ultrasonic vibration, EDM gains a high efficiency which can be used to enhance the circulation of the dielectric which accelerates the removal of waste particles [13]. The use of a DC supply in the place of traditional pulse power supply to spark erosion with ultrasonic frequency was suggested by “Zhang et al.” [14].

3.1.1 Machining of Micromoles

To make holes in ceramics material, Jia et al. introduced an “ultrasonic vibration pulse electro-discharge machining (UVPEDM)” technique in 1995 [15]. In an experimental study, they proved that this technique is good to get the maximum MRR. By using ultrasonic vibration, the depth of micro-holes can be double in comparison of without ultrasonic vibration this is confirmed by Ogawa et al. [16]. In a study of machining the ceramic-coated nickel alloy with ultrasonic vibration, “Thoe et al.” found following information: the most resilient material is mild steel while drilling the 1 mm diameter hole using different electrode material with boron carbide abrasive slurry on ceramic coated nickel alloy workpiece [17, 18].

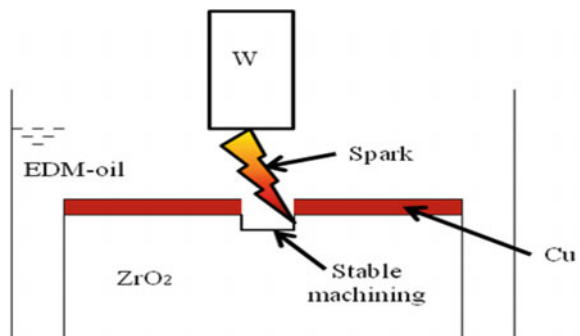
3.1.2 Specimen Vibration

Egashira et al. [19] developed a novel technique for micro-ultrasonic machining. The specimen was shaken throughout machining, and they have proceeded in machining micromoles. A frittage tool was inspected and precision accuracy to solve the problem Gao and Liu [20]. Get the outcome ultrasonic micro-EDM is 8 times superior to micro-EDM when stainless steel specimen is 0.5 mm thick and the tungsten electrode is 43 mm diameter “Prihandana et al.” [21]. Researchers have learned effect of vibrated job piece. They found out, higher amplitude with higher frequency increases the material removal rate.

3.2 EDM of Non-conductive Materials

Utilizing EDM, the electrical conductivity of materials is 0.1 Scm^{-1} to be prepared, which is minimum. Along these lines, this strategy is utilized to metals and conductive earthenware production can machine [22–24]. To machine earthenware production, EDM and smaller-scale EDM are used regular cutting procedures [25, 26]. The result of ultrasonic vitality can help with making flash disintegration and break arrangement that causes spalling [27]. Utilizing helping anode strategy (AEM), non-conductive pottery was machined effectively by EDM (Fig. 4) with barely any changes done in the strategy which is one of the regular techniques utilized [28]. In AEM, a conductive film is covered on the head of non-conductive earthenware to think of sparkle between the specimen and electrode. Because of high-temperature degeneration of polymer chains can occur around the dielectric liquid, it makes carbon components from split polymer chains. The carbon components, alongside the conductive flotsam and jetsam, spread the earthenware surface to support the conductivity [29–31].

Fig. 4 Schematic diagram of micro-EDM of non-conductive zirconia [29]



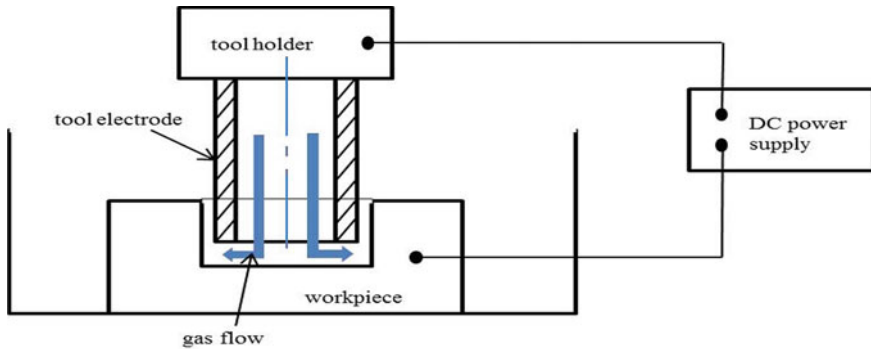


Fig. 5 Schematic diagram of dry EDM

3.3 Dry EDM

In dry EDM, the DC power supply is connected with a specimen and tool holder. Gas flow is between the tool electrodes. Dielectric is flow in the chamber between the specimen and tool holder. A fine particle of powder is assorted in a dielectric. For better performance of the EDM, to prepare the good characteristics of powder has fine grain particle and concentration. “Lin et al.” [32] studied behaviour of dry EDM with the association of vibrations and abrasive jet, and he finds out that the MRR, TWR and SR were increased and the surface nobility was reduced. Figure 5 shows the process diagram of dry EDM.

3.4 Near-Dry EDM

Dry EDM has some disadvantages like debris deposition on the electrode, low MRR obtains by using non-oxygen gases, bad odour and blockage of the gas pipe by the debris. In 1989, Tanimura et al. [33] developed a new variant of the EDM called near-dry EDM (ND-EDM) to overcome the disadvantages of the dry EDM. Two-phase movement of gas and liquids is used in place of the dielectric fluid. The liquid present in flow removed all the debris from the electrode and at the pipe opening [34]. In a study, Tao et al. [35] found out the better surface finish and mostly zero taper angle in the hole making with low discharge current and low pulse duration. ND-EDM gives mirror-like surface finish. In a comparison study of effects of different dielectric mixture on MRR, Dhakar et al. [36] find out that glycerine–air mixture gives higher MRR.

Near-dry EDM is used with different approaches to enhance its performance and creates a different variant of EDM like ND-EDM by using a magnetic field, “high-speed ND-EDM, 5-axis milling with ND-EDM, ND-EDM with high viscosity dielectric medium, and rotary tool near-dry EDM (RT-ND-EDM)” [37].

3.5 EDM with Powder Additives

The sheer abrasive powder is added in dielectric medium. Powder mixed EDM (PMEDM) is called another name of the hybrid material removal process; it runs at low pulse energy [38]. It also disturbs execution of electrical discharge machine technique. The electrically conductive powder was used to reduce the cut off the power of dielectric medium and enhanced spark gap between specimens and tools. EDM is more steady through this method and enhances machining output, MRR and surface quality. Characteristics of powder-like fine grain size, type and concentration affect dielectric quality [39].

3.6 EDM in Water

Water as dielectric is an alternate of carbon-based oil. To push a much superior health and nontoxic atmosphere, this approach is adopted while working with EDM. Decomposed and toxic vapours (CO and CH₄) are discharged by hydrocarbon oil like kerosene [40]. Utilization of distilled water and water with additives is involved in research studies in the last 25 years.

3.7 Pure water

In 1981, Jeswani [41] published the primary paper on the consumption of water as the dielectric. In his analysis, he compared kerosene and pure water output over pulse energy range 72–288 mJ. Machining in pure water resulted an unusually greater material removal rate and slower TWR ratio of the device than kerosene, after using wide variety of pulsed electricity. The machining precision was inferior but with distilled water, the surface finish became more improved. By using copper equipment with negative polarities, the most efficient machining rates are obtained with tap water, and machining in water has chance to achieve zero electrode wear.

3.8 Water with Additives

Extremely concerted aqueous glycerine solution has benefits as equated to hydrocarbon dielectrics when running through lengthy pulse intervals also with great pulse duty factors and discharge currents, progressive polarity tool electrode [42]. To boost the performance of demonized water, few scholars have study the possibility of putting an organic compound that “ethylene glycol, polyethylene glycol 200, polyethylene glycol 400, polyethylene glycol 600, dextrose and sucrose” [43].

Titanium surface was affected by use of urea solution dielectric in water [44, 45]. Nitrogen portion decayed from urea, transferred to a piece of work preparing a hard TiN layer that was significant for better wear resistance after the EDM.

4 Flushing Method

Flushing plays the greatest key role in the EDM providing control circulation of coolant [46]. It is very necessary to remove the waste particles completely, if they stay in the space between the tool and specimen, they will work as barricades within the sparking space. Flushing is the method of providing neat and clean dielectric medium between the sparking gap. There are various ways of using the flushing system like pressure flushing, side flushing and suction flushing.

5 Conclusion

EDM of powder additives, water EDM and modelling techniques is discussed in this review paper. The progress of the development of the EDM technique is presented using charts. For micromachining, the best suitable method is ultrasonic vibration, dry machining is cheaper, for safer and more conducive working environment water EDM takes place, for increasing surface quality and MRR, EDM with powder additives is considered, and it also decreases the TWR using dielectric oil, and by using EDM modelling, it will be very easy to analysis the output parameters that helps in the growth of specific and precise EDM performance. For every new technique developed for the EDM, the aim is the same, i.e. increase MRR and SQ and decrease TWR, developing techniques for new material introduced, and create a safer working environment.

References

1. Ho KH, Newman ST (2003) State of the art electrical discharge machining (EDM). *Int J Mach Tools Manuf* 43:1287–1300
2. Meshram DB, Puri YM (2017) Review of research work in die sinking EDM for machining curved hole. *J Braz Soc Mech Sci Eng* 39:2593–2605
3. Saini KS, Singh S, Datt M (2017) Electrical discharge machining: state of the art and future prospects. *Int J Latest Trends Eng Technol Spec Issue AFTMME* 123–130
4. Ramani V, Cassidenti ML (1985) Inert-gas electrical discharge machining. NASA Tech. Br. No. NPO-15660
5. Jamwal A, Aggarwal A, Gautam N, Devarapalli A (2018) Electro-discharge machining: recent developments and trends. *Int Res J Eng Technol (IRJET)* 05(02). e-ISSN: 2395-0056
6. Aspinwall DK, Wise MLH, Stout KJ, Goh THA, Zhao FL, El-Menshawly MF (1992) Electrical discharge texturing. *Int J Mach Tools Manuf* 32(1/2):183–193

7. Kozak J, Rajurkar KP, Wang SZ (1994) Material removal in EDWM of PCD blanks. *J Eng Ind (Trans ASME)* 116(3):363–369
8. Rajurkar KP (1994) Handbook of design, manufacturing and automation. In: *Non-traditional manufacturing processes*. Wiley, USA (Chapter 13)
9. Vijayanand AM, Mathiyalagan M, Sabarigiri SS, Madhesh A, Muthukrishnan M (2018) Optimization of machining parameter in die sinking EDM cut over aluminium using copper tool. *Int J Innov Res Sci Technol* 4(11). ISSN (online): 2349-6010
10. Azar K, Tavassoli B (2008) *Qpedia Thermal Management—Electronics Cooling Book*. 1(1). Advanced Thermal Solutions, USA
11. Gov K (2017) The effects of the dielectric liquid temperature on the hole geometries drilled by electro erosion. *Int J Adv Manuf Technol* 92:1255–1262
12. Basu B, Kalin M, Venkata Manoj Kumar B (2020) *Conventional and advanced machining processes*. Wiley
13. Guo ZN, Lee TC, Yue TM, Lau WS (1997) A study of ultrasonic aided wire electrical discharge machining. *J Mater Process Technol* 63:823–828
14. Zhang JH, Lee TC, Lau WS, Ai X (1997) Spark erosion with ultrasonic frequency. *J Mater Process Technol* 68:83–88
15. Zhixin J, Jianhua Z, Xing A (1995) Ultrasonic vibration pulse electro-discharge machining of holes in engineering ceramics. *J Mater Process Technol* 53:811–816
16. Hitoshi O, Teruo N, Iwao M (1999–2001) Study of micro machining of metals by EDM with high frequency vibration. Takushima Prefectural Industrial Technology Centre
17. Thoe TH, Aspinwall DK, Killey N (1999) Combined ultrasonic and electrical discharge machining of ceramic coated nickel alloy. *J Mater Process Technol* 92–93:323–328
18. Wansheng Z, Zhenlong W, Shichun D, Guanxin C, Hongyu W (2002) Ultrasonic and electric discharge machining to deep and small hole on titanium alloy. *J Mater Process Technol* 120:101–106
19. Egashira K, Masuzawa T (1999) Micro ultrasonic machining by the application of work piece vibration. *CIRP Ann Manufact Technol* 48:131–134
20. Gao C, Liu Z (2003) a study of ultrasonically aided micro-electrical discharge machining by the application of work piece vibration. *J Mater Process Technol* 139:226–228
21. Prihandana GS, Hamdi M, Wong YS, Mitsui K (2006) Effect of vibrated electrode in electrical discharge machining. In: *Proceedings of the first international conference and seventh AUN/SEED-net field wise seminar on manufacturing and material processing*. Kuala Lumpur, 14–15 Mar 2006, pp 133–138. ISBN: 983-42876-0-7
22. Asfana A, Ali MY, Mohamed AR, Hung WNP (2015) Material removal rate of zirconia in electro discharge micromachining. *Adv Mater Res* 1115:20–23
23. Hosel T, Cvanara T, Ganz T, Muller C, Reinecke H (2011) Characterization of high aspect ratio non-conductive ceramic microstructures made by spark erosion. *Microsyst Technol* 17:313–318
24. Hosel T, Muller C, Reinecke H (2011) Spark erosive structuring of electrically nonconductive zirconia with an assisting electrode. *CIRP J Manuf Sci Technol* 4:357–361
25. Schubert, A. & Zeidler, H. (2009). Machining of nonconductive ZrO₂ ceramics with micro-EDM. In: Van Brussel H, Brinks Meier E, Spaan H (eds) *Proceedings of the 9th international conference of the European society for precision engineering and nanotechnology*, vol 2, pp 6–9. ISBN: 978-0-9553082-6-0
26. Mutt Amara A, Janmanee P, Fukuzawa Y (2010) A study of micro-EDM on silicon nitride using electrode materials. *Int Trans J Eng Manag Appl Sci Technol* 1(1):001–007
27. Mohri N, Fukuzawa Y, Tani T, Saito N, Furutani K (1996) Assisting electrode method for machining insulating ceramics. *Ann CIRP* 45:201–204
28. Chen YF, Lin YC, Chen SL, Hsu LR (2009) Optimization of electro discharge machining parameters on ZrO₂ ceramic using the Taguchi method. *J Eng Manufact* 224:195–205
29. Banu A, Ali MY, Rahman MA (2014) Micro-electro discharge machining of non-conductive zirconia ceramic: investigation of MRR and recast layer hardness. *Int J Adv Manuf Technol* 75:257–267

30. Liu YH, Li XP, Ji RJ, Yu LL, Zhang HF, Li QY (2008) Effect of technological parameter on the process performance for electric discharge milling of insulating Al₂O₃ ceramic. *J Mater Process Technol* 208:245–250
31. Fukuzawa Y, Mohri N, Tani T, Muttamara A (2004) Electrical discharge machining properties of noble crystals. *J Mater Process Technol* 149:393–397
32. Lin Y-C, Hung J-C, Chow H-M, Wang A-C, Chen J-T (2016) Machining characteristics of a hybrid process of EDM in gas combined with ultrasonic vibration and AJM. *Proc CIRP* 42:167–172
33. Tanimura T, Isuzugawa K, Fujita I, Iwamoto A, Kamitani T (1989) Development of EDM in the mist. In: *Proceedings of ninth international symposium of electro machining (ISEM IX)*. Nagoya, Japan, pp 313–316
34. Yadav VK, Kumar P, Dvivedi A (2017) Investigations on rotary tool near-dry electric discharge machining. In: Wang S, Free ML, Alam S, Zhang M, Taylor PR (eds) *Applications of process engineering principles in materials processing, energy and environmental technologies*. Springer, Cham, pp 327–334
35. Tao J, Shih AJ, Ni J (2008) Experimental study of the dry and near-dry electrical discharge milling processes. *J Manuf Sci Eng* 130:11002–11009
36. Dhakar K, Dvivedi A, Dhiman A (2016) Experimental Investigation on effects of dielectric mediums in near-dry electric discharge machining. *J Mech Sci Technol* 30:2179–2185
37. Yadav VK, Kumar P, Dvivedi A (2019) Effect of tool rotation in near-dry EDM process on machining characteristics of HSS. *Mater Manuf Process*. <https://doi.org/10.1080/10426914.2019.1605171>
38. Zhao F-L, Lu Z-Z, Wang H, Qian Z-Q (2005) Research on effecting mechanism of particles in powder-mixed EDM. *Dalian Ligong Daxue Xuebao J Dalian Univ Technol* 45:668–671
39. Pecas P, Henriques E (2003) Influence of silicon powder-mixed dielectric on conventional electrical discharge machining. *Int J Mach Tools Manuf* 43:1465–1471
40. Zhang QH, Du R, Zhang JH, Zhang Q (2006) An investigation of ultrasonic-assisted electrical discharge machining in gas. *Int J Mach Tools Manufact*. <https://doi.org/10.1016/j.ijmactools.2005.09.023>
41. Jeswani ML (1981) Electrical discharge machining in distilled water. *Wear* 72:81–88
42. Konig W, Siebers F-J (1993) Influence of the working medium on the removal process in EDM sinking. *Am Soc Mech Eng Prod Eng Div Publ PED* 64:649–658
43. Leao FN, Pashby IR (2004) A review on the use of environmentally-friendly dielectric fluids in electrical discharge machining. *J Mater Process Technol* 149:341346
44. Yan BH, Tsai HC, Huang FY (2005) the effect in EDM of a dielectric of a urea solution in the water on modifying the surface of titanium. *Int J Mach Tools Manuf* 45:194–200
45. Abbas NM, Solomon DG, Bahari MF (2007) A review on current research trends in electrical discharge machining (EDM). *Int J Mach Tools Manufact* 47(7–8):1214–1228
46. Pal NK (2014) Thesis on parametric optimization of process parameters for EDM of stainless steel 304. National Institute of Technology Rourkela Odisha, India, May 2014

Biodiesel Prepared from Used Palm Oil Collected from Hostel Mess is a Promising Supplement for Diesel Fuel



Santosh Kumar Dash, P. S. Ranjit, Bhemuni Varaprasad, Nabam Hina Papu, and P. V. V. S. S. Manikanta

Abstract The demand for energy is increasingly growing, because of the exponential rise in the number of industries and automobiles due to population growth. Petroleum, natural gas, coal, hydrocarbon, and nuclear are the sources of the energy. Fossil fuels are commodities and are not renewable energies. Though these fuels largely contribute to the world's energy supply, consumption of these sources has increased environmental concerns. Biodiesel prepared from waste and non-edible feedstock is the need of the hour as a diesel supplementary fuel. In this study, waste fried palm oil has been used to produce biodiesel, and subsequent diesel engine performance test is carried out. Test parameters have been optimized for quality checkup. Efficient production potential and excellent fuel properties have been ensured from this study. Up to B40 blend, the performance and emanation trend of CO, HC, NO_x, and smoke observed to be astounding. It is encouraged to use waste fried palm-based biodiesel for agricultural applications for power in rural areas.

Keywords Energy · Waste cooking oil · Performance · Diesel engine · Biodiesel

1 Introduction

The main challenge for this century has become to reduce carbon emissions and meet the ever-increasing demand for energy. It has been reported that almost 90% of carbon emissions are caused by combustion of fossil fuels. As a synthetic fuel, biodiesel (BD) has become a key source and is making its position as a primary future source of renewable energy [1, 2]. The use by transesterification of liquid fuels such as biodiesel generated from used cooking oil is one of the most promising

S. K. Dash (✉) · P. S. Ranjit · B. Varaprasad · P. V. V. S. S. Manikanta
Department of Mechanical Engineering, AEC, Surampalem, Andhra Pradesh 533437, India
e-mail: santoshdash@aec.edu.in

N. H. Papu
Department of Mechanical Engineering, NERIST, Nirjuli, Arunachal Pradesh 791109, India

options for the supplement of conventional fossil fuels [3]. BD made from edible oils is not commercially feasible at this time [4, 5]. Moreover, the large-scale use of edible oils to produce biodiesel may lead to edible crisis [6, 7]. Such problems can be addressed by using low-cost feedstocks for the production of BD, such as unused oils and waste cooking oils [8–10]. Present biofuel policy stressed on the use of waste-based energy utilization to serve the dual objective of atmospheric contamination and energy yield to meet the increased demand for clean energy [11–13]. Muralidharan et al. [14] studied the various performance data to correlate the feasibility of using biodiesel prepared from waste oil. They found reduction in CO, HC, CO₂ emissions at the penalty of NO_x emanation. Abubakar et al. [15] optimized the production process parameters and obtained 90% biodiesel yield at optimum parameters. They observed the properties to be comparable with earlier literatures and standard biodiesel specifications. Singh et al. [16] produced biodiesel from waste fried mustard oil collected from local restaurants and utilized the biodiesel to prepare various lower order biodiesel diesel blends (B5, B8, and B10) for the experimental investigation in diesel engine. However, detail performance and emission study for higher order blends of waste cooking biodiesel prepared from used palm oil has not been reported. This project deals with the preparation of biodiesel and its blends from waste cooking palm oil collected from Aditya Engineering College hostel mess, measuring its properties and testing them on diesel engine to study the performance of biodiesel and its blends.

2 Materials and Methods

Waste fried palm oil is collected from Aditya Engineering College hostel mess, Andhra Pradesh, India. Methanol, NaOH, and phenolphthalein indicator were purchased from Merck Private Limited, Maharashtra, India. Engine test is carried out in Apex innovations, Sangli, Pune, Maharashtra, and India. AVL smoke meter and modern sensor-based gas analyzer were used for measuring emission parameters.

3 Production of Biodiesel

Free fatty acid % for waste cooking palm oil is obtained to be 1.76% from the titration test. Base catalyzed transesterification is followed for the biodiesel production as FFA is lower [17, 18]. Mixing of catalyst with hot oil is done by using three neck conical flasks, hot plate with magnetic stirrer. In this study, we have taken 500 ml of used cooking oil, 100 ml of methanol, and 5 g of sodium hydroxide as catalyst. Methanol and NaOH catalyst initially measured and transferred into the flask. The oil (500 ml) using hot pan was warmed and was added with 100 ml of methanol and required amount of sodium hydroxide as catalyst and mixed properly so that no precipitate should present. Constant reaction speed 800 rpm is maintained throughout

Table 1 Properties of test fuels

Blends	Diesel	WB10	WB20	WB30	WB40	WB50	WB100
Properties							
Viscosity at 40 °C (mm ² /s)	2.6	2.74	2.83	2.98	3.22	3.36	4.17
Density (kg/m ³)	824	829	834	840	846	852	878
Flash point (°C)	66.5	78.5	87	99	112	120	172
Fire point (°C)	72.2	82	93.5	106	119	132	185
Calorific value (MJ/kg)	43.25	43.1	42.83	42.71	42.56	42.27	39.41

the reaction. This mixture is added to waste cooking oil at 65 °C constant temperatures and heated for 60 min maintaining that constant temperature. The resultant mixture is kept undisturbed for 12 h. So that two layers are formed; one is glycerol that is present as precipitate at the bottom and the unpurified BD at the top.

The unpurified biodiesel was washed with normal tap water for 5 times to separate soaps and impurities formed in reaction. This process is done until no foam forms when water is mixed with waste cooking oil biodiesel (WB). At the end of 5th wash, we got 498 ml of washed waste cooking oil biodiesel. Now, the washed biodiesel is heated at certain temperature so that any water content present in oil gets evaporated. The biodiesel is separated from the glycerol using a separating funnel. After separation, water washing, and heating, we got 480 ml of biodiesel, i.e., yield efficiency of 96%. Finally, pure biodiesel is prepared which has been taken for the experimental investigation. Table 1 presents the properties of the test fuels.

4 Results and Discussion

Experiments have been carried out to determine the performance health as well as emanation health of a diesel engine for distinct load settings (0, 25, 50, 75, and 100%). Here, in this work, BTE, EGT, HC, CO, NO_x, and smoke density are studied.

4.1 Brake Thermal Efficiency

Brake thermal efficiency (BTE) is the ratio of power output of the engine and the energy of the combusted hydrocarbons. BTE increases with the rise in load (Fig. 1). This is due to the increase in brake power and lower rate of losses with increase in loads [19]. Considering the higher share of BD in the blends, the BTE typically reduces. It is attributed to an increase in low heating value diesel fuel consumption that raises BTE. Lower calorific value of the blends resulted in lower BTE in contrast to diesel. At full throttle, the BTE for diesel, WB10, WB20, WB30, WB40, WB50, and WB100 is observed to be 33.1%, 32.46%, 31.86%, 31.25%, 30.77%, 30.16%,

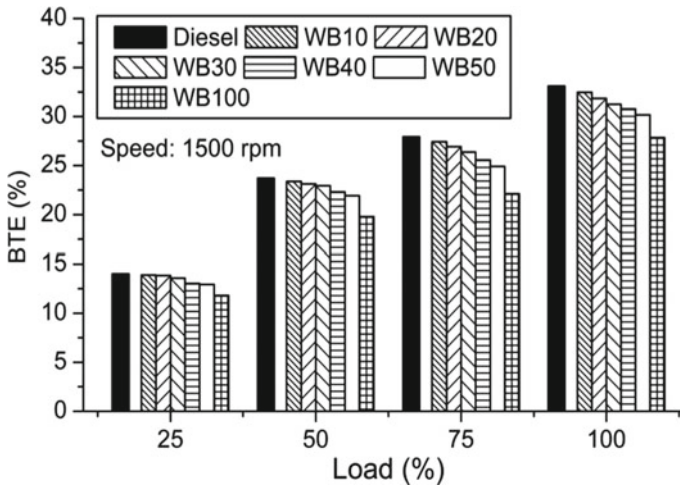


Fig. 1 Brake thermal efficiency of different blends with loads

and 27.84%, respectively. Having the BTE more than 30% is very impressive for an engine without turbo and supercharger. The noise level also found to be in usual range while in operation.

4.2 Exhaust Gas Temperature

The temperature of the exhaust gas (EGT) is proportional to that of the cylinder temperature. This helps to research rising NO_x emissions. The graph of EGT with load is shown in Fig. 2. As load ascends, the amount of fuel consumed grows, increasing the energy emitted as a result of the combustion. Therefore, EGT uprises with increased load. The exhaust gas temperature for WB30 observed to be least amongst all fuels, which changes from 143.29 °C at 0 load to 332 °C at 100% load. For DF, the EGT alters from 150 °C at 0 load to 349.8 °C at 100% torque condition [20]. This is due to more heating value of diesel while compared with remaining biodiesel blends. The lower the EGT value the better for the engines durability and life. High temperature has huge limitations for the engine. The lubrication also hampered with high temperature. Various correlations are also available that show the EGT relations with other engine factor.

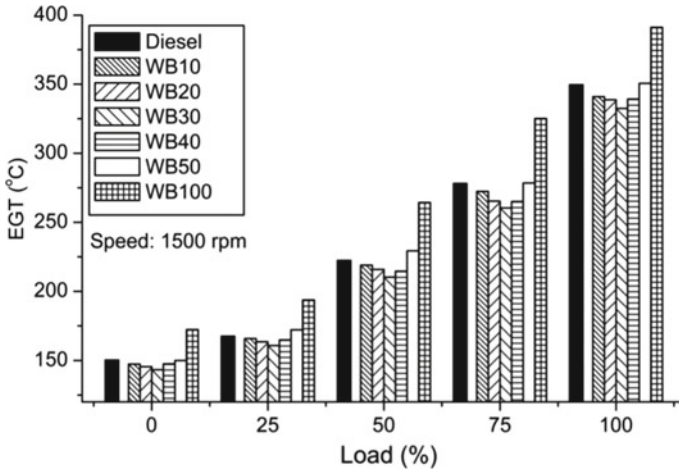


Fig. 2 Exhaust gas temperature of different blends with loads

4.3 Hydrocarbons (HC)

The emissions CO and HC are indicators of incomplete fuel combustion [21]. When fuel combustion efficiency decreases, it results in more CO and HC emissions. With load the variation of HC is shown in Fig. 3. It is seen that B10, B20, and B30 blends have resulted in decreased HC emission. From the graph, it can be seen that the emissions of HC reduced with uprise of load. At full load, the emissions from B20, B30, and B40 are less than other blends. B50 and B100 blend is observed to be

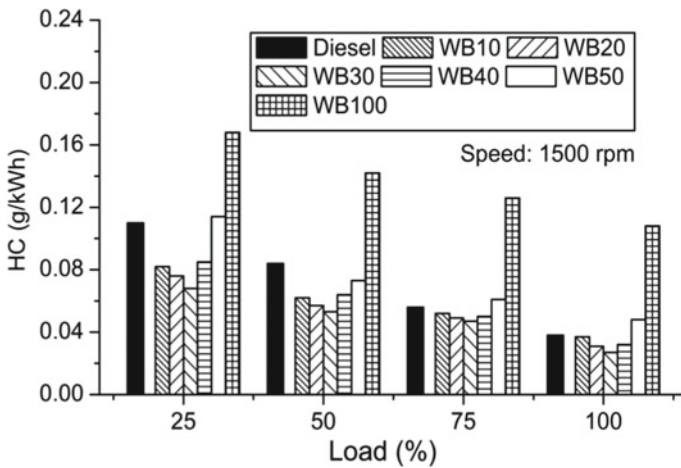


Fig. 3 HC emissions at different load

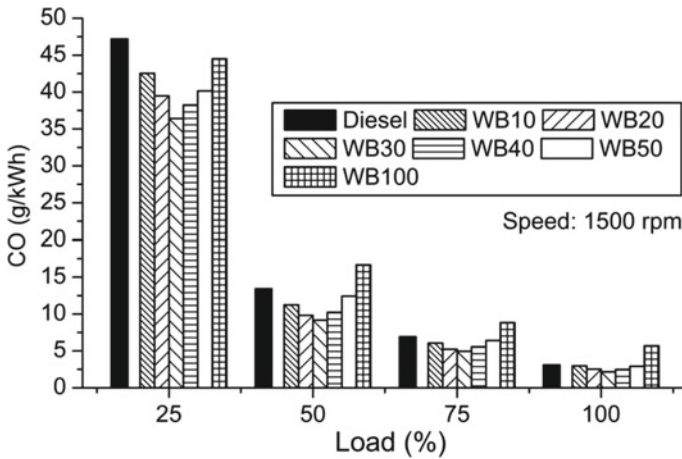


Fig. 4 CO emission at different load

increased significantly compared to other blends. At the upper circuit load, the HC emission for diesel, WB10, WB20, WB30, WB40, WB50, and WB100 is observed to be 0.038, 0.037, 0.031, 0.027, 0.032, 0.048, and 0.108 g/kWh, respectively. Some complexities are there when we discuss about the HC emission as it is affected by many things. However, the present work involves very lower HC figure that addresses the efficacy of the derived fuel as well as the quality of the engine.

4.4 Carbon Monoxide (CO)

The change of CO with regard to load is shown in Fig. 4. It is seen that B10, B20, and B30 blends have resulted in decreased CO. The emissions of CO reduced with an uprise in load. At higher load, the temperature is higher, which improves the reactivity which ultimately balances the incompletely burned carbon molecules. B50 and B100 blend is observed to be increased significantly compared to other blends. At full throttle, the CO for diesel and all blends is observed to be 3.1, 2.96, 2.53, 2.15, 2.48, 2.91, and 5.7 g/kWh, respectively. The present norms are getting stricter as a safeguard against carboniferous pollutions. It is also predicted that in the coming days it will be crucial to reduce CO in order to run a vehicle or engine.

4.5 Nitrogen Oxides (NO_x)

The NO_x emission with load is shown in Fig. 5. It is seen that up to B30 biodiesel diesel blends resulted in higher emissions of NO_x, while B40 blends onwards the

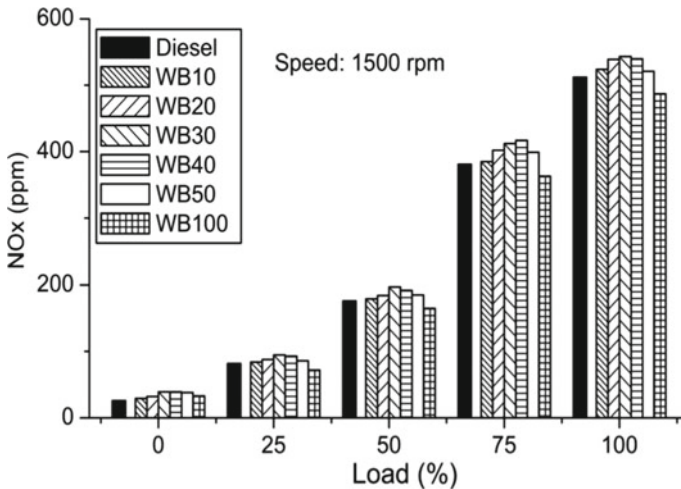


Fig. 5 NO_x emissions at different load

NO_x emission decreases at all load conditions. The NO_x strongly depends on the hotness within the cylinder, adiabatic temperature, mole of oxygen, etc. The NO_x emissions are higher for B30 at full throttle condition. The additional oxygen of biodiesel fuel is responsible for higher NO_x emission [22]. The NO_x emission at full throttle is observed to be within 600 ppm for all test fuels. This is a kind of emission that has very harmful impact on humanity. It causes very poisonous atmosphere by mixing with other harmful light compounds.

4.6 Smoke Opacity

The smoke with load is shown in Fig. 6. It can be observed that smoke increases with uprise in load. At full throttle condition, the smoke from B30 is less than other biodiesel blends. Higher order blends possess more density and viscosity for which the fuel mixture could not ignite properly and resulted in incomplete combustion and more smoke [23, 24]. Everyone is aware that smoke has huge potential to damage the ecosystem. It must be kept in limit. The smoke value indicates the health of the engine. It can be said that the inferior the engine digest the fuel, the more the smoke value. So, by studying the quality of the exhaust, the quality of the engine and its efficacy can be interpreted. It is always encouraged to establish correlation between several factors so that by testing any particular characteristics others can be predicted [25].

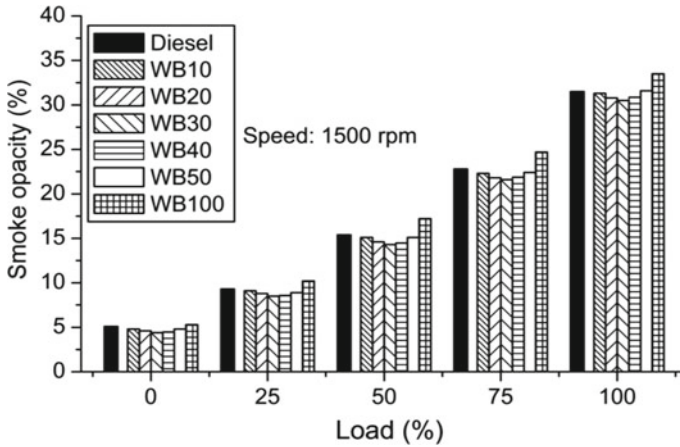


Fig. 6 Smoke opacity at different load

5 Conclusions

The biodiesel of waste cooking biodiesel oil is prepared by using transesterification process. These blends are tested on VCR diesel engine at different loads, and different performance characteristics and emissions are studied.

- With optimum reaction parameters of molar ratio 6:1, reaction speed 800 rpm, temperature 65 °C, and time 60 min, the yield efficiency of 96% obtained.
- The VCR diesel engine investigation for performance and emissions characteristics reveals that waste cooking biodiesel up to B40 is best for the undertaken engine.
- The main results indicate that the fuels are of sufficient quality for the emanation reduction.
- The long-term durability analysis is suggested for further investigation.

References

1. Dash SK, Lingfa P (2017) A review on production of biodiesel using catalyzed transesterification. AIP Conf Proc 1859:020100. <https://doi.org/10.1063/1.4990253>
2. Dash SK, Lingfa P (2018) Performance evaluation of Nahar oil-diesel blends in a single cylinder direct injection diesel engine. Int J Green Energy 15:400–405
3. Dash SK, Lingfa P (2018) An overview of biodiesel production and its utilization in diesel engines. IOP Conf Ser Mater Sci Eng 377:012006. <https://doi.org/10.1088/1757-899X/377/1/012006>
4. Mofijur M, Atabani AE, Masjuki HH, Kalam MA, Masum BM (2013) A study on the effects of promising edible and non-edible biodiesel feedstocks on engine performance and emissions production: a comparative evaluation. Renew Sustain Energy Rev 23:391–404

5. Azam MM, Waris A, Nahar NM (2005) Prospects and potential of fatty acid methyl esters of some non-traditional seed oils for use as biodiesel in India. *Biomass Bioenergy* 29:293–302
6. Dash SK, Dash S, Lingfa P (2017) Comparative assessment of performance and emission analysis of a diesel engine fueled with biodiesel prepared from different sources. *J Ind Pollut Control* 33(2):1114–1119
7. Dhar A, Kevin R, Agarwal AK (2012) Production of biodiesel from high-FFA neem oil and its performance, emission and combustion characterization in a single cylinder DIC I engine. *Fuel* 97:118–129
8. Ranjit PS, Chintala V (2020) Impact of liquid fuel injection timings on gaseous hydrogen supplemented pre-heated straight vegetable oil (SVO) operated compression ignition engine. *Energy Sources Part A Recov Utiliz Environ Eff.* <https://doi.org/10.1080/15567036.2020.1745333>
9. Kumar A, Dash SK, Ahamed MS, Lingfa P (2019) Study on conversion techniques of alternative fuels from waste plastics. In: Ghosh S (eds) *Energy recovery processes from wastes.* https://doi.org/10.1007/978-981-32-9228-4_18
10. Dewangan A, Yadav AK, Mallick A (2018) Current scenario of biodiesel development in India: prospects and challenges. *Energy Sources Part A Recov Utiliz Environ Eff.* <https://doi.org/10.1080/15567036.2018.1502849>
11. Dash SK, Lingfa P, Chavan SB (2019) Combustion analysis of a single cylinder variable compression ratio small size agricultural DI diesel engine run by Nahar biodiesel and its diesel blends. *Energy Sources Part A Recov Utiliz Environ Eff.* <https://doi.org/10.1080/15567036.2019.1604878>
12. Naik M, Meher LC, Naik SN, Das LM (2008) Production of biodiesel from high free fatty acid karanja (*Pongamia pinnata*) oil. *Biomass Bioenergy* 32:354–357
13. Dash SK, Lingfa P (2018) Production of biodiesel from high FFA non-edible Nahar oil and optimization of yield. *Adv Manuf Mater Sci* 431–439. https://doi.org/10.1007/978-3-319-76276-0_44
14. Muralidharan K, Vasudevan D, Sheeba KN (2011) Performance, emission and combustion characteristics of biodiesel fuelled variable compression ratio engine. *Energy* 36:5385–5393
15. Abubakar HG, Abdulkareem AS, Jimoh A, Agbajelola OD, Okafor JO, Afolabi EA (2016) Optimization of biodiesel production from waste cooking oil. *Energy Sources Part A Recov Utiliz Environ Eff* 38(16):2355–2361
16. Singh B, Kaur J, Singh K (2010) Production of biodiesel from used mustard oil and its performance analysis in internal combustion engine. *J Energy Res Technol* 132:031001
17. Moser BR (2009) Biodiesel production, properties, and feedstocks. *Vitro Cell Dev Biol Plant* 45:229–266. <https://doi.org/10.1007/s11627-009-9204-z>
18. Shahid EM, Jamal Y (2011) Production of biodiesel: a technical review. *Renew Sustain Energy Rev* 15:4732–4745
19. Dash SK, Lingfa P, Chavan SB (2018) An experimental investigation on the application potential of heterogeneous catalyzed Nahar biodiesel and its diesel blends as diesel engine fuels. *Energy Sources Part A Recov Utiliz Environ Eff* 40:2923–2932
20. Papu NH, Lingfa P, Dash SK (2020) *Euglena Sanguinea* algal biodiesel and its various diesel blends as diesel engine fuels: a study on the performance and emission characteristics. *Energy Sources Part A Recov Utiliz Environ Eff.* <https://doi.org/10.1080/15567036.2020.1798566>
21. Dash SK, Lingfa P, Barik D (2020) Combined adjustment of injection timing and compression ratio for an agricultural diesel engine fuelled with Nahar methyl ester. *Int J Ambient Energy.* <https://doi.org/10.1080/01430750.2020.1712250>
22. Bhurat S, Ranjit PS et al (2019) Technical barriers and their solutions for deployment of HCCI engine technologies—a review. *Int J Ambient Energy.* <https://doi.org/10.1080/01430750.2019.1611644>
23. Dash SK, Chavan SB, Kumar A, Ahamed MS, Lingfa P (2020) *Jatropha* biodiesel blends as renewable diesel fuel additives. In: Ghosh S, Sen R, Chanakya H, Pariatamby A (eds) *Bioresource utilization and bioprocess.* Springer, Singapore. https://doi.org/10.1007/978-981-15-1607-8_11

24. Dash SK, Lingfa P, Dash D (2020) Effect of compression ratio and injection timing on the performance of a B20 biodiesel blend fueled diesel engine. In: Satapathy S, Raju K, Molugaram K, Krishnaiah A, Tsihrintzis G (eds) International conference on emerging trends in engineering (ICETE). Learning and analytics in intelligent systems, vol 2. Springer, Cham. https://doi.org/10.1007/978-3-030-24314-2_91
25. Ranjit PS, Dash SK, Kamesh VV (2021) Experimental investigation on influence of injection pressure on gaseous hydrogen supplemented SVO operated IDI CI engine. Mater Today Proc. <https://doi.org/10.1016/j.matpr.2020.11.660>

Mapping, Trajectory Planning, and Navigation for Hexapod Robots Using ROS



Jovan Menezes, Shubhankar Das, Bhavik Panchal, Nitesh P. Yelve, and Praseed Kumar

Abstract The paper focuses on the design, modeling, and control of Razbot, an autonomous, dynamically stable hexapod robot possessing three actuated degrees of freedom in each leg. Razbot's design emphasizes mechanical stability accompanied by robustness to achieve power and computational autonomy providing it a wonderful advantage to maneuver over complex terrains. The project implements robot operating system (ROS) to build simulation and at the same time attain live feedback of Razbot's location. Such hexapod robots can serve applications in numerous fields such as terrain mapping and navigation for search and rescue operations, military stealth or other surveillance operations, aerospace operations to map and navigate on exoplanets, and many more.

Keywords Hexapod robots · Kinematics · Mapping and navigation · Simultaneous localization and mapping · ROS

1 Introduction

Wheeled robots suffer a disadvantage while traveling over rocky and uneven terrains unless they are imbued with greater flexibility which is accompanied by structural complexity. Instead, the use of legged robots in such instances can not only overcome such hurdles but also achieve the same at a reasonable cost. Legged robots are essentially bio-mimicked robots, i.e., their structural design is inspired by various biological life-forms such as cheetahs, ants, spiders, and even humans [1]. The study

J. Menezes (✉) · S. Das · B. Panchal · N. P. Yelve · P. Kumar
Department of Mechanical Engineering, Fr. C. Rodrigues Institute of Technology, Vashi, Navi Mumbai, India

N. P. Yelve
e-mail: niteshyelve@fcrit.ac.in

P. Kumar
e-mail: praseedkumar@fcrit.ac.in

of these robots provides hindsight into the principles behind the locomotion mechanism of animals as well as human beings. Such research, other than the field of robotics and automation, can even prove to be of essential assistance in the field of medicine and surgery, particularly in the development of prosthetics and other artificial motion mechanisms. Unmanned ground vehicles (UGVs) can be assigned different search and rescue (SaR) missions in forest fires, mapping, reconnaissance, damage inspection, acting as a repeater for transmissions [2]. In the aforementioned applications, it is evident that legged robots essentially dominate over wheeled robots. Based on the number of legs, these robots can be classified as bipods, quadrupods, hexapods, octopods, etc. Hexapods, as the name suggests, are a specific class of bio-mimicked robots consisting of six legs and their design inspired by that of ants. Hexapods possess a greater sense of stability due to the presence of three legs on each side as compared to the bipedal humanoid robots like the Atlas [3], developed by Boston Dynamics for search and rescue or the four-legged Cheetah robot [4], developed by the Massachusetts Institute of Technology. Also, any number of legs greater than six can induce a sense of redundancy from the point of stability and locomotion resulting in an unwanted increase in cost as well. Hence, hexapod robots have been in the limelight of roboticists ever since their inception with Stiquito [5], one of the initial and simplest hexapod robots developed by the Computer Science department at the Indiana University. The robot is intended for use as a research and educational platform to study computational sensors, subsumption architectures, neural gait control, the behavior of social insects, and machine vision. The robot is 60 mm long \times 70 mm wide \times 25 mm high and weighs 10 g. Stiquito's body is constructed of 32 parts of which 12 move. Six legs of Stiquito bend in response to six nitinol actuator wires. The RHex is a power autonomous six-legged vehicle that easily traverses terrain approaching the complexity and diversity of the natural landscape [6]. RHex consists of a rigid body with six compliant legs, each possessing only one independently actuated revolute degree of freedom. The attachment points of the legs as well as the joint orientations are all fixed relative to the body.

In their 2002 research paper, Pratihari et al. [7] described the use of a GA-fuzzy approach for generating optimal path and gait simultaneously for a hexapod robot. In their research, a genetic fuzzy system is developed in which a genetic algorithm (GA) finds the optimal rule-base of the fuzzy logic controllers (FLCs) to solve the problem of combined path and gait generations simultaneously of a hexapod robot. All-Terrain Hex-Limbed Extra-Terrestrial Explorer (ATHLETE), a large hexapod robot developed by the Jet Propulsion Laboratory (JPL), is a flexible platform designed to serve a variety of operations during manned and unmanned missions to the moon [8]. ATHLETE can perform tasks such as transportation, construction, and exploration while being operated by astronauts on the moon or remotely operated from the earth. Xin et al. [9–11] demonstrate the development of dynamic analysis and hybrid control followed by a novel control strategy based on rolling gait and trajectory planning to enable six-legged robots walk in dynamic environments using PH-robot. The robot utilizes a parallel mechanism, instead of the traditional revolute joint mechanism, which helps to improve payload capacity. The central intent of the research is to develop a control strategy to change gait and trajectory based on the ever-changing

environment and the status of the robot to achieve balance and serve the operations of search and rescue. Zhao et al. [12] described the development of Octopus-III, a hexapod robot with each leg consisting of a universal, a prismatic, and a spherical joint. A novel scheme is developed for obstacle avoidance and motion planning for Octopus-III wherein the trajectory planning method computes the walking direction by formulating the obstacle avoidance issue as an optimization problem. A drawback of the algorithm proposed in the research is that the obstacles are simplified as circles which lacks terrain classification to decide walking gait. Espenschied et al. [13] developed a biologically based distributed control instead of the traditional centralized control scheme to develop localized leg reflexes for the hexapod robot to walk over uneven terrains. The research described the integration of multiple biological reflexes such as an elevator and searching reflex into a hexapod robot with each leg possessing three active independent revolute degrees of freedom with angle sensors and one passive spring-loaded prismatic degree of freedom with a force sensor. Research at the Goddard Space Flight Center's Robotic Operations Center of NASA involved the testing of a hexapod robot with six degrees of freedom (three translational and three rotational) which is used to mimic the motion of satellites in zero gravity [14]. The 10 ft tall and 16 ft wide hexapod robot, which can move up to 8 inches/s and even extend to 13 ft, tests mission elements in the absence of humans. From the point of view of planning and navigation, various milestones are being achieved by the use of Intel tracking cameras [15], fuzzy Q -learning [16], biologically inspired adaptive obstacle negotiation behavior for obstacle avoidance [17], and RGB-D sensors for locomotion in uneven terrains [18].

In the literature presented, the focus has been on achieving greater mobility of hexapod robots over a variety of terrain incorporating various schemes, from biologically based distributed control to the use of genetic algorithms. The diverse applications presented above coupled with the mobility of hexapod robots have been inspiring in the development of a prototype of a hexapod robot that can first localize itself while simultaneously mapping the geometry and topography of its surroundings using human assistance, then navigate through the environment without any human intervention, and perform the necessary operation. The present study also implements ROS packages on hexapods robots to achieve the required degree of applicability. The paper is divided into five major sections. Having introduced the research in Sect. 1 and Sect. 2 deals with the design and modeling of the hexapod. The control philosophy is given in Sect. 3, and Sect. 4 deals with the experiments and its outputs. The concluding remarks on the study are given in Sect. 5.

2 Design and Modeling

2.1 Design and Morphology

Various complications can be experienced while executing the motion strategy if proper focus is not provided on the structural design and integrity of the hexapod robot [19]. Therefore, while designing the prototype, as shown in Fig. 1, the main objective has been to develop a hexapod robot with a great degree of flexibility accompanied by mechanical stability at minimum cost. To achieve this, each leg of the robot consists of three independent revolute joints, i.e., the coxa, femur, and tibia starting from the body to the end of the leg. These joints constitute the three degrees of freedom per leg and an overall 18 degrees of kinematic freedom, thus resembling its legs to those of the ants to a greater extent. On the other hand, the design of the body constitutes symmetry about the lateral as well as the vertical axis to facilitate better stability while in motion as well as better implementation of the navigation script during independent functioning. The tibia links for each leg are fabricated using the fused deposition modeling (FDM) technique, while the body consists of two plates (upper and lower plate, between which space is provided to accommodate the hardware) made of 4 mm thick acrylic sheet manufactured by laser cutting. This structure provides the necessary strength and durability for the prototype and also ensures that the center of gravity (COG) of the robot is close to the ground.

The control scheme of Razbot is shown in Fig. 2. Dynamixel AX-12A servomotors are used as actuators at each of the 18 joints of the robot, providing Razbot a programmable resolution of 0.29° as well as the required torque and speed at a considerable cost. These servomotors are powered using a 12.6 V, 5000 mAh lithium polymer (LiPo) battery using a servo distributor. A U2D2 servo controller is used to operate the servos using an onboard Intel NUC7PJYH. The Next Unit of Computing (NUC) provides the required computational capability onboard with a quad-core

Fig. 1 Prototype Razbot

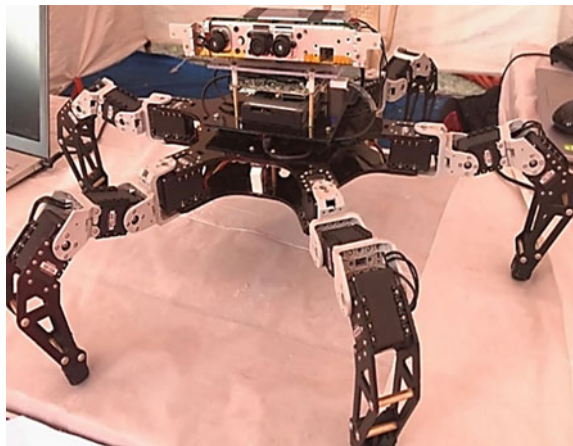
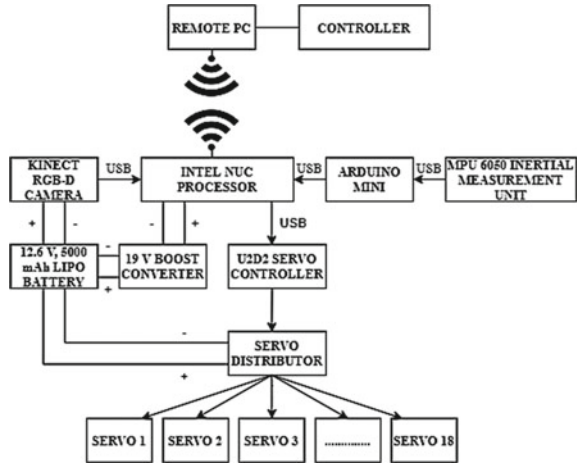


Fig. 2 Control scheme for Razbot



Intel Pentium Silver processor, reduces onboard weight as well as communicates with the operator’s laptop using the Intel Wireless-AC 9462 with Bluetooth v5, thus avoiding the need for a wire bus from the laptop to the robot. The NUC operates at 19 V, thus requiring a 19 V voltage booster from the 12.6 V supplied by the LiPo battery. Two feedback devices are used to help Razbot map and localize in the given environment, i.e., Microsoft XBOX 360 Kinect Sensor and the MPU 6050 inertial measurement unit with triple axis accelerometer and gyro breakout coupled to the NUC through Arduino Mini. Razbot can also be controlled manually using a joystick controller connected to the laptop.

2.2 Kinematic Equations

While developing the kinematic equations of motion for Razbot, it is assumed that the end/tip of the leg makes a point (or hard) contact with the ground instead of the actual area (or soft) contact. For achieving the necessary accuracy during locomotion as well as the required rate of computation, the matrix algebra approach is used to determine the inverse kinematic (IK) equations [20, 21]. The idea is to define the homogeneous transformation matrix from the center of Razbot’s body to the end of each leg, i.e., of the individual tibia links. The Denavit–Hartenberg (D–H) parameters for a single leg (rear left leg when viewed in the forward direction) are defined as shown in Table 1, while the notations used in the equations are given in Table 2.

Similarly, the D–H parameters for other legs can be defined by simply changing the value of θ from 60° to 120° , 180° , and so on for the body links. Based on these D–H parameters, each transformation matrix is defined, and by multiplying them together, the final transformation matrix is obtained as

Table 1 D–H parameters for rear left leg

Link	θ	d	α	a
1 (body link)	60°	0	0°	d_{bl}
2 (coxa link)	q_1°	0	90°	d_{cl}
3 (femur link)	q_2°	0	0°	d_{fl}
4 (tibia link)	q_3°	0	0°	d_{tl}

Table 2 List of notations

S. No.	Notation	Description
1	θ	Rotation about Z-axis
2	d	Translation about Z-axis
3	α	Rotation about X-axis
4	a	Translation about X-axis
5	d_{bl}	Distance from body center to coxa joint
6	d_{cl}	Length of coxa link
7	d_{fl}	Length of femur link
8	d_{tl}	Length of tibia link
9	q_1°	Coxa servo rotation angle
10	q_2°	Femur servo rotation angle
11	q_3°	Tibia servo rotation angle

$$T = \begin{bmatrix} \cos(q_1 + 60) \times \cos(q_2 + q_3) & -\cos(q_1 + 60) \times \sin(q_2 + q_3) & \sin(q_1 + 60) & \cos(q_1 + 60) \times r - d_{bl}/2 & \\ \sin(q_1 + 60) \times \cos(q_2 + q_3) & -\sin(q_1 + 60) \times \sin(q_2 + q_3) & -\cos(q_1 + 60) & \sin(q_1 + 60) \times r + \sqrt{3} \times d_{bl}/2 & \\ \sin(q_2 + q_3) & \cos(q_2 + q_3) & 0 & d_{fl} \times \sin(q_2) + d_{tl} \times \sin(q_2 + q_3) & \\ 0 & 0 & 0 & 1 & \end{bmatrix} \quad (1)$$

where $r = d_{cl} + d_{tl} \times \cos(q_2 + q_3) + d_{fl} \times \cos(q_2)$.

By solving the above matrix given in Eq. (1), the information regarding the position as well as the orientation of the tibia link of the leg based on the rotation angle of each joint motor is obtained. Inverse kinematics, on the other hand, determines the rotation angle of each joint motor based on the end position provided. The upper left 3×3 matrix provides information regarding the orientation, while the fourth column provides the position of the tip of the leg. Based on the assumption made earlier, for the requirement to plan the trajectory of Razbot, only the position elements of the above matrix are of importance. Accordingly, these position elements are used in the IK solver engine and are given below:

$$x = \cos(q_1 + 60) \times r - d_{bl}/2, \quad (2)$$

$$y = \sin(q_1 + 60) \times r + \sqrt{3} \times d_{bl}/2, \quad \text{and} \quad (3)$$

$$z = d_{fl} \times \sin(q_2) + d_{tl} \times \sin(q_2 + q_3). \quad (4)$$

Having known the values for d_{b1} , d_{c1} , d_{f1} , and d_{t1} as 144.53, 52, 66.061, and 133 mm and the end coordinates (x, y, z) obtained from the controller, the IK engine provides the values for the angle of rotation of each motor (q_1 , q_2 , and q_3).

3 Control Philosophy

The developed CAD model of Razbot (shown in Fig. 3) is converted into the unified robot description format (URDF) model as shown in Fig. 4 to obtain the real-time data/information regarding the motion and operation of each joint and links, i.e., the joint angles. This model is then used to simulate and navigate in robot visualization (RVIZ), an application of the robot operating system. RVIZ also assists in visualizing the transformations of each joint as shown in Fig. 5. Depending upon the terrain and its stability, Razbot can walk, turn, and lean using three different gaits. During the tripod gait 3 alternate legs move at a time while during the ripple gait 2 legs move

Fig. 3 CAD model of Razbot

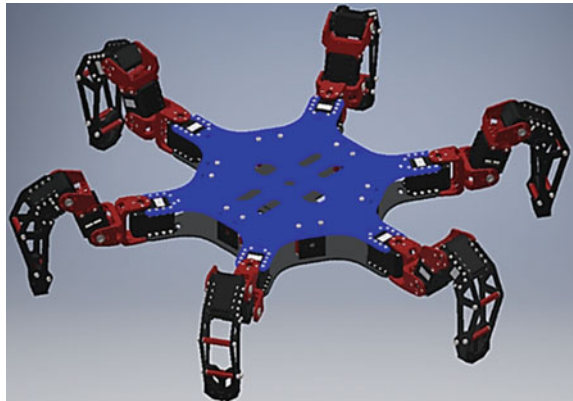


Fig. 4 URDF model of Razbot in RVIZ

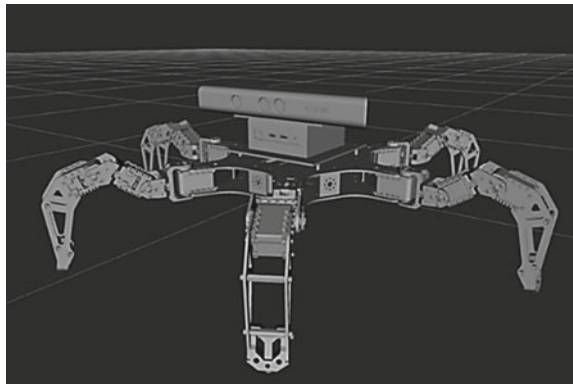
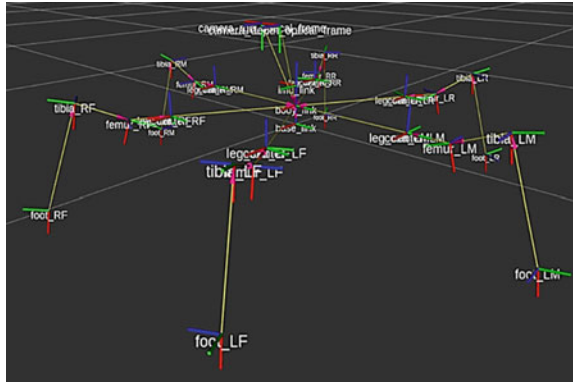


Fig. 5 Transformations defined for Razbot and visualized in RVIZ

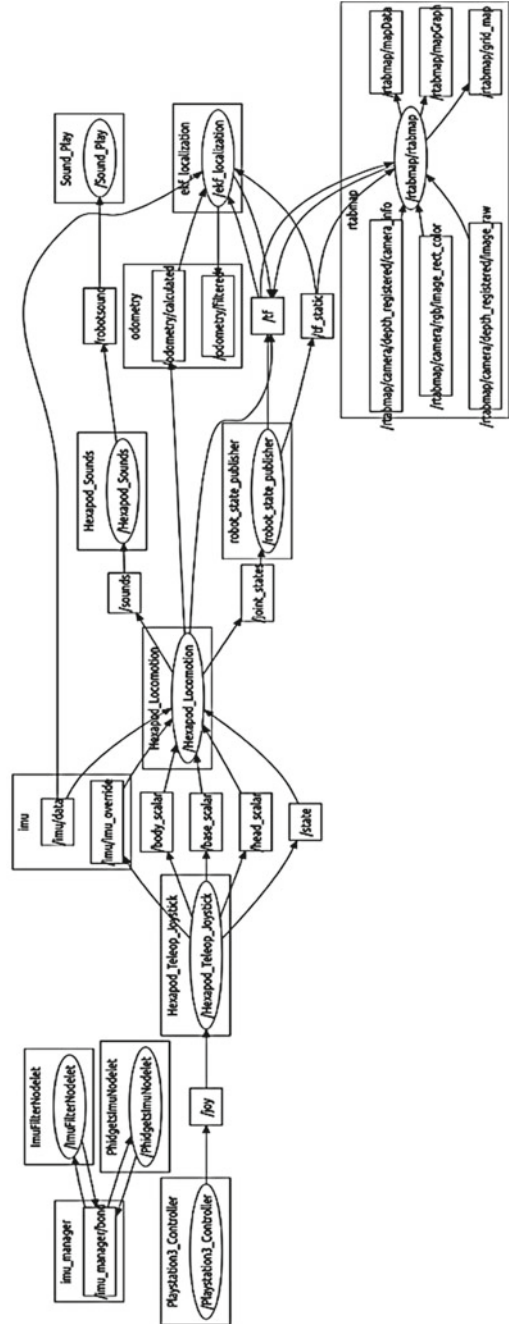


at a time, and only one leg moves in the crawl gait. Out of the three gaits, the tripod gait provides the fastest maneuverability and is commonly used over even surfaces, while the crawl gait is the slowest and is used where the terrain is complex and difficult to navigate through. Razbot is also capable of an extended leg lift gait in which the height of the lift is greater than usual. This gait is mainly helpful while climbing stairs or rocky regions. However, it is important to note that the shifting of gaits needs to be done manually by the operator and cannot be executed by Razbot during autonomous navigation.

3.1 Mapping and Locomotion

The script for locomotion, mapping, and navigation is developed in ROS using C++ language, which is summarized in the flowchart shown in Fig. 6. The backend script begins by defining a node *joy* to take in navigation or motion values from the joystick/controller node (*Playstation3_Controller*) and publish the same to the *Hexapod_Teleop_Joystick*. These values are then used to calculate the body scalar, base scalar, head scalar, and state of the robot (i.e., whether Razbot is in a state of motion or at rest or simply just standing) with the help of the URDF model developed earlier. These parameters are then published to the locomotion node (*Hexapod_Locomotion*) which is used for moving Razbot. The hexapod locomotion node also stores the values published by the IMU (*imu/data*) through the Arduino. The locomotion node can also publish the state of Razbot to the *Hexapod_Sounds* which provides an audio description of the state of the robot through the *Sound_Play* node. The *Hexapod_Sounds* node contains individual script based on the state of Razbot published by the *Hexapod_Locomotion* node which provides the audio output. This feature however requires Razbot to be connected to a laptop since the NUC does not have audio output and would need to integrate an onboard speaker. The locomotion node publishes the joint states to the *robot_state_publisher* node which provides the URDF transform values in the */tf & /tf_static* node.

Fig. 6 Control architecture for Razbot in ROS



Now, based on the transforms and the joint states of the robot obtained from the locomotion node, raw odometry values are calculated. These values along with the IMU data are sent into the extended Kalman filter (*ekf_localization*) node which provides the final filtered odometry values which are useful for the localization of Razbot. The present approach uses visual simultaneous localization and mapping (V-SLAM) which is based on the real-time appearance-based (RTAB) mapping using an RGB-D camera to help create a map and localize the robot in it [22]. This approach is opposed to the initial use of ultrasonic sensing accompanied with multiple servo-mounted sonar sensors for SLAM [23] and adept to the more recent ORB-SLAM [24, 25], VPS-SLAM used in drones for indoor mapping [26] and vision-based controller adaptation for hexapod robots [27, 28]. V-SLAM uses the key points in the point cloud image obtained from the KINECT camera to match with other key points in the new image obtained to determine as to what extent has the robot moved while also performing large-scale optimization on the 3D point positions and camera poses using the iterative closest point algorithm. To obtain the RTAB map, the filtered odometry values are provided as an input to the *rtabmap* node through the */tf* node along with the static transform values. The RGB image obtained from KINECT camera and the infrared depth details obtained from the infrared camera are also provided as inputs to develop the RTAB map. Now, the *rtabmap* publishes three details: the RTAB map itself, a graph on the map, and a grid on the map which can be viewed in RVIZ as shown in Fig. 7.



Fig. 7 Indoor RGB-D mapping using V-SLAM and KINECT as seen in RVIZ

3.2 Trajectory Planning and Navigation

The ROS navigation stack is implemented to achieve trajectory planning and navigation of Razbot in any given environment. The goal of the navigation stack is to move Razbot from one position to another safely without colliding or getting lost. The navigation stack takes inputs from the RTAB map generated earlier, the IMU and joint angle data, and provides output in the form of velocity commands to each motor. The original navigation stack, developed to handle mainly wheeled robots and not robots that can move sideways, is upgraded to account for the additional degrees of freedom made available from Razbot's structure. The map generated by V-SLAM technique (*gmapping* package) is fed in as ROS service through the *map_server* package for the navigation stack. The adaptive Monte Carlo localization (*amcl*) package, which is a probabilistic localization system, is used to track the posture of Razbot against the map generated earlier. The global navigation stack (*global_planner*) generates trajectories for the end task in the map or at a distant location by developing the global costmap to determine the minimum cost plan for achieving the endpoint using the Dijkstra's algorithm. On the other hand, the local navigation stack (*local_planner*) generates trajectories in the local region and avoids obstacles by executing the trajectory rollout and dynamic window algorithm. Finally, the *move_base* package integrates the global and local planner to achieve the holistic navigation and occasionally recovers behavior when Razbot perceives itself as stuck.

4 Experimentation and Discussion

4.1 Traversing Over Uneven Terrain

Since the primary purpose of developing Razbot is for potential use in dynamic and uneven terrain, the testing began by traversing Razbot in the outdoor environment. This is conducted on two stages; first on rocky and unstable terrain, such as the one found in gardens and grounds, second over speed breakers for automobiles to demonstrate its ability to climb over surfaces. While moving in uneven terrains, it is crucial that the COG of the body must be as close to the ground as possible, thus ensuring better stability and motion. As seen in Fig. 8, Razbot can easily travel over rocky surfaces using the tripod gait with the normal leg lift. This ensures promising results that can be achieved with the use of extended leg lift and crawl gait for even more complex terrains. This ability proves to be useful in applications such as landmine detection for military purposes and navigation on extraterrestrial planets. Figure 9 shows Razbot climbing over speed breakers which have a height of 10 cm. Again, this is achieved with the tripod gait and normal leg lift. While moving in the external environment, due to increased surrounding light (sunlight), the mapping achieved through KINECT is not sufficient to achieve independent navigation. Advanced

Fig. 8 Razbot traversing rocky surfaces



Fig. 9 Razbot traveling over elevated surfaces



cameras and sensors can improve the quality of the map provided which will provide better navigation outdoors.

4.2 Indoor Mapping and Navigation

The quality of the map obtained is relatively better for indoor operations than outdoor, the reason being that the infrared projector and camera used in KINECT are best suitable for indoor applications. As shown in Fig. 10, Razbot is able to localize and navigate better indoors as the feature detection process in V-SLAM is enhanced. Razbot can detect obstacles such as chairs, tables, and beds and can also navigate itself through such environments. While switching to autonomy indoors, it was found that the time taken for Razbot to detect changes in the environment and localize itself is relatively long. KINECT, on average, has a frame rate of around 9–30 Hz which is comparatively lower for achieving rapid autonomous operation. Also, on average, KINECT has a practical ranging limit of 1.2–3.5 m. These drawbacks, however, can be easily overcome with the use of a better camera for mapping such

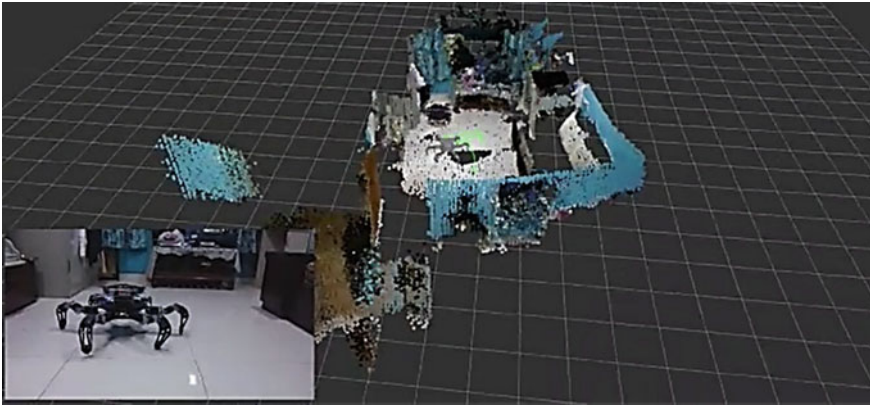


Fig. 10 Razbot performing indoor mapping and navigation. Inserted window shows camera shot of the room where Razbot is

as a commercial LiDAR [29, 30]. With the use of such sensors, the autonomous navigation of Razbot can be enhanced to a much higher extent and can even easily serve outdoor applications.

4.3 Discussion

Based on the observations of the above tests and analysis, it is evident that the method proposed is effective, agile, and easy to implement on hexapod robots to improve their efficacy in performing a wide range of operations. However, it is imperative to note that the complete potential of the V-SLAM technique for Razbot cannot be determined by the use of KINECT. KINECT serves as a viable solution for RGB-D mapping at low cost; however, the use of enhanced sensors such as the RPLiDAR A1M8 which has the ability to rotate 360° with an improved frame rate of nearly 8000 Hz and range of nearly 6 m can provide better and faster mapping which will directly help achieve better navigation. Evidently, with the implementation of such enhanced sensors, better results can be obtained in the above tests, and it can even expand the horizons of Razbot's ability to perform autonomously in almost any given environment. The V-SLAM technique and the navigation stack, with the available hardware, proved to be effective and successful in achieving the required results for mapping, planning, and navigation of Razbot. The robust structure of Razbot as well the 18 degrees of kinematic freedom imbues Razbot with the ability to twist and tilt, allowing it to operate in various fields where perhaps humans cannot venture. With the variety of gaits that can be achieved as well as the extended height that can be reached, Razbot can move on much more complex terrains than the ones presented in the above tests. The V-SLAM technique proves to be more effective than earlier proposed techniques (such as ultrasonic, GSLAM, ORB-SLAM, or other methods)

and can be used on hexapod robots in any surrounding. Another advantage of this is that Razbot does not require any prior information about the topography of the environment and can localize and map itself in it rather than first providing the map and then navigating the robot.

5 Conclusion

The paper focuses on the issues of hexapod robot related to its mapping and navigation in any environment using ROS. The prototype built is simple, and at the same time, it is agile to demonstrate the results. Clearly, structural integrity can be enhanced to serve the desired field of application. With the use of spring-actuated joints, the robot can perform activities involving jumping, while using advanced sensors and actuators, it can locomote faster. Hexapod robots are more stable than humanoid, biped, or quadruped robots which make it simpler to control and navigate. ROS provides a window of opportunities to explore with hexapod robots making it easier to integrate and achieve multiple tasks for any given structure. A step further in this work could be the implementation of autonomy from the moment the robot is turned on, allowing it to even construct the map of its surroundings without any intervention. With the development of better SLAM techniques and improved hardware, this does not seem too farfetched. A swarm of such robots could perform coordinated activities that would help in the field of post-disaster rescue. Further development in achieving autonomy of legged robots, in particular, can serve beneficial to different fields of study and industry.

References

1. Diftler MA, Mehling JS, Abdallah ME, Radford NA, Bridgwater LB, Sanders AM, Askew RS, Linn DM, Yamokoski DM, Permenter FA, Hargrave BK, Platt R, Savely RT, Ambrose RO (2011) Robonaut 2—the first humanoid robot in space. In: Proceedings of IEEE international conference on robotics and automation. Shanghai, China, pp 2178–2183. <https://doi.org/10.1109/ICRA.2011.5979830>
2. Karma S, Zorba E, Pallis GC, Statheropoulos G, Balta I, Mikedi K, Vamvakari J, Pappa A, Chalaris M, Xanthopoulos G, Statheropoulos M (2015) Use of unmanned vehicles in search and rescue operations in forest fires: advantages and limitations observed in a field trial. *Int J Disaster Risk Reduct* 13:307–312. <https://doi.org/10.1016/j.ijdrr.2015.07.009>
3. Koolen T, Bertrand S, Thomas G, De Boer T, Wu T, Smith J, Engelsberger J, Pratt J (2016) Design of a momentum-based control framework and application to the humanoid robot atlas. *Int J Humanoid Rob* 13(1):1650007. <https://doi.org/10.1142/S0219843616500079>
4. Seok S, Wang A, Chuah MY, Otten D, Lang J, Kim S (2013) Design principles for highly efficient quadrupeds and implementation on the MIT Cheetah robot. In: Proceedings of IEEE international conference on robotics and automation. Karlsruhe, Germany, pp 3307–3312. <https://doi.org/10.1109/ICRA.2013.6631038>
5. Mills JW (1992) Stiquito: a small, simple, inexpensive hexapod robot. Technical report, 363A. Indiana University Computer Science Department, pp 1–48

6. Saranlı U, Buehler M, Koditschek DE (2000) Design, modeling and preliminary control of a compliant hexapod robot. In: Proceedings of IEEE international conference on robotics and automation. San Francisco, CA, USA, pp 2589–2596. <https://doi.org/10.1109/ROBOT.2000.846418>
7. Pratihari DK, Deb K, Ghosh A (2002) Optimal path and gait generations simultaneously of a six-legged robot using a GA-fuzzy approach. *Robot Auton Syst* 41(1):1–20. [https://doi.org/10.1016/S0921-8890\(02\)00273-7](https://doi.org/10.1016/S0921-8890(02)00273-7)
8. Smith TB, Barreiro J, Smith DE, Sunspiral V, Chavez-Clemente D (2008) ATHLETE's feet: multi-resolution planning for a hexapod robot. In: Proceedings of ICAPS-08 scheduling and planning applications workshop. Sydney, Australia
9. Xin G, Deng H, Zhong G, Wang H (2015) Dynamic analysis of a hexapod robot with parallel leg mechanisms for high payloads. In: Proceedings of 10th Asian control conference. ASCC, 2015, pp 1–6
10. Zhong G, Deng H, Xin G, Wang H (2016) Dynamic hybrid control of a hexapod walking robot: experimental verification. *IEEE Trans Ind Electron* 63:5001–5011. [https://www.sciencedirect.com/science/refhub/S0921-8890\(17\)30020-9/sb3](https://www.sciencedirect.com/science/refhub/S0921-8890(17)30020-9/sb3)
11. Deng H, Xin G, Zhong G, Mistry M (2017) Gait and trajectory rolling planning and control of hexapod robots for disaster rescue applications. *Robot Auton Syst* 95:13–24. <https://doi.org/10.1016/j.robot.2017.05.007>
12. Zhao Y, Chai X, Gao F, Qi C (2018) Obstacle avoidance and motion planning scheme for a hexapod robot Octopus-III. *Robot Auton Syst* 103:199–212. <https://doi.org/10.1016/j.robot.2018.01.007>
13. Espenschied KS, Quinn RD, Beer RD, Chiel HJ (1996) Biologically based distributed control and local reflexes improve rough terrain locomotion in a hexapod robot. *Robot Auton Syst* 18(1–2):59–64
14. <https://nasa.tumblr.com/post/175779680559/6-fun-facts-about-our-new-hexapod-robot>. Accessed on 30 Aug 2020
15. Bayer J, Faigl J (2019) On autonomous spatial exploration with small hexapod walking robot using tracking camera intel RealSense T265. In: 2019 European conference on mobile robots. ECMR 2019—proceedings, pp 1–6. <https://doi.org/10.1109/ECMR.2019.8870968>
16. Hong J, Tang K, Chen C (2018) Obstacle avoidance of hexapod robots using fuzzy Q-learning. In: 2017 IEEE symposium series on computational intelligence. SSCI 2017—proceedings, Jan 2018, pp 1–6. <https://doi.org/10.1109/SSCI.2017.8280907>
17. Goldschmidt D, Wörgötter F, Manoonpong P (2014) Biologically-inspired adaptive obstacle negotiation behavior of hexapod robots. *Front Neurobot* 8:1–16. <https://doi.org/10.3389/fnbot.2014.00003>
18. Cizek P, Faigl J (2017) On localization and mapping with RGB-D sensor and hexapod walking robot in rough terrains. In: 2016 IEEE international conference on systems, man, and cybernetics. SMC 2016—conference proceedings, pp 2273–2278. <https://doi.org/10.1109/SMC.2016.7844577>
19. Tedeschi F, Carbone G (2014) Design issues for hexapod walking robots design issues for hexapod walking robots. *Robotics* 3(2):181–206. <https://doi.org/10.3390/robotics3020181>
20. Roy SS, Pratihari DK (2014) Kinematics, dynamics and power consumption analyses for turning motion of a six-legged robot. *J Intell Robot Syst Theory Appl* 74(3–4):663–688. <https://doi.org/10.1007/s10846-013-9850-6>
21. Xin G, Deng H, Zhong G, Wang H (2015) Hierarchical kinematic modelling and optimal design of a novel hexapod robot with integrated limb mechanism. *Int J Adv Robot Syst* 12(9):123. <https://doi.org/10.5772/59989>
22. Omara HIMA, Sahari KSM (2016) Indoor mapping using kinect and ROS. In: 2015 international symposium on agents, multi-agent systems and robotics. ISAMSR 2015, pp 110–116. <https://doi.org/10.1109/ISAMSR.2015.7379780>
23. Leonard JJ, Durrant-Whyte HF (2002) Simultaneous map building and localization for an autonomous mobile robot. In: Proceedings of IEEE/RSJ international workshop on intelligent robots and systems, vol 3. Osaka, Japan, pp 1442–1447. <https://doi.org/10.1109/iros.1991.174711>

24. Mur-Artal R, Montiel JMM, Tardos JD (2015) ORB-SLAM: a versatile and accurate monocular SLAM system. *IEEE Trans Robot* 31(5):1147–1163. <https://doi.org/10.1109/TRO.2015.2463671>
25. Mur-Artal R, Tardos JD (2017) ORB-SLAM2: an open-source SLAM system for monocular, stereo, and RGB-D Cameras. *IEEE Trans Robot* 33(5):1255–1262
26. Bavle H, De La Puente P, How JP, Campoy P (2020) VPS-SLAM: Visual planar semantic SLAM for aerial robotic systems. *IEEE Access* 8:60704–60718. <https://doi.org/10.1109/ACCESS.2020.2983121>
27. Bjelonic M, Homberger T, Kottege N, Borges P, Chli M, Beckerle P (2017) Autonomous navigation of hexapod robots with vision-based controller adaptation. In: *Proceedings—IEEE international conference on robotics and automation*, pp 5561–5568. <https://doi.org/10.1109/ICRA.2017.7989655>
28. Bjelonic M, Kottege N, Homberger T, Borges P, Beckerle P, Chli M (2018) Weaver: Hexapod robot for autonomous navigation on unstructured terrain. *J Field Robot* 35(7):1063–1079. <https://doi.org/10.1002/rob.21795>
29. Hess W, Kohler D, Rapp H, Andor D (2016) Real-time loop closure in 2D LIDAR SLAM. In: *IEEE international conference on robotics and automation (ICRA)*, 12–13. <https://doi.org/10.2307/j.ctv6wgf4q.9>
30. Pierzchała M, Giguère P, Astrup R (2018) Mapping forests using an unmanned ground vehicle with 3D LiDAR and graph-SLAM. *Comput Electron Agric* 145:217–225. <https://doi.org/10.1016/j.compag.2017.12.034>

Voronoi Diagram Approximated Austenite Grain Mapping and Voronoi Algorithm-Based Microstructure Prediction of Quenched C35 Steel



S. Sanchu, N. Biju, and V. N. N. Namboothiri

Abstract Ability of Voronoi diagram in predicting the microstructure evolution during martensite transformation in C35 steel quenched from complete austenite range is analyzed in this work. The input needed for constructing Voronoi diagram is the position of individual seeds. Since diffusionless transformation is considered in this work, knowledge about the grain boundary is essential. Using image processing software ImageJ, from the micrograph obtained experimentally, austenite grain map is identified. This grain map is converted into equivalent Voronoi diagram. The micrograph of quenched steel is analyzed to determine number of martensite blocks in the final structure. Using these two inputs, Voronoi diagram is constructed. The result represents the microstructure in quenched condition. On comparison between simulated microstructure and micrograph, it is evident that Voronoi diagram-based simulation technique can effectively be used for modeling microstructure evolution during quenching of C35 steel.

Keywords Microstructure modeling · Voronoi diagram · Micrograph · Grain map · Martensite formation

1 Introduction

Microstructure is one of the key factors, which determines the mechanical properties of materials. Knowledge about microstructure evolution during processing helps to develop efficient and cost-effective processes that can contribute for development of materials with desired properties. Effective use of computational material science plays an important role in reduction of expensive experimental approach for building process structure property (PSP) links [1]. Main steps involved in computational microstructure characterization and reconstruction (MCR) are quantitatively represent microstructure and build statistically equivalent microstructure [1, 2]. A

S. Sanchu (✉) · N. Biju · V. N. N. Namboothiri
Division of Mechanical Engineering, School of Engineering, Cochin University of Science and Technology, Kochi, India

brief review of various type of characterization and reconstruction methods can be found in Ref. [1].

Voronoi algorithm-based methods plays an important role in reconstruction of statistically similar microstructure from micrograph. Voronoi diagram is a portioning technique used for dividing n dimensional Euclidian space based on some criteria [3]. Burtseva et al. [4] done a review of Voronoi diagram-based techniques applied to modeling of material structure as sphere packing models. Modeling of microstructure from scanning electron microscope (SEM) images is also reported by various researchers. Katani et al. [5] created finite element models from SEM images using two distinct methods. One method directly creates microstructure from the image, and the second model uses Voronoi algorithm to construct statistically similar microstructure. The influence of fiber content on mechanical properties is analyzed by Bertoncelej et al. [6] using the microstructure model based on Voronoi algorithm. They pointed out that the crucial step is the effectiveness in tessellation of microstructure, into Voronoi polygon. Voronoi algorithm is also used to create microstructure geometry of ceramic grains, which is statistically similar to images obtained through experiments [7]. Bertolino et al. [8] use experimentally measured characteristics like grain size, grain shape, size distribution and texture distribution to simulate realistic two-dimensional microstructure. If the seeds of Voronoi diagram are determined using homogeneous Poisson point process, then it can be considered as Poission–Voronoi diagram [3]. In most of the cases, the seed generation is considered as homogeneous. Schnelder et al. [9] suggested a numerical method based on hierarchical Poisson Voronoi tessellation for constructing two-dimensional or three-dimensional artificial microstructure. In this model, the nuclei generation is considered as inhomogeneous. Based on the morphological and cryptographic data obtained from electron back scattered diffraction (EBSD) analysis, the development of 3D microstructure is reported by St-Pierre et al. [10]. The ability of Voronoi algorithm for developing realistic microstructure in the case of 2D foam-like representative element is examined by Alsayednoor et al. [11]. They evaluate the effectiveness both from mechanical and morphological perspectives.

Among heat treatment processes, quenching is the most studied one because of its importance in industrial fields. For the accurate prediction of properties of materials and for efficient process development, knowledge about the transformation kinetics and its relation to evolved microstructure is important. Kinetics of martensite transformation largely depends on slower one among nucleation and growth [12]. As formed martensite plates suddenly grow into its final size [13], kinetics depends only on nucleation rate. Detailed studies about the various aspects of martensite nucleation [14] and transformation including modeling methods are available in the literature. Fisher et al. assumed that austenite to martensite transformation happens through nucleation and growth. Based on this assumptions, they calculated martensite start temperature and martensite transformation curve [15]. Zaho et al. [16] suggested that thermal activation can stimulate homogeneous nucleation in iron-based alloys. Hsu et al. introduced an approach for evolution of critical driving force [17]. Studies about the crystallographic features of lath martensite are also available [18]. Analysis on the effect of prior austenite grain size in martensite transformation showed that

Table 1 Composition of C35 in weight percentage [28]

C	Mn	Si	Cu	Cr	Ni	Mo	Sn	P	S
0.364	0.656	0.305	0.226	0.177	0.092	0.016	0.017	0.014	0.021

grain refinement shifts M_s to a lower state [19]. Efficient simulation methods for prediction of microstructure developed during various processes will considerably reduce the cost of experiments. Variety of simulation methods including geometrical methods [20], phase field method [21], Monte Carlo simulation [22], cellular automata [23], etc., are available in the literature. Out of which geometric simulation methods are computationally efficient. Alavi et al. [24] used combination of finite element method and cellular automata to predict microstructure changes during non-isothermal heat treatment process. Jia et al. [25] developed cellular automata model to study the microstructure evolution and solute distribution during intercritical annealing. Carlsson et al. [26] reported the effectiveness of combined model based on phase field method and statistical geometry random Voronoi tessellation for studying fracture and strength of porous microstructure. Simulation based on finite element method is also available to analyze the effect of stress on martensite transformation to predict temperature history, microstructure evolved and internal stresses [27].

This work is an attempt to predict the microstructure developed during quenching of C35 steel from complete austenite range using the properties of ordinary Voronoi diagram. The grain map obtained at complete austenite range is taken as the initial microstructure. Using the number of martensite grains evolved during undercooling from martensite start temperature (M_s) to room temperature and initial microstructure as input, ordinary Voronoi diagram is constructed. The properties of constructed diagram are compared with the experimental result. As geometrical simulation method is used here, computational efficiency is higher than other simulation methods like phase field simulation and cellular automata, etc.

2 Material Used

Material used in this work is C35. Composition of the material in terms of weight percentage is shown in Table 1.

3 Experimental Procedure

The material is cut into 10 mm \times 10 mm \times 10 mm size. Sample is heated to 900 °C using electric furnace and keep it at that temperature for 30 min. After the holding duration, sample is water quenched to get martensite microstructure.

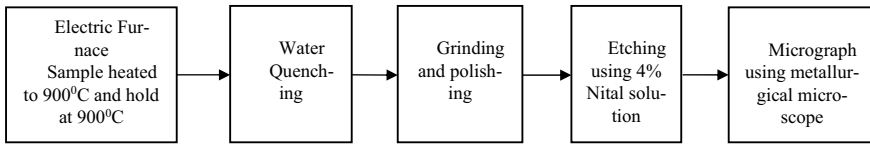


Fig. 1 Schematic experimental setup

For metallographic analysis, the sample is grinded using 240, 400, 800 and 1000 grade papers and then polished using diamond paste. After polishing, the material is etched using 4% Nital solution. Micrographs at $50\times$ magnification are taken using metallurgical microscope for metallographic analysis. Schematic representation of experimental setup is shown in Fig. 1.

4 Simulation Procedure

This work is attempted to predict the microstructure of C35 steel quenched from complete austenite range, using algorithm for Voronoi diagram construction. Ordinary Voronoi diagram divides the space into n cells, where n (seeds) is any integer greater than or equal to two and less than infinity, in such a way that the distance between any point in space to its seed is less than the distance between that point to any other seed [3]. The input needed for constructing Voronoi diagram is position of individual seeds. Here, there will be an additional constraint that is the austenite grain structure. Since the displacive transformation cannot be sustained across grain boundaries [29], martensite plates evolved cannot grow beyond austenite grain boundaries. Thus, the inputs for simulation are (1) Initial Voronoi diagram which is equivalent to austenite grain map, (2) Number of martensite nuclei evolved.

The seeds of initial Voronoi diagram are stored in initial seed matrix. A weight matrix is created to store identifiers of different phases. 0 represents austenite and 1 represents martensite. As there is only austenite phase in initial microstructure weight matrix is initiated with 0 corresponding to each polygon. Number of martensite grains evolved after quenching (calculated from micrograph) is taken as NM. Generate NM number of new coordinates randomly to fix the position of newly generated martensite nuclei. The new coordinates added to seed matrix and weight matrix is updated with assigning weight 1 corresponding to newly generated nuclei. The number of austenite nuclei remain in the structure is modified using the position of martensite nuclei generated. Update the seed matrix and id matrix. From the initial Voronoi diagram, each polygon is identified. From the updated seed matrix, the martensite nuclei formed in each polygon can be identified. Construct Voronoi diagram within the polygon using nuclei formed inside it as seed. Region occupied by martensite phase can be identified using the seed and corresponding weight. The polygon corresponding to the seeds with weight 1 is martensite phase and with 0 weight is austenite phase. By dividing the area occupied by martensite phase with

whole area, transformed fraction of martensite can be obtained. From the resulting Voronoi diagram, it is possible to identify grain area and grain area distribution mathematically.

5 Micrograph Analysis

For analyzing micrographs, open source software ImageJ [30] is used. Here, image analysis is used to determine inputs for simulation and also for comparison of simulated results with experimental results. For the simulation, inputs needed are initial grain map in austenite range and number of martensite nuclei evolved during quenching. For the comparison between experimental and simulated results fraction of martensite evolved, grain area of martensite and grain area distribution are needed. Besides these, austenite grain area and austenite grain area distribution are needed to compare the grain map and equivalent Voronoi diagram.

For the simulation, first input needed is the austenite grain map. The grain map of sample in complete austenite range is derived from micrograph using the procedure summarized below. After scaling of initial micrograph, $500\mu\text{m}\times 500\mu\text{m}$ is taken as region of interest and is represented in Fig. 2. The selected image is filtered using band pass filtering technique (result is shown in Fig. 3). Then, the image is segmented using morphological segmentation (*MorphoLibJ*) [31], in order to get the grain map. Results are shown in Fig. 4a, b. The grain map image obtained in Fig. 4 is converted to polygon using available MATLAB code [32]. Polygon approximated grain map image is represented in Fig. 5a. The centroid of each polygon is calculated [33] and is considered as seeds for constructing initial Voronoi diagram. Using this seeds, Voronoi diagram equivalent to grain map is constructed and is shown in Fig. 5b. This seeds and corresponding Voronoi diagram are used as input for simulation.

Another input needed for simulation is number of martensite grains evolved during quenching. For this, morphological segmentation is done on the micrograph. The results are shown in Fig. 6a, b. From the image (a), number of martensite blocks

Fig. 2 Original image
 $500\mu\text{m} \times 500\mu\text{m}$

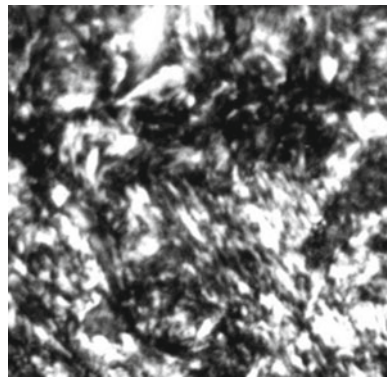


Fig. 3 Image after band pass filtering

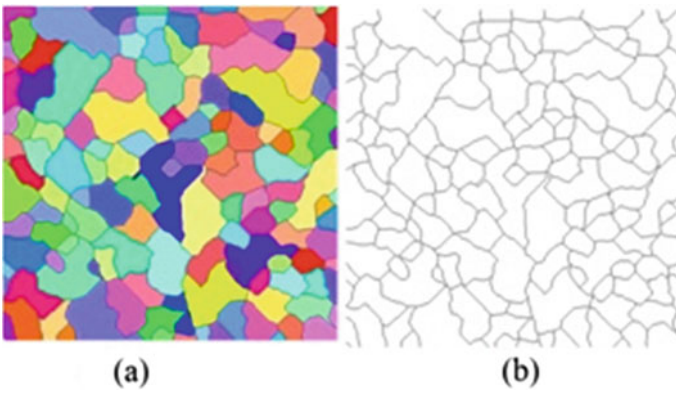
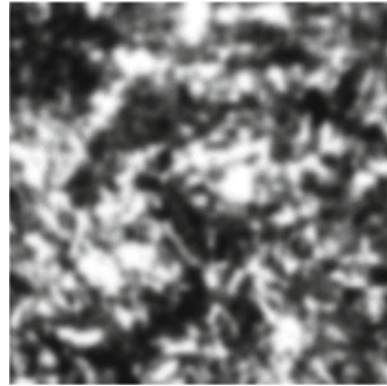


Fig. 4 Images after morphological segmentation of band pass filtered image **a** catchment basins **b** watershed lines

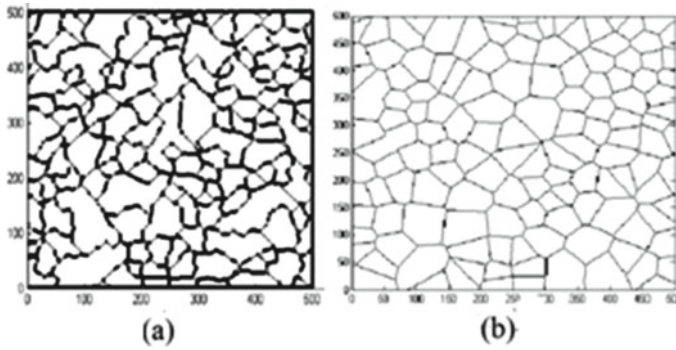


Fig. 5 Images after morphological segmentation of band pass filtered image. **a** Polygon approximated grain map. **b** Voronoi equivalent of grain map

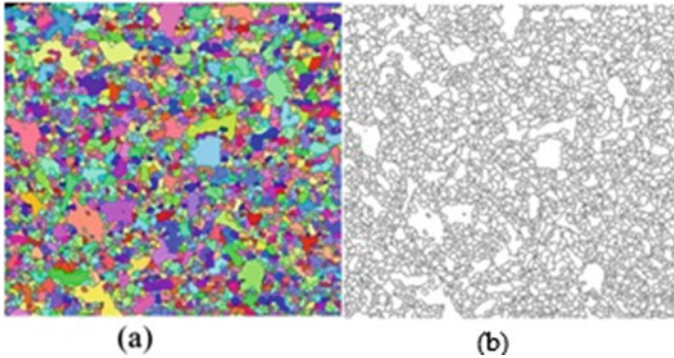
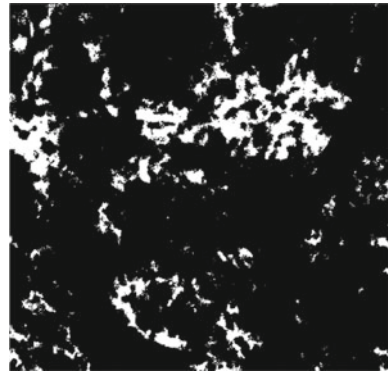


Fig. 6 Images after morphological segmentation **a** catchment basins **b** watershed lines

Fig. 7 Image after threshold



generated are counted using cell counting. This is used as the second input for the simulation.

In order to compare the grain area and grain area distribution in grain map image and simulated initial microstructure, the area occupied by each cell in Fig. 4a is calculated using measurement function in ImageJ. The result obtained is analyzed to get average area and grain area distribution. To find fraction of martensite formed, threshold function is used. Image obtained after applying threshold function is shown in Fig. 7. Packet area and area distribution of martensite are calculated using the same procedure used in the case of austenite.

6 Result and Discussions

First, experimentally determined average area and area distribution of austenite grains are compared with that of equivalent Voronoi diagram represented in Fig. 4b. The average area of austenite grains calculated from micrograph using the procedure

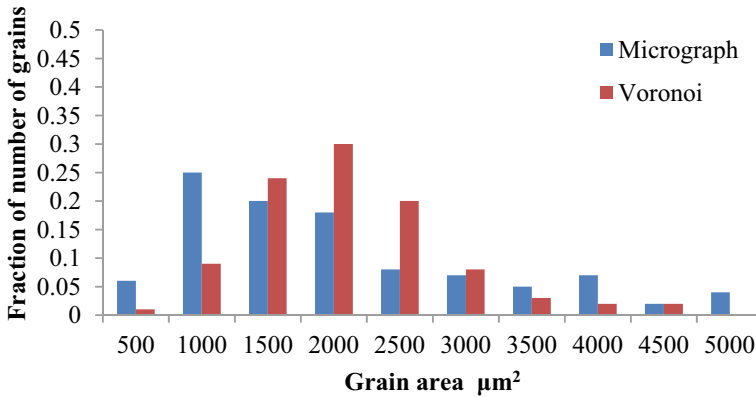


Fig. 8 Austenite grain area distribution

mentioned in previous section and area mathematically calculated from Voronoi diagram are same ($1811 \mu\text{m}^2$), because the number of austenite grains are equal. The area distribution in both cases is represented in Fig. 8. From the figure, it is clear that the area distribution is almost same in both cases. Most of the grains have area between 1000 and $3000 \mu\text{m}^2$.

For simulation, the inputs needed are initial grain map and number of martensite nuclei generated. The seeds of Voronoi equivalent of grain map, which is shown in Fig. 5b, are taken as one input, and the number of martensite nuclei evolved, which is calculated using the procedure explained in previous section, is taken as second input. The simulation result is shown in Fig. 9. The red portion indicates martensite and white corresponding to austenite phases.

Fraction of martensite phase evolved calculated from micrograph using threshold is 88.37% and from the simulated microstructure is 87.35% . The error percentage is 1.15% . Mean area occupied by martensite block determined experimentally is $465 \mu\text{m}^2$ and that determined through simulation is $453 \mu\text{m}^2$. The error percentage is

Fig. 9 Microstructure modeled using Voronoi algorithm

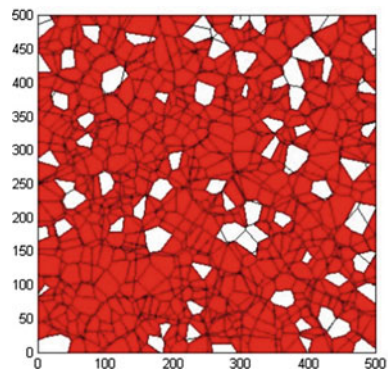
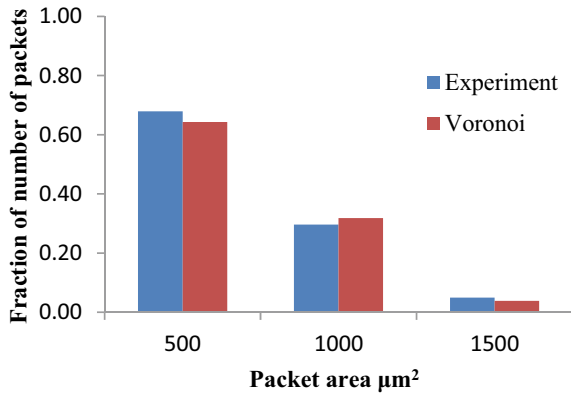


Fig. 10 Martensite Packet area distribution



2.61%. The area distribution of martensite packets in both cases are shown in Fig. 10. The distribution is almost similar in this case also.

7 Conclusion

The microstructure evolution during martensite transformation from complete austenite range is simulated using ordinary Voronoi diagram. The inputs for the simulation are austenite grain map and number of martensite nuclei generated during quenching. Austenite grain map is derived from experimentally obtained micrograph. The obtained grain map is converted into Voronoi diagram equivalent. The average austenite grain area, determined experimentally and calculated from Voronoi diagram, are seems to be similar. Grain area distribution also shows similar characteristics. Number of martensite nuclei generated is calculated from micrograph. Using these inputs, microstructure evolution during martensite transformation is predicted. Fraction of martensite evolved, average area of martensite packets and area distribution are compared with values obtained from experiment. In all cases, results show good agreement. Thus, ordinary Voronoi diagram can successfully used for representing micrograph and to predict microstructure evolution during quenching of C35 steel.

References

1. Bostanadad R, Zhang Y, Li X, Kearney T, Brinson C, Apley DW, Liu WK, Chen W (2018) Computational microstructure characterization and reconstruction: review of state of art techniques. *Prog Mater Sci* 95:1–41

2. Greene S, Liu Yu, Chen W, Liu W (2011) Computational uncertainty analysis in multiresolution materials via stochastic constitutive theory. *Comput Methods Appl Mech Eng* 200(1–4):309–325
3. Okabe A, Boots B, Sugihara K, Chiu SN (2000) Spatial tessellations concepts and applications of Voronoi diagram, 2nd edn. Wiley Publications
4. Burtseva L, Werner F, Salas BV, Pestryakov A, Romero R, Petranovskii V (2005) Modeling of material structure using Voronoi diagram and tessellation methods. *Appl Mech Mater* 756:426–435
5. Katani S, Ziaei-Rad S, Nouri N, Saeidi N, Kadkhodapour J, Torabian N, Schmauder S (2013) Microstructure modeling of dual phase steel using SEM micro graphs and Voronoi polycrystal model. *Metallogr Microstruct Anal* 2:156–169
6. Bertoneclj B, Vojisavljevic K, Rihtarsic J, Trefalt G, Huskic M, Zagar E, Malic B (2016) A Voronoi-diagram analysis of the microstructures in bulk-molding compounds and its correlation with the mechanical properties. *eXPRESS Polym Lett* 10(6):493–505
7. Braga FL (2018) 2D ceramic grains image manipulations: a simple geometrical characterization and grain domain recreation algorithm. *Appl Comput Inform* 14:159–165
8. Bertolino G, Bilger N, Crepin J (2007) Modeling microstructures and microstructural effects on macroscopic and intragranular mechanical behavior. *Comput Mater Sci* 40:408–416
9. Schneider Y, Weber U, Wasserbäch W et al (2020) A numerical method for the generation of hierarchical Poisson Voronoi microstructures applied in micromechanical finite element simulations—part I: method. *Comput Mech* 66:651–667
10. St-Pierre L, Heripre E, Dexet M, Crepin J, Bertolino G, Bilger N (2008) 3D simulations of microstructure and comparison with experimental microstructure coming from O.I.M. image. *Int J Plast* 24:1516–1532
11. Alsayednoor J, Harrison P (2016) Evaluating the performance of microstructure generation algorithms for 2-d foam like representative volume elements. *Mech Mater* 98:44–58
12. Gur CH, Pan J (2009) Thermal process modeling of steels. CRC Press
13. Kaufman L, Cohen M (1956) *Trans Am Inst Min Metall Eng* 206:1939
14. Olson GB, Cohen M (1976) General mechanism of martensite nucleation: part III. Kinetics of martensite nucleation. *Metall Trans A* 7:1897–1904
15. Fisher JC, Holloman JH, Turnbull D (1949) Kinetics of austenite-martensite transformations. *Metal Trans* 185:691–700
16. Zaho XQ, Han YF (1999) Kinetics of homogeneous martensitic nucleation in iron-based alloys. *Metall Mater Trans A* 30(3):884–886
17. Hsu TY, Chang H (1984) On the calculation of Ms and driving force for martensitic transformation in Fe-C. *Acta Metall* 32:343–348
18. Kitahara H, Ujei R, Tsuji N, Minamino Y (2006) Crystallographic features of lath martensite in low carbon steel. *Acta Mater* 54:1279–1288
19. Casero C, Siesma J, Santofimina MJ (2019) The role of austenite grain in martensitic transformation in low carbon steel. *Mater Des* 54(5):1279–1288
20. Jensen DJ (1992) Modelling of microstructure development during recrystallization. *Scr Metall* 27:1551–1556
21. Chen LQ (2002) Phase field models for microstructure evolution. *Annu Rev Mater Res* 32(1):113–140
22. Rollett AD, Manohar P (2004) Continuum scale simulation of engineering materials chapter. In: *The Monte Carlo method*. Wiley- VCH, pp 77–114
23. Rabbe D (2002) Cellular automata in material science with particular references to recrystallization simulation. *Annu Rev Mater Res* 32(1):53–76
24. Alavi P, Serajzadeh S (2020) Microstructural changes during static recrystallization of austenitic stainless steel 304L: cellular automata simulation. *Metallogr Microstruct Anal* 9:223–238
25. Jia C, Zheng C, Li D (2020) Cellular automaton modeling of austenite formation from ferrite plus pearlite microstructures during intercritical annealing of a C-Mn steel. *J Mater Sci Technol* 47:1–9

26. Carlsson J, Isaksson P (2020) A statistical geometry approach to length scales in phase field modelling of fracture and strength of porous microstructures. *Int J Solids Struct* 200–201:83–93
27. Esfahani AK, Babaei M, Sarrami-Foroushani S (2021) A numerical model coupling phase transformation to predict microstructure evolution and residual stress during quenching of 1045 steel. *Math Comput Simul* 179:1–22
28. Offerman SE, van Dijk NH, Sietsma J, Lauridsen EM, Margulies L, Grigull S, Poulsen HF, van der Zwagg S (2006) Phase transformations in steel studied by 3DXRD microscopy. *Nucl Instrum Methods Phys Res B* 246:194–200D
29. Bhadeshia HKDH, Interpretation of the microstructure of steels. http://www.phase-trans.msm.cam.ac.uk/2008/Steel_Microstructure/SM.html
30. Schindelin J, Arganda-Carreras I, Frise E et al (2012) Fiji: an open-source platform for biological-image analysis. *Nat Methods* 9(7):676–682. PMID 22743772. <https://doi.org/10.1038/nmeth.2019>
31. Legland D, Arganda-Carreras I, Andrey P (2016) *MorphoLibJ*: integrated library and plugins for mathematical morphology with ImageJ. *Bioinformatics* 32(22):3532–3534 (Oxford University Press). PMID 27412086. <https://doi.org/10.1093/bioinformatics/btw413>
32. Ikuma K (2020) Mask2poly(mask). MATLAB central file exchange. <https://www.mathworks.com/matlabcentral/fileexchange/45980-mask2poly-mask>
33. Polygon, MATLAB central file exchange. <https://www.mathworks.com/matlabcentral/fileexchange/70090-area-centroid-and-moment-of-inertia-of-a-polygon>

Development and Fabrication of Nylon 6 Standard and Asymmetric Spur Gear Using Injection Moulding



Mohit Jain, Santosh Patil, and S. S. Ghosh

Abstract In the present study, Nylon 6 standard and asymmetric spur gear manufacturing using injection moulding technique has been carried out. Development and fabrication challenges of these gears have been focused and discussed explicitly in this work. A separate die (core–cavity) is designed to fabricate standard and asymmetric Nylon 6 spur gear of specific dimension. The process of producing injection moulded gears is gone through several trials to achieve the required combination of operating parameters. These combinations of operating parameters are categorized into three groups such as process optimization, barrel temperature and ejector set-up. Finally, the essential operating parameters such as injection pressure, holding time, cycle time and barrel temperature are investigated and presented in this paper. Operating parameters are found similar with a little deviation in injection time of 02 s more in asymmetric gear in comparison with standard gear. Further, it can also be observed that the appropriate injection gate size opening helps the proper dispersion of the molten polymer into the gear cavity edges. A gate size opening of 0.18 mm² cross-sectional area is considered during development of die. It greatly affects the surface finish of the gear edges of the final component produced by this technique. A trough region of approximately 0.06 mm is also observed on lateral surface of finished gear tooth.

Keywords Injection moulding · Mould · Polymer · Nylon · Fabrication · Asymmetric spur gear

1 Introduction

In the past, metallic gears have been used widely as a machine component in various power and motion transmission systems. However, in low- and medium-torque transmission systems, polymer gears are now being preferable over metallic gears due to

M. Jain (✉) · S. Patil · S. S. Ghosh
Department of Mechanical Engineering, Manipal University Jaipur, Jaipur, Rajasthan 303007,
India
e-mail: mohit.jain@jaipur.manipal.edu

© The Author(s), under exclusive license to Springer Nature Singapore Pte Ltd. 2022
K. Govindan et al. (eds.), *Advances in Mechanical and Materials Technology*,
Lecture Notes in Mechanical Engineering,
https://doi.org/10.1007/978-981-16-2794-1_78

879

largely observed advantages such as reduced noise, costs and low weight to power consumption [1]. Performance characteristics such as bending fatigue, wear, contact stress, friction, vibration, noise, etc., are some of the domains of polymer gear which is being researched extensively by many researchers [2–7]. Polymer gears can be manufactured by conventional way of machining process, but it becomes difficult when tooth profile is non-standard involute, i.e. asymmetric, etc. Therefore, presently, recent unconventional techniques are preferred and are used very frequently, and injection moulding is one such unconventional technique which provides ease of processing and fabricating of any standard and modified polymer gears. Hence, injection moulding technique has vastly increased its usage in gear industry applications. Most of the researches have been extensively carried out on injection moulded polymer gears like Nylon, acetal, polypropylene (PP), polyoxymethylene (POM), etc. [8–17], compared to machined polymer gears [18–20]. Basic weakness of plastic spur gear teeth is tooth fracture brought on by the accumulation of stress at the root of the tooth. This problem can be solved by asymmetric gear. Gear forming injection moulding technology [21] is one of the most important methods for manufacturing of asymmetric gear. Injection moulded manufacturing technique is a method to obtain moulded product say polymer gear, by injecting molten polymer material into a mould and then cooling and solidifying them. Recent studies [22–25] on performance and operational characteristics of injection moulded polymer gears have been investigated for their errors and other manufacturing difficulties. Injection moulding process involves six steps such as clamping, injection, dwelling, cooling, mould opening and removal of products. During the process, various operating parameters like injection pressure, injection speed, holding pressure, barrel temperature, nozzle temperature, etc., are involved and required in proper combination to achieve finished polymer gear. A die is to be designed and fabricated as per the required gear dimension after consideration of shrinkage allowance of polymer material. It is observed that injection gate size opening plays an important role in filling up the cavities and corners of the mould. Mould gate is a gate way to enter molten material into the mould's cavity. If gate size is small, mould does not fill completely, and if too large then material may get accumulated or mould may become too hard to shear. Main objective of this work is to investigate the suitable combination of injection moulding parameters and appropriate dimension of gate size to overcome the manufacturing defects in production of injection moulded Nylon 6 spur gear.

2 Methodology

Nylon 6 spur gear fabricated in the present study is of two types: (i) standard involute and (ii) asymmetric profiled spur gear. Respective gear specifications and geometry are shown in Table 1 and Fig. 1. Methodology involves three stages: (i) gear material preparation, (ii) design and development of die and (iii) injection moulding operation.

Table 1 Gear specification and details

Standard gear	Asymmetric gear
Module (mm): 4.5	Module (mm): 4.5
Number of teeth: 18	Number of teeth: 18
Pitch circle diameter (mm): 81	Pitch circle diameter (mm): 81
Pressure angle (degree): 20	Pressure angle (degree): 20–34
Root fillet radius (mm): 1.71	Root fillet radius (mm): 1.71
Centre distance (mm): 90	Centre distance (mm): 90

2.1 Gear Material Preparation

Nylon 6 material is used to produce injection moulded standard and asymmetric spur gear. Generally, Nylons are noted for their strength, toughness and abrasion resistance. Granules of Nylon 6 as shown in Fig. 2 were procured from Ester Industries Limited (Uttarakhand, India). Since PA6 absorbs moisture readily [26], the granules were preheated at 80 °C for 6 h prior to injection moulding to remove moisture content [27] (Fig. 3).

2.2 Design and Development of Die

In injection moulding, die plays an important role in the process. Die is used to mould the melted material which takes shape of the dies after its solidification. In this work, a die for standard and asymmetric gear is modelled in Fusion 360 as shown in Fig. 4 as per the required gear dimension specified in Table 1. Die consists of two parts: (i) core and (ii) cavity. One core plate and two different cavity plates were designed for both standard and asymmetric gears. A complete die assembly and die parts are shown in Fig. 4a, b, respectively.

Injection gate opening from where the molten polymer would be assumed to flow into the cavity plate is also shown in Fig. 4c. After die designing, dies were fabricated and got mounted over the injection moulded machine as shown in Fig. 4d, e.

2.3 Injection Moulding Operation

The injection moulding operation has been carried out on ‘De-Tech85 LNC5’ machine at Central Institute of Plastics Engineering and Technology (CIPET), Jaipur, as shown in Fig. 3. The whole injection process comprises two units: (i) injection unit and (ii) clamping unit as shown in Fig. 5. Heating and injection of Nylon 6 into the mould take place in injection unit. Through an opening at the bottom of the hopper, material was fed into the barrel at a temperature of 118 °C. The material

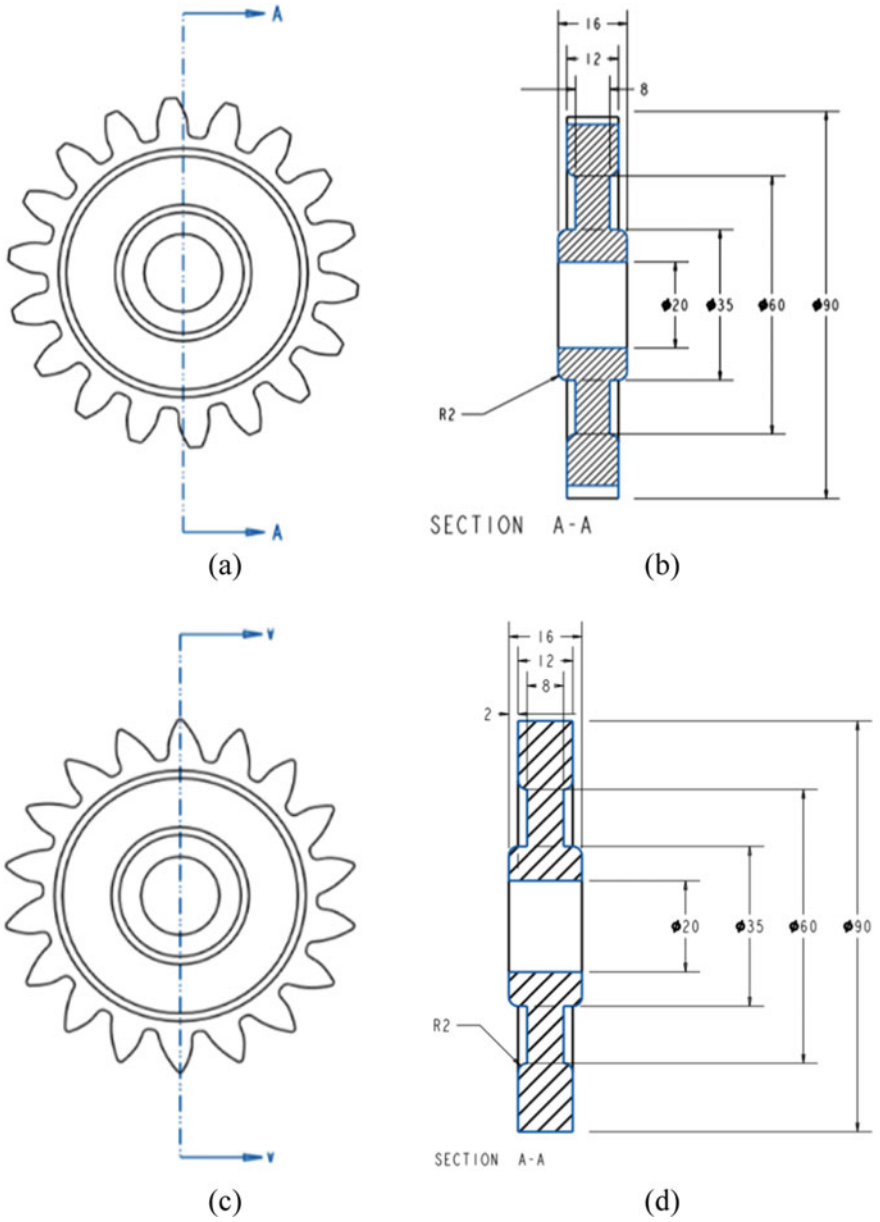


Fig. 1 Gear geometry: **a, b** front view and cross-sectional view of standard gear, respectively, **c, d** front view and cross-sectional view of asymmetric gear, respectively (all dimensions are in mm)

Fig. 2 Nylon 6 granules**Fig. 3** Injection moulded machine 'De-Tech85 LNC5' at CIPET, Jaipur

was melted by three consecutive heaters, viz. MH1, MH2 and MH3, at different temperatures and injected into the mould through nozzle at the end of the barrel. The screw is rotated to let the molten material to accumulate in front of the screw. And, once the required amount of molten plastic is accumulated, injection process started. Moving speed of the screw, i.e. injection speed, is controlled by machine during flowing of molten material into the mould. Initially, the barrel temperature and processing parameters such as temperature, injection pressure, injection speed and holding time were not correctly known. Therefore, several trials were conducted

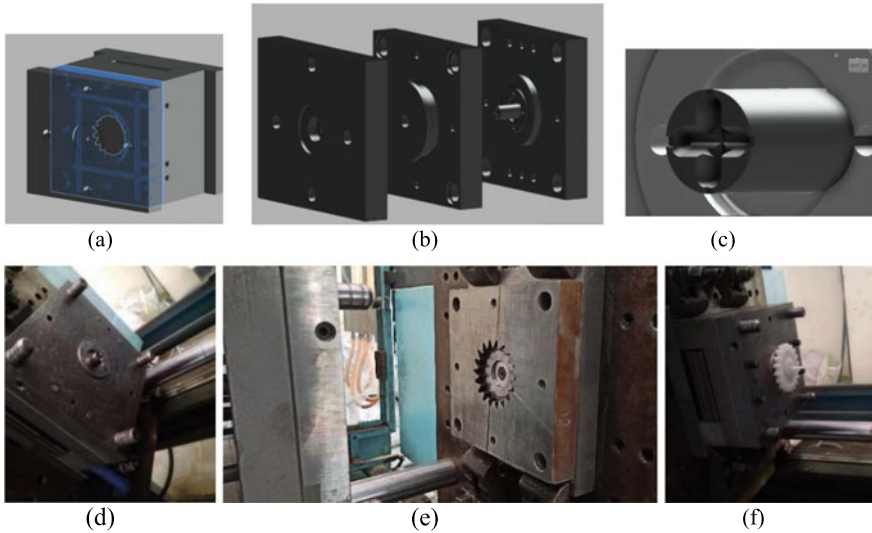


Fig. 4 Design and development of die: **a** CAD model of die assembly. **b** CAD model of die parts. **c** CAD model of gate opening of die. **d** Asymmetric gear core. **e** Asymmetric gear cavity. **f** Produced gear on die

to investigate the correct barrel temperature and processing parameters. Trials were repeated to narrow down the optimal temperature and other parameters, to achieve the final finished gear component. However, the material was injected at a pressure of 85 bar with a holding time of 04 s. After the required cooling time of 95 s, the melted Nylon 6 took the shape of desired gear as shown in Fig. 4f and then was opened by hydraulically powered clamping motor. Ejector bar pushed out the solidified gear out of the open cavity. Silicon spray was done over cavity surface before injecting molten material to avoid any clinging of material over die surface.

3 Results and Discussion

During injection moulding process, melted Nylon 6 entered the injection unit. It was heated using three consecutive heaters and injected at certain pressure. As mentioned above in methodology, the temperature of heaters and operating parameters were not known. Hence, at the start based on initially knowledge trials were made and the temperature of heaters and nozzle were set to 230, 250, 260 and 270 °C. Also, injection pressure and holding pressure were kept at 110 bar and 75 bar, respectively. Figure 6a, b shows the prefinished state of standard gear. Further, a distorted gear was obtained with deformed tooth shape as observed in Fig. 6c, e. It is due to the reason that material could not have reached at the tip of the tooth and not solidify properly.

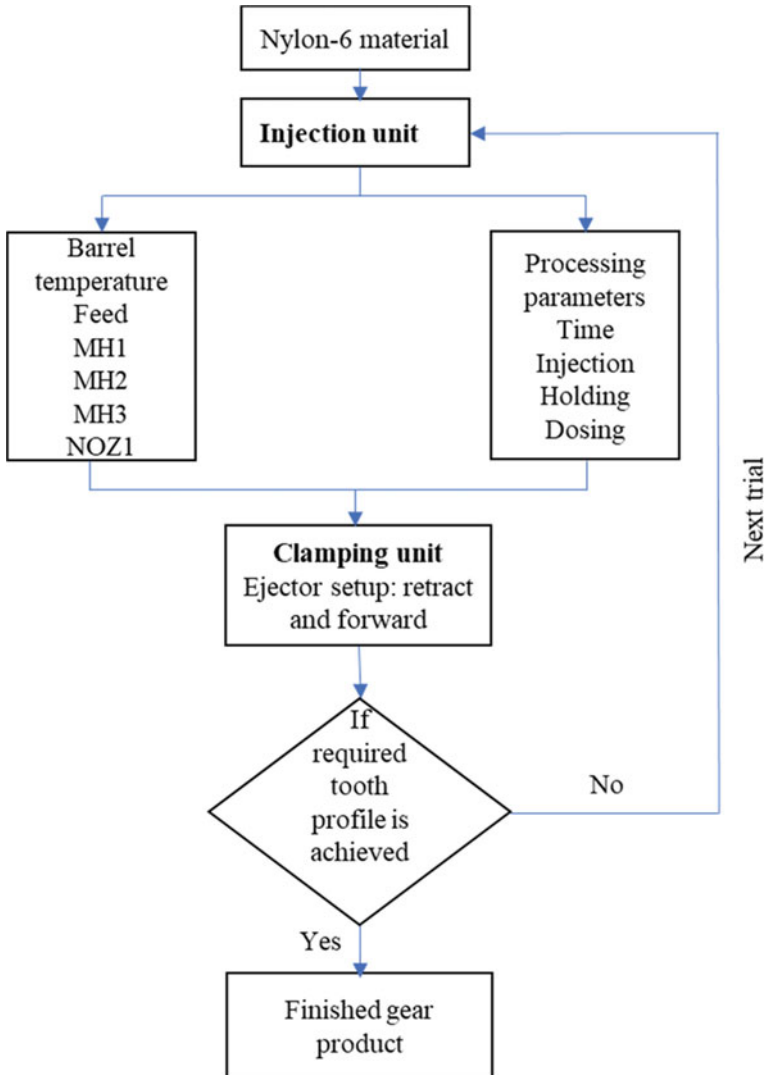


Fig.5 Injection moulding operation flow chart

Hence, it was required to conduct more such trials by varying barrel temperatures and operating parameters. Therefore, the temperature and operating parameter like pressure were varied down with a unit of 5 °C and 5 bar, respectively, with several combinations. And each time, the better gear mould was obtained compared to previous one as observed in Fig. 6.

In Fig. 6f, tooth shape was comparatively found better than previous one in Fig. 6c, but material accumulates unevenly over tooth and gear surface. This is due to the

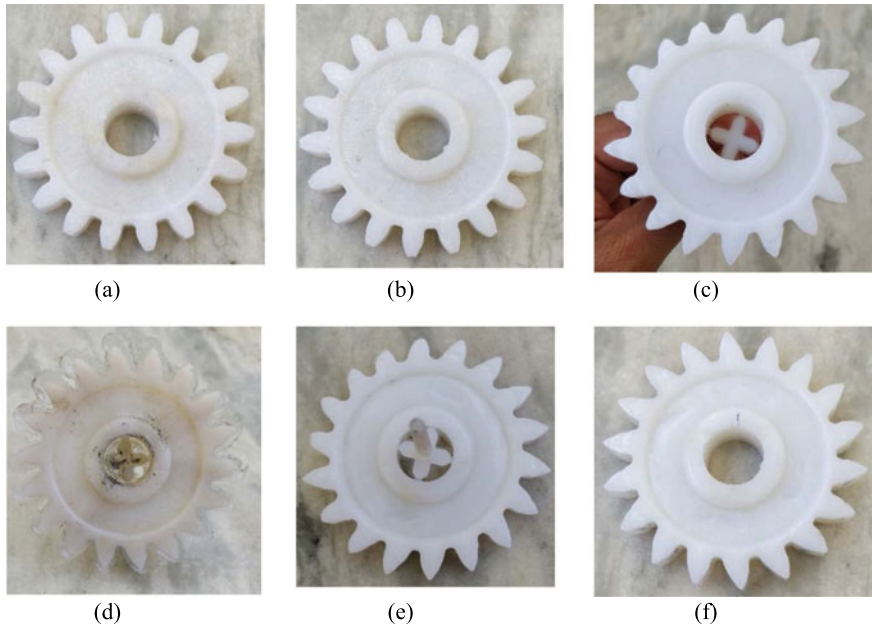


Fig. 6 Development and fabrication of injection moulded standard and asymmetric spur gear gone through several trials

fact that injection gate opening size was not big enough, and therefore, the material cannot reach evenly inside the cavity. Therefore, the gate size was slightly increased by increasing the width and depth by 0.5 mm. The cross-sectional area of 0.18 mm² of gate size was kept finally. It was kept same for both standard and asymmetric gear tooth profiles. The increase in gate size maintained the flow and quantity of molten material. Gate design has been shown in Fig. 4c. However, due to overvaluation of operating parameter like injection pressure, holding time, etc., a thin polymer layer is developed at the back of gear surface as shown in Fig. 6d. Hence, it was necessary to find the correct values of those parameters as well.

After several trials, a right combination of all parameters has been investigated and recorded as shown in Table 2 to produce finished gears as shown in Fig. 7a, b. Finished gears were produced at an injection pressure of 85 bar with holding time and cooling time of 04 s and 95 s, respectively, as shown in Table 2. However, the injection time for asymmetric gear was found 02 s more than standard gear, because of the curved asymmetric tooth profile. Senthilvelan et al. [10] produced injection moulded reinforced and unreinforced Nylon 66 spur gear at an injection pressure of 125 MPa with a holding time of 02 s and cooling time of 20 s.

Reinforced Nylon is comparatively harder and stronger than pristine Nylon; hence, it yields comparatively more injection pressure. The temperatures of 215.9 °C, 230 °C and 241.5 °C have been observed of three consecutive heaters inside barrel for both symmetric and asymmetric gears. The temperature of 118.3 °C at feed and 236.6 °C

Table 2 Injection moulding operation parameters

Process optimization												
	Set	Act	Injection	Set	Holding	Set	Act	Dosing	Set	Act	Switch over criteria	Act
Cycle monitor (s)	150	87.6	Pressure (bar)	85	Time (s)	4	-	Dosing time (s)	-	6.3	Stroke (mm)	81
Cooling (s)	95	81.8	Speed (mm/s)	35	Pressure (bar)	65	59	Dosing stop (mm)	71	71	Pressure (bar)	21
					Speed (mm/s)	35	-	Screw retract (mm)	77	81		
Barrel temperature												
	Set											
Feed (°C)	Act											
MH1 (°C)	100											
MH2 (°C)	215											
MH3 (°C)	230											
NOZ1 (°C)	240											
Oil prewarming (°C)	240											
Ejector set-up	40											
Retract												
Pressure (bar)	Forward											
	30											
Time (s)	20											
	0.6											
	0.44											

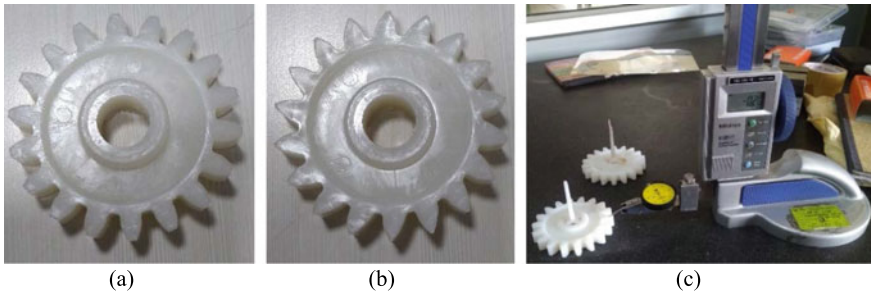


Fig. 7 Finished gears: **a** standard gear. **b** Asymmetric gear. **c** Measurements of lateral surface of gear on height gauge

at nozzle is recorded. Similar heater temperatures were found in Sardar et al. [28], who developed and fabricated injection moulded composite polypropylene spur gear and kept heaters at temperatures of 220, 225 and 230 °C. Other works [29–31] which show relevant barrel temperatures range from 200 to 300 °C for polymer gears were also observed.

As it can be observed from Fig. 7a, b, the gear tooth profile and surface finish have been checked and found good on areas such as flanks, hub and other edges. But still, the trough of 0.06 mm was observed over the lateral surface of gear measured by height gauge as shown in Fig. 7c. Since the die was designed as per the shrinkage allowance, this trough region was inevitable. However, it does not directly affect the performance of gears; nevertheless, this error needs to be considered during further testing of gears.

4 Conclusions

Production of injection moulded standard and asymmetric Nylon 6 spur gears was carried out for a various testing. Various challenges during injection process were handled and come up with following conclusions:

1. The polymer material Nylon 6 was fed at a temperature of 118.3 °C, and temperature of three consecutive heaters was kept at 215.9, 230 and 241.5 °C. And nozzle temperature was kept at 236.6 °C.
2. During injection process, pressure is maintained at 85 bar with injection speed of 35 mm/s. Holding pressure is recorded 59.3 bar with holding time of 04 s. Cooling time of 95 s is recorded.
3. Die has been developed and fabricated considering the shrinkage allowance of Nylon 6 material with a cross-sectional area of 0.18 mm² of gate size to obtain a finished tooth profile of standard and asymmetric gear.

4. For well-finished standard and asymmetric gear tooth profile, injection moulding operation parameters are found similar with a little deviation in injection time of 0.2 s more in asymmetric gear in comparison with standard gear.
5. A trough region of approximately 0.06 mm is observed on lateral surface of finished gear tooth. It occurs because of shrinkage property of polymer material, even after consideration of shrinkage allowance.

Acknowledgements The authors gratefully acknowledge the financial support provided by Manipal University Jaipur (MUJ) through the scheme Endowment Seed Grant 'EF/2017-18/QE04-08'.

References

1. Walton D, Shi YW (1989) A comparison of ratings for plastic gears. *J Mech Eng Sci* 203(4):31–38
2. Li W, Wood A, Weidig R, Mao K (2011) An investigation on the wear behaviour of dissimilar polymer gear engagements. *Wear* 271(9–10):2176–2183
3. Mao K, Li W, Hooke CJ, Walton D (2009) Friction and wear behaviour of acetal and nylon gears. *Wear* 267(1):639–645
4. Mertens AJ, Senthilvelan S (2016) Durability of injection moulded asymmetric involute polymer spur gears. *Int J Powertrains* 5(3):264–280
5. Ghosh SS, Chakraborty G (2016) On optimal tooth profile modification for reduction of vibration and noise in spur gear pairs. *Mech Mach Theory* 105:145–163
6. Maper A, Karuppanan S, Patil SS (2019) Analysis and formulation of spur gear stresses with different tip modifications. *J Cent South Univ* 26(9):2368–2378
7. Patil SS, Karuppanan S (2020) Evaluation of the effect of friction in gear contact stresses. *Tribol Mater Appl* 227–242
8. Breeds AR, Kukureka SN, Mao K, Walton D, Hooke CJ (1993) Wear behaviour of acetal gear pairs. *Wear* 166:85–91
9. Senthilvelan S, Gnanamoorthy R (2004) Damage mechanisms in injection molded unreinforced, glass and carbon reinforced nylon 66 spur gears. *Appl Compos Mater* 11(6):377–397
10. Senthilvelan S, Gnanamoorthy R (2006) Selective carbon fiber reinforced nylon 66 spur gears: Development and performance. *Appl Compos Mater* 13(1):43–56
11. Gurunathan C, Kirupasankar S, Gnanamoorthy R (2011) Wear characteristics of polyamide nanocomposite spur gears. *Proc Inst Mech Eng Part J J Eng Tribol* 225(5):299–306
12. Duhovnik J, Zorko D, Sedej L (2016) The effect of the teeth profile shape on polymer gear pair properties. *Tech Gaz* 23(1):199–207
13. Mertens AJ, Senthilvelan S (2016) Durability of polymer gear-paired with steel gear manufactured by wire cut electric discharge machining and hobbing. *Int J Precis Eng Manuf* 17(2):181–188
14. Jain M, Patil S, Ghosh SS (2016) A review on failure characteristics of polymer gear. In: ICAMEN 2019, vol 90
15. Roda-Casanova V, Sanchez-Marin F (2019) A 2D finite element based approach to predict the temperature field in polymer spur gear transmissions. *Mech Mach Theory* 133:195–210
16. Zorko D, Kulovec S, Duhovnik J, Tavčar J (2019) Durability and design parameters of a Steel/PEEK gear pair. *Mech Mach Theory* 140:825–846
17. Zhang Y, Mao K, Leigh S, Shah A, Chao Z, Ma G (2020) A parametric study of 3D printed polymer gears. *Int J Adv Manuf Technol* 107(11–12):4481–4492

18. Imrek H (2009) Performance improvement method for nylon 6 spur gears. *Tribol Int* 42(3):503–510
19. Kim CH (2006) Durability improvement method for plastic spur gears. *Tribol Int* 39(11):1454–1461
20. Dighe AD, Mishra AK, Wakchaure VD (2014) Investigation of wear resistance and torque transmission capacity of glass filled polyamide and Peek composite spur gears. *Int J Eng Adv Technol* 3(3):299–303
21. Kapelevich AL, Shekhtman YV (2010) Fabrication of directly designed gears with symmetric and asymmetric teeth. *Gear Technol* 86–91
22. Singh PK, Siddhartha, Singh AK (2017) An investigation on the effects of the various techniques over the performance and durability of polymer gears. *Mater Today Proc* 4(2):1606–1614
23. Singh AK, Siddhartha (2018) Noise emission from functionally graded materials based polypropylene spur gears—a tribological investigation. *Mater Today Proc* 5(2):8199–8205
24. Singh AK, Siddhartha, Singh PK (2018) Noise emission from ABS, POM and HDPE spur gears—a comparative study. *Mater Today Proc* 5(9):18038–18044
25. Schubert D, Hertle S, Drummer D (2019) Influence of titanium oxide-based colourants on the morphological and tribomechanical properties of injection-moulded polyoxymethylene spur gears. *J Polym Eng* 39(8):774–783
26. Targett J, Nightingale JE (1970) Paper 23: thermoplastic gears. *Proc Inst Mech Eng Conf Proc* 184:184–226
27. Senthilvelan S, Gnanamoorthy R (2007) Effect of rotational speed on the performance of unreinforced and glass fiber reinforced nylon 6 spur gears. *Mater Des* 28(3):765–772
28. Sardar J, Bandopadhyaya D (2014) Development and fabrication of cement reinforced polypropylene composite material spur gear. *J Polym Eng* 34(8):775–786
29. Singh AK, Siddhartha (2018) Thermal and wear behavior of glass fiber-filled functionally graded material-based polyamide 66 spur gears manufactured by a novel technique. *J Tribol* 140(2):1–16
30. Ramanjaneyulu S, Suman KNS, Phani Kumar S, Suresh Babu V (2017) Design and development of graphene reinforced acetal copolymer plastic gears and its performance evaluation. *Mater Today Proc* 4(8):8678–8687
31. Kodeeswaran M, Suresh R, Senthilvelan S (2019) Effect of strain rate on bending and transmission characteristics of injection molded polyamide 66 spur gears. *Proc Inst Mech Eng Part L J Mater Des Appl* 233(6):1145–1155

Investigates the Impact of Insulation Material on the Building Performance in Different Weather Zones of India



Shaheen Hasan, Sabah Khan, and Saif Uddin

Abstract India is a developing country with a continuous rise in almost all energy-related sectors like construction, industrialization, agriculture, etc. However, like the whole world, India too is facing an acute energy crisis due to its fast-depleting energy resources. In the urban part of the country, the energy consumption by the residential building sector becomes very important since this energy consumption uses an ample amount of the total delivered energy consumption for the country. There are two approaches to reduce the building energy one is active and the other one is passive methodology. In this work, the focus is on passive technology by using the optimum insulation thickness technique to reduce energy consumption. This manual calculation is based on using five different fuels (Coal, Oil, LPG, Natural gas, and water) in the different climatic zones in different geographical regions of India. In this method, five different insulation materials (EPS, XPS, PUF, GW, and RW) will be used. The technology involves applying different insulation materials under different weather conditions to obtain different insulation thickness.

Keywords Extended polystyrene (EPS) · Extruded polystyrene (XPS) · Polyurethane foam (PUF) · Glass wool (GW) · Rockwool (RW) · Liquid petroleum gas (LPG)

S. Hasan (✉) · S. Khan

Department of Mechanical Engineering, Jamia Millia Islamia, New Delhi 110025, India

S. Khan

e-mail: skhan2@jmi.ac.in

S. Uddin

Global Evolutionary Energy Design, New Delhi 110025, India

e-mail: saif@geedindia.org

1 Introduction

The Indian energy sector consumes a large amount of thermal fuel, for example, coal, oil, and gas, which emit a massive amount of harmful gases that are injurious to the environment as well as human health. Energy is a very crucial element for developing any nation [1], thus making an energy-saving concept mandatory or necessary for any nation. As a consequence, energy saving is an essential factor for development. The Indian economy in recent times is undergoing a crisis due to the large population, unemployment, corruption, and now the pandemic COVID 19. According to EIA's international energy reports 2017 explained that the rapid growth of building energy consumption in India, and it is expected it will have been grown fastest among all the countries since 2040. IEO2017, reports also explained that residential and commercial building has also increased their energy consumption around 2.7% per year in the duration of 2015–2040, which is almost double the global average consumption around the world [2]. As per the recent scenario of energy consumption in the building, building envelope plays an important role to affect the thermal comfort inside the building and reduction of energy consumption. After applying insulation layers into the building wall, it controls the transient heat conduction through the walls and provides almost a constant temperature inside wall zones. Before insulation application, intense heat conduction takes place which increases the heat temperature inside wall zones and vice versa in summer and winter duration. So after reviewing a lot of research work authors conclude that building insulation materials have the potential of saving of energy on a large scale and provide suitable human thermal comfort inside the building zones [3, 4]. Insulation thickness in a building is a vital parameter in the design of exterior wall [3, 5] since low insulation thickness easily allows heat transfer from the inside to the outside or from the outside to the inside, resulting in a negative effect on thermal comfort and energy savings. On the other hand, increasing the insulation thickness reduces heat loss and the subsequent heating load and fuel cost. However, an increase in insulation thickness results in an increase in insulation investment costs also. India has diverse weather conditions, so the selection of correct insulation material is a challenging task. The aim of this study is the selection of the insulant material, applying the selected optimum material up-to-the correct level, and analyzing its cost for five different fuels. The different types of insulation materials chosen are expanded polystyrene foam (EPS), extruded polystyrene foam (XPS), polyurethane foam (PUF), glass wool (GW), and rock wool (RW) [6–8]. The EPS and XPS insulation in building construction provides high flexibility, compatibility, and thermal efficiency for use in all areas of a building envelope.

Insulation materials have been made an important part in building construction industry because of major benefits; they also contribute in saving and protect environment condition. Nowadays, biodegradable insulation material also available to replace non-biodegradable material, and they also contribute same benefit; apart from this, they protect environment and reach to sustainable production goal. But they may be less economical to owner in starting phase but they are beneficial in long term.

In this work, the heating degree day (HDD) and cooling degree day (CDD) methods are used for the building to find the required energy load for a particular facility. Degree days can be calculated by three different methods, i.e.,

- (1) Averaging Method
- (2) Baskerville-Emin (BE) Method
- (3) Electronic Real-time Data Collection.

All these procedures acquired a minimum-based temperature which is a reference temperature, above and below this temperature either required load for heating and cooling purpose. Bhatnagar and Mathur have been found in their study that for the cooling purpose, base temperature may be varied from 6.8 °C to 28.6 °C for the large building and 8.7–28.1 °C for office purpose, while the heating purpose base temperature may be varied 13.8 °C to 21.4 °C for the large building and 10.4–18.7 °C, respectively, for different location of India. For removing complication in research work, mostly preferred-based temperature is 18 °C for India. This work is done by considering India's base temperature as 18 °C for both heating and cooling [5].

2 Methodology

2.1 Structure of the Wall

In the building structure, mainly heat exchange takes place either inside to outside or vice versa through the walls, doors, cavities, windows and the roofs, etc. The building structure comprises both opaque and transparent portions of the walls and the roof which are connected to both the floor and the external environment. In this work, only wall portions are considered to reduce the effect of the outside environment in the building zones. These may be single or multi-layer and represent the partition between the external and internal environment. The average method is used to calculate heating and cooling degree day is defined in Eqs. 1 and 2. The building construction, composition is as 13 mm cement, 200 mm burnt brick, 15 mm thick cement plaster, and insulating material. In this analysis, an important assumption is that all heat transactions occur through walls only.

$$\text{HDD} = \left(T_b - \frac{T_{\max} + T_{\min}}{2} \right)^+ \quad (1)$$

$$\text{CDD} = \left(\frac{T_{\max} + T_{\min}}{2} - T_b \right)^+ \quad (2)$$

T_{\max} and T_{\min} are daily maximum and minimum temperature.

T_b is base temperature, which is 18 °C for India.

The general building specifications are described in Table 1, and these values are taken according to ECBC 2007 (Energy conservation building code).

The thermal conductivity and insulation cost are two main parameters that should be considered to select the insulation material. Tables 2 and 3 describe the selected fuel and insulation material properties and their price (Indian market). Figure 1 explains the details of the internal structure of the building.

Table 1 Building specifications

Material	Unit	Values
Planum	(W/m ² -K)	0.4
Envelope	(W/m ² -K)	0.7
Floor	(W/m ² -K)	2
Glazing	W/m ² -K	1.2
Glass visible transmittance		0.301
Glass solar heat gain coeff.		0.31
WWR		28
Lighting power density	W/m ²	Corridor 5.3820 Space 18.29 Stair 6.45 Visiting 13.99 Lift 6.45 Toilet 9.68 Reception lobby: 14

Table 2 Selected insulation material characteristics [9]

Insulation	ρ (kg/m ³)	Thermal conductivity k (W/mk)	Embodied energy kWh/m	Cost in Rs./m ³
EPS	25	0.04	1125	2400
XPS	30	0.0321	1125	11,500
PUF	36	0.0372	1125	10,000
GW	16	0.035	–	4279
RW	150	0.045	–	3500

Table 3 Fuels heating values, prices, and efficiencies [3]

Fuels	Hu	η	Cost in Rs.
Natural gas	34.5 M J/m ³	0.9	0.4/kg
Coal	25 M J/kg	0.7	25/kg
Fuel oil	40 M J/kg	0.80	4/m ³
LPG	46 M J/kg	0.89	40/kg
Hydro	36 MJ/kWh	0.99	8/kWh

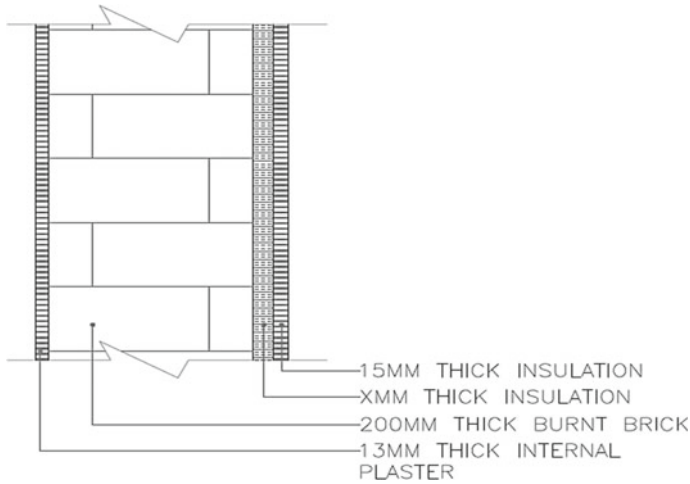


Fig. 1 Building wall internal structure

2.2 Energy Consumption Calculation

Heat flux calculate by using Eq. (3) for an external wall

$$q = U \cdot \Delta t \tag{3}$$

U = heat transfer coefficient, Δt = temperature difference between inside and ambient temperature.

The energy expenditure through heating and cooling of the building is calculated by using Eqs. (4) and (5) for the whole year.

$$Q_{\text{year}, H} = 86,400 \times \text{HDD} \times U \tag{4}$$

$$Q_{\text{year}, C} = 86,400 \times \text{CDD} \times U \tag{5}$$

The overall heat transfer coefficient for the building calculate by using Eq. (6)

$$U = \frac{1}{R_i + R_{\text{ins}} + R_o + R_w} \tag{6}$$

where R_i and R_o are the building inside and outside zone resistance to heat flow, R_w is the wall resistance without applying insulation and R_{ins} is the insulant resistant, and R -value is measured in ($\text{m}^2\text{K}/\text{W}$).

The building design criteria are set up by the material, and material is govern by either thermal conductivity or R -value, as per ECBC-2007 guideline book. The ability of material is defined through how much heat is resist by the material during

heat transient through it [10].

$$R_{\text{ins}} = \frac{x}{k} \quad (7)$$

where x and k are the insulant thickness (mm) and thermal conductivity (W/mK), respectively.

Over the years, researchers are trying to adjust the R -values according to outside weather condition throughout the year. However, it may happen that after increasing R -value may decrease energy load of the building. But due to this increasing embodied energy of the material and decreasing operational cost, thus it may become unproductive [10].

2.3 Determine Optimum Insulation Material Thickness

After applying the insulation material, heat consumption in the building was significantly reduced. The cost analysis is also necessary to calculate the worth level of selected insulant material. After applying insulation material into the wall, it only reduces heat transition, but does not terminate it completely. As continuous increasing building insulation thickness, increasing insulation material and installation cost correspondingly. But after reaching a certain point if these are drawn on graph, curve will have become asymptotic curve. So it is necessary to calculate an average cost of all input variable and find out an optimum insulation thickness cost, which is suitable for both purpose, i.e., optimum for energy saving and for building owner. Reduction of building load is directly influence the environment condition.

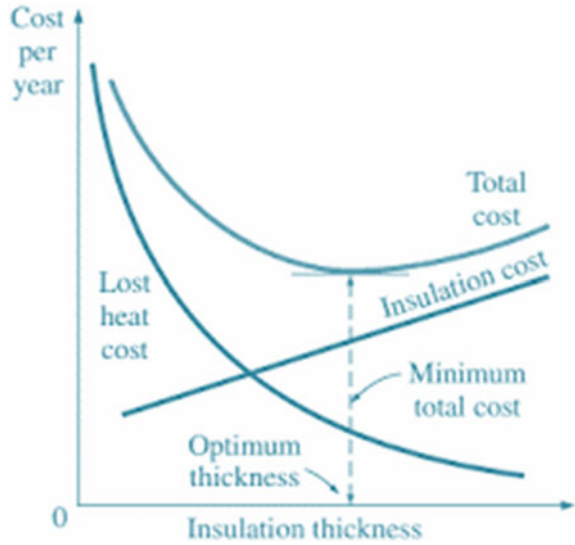
The determination of the optimum thickness of insulation is shown in Fig. 2 [11]. This point where the graph goes down is known as the critical point, and the corresponding thickness is called the critical thickness or optimum thickness. It can be seen that the cost of insulation increases linearly with its thickness, while the cost of heat loss decreases exponentially.

The prominent factor in the application of a thermal insulation system is to analyze the thermal insulation with respect to its cost. Many economical methods are available to optimize the thermal insulation thickness of external walls, out of which the life cycle cost (LCC) analysis is very simple and easy method that's why authors opted this method (5). Thus, LCC is chosen to find the cost. The annual energy cost for unit surface (C_A, H) and (C_A, C) is calculated by using the following Eqs. (8) and (9):

$$C_A, H = \frac{86,400 * HDD * C_{\text{fuel}}}{(R_{\text{wt}} + R_{\text{ins}}) * Hu * \eta} \quad (8)$$

$$C_A, C = \frac{86,400 * CDD * Ce}{(R_{\text{wt}} + R_{\text{ins}}) * COP} \quad (9)$$

Fig. 2 Computation of the optimum thickness of insulation [11]



C_{fuel} is the fuel price, H_u is fuel lower heating value, and η is the efficiency of the fuel operating system. C_e is electricity cost. R_{ins} is the insulant resistant, and R-value is measured in (m^2K/W) from Eq. (7).

Here we have used the life cycle cost methodology to calculate the optimum insulation thickness [5, 12, 13]. Yearly energy cost can be calculated by using present worth (PW) factor, and PW depends on inflation and interest rate as shown in Eqs. (10) and (11). The following parameters values such as $PW = 9.05$, the interest rate $i = 8\%$, inflation rate $g = 7.5\%$, and life span $N = 10$, were selected from the literature review [13–16].

If $i > g$

$$r = \frac{i - g}{i + g} \tag{10}$$

$$PW = \frac{(1 + N)^N - 1}{r * (1 + r)^N} \tag{11}$$

where $N =$ life time span of the building.

Optimum insulation thickness of the building is calculated by using this Eq. (12) [14].

$$X_{opt,H,C} = 293.94 * \left(\frac{HDD * C_{fuel} * PWF * k}{H_u * C_y * \eta} + \frac{CDD * C_e * PWF * k}{C_y * COP} \right)^{0.5} - k * R_{w,t} \tag{12}$$

where

C_y = insulation material cost.

$R_{w,t}$ = insulation thermal resistance with wall and insulation material.

3 Results and Discussion

The increasing insulation thickness raises the initial construction cost of the building and, at the same time, decreases the operating cost. In the present research, the HDD technique was employed to determine the optimum insulation thickness for application to the outer walls by carrying out calculations using different relations. Indian weather has variation, so the prediction of one insulation material is impossible. Each region has shown different results with the five chosen insulating materials. However, the type of fuel does not indicate many variations for each climatic zone and insulating material. Ahmedabad and Amritsar have a hot semi-arid climate. The calculations indicate that the type of fuel does not affect the thickness parameter of each wall material. The minimum thickness is about 55.3 for Ahmedabad and 45.2 for Amritsar for XPS insulating material. Bangalore, Bhopal, and Akola have tropical climate and here too the minimum thickness was observed for XPS for all the five fuels. Prayagraj has humid sub-tropical, and XPS gives the minimum thickness here too. Barmer is tropical sub-tropical desert climate, and XPS thickness was observed to be minimum in this climatic zone too. Bhuj has arid desert hot climate, and all materials indicated variation with the type of fuel, but average XPS thickness was observed to be minimum here too. The insulation thickness for different regions for the five materials is given in Table 4.

After getting results, can say that XPS material is also optimum insulation material in most of the cities but can't say directly that it works same for all cities. And reason behind it has closed cell structure and show better mechanical performance, with a good density, range lies in between 25 and 50 kg/m³ and has suitable thermal conductivity which provide good efficiency in different weather conditions. Raw material for XPS is same as EPS that's why crude oil is present at its basis.

Since thermal insulation of buildings depends on the low thermal conductivity of the insulating materials, gases are preferred as they display poor thermal conduction in comparison to liquids and solids. Air and gases also used as insulation within the wall or in the window, in the absence of convection heat transfer.

Therefore, several insulating materials (e.g., polystyrene) function simply contains lots of gas-filled packet which help in reducing convection through it. After adding gas pocket in alternation manner and solid material required that heat should be transferred through a number of interfaces causing rapid decrease in heat transfer coefficient. Air and gases exhibit negligible convection. Thus, XPS functions simply by having a large number of gas-filled pockets prevent large-scale convection [15]. Nonmetals, such as glass, ceramics and polymers, etc., shows low thermal conductivity since they have less number of free electrons and phonons which actually responsible for thermal heat conduction, also good insulation material. But,

Table 4 Insulation material thickness for different materials for different climatic zones

City	Fuels	HDD	CDD	EPS	XPS	GW	RW	PUF
Ahmedabad	Coal	150	3588	68.3	55.3	99.2	124.3	66.6
	Oil			68.4	55.4	99.4	124.4	64.1
	Gas			68.3	55.3	99.3	124.3	64
	LPG			68.4	55.7	99.4	124.4	64.1
	Hydro			68.6	55.5	99.5	124.1	64.3
Akola	Coal	400	3450	8.41	7.05	16	20	8
	Oil			86	69.5	123	156.2	80.1
	Gas			30	25	46	57.6	28.2
	LPG			98	80	140.4	175.8	92
	Hydro			152	123.4	215.2	270	142.2
Prayagraj	Coal	0	2938	62.4	59	91.03	114	57
	Oil			64.14	52.3	94	117	63
	Gas			62	51	90.48	113.3	58.1
	LPG			65	52.8	95	118.3	61
	Hydro			69	56.1	100	125.3	64.54
Amritsar	Coal	49	2378	54.2	44.2	79.8	98	51
	Oil			62	50.4	90.3	113	57.98
	Gas			55.04	45.2	81.35	101.8	51.2
	LPG			64	52	93.2	117	59.9
	Hydro			74.8	61	108.4	135.6	70.12
Aurangabad	Coal	0	2830	6.8	5.8	14	17.3	6.5
	Oil			79.6	62.4	110.8	138.7	72
	Gas			26.4	22	41.1	51.3	25
	LPG			88	71.5	126.5	158.4	82.35
	Hydro			136.5	111	194.3	243.3	128
Barmer	Coal	57	3540	68	55.3	98.6	123.5	65.6
	Oil			68.6	55.9	99.8	124.95	64.4
	Gas			68	55.4	98.8	123.7	63.7
	LPG			68.9	56.14	100.2	125.4	64.5
	Hydro			70.3	57.3	102.1	127.8	66
Belgaum	Coal	0	2340	5.1	4.2	11	14.2	4.9
	Oil			67.2	55.7	98.7	121.6	63.7
	Gas			21.2	18.5	38.9	45.5	21.5
	LPG			78	63.5	112.5	142.5	76.5
	Hydro			121.5	98.9	112.8	218.5	113.4
Bengaluru	Coal	0	2345	5.5	4.6	12.5	15	5.2

(continued)

Table 4 (continued)

City	Fuels	HDD	CDD	EPS	XPS	GW	RW	PUF
	Oil			69	56.2	100.3	125.5	64.7
	Gas			23.3	19.1	40	46	22
	LPG			79.3	64.5	114.5	143.4	79
	Hydro			123.7	100.6	176.2	221	115.6
Bhagalpur	Coal	10	3249	8	6.64	15.4	19.2	7.5
	Oil			82.7	67.3	119.2	149.3	77.45
	Gas			29	53.8	44.5	55.6	27
	LPG			95	77.06	135.9	170.3	88.75
	Hydro			147	119.4	208.5	261.2	137.7
Bhopal	Coal	20	2489	60.1	49	88	110	56.2
	Oil			60.99	49.63	89	111.4	57
	Gas			60.4	50	88	110.34	57.3
	LPG			61.3	49.78	89.2	111.85	57.4
	Hydro			62.8	51.23	89.5	112	58.9
Bhubaneshwar	Coal	0	3386	8.5	8	16.24	20.15	8
	Oil			85.96	70	123.8	157.96	80.5
	Gas			29.4	24.7	46.4	57.9	28.3
	LPG			98.5	80.06	143.2	176.7	92.2
	Hydro			152.6	123.9	216.3	270.9	142.89
Bhuj	Coal	21	3459	8.43	7	16	20	7.5
	Oil			85.1	69.5	122.5	158	79.5
	Gas			28.7	24	45.9	58	28
	L LPG			97.5	79.8	142.5	175.8	91.5
	Hydro			152	122.5	216	269.4	142
Bikaner	Coal	240	3300	65.3	53.2	95.2	119	61.2
	Oil			69.3	56.4	100.6	125.9	65
	Gas			65.9	53.7	95.9	120	61.7
	LPG			70.4	57.3	102.14	128	65
	Hydro			76.5	62	111	138.5	71.6

these materials have low strength or brittleness nature, which used only for selective purpose [16].

Thus, due to low thermal conductivity, XPS is suitable in all climatic zones. Thermal conductivity is crucial when considering XPS foams applied as insulation panels in buildings and construction [17].

4 Conclusion

The objective of this paper is to determine the optimum thickness of a building wall by using various fuels for different climatic zones of India so as to identify material suitability along with economics. From the analysis carried out, it is concluded that the optimum insulation thickness is highly affected by the wall structure, degree days, and the insulation material, whereas the type of fuel does not have much effect. The inside temperature of a building depends upon the building design, orientation, and envelope. These three parameters are affected by ventilation, solar radiation, ambient temperature, and relative humidity. The building has to satisfy two contrasting functions: keeping the heat out in summer and keeping the heat inside in winter. Different insulation materials, different optimization methods, and the economic analysis methods were used in the present work. The five different insulation materials used were EPS, XPS, PUF, GW, and RW. It was observed that for most of the cities in different climatic zones based on Köppen-Geiger climate classification for India, XPS gave the best results, since it functions by having a large number of gas-filled pockets which prevent large-scale convection. The choice on the type of insulation material has great environmental implications. The thermal performance of external walls constitutes a key factor to increase the energy efficiency of the construction sector and to reduce greenhouse gases emissions. Thermal insulation is, thus, one of the best ways to reduce the energy consumption due to both winter heating and summer cooling.

References

1. Bolattürk A (2006) Determination of optimum insulation thickness for building walls with respect to various fuels and climate zones in Turkey. *Appl Therm Eng* 26:1301–1309
2. Aytac A, Aksoy UT (2006) Enerji Tasarrufu İçin Dış Duvarlarda Optimum Yalıtım Kalınlığı Ve Isıtma Maliyeti İlişkisi. *J Gazi Univ Fac Eng Archit* 26:753–758
3. <https://www.eia.gov/todayinenergy/detail>
4. Simona PL, Spiru P, Ion IV (2017) Increasing the energy efficiency of buildings by thermal insulation. *Energy Proc* 128:393–399
5. Bhatnagar M, Mathur J, Garg V (2018) Determining base temperature for heating and cooling degree-days for India. *J Build Eng* 18:270–280
6. Kaynakli O (2012) A review of the economical and optimum thermal insulation thickness for building applications. *Renew Sustain Energy Rev* 16:415–425
7. Sundaram AS, Bhaskaran A (2014) Optimum insulation thickness of walls for energy saving in hot regions of India. *Int J Sustain Energy* 33(1):213–226
8. Aksit M, Zhao C, Klose B, Kreger K, Schmidt H-W, Altstädt V (2019) Extruded polystyrene foams with enhanced insulation and mechanical properties by a benzene-trisamide-based additive. *Polymers* 11:268
9. Adityaa L, Mahliaa TMI, Rismanchic B, Nge HM, Hasane MH, Metselaare HSC, Murazaf O, Aditiya HB (2017) A review on insulation materials for energy conservation in buildings. *Renew Sustain Energy Rev* 73:1352–1365
10. Raouf AM, Al-Ghamdi SG (2020) Effect of *R*-values changes in the baseline codes: embodied energy and environmental life cycle impacts of building envelopes. *Energy Rep* 6:554–560

11. Abdelgadir EKM, Mohammed A, Adam H, Younis O, Hussein AK (2019) Optimum thermal insulation thickness for building under different climate regions—a review. *J Adv Res Fluid Mech Therm Sci* 59(2):254–268
12. Prices of Fuel (2015) www.igdas.com.tr
13. Kaygusuz K, Kaygusuz A (2004) Energy and sustainable development part II: environmental impacts of energy use. *Energy Sources* 26(11):1071–1082
14. Dombaycı A, Gölcü M, Pancar Y (2006) Optimization of insulation thickness for external walls using different energy-sources. *Appl Energy* 83:921–928
15. <https://www.nuclear-power.net/nuclear-engineering/heat-transfer/heat-losses/insulation-materials/extruded-polystyrene-xps/>
16. Almadhoni K, Khan S (2015) Evaluation of the effective thermal properties of aluminum metal matrix composites reinforced by ceramic particles. *Int J Curr Eng Technol* 5:2884–2897
17. De Micco C, Aldao CM (2006) On the prediction of the radiation term in the thermal conductivity of plastic foams. *Lat Am Appl Res* 36:193–197

Performance Comparison Between Pure Diesel and 5% Butanol Blended Diesel in a Multi-cylinder Engine



Jitendra Kumar, Naushad Ahamad Ansari, Samsher,
and Irwin Osmond Toppo

Abstract In this paper, the combustion characteristics of pure diesel and 5% butanol blended diesel (95% diesel and 5% *n*-butanol by volume) were compared when used as fuel for a multi-cylinder engine. The IC engine test rig chosen was TATA Turbo Engine 226 having power 52 kW, four-stroke, four-cylinder, water-cooled, variable speed, compression ignition (CI) engine using IEngineSoft_9.0 software. The combustion reports for both the fuels were obtained under constant pre-defined ambient conditions. The engine was run at a specified steady speed of approximately 1050 revolutions per minute. The comparison graphs were generated at no-load engine conditions. In this study, the curves for the following parameters such as cylinder pressure, net heat release, rate of pressure rise and mean gas temperature were analysed. From the acquired results, it was concluded that the 5% butanol blended diesel advances the combustion process in comparison with pure diesel fuel. It was also inferred that the butanol blended fuel would ensure sustainable and progressive use of biodegradable fuels. This work is an attempt to promote the use of biofuels as an alternative for the conventionally used fossil fuels.

Keywords *n*-butanol · Pure diesel · Crank angle · Cylinder pressure · Mean gas temperature

Abbreviations

BDC	Bottom dead centre
CA	Crank angle
CI	Compression ignition
CN	Cetane number

J. Kumar (✉) · I. O. Toppo
G. B. Pant Government Engineering College, New Delhi 110020, India
e-mail: jitendra@gbpec.edu.in

N. A. Ansari · Samsher
Delhi Technological University, New Delhi 110042, India

EOC	End of combustion
HC	Hydrocarbon
IC engine	Internal combustion engine
rpm	Revolutions per minute
SOC	Start of combustion
TDC	Top dead centre

1 Introduction

As with the increase in the number of vehicles on road, the demand for adequate fuel infrastructure is escalating at an extremely high rate. With the elevation in a requirement for conventional fuel (diesel), the major green house gas contributor (fossil fuels) is getting exhausted day by day. These fossils are also the prime cause of uncertainty in climatic conditions worldwide [1]. To overcome the deficiency of fuel resources, switching towards alternate fuels is very much necessary. Biodegradable fuels are the one which can act as the best suitable alternate fuels. Oxygenated fuels like alcohol are the biofuels to be used, as they combust much cleaner than the traditionally available conventional fuels [2]. Alcohols as fuel have many advantages [3], (i) less viscous than diesel, leading to much better atomization, injection and vaporization of fuel, (ii) better stoichiometric air–fuel ratio in comparison with diesel makes alcohols to release less harmful gases and (iii) shortens and enhances the entire combustion process, due to higher laminar flame propagation than diesel fuel. Ethanol has a wider set of applications [4–7]; however, it is poor auto-ignition quality that makes the fuel inappropriate to be used in CI engines [8]. From the higher-order HCs, butanol can be used as a blend with pure diesel fuel as it has higher CN, is less hydrophilic [9] and has a higher miscibility factor in pure diesel than ethanol [10]. Hence, the possible use of butanol blended diesel as fuel remains to be explored. The properties of butanol and pure diesel are mentioned in Table 2 [11–14]. The principle process for the production of butanol was invented by Pasteur in 1861. Fermentation plays a crucial role in the production of butanol during World War I and World War II. The worldwide annual production of butanol has been of the order 2.5×10^9 kg. In automobile fuel, butanol works as an air cleaner in the tailpipe exhaust having the motor octane value of butanol 113 and 94 in comparison with ethanol 111 and 92, respectively [15]. Isobutanol as an isomer of *n*-butanol is currently used as a biofuel. Despite biobutanol, it is generally pronounced as butanol [16]. Butanol is easier to mix with hydrocarbons, including gasoline because of the length of butanol's chain [17]. Productions of side products, like acetone and ethanol, and inhibition at low concentrations are two major drawbacks of butanol fermentation [18]. This study was done for evaluating the combustion curves of 5% butanol blended diesel in a multi-cylinder engine and compared with the results for pure diesel.



Fig. 1 Four-cylinder, four-stroke TATA turbo engine

2 Methods and Materials

2.1 Experimental Set-Up

Figure 1 shows the experimental set-up which was used.

All experimental work was performed on a four-cylinder, four-stroke, 1404.88 cc, 52.0 kW, variable speed, water-cooled TATA Turbo Engine 226. Pure diesel was used as a reference fuel for comparing the combustion curves of 5% butanol blended diesel with it. The engine was run at a steady speed of approximately 1050 rpm before generating the reports. The engine and fuel specifications are mentioned in Table 1.

The properties of butanol and pure diesel are mentioned in Table 2, taken from the sources [13, 14].

Firstly, the engine was run with pure diesel, and thereafter, 5% butanol blended diesel was used as fuel for the engine. The combustion reports for both fuels were obtained under constant pre-defined ambient conditions. The combustion parameters for both the fuels are listed in Table 3. The graphs for comparison between both the fuels were generated using ICEngineSoft_9.0 software.

3 Result and Discussion

An experimental study was done on a multi-cylinder, four-stroke, diesel engine with compression ratio of 18.5:1 and bore \times stroke as 75.0 mm \times 79.5 mm. The

Table 1 Engine and fuel specifications

Name	Specification
Engine type	Four-stroke, four-cylinder, water-cooled, variable speed, CI engine
Company	TATA
Rated power	52.0 kW @ 4000 rpm
Bore × stroke	75.0 mm × 79.5 mm
Compression ratio	18.5:1
Swept volume	1404.88 cc
Connecting rod length	141.0 mm
Ambient temperature	27 °C
Fuel density (pure diesel)	830 kg/m ³
Calorific value (pure diesel)	42,000 kJ/kg
Fuel density (5% butanol blended diesel)	742 kg/m ³
Calorific value (5% butanol blended diesel)	42,627 kJ/m ³

Table 2 Properties of *n*-butanol and pure diesel [11–14]

Fuel properties	Butanol (C ₄ H ₉ OH)	Diesel (C ₁₂ H ₂₄)
Density @ 20 (°C, kg/m ³)	810	837
CN	~25	~51
Boiling point (°C)	118	180–360
Latent heat of evaporation (kJ/kg)	585	250
Oxygen, %wt	21.6	0
Stoichiometric air–fuel ratio	11.2	15
Molecular weight	74	170
Auto-ignition temperature (°C)	355	204

Table 3 Combustion parameters

Parameter	Value
Specific gas constant	1 kJ/kg-K
Air density	1.17 kg/m ³
Adiabatic index	1.41

combustion curves for 5% butanol blended diesel and pure diesel used as fuel were procured.

Figure 2a, b plots cylinder pressure versus crank angle for pure diesel and 5% butanol blended diesel.

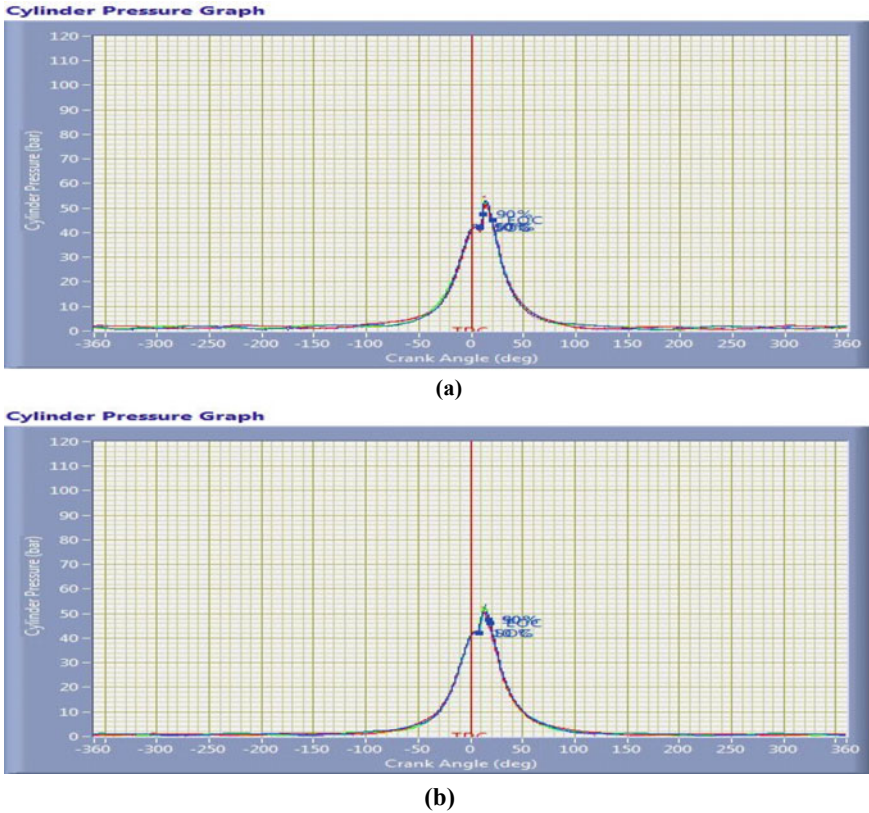


Fig. 2 a Pure diesel and b 5% butanol blended diesel

Figure 3a, b plots rate of pressure rise versus crank angle for pure diesel and 5% butanol blended diesel.

Figures 2a, b and 3a, b depict the comparison of the rate of pressure rise and cylinder pressure for both, pure diesel and 5% butanol blended diesel. The cylinder pressure graph shows the pressure variation within the cylinder during the complete cycle with CA. From the graphs, it can be inferred that (a) the SOC & 50% combustion for both the fuels takes place at a similar pressure, i.e. 42 bar; (b) the 90% combustion for pure diesel occurs before reaching the peak cylinder pressure, whereas in case of 5% butanol blended diesel it takes place after reaching the peak cylinder pressure; (c) after the completion of 90% combustion process the EOC occurs instantly at a constant CA of 20° for 5% butanol blended fuel, whereas for pure diesel fuel there exists a delay of approximately 10° between the occurrences of these two stages; and (d) the rate of pressure rise reaches its positive peak value within 10° of crank rotation, and the maximum value for the rate of pressure rise for pure diesel and 5% butanol blended diesel lies below and above 5 bar/degree, respectively.

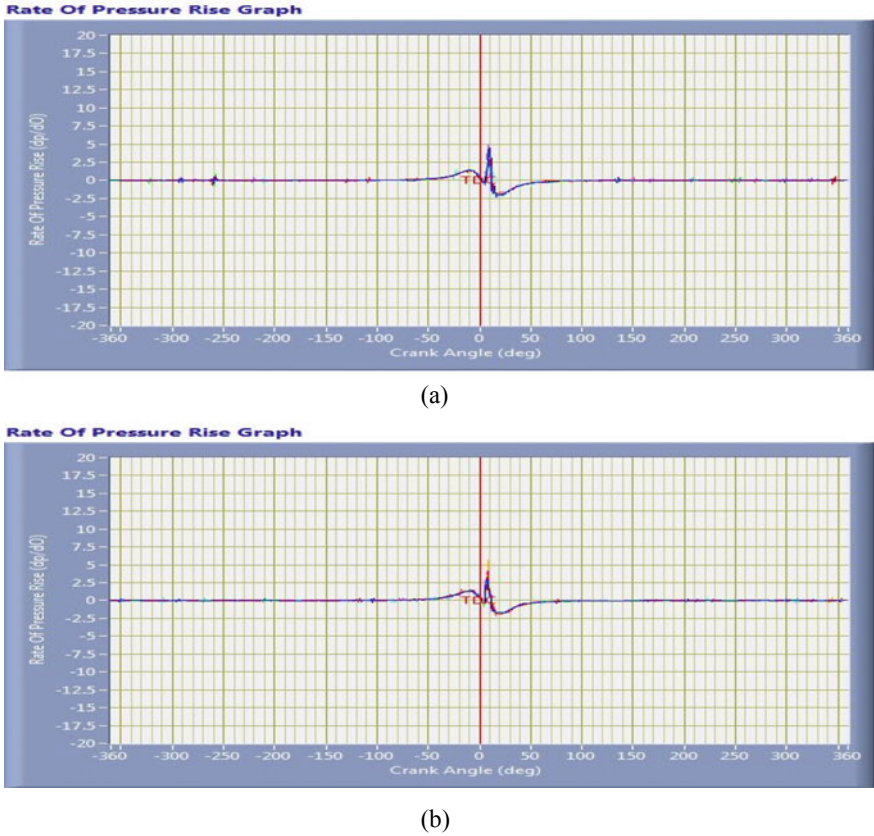


Fig. 3 a Pure diesel and b 5% butanol blended diesel

Figure 4a, b plots net heat release versus crank angle for pure diesel and 5% butanol blended diesel.

Figure 4a, b illustrates that (i) there is a significant decrease (approximately 12 J/degree) in the maximum value of net heat release from the engine when butanol blended diesel is used as fuel, and (ii) the process of heat release for 5% butanol blended diesel starts and reaches its peak value earlier than pure diesel.

Figure 5a, b plots mean gas temperature versus crank angle for pure diesel and 5% butanol blended diesel.

From Fig. 5a, b, it can be obtained that there is a slight drop in mean gas temperature of combustion gases during the initial and peak stages of the graph, whereas for final stage the observed mean gas temperature is moderately higher for 5% butanol blended fuel than pure diesel.

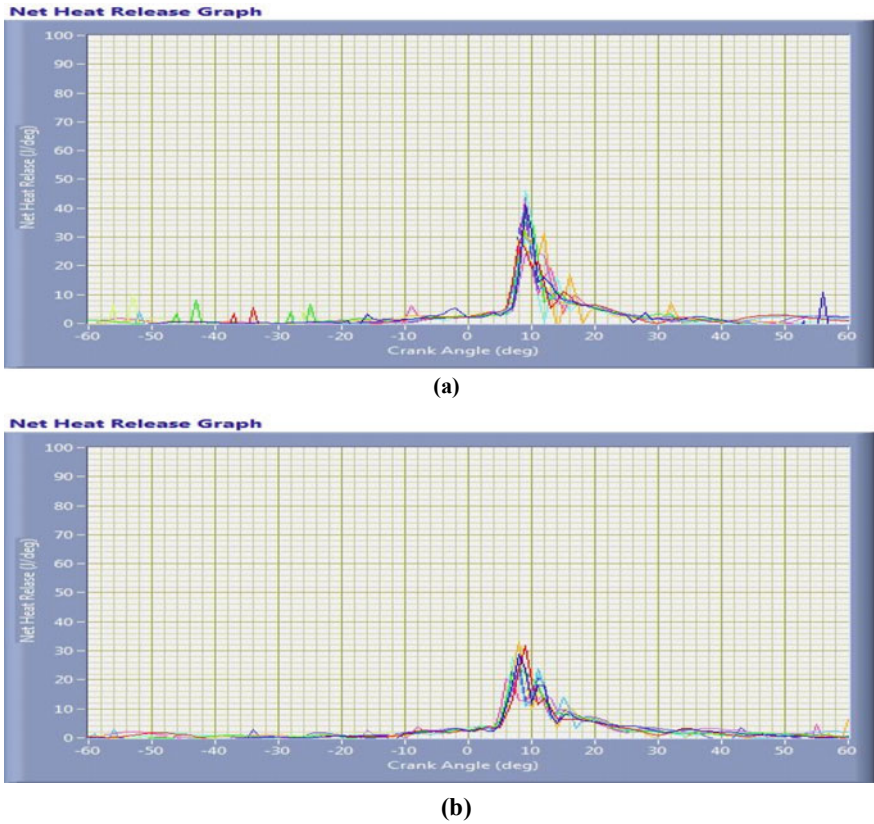


Fig. 4 a Pure diesel and b 5% butanol blended diesel

4 Conclusions

The motive of this study was to compare the combustion of 5% butanol blended diesel with pure diesel as fuel for four-cylinder, variable speed, water-cooled, four-stroke, compression ignition engine.

- The 5% butanol blended diesel advances the combustion process in comparison with pure diesel fuel.
- There is an increment in the peak value of the rate of pressure rise, upon the addition of a small quantity of *n*-butanol in diesel fuel.
- With the use of butanol blended diesel as a fuel, the peak value of net heat release from the engine decreases.
- The butanol blended fuel caused the mean gas temperature to vary slightly in the proximity of TDC when compared with pure diesel.

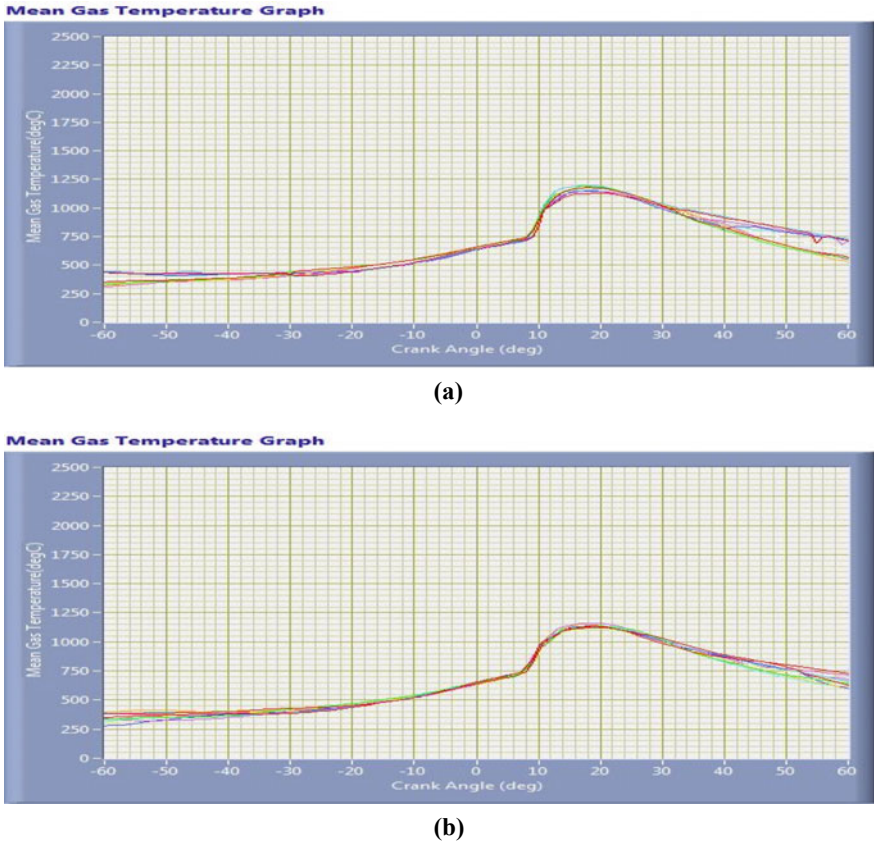


Fig. 5 a Pure diesel and b 5% butanol blended diesel

References

1. Singh P, Singh A (2011) Production of liquid biofuels from renewable sources. *Prog Energy Combust Sci* 37:52–68
2. Oguzhan D (2011) The influence of *n*-butanol/diesel fuel blends utilization on a small diesel engine performance and emissions. *Fuel* 90(7):2467–2472
3. Sayin C (2010) Engine performance and exhaust gas emissions of methanol and ethanol-diesel blends. *Fuel* 89(11):3410–3415
4. Szwaja S, Naber JD (2010) Combustion of *n*-butanol in a spark-ignition IC engine. *Fuel* 89(7):1573–1582
5. D'urre P (2008) Fermentative butanol production bulk chemical and biofuel. *Ann N Y Acad Sci* 1125:353–362
6. Dermotte J, Rouselle M, Halter F, Seers P (2010) Evaluation of butanol-gasoline blends in port fuel-injection, spark-ignition engine. *Oil Gas Sci Technol Rev* 65(2):345–351
7. Singliar MDM (2008) Emerging technologies for second generation of biofuels. *MOL scientific magazine, SD and HSE special*, pp 67–80
8. Murat C, Yuksel F, Hus H (2009) Emission characteristics of a converted diesel engine using ethanol as fuel. *Energy Sustain Dev* 13:250–254

9. Bryan W, Kumar K, Zhang Y, Sung-chin J (2011) Autoignition of *n*-butanol at elevated pressure and low-to-intermediate temperature. *Combust Flame* 158:809–819
10. Rakopoulos DC, Rakopoulos CD, Giakoumis EG, Dimaratos AM, Kyritsis DC (2010) Effects of butanol-diesel fuel blends on the performance and emissions of a high-speed DI diesel engine. *Energy Convers Manage* 51(10):1989–1997
11. Liu Y, Jiao W, Qi G (2011) Preparation and properties of methanol-diesel oil emulsified fuel under high-gravity environment. *Renew Energy* 36(5):1463–1468
12. Pukalskas S, Bodanovicus Z, Makareviciene V, Sendžikiene E, Janulis P (2009) The mixture of Biobutanol and petrol for otto engines. *Transport* 24(4):301–307
13. The DOW chemical company (2012) Technical data sheet, 2012. http://msdssearch.dow.com/PublishedLiteratureDOWCOM/dh_08ac/0901b803808ac9ed.pdf?filepathoxsolvents/pdfs/noreg/327-00014.pdf&fromPageGetDoc
14. Bharat Petroleum, High-speed diesel BS-IV. <https://www.bharatpetroleum.in/pdf/MRHighSpeedDieselOilBharatStageIV.pdf>
15. Qureshi N (2009) Solvent production, applied microbiology: industrial. Elsevier Inc. pp 512–528
16. Roberts LG, Patterson TJ (2014) Encyclopedia of toxicology Chevron Energy Technology Company, San Ramon, CA, USA @2014 Elsevier Inc., Volume 1, pp. 469–475
17. Ramanjaneyulu G, Rajasekhar B (2019) Reddy emerging trends of microorganism in the production of alternative energy recent developments in applied microbiology and biochemistry. © 2019 Elsevier Inc., pp 275–300 (Chapter-21)
18. Tirado-Acevedo O (2010) Production of biofuels from synthesis gas using microbial catalysts. In: *Advances in applied microbiology*, vol 70. @2010 Elsevier Inc., pp 58–83. ISSN 0065-2164 (Chapter 2)

Gamma Radiation Effects on Pre- and Post-welding SS304 and SS316 Stainless Steels' Ductility and Hardness



Parveen Kumar, Rajinder Kumar Soni, and B. S. Dehiya

Abstract The use of stainless steel is commonplace in nuclear reactors and other situations where nuclear radiations may be present. The effects of the nuclear radiation on structural steels are, therefore, a matter of great concern for anticipating the flaws and failures of the structures exposed to such high-energy radiations. This information can also be useful in the design of radiation-proof buildings, vessels, and shelters, etc. In the present work, we have studied the changes in mechanical properties, specifically plasticity, ductility, and hardness of two common types of commonly used stainless steels viz. SS304 and SS316, after exposure to high-energy gamma radiation from a Co^{60} source with a radiation dose rate of 2.875 kGy/h for up to 96 hr duration. The plasticity and failure properties were measured by tensile tests using a Tensometer, and the hardness was measured using a Rockwell micro-indenter. It was found that percentage elongation or ductility decreases only slightly for either type of steel alloy, even after 96 hr of gamma radiation. No major changes in tensile properties were observed for unwelded samples except for a substantial increase in surface hardness for both types of steels. For tensile specimens with welded joints, however, in case of SS316, the exposure to gamma irradiation greatly reduced the ductility from 43% to 24% while it increased the yield stress only slightly. The effects on the welded joint specimens of SS304 were a lot less pronounced. This difference may be attributed to the Molybdenum content of SS316 and its behaviour upon irradiation after the welding process.

Keywords SS304 · SS316 · Gamma radiation · Mechanical properties · Welded joints

Parveen Kumar · R. K. Soni

Department of Mechanical Engineering, Deenbandhu Chhotu Ram University of Science and Technology, Murthal, Sonapat, Haryana 131039, India

B. S. Dehiya (✉)

Department of Materials Science and Nanotechnology, Deenbandhu Chhotu Ram University of Science and Technology, Murthal, Sonapat, Haryana 131039, India
e-mail: drbrijdehiya.msn@dcrustm.org

Department of Chemical Engineering, Deenbandhu Chhotu Ram University of Science and Technology, Murthal, Sonapat, Haryana 131039, India

1 Introduction

Austenitic stainless steels (such as 304 and 316) are generally utilized in structural parts of industrial plants, for example, in pressure vessels, synthetic apparatuses, and channels, since they have fantastic erosion obstruction, corrosive opposition, formability, and weldability. These are also used in gas turbines, stream forces, and atomic power plants in light of their excellent durability in high-temperature and high-pressure situations. Industries that use SS316 include chemical manufacturing and storage, mining and petroleum activities, and marine engineering, medicine industry, pulp, and paper industry, automobile and transportation sector, and several others. A large number of products are made of SS304 or 316, including structural beams and rods, machines, bearings and valves, pipes and fittings, heat exchangers, laboratory equipments, and springs, locks, chains, meshes, scalpels, pincers, strainers, and many others [1, 2].

The addition of nickel to iron is the primary method used to change the BCC structure (ferrite) of iron to an FCC structure (austenite) (Fig. 1).

Austenitic stainless steels, in general, have superior toughness and ductility as compared to ferritic steels. Several elements have been identified as promoters of the BCC structure while others promote the FCC structure in stainless steel (see Table 1).

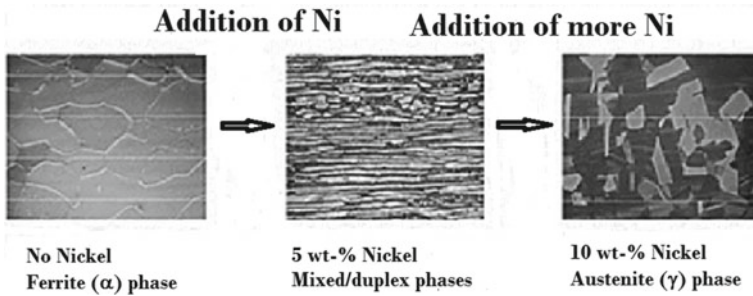


Fig. 1 Figure shows the characteristic changes from ferrite to austenite structure by the addition of nickel (generic representational images [e.g. 3])

Table 1 Additive elements that are known to promote either the ferrite or the austenite unit cell structure of stainless steels [2, 3]

Ferrite (α) phase promoters	Austenite (γ) phase promoters
Iron (Fe)	Nickel (Ni)
Chromium (Cr)	Nitrogen (N)
Molybdenum (Mo)	Carbon (C)
Silicon (Si)	Manganese (Mn)
	Copper (Cu)

The SS304 stainless steel contains high amounts of chromium (up to 24%) and up to 35% nickel, and small amounts of carbon and manganese. SS304 is one of the most commonly available forms of stainless steel in the world, preferred due to its excellent corrosion resistance as well as other mechanical properties. The corrosion/oxidation resistance is attributed to the formation of a chemically inert chromium oxide film on the surface. The SS316 grade is another common form of stainless steel. It has almost similar material characteristics as SS304, with one key difference: the SS316 steel contains 2–3% of dissolved molybdenum. The presence of molybdenum increases corrosion resistance against chemically reactive species and solvents. Molybdenum, however, is also a ferrite (bcc) phase promoter, and thus, it is used in smaller quantities. The addition of molybdenum to ferritic stainless steels also considerably enhances their corrosion resistance as well as their high-temperature mechanical properties [4].

Since structural steels necessarily have to be welded in applications, their mechanical properties are subject to change/degradation upon the formation of a welded joint. The welded joint may be considered a separate phase from the steel owing to the time–temperature treatment given to the welded area being different from that of the parent steel(s). The technique of arc welding is widely used for in stainless steel structures. The metal inert gas (MIG) welding/gas metal arc welding technique is quite commonly employed. An effective welded joint can be produced by passing a very large current through filler wires of several types viz. E-308L, 309L, 316L, etc., to bond together two stainless steel pieces. Rapid and controllable solidification can be carried out after welding thus helping to improve the quality of the weld [5].

As there is a tremendous amount of heat generation during the welding process, this can result in a structural and mechanical degradation of microstructure and mechanical properties of the stainless steels. The loss of homogeneity of the microstructure, the precipitation of secondary phases, and changes in plastic flow properties are the main underlying factors for this degradation. A post-weld heat treatment (PWHT) is typically used to control and minimize such deterioration of structure and mechanical properties. An appropriate PWHT can aid in retaining the steel's mechanical properties through homogenization of the microstructure of the welded area and by avoiding/dissolving the secondary phases that may have precipitated, leading to microstructural uniformity with the parent steel base [6, 7].

The current investigation has been carried out to look at the effects of high-energy (gamma) radiation on austenitic stainless steel components, specifically steels with welded joints. Microstructural changes can be created in austenitic steels depending upon the material and test conditions through radiation [7]. High-energy radiation environments are encountered in several critical applications—such as nuclear reactors, radioactive materials storage and containment, research/biomedical instruments such as x-ray imaging devices, and design of radiation-proof structures, among others [8].

2 Experimental

2.1 Test Materials

The two materials used in this study are SS304 and SS316 steels because these materials are commonly used to construct structural components in the nuclear power plants. These components are exposed in service to high-energy radiation damage at very high concentrations and different temperature and environmental conditions.

Tensile tests were carried out in concordance with the ASTM A370-E8/EM standard tests protocols. The mechanical and failure properties were estimated by tensile tests utilizing a Tensometer [8, 9].

2.2 Chemical Compositions

The chemical compositions of SS304 and SS316 were analysed chemically and are given in Table 2:

2.3 ASTM Standard

The tensile strength of the material was analysed using the ASTM A370 (or E8) standards. This standard is specifically meant for testing small-sized samples. The geometry of the tensile test specimens specified in this standard is shown in the following diagram (Fig. 2):

To find the impact of the change in microstructures, we also utilized a micro-hardness test as per the ASTM standards, both pre- and post-irradiation by gamma rays. Micro-hardness was measured in two distinct zones: the base material zone (BM) in the thermally influenced zone (TAZ) for welded samples. The testing speed at which the tensile tests were carried out was kept at 300 N/s. The samples were mechanically polished using a diamond paste to a submicron finish before the tensile (and hardness) tests.

2.4 Finishing and Exposure to Gamma Radiation

Polished surfaces of steel specimens from each sample were prepared by conventional machining grinding and polished technique. 1 cm² square samples were prepared for characterization of the material, and ASTM standards were also used for the tensile specimen exposed to gamma radiation. The polished samples were exposed to gamma radiation in the gamma chamber of GC1200TM with compact shielded ⁶⁰Co

Table 2 The chemically analysed compositions of the two SS304 and SS316 steels used in this study are described below:

Chemical composition of the tested stainless steels (in wt%)										
Stainless steel used	Fe	Cr	Ni	Mo	Mn	Si	C	P	S	N
SS304	Remaining	18.9	8.5	-	1.96	0.77	0.07	0.04	0.03	0.4
SS316	Remaining	16.3	11.8	2.08	2.03	0.75	0.08	0.05	0.03	0.4

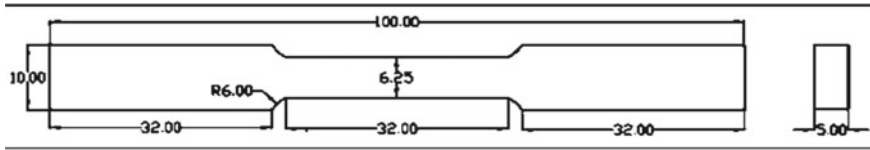


Fig. 2 Test specimen dimensions for the A370 tensile test samples [e.g. 9]. All dimensions are in mm (*Reproduced from the ASTM manual for A370—testing of steel samples*)

gamma irradiator rendering an irradiation volume of approximately 1200 cc. This work was carried out at the Inter-University Accelerator Center, New Delhi. The synthetic radioactive isotope of cobalt ^{60}Co is used as the radiation source in the gamma chamber and is the most commonly used gamma radiation source.

2.5 Mechanical Testing

The tensile test is the most common type to test used to measure the mechanical properties of a material, especially metals and alloys. In addition to the tensile tests in this work, hardness tests were also carried out to evaluate the changes in surface plastic flow properties.

2.6 Tensile Tests

A Tensometer device was used for the tensile testing of the material at the facility in Jamia Millia Islamia University, New Delhi, with tensile specimens made up of both before and after the gamma radiation exposure. The major parameters from the engineering stress–strain curves obtained during the tension test were the tensile strength, yield strength, and the percentage elongation before fracture/ductility.

2.7 Hardness

Multiple micro-hardness tests were performed on the gamma-exposed (duration of exposure was from 24 to 96 hr) welded and unwelded samples of the stainless steels. The device used for the micro-hardness testing was a Rockwell micro-indenter. In this test, a spherical indenter is pushed into a metallic surface with a specific known force, causing an indentation on the surface. There are many Rockwell hardness scales, depending on the type of indenter and load used. The Rockwell-B hardness measurement is then inversely proportional to the depth of penetration (in HRB

units). The Rockwell-B scale is used for softer steels and comprises of a 1/16-inch diameter ball indenter applied with a 100-kg load.

3 Results and Discussion

3.1 Tensile Tests

The combined tensile test results for the two stainless steels, *with* and *without* welded joints and both with/without gamma irradiation, are shown in Fig. 3:

As can be observed from the plots of Fig. 3, the effect of gamma radiation on the unwelded steel samples of SS304 and SS316 is very small, even negligible.

However, in the case of tensile specimens with welded joints, the gamma irradiation causes ~ 40% reduction in the strain to failure for the SS316 specimen, while producing no significant change in ductility for the SS304 steel (Figs. 4 a and b).

In both cases, however, a small increase in yield strength is observed, which can be attributed to the generation of point defects in the steels by the high-intensity gamma radiation [10, 11].

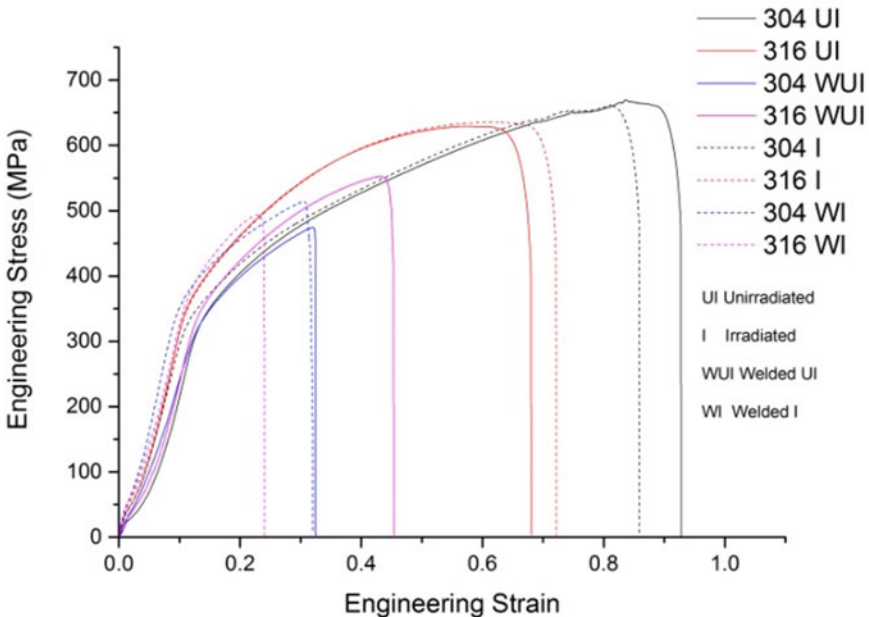


Fig. 3 The tensile tests' results are shown here as plotted graphs between engineering stress and engineering strain before and after the irradiations of welded samples of SS304 and SS316 steel

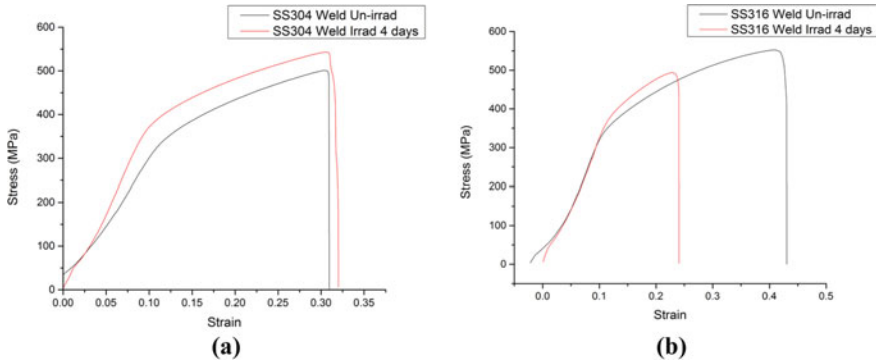


Fig. 4 a, b The engineering stress–strain diagrams of **a.** SS304 and **b.** SS316 steels’ tensile tests that compare the un-irradiated and gamma-irradiated welded steel tensile samples after four days of gamma irradiation, are shown here. The effects on SS316 steel are quite pronounced after welding

3.2 Hardness

This part of the tests was carried out by following the ASTM E18 Rockwell’s hardness test for metallic materials, and the following graphs were obtained (Fig. 5):

The welded-joint samples exhibit larger increases in surface hardness after gamma radiation of 4-days duration in comparison to the unirradiated welded-joint samples.

The considerable increase in hardness upon irradiation found for both the types of steels which we have tested, exhibits the promise of the use of gamma radiation for surface enhancement of structural/automobile components that need high tribological/frictional resistance when in practical use.

3.3 Carbide Precipitation and Mo Content in SS316

When the 300 series stainless steels are held in the temperature range above 600 °C, the chromium and carbon atoms migrate towards each other through random diffusion. After a while, the chromium and carbon atoms can combine to form chromium carbides precipitates [12, 13]. The primary disadvantage here is that in addition to the secondary phases formed, this process creates chromium deficient areas at the grain boundaries of the steel. Since chromium is the main element that provides corrosion resistance to the steel, after the grain boundaries become depleted of chromium, intergranular corrosion occurs much more rapidly at the grain boundaries, severely weakening the steel through surface cavitation.

The octahedral interstitial site of BCC ferrite is much smaller than that of FCC austenite. Hence the solubility of carbon in ferrite is much smaller than solubility of carbon in austenite. Since molybdenum is a ferrite promoter, it is possible that under high-energy radiation, Mo promotes the growth of the ferrite phase (XRD

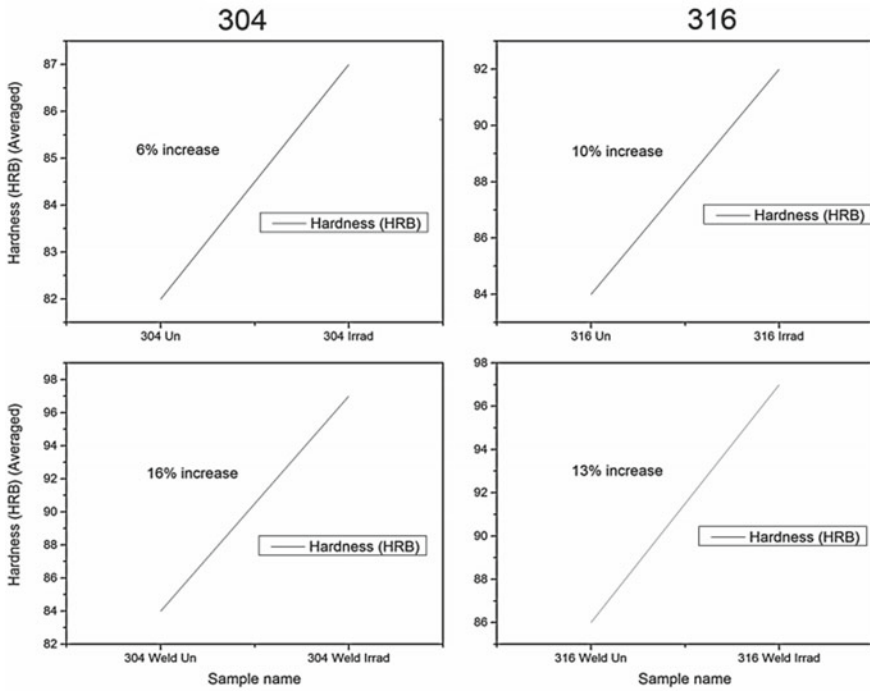


Fig. 5 The figures below show the Rockwell B hardness values. These charts show an increase of surface hardness with gamma radiation, by 6–10% for SS304 and 10–13% for SS316 steels

studies we are carrying out seem to indicate this is true). Thus, upon formation of ferrite from austenite in the welded-SS316 specimen, upon gamma radiation, there would be some free carbon interstitials liberated from the austenitic structure. These could then combine with chromium to generate carbides which are known to occur in heat-treated stainless steels. The presence of the carbides would increase the yield strength slightly, but at the same time, these would also cause weakness in the grain boundaries due to chromium depletion, leading to a reduction in ductility.

4 Conclusion

SS304 and SS316 hardened steels were researched against high energy radiation from a Co-60 gamma radioisotope source. The measurements of the gamma radiation properties of the steels were carried out for up to 4 days of gamma irradiation. In addition, the impact of radiations on the microstructure and mechanical properties of welded SS304 and SS316 stainless steel was examined.

While the effect of gamma radiation on the plastic flow properties SS304 was minimal, it did have the effect of increasing the surface hardness of the alloy by up to ~ 13%.

The samples with welded joints of SS304 did not show any appreciable change in plastic flow properties upon gamma radiation, which is a good sign from the point of view of the applicability of this alloy in high-energy radiation environments.

For the SS316 alloy, the gamma radiation again did not produce any appreciable change in plastic flow properties, but in the case of a welded joint in SS316 sample, the ductility decreased by nearly 40%. The x-ray diffraction plots show a gradual appearance of a ferrite phase upon prolonged exposure to gamma radiation, which can be ascribed to the radiation-enhanced diffusion of molybdenum in SS316, which is a known ferrite stabilizer. The formation of ferrite would release carbon into the matrix that can lead to the generation of carbide precipitates at the grain boundaries, which can explain the reduction in ductility for the welded SS316 to a great extent.

References

1. Narayana Rao M (2011) Materials development for Indian nuclear power programme: an industry perspective. *Energy Procedia* 7:199–204, ISSN 1876-6102, <https://doi.org/10.1016/j.egypro.2011.06.026>
2. Allen TR, Sridharan K, Tan L, Windes WE, Cole JI, Crawford DC, Was GS (2008) Materials challenges for generation IV nuclear energy systems. *Nucl Technol* 162(3):342
<https://www.totalmateria.com/page.aspx?ID=CheckArticle&site=kts&NM=208>
3. Syed R (2014) Fatigue crack behavior of stainless steel SS304 by the addition of carbon nanotubes. *Directory Open Access J (Sweden)*
5. Wang C, Luo J, Guo N, Tu J, Ye H, Zhang P, Yan Q (2019) Effect of yttrium contents on the microstructure of a hot-rolled tantalum-containing 12Cr-ODS steel. *Front Mater* 6:317. <https://doi.org/10.3389/fmats.2019.00317>
6. Li Y, Huang Q, Wu Y, Nagasaka T, Muroga T (2007) Mechanical properties and microstructures of China low activation martensitic steel compared with JLF-1. *J Nucl Mater* 367–370:117–121. <https://doi.org/10.1016/j.jnucmat.2007.03.012>
7. Tan L, Stoller RE, Field KG, Yang Y, Nam H, Morgan D, Wirth BD, Gussev MN, Busby JT (2016) Microstructural evolution of type SS304 and SS316 stainless steels under neutron irradiation at LWR relevant conditions. *JOM*
8. Kuksenko V, Pareige C, Genevois C, Cuvilly F, Roussel M, Pareige P (2011) Effect of neutron-irradiation on the microstructure of a Fe–12 at% Cr alloy. *J Nucl Mater* 415(1), 61–66. <https://doi.org/10.1016/j.jnucmat.2011.05.042>
9. ASTM A370-20, Standard test methods and definitions for mechanical testing of steel products, ASTM International, West Conshohocken, PA, 2020, <https://www.astm.org>
10. Allen T, Cole J, Trybus C, Porter D, Tsai H, Garner F, Kenik E, Yoshitake T, Ohta J (2006) The effect of dose rate on the response of austenitic stainless steels to neutron radiation. *J Nucl Mater* 348(1–2):148–164. <https://doi.org/10.1016/j.jnucmat.2005.09.011>
11. Zhang Z, Dong Q, Song B, He H, Chai L, Guo N et al (2019) Effect of shear strain rate on microstructure and properties of austenitic steel processed by cyclic forward/reverse torsion. *Materials* 12:506. <https://doi.org/10.3390/ma12030506>

12. Chowdhury MA, Nuruzzaman DM (2016) Investigation of thin film deposition on stainless steel SS304 substrates under different operating conditions. *Int Nucl Inf Syst (INIS)*
13. Jublot-Leclerc S, Li X, Legras L, Lescoat M-L, Fortuna F, Gentils A (2016) Microstructure of Au-ion irradiated 316L and FeNiCr austenitic stainless steels. *J Nucl Mater* 480:436–446. <https://doi.org/10.1016/j.jnucmat.2016.08.006>

Design and Analysis of Multi-purpose Shopfloor Vice



Jash H. Patel, Jay S. Shah, Mili D. Shah, Monil K. Shah,
and Vinayak H. Khatawate

Abstract The paper is about the design and analysis of a prototype of a bench vice which can be used for several purposes. The paper aims at increasing the degrees of freedom of a simple bench vice without any increase in weight or cost of the product. The vice is made portable in order to increase its compatibility with other machine tools. Rotating motion and tilting motion are the major features of the prototype. Ease of manufacturing was considered while designing, and thus, authors made a simple and intuitive design. The integration of various functions and features from the existing vices in the market was taken into account.

Keywords Vice · Rotating · Tilting · Portable

1 Introduction

“Simple things have more scope for improvement”—a wise quote signifying the importance of keeping a keen eye for improvising things at its minutest detail. Detailed study of a product is the job of an engineer for the betterment of the customers around him. Bench Vice—a simple mechanical tool found in almost all the workshops around the world is helpful in many ways for mechanical engineers to carry out operations on a work piece that requires accuracy and stability while working on it. The clamping technique was originally developed in the middle ages with the introduction of clamps with threads. In recent times, a vice has a definition as—A mechanical apparatus used to secure an object to allow work to be performed on it. Vices have two parallel jaws, one fixed and the other movable, threaded in and out by a screw and lever. The major hardship face by the worker of the small-scale industries is that they have to use unifunctional vice because multifunctional vice are expensive. We have alter the current multifunctional vice, so that even the small-scale industries can have it and perform the operation on it and also there by can increase the production efficiency. The vice available that has all the operations such as tilting

J. H. Patel (✉) · J. S. Shah · M. D. Shah · M. K. Shah · V. H. Khatawate
Department of Mechanical Engineering, DJSCE, Mumbai, India

and rotating has being in uses in now a day in various industries. The tilting of the vice has been possible with the help of mechanism. The latest vice has hydraulic system which helps in the tilting of the vice. It also has a slot mechanism which helps in tilt of the vice. The information obtain from the papers shows that the weight of the vice increases while using hydraulic systems. The cost of such vice is also high [1–3]. The rotating of the vice is carried out by using a 90° transmission system such as bevel gears, cam mechanisms, etc.[4, 5] The manufacturing process has also change from wood to casting metal to CNC machining.[6] The current multifunctional vice is bulky, expensive, stationary, etc. This all problem has been solved by using square section to reduce weight, using traditional manufacturing method to minimize the cost, using bolts and screws for assembly there by making it portable.

2 Design

See Figs. 1, 2, and 3.

Fig. 1 Prototype vice 1

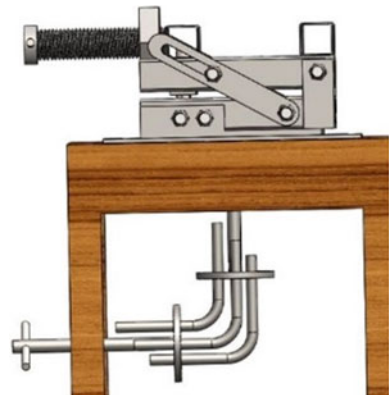


Fig. 2 Prototype vice 2

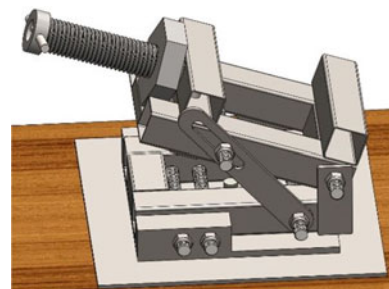
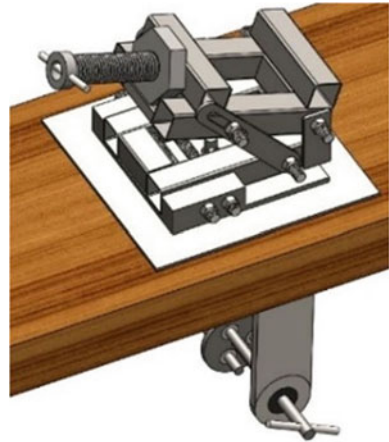


Fig. 3 Prototype vice 3



2.1 Tilting and Clamping Body

A standard bench vice only has the clamping part with a fixed and movable jaw. Movable jaw generally slides in a slot with the use of a screw. On the similar lines, this component in proposed design comprises of movable jaw, fixed jaw, body, and handle attached to the screw and nut. Major features of this component are listed below:

1. It comprises of the slotted link which aids the tilting motion of the vice.
2. Screw diameter is calculated using 100 N clamping force.
3. Screw diameter is set such that it satisfies self-locking condition
4. The clamping mechanism is made such that it holds 70 mm × 70 mm × 70 mm of the material desired to be machined.
5. Butterfly nuts are used to fix the position of the tilting mechanism at a particular angle (Figs. 4 and 5).

Fig. 4 Slotted link

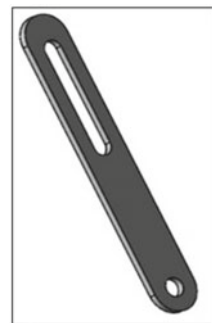
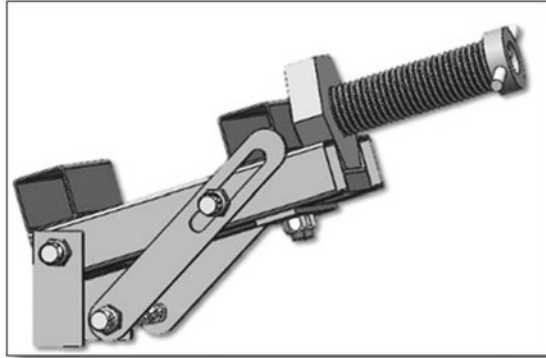


Fig. 5 Tilting and clamping body



2.2 Rotating Body with Fixed Plate

This component is not a part of a standard bench vice. A fixed plate is attached to the work table permanently and provides surface for rotation of the rotating body. This component comprises of fixed plate, rotating base, main body of vice, and tabs for tilting and clamping body. Major features of this component are listed below:

1. Material for fixed plate is steel with the view that steel–steel interface having high co-efficient of friction than the steel-wood interface.
2. Rotating body comprises of rotating base and the main body holding the tilting mechanism via tabs.
3. Rotating base is coupled with the elbow-rod transmission via studs.
4. The main body of vice acts as a link between rotating base and tilting and clamping body (Figs. 6, 7 and 8).

Fig. 6 Main body

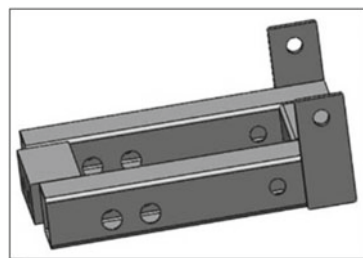
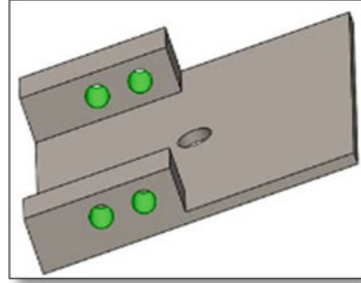
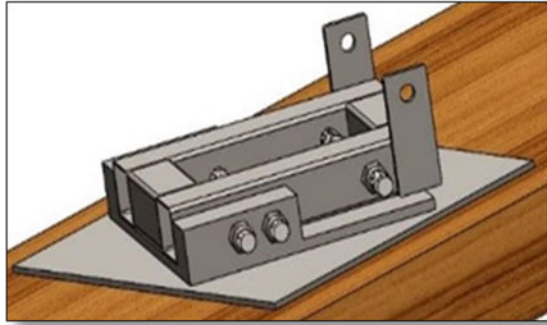


Fig. 7 Rotating body**Fig. 8** Rotating body with fixed plate

2.3 Gearless Elbow-Rod Transmission

The standard vice available in market with rotating feature has bevel gear mechanism to transmit the rotation motion from input by the operator to the output at vice main body. Here, unlike the standard vice, bent rods are used which slide to and fro in the slots provided while transmitting power. The elbow-rod transmission consists of bent rods, slotted disc, shafts, bearings, and nylon bushings. Major features of this mechanism are listed below:

1. Elbow-rod transmission comprises of three solid rods bent at an angle ranging from 90 to 95°.
2. The input shaft transmits the motion to the output shaft (attached to the rotating base) at an angle via circular plates with holes at a PCD of 30 mm.
3. The diameter of bent rods is calculated considering shearing condition.
4. Input shaft of the elbow-rod transmission is supported using bearings.
5. The bearing housing component is attached to the work Table 1 (Figs. 9, 10 and 11).

Table 1 Materials and their properties

SI. No.	Material	Yield strength (MPa)	Ultimate strength (MPa)	Elongation percent
1	Mild steel	210	330	20
2	Aluminum	145	276	10
3	Stainless steel	235	360	26

Fig. 9 Bent elbow-rods

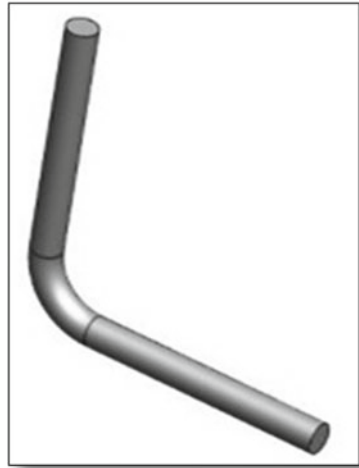


Fig. 10 Slotted rotating disc

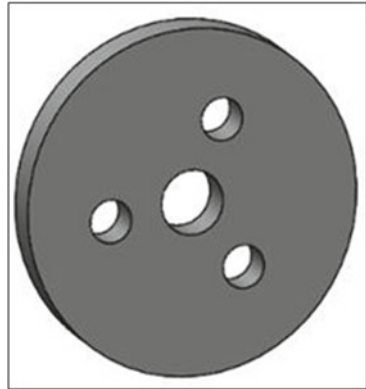
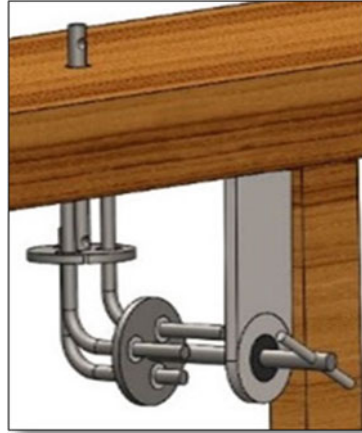


Fig. 11 Elbow-rod transmission



3 Analytical Calculations

3.1 Material Selection

After analyzing the mechanical properties of the materials, mild steel, aluminum, and stainless steel were selected for the prototype vice. Another consideration was the cost of the material, the cost of aluminum hollow square section was higher than that of the mild steel hollow square section.

Mild steel was selected as the material for the manufacturing of vice because it was easily available as compared to stainless steel. Mild steel had various cross-section available and was easy to choose from it. By selecting the mild steel, the welding process also gets easier because mild steel-based filler is also easily available in the market. Material for the plate was also mild steel.

The dimensions of the square section used were 1 inch \times 1 inch with 1 mm thickness.

3.2 C-Clamp Calculation

Maximum clamping force (W) = 4 KN

Co-efficient of screw friction (μ_s) = 0.14

Co-efficient of collar friction (μ_c) = 0.16

Force applied by an operator = 100 N

Distance between axis of screw and centroidal axis of vertical column = 100 mm

Material = MS1018

Yield strength = $S_{yt} = 370 \text{ N/mm}^2$

Factor of safety = $\text{fos} = 3$

Now,

$$\sigma_t = \frac{S_{yt}}{\text{fos}} = 123.33 \text{ N/mm}^2$$

$$\sigma_c = 1.4 * \sigma_t = 172.66 \text{ N/mm}^2$$

$$\tau = 0.5 * \sigma_t = 61.67 \text{ N/mm}^2$$

(1) Design of screw body [7, 8]

$$\sigma_c = \frac{W}{\frac{\pi}{4} * d_c^2} = 172.66$$

$$d_c = 5.43 \text{ mm} \approx 10 \text{ mm}$$

Select standard square thread for screw

$$d_c = 17 \text{ mm.}$$

$$d = 22 \text{ m}$$

$$p = 5 \text{ mm}$$

$$d_m = d - 0.5 * p = 19.5 \text{ mm}$$

Torque required to overcome thread friction T_t

$$\lambda = \tan^{-1} \left(\frac{p}{\pi * d_m} \right) = 4.66^\circ$$

$$\phi = \tan^{-1} \mu_s = 7.969^\circ$$

$$T_t = \frac{W * d_m}{2} * \tan(\phi + \lambda) = 8.743 \text{ Nm}$$

Torque required to overcome collar friction T_c

$$R_o = 0.75 * d = 16.5 \text{ mm}$$

$$R_i = 0.25 * R_o = 5 \text{ mm}$$

$$R_m = 11.775 \text{ mm}$$

$$T_c = W * R_m * \mu_c = 7.536 \text{ Nm}$$

Total torque T

$$T = T_c + T_t = 16.279 \text{ Nm}$$

(2) Determination of stresses

Stresses at section X-X

Torsional shear stress

$$\tau = \frac{16 * T}{\pi * d_c^3} = 16.88 \text{ N/mm}^2$$

Bending stress

$$M = F * l = 100 * 100 = 10,000 \text{ N mm}$$

$$\sigma_b = \frac{32 * M}{\pi * d_c^3} = 20.73 \text{ N/mm}^2$$

Maximum shear stress

$$\tau_{\max} = \sqrt{\left(\frac{\sigma_b}{2}\right)^2 + \tau^2} = 19.81 \text{ N/mm}^2$$

$$\text{but, } \tau = 61.69 \text{ N/mm}^2$$

Since $\tau_{\max} < \tau$

Therefore, design is safe.

Stresses at section Y–Y

Direct compressive stress

$$\sigma = \frac{W}{\frac{\pi}{4} * d_c^2} = 17.62 \text{ N/mm}^2$$

Torsional shear Stress

$$\tau \frac{16 * T_c}{\pi * d_c^3} = 7.81 \text{ N/mm}^2.$$

Maximum shear stress

$$\tau_{\max} \sqrt{\left(\frac{\sigma_b}{2}\right)^2 + \tau^2} = 11.77 \text{ N/mm}^2$$

Since $\tau_{\max} < \tau$

Therefore, design is safe.

(3) Checking for self-locking condition:

$$d_m = d - 0.5 * p$$

$$\mu = 0.12 \text{ (standard)}$$

$$\frac{1}{\pi d_m} = \frac{1}{\pi (22 - 0.5 * 5)} = 0.0160$$

$$\text{thus, } \mu > \frac{1}{\pi d_m} \text{ satisfied}$$

SCREW DIMENSION

$$d = 22 \text{ mm}$$

$$p = 5 \text{ mm}$$

3.3 Rod Calculation

Torque required for rotation

Data:

$$\text{Force} = 100 \text{ N}$$

$$\text{Co-efficient of friction } f = 0.6$$

$$R_o = 0.1 \text{ m}$$

$$R_i = 0.015 \text{ m}$$

$$T = \frac{2 \cdot F \cdot f \cdot (R_o^3 - R_i^3)}{3(R_o^2 - R_i^2)} \quad [9]$$

$$= \frac{2 \times 100 \times 0.6(0.1^3 - 0.015^3)}{3(0.1^2 - 0.015^2)}$$

Torque = 4.07 N m
 Diameter of Rod
 Data:
 Torque = 4070 N mm
 $R = 15$ mm
 Material: MS 1010
 Shear stress = 180 N/mm²
 Fos = 20

$$T = F \times R$$

$$F = \frac{T}{R} = \frac{4070}{15}$$

Force = 271.3 N

$$\text{Stress} = \frac{\text{Shear Stress}}{\text{Fos}} = \frac{180}{20}$$

Therefore, Stress = 9 N/mm².

Also, Stress = $\frac{F}{A}$

$$9 = \frac{271.3}{\frac{\pi \times d^2}{4}}$$

$$d^2 = \frac{271.3 \times 4 \times 20}{180 \times \pi}$$

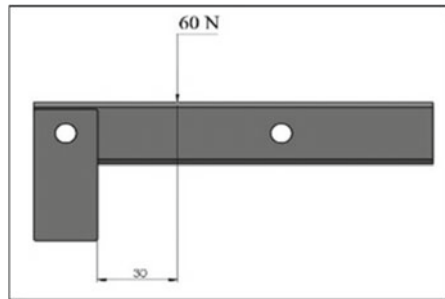
$$d = 6.195$$

d = 8 mm
 Diameter of Rods = 8 mm

3.4 Tab Calculation

Data:
 Force = 60 N
 Material: MS 1010
 $S_{yt} = 250$ N/mm²
 Fos = 20 (Fig. 12).
 $\tau = \frac{0.5 \times S_{yt}}{\text{fos}} = 6.25$ N/mm²

Fig. 12 Tab calculation



$$\tau = \frac{F}{A_c} \rightarrow A_c = \frac{F}{\tau}$$

$$\frac{\pi \times d_c^2}{4} = \frac{60}{6.25}$$

$$d_c^2 = 12.23 \text{ mm}$$

$$d_c = 3.5 \text{ mm}$$

$$d = 1.19 \times d_c$$

$$= 1.19 \times 3.5$$

$$= 4.2 \text{ mm}$$

Therefore, $d = 6 \text{ mm}$

Therefore, M6 bolt is selected.

4 Analysis

The 3D CAD model is made in SolidWorks 2017 [10]. The analysis is done on ANSYS Workbench 18.1 [11].

4.1 Tilting Mechanism Tab

Static structural analysis is done on the tab. While carrying out the simulation, the base of the plate and the mounting points were considered as fixed support. The overall weight of the object and tilting body (movable jaw, fixed jaw and screw with handle) was considered to be 6 kg and applied on the top of the face (Figs. 13 and 14).

Fig. 13 Geometry (Tab)

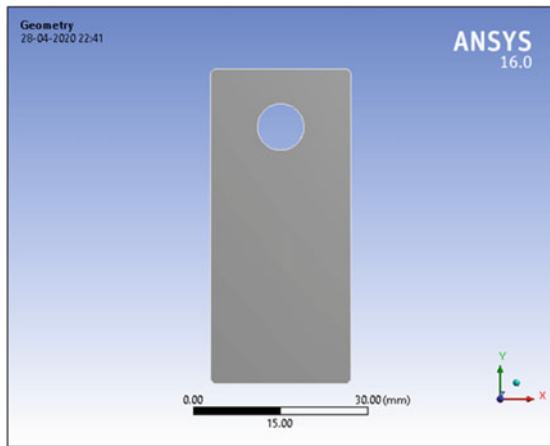
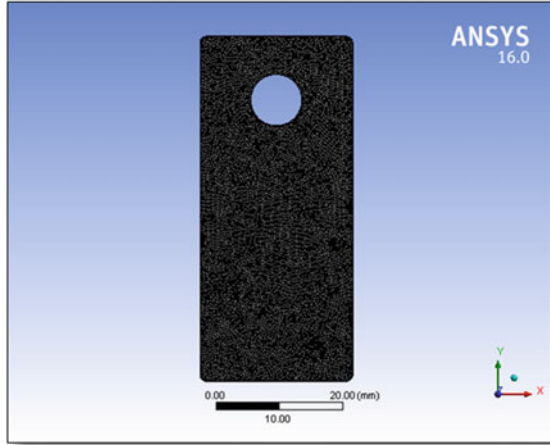


Fig. 14 Meshing (Tab)



4.2 Gearless Elbow-Rod Transmission

Transient structural is used for analysis of elbow transmission. The disc was given rotation motion with respect to time because transient analysis is used for time dependent load (Figs. 15 and 16).

Fig. 15 Geometry (gearless transmission)

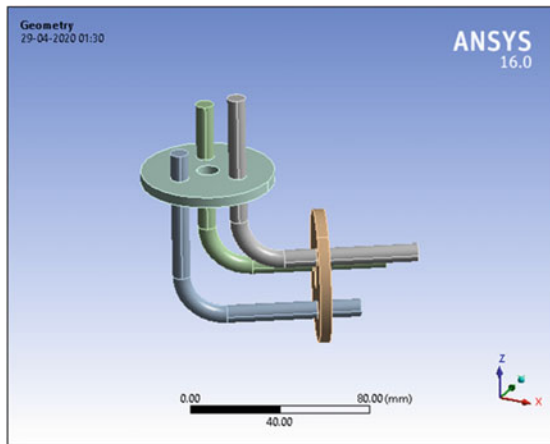
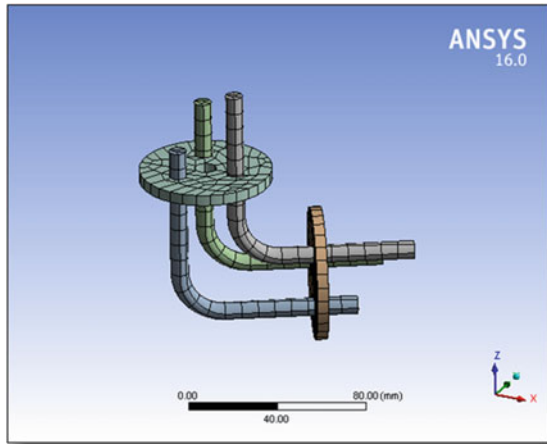


Fig. 16 Meshing (gearless transmission)



5 Results and Discussion

Statics analysis result of tilting mechanism tab for maximum stress is 2.0847 MPa with factor of safety of 15 and maximum deformation of 6.35×10^{-5} mm. Transient structural analysis result of gearless elbow transmission is it has maximum stress of 0.398 MPa and factor of safety of 15. These values indicated that it is in the over design condition, but one can change the material as per the requirement of the system, and still it will satisfy the necessary values of the industries. It can be also change according to the task perform on it (Figs. 17, 18, 19, 20, 21, and 22).

Fig. 17 Total deformation (Tab)

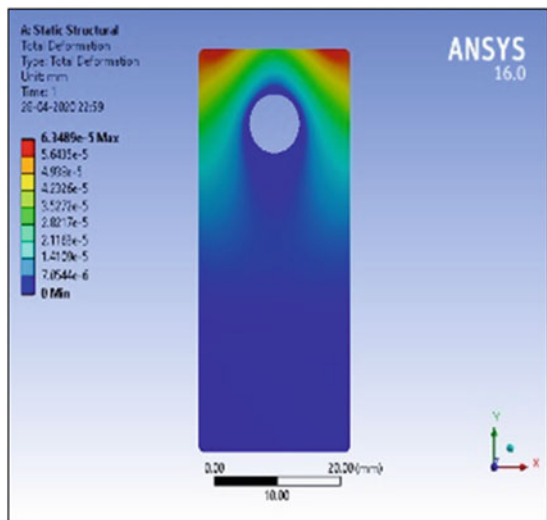


Fig. 18 Eq. stress (Tab)

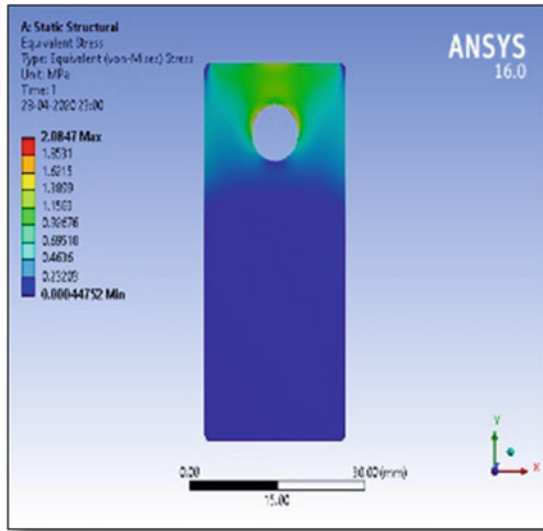


Fig. 19 Safety factor (Tab)

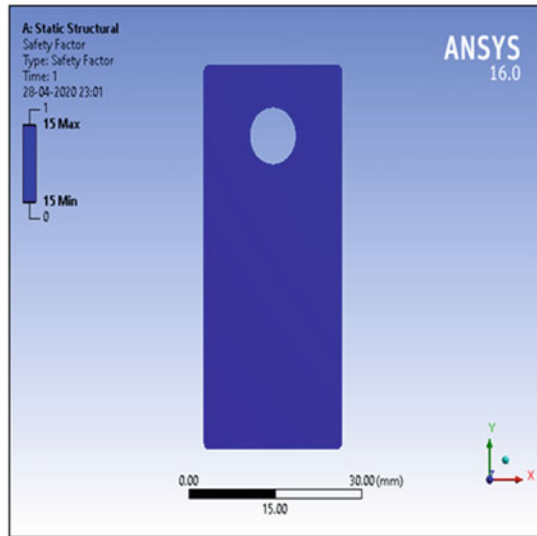


Fig. 20 Total deformation (gearless transmission)

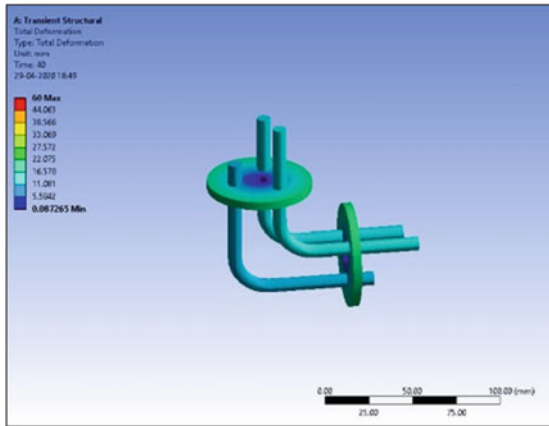


Fig. 21 Eq. stress (gearless transmission)

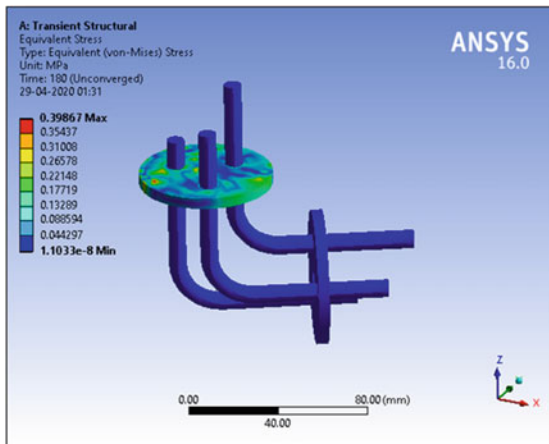
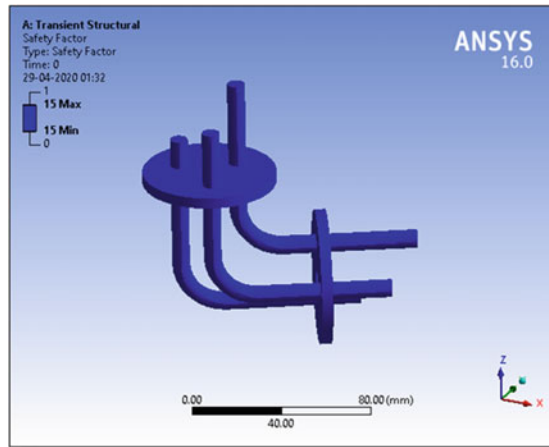


Fig. 22 Safety factor
(gearless transmission)



6 Conclusion

The design of the vice shows the reduction in the weight and the cost of the vice.

The functions such as rotating, tilting, etc., are well performed within the set limit. The factor of safety of whole assembly is more than ten which show the stability of the vice. The purpose of making it portable has also fulfilled. It shows a change from the existing vice and also shows the area of improvement done such as design, weight, manufacturing, and cost.

References

1. Chougule SM, Waghmare DB (2015) Design and manufacturing of components of modified bench vice on rapid prototype machine. *Int J Appl Innov Eng Manag (IJAIEM)* 4(7) July
2. Kadam AS, Rupanawar RM, Daundkar TV, Tanpure SR, Saidpatil VV (2016) Design and modification of bench vice by increasing the degrees of freedom. *GRD J Glob Res Dev J Eng* 1(11) (Oct 2016) ISSN: 2455-5703
3. Anuchandran C, Praveen M, Karthikeyan R, Arun R, Marimuthu K (2017) Design and fabrication of automatic machine vice using microcontroller. *IJSRD—Int J Sci Res Dev* 5(07) ISSN (online): 2321-0613
4. Logesh B, Vignesh R, Pugazhenth J, Vigneshan N, Vigneshwaran N (2018) A systematic design, development and fabrication of a safe cam operated machine vice. *Int J Res Eng Sci Manag (IJRESM)* 1(2) (Feb)
5. Rajendra Babu P, Mani Kumar Ch, Daniel K (2019) Design and fabrication of rotating and tilting vice (New technique) for radial drilling machine. *Int J Res Appl Sci Eng Technol (IJRASET)* 7(III) (Mar)
6. Sivasankaran P (2018) Design and analysis of modular fixture for machine vice. *Int J Ind Prod Eng Technol* 8(1):1–6. ISSN 2249-4219
7. Bhandari B (2017) *Design of machine elements*, 4th edn. Mc.Graw Hill Education, India
8. Nelson A (2009) *Engineering mechanics*. Tata Mc.Graw Hill Education, India

9. Ratan SS (2014) Theory of machines. Tata-McGraw Hill, India
10. Solidworks (2017) Introducing solidworks. Dassault Systemes
11. Autodesk ANSYS 2018, ANSYS theory reference, 11th edn. SAS IP. Inc., pp 77–84

Selection of a Best Humanoid Robot Using “TOPSIS” for Rescue Operation



K. Krishna Kumar, Abinav Karthikeyan, and Murugappan Elango

Abstract A rescue robot is introduced and built to reduce people’s work and to rescue people. The rescue robots are needed in cases of urban disasters, mining accidents, research endeavors, high-powered explosions, hostage situations, and military operations involving victim location and explosives detection. Rescue robots prove worthy since they reduce people’s work, reduce corresponding fatigue, and withstand high temperature since robots are made up of high temperature withstanding materials like aluminum. A rescue robot can access areas with ease, where humans find it difficult to reach. The advances in the field of robotic technologies are quite high these days. Recent developments are oriented on producing machines that have the capability of traversing along debris in building collapses, rescuing people from marine disasters, military reconnaissance and mapping, aiding in surgeries, and meticulous evacuations. This research paper proposes a selection method of an ideal humanoid robot by utilizing the multiple criterion decision model: “technique for order of preference by similarity to ideal solution” (TOPSIS) for rescue operation. Five important attributes of the robot were shortlisted to function as the criterion for selection. The simulated study of the robotic structure’s capabilities pertaining to rescue missions is considered.

Keywords TOPSIS · AHP · Factors · Criteria weight · Selection process · Specifications

Abbreviations

AHP	Analytic hierarchy process
TOPSIS	Technique for order of preference by similarity to ideal solution
PM	Preference matrix
NM	Normalization matrix

K. Krishna Kumar (✉) · A. Karthikeyan · M. Elango
Department of Mechanical Engineering, Thiagarajar College of Engineering, Madurai,
Thiruparankundram, Tamil Nadu, India

WNM Weighted normalized matrix

1 Introduction

Rescue robots have various applications like rescuing to search victims, in research and development. Researchers are keen in designing **humanoid robots** which help in surveying and overseeing damage, in regions of target and perform critical tasks like accessing and deciphering information from instrumentation panels or help in transporting first-aid equipment and vital medical supply. Tele-operated **robots** find uses in industrial, aerospace, and underwater settings. Recent advances in robotics and artificial intelligence techniques, have yielded advanced humanoid robots, which have substantially minimized human efforts also providing a multitude of useful features.

Many related works are explained while performing a literature survey, with ambitions to select an ideal robot for a mentioned target task work. The study explained in [1] introduces selected qualitative parameters for the selection of the ideal alternatives for a mobile robot use case, using fuzzy approach. The work presented in [2] explains about a method based on intelligent task planning and consequent action selection scheme, centered on a mobile robot plying on a robotic soccer system through the fuzzy-based neural network methodology. The work explained in [3] suggests a scheme centered on the analytic hierarchy process (AHP) with motives to select the ideal industrial robot for a distinctive milling application case. The work presented in [4] explains a decision-making process for choosing among CNC milling, robotic milling, and a process of the cards of additive manufacturing (DMLS) for a certain class of parts. The work presented in [5] depicts a fuzzy set-based multi-criteria decision approach. The work presented in [6] clarifies the robot selection dilemma using approaches, namely the fuzzy best–worst method and PROMETHEE. The work presented in [7] attempts to solve the robot selection debacle by weighing two related methods, on an industrial note, and consequently assert the importance of one over the other. The work presented in [8] proposes a grouped decision-making (GDM) methodology to analyze a typical multi-robot selection program. The work presented in [9] puts forward the notion of a decision model plying on a fuzzy linear regression approach on motives for picking an industrial robot. The work presented in [10] proposes a robot selection strategy by means of an integrated approach on the lines of quality function deployment and further justified by fuzzy regression. The work presented in [11] proposes a multi-criteria robot selection strategy, justified by a distance measure. The work presented in [12] puts forward an integrated linguistic MCDM approach, to comply with the evaluation of robots, with inputs from incomplete weight information. The work presented in [13] proposes an interval 2-tuple linguistic MCDM method with aims to evaluate and select the ideal industrial robot. The work presented in [14] determines the primary Weights with regards to specific customer needs layered on a FUZZY AHP approach in tandem with the approach of

Table 1 Considered robotic system

Attribute or criteria	Processor (MHz)	Battery (KWH)	Motor (V DC)	Speed (MPH)	Cost
ROBOTHESPIAN	1600	2.6	12	15	\$3,200,000
VALKYRIE	133	1.8	12	14	\$2,000,000
DARWIN OP2	1600	1.7	12	5.6	\$3,000,000
ATLAS	1000	3.7	24	20	\$4,000,000
HRP-5P	2800	1.08	24	20	\$2,600,000
NAO	1600	4.8	12	6	\$16,000

extent analysis. The work presented in [15] proposes the AHP-MOORA approach, a hybrid decision-making strategy used to detect materials with appreciable wear resistance properties. The work presented in [16] clouds over a bi-phased approach dubbed as ROBSEL, with motives to aid in robot selection decisions. The work presented in [17] defines an analysis, aimed at the hospitality sector, through a digital transformation perspective. The work presented in [18] proposes about the selection of CMS, which in reality is another of the broad spectrum of MCDA schema. The work presented in [19] explains a digraph methodology, buttressed with matrix methods, with aims to differentiate alternative industrial robots.

2 Methodology

For this approach, six humanoid robots, which have got the capability to perform rescue operations, were chosen to be studied. Pertaining characteristics and attributes of the chosen robotic systems are given as follows (Table 1).

3 Factors Needed for the Selection of Best Humanoid Robot Related to Rescue Operation

Processor It is the brain of the robot. It collects and stores all the information. It helps the robot to react to the commands and instructions given by people.

Battery It is the source of energy for the robot, which enables it to perform the desired tasks.

Motor It converts electrical energy to useful physical motion. It also makes the robot to move and helps in the movement of arms, ankles, and head.

Speed It implies how fast the robot can move per second or per hour.

Cost The parameter governing the price invested in the robot.

4 Calculation of Criteria Weight Using Analytical Hierarchy Process (AHP)

The ANALYTIC HIERARCHY PROCESS (AHP) was introduced by Thomas L. Saaty, and it deals with pairwise comparisons, by pitting the elements i and j , finding the desired value finding the value a_{ij} as result. This comparison is made on the lines of the mentioned hierarchical descriptions.

$$a_{ij} = 1 \text{ for } i = j, \text{ where } i, j = 1, 2, \dots n$$

$$a_{ij} = 1/a_{ji} \text{ for } i \text{ not equal to } j$$

The judgment scale that is taken for consideration here is the one found by Saaty: 1—equal important; 3—weakly very important; 5—strongly very important; 7—demonstrably very important; and 9—absolutely very important. Values in the domain of (2, 4, 6, and 8) indicate compromising judgments. A pairwise comparison is performed, consequently tabulating the preference matrix (Table 2).

Up next, the sum of each column is obtained and given (Table 3).

$$\text{sum}_j = \sum_{j=1}^n a_j, \text{ where } j \text{ denotes the column index}$$

Table 2 Formation of preference matrix

Attribute or criteria	Processor	Battery	Motor	Speed	Cost
Processor	1	2	3	4	5
Battery	1/2	1	2	3	4
Motor	1/3	1/2	1	2	3
Speed	1/4	1/3	1/2	1	2
Cost	1/5	1/4	1/3	1/2	1

Table 3 Summing all the columns

Attribute or criteria	Processor	Battery	Motor	Speed	Cost
Processor	1	2	3	4	5
Battery	0.5	1	2	3	4
Motor	0.33333333	0.5	1	2	3
Speed	0.25	0.333333	0.5	1	2
Cost	0.2	0.25	0.33333333	0.5	1
Column sum	2.28333333	4.083333	6.83333333	10.5	15

The normalized values are obtained by dividing individual values and the corresponding column sum.

$$N_{ij} = \frac{a_{ij}}{\text{sum}_j}$$

For each criterion, the average is taken and is given as the criteria weight (Table 4).

$$\text{Criteria Weight}_i = \frac{\sum_{i=1}^n N_i}{n}, \text{ where } i \text{ denotes the row index}$$

The obtained criteria weights are further used in the TOPSIS approach.

Selecting the Best Humanoid Robot Among The Chosen Using Technique For Of preference by Similarity to Ideal Solution (TOPSIS) Approach:

The Technique for order preference by Similarity to Ideal solution, a brain-child of Ching, Lai. Hwang and Yoon, is a methodology deployed in order to evaluate the performance of competing strategies, by analyzing each attribute’s closeness with the ideal solution [20].

Table 4 Formation of normalized matrix

Attribute or criteria	Processor	Battery	Motor	Speed	Cost	Criteria weight
Processor	0.437956204	0.489796	0.43902439	0.380952381	0.333333	0.416212445
Battery	0.218978102	0.244898	0.292682927	0.285714286	0.266667	0.261787988
Motor	0.145985401	0.122449	0.146341463	0.19047619	0.2	0.161050407
Speed	0.109489051	0.081633	0.073170732	0.095238095	0.133333	0.098572773
Cost	0.087591241	0.061224	0.048780488	0.047619048	0.066667	0.062376387

Table 5 Considered robotic systems

Criteria weight	0.41621245	0.261788	0.16105	0.098573	0.062376
Attribute or criteria	Processor	Battery	Motor	Speed	Cost
ROBOTHESPIAN	1600	2.6	12	15	3,200,000
VALKYRIE	134	1.8	12	14	2,000,000
DARWIN OP2	1600	1.7	12	5.6	3,000,000
ATLAS	1000	3.7	24	20	4,000,000
HRP-5P	2800	1.08	24	20	2,600,000
NAO	1600	4.8	12	6	16,000

Table 6 Calculation of the normalized matrix

Criteria weight	0.41621245	0.261788	0.16105	0.098573	0.062376
Attribute or criteria	Processor	Battery	Motor	Speed	Cost
ROBOTHESPIAN	0.393440503	0.364837636	0.288675135	0.417900261	0.471812947
VALKYRIE	0.032950642	0.252579902	0.288675135	0.390040244	0.294883092
DARWIN OP2	0.393440503	0.238547685	0.288675135	0.156016098	0.442324638
ATLAS	0.245900314	0.519192021	0.577350269	0.557200348	0.589766184
HRP-5P	0.68852088	0.151547941	0.577350269	0.557200348	0.383348019
NAO	0.393440503	0.673546406	0.288675135	0.167160105	0.002359065

Selection of the robot is done using the technique for order of preference by similarity to ideal solution (TOPSIS) approach by the following steps given. The attributes corresponding to each parameter are provided for each robot variant (Table 5).

Up next, the values are normalized resulting in a normalization matrix. It is done using the formula given below (Table 6)

$$\bar{x}_{ij} = \frac{x_{ij}}{\sqrt{\sum_{j=1}^n x_{ij}^2}}$$

Each attribute in the normalization matrix is now multiplied with the weights affixed to each attribute, from the AHP. The corresponding formula is given below (Table 7).

$$V_{ij} = \bar{x}_{ij} * W_j$$

For each attribute class, we obtain the ideal best and worst terms, with the former denoting the maximum value pertaining to an attribute class, while the latter denotes

Table 7 Calculation of the weighted normalized matrix

Attribute or criteria	Processor	Battery	Motor	Speed	Cost
ROBOTHESPIAN	0.163754836	0.095510115	0.04649113	0.041193682	0.029429804
VALKYRIE	0.013714467	0.066122387	0.04649113	0.038447437	0.018393628
DARWIN OP2	0.163754836	0.062448921	0.04649113	0.015378975	0.027590442
ATLAS	0.102346772	0.135918241	0.092982261	0.05492491	0.036787255
HRP-5P	0.286570962	0.039673432	0.092982261	0.05492491	0.023911716
NAO	0.163754836	0.176326366	0.04649113	0.016477473	0.000147149

Table 8 Calculation of ideal best value and ideal worst value

Attribute or criteria	Processor	Battery	Motor	Speed	Cost
ROBOTHESPIAN	0.163754836	0.095510115	0.04649113	0.041193682	0.029429804
VALKYRIE	0.013714467	0.066122387	0.04649113	0.038447437	0.018393628
DARWIN OP2	0.163754836	0.062448921	0.04649113	0.015378975	0.027590442
ATLAS	0.102346772	0.135918241	0.092982261	0.05492491	0.036787255
HRP-5P	0.286570962	0.039673432	0.092982261	0.05492491	0.023911716
NAO	0.163754836	0.176326366	0.04649113	0.016477473	0.000147149
V +	0.286570962	0.176326366	0.092982261	0.05492491	0.036787255
V –	0.013714467	0.039673432	0.04649113	0.015378975	0.000147149

the minimum value of the same class. For each attribute/column, the ideal best and worst values are computed (Table 8).

For each attribute, the Euclidean distance from the ideally best and worst values is obtained. The Euclidean distance approach is done using the formula given below.

$s_i^+ = \left\{ \sum (v_{ij} - v_j^-)^2 \right\}^{0.5}$ with **i:** $i \in (1, 2, \dots, n)$ and **j:** $j \in (1, 2, \dots, m)$ where s_i^+ is the Euclidean distance of the ideal best from the persisting values.

$s_i^- = \left\{ \sum (v_{ij} - v_j^+) ^2 \right\}^{0.5}$ with **i:** $i \in (1, 2, \dots, n)$ and **j:** $j \in (1, 2, \dots, m)$ where s_i^- is the Euclidean distance of the ideal worst from the persisting values.

The performance score metric is used to rank the various proposals put forward. A higher performance score indicates that the considered proposal is relatively closer to the positive ideal solution and further from the negative ideal solution computed.

The performance score is calculated using the formula given below (Table 9):

$$P = \frac{s_i^-}{s_i^- + s_i^+}$$

Based on the results computed, we find that the Robot **HRP-5P** has the highest performance score than others.

Thus, we have come to a conclusion that TOPSIS has chosen **HRP-5P** robot as the best humanoid robot among all the six chosen for selection.

5 Conclusion

With rescue robots becoming ubiquitous in rescue operations, the industry has a lot to offer. Rescue robots of late are becoming more advanced and capable, with a select few requiring absolutely zero human assistance. Choosing the ideal humanoid robot based on the situation encountered is the most important prerequisite of initiating a robot-aided rescue. The multitude of features offered by each robot variant initially

Table 9 Calculation of the Euclidean distance metric from the ideal best (S +) and ideal worst value (S -) and performance score

Attribute or criteria	Processor	Battery	Motor	Speed	Cost	s_i^+ (Ideal best)	s_i^- (Ideal worst)	P	Rank
ROBOTHESPIAN	0.163754836	0.095510115	0.04649113	0.041193682	0.029429804	0.1549812	0.16478386	0.515328	3
VALKYRIE	0.013714467	0.066122387	0.04649113	0.038447437	0.018393628	0.29894287	0.03955547	0.116856	6
DARWIN OP2	0.163754836	0.062448921	0.04649113	0.015378975	0.027590442	0.17849863	0.15422052	0.463516	4
ATLAS	0.102346772	0.135918241	0.092982261	0.05492491	0.036787255	0.18860373	0.14895151	0.441266	5
HRP-5P	0.286570962	0.039673432	0.092982261	0.05492491	0.023911716	0.13725817	0.28060778	0.671526*	1*
NAO	0.163754836	0.176326366	0.04649113	0.016477473	0.000147149	0.14165426	0.20294665	0.588932	2
V +	0.286570962	0.176326366	0.092982261	0.05492491	0.036787255				
V -	0.013714467	0.039673432	0.04649113	0.015378975	0.000147149				

* Indicates the ideal robot based on the highest performance score

puts the monitoring team in jeopardy, thus requiring an adaptable selection methodology. This research work proposes a method based on selection of a best humanoid robot using **TOPSIS** for rescue operation. For this approach, **five attributes** of the robots were chosen. These five criteria were used for **pairwise comparisons**. The five factors taken into consideration are **battery, motor, processor, speed, and cost**. These factors were taken in accordance with the rescue operation. The factor **processor** influences how fast the robot could react according to the commands given and consequently storing the information, which is more important in rescue operations. Generally, most of the humanoid robots are programmed with artificial intelligence techniques which enable the robots to think on their own and make decisions, according to the situation. The factor **battery** is another essential factor, since it provides electrical power to the robot thus making it to work. The robot is expected to deliver its optimal performance for a lengthy period, without requiring an intermediate charging period. The robot losing power and consequently stalling amidst a rescue operation could prove perilous. The factor **motor** aids in the robot motion, and it is pivotal in influencing the movement robot arms, ankle, elbow, leg, etc. The robotic arms and other moving parts are expected to be delicate, while dealing with situations involving a lot of intricate debris. The factor **speed** is vital for the rescue operations, especially in those desired to rescue people. A timely rescue can save a lot of lives, as well as saving millions of bucks of vital property. The factor **cost** implies that price of the robot should be reasonable and enough to be employed in any particular type of rescue operation. The AHP process yielded the weights of each parameter considered, and it ranked the **processor** criterion as the one with the highest weight, followed by **battery, motor, speed, and cost**. The **cost** parameter was attributed with minimal weights, owing to the factor that almost all rescue robot systems cost similarly in lieu of the present competitive global market.

The preference matrix was formulated, and weights of each individual criterion were computed using AHP. The criteria weights from the AHP approach were used on the TOPSIS approach. The ideal best and the ideal worst values were computed by the TOPSIS approach. The former is the one that maximized the benefit criterion considered, simultaneously minimizing the expense criteria, while the latter is the one that maximized the expense criterion and simultaneously minimizing the benefit criterion. The Euclidian distance of each attribute value from the ideal best and ideal worst values is computed finally computing the performance score, which settles the debacle of selecting the best rescue robot, among its competitors. Thus, after weighing each preference parameter and defining selection metrics using **TOPSIS**, the robot **HRP-5P** is chosen as the best and ideal humanoid robot for rescue operations, based on the higher value of performance score.

References

1. Sahu J, Choudhury BB, Muni MK, Patra MR (2015) An effective selection of mobile robot model using fuzzy logic approach. *Mater Today: Proc* 2(4–5):2605–2614. ISSN 2214-7853. <https://doi.org/10.1016/j.matpr.2015.0>
2. Jolly KG, Sreerama Kumar R, Vijayakumar R (2010) Intelligent task planning and action selection of a mobile robot in a multi-agent system through a fuzzy neural network approach. *Eng Appl Artif Intell* 23(6):923–933. ISSN 0952-1976. <https://doi.org/10.1016/j.engappai.2010.04.0>
3. Breaz R, Bologa O, Racz S-G (2017) Selecting industrial Robots for milling applications using AHP. *Procedia Comput Sci* 122:346–353. <https://doi.org/10.1016/j.procs.2017.11.379>
4. Breaz RE, Bologa O, Racz SG (2017) Selecting between CNC milling, robot milling and DMLS processes using a combined AHP and fuzzy approach. *Procedia Comput Sci* 122:796–803. ISSN 1877-0509. <https://doi.org/10.1016/j.procs.2017.11.439>
5. Keshavarz-Ghorabae M (2015) Developing an MCDM method for robot selection with interval type-2 fuzzy sets. *Robot Comput-Integr Manuf*. <https://doi.org/10.1016/j.rcim.2015.04.007>
6. Nasrollahi M, Ramezani J, Sadraei M (2020) A FBWM-PROMETHEE approach for industrial robot selection. *Heliyon* 6:e03859. <https://doi.org/10.1016/j.heliyon.2020.e03859>
7. Chatterjee P, Athawale V, Chakraborty S (2010) Selection of industrial robots using compromise ranking and outranking methods. *Robot Comput-Integr Manuf* 26:483–489. <https://doi.org/10.1016/j.rcim.2010.03.007>
8. Fu Y, Li M, Luo H, Huang G (2019) Industrial robot selection using stochastic multicriteria acceptability analysis for group decision making. *Robot Auton Syst* 122:103304. <https://doi.org/10.1016/j.robot.2019.103304>
9. Rajkumar, Kanansukuntha selection of robots using fuzzy for plant operation. [http://refhub.elsevier.com/S2405-8440\(20\)30704-0/sref12](http://refhub.elsevier.com/S2405-8440(20)30704-0/sref12)
10. Karsak E (2008) Robot selection using an integrated approach based on quality function deployment and fuzzy regression. *Int J Prod Res* 46:723–738. <https://doi.org/10.1080/00207540600919571>
11. Vithuin, anthraje selection of best robot using tops is for hotel server operation. <https://www.tandfonline.com/doi/full/>, <https://doi.org/10.1080/00207543.2010.530623?src=recsys>
12. Liu H-C, Ren M-L, Wu J, Lin Q-L (2014) An interval 2-tuple linguistic MCDM method for robot evaluation and selection. *Int J Prod Res* 52. <https://doi.org/10.1080/00207543.2013.854939>
13. Xue Y, You J, Zhao X, Liu H-C (2016) An integrated linguistic MCDM approach for robot evaluation and selection with incomplete weight information. *Int J Prod Res* 1–16. <https://doi.org/10.1080/00207543.2016.1146418>
14. Kwong CK, Bai H, Kwong CK, Bai H (2003) Determining the importance weights for the customer requirements in QFD using a fuzzy AHP with an extent analysis approach. *IIE Trans* 35:619–626. <https://doi.org/10.1080/07408170304355>
15. Yusuf T, Mustafa Y, Berna D (2013) Robotics and computer-integrated manufacturing, vol 29, Issue 4, August. <https://www.sciencedirect.com/science/journal/07365845>
16. Büyükoçkan G, Feyzioğlu O, Havle CA (2019) Intuitionistic Fuzzy AHP based strategic analysis of service quality in digital hospitality industry. *IFAC-PapersOnLine* 52:1687–1692. <https://doi.org/10.1016/j.ifacol.2019.11.443>
17. Başar O (2014) A decision model for information technology selection using AHP integrated TOPSIS-Grey: the case of content management systems. *Knowl-Based Syst* 70. <https://doi.org/10.1016/j.knosys.2014.02.010>
18. Pamucar D, Ćirović G (2015) The selection of transport and handling resources in logistics centers using multi-attributive border approximation area comparison (MABAC). *Expert Syst Appl* 42:3016–3028. <https://doi.org/10.1016/j.eswa.2014.11.057>

19. Kumar R, Garg R (2010) Optimal selection of robots by using distance based approach method. *Robot Comput-Integr Manuf* 26:500–506. <https://doi.org/10.1016/j.rcim.2010.03.012>
20. Krohling RA, Pacheco AGC (2015) TOPSIS—an approach based on TOPSIS for ranking evolutionary algorithms. *Procedia Comput Sci* 55:308–317. ISSN 1877-0509, <https://doi.org/10.1016/j.procs.2015.07.054>

Experimental Investigation on Performance and Emission Characteristics of Low Heat Rejection Engine Operating on Biodiesel



A. Vadivel, S. Periyasamy, V. V. Mithun Kumar, and M. Praveen

Abstract The aim of this experimental work is to explore the effect of a thermal barrier coating (TBC) on an Annona biodiesel-fueled diesel engine, where NiCrAl was a bond coat in which the cylinder head, piston crown, and valves were coated with a plasma spray process consisting of two layers. Furthermore, the mixing of Al_2O_3 and TiO_2 was selected as a second layer. The conversion of Annona squamosa seed oil to Annona methyl ester was achieved through the transesterification process. For testing, a Kirloskar TV1 model was used with a highly precise eddy current dynamometer for a direct injection single-cylinder diesel engine. In terms of performance characteristics, the brake thermal efficiency is raised by 5.59%, and the specific fuel consumption of the Annona biodiesel-coated engine was reduced by 10.81% compared to the diesel-coated engine. As the carbon test concerned CO, HC, and CO_2 were reduced in the Annona biodiesel-coated engine, the NO_x emission improved in biodiesel in comparison to diesel fuel.

Keywords Annona methyl ester · Thermal barrier coating · Low heat rejection

1 Introduction

The performance, emission, and combustion features of a diesel engine fueled with Annona biodiesel were explored by Ramalingam et al. [1]. 20% of Annona methyl ester (AME) with 80% diesel blends demonstrated improved engine performance and lower emissions relative to pure diesel. Experiments on the use of AME and the blends in the four-stroke diesel engine have been performed by R. Senthil et al. The experimental findings indicate that the BTE is 30% for A20 and 33% for diesel fuel.

A. Vadivel (✉) · V. V. Mithun Kumar · M. Praveen
Department of Mechanical Engineering, Sri Ramakrishna Engineering College, Coimbatore,
Tamil Nadu 641022, India
e-mail: vadivel.ayyakkannu@srec.ac.in

S. Periyasamy
Department of Mechanical Engineering, Government College of Technology, Coimbatore, Tamil
Nadu 641013, India

Without any change, the engine can work on biodiesel and its blends [2]. From their experiment, Varatharaju Perumal et al. found that the use of C. Viscose biodiesel lowers greenhouse gases like CO and HC to 30% and 20%, respectively, in diesel engines. While smoke and No_x are rising to 9.03 and 6.04% [3].

Hanley Hazar et al. found that the efficiency of coated engines was enhanced and the emission rate was reduced by thermal barrier layers in their experiment by using linseed oil and diesel blend as fuels in diesel engines in which the combustion chambers are coated with tungsten carbide by the plasma spray process [4]. From their examination using biodiesel-energized diesel engine with alumina-covered piston, Srinivasan Senthil Kumar et al. found that the BTE was improved by 4%, and the fuel consumption reduced by nine percent for B25 with coated engine compared to the base engine. Exhaust parameters were lowered relative to the uncoated piston engine for the B25 blend with coated piston [5]. Mohamed Musthafa concluded that partially stabilized zirconia is known as the best TBC material for an engine, and the process of plasma spray is commonly used to build a TBC on engine [6].

The efficiency and emission characteristics of the TBC-coated low heat rejection engine have been investigated by G. Vidyasagar Reddy et al. They used three separate TBC materials and observed that with the three coatings, nitrogen oxide emissions rose by 5.52, 10.1, and 14.87% relative to the base engine. This was attributed to the engine having a higher running temperature. Smoke opacity in LHR engines was also found to have been reduced by a greater amount compared to the uncoated engine [7]. Experiments using Annona biodiesel in the LHR engine have been investigated by Senthil Ramalingam et al. They observed that BSFC is lower for all test fuel when used in coated engines and also found that when replacing diesel fuel with biodiesel, CO and HC emissions were seen declined equally and that No_x emissions of the coated engine were increased [8]. M. J. Abedin et al. concluded that all LHR engines displayed improved engine efficiency and emission characteristics except that of No_x due to elevated combustion temperature by referring to separate papers on LHR engines and biodiesels [9]. An experiment on a single-cylinder thermal barrier-coated engine with AME as fuel was investigated by Senthil Ramalingam et al. They are combined with B20, B40, B60, and B80 diesel fuel and pure biodiesel. Finally, they disclosed that the B20 AME blended with diesel can be used without modifications as an alternative fuel in the LHR engine [10].

This experimental work, based on the literature survey, focused on efficiency, emission, and combustion attributes of the single-cylinder-computerized VCR engine coated with aluminum oxide and titanium oxide thermal barrier coating and used B20 AME biodiesel, to explore its viability as fuel over pure diesel.

2 Materials and Methods

2.1 Test Fuel

Annona squamosa seeds are obtained from Greenfield Agro Products Pvt. Ltd., Maharashtra, India. *Annona squamosa* seeds have been dried for a week, and afterward, the hard nuts have been isolated physically and the seeds have been extracted. For the production of oil, the seeds are crushed with a mechanical expeller. Five kilograms of seeds are taken to be crushed for a batch, with each batch of seed passing five times to obtain the maximum amount of oil. The oil obtained by filtering it with filters has been stored in a glass reagent bottle. For 10–12 h, the filtered oil was left to settle the minute particles of dust. Once the oil was filtered and settled, it was stored in a glass reagent bottle. Figure 1 shows the production of *Annona squamosa* seed oil by mechanical oil expellers.

The readied arrangement was more than once heated up to 55 °C before treatment. The heating arrangement was blended in with 10 g of potassium hydroxide and broke up in 300 ml methanol, and at that point, it is warmed constantly and mixed for an hour and a half. The arrangement was moved to a different walled-in area after the predefined period and permitted to agree it over a day with no interruption. Unrefined glycerin starts to settle, and AME ascends to the top one. The AME segregated and sifted with delicate sterile with water multiple times. It was warmed for the extraction of water particles prior to utilizing the arrangement gathered in the engine. Figure 2 shows the development of *Annona methyl ester* seed oil. Table 1 shows the distinctive physical and compound properties of clean diesel fuel, *Annona squamosa* seed oil, and B20 *Annona squamosa* seed methyl ester.



Fig. 1 a *Annona squamosa* seed, b mechanical oil expeller, and c *Annona squamosa* seed oil

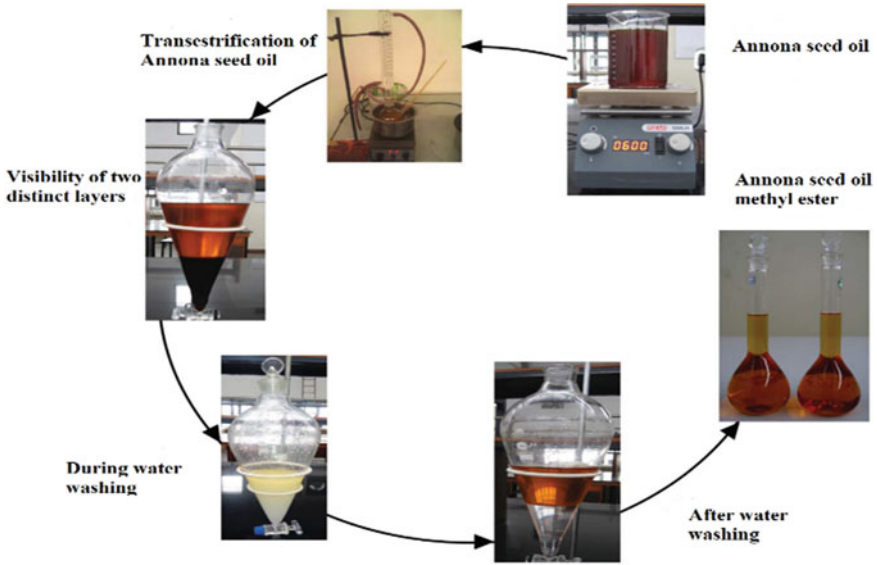


Fig. 2 Production of Annona biodiesel

Table 1 Thermal and chemical properties of neat diesel fuel, Annona squamosa seed oil and B20 Annona seed squamosa oil methyl ester

Property	Testing methods	Diesel	Annona oil	AME	B20 AME
Density (kg/m ³)	EN ISO 3675	830	880	872	750
Kinematic viscosity at 40 °C (mm ² /s)	EN ISO 3104	3.9	5.18	5.18	3.8
Gross calorific value (kJ/kg)	DIN 51,900	43,000	41,000	39,575	41,200
Flash point (°C)	EN ISO 3679	56	76	76	68
Fire point (°C)	EN 2301	64	92	92	73

2.2 Thermal Barrier Coating

Utilizing a plasma spray coating measure, TBC was added in the combustion chamber to the cylindrical form of the piston and the manifold. Figure 3 displays the uncoated and coated parts of the engine, such as the piston, the cylinder head, and even the inlet exhaust manifold. Figure 4 demonstrates the workings of the plasma spray coating technique. To build the erosion opposition of the covering in this work, the cylinder crown covered with 100 μm thickness of NiCrAl as a liner layer was covered with a combination of 150 μm thickness made out of aluminum and titanium oxide by plasma splash covering on the engine parts. The erosion resistance of the covering is improved with the extension of TiO₂ present in the YSZ. The motivation behind this

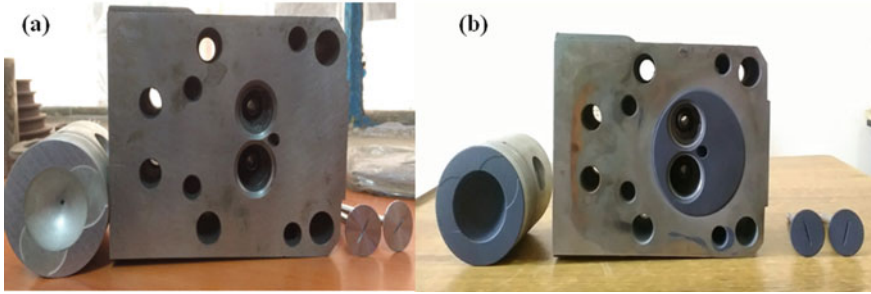


Fig. 3 a Uncoated engine and b coated engine parts

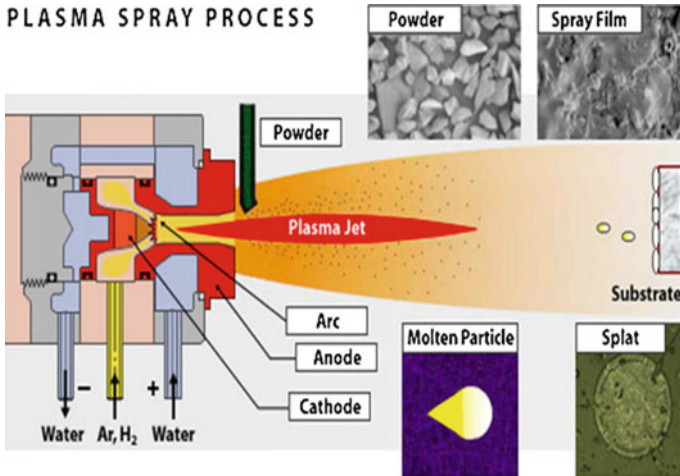


Fig. 4 Plasma spray coating technique

exploratory work is to investigate how the combination of aluminum and titanium oxide improves the IC engines' exhibition and outflow attributes. Table 2 shows the details of the plasma spray covering technique.

3 Experimental Setup

Table 3 lists out the detailed view of the test engine. The test rig comprises of a VCR engine, an eddy current dynamometer, a fluid cooling line, a fuel conveyance line and an electronic information assortment greasing up framework.

The visual view and model diagram of the laboratory test device with specimens of TBC and test fuel are shown in Figs. 5 and 6. The examination was led out utilizing an eddy current dynamometer. Using the AVL five-gas analyzer, engine discharge

Table 2 Detailed view of plasma spray coating technique

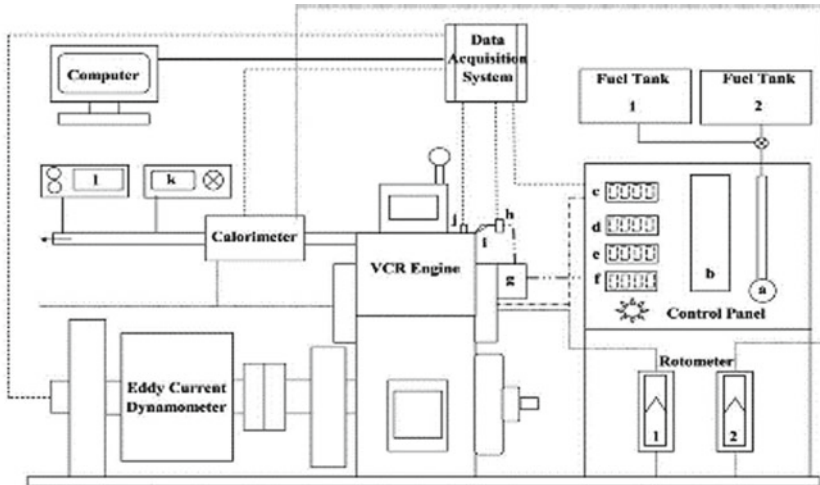
Coating parameters	Specifications
Distance of spraying	7.6–12.7 m
Current (A)	490–500
Plasma gun	3 MB plasma spray gun
Nozzle	GH-type nozzle
Voltage (V)	60–70
Particle velocity	Up to 450 m/s
Arc temperature	16,000 °C

Table 3 Specification of the test engine

Make and model	Kirloskar TV1
Type	Four-stroke, single-cylinder DI diesel engine
Bore × Stroke	87.5 mm × 110 mm
Rated power	5.2 kW
Compression ratio	17.5:1
Type of cooling	Water
Fuel injection	23° bTDC



Fig. 5 A visual view of the test engine



Control panel- a. Fuel measuring burette, b. U- tube manometer, c. Air box with sensors, d. Temperature indicator, e. Speed indicator, f. Load indicator with load adjuster. VCR Engine- g. Fuel filter and pump, h- Fuel line pressure sensor, i- Fuel injector, j- Combustion analyser. Rotometer- (i) Engine water supply, (ii) Calorimeter water supply. Engine exhaust line- k. AVL Five gas analyser, l. AVL Smokemeter.

- Water line for engine and calorimeter
- Electrical line from various sensors to DAQ
- Air flow line for engine
- . . . Diesel fuel line to engine
- Main interface line between DAQ and Computer

Fig. 6 Schematic of the experimental setup

qualities such as CO₂, CO, HC, and NO_x were estimated. Table 4 represents the attributes of the exhaust gas analyzer. Both yield and emanation attributes were done by utilizing the ARAI-EDACS regulator arrangement.

Table 4 Specification of AVL gas analyzer

Measures	CO, HC, NO _x
Range	CO: 0–10 (% volume) HC: 0–2000 (ppm) NO _x : 0–5000 (ppm)
Measurement frequency	About 1 Hz
Power supply	Built-in rechargeable battery 900 mAh
Dimensions	270 × 106 × 43 mm
Diameter of gas pipe	6 mm

3.1 Error Analysis

In particular, to evaluate the discrepancies in the experiments, an error assessment was conducted. As mentioned below, some uncertainties are assumed for the procedure: (a) calibration of equipment, (b) environmental and experimental conditions, (c) observations during the experiment, (d) and methods used for the experiment. During experimentation, the error is calculated by the propagation of error techniques following the Holman technique [15]. During the experiment, the total uncertainty was found to be $\pm 2.29\%$.

4 Results and Discussion

4.1 Brake Thermal Efficiency (BTE)

The BTE of different stacking conditions and diverse test fuel extents is given in Fig. 7 to infusion timing of 24° TDC at 220 bar infusion pressure. The BTE even improved from no load to full load conditions when the engine burden was expanded. For neat

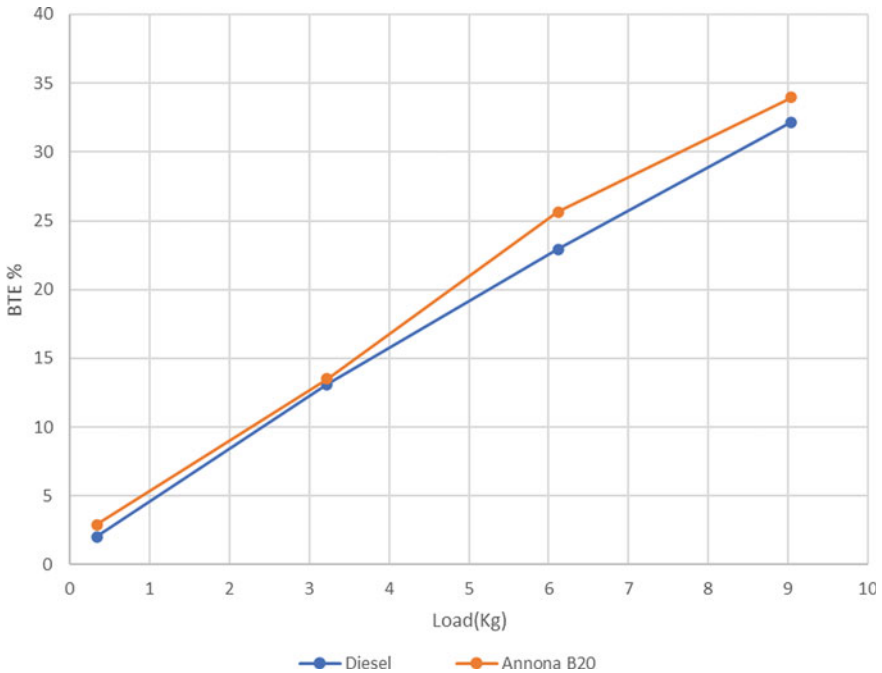


Fig. 7 BTE versus load

diesel fuel, yet for its higher calorific worth and lower viscosity, the BTE likewise improved when the engine load was expanded. In this way, the BTE was improved by 5.59% to the efficiency estimation of neat diesel at full burden conditions for the B20 biodiesel mix. From the examination information, it is to be sure certain that the peak BTE was obtained at full load conditions with B20 biofuel. This is on the grounds that the TBC does not permit the heat energy of the cylinder crown to be moved by cooling water or some other medium to the air.

4.2 Specific Fuel Consumption (SFC)

Figure 8 reveals SFC differences for diverse engine loads and 24° TDC infusion and 220 bar injection pressure. The SFC was higher than the mixed fuel in diverse charging conditions for neat diesel fuel. The B20 blend results in the SFC value 10.81% lower than the pure diesel fuel at full load and improved progressively for full load conditions. SFC drops due to reduction in fuel utilization and increased rate of energy transition in the TBC-coated engine under all load conditions.

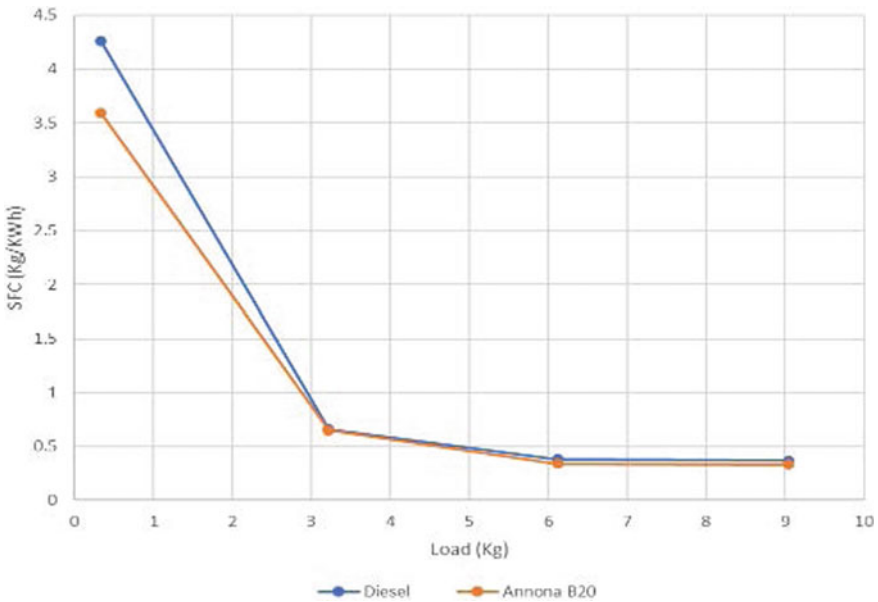


Fig. 8 SFC versus load

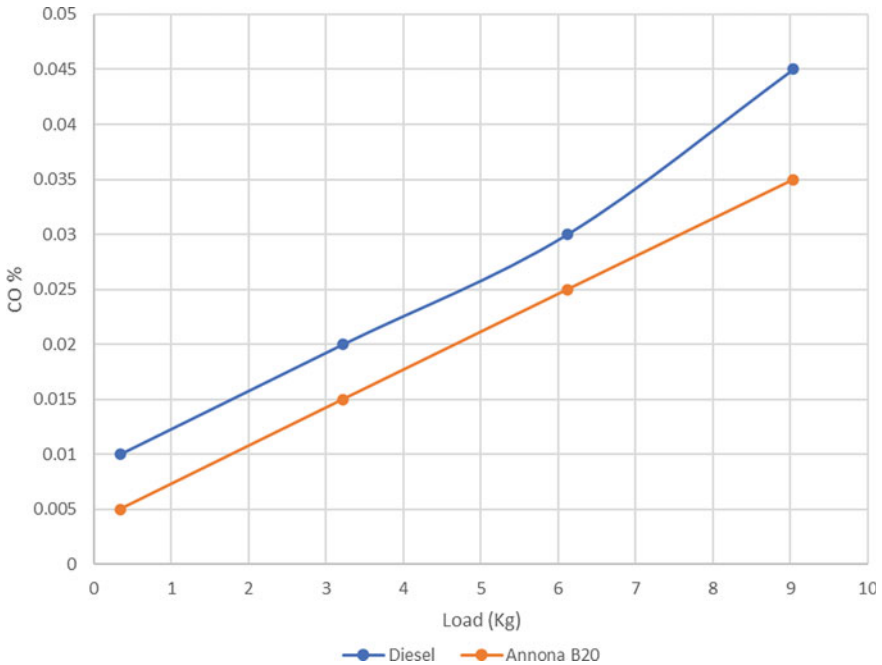


Fig. 9 Carbon monoxide versus load

4.3 Carbon Monoxide (CO)

Figure 9 indicates the carbon monoxide emissions for multiple engine loads and the mixture of biodiesel and gasoline. Based on the experimental findings, the biodiesel blend B20 has been shown to yield very low CO relative to pure diesel fuels began in no load to full load. Under no load environment, CO emissions of all test fuels were lowered by 22.22% relative to the pure diesel value and the overall load condition. The emission of CO from the LHR engine was significantly lower than normal vegetable oil engine. The oxygen intake of vegetable oil was also higher. The key reason behind the decline of CO emissions in a TBC engine is full combustion of gasoline.

4.4 Unburned Hydrocarbon (UHC)

Figure 10 indicates a difference of UHC with regard to a load for biomixing biofuel and diesel for the 220 bar injection pressure. The Annona B20 biodiesel fuel was less UHC than regular diesel when the load was up from 0 to 100% condition. The use of Annona B20 fuel showed a 7.27% reduction in UHC emissions relative to full load diesel fuel. We assume from the findings that the properties of combustion are

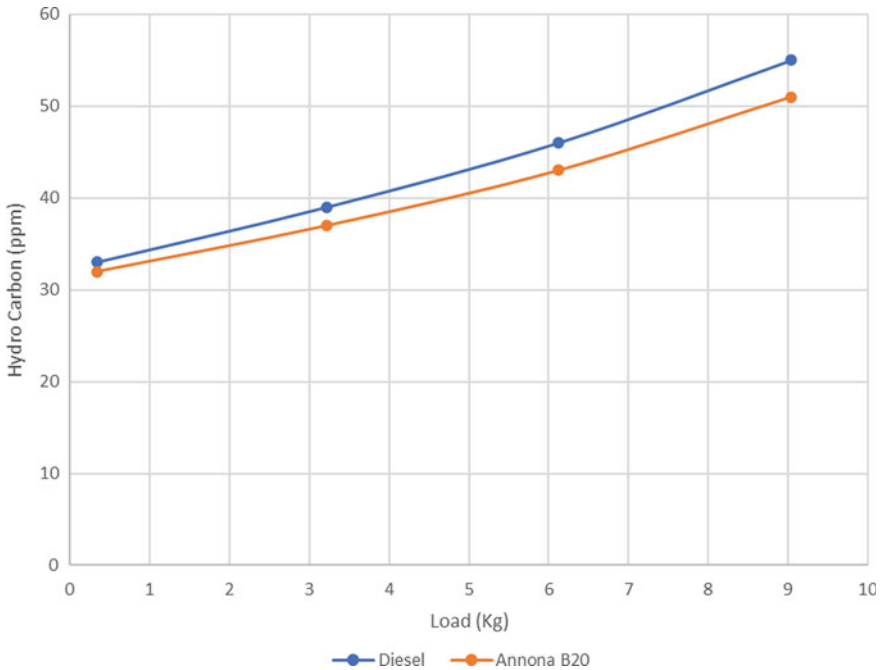


Fig. 10 Unburned hydrocarbon versus load

enhanced with the Annona B20. The key source of decreased HC emissions on the TBC-coated engine is the progressive lift in ignition temperature after a burning stage and the reduction in thermal degradation, and the TBC also tends to vaporize gasoline, resulting in lower hydrocarbon emission due to higher combustion temperatures.

4.5 Carbon Dioxide (CO₂)

Figure 11 indicates the carbon dioxide emission of biodiesel and diesel. It indicates that the carbon dioxide reduced when the biodiesel used during the combustible. Based on the experimental findings, the diesel fuel emitted high CO₂ emissions ranging from 1% at no charge to 1.8% at full load. Under no conditions of load, all B20 mixtures contain less CO₂ and do not bill for maximum load. With respect to the biodiesel mix, CO₂ emissions range from 0.9 to 1.7%, from no charge to full load. The findings from preliminary studies revealed a 5.55% reduction in CO₂ emissions from pure diesel fuel for the B20 mix.

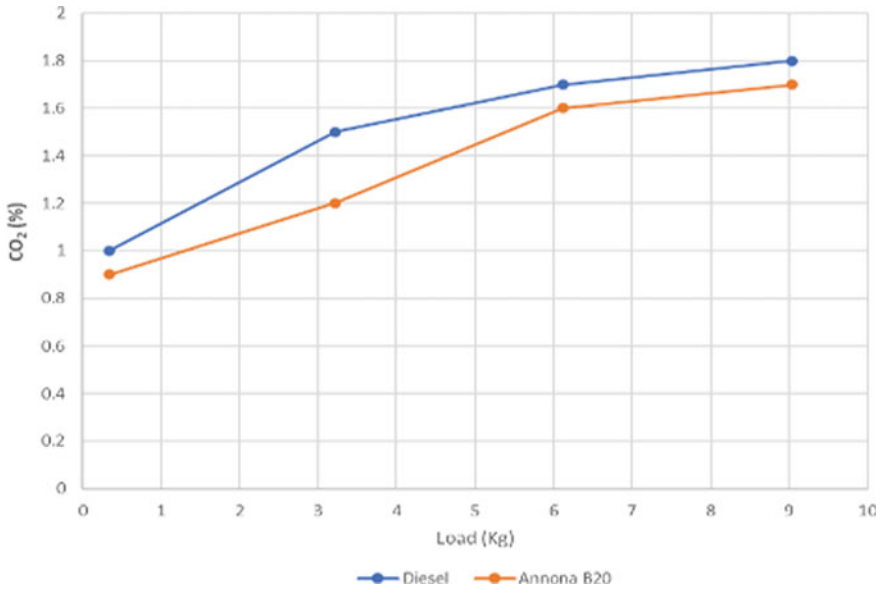


Fig. 11 CO versus load

4.6 Oxides of Nitrogen (NO_x)

Figure 12 reveals NO_x emissions for diesel and Annona B20 as fuels for different engine load conditions. The pollution in the biodiesel blend B20 rose by 12.9% in comparison to diesel at full load. The oxygen content and temperature accompanying the emission of NO_x are important considerations. Owing to the high combustion temperature, NO_x emissions in the LHR engine are even higher. Due to its higher oxygen ratio, biodiesel emissions showed greater NO_x in both the LHR and regular engines than diesel fuel. The engine has a more homogenous fuel–air combination and higher engine speeds. Consequently, at higher engine speeds, emissions of NO_x rise. The findings show that in contrast to unadulterated diesel fuel, the pollution results of NO_x improved in mixed fuel.

5 Conclusion

The study on single-cylinder engine, neat diesel fuel stacked with B20 biodiesel Annona, has been conducted out at constant speed. The plasma spraying process for turning one-cylinder diesel engine into such an LHR engine has been employed with bond layer of NiCrAl with 100-μm-thickness ceramic coating and aluminum and titanium oxide-coated with 150 μm thickness. The following findings were taken on the basis of the research observations. In contrast to pure diesel, the thermal effective

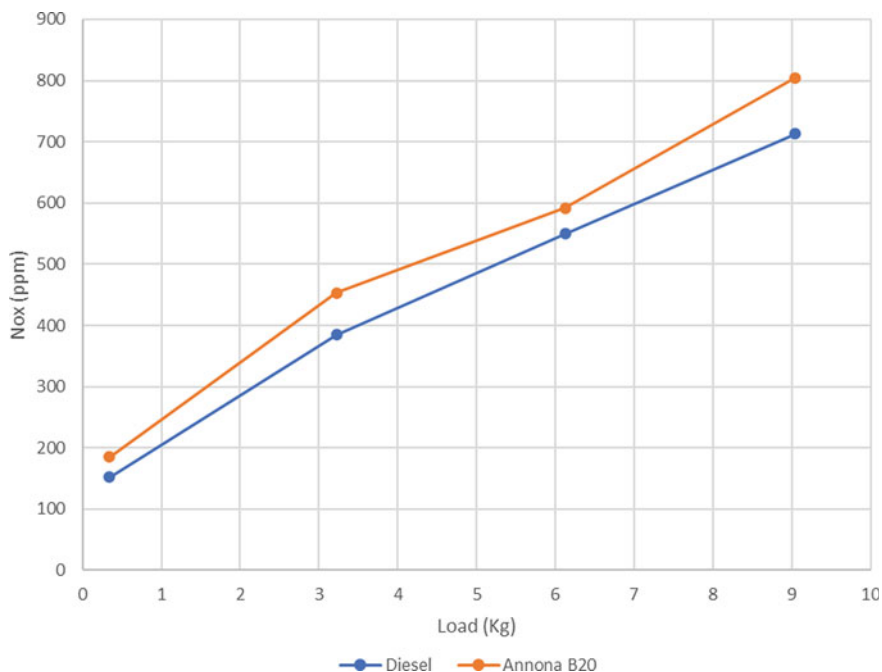


Fig. 12 NO_x versus load

braking power in the AME B20 improved 5.59% as the load of engines increased from no load to full load conditions. The B20 blend results in the SFC value 10.81% lower than neat diesel fuel at full load and improved progressively for full load conditions. The CO emissions were lowered by 22.22% relative to the value of pure diesel in the maximum load. Usage of Annona B20 fuel indicates a 7.27% reduction in UHC emissions in contrast to full load diesel fuel. The NO_x pollution in the biodiesel blend B20 climbed 12.9% as contrast to pure diesel fuel at maximum load conditions. In contrast with pure diesel fuel, emissions of B20 fuel have decreased by 5.55%. The findings obtained above demonstrate that the Annona seed oil methyl ester can be employed as a promising substitute in coated engine to conventional fuel.

References

1. Ramalingam S et al (2009) Use of antioxidant additives for NO_x mitigation in compression ignition engine operated with biodiesel from Annona oil. *Therm Sci* 20(4):S967–S972
2. Senthil R, Silambarasan R (2014) Annona: a new biodiesel for diesel engine: a comparative experimental investigation. *J Energy Inst* 88(4):459–469
3. Perumal V, Ilangkumaran M (2018) Experimental analysis of operating characteristics of a direct injection diesel engine fuelled with Cleome viscosa biodiesel. *Fuel* 224:379–384

4. Hazar H, Sevinc H (2019) Investigation of the effects of pre-heated linseed oil on performance and exhaust emission at a coated diesel engine. *Renew Energy* 130:961–967
5. Senthil Kumar S et al (2014) Performance analysis of a biodiesel fuelled diesel engine with the effect of alumina coated piston. *Therm Sci* 21:489–498
6. M. Mohamed Musthafa (2017): Thermal barrier coated diesel engine running on biodiesel: a review. *Int J Sustain Eng* 11(3) (2018)
7. Vidyasagar Reddy G, Govindha Rasu N, Hari Prasad T (2019) Analysis of performance and emission characteristics of TBC coated low heat rejection engine. *Int J Ambient Energy*. <https://doi.org/10.1080/01430750.2019.1567581>
8. Ramalingam S et al (2014) Application of thermal barrier coating for improving the suitability of annona biodiesel in a diesel engine. *Therm Sci* 20(Suppl. 4):S973–S979
9. Abedin MJ, Masjuki HH, Kalam MA, Sanjid A, Ashraful AM (2014) Combustion, performance, and emission characteristics of low heat rejection engine operating on various biodiesels and vegetable oils. *Energy Convers Manage* 85:173–189
10. Karthickeyan V (2019) Effect of cetane enhancer on Moringa oleifera biodiesel in a thermal coated direct injection diesel engine. *Fuel* 235:538–550

An Analytical Implementation of AHP in Supply Chain Working Environment



V. K. Pathak, N. Kumar, and R. K. Patel

Abstract As every organization wants to go parallel with the market demands to gain maximum profits, for achieving it, supply chain processes and demand forecasting of inventories play a vital role. On the basis of different parameters, inventories and supply chain will be planned accordingly and amended. For any company to work efficiently, the relation and trust between the consumer and consuming organization are very important. The idea of supply chain management has an extensive concern over worldwide economy. So in this research, article supply chain is so planned that the flow between them is always smooth and flexible according to the need of the consumer. After studying of various processes undergoing in the organization for efficient working of their supply chain, different criteria are selected. In this paper, analytic hierarchy process (AHP) is used for evaluation and ranking the supplier on the basis of their priority. The ranking of the suppliers according to those major criteria is obtained so that most efficient working supply chain for that particular organization is achieved, which makes supply chain smoother and efficient. This ultimately improves market share and customer satisfaction.

Keywords Supply chain · MCDM (AHP) · Ranking · Effective utilization

1 Introduction

In today's competitive international markets, the introduction of products with shorter existence cycles and the heightened expectancies of clients have forced enterprise establishments to put money and awareness interest on their deliver chains. This

V. K. Pathak (✉) · N. Kumar · R. K. Patel
Mechanical Engineering Department, KIET Group of Institutions, Ghaziabad, Uttar Pradesh, India
e-mail: vivek.pathak@kiet.edu

R. K. Patel
e-mail: rajesh.patel@kiet.edu

© The Author(s), under exclusive license to Springer Nature Singapore Pte Ltd. 2022
K. Govindan et al. (eds.), *Advances in Mechanical and Materials Technology*,
Lecture Notes in Mechanical Engineering,
https://doi.org/10.1007/978-981-16-2794-1_85

969

collectively with continuing advances in communications and transportation technology (e.g., cell verbal exchange, Internet, and in a single day transport), has stimulated the non-stop evolution of the deliver chain and of the techniques to manage it efficiently. In a standard supply chain, unprepared materials are procured, and objects are produced at one or more factories, shipped to warehouses for intermediate storage. After that it shipped to shops or customers [2]. Consequently, to reduce fee and enhance service levels, powerful deliver chain techniques have to recollect the interactions on the various levels within the deliver chain.

1.1 Principles of SCM

It has ended up top management's new "religion," and then, it needs a guideline. Andersen consulting has progressed to offer the needed steering, espousing what it calls the "Seven Principles" of supply chain control [4]. When always and comprehensively followed, the consulting firm says, those seven concepts carry a bunch of competitive advantages.

The seven standards as articulated through Andersen consulting are as follows:

- (a) Segment clients primarily based on provider desires
- (b) Customize the supply chain management community
- (c) Listen to indicators of marketplace demand and plan accordingly
- (d) Differentiate product closer to the purchaser
- (e) Strategically control the resources of supply
- (f) Develop a deliver chain-wide technology method
- (g) Adopt channel-spanning overall performance measures.

1.2 Decisions in SCM

When running in a delivery chain control framework one of the significant result to perceive roughly the importance of dynamic and furthermore knowing the expense of forces. Delivery chain decision making is classified by using Ram Ganeshan and Terry Harrison. They broadly classified deliver chain decisions into:

- Location decisions
- Production decisions
- Inventory decisions
- Transportation decisions.

These decisions are responsible for smooth flow of supply chain. Various researchers found that these decisions are highly important when we implement it on supply chain.

2 Literature Review

The literature review highlights developments in the supply chain. The literature covers various areas like stochastic demand, transportation, operational cost, traffic congestion, levels of customer service and multi-source shipping, travel time and distance, and buyer-to-buyer relationships. There are many researchers find different methodology for supplier selection in the field of supply chain. To capture the interests of various stakeholders, (Harrington et al. 2016) proposed a research work. Researchers applied ANP and AHP techniques in supply chain coordination research (Shukla et al. 2018). Wohlrab (2016) identified design criteria for urban system “last mile” solutions. Singh et al. [6] studied “Assessment and optimization of distinct network using an AHP approach,” and Singh et al. [5] analyzed “Robust strategies for mitigating operational and disruption risks using a fuzzy AHP approach.”

Kumar et al. (2011) recommend an alternator/supplier assortment technique designed for price modeling that allows the selection of the best inclusive dealer through allowing for low-value packing substances used in huge measures for deal with meals merchandise Grimm et al. (2014). Discover the controller of sub-suppliers’ agreement with recognize to sustainability components. Govindan et al. (2017) explain a dealer assortment problem inside the meals resource sequence using a mixture technique that consists of the reviewed similar manner.

On the basis of different survey, this paper provides a best solution to select supplier for particular organization in the supply chain.

3 Methodology

3.1 *Multi-criteria Decision-Making Analysis (MCDMA) [2]*

This is a valuable device that we can practice to many complex decisions. It is most applicable to fixing problems which are characterized as a choice among alternatives. It has all of the traits of a useful selection aid tool. It helps us to focus on what is essential, logical and steady, and is straightforward to apply. MCDA is used for:

- Dividing the decision into smaller, more understandable parts.
- Analyzing each part.
- Integrating the parts to produce a meaningful solution.

When used for group decision making, MCDA allows corporations speak about their decision opportunity (the trouble to be solved) in a manner that allows them to do not forget the values that each perspectives as important. It also affords a unique ability for human beings to recollect and communicate about complicated change-offs among alternatives.

3.2 Analytic Hierarchy Process (AHP)

AHP is a multi-criterion decision-making technique dependent on the priority hypothesis. It offers with complex issues that include the consideration of various criteria/options at the same time [6]. Saaty (1980) at first developed AHP to allow selection making in situations characterized by using a couple of attributes and options. Four important steps in making use of the AHP technique are as follows:

- Build up a chain of importance of variables affecting an ultimate choice. This is known as the AHP choice model.
- Inspire pairwise examinations between the elements utilizing contributions from clients/supervisors.
- Assess relative significance loads at each degree of the chain of importance.
- Consolidate relative significance loads to acquire a general positioning of the three competitors.

So we are discussing to select the excellent dealer for the company A in order that a non-stop glide in the deliver chain of the business enterprise is maintained. We should perform the system for four dealers available the choice is to be accomplished on the basis of the attributes. It might be most essential for the employer. It has furnished with the four most critical criteria. The statistics of the entire characteristic for all the dealers is also supplied.

There are four criteria selected:

- License (L)
- Turnover (T)
- Experience (E)
- Repeatability in billing (R).

License As enquired through the company in which we are working on, we got here to end that license is one of the maximum important attribute as without license no provider is authorized to do enterprise with the organization. Dealer should possess the legitimate seed license in conjunction with store/sale counter ownership proof.

Turnover It is the yearly common commercial enterprise that the provider does with the corporation. Dealer has to have done an annual average commercial enterprise of at least three lakh from sales of seeds during that duration.

Experience It is the degree of earlier knowledge that a dealer should have before it may begin enterprise with the agency. They have to have as a minimum 1 year experience within the seed business.

Repeatability in Billing The company prefers a provider that is ordinary in taking the orders and is likewise regular in the quantity of order it takes. They must at least repeat the order in a regular sample for one season of the seed (Table 1).

Table 1 Dealer detail

Dealer	License	Turnover (Rs.)	Experience (Years)	Repeatability in billing (months)
Dealer 1	Yes	23,31,354.93	25	3
Dealer 2	Yes	1,41,372.14	7	5
Dealer 3	Yes	10,38,093.14	10	4
Dealer 4	Yes	48,180.00	3	3

Table 2 AHP importance comparison

AHP scale of significance	Numeric value	Reciprocal
Extreme importance	9	1/9
Very strong to extremely	8	1/8
Very strong importance	7	1/7
Strong to very strong	6	1/6
Strong importance	5	1/5
Moderately to strong	4	¼
Moderate importance	3	1/3
Equally to moderately	2	½
Equal importance	1	1

These details are approximated data which were acquired from company A, and this data will help in the analyzing the problem and coming to the solution of the numerical value.

Step 1 Decompose the problem into hierarchy of criteria, sub-criteria, and alternative (Table 2).

Step 2 Normalize—Each entry divide by column sum and take over all row range.

Step 3 Calculate consistency ratio (C.R).

C.R. = C.I./R.I.,

and C.I. = $\frac{\lambda_{max} - n}{n - 1}$,

If C.R. is less than 0.1 or 10%, matrix is consistent.

If C.R. is more than 0.1 or 10%, matrix is inconsistent (Table 3).

Table 3 Standard table for random index

N	1	2	3	4	5	6
Random index	0	0	0.52	0.90	1.11	1.25

4 Calculations for Each Criteria

- **License:** Formulation of initial matrix (Table 4)

Normalize matrix (Table 5).

Calculate Consistency Ratio

$$\text{Max. eigenvalue} = (4 * 0.25) + (4 * 0.25) + (4 * 0.25) + (4 * 0.25) = 4$$

$$\text{C.I.} = 4 - 4 / (4 - 1) = 0, \quad \text{C.R.} = 0$$

Now, as the value of C.R. for license is zero, this means that it is less than 0.1 or 10%; therefore, the matrix is consistence. Thus, the comparison is reliable and will give a predictable result.

- **Turnover**

(a) Formulation of initial matrix (Table 6)

(b) Normalize matrix (Table 7)

Calculate Consistency Ratio

For this, following calculation is required of max. eigenvalue.

$$= (1.58 * 0.6022) + (13.5 * 0.0852) + (4.533 * 0.25) + (15 * 0.0618).$$

$$= 4.167$$

$$\text{C.I.} = 0.055, \quad \text{C.R.} = 0.06172$$

Table 4 Formulation

1	1	1	1
1	1	1	1
1	1	1	1
1	1	1	1

Table 5 Normalization

0.25	0.25	0.25	0.25
0.25	0.25	0.25	0.25
0.25	0.25	0.25	0.25
0.25	0.25	0.25	0.25

Table 6 Formulization

1	7	3	9
1/7	1	1/5	2
1/3	5	1	3
1/9	1/2	1/3	1

Table 7 Normalization

0.63	0.51	0.66	0.60
0.09	0.074	0.044	0.13
0.21	0.370	0.220	0.2
0.07	0.037	0.073	0.067

Now, as the value of C.R. for license is 0.06172, this means that it is less than 0.1 or 10%; therefore, the matrix is consistence. Thus, the comparison is reliable and will give a predictable result.

• **Experience**

- Formulation of initial matrix (Table 8)
- Normalize matrix (Table 9)

Calculate Consistency Ratio

For this, following calculation is required of max. eigenvalue.

$$= (1.453 * 0.667) + (8.5 * 0.1112) + (8.833 * 0.1616) + (15 * 0.059).$$

$$= 4.225$$

$$C.I. = 0.07502, \quad C.R. = 0.0833$$

Now, as the value of C.R. for license is 0.0833, this means that it is less than 0.1 or 10%; therefore, the matrix is consistence. Thus, the comparison is reliable and will give a predictable result.

• **Repeatability in billing**

- Formulation of initial matrix (Table 10)
- Normalize matrix (Table 11)

Calculate consistency ratio

For this, following calculation is required of max. eigenvalue.

Table 8 Formulation

1	5	7	9
1/5	1	1/2	2
1/7	2	1	3
1/9	1/2	1/3	1

Table 9 Normalization

0.688	0.588	0.792	0.60
0.1376	0.1176	0.0566	0.133
0.098	0.235	0.113	0.20
0.0764	0.058	0.0377	0.066

Table 10 Formulation

1	7	5	1
1/7	1	1/5	1/7
1/5	5	1	1/5
1	7	5	1

Table 11 Normalization

0.427	0.35	0.446	0.427
0.00610	0.05	0.0178	0.0610
0.085	0.25	0.089	0.085
0.427	0.35	0.446	0.42

$$= (2.34 * 0.4125) + (20 * 0.047) + (11.2 * 0.127) + (2.34 * 0.4125).$$

$$= 4.3037$$

$$C.I. = 0.1012, \quad C.R. = 0.0112$$

As the value of C.R. for license is 0.0112, this means that it is less than 0.1 or 10%; therefore, the matrix is consistence. Thus, the comparison is reliable and will give a predictable result.

So making an initial matrix by comparing the criteria among themselves and the checking for its consistency (Table 12).

Formulation of Initial Matrix

- Normalize matrix (Table 13)

Calculate Consistency Ratio

For this, following calculation is required of max. eigenvalue.

Table 12 Formulation

Attributes	License	Turnover	Exp	Repeatability in billing
License	1	5	7	9
Turnover	1/5	1	4	3
Experience	1/7	1/4	1	2
Repeatability in billing	1/9	1/3	1/2	1

Table 13 Normalization

0.688	0.759	0.56	0.6
0.1376	0.1519	0.32	0.2
0.764	0.037	0.08	0.133
0.0764	0.0506	0.04	0.067

Table 14 Multiplication of row average of attributes with row average of normalized matrix of attributes

0.25	0.6022	0.667	0.4125	0.651
0.25	0.0852	0.112	0.0474 × 0.2023	
0.25	0.25	0.1616	0.1272	0.0873
0.25	0.0618	0.059	0.4125	0.0585

$$= (1.45 * 0.65) + (6.583 * 0.2023) + (12.5 * 0.0873) + (15 * 0.0585).$$

$$= 4.246$$

$$C.I. = 0.08213, \quad C.R. = 0.0912$$

Now, as the value of C.R. for all the selected attributes is 0.0912, this means that it is less than 0.1 or 10%; therefore, the matrix is consistence. Thus, the comparison is reliable and will give a predictable result.

So to calculate the ranking of the dealer we must multiply the matrix comprised of row average of particular attribute with the row average of the normalize matrix of attribute comparison matrix.

On solving Table 14, we get following results:

$$\text{Dealer 1} = 0.3669 = 36.69\%$$

$$\text{Dealer 2} = 0.1924 = 19.24\%$$

$$\text{Dealer 3} = 0.2348 = 23.48\%$$

$$\text{Dealer 4} = 0.2045 = 20.45\%.$$

5 Result

The percentage calculated above is the representation of which dealer is most consistent and reliable. It will give the smoothest flow in the supply chain of the company ranking on the basis of calculation. It is observed that dealer 1 is most reliable with 36.69% consistency. Dealer 3 is second most reliable with 23.48% consistency. Dealer 4 is third most reliable with 20.45% consistency. Dealer 2 is least reliable with 19.24% consistency. The initial comparison matrix is made and solved to know which attribute is having more value than the other. It may be possible that an ideal dealer is created to compare other dealers with it and prepare an initial matrix. But a drawback in that approach will be that a true solution will not be achieved as in every comparison. The comparison was done according to the criteria given by the company, and the importance of criteria over the other is assumed because of effectiveness on the selection, and then, the assumption is validated using comparison matrix and calculating consistency.

6 Conclusion

Supply chain is a growing and very important field for the development of the organization. It is not only improving the customer manufacturer relation but also helps in reduction of losses and also optimizing the processing. Supply chain has become a very important part of the rapidly developing world. It quantifies the decisions which were formerly achieved only by the assumption of the most experienced and predictable person of the organization. Thus, supply chain is a vast and growing subject which can be applied in most easy problems at domestic to the complex problem in industries. Every organization to improve its customer relation reduces its processing time and improves quality. So the main focus to maximize the profit must apply supply chain in its organization. From different methods for solving the problem, to choose best dealer in order to maintain the profit, we apply the AHP technique for analysis of different dealers such that which dealer is good in respective field. We obtained the information regarding the dealer from XYZ in supply of seeds for loading and unloading in the market. We try to form the rank of dealer by solving the different matrix and obtain which dealer will be perfect for assisting the supply chain cycle from supplier to dealer and dealer to farmer. So the losses in supply of product under different circumstance can be minimizing. To conclude, a supply chain is a key of success in every company and methods like MCDM helps in quantitating the problems and gain a permanent and practical solution.

References

1. Agarwal A, Shankar R (2003) On-line trust building in e-enabled supply chain. *Supply Chain Manag Int J* 8(4):324–334
2. Agarwal A, Shankar R, Tiwari MK (2007) Modeling agility of supply chain. *J Ind Mark Manag* 36(4):443–457
3. Agarwal A, Shankar R, Tiwari MK (2006) Modeling the metrics of lean, agile and leagile supply chain: an ANP-based approach. *Eur J Oper Res* 173:211–225
4. Chopra S, Meindl P, Kalra DV (2012) *Supply chain management: strategy, planning and operations*, 3rd edn. Pearson Education, INC
5. Singh AR, Mishra PK, Rajeev J, Khurana MK (2012) Robust strategies for mitigating operational and disruption risks—a fuzzy AHP approach. *Int J Multicriteria Decis Making* 2(1):1–28
6. Singh AR, Mishra PK, Rajeev J, Animesh M (2010) Assessment and optimization of distinct network- An AHP approach. In: *Proceedings of international conference on science, engineering and spirituality*, Navalnagar, 1–2 April
7. Morgan C (2004) Structure, speed and salience: performance measurement in the supply chain. *Bus Process Manag J* 10:522–536
8. Brewer PC, Speh TW (2000) Using the balanced scorecard to measure supply chain performance. *J Bus Logist* 21:75–94

9. Chen ZH, Wang HS (2008) Supplier selection and supply quantity allocation of common and non-common parts with multiple criteria under multiple products. *Comput Ind Eng* 55(1):110–133
10. Luthra S, Garg D, Haleem A (2016) The impacts of critical success factors for implementing green supply chain management towards sustainability: an empirical investigation of Indian automobile industry. *J Cleaner Prod* 121:142–158 (10 May 2016)

Simulation and Experimental Analysis of Multi-fragment Directional Warhead



Pankaj K. Choudha  and A. Kumaraswamy

Abstract Multi-fragment directional warheads are used for military applications. Directional fragmentation warhead having double profile, i.e. convex in azimuth and concave in elevation has been designed to direct the premade fragments in the angular zone of $70^\circ \times 5^\circ$. The design was finalized using theoretical calculations of fragment velocities, ejection angles and numerical analysis using 3D quarter symmetric model in ANSYS-AUTODYN software. Explosive PBX was modelled using JWL equation and stainless steel spherical fragments using shock equation of state and Steinberg–Guinan strength model. Simulation results were analysed for fragment velocities and its ejection angles. The effect of plastic casing of warhead on fragment velocity and ejection angles is studied. Further, the warhead was fabricated and tested for its performance. Experimental results matched very closely with numerical predictions.

Keywords JWL equation · Fragment velocity · Ejection angles

Nomenclature

ρ_e	Explosive density; kg/m^3
a, b	JWL constant; Pa
R_1, R_2, ω	JWL constant;
V_d	Detonation velocity; m/s
e	Specific internal energy; J/m^3
P_{cj}	CJ detonation pressure; Pa
P	Current pressure; Pa
ρ_s	Density of steel; kg/m^3
ν	Poisson's ratio;

P. K. Choudha (✉)

Armament Research & Development Establishment, Pashan, Pune 411021, India

A. Kumaraswamy

Defence Institute of Advanced Technology, Girinagar, Pune 411025, India

q	Specific heat; J/kg °K
Y_0	Initial yield stress; Pa
β	Hardening constant; Pa
n	Hardening exponent;
C, C_1, C_2	Bulk sound speed; m/s
S, S_1, S_2	Constant for linear and quadratic term;
T_m	Melting temperature; °K
ε_p	Effective plastic strain;
V_0	Initial volume;
V	Current volume;
l	Length of charge; mm
w	Width of charge; mm
t	Charge thickness; mm
L_n	Distance of n th fragment along length; mm
L_{\max}	Length of charge from centre; mm
W_n	Distance of n th fragment along width; mm
W_{\max}	Width of charge from centre; mm
r	Radial location of fragment; mm
r_{\max}	Maximum radius of cylindrical warhead; mm
θ	Ejection angle of fragment with normal to the explosive/metal interface;
δ	Angle between detonation point and normal to the explosive/metal interface location;
T	Current temperature; 0 K
G_0	Initial shear modulus; Pa
G'_p	Shear modulus derivative of pressure;
G'_T	Shear modulus derivative of temperature; Pa/°K
Y'_p	Yield stress derivative of pressure;
Y_{pc}	Plastic stress of polycarbonate;
Γ	Gruneisen Gamma;
ε_f	Geometric failure strain;
$\sqrt{2E}$	Gurney constant; m/s
C_o	Overall explosive mass; kg
M_o	Overall metal mass; kg
k	Velocity correction factor;
ρ_s	Fragment density; kg/m ³
V_{\max}	Maximum fragment velocity; m/s
V_f	Fragment velocity; m/s
\varnothing_e	Elevation angle from central axis; 0
\varnothing_a	Azimuth angle from central axis; 0

1 Introduction

Multi-fragment directional warheads are used in missile, rockets and ammunition systems for military applications to destroy the enemy targets. A fragmentation warhead consists of an explosive charge surrounded by a solid or scored metal casing or preformed metal fragments held together by adhesive in outer casing. During fragmentation process, they generate a large number of fragments. Projectile uses natural fragmentation generating different shapes and masses of fragments which depends on the casing material and its grain structure [1]. For rocket, missile and land-based munitions, preformed fragmentation warheads are preferred. Preformed fragment of various shapes, i.e. sphere, cube, rods, wire weighing from 0.38 to 14.25 g, are used in these devices [2].

Fragment lethal range depends on its initial velocity, mass and shape. Fragment velocity is estimated using Gurney equation for spherical, cylindrical and sandwich warheads [3, 4]. The ejection angles of fragments are estimated based on Taylor equation. The shock loading, i.e. head on and side on, will affect the ejection velocities and directions of fragments [5]. HEMP hydro code was used for calculating the fragment velocity and ejection angles considering leakage of gases [6]. Zhou et al. discussed the effect of gas leakage along with the disintegration of cylindrical shell on fragment acceleration [7]. König suggested a method for correction of ejection angle of fragments from a cylindrical warhead [8]. Parallel control of fragments using concave contour has been studied [9]. Influence of peripheral frame parameters on fragments dispersion was discussed for directional warhead [10].

Asymmetric initiation of cylindrical warhead affects the distribution of radial fragment velocity [11]. The influence of initiation of charge on the fragment scattering characteristics is studied by Wang et al. [12]. Guang et al. have discussed the effect of the rarefaction wave on fragment velocity distribution at both the ends of cylindrical warhead [13]. Further, cylindrical hollow core and non-cylindrical symmetry geometrics were studied for fragment velocities distribution along the length [14, 15]. Liangliang et al. have investigated 'D' shape cylindrical with convex and concave curvature for fragment velocities and spatial distributions [16]. Theory of oblique shock is proposed for correction of ejection angles estimation for 'D' shaped warheads [17]. The concave curvature can be worked out based on proposed optical theory [18]. A multilayer 'D' shaped warheads were studied using x-ray technique for velocity of different layers [19]. Determination of velocity characteristics of fragments of a prismatic casing is proposed [20]. The experimental studies were conducted for dispersion angles of concave disc with 160°, 170° and 175° warheads [21]. Dhote et al. have studied the standard deviations for ejection angles [22].

Comprehensive review of literature revealed that directional fragment devices of cylindrical or rectangular shape having either convex or concave curvature with uniform cross section have been analysed. Dhote et al. [23] proposed a design methodology of directional warhead using modified Gurney equation for fragment velocity and modified Tylor equation for ejection angles of convex profile. However, modified Tylor equation for ejection angle is not suitable for narrow fragment beam with

concave profile. In view of the above albeit partially, in the present study, a rectangular double curvature warhead was analysed to achieve the azimuth angle (\varnothing_a) of 70° while the elevation beam angle (\varnothing_e) is just 5° . To meet this requirement, convex profile for larger dispersion in azimuth direction and concave profile in elevation for narrow beam is considered. The design was analysed in detail and experimentally verified.

2 Design Methodology

The basic design of warhead was carried out using based on the fragment velocity and ejection angles of fragments. The parameters affecting the fragment velocity are C_o/M_o ratio, t , w and l of a given explosive charge. The modified Gurney Eq. (1) is used for estimation of maximum fragment velocity using correction factor k of 0.9 [23]. The Gurney constant value can be estimated using various methods proposed by Dany [24]. $\sqrt{2E}$ for PBX is considered 2600 m/s. Similar correction factor value of k is also suggested as 0.8 for open sandwich cylindrical charge without liner configuration [10]. Correction factor k depends upon the warhead construction having fragments with metallic liner, glued in composite matrix or only fragments (spherical or cubical). Variation of fragment velocity along radial direction is given by Eq. (2). The ejection angles were estimated in azimuth direction by Eq. (3) [4].

$$V_{\max} = k\sqrt{2E} \frac{\sqrt{3}\left(\frac{C_o}{M_o}\right)}{\left\{\left(\frac{C_o}{M_o} + 4\right)\left(\frac{C_o}{M_o} + 1\right)\left(1 + \frac{t}{l} + \frac{t}{w}\right)\right\}^{1/2}} \tag{1}$$

$$V_f = V_{\max} \left(\frac{2}{3} + \frac{1}{3} \sqrt{1 - \left(\frac{r}{r_{\max}}\right)^2} \right) \tag{2}$$

$$\sin(\theta) = \sin(\delta) \left(\frac{V_f}{2V_d} \right) \tag{3}$$

Based on above equations, the basic configuration was finalized. The azimuth profile of radius 232.97 mm was selected based on theoretical ejection angle. The elevation profile was designed based on a parametric study of concave curvature.

3 Numerical Modelling

Numerical modelling of fragmentation warhead was carried out using ANSYS-AUTODYN software. Design configuration involves the modelling of explosive,

fragments, plastic casing and Euler domain. The geometry, materials, modelling and validation details are discussed in subsequent sections.

3.1 Geometry Details

MFELD consists of explosive with rectangular geometry ($228 \times 126 \text{ mm}^2$) and a single layer of fragments as shown in Fig. 1c. The PBX explosive thickness of 45 mm at centre is selected such that minimum charge to metal ratio is achieved for lethality requirements. The front side of explosive shape, adjacent to fragments has double curvature. A composite half-concave profile was constructed with radius of 600 mm at centre of the charge for 35 mm width and radius of 120 mm for a width of 28.5 mm at the end of explosive charge as shown in Fig. 1c. Stainless steel fragments of $\phi 6 \text{ mm}$ having mass of 0.89 g are positioned. 172 fragments are arranged, in a rectangular pattern of 10 rows and 19 columns in a quarter. The charge and metal

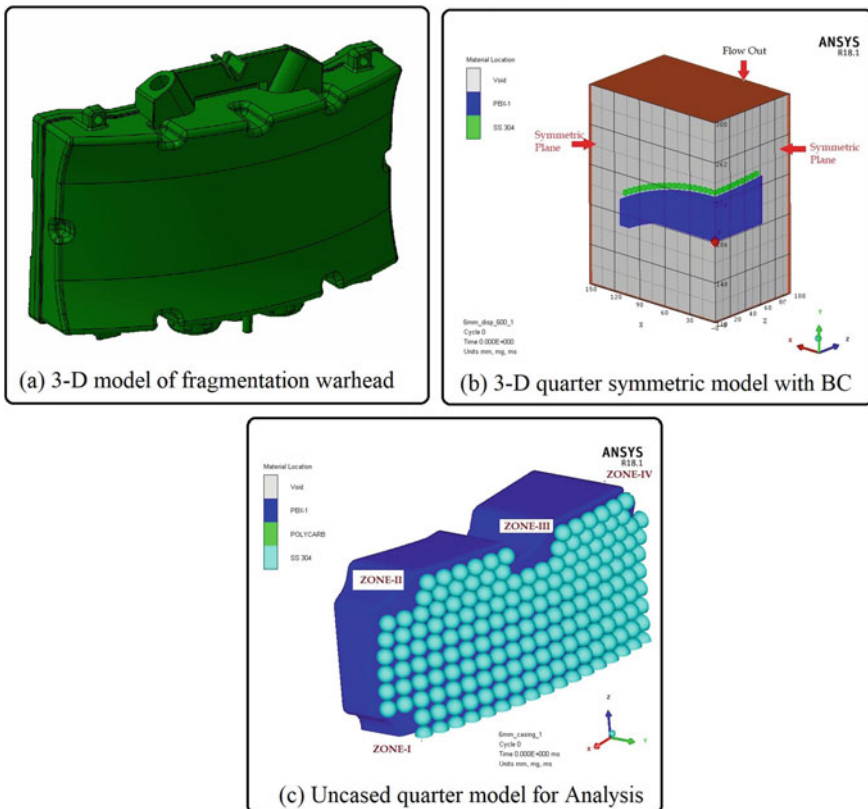


Fig. 1 Details of fragmentation warhead modelling for simulation

fragments enclosed in a plastic casing of 3 mm thickness of polycarbonate along with other design constraints have been simulated considering high strain rate material behaviour as presented in the literature [25, 26]. The material piecewise JC material model was considered as proposed in AUTODYN material library. The plastic stress and plastic strains were considered in four pieces as given in Tables 4 and 5. The casing is modified in such a way that it can accommodate the screws for back lid, and hence, no explosives and fragments can be placed in casing as shown in zone I, II, III and IV. The detonation point is fixed at the centre on the rear side of explosive as shown in Fig. 1b. The rear face is considered flat at the centre of explosive.

3.2 Details of Model and Simulation Methodology

3D geometry is created in CATIA and then this geometry is exported to ANSYS using the standard translator. This quarter geometry is converted to FE mesh and then transferred to AUTODYN. The 3D quarter symmetry model is as shown in Fig. 1b. Further, the Euler domain of $150 \times 190 \times 100 \text{ mm}^3$ is created with 1 mm element size in x , y and z directions. The spheres were meshed using unstructured Lagrange elements of tetrahedral and hexahedral combinations of 1 mm size. The interaction of explosive and fragments was fully coupled using Euler–Lagrange interaction algorithm.

All the boundary conditions were defined in the model. The symmetry boundary conditions are defined in XY and YZ plane. All the nodes of fragments lying on XY plane were applied zero velocity in the z direction. Similarly, all the nodes of fragments lying on YZ plane were constrained in x direction. Flow out boundary conditions are applied as shown in Fig. 1b, on all the four sides to allow the expanded explosive gases to flow out. Once the explosion is initiated through the detonation point, the detonation wave travels through the explosive and converts it into a high-pressure shock wave. In addition, the explosive is converted to ideal gas. These high-pressure gases expand and interact with fragments. Hence, the effect of modelling of air at atmospheric pressure around the fragment module is ignored.

The simulation time is considered such that the absolute velocities of fragments become constant. Then, the velocities along x , y and z -axis are extracted. The directions are determined for azimuth (\varnothing_a) and elevation (\varnothing_e) ejection angles for each fragment.

3.3 Material Properties

Modelling of explosive for describes the detonation product expansion for high-energy explosive materials is carried out using JWL equation of state given in Eq. (4). JWL parameters of PBX explosive, i.e. RDX/PU (80/20) are given in Table 1.

Table 1 JWL parameters for PBX (RDX/HTPB: 80/20)

ρ_c	a	b	R_1	R_2	ω	D	e	P_{cj}
1.53×10^3	6.1691×10^{11}	1.0762×10^{10}	5.2391	1.25159	0.2693	7700	7.82×10^9	2.03×10^{10}

$$P = a \left(1 - \frac{\omega \eta}{R_1} \right) e^{-\frac{R_1}{\eta}} + b \left(1 - \frac{\omega \eta}{R_2} \right) e^{-\frac{R_2}{\eta}} + \omega \rho e; \text{ Where } \eta = \frac{\rho}{\rho_e} \quad (4)$$

The properties of stainless steel fragment are provided in Tables 2 and 3. The shock equation of state along with Steinberg–Guinan strength model was used. The high strain rate constitutive relationships for G and Y are mentioned in Eqs. (5) and (6). The Polycarbonate material properties are given in Tables 4 and 5.

$$G = G_0 \left\{ 1 + \left(\frac{G'_p}{G_0} \right) \frac{P}{\eta_1^{1/3}} + \left(\frac{G'_T}{G_0} \right) (T - 300) \right\} \quad (5)$$

$$Y = Y_0 \left\{ 1 + \left(\frac{Y'_p}{Y_0} \right) \frac{P}{\eta_1^{1/3}} + \left(\frac{G'_T}{G_0} \right) (T - 300) (1 + \beta \epsilon)^n \right\} \quad (6)$$

$$Y_0 (1 + \beta \epsilon)^n \leq Y_{\max}; \text{ Where } \eta_1 = \frac{V_0}{V}$$

Table 2 Material parameters for Steinberg–Guinan for stainless steel

ρ_s	C	S	N	Γ	N	q	G_0	G'_p
7.9×10^3	4.57×10^3	1.49	0.35	1.93	0.33	423	7.7×10^{10}	1.74

Table 3 Material parameters for Steinberg–Guinan material model for stainless steel

G'_T	Y_0	Y'_p	β	T_m	ϵ_p	Y_{\max}
-3.504×10^{07}	3.4×10^{08}	7.684×10^{-3}	43	2380	0.3	2.5×10^{09}

Table 4 Polycarbonate material parameters for shock equation of state

P_p	C_1	S_1	C_2	S_2	Γ	ϵ_f	n	G_p
1.2×10^3	1.933×10^3	2.65	2.35×10^3	1.62	0.61	2.0	0.04	1.0×10^6

Table 5 Material parameters for piecewise JC equation

Y_{pc}	ϵ_{pc1}	Y_{pc1}	ϵ_{pc2}	Y_{pc2}	ϵ_{pc3}	Y_{pc3}	ϵ_{pc4}	Y_{pc4}
8.06×10^7	0.1	8.8×10^7	0.5	1.42×10^7	0.6	1.68×10^7	0.7	1.87×10^7

3.4 Discussion of Simulation Results

Validation of numerical model. In order to establish the simulation methodology, standard fragment generator problem was chosen from the literature. The details for validation are presented in Ref. [27].

Analysis of directional fragmentation warhead. Two simulations were carried out for this design. In first case, the explosive and fragments were modelled and in second case, casing over the explosive and fragments was also considered. The contour plot for absolute velocity and velocity in y-axis for all balls are plotted in Fig. 2.

To evaluate V_f , θ_a and θ_e , simulations were carried out with and without the casing. The effect of the casing on these parameters is presented in Figs. 3, 4 and 5. The details about these are given in Tables 6 and 7. Fragments which are further supported by other neighbour fragments is designated as SP, and similarly, USP denotes unsupported fragments. The charge to metal ratio is less for an encased charge, resulting in the reduction of fragment velocity. The surface plot of velocity is given in Fig. 3. In case of uncased charge, θ_a of fragments increases in the SP zone from 34.43° to 37.18° , which further increases to 45.36° in USP zone. This is purely due to non-availability of shock pressure beyond the location where $L_n/L_{max} = 0.84$. However, azimuth angle increases for SP fragment from 18.41° to 27.7° in zone III, since there is no further explosive support on left side. In this zone, the direct shock reaches to further SP fragment causing it to eject at an angle of 12.9° due to no support on right side as shown in Fig. 4. Similarly, elevation angles in SP and

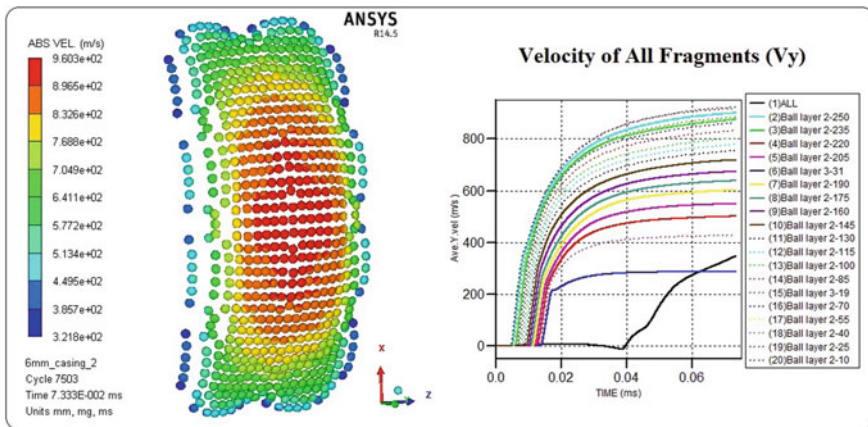


Fig. 2 Absolute and V_y velocities of all the fragments of cased charge

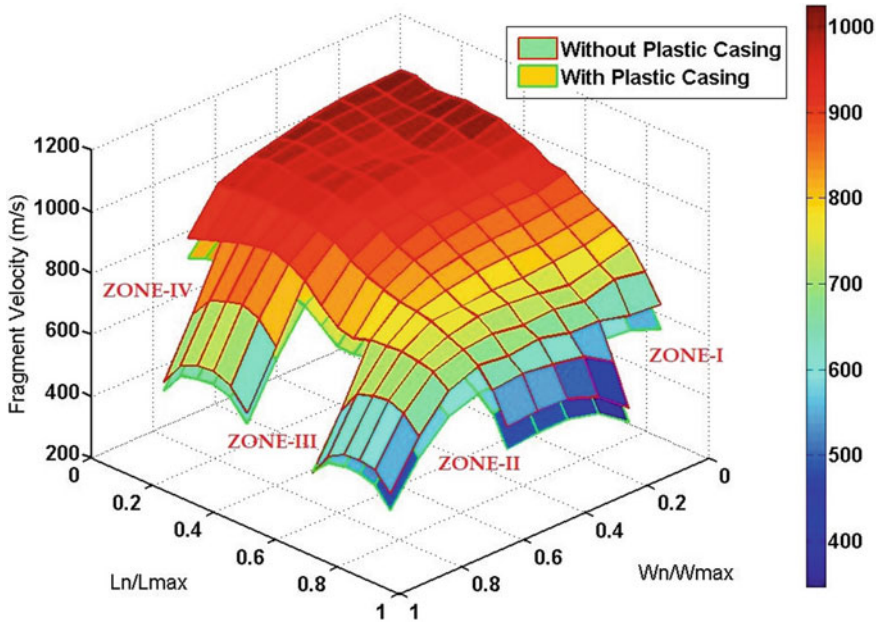


Fig. 3 Effect of casing on V_f

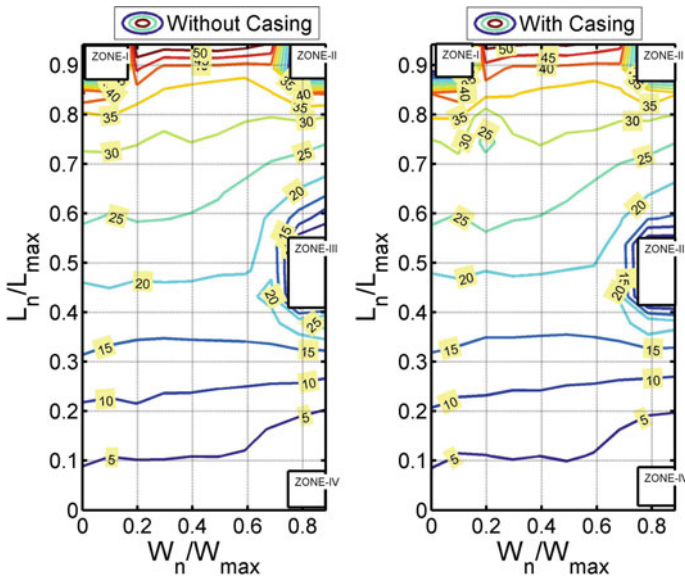


Fig. 4 Effect of casing on azimuth angle

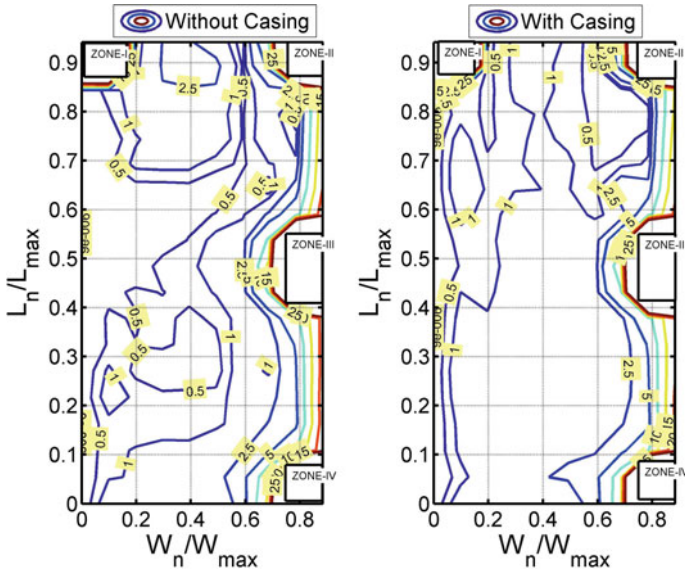


Fig. 5 Effect of casing on elevation angle

Table 6 Fragment velocity for uncased and cased charge

Type of charge	C_0/M_0	V_f (m/s), Centre
Uncased	1.53	1021.17
Cased	0.95	933.23

Table 7 Fragment velocity and ejection angles for uncased and cased charge

Type of charge	Zone	Fragment velocity (m/s)		Azimuth angle (°)		Elevation angle (°)	
		SP	USP	SP	USP	SP	USP
Uncased	I	667	633	37.18	45.36	1.36	0.7
	II	655	586	34.87	40.46	1.91	5.63
	III	807	688	18.41/19.08	27.70/12.90	2.43	10.78
	IV	815	777	1.48	0.64	4.37	16.38
Cased	I	602	533	36.97	42.81	1.29	2.06
	II	570	502	34.28	39.81	1.10	5.94
	III	724	639	17.71/20.39	24.02/15.30	1.82	9.46
	IV	746	711	1.92	1.68	3.92	13.42

USP fragments in zone III and IV have increased significantly from 2.43° to 10.78° and 4.37° to 16.38° , respectively. The azimuth angle slightly improved for cased charges in zone III. Therefore, the direction of ejection of fragments is influenced by location of initiation point, explosive support for fragments, casing and direction of propagation of shock.

4 Experimental Validation

To validate the simulation, the fragmentation warhead was experimentally evaluated. The fragmentation module casings were fabricated from polycarbonate plastic. Stainless steel fragments were accommodated in the casings using epoxy resin. Subsequently, PBX explosive was casted in the casing. These fragmentation modules were tested for their performance.

To evaluate the warhead, the fragment ejection velocity and direction were recorded on target plates. Four target plates of size $2.4 \times 1.2 \text{ m}^2$ and 1.6 mm thickness were erected at 7.5 m distance from the location of fragment module. They covered 36.8° in azimuth direction for half of fragment module. Additional plates located remotely at 50, 60 and 70 m distances covering in azimuth direction of 36.8° on left side for lethality aspects, i.e. perforation capability. Four velocity screens (printed circuit boards with tracts at 3 mm distance) were mounted on plates erected at 7.5 m. Two velocity screens were mounted at the height of 1.2 m on target plate, one at the centre of the plate at zero azimuth angle and another at azimuth angle of 36.8° . Two more velocity screens were mounted just above the ground as shown in Fig. 6. The fragmentation module was kept on wooden platform at 1.2 m height such that, half of the fragment hits are covered at central zone (0° – 36.8° azimuth angles) and another half on the remotely located targets. Fragment module was fired using electrical detonator fix with an adopter that accommodates a booster of $\phi 20 \text{ mm} \times 10 \text{ mm}$ height (Fig. 7).

Fragment hits were observed on target plates kept at 7.5 m distance. Hits were observed on first and second velocity screens. However, no hits were observed on

Fig. 6 Experimental setup for evaluation



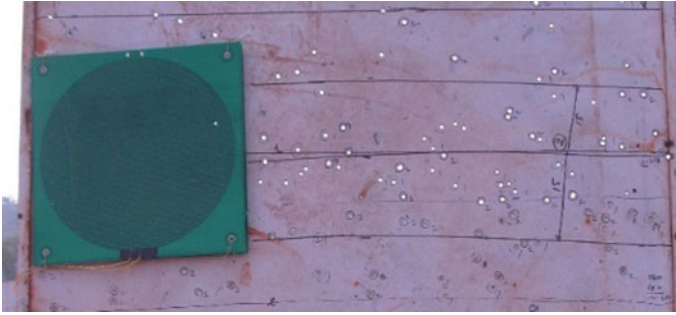


Fig. 7 Fragment hits in zone of 650 mm at 7.5 m

third and fourth screen. The time elapsed between firing trigger and perforations of the first and second screen (shortening of tracks) were 8 ms and 11.2 ms, respectively. Initial fragment velocity is 1.07862 times (estimated based on the exponential decay equation) of average velocity at the distance of 7.5 m. It has been estimated based on the drag coefficient and exponential decay of velocity. Initial fragment velocities were estimated as given in Table 8. Number of fragment hits was recorded in the zone of 650 mm as shown in Fig. 7, which constitute about 50 of elevation angle at a distance of 7.5 m from fragment module. The four target plates in the azimuth direction (~ 36.8°) cover half of the fragments of fragment module. The total hits observed in elevation zone of 50 were 236 experimentally against 256 as predicted by simulation as given in Table 9. Total 78% of fragments could be focused in 5° angular zone of elevation. Warhead design was thus validated experimentally.

Table 8 Comparison of fragment velocity (simulation and experiment)

Avg V_f (m/s)	Centre	At azimuth (36.8°)
Simulation	933	686
Experiment	1010	721
% Error	+ 8.25	+ 5.10

Table 9 Details of no of fragment hits expected and observed

Azimuth angle	0–9.2°	9.2°–18.4°	18.4°–27.6°	27.6°–36.8°	36.8–60°	Total
Total fragments	80	70	97	50	31	328
No of fragment hits observed within 5° elevation angle						
Simulations	54	56	77	42	27	256
Experimental	53	59	70	54	Not recorded	236

5 Conclusions

It is concluded that convex curvature spreads the fragments in wide beam angle (70°), whereas concave curvature produces focusing of fragments in narrow angular zone (5°) for any warhead directional profile. The directional warhead simulation predicted the fragment velocity and ejection angle very well and can predict the lethality performance. This would help in reducing the number of experimental iteration in finalization of warhead designs. The removal of explosive at edges of warheads and areas in its vicinity affected the fragment parameters, i.e. drop in fragment velocity and change in direction significantly. The plastic casing of warhead reduced the fragment velocity and affected azimuth and elevation angles. The fragment velocity and number of fragments hit estimated from numerical study are consistent with the experimental results.

Acknowledgements The authors are thankful to Shri A. K. Srivastava in supporting experimental studies and Shri Mahesh Vakchure, JRF for pre-processing of data. Shri Haribhau Markale, Shri V. K. Dixit and Dr. V. V. Rao, Director, ARDE, Pune, for their motivation in completing above work. One of the authors Mr. Pankaj Choudha is grateful to Vice Chancellor, DIAT (DU), Pune, for allowing to pursue doctoral work.

References

1. Zhao C, Wang S, Guo C, Liu D, Ma F (2020) Experimental study on fragmentation of explosive loaded steel projectile. *Int J Impact Eng* 144:103610. <https://doi.org/10.1016/j.ijimpeng.2020.103610>
2. Smith SD (1964) *Engineering design handbook warheads: General (U)*. US Army Material Command, Washinton, D. C. 20315
3. Cooper P (1996) *Explosives engineering*. Wiley-VCH, New York, USA, New York
4. Lloyd RM (2001) Physics of direct hit and near miss warhead technology. In: Zarchan P (ed) *Progress in astronautics and aeronautics*. American Institute of Aeronautics and Astronautics, USA, pp 250–254
5. Carleone J (1993) Tactical missile warheads. In: Seebass AR (ed) *Prog Astronaut Aeronaut*, pp 454–459. American Institute of Aeronautics and Astronautics, USA
6. Charles E, Anderson J, Predebon W (1985) Computational modeling of explosive-filled cylinders. *Int J Eng Sci* 23:1317–1330. [https://doi.org/10.1016/0020-7225\(85\)90110-7](https://doi.org/10.1016/0020-7225(85)90110-7)
7. Zhou M, Wu C, An F, Liao S, Yuan X, Xue D, Liu J (2020) Acceleration characteristics of discrete fragments generated from explosively-driven cylindrical metal shells. *Materials (Basel)* 13. <https://doi.org/10.3390/ma13092066>
8. Konig PJ (1987) A correction for ejection angles of fragments from cylindrical warheads. *Propellants, Explos Pyrotech* 12:154–157
9. Chen W, Li X, Lu F, Li Z, Zhang Z (2015) Parallel control to fragments of a cylindrical structure driven by explosive inside. *Math Probl Eng*. <https://doi.org/10.1155/2015/723463>
10. Zlatkis A, Korin N, Touati D, Evgeny G (2008) Influence of peripheral frame parameters on fragments dispersion. In: Bless S (ed) *24th International symposium on ballistics*. DEStech Publ., Lancaster, PA, pp 1077–1084. ISBN 9781932078930
11. Li Y, Li Y, Wen Y (2017) Radial distribution of fragment velocity of asymmetrically initiated warhead. *Int J Impact Eng* 99:39–47. <https://doi.org/10.1016/j.ijimpeng.2016.09.007>

12. Wang X, Kong X, Zheng C, Wu W (2018) Effect of initiation manners on the scattering characteristics of semi-preformed fragment warhead. *Def Technol* 14:578–584. <https://doi.org/10.1016/j.dt.2018.07.018>
13. Huang GY, Li W, Feng SS (2015) Axial distribution of fragment velocities from cylindrical casing under explosive loading. *Int J Impact Eng* 76:20–27. <https://doi.org/10.1016/j.ijimpeng.2014.08.007>
14. Guo Z, Huang G, Liu C, Feng S (2018) Velocity axial distribution of fragments from non-cylindrical symmetry explosive-filled casing. *Int J Impact Eng* 118:1–10. <https://doi.org/10.1016/j.ijimpeng.2018.03.011>
15. An X, Liu J, Ye P, Tian C, Feng S, Dong Y (2018) Axial distribution characteristics of fragments of the warhead with a hollow core. *Int J Impact Eng*. <https://doi.org/10.1016/j.ijimpeng.2018.08.003>
16. Ding L, Li Z, Liang M, Li X, Lu F (2017) The dispersion rule of fragments about the asymmetric shell. *Hindawi Shock Vib* 1–13. <https://doi.org/10.1155/2017/9810978>
17. Wang M, Lu F, Li X, Cao L (2013) A new method to estimate the projection angles of fragments from a D shape configuration. *Appl Mech Mater* 275–277:122–127. <https://doi.org/10.4028/www.scientific.net/AMM.275-277.122>
18. Huang G, Feng S, Wang F, Zhou T (2012) An optical design theory for focused fragmentation warhead aperture angle. *Def Sci J* 62:205–211. <https://doi.org/10.14429/dsj.62.1066>
19. Guo Z, Huang G, Zhu W, Feng S (2019) Fragment velocity distribution of D-shaped casing with multiple fragment layers. *Int J Impact Eng* 131:85–93. <https://doi.org/10.1016/j.ijimpeng.2019.04.027>
20. Ning J, Duan Y, Xu X, Ren H (2017) Velocity characteristics of fragments from prismatic casing under internal explosive loading. *Int J Impact Eng* 109:29–38. <https://doi.org/10.1016/j.ijimpeng.2017.05.018>
21. Dhote KD, Murthy KPS, Rajan KM, Sucheendran MM (2014) Quantification of projection angle in fragment generator warhead. *Def Technol* 10:177–183. <https://doi.org/10.1016/j.dt.2014.05.001>
22. Dhote KD, Murthy KPS, Rajan KM, Sucheendran MM (2016) Statistics of fragment dispersion by explosion in a fragment generator warhead. *Cent Eur J Energ Mater* 13:183–197. <https://doi.org/10.22211/cejem/64971>
23. Dhote KD, Murthy KPS, Rajan KM, Sucheendran MM (2015) Directional warhead design methodology for a tailored fragment beam. *Cent Eur J Energ Mater* 12:637–650
24. Frem D (2020) Estimating the metal acceleration ability of high explosives. *Def Technol* 16:225–231. <https://doi.org/10.1016/j.dt.2019.07.002>
25. Walley SM, Field JE (1994) Strain rate sensitivity of polymers in compression from low to high Rates. *DYMAT J* 1:211–227
26. Sarva SS, Boyce CM (2007) Mechanics of polycarbonate during high-rate tension. *J Mech Mater Struct* 2:1853–1880
27. Choudha PK, Kumaraswamy A (2019) Simulation of multi-fragment launch device for prediction of ejection. In: 12th international high energy materials conference & exhibits, HEMCE-2019, pp 1–3. IIT Madras, Chennai, India

FEA Analysis of the Knee Joint at Different Q Angle



Richa Rai and Vikas Rastogi

Abstract Three-dimensional model of the knee joint was constructed or built by using “Mimics” software. MRI scan two-dimensional images (DICOM) are only used to create a model of the knee joint which only includes femur and tibia. For the soft tissues of the knee, we require CT scan images that were not easy to get in this time, so trying to review the paper based on previous work. This paper is all about the basic knowledge of biomechanics and useful to interpret and realization of forces act on tibia and femur, and anatomy of knee joint (beneficial for non-biological background people). In this review paper, discuss dynamic (explicit) analysis Ansys software) of knee joint, at different Q angles and also theoretical approach of “data science” to quick analysis of knee joint.

Keywords Knee joint biomechanics and knee joint forces · Macroscopic · “Q” angle · Free fall and knee anatomy

1 Introduction

Artificial knee replacement success rate nowadays is about 90–92%. It happened because of improvement of surgical technique, though it can prognosis any potential defect/weakness, ultimately leading to the failure of the concerned body part. So we could see the importance of biomechanics in our life, whether it is related to machines or human being. Scientist “hetzes” said biomechanics is the study of the movement of living things. Biomechanics is a combination of biology and mechanics. This paper discusses knee so the term biomechanics of knee is nothing but study and analysis of knee joint, bones, ligaments and muscles. What if add those medical data with AI, it will improve the medical analysis and reduce time to diagnosis the problems. This combination is a dream for me to do my further research or study. Given an opportunity, I have a vision to expand scope of my research to entire mechanical joints of the human body and create a DIGNIFIED, PAINFREE

R. Rai (✉) · V. Rastogi
Delhi Technological University, Shahbad Daultapur, Main Bawana Road, Delhi 110042, India
URL: <http://www.dtu.ac.in/Incs>

© The Author(s), under exclusive license to Springer Nature Singapore Pte Ltd. 2022
K. Govindan et al. (eds.), *Advances in Mechanical and Materials Technology*,
Lecture Notes in Mechanical Engineering,
https://doi.org/10.1007/978-981-16-2794-1_87

995

WORLD for the vulnerable population. Data science is a multidisciplinary field, uses scientific methods, and processes, through algorithm, systems to extract knowledge and insights from structured and unstructured data. Data science is related to data mining and big data. Knee joint is “hinge joint” made of two bones—thigh bone and shin bone. It was challenging to study the anatomy of knee because who belong to non-biological background very help-full for them, so decided to write full anatomy and problem-solving process in only on paper.

1.1 A Basic Mechanism of the Knee

Femur (upper bone of the leg). The head forms a socket and ball joint with the pelvic arch, being held in place by a ligament within the socket and by strong surrounding ligaments. In humans, the neck of the femur connects the shaft and head at a 125° angle, which is efficient for walking. Tibia (shin bone) located in the lower front portion of the leg. Tibia is second largest bone in the body. Knee joint is the largest joint of human body, and the function of knee joint is to allow movement of the leg and is critical to normal walking. Inside the knee, a smooth articular cartilage that covers the joint surface, resting on the top of tibial cartilage, is meniscus which improves the stability of joint and helps to distribute weight. Ligaments are important to controlling excessive motion by limiting joint mobility especially side-to-side movement. Together these tendons and ligaments provide extension and flexion as well as medial and lateral rotation of knee joint. The quadriceps muscles play a vital role in the stability of the knee and are anchored onto the top of the patella. Knee is made of three bones, the femur, patella and tibia. Here we are taking right knee of human and looking straight at it (Fig. 1).

Knee joint and Q angle Femur is a thigh bone. Tibia is a shin bone. Patella is a knee cap. Knee is complex joint with many different combinations of parts: Tendon ligament bones muscle movement of the bones causes friction in the articulating surface, to reduce this friction between all articulating surfaces involving in movement, are covered with a quite shiny and slippery layer called cartilage. Articulating surface of femoral condyle and tibia plateaus cartilage and the back of the petal cartilage is covered with the cartilage. This provides smooth surface that facilitates easy movement and further reduces friction between articulating surface of the bones or “knee joints”. Q angle in our knee must be able to support the weight of body during walking and running. Q angle is angle between quadriceps tendons and patella tendons. If we increase Q angle, it will lead to fracture of patella. Take patella periphery and patella center and tibia and draw a line from center of patella, and the second is from tibia to periphery of patella to measure Q angle (Fig. 2).

Role of knee joint in human gaiting system It is important to set method of biomechanical feature of knee joint motion and stress during high flexion which we can feel in daily life. It is very difficult to analyze knee joint stress and motion, but there are some effective analysis methods through we could easily analyze them. Some

Fig. 1 Knee anatomy

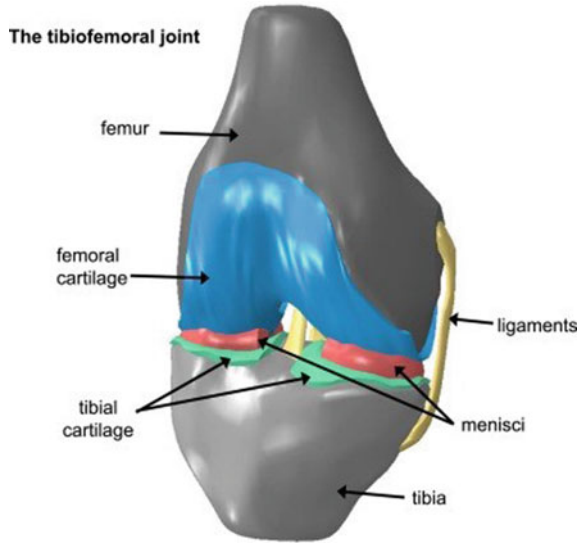
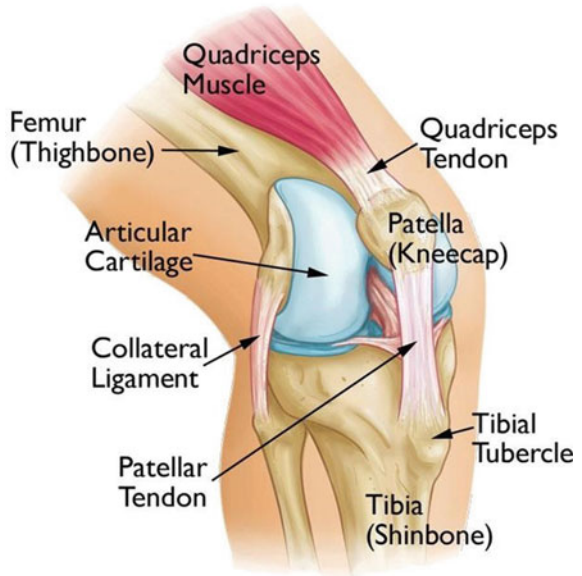


Fig. 2 Knee bones and muscles



methods are done in laboratory and some based on software. My analysis is based on software. For the analysis of knee flexion, firstly we have to build a 3D model which includes tibia, femur and soft tissues of knee. It is very difficult to analyze soft tissues of knee, so my word is limited to dynamic analysis of femur and tibia.

Methods of creating 3D model and Research Motivation Nowadays, we have several methods to build 3D model of the knee because of highly specific software including “Mimics”, X-ray image to construct 3D model, laser scan technique, image processing, slicer reverse engineering and rapid prototype. We are focused only on “Mimics” software and some necessary information about Mimics software. “Mimics” is a materialized interactive medical image control system or software which used to build 3D model of complex shapes and also used in 3D printing. For the construction of the 3D model of knee, we need an MRI scan and CT scan of the knee of a healthy human. Moreover, by importing that images in Mimics software using thresholding and segmentation, we can quickly develop a 3D model of the knee. Motivation biomechanics is the part of mechanical engineering and principles of living things. It deals with organisms at a different level. A combination of engineering fields deals with different levels of complexity, which is not possible by only the biomedical field, like analyzing the forces before actual practice is the basic need of engineering in the medical field. Small strain behavior in tissue and the bone scan show large changing shape, and this changing shape is because of applying external force remodeling. Everything there makes bone a very good living tissue model of the prototype for the applications of the methods of finite element analysis or in continuum mechanics. This modeling process is open system mechanics to deal with the biomechanics system. This may be responsible for bone growth and analysis across the scales.

2 Literature Review

Author Blankevoort in 1988, Kempton in 1980, Mow in 1982, Walker 1972 and Roth 1977 were worked in the very beginning, and their title was to find how we do FEA on knee joint. Their research work based on effects of articular contact 3D shows the mathematical model of knee joint and finds the value of joint kinematics, at two different positions, and result is indirect motion of knee joint and their motion characteristics were simulated. Contact study of knee show that FEA can do 2D and 3D analyses. In 1991, Author Blankevoort and Walker develop articular contact 1991, title of their research was Effects of articular contact 3D mathematical model of knee Joint, and their research is mainly based on finding the value of joint kinematics, at two different positions. The result is that ligaments and articular cartilage’s mechanical property were found. Author Mr. Vaziri in 2008 constructed the first 2D model of the knee. Their title of research was on, The asymmetric 2D model was constructed, Vaziri research work was mainly based on studies and analysis of contact position of knee joint, result is knee kinematics and nonlinearity of the model, Author Herzog and Donzelli in 1999, Mr. Un and Wilson in 2001 and 2005, Dar, Aspen and Wilson in 2003, Vadher and team in 2006, Modified form of Vaziri et al. 2008 model. Title of their work was The geometry of 2D model taken, and research work was mainly based on axisymmetric and lot equivalent to the 3D model. The result provides necessary information about the knee. Author Penrose and team in 2002, Blecha in

2005, Author Halonen and team in 2013, Zheng and Yang in 2014 and 2010. Author Wang and Kiapour in 2014, Author Miyoshi and team in 2002. Author Gardiner and Weiss in 2003, Author Guess in 2010, Author Li in 1999a, Author and team in 2008, Author Mootanah and team in 2014, Yao and song in 2006b and 2004, Author Son Monomer in 2012 Peña et al. 2007 and 2008. Their work title was 3D model of human knee (with soft and hard tissues) by using MRI and CT scans. Research work of their work was three-dimensional of the knee first developed and was a very big achievement in the biomechanical field, and finite element of the knee includes tibia and femur and predicts or analyzes knee forces and knee kinematics, while a load is applied (external). Result based on ligament and articular data was taken from “Blankevoort et al.” and mechanical behavior of knee was analyzed. Author Li and team in 2001a, 2002 and 2005 work title was 3D model of the human knee (with soft and hard tissues) by using MRI and CT scans. Their research work was Modify, the above work Study of Author Li of the knee, is provide a contact of articulate surface, and Result articulate surface and experiment of damage of ligament and articular surface when the load is applied. Authors Wang, Kun Tao, Li and Chengtao Wang in 2014 work title was Modeling and analysis on biomechanical dynamic, characteristics of knee flexion movement. Research work based on 3D model of the knee was build including tibia, femur and soft tissues of knee. And FEA was done at 30 degree of knee flexion. Result is patellofemoral contact joint unsteady, 30–90° it will drift from its original position. At 0 to 90° stress, 9 MPa was applied and simulated, contact above 90–130° it will reach to 22 MPa. Result was to find out von Mises stress and displacement, and there is no difference in their values. Model and biomechanics review Basic idea of knee implant. In case of aseptic loosening, it is very difficult to do surgery for the second time, and it may fail the implant of the knee.

Literature review based on FEA analysis. [1] Three-dimensional cases are to be analyzed. “Four” cases studied, types of nodes and elements 12,388 elements of tibial meshed part and 2238 nodes. Meshing-type “Triangle” and the boundary conditions were type of element mesh frictionless contact between tibia and femur, tibia bottom edge eight nodes full restricted. Separate and reduce top model.

Reference [2] Two-dimensional cases are to be analyzed. “Eight”, number of elements and nodes “Four” femur contents and “two” direct contact condition. Total 3116 Nodes and 4615 elements, types of elements “Tetrahedral” type of elements mesh Left edge of and the boundary conditions is the femur is fixed to create static symmetry, the bottom surface of tibia restricted to avoid motion. [3] 3-Dimensional analysis Total “Six” cases I have analyzed. Contact analysis between tibia and femur is under 3200 N load and 45-degree flexion, 2200 N load and 15° and 2800 N load at 60°. And for fatigue analysis, there are three loading conditions 4000 N, 2000 N and 500 N. Total number of meshing elements is 256705 for contact analysis. And for fatigue analysis, number for meshing elements is 109643 “Four” element nodes. “Tetrahedral” element type is used for tibia and femur. Ten nodes are used to analyze tibia. Boundary condition of contact analysis could be done by fixing the tibial base. Fatigue test can be done by specifying half of the tibial base and free another half. [4]

Two-dimensional analysis of total “Four” cases is analyzed, and this paper is based on femur components of the knee joint. A total number of elements are 1280, and 560 node value is used. Direct strain condition is used, and it will be applied at the center of straight strain. Boundary conditions of the femur center component are fixed and constrained in both vertical and horizontal directions. [5] Two-dimensional analysis for direct material property and three-dimensional analysis for finite element of the knee. “Two” cases were studied based on contact of knee bones, and “Eight” cases are analyzed based on loading condition. A total of 560 nodes and 1280 elements were used during meshing of the knee for FEA. “Eight” nodes is used for translation in plane strain condition. And “Four” node element is used for rigid FEA analysis of knee. In boundary conditions, only tibial element is allowed for FEA analysis of knee and gives freedom of movement.

3 Modeling and Analysis of Knee Using Q Angle

Knee joint geometry Knee geometry is build by using MRI and CT scan DICOM files; CT scan file is used to construct bones, and MRI is used for soft tissues. Images are margin of 0.0015 m in coronal, sagittal and axial planes. Knee flexion has been taken as 0°. The knee is a very complex structure in our body, complicated to model without having any flaws because flaws in construction could exploit our calculation, so we will use MRI data to create a 3D model of the knee in Mimics or SLICER. MRI is magnetic resonance imaging; firstly, we need MRI of a healthy volunteer (5.6 feet, weight 60 kg) and a DICOM image file of MRI. The 3D model depends heavily on images and what we want our final images to look like and how the model used. We start from segmenting (is a process to increase the resolution of images). DICOM image export is the software and chooses threshold menu, and after thresholding click on 3D preview, and we will get mask segmentation. Now 3D model of the knee has soft tissues and bones (Fig. 3).

Procedure Materials For the analysis of knee, it is very important to know about mechanical properties of bones, and property of bones depends on gender, age and in which environment we are living. Here is table which shows the material property of knee which we are going to use in our analysis. Many references have taken by the authors Jacob and Hull Rashid journals that a healthy man weight is 30 years, 5 feet 6 inch tall and weight is about 70 kg, force of 1400 N is applied; normally, it would be double of weight. This loading condition has been taken from Ayala and Morales. We have applied displacement approximately 0.010 m, and all the data which we have been taken will be very useful to analyzing maximum and minimum deformation that soft tissues can swear without failure. All the tables given in this paper are taken from different journals, some authors' names are given below: Mr. Jolivet in 2001 and W. Li et al. 2009, Limbert and Little et al. in 2004 and 1986, Meakin 2003, Pandey 1997, Penrose 2002 (Table 1).

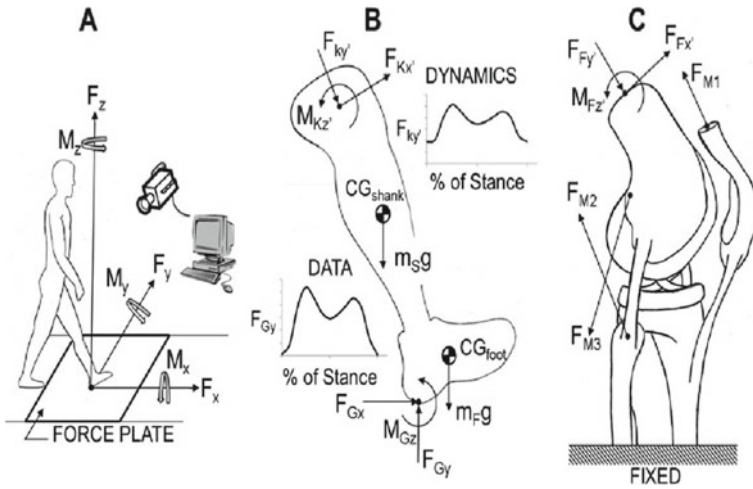


Fig. 3 Knee geometry

Table 1 Properties of material

Material	Young's modulus	Poisson's ratio
Bones	17,400	0.3
Ligaments	60	0.3
Cartilage	12	0.49
Menisci	59	0.45

FEA Model FEA is a finite element analysis based on the finite element method. This method we used is to predict the behavior of heat flow, the behavior of solids, heat conduction of fluid flow, Euler's equation, displacement estimate is 10 mm. Model— This paper includes a combination of tibia, femur, patella and menisci. Only external load will be applied. The complexity of the model of knee pushes to take 0° flexion of extension. Moreover, bones are based on linear analysis, and soft tissues include nonlinearity: static analysis and many more. FEA provides results with precision and real-life scenarios with accuracy. Differential equations connect everything like changes in displacement, the geometry of objects, physical properties, temperature and pressure, and more. It is very difficult to the analyze the soft tissues, so in many research papers, authors have described finite element model of the knee, which includes bones and soft tissues of the knee like tendon, patella, menisci and bones.

Importing medical data in Mimics software In Mimics software, we can import 420 DICOM images of CT scan, so I have taken CT scan of 30-year-old man's left knee. FE model of knee has been created, and meshing is also done through Mimics software very easily. Meshing is very important while analyzing the model and reducing analysis time. Most important thing is how to import CT scan or MRI report images (DICOM format) to Mimics software. Go to file, choose new project wizard and

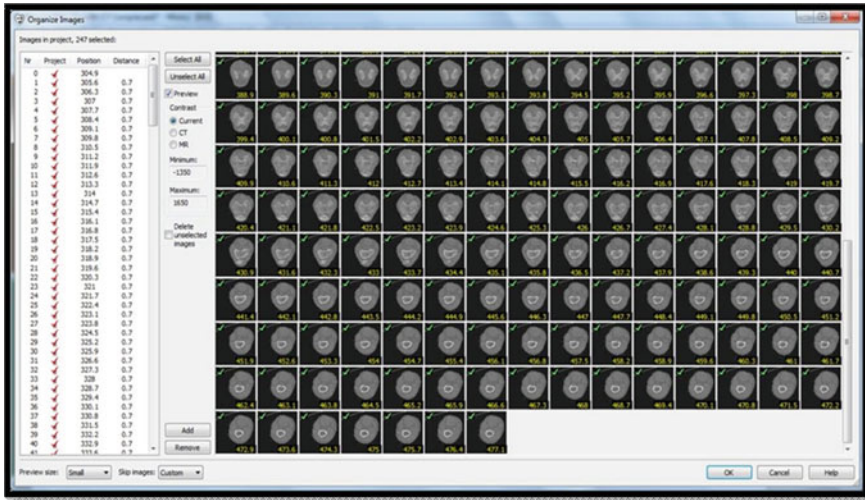


Fig. 4 DICOM images in mimics

import my raw DICOM images or file of knee, then hit next. Segmentation and thresholding segmentation of an MRI or CT scan image is imported in Mimics software. This software converts the two-dimensional image into the three-dimensional solid geometry. Threshold operation is used to create mask. This mask connects all the region in same threshold area. The mask which creates automatically is green mask; it shows after completing the threshold in cropping region. So “thresholding” is the process of choosing the range and intensity values that used in any of the pixels that will fall within a range get highlighted or selected and put into our segmentation. Number of pixel on Y-axis and value of image are along the x-axis. So we can see as we drag the mouse, the pixel will update in real time as well as my 3D view. It has some predefined sets of CT scan. Coefficient of friction has been taken 0.038 to articular surface. Calculation of knee joint is easy and flawless when we formulate knee joint torque (Figs. 4 and 5).

4 Dynamic Analysis at “Q” Angle

Meshing had been performed in Mimics software. Meshed three-dimensional model of knee joint is imported into the Ansys software. This FE model has 258,222 elements and 456,300 nodes. Femur, tibia and patellar mesh density input is 2 mm. Mesh refinement is very important part of any finite element analysis, which provides accurate and error-free result. But very refined meshing would take so much of time, that’s why we refined the mesh where we need accurate result. Angular distortion of any shell element reaches to zero. The value of orthogonal quality (taken from

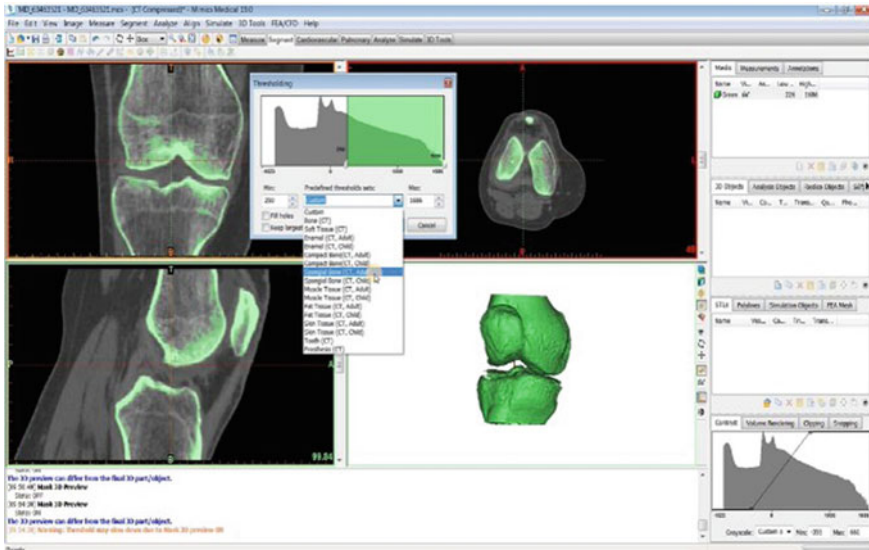


Fig. 5 Thresholding

Emrah and farukh) is greater than 0.1, and maximum is less than 0.95, average value of skew is taken as 0.46, average orthogonal value is 0.69, and according to the mesh refinement, this is quite good result. Loading—We imposed 350 N load on femur in axial direction, and other 56 N is on the tendon. According to FEA, we will talk about von Mises stress. Our focus is on the daily gaing system of human based on Q angle. Q angle has been taken 10°, 15° and 22°. The most effected part by above loading condition is at 22°, at which tibia, femur and patella have most deformation compared with 10° and 15° angles (Fig. 6).

Results Here is the result which describes the stresses at different “Q” angle and at different loading condition. At angle 22°, stresses in femur, tibia and patella are 14.6, 9.2 and 2.2 MPa. At 15° angle, stresses in femur, tibia and patella are 4.3, 4.9 and 1.2 MPa, and same goes to 10° angle stresses which are 12.5, 8.4 and 3.8 MPa. Below in given table I have described the material (femur, tibia, cartilage and menisci) properties. And in second table, we can see the value of stresses at different “Q” angle. All the table and material properties are taken from different journals (Tables 2 and 3),

Stresses in femoral cartilage stresses in femoral cartilage at different Q angle are at 22°. The value of stress is 9.24 MPa, the value of stress at 15° is 4.86 MPa, and value of stress at 10° is 8.39 MPa. From above result, we could see the major deformation to find in femoral cartilage, i.e., at 22° at given loading conditions. Stresses in patellar cartilage stresses in patellar cartilage at different Q angle are at 22°. The value of stress is 2.226 MPa, the value of stress at 15° is 1.206 MPa, and value of stress at 10° is 3.78 MPa. From above result, we could see the major deformation to find in Patellar cartilage at 10° at given loading conditions. Stresses in tibial cartilage. Stresses in

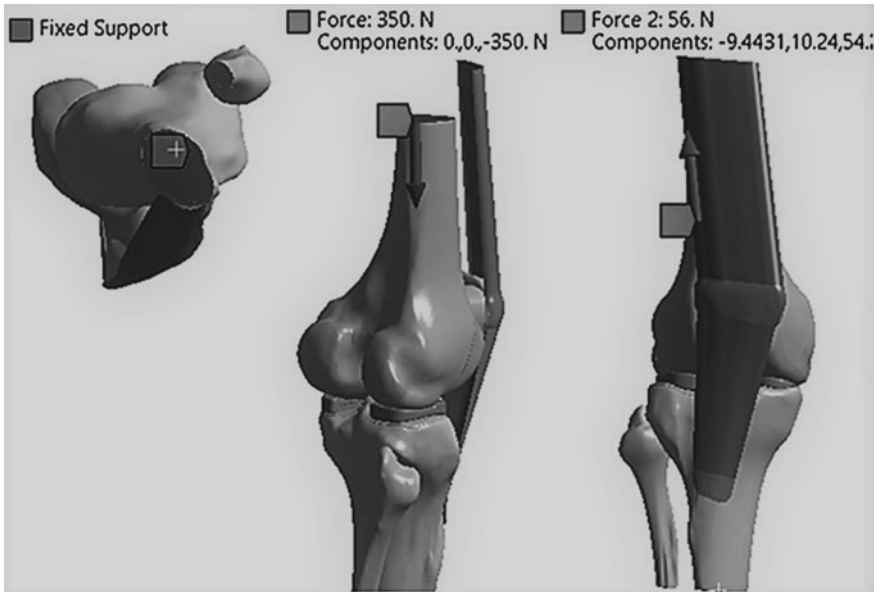


Fig. 6 Loading condition

Table 2 Different stress condition property of material

Materials	Young’s modulus (MPa)	Poisson’s ratio	Bulk modulus (MPa)	Shear stress (MPa)
Femur	17,000	0.3	14,167	6538.5
Tibia	14,000	0.3	11,667	5384.6
Cartilage	5	0.46	20.833	1.7123
Menisci	59	0.49	983.33	19.799

Table 3 Value of stress at Q angle

Q angle	Tibial cartilage(MPa)	Femural cartilage(MPa)	Patellar cartilage(MPa)
10	12.5	8.3	3.6
15	4.3	4.8	1.2
22	14.6	9.1	2.2

patellar cartilage at different Q angle is at 22°. The value of stress is 14.592 MPa, the value of stress at 15° is 4.27 MPa, and value of stress at 10° is 12.418 MPa. From above result, we could see the major deformation to find in patellar cartilage, i.e., at 22° at given loading conditions. So we can see the above discussion and classified that in above three discussions, the patellar cartilage at 15° Q angle will be lower

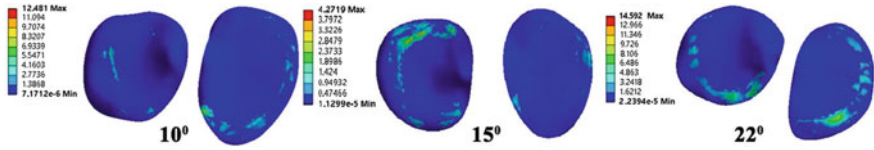


Fig. 7 Stresses in tibial cartilage

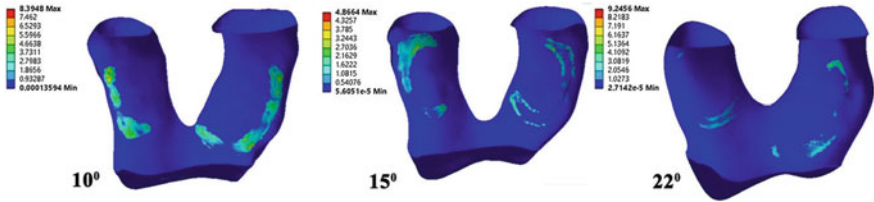


Fig. 8 Stresses in femoral cartilage

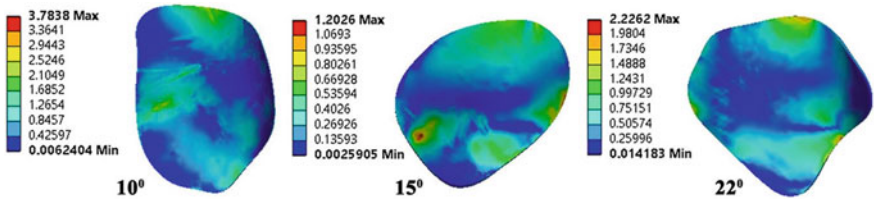


Fig. 9 Stresses in patellar cartilage

middle region at which we could see lowest stress in all Q angle and also when we comparing with others (Figs. 7, 8 and 9).

5 Discussion

For females, an increased Q angle is linked to knee pain, anterior cruciate ligaments (ACL) injury and patellofemoral pain. The alignment of patellofemoral joint is affected by the patellar tendon length and Q angle, after Q angle extension, first one is external tibial torsion and second is femoral anteversion and many stresses. Impact of knee when free fall on ground and flexion and extension, quadriceps muscles play very important role and it anchored on the top of patella. Patellar tendon acts in downward direction. The menisci of knee varied between 0.98 MPa in compressive stress in the externally is 3.96 MPa and the internally, under a compressive force of 1300 N. Author Dong found a compressive stress on both the lateral and medial meniscus as 3.00 and 2.83 MPa. Found that the compressive stress on the medial meniscus was

3.31 MPa. The compressive stresses on the lateral and medial meniscus were found as 3.5 MPa and 2.1 MPa.

6 Conclusion

A 3D model of the healthy volunteer knee is built in Mimics software, and it has bones and soft tissues.

Author Y.H. Lee² discusses cartilages, tendons, ligaments, menisci and bones and analyzed under compressive force. The force is of full flexion position. The analysis of final model is compared with the literature results which are fully established, that was true and based on actual.

Author N. Reddy told that the high load-bearing and low load-bearing areas were situated on the anterior and posterior parts of the femoral cartilage.

Authors Ham Mamet and Tunisia have told that modeling of three-dimensional human knee joint in Mimics software is very useful for kinematic and dynamic analysis of knee joint on FEA or finite element analysis to avoid complexity in the analysis.

7 Future Scope

Through supervised learning, which is part of artificial intelligence, easily performed on previous data from “NIMHDataArchive”, is a government data collection, which is used for storing data of patients, and through the Supervised learning. During analyzing the data, it needs (1) exploratory data analysis, (2) feature engineering, (3) treating missing values and (4) machine learning using random forest. Reading of data is important, read in the train and test datasets and then bind the two sets, using `bind rows()` from the “NIMHDataArchive” data, and it needs to do all feature engineering and data preparation on both datasets and then divides our data into train and test sets again later before creating our model. One which is less messier requires little or no cleaning, and second is attribute which looks quite messy and will extract appropriate information from them before using the model. The random forest model will give results near the actual experimental results, which has error, importance for predictors of problems, ratio of knee cap dislocation compare to young age and old age people, what kind of fracture happened and what we need to analyze with unknown problems which is related to previous data. The prediction of 4397 test data was saved. Random forest (formula = revenue data = train, n tree =) (Fig. 10).

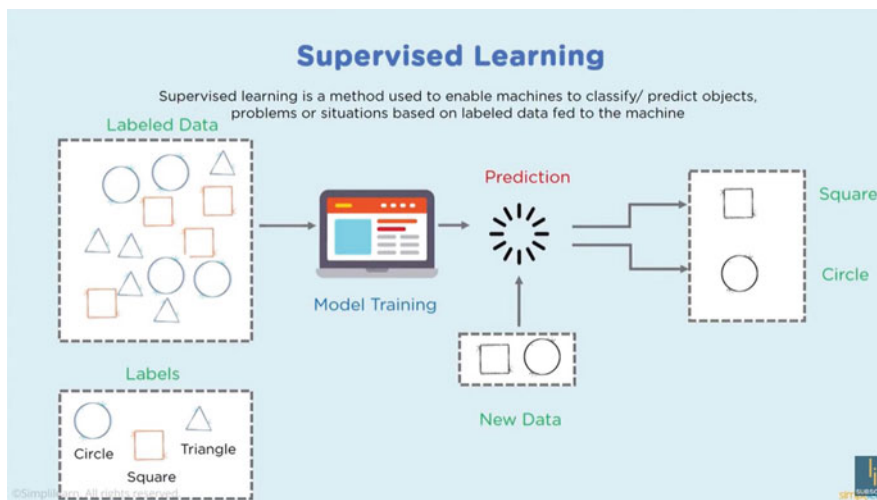


Fig. 10 Supervised learning

Acknowledgements This paper is based on previous research work. Research is a higher concept. Research work brings to test our dedication, patience and state of mind. Every result arrived is a beginning for higher achievement.

References

1. Gurtin ME (1982) An introduction to continuum mechanics, vol 158, 1st edn. Academic Press Inc., London
2. Oden T (2006) Finite element of non-linear continua. Dover Publication Inc., New York
3. Miyoshi S et al. Analysis of the shape of the tibial tray in total knee arthroplasty using a three dimension finite element model
4. Goswami T. Development of creep-fatigue of life prediction models
5. Wang J, Tao K, Li H. Modelling and analysis on biomechanical dynamic, characteristics of knee flexion movement under squatting

Fault Diagnosis of Ball Bearing Using EEMD IMF Features, ReliefF, and Machine Learning



V. Dave and V. Vakharia 

Abstract Bearing may widely use rotating component in most engineering machinery. To prevent failure in bearing during operation, it is obligatory to spot faults that happen in bearings. To identify the faults, vibration signals from vigorous, internal defect, external defect, and ball failings are considered. During this paper, features are acquired from signal processing skills like ensemble empirical mode decomposition (EEMD) to distinguish the bearing fault. Three vital features like RMS, kurtosis, and skewness are considered for altogether fifteen IMFs. ReliefF feature ranking algorithm is employed to pick the appropriate features. The results designate that the features supported individual IMF will give better fault diagnosis accuracy. Totally, fifteen IMFs have been calculated for the given signal. It is observed that mostly the primary two IMF features are selected. Results disclose that random forest contributes 100% training precision through thirty-five features and 96.42% tenfold cross-validation precision thereupon that features and SVM gives 100% training accuracy at fourteen features and 92.85%. Consequently, the methodology used is reliable and may be considered as a possible technique for fault analysis.

Keywords EEMD · Support vector machine · Random forest · ReliefF · IMF

V. Dave · V. Vakharia (✉)

School of Technology, Pandit Deendayal Petroleum University, Gandhinagar, Gujarat 382007, India

e-mail: vinay.vakharia@sot.pdpu.ac.in

1 Introduction

Nowadays, revealing of bearing errors is a crucial question for extensive time–frequency resolutions, but the choice of mother wavelet may be a difficult task [1]. Empirical mode decomposition (EMD) is one among the signal decomposition method, which separates the signals into a different intrinsic mode function (IMF) in which useful information regarding bearing condition may reveal. Mode mixing is considered as a major drawback of EMD which specifies as either a single IMF residing of mechanisms of usually contrasting scales or a component of like scale residing in several IMFs [2]. To resolve this problem, EEMD is developed. Feature vectors are constructed which consists of statistical parameters like RMS, kurtosis, skewness etc. and features are selected using Relief feature ranking approach. Similarly, the utility of the rated feature subclass is analyzed with support vector machine (SVM) and random forest classifiers. The EEMD methodology to diagnose the bearing faults is shown in Fig. 1 research. During working, various sorts of faults are developed in bearing. Proper and accurate diagnosis procedures can eliminate the issue of machinery. Bearing, shaft, and motors are arranged in a linear direction, which may cause the problem of balancing and irregularity [3]. Vibration signals comprise necessary information about bearing health conditions which can be revealed by applications of proper signal processing strategies. Fast Fourier transform (FFT), wavelet transform, empirical mode decomposition, Hilbert transform, and so forth are the procedures where signals amassed from operating conditions of bearing with proper setup of accelerometer, motor, shaft, and different devices. The signals are non-stationary in environment; thus, wavelet transform works well over FFT.

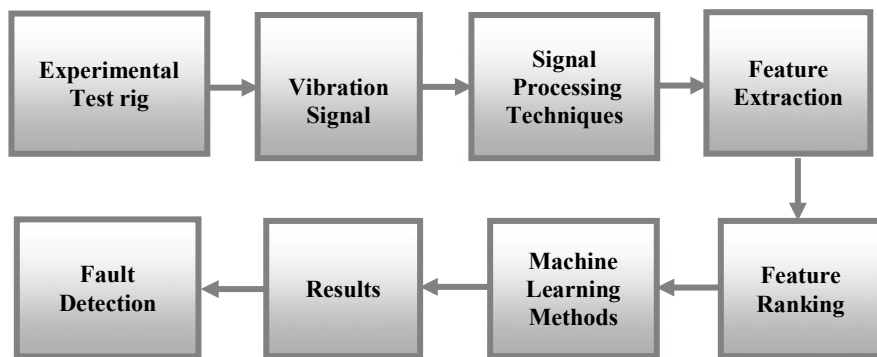


Fig. 1 Stream graph of the projected system

2 Ensemble Empirical Mode Decomposition (EEMD)

Generally in the roller bearing, because of some defects like spalls, cracks, pits, etc., when the ball passes over, the raceway causes variation in the contact forces. The impact of vibration at that contact surface is different than other surfaces with different frequencies. Because of some unsolved problems of time frequencies, Fourier transform cannot apply for fault diagnosis. Hilbert–Huang transform (HHT) is one of the popular methods which can use EMD as a time adaptive decomposition operation. However due to some issues like the presence of low-amplitude IMF at the low frequency and extensive frequency range at the high-frequency region, it is not considered as a suitable method for fault analysis [4]. The above problem can be solved by an improved version of EMD which is known as EEMD, which also can help to select the suitable IMF which contains fault information and resolve the problem of mode mixing. The definite disintegration method changes to the following steps [5].

1. Input white noise to the signal $X(t)$ then controlling the modified signal.
2. Decompose the modified signal.
3. Above steps should be repetitive N times, with addition of white noise all time.
4. The average calculating task for the matching decomposed collective IMF to offset the effect of several Gaussian white noises at the actual IMF.

At last, the highlights are separated from individual IMFs of signals which can be mathematically calculated as:

1. RMS: The root mean square is described as the square root of the mean square and defined by

$$\text{RMS} = \sqrt{\frac{\sum_{i=1}^n x_i^2}{n}} \tag{1}$$

2. Kurtosis: It is dimensionless parameter and can be defined by

$$K = \frac{1}{n-1} \sum_{i=1}^n \frac{(X_i - \bar{X})^4}{\sigma^4} \tag{2}$$

3. Skewness: Skewness represents the asymmetry of vibration signal, which can be quantified with the calculations of probability density functions from the standard normal distribution which is define as

$$S = \frac{1}{n-1} \sum_{i=1}^n \frac{(X_i - \bar{X})^3}{\sigma^3} \tag{3}$$

where x_i represents data, n is a sample size, σ is standard deviation, and \bar{x} is the mean of data.

3 Feature Selection Using ReliefF

ReliefF may be a feature selection algorithm useful for feature ranking. While handling multi-class complications, the ReliefF algorithm picks the adjoining neighbor samples from each of the samples within exclusive sets [7]. Within the beginning, we randomly select a sample x from the training sample, determine k nearest neighbor samples from x , and then randomly determine k number almost like the closest neighbor samples from the neighbors of various classes. To switch the feature, additional weights are often obtained by equating within-class space and between-class space from the neighboring samples. The above procedure is often repeated on each feature, and at the end, the weighted value of every feature is obtained [8].

4 Fault Identification Techniques

Based on features extracted from adopted signal processing technique and ranked by ReliefF, fault identification accuracy of features using different classifiers has to be determined. In this paper, two different classifiers are used for training and tenfold accuracy estimation which are explained below.

4.1 Support Vector Machine

The utility of the support vector machine (SVM) lies in its proven multidisciplinary applications in numerous fields of engineering, applied math, medical and biological sciences, and so on. For small samples, like fault diagnosis, it is a suitable technique for classification and regression. For data which will be linear or nonlinear, a hyperplane is made which splits hyperspace to realize maximum segregation among the classes referred to as margin [9]. The features which are close to the require margin are accepted as support vectors as shown in Fig. 3 a training model set $\{(x_i, y_i)\}: i = 1 - k$ is considered, where k is a total range of samples. The hyperplane $f(x) = 0$ which classifies the features will reflect as a solution to the optimization formulation revealed below [10].

$$\text{Minimize } \frac{1}{2} \|w^2\| + C \sum_{i=1}^K \xi_i \quad (4)$$

$$\text{Subjected to } \{y_i (w^T x_i + b) \geq 1 - \xi_i, \xi_i \geq 0, \quad i = 1, 2, \dots, K \quad (5)$$

where C is an endless demonstrating error forfeit.

4.2 Random Forest

In this machine learning classifier, classifications can be performed in two parts, where in one part some data are considered for training, in another part, some data are considered as accuracy validations, and the process is repeated for several turns. The random forest algorithm which employs the ensemble of bagged trees works similarly, by taking decision trees of various depths and splits randomly and creating an ensemble of trees. Bootstrap aggregation (Bagging) makes different sets for preparing from a single data set [11].

5 Experimental Procedure

The bearing involves four components: the external race, internal race, ball, and cage. Figure 2 displays the graphic setup of the investigational test rig from CWRU [6]. The bearing shaft turning speed diverse is 1730, 1750, 1772, and 1797 rpm with a rate of 12 kHz. Different sizes of defects at different speeds are introduced. 6205-2RSL JEM SKF deep groove ball bearing is used at each end whose proportions and specifications are set in Table 1. In total, there are 56 instances related to inner race diameter (IRD), outer race diameter (ORD), ball diameter (BD), and healthy bearing (HB) with various fault sizes, and differences in revolving speed of the shaft are taken into account. After collecting signals, signal processing technique EEMD is applied, which reveals the fault information within the sort of IMF. For all calculated IMF,

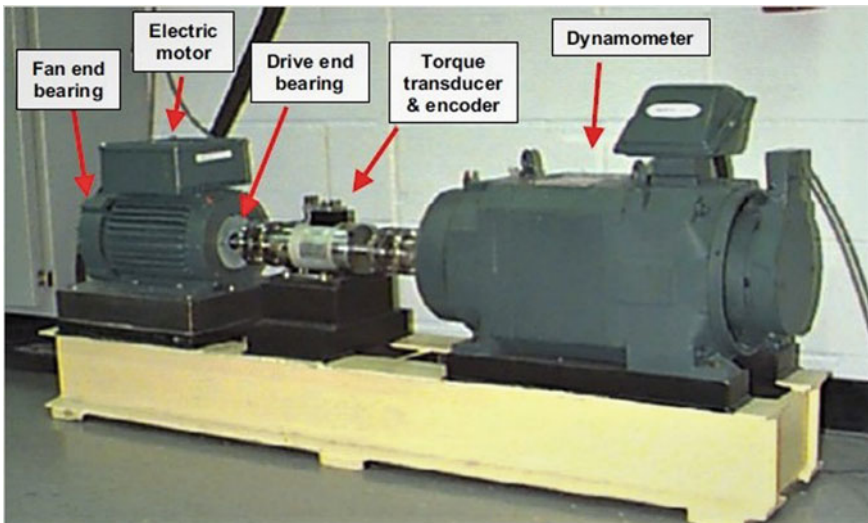
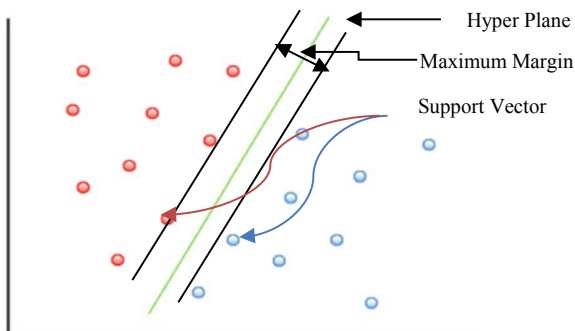


Fig. 2 CWRU bearing test rig [6]

Table 1 Bearing specifications

Bearing type	SKF 6205
External diameter (mm)	52
Internal diameter (mm)	25
Sphere diameter (mm)	7.94
Bearing pitch diameter (mm)	39
Sphere number	9
Contact position	0°

Fig. 3 Support vector machine [9]



three features for every IMF are calculated, namely RMS, kurtosis, and skewness, so a feature vector consisting of 45 features related to fifteen IMFs with 56 instances fed into machine learning algorithms. Afterward, feature ranking is performed with the help of ReliefF method followed by training and tenfold accuracy with the help of random forest and SVM classifier (Fig. 3).

6 Outcomes and Discussion

In this research, training and tenfold cross-validation of classifiers, random forest, and SVM perform for bearing fault diagnosis. Within the tenfold cross-validation method, the developed feature set splits into ten equal-sized bends and ten repetitions perform. In each repetition, one among the tenfold is employed for testing and therefore remaining ninefold is used for training. A total of 56 occurrences and 45 features are used for constructing a feature vector. For random forest, bag size and batch length were considered as 100 and 56. whereas the forfeit parameter C of SVM was agreed to 10 and therefore the PUK kernel preferred. Table 2 shows the average values of features calculated from each IMF. It is observed that the previous couple of values for RMS are not changing; similarly, for skewness and kurtosis, the changes within the last values are nominal. Figure 4a, b shows the variation of accuracy with features related to all IMF. Table 3 shows that thirty-five ranked

Table 2 Average values of statistical features

IMF	RMS value	Kurtosis	Skewness
1	0.315	10.389	0.024
2	0.294	10.763	0.002
3	0.060	8.002	0.012
4	0.051	4.648	0.010
5	0.022	5.451	0.021
6	0.013	3.872	0.023
7	0.006	3.958	0.037
8	0.004	3.698	0.033
9	0.002	4.162	0.039
10	0.002	4.131	0.002
11	0.001	4.189	0.029
12	0.001	4.664	0.078
13	0.001	4.366	0.103
14	0.001	3.979	0.014
15	0.001	3.206	0.010

features using ReliefF and random forest classifier give 100% training and 96.42% tenfold accuracy. With another classifier, it can be additionally judged that SVM provides tenfold cross-validation efficiency (92.85%) thru fourteen ranked features. The feature selected by ReliefF gives maximum tenfold cross-validation accuracy with the random forest, while with SVM tenfold cross-validation accuracy achieved is 92.85% with fourteen selected features only. The proposed work is compared in terms of the machine learning method. Table 4 shows the comparison table for demonstrating the effectiveness of the proposed methodology. Authors have included the literature of the authors during which study is performed on CWRU data. Results are compared in terms of training, testing, and cross-validation accuracy considering various bearing faults with different numbers of features and signal processing techniques proposed by various authors in recent years. The result obtained shows the efficacy of the proposed methodology which may be useful for fault identification.

7 Conclusion

In this paper, EEMD is used as a signal processing method and ReliefF is used as a feature ranking tool. The result can be summarized as follows.

1. Considerations of all IMF values for feature calculation give ease of calculations. IMF contains the fault information, which further helps to diagnose the bearing fault.

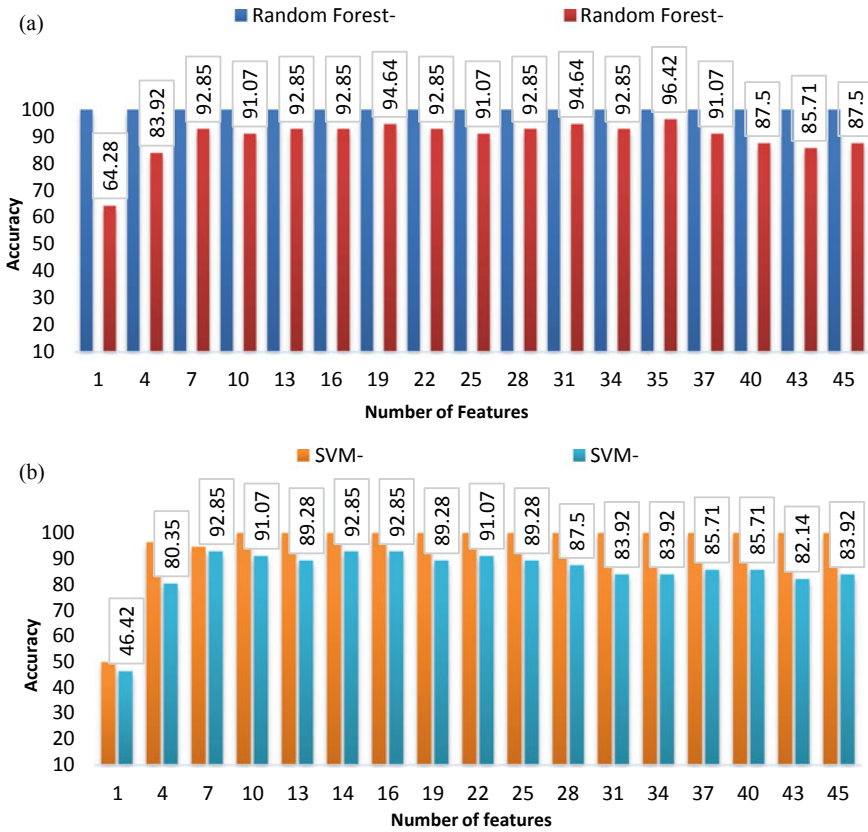


Fig. 4 a and b Training and tenfold accurateness of random forest and SVM, respectively

2. Random forest and SVM correctly identify the data with good accuracy.
3. Characteristic parameters like RMS, kurtosis, and skewness reveal the difference of features.
4. Significant improvement has been observed in fault identification.

Table 3 Confusion matrix

Name	Feature numbers	Training accuracy				Tenfold accuracy					
		HR	IR	OR	BALL	Condition	HR	IR	OR	BALL	Condition
Random forest	35	4	0	0	0	HR	4	0	0	0	HR
		0	12	0	0	IR	0	11	1	0	IR
		0	0	28	0	OR	0	0	27	1	OR
		0	0	0	12	BALL	0	0	0	12	BALL
SVM	14	4	0	0	0	HR	4	0	0	0	HR
		0	12	0	0	IR	0	9	2	1	IR
		0	0	28	0	OR	0	0	28	0	OR
		0	0	0	12	BALL	0	0	1	11	BALL

Table 4 A comparison table showing utility of proposed methodology

References	Machine learning methods	Vibration analysis techniques	Features considered	Maximum accuracy (%)	Remarks
Li et al. [12]	SVN-BT	NA	One hundred eighty	100	Training
Wu et al. [13]	SVM	Multiscale permutation entropy	16 TDFDSFs features, 16 MSEs features, a single P feature, and 16 MPEs	SVM (100)	Training
				SVM (97)	Testing
Yaqub et al. [14]	KNN	Stationery wavelet transform and Db5	NA	KNN (91.23)	Training
				KNN (91.23)	Testing
Vakharia et al. [15]	ANN and random forest	Discrete wavelet transform	Forty statistical features	ANN (93.54)	Tenfold cross-validation
				Random forest (77.41)	Tenfold cross-validation
Present work	SVM and random forest	EEMD signal processing method	Statistical features namely kurtosis, skewness, and RMS	SVM (100)	Training
				SVM (92.85)	Tenfold cross-validation
				Random forest (100)	Training
				Random forest (96.42)	Tenfold cross-validation

Acknowledgements The authors might truly want to express gratitude toward Prof. K. A. Loparo of Case Western Reserve University for giving bearing vibration informational indexes that are used in the investigation. The authors likewise are appreciative to PDPU Gandhinagar for offering the necessary help for finishing these investigations.

References

1. Kankar PK, Sharma SC, Harsha SP (2011) Rolling element bearing fault diagnosis using wavelet transform. *Neurocomputing* 74(10):1638–1645
2. Gao C, Wu T, Fu Z (2018) Advanced rolling bearing fault diagnosis using ensemble empirical mode decomposition, principal component analysis and probabilistic neural network. *J Robot Networking Artif Life* 5(1):10–14
3. Feng Z, Liang M, Chu F (2013) Recent advances in time–frequency analysis methods for machinery fault diagnosis: a review with application examples. *Mech Syst Signal Process* 38(1):165–205

4. Wang D, Yi C, Tsui KL (2018) Making EEMD more effective in extracting bearing fault features for intelligent bearing fault diagnosis by using blind fault component separation. *J Intell Fuzzy Syst* 34(6):3429–3441
5. Lei Y, He Z, Zi Y (2009) Application of the EEMD method to rotor fault diagnosis of rotating machinery. *Mech Syst Signal Process* 23(4):1327–1338
6. Loparo KA (2020) Bearing vibration dataset. Case Western Reserve University. Available at: www.eecs.cwru.edu/laboratory/bearing. Last accessed June 2020
7. Vakharia V, Gujar R (2019) Prediction of compressive strength and Portland cement composition using cross-validation and feature ranking techniques. *Constr Build Mater* 225:292–301
8. Vakharia V, Kiran MB, Dave NJ, Kagathara U (2017) Feature extraction and classification of machined component texture images using wavelet and artificial intelligence techniques. In: 8th international conference on mechanical and aerospace engineering (ICMAE), IEEE, pp 140–144
9. Gujar R, Vakharia V (2019) Prediction and validation of alternative fillers used in micro surfacing mix-design using machine learning techniques. *Constr Build Mater* 207:519–527
10. Widodo A, Yang BS (2007) Support vector machine in machine condition monitoring and fault diagnosis. *Mech Syst Signal Process* 21(6):2560–2574
11. Breimans L (2001) Random forests. *Mach Learn* 45(1):5–32
12. Li Y, Xu M, Wei Y, Huang W (2016) A new rolling bearing fault diagnosis method based on multiscale permutation entropy and improved support vector machine based binary tree. *Measurement* 77:80–94
13. Wu SD, Wu PH, Wu CW, Ding JJ, Wang CC (2012) Bearing fault diagnosis based on multiscale permutation entropy and support vector machine. *Entropy* 14(8):1343–1356
14. Yaqub MF, Gondal I, Kamruzzaman J (2011) Inchoate fault detection framework: adaptive selection of wavelet nodes and cumulant orders. *IEEE Trans Instrum Meas* 61(3):685–695
15. Vakharia V, Gupta VK, Kankar PK (2016) Bearing fault diagnosis using feature ranking methods and fault identification algorithms. *Procedia Eng* 144:343–350

Design of External Wall Painting Robot for High-Rise Buildings



Supreet Thale, Prathamesh Sawant, Saurabh Bagwe,
and N. S. Chandrashekhar

Abstract The external walls of buildings have traditionally been painted by human beings being suspended down from the terraces using gondolas. This is a job which has high risk of fatality. The objective of the project is to reduce this risk and increase productivity by developing an automated programmable and/ or an autonomous external wall painting robot for high-rise buildings which can paint and clean the external walls of buildings without the need of any human intervention. The robot consists of a crane, which is located on the terrace of the building. The crane supports the load of the painting robot via suspended cables and also controls its motion along the vertical wall, while vacuum pads are deployed as an anti-swing mechanism on the wall to prevent the robot from oscillating due to high winds. An arm equipped with a nozzle is programmed to perform painting as it moves along the coordinate axes. This project uses design and simulation software Solidworks, Autodesk Fusion 360 and ANSYS to test the functioning and safety of the machine and provides the customers with a range of product options based on various working conditions which might potentially be present on different working sites.

Keywords Painting technique · Autonomous robot · High-rise buildings · Construction safety · Design concept

1 Introduction

The number of newly constructed high-rise buildings in developing countries like India continues to increase by manifolds each year. The exterior walls of these buildings require to be painted; this increases the demand for exterior wall painting. Exterior wall painting is performed by workers working on suspended gondola or scaffold. They must work with high risk of accidents, such as falls or collisions with protruding walls. The workers need to perform painting and cleaning operation on high-rise buildings at altitudes as high as 200 m and experience high wind forces.

S. Thale (✉) · P. Sawant · S. Bagwe · N. S. Chandrashekhar
K. J. Somaiya College of Engineering, Vidyavihar, Mumbai 400077, India
e-mail: supreet.t@somaiya.edu

© The Author(s), under exclusive license to Springer Nature Singapore Pte Ltd. 2022
K. Govindan et al. (eds.), *Advances in Mechanical and Materials Technology*,
Lecture Notes in Mechanical Engineering,
https://doi.org/10.1007/978-981-16-2794-1_89

1021

This presents a physical and mental challenge to them as well as severely risks their safety. The fundamental element of safety of skilled workers must be addressed to ensure their sustainability. Our project aims to develop an automated robot which paints the external walls of buildings without the need of any human intervention. It consists of a painting robot suspended from the rooftops of buildings using portable crane and winch technology. The painting robot identifies the surfaces which need to be painted using image processing and employs vacuum pads to ensure stability while painting. Various studies and developments with similar concepts have been explored in the section below.

2 Literature Review

Lim [1] patented a six-axis robotic arm mounted on a mini-gondola for painting the external walls of buildings. It uses motor-controlled pulley system which drives the mini-gondola to traverse laterally on a set of twin-rails on the rooftop of the building. It has four vacuum cups mounted on the mini-gondola to secure it to the wall. Takeno et al. [2] patented a system for external wall painting robot with a painting apparatus. It is suspended from a hoist apparatus disposed on the roof of the building. References [3, 4] conducted technical–economic feasibility analysis and life cycle cost analysis, respectively, for versions of automated exterior wall painting robots and concluded that the automated painting robots are technically and economically feasible, enhance safety, productivity and quality compared to the conventional method. Vempati et al. [5] developed an autonomous spray-painting robot using an unmanned aerial vehicle (UAV). It consists of components which captures a 3D model of the target surface, designs its surface appearance and generates commands for robotic painting. Window-cleaning robots employ crane, winch and obstacle avoidance technology which is similar to that required for wall painting robots. Similar developments [6–8] employ a UAV for performing the task of painting using real-time image processing. Kim et al. [9] developed an external window-cleaning robot with a driving mechanism that uses renewable energy. They reviewed the risks of window cleaners falling from gondolas and scaffolding, analysed various patented technologies related to cleaning machines and identified the possibility of having continuous obstacle avoidance for the robot. Lee et al. [10] studied the control system of a wall building façade cleaning robot which uses a crane and winch system. It has three stages, namely preparation stage, cleaning stage and return stage. According to the stages, the robot performs tasks such as cleaning, moving and obstacle detection. The pros and cons of employing a six degrees of Freedom (DOF) robotic arm for painting were studied. Previous developments [11–13] employed a six DOF robotic arm for spray-painting the interior wall surface. They have visualized the main requirements of a reliable robotic arm such as its reach, stability, safety and painting efficiency. These works have also studied the design of end-paint-head, motion and path required for painting and the economic

cost analysis of the robotic painting arm. Teoh et al. [14] developed a fully functional wall painting robot prototype for indoor and outdoor environments. They have used MATLAB and C programming for generating the coordinates of the workspace which is then used to specify the changes in length for the supporting string. The robot paints the workspace specified by the user by avoiding windows. Past studies [15–20] have developed automated interior wall painting robots having mobile robot base as a common feature and by using mechanical mechanisms for the movement of an arm and sprayer nozzle.

Javier et al. [21] developed a wall painting machine comprising a securing device with multiple cables which allow the main painting body to be positioned on any point of the facade of the building and an assembly of omnidirectional wheels which enable it to move over any obstacle or irregularity on the surface whether the surface is regular or irregular.

The scope of the present study is to design an external wall painting robot by exploring motion systems that can be suitable for painting. The robot should incorporate a quick changing and easily mountable crane system on the rooftop of the building to minimize the time wastage and should also be portable, lightweight and cost-effective.

3 Design and Development

A detailed research and study have been carried out for the design and selection of various components involved in the assembly of the robot. The robot consists of the crane system, lifting and rigging system, motion system, painting system, pressure water cleaning system, vacuum system and electronic control system whose general layout has been shown in Fig. 1.

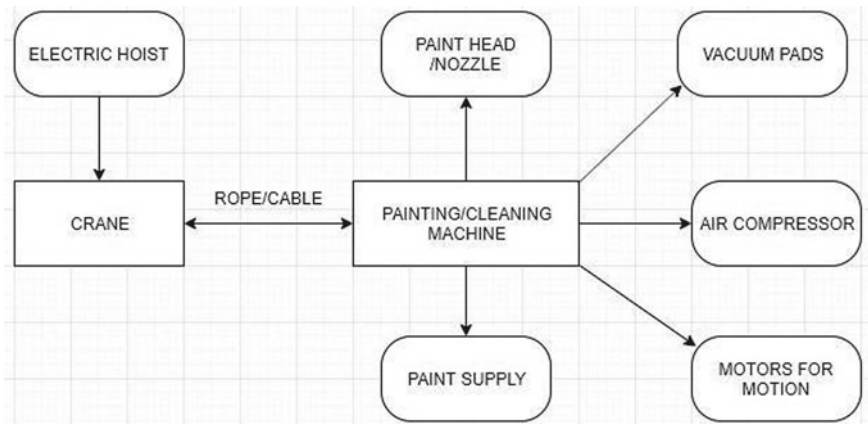


Fig. 1 Layout of external wall painting robot

Table 1 Wind speeds in Mumbai at different altitudes [23]

Altitude (m)	Maximum wind speed (m/s)	Minimum wind speed (m/s)
50	5.84	4.20
100	7.50	4.00
200	8.0	5.25

3.1 Operating Conditions

The study of the topology of skyscrapers and wind speeds in an area is essential in determining the operating characteristics of the robot. The wind speed and the corresponding risk of component failure increase with altitude, and any failure can be dangerous to both, human beings residing in the building and to the machine itself. The study of topology of skyscrapers in Mumbai was done using the data presented in The Skyscraper Centre, a Global Tall Building Database of the Council on Tall Buildings and Urban Habitat [22], and the study of wind speeds corresponding to the operating range was carried out using the Global Wind Atlas [23]. It was found that most buildings in Mumbai range between 15 and 200 m in height and the wind speeds for the aforementioned range lie between 4 and 8 m/s [23]. These are taken as the operating condition for which the robot is designed. The machine is initially designed to operate on a plain wall without having any extra features like balcony, roof, etc. Table 1 shows the maximum and minimum wind speeds in Mumbai at different altitudes.

3.2 Crane Design

Crane is used to suspend the painting robot from the terrace of buildings. It needs to be compact having a capacity of 100 kgs. The two types of crane selected are the mobile crane and the parapet clamp. The mobile crane is made of mild steel whose base is 1500 mm in length and 750 mm in width. The column height is taken as 625 mm, and the beam length is 2100 mm. A hollow rectangular cross section was chosen to reduce bending stresses on the column and beam. The parapet clamp with two clamps made of mild steel is chosen as an alternative to mobile crane in the scenario where the space available on the terrace is not sufficient to mount the mobile crane. The design of mobile crane and parapet clamp is shown in Fig. 2a and b.

The finite element analysis (FEA) of parapet clamp was carried out in Fusion 360 in which the parapet clamp was fixed at three faces which are directly in contact with the parapet wall, and a point load of 150 kg was applied on the leading pair of pulleys of the clamp to simulate the load applied by cable on the pulley. Finally, the anchorage hook at the back of the parapet clamp was fixed in position to simulate the anchoring of the clamp. The deformation was found to be 0.005 mm which is

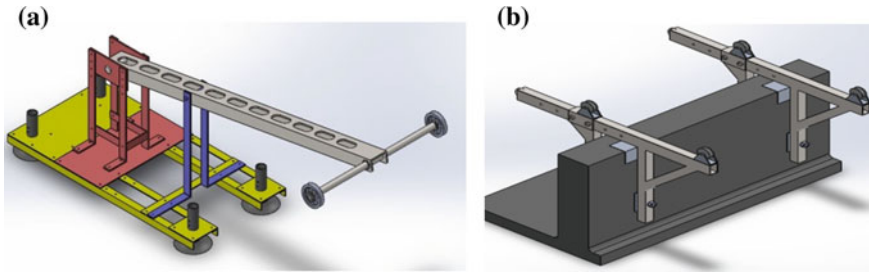


Fig. 2 a Design of mobile crane b Design of parapet clamp

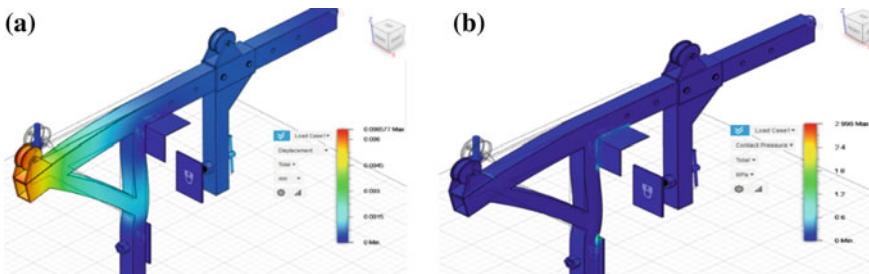


Fig. 3 Exaggerated scale plot for a Total deformation b Contact pressure plot

negligible, the contact pressure at the support plates is 2.9 MPa, and the maximum reaction was found to be 73 N. Figure 3a and b shows the analysis results of parapet clamp.

3.3 Lifting and Rigging

Rope Selection. A wire rope is selected as a medium to lift the robot because it provides flexibility, strength in a smaller diameter design and the ability to handle bending stresses. The selection of wire rope and sheave diameter is done using Design Data: Data Book of Engineers [24].

Maximum payload of the robot considered as 100 kg, calculating for three floor height of building (9.144 m), initially selecting wire rope of 6 × 19 class 3 and standard rope of diameter (d) = 10 mm based on factors such as flexibility, strength and availability.

We obtain a maximum number of wires to support the robot as 4.

From the standard rope diameter, the dimensions selected for the sheave to be used on parapet clamp are $d = 11$ mm, $a = 40$ mm, $b = 30$ mm and $c = 7$ mm.

The specifications of the selected wire rope which is commercially available are displayed in Table 2.

Table 2 Specifications of galvanized rope

Parameters	6 × 19 galvanized (10 mm)
Tensile strength	1960 N/mm ²
Weight	0.346 kg/m
Minimum breaking load	6427 kg

Electric Hoist. For our application of external painting, the hoist should have a lifting capacity of 100 kg considering factor of safety (FOS) as 2 and have a cable length of at least 30 m. The spool should be able to accommodate a wide range of cable diameters, and the working temperature should be around 20–50 °C. The space required and the weight of the hoist should be minimum.

3.4 Motion System

The motion system should be able to move the paint head in required motion to paint any intrinsic surface of the building without altering the position of the main robot platform and be self-locking so as to withstand high wind loads and retain its painting accuracy. The Cartesian robot is selected as it can carry maximum payload without reduction in accuracy as it depends on that of the lead screw rather than the motors. A five axis Cartesian motion system is selected and designed as per our requirements which is shown in Fig. 6a. The motion of the machine in the vertical Y-axis is carried out by the electric hoist. The stroke length is taken as 900 mm so as to replicate the span of human arms in one stroke with the width of the carriage being 290 mm. Aluminium 1060 is selected as the material for the frame because it has adequate strength and lighter in weight as compared to mild steel.

3.5 Painting System

A rotary mechanism is incorporated in the motion system to attach the paint nozzle head to perform painting. The air-assisted spraying system is chosen as its design architecture is simple and works on low pressures, thereby minimizing the power requirement. It is also light in weight (0.6–1.0 kg) as compared to other systems. A flat fan nozzle was selected as it provides good atomization of the liquid paint for the application on the wall and provides efficient utilization of the paint. It also gives variable fan height by varying the pressure. In the project, the paint head will be travelling only in the x-direction, and hence, it is favourable to use flat fan nozzles which will cover sufficient area linearly. The selection of nozzle tip size for acrylic masonry paint is done by following the method used by Sumner [25]. The calculation of nozzle tip size is as follows:

$$\text{For paint coverage capacity} = 14.87 \text{ m}^2/\text{l}$$

Table 3 Specifications of flat fan nozzle [26]

Type	A (mm)	E (mm)	V (l/min) P (bar)				Spray width at P = 2 bar	
632.275	0.60	0.30	0.5	1.0	2.0	5.0	H = 200 mm	H = 500 mm
			0.11	0.16	0.22	0.35	310	590

Speed of painting (horizontal speed of nozzle head) = 0.5 feet/s = 0.340 MPH.

We obtain, flow rate = 0.0551 GPM = 0.208 l/min.

Selecting the nozzle based on flow rate from Lechler catalogue [26]

- Nozzle type = 632.275, fan angle = 75°
- Spray height (H) = 500 mm, spray width (B) = 590 mm (Table 3).

3.6 Vacuum System

The robot will experience oscillation as it is suspended from the terrace and also due to high wind forces acting on the machine at high altitudes. A vacuum mechanism is needed to ensure its stability. Atmospheric pressure varies at different altitudes and has an effect on the level of vacuum pressure. Hence, it is accounted for while calculating the diameter of the vacuum cups. Designing the vacuum cup for the maximum operating range of altitude of 200 m, the atmospheric pressure drops to 0.9866 Bar, the corresponding vacuum gauge drops to 72.3 kPa, and this results in decrease in the suction pressure.

Calculating vacuum cup diameter using Vuototecnica vacuum solutions catalogue [27]:

$$D = 113 \times \sqrt{((m \times s)) / (P_u \times n)}$$

$$m = 25 \text{ kg}, s = 3, P_u = 72.3 \text{ KPa}, n = 2$$

We get the diameter of suction cup (D) = 81.38 mm. Hence, two vacuum cups with a diameter equal to or greater than 81.38 mm will therefore be required. Selecting from standard available suction cups: Vuototecnica round flat foam rubber vacuum cup 08 92 15, D = 92 mm.

Based on diameter of the suction cup selecting the suction rate of vacuum generator:

Suction capacity for single cup (Vs) = 1 m³/h = 16.6 l/min.

Calculating total suction rate (V) for the system

$$V = n \times V_s = 2 \times 16.6 = 33.2 \text{ l/min}$$

The suction cup is selected based on the conditions that it is able to withstand wind speeds in range of 4–8 m/s [23] at 200 m altitude above sea level and a horizontal load of 25 kg. External wall surface roughness considered as 0.7.

3.7 Supporting Wheel

The supporting wheels are mounted on the top of the robotic arm to provide stability and support to the painting robot and to safeguard the robot and position it at a fixed distance from the wall to withstand high wind speeds. The wheel assembly shown in Fig. 6a is controlled by an actuating mechanism which gives feedback to the electronic control unit.

3.8 Analysis of Painting Robot

The static structural analysis of the robot was carried to check for possible failures and safety. The hooks of the main frame were fixed in position with zero degrees of freedom emulating the condition where the wire ropes will be connected from the crane to the robot, and a pressure load of 500 N was applied at the bottom of the container plate to simulate the weight of the components attached to it. A point load was applied where the painting nozzle is connected to the robot arm to simulate the weight and forces on the nozzle. Figure 4a and b shows total deformation and contact pressure plot, respectively, and the deformation was found out to be 0.35 mm maximum on the nozzle holder when subjected to 10 N load which is taken extra as a safety measure. The maximum stress was 13 MPa (Fig. 4).

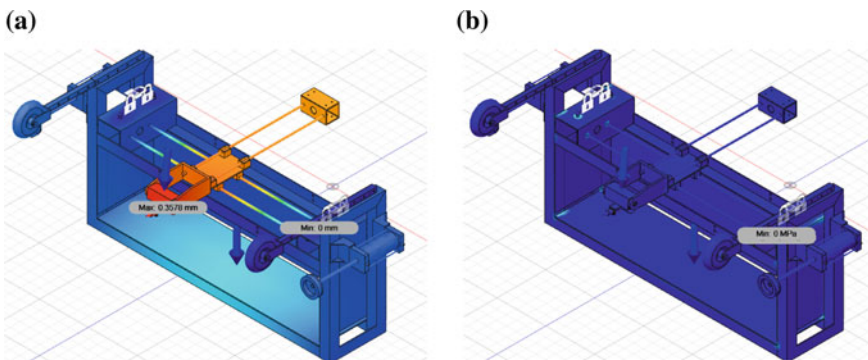


Fig. 4 a Total deformation plot b Contact pressure plot

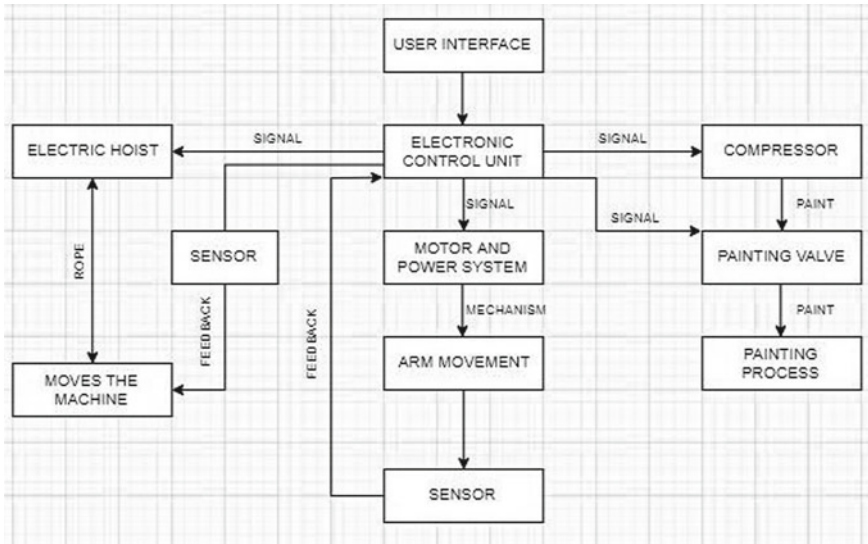


Fig. 5 General layout and working of the electronic control system for the painting robot

3.9 Working and Assembly

The crane is mounted on the terrace of a building to which the painting robot is suspended with the help of wire rope. The area of the wall to be painted is first captured by the ESP32-CAM camera module of the image processing unit, and it determines the areas which are to be painted. The ultrasonic sensor determines the distance between the wall and the nozzle, and it along with the camera module sends signals to the Arduino Uno development board and electronic control unit which instructs the NEMA 17 stepper motors of the motion system to actuate and position itself according to the required proximity w to the wall and the painting system to start the supply of paint through the nozzle.

The motion system completes a horizontal painting stroke and returns to the previous position, thereby applying two layers of paint. The electric hoist then lowers the robot by a fixed distance, and the cycle is repeated until the entire area is painted. Figures 5 and 6 show the general working layout and assembly of the robot.

4 Conclusion

The design of the wall painting robot has been presented in this project. It has been tested for safety in a virtual simulation lab like ANSYS and Fusion 360 according to the on-site working conditions. The robot has the ability to spray an area of about 0.54 m² in a single stroke, and the components are designed and selected with

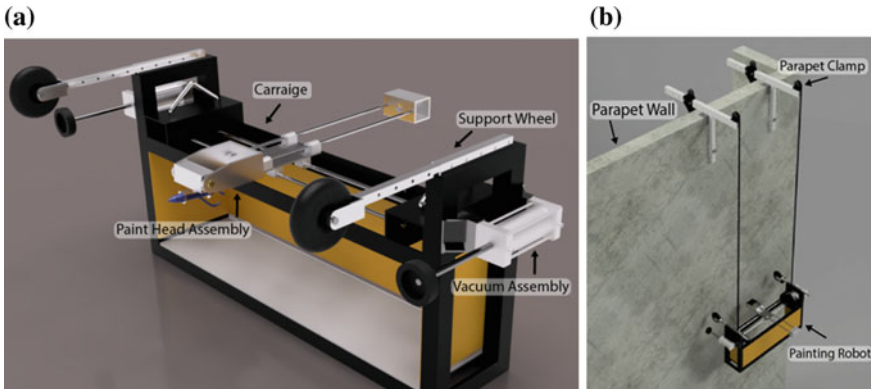


Fig. 6 Rendered isometric view of **a** External wall painting robot **b** Assembly

consideration to reduce the weight of the robot and at the same time be safe and efficient. The lateral dynamic force experienced on the robot due to wind speeds was negligible compared to the suction force provided by the vacuum pads, and hence, only static structural analysis has been carried out. The current scenario has restricted further attempts of prototyping and testing the robot on-site. The fabrication and rigorous testing of the robot is the next stage in this project. The risk of fatality of human life during painting operation can be reduced to negligible, and the manpower required to operate the robot is reduced to a maximum of 2–3. It has the potential to speed up the painting and cleaning process by about 30% since the robot does not need a break. The automated system also minimizes wastage and can save up to 20% of paint. The external wall painting robot can be a potential substitute to the traditional techniques present in the industry. It aims to improve the safety and efficiency of the painting industry.

References

1. Lim HE (2017) System and method for spray painting external walls of building. US20170282202A1
2. Takeno M, Sakai Y, Shirato A. Apparatus for automatically painting external wall of building, US4944243A
3. Kim YS, Jung MH, Cho YK, Lee J, Jung U (2007) Conceptual design and feasibility analyses of a robotic system for automated exterior wall painting. *Int J Adv Rob Syst* 4(4):49
4. Yeom D-J, Na E-J, Lee M-Y, Kim Y-J, Kim YS, Cho C-S (2017) Performance evaluation and life cycle cost analysis model of a gondola-type exterior wall painting robot. *Sustainability* 9(10):1809
5. Vempati AS, Kamel M, Stilinovic N, Zhang Q, Reusser D, Sa I, Nieto J, Siegwart R, Beardsley P (2018) PaintCopter: an autonomous UAV for spray painting on 3D surfaces. *IEEE Robot Autom Lett* 3(4):2862–2869
6. Dahlstrom RL (2020). Apellix, State of technology: cleaning and coating UAV systems—industrial spray painting drones. *Offshore Technology Conference*

7. Lai J-H, Ma Y, Shi C, Xia Y (2016) Automatic painting system with drone, user interface and computer vision. US10023311B2
8. Busby LA, Iverson T, McMaster R (2014) Systems and methods for unmanned aerial painting applications, US9776200B2
9. Kim K, Jun Y (2016) Development of a window-cleaning robot powered by new renewable energy capable of continuous operation during obstacle avoidance. *Int J Sustain Build Technol Urban Dev* 7(3–4):214–218
10. Lee Y-S, Kim S-H, Gil M-S, Lee S-H, Kang M-S, Jang S-H, Bo-Hyun Yu, Ryu B-G, Hong D, Han C-S (2018) The study on the integrated control system for curtain wall building façade cleaning robot. *Autom Constr* 94:39–46
11. Yang G, Hu C, Meng H, Wang SY (2019) Constraint path planning for an autonomous wall spray coating robot. In: *International conference on robotics and biomimetics*, China
12. Asadi E, Li B, Chen IM (2018) Pictobot: a cooperative painting robot for interior finishing of industrial developments. *IEEE Robot Autom Mag* 25(2):82–94
13. Kahane B, Rosenfeld Y (2004) Balancing human-and-robot integration in building tasks. *Comput-Aided Civil Infrastruct Eng* 19(6):393–410
14. Teoh BE, Ragavan SV (2011) PAINTbot—FPGA based wall painting service robot prototype. *IEEE Recent Adva Intell Comput Syst*
15. Sorour M, Abdellatif M, Ramadan AA, Abo-Ismael AA (2011) Development of roller-based interior wall painting robot. *Int J Mech Mech Eng* 5(11)
16. Abdellatif M (2013) System design considerations for autonomous wall painting robot. *Int J Eng Res Technol* 2(10)
17. Keerthana P, Jeevitha K, Navina V, Indira G, Jayamani S (2013) Automatic wall painting robot. *Int J Innov Res Sci Eng Technol* 2(7)
18. Sorour M (2015) RoboPainter—a detailed robot design for interior wall painting. *IEEE Int Workshop Adv Robot Its Soc Impacts*
19. Vani M, Mohamed Sirajudeen KI, Nidhinsha, Sheron BJ (2017) Automatic sensor based wall painting robot. *Int J Adv Eng Sci Res* 4(1):49–56
20. Raman S, Jennings B, Giovacchini RJ, Cherbaka E, Slater TC, Ye TH (2017) Autonomous painting systems and related methods. US10124359B2
21. Javier R, George C, Merchan F, Berbey A (2017) Wall-painting machine. WO2017042729A1
22. The Skyscraper Center, Global Tall Building Database of the CTBUH. Retrieved Oct 2019. <https://www.skyscrapercenter.com/city/mumbai>
23. Global Wind Atlas. Retrieved Oct 2019. <https://globalwindatlas.info/>
24. Achchagam K, PSG College of Technology, Coimbatore, India (2017) Design data, data book of engineers, pp 9.1–9.10, Oct 2017. ISBN 978-81-927355-0-4
25. Sumner PE (2012) “Sprayer nozzle selection”. *Cooperative Extension (Bulletin 1158)*, The University of Georgia
26. Lechler Catalogue: Flat fan nozzles Series 632 /633, (2017) https://www.lechler.com/fileadmin/media/kataloge/pdfs/industrie/katalog/EN/04_flatstrahl/lechler_flat_fan_nozzles_series_632_633.pdf
27. Vuototecnica-Vacuum Solutions Catalogue, pp 23–37, 1.24–1.26

Optimization of Wear Behaviour of Sugarcane Bagasse-Based Epoxy Particulate Composite Using Taguchi Method and Grey Relational Analysis



Ankit, Rajesh , and Anil Kumar

Abstract The evolving world of composite materials needs to adopt cheap and easily available green material as the reinforcement. In this study, sugarcane bagasse is used as the reinforcement in the epoxy matrix. This study is based on the analysis of wear behaviour of sugarcane bagasse epoxy composite for varying sliding speed, sliding time and applied load. Epoxy composite reinforced with sugarcane bagasse is made up by hand lay-up process using epoxy, hardener and sugarcane bagasse in powdered form. This material is subjected to the wear testing on pin on disc wear testing machine under dry conditions. A plan of experiment was made ready by using Taguchi L9 orthogonal array to find out the wear behaviour in form of wear and frictional force in a controlled manner. In this study, analysis of variance is used to find out the correlation of process parameters with applied load, sliding distance and sliding time of epoxy composite. It was observed that the varying applied load, sliding time and sliding speed relatively affect the wear property of epoxy composite. The optimal combination of process parameters resulted in minimum dry sliding wear.

Keywords Epoxy · Wear · Sugarcane bagasse reinforced particulate composite · Taguchi · GRA

1 Introduction

Recently, industrialists and researchers have shown their great interest in natural fibres or their powder form as reinforcements for composites. Natural fibres are originated from different sources such as bamboo, cereal, cotton, wool, jute, hemp and sisal. The fibres contain mainly cellulose and lignin with pectins [1–3]. Natural fibres have many advantages over synthetic fibres, such as biodegradable nature, low

Ankit · Rajesh (✉)
Department of Mechanical Engineering, UIET, MDU, Rohtak, India

A. Kumar
Department of Mechanical and Automation Engineering, G.B. Pant Engineering College, New Delhi, India

cost, abundant availability and flexibility in processing which results in less machine wear. Less density makes them light in weight compared to synthetic fibres. Less machining wear minimizes the danger in processing [4, 5]. This study is focused on the sugarcane bagasse-reinforced composites. Sugarcane bagasse is a natural waste material left out after the extraction of juice from sugarcane [6]. It is easily available in sugar mills. Like any lignocellulosic material. Sugarcane bagasse is constituted of cellulose, hemicelluloses and lignin, with a small amount of ash and extractive. Bagasse can be used to make disposable food containers and to make papers [7, 8].

2 Literature Review

Juliana et al. [1] explained the use of sugarcane bagasse fibres as the reinforcement to make the polypropylene composite and observed that most of the properties of both the composites are similar to each other. Sergio et al. [2] tried to find out the impact nature of the sugarcane bagasse fibres and waste particles of rubber-reinforced hybrid composite. They observed more amount of rubber, and longer bagasse fibres give higher energy absorption. Fabio et al. [3] explained that sugarcane bagasse can be used as the semi-reinforcement in the manufacturing of sandals of composites of natural rubber. Marwa et al. [4] gave explanations about some mechanical properties of sugarcane bagasse and glass and/or polyester composite. They concluded that the mechanical properties of a composite material of sugarcane bagasse and polyester are improved in cooperation with the mat of E-glass. Ruano et al. [5] introduced bagasse and hemp fibre-reinforced cementitious composites. Bagasse fibres broken with little displacement and hemp fibres were pulled out completely in the pull-out test. Arjun et al. [6] used the bagasse of sugarcane to prepare the reinforced composite and studied that the alkali-treated reinforced composite of sugarcane bagasse has improved properties over the untreated composite. Elammaran et al. [7] tried composites reinforced with fly ash and sugarcane bagasse fibre. They concluded that the addition of 4 wt% of bagasse fibres and 2 wt% of ash gave enhanced hardness and tensile strength. Dhiwakar et al. [8] prepared a hybrid composite of sugarcane bagasse fibres and glass fibres. They concluded that there is approximately a 15 percent difference in outcomes of tensile strength and bending strength by both the methods. Narinder et al. [9] used aluminium alloy AA60636 metal matrix for SiC particles of size 37 μm and found that optimum value of wear and frictional force was at 20 N load, 1570 m sliding distance and 10.5% of SiC by weight. Arun et al. [10] described the fabrication of carbon fibre composites using nano-SiC particles and observed increased tensile strength and compressive strength by the addition of SiC particles.

3 Objective of the Study

This study is based on identifying the wear behaviour of the reinforced composite using sugarcane bagasse in the powder form as the reinforcement and to optimize the frictional force and wear from pin-on-disc sliding wear test in dry conditions with utilization of Taguchi analysis and using the grey relational analysis tool (GRA tool).

4 Methodology

1. Collecting of the raw material, sugarcane bagasse and epoxy resin and hardener, fabrication of the sugarcane bagasse-reinforced particulate composite and to cut them in the different sample sizes.
2. Preparation of L9 orthogonal array in Taguchi design for three factors with three levels, performing the pin-on-disc sliding wear test on the different sample sizes to obtain frictional force and wear values.
3. To optimize the results using Taguchi method with GRA.

5 Experimental Work

5.1 Composite Preparation

The fabrication of sugarcane bagasse powder-reinforced composite was done by hand lay-up technique. First, a plane surface of glass was polished and cleaned with a release agent. A mixture was prepared with 50% by volume of sugarcane bagasse powder with the epoxy resins in 10:1 ratio with hardener. Then, the fabrication was left to cure for 24 h at normal room temperature (Figs. 1 and 2).

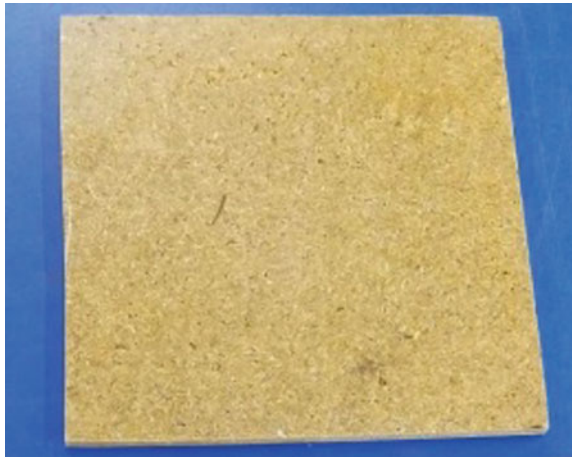
5.2 Pin-on-Disc Wear Test

The samples have been tested on DUCOM (TR-20LE) pin-on-disc tribometer. The samples are cut of size 25 mm × 6 mm × 6 mm as shown in Fig. 2. Dry sliding wear tests of samples have to be done at normal room temperature conditions. The readings of the wear, in micrometer, and the frictional force, in newton, made available on the screen simultaneously (Figs. 3 and 4; Table 1).

Fig. 1 Sugarcane bagasse powder



Fig. 2 Reinforced composite



5.3 Taguchi Design

Three factors, viz. load placed in Newton, time for sliding in minutes and speed of rotating disc in RPM, were considered at three different levels for the wear test. The analysis of process parameters has been done with the Taguchi L9 array using MINITAB software (Table 2).

From the above orthogonal array, sample no. 1 was taken at randomly, and pin-on-disc test was performed on this sample. From pin-on-disc test, we have obtained the following graphs (Figs. 5 and 6).

Similarly, the test is conducted with remaining samples. The values of frictional force and wear obtained by the pin-on-disc wear test on all nine samples are shown in Table 3.

Fig. 3 Pin-on-disc wear test machine



Fig. 4 Samples to be tested



Table 1 Process parameters in input and their different levels

SI. No.	Process parameters	Levels		
		1	2	3
1	Normal load (N)	10	20	30
2	Time for sliding (min)	2	3	4
3	Speed for sliding (rpm)	400	500	600

Table 2 Taguchi L9 array of input process parameters

SI. No.	Load (N)	Time (min.)	Rpm
1	10	2	400
2	10	3	500
3	10	4	600
4	20	2	500
5	20	3	600
6	20	4	400
7	30	2	600
8	30	3	400
9	30	4	500

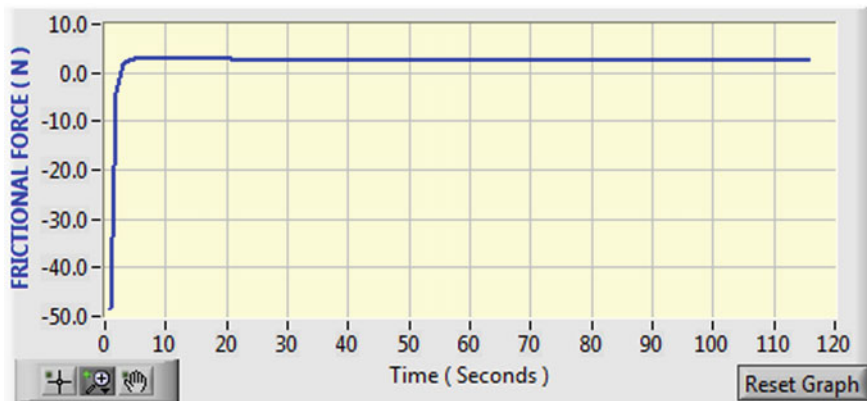


Fig. 5 Frictional force versus time

5.4 Taguchi and GRA Analysis to Optimize the Wear Behaviour

Taguchi analysis is one of the most helpful and important tools to optimize and utilize the various problems in designing with utilization of the beautiful GRA tool. A statistical data tool signal-to-noise (S/N) ratio, utilized by Taguchi tool, has been used to investigate the obtained results in pin-on-disc test. Whole behaviour responses as frictional force and wear are “smaller-is-better” type so to calculate S/N (M) ratio in Taguchi analysis with the help of given equation:

$$M_{ij} = -10 \log_{10} \left(\frac{1}{n} \sum_{j=1}^n y_{ij}^2 \right) \quad (\text{smaller-is-better}) \quad (1)$$

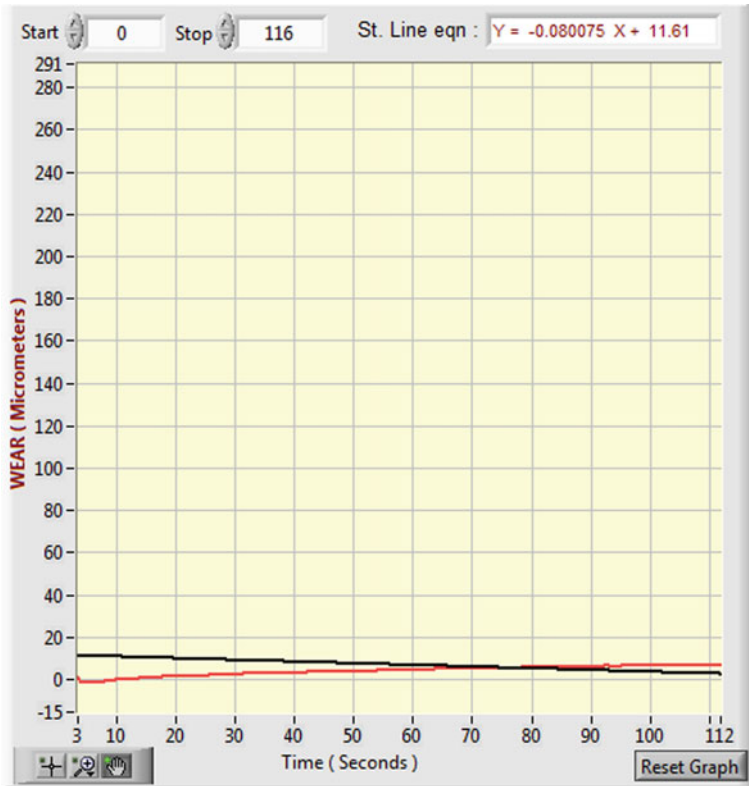


Fig. 6 Wear versus time

Table 3 Data for response behaviour on all samples

SI. No.	Load (N)	Time (min.)	Rpm	Wear	Friction force (N)
1	10	2	400	7	2.6
2	10	3	500	6	2.5
3	10	4	600	9	3.8
4	20	2	500	8	3.2
5	20	3	600	4	3.2
6	20	4	400	24	6.3
7	30	2	600	16	9.7
8	30	3	400	20	3.7
9	30	4	500	10	4.9

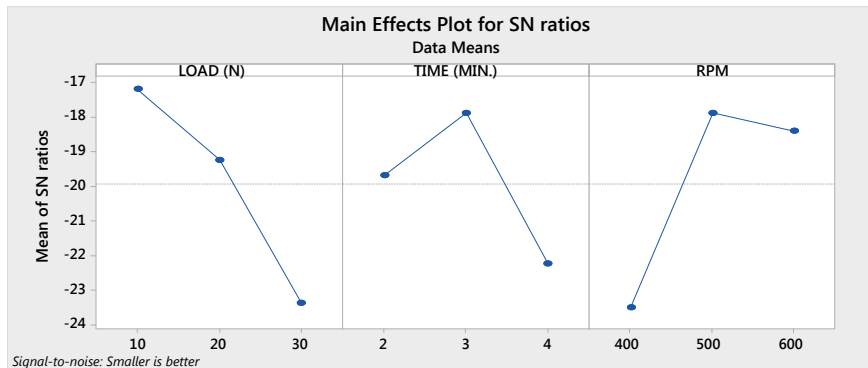


Fig. 7 Main effects plot of S/N ratio for wear

Table 4 Table of responses showing signal-to-noise (S/N) ratios (smaller-is-better)

Level	Load (N)	Time (min.)	Rpm
1	-17.18	-19.68	-23.51
2	-19.24	-17.87	-17.87
3	-23.37	-22.23	-18.40
Delta	6.18	4.35	5.63
Rank	1	3	2

• **Taguchi analysis: wear versus load (n), time (min.), rpm** (Fig. 7; Table 4)

The table of responses and the main effects plot of wear give a clear view that the entire chosen factor is almost equally responsible for the wear of the samples. Also, it has been observed that the optimum wear can be achieved at load of 10 N, time of test 3 min and at RPM 500.

Taguchi Analysis: Friction force versus load (n), time (min.), rpm (Fig. 8; Table 5):

The table of responses and the main effects plot of friction force show clearly that the entire chosen factor is almost equally responsible for the wear of the samples, but load variation can cause a greater effect. Also, it has been observed that the optimum wear can be achieved at load of 10 N, time of test 3 min and at RPM 500.

5.5 Grey Relational Analysis (GRA)

GRA, discovered by Ju-Long in 1982, is a special tool requiring knowing and unknowing elements setting up together to obtain optimal values of the behaviour responses. Grey relational coefficient (GRC) and grey relational grade (GRG),

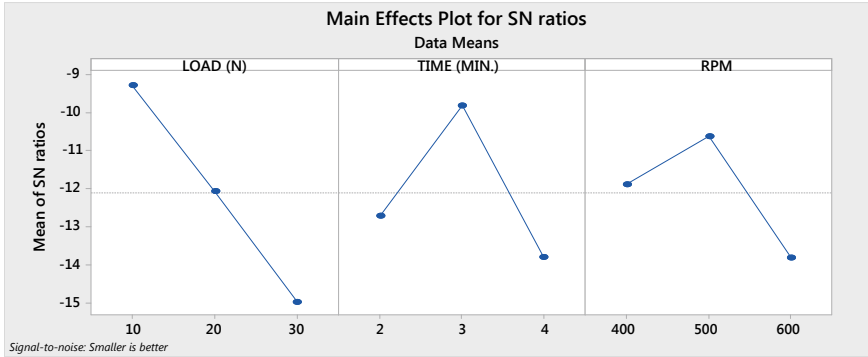


Fig. 8 Main effects plot of S/N ratio for friction force

Table 5 Table of responses showing signal-to-noise (S/N) ratios (smaller-is-better)

Level	Load (N)	Time (min.)	Rpm
1	-9.285	-12.713	-11.883
2	-12.064	-9.809	-10.622
3	-14.968	-13.795	-13.811
Delta	5.683	3.987	3.189
Rank	1	2	3

computed for the normalization of obtained experimental values, were used by GRA. Frictional force and wear of the fabricated composite structure are main quality elements. Each of these quality elements is “smaller-is-better” type. The first step was to prepare GR formulation with data of 0 and 1. This formulation is done for both the quality elements. In this examination, both the chosen quality elements are “smaller-is-better” type (Tables 6 and 7).

The higher GRG value shows improved relation of process parameters at the given level, and that level has been estimated as the optimized level of process parameters. Here in table, it has been observed that as per GRA, the optimum parameters are load 10 N, time of operation 3 min and 500 rpm for optimum wear and friction force.

6 Results and Discussions

- **Taguchi Analysis: WEAR Versus LOAD (N), TIME (MIN.), RPM:** The response table and the main effects plot of wear show clearly that the entire chosen factor is almost equally responsible for the wear of the samples. Also, it has been observed that the optimum wear can be achieved at load of 10 N, time of test 3 min and at RPM 500.

Table 6 Calculation of GR coefficients and GR grade

Load (N)	Time (Min.)	Rpm	Wear	Friction force (N)	GR coefficient		GR grade
					Wear	FF	
10	2	400	7	2.6	0.769	0.972	0.871
10	3	500	6	2.5	0.833	1	0.916
10	4	600	9	3.8	0.666	0.734	0.700
20	2	500	8	3.2	0.714	0.837	0.775
20	3	600	4	3.2	1	0.837	0.918
20	4	400	24	6.3	0.333	0.486	0.409
30	2	600	16	9.7	0.454	0.333	0.393
30	3	400	20	3.7	0.384	0.75	0.567
30	4	500	10	4.9	0.625	0.6	0.612

Table 7 Average GR grade for factors and levels of the experiment

Level	Load	Time	Rpm
1	0.82948	0.68026	0.61611
2	0.70142	0.80008	0.7683
3	0.52445	0.57436	0.67107

- **Taguchi Analysis: Friction Force Versus LOAD (N), Time (MIN.), RPM:** The table of responses and the main effects plot of friction force show clearly that the entire chosen factor is almost equally responsible for the wear of the samples, but load variation can cause a greater effect. Also, it has been observed that the optimum wear can be achieved at load of 10 N, time of test 3 min and at RPM 500.
- **Grey relational analysis (GRA):** In GRA, knowing and unknowing elements are set up together for getting optimal values of the behaviour responses. Grey relational coefficient (GRC) and grey relational grade (GRG), computed for the normalization of obtained experimental values, were used by GRA. Frictional force and wear are main quality elements. Each of these quality elements is “smaller-is-better” type. It has been observed that as per GRA, the optimum parameters are load 10 N, time of operation 3 min and 500 rpm for optimum wear and friction force.

7 Conclusion

Main aim of this research is optimizing the wear behaviour characteristics, frictional force and wear, of the sugarcane bagasse-reinforced particulate composite using Taguchi and GRA—the multi-step optimizing tools. S/N ratio values for both

performance factors have been computed. The lower frictional force and wear values are required for the improved wear behaviour. Equation 1 has been utilized to calculate the S/N ratio with the help of the MINITAB 178 software system. It has been observed that optimum wear can be achieved at load of 10 N, time of test 3 min and at RPM 500. It has also been observed that as per GRA, the optimum parameters are load 10 N, time of operation 3 min and 500 rpm for optimum wear and friction force. Also, it has been clear that the results of the GRA are in total agreement with the results of the Taguchi analysis. Therefore, finally it has been found that the optimum parameters for wear and friction force are (a) load—10 N, (b) time of operation—3 min and (c) RPM—500.

References

1. Anggono J, Farkas AE, Bartos A, Moczo J, Antoni, Purwaningsih H, Pukanszky B (2019) Deformation and failure of sugarcane bagasse reinforced PP. *European Polym J* 112:153–160
2. Ribeiro Filho SLM, Oliveira PR, Panzera TH, Scarpa F (2018) Impact of hybrid composites based on rubber tyres particles and sugarcane bagasse fibers. *Compos Part B*. <https://doi.org/10.1016/j.compositesb.2018.09.054>
3. de Paiva FFG, de Maria VPK, Torres GB, Dognani G, dos Santos RJ, Cabrera FC, Job AE (2019) Sugarcane bagasse fiber as semi-reinforcement filler in natural rubber composite sandals. *J Mater Cycles Waste Manag* 21:326–335
4. Abd El-Baky MA, Megahed M, El-Saqqa HH, Alshorbagy AE (2019) Mechanical properties evaluation of sugarcane bagasse-glass/polyester composites. *J Nat Fibres*. <https://doi.org/10.1080/15440478.2019.1687069> (2019)
5. Ruano G, Bellomo F, Lopez G, Bertuzzi A, Nallim L, Oller S (2019) Mechanical behaviour of cementitious composites reinforced with bagasse and hemp fibres. *Constr Build Mater* <https://doi.org/10.1016/j.conbuildmat.2019.117856>
6. Ramesh AV, Paul E, Irfan CH, Sadiq Ali KK, Anjaldev VV (2018) Comparative study of the mechanical properties of alkali treated and untreated sugarcane bagasse fibre reinforced composite material. *Int Res J Eng Technol (IRJET)*, vol 05
7. Jayamami E, Rahman MR, Benhur DA, Bakri MKB, Kakar A, Khan A (2020) Comparative study of fly ash/sugarcane fibre reinforced polymer composites properties. *BioResources* 15(3):5514–5531
8. Ram DS, Bharath Kumar PN, Sandeep Kumar R, Vijaya Ramnath B (2020) Evaluation of mechanical properties of sugarcane reinforced hybrid natural fibre composites by conventional fabrication and finite element method, vol 841. <https://doi.org/10.4028/www.scientific.net/KEM.841.327>
9. Kaushik N, Singhal S (2018) Optimisation of wear properties in aluminium metal matrix composites using hybrid Taguchi-GRA-PCA. *Int J Performability Eng* 14(5):857–870. <https://doi.org/10.23940/inpe.18.05.p4.857870>
10. Arun Premnath A (2018) Wear studies on carbon fibre nano SiC composites—a Gray-Taguchi method Optimisation. *Parts Sci Technol*. <https://doi.org/10.1080/02726351.2018.1498041> (2018)

Parametric Investigation of Ballastless Railway Track for High-Speed Railway



Yamika Patel, Vikas Rastogi, and Wolfgang Borutzky

Abstract Increasing population and high population density of India have put intense pressure on existing railway track. They are operating at a way more than their capacity, and this has strained many rail lines which lead to derailment and other mishaps. This high population density suits high-speed railway in the country. To fight with increased traffic with regard to speed and loading, the stresses variation in various components must be known accurately to evaluate useful life of each component for its life assessment. To assess, this detailed analysis is necessary to develop methodology for every track component under actual loading condition. In this paper, a comprehensive study of the behavior of ballastless track structure for high-speed train under static load has been carried out. For the analysis, three-slab track model has been developed which are simple track model, standard track model, and shinkansen track model. Deflection and stresses are the parameters which are used to analyze the performance of track system. Different track structures are analyzed under stationary wheel loads using finite element method of analysis. The influence of various parameters, i.e., change in material properties of track components on the behavior of track structures, is also investigated.

Keywords High-speed track · ANSYS · Parametric study · Ballastless track

1 Introduction

Train transport is known to be one of the earliest modes for locomotion. With continuous advancements, this mode of service is becoming better day by day. The arrival and development of the concept of high-speed trains brought a new revolution to this mode of traveling, with the large operational ranges getting covered in such a short

Y. Patel (✉) · V. Rastogi
Delhi Technological University, Delhi, India
e-mail: yamika_phd2k17@dtu.ac.in

W. Borutzky
Bonn-Rhein-Sieg University of Applied Sciences, Sankt Augustin, Germany

time span. This is taking the competition with airplanes to an all new height as more comfort and safety can be provided and that too at such a minimal cost. Though the average traveling time of airplanes is still far lesser than trains, the convenience and comfort compensate for the total time in some cases for the passengers. While calculating the time duration between the origin and the destination, many factors play a vital role such as distance between infrastructure and point of starting, time taken to access the vehicle, the lines of waiting, time span needed for passengers' control, etc. Considering all these vital factors and considering that though airplanes take lesser time, the time of displacement for passengers is lesser in trains compared to them. Thus, this reason along with petrol price hike and ever-increasing pollution has resulted in much support toward this development. The basis of analysis of the track structure was to provide and prove a system which would predict the stresses, elastic deflections, and settlements which occur in the different components of track structure under stationary vertical wheel loads. Rail track models were simulated for deciding the reactions caused by the moving train load. In rail track models, all the components of tracks were interrelated. These models are quite effective and accurate tool for predicting the rendition of the tracks. The forces generated on the topmost surface of rails were transmitted to the concrete slab. The longitudinal forces were developed while braking and accelerating operations were imparted to the track structure. Lateral forces are evenly distributed on the rail side surfaces [1]. Setu et al. [2] presented analytical formulation of rail track system. A change in track model brings in wide change in receptance and track decay rate in frequency domain. Li and Berggren [3] examine the rendition of the tracks while considering the effect of track stiffness along the vertical direction and also its variation along the track. Setu et al. [2] presented governing differential equation and finite element formulation of the beam on elastic foundation of Winkler type is taken into the account. The results from two-loading pattern, single point load of 98 kN [4] corresponding to a single wheel and two pair of wheels of same magnitude at each of the contact point, are provided for track displacement, bending moment, and shear force variation in and around the contact region by considering different boundary conditions. Sadeghi et al. [5] investigate the dynamic behavior of ballastless track under unsupported sleeper. By incorporating the nonlinear behavior of fastening system, Oregui et al. [6] examined the vertical dynamics of track structure. Khajehdezfuly [7] study the effect of rail pad stiffness on the contact force developed at wheel rail interface.

2 FE Modeling

The rail track system is a convoluted system. It is a collection of rails, pads, sleeper, slab, concrete, and foundation. For analysis, three-slab track model has been developed which are simple track model (model1), standard track model(model2), and shinkansen track model (model3). Simple track model is formed by integrating rail, rail pad, concrete slab, hydraulic bearing layer (HBL), and foundation. The geometry

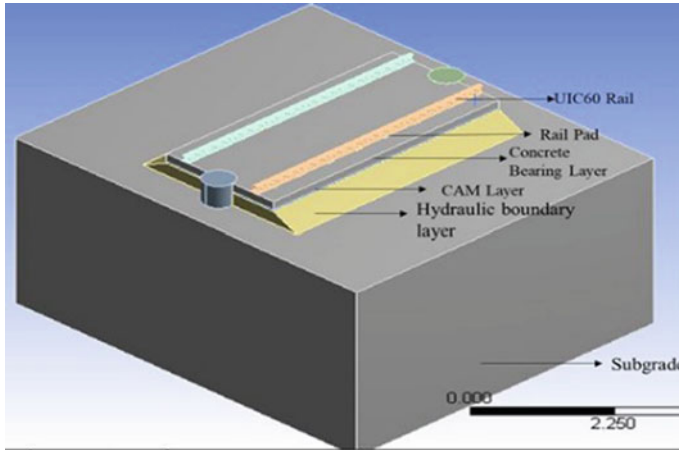


Fig. 3 Shinkansen track model

it. Geometrical and material properties of different track components are shown in Table 4. The geometric model of shinkansen track is shown in Fig. 3.

3 Simulation

Static structural analysis of high-speed railway track has been done on ANSYS 18.1 which is based on finite element method. Whole model is discretized into finite element using mesh features listed in Table 1 and Fig. 4.

3.1 Track Characteristics

Geometrical and material properties of different track components are shown in Table 2. All the properties are represented in terms of elastic modulus, Poisson’s ratio, and density of materials.

Table 1 Mesh details

Mesh size	Fine
Mesh type	Quadrilateral
Edge length	0.00216 m
No. of elements	60,394

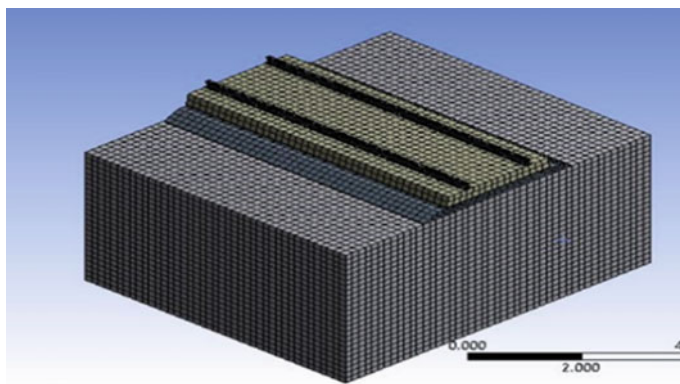


Fig. 4 Mesh generation

Table 2 Shinkansen track properties

	Dimensions/parameter	Young's modulus (MPa)	Poisson's ratio (ν)	Density (kg/m^3)
Rail	UIC 60	205,800	0.3	7872
Rail pad	Stiffness = 70 kN/m Thickness = 9 mm	1100	0.42	950
Slab	Length = 4.95 m Width = 2340 mm Thickness = 190 mm	38,000	0.2	2400
Concrete asphalt mortar layer	Length = 4.95 m Width = 2340 mm Thickness = 40 mm	8000	0.25	1800
Hydraulic bearing layer	Length = 4.95 m Width = 2950 mm Thickness = 200 mm	23,000	0.25	2400
Subgrade	Length = 5.5 m Width = 7.5 m Thickness = 4 m	100	0.3	1800

3.2 Boundary Conditions

In Fig. 5a, the complete load model is presented. For the loading conditions, stationary multiple vertical wheel loads are considered for the present study. Research Designs and Standards Organization (RDSO) has defined several wheel load configurations for coaches, locomotives, and wagons. For present study, maximum axle load defined by RDSO to consider for high-speed railway track is considered. India has moved to axle load of 22 tons.

This load is provided in the form of pressure acting on an elliptical patch on the rail. This elliptical patch shown in Fig. 5b represents the contact area between wheel

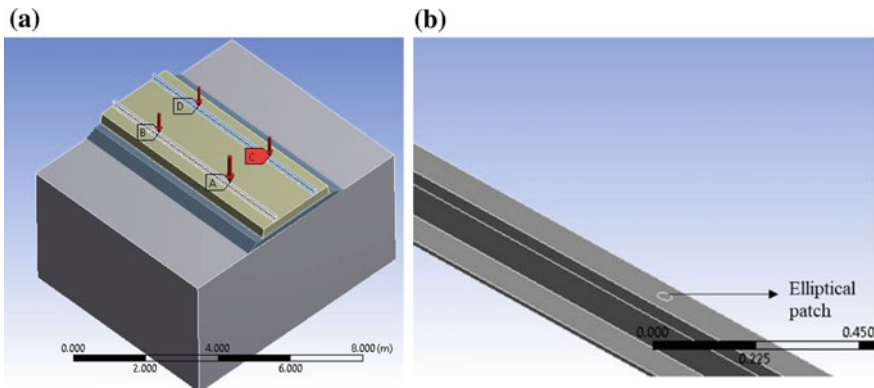


Fig. 5 a Loading condition, b elliptical contact patch

and rail. Two patches on each rail are made at a distance of 2800 mm showing the distance between wheels of bogie as defined by RDSO as shown in Fig. 5a.

$$\text{Area of elliptical patch} = 8.905 \times 10^{-4} \text{ m}^2$$

$$\text{Load per wheel} = 22/2 = 11 \text{ tons}$$

$$= 11 \times 9.81 = 107.91 \text{ kN}$$

$$\text{Therefore, Applied pressure force} = 121184556.3 \text{ Pa}$$

The influence of various parameters on the behavior of ballastless track structure under stationary wheel load (22t/axle) condition is investigated as under. The track with rail, rail pad, concrete slab, cement asphalt layer, concrete treated hydraulic bounded layer, and subgrade is considered for analysis. Variations in the parameters were made, and comparison is done based on deformations produced in the rail and the concrete slab.

4 Result and Discussion

The wheel load of 22tons/axles is applied on the rail to evaluate the displacement in rail section and concrete slab. The vertical displacement varying with depth in all the three models (model1, model2, model3, i.e. simple track model, standard track model, and shinkansen track model, respectively) is shown in Fig. 6a–c, respectively. The maximum vertical deflection occurs at the contact area patch formed where the load is applied. With an increase in depth, the vertical displacement decreases. All the graphs shows same trend of decrease in deflection with depth.

It is observed from the graphs that maximum displacement has occurred in the simple model shows a very high deflection of 1.96 mm (Fig. 6a). To mitigate the

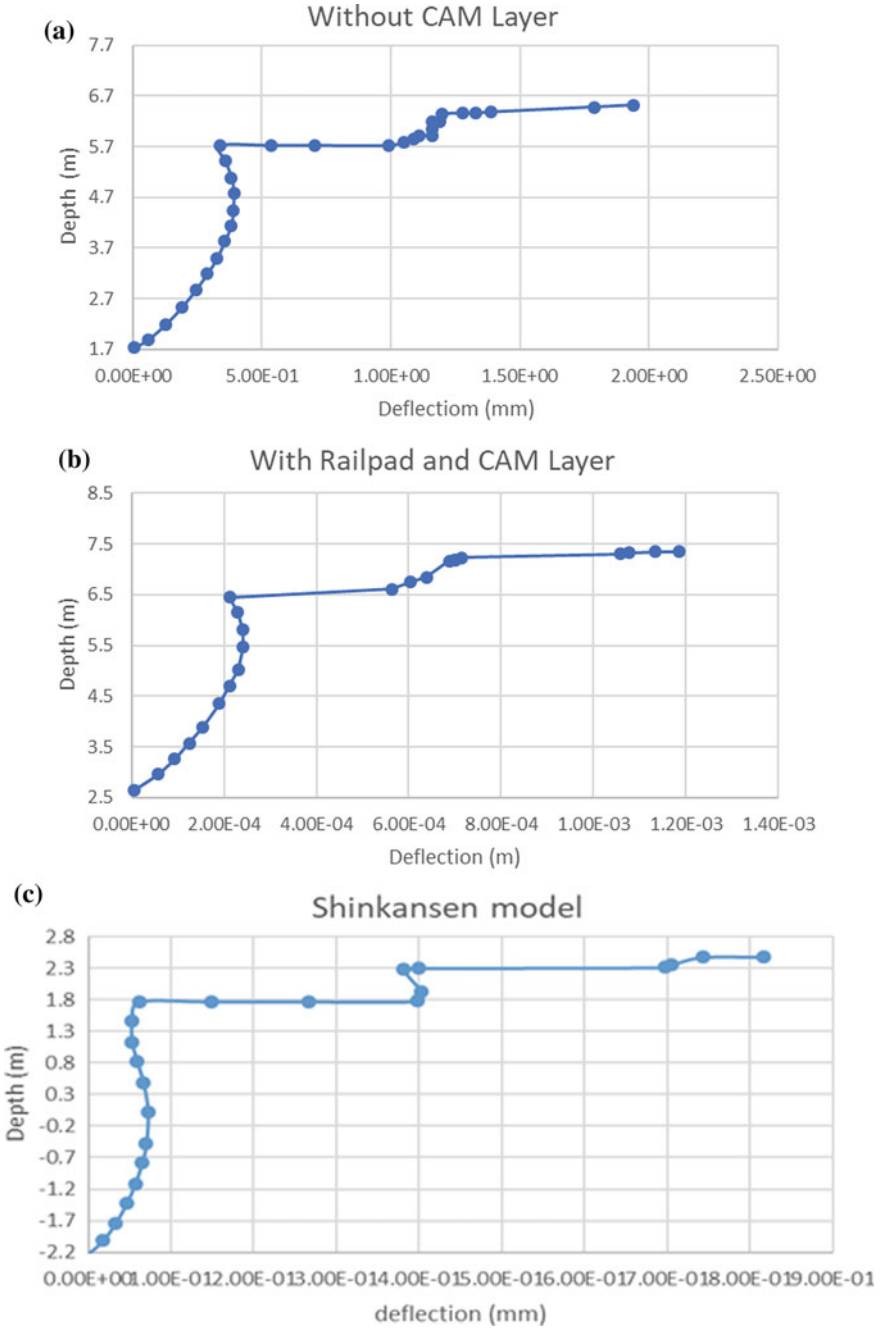
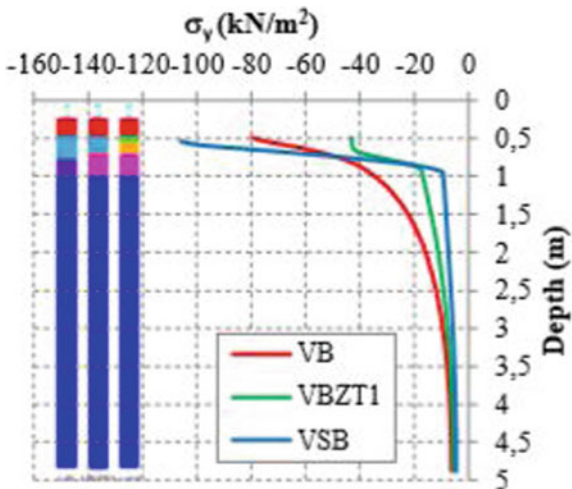


Fig. 6 Deflection in various model1, model2, model3 at standard value taken from Sun et al. [8]

Fig. 7 Vertical displacements in depth for VB, VBZT1, and VSB [9]



rider’s discomfort due to high deflection, rail pad property can be changed for considerable decrease in deflection. Further, the introduction of interface CAM layer along with rail pad (model 2) also causes more reduction in deflection. The result of displacement in shinkansen model is shown in Fig. 6c which is less than previous results because of additional stability due to stopper. The results obtained from the design model are compared with the results of the model of Matias [9] as shown in Fig. 7. A model with rail pad and CAM represents the result in accordance with VSB track structure in Matias [9] model. The slight variation in the result is due to the conditions applied and software simulation criteria (Fig. 8).

4.1 Parametric Study

Parametric studies have been done to investigate the behavior of track structure by varying the material properties of various track components like varying the modulus of elasticity of CAM layer, concrete bearing layer, subgrade/foundation, and rail pad stiffness. Deflection in the rail and slab has been obtained by varying the properties as shown in Figs. 9 and 10 given. Variations in the parameter have been shown in Table 3.

A parametric study is carried out and deflection in rail, and concrete slab is computed. Table 4 represents the variation of different parameters from benchmark value, and data is analyzed for deflection. Figures 9 and 10 are plotted to understand the effect of design parameters on the deflection of the track system.

Figure 9 shows that deflection in rail has shown negligible change by changing the modulus of elasticity of CAM layer and concrete slab. But the change in stiffness of the rail pad has greatly impacted the deformation. It is observed that around 42%

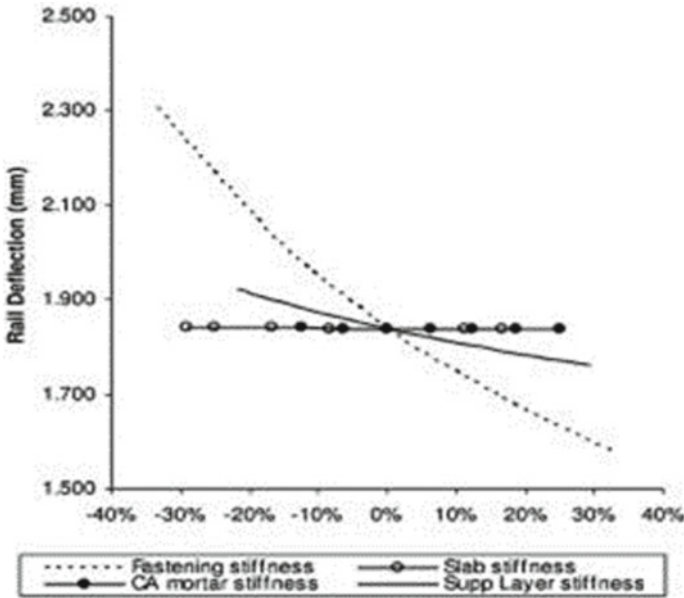


Fig. 8 Effect of design parameter in CRTS 11 [8]

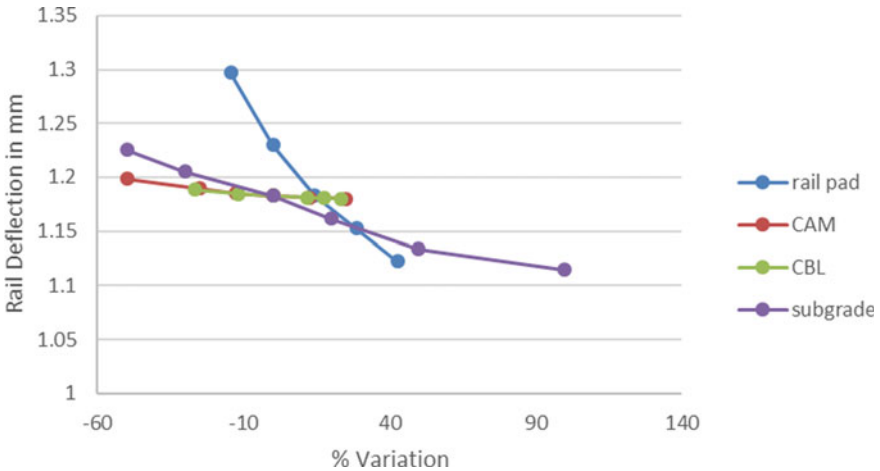


Fig. 9 Effect of design parameters on the deflection of rail

increase in stiffness rail pad fastening system decreases the deflection of rail by 18%. Also, variation in modulus of elasticity of subgrade shows minor changes in the deflection of rail. Increase in modulus of elasticity of subgrade by 50% decrease the deflection in rail by 4%. The change in stiffness of rail pad greatly affects the deflection in concrete slab also while variation in other parameters shows negligible

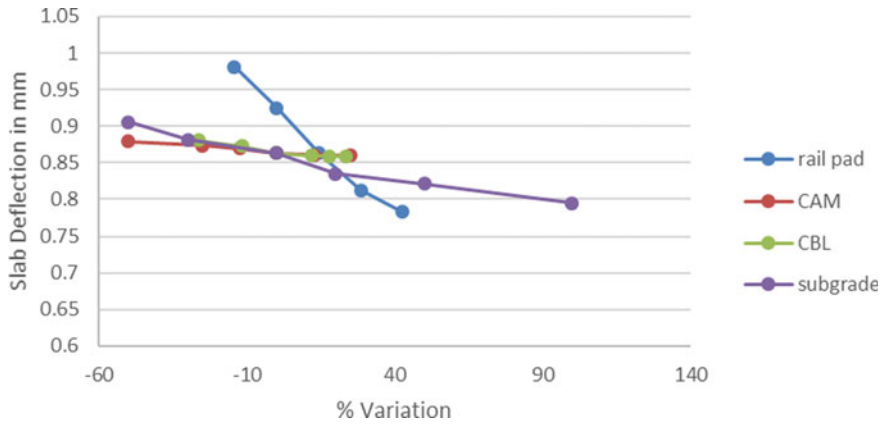


Fig. 10 Effect of design parameters on the deflection of slab

Table 3 Variation in values of parameters used in the analysis

Stiffness of rail pad (kN/mm)	50	60	70	80	90	100
Modulus of CAM layer (MPa)	4000	6000	7000	8000	9000	10,000
Modulus of CBL (MPa)	25,000	30,000	34,000	38,000	40,000	42,000
Modulus of subgrade (MPa)	50	70	100	120	150	200

Table 4 % variation of parameters from benchmark value

Stiffness of rail pad (kN/mm)	50	60	70	80	90	100
% variation	- 28.57	- 14.28	0	14.28	28.57	42.58
Modulus of CAM layer (MPa)	4000	6000	7000	8000	9000	10,000
% variation	- 50	- 25	- 12.5	0	12.5	25
Modulus of CBL (MPa)	25,000	30,000	34,000	38,000	40,000	42,000
% variation	- 26.47	- 11.76	0	11.76	17.65	23.53
Modulus of subgrade (MPa)	50	70	100	120	150	200
% variation	- 50	- 30	0	20	50	100

effect. The comparison between the results obtained from the designed model to that of the reported model taken from Sun et al. [8] model is shown in Figs. 8 and 9, respectively. The design model and Sun et al. [8] model show similar variation in the results due to change in parameters.

5 Conclusion

A parametric investigation is carried out, and it is concluded that escalation in stiffness of the rail pad decreases the maximum vertical deflection which occurred in rail and decreases the deflection in concrete slab also. The variation in modulus of elasticity of CAM layer and modulus of elasticity of concrete slab shows no change in the vertical deflection. At the same time, increase in modulus of elasticity of subgrade produces slight increase in deflection. The result of the deflection by varying material parameters obtained from design model was obtained from design model and was compared with reported model by Sun et al. [8] for similar studies. The graph of deflection obtained in the current model and Sun et al. [8] model shows similar pattern which emphasizes the correctness of the model.

References

1. Gao Y (2013) A 3D dynamic train-track interaction model to study track performance under trains running at a critical speed
2. Setu G, Mohanta M, Srivastava J, Sarkar P (2015) Analytical modeling of rail track system, PP design50-1 to design 50-6
3. Li MXD, Berggren EG (2010) A study of the effect of global track stiffness and its variations on track performance: simulation and measurement. Proc Inst Mech Eng Part F: J Rail nd Rapid Transit 224(5):375–382
4. Srivastava JP, Sarkar PK, Ranjan V (2014) Contact stress analysis in wheel-rail by hertzian method and finite element method. J Inst Eng (India): Series C 95(4):319–325
5. Sadeghi J, Zakeri JA, Tolou Kian AR (2018) Effect of unsupported sleepers on rail track dynamic behavior. P I Civil Eng Transp 171:286–298
6. Oregui M, Nunez A, Dollevoet R, Li Z (2017) Sensitivity analysis of rail pad parameters on vertical railway track dynamics. J Eng Mech 143(5):04017011
7. Khajehdezfuly A (2019) Effect of rail pad stiffness on the wheel/rail force intensity in a railway slab track with short-wave irregularity. Proc Inst Mech Eng Part F: J Rail Rapid Transit 095440971882541
8. Sun L, Chen L, Zelelew HH (2013) Stress and deflection parametric study of high-speed railway CRTS-II ballastless track slab. J Transp Eng 139(12):1224–1234
9. Matias S (2015) Numerical modeling and design of slab tracks. University of Lisbon, pp 425
10. https://www.alibaba.com/product-detail/heavy-steel-rail-UIC-60-heavy_6246710893 last access 2019/09/09

Determining the Fiber Loading on Mechanical Behavior of Kenaf and Sisal Fibers Reinforced Polyester Composites



R. Muthalagu, V. Srinivasan, S. Sathees Kumar, and V. Murali Krishna

Abstract In this study elastic, flexural, effect, and hardness characteristics of sisal fiber and kenaf rein constrained with polyester mixtures are portrayed unexpectedly. The composite samples are manufactured for various fiber loads by injection molding technique. Kenaf filaments are having better elasticity contrasted and sisal. Because of that reason, kenaf is as base material and sisal is as filler. To research the mechanical traits of elastic, flexural, sway, and hardness tests were proceeded according to American Society for Testing and Materials (ASTM) standard. The mechanical experiment outcomes uncovered an ordinary pattern of an expansion in malleable, flexural, effect, and hardness attributes to including common filaments. Great grip between the normal filaments and the polyester matrix is additionally liable for the successful mechanical ability. This outcome infers that kenaf and sisal fiber have.

Keywords Flexural · Hardness · Impact · Kenaf · Sisal · Tensile

1 Introduction

Characteristic strands have starting late pulled in the thought of scientists and technologists because of the central focuses that these strands provide more traditional strengthening substances, and the unforeseen development of NFC has been a matter of astuteness as far back as relatively few years [1–3]; these NF are easy strands with low width and great express attributes. These are decomposable and non-abrasive, not in any way like other fortifying strands. Moreover, they are speedily open and

R. Muthalagu · V. Srinivasan

Department of Manufacturing Engineering, Annamalai University, Chidambaram, Tamil Nadu, India

S. Sathees Kumar (✉)

Department of Mechanical Engineering, CMR Institute of Technology, Hyderabad, Telangana, India

V. M. Krishna

Department of Mechanical Engineering, B.V. Raju Institute of Technology, Narsapur, Medak, Telangana, India

their specific attributes are equal to those of various strands used for fortifications. In any case, certain drawbacks, for instance, logical inconsistency with the hydrophobic polymer form, the inclination to structure accumulates through preparing, a helpless resistance from dampness gigantically decreases the ability of NF to be used as reinforcements in polymers [4]. Prior articles have shown that by behaving synthetic usage strategies, for instance, external alteration, the idea of the trademark strands can be improved for well fiber-framework joining [5]. Furthermore, NFC has engaging natural and monetary points of view and the capacity to address individual issues. Green fiber mixtures expose imperative open doors for norm in the aviation and car domains [6]. NF a natural substance basically includes hemicellulose, lignin, and cellulose. The extended cellulose substance supplements the potency [7] of the fibers, viz. flax, banana, kenaf, and sisal, are well-completed another plant fibers have developed pressure change and interconnection extending between sap and strands. Various specialists had uncovered that crossover strand braced with polyester matrix progresses the mechanical nature of the mixture. Only some assessments task definite that the incorporated of filler with volume decline from more modest scope to nano-enhance the fibers/resin interfacial extending. The filler substances, for instance, titanium oxide, graphene (Gr), and Al_2O_3 are utilized to redesign the interconnection attributes of sap in order to enhance excellent trademark fiber invigorated polymer cross-sectional composite [8–10]. Regardless, these regular filler materials are a critical cost; from this time forward, there is a necessary vital to find an elective source of filler effortlessly. The plentifully available biomass endures, viz. bamboo and rice husk, are reflected as the good replacement above common fillers with respect to cost. These mineral bio-flotsam and jetsam fillers in polymer cross-sectional mixture are seen as a better decision than accomplish developed attributes like that of critical cost fillers [11, 12]. The element action enhances the fiber–gum interaction attributes by extending the exterior harshness of fibers by abstaining from the hydroxyl social events. The antacid method is viewed as a convincing strategy in extending the possessing among organizations and filaments [13]. This sequence decreases the oil, hydroxyl, and surplus contagions that assistance to develop the keeping idea of strands [14–18]. Killing hemicellulose and lignin stimulate unparallel squeezing of the cellulose series, thus upgrading the qualities of mixtures [19]. The mixtures fortified with 5% of NaOH treated trademark strands truth be told updated the mechanical characteristics [20]. In this work, two vary filaments one from the leaf (sisal) and another from the bast class. These two filaments having more elastic and bending attributes. Be that as it may, adding up these two strands in this task are depicted the accompanying purposes. Sisal is a usually happening plant with a yearly overall fiber formation stated to achieve five million ton [21]. The cellulose substance of sisal shifts among 50 and 62 %wt., contingent upon the phase of the plant [22]. The utilization of sisal as new source substance will permit us to get nanoparticle measurements, augment the scope of possible functions and increment the flexibly of cellulosic substance functional for nanocomposite materials [23–25]. Furthermore, the kenaf plant is made out of various significant parts and inner each of these there are distinctive functional pieces [26, 27]. Kenaf filaments include discrete individual strands, of generally 2–6 mm. The branch is vertical and

unbranching and is made out of an outside level and a trot [28]. The branch comprises 35–45% of the branch dry heaviness and displays a fairly heavy arrangement [29]. In this investigation, different fibers are fortified with polyester medium by dissimilar wt. %. The mechanical attributes of the mixtures were identified.

2 Experimental Details

2.1 Extraction of Sisal Fibers

The sisal greeneries are cutback from sisal plant and incorporated with bunches with consuming packs. By afterward, packs comprise the greeneries are soaked in storage reservoir for 2–3 days. The soaked leafages are rinsed in flowing stream, and the upper piece of the leafages are taken out genuinely to get the strand freely and scrubbed and rubbed out in the sunlight. Each strand is destroying based on to strand appraises and collected properly [30, 31].

2.2 Extraction of Kenaf Fibers

The removal of the filament from the Kenaf plant was finished by water soaking measure. The stalk of the kenaf was brought down in a water wash and made sure about with water jacinth for 28 days [32].

2.3 Alkaline Treatment of Fibers

Soluble treatment is a run of the mill fiber exterior treatment that can in like manner be used as initial treatment when gotten together with additional compound changes. At first, these medicines were finished to improve fiber's color loving and radiance [33]. Re-searchers consequently found that alkalization similarly emphatically influences the mechanical attributes of strand reinforced mixtures, yielding substantial updates in the interbonding execution [34, 35]. The exterior handling of the strands was done utilizing alkali to enhance its quality. The strands with same mass extent were ingested 5 percentage of sodium hydroxide centers for 5 h with physical blending at each 40 min was washed in refined liquid and makes dry at room temperature. The low-thick polyester gum of business-quality methyl ethyl ketone peroxide and Denverpoly 754 creation some gel recollections of 130–200 min is consumed as a grid source. Actual traits of NF are appeared in Table 1.

Table 1 Natural attributes of NF

Filaments	Density (g/cm ³)	Diameter (μm)	Tensile strength (MPa)	Tensile modulus (GPa)	Elongation at break (%)	Sources
Kenaf	0.749	43.3–140	223–624	11–14.5	2.7–5.7	[36–38]
Sisal	1.45	50–200	80–240	1.46–15.8	3–15	[39–41]

Table 2 Working constraints on the molding machine

Setting temperature (°C)	Pressure zones (bar)	Time (s)
Chamber—200	Insertion pressure—85	Fusion time—12
Melting—180	Holding pressure—67	Cool off time—27
Molding—25	Back up pressure—13	

2.4 Fabrication of Samples

Refined substances were dried up in an oven at 75 °C for 3 h before forming. This is to hinder the plan of airborne ascends in the examples which might cut downward their mechanical ascribes. Table 2 exposes the molding constraints for the fiber/polyester mixtures. The stuff including layers of fiber was pressed in a four-sided framed form (160 mm × 140 mm × 4 mm) under a pressure of 10 MPa and at a hotness of 195 °C for 15 min (Fig. 1 and Table 3).

3 Materials Categorization

3.1 Tensile Strength

The sample was set up as indicated by the ASTM—D638. The ductile trial was directed on a Tinius Olsen 10 KN Universal Testing Machine with a measurement of 70 mm and crosshead pace of 3 mm/min. The sample shape for tractable trial is 120 × 15 × 3 mm. The examinations were led multiple times, and every arrangement and the normal qualities are considered for outcomes [16].

3.2 Flexural Strength

In this test, a three-point twisting technique was utilized for discovering the bending of an example. The shape of example for bending trial is 115 × 20 × 3 mm as per ASTM/D790. The three-point bending trial is the best well-known bending test and

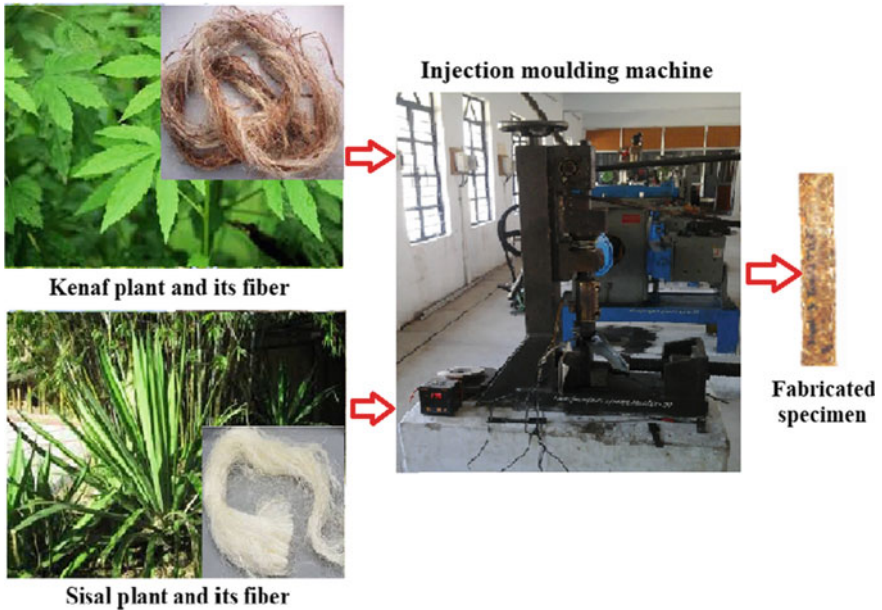


Fig. 1 Made-up method of NF composite specimen

Table 3 Formation of made-up specimens

Description of samples	Structure of NF	
	Kenaf (wt.%)	Sisal (wt.%)
A	90	10
B	80	20
C	70	30
D	60	40
E	50	50

operated in this trial for testing the bowing strength of the mixture substances with a support range measurement of 75 mm, and the x-head pace was fixed at 3 mm/min. The testing cycle comprises stroking the trial sample in the UTM and employing strength to it till it flaws and fractures.

3.3 Impact Strength

The Izod trial sample according to measurements is 65 × 15 × 3 mm. Throughout the examination cycle, the sample should be stacked in the UTM and permits the

swing until it cracks or fractures. Utilizing the effect test, the strength expected to fracture the substance can be estimated effectively and can be utilized to quantify the sturdiness of the substance and the yield force. The impact of straining value on crack and ductile of the substance can be investigated by utilizing the effect trial.

3.4 Hardness

The hardness trial is led on a shore durometer tester. The ASTM/ D2240 sample is completed in the shore durometer hardness analyzer. Every hardness sample is ready for the dimension of $35 \times 15 \times 3$ mm [42]. Hardness is a proportion of the protection from confined plastic twisting instigated by whichever mechanical space or scraped spot.

4 Results and Discussions

4.1 Tensile Characteristics

It very well may be seen from Fig. 2 that the elasticity and malleable moduli of the polyester mixture increments with regular strand stacking in all events. The antacid treated mixtures A, B, C, and D expose slow improvement of flexible attribute. The mixtures exhibited a beneficial outcome up to the wt.% of kenaf (60%) and sisal (40%) in the example (D). Figure 2 exposes at the point when the fiber substance of kenaf and sisal strands are raised, the rigidity and elastic moduli of the mixtures are upgraded. From the outcomes, the most extreme wt.% of the kenaf and sisal fiber

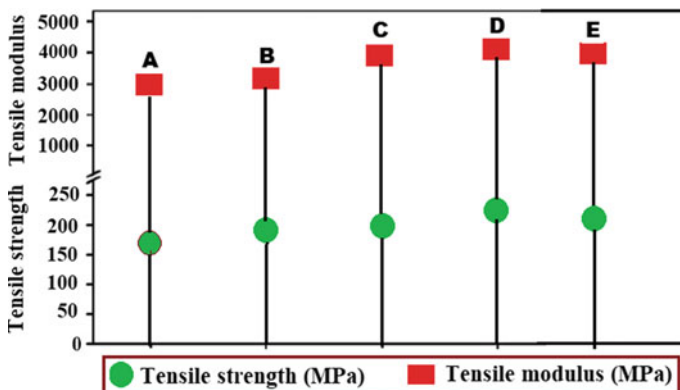


Fig. 2 Ductile characteristics of composite specimens

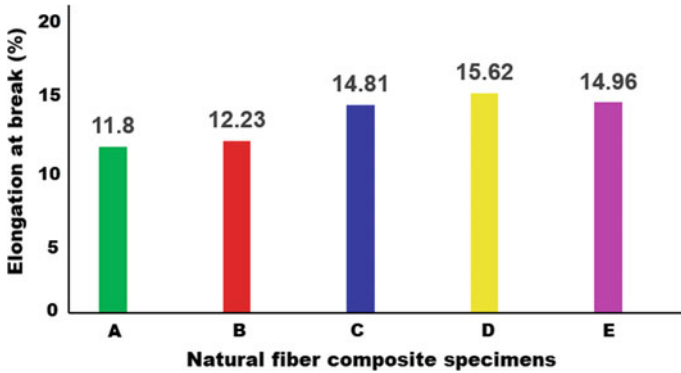


Fig. 3 Extension of composite specimens

contents grasps the pliable qualities of mixtures. In E specimen, the ductile strength was gradually diminished, due to the partial part of both fibers as the ductile attribute converted into brittleness. The investigational outcomes of sample D have improved the complete tensile performance matched with another samples, for instance A, B, C, and E. The evaluation rates are noticed in 15.54, 11.03, 5.07, 3.15% correspondingly. However, the ductile moduli of NF mixtures were improved progressively from A, B, C, and D specimen. In E sample, the moduli has been diminished, higher inclusion of sisal enhanced the brittle attribute. The strength was diminishing due to the incapability of the strand to help stresses conveyed from the polymer medium [43, 44]. The ductile moduli of specimen D matched with another samples, for example, A, B, C, and E. The moduli rates are considered in 28.42%, 15.16%, and 5.26%, respectively.

The extension of samples is exposed in Fig. 3. The extension characteristics steadily developed from the specimens A, B, C, and D. The enhancement of extension attributes of specimens evidenced the better interaction network among the fibers/polyester medium [45–47]. Specimen E is suddenly reducing the elongation at break. Upsurge of sisal fiber fillings in the sample E, the extension possessing character of fiber may be distressed.

4.2 Flexural Characteristics

Figure 4 exposes that the bending quality of the mixture increments with normal strand stacking in entire specimens. The samples A, B, C, and D expose continuous upgrade of twisting potency. Figure 4 implies that the expansion of kenaf and sisal strands to the polyester improves the bending quality and decreases the diversion. Well-maintaining areas between filaments and gum are essentially nope warnings of filaments improper bonding, parting structures at the treated kenaf strand mixture break exterior afterward bendable packing. This result recommends that

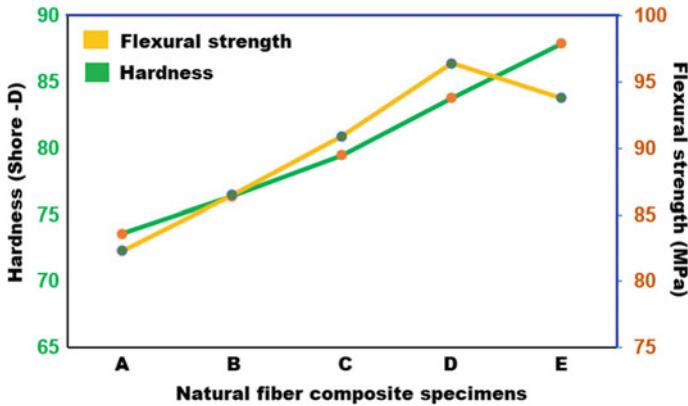


Fig. 4 Bendable and hardness quality of composite specimens

interbonding connection among the kenaf fibers/polyester medium has gotten appreciably further encouraging and limitless contribute of fibers. Bendable characteristics also developed with filler inclusion [48].

Moreover, the bending moduli of mixtures are shown in Fig. 5. As the sisal fiber wt.% moves above 40 %wt., the bending moduli declines observably in polyester fortified mixtures. This disappointment is an away from of insufficient burden move among the lattice and fiber. Pressure move of the composites expanded by solid fiber and grid holding, permitting versatile disfigurement [49]. It is successively apparent that the attached alkali treatment primarily magnifies the pliability of mixtures.

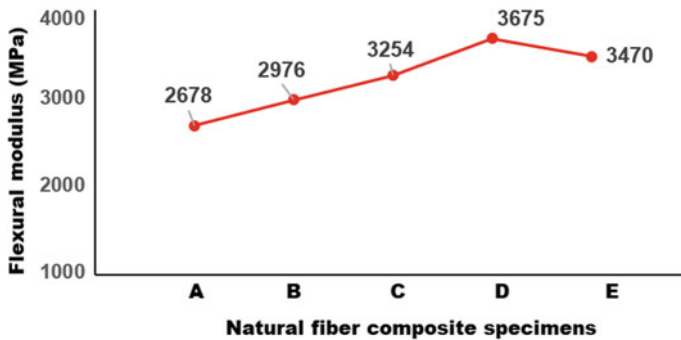


Fig. 5 Flexural modulus of composite specimens

4.3 Hardness Attributes

Figure 4 signifies the rigidity of the kenaf/sisal mixtures. Alkali treated filaments exposes the speedy augmentation of rigidity quantities. In specimen A, it has small limit of 73.6 then it has developed to 87.9 on specimen E. The equivalent part of NF boosted the rigidity characteristics of the polyester medium [50]. The purpose behind expanding the rigidity is the well-scattering of strands into the fibers network more grounded interaction attachment to the fiber grid.

4.4 Impact Attributes

Figure 6 shows the effect of mixtures improves as of A, B, C, and D gradually. The wt.% of kenaf fiber (60%) and sisal (40%) filaments is stretched the excessive effect of around 31 J/m². Sample D evaluated with remaining samples like A, B, C, and E is achieved the good effect of 47.6%, 29.16%, 14.8%, 82.8%, and 6.89%, respectively.

The extended fiber element will intensify the interaction external among the strand and polyester medium if there is suitable saturation of filaments in the polyester gum. By the side of greater fiber filling, the outcome transfer ought to be additional capable [51]. Substantial connection among the strand and polyester medium is too accountable for the excessive fortification from interruption extent throughout impact tests.

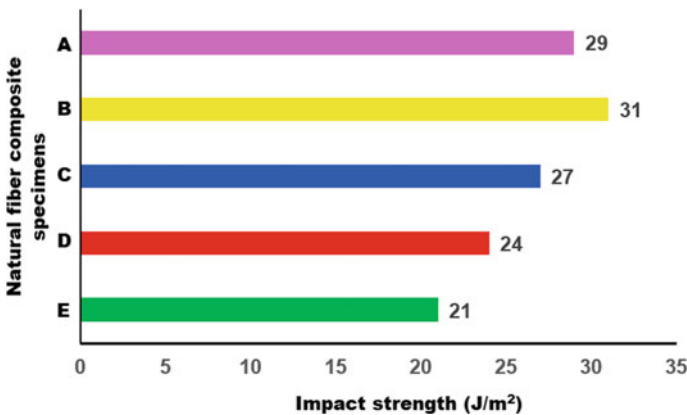


Fig. 6 Impact strength of composite specimens

5 Conclusion

The kenaf and sisal strands are fortified polyester mixtures are made up on different wt.% throughout molding technique. The mechanical characteristics of mixture were illustrated.

- In the malleable experiment, the most extreme elasticity, ductile modulus, and prolongation of polyester mixtures example *D* achieved at 219.3, 4382 MPa, and 15.62%, respectively. By expanding the substance of sisal wt% upto 40%, the bendable property has been upgraded
- Specimen *D* achieved the greatest bending strength and moduli about 96.4 MPa and 3675 individually. The consideration of half sisal accomplished a negative impact in *E* example. The unvarying scattering of characteristic strand outcomes may be expanding the estimation of the bending attribute.
- The impact is accomplished greatest at 31 J/m² in *D* example. Great bond among the normal strand and polyester medium is answerable for the well effect potency.
- The most extreme hardness accomplished at 87.9 in *E* example. The rigidity of a mixture relies upon the dissemination of the filaments keen on the resin grid.
- This sort of mixture material can be valuable for bundling, lightweight vehicle parts, packing materials in an industry, and civil engineering fields.

References

1. Schneider JP, Myers GE, Clemons CM, English BW (1995) Biofibers as reinforcing fillers in thermoplastic composites. *Eng Plast* 8(3):207–222
2. Pothan LA, Thomas S, Neelakantan NR (1997) Short banana fiber reinforced polyester composites: mechanical, failure and aging characteristics. *J Reinf Plast Compos* 16(8):744–765
3. Francis R (2016) *Recycling of polymers: methods, characterization and applications*. Wiley
4. Saheb DN, Jog JP (1999) Natural fiber polymer composites: a review. *Adv Polym Technol J Polym Process Inst* 18(4):351–363
5. Furqan A, Choi HS, Park MK (2014) Natural fiber composites selection in view of mechanical, light weight, and economic properties. *Macromol Mater Eng* 300:10–24
6. Biagiotti J, Puglia D, Kenny JM (2008) Effect of surface treatment of jute fibers on the interfacial adhesion in poly (lactic acid)/jute fiber biocomposites. *Fibers Polym* 17:266–274
7. Moran JI, Alvarez VA, Cyras VP, Vazquez A (2008) Extraction of cellulose and preparation of nanocellulose from sisal fibers. *Cellulose* 5:149–159
8. Kavimani V, Soorya Prakash K, Thankachan T, Udayakumar R (2020) Synergistic improvement of epoxy derived polymer composites reinforced with Graphene Oxide (GO) plus Titanium di oxide (TiO₂). *Compos B Eng* 107911:191
9. Duongthipthewa A, Su YY, Zhou LM (2020) Electrical conductivity and mechanical property improvement by low-temperature carbon nanotube growth on carbon fiber fabric with nanofiller incorporation. *Compos B Eng* 107581:182
10. Megahed M, Abd El-baky MA, Alsaedy AM, Alshorbagy AE (2019) An experimental investigation on the effect of incorporation of different nanofillers on the mechanical characterization of fiber metal laminate. *Compos B Eng* 107277:176

11. Abdul Khalil HPS, Fizree HM, Bhat AH, Jawaid M, Abdullah CK (2013) Development and characterization of epoxy nanocomposites based on nano-structured oil palm ash. *Compos B Eng* 53:324–333
12. Sitticharoen W, Chainawakul A, Sangkas T, Kuntham Y (2016) Rheological and mechanical properties of silica-based bagasse-fiber-ash-reinforced recycled HDPE composites. *Mech Compos Mater* 52:421–432
13. Feng NL, Malingam SD, Razali N, Subramonian S (2020) Alkali and silane treatments towards exemplary mechanical properties of kenaf and pineapple leaf fiber-reinforced composites. *J Bionic Eng* 17:380–392
14. Ouahrhim W, Essabir H, Bensalah MO, Zari N, Bouhfid R, Qaiss A et al (2018) Structural laminated hybrid composites based on raffia and glass fibers: effect of alkali treatment, mechanical and thermal properties. *Compos Part B Eng* 154:128–137
15. Huan XH, Shi K, Yan JQ, Lin S, Li YJ, Jia XL, Yang XP (2020) High performance epoxy composites prepared using recycled short carbon fiber with enhanced dispersibility and interfacial bonding through polydopamine surface modification. *Compos B Eng* 107987:193
16. Vilaseca F, Del Rey R, Serrat R, Alba J, Mutje P, Espinach FX (2018) Macro and micro-mechanics behavior of stiffness in alkaline treated hemp core fibers polypropylene-based composites. *Compos B Eng* 144:118–125
17. Yan F, Lin ZB, Zhang DL, Gao ZL, Li ML (2017) Experimental study on bond durability of glass fiber reinforced polymer bars in concrete exposed to harsh environmental agents: freeze-thaw cycles and alkaline-saline solution. *Compos B Eng* 116:406–421
18. Barreto ACH, Costa MM, Sombra ASB, Rosa DS, Nascimento RF, Mazzetto SE, Fechine PBA (2010) Chemically modified banana fiber: structure, dielectrical properties and biodegradability. *J Polym Environ* 18:523–531
19. Gassan J, Bledzki AK (1999) Possibilities for improving the mechanical properties of jute/epoxy composites by alkali treatment of fibers. *Compos Sci Technol* 59:1303–1309
20. Ouahrhim W, Essabir H, Bensalah MO, Rodrigue D, Bouhfid R, Qaiss A et al (2019) A comparison between sabra and alfa fibers in rubber biocomposites. *J Bionic Eng* 16:754–767
21. Chand N, Tiwary RK, Rohatgi PK (1988) Bibliography resource structure properties of natural cellulosic fibers—an annotated bibliography. *J Mater Sci* 23(2):381–387
22. Hashmi SAR, Naik A, Chand N (2006) Effects of hybrid composition of LCP and glass fibers on abrasive wear of reinforced LLDPE. *Bull Mater Sci* 29(1):49–54
23. Li Y, Mai YW, Ye L (2000) Sisal fiber and its composites: a review of recent developments. *Compos Sci Technol* 60(11):2037–2055
24. Mukherjee PS, Satyanarayana KG (1984) Structure and properties of some vegetable fibers. *J Mater Sci* 19(12):3925–3934
25. De Rodriguez NLG, Thielemans W, Dufresne A (2006) Sisal cellulose whiskers reinforced polyvinyl acetate nanocomposites. *Cellulose* 13(3):261–270
26. Idicula M, Malhotra SK, Joseph K, Thomas S (2005) Dynamic mechanical analysis of randomly oriented intimately mixed short banana/sisal hybrid fiber reinforced polyester composites. *Compos Sci Technol* 65(7–8):1077–1087
27. Webber CL III, Bledsoe VK (2002) Kenaf yield components and plant composition, trends in new crops and new uses. ASHS Press, Alexandria, VA, EUA, pp 348–357
28. Ogbonnaya C, Roy-Macauley H, Nwalozie M, Annerose D (1997) Physical and histochemical properties of kenaf (*Hibiscus cannabinus* L.) grown under water deficit on a sandy soil. *Ind Crops Prod* 7:9–18
29. Lee SA, Eiteman MA (2001) Ground kenaf core as a filtration aid. *Ind Crops Prod* 13(2):155–161
30. Sathees Kumar S (2020) Dataset on mechanical properties of natural fiber reinforced polyester composites for engineering applications. *Data Brief* 28:105054
31. Sathees Kumar S (2020) Effect of natural fiber loading on mechanical properties and thermal characteristics of hybrid polyester composites for industrial and construction fields. *Fibers Polym* 21(7):1508–1514

32. Tahir Mohd P, Ahmer BA, Saifulazry SOA, Ahmed Z (2011) Retting process of some bast plant fibers and its effect on fiber quality: a review. *Bioresources* 6(4):5260–5281
33. Vandeweyenberg I, Chitruong T, Vangrimde B, Verpoest I (2006) Improving the properties of UD flax fiber reinforced composites by applying an alkaline fiber treatment. *Compos A Appl Sci Manuf* 37:1368–1376
34. Valadez-Gonzalez A (1999) Chemical modification of henequen fibers with an organosilane coupling agent. *Compos B Eng* 30:321–331
35. Valadez-Gonzalez A (1999) Effect of fiber surface treatment on the fiber matrix bond strength of natural fiber reinforced composites. *Compos B Eng* 30:309–320
36. Malkapuram R, Kumar V (2008) Recent development in natural fiber reinforced polypropylene composites. *J Reinf Plast Compos* 28:1169–1189
37. Graupner N, Herrmann AS, Mussig J (2009) Natural and man-made cellulose fiber-reinforced poly(lactic acid) (PLA) composites: an overview about mechanical characteristics and application areas. *Compos A Appl Sci Manuf* 40:810–821
38. Shibata S, Cao Y, Fukumoto I (2005) Press forming of short natural fiber-reinforced biodegradable resin: effects of fiber volume and length on flexural properties. *Polym Testing* 24:1005–1011
39. Satyanarayana K, Sukumaran K, Kulkarni A, Pillai S, Rohatgi P (1984) Performance of banana fabric-polyester composites. In: Marshall I (ed) *Proceedings of second international conference on composite structures*. Applied Science Publishers, London, pp 535–538
40. Satyanarayana K, Sukumaran K, Mukherjee P, Pillai S (1986) Materials science of some lignocellulosic fibers. *Metallography* 19:389–400
41. Jayaraman K (2003) Manufacturing sisal/polypropylene composites with minimum fiber degradation. *Compos Sci Technol* 63:367–374
42. Benítez AN, Monzón MD, Angulo I, Ortega Z, Hernández PM, Marrero MD (2013) Treatment of banana fiber for use in the reinforcement of polymeric matrices. *Measurement* 46:1065–1073
43. Karmani R, Krishan M, Narayan R (1997) Biofiber reinforced polypropylene composites. *Polym Eng Sci* 37(2):476–483
44. Åkesson D, Skrifvars M, Seppälä J, Turunen M (2011) Thermoset lactic acid-based resin as a matrix for flax fibers. *J Appl Polym Sci* 119(5):3004–3009
45. Sudhagar S, Raja VM, Sathees Kumar S, Samuel AJ (2019) The wear behaviour and service life of Madar and Bauhinia Racemosa reinforced polyester hybrid composites for gear applications. *Mater Today Proc* 19:589–593
46. Sathees Kumar S, Mugesh Raja V, Sridhar Babu B, Tirupathi K (2020) Comparison of ductile, flexural, impact and hardness attributes of sisal fiber-reinforced polyester composites. In: *Intelligent manufacturing and energy sustainability*. Springer, Singapore, pp 645–654
47. Sathees Kumar S (2019) Tribological characteristics of natural fiber reinforced polyester hybrid composites. *Int J Innov Technol Explore Eng* 8(10):947–952
48. Sathees Kumar S (2019) Mechanical and Water absorption properties of Madar and Bauhinia Racemosa natural fiber composites. *Int J Recent Technol Eng* 8(2):2338–2342
49. Threepopnatkul P, Kaerkitcha N, Athipongarporn N (2009) Effect of surface treatment on performance of pineapple leaf fiber polycarbonate composites. *Compos Part B* 40:628–632
50. Velusamy Mugesh R, Sathees Kumar S (2019) Determination of static and fatigue characteristics of carbon fiber reinforced polyester composites for automobile applications. *Mater Res* 22:6
51. Sathees Kumar S, Mugesh Raja V, Nithin Chakravarthy CH, Muthalagu R (2020) Determination of mechanical properties and characterization of alkali treated sugarcane bagasse, pine apple leaf and sisal fibers reinforced hybrid polyester composites for various applications. *Fibers Polym* vol.to appear 2020

An Experimental Investigation of Influence of Coated Piston Ring Surface Under Different Lubrication Condition Against Uncoated Surface on Diesel Engine



Anshul Kumar, Rajiv Chaudhary, and Ramesh Chand Singh

Abstract In diesel engine, the loss of power occurs via various means like mechanical losses, cylinder cooling and exhaust from the engine. Frictional losses in diesel engine play a predominant role in mechanical losses. In this study, a chrome plated surface of piston ring material is tested for determining coefficient of friction and specific wear rate of the material against the uncoated surfaced material. The tribological analysis was conducted on pin-on-disc tribotester (ASTM-G99) under the full flooded and starved lubrication condition. The lubricant used for the experimental purpose is the standard 15W40 lubricant used in diesel engine. It was found that the coefficient of friction and specific wear rate (SWR) were reduced by using the chrome-coated piston ring surface as compared to the uncoated surface.

Keywords Chrome plating · Piston ring · Cylinder liner

1 Introduction

A surface interaction controls the functioning of every device available with surface contact. Every device made by human is subjected to friction and wear which the result of the relative motion between the surfaces. Human body also has many interacting surfaces, e.g. knee joints, finger knuckles; hence, these parts also subjected to the lubrication and wear [1].

Wear mechanism causes loss of material from the interacting surfaces and hence mechanical performance of the surface degrades. Any reduction in the wear amount can save considerable amount of money and material. The main culprit behind the wear mechanism and energy dissipation is friction. Around one-third of the world's energy gets consumed to overcome the friction in one form or another [2]. Lubrication proved to be the effective means of controlling the friction [3].

A. Kumar (✉) · R. Chaudhary · R. C. Singh
Delhi Technological University, Delhi, India

The tribological losses of power contribute around 80% of the mechanical losses in a diesel engine. Mechanical losses contain losses in piston assembly (approx. 45%), bearings (approx. 25%), valve train (approx. 10%) and pumping losses (approx. 20%) [4]. Many researchers have made attempts to overcome the frictional losses by modifying the contact surfaces. Broszeit et al. [5] investigated the deposition and application of CrN coating deposited by physical vapour deposition (PVD) and discussed the problems associated with chromium (Cr) electroplating and behaviour of titanium nitride (TiN) which are not up to the mark with various process parameters. Electroplated chromium (Cr) shows highest deposition rate but deposition rate of TiN and CrN, chromium nitride shows higher deposition rate. It replaces the TiN and electroplating of Cr with their promising corrosion resistance and several applications. Mishra et al. [6] have modelled a 4-strokes 4-cylinder engine to obtain the performance of lubrication. The parameters related to the engine tribology, i.e. engine friction and lubrication, were calculated numerically for firing order of 1–3–4–2 [7]. In order to prevent friction and its posterior wear, the surface of cylinder liner was textured with cross-h pattern and also the surface of piston ring was coated with the wear resisting coating [8].

Surface texturing technique is used to reduce the friction and wear of the contacting surfaces. The surface texture can be improved by generating dimples on the surface using the laser technology. By using the dimpled surface, the wear rate between the surfaces reduced by 72% [9]. One of the methods for improving the surface properties is coating with the suitable material on the surface of the specimen. This will enhance the surface hardness, wear resistance of the surface and also the life of mating surfaces [10].

Chromium coating is a wear resistance coating applied over the steel surface and also on the other metallic surfaces. A hard chromium coating differs from ornamental chromium coating in the manner of thickness deposited on the metallic surface. For hard chromium coating, the thickness of coating varies from 12 to 250 μm [10, 11]. Cast iron and mild steel are the common material used for the manufacturing of piston ring and cylinder liner. Chrome coating is done on the cast iron specimen by the process of electro-deposition. Hard chrome deposit has low surface energy, and it is deposited mainly on sliding or revolving machine element like engines and pumps. A hard chrome deposit is in demand as it has high resistance to corrosion and hence primarily used in the situations where corrosion is highly detrimental to the working surface [12].

The lubrication between the contacting surfaces helps in reducing the friction and wear between the surfaces. The interacting surface between the piston ring and cylinder liner is quite important in an internal combustion engine [13]. The clearance between the piston ring and cylinder liner gets wider due to the friction and wear mechanisms. This causes the less compression of the gaseous fuel mixture above the piston head. During the compression stroke, the fuel gaseous mixture moves to the crankshaft side from the compression chamber through the wider clearance between the piston ring and cylinder liner [14]. This will reduce the power generated by the internal combustion engine and hence causes loss of energy. This condition is known as blow-by condition.

Under full flooded lubrication, a continuous supply of lubricant is done between the interacting surfaces. This will create a thick layer of lubricant between the surfaces and reduces the metal to metal contact of piston ring and the cylinder liner. Hence, the wear and friction reduce and the power produced from engine increases [15]. The use of the hard chrome coating over the piston ring surface will reduce the wear rate between the piston ring and the cylinder liner. This will ensure a prolonged life of the said mating parts and also reduces the chances of blow-by to occur in the engine. Hence, the power of the engine increased.

2 Experimental Conditions

A rotating type of pin-on-disc tribotester (ASTM G99) is used for determining the coefficient of friction, and the amount of wear occurred on the specimen surface. A schematic diagram of the apparatus is shown in Fig. 1. A specimen circular disc of mild steel having a diameter of 265 mm and thickness of 10 mm and a cylindrical pin of cast iron of diameter 10 mm and length 30 mm was prepared. Mild steel selected for circular disc specimen is having following properties (Table 1).

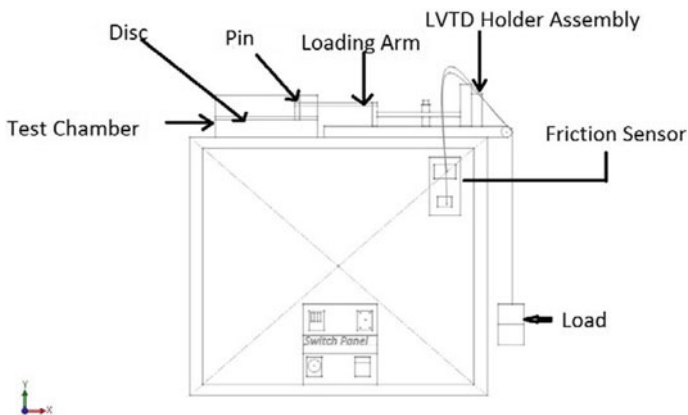


Fig. 1 Schematic diagram of pin-on-disc tribotester [3]

Table 1 Properties of mild steel

Density (kg/m ³)	7890
Young's modulus (Pa)	2E11
Specific heat (J/kg K)	465
Thermal conductivity (W/m K)	53.6
Poisson's ratio	0.3

Table 2 Properties of cast iron

Density (kg/m ³)	7085.5
Young's modulus (Pa)	1.4E11
Specific heat (J/kg K)	460
Thermal conductivity (W/m K)	46
Poisson's ratio	0.26

Cast iron is used for preparing specimen pin. The following are the properties of cast iron (Table 2).

The chrome coating was done on the tip of the cast iron pin by the process of electro-deposition. The thickness of the chrome coating was kept at 25 μm , which is well within the prescribed limit of 10–225 μm . The hardness and elastic modulus of the chrome coating over the cast iron pin were found by using the micro-indentation tester MHT³ (ASTM E2546). The hardness of the chrome coating is 984.6 Vickers, and its Young's modulus is 226.62 GPa. For the lubrication purpose, a standard diesel lubricant, 15W40, was used. A kinematic viscometer (ASTMD445) was used to measure the kinematic viscosity of the lubricant. The kinematic viscosity came out to be 97.35 mPa s. The density of the 15W40 lubricant was measured using a density analyzer (ASTMD4052), and its value came out to be 870.35 kg/m³ at 40 °C. A full flooded lubrication condition and starved lubrication condition was used for determining the wear and friction between the mild steel disc and chrome-coated cast iron pin. In full flooded lubrication condition, there is a continuous supply of lubricant at the contact surface of the mating parts. This will maintain a uniformly thick layer of lubricant between the contacting surfaces. In starved lubrication condition, a small amount of lubricant is placed between the contacting surfaces before the surfaces were put in motion. This will generate a thin layer of lubricant around the contact region.

For determining the amount of wear and friction in a tribotester, three different normal loads (20, 40 and 60 N) at three different sliding speed were used. A total distance of running the contact surface for the test is kept at 2000 m. The test conditions were shown below (Table 3).

The specific wear rate (SWR) was determined as the amount of material lost per normal load applied per sliding distance covered by the sliding surface. SWR was

Table 3 Test conditions on tribotester

S. No.	Sliding speed (m/s)	Track diameter	RPM	Time of test run (s)
1	2.61	50	1000	764
2	3.66	70	1000	546
3	5.26	100	1000	380
4	7.33	70	2000	272
5	10.47	100	2000	192
6	13.60	130	2000	147

calculated by the following equation:

$$\text{SWR} = \frac{V_w}{\text{Nr} \times L}$$

where SWR = Specific wear rate, mm³/N m

V_w = Volume of wear loss, in mm³

Nr = Applied normal load in N

L = Sliding distance, m.

3 Results and Discussion

A comparison was made between the behaviour of chrome-coated cast iron pin and the uncoated cast iron pin under full flooded and starved lubrication condition at various sliding speed and normal loads.

3.1 Behaviour Under Starved Lubrication Condition

It is clearly observed from Fig. 2 that the specific wear rate gets reduced at the contact surfaces of chrome-coated C.I pin and M.S disc. The specific wear rate increases at low-speed ranges and further decreases during the transition from low speed-to-medium speed ranges. At high-speed ranges, the rate of increase of the specific wear rate was slower. The hard surface of the chrome coating reduces the wear between the contacting surfaces as compared to the uncoated contacting surfaces. Also, from Fig. 3, it is observed that the coefficient of friction between the surfaces gets reduced while using the chrome coating over the cast iron pin. The high surface finish of the chrome-coated pin reduces the surface asperities interaction with each other and hence further reduces the coefficient of friction.

3.2 Behaviour Under Full Flooded Lubrication Condition

From Figs. 4 and 5, it was found that the SWR and friction coefficient between the contacting surfaces gets reduced by employing chrome coating on the cast iron pin. Along with the high hardness and wear resistance of the chrome-coated pin, the full flooded lubrication forms a thick layer of lubricant between the surfaces, which helps in reducing the specific wear rate and coefficient of friction between the contacting surfaces. The aftermath of this reduction in SWR is the increased of service life of

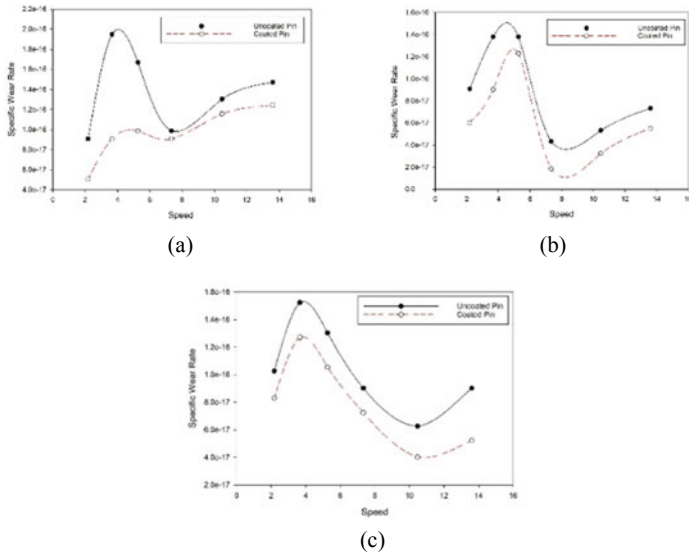


Fig. 2 Specific wear rate comparison between uncoated and chrome-coated pin under different normal loads **a** 20 N, **b** 40 N, **c** 60 N and starved lubrication

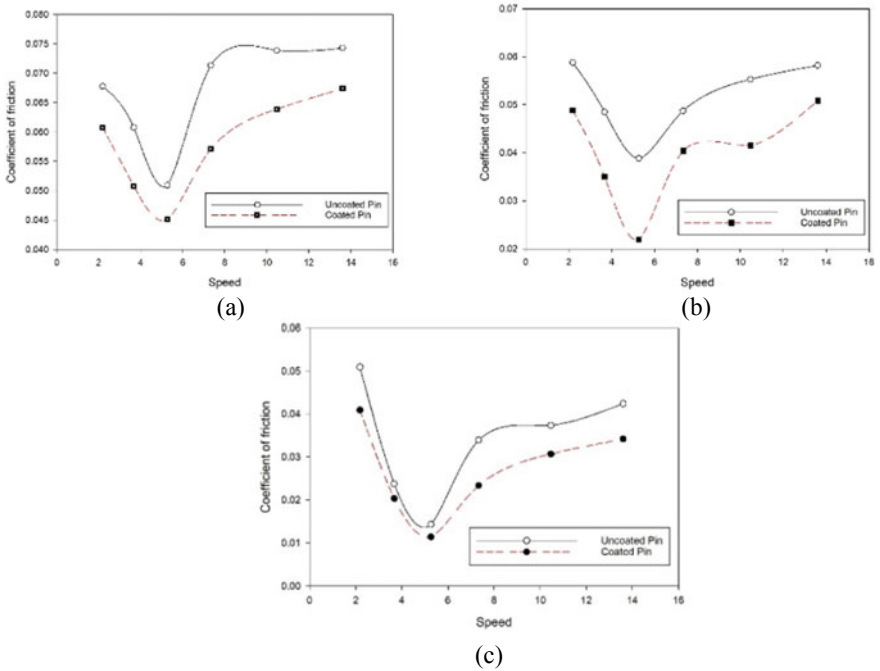


Fig. 3 Coefficient of friction comparison between uncoated and chrome-coated pin under different normal loads **a** 20 N, **b** 40 N, **c** 60 N and starved lubrication

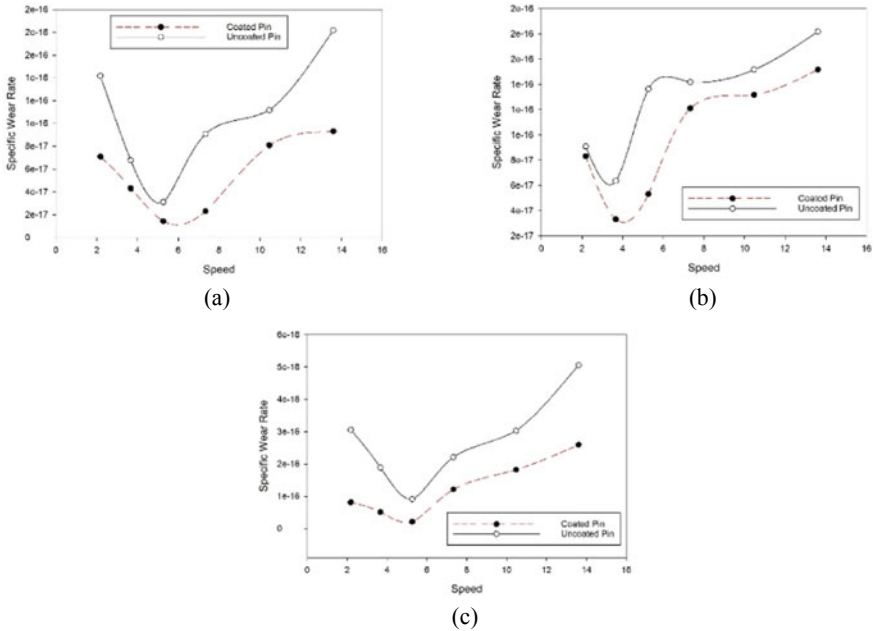


Fig. 4 Specific wear rate comparison between uncoated and chrome-coated pin under different normal loads **a** 20 N, **b** 40 N, **c** 60 N and full flooded lubrication

the piston ring. Also, the blow-by of combustible gases in the internal combustion engine could also be reduced by using the chrome plating on the piston ring. The gap between the piston ring and the cylinder liner is maintained for the longer period of time. This also makes the reduction in maintenance cost.

4 Conclusion

It is definitely observed that the use of coated component over uncoated ones improves the life of the rubbing components. The coefficient of friction is reduced by a considerable amount after using the chrome-coated pin instead of the uncoated pin. Hence, it is desirable to use the chrome plating in piston ring assembly. Chrome coating done by electro deposition is quite a reliable technique of coating. The specific wear rate is also be reduced for the rubbing surfaces by the use of chrome-coated components. The use of the chrome-coated piston ring and cylinder liner could be beneficial as it would improve the life of the piston ring, the problem of blow-by and blow back could be reduced, and hence, the amount of energy loss would be reduced.

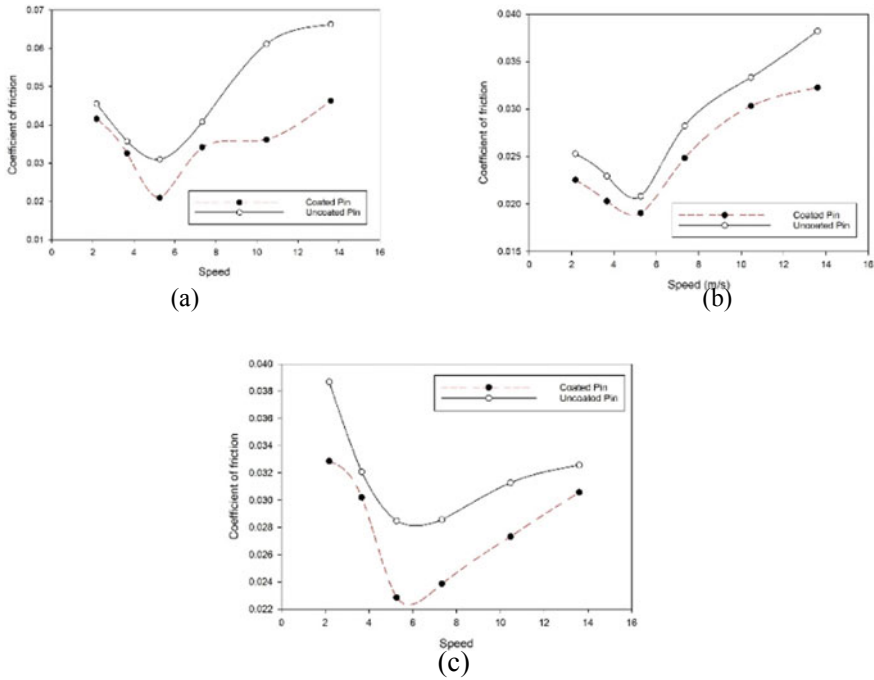


Fig. 5 Coefficient of friction comparison between uncoated and chrome-coated pin under different normal loads **a** 20 N, **b** 40 N, **c** 60 N and full flooded lubrication

References

- Holmberg K, Andersson P, Nylund N, Mäkelä K, Erdemir A (2014) Tribology International Global energy consumption due to friction in trucks and buses. *Tribology Int* 78:94–114
- Bhatt DV, Sutaria BM, Bhatt MK, Sonigra BK (2013) ASTM performance tests to study the effect of blend oil with based oil analysis for automobile engines. *International Conference on Mechanical, Production and Automobile Engineering* 2013
- Chaudhary S, Singh RC, Chaudhary R (2017) Experimental Investigation of Influence of SiO₂ nanoparticles on the tribological and rheological properties of SAE 40 lubricating oil. *Int Eng Technol* 9(6):4307–4314
- Sonia SC (2020) Preparation and tribological analysis of Mustard oil bio lubricant blend using four ball testing machine. *Int J Mech Prod* 279–286
- Broszeit E et al (1999) Deposition, properties and applications of PVD CrN coatings. *Surf Coat Technol* 115(1):9–16
- Mishra PC (2013) Modeling for friction of four stroke four cylinder in-line petrol engine. *Fac Eng* 35(3):237–245
- Mishra PC (2014) A review of piston compression ring tribology. *Tribol Ind* 36(3):269–280
- Mistry HR, Bhatt DV (2011) Study of tribological parameters on SI engine – a case study. *Int J Advan Eng Technol* 6–10
- Ezhilmaran V et al (2018) Investigation on generation of laser assisted dimples on piston ring surface and influence of dimple parameters on friction. *Surf Coating Technol* 335:315–326
- Navinšek B, Panjan P, Milošev I (1997) Industrial applications of CrN (PVD) coatings, deposited at high and low temperatures. *Surf Coat Technol* 97(1–3):182–191

11. Unal H, Mimaroglu A, Kadiloglu U, Ekiz H (2004) Sliding friction and wear behaviour of polytetrafluoroethylene and its composites under dry conditions. *Mat Design* 25(3):239–245
12. Costa MYP et al (2010) An investigation on sliding wear behavior of PVD coatings. *Tribol Int* 43(11):2196–2202
13. Moosavian A, Najafi G, Ghobadian B, Mirsalim M, Jafari SM, Sharghi P (2016) Piston scuffing fault and its identification in an IC engine by vibration analysis. *App Acous* 102:40–48
14. Shah AS, Bhatt DV (2014) Experimental study to measure piston ring assembly friction of multi cylinder I.C. Engine on motorized engine test rig: a case study. *International conference on Advances in Tribology and engineering systems*, springer Indian 2014, pp 60–63
15. Sonia SC et al (2020) Tribological investigation of bio-lubricant based on Madhuca Longifolia and Sesamum Indicum. *Int J Advan Sci Technol* 5885–5892

Numerical Study of Traction at Grouser–Soft Seabed Interface Incorporating Experimentally Validated Constitutive Model



S. Sumith , K. Shankar, and K. Kannan

Abstract This paper presents the tractive performance of different grouser shapes in extremely soft seabed soil using finite element analysis (FEA). Consequently, the deformation characteristics and pattern of shear failure in the seabed soil can be predicted, eliminating expensive full-scale experiments. A three-dimensional FEA with the incorporation of geometric nonlinearity of shear rheometry is performed using coupled Eulerian–Lagrangian (CEL) technique in ABAQUS Explicit. The Mohr–Coulomb criterion is used to define the constitutive behaviour of the seabed soil sample used. To validate the model, the CEL simulation results are corroborated with experimental observations. The study reveals that the Mohr–Coulomb model with the governing parameters is able to capture the maximum rotational moment obtained from the experimental results with a maximum error of 3.5%. The Mohr–Coulomb model is therefore used to determine the maximum traction developed from two distinct grouser profiles to evaluate their tractive efficiency. It is observed that a triangular grouser offers better traction than an involute grouser.

Keywords Seabed soil · Shear rheometry · Mohr–Coulomb model · Coupled Eulerian–Lagrangian technique · Finite element analysis · Grousers

1 Introduction

In recent times, the investigation of deep sea mineral resources is of profound interest due to the gradual exhaustion of land mineral resources [1]. Recent technologies have resulted in the use of tracked undercarriage vehicles (underwater crawler) to extract deep sea minerals from the potential mining sites [2, 3].

Seabed surface has very soft clays having shear strength not more than 2 kPa [4, 5]. Since the mobility of tracked vehicles is firmly decided by shear resistance of seabed, it is incumbent upon us to consider the study of soft soil track interaction characteristics. The interaction of the vehicle with the soft clay is maintained through

S. Sumith (✉) · K. Shankar · K. Kannan

Department of Mechanical Engineering, Indian Institute of Technology Madras, Chennai 600036, India

grouser systems. A grouser is a projection on the continuous track belt surface, designed for enhancing the tractive force over deep-seabed surface. Grousers may take the shape of triangular or complex involute form based on the type of terrain and desired vehicle performance. Grousers may be permanently attached or bolted to the track segment for the purpose of replacement. For a viable track design, considering the involvement of the grouser in the development of tractive forces in the running gear system is significant [6].

Arising from the previous studies, it is obvious that the grouser geometries in a track can significantly affect the performance of the tracked vehicle [7]. The grouser–terrain interaction is of much relevance since it determines the thrust development. Moreover, it is required to investigate the kinds of deformation and shear patterns in soil. Nevertheless, performing field tests are more expensive and time-consuming and cannot be easily repeated.

From the literature survey, it is noticed that finite element method (FEM) is being used in recent decades for modelling a cutting blade–soil interaction [8]. In view of this, a dynamic analysis is carried out using FEM to investigate the soft soil–grouser interaction characteristics. The effect of grouser geometries on the total horizontal reaction forces developed is mainly considered. Thus, the analysis is motivated in the a priori evaluation of the tractive performance of different grouser shapes without exhorting expensive and time-consuming experiments. This paper also discusses the effectiveness of the constitutive model used in finite element analysis of soft soil–grouser interaction. The efficacy of the model is validated by simulating the large deformation shear rheometry using the CEL technique in ABAQUS and corroborating simulation results with experimental observations.

2 Materials and Methods

The constitutive behaviour of soft cohesive soil is effectively modelled based on the elastic perfectly plastic failure criterion. The Mohr–Coulomb elasto-plastic model is used here to depict the characteristics of soil [9]. Generally, the model's stress–strain behaviour is linear within the elastic range and is described by using two parameters from Hooke's law (Young's modulus, E and Poisson's ratio, ν). The failure criterion is represented by two parameters, namely (the friction angle, φ and cohesion, c) and another parameter which defines the flow rule (dilatancy angle, θ). The dilatancy angle arises from the non-associated flow rule that is commonly employed to model a realistic irreversible volume change by virtue of shearing effects. The Mohr–Coulomb failure criterion is given by

$$\tau_f = c + \sigma_f \tan \varphi \quad (1)$$

where c , φ are parameters and are discussed above. τ_f and σ_f are the shear and normal stresses act on the plane where failure takes place.

Table 1 Parameters associated with Mohr–Coulomb model

S. No.	Parameters	Value	Units
1	Density	1.2×10^{-9}	tonnes/mm ³
2	Young's modulus	500×10^{-3}	MPa
3	Poisson's ratio	0.49	Number
4	Friction angle	1.0	°
5	Dilation angle	0.85	°
6	Cohesion yield stress	1×10^{-3}	MPa

The model parameters are estimated by considering the deep sea soils having shear strength of 1 kPa. The parameters used to model the deep seabed soil are given in Table 1. Here, the undrained soil response is modelled by considering Poisson's ratio, $\nu = 0.49$ and the key factor governing the result is cohesion. In order to prevent any instability in numerical simulations, small but nonzero dilation and friction angle values are regarded.

3 Validation of the Model

The objective of this section is two-pronged. One is to provide accurate prediction of mechanical behaviour of soft soil under consideration based on the standard experimental technique namely the shear rheological test and second, to numerically simulate the shear rheological test using the Mohr–Coulomb model available in ABAQUS and experimentally validate the simulation result. The above goals are targeted to determine the efficacy of the model for further grouser–soft soil interaction analysis.

3.1 Experiment

To conduct the shear rheometry tests, initially, the substitute for soft seabed soil with shear strength 1 kPa (average shear strength) is prepared by using 20 wt% bentonite–water mixtures. The bentonite–water mixture resembles the mechanical and physical features of the original deep-sea sediment in most respects [10, 11]. Anton-Paar MCR 301 Rheometer is used in the present study (see Fig. 1a). The parallel plate geometry has been identified to be convenient for shearing this type of clay dispersion [12].

In this measuring geometry, the sample is placed between an upper rotating disc and a stationary lower disc having a common axis as shown in Fig. 1b. The response of simulative soil is investigated by keeping the sample at a constant shear rate of 10 s^{-1} , and the reaction moment is determined as a function of time. The diameter of the discs (ϕ) is 25 mm, and a constant gap (h) of 2 mm is sustained during

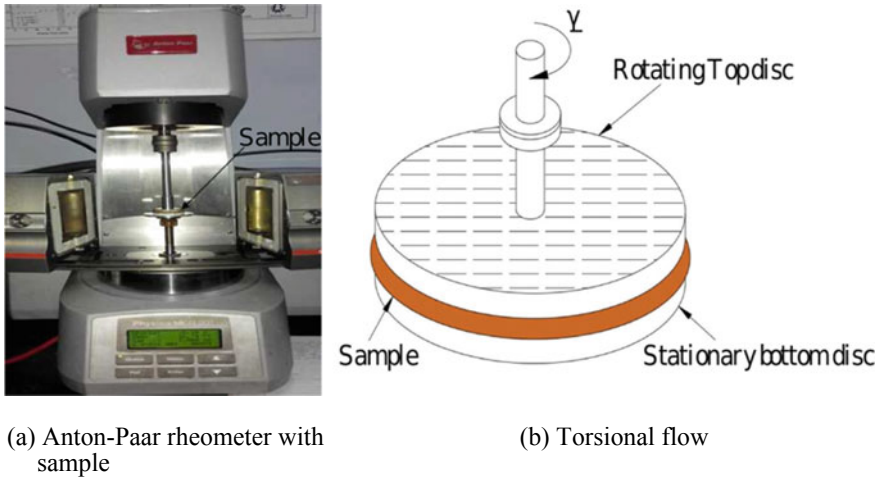


Fig. 1 Parallel plate geometry

measurements. The test is performed at constant temperature of 25 °C. The variation of rotation moment with time can be seen in Fig. 2.

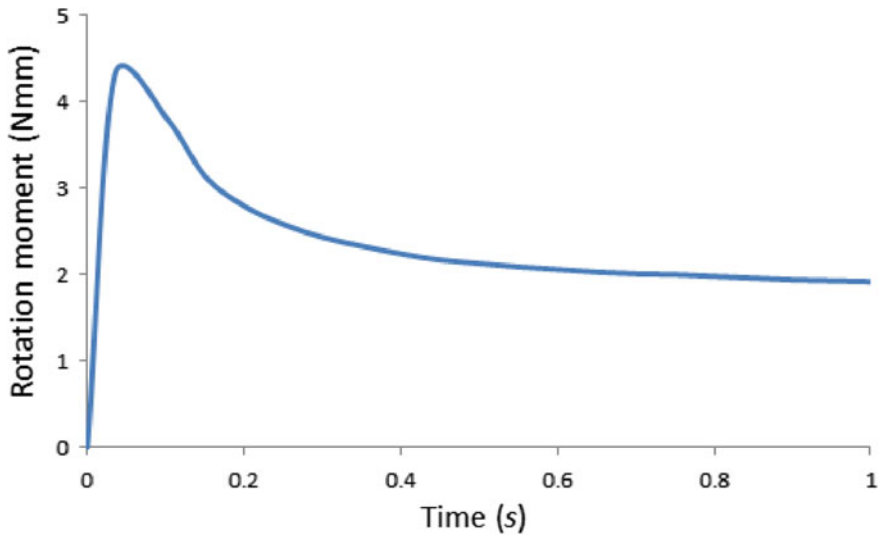


Fig. 2 Variation of torque with time at 10 s⁻¹

3.2 Numerical Modelling of Shear Rheometry

To evaluate the validity of the model, the numerical simulation of shear rheological experiment is performed. Here the soil domain and the rotating discs are modelled as two different parts. The soil domain is 25 mm in diameter and 2 mm in height. From the experiment, it is observed that as the disc starts rotating, the sample will flow towards outside through periphery. Therefore, a void (material free) of 1.5 mm has been created at the periphery of the soil domain.

Previous experimental and numerical studies on seabed modelling indicate that substantial deformation of the seabed surface occurs when subjected to loading [13]. Such large deformation inherently present in seabed soil seeks an Eulerian-based approach for their numerical modelling [14]. The advantage of the Eulerian over Lagrangian approach is that the mesh undergoes no distortion, and thus, large deformations can be readily handled.

The simulation of rheological tests relies on the CEL features available with in commercially available finite element package ABAQUS (ABAQUS/CAE 6.14). Lagrangian and Eulerian elements are combined using a method known as coupled Eulerian–Lagrangian (CEL) analysis. In CEL analysis, soft soils which undergoing significant deformations are meshed with Eulerian elements, while disc attached to the soil is meshed with Lagrangian elements. The soil domain is discretized using eight-node linear reduced integration Eulerian hexahedral elements (EC3D8R) and the disc is modelled using three-dimensional rigid elements (R3D3 and R3D4) alongside rigid body constraint with reference node at the centre of the disc. The description of mesh sizes used in the soil domain for mesh convergence study is shown in Table 2. Figure 3 depicts the finite element model of the shear rheometry performed using automatic mesh generator of ABAQUS.

The stress–strain response of the soft soil is simulated using Mohr–Coulomb model, and the parameters available in Table 1 are used. In order to replicate the shear rheometry boundary conditions, the bottom base nodes of the soil domain are fully constrained. To define the interaction of contacting surfaces between the disc and the soft soil, Coulomb friction model with a high coefficient of friction is used. Thus, the analysis takes into account frictional forces, which resist the relative sliding of the surfaces. In order to apply a constant shear rate, the disc is allowed to move in the clockwise direction by giving a prescribed angular velocity (Ω) by considering the relation shear rate $\dot{\gamma} = \Omega R/h$. Thus, the shear rate has been given by applying angular velocity at the reference node of rigid disc and is maintained constant throughout the analysis. By making use of the rigid body constraint feature in ABAQUS, one can predict the resultant reaction moment induced on the whole disc by means of a single reference node.

Table 2 Mesh details for soil model

Mesh	Coarse	Medium	Fine
Number of elements	102	1672	12,288

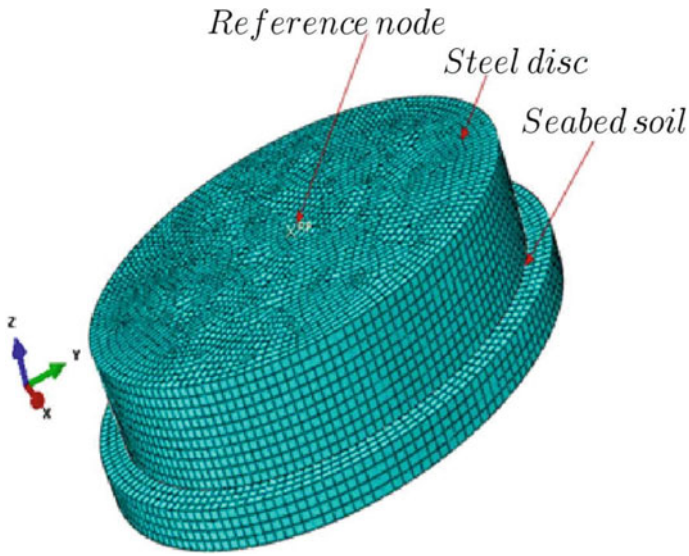


Fig. 3 Meshed model of shear rheometry

Figure 4 depicts the rotational moment (torque) evaluated from numerical analysis of shear rheometry for various mesh sizes of soil domain. The fine mesh with 12,288

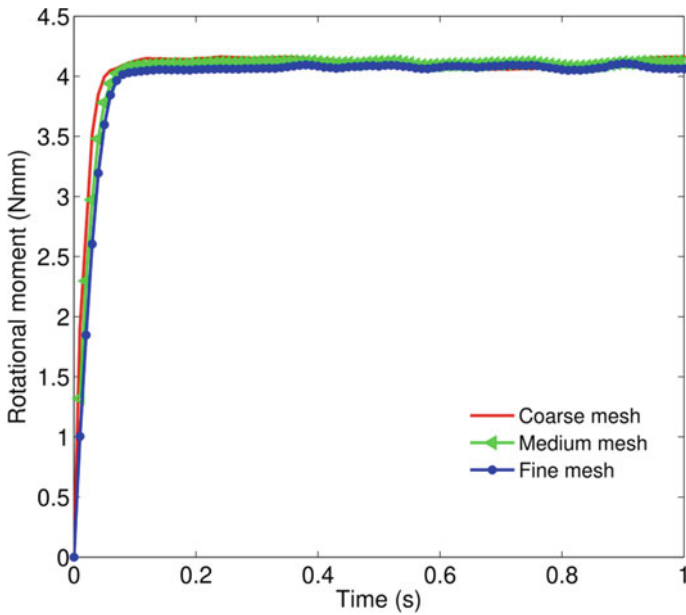


Fig. 4 Mesh independence study of soil domain

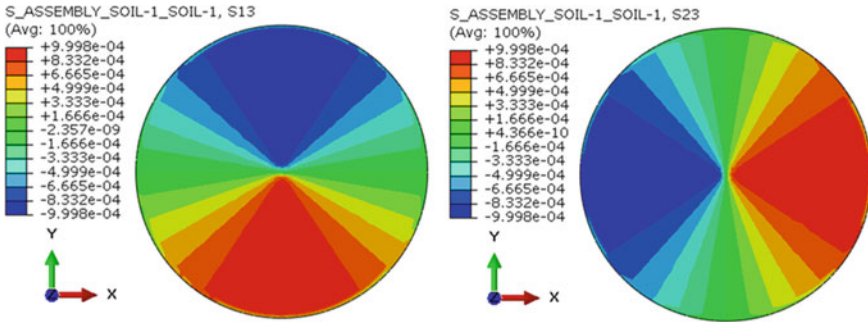


Fig. 5 Distribution of shear stress along horizontal cross section at the top surface of the soil domain

number of elements are used for the comparison herein. The reaction torque obtained from numerical analysis is compared with experimental torque for the same value of simulation input cohesive yield stress and experimental undrained shear strength. From shear rheometry, it is noticed that the phenomenon of torque overshoots prior to torque relaxation occurs within a short period of time. The Mohr–Coulomb model parameters are unable to capture the post-failure phenomenon in the experiment once the shear failure occurs. However, the most significant feature observed is that the peak value of rotational moment from FEA matches with that of the shear rheological experimental results. The maximum torque attained from CEL modelling of shear rheometry (4.17×10^{-3} Nm) is about 96.5% compared to the experimentally obtained moment (4.32×10^{-3} Nm). This slight reduction in numerical results is attributed to the small variation in shear stress distributions induced from the numerical analysis. The shear stress distribution along the horizontal cross section at the top surface of the soil domain is investigated using Cartesian coordinates and is shown in Fig. 5. It is noticed that the magnitudes of shear stresses are maximum at the extreme ends of 1st and 2nd axis as anticipated. Furthermore, the maximum value of shear stress say 0.99 kPa is nearly equivalent to the input undrained cohesion yield stress value given in Table 1. Thus, it can be inferred from the results that the Mohr–Coulomb model parameters are suitable for investigating the effect of different grouser shapes on the maximum traction performance of the underwater tracked vehicle.

4 An Application of the Model to Dynamic Analysis

Single grousers with two different shapes are numerically studied using ABAQUS in this section. Here FEA is conducted to study the effect of maximum reaction forces on the grouser with respect to displacement and time. The validated Mohr–Coulomb model parameters are employed to describe the seabed soil behaviour as shown in Table 1. To study the dynamic effects of the soil–track interface, velocity of 100 mm/s (refer [15]) is applied to the grousers. Two different grouser shapes with same height

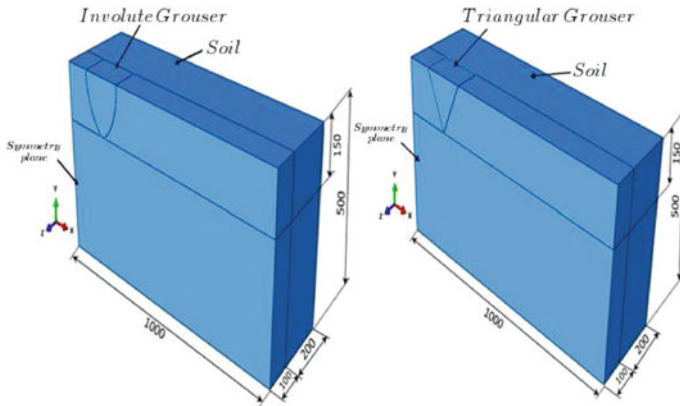


Fig. 6 Geometry of the soil model with different grousers

and width are used here in the simulation as shown in Fig. 6. These grouser shapes are predominately used in the underwater tracked vehicles operating on very soft sediments of the deep-seafloor. Further, the experimental studies have shown that these shapes are able to provide more traction as compared to other grouser shapes [7, 16].

5 Model Geometry

A three-dimensional soil model is developed as shown in Fig. 6. The model consists of lateral bound width having 200 mm, 200 mm is the grouser moving width, 1000 mm is the soil bin length, 500 mm is the soil bin height, 150 mm is the sinkage depth of the grouser. Owing to the geometric symmetry, half of the model is taken into account for simulation.

6 Meshing and Boundary Conditions

The automatic mesh generator of ABAQUS is used here. A general purpose 8-node linear brick continuum element (C3D8R) with reduced integration (one integration point) is used to characterize the soft seabed soil in the finite element model. To obtain reliable results, fine meshes are generated near grousers, while meshes of other regions are relatively coarse. Here 23,670 numbers of elements have been used in soil domain based on the grid independence test. The dynamic explicit scheme in ABAQUS is used to perform the analysis, and the grousers are represented as a rigid body with a reference node. The movement of grousers is governed by prescribed

velocity at the reference node kinematically attached to it. The grousers are simulated by making use of the rigid body feature in ABAQUS. This allows in finding the reaction forces developed on the different grouser shapes by means of a single reference node.

In the analysis, bottom base nodes of the seabed soil domain are totally constrained. The vertical boundary nodes parallel to $Y-Z$ plane, at $X = 0$ and $X = 1000$ mm, are confined horizontally along the X -axis. Similarly, the vertical boundary nodes parallel to $X-Y$ plane, at $Z = 0$ and $Z = 300$ mm (symmetry plane), are confined laterally along the Z -axis. The movement of grousers is restricted in the vertical direction as well as rotation. However, it is mobile in the horizontal direction. Furthermore, the constant velocity of 100 mm/s has been given to grousers.

7 Result and Discussion

In FEA, the grousers are moved horizontally at a distance of 15 mm and the maximum reaction developed has been analysed. From this analysis, it has been observed that the total horizontal reaction force predicted for a triangularly shaped grouser in seabed soil is higher than that of an involute grouser and is shown in Fig. 7. The steep rise of the reaction forces at the starting of the motion could be attributed to the momentum exchange between bodies under contact, the grouser with the starting velocity and the soil being stationary. Moreover, one can readily predict the maximum tractive force of different grousers based on the terrain shear strength and grouser contact area (Table 3).

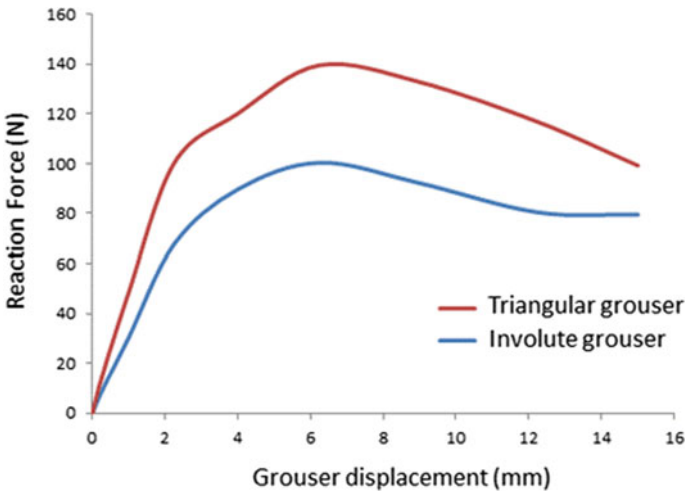


Fig. 7 Variation of force with respect to displacement for different grousers

Table 3 Maximum reaction force induced in involute and triangular grouser

Geometry	Maximum reaction force
Involute	105 N
Triangular	140 N

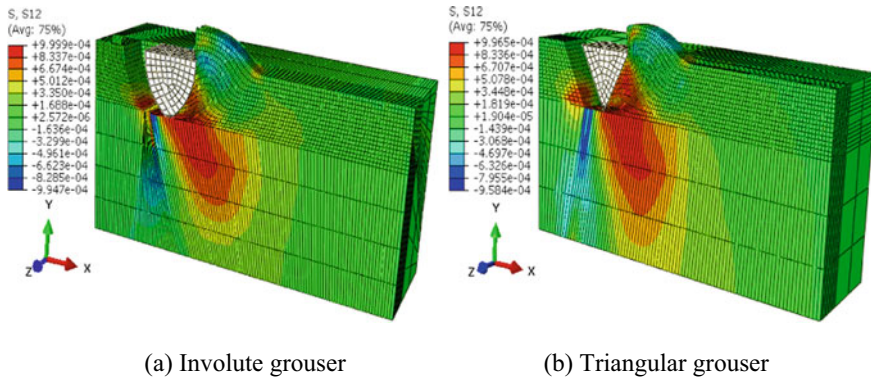


Fig. 8 Vertical shear stress distribution in soil domain for different grousers

Figure 8 shows the contour for vertical shear stress distribution in soil domain due to the displacement of different grouser geometries. The development of a shear band during shearing is observed as a hemisphere or a conical zone in the vicinity of the grouser. Furthermore, the maximum shear stress is found to be around $(0.99 \times 10^{-3} \text{ MPa})$ which agrees with the shear strength of the simulated soil. Thus, this study can be used as a benchmark which allows investigating the effect of different grouser geometry on trafficability of soft seabed soils without performing expensive full-scale experiments.

8 Conclusion

In this paper, FEA was performed on an extremely soft seabed with shear strength of 1 kPa for a priori evaluation of the tractive performance of different grouser geometries. The Mohr–Coulomb model was found to be suitable for predicting the constitutive behaviour of seabed soil. The efficacy of the model was validated based on the large deformation finite element analysis of shear rheometry using CEL technique in ABAQUS. From this study, it was observed that the model is capable of capturing the torque required at failure observed in the experiment with a maximum percentage error of 3.5. Therefore, the parameters of the Mohr–Coulomb model were subsequently used in further dynamic analysis of triangle and involute grouser shapes mainly used in underwater tracked vehicles. The dynamic analysis mainly

elucidated the total horizontal reaction forces developed during the movement of different grousers in seabed soil, which in turn predicts the maximum power requirement. From this analysis, it was noticed that the tractive force developed in a triangularly shaped grouser is higher than that of an involute grouser. Thus, without performing expensive field testing experiments, this novel study provides valuable information about the effect of different grouser geometry as well as the optimal grouser shape on gross tractive effort in extremely soft seabed soil.

References

1. Kato Y, Fujinaga K, Nakamura K, Takaya Y, Kitamura K, Ohta J, Toda R, Nakashima T, Iwamori H (2011) Deep-sea mud in the pacific ocean as a potential resource for rare-earth elements. *Nat Geosci* 4(8):535–539
2. Dai Y, Liu SJ (2013) Theoretical design and dynamic simulation of new mining paths of tracked miner on deep sea floor. *J Central South Univ* 20(4):918–923
3. Hong S, Kim HW, Choi JS et al (2002) Transient dynamic analysis of tracked vehicles on extremely soft cohesive soil. In: The fifth ISOPE Pacific/Asia offshore mechanics symposium. International society of offshore and polar engineers, pp 100–107
4. Babu SM, Ramesh N, Muthuvel P, Ramesh R, Deepak C, Atmanand M et al (2013) In-situ soil testing in the central indian ocean basin at 5462-m water depth. In: Tenth ISOPE ocean mining and gas hydrates symposium. International society of offshore and polar engineers, pp 190–197
5. Choi JS, Hong S, Chi SB, Lee HB, Park CK, Kim HW, Yeu TK, Lee TH (2011) Probability distribution for the shear strength of sea floor sediment in the KR5 area for the development of manganese nodule miner. *Ocean Eng* 38(17–18):2033–2041
6. Ma W, Rao Q, Feng K, Xu F (2015) Experimental research on grouser traction of deep-sea mining machine. *Appl Math Mech* 36(9):1243–1252
7. Hong S, Choi JS et al (2001) Experimental study on grouser shape effects on trafficability of extremely soft seabed. In: Fourth ISOPE ocean mining symposium. International society of offshore and polar engineers, pp 115–121
8. Abo-Elnor M, Hamilton R, Boyle J (2003) 3D dynamic analysis of soil-tool interaction using the finite element method. *J Terramech* 40(1):51–62
9. Rani RS, Prasad K, Krishna T (2014) Applicability of mohr-coulomb and drucker-prager models for assessment of undrained shear behaviour of clayey soils. *Int J Civ Eng Technol* 5(10):104–123
10. Ma WB, Rao QH, Li P, Guo SC, Feng K (2014) Shear creep parameters of simulative soil for deep-sea sediment. *J Central South Univ* 21(12):4682–4689
11. Sumith S, Sangam K, Kannan K, Shankar K (2020) Prediction of nonlinear viscoelastic behaviour of simulative soil for deep-sea sediment using a thermodynamically compatible model. *Inverse Prob Sci Eng* 28(6):777–795
12. Sumith S, Kannan K, Shankar K (2020) A constitutive model for bentonite-water mixture and the effect of wall slip boundary conditions on its mechanical response. *Int J Non-Linear Mech* 119:103318
13. Fadaifard H, Tassoulas JL (2014) Numerical modeling of coupled seabed scour and pipe interaction. *Int J Solids Struct* 51(19–20):3449–3460
14. Qiu G, Henke S, Grabe J (2011) Application of a coupled Eulerian-lagrangian approach on geomechanical problems involving large deformations. *Comput Geotech* 38(1):30–39
15. Grebe H, Schulte ES et al (2005) Determination of soil parameters based on the operational data of a ground operated tracked vehicle. In: Sixth ISOPE ocean mining symposium. International society of offshore and polar engineers, pp 149–156

16. Janarthanan C, Reshma K, Rajesh S, Ramesh N, Raj TR, Sundaramoorthi V, Muthuvel P, Gopakumar K, Ramadass G, Atmanand M (2015) Traction and drawbar pull experimental study for development of deep sea mining machine. In: 2015 IEEE underwater technology (UT) IEEE, pp 1–7

Performance Characteristics of Asymmetric Body in Hypersonic Flow



D. Nithin and Vinod Kotebavi

Abstract Increase in the angle of attack in high-speed flows offers the possibility of more efficient aerodynamic flow, and this phenomenon is being looked into for improving the performance of high-speed vehicles, from reusable space vehicles to military applications. By increasing this bite angle, there are opportunities to reduce the thermal loads on objects under hypersonic flows, thus reducing the need for higher degrees of thermal dissipation. But even a simple structure can induce complex flow at those speeds and angles of attack, including leeward side separations and vortices. The principal objective of this report was to obtain detailed flow field and surface pressure measurements over asymmetric body like elliptic cone. Detailed measurements of the distribution of pressure were made along the leading edges and on the windward and leeward sides of the models. Furthermore, drag and lift characteristics were calculated using Spalart–Allmaras model and compared to the drag and lift performance on circular cones with same base dimensions to show the advantages of the elliptical cones as a better carrier in hypersonic flows.

Keywords Elliptical cones · Hypersonic flow · Aerodynamic characteristics

1 Introduction

Hypersonic aerodynamics has gathered immense momentum in the past few years, with its perceived advantages in its utility in military and commercial applications. But it remains a fact that there is still a lot of work to be done before we are at a position where hypersonic flights become common place. For that matter, concorde still remains the only commercial application of supersonic flights. Hypersonic study is not a new concept, and it was researched extensively in the 1950s, when the spacecrafts were being developed, but due to the difficulty in testing and a lack of computational methods during the time, the processes were deferred.

D. Nithin · V. Kotebavi (✉)

Department of Mechanical Engineering, Amrita School of Engineering, Amrita Vishwa Vidyapeetham, Bengaluru, India
e-mail: k_vinod@blr.amrita.edu

The symmetrical body like circular cone has always been a reference when it comes to any form of supersonic or hypersonic flow past revolving objects, but elliptical objects which are asymmetric assume that role when considering objects with non-circular dimensions. This is because elliptical geometry provides higher lift values while maintaining a usable amount of surface area. The first approximate solution for supersonic flow over elliptical bodies was derived by Fraekel [1], following the work done by Ward [2] who defined the supersonic slender body theory. The second-order approximations for circular objects were derived by Lighthill [3] and were extended to elliptical cones by Van Dyke [4].

For a very long time, no generalised flow field characteristics were set forth for hypersonic flow over elliptical cones, due to the difficulty in deriving such theoretical solutions and the lack of machine computation available during the 1960s and 1970s. Chapkis [5] applied the linearised theory put forth by Ferri [6] to elliptical cones and found them to agree with the experimental results at zero degree of attack, but the Newtonian approximations were found to be more accurate at higher angles of attack. Kaattari [7] presented a method for approximating pressure distribution over elliptical cones based on correlation with experimental values and those from two-dimensional shock theory, which can be used to estimate pressure on surfaces at different Mach numbers, cone geometry and angles of attack, but limited to a maximum semi-apex angle of 30° .

Quite a few experimental literature has since been published with very specific goals. Jorgensen [8] performed detailed testing on elliptical cones at Mach 2.97 using both linearised and slender body theory as comparison. Chapkis [5] performed the earliest experiment on hypersonic flow over elliptical cones. Holden et al. [9] drove multiple projects in understanding the hypersonic flow over elliptical cones, including laminar, transitional and turbulent flow. The process was carried out over Mach numbers from 8 to 12, and detailed measurements were made for both the heating and pressures along the leading edges as well as windward and leeward sides. Huntley et al. [10] studied transition characteristics of high-speed flows over elliptical cones at Mach 8 using filtered Rayleigh scattering and provided visual insights into travelling wave instabilities at their centreline. Spikes are also used to reduce the drag on the object [11, 12] in hypersonic flow. Rajesh et al. [13] concluded that introduction of spikes reduces the drag but the same time it introduces pulsation phenomenon in many cases. Rajesh et al. [14] also conducted study on spiked cylinders with different shapes of spikes. They found that aerodisk will not produce buzz phenomenon for any L/D ratios they used.

2 Formulation of the Problem

Shockwaves in supersonic aerodynamics are considered mathematical and physical discontinuities. Increase in Mach numbers to hypersonic speeds brings no dramatic changes with regard to the physics of this, as explained by Anderson [15]. However, there are some peculiarities associated with hypersonic flow, mainly the

small distance between the body and the shockwave, as well as the thinness of the shockwave associated. Including the temperature and chemical effects of the hypersonic interaction further reduces the shock angle creating a merged shockwave with the boundary layer at low Reynolds number. But this issue turns into a blessing at higher Reynolds number where the shock layer can be considered inviscid. The study of this phenomenon was merged to form the thin shock layer theory.

The interaction of any object with a flowing gas produces two forces, lift and the drag relative to the direction of the flow. These forces are expressed as non-dimensional coefficients in this report to visualise their significance in comparison with various geometric structures.

$$C_L = \frac{L}{q_\infty S} \tag{1}$$

$$C_D = \frac{D}{q_\infty S} \tag{2}$$

$$q_\infty = \frac{1}{2} \rho_\infty V_\infty^2 \tag{3}$$

Spalart–Allmaras [16] model was used in Ansys Fluent to solve for the above aerodynamic properties. This model was originally designed for “aerospace applications involving wall-bounded flows”, and it gives proper results for boundary layer problems which are subjected to extreme pressure gradients, as is applicable in our report.

The solution equation for the transport property in the SA model is given by

$$\frac{\partial}{\partial t}(\rho \tilde{\nu}) + \frac{\partial}{\partial t}(\rho \tilde{\nu} u_i) = G_\nu + \frac{1}{\sigma_{\tilde{\nu}}} \left[\frac{\partial}{\partial x_i} \left\{ \left((\mu + \rho \tilde{\nu}) \frac{\partial \tilde{\nu}}{\partial x_j} \right) \right\} + C_1 \rho \left(\frac{\partial \tilde{\nu}}{\partial x_j} \right)^2 \right] - T_\nu + S_{\tilde{\nu}} \tag{4}$$

where G_ν is the turbulent viscosity generation source, and T_ν is the distorted turbulent viscosity at the near-wall region due to wall blocking and viscous damping. $\sigma_{\tilde{\nu}}$ and C_1 are constants and ν is the kinematic viscosity. $S_{\tilde{\nu}}$ is a user-defined transport property source. Note that since the turbulent kinetic energy, κ is ignored in the SA model, the last term in (5) is eliminated while estimating Reynolds stresses;

$$-\overline{\rho u'_i u'_j} = \mu_t \left(\frac{\partial u_i}{\partial x_j} + \frac{\partial u_j}{\partial x_i} \right) - \frac{2}{3} (\rho \kappa + \frac{\partial u_k}{\partial x_k}) \delta_{ij} \tag{5}$$

The above solution is obtained by the RANS equation

$$\frac{\partial}{\partial t}(\rho u_i) + \frac{\partial}{\partial x_j}(\rho u_i u_j) = -\frac{\partial p}{\partial x_i} + \frac{\partial}{\partial x_j} \left[\mu \left(\frac{\partial u_i}{\partial x_j} + \frac{\partial u_j}{\partial x_i} - \frac{2}{3} \delta_{ij} \frac{\partial u_n}{\partial x_n} \right) \right]$$

$$+ \frac{\partial}{\partial x_j} \left(-\rho \overline{u'_i u'_j} \right) \tag{6}$$

where $\overline{u'_i}$ and u'_i are the mean and instantaneous velocity components, which mandates Reynolds stresses be calculated to close out (6).

Models. Eight models were analysed, two sets of elliptical cones with varying semi-apex angles and circular cones with the same angles. The elliptical cones have varying ellipse ratio to understand its impact on the performance characteristics. The base area for all the models is kept constant to study the variation of aerodynamic properties on each geometry. The defined geometry can be classified as below;

1. Elliptical cone with 30° semi-major axis
 - a. 3 ellipse ratios of 2, 1.5 and 1.25
2. Elliptical cone with 30° semi-minor axis
 - b. 3 ellipse ratios of 2, 1.5 and 1.25
3. Circular cone with semi-cone angle of 20° and 30°.

All of these models were analysed at different angles of attack of 0°, 2°, 4°, 6°, 8°, 10° and 15° at Mach 8, at standard operating conditions.

Grid independence study has been carried out on the models to study the impact of the mesh sizes and the accuracy of the solution, to account for the limited computational power the report was restricted to. As evident from the plot, the progression of accuracy reduced beyond the fine mesh preset on the object (Fig. 1).

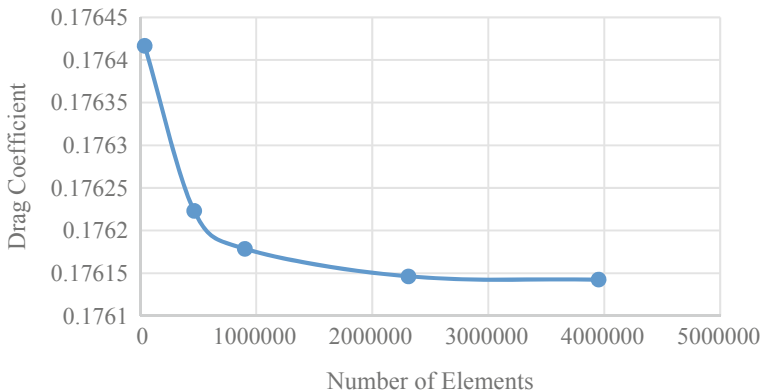


Fig. 1 Grid independence result

3 Results and Discussion

The results presented in this report are measured to reflect the progression along the angle of attack. This section can be divided into the two, the aerodynamic performance with the drag and lift performance and the surface pressure distribution obtained along the windward and the leeward sides of the elliptical cone. We can start by looking at the drag and lift characteristics of the models to assess the improvements which can be achieved with an elliptical cone over the circular cone.

For the elliptical cones, there is increase in the wetted-form area with the increase in the ellipse ratio with base area remaining the same. Figure 2b illustrates the appreciable increase in lift witnessed at all angles of attack of the elliptical cone geometry. The other pattern to be observed is the decrease in the drag as ellipse ratio is increased. this is a very important inference since we can use this in design of hypersonic vehicles, but it does beg the question as to how far this trend continues or is there is a low point in that curve, which can be further studied upon. As evident from the work of Jorgensen [8], the lift does regress once the major axis goes onto the vertical, thus reducing the wetted area.

The work of Jorgensen does remain the primary work of validation for the trends obtained in this paper, despite its lack of hypersonic study, since it provides us with a direct comparison to supersonic flows with similar criteria of study, creating a suitable frame for comparison of performance of objects between hypersonic and supersonic flows.

The values in Fig. 3 show conclusively in analysis the improvements in the aerodynamic efficiency obtained with use of the elliptical geometry for an object in hypersonic flow as compared to the circular cone. It is interesting to note that the slenderer the cone, the greater the performance obtained, giving some credence to the slender body theory as postulated by Ward [3]. The results also point towards greater performance in lesser apex angles with smaller ellipse ratios being more efficient, but possessing less lift compared to those with greater ellipse ratios as shown in Fig. 2b.

Earlier theories introduced on the hypersonic flow predicted nonlinear lift curve at very high-speed flow due to the presence of shed vortices, but the lift values obtained here are very linear, as predicted by the flat-plate theory and later by the slender body theories. Another inference we must be careful with while utilising the result obtained is the increase in the drag experienced on the elliptical cones as the angle of attack increases beyond a certain range, which must be calculated and analysed. This is important to note while designing for the higher aerodynamic efficiency which is evident from the above results. We can now have a look at the pressure distribution along the windward and leeward side of the models with the increase in the angle of attack (Fig. 4).

The distribution of the pressures observed on the elliptical cone surfaces is aligned with our understanding of the fluid behaviour when considering inviscid hypersonic flow with minimal turbulent viscosity in consideration. The variations in the pressure observed are either due to the presence of surface shocks or separation vortices.

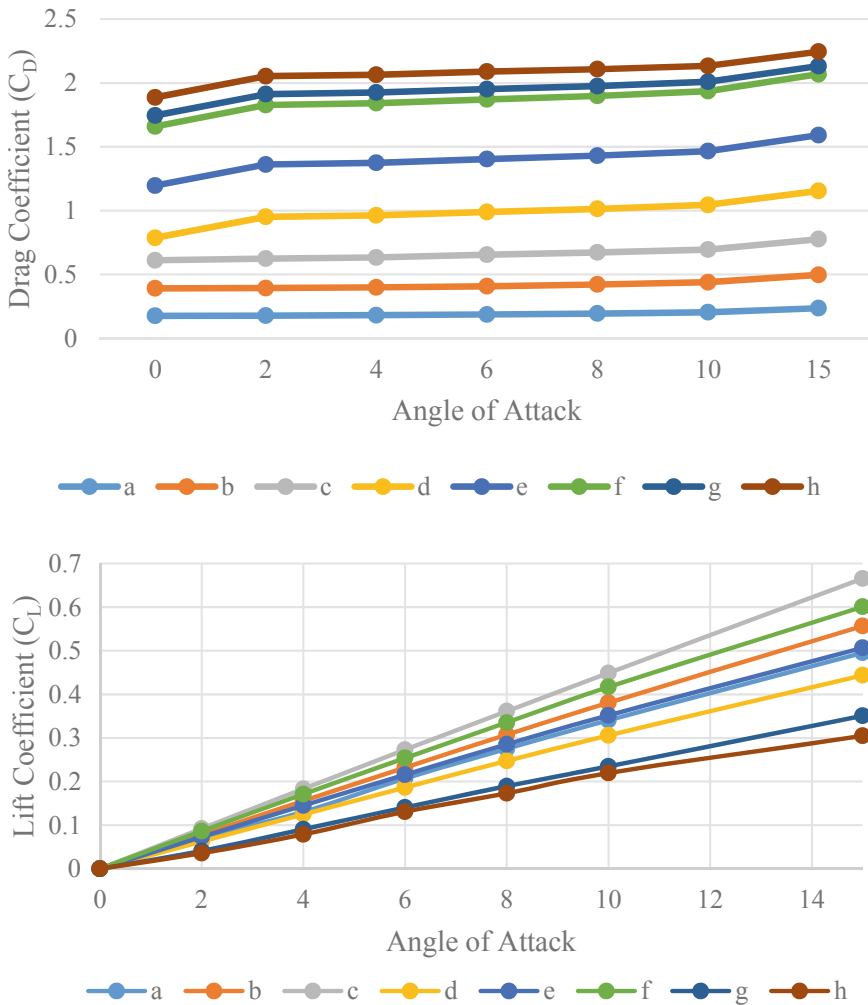


Fig. 2 (i) C_D versus AoA figure (ii) C_L versus AoA where (a) EC with $\alpha = 20^\circ$ and $\epsilon = 2$, (b) EC with $\alpha = 20^\circ$ and $\epsilon = 1.5$, (c) EC with $\alpha = 20^\circ$ and $\epsilon = 1.25$, (d) EC with $\alpha = 30^\circ$ and $\epsilon = 2$, (e) EC with $\alpha = 30^\circ$ and $\epsilon = 1.5$, (f) EC with $\alpha = 30^\circ$ and $\epsilon = 1.25$, (g) cone with $\alpha = 20^\circ$, (h) Cone with $\alpha = 30^\circ$ [AoA is the angle of attack, EC is elliptical cones, α is semi-apex angle and ϵ is the ellipse ratio]

Significant drop off in the pressure visible in the leeward side indicates the presence of flow separation.

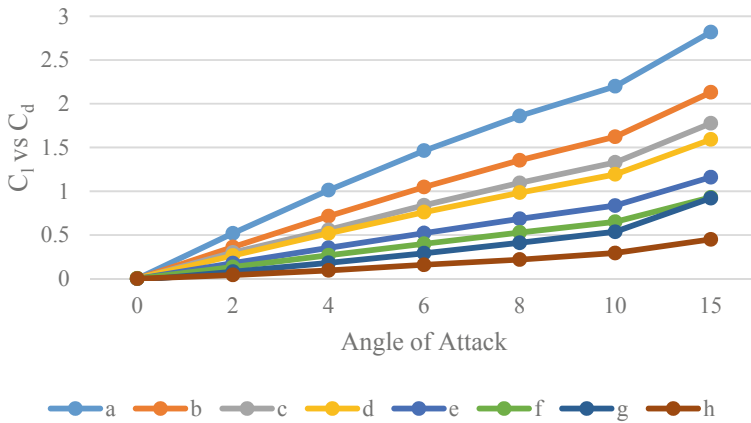


Fig. 3 C_L/C_D versus AoA where (a) EC with $\alpha = 20^\circ$ and $\epsilon = 2$, (b) EC with $\alpha = 20^\circ$ and $\epsilon = 1.5$, (c) EC with $\alpha = 20^\circ$ and $\epsilon = 1.25$, (d) EC with $\alpha = 30^\circ$ and $\epsilon = 2$, (e) EC with $\alpha = 30^\circ$ and $\epsilon = 1.5$, (f) EC with $\alpha = 30^\circ$ and $\epsilon = 1.25$, (g) Cone with $\alpha = 20^\circ$, (h) cone with $\alpha = 30^\circ$ [AoA is the angle of attack, EC is elliptical cones, α is semi-apex angle and ϵ is the ellipse ratio]

4 Conclusion

The aim of this report was to survey the pressure distribution along the surface of the elliptical cone, as well as understanding the behaviour of the drag and lift performance at different geometry configuration and understanding the effect on the flow characteristics, namely the lift and drag on increase in the angle of attack on the ellipse using analytical methods. Elliptical cones with ellipse ratios of 1.25, 1.5 and 2 were considered with the angle of attack increasing from 0° to 15° .

The aerodynamic efficiency of the elliptical cones was found to have significant improvement when compared to those of the circular cone at similar conditions and dimensions. The effect of the increase in the angle of attack on the flow characteristics was apparent as well, with improvements seen across the model dimensions. The slenderer elliptical cone was found to have the best performance, agreeing with the theory of slender body mechanics. One interesting effect of the upper-surface flow phenomenon on the elliptical cones observed was the difference in the rate at which drag changes with the lift.

While this report does not go into the temperature interaction of hypersonic flow, it is imperative to understand its effect on it nevertheless. The viscous interaction and the chemical disassociation are a very serious issue; one whose physics are yet to be deciphered in any predictable manner. If hypersonic vehicles are to be realised in the near future, this is a very important roadblock to overcome. Another challenge faced during the realisation of a credible validation for the above profiles is the lack of unified or accepted data availability, due to the cost incurred during such testing and the reluctance of researchers in larger corporations who do perform such testing in publishing the results.

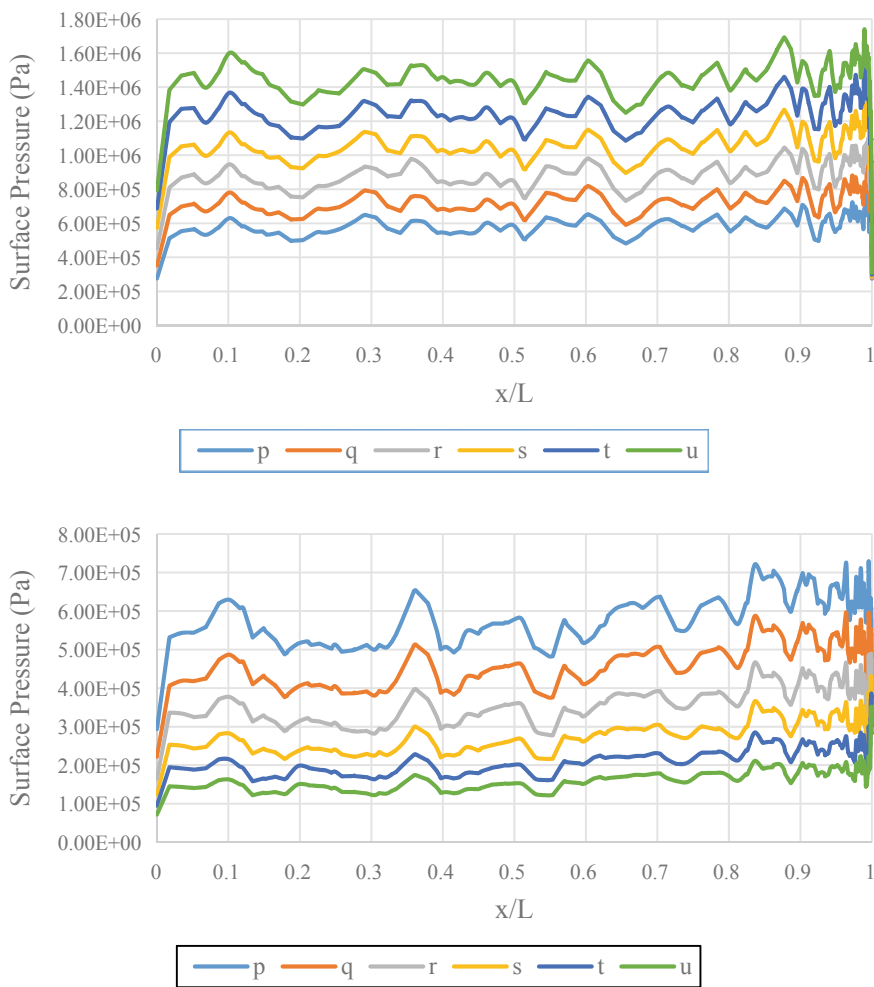


Fig. 4 Surface pressure distribution along (i) Windward Side (ii) Leeward Side where (p) EC with $\alpha = 20^\circ$ and $\varepsilon = 2$ (q) EC with $\alpha = 20^\circ$ and $\varepsilon = 1.5$ (r) EC with $\alpha = 20^\circ$ and $\varepsilon = 1.25$ (s) EC with $\alpha = 30^\circ$ and $\varepsilon = 2$ (t) EC with $\alpha = 30^\circ$ and $\varepsilon = 1.5$ (u) EC with $\alpha = 30^\circ$ and $\varepsilon = 1.25$ [EC is elliptical cones, α is semi-apex angle and ε is the ellipse ratio]

References

1. Fraenkel LE (1955) Supersonic flow past slender bodies of elliptic cross-section. HM Stationery Office
2. Ward GN (1949) Supersonic flow past slender pointed bodies. Q J Mech Appl Math 2(1):75–97
3. Lighthill MJ (1948) Q J Mech Appl Math 1(1):76–89
4. Van Dyke MD (1956) The slender elliptic cone as a model for non-linear supersonic flow theory. J Fluid Mech 1.1:1–15

5. Chapkis RL (1961) Hypersonic flow over an elliptic cone: theory and experiment. *J Aerosp Sci* 28(11):844–854
6. Ferri A (1951) The linearized characteristics method and its application to practical nonlinear supersonic problems. National Aeronautics and Space Administration, Hampton VA Langley Research Center
7. Kaattari GE (1970) A method for predicting pressures on elliptic cones at supersonic speeds. National Aeronautics and Space Administration, Hampton VA Langley Research Center
8. Jorgensen LH (1957) Elliptic cones alone and with wings at supersonic speeds. Ames Aeronautical Laboratory Moffett Field, California
9. Holden M (1972) Shock wave-turbulent boundary layer interaction in hypersonic flow. In: 15th aerospace sciences meeting. Los Angeles, p 45
10. Huntley M, Alexander S (2000) Transition studies on an elliptic cone in Mach 8 flow using filtered Rayleigh scattering. *Eur J Mech B/Fluids* 19.5:695–706
11. Gopala Krishnan G, Akhil, Nagaraja SR (2017) Drag reduction for hypersonic vehicles. *Int J Mech Eng Technol (IJMET)* 8(10):878–885
12. Sreekanth N, Akhil J, Nagaraja SR (2016) Design and analysis of secondary spike on blunt head. *Indian J Sci Technol* 9(45):1–8
13. Rajesh R, Rakesh SG (2020) Effect on the drag coefficient of various spiked cylinders during buzz phenomenon subjected to hypersonic flows. *J Brazil Soc Mech Sci Eng* 42(6). ISSN 1678-5878
14. Rajesh R, Rakesh SG (2018) Effect of dimensions of various spikes of a spiked cylinder on the buzz phenomenon subjected to hypersonic flows. *Int J Fluid Mech Res* 45(5):377–388
15. Anderson JD (2006) Hypersonic and high-temperature gas dynamics. American Institute of Aeronautics and Astronautics, Virginia
16. Spalart P, Allmaras S (1992) A one-equation turbulence model for aerodynamic flows. In: 30th aerospace sciences meeting and exhibit, Reno

Experimental and Theoretical Investigations of Support Structure Features and Build Time Management in PolyJet Technology



Arivazhagan Pugalendhi, Rajesh Ranganathan,
and Balamurugan Gopalakrishnan

Abstract Additive manufacturing (AM) is rapidly revolutionizing the many fields, especially in manufacturing and research. Comparing to the conventional manufacturing, it is a unique method of layer by layer manufacturing. One such technology is the PolyJet technology, which can print more accurate parts with superior surface finish even with complex geometries. Quality of the 3D printed part is influenced by support structures. Additional support structure affects the material consumption, build time, and process energy consumption. Currently, limited evidence is available about the effects of support structure and its optimization. Research in support structure gives a great leap in the future of AM. The aim of the paper is to study the features of support structure and build time calculation of Objet260 Connex printer. Rigid materials of VeroClear (VC), VeroWhite (VW), and flexible material of TangoPlus (T+) are grouped by two different Taguchi designs of experiments. Here, thickness of the samples, type of model material, printing modes, type of finish, and shape of the samples are considered as control factors. Evaluating the robustness of the design and finding the optimal combination of selected process parameters were accomplished by signal-to-noise (S/N) ratio analysis. Features of support structure include length, width, and height which is to be determined. Thereby, total printing time is derived from the mathematical formula and the values are compared with obtained values. Finally, a case study was carried out to validate the developed method. Results of the findings are useful to predict the build time of the PolyJet printed parts without using the Objet Studio software. These results would be valuable to practitioners and researchers who use the Objet printers. Describing the state of the art in support structures and reduction in support waste lead in making AM a more sustainable manufacturing system.

Keywords Additive manufacturing · PolyJet · Support structure · Design of experiments · Taguchi approach · Build time

A. Pugalendhi (✉) · R. Ranganathan · B. Gopalakrishnan
Department of Mechanical Engineering, Coimbatore Institute of Technology, Coimbatore, Tamil Nadu 641014, India

1 Introduction

Additive manufacturing (AM) technologies is one of the most promising manufacturing technologies to produce parts with zero-cost geometry flexibility. Capabilities of AM include, it is used in many industrial sectors for its design flexibility, decentralization of manufacturing process, integrated design, shorter lead time, flexibility in manufacturing, reduction of material waste, storage and transportation costs [1]. Presently, AM technologies are grouped into seven different categories such as vat photo polymerization, material extrusion, material jetting, binder jetting, directed energy deposition, powder bed fusion, and sheet lamination. The above-mentioned seven categories, except for sheet lamination technique, support structure is inevitable in all the technologies for printability, balancing, and thermal dissipation [2].

In AM, support structures are used to manufacture the overhanging geometries such as angled overhangs, bridging, bores, and channels successfully without any additional cost compared to conventional manufacturing techniques. Support structures reduce the efficiency of the material, process build time, increase process cost, post-processing equipment utilization time, surface quality, and oppose the near net shape manufacturing [3]. Reducing the need for support structures is controlled by optimal part orientation, support structures optimization, and redesigning the original part in terms of topology optimization [4]. Dimensional accuracy and surface roughness are affected by post-processing techniques such as tumbling, shot peening, hand finishing, spray painting, chemical treatment, and computer numerical control (CNC) machining. Dimensional accuracy of the acrylonitrile butadiene styrene (ABS) test pieces is improved while using the acetone bath immersion [5].

In directed energy deposition (DED) method, carbon steel sacrificial support is used to fabricate a stainless steel bridge and the metallic supports are removed by electrochemically etching without any machining operations [6]. In powder bed fusion (PBF), fabricated stainless steel utilizes dissolving supports, and then it is removed by using a sensitization process and etching process which minimizes the internal stresses and self-terminate, respectively [7].

Topology optimization is an uprising field for developing innovative 3D printed parts with soft and lightweight applications. This is without sacrificing the performance of the final part [8]. Topological optimization of internal patterns and supports reduces the volume of material as well as weight [9]. Level set method optimizes the shape and topology of supports, and Hadamard method optimizes both supports and its structure [10]. A MATLAB algorithm of cellular support structures unveils an increase in the efficiency of process: deliver time, material, and energy savings [11]. Dijkstra's shortest path algorithm generates the least cellular structure and minimizes the difficulties in supports removal from the 3D printed parts [12]. Discrete-marking fast generation algorithm is utilized for improving the efficiency of support calculations [13].

Effective print path planning is to decrease the consumption of support material, and it also reduces the finish surface deterioration for flat features by minimizing the post-processing efforts [14]. Skeleton-based path planning method reduces the material consumption as well as saves the build time by minimizes the filled volume of the final part with accounting the self-supporting capability and required minimum wall thickness [15]. Volume of support structures for a specified part orientation is determined by voxel-based algorithms. From this method, form errors of flatness and cylindricity were minimized by the optimal selection due to the reduction of support structures [16].

In recent work, Walker et al. reported about the study conducted on zero-support 3D printing of thermoset silicone by utilizing the transient material properties and determining the temperature boundaries and optimal time. Printing time of the extruded material is minimized due to increase in the number of cross-links. Weight of the recently deposited material affects the printed structure [17]. Reusable and easy to remove the novel support material was created by methylcellulose mixed in propylene glycol or butylene glycol. Measured surface tension, viscosity, and texture analysis of support material meet the properties of jetting-based AM processes [18]. Under direct ink writing (DIW) 3D printing, polyimine inks are capable to print five times recycled with superb printability [19]. In multi-axis AM (MAAM), free form models have better surface quality and offer efficient tool paths due to the elimination of support structures [20].

Required number of samples for study is limited by an orthogonal array (OA) of Taguchi method [21]. Total number of samples or trails and OA size is defined by a number of factors, the levels of each factor and interactions between the factors [22]. Systematic Taguchi approach is used in many manufacturing processes which are highly difficult to manufacture such as 3D printing or injection molding processes [23]. The Taguchi method optimizes the 3D printing parameters of screw-type extrusion (STE) process to accurately control ceramics [24]. Taguchi design of experiments (DOE) is utilized for parametric optimization of fused deposition modeling (FDM) process. Proposed methodology is used to calculate the significance of experimental error with the help of signal-to-noise (S/N) ratio and analysis of variance (ANOVA) [25]. Durão et al. utilized DOE to investigate and optimize manufacturing time, material consumption, and dimensional accuracy for FDM. Results of study reveal that quality of the FDMs that are 3D printed is highly influenced by print speed and number of contours [26].

This paper focuses on calculating the effect of build time by utilizing optimal support material consumption in PolyJet technology. PolyJet process selectively jets the photopolymer droplets onto a build platform, and then instant curing is performed by ultraviolet (UV) lamps [27]. In material jetting process, part orientation significantly affects the dimensional distortion [28]. PolyJet printed parts have the best ranking in surface quality but the greatest environmental impact and highest manufacturing cost than FDM and SLA [29]. Total cost of the AM part is calculated by build time, total energy consumption, and indirect costs. Additional support structure increases the build time, and it requires extra energy for creating the supports during

manufacturing and removing the supports from the final part during post-processing [30].

This research paper studies about the features of PolyJet support structures and predicts the total build time by using the total number of layers and height of the printed specimen. Three different model materials are printed in single material mode, and the number of samples is derived by two different DOE based on nature of material. Then, optimum combination is determined by signal-to-noise (S/N) ratio. These results are very useful for close packing of the parts and manufacturing the self-assembled products.

2 Materials and Methods

Objet260 Connex (Make: Stratasys) of PolyJet technology is used for this study. This machine is appropriate for numerous applications like varying the shore hardness, transparent applications, self-assembled products, and manufacture of multi-material parts with better accuracy. Size of build platform is $255 \times 252 \times 200$ mm; it offers 105 material combinations derived from 15 pure materials [31]. Model materials (actual material) and support materials (protect the model materials from collapsing) are deposited from print heads. It simultaneously jets the photocurable resins on to a build platform, where UV light solidifies the thin layer of the object. The steps are continued until the final layer of the job is completed. Here, print head moves in X -, Y -directions and build platform moves in Z -direction. Finished job is removed from build tray, following which in post-processing water jet removes the support materials [32–34]. Objet printer offers three grid styles of support material: standard, heavy, and lite. There are three printing modes which are available such as high-quality (16μ), high-speed (30μ), and digital-material (30μ). PolyJet printed parts have the surface finish of matte or glossy [35].

SolidWorks, Objet Studio, and Minitab softwares are used for this study. Design of the samples and STL file conversion are done in SolidWorks. Converted STL file is loaded in Objet Studio software to communicate with machine. Creation of support structure, part orientation, tool path generations, selection of surface finish, and printing modes are performed by Objet Studio. The machine predicts the material consumptions of both model and support materials, total printing time, and total number of layers required to complete the build operation.

Number of experiments/samples is derived by statistical method of Taguchi orthogonal array by using Minitab software. Each experiment was conducted three times randomly, and average response values are recorded. From this OA, analysis of signal-to-noise ratio (S/N) determines the significance of the individual parameters with their optimum combination of experiment. In this study, all the responses such as build time, height of the printed specimen, and number of layers should be minimum for reducing the manufacturing cost and faster production of 3D printed parts. Thereby, lower-the-better quality characteristic is estimated by using Eq. 1.

$$S/N = -10 \log \frac{1}{n} \sum_{i=1}^n y_i^2 \tag{1}$$

where y_i = measured data at the i th experiment; n = number of observation in an experiments.

Broadly used are three different model materials which are chosen for this study, namely VeroClear (VC), VeroWhite (VW), and TangoPlus (T+). Support material used for this study is FullCure 705. Initially, standard grid style is chosen for this study. Determination of appropriate test sample is itself a research of its own. VC and VW samples of square and circular profile are printed in high-quality (HQ) and high-speed (HS) of single material mode with varying thickness (1, 3, 6, and 9 mm). The entire samples are printed in both glossy and matte finish. So, L_8 orthogonal array results that eight different samples are printed in different combinations for both rigid materials, and it is referred as a first DOE. Correspondingly, T+ samples are printed in HS and digital-material (DM) mode of single material mode. Practically, HQ printing mode is not applicable for T+ material. So, different L_8 orthogonal array is used for flexible T+ material and it is referred as second DOE. Table 1 displays the levels of process parameters of first DOE ($4^1 1, 2^4$) and second DOE ($4^1 1, 2^3$).

Figure 1 illustrates the profile and dimensions of test samples which are used for this study. In glossy finish, top surface of the samples is free from support. But in matte finish, printed sample is fully immersed in support material. Support structure dimensions of the glossy finished square samples are obtained by following equations,

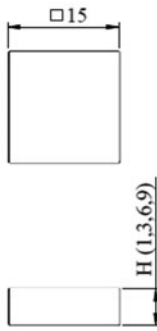
$$L_{sg} = (L_g - L)/2 \tag{2}$$

$$B_{sg} = (B_g - B)/2 \tag{3}$$

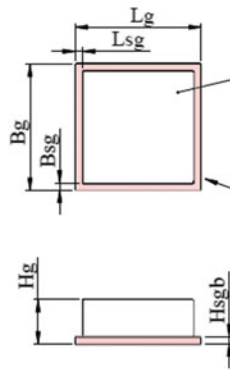
Table 1 Process parameters and its levels for first and second DOE

DOE	Control factor	Symbol	Unit	Level 1	Level 2	Level 3	Level 4
First	Thickness	<i>A</i>	mm	1	3	6	9
	Material	<i>B</i>	–	VeroClear	VeroWhite	–	–
	Printing mode	<i>C</i>	–	High-quality	High-speed	–	–
	Finish type	<i>D</i>	–	Matte	Glossy	–	–
	Shape	<i>E</i>	–	Square	Circle	–	–
Second	Thickness	<i>A</i>	mm	1	3	6	9
	Material	<i>B</i>	–	TangoPlus	–	–	–
	Printing mode	<i>C</i>	–	High-speed	Digital-material	–	–
	Finish type	<i>D</i>	–	Matte	Glossy	–	–
	Shape	<i>E</i>	–	Square	Circle	–	–

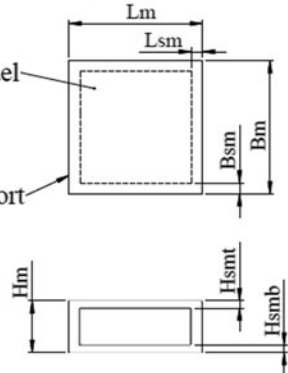
Sample 1 Dimensions



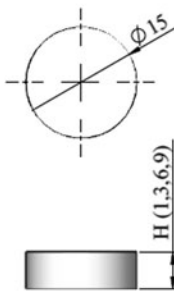
Glossy Finish



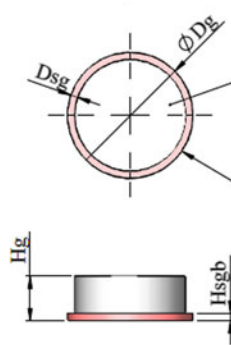
Matte Finish



Sample 2 Dimensions



Glossy Finish



Matte Finish

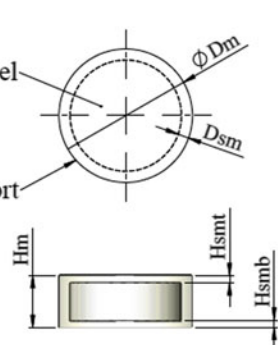


Fig. 1 Dimensions of samples and supports with different finishes

$$H_{sg} = (H_g - H) \tag{4}$$

where L_g —Total length of the sample in glossy finish, L_{sg} —Length of the support in glossy finish, B_g —Total breadth of the sample in glossy finish, B_{sg} —Breadth of the support in glossy finish, H_g —Total height of the sample in glossy finish, H_{sgb} —Height of the support in glossy finish.

Length, breadth, and height of the samples are represented in L , B , and H . Similarly, L_m , B_m , and H_m indicate the length, breadth, and height of the matte finished samples, respectively. L_{sm} and B_{sm} are length and breadth of the support in matte finish which is calculated by Eqs. 2 and 3. H_{smt} is a height of the top support, and H_{smb} is a height of the bottom support.

$$H_{sm} = (H_m - (H_{smt} + H_{smb})) \tag{5}$$

Here, H_{smb} is equal to H_{sgb} . Now, the H_{smt} is calculated by,

$$H_{\text{smt}} = H_{\text{sm}} - H_{\text{smb}} \quad (6)$$

The dimensions of PolyJet printed samples with support and without support are measured by digital Vernier caliper. Mitutoyo's Digimatic Caliper having the range of 0–300 mm is used to measure the 3D printed samples. Total number of layers (T_{Layer}) required to complete the job is calculated by below equation.

$$T_{\text{Layer}} = H_{\text{Job}}/t \quad (7)$$

where H_{Job} = Total job height, t = layer thickness or thickness of single layer.

Total build time (T_{Build}) is calculated by following equation, [36]

$$T_{\text{Build}} = T_{\text{Job}} + (\alpha_1 \times T_{\text{Layer}}) \times O \quad (8)$$

where T_{Job} = Machine warm up time, α_1 = Time consumed for the completion of each layer, O = Number of print head offsets in Y -direction.

In Objet260 Connex, print head offsets maximum 5 times in Y -direction based on the dimension and orientation of the job. For example, dimension of job is $150 \times 50 \times 1$ mm and the job is oriented in YX -direction revealing, print head will offset 3 times in Y -direction to complete the single layer. Material usage efficiency (η) or yield can be calculated as the proportion of mass of the deposited material (M_d) (i.e., total mass of job with support material) to mass of the job (M_j) [36]. Mass of samples is measured by durable and accurate electronic scale of JS-100xV having the $100 \text{ g} \times 0.1 \text{ g}$.

$$\eta = M_d/M_j \quad (9)$$

3 Results and Discussion

Objet printers need extra support materials to protect the actual material and improve the quality of 3D printed parts. Bottom support layer is mandatory to prevent the damage of the job during the removal of job from build platform in any type of printing mode and finish type. Bonding between the bottom support layer and build platform is stronger in flexible material compared to rigid materials. Thereby, flexible materials need extra care for removal of the job from build platform and measuring the dimensions. In matte finish, top surface of job is also covered by support materials. This is to achieve uniform surface finish and improved quality of the part. Top support layer depends on type of model material to be used. Difference between the matte finish and glossy finish in terms of support material is shown in Fig. 2.

Orthogonal array (L_8) for first DoE and its printing details are displayed in Table 2. Required printing time of all combinations and its height of the printed specimen, number of layers in Objet Studio are discussed. Here, all the readings are taken from

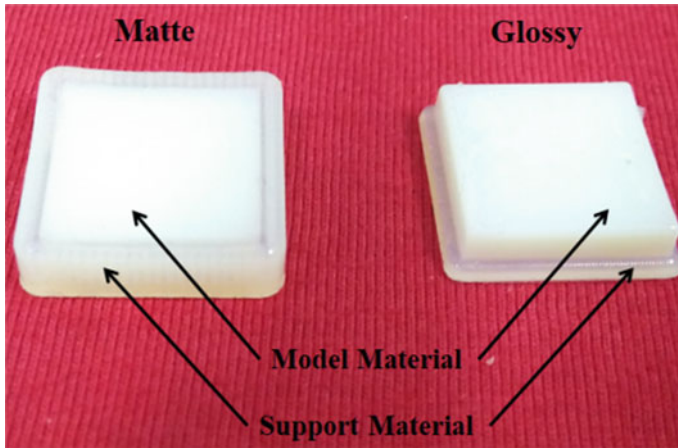


Fig. 2 Matte and glossy finished VeroWhite samples with supports

Table 2 Orthogonal array (L_8) for first DoE and its printing details

Experiment	Control factors					Build time (min)	Height of the printed specimen in Objet (mm)	Number of layers in Objet
	A	B	C	D	E			
a	1	1	1	1	1	15.14	3.69	223
b	1	2	2	2	2	8.30	2.05	69
c	2	1	1	2	2	14.38	4.05	245
d	2	2	2	1	1	9.46	4.36	146
e	3	1	2	1	2	20.53	10.06	336
f	3	2	1	2	1	27.27	7.05	427
g	4	1	2	2	1	20.15	10.07	336
h	4	2	1	1	2	35.47	10.22	619

job manager window after completing the job. Because tray setting readings differ from job manager readings, it gives only the estimated value. Similarly, orthogonal array (L_8) for second DoE and its printing details are displayed in Table 3.

Using the values from Tables 2 and 3, layer thickness was calculated by utilizing Eq. 7, and with reference to Objet Studio machine window. Here, layer thickness of the HQ mode is 16.5μ instead of 16μ . This small fractional value created major difference in larger components. Layer thickness of HS and DM mode value of 30μ perfectly match with calculations. Dimensions of supports for selected materials are calculated by Eqs. 2–6. The obtained dimensions of supports are displayed in Table 4.

Table 4 values are very useful for close packing of multiple jobs printed in a single print. Number of layers is the main factor to calculate total build time. Time

Table 3 Orthogonal array (L_8) for second DoE and its printing details

Experiment	Control Factors				Build time (min)	Height of the printed specimen in Objet (mm)	Number of layers in Objet
	A	C	D	E			
i	1	1	1	1	5.57	2.35	79
j	1	2	2	2	5.24	2.05	69
k	2	1	1	2	11.10	4.36	146
l	2	2	2	1	9.05	4.06	136
m	3	1	2	1	14.43	7.06	236
n	3	2	1	2	15.03	7.36	246
o	4	1	2	2	20.09	10.07	336
p	4	2	1	1	24.42	10.37	346

Table 4 Dimensions of supports

S. No.	Description	Dimensions of supports (mm)					
		VeroClear		VeroWhite		TangoPlus	
		HQ	HS	HQ	HS	HS	DM
1	L_{sg}	1.00	1.00	1.00	1.00	1.00	1.00
2	B_{sg}	1.00	1.00	1.00	1.00	1.00	1.00
3	H_{sgb}	1.05	1.05	1.05	1.05	1.05	1.05
4	D_{sg}	1.00	1.00	1.00	1.00	1.00	1.00
5	L_{sm}	1.65	1.65	1.65	1.65	1.65	1.65
6	B_{sm}	1.65	1.65	1.65	1.65	1.65	1.65
7	H_{smb}	1.05	1.05	1.05	1.05	1.05	1.05
8	H_{smt}	1.65	3.00	0.16	0.30	0.30	0.30

study is conducted during job printing to determine the machine warm up (T_{Job}) time and required time to complete a single layer (α_1). This time study reveals that the warm up time of the machine depends upon the temperature of print heads and tray temperature. So, warm up time of initial printing only takes longer time than upcoming instant printing. It takes maximum 4.5 min for initial printing from 30 °C of print heads, and it takes maximum 2.0 min for immediate printing while the print heads are in 65–66 °C.

By observation through this study, Objet260 machine takes 4.5 min for warming up the machine and time required for completion of single layer is 3.3 s. After completing the final layer, machine takes an additional of 17–19 s for final scanning and curing the job. Weight of the samples with support material and without support material is recorded by using weighing scale. Figure 3 illustrates the PolyJet printed samples with support material and without support material.

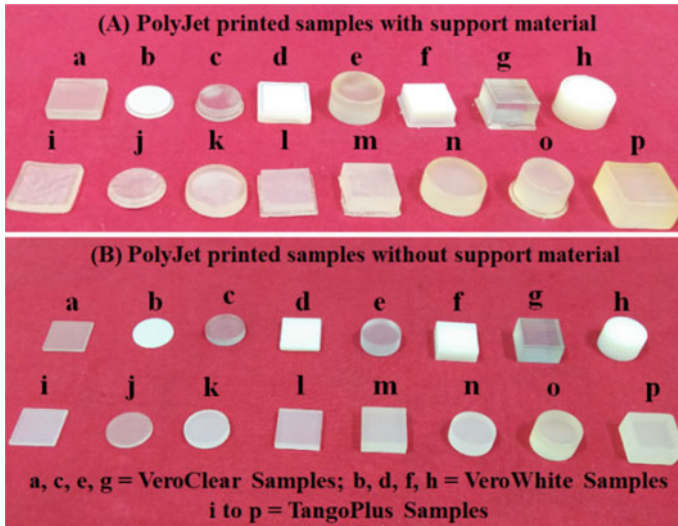


Fig. 3 PolyJet printed samples

Table 5 Percentage of deviation in build time and yield

Sample Name	Build time in objet studio (min)	Calculated build time (min)	Percentage of deviation (%)	Mass of the job with support material (g)	Mass of the job without support material (g)	Yield (%)
a	15.14	14.16	6.79	1.50	0.27	18.00
b	8.30	8.18	2.47	0.47	0.22	46.81
c	14.38	15.29	5.44	0.93	0.62	66.67
d	9.46	10.02	2.63	1.69	0.82	48.52
e	20.53	20.29	1.97	3.06	1.26	41.18
f	27.27	25.29	7.71	1.97	1.58	80.20
g	20.15	20.29	1.12	2.74	2.38	86.86
h	35.47	36.03	0.73	3.18	1.89	59.43
i	5.57	6.21	6.23	0.96	0.27	28.13
j	5.24	5.48	6.82	0.52	0.22	42.31
k	11.10	10.02	11.33	1.37	0.61	44.53
l	9.05	9.29	4.18	1.17	0.79	67.52
m	14.43	14.59	1.76	1.90	1.53	80.53
n	15.03	15.32	3.09	2.18	1.19	54.59
o	20.09	20.29	1.61	2.07	1.79	86.47
p	24.42	23.32	4.97	3.88	2.23	57.47

Percentage of deviation in build time and material yield is populated in Table 5. Except sample b and p, all samples are printed instantly. While printing the samples of a, c, and k, print heads take some time to refresh the print heads and the times are 156 s, 94 s, and 95 s, respectively. Except sample k, all the sample values are very similar to software values, with below 8% deviations. Percentage of build time deviation for the sample k is 11.33%. Yield of the matte finish samples is lower than that of glossy finished samples. Matte finished VC sample 'a' has the lowest yield (18%) than others while printed in HQ mode. Similarly, glossy finished VC sample 'g' has the highest yield (86.86%) than others while printed in HS mode. Despite that, surface finish of matte finished sample is uniform throughout the job than glossy finished samples. This is because, top surface of the glossy finished sample is free from the supports and it is different from other portions of the job.

Analysis of signal-to-noise ratio is performed on first and second DOE to determine the optimum combination and significance of the each parameter of the experiment. *S/N* response table for build time of first and second DOE is populated in Table 6. From this table, thickness of the sample is of major significance on build time for the first and second DOE. Similarly, there is no significant effect in shape of the sample on build time. *S/N* response table for the height of the printed specimen and number of layers for the first and second DOE are populated in Tables 7 and 8, respectively. Results of the analysis reveal that, thickness of the sample is of major significance on height of the printed specimen and number of layers for first and second DOE. Printing mode and shape of the sample are the least significant parameter on height of the printed specimen for first and second DOE, respectively. Similarly, there is no significant effect in shape of the sample on number of layers for first and second DOE.

All the analysis results reveal that, second DOE has similar ranking order of thickness, finish type, printing mode, and shape for all responses. For first DOE, ranking order of the responses of build time and number of layer is thickness, printing mode, finish type, material, and shape. Ranking order of the response for height of the printed specimen is thickness, finish type, material, shape, and printing mode. The optimum conditions of input parameters for first and second DOE were identified and are given in Table 9. From this table, glossy finished 1 mm thick VW circular sample printed in HS mode is optimum for first DOE. Similarly, glossy finished 1mm thick circular sample printed in DM mode is optimum for second DOE.

Build time is significantly affected by dimension of the object in Z-axis. Owing to back and forth movement of the print heads in X-axis, it requires shorter build time when compared to Y- and Z-axes. Print heads measure about 50 mm on the Y-axis, models measure less than this which are printed in one pass. Thereby, placing the object's smallest dimension along the Z-axis, largest dimension along the X-axis and intermediate dimension along the Y-axis is advisable. This study is very useful for predicting the build time of the 3D printed part without using the Objet Studio software. These results are beneficial for researchers and practitioners of Objet printers to reduce the supports in terms of nesting and optimal selection of printing parameters. All the results are helpful for generating the algorithms such as topology optimization, support structure generation, and optimization in build orientation.

Table 6 S/N response table for the build time for first DOE and second DOE

S. No.	First DoE					Second DoE				
	Level 1	Level 2	Level 3	Level 4	Rank	Level 1	Level 2	Level 3	Level 4	Rank
A	- 20.99	- 21.34	- 27.48	- 28.54	1	- 14.65	- 20.02	- 23.36	- 26.91	1
B	- 24.77	- 24.40	-	-	4	-	-	-	-	-
C	- 26.62	- 22.56	-	-	2	- 21.27	- 21.20	-	-	3
D	- 25.09	- 24.08	-	-	3	- 21.78	- 20.69	-	-	2
E	- 24.48	- 24.70	-	-	5	- 21.25	- 21.22	-	-	4

Table 7 *S/N* response table for the height of the specimen in Objet Studio for first DOE and second DOE

S. No.	First DoE				Second DoE					
	Level 1	Level 2	Level 3	Level 4	Rank	Level 1	Level 2	Level 3	Level 4	Rank
<i>A</i>	- 8.78	- 12.46	- 18.50	- 20.12	1	- 6.82	- 12.48	- 17.15	- 20.18	1
<i>B</i>	- 15.90	- 14.04	-	-	3	-	-	-	-	-
<i>C</i>	- 15.16	- 14.78	-	-	5	- 14.31	- 14.01	-	-	3
<i>D</i>	- 16.09	- 13.85	-	-	2	- 14.46	- 13.86	-	-	2
<i>E</i>	- 15.28	- 14.65	-	-	4	- 14.22	- 14.10	-	-	4

Table 8 S/N response table for the number of layers in objet studio for first DOE and second DOE

S. No.	First DoE					Second DoE				
	Level 1	Level 2	Level 3	Level 4	Rank	Level 1	Level 2	Level 3	Level 4	Rank
A	- 41.87	- 45.54	- 51.57	- 53.18	1	- 37.36	- 42.98	- 47.64	- 50.65	1
B	- 48.95	- 47.13	-	-	4	-	-	-	-	-
C	- 50.80	- 45.28	-	-	2	- 44.81	- 44.51	-	-	3
D	- 49.15	- 46.92	-	-	3	- 44.96	- 44.36	-	-	2
E	- 48.35	- 47.73	-	-	5	- 44.72	- 44.60	-	-	4

Table 9 Optimum values of first DOE and second DOE

Response	First DOE					Second DOE				
	Thickness	Material	Printing mode	Finish	Shape	Thickness	Printing mode	Finish	Shape	
Build time	A1	B2	C2	D2	E1	A1	C2	D2	E2	
Height of the printed specimen	A1	B2	C2	D2	E2	A1	C2	D2	E2	
Number of layers	A1	B2	C2	D2	E2	A1	C2	D2	E2	

4 Case Study

Developed method is validated using a case example. In this case, job of grooved cover is printed in Objet260 printer. Grooved cover acts as a coupling and prevents the leaks from water. The final job is assembled with other components and the prototype for proving the design concepts. Dimensions of the grooved cover are $100 \times 100 \times 32.4$ mm. For this application, VW material is used for making the glossy finished prototype and printed in HS mode. Job is placed in flat XY orientation in build platform, and smallest dimension of the job is placed in Z-axis. Figure 4 illustrates the PolyJet printed grooved cover prototype in build platform.

Before loading the STL file into the Objet Studio software, following steps are carried out to predict the manual build time of the job without using Objet Studio software.

Step 1: Calculate the job height by using Eq. 4. i.e., $(H_{Job} = 32.4 + 1.06 = 33.46$ mm).

Step 2: Required total number of layer is calculated by using Eq. 7. $(T_{Layer} = 33.46/0.03 = 1116$ no's).

Step 3: Finally, build time is calculated by using Eq. 8. $(T_{Build} = 4.5 + (1116 \times 3.3) \times 2 = 127.25$ min).

Once the printing is completed, semifinished grooved cover is sent for post processing to clean the support materials. Prototype consumes 33 g of VW, 5 g of support material, and it takes 118 min to build the job. Yield of grooved model is 90.68%, and difference between the calculated values and actual values is displayed in Table 10. Developed method is 7.26% which deviates from actual values.

Fig. 4 PolyJet printed grooved cover on build tray

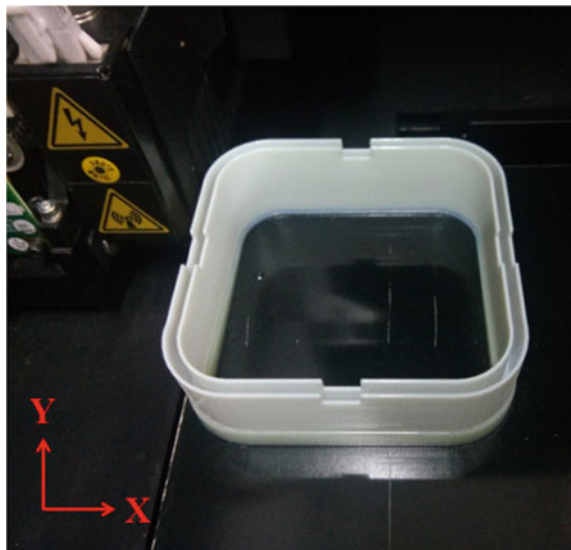


Table 10 Difference between calculated and actual values

S. No.	Description	Calculated values	Actual values	Percentage of deviation
1	H_{Job} (mm)	33.46	33.51	0.149432
2	T_{Layer} (no's)	1116	1118	0.179211
3	T_{Build} (min)	127.25	118	7.26916

5 Conclusion

In this study, the features of support structure and build time calculations of Objet260 printer were identified. The number of experiments required for calculating the responses was conducted using Taguchi orthogonal array which leads to minimize the production cost and time. Significance of input parameters was also identified through S/N ratio value. Initially, small size samples are printed in single material mode by using VC, VW, and T+ materials. Matte finished VC samples have the highest top support layer and build time than other samples. Especially, in HS mode of matte finished VC samples has 3.00 mm of top support layer, whereas HQ matte finished VC samples has the 1.65 mm of top support layer. Layer thickness of the HQ mode is 16.5 μ instead of 16 μ .

In addition, time required for completion of single layer of all sample is 3.3 s and observed machine warm up time is 4.5 min. Difference between the calculated build time and Objet Studio is below 7.3%. Matte finished VC sample has the lowest yield of 18%, and glossy finished VC sample has the highest yield of 86.86%. Research was also validated by appropriately selected case study. Through this work, support materials and its build time will vary depending upon the type of model material and its finish type. All the results gave a clear understanding for nesting of multiple components and prediction of the total build time by mathematical calculations. This optimal selection is also used in the development of optimized algorithm for support materials. Further, this study could be extended to other available materials in PolyJet machine with larger samples and multiple parts printed in a single print. DM mode also can be evaluated in other PolyJet materials. Similarly, material consumption and cost factors can also be added in calculation to predict before printing and to develop a new optimized algorithm for Objet printers.

Acknowledgements Thanks to the Centre of Excellence in Manufacturing Sciences (CoEMS), Coimbatore Institute of Technology, Coimbatore, India, where the sample/R&D work is carried out.

References

1. Uz Zaman UK, Rivette M, Siadat A, Mousavi SM (2018) Integrated product-process design: material and manufacturing process selection for additive manufacturing using multi-criteria decision making. *Robot Comput Integr Manuf* 51:169–180

2. Culmone C, Smit G, Breedveld P (2019) Additive manufacturing of medical instruments: a state-of-the-art review. *Addit Manuf* 27:461–473
3. Bikas H, Lianos AK, Stavropoulos P (2019) A design framework for additive manufacturing. *Int J Adv Manuf Technol* 103(9–12):3769–3783
4. Jiang J, Xu X, Stringer J (2018) Support structures for additive manufacturing: a review. *J Manuf Mater Process* 2(4):64
5. Nsengimana J, Van der Walt J, Pei E, Miah M (2019) Effect of post-processing on the dimensional accuracy of small plastic additive manufactured parts. *Rapid Prototyping J* 25(1):1–12
6. Hildreth OJ, Nassar AR, Chasse KR, Simpson TW (2016) Dissolvable metal supports for 3D direct metal printing. *3D Print Additive Manuf* 3(2):90–97
7. Lefky CS, Zucker B, Wright D, Nassar AR, Simpson TW, Hildreth OJ (2017) Dissolvable supports in powder bed fusion-printed stainless steel. *3D Print Additive Manuf* 4(1):3–11
8. Zhang H, Kumar AS, Fuh JYH, Wang MY (2018) Design and development of a topology-optimized three-dimensional printed soft gripper. *Soft Rob* 5(5):650–661
9. Gardan N, Schneider A (2015) Topological optimization of internal patterns and support in additive manufacturing. *J Manuf Syst* 37:417–425
10. Allaire G, Bogosel B (2018) Optimizing supports for additive manufacturing. *Struct Multidiscip Optim* 58(6):2493–2515
11. Strano G, Hao L, Everson RM, Evans KE (2013) A new approach to the design and optimisation of support structures in additive manufacturing. *Int J Adv Manuf Technol* 66(9–12):1247–1254
12. Vaidya R, Anand S (2016) Optimum support structure generation for additive manufacturing using unit cell structures and support removal constraint. *Procedia Manuf* 5:1043–1059
13. Bo Q, Lichao Z, Yusheng S, Guocheng L (2011) Support fast generation algorithm based on discrete-marking in stereolithography rapid prototyping. *Rapid Prototyping J* 17(6):451–457
14. Jiang J, Stringer J, Xu X (2019) Support optimization for flat features via path planning in additive manufacturing. *3D Print Additive Manuf* 6(3):171–179
15. Jin Y, Du J, He Y (2017) Optimization of process planning for reducing material consumption in additive manufacturing. *J Manuf Syst* 44:65–78
16. Paul R, Anand S (2015) Optimization of layered manufacturing process for reducing form errors with minimal support structures. *J Manuf Syst* 36:231–243
17. Walker S, Daalkhajav U, Thrush D, Branyan C, Yirmibesoglu OD, Olson G, Menguc Y (2019) Zero-support 3D printing of thermoset silicone via simultaneous control of both reaction kinetics and transient rheology. *3D Print Additive Manuf* 6(3):139–147
18. Fahad M, Dickens P, Gilbert M (2013) Novel polymeric support materials for jetting based additive manufacturing processes. *Rapid Prototyping J* 19(4):230–239
19. He X, Lei Z, Zhang W, Yu K (2019) Recyclable 3D printing of polyimine-based covalent adaptable network polymers. *3D Print Additive Manuf* 6(1):31–39
20. Isa MA, Lazoglu I (2019) Five-axis additive manufacturing of freeform models through buildup of transition layers. *J Manuf Syst* 50:69–80
21. Hodder KJ, Chalaturnyk RJ (2019) Bridging additive manufacturing and sand casting: utilizing foundry sand. *Addit Manuf* 28:649–660
22. Papazetis G, Vosniakos GC (2019) Mapping of deposition-stable and defect-free additive manufacturing via material extrusion from minimal experiments. *Int J Adv Manuf Technol* 100(9):2207–2219
23. Chen JC, Cox J (2017) Taguchi-based optimization of surface roughness and dimensional accuracy in wire EDM process with S7 heat treated steel. *World Acad Sci Eng Technol Int J Chem Mol Nucl Mater Metall Eng* 11(8):551–556
24. Kim NP, Cho D, Zielewski M (2019) Optimization of 3D printing parameters of screw type extrusion (STE) for ceramics using the Taguchi method. *Ceram Int* 45(2):2351–2360
25. uz Zaman UK, Boesch E, Siadat A, Rivette M, Baqai AA (2019) Impact of fused deposition modeling (FDM) process parameters on strength of built parts using Taguchi's design of experiments. *Int J Adv Manuf Technol* 101(5–8):1215–1226

26. Durão LFC, Barkoczy R, Zancul E, Ho LL, Bonnard R (2019) Optimizing additive manufacturing parameters for the fused deposition modeling technology using a design of experiments. *Prog Additive Manuf* 4(3):291–313
27. Kampker A, Kreisköther K, Reinders C (2017) Material and parameter analysis of the PolyJet process for mold making using design of experiments. *Int J Mater Metal Eng* 11(3):242–249
28. Khoshkhoo A, Carrano AL, Blersch DM (2019) Effect of build orientation and part thickness on dimensional distortion in material jetting processes. *Rapid Prototyping J* 24(9):1563–1571
29. Li Y, Linke BS, Voet H, Falk B, Schmitt R, Lam M (2017) Cost, sustainability and surface roughness quality—a comprehensive analysis of products made with personal 3D printers. *CIRP J Manuf Sci Technol* 16:1–11
30. Baumers M, Wildman R, Tuck C, Dickens P, Hague R (2015) Modeling build time, process energy consumption and cost of material jetting-based Additive Manufacturing. In: *NIP and digital fabrication conference*, vol 2015, No 1. Society for Imaging Science and Technology, pp 311–316
31. Palanisamy M, Pugalendhi A, Ranganathan R (2020) Selection of suitable additive manufacturing machine and materials through best–worst method (BWM). *Int J Adv Manuf Technol* 1–18
32. Espera AH, Dizon JRC, Chen Q, Advincula RC (2019) 3D-printing and advanced manufacturing for electronics. *Prog Additive Manuf* 1–23
33. Touri M, Kabirian F, Saadati M, Ramakrishna S, Mozafari M (2019) Additive manufacturing of biomaterials—the evolution of rapid prototyping. *Adv Eng Mater* 21(2):1800511
34. Singh R (2011) Process capability study of polyjet printing for plastic components. *J Mech Sci Technol* 25(4):1011–1015
35. Reichl KK, Inman DJ (2018) Dynamic mechanical and thermal analyses of object connex 3D printed materials. *Exp Tech* 42(1):19–25
36. Demir AG (2018) Micro laser metal wire deposition for additive manufacturing of thin-walled structures. *Opt Lasers Eng* 100:9–17

Fluid Flow Analysis of a Rotating Vaneless Diffuser Using CFD



Gnanadurai Ravikumar Solomon, R. Rahul, R. Balaji, and Ashish Selokar

Abstract The main aim of the work is to analyze the losses of the fluid flow in a stationary vaneless diffuser. This involves with the computational procedure to investigate the flow at the exit of a centrifugal impeller and flow through the diffuser by applying various turbulence models. Single-bladed fluid domain has been modeled in ANSYS ICEM CFD and meshed tetrahedral accompanied with prism mesh for capturing the viscous effect near the walls. The meshed model was exported to ANSYS CFX for simulation process, and results were generated for various turbulence models corresponding to various flow parameter and the boundary conditions to the code. The various boundary conditions used are inlet, outlet, wall, periodic, no-slip condition along the walls. The cases had been run for turbulence models like $k-\varepsilon$, $k-\omega$ and SST. It has been found that turbulence model $k-\omega$ shows the least deviation from the experimental data. Grid independency study has been done for 3 different meshes, i.e., 6 lakhs, 8 lakhs and 9 lakhs, and it was found that the results are independent of the mesh. Further, all the cases were run for the $k-\omega$ turbulence model. Here, basic model is modified by extending the shroud for two different cases RVD 10 and RVD 40. Simulation has been done, and contours are plotted for both the cases. It has been found that there is considerable improvement in the desired parameters for the cases RVD 10 but RVD 40 has shown improvement for some of the desired parameters.

Keywords Fluid flow · Vaneless diffuser · ANSYS · Centrifugal impeller

G. R. Solomon · R. Rahul · R. Balaji

Department of Mechanical Engineering, Hindustan Institute of Technology and Science, Chennai 603103, India

e-mail: sridharabala@gmail.com; rksolomon@hindustanuniv.ac.in

A. Selokar (✉)

Department of Physics, Desaiganj (Wadsa), Mohsinbhai Zaweri Mahavidyalaya, Maharashtra 441207, India

© The Author(s), under exclusive license to Springer Nature Singapore Pte Ltd. 2022

1121

K. Govindan et al. (eds.), *Advances in Mechanical and Materials Technology*,

Lecture Notes in Mechanical Engineering,

https://doi.org/10.1007/978-981-16-2794-1_97

1 Introduction

Centrifugal blowers otherwise called radial blowers are a subclass of dynamic axisymmetric work-absorbing turbomachinery. The proficiency of this machinery relies upon flow in impeller and misfortunes in diffuser [1]. The exhibition of the centrifugal blower relies upon the individual execution of its segments. Two-thirds of the all-out vitality misfortunes in a centrifugal blower happens in the diffuser [2]. It is important to create strategies that diminish the vitality misfortunes related to diffusion and likewise increment in the stable working scopes of diffusion frameworks [3]. The velocity of the liquid is changed over to pressure, incompletely in the impeller and mostly in the stationary diffuser. The greater part of the velocity leaving the impeller is changed over into pressure vitality in the diffuser. A large portion of the pressure rise happens in the impeller and the rest in the diffuser [4]. The diffuser comprises basically vanes, which are extraneous to the impeller. These vane entries separate to change over the velocity head into pressure energy. Rotating vaneless diffusers are of two sorts: free and forced [5]. Free-rotating diffusers are segregated substance and turn at a modest quantity of the impeller speed by using a sensible course of action, while forced rotating diffusers are fundamental with the impeller and rotate at a comparative speed as that of impeller. In free-rotating vaneless diffuser, the dividers of the vaneless territory were turned self-governing of the impeller. The diffuser speed transforms into a modest quantity of the impeller speed, so the shear powers between the flow and diffuser divider are inconceivably reduced [6]. Thus, the breaking point layer advancement inside the rotating diffuser is more diminutive than in looking at stationary diffuser, and the blower execution improves from both frictional and flow profile contemplations [7]. In the work, a numerical approach is used to investigate the losses associated with diffuser and to minimize these losses using varying diffuser geometry by extending the shroud (10% and 40%) and making a rotating passage. The numerical approach used to solve the problem considered different diffuser configurations, and optimum configuration will be validated with the reference in earlier research data.

Rodgers and Mnew observed that the Diffuser execution under braked and free-rotating conditions at section Mach numbers up to upto unity. Huge improvement in diffuser execution was accomplished under free-rotating conditions despite the fact that the enormous wakes were produced by upstream stationary whirl spouts [8]. By and large, static pressure recuperation for the total diffusion framework expanded roughly 20% at free-rotating conditions relating to a distracting velocity proportion (diffuser rotor/occurrence stream) of 0.43. This was ascribed to the limit layer development inside the stationary diffuser, and the blower execution improved from both frictional and flow profile considerations. Harold and Schenectady explored the improvement in the effectiveness of the blower by the utilization of rotating vaneless diffuser [9]. The high-velocity spillage flow getting away digressively through the freedom space between the impeller and rotating diffuser was used to control a turbine. Anish and Sitaram concentrated numerically on the impact of the outspread

Table 1 Geometrical details

Diameter at impeller inlet D_i	180 mm
Diameter at impeller exit D_o	550 mm
The ratio of inlet to diameter to the exit diameter	0.3272
Width at exit b_2	50 mm
Width at inlet b_1	50 mm
Inlet blade angle β_1	40°
Outlet blade angle β_2	78°
Speed of rotation n	1800 rpm
No. of blades Z	24

hole between the impeller and diffuser on the presentation and flow field of a low-speed centrifugal blower stage. It was seen that the stable working reach and the measure of pressure rise were intensely reliant on the sort of diffusers utilized in the centrifugal compressors [10]. Ozturk et al. investigated the flow through the vaneless diffuser in low-speed backswept centrifugal blower utilizing finite volume method (FVM). Flow field at diffuser section plainly indicated the impeller jet-wake flow design and the cutting-edge wake [11]. Entry wake was situated on the cover side of the diffuser and blends out gradually as the flow travels through a diffuser.

1.1 Model Description and Computational Method

The impeller blade was modeled in ANSYS ICEM CFD software by adopting the point-by-point method. Compressor has 24 backward curved blades followed by vaneless diffuser. The geometrical details of the impeller are given in Table 1. Initially, the blade of the impeller is designed as per the data available in Table 1. The impeller blade is modeled in ANSYS ICEM CFD software by using point-by-point method which is shown in Table 2 (Fig. 1).

1.2 Mesh Details

The fluid domain is modeled on either side of the blade. The dimensions of the fluid domain at the inlet part are about half of the chord length of the blade. And the dimensions of the fluid domain at outlet part are one-fourth of the chord length of the blade. Unstructured tetrahedral mesh is used to mesh the fluid model in ICEM CFG with prism mesh near the wall (Table 3).

Single-bladed meshed fluid domain with prism mesh on the wall portions is shown in Fig. 2. Once the mesh is generated, the fluid domain is imported to ANSYS CFX-Pre where boundary conditions and flow parameters are applied for various

Table 2 Point-by-point method

S. no.	r (m)	B	β (rad)	$\tan \beta$	$(r \tan \beta)$	$(r \tan \beta)$ avg	$dr/(r \tan \beta)$ avg	$\Delta\theta$ (rad)	$\Delta\theta^\circ$	θ (in degrees)
1	0.09	40	0.698	0.839	0.076	0.085	0.145611765	0.14459554	8.28	0
2	0.10233	42.53	0.742	0.917	0.094	0.104	0.118126784	0.11758189	6.74	8.28
3	0.11467	45.06	0.787	1.002	0.115	0.127	0.097106266	0.09680276	5.55	15.02
4	0.127	47.6	0.831	1.095	0.139	0.153	0.080630703	0.08045665	4.61	20.57
5	0.13933	50.13	0.875	1.197	0.167	0.183	0.067452435	0.06735041	3.86	25.18
6	0.15167	52.66	0.919	1.311	0.199	0.217	0.056728832	0.0566681	3.25	29.04
7	0.164	55.2	0.963	1.439	0.236	0.258	0.047872474	0.04783595	2.74	32.28
8	0.17633	57.73	1.008	1.584	0.279	0.305	0.040462749	0.04044069	2.32	35.02
9	0.18867	60.26	1.052	1.751	0.330	0.361	0.034191501	0.03417819	1.96	37.34
10	0.201	62.8	1.096	1.946	0.391	0.428	0.028828404	0.02882042	1.65	39.30
11	0.21333	65.33	1.140	2.177	0.465	0.510	0.024198234	0.02419351	1.39	40.95
12	0.22567	67.86	1.184	2.459	0.555	0.612	0.020165542	0.02016281	1.16	42.34
13	0.238	70.4	1.229	2.808	0.668	0.742	0.016624045	0.01662251	0.95	43.49
14	0.25033	72.93	1.273	3.257	0.815	0.914	0.01348909	0.01348827	0.77	44.44
15	0.26267	75.46	1.317	3.857	1.013	1.153	0.010692078	0.01069167	0.61	45.22
16	0.275	78	1.361	4.705	1.294	0.647	0.019065628	0.01906332	1.09	45.83

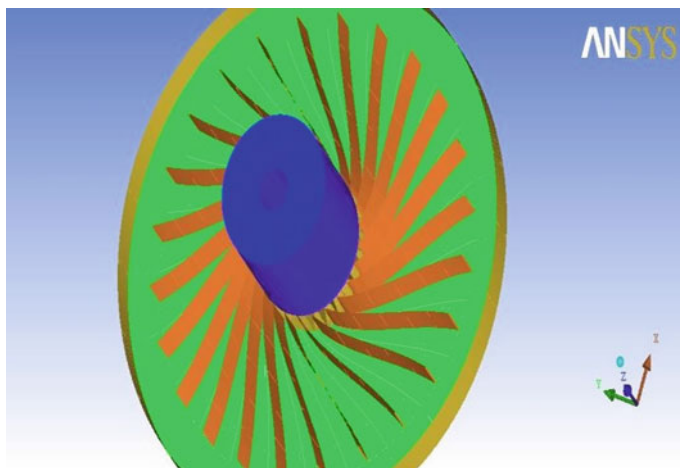


Fig. 1 Impeller with 24 blades

Table 3 Mesh data

Model types	No. of elements	No. of nodes
SVD	474,418	145,791
RVD 10	529,201	173,866
RVD 40	476,450	146,560
Full RVD	474,418	145,791

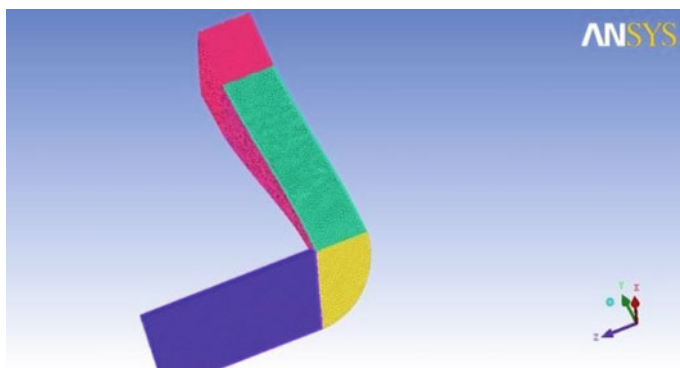


Fig. 2 Unstructured tetrahedral mesh fluid domain model

turbulence models ($K-\epsilon$, $k-\omega$, SST). The model simulation is done in ANSYS CFX SOLVER to validate with the reference values.

2 Experimental Methods

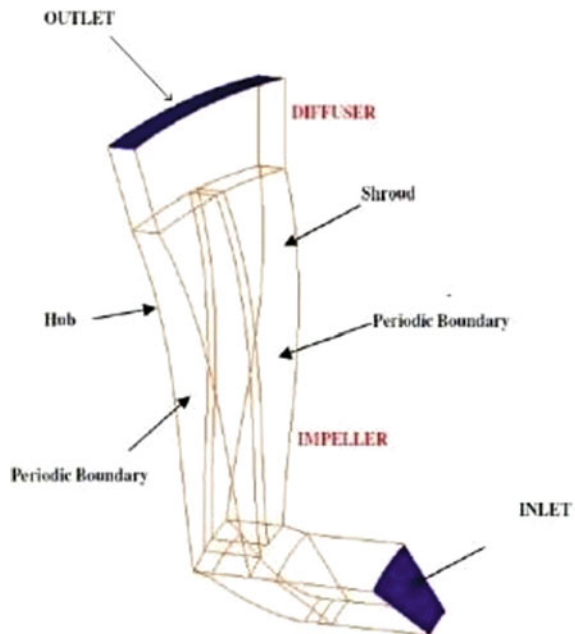
2.1 Turbulent Models

A superior forecast on stream division requires good modeling of turbulence. For this standard estimation of k - ω - and k - ω -based shear stress transport (SST), turbulence models were utilized. The outcomes acquired were contrasted and exploratory qualities. The examination of the qualities indicated that the numerical estimations of k - ω are nearer to the exploratory qualities. Along these lines, further examination was completed with this model.

2.2 Boundary Conditions

Every boundary definition appears in Fig. 3. Inlet boundary condition utilizes total pressure with a boundary layer profile. At outlet, mass stream rate is given. From the total stream coefficient, the mass stream rate is determined. In this manner, from inside the space, the velocity and pressure dispersion can be registered with the mass stream rate at the outlet and total pressure, particularly at the channel. As passage, with half the pitch on either side of the blade is being solved; the planes on either side of the blade will make periodic pair of surfaces. On the sides of space, occasional

Fig. 3 Boundary conditions for centrifugal impeller and vaneless diffuser



boundary conditions are given. Divider boundary condition pivoting with angular velocity equivalent to that of space is given to the edges, center point, cover, and turning diffuser. The walls were implemented with no-slip conditions.

3 Results and Discussion

The flow through impeller is computationally analyzed, and hence, the performance of the impeller is predicted which may differ from that experimental value. In this, four flow coefficients are considered one at design flow conditions, i.e., 0.208, and rest three are at off design conditions, i.e., 0.156, 0.227 and 0.266. The results for all three turbulence models are compared with experimental data available, the mode, which achieving less deviation is selected for further analysis at various mass flow rates and number of cells. Table 4 compares the experimental values for the energy coefficient (Ψ) has been compared with the energy coefficient calculated by different turbulence models along with the estimated error. Figure 4 gives the graphical comparison for better understanding.

Table 4 Comparison of Ψ for various turbulence models with experimental data

Flow coefficient, ϕ	Experimental value, Ψ	$\Psi (k-\omega)$	$\Psi (k-\epsilon)$	$\Psi (SST)$	Error for $k-\omega$ %
0.10	1.4	1.6	1.75	1.69	12.5
0.15	1.3	1.5	1.68	1.61	13.33
0.19	1.2	1.45	1.58	1.57	17.24
0.22	1.1	1.4	1.58	1.58	21.42

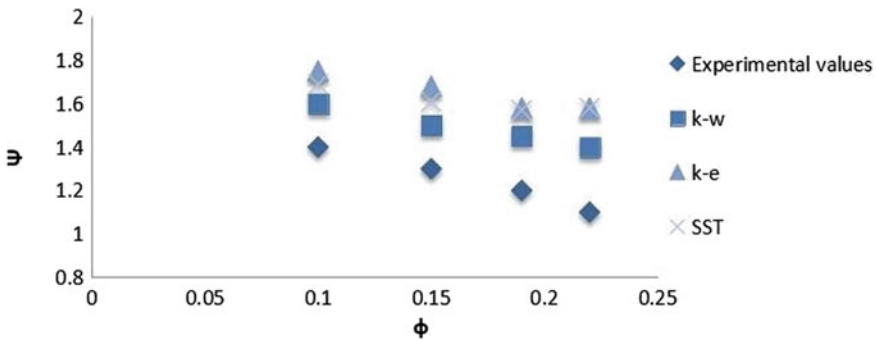


Fig. 4 Comparison between Ψ and ϕ for different turbulence models

3.1 Static Pressure Contours

As the radius increases, static pressure likewise increases because of flow diffusion. The angular velocity of the liquid particles holding fast to the outskirts of the plate is equivalent to the circle. As the good ways from the divider diminish, there will be a decline in the angular velocity of the liquid particles. As the flow moves to the higher span, the static pressure gain is the consequence of the expanded dynamic vitality of the. Among center point and cover, the turbo surfaces are taken at five unique positions. Consequently, the static pressure is marginally lower at mid-pivotal area ($x/b = 0.5$) contrasted with an area close to the dividers ($x/b = 0.05$ and $x/b = 0.95$) where the plate gives the rotational velocity to the liquid particles.

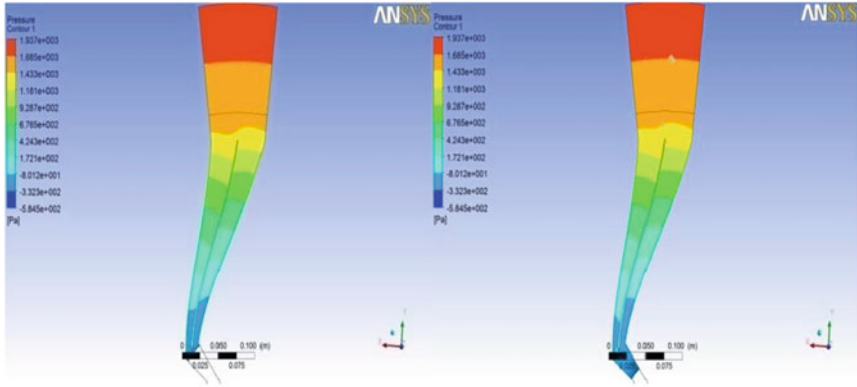
It has been discovered that there is an impressive increment in static pressure subsequent to expanding the cover, which can be obviously found in forms that appeared. As the region of the pivoting entry in the cover expands, the static pressure increases. The mass flow rate additionally assumes a significant job in the ascent of the static pressure. As it tends to be found in the forms for higher mass flow rates, the expansion in static pressure is additionally higher (Figs. 5, 6, 7 and 8).

The contour pattern for shroud extension 10% is shown in the above figures. With the help of these contours, the changes in the static pressure are estimated. These contours are taken across five different spans across hub to shroud to understand the changes in pressure taking place inside the fluid. The span value 0.95 is the closest to the wall of shroud, whereas the span value 0.05 is the closest to the wall of the hub. It has been observed that the maximum rise in static pressure has taken place for design value that is 0.208. Design value 0.156 has shown the highest rise in the static pressure for off design values, whereas for the case 0.227 and 0.226 it has reduced gradually.

The maximum rise in static pressure is shown by red color. It has been observed that for lower flow coefficient the area covered by maximum, i.e., red color, is less compared to the higher flow coefficient. It is clearly seen that the flow coefficient 0.266 covers the highest red color area when compared with flow coefficient 0.156 which is lowest of all coefficient. The static pressure distribution is almost same for the rest of the blade. It has also been noted that the lowest pressure rise which is shown by navy blue color is prominent at some of the places near to the entry point for the lowest flow coefficient, but in the case of higher flow coefficient there is no such thing pressure has started increasing from the very beginning (Figs. 9, 10, 11 and 12).

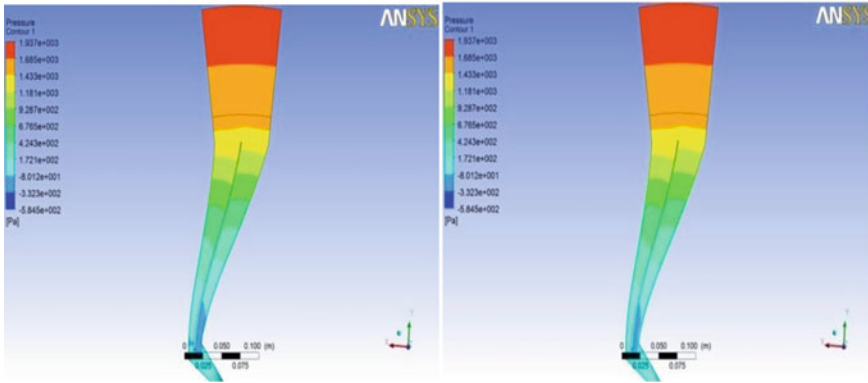
The contour pattern for shroud extension 40% is shown in the above figures. With the help of these contours, the changes in the static pressure are estimated. These contours are taken across five different spans across hub to shroud to understand the changes in pressure taking place inside the fluid. The span value 0.95 is the closest to the wall of shroud, whereas the span value 0.05 is the closest to the wall of the hub. From the above shown contours, the design flow coefficient 0.156 has the highest range of static pressure for RVD 40.

Static Pressure contour at constant span values (RVD 10)



Static Pressure (x/b) = 0.05

Static Pressure (x/b) = 0.5



Static Pressure (x/b) = 0.75

Static Pressure (x/b) = 0.95

Fig. 5 Static pressure contours for $\phi = 0.208$ from hub to shroud

It is observed that the highest static pressure region has reduced when compared to previous case. The lowest pressure is also dropped in comparison with RVD 10 model. In that, there was no blue region but here blue region can be prominently seen at the entrance of the model. So, it can be concluded that the quality of the required parameters has degraded with the further extension of the shroud.

4 Graphs

The graphs have been plotted for all four mass flow rates at the dimensionless values. It is clearly visible that there is a considerable rise in static pressure by comparing all four graphs for all four modifications. On comparing the models, it was found that

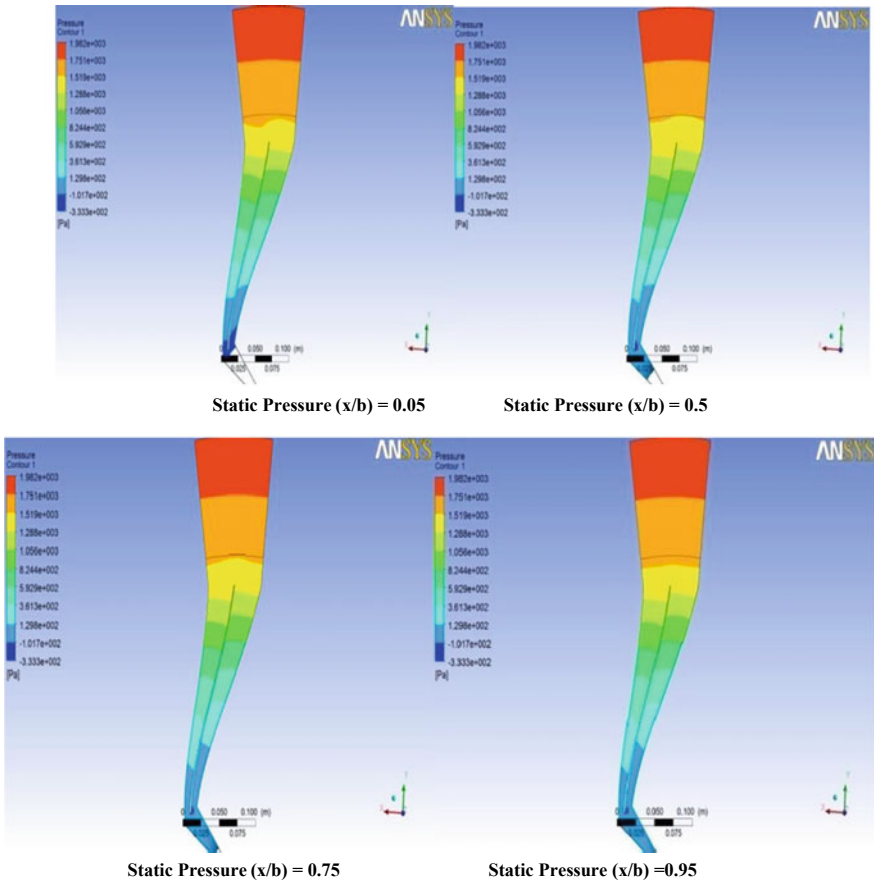


Fig. 6 Static pressure contours for $\phi = 0.156$ from hub to shroud

there is increase in static pressure coefficient. Even on considering the full rotating model, it will show the maximum rise in the static pressure coefficient, but it is not practically possible to create a centrifugal compressor with all its parts rotating. Further on comparing all four mass flow rates, the graph is almost straight line, which shows that the flow is uniform from hub to shroud and there is not much difference between the pressure at hub and the pressure calculated at the shroud (Figs. 13 and 14).

5 Conclusion

- Above figures show the distribution of pressure across the width of the impeller fluid model at different flow coefficients 0.208, 0.156, 0.227 and 0.266.

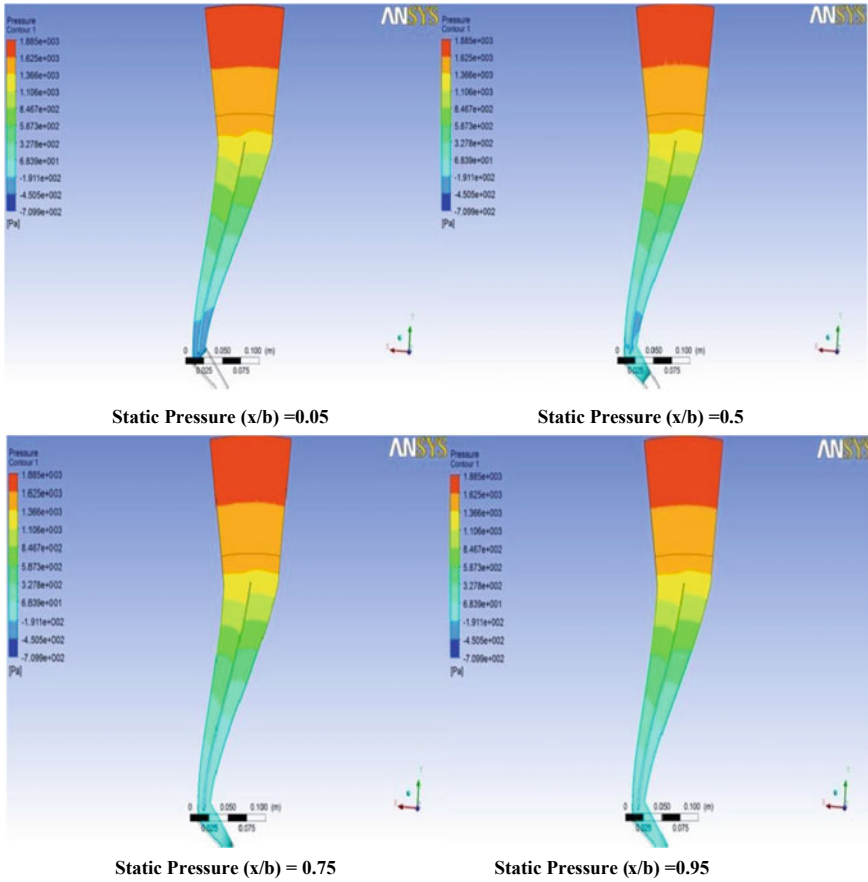


Fig. 7 Static pressure contours for $\phi = 0.227$ from hub to shroud

- The static pressure is calculated at the turbo-surface and analyzed at various spans (0.05; 0.5; 0.75; 0.95) across the impeller from hub to shroud for each flow coefficient.
- At the suction point, the pressure distribution of the fluid is low which gradually increases due to centrifugal force. By increasing the shroud, there is rise in the static pressure.
- For lower mass flow rates, the increase in static pressure is higher. Across the impeller from hub to shroud, the distribution is almost uniform.
- With RVD 10, higher static pressure increase rate with lower losses over SVD is obtained. This explains that in shroud extension the rate of diffusion is greater compared to SVD.
- The less frictional losses in shroud extension are caused by shorter flow path length and higher relative flow angle compared to SVD.

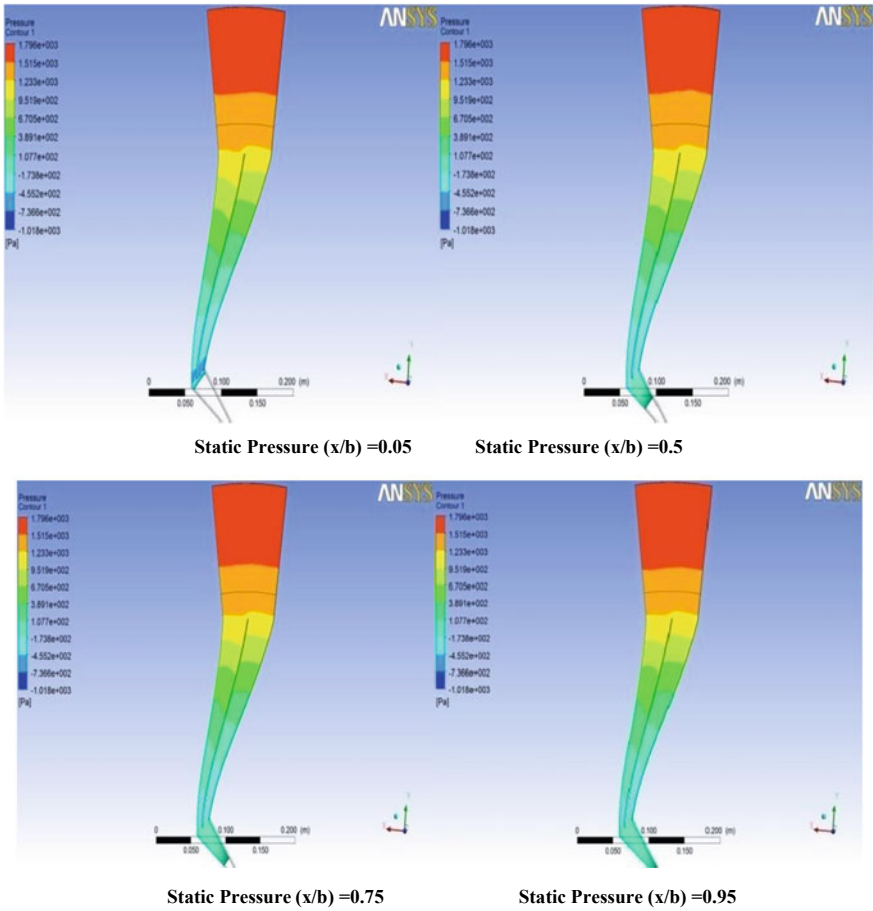
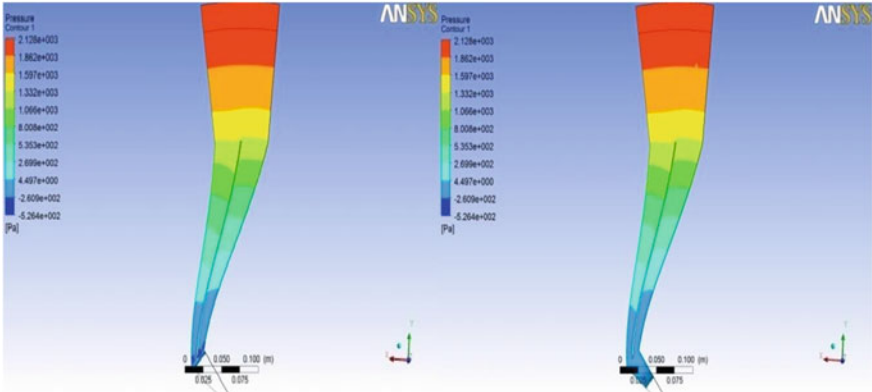


Fig. 8 Static pressure contours for $\phi = 0.266$ from hub to shroud

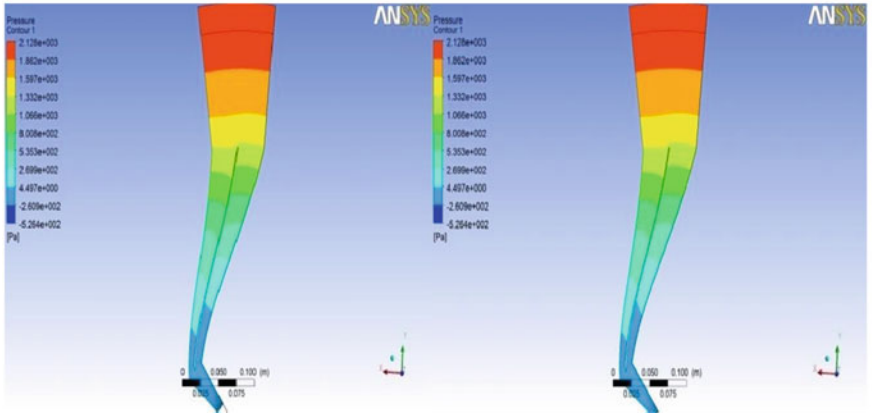
- At the end, it can be concluded that RVD 10 has shown a considerable improvement in all the desired parameters, whereas in case of RVD 40 there is improvement in static pressure coefficient but total pressure coefficient has declined from the original case.

Static Pressure contour at constant span values (RVD 40)



Static Pressure (x/b) = 0.05

Static Pressure at (x/b) = 0.5



Static Pressure (x/b) = 0.75

Static Pressure (x/b) = 0.95

Fig. 9 Static pressure contours for $\phi = 0.208$ from hub to shroud

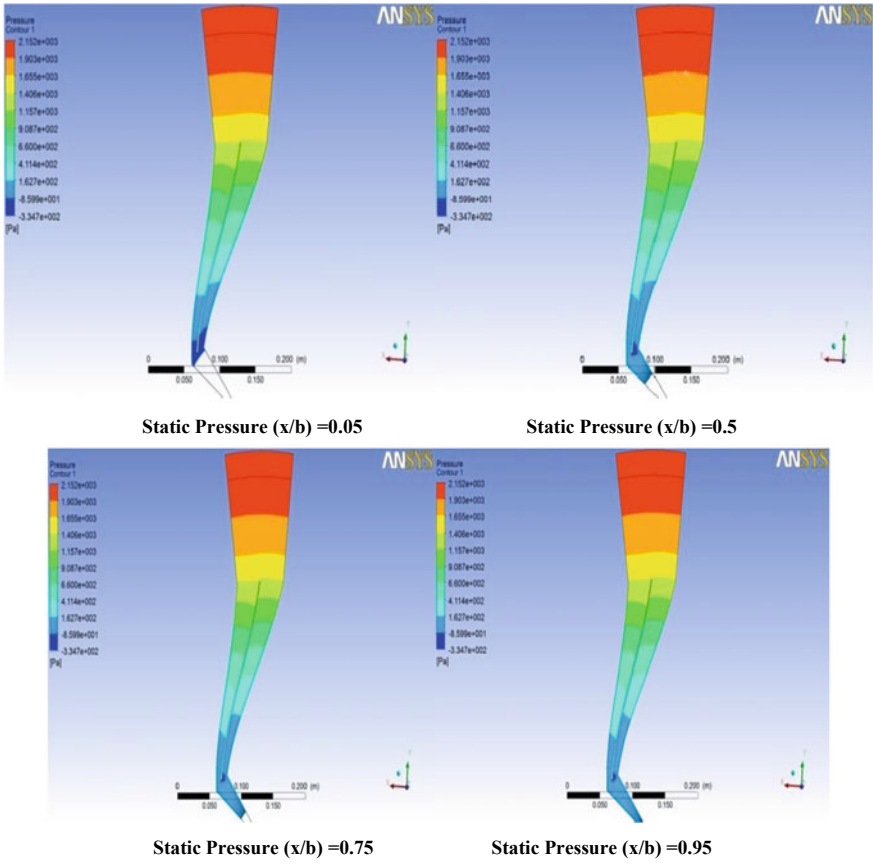


Fig. 10 Static pressure contours for $\phi = 0.156$ from hub to shroud

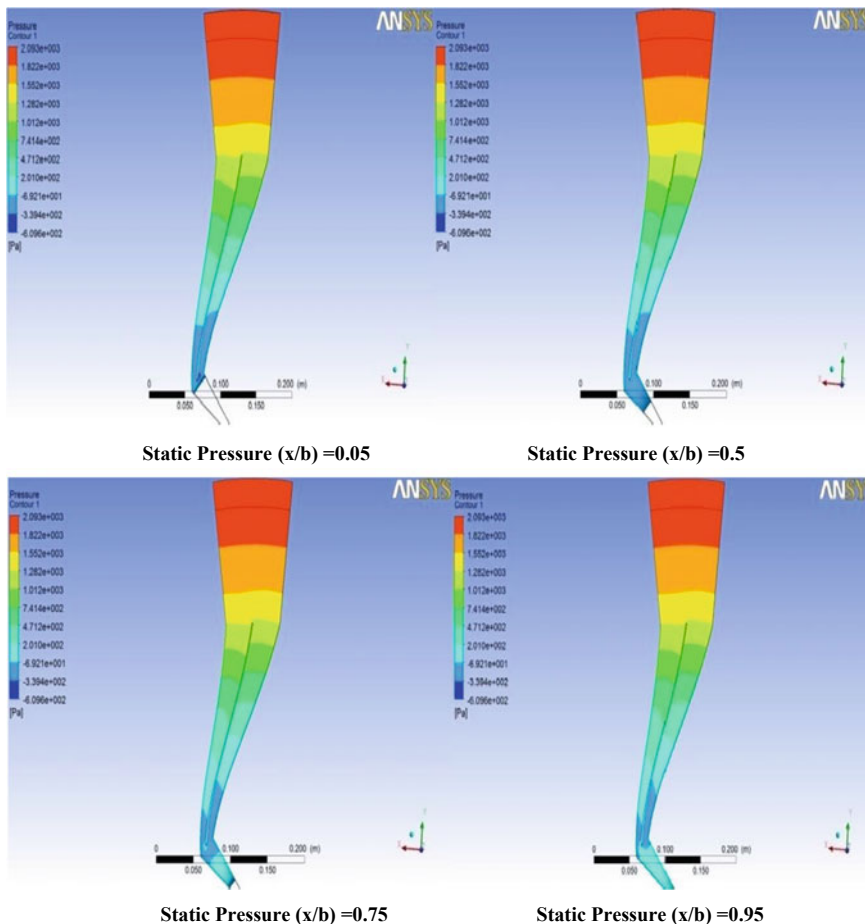


Fig. 11 Static pressure contours for $\phi = 0.227$ from hub to shroud

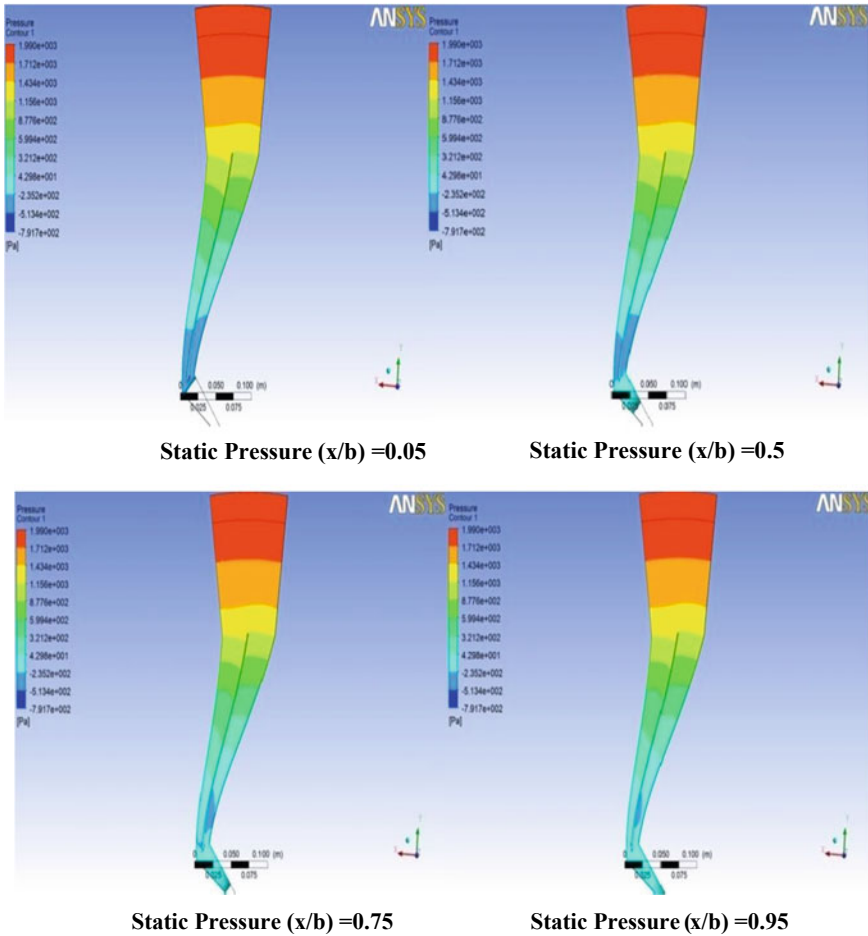


Fig. 12 Static pressure contours for $\phi = 0.266$ from hub to shroud

Fig. 13 Static pressure coefficient distribution for RVD 10 along hub to shroud measured at 10 mm from the tip of impeller for various flow coefficients

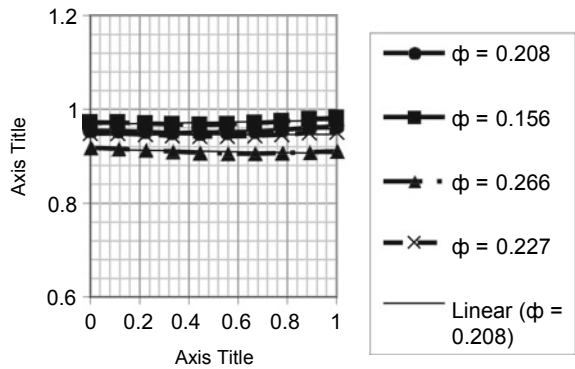
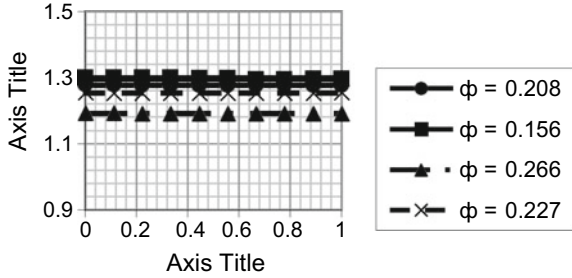


Fig. 14 Static pressure coefficient distribution for RVD 40 along hub to shroud measured at 40 mm from the tip of impeller for various flow coefficients



References

1. Rodgers C, Mnew H (1975) Rotating vane less diffuser study. *J Eng Power* 231–242
2. Harold L, Schenectady NY (1975) Centrifugal compressor with rotating vane less diffuser powered by leakage flow. US Patent, Appl. No.: 456129
3. Anish S, Sitaram N (2009) Computational investigation of impeller–diffuser interaction in a centrifugal compressor with different types of diffusers. *Power Energy* 223:167–178
4. OzturkT OA, Ali P (2008) Flow analysis in centrifugal compressor vaneless diffusers. *J Sci Ind Res* 67:348–354
5. Dubitsky O, Japikse D (2008) Vaneless diffuser advanced model. *J Turbomach* 130
6. Lee YT, Luo L, Bein TW (2001) Direct method for optimization of a centrifugal compressor vaneless diffuser. *J Turbomach* 123/73
7. SchleerMandAbhari RS (2008) Clearance effects on the evolution of the flow in the vaneless diffuser of a centrifugal compressor at part load condition. *J Turbomach* 130/031009-1
8. Anish S, Sitaram N (2010) Steady and transient computations of interaction effects in a centrifugal compressor with different types of diffusers. *ASME Turbo Expo 2010: Power For Land, Sea And Air* GT2010
9. Cui MM (2005) Comparative study of unsteady flows in a transonic centrifugal compressor with vaneless and vaned diffusers. *Int J Rotating Mach* 90–103
10. Ubaldi M, PietroZunino AG (1998) Detailed flow measurements within the impeller and the vaneless diffuser of a centrifugal turbomachine. *Exp Thermal Fluid Sci* 17:147–155
11. Hildebrandt, Genrup M (2007) Numerical investigation of the effect of different back sweep angle and exducer width on the impeller outlet flow pattern of a centrifugal compressor with vaneless diffuser. *J Turbomach* 129/421

Design and Performance of Wick-Type Solar Water Distillation Unit



Ashwini Shrivastava, Devendra Singh, Ajay Kumar Sharma,
and Ashok K. Dewangan

Abstract Present work deals with impact of different parameter and operating parameters on distillation of water, utilizing a basin-type solar still with a wick cloth and polythene sheet. In the current investigation, two glass plates and numerous jute wick and polythene sheets are utilized to increase productivity of freshwater. The investigation has been directed at Sachdeva Institute of Technology, Farah, Mathura, Uttar Pradesh, India [(Latitude: 24.50 N) (Longitude, 81.30 E)]. The test arrangement comprises of three layers: First layer consists of black polythene sheet of 900 mm × 895 mm cover bottom area and jute wick cover of area 895 mm × 895 mm, the second layer consists of 880 mm × 875 mm black polythene sheet area and 875 mm × 895 mm jute wick area, and third and last layer consist of black polythene sheet of area 870 mm × 895 mm and 865 mm × 895 mm jute wick area. The result shows that the water yield is 980 mL/day/m² in single layer, 1250 mL/day/m² in double layer, and 1500 mL/day/m² in third layer at solar radiation of 5.19 kWh/m²/day. The estimation of evaporation heat move is higher than radiative heat move, and the most extreme water yield got is 1500 mL/day on 30/10/2019. The value of maximum water yield obtained is 1500 mL/day on 30/10/2019.

Keywords Desalination · Jute wick layer · Solar still efficiency · Basin temperature

Nomenclature

P_w Water pressure (bar)

A. Shrivastava (✉) · D. Singh

Department of Mechanical Engineering, Sachdeva Institute of Technology, Farah Mathura, India

A. K. Sharma

Department of Mechanical Engineering, Institute of Engineering and Technology, Lucknow, India

A. K. Dewangan

Department of Mechanical Engineering, National Institute of Technology, Delhi, India

© The Author(s), under exclusive license to Springer Nature Singapore Pte Ltd. 2022

1139

K. Govindan et al. (eds.), *Advances in Mechanical and Materials Technology*,

Lecture Notes in Mechanical Engineering,

https://doi.org/10.1007/978-981-16-2794-1_99

$T_{\text{mini}} (w)$	Minimum climate temperature ($^{\circ}\text{C}$)
Q	Total convective heat transfer by glass plate 1 to glass plate 2
τ_2	Fraction of energy incident on the glass plate 2 absorb by jute wick
τ_1	Fraction of solar energy absorb by first glass plate
h_{ca}	Convective heat transfer coefficient $\text{W/m } ^{\circ}\text{C}$
V	Airspeed (m/s)
M_w	Mass of water (kg/s)
η	Total Efficiency of still unit.

1 Introduction

The increasing shortage of potable water has pushed technologies to provide highly purified water as faster rate. Kalita et al. [1] investigated and operating parameter on distillate produce by a solar still using absorber plate and fabricated and also using baffle plate. Dunkle [2] suggests the mathematical calculation of heat transfer coefficient for solar still and develops empirical formula. Pal et al. [3] worked on double slope multi-jute wick solar still by presenting wick, and they work on black cotton wick and jute wick and in comparison with both thermal efficiencies. This paper aims to reduce the problem of distilled water at low cost and less wastage of water at appropriate prototype which resolves the problem of water distillation through renewable energy resources will use. This paper is help to find how much water is distilled in day by solar energy using jute wick, black polythene sheet arrangement, and other factor/obstacle (like pipe friction, smoothness of work piece, wick) will not be considered. Various types of setup are used like simple distillation, fractionation distillation, vacuum distillation, steam distillation, new hybrid distillation using wick/solar still, absorption cooling distillation system, purification of salty water distillation, PVC solar water distillation, nanoparticle solar distillation, and other. This paperwork on two glass plate with same thickness and maintained gap in between is 12 mm. Agrawal and Rana [4] developed an experimental setup which based on single-slope solar still and various parameters like heat transfer coefficient, convective, and radiative heat transfer coefficients analysis. Fanga et al. [5] discussed the plentiful sun powered energy assets in Xinjiang, wherein the low-temperature layer refining innovation is utilized to heat the saline water into a drinkable refined water. The sun-based energy replaces the electric energy for refining and distillation of water, which significantly decreases the activity and upkeep cost of system. Torchia et al. [6] worked on various components of passive solar still work on collector plate, brine, and solar still with thermal efficiency is 12.9%, 6%, 5%, respectively. Dev and Tiwari [7] developed characteristic equation for active solar still and passive solar still with various angles 15° , 30° , 45° S. Kharabsheh and Yogi [8] worked on innovative solar water desalination system utilizing a passive vacuum technique in which vacuum create by nature force and conventional concept and make water

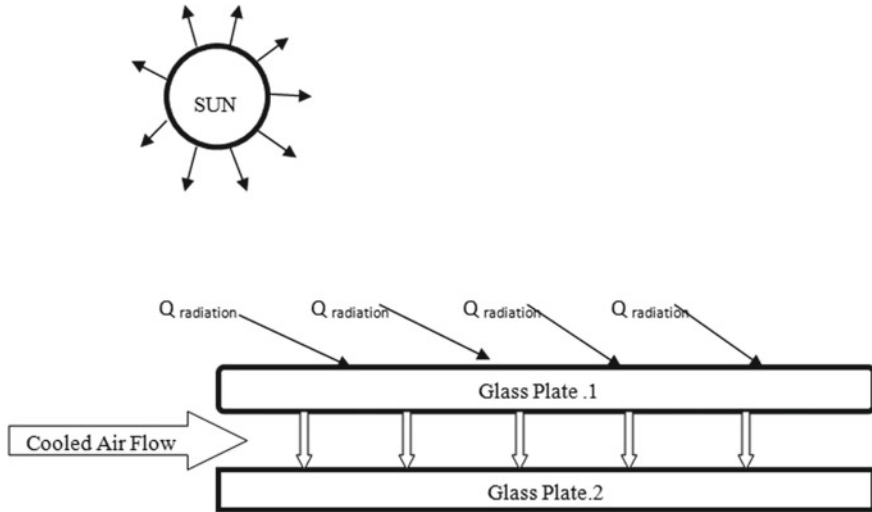


Fig. 1 Air carries temperature by convection and advection

distilled. Agrawal and Rana [4] worked on experimental performance evaluation of single-slope single-basin solar still with multiple V-shaped floating wicks.

They observed the impact of climatic condition like sunlight-based radiation, operational condition, temperature examination at hourly, water TDS value after distillation, and wick material temperature on solar still. Singh et al. [9] studied the effect of mass in fluid flow for enhancing the efficiency of solar desalination unit coupled with evacuated tubular collectors. Dev et al. [10] developed a characteristic equation to observe the performance analysis of solar still. Mohammadia et al. [11] discussed on hybrid type solar power systems. The solar system was modified with perforated plate and wick to analysis the performance of the system [12, 13]. In present work, a basin-type slope multi-wick solar still using the E, W, S walls of acrylic is used to increase output day to day. Layout of experimentation has been presented in Fig. 1.

2 Experimental Setup

This wick-type solar water distillation installed at Mathura, (Fig. 2). The solar still basin is of area 1 m^2 (1 m Length and 1 m breath), which is made up of GP (Alvalume plain sheet) sheet with 0.68 mm thickness and 220 MPa strength, and its sheet is AZ coating (GSM 70, 100, 120, 185), and its yielding strength is 240, 550, 340 MPa, and three layers of jute cloth and three layers or black polythene sheet arrange in three layers, and using top as two glass sheet (5 mm thickness) which absorb more energy from sun. The average yield of distilled water was $980 \text{ mL/m}^2/\text{day}$ (25/10/2019)

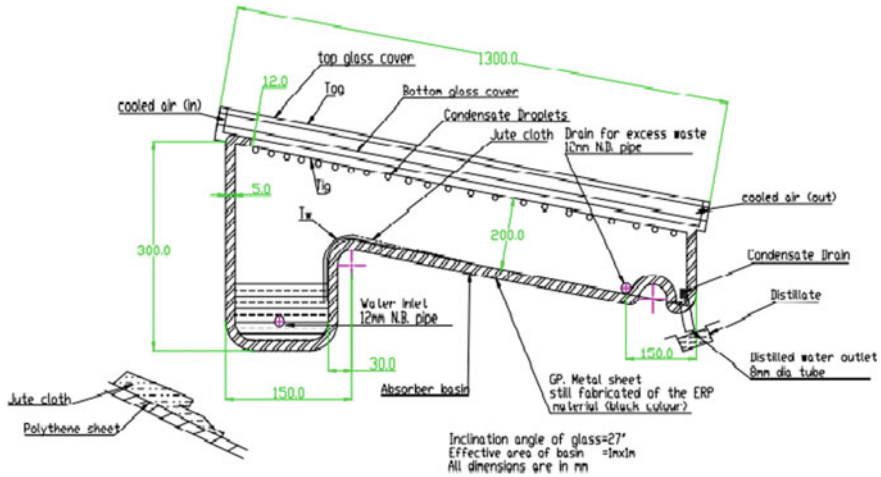


Fig. 2 Operating principle and arrangement of solar still

and 1250 mL/m²/day (27/10/2019), 1500 mL/m²/day (30/10/2019) at Mathura with weather maximum temperature of 31 °C and minimum temperature of 17 °C. The result with efficiency is 65% of an analysis based on Dunkle method. This setup established angle of elevation 27° from ground level and using two normal glass with 5 mm thickness and maintain 12 mm thickness in between them and also use cooling fan device at various place as water distilled by condensed water vapor, and its water vapor converts into water droplets and makes water distilled, and some water are distilled due to capillary action of jute wick. With the help of this setup, impure water that converts into distilled water with TDS value is 23 ppm. In this, we use jute wick, black polythene sheet which makes as bed which thickness is 15 mm. It is placed inside the setup, top surface covers by glass plate and makes glass plate fully make insulation using black brown tapping and other glass placed 12 mm on it. The jute cloth absorb maximum solar radiation and easily developed moisture environment inside the leak proof setup. The jute cloth and polythene sheet arrange in three layers. In these layer a black ploythene is used as base sheet. The jute cloth behaves as capillary action, and polythene sheet-jute cloth maintain temperature inside the setup. A tube of 8 mm diameter is used to discharge the excess water and measured 65 ppm TDS value. In this, we also use black paint inside and outside the setup which increase the efficiency of the setup. Whenever we have not painted black paint inside and outside, then we analyze that quantity of water distilled is less 910 mL/m²/day than after doing black paint which efficiency improve but certain limit. We also used a solar energy panel system to work the condensate equipment. We used cooling fan unit which placed between two glasses, and this cooling fan unit is operated by solar energy. We use solar plate and inverter and battery which is it make fully solar energy-based system. The cooling fan (DC brushless fan, 12 V, 0.09 A) flow air with 2 m/s velocity takes heat to other end or condensate the water and collected it. The

jute wick has wicking characteristic, and its heat transfer coefficient is $13.5 \text{ W/m}^2 \text{ } ^\circ\text{C}$, capillary rise 78 mm/h , and dip portion of first wick is 10 cm , second wick is 15 cm , and third wick is 19 cm and water suction by capillary action.

All materials have different thermal conductivity and different convective heat transfer coefficient. The detail experimental setup is shown in Fig. 3a, b; for experimentation, we take ground water containing initial TDS value 225 ppm .



Fig. 3 **a** Photograph of experimental setup of solar still (1) water input device (2) water circulation (3) condensate water collection (4) cooling fan unit (5) battery (6) inverter (7) AC to DC converter, PVC cable (8) temperature measuring device (9) solar plate (10) distillate water collected after condensate. **b** Photograph of start of distillation through solar energy with condensate droplet

3 Formulation

Utilizing Dunkle's relation Q_c , Q_e , and Q_r and disregarding the heat capacity (C_p , C_v) of the irradiation was of water and glass spread, and the energy adjusted by first law of thermodynamics for glass spread and water sheet might be express as:

$$\tau_1 H_s + Q_r + Q_e + Q_c - Q = 0 \quad (1)$$

$$\tau_2 H_s - Q_r - Q_e - Q_c - h'(T_w - T_g) = 0 \quad (2)$$

The following parameter has been used to evaluate to water surface and glass temperature absorbed by the atmospheric condition.

where parameters are:

$\tau_1 = 0.06$ (Experimental value); $\tau_2 = 0.088$ (Best value from available experiment).

$l = 1300$ mm; $h_i = 22.85$ W/m²⁰C

$$Q_c = 0.884 \left[((T_w - T_g) + \{(P_w - P_g)(T_w + 273.15)/(268.9 * 10^3 + P_w)\})^{1/3} \right]$$

$$Q_e = 16.273 * 10^3 * Q_c [(P_w - P_g)/(T_w - T_g)]$$

$$Q_r = \sigma [(T_w + 273.15)^4 - (T_g - 273.15)^4]$$

$$Q = [h_{ca} T_g + \sigma (T_g + 273.15)^4 - (T_w + 273.15)^4]$$

Put values of Q_c , Q_r , Q_e , Q in Eqs. (1) and (2)

Calculation of h_{ca}

$$h_{ca} = 5.7 + 3.8v \text{ and } 1/h = 1/k + 1/h''.$$

Quantity of distilled water

$$M_w = 16.273 * 10^3 [Q_c (P_w - P_g)/(T_w - T_g)] \quad (3)$$

where T_w , and T_g are calculated by Eqs. (1) and (2), and corresponding vapor pressure can find from steam table (R. S. Khurmi).

Then find efficiency of still by using Eq. (4)

$$\eta = \left(\int Q_e dt \right) / \left(\int H_s dt \right) \quad (4)$$

4 Experimentation

The tests are led for a few days during the sunny mornings of winter beginning at Mathura, (U.P), India. Among nowadays, the best perceptions were recorded on

Table 1 Amount of water distillation per day

Date	Atmospheric pressure (mb)	Maximum (°C)	Minimum (°C)	Water distillation per day amount (mL)	Solar radiation (KWh/m ² year)
21/10/19	1013	33	19	250	3035.20
22/10/19	1011	32	18	560	3035.20
23/10/19	1010	33	17	910	3035.20
24/10/19	1010	35	17	820	3035.20
25/10/19	1013	31	17	980	3035.20
26/10/19	1011	32	17	940	3035.20
27/10/19	1013	31	19	1250	3035.20
28/10/19	1013	30	21	1210	3035.20
29/10/19	1014	31	21	1305	3035.20
30/10/19	1011	30	19	1500	3035.20
31/10/19	1011	32	21	1357	3035.20

30 October 2019 and 25 October 2019. The direction of the sun oriented despite everything is continued along the east-west bearing with the glass spread confronting south to boost episode sunlight-based radiation.

Test of the sun-based refining framework was completed with different factors (Table 3). Outdoor tests of the solar still were conducted on various sunny days and cloudy days, respectively; by varying the input, water with TDS is 200 ppm, and after distillation, it is converted to TDS of 23–25 ppm (Table2). Table 1 represents daily reading of water yield.

5 Results and Discussion

The following is the description of result and discussion. The data observed during the experiment was calibrated and used for the analysis. Figure 4 displays that the convective heat transfer coefficient is 20.38 W/m °C, and water distillation amount is 250 mL/day, and first-day solar still setup efficiency is 12.28%. Figure 5 shows the variation of temperature in between inner glass and outer glass and water temperature difference in 21/10/2019 for morning 7 am to 6 pm. It presents the variation of temperature on an hourly basis which affects water yield value. Temperature difference is maximum on 25/10/2019 is 5.2 °C, and variation of outer glass temperature is maximum at 58.9 °C on 27/10/2019.

Another comparative study is completed between inner and outer glass temperature in Fig. 5. Inner glass temperature increases compared to outer glass temperature because outer glass continuously heat loss by the surrounding. Basically, the inner glass gains heat from top glass plate temperature. The difference of inner and outer

Table 2 Temperature analysis hourly

Daily temperature of experiment															
Temp. (°C)	T_i	T_o	T_w	T_i	T_o	T_w	T_i	T_o	T_w	T_i	T_o				
Time/date	21-10-2019			22-10-2019			23-10-2019			24-10-2019					
7 am	19.3	20.2	20.3	17.8	16.9	19	19	17	20	19.9	19	21.4	17.9	18.4	19.4
8 am	23.4	21.8	22.9	29.3	26.6	29.3	37	33	35	32	31	35	22.4	21.8	22.9
9 am	38.4	32.8	35.8	41.8	35.2	38.2	45	39	42	36.1	33	35.4	43.9	36.5	38.4
10 am	49.7	41.8	44.3	51.4	41.9	44.1	60	50	53	52.3	46	49.4	50.2	40.1	43.5
11 am	59.4	49.1	52.3	62.4	50.4	53.6	65	54	58	63.6	53	58.3	65.8	53.9	59.1
12 noon	63.3	51.5	54.7	64	52.1	55.5	68	58	62	67.3	55	59.8	63.6	52.6	57.5
1 pm	63.8	51.7	53.8	64.8	51.4	55.8	67	55	58	67	55	59.6	62.4	51.3	54.7
2 pm	58.8	47.7	50	56.3	58.5	52	65	53	59	59.8	55	51.6	57.1	48.3	52.1
3 pm	54.4	45.9	48.4	55	43.5	49.4	45	55	50	59.8	55	55.1	54.1	47	52
4 pm	47.5	40.3	42.9	44.1	36.3	41	43	54	48	50.4	49	48.6	42.3	36.2	40.4
5 pm	44.1	37.7	38.9	33.4	29.2	33.5	38	31	37	45.2	42	41.5	40.1	32.1	38.2
6 pm	34.5	35.4	35.5	30	24.3	28.4	35	30	33	37.2	31	34.2	31.5	27.9	31.9
Time/date	26-10-2019			27-10-2019			28-10-2019			29-10-2019			30-10-2019		
7 am	21.3	20.1	22.3	20.4	18.1	19.4	24	20	25	20.9	20	27.3	17	21.3	19.5
8 am	26.5	25.8	25.8	24.8	20.4	18.6	26	28	27	22.4	24	24.7	25.4	27.3	22.4
9 am	44.7	38.3	39.6	40.3	35.3	38.7	34	34	22	49.4	31	32.8	28.8	26.9	29.7
10 am	52.4	40.8	50.4	51.4	48.7	50.3	49	36	34	45.4	39	40.9	38.1	30.4	35.6
11 am	52.4	46.8	51.4	54.3	48.3	52.3	54	48	50	54.3	45	40.9	48.4	41.1	45.8
12 noon	58.1	50.8	55.5	58.9	50.7	54.5	62	51	54	61	40	48.8	47.7	40	46.7

(continued)

Table 2 (continued)

Daily temperature of experiment															
1 pm	62.5	51.4	54.2	62.1	58.9	60.1	63	55	57	45	50	44.9	43.3	37.5	42
2 pm	60.4	50.9	48.3	60.3	57.3	58.4	62	51	50	54.1	57	61.3	41.6	36.3	40.8
3 pm	48.3	48.3	32.5	54.9	48.8	51.3	45	38	45	46.3	41	42.4	38.2	36.5	37.4
4 pm	42.5	33.4	33.3	42.1	35.3	33.5	32	28	32	48.5	35	46.4	37.2	32.5	37.2
5 pm	32.1	28.1	29.4	30.7	25.9	23.4	31	27	31	42.1	30	37.8	30.8	25.9	31.2
6 pm	28.4	24.3	21.3	25.3	23.1	27.8	28	25	29	33.4	27	33.1	27.3	23.2	29.1

Table 3 Velocity and TDS value

Date	T_w (°C)	T_o (°C)	$T_w - T_o$ (°C)	P_w (KPa)	V (m/s)	Cloud cover (%)	Humidity (%)	TDS (ppm)
21-10-2019	54.7	51.5	3.2	157	1.47	35–45	28–77	70
22-10-2019	55.8	51.4	4.4	168	2.44	31–45	26–70	67
23-10-2019	62	58	4	218	1.028	31–42	24–87	35
24-10-2019	59.8	55	4.8	199	1.78	48–57	28–78	25
25-10-2019	59.1	53.9	5.2	150	3.3	51–65	38–80	29
26-10-2019	55.5	50.8	4.7	157	2.63	46–60	25–87	27
27-10-2019	60.1	58.9	1.2	199	1.93	51–75	30–88	30
28-10-2019	57.3	55.2	2.1	173	0.73	41–54	36–71	28
29-10-2019	61.3	57.3	4	208	2.32	72–95	36–74	26
30-10-2019	46.7	40	6.7	103	3.48	70–90	28–84	25

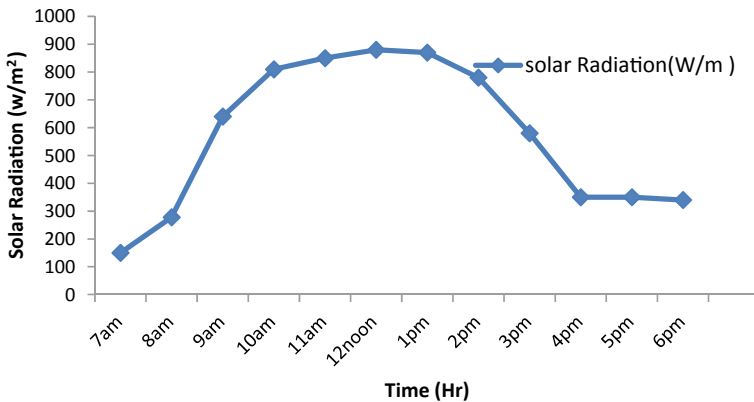


Fig. 4 Variation of solar radiation (hr)

glass temperature is in range of (1–13 °C). This inner glass has inner side to collect water vapor; this temperature is reduced by cooling fan unit and condense water droplet and collected as can be shown in Fig. 3. Figure 6 shows water distillation productivity (mL/day). The maximum value of heat transfer convective and radiative and evaporative obtained on 22/10/2019 and 24/10/2019 is 18.39 W/m² °C and 18.21 W/m² °C, respectively, and TDS value also varies day to day. The yield obtained with black polythene sheet and jute wick which absorbed more solar radiation than black polythene sheet. Due to jute wick, capillary action performs layer to layer. The water absorbs by jute and evaporated under the still due to high temperature developed by glass plate. Thus, on first day (21/10/2019) 250 mL/day distilled amount of water and on 30/10/2019 1500 mL/day amounts of water are distilled, which improves the efficiency is about 65.43%. The dates of experiments for basin

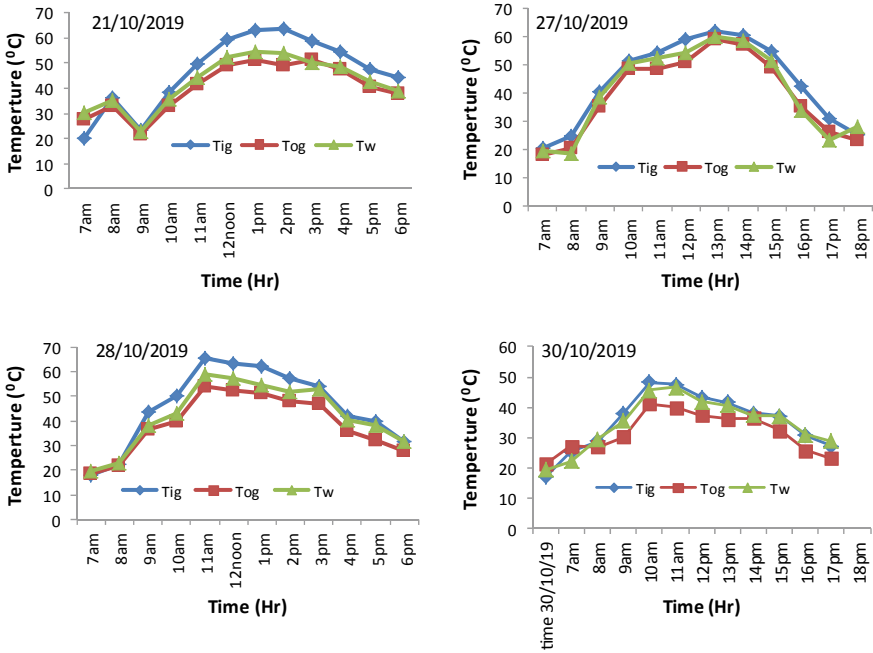


Fig. 5 Temperature variations on an hourly basis on 21/10/2019 to 30/10/2019

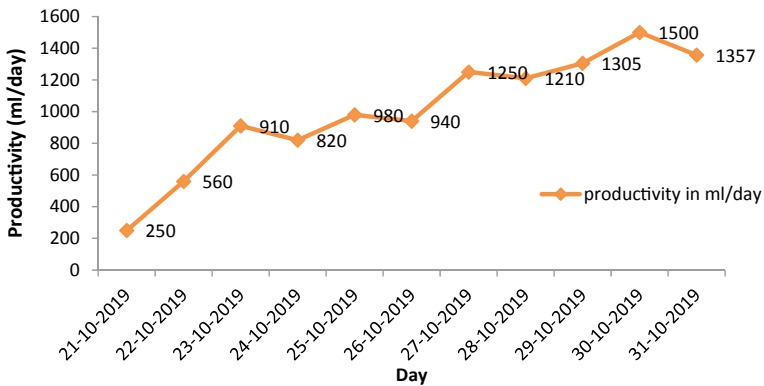


Fig. 6 Water distillation productivity (mL/day)

and daily yield are presented in (Table1). The TDS value of water was 225 ppm at starting, and after distillation, this value goes best up to 65–23 ppm. This distilled water after distillation process has clean and eliminating harmful elements. It can be used in hospital, laboratory, chemical industry, batteries, etc. In this basin, moisture content rate higher than amount of water distilled increased. These results are analyzed for individual 10 day. Figure 6 shows the hourly variation of temperature,

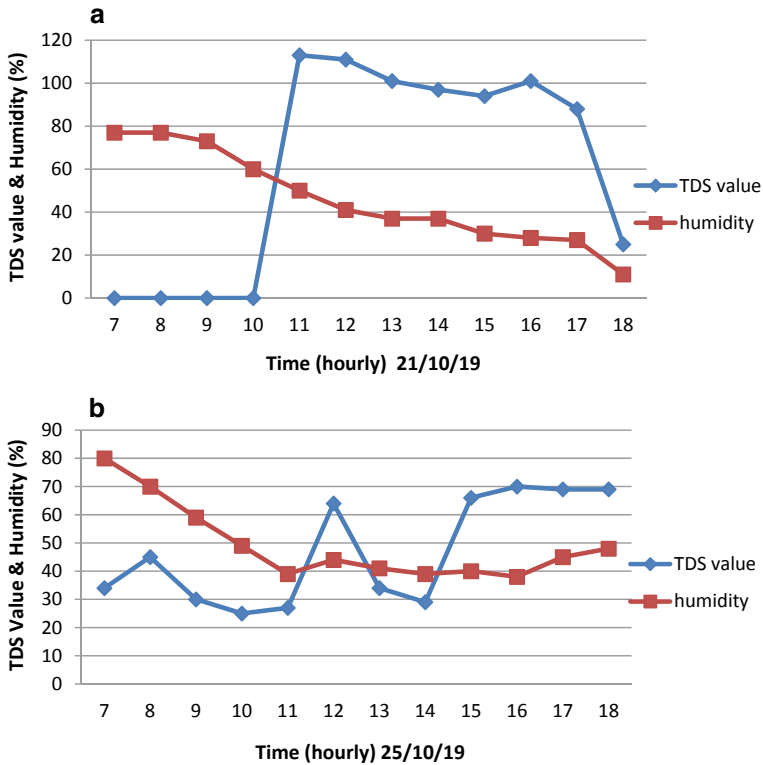


Fig. 7 Experimental value of TDS and water temperature and outer glass temperature

heat transfer coefficient, and heat transfer like convective, radiative, and evaporative. The maximum value of heat transfer coefficient is $24.47 \text{ W/m}^2 \text{ }^\circ\text{C}$ on 27/10/2019, and heat transfer coefficient is $16.80 \text{ W/m}^2 \text{ }^\circ\text{C}$ on 30/10/2019 on that day amount of water distilled is 1500 mL/day. In Fig. 7, value of TDS and water temperature and outer glass temperature has been presented. It can be observed that the maximum water temperature is $54.7 \text{ }^\circ\text{C}$, and pressure is 0.15741 bar with wind velocity of 1.47 m/s. Figure 8 presents heat transfer rate for 10 days. Solar radiation is 815 W/m^2 at first day, and other day readings are calculated.

6 Conclusions

Based on the experimental work, the values of evaporative and radiative heat transfers (Q_e and Q_r) more than the value of heat transfer Q_c are observed. The extreme value of water evaporated is 847 g/m^2 on 30/10/2019. The yield obtained in typical days of October with jute wick and black polythene was 1500 mL/day/m^2 , and starting day

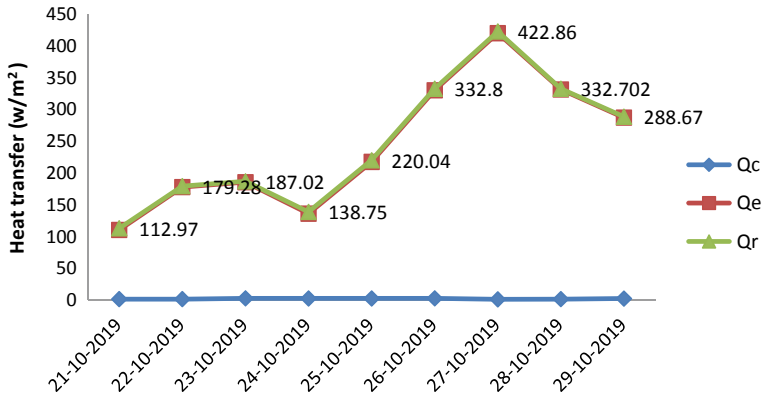


Fig. 8 Heat transfer rate on different dates

is 250 mL/day/m². Thus, an increase in 8.33% of yield obtained from present still, low wastage of water when water is distillation. The maximum thermal efficiency with jute and black polythene was 59%. The amount of yield is also increased when we using cooling fan unit in between two glass plate. At night time without feeding water, distilled water amount near about 170–200 mL is collected. The most extreme yield acquired was 1500 mL/day on October 30, 2019 at 2 cm with single-slope water distillation arrangement with jute wick and black polythene individually. The ideal yearly expense of distillation water per liter is Rs. 2.50 (0.035USD) with the jute wick, black polythene sheet, when first all establishment cost of arrangement was Rs. 8000.

References

1. Kalita P, Borah S, Dudul D (2017) Design and performance evaluation of a novel solar distillation unit. *Desalination* 416:65–75
2. Dunkle RV (1961) Solar water distillation: the roof type still and multiple effect diffusion still. In: *International developments in heat transfer*, ASME, proceedings of international heat transfer conference. University of Colorado, pp 895–902
3. Pal P, Yadav P, Dev R (2015) Design of modified basin type double slope multi-wick solar still. *BLB-Int J Sci Technol* 304–309
4. Agrawal A, Rana RS (2018) Energy and exergy analysis of single slope single basin solar still in Indian condition: an experimental analysis. *Mater Today Proc* 5:19656–19666
5. Fanga S, Tuc W, Lin M, Sunc ZL, Qiuyue H, Yangd Y (2019) Saline alkali water desalination project in Southern Xinjiang of China: a review of desalination planning, desalination schemes and economic analysis. *Renew Sustain Energy Rev* 11:3109268
6. Torchia NJC, Porta GMA, Cervantes GJG (2008) Exergy analysis of a passive solar still. *Renew Energy* 33:608–616
7. Dev R, Tiwari GN (2009) Characteristic equation of a passive solar still. *Desalination* 245:246–265
8. AlKharabsheh S, Goswami D (2003) Experimental study of an innovative solar water desalination system utilizing a passive vacuum technique. *Sol Energy* 75:395–401

9. Singh DB, Raturi A, Kumar N et al (2020) Effect of flow of fluid mass per unit time on life cycle conversion efficiency of single slope solar desalination unit coupled with N identical evacuated tubular collectors. *Mater Today Proc.* <https://doi.org/10.1016/j.matpr.2020.03.245>
10. Dev R, Singh HN, Tiwari GN (2011) Characteristic equation of double slope passive solar still. *Desalination* 267:261–266
11. Mohammadia K, Mohammad S, Ellingwood K, Kody P (2019) Hybrid concentrated solar power (CSP)-desalination systems: a review. *Desalination* 468:114083
12. Nafey AS, Abdelkader M, Abdelmotalip A, Mabrouk AA (2002) Enhancement of solar still productivity using floating perforated black plate. *Energy Convers Manag* 43:937–946
13. Pala P, Yadava P, Dev R, Singh D (2017) Performance analysis of modified basin type double slope multi-wick solar still 422:68–82

Investigation of Tribological-Based Thermal Behaviours of Lubricating Oil of Worm Gearbox: A Review



J. S. Bhat, A. B. Chougale, and B. U. Sonawane

Abstract This paper presents the importance of the study of the thermal behaviours of lubricant oil of worm gearbox. Worm gearbox due to sliding motion between teeth's of worm and worm wheel causes friction energy loss. The friction energy loss is converted into heat energy and that heat energy is dissipated into lubricating oil of worm gearbox. The performance of lubricating oil is decreasing due to an increase in the temperature which causes decreases in the overall performance of gearbox. When the lubricant oil temperature is the response parameter, then many factors are affecting on that response parameter those are called process parameters. The viscosity of lubricant oil, additives in the oil, load on the worm wheel, the speed of worm, the geometry of gear, the oil level, the clearance, position of the worm, etc., is the process parameters. Selecting some process parameters and response parameters, the thermal behaviour of the lubricant oil of the worm gearbox can be analysed for optimum levels of process parameters. This special test rig of the worm gearbox must be developed based on temperature sensors which gives response parameter readings under different process parameters at their different levels. The results obtained by experimentation can be validated with simulation results. The Taguchi optimization technique can be used for the optimization of experiments. Grey relational analysis (GRA) can be used to determine optimum process parameters. ANOVA analysis can be used to find the relative contribution of process parameters on response parameters.

Keywords Tribology · Lubricating oil · Thermal behaviours · Worm gearbox

J. S. Bhat (✉) · B. U. Sonawane

Department of Production Engineering and Industrial Management, College of Engineering Pune, Pune, India

B. U. Sonawane

e-mail: bus.prod@coep.ac.in

A. B. Chougale

Department of Mechanical Engineering, K.I.T.'s College of Engineering, Kolhapur, Maharashtra, India

1 Introduction

Tribology is the study of wear, friction and lubrication under applied load when two surfaces are in relative motion. Worm gearbox is used for the nonparallel, right angle and non-intersecting gear drive system applications where a high-speed reduction is required. As compared to other gear drive systems, worm gearbox offers a more compact solution. Usually, a worm is made of harder metal like steel, and worm wheel is made of softer metal like bronze. Worm gearbox rolling and sliding motion occur simultaneously. The sliding action creates friction energy loss, that friction energy loss is mainly converted into heat energy which could raise the temperature of gearbox and also of lubricant oil [1–7]. The viscosity of lubricant oil is due to the cohesive force of attraction between the molecules. Increase of temperature of lubricant oil decreases the viscosity of lubricant oil which reduces the overall performance of gearbox. So, the lubricant oil temperature and viscosity of oil can be chosen as the response parameters for the thermal behaviour of the lubricant oil of the worm gearbox. It is observed that many factors affect on the temperature increment of lubricant oil of worm gearbox, such as the rotational speed of worm, the geometry of gear, oil level, viscosity of the oil, load on worm wheel, clearance, type of oil, additives in oil, etc., which are called as process parameters [8–16]. Special test rig should be developed based upon temperature sensors which will give response parameter readings at different process parameters at their different levels. By selecting some process parameters at their different levels analysis of thermal behaviours of lubricant oil of worm gearbox is possible to determine the optimum levels of process parameters. The result obtained by experimentation can be validated with FEA. The Taguchi optimization technique can be used for the optimization of experiments. Minitab software is available for experimental setup values based on the Taguchi optimization method [17–23]. Grey relational analysis should be used to determine optimum process parameters. ANOVA analysis should be used to find the relative contribution of process parameters on response parameters [24–30].

2 Literature Review

2.1 Importance of Tribology

In total world energy, 23% of energy is related to tribological contacts, from that 20% of energy is utilised to overcome the friction, and 3% of energy is utilised to remanufacture wear parts. By taking advantage of new materials, lubrication, surface coatings and tribological study, these energy losses can be reduced to 40% in 15 years and 18% in 8 years [1]. Maintenance depends on the rate of friction as well as wear, through the tribological improvement of tribomechanical systems approximately 90% saving can be possible in maintenance [2].

2.2 *Materials for Worm Gearbox*

The worm is made of harder metal like steel and worm wheel made of softer metal like bronze. To observe tribological behaviour of quenched bronze and tempered steel material pair, disc on disc experiment arrangement is used, and it is observed that the microstructure of CuSn12 alloy is an important factor for surface damage [3]. The gear pair's 42CrMo4V steel against itself and GJS700 cast iron against 42CrMo4V steel, respectively, can be alternative materials solution for worm and worm wheel [4]. By providing modifications on the surface (i.e. DLC, WC-CrN, WC/C coatings, plasma nitriding) on steel-steel pair that can be an alternative material solution for worm gearbox drive [5].

2.3 *Wear Analysis*

Due to high sliding relative motion between teeth, worm gear drive suffers from wear. Wear depends on many parameters, i.e. material pair, the viscosity of the oil, film thickness, sliding distance, normal force, lubrication method and roll to slide ratio, etc. Ferrographic analysis is used to calculate the wear of worm gearbox to operating hours. By calculating wear severity index and wear particle concentration, concerning operating time earliest advice can be given for the prevention of breakdown [6]. According to the wear model of Archard's, the tooth surface is calculated and modifies the geometry, and the calculation process is repeated in a series of wear steps [7].

2.4 *Power Losses*

Due to sliding motion between teeth, worm gearbox has low efficiency. Power losses in worm gearbox are divided into two types, i.e. churning power loss (CPL) and total power loss (TPL). Churning power loss is no load-dependent loss, while total power loss consists of all types of losses. ANOVA result shows that immersion depth mostly effects on CPL, and speed of worm gear has a minimum impact on CPL. The worm speed has a maximum impact on TPL, and immersion depth has minimum impact on TPL [8]. The MPS-implicit method is applied to determine the impact of immersion depth, the lubricant viscosity, rotational speed and worm arrangement on oil pressure distribution and CPL of the worm gear drive. As rotational speed increases, churning losses also increase. Churning losses are very less when worm gear is placed at the top as compared to worm gear at the bottom. Churning losses are increased with an increase in lubricant viscosity [9]. CFD software is the best tool to calculate power loss in gears and its influence parameters. Results show that power loss is proportional to the cube of velocity, linearly proportional to tooth width and significant increases with tip diameter [10]. Pin on disc setup used for calculating the correlation between

normal load, wear volume and dissipated energy [11]. Magyar and Sauer explain the method for calculating the efficiency of the worm gearbox. Along with tooth friction losses, other power losses such as oil churning, the bearings and seals power losses are considered [12].

2.5 Thermal Analysis

Sliding action in worm gearbox causes friction energy loss which converted into heat energy which raises the temperature of gearbox and also lubricating oil. An experimental investigation carried out to determine optimum working conditions for worm gearbox. Input torque required and lubricant heating time are chosen as response variables, while the type of lubricant, the volume of lubricant and speed of worm are selected as a control variable. For the three-level three-factor, the Taguchi L9 optimization technique is used [13]. FEA is to be used to analyse the thermal behaviour of the worm gearbox. In gear, at contact surface temperature is high, so gear failure sometimes occurs due to high temperature. The surface temperature of the gear tooth is carried out using finite element analysis in ANSYS [14]. For calculating the tooth, surface temperature rise of spiral bevel gear EHL and loaded tooth contact is applied and transient, and steady analysis is carried out [15]. Thermal characteristics can be improved by machine-setting parameter adjustment of spiral bevel gear, and an FEA 3D model is developed to analyse transient thermal behaviour and the frictional heat generation [16]. The temperature of the interface increases with an increase in sliding distance. Due to sliding motion, heat is generated at contact and that heat melts wear debris due to that coefficient of friction increases [17].

2.6 Oil Temperature and Viscosity

Due to temperature increases, the viscosity of oil decreases results in the performance of lubricant oil decreases. The viscosity of oil depends on many parameters. The viscosity decrement is sensitive to the nanoparticle types, the concentration of nanoparticles and temperature of fluid [18]. The viscosity of the lubricant is strongly affected by the wear. There is an inverse relationship between wear and lubricant viscosity and also wear and specific film thickness [19]. Proper lubrication in the gear drive system can decrease friction, scuffing and suppress wear and also increase torque capacity and fatigue life of the gear. Higher viscosity and EP oils provide a higher fatigue life. Gear performance such as dynamics, fatigue and mechanical efficiency highly influenced by lubricant viscosity, lubrication method and lubrication condition [20]. The lubricating oil temperature of the worm gearbox linearly increases with output torque [21]. Through the use of viscometer, the viscosity of the oil is measured, and total acid number (TAN) is measured with acid number

device. Total acid number changes due to oxidation [22]. Rise of the temperature of oil depends on oil viscosity and additives in the oil [23].

2.7 Grey Relational Analysis and ANOVA

Grey relational analysis is used to determine optimum levels of process parameters. GRA converts experimental results into equivalent grades between 0 to 1. ANOVA analysis is used to find the relative contribution of process parameters on response parameters. Minitab software is available to perform grey relational analysis and ANOVA [24–30].

3 Research and Gaps

3.1 Summary of the Literature Review

1. Importance of tribological study.
2. Materials and alternative materials for worm gearbox.
3. Ferrographic analysis of worm gearbox for preventive maintenance.
4. Maximum efficiency, compactness, vibration, thermal efficiency and weight, etc.
5. Effect of load, viscosity and speed of worm gear on wear and surface temperature rise.
6. Effect of speed, oil volume and type of oil on input torque required and oil temperature rise.
7. Cause of wear and failure mechanism.
8. CPL and TPL and its affecting parameters.
9. Process parameters and response parameters for worm gearbox.
10. Thermal analysis of spiral bevel gear.
11. Taguchi method for optimization of experiments.
12. Grey relational analysis for optimization of levels of process parameters.
13. ANOVA analysis to find the relative contribution of process parameters on response parameters.

3.2 Gaps from Literature Review

1. Many researchers worked on tribological properties of gears, but the worm drive is getting lesser attention.

2. Due to sliding motion at the interface of tooth, large heat is generated, the outcome in the temperature rise of the gearbox and also of lubricating oil, this is less attention part.
3. Less attention is given on the thermal analysis of worm gearbox.
4. Less attention to thermal behaviours of lubricating oil due to raising of temperature.
5. Due to temperature raise, thermal stresses induced in worm and worm wheel that is a less studied part.
6. Less use of finite element analysis (FEA) to analyse the worm gearbox system.

4 Methodology

4.1 Problem Definition

Worm gearbox rolling and sliding motion occur simultaneously. The sliding action creates friction energy loss that friction energy loss is mainly converted into heat energy which raises the temperature of lubricating oil of worm gearbox which reduces the performance of lubricating oil and also of worm gearbox. So to study the thermal behaviour of lubricating oil of worm gearbox is necessary to improve the performance of the worm gear drive system.

4.2 Objectives of Review Work

Objectives of the review work are as follows:

- (1) To explain the importance of thermal analysis of lubricant oil of worm gearbox.
- (2) To suggest some response parameters and process parameters to analyse the thermal behaviour of lubricant oil of worm gearbox.
- (3) To suggest Taguchi, grey relational analysis and ANOVA determine optimum levels of process parameters and their relative contribution.
- (4) To suggest the use of FEA analysis to analyse the thermal behaviour of worm gearbox and lubricant oil.

4.3 Experimental Test

To analyse the thermal behaviour of lubricant oil of worm gearbox, an experimental setup should be consist of multiple response worm gearbox with casing over it. The material used, speed reduction ratio and size of worm gearbox should be standard. A motor with variables frequency drive (VFD) is to be connected to the input shaft to rotate worm gearbox at various speeds. An oil level indicator, temperature sensors

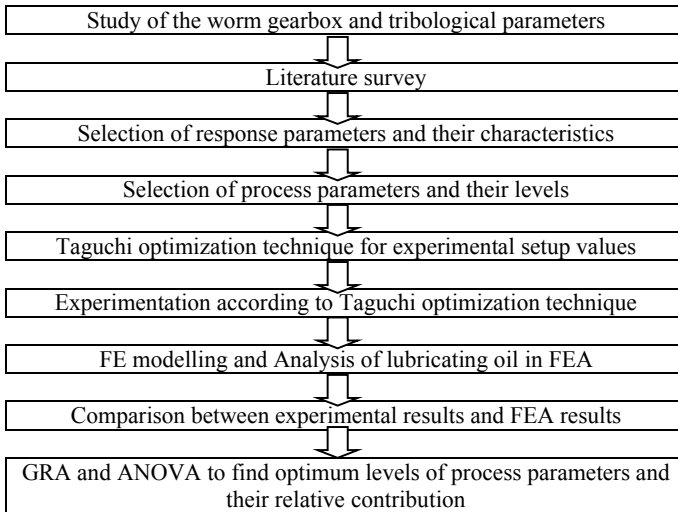


Fig. 1 Flow chart of the methodology

and torque sensors are to be used to measure response and operating parameters. The output shaft of worm gear should be connected to a load cell to indicate load on the worm wheel. Thermal analysis in ANSYS software and flow analysis in CFD software is required for simulation results. For achieving mentioned objectives, following methodology should be followed (Fig. 1).

5 Conclusion

- (1) Study of thermal behaviour of lubricant oil of worm gearbox is necessary to improve the performance of the worm gearbox.
- (2) For thermal analysis of lubricant oil of worm gearbox, lubricant oil temperature, the viscosity of lubricant oil, etc., can be considered as response parameters.
- (3) The rotational speed of worm, the geometry of gear, oil level, viscosity of the oil, type of oil, additives in the oil, load on worm wheel, clearance, worm gear position, etc., can be considered as a process parameters.
- (4) Special test rig needs to develop with temperature sensors which give response parameter readings at different process parameter at their different levels. Results obtained by experimentation can be validated with finite element analysis (FEA).
- (5) Taguchi method is used for experiments optimization. Grey relational analysis is used to determine optimum levels of process parameters, and ANOVA is used to find the relative contribution of each process parameter on the response parameter.

References

1. Holmberg K, Erdemir A (2017) Influence of tribology on global energy consumption, costs and emissions. *Friction* 5(3):263–284
2. Dr. BABIC (2001) Nature of the tribology—maintenance relation. *Tribol Ind* 23(1 and 2)
3. Fontanari V et al (2013) Tribological behavior of the bronze–steel pair for worm gearing. *Wear* 302(1):1520–1527
4. Fontanari V et al (2016) Investigation of the lubricated wear behaviour of ductile cast iron and quenched and tempered alloy steel for possible use in worm gearing. *Wear* 350:68–73
5. Benedetti M et al (2017) Investigation of lubricated rolling sliding behaviour of WC/C, WC/C-CrN, DLC based coatings and plasma nitriding of steel for possible use in worm gearing. *Wear* 378:106–113
6. Magyar B, Sauer B (2015) Calculation of the efficiency of worm gear drives.
7. Thyla PR, Rudramoorthy R (2004) Investigations on gear tooth surface and bulk temperatures using ANSYS. PSG College of Technology, Coimbatore
8. Singh RN, Vanalkar AV (2012) Analysis of wear phenomena in sliding contact surfaces. *Int J Eng Res Appl (IJERA)* ISSN: 2248-9622
9. Al-Bender F, De Moerlooze K (2011) Characterization and modeling of friction and wear: an overview. *Sustain Construct Des* 2(1)
10. Chothani HG, Maniya KD (2020) Experimental investigation of churning power loss of single start worm gear drive through optimization technique. In: *Materials today: proceedings*
11. Deng X et al (2020) A combined experimental and computational study of lubrication mechanism of high precision reducer adopting a worm gear drive with complicated space surface contact. *Tribol Int* 146:106261
12. Palanikumar P et al (2019) Effect of sliding speed and rise in temperature at the contact interface on coefficient of friction during full sliding of SS304. In: *Materials today: proceedings*
13. Chothani HG, Maniya KD (2019) Determination of optimum working parameters for multiple response characteristics of worm gear box. *Int J Recent Technol Eng (IJRTE)* 8(3). ISSN: 2277-3878
14. . Bhat JS, Sonawane BU (2019) Analysis of wear particles in lubricating oil of worm gearbox using ferrography. *Manuf Technol Today* 18(5)
15. Pei X et al (2019) Surface topography and friction coefficient evolution during sliding wear in a mixed lubricated rolling-sliding contact. *Tribol Int* 137:303–312
16. Liu H, Liu H, Zhu C, Parker RG (2020) Effects of lubrication on gear performance: a review. *Mech Mach Theory* 145:10370
17. Krantz TL, Kahraman A (2004) An experimental investigation of the influence of the lubricant viscosity and additives on gear wear. *Tribol Trans* 47(1):138–148
18. Gorla C, Concli F, Stahl K, Höhn BR, Michaelis K, Schultzeiß H, Stemplinger JP (2013) Hydraulic losses of a gearbox: CFD analysis and experiments. *Tribol Int* 66:337–344
19. Tica M, Miltenović D, Banić M, Miltenović A (2017) Permissible temperatures and thermal stability of worm gears. *Annals Faculty Eng Hunedoara* 15(3):61
20. Bhat JS, Sonawane BU (2018) Evaluation of performance deterioration of the used equipment oil in sliding pair. *Int J Res Advent Technol* 6(8):2061–2066
21. Desai MR, Bhat JS, Sonawane BU (2019) Review on tribological modelling of worm gear
22. Zhang J-g, Liu S-J, Fang Te (2017) Determination of surface temperature rise with the coupled thermo-elasto-hydrodynamic analysis of spiral bevel gears. *Appl Therm Eng* 124:494–503
23. Wang Y et al (2019) Investigation into the meshing friction heat generation and transient thermal characteristics of spiral bevel gears. *Appl Thermal Eng* 119:245–253
24. Sharif KJ et al (2001) Contact and elasto-hydrodynamic analysis of worm gears part 1: theoretical formulation. *Proc Inst Mech Eng Part C J Mech Eng Sci* 215:817
25. Perumal S, Udaya Prakash J (2016) Multi-objective optimization of tribological parameters of hybrid composites using grey relational analysis. *Int J Chem Sci* 14(2):1172–1182
26. Mahajan VN, Nikalje AM, Patil YS (2017) Influence of parameters and wear analysis of aluminium-bronze (CuAl. *Indian J Sci Technol* 10:27

27. Yunus M, Alsoufi MS (2016) Multi-output optimization of tribological characteristics control factors of thermally sprayed industrial ceramic coatings using hybrid Taguchi-grey relation analysis. *Friction* 4(3):208–216
28. Hasani H, Tabatabaei SA, Amiri G (2012) Grey relational analysis to determine the optimum process parameters for open-end spinning yarns. *J Eng Fibers Fabr* 7(2):155892501200700220
29. Pathan F, Gurav H, Gujrathi S (2016) Optimization for tribological properties of glass fiber-reinforced PTFE composites with grey relational analysis. *J Mater*
30. Mishra P, Kumar AKV, Srivastava RK (2014) Optimization of tribological performance of Al-6061T6–15% SiCp-15% Al₂O₃ hybrid metal matrix composites using Taguchi method and grey relational analysis. *J Min Materials Charact Eng*

Prediction and Modelling of Nodal Temperature in Turning Operation



Rishish Mishra, Vineet Dubey, Rabesh Kumar Singh,
and Anuj Kumar Sharma

Abstract Accurate temperature determination of the tool tip, rake face and the flank face during the machining operation has always been topic of interest among the researchers. Computational fluid dynamics and the MATLAB have been used as a tool to determine the temperature distribution on the carbide tool insert during different machining environments. In the present work, four conditions, namely dry cutting with different boundary conditions, flooded water cooling and the mist flow environment have been considered in turning. Computer-aided design of tool insert, mesh generation and the solution the several governing equations has been performed by using ANSYS fluent solver. The prediction model developed to compute the temperature across the profile through different numerical equations. Furthermore the simulated data have also been verified through experimental validation, and the variation of 25–35% has been observed, in different cases. A comparison has also been drawn from the obtained result to analyse the better cooling environment.

Keywords Nodal temperature · CFD · Turning · Cutting tool · Machining

1 Introduction

The ever increasing demand rate and need for precision had put a huge load on the manufacturing industries and the machine operators. Industrialization with its every next version seeks updating from the previous shortcomings. The twenty-first century marked itself as the industrial revolution 4.0, every bit is automated, and it is not only because of meeting daily manufacturer's demand, but also to be precise in its deliverance of product. Conventional machining process involves a direct contact between the tool and work piece which causes the plastic deformation with increase in shear strain and the frictional losses that result to heat generation on the tool insert. Heat generation becomes a major concern when the machining is performed with high speed and on tougher materials, high rate of heat generation with improper heat

R. Mishra · V. Dubey · R. K. Singh (✉) · A. K. Sharma
Mechatronics, Centre for Advanced Studies, Dr. A.P.J. Abdul Kalam Technical University,
Lucknow 226031, India

© The Author(s), under exclusive license to Springer Nature Singapore Pte Ltd. 2022
K. Govindan et al. (eds.), *Advances in Mechanical and Materials Technology*,
Lecture Notes in Mechanical Engineering,
https://doi.org/10.1007/978-981-16-2794-1_101

1163

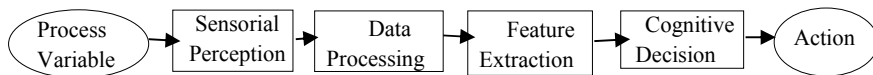


Fig. 1 Process of temperature monitoring technique

disposal may lead to tool wear, shorter tool life and inferior quality of surface finish [1, 2]. Flank and the rake face of the tool insert are the main areas of concern, because of its susceptibility to high temperature. Process variables such as cutting force, torque, temperature, and acoustic emission have been used in the past to monitor the conventional machining process.

In order to develop an online tool wear monitoring system, several different approaches are made. Teti et al. [3] have described it in a direct and indirect tool wear measurement technique. The direct techniques use cameras, radioactive isotopes and laser-beams, while the indirect techniques use sensorial perception using process variables as shown in Fig. 1, such as temperature, acoustics, noise, vibration, cutting forces and strains [4–6]. Research suggests that the direct techniques are comparatively more accurate but only limited to laboratory findings, while the indirect techniques can be of broad industrial applications. The advanced tool monitoring systems have also been reported that uses perceptron learning, ANN, fuzzy logic and image processing [7–10]. The only problem reported with these advanced monitoring techniques is the requirement of separate endeavour of knowledge to execute it, which generally a conventional machining operator lags in.

Among these various factors, cutting temperature has been considered as a perfect variable for control reason, as a result of its connection with tool wear [2]. Takeyama and Murata [11] in their investigation on tool wear have given a relationship between the mechanical wear, and the absolute temperature generated during machining operation as discussed in Eq. 1. The research done by Takeyama and Murata clearly shows the evidence of temperature monitoring to determine the tool wear.

$$w = e^{\left[\frac{-Q}{K\theta}\right]} \tag{1}$$

where w is mechanical wear, Q is activation energy, K is a constant and θ is absolute temperature at cutting edge.

During turning operation tool tip, the work piece is the prime interface for study in a research topic, and there has always been a debate on the methods and methodology to determine the tool tip temperature. In order to find this, we need to first understand why it is very difficult to determine tool tip temperature. Sharma et al. [2] provide insight to that, by stating the nature of contact between tool and work piece in conventional machining operation, which is in constant continuous relative motion. Abukhshim et al. [1] elaborate about high strains, high localised temperature and pressure, and it also discusses on narrow shear bands and about chip obstacles.

Furthermore, the surge in temperature causes the tool wear, and hence, researchers have understood the necessity of cutting fluid in machining operations. Several researches have been conducted with time to determine the need and influence of

cutting fluid on tool wear, which urges the need of cutting fluid to overcome the limitations posed by dry machining operations [1, 2, 15–17]. In order to enhance the heat dissipation, properties of conventional cutting fluid researchers have incorporated the use of hybrid nanofluid [13, 14]. Taylor [18] was the first to use water as cutting fluid and reported an increase in the cutting speed by 40%. Further he suggested that during machining operation, the basic need is to improve the tribological properties of finished workpiece.

Researchers in past history have been working on the different methodologies to determine the temperature distribution over the tool insert by using thermal or mathematical modelling. The evidence for same can be sought from different literature of Parveiza [15–17] and Sharma [2] with experimental validations. Scientific innovations, numerical modelling and the ability to solve the higher order differential equation by using software solvers have been a popular trend among the scientific community. This merely because of economic aspects that prevent a huge initial investment cost to set up the machinery, and also, it provides an opportunity to do multiple iterations without creating any newer setups. Hence, the following study has also been conducted using ANSYS CFD fluent solver to determine and predict the thermal behaviour of tool insert in turning operation under different fluid flow environments.

2 Methodology

2.1 *Experimental Setup*

The proposed methodology in complies turning operation with a tungsten carbide tool insert on a steel 304 AISI work piece, which is subjected to different flow condition of cutting fluid. A carbide tool insert with a tool holder has been bolted together, and a blind hole of diameter 1.6 mm is drilled inside, through the electron discharge machining operation because a carbide tool is very hard to get drilled by any conventional machining operation. A MI k-type thermocouple of sheath diameter 1.5 mm is silver brazed inside the drilled hole up to the 2 mm distance from the rake profile of tool insert. Major findings from the literature survey support that the k-type thermocouple's range would be enough to determine the maximum temperature. The embedded thermocouple is at a 2 mm distance apart from the tool tip. A National Instruments USB-TC01 data acquisition system has been used along with a computer (shown in Fig. 2.) to record the nodal temperature of tool insert. A conventional lathe machine has been used to perform the turning operation.

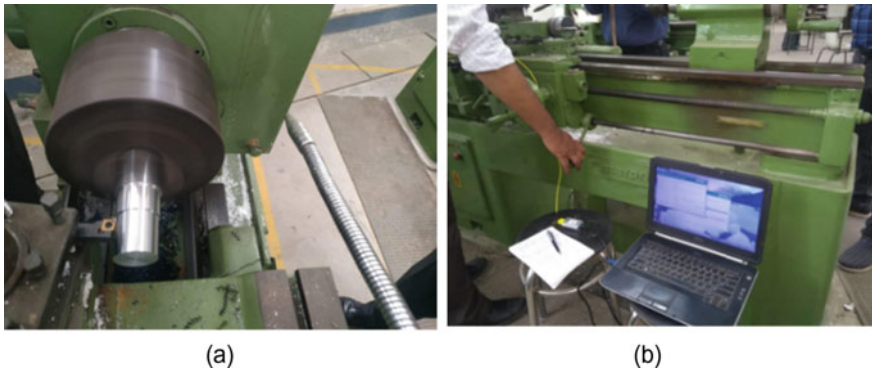


Fig. 2 **a** Turning in dry conditions, **b** complete machine setup

2.2 Thermal Modelling and Simulation

The tool insert designated as CCMT090304 is designed on SOLIDWORKS software by using WIDIA catalogue [19]. The designed tool insert geometry is then imported into the fluent solver by appointing a constant heat source at the tool tip by calculating the cutting force of 160 N at depth of cut 0.9 mm, feed rate 0.12 mm/rev and cutting velocity 90 m/min.

The heat generated is introduced, and a constant heat generation source that has been appointed over the node is shown in Fig. 3a, and the thermal simulation has been performed under the following four different machining condition as discussed in Table 1.

3 Mathematical Modelling

MATLAB 2016b software has been used to perform the mathematical modelling of the temperature profile. The temperature distribution data of simulated results

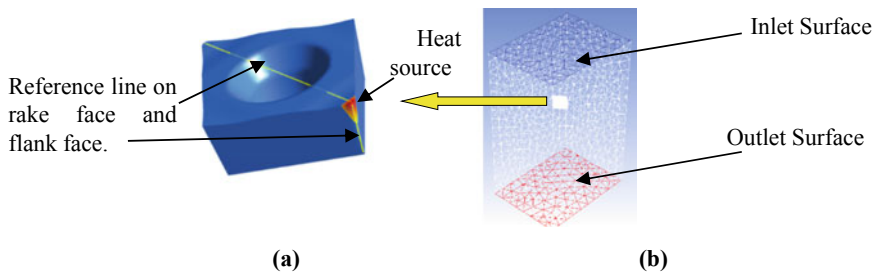


Fig. 3 **a** CAD geometry of tool insert, **b** Enclosure creation around tool insert

Table 1 Different environmental conditions used in simulation

Conditions	Environment
Condition—1	Dry machining (air as surrounding media with 0 m/s inlet velocity)
Condition—2	Machining under air cooling with inlet velocity of 26 m/s
Condition—3	Flooded machining (water as surrounding media with 26 m/s inlet velocity)
Condition—4	Multiphase mist machining (mixture of water droplet and air as with 26 m/s inlet velocity)

Table 2 Thermo physical properties of carbide tool insert [20, 21]

Properties	Value	Unit
Density	15,000	kg/m ³
Specific heat	480	j/kg k
Thermal conductivity	110	w/m k

along the reference line, shown in Fig. 3a, have been imported from CFD thermal modelling done on ANSYS 19.2 fluent solver. An enclosure has been created around the tool inset with inlet and outlet surfaces for fluid flow as shown in Fig. 3b. A controlled mesh has been generated with around 282,354 meshing elements and maintaining the minimum orthogonal quality at 0.263. Furthermore the continuity, energy and momentum conservation equations have been taken care of while solving in the CFD fluent solver. The thermo physical property of tungsten carbide has also been imported in solver as mentioned in Table 2. The literature survey supports the implementation of $k-\omega$ shear stress transport (SST) turbulence model for such boundary conditions [2], and same has been used in this study. The root mean square (RMS) errors have also been calculated to determine the accuracy of our predicted model to the simulated model.

4 Results and Discussion

Every graph plotted in this section explains the temperature profile distribution along a reference line, shown in Fig. 3a, drawn on the rake and flank face of tool insert.

4.1 Dry Machining (Air as Surrounding Media with 0 m/s Inlet Velocity)

The temperature distribution pattern is uneven on the rake face, so the mathematical modelling demands a higher degree polynomial equation. It has found through a

number of iterations that the 12th degree of polynomial with reported RMS value 71.935.

The predicted mathematical equation of temperature profile for rake face shown in Fig. 4a along the reference line with the distance(x) is:

$$\begin{aligned}
 t_x = & 119x^{12} - 49x^{11} - 1332x^{10} + 350x^9 + 5624x^8 - 1001x^7 \\
 & - 10856x^6 + 1185x^5 + 8978x^4 - 466x^3 \\
 & - 1786x^2 + 37x^1 + 344
 \end{aligned}
 \tag{2}$$

The predicted mathematical equation as shown in Fig. 4b of temperature profile on the reference line drawn across the flank face with distance(x) is:

$$t_x = -15.9x^4 + 0.5x^3 + 97.1x^2 + 135.9x^1 + 1151.3
 \tag{3}$$

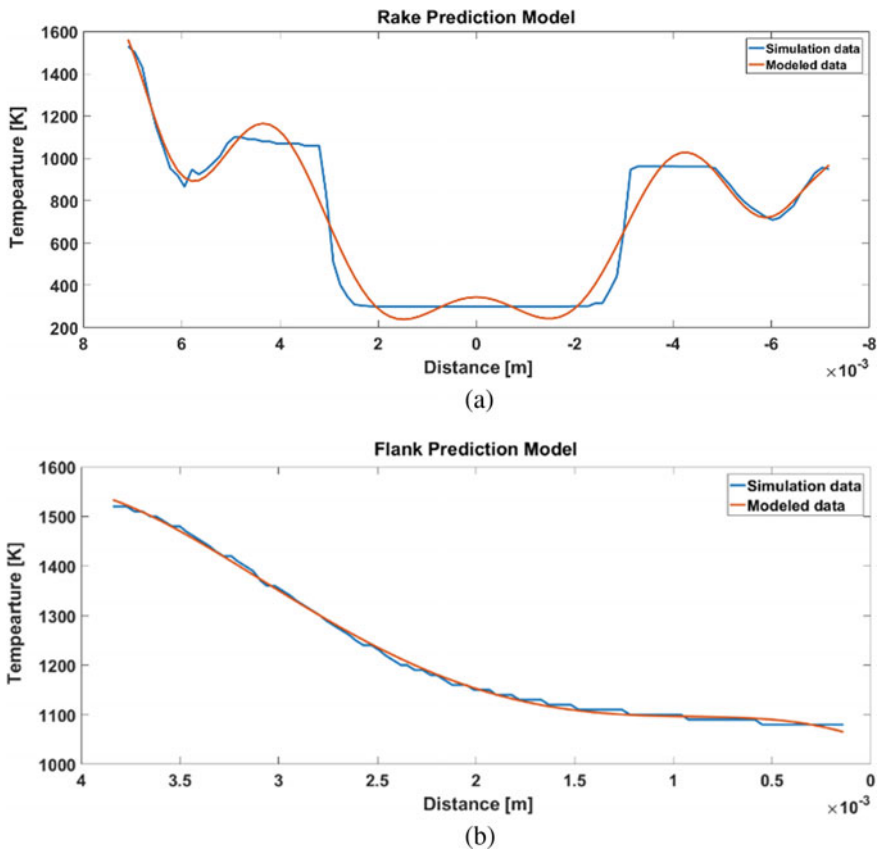


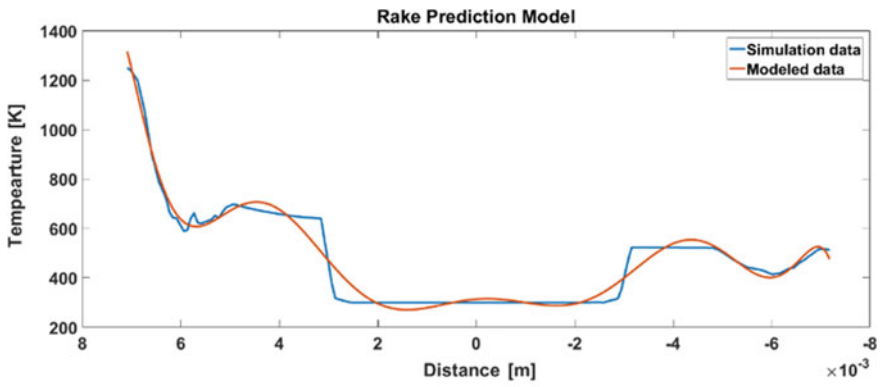
Fig. 4 Temperature prediction model for a rake face, b flank face, under dry machining conditions

And the reported RMS value is 6.1253.

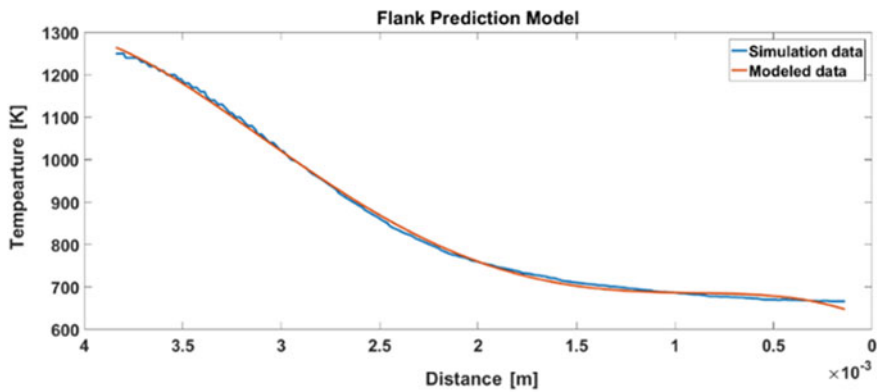
4.2 Machining Under Air Cooling with Inlet Velocity of 26 m/s

The predicted mathematical equation of temperature profile for rake face as shown in Fig. 5a along the reference line with the distance(x) is:

$$t_x = -130.2x^{10} + 7.6x^9 + 1013.7x^8 + 4.1x^7 - 2672.4x^6 - 123.0x^5 + 2665.8x^4 + 231.8x^3 - 571.3x^2 - 51.4x^1 + 314 \tag{4}$$



(a)



(b)

Fig. 5 Model prediction for a rake face, b flank face under air cooling with 26 m/s inlet velocity

The root mean square error value of the predicted model is 35.54.

The predicted mathematical equation of temperature profile of flank face as shown in Fig. 5b along the reference line with the distance(x) is

$$t_x = -19.91x^4 + 0.827x^3 + 125.93x^2 + 177.204x^1 + 757.883 \quad (5)$$

The root mean square error value of the predicted model is 7.0086.

4.3 Flooded Machining (Water as Surrounding Media with 26 m/s Inlet Velocity)

The graph plotted in Fig. 6a that is for the reference line drawn on rake profile. The temperature distribution in this condition is comparatively less uneven as reported in previous case, so the mathematical model of 5th order polynomial equation does well with the RMS value.

$$t_x = 12.913x^5 + 14.242x^4 - 28.299x^3 - 22.982x^2 + 12.232x^1 + 304.25 \quad (6)$$

The root mean square error value of the predicted model is 7.9186.

The predicted mathematical equation of temperature profile for flank face as shown in Fig. 6b along the reference line with the distance(x) is

$$t_x = -7.733x^4 + 4.84x^3 + 48.59x^2 + 39.081x^1 + 306.527 \quad (7)$$

The root mean square error value of the predicted model is: 4.389.

4.4 Multiphase Mist Machining (Mixture of Water Droplet and Air as with 26 m/s Inlet Velocity)

In the fourth condition, 0.5 volume by fraction of water droplets of diameter 10^{-5} m is mixed in continuous air phase, at an inlet speed of 26 m/s. So, a higher degree polynomial equation will be required to monitor the temperature distribution over the reference line drawn on rake profile as shown in Fig. 7a. The determined equation of 7th degree polynomial is selected, and the reported RMS value for the predicted model is 13.4137.

$$t_x = 29.81x^7 + 25.654x^6 - 121.126x^5 - 83.864x^4 + 157.76x^3 + 93.37x^2 - 36.671x^1 + 290.603 \quad (8)$$

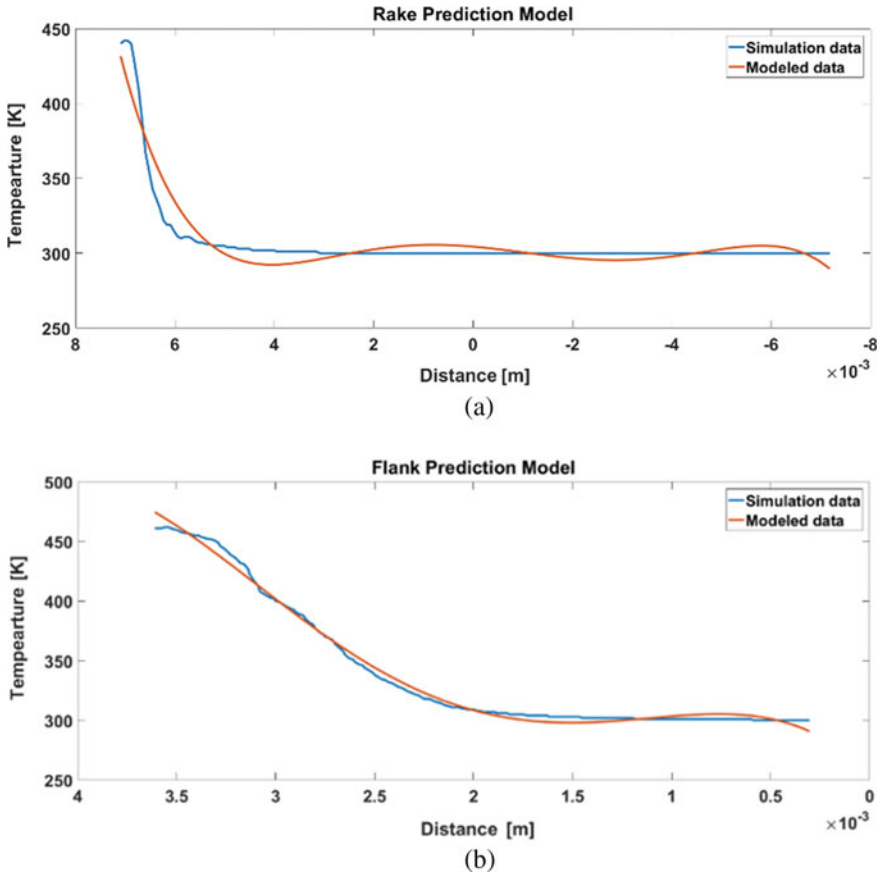


Fig. 6 Model prediction for **a** rake face, **b** flank face under flooded water cooling with 26 m/s inlet velocity

The predicted mathematical equation of temperature profile of flank face as shown in Fig. 7b along the reference line with the distance(x) is:

$$t_x = -15.723x^4 + 4.263x^3 + 105.033x^2 + 133.693x^1 + 422.983 \quad (9)$$

The reported RMS value is 6.56.

It can be clearly observed from the research that the different cutting fluid flow environments provide a distinct temperature distribution over the rake and flank face of tool insert. The nature of rake profile temperature distribution as shown in Figs. 4a and 5a is different in symmetry with the rest of rake profile curves, and this is because of slow heat dissipation rate in case of dry and air cooling. The reported maximum temperature in dry machining environment is comparatively very high as compared to other cases as water and mist cooling condition. The practical validation results,

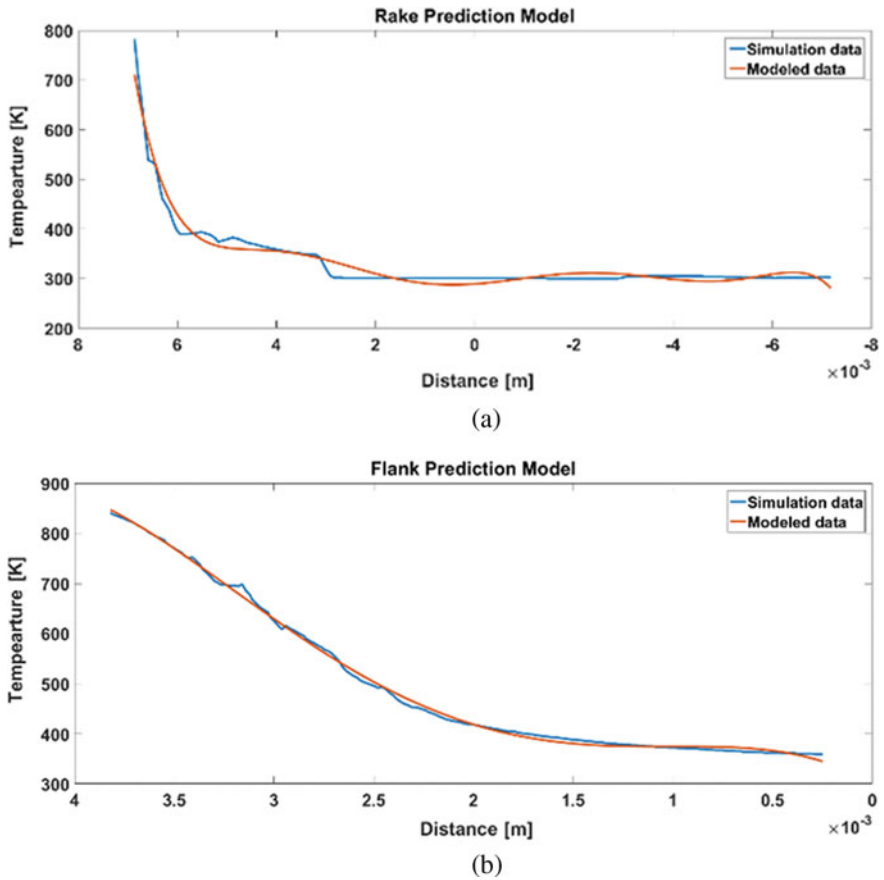


Fig. 7 Model prediction for a rake face, b flank face under mist condition with 26 m/s inlet velocity

as shown in Fig. 8, for conditions 1 to 4 gives the deviation of 29.2%, 32%, 25%, and 35% respectively, to the simulated results, which might be because of factors affecting the workshop machining conditions and other manual factors, including the positioning of thermocouple.

5 Conclusions

- The results provide enough evidence to the fact that the temperature generation and distribution is lowest in the case of flooded water cutting fluid environment.
- The result obtained from CFD simulation complies closely with the experimental data.

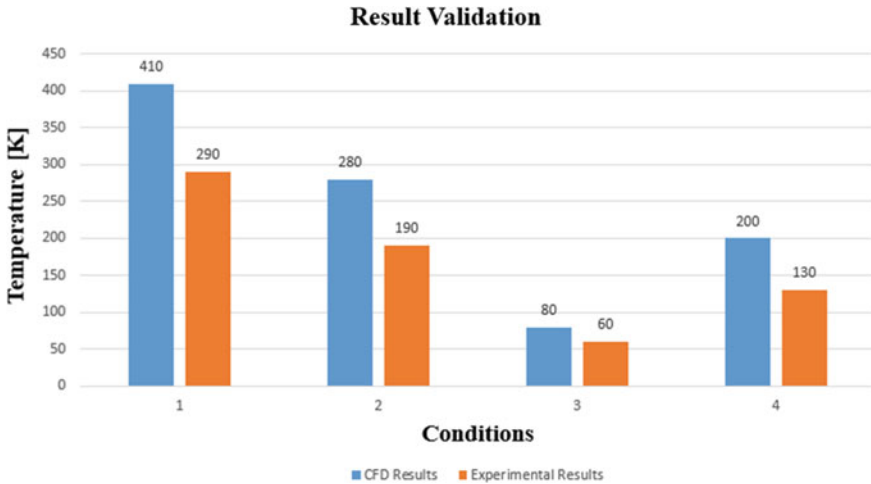


Fig. 8 Comparison of CFD and experimental values of nodal temperatures during turning at 2 mm distance from the rake face

- It is also reported that mist flow cutting fluid environment gives approximately the same heat distribution as reported in flooded water environment which reduces the wastage of cutting fluid.

Acknowledgements The authors wish to express their gratitude to the Dr. A.P.J.Abdul Kalam Technical University Uttar Pradesh, Lucknow for the financial assistance provided to this study under Visvesvaraya Research Promotion Scheme (VRPS), letter no. Ref.: Dr.APJAKTU/Dean-PGSR/2019/4236-46/5109 dated 8th June 2019.

References

1. Abukhshim NA, Mativenga PT, Sheikh MA (2006) Heat generation and temperature prediction in metal cutting: a review and implications for high speed machining. *Int J Mach Tools Manuf* 46(7–8):782–800
2. Sharma AK, Tiwari AK, Dixit AR (2016) Effects of Minimum Quantity Lubrication (MQL) in machining processes using conventional and nanofluid based cutting fluids: A comprehensive review. *J Clean Prod* 127:1–18
3. Teti R, Jemielniak K, O’Donnell G, Dornfeld D (2010) Advanced monitoring of machining operations. *CIRP Ann* 59(2):717–739
4. Hundt W, Leuenberger D, Rehsteiner F (1994) An approach to monitoring of the grinding process using acoustic emission techniques. *CIRP Ann* 43(1):295–298
5. Rogers LM (1979) The application of vibration analysis and acoustic emission source location to on-line condition monitoring of anti-friction bearings. *Tribol Int*, 51–59
6. Inasaki I (1998) Application of acoustic emission sensor for monitoring machining processes. *Ultrasonics* 36:273–281

7. Achichea S, Balazinski M, Baron L, Jemielniak K (2002) Tool wear monitoring using genetically-generated, fuzzy knowledge bases. *Eng Appl Artif Intell* 15:303–314
8. Kuo RJ, Cohen PH (1999) Multi-sensor integration for on-line tool wear estimation through radial basis function networks and fuzzy neural network. *Neural Netw* 12(2):355–370
9. Axinte D (2006) Approach into the use of probabilistic neural networks for automated classification of tool malfunctions in broaching. *Int J Mach Tools Manuf* 46(12–13):1445–1448
10. Mohanta N, Singh RK, Sharma AK (2020) Online monitoring system for tool wear and fault prediction using artificial intelligence. In: 2020 international conference on contemporary computing and applications (IC3A). IEEE, pp 310–314
11. Takeyama, H., & Murata, R.: Basic investigation of tool wear (1963).
12. Sharma, A. K., Singh, R. K., Dixit, A. R., Tiwari, A. K., & Singh, M. An investigation on tool flank wear using Alumina/MoS₂ hybrid nanofluid in turning operation. In *Advances in Manufacturing Engineering and Materials* (pp. 213–219). Springer, Cham (2019).
13. Singh RK, Sharma AK, Mandal V, Gaurav K, Sharma A, Kumar A, Dixit AR, Mandal A, Das AK (2018) Effect of multi-walled carbon nanotubes based nanofluid on surface roughness and cutting temperature in turning operation using minimum quantity lubrication. In: International conference on mechanical, materials and renewable energy, vol 377, p 012017
14. Singh RK, Dixit AR, Sharma AK, Tiwari AK, Mandal V, Pramanik A (2018) Influence of graphene and multi-walled carbon nanotube additives on tribological behaviour of lubricants. *Int J Surf Sci Eng* 12(3):207–227
15. Pervaiz S, Deiab I, Wahba E, Rashid A, Nicolescu CM (2015) A novel numerical modeling approach to determine the temperature distribution in the cutting tool using conjugate heat transfer (CHT) analysis. *The International Journal of Advanced Manufacturing Technology* 80(5–8):1039–1047
16. Pervaiz S, Deiab I, Wahba EM, Rashid A, Nicolescu M (2014) A coupled FE and CFD approach to predict the cutting tool temperature profile in machining. *Procedia CIRP* 17:750–754
17. Pervaiz S, Deiab I, Wahba E, Rashid A, Nicolescu M (2018) A numerical and experimental study to investigate convective heat transfer and associated cutting temperature distribution in single point turning. *Int J Adv Manuf Technol* 94(1–4):897–910
18. Taylor FW (1907) On the art of metal cutting. *Trans ASME* 28:31–35
19. ISO CCMT 090304TN2000 Widiacatalog
20. Gopal AV, Rao PV (2003) Selection of optimum conditions for maximum material removal rate with surface finish and damage as constraints in SiC grinding. *Int J Mach Tool Manu* 43:1327–1336
21. <http://www.matweb.com/search/DataSheet.aspx?>

Sensitivity of Al/Mg/Ti/Cu/SiC Hybrid Composite to Static Loads



Kumar Prakash and N. K. Singh

Abstract Aluminium hybrid composites are widely used for lightweight and crash-worthy structures due to their improved mechanical and tribological properties. Therefore, it is necessary to investigate the deformation behaviour of these composites for enhancing the performance of their structures while in service. In this paper, an experimental investigation on the strain rate sensitivity of the newly developed aluminium hybrid composite (Al–2Mg–1.5Ti–1Cu–5SiC) through the stir casting process is presented under quasi-static compressive ($0.001\text{--}0.1\text{ s}^{-1}$) and bending/flexural ($1\text{--}100\text{ mm/min}$) loads. Different mechanical tests (compression and three-point bending) are carried out on universal testing machine at low strain rates/speeds. Effects of geometry and heat treatment of specimens are also observed under compression. Johnson–Cook material model predicts the flow stress of the composite under compression well as compared to the experimental results.

Keywords Aluminium hybrid composites · Strain rate sensitivity · Material model · Compression and bending

1 Introduction

The growing demand of aluminium hybrid composites (AHCs) in automobile, aerospace, marine and defence sectors due to high strength-to-weight ratio, high specific stiffness, superior damping capacities, good corrosion and wear resistance, low coefficient thermal expansion and high thermal/electrical conductivity attracts the researchers to investigate their mechanical characteristics for structural design and its mass production. Aluminium hybrid composites are prepared using aluminium alloy as a matrix reinforced with the particles of SiC, Al_2O_3 , SiO_2 , B_4C , BN, etc. Several researchers [1–5] fabricated the composites using varying compositions of

K. Prakash (✉) · N. K. Singh

Department of Mechanical Engineering, National Institute of Technology Patna, Patna, India

N. K. Singh

e-mail: nilambersingh@nitp.ac.in

organic/inorganic particulate reinforcements and investigated the mechanical and tribological properties. Alidokht et al. [6] evaluated wear properties of friction stir-processed cast aluminium alloy, whereas Tang et al. [7] observed the influence of temperatures (250–450 °C) and loading rates ($0.001\text{--}1\text{ s}^{-1}$) on the composites. Effects of machining parameters on AHCs are presented by Rasagopal et al. [8]. Ramadoss et al. [9] studied the hybrid composites (Al7075 + B₄C + BN) for marine applications. Gowrishankar et al. [10] found increased hardness (50–80%) and tensile strength (40–50%) in the as-cast composites by reinforcing SiC and B₄C as compared to aluminium alloy. Some discussion on mechanical [11–16] and wear [17–19] responses of AHCs is available in the published paper. Both the mechanical and tribological behaviours of the composites are presented by a number of researchers [20–23]. However, there are lots of variations in these properties of the composites in the available literature. Therefore, in this paper, the authors investigated the strain rate sensitivity of the stress–strain behaviour of the aluminium hybrid composite developed by stir casting route under compression and three-point bending. Effects of geometry and heat treatment are observed under compression. It is found that the composite is sensitive to the loading rates under compressive and bending loads. The material parameters of Johnson–Cook model are evaluated by curve fitting method based on experimental data.

2 Experiments

The experimental set-up (universal testing machine, Zwick Roell, 250 kN) used to test the composites under quasi-static compressive and flexural (three-point bending) loads is shown in Fig. 1a, b, respectively.

The composite is developed through stir casting process in which LM6 aluminium alloy (Al: 85.95, in weight %) is matrix and dried powders (99% purity level) of Mg, Ti, Cu and SiC are particulate reinforcements in the ratio 2:1.5:1:5. The particle size of Mg, Ti or SiC is 60 μm, whereas the particle size of Cu powder is 100 μm. For compressive tests, the cylindrical specimens (Fig. 1c) of lengths (L) 5 mm, 10 mm and 15 mm are prepared for the diameter (D) 10 mm. Flexural specimens (Fig. 1d) of size 120 mm × 10 mm × 4 mm are used for three-point bending tests at different cross head speeds (1 mm/min, 10 mm/min, 100 mm/min). During bending tests, the flexural specimen is placed on two hemispherical supports of 25 mm radius each, while the radius of indenter is 10 mm.

3 Results and Discussion

Specimens of aluminium hybrid composite are tested at different loading rates under compression and flexure. The obtained experimental data are analysed, and then stress–strain curves are plotted to study the deformation behaviour of the composite

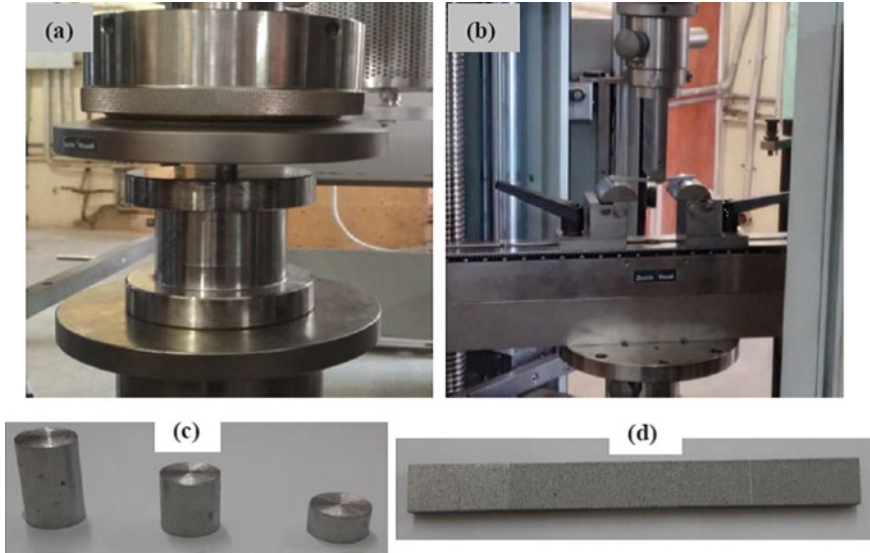


Fig. 1 Quasi-static tests **a** under compression, **b** under three-point bending, **c** compressive specimens and **d** flexural specimens

under various loading rates. Yield strength (Y.S.) is considered as 0.2% of strain. Experiment at each strain rate/speed is repeated 3 times to check the closeness of experimental data. True stress and true strain under compression and bending loads are evaluated from Eqs. (1) and (2), respectively [24, 25].

$$\text{For compression: } \sigma_T = (1 - \varepsilon_s) \text{ and } \varepsilon_T = -\ln(1 - \varepsilon_s) \quad (1)$$

$$\text{For flexure: } \sigma_T = (1 + \varepsilon_s) \text{ and } \varepsilon_T = \ln(1 + \varepsilon_s) \quad (2)$$

3.1 Strain Rate Sensitivity Under Compression

It is observed that on increasing loading rate ($0.001\text{--}0.1 \text{ s}^{-1}$) at L/D ratio 1 (Fig. 2a), the dissipation energy increases. On increasing L/D ratio, the yield strength/ultimate compressive strength decreases while malleability increases as shown in Fig. 2b. The decreased true ultimate compressive strength (U.C.S.) at 0.1 s^{-1} is due to large strain (Eq. 1) induced in the specimen. The compressive specimens of L/D ratios 1 and 1.5 are fractured, whereas the specimen at L/D ratio 0.5 is not fractured; however, some cracks are observed at the edge and on curved surface at strain rate 0.1 s^{-1} . Experimental results of the compression tests under different loading conditions are presented in Table 1.

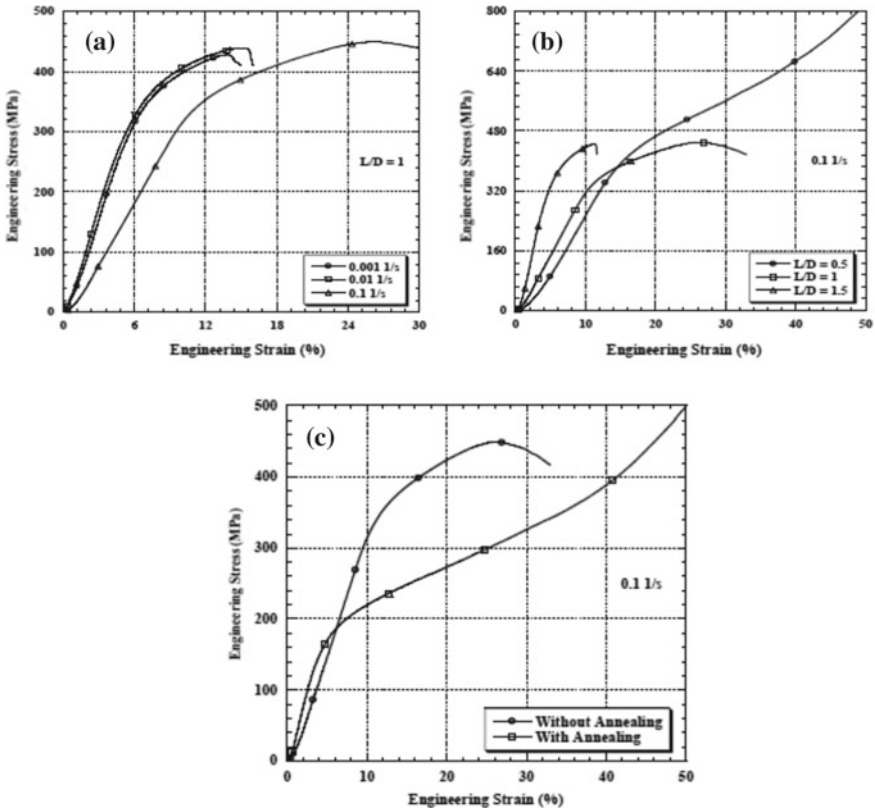


Fig. 2 Compression tests **a** at different strain rates, **b** at different L/D ratios and **c** with and without annealing

Figure 2c shows that after annealing, flow stress decreases but malleability (compression) increases. The deformed specimens under various strain rates, L/D ratios and annealed conditions are shown in Fig. 3.

3.1.1 Material Model

The Johnson–Cook model evaluated in this work is as below [25]:

$$\sigma = [A + B\varepsilon^n] \cdot [1 + C \ln \dot{\varepsilon}^*]$$

The material parameters are determined based on experimental results under compression using curve fitting method.

$$A = 258 \text{ MPa}, B = 1387.1 \text{ MPa}, n = 1.2101, C = 0.00088746(\text{at } 0.01 \text{ s}^{-1})$$

Table 1 Experimental results under compression tests

Conditions	L/D ratio	Strain rate (s^{-1})	Engineering stress-strain			Compressive toughness (MI/m^3)	True stress-strain		
			Y.S. (MPa)	U.C.S (MPa)	Compression (%)		Y.S. (MPa)	U.C.S (MPa)	
Room temperature	0.5	0.1	343 ± 3	667 ± 6 (up to 40% compression)	Not fractured	161 ± 2 (up to 40% compression)	299 ± 3	400 ± 5 (up to 40% compression)	
			0.001	271 ± 3	428 ± 3	15 ± 0.5	44 ± 1	258 ± 2	369 ± 3
			0.01	268 ± 2	439 ± 4	16 ± 0.6	50 ± 1	255 ± 2	373 ± 4
Annealing	1	0.1	319 ± 3	450 ± 5	33 ± 0.5	110 ± 1.5	286 ± 3	332 ± 3	
		0.1	280 ± 2	445 ± 3	11 ± 0.5	34 ± 0.5	268 ± 2	395 ± 3	
Annealing	1	0.1	125 ± 2	389 ± 3 (up to 40% compression)	Not fractured	105 ± 1.5 (up to 40% compression)	121 ± 2	233 ± 3 (up to 40% compression)	
			0.1	125 ± 2	389 ± 3 (up to 40% compression)	Not fractured	105 ± 1.5 (up to 40% compression)	121 ± 2	233 ± 3 (up to 40% compression)

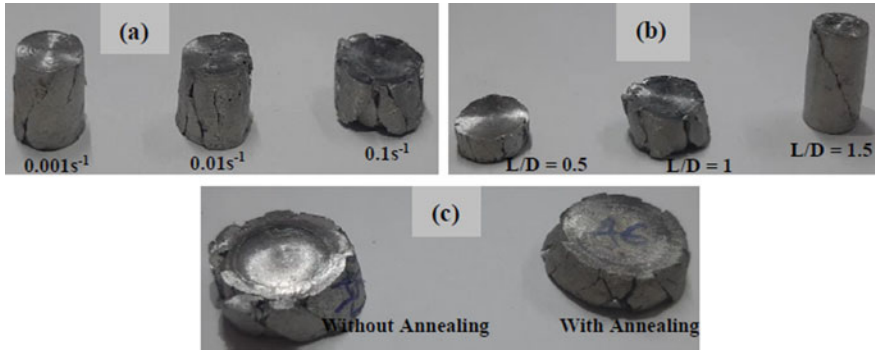


Fig. 3 Deformed specimens **a** at different strain rates, **b** at different L/D ratios and **c** with and without annealing

and $C = -0.062188$ (at 0.1 s^{-1}).

The negative value of “ C ” parameter at 0.1 s^{-1} is due to more crushing of the specimen. Figure 4 shows the comparison of the predicted results with the experimental results.

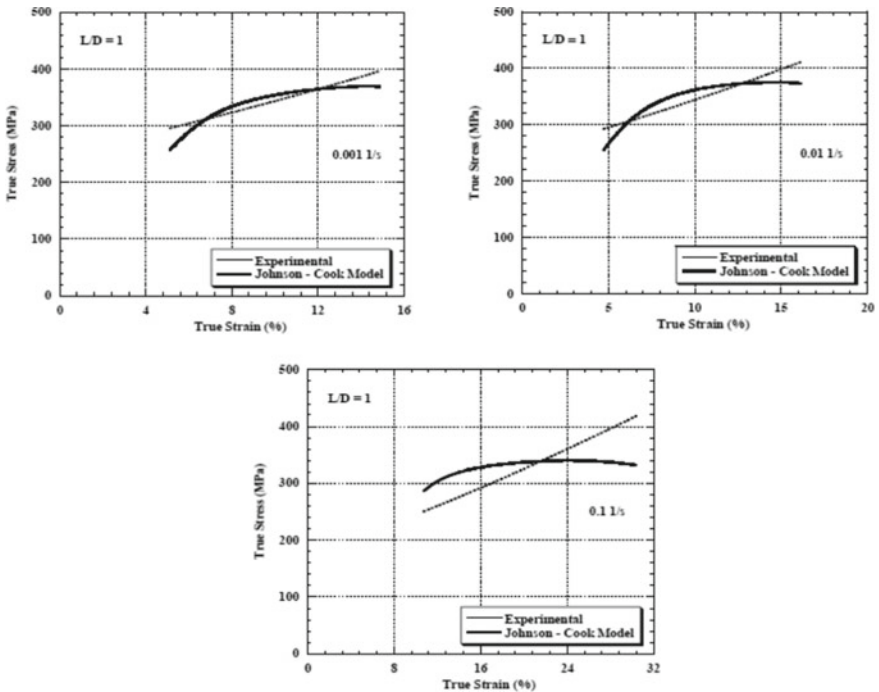


Fig. 4 Comparison of the predicted results with the experimental results

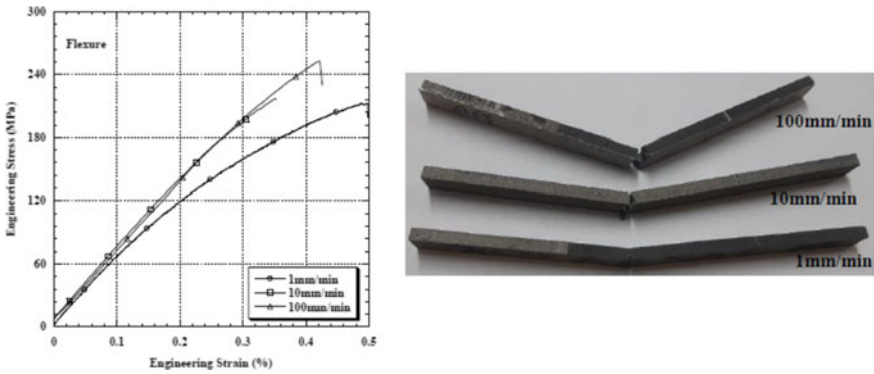


Fig. 5 Different stress–strain curves (flexure) with deformed specimens

Table 2 Bending test results at room temperature

Span length (mm)	Cross head speed (mm/min)	Engineering stress–strain			Flexural toughness (MJ/m ³)	True stress–strain	
		Y.S. (MPa)	U.F.S. (MPa)	Elongation (%)		Y.S. (MPa)	U.F.S. (MPa)
100	1	–	213 ± 2	0.5 ± 0.01	0.65 ± 0.02	–	214 ± 2
	10	–	217 ± 2	0.35 ± 0.01	0.43 ± 0.01	–	218 ± 2
	100	–	253 ± 3	0.43 ± 0.01	0.60 ± 0.02	–	254 ± 3

3.2 Strain Rate Sensitivity Under Three-Point Bending

Stress–strain curves are compared at different cross head speeds (1–100 mm/min) for span length 100 mm in Fig. 5 under bending loads. Experimental results of bending tests at room temperature are given in Table 2. The ultimate flexural strength (U.F.S.) increases with increasing cross head speed. The composites fractured at U.F.S., and no yield point is observed. On increasing the cross head speed from 1 to 100 mm/min, the U.F.S. increases approximately by 18%. The dissipation energy decreases slightly on increasing cross head speed under bending loads. All the flexural specimens (loading along thickness) are fractured during three-point bending (1–100 mm/min).

4 Conclusions

The outcomes of the present study are as below:

1. Aluminium hybrid composite is sensitive to the compressive and bending loads.
2. Mechanical behaviour of the composite under compression depends on the geometry of the tested specimens.

3. The dissipation energy increases with increasing compressive loads ($0.0010.1 \text{ s}^{-1}$) at L/D ratio 1 while decreases with increasing bending loads (100 mm/min).
4. All the specimens are fractured under compression (length: 10 mm and 15 mm) and flexure.
5. Compressive stress decreases, and malleability increases during crushing of the cylindrical specimens after annealing.
6. Johnson–Cook model predicted the flow behaviour of the composite well with the experimental results of compression tests.

References

1. Bose S, Pandey A, Mondal A (2018) Comparative analysis on aluminum-silicon carbide hybrid green metal matrix composite materials using waste egg shells and snail shell ash as reinforcements. *Mater Today Proc* 5(14), Part 2:27757–27766
2. Chak V, Chattopadhyay H, Dora TL (2020) A review on fabrication methods, reinforcements and mechanical properties of aluminum matrix composites. *J Manuf Process* 56(A):1059–1074
3. Moona G, Walia RS, Rastogi V, Sharma R (2020) Parametric optimization of fatigue behaviour of hybrid aluminium metal matrix composites. *Mater Today: Proc* 21, Part 3:1441–1445
4. Pawar SY, Kharde YR (2020) Tribological characterization of LM26/SiC/Ni.-Gr. Hybrid aluminium matrix composites (HAMCs) for high temperature applications. *Mater Today Proc.* <https://doi.org/10.1016/j.matpr.2020.06.003>.
5. Sharma A, Mishra PM (2019) Effects of various reinforcements on mechanical behavior of AA7075 hybrid composites. *Mater Today: Proc* 18(7):5258–5263
6. Alidokht SA, Abdollah-zadeh A, Soleymani S, Saeid T, Assadi H (2012) Evaluation of microstructure and wear behavior of friction stir processed cast aluminum alloy. *Mater Charact* 63:90–97
7. Tang B, Wang H, Jin P, Jiang X (2020) Constitutive flow behavior and microstructural evolution of 17 vol% SiCp/7055Al composite during compression at elevated temperature. *J Mater Res Technol* 9(3):6386–6396
8. Rasagopal P, Senthilkumar P, Nallakumarasamy G, Magibalan S (2020) A study surface integrity of aluminum hybrid composites during milling operation. *J Mater Res Technol* 9(3):4884–4893
9. Ramadoss N, Pazhanivel K, Anbuechziyan G (2020) Synthesis of B4C and BN reinforced Al7075 hybrid composites using stir casting method. *J Mater Res Technol* 9(3):6297–6304
10. Gowrishankar MC, Hiremath P, Shettar M, Sharma S, Rao SU (2020) Experimental validity on the casting characteristics of stir cast aluminium composites. *J Mater Res Technol* 9(3):3340–3347
11. Rajeswari B, Amirthagadeswaran KS, Anbarasu K (2015) Investigation of mechanical properties of aluminium 7075–silicon carbide–alumina hybrid composite using Taguchi method. *Aust J Mech Eng* 3:127–135
12. Nyanor P, Bahador A, El-Kady OA, Umeda J, Kondoh K, Hassan MA (2020) Improved ductility of spark plasma sintered aluminium-carbon nanotube composite through the addition of titanium carbide microparticles. *Mater Sci Eng, A* 795:139959
13. Kim CS, Cho K, Manjili MH, Nezafati M (2017) Mechanical performance of particulate reinforced Al metal-matrix composites (MMCs) and Al metal-matrix nano-composites (MMNCs). *J Mater Sci* 52:13319–13349

14. Hu J, Wu G, Zhang Q, Gou H (2014) Mechanical properties and damping capacity of SiC_p/TiNi_f/Al composite with different volume fraction of SiC particle. *Compos B Eng* 66:400–406
15. Zhou MY, Ren LB, Fan LL, Zhang YWX, Lu TH, Quan GF, Gupta M (2020) Progress in research on hybrid metal matrix composites. *J Alloy Compd* 838:155274
16. Sasikumar KSK, Dineshkumar K, Deeban K, Sambathkumar M, Saravanan N (2020) Effect of shot peening on surface properties of Al7075 hybrid aluminum metal matrix composites. <https://doi.org/10.1016/j.matpr.2020.02.676>
17. Idusuyi N, Olayinka JI (2019) Dry sliding wear characteristics of aluminium metal matrix composites: a brief overview. *J Mater Res Technol* 8(3):3338–3346
18. Walczak M, Pieniak D, Zwierzchowski M (2014) The tribological characteristics of SiC particle reinforced aluminium composites. *Arch Civ Mech Eng*, 4–11. <https://doi.org/10.1016/j.acme.2014.05.003>
19. Nieto A, Yang H, Jiang L, Schoenung JM (2017) Reinforcement size effects on the abrasive wear of boron carbide reinforced aluminum composites. *Wear* 390–391:228–235
20. Alaneme KK, Fajemisin AV, Maledi NB (2019) Development of aluminium-based composites reinforced with steel and graphite particles: structural, mechanical and wear characterization. *J Mater Res Technol* 8(1):670–682
21. Imran M, Khan ARA (2019) Characterization of Al-7075 metal matrix composites: a review. *J Mater Res Technol* 8(3):3347–3356
22. Liu S, Wang Y, Muthuramalingam T, Anbuhezhiyan G (2019) Effect of B₄C and MOS₂ reinforcement on micro structure and wear properties of aluminum hybrid composite for automotive applications. *Compos B Eng* 176:107329
23. Kumar RA, Devaraju A, Kumar SA (2018) Experimental investigation on mechanical behaviour and wear parameters of TiC and graphite reinforced aluminium hybrid composites. *Mater Today: Proc* 5(6), Part 2:14244–14251. <https://doi.org/10.1016/j.matpr.2018.03.005>
24. Prakash G, Singh NK, Sharma P, Gupta NK (2020) Tensile, compressive, and flexural behaviors of Al5052-H32 in a wide range of strain rates and temperatures. *J Mater Civ Eng* 32(5):04020090
25. Prakash G, Singh NK, Gupta NK (2020) Mechanical behavior of magnesium Alloy AZ61 at different strain rates and temperatures under tensile, compressive and flexural loads. *J Mater Civ Eng* 32(11):04020336

The Effect of Geometric Parameters of a Container on Thermal Charging of Latent Heat Thermal Energy Storage System: A Review



Jayesh Kumar, Pushpendra Singh, and Rajesh Kumar

Abstract The latent heat thermal energy storage (LHTES) by phase change material (PCM) is more promising than supplementary technologies due to elevated heat capacity per unit volume and small volume change during heat exchange. The efficiency of the LHTES system mainly determines upon the thermophysical properties of PCM, operating conditions, and geometric parameters of a heat exchanger or PCM container. Geometric parameters like shape, size, height, type, and orientation of heat exchanger have greatly influenced the heat convey rate in between heat convey fluid and PCM. The tube and shell-type heat exchangers are most widely studied and analyzed by the researchers. This review presents and summarizes the different types of PCM container/heat exchanger which are used in the case of PCM along with geometric heat transfer enhancement techniques like fins, heat pipes, and multiple tubes, etc. The main focus is on the melting behavior of PCM interior the containers/heat exchangers which is an important variable to magnify the thermal charging capabilities of the LHTES system.

Keywords PCM · Heat transfer enhancement · LHTES · PCM heat exchanger · PCM container

1 Introduction

Thermal energy can be accumulated in three methods, i.e., “sensible heat, latent heat, and thermochemical heat storage” [1–3]. In sensible heat storage, heat is accumulated by altering the temperature without phase transformation. But heat is accumulated by the transition of the phase of material in latent heat storage [3]. Heat is stored during material melting known as thermal charging. This heat is released during

J. Kumar (✉)

Applied Sciences Department, Maharaja Surajmal Institute of Technology, New Delhi, India
e-mail: jayesh2117@gmail.com

J. Kumar · P. Singh · R. Kumar

Department of Mechanical Engineering, Delhi Technological University, New Delhi, India

solidification considered as thermal discharging. Latent heat storage more fascinates in solid to liquid transition as compared to sensible heat storage. This is because it is demanded low volume and weight of material to accumulate a specified amount of energy due to the high heat of melting per unit volume [1, 2]. Moreover, it provides the heat at a nearly fixed temperature which depends upon the melting temperature of a material [3]. Heat convey rate in between heat transfer fluid (HTF) and PCM depends upon the thermophysical properties of PCM mainly thermal conductivity, thermal gradient (between HTF and PCM), operating conditions of the HTF, and geometric characteristics of heat exchanger (HX)/PCM container. The total time requires for the thermal charging of LHTES mainly depends upon the liquefaction rate of PCM. But due to the inadequate thermal conductivity of most PCM [3], the liquefaction rate of PCM is not adequate to minimize the total thermal charging time. Thermal conductivity enhancement of PCM by adding nanoparticle, etc., is one way to overcome this limitation. But it creates a further burden on the cost of LHTES. The second approach is a modification in the fusion mechanism inside the container to expedite the liquefaction rate of PCM. Initially, conduction is the governing mode of heat transport due to solid PCM. But, as sufficient melting occurs, the convection mode is going to be more pronounced due natural current of liquid which is set up by temperature stratification. The convection process in the liquid PCM accelerates heat transport in the remaining unmelt portion of PCM which diminishes the total fusion time of PCM. The geometric parameters of the container significantly influence the thermal charging of PCM. Heat transport mechanisms, heat convey rate, and movement of solid–liquid front movement, temperature gradient inside PCM, and aggregate melting time are greatly impacted by the geometric characteristics of HX/PCM container.

2 Classification of PCM-Based LHTES System HX/container

In this review, the melting mechanism of PCM, the melting gradient of PCM, solid–liquid front movement, and the developed natural convection within PCM are discussed and summarized that contained in the different type of the geometry of the container. These shapes of HX mainly include spherical, rectangular, shell, and tube type containers and cylindrical (both horizontal and vertical) as shown in Fig. 1. The researchers found that geometric parameters like container shape, container height, width, the orientation of container, interior tube diameter, and shape, quantity, and shape of thermal conductivity enhancers like fins and heat pipes are deciding factor for total thermal charging time and heat transport rate.

2.1 Thermal Charging in a Spherical Vessel as LHTES System

Researchers mainly analyzed the melting of PCM inside the sphere by considering constraint and unconstraint mechanism. Spherical containers give the advantage of easy accumulation of PCM during packing and low volume to heat transfer ratio [4]. Tan [4] experimentally probed the melting mechanism and performed the comparative study of constraint and unconstraint melting by submerging the sphere in a hot bath. In the early stage, conduction was the governing mode of heat transfer. After melting, buoyancy-controlled convection was dominant in the PCM, and the heat transport rate was enhanced. In unconstraint melting, the unmelt portion was submerged at the base of the vessel due to the larger density than that of liquid PCM. Conduction through vessel was mode of heat transport in the submerged solid PCM at the base. But in the upper half, natural convection was governed the heat transport mechanism.

Two natural convection cells were developed in the upper half which is symmetric about the vertical axis. But in the constraint melting, solid PCM was suspended in the core of the sphere by hanging around the tube. Melting of PCM was all around the hanging solid PCM by natural convection mainly. Waviness was formed at the base of hanging solid PCM due to three natural convection cells. The liquefaction rate of PCM is more in the unconstrained melting due to the direct conduction from the bottom sphere surface to the submerged solid PCM. Sattari et al. [1] probed the liquefaction characteristics of PCM in the spherical capsule by CFD simulation. They found that waviness is formed in the bottom portion of capsules due to the unstable liquid of PCM. It concluded that 27% enhancement of diameters imparts to the 80% intensification of the liquefaction time of PCM. Li et al. [5] probed the constrained liquefaction of PCM inside the spherical vessel. It concluded that a

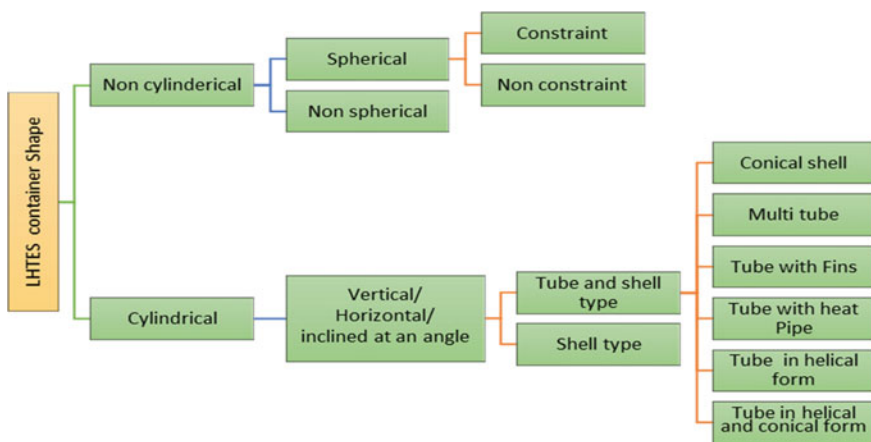


Fig. 1 Classification-PCM embedded HX container [1, 5-15, 19-28]

smaller radius sphere demonstrated the high melting rate of PCM. A high thermal conductive material is recommended for the spherical vessel to decrease the thermal charging time. It is advantageous to use a greater number of spheres of a smaller radius instead of a smaller number of spheres of larger radius.

2.2 Thermal Charging in a Non-cylindrical and Non-spherical Vessel as LHTES

Kamkari et al. [6] probed experimentally the fusion behavior of PCM material in the rectangular container with 90° , 45° , and 0° inclination angle with a horizontal plane. They provided the heat source on the right wall of the container. They probed that reducing the height of a container is beneficial for diminishing the total melting time in 90° and 45° inclination of the container. But there was no significant change in the horizontal configuration. It revealed that 0° and 45° inclined container had taken 53% and 35% less melting time compared to the vertical container. Horizontally placed container demonstrated the least melting time for the PCM but it was occupying more space. Further, they [7] probed the impact of fins by placing in their only vertical configuration of a container as their earlier work. Initially, the conduction mode was dominated during heat transport until a thin layer of liquid PCM was developed near the wall of the container. At this time, the thickness of liquid PCM was uniform near the container wall height. As melting continues, the thickness of liquid PCM was more at the top of the container as compared to the bottom of the container. At this time, the buoyancy force was dominating the viscous forces. Liquid PCM moved upward with hot wall and cold liquid returned downward with a solid–liquid interface. Consequently, a circulating convection current was developed between the container wall and solid–liquid interface which further enhance the heat transport rate. The circulating convection current zone was divided into parts as the insertion of fins. The heat transport rate was more above the fin surface due to strong vortex motion in the liquid PCM near the fin surface. They stated that fins (three) were reduced the melting time by about 37% as compared to the unfinned container due to the magnification of the heat transport area. But fins also developed the obstruction in circulating convection current which diminishes the heat transport rate. As a result, there was a requirement of an optimal number of fins. Further, they found that the fins impact was more at the lower wall temperature. Haddad et al. [8] numerically probed the liquefaction characteristics of paraffin in the wavy (bottom surface) trapezoidal cavity which is heated from below. It stated that the liquefaction duration in the flat surface is nearly 2.5 times quicker than that in the wavy surface at a temperature gradient of 50°C .

2.3 *Thermal Charging in the Cylindrical Container as LHTES System*

Different orientation of the cylinder like horizontal, vertical, and inclined was studied by the researchers during thermal charging. Seddegh et al. [9] simulated and compared the liquefaction characteristics of PCM in the “vertical and horizontal shell and tube” LHTES system. It found that the convective heat convey mode is dominating in the upper half portion of the horizontal container during heat absorption in the PCM. Hence, the rate of liquefaction is inflated at the inceptive stage of the charging operation. But the liquefaction rate is going to decrease as the melting of the lower portion start due to the absence of the buoyancy effect. Vertical container shows the greater liquefaction rate of PCM in the lower portion than that of horizontal. The liquefaction rate is more uniform in the vertical container than that of horizontal. A horizontal container is recommended for part load application as a better melting rate of the upper portion. Recently, Mahdi et al. [10] numerically probed the effect of PCM location on the thermal capabilities in the concentric pipe by Ansys Fluent. PCM was settled in the annulus and inner tube in the first and second cases, respectively. PCM accumulation in the inner tube is diminished the melting time about 50% than that of other case. This is happened because convection is dominated in the larger portion in the case second (inner tube PCM packing), but it is mainly restricted in the top portion in the case first after initial melting. Bechiri et al. [11] presented a numerical analysis to probe the liquefaction of PCM partially occupied in a perpendicular cylindrical tube with a constant temperature wall surface. It stated that at the inception of liquefaction (initial four minutes), the height of PCM does not influence the fusion process because thermal energy is disseminated by conduction inside PCM. Subsequently, after four minutes, the liquefaction time intensifies as PCM container height increases. The natural convection fluctuation actuated by altering the tube diameter and exterior wall surface temperature impacts remarkably the liquefaction process. Saraswat et al. [12] probed the liquefaction process of “industrial-grade paraffin wax” [12] occupied in a semi-cylindrical vessel with a heating strips (heat pipe) attached axially along with the core of semi-cylinder. It was found that the integration of heat pipes with PCM assists to extent convey of heat in the PCM, and hence, a remarkable diminishes in the aggregate required liquefaction time of PCM. Joybari et al. [13] experimentally investigated single and multiple (five) tube with PCM incorporated in the shell. It was revealed that the multitube HX exhibited better performance than the single tube HX in terms of fusion duration and energy storage capacity due to extended heat convey surface area.

2.4 Thermal Charging in the Shell and Tube Model HX as LHTES System

Researchers probed the impact of a different configuration of the tube carrying HTF with PCM embedded in the shell-like single tube, multitube, coil form tube, and conical coil type, etc. In the research literature, nearly two-third studies of PCM embedded in the container is related to shell and tube container due to low heat loss in the cylindrical container than that of other [2]. Shell and tube diameter ratio " λ " should be less than four to maximum the accumulated energy density [2]. But the " λ " value should be 5.4 to optimize the total accumulated energy density and melting time. Hosseini et al. [14] probed the melting characteristics of material experimentally and numerically in tube and shell model in horizontal configurations. As time progress, natural convection is governed the heat transport in the liquid PCM. Sodhi et al. [15] numerically studied phase transformation attributes of PCM (Sodium Nitrate) in the horizontal conical vessel and tube type HX. They stated that 3.4° are the optimized angle of cone and 98.6 mm, 54 mm is the inlet and outlet optimized diameter of the conical vessel to reduce the charging duration for 96% portion melting. Fins increase the heat convey rate in conduction mode at the inlet portion of the conical shell, but they are insignificant at the outer portion of the conical shell. Recently, Al Siyabi et al. [16] analyzed charging and discharging characteristics of inclined (0° , 45° , 90°) tube and shell-type containers for PCM (Paraffin). 45° inclination angle was demonstrated the highest melting rate than that of the other two inclination. PCM melting gradient is dominated in the axial orientation than that of radial orientation in the inclination of 0° . But the liquefaction rate behavior is just the opposite in the inclination of 90° . The region which faces the buoyant force in convection mode has a remarkable influence on the melting rate. Mahdi et al. [17] experimentally examined the liquefaction characteristics of "paraffin wax in a conical coil" LHTES system in the cylindrical container. Their probes revealed that the liquefaction rate in the conical coil LHTES system is intensified by 22% in comparison with that of normal coil LHTES system due to the hike in the HTF pipe surface at the lower zone of a cylinder where the solid PCM subsided due to its relatively elevated density. Mao et al. [18] numerically probed heat convey characteristics during the melting of PCM in a "novel truncated cone shell and tube" LHTES vessel. It stated that aggregate liquefaction time diminishes nearly 30.69% compared with the traditional cylindrical vessel. Seddegh et al. [19] probed the thermal characteristics of the "conical and cylindrical" vessels. Their results showed that the conical vessel can accumulate thermal energy much quicker than the cylindrical vessel at the same working situation. Recently, Mahdi et al. [20] did a fascinating simulation and experiment by double pipe helical coil with PCM such that both the outer shell and interior tube are coiled. PCM is embedded in between the interior tube and shell. They revealed that melting time is diminished by about 25% and 67% for the same heat exchange surface area than that of straight horizontal and vertical HX. Melting is started from the top portion due to the buoyancy effect and move downward in all the cases. They gave the same result which verified by other researchers that after initial melting, the effect of convection

current is more in the top portion in the straight horizontal HX than that of straight vertical. But, in vertical HX, convection current is more dominating in the axial direction. The conduction mode of heat transport in bottom portion diminishes the heat transfer in the later stages. The innovative design took the advantage of both horizontal and vertical HX and reduced the limitations of the other two cases.

2.5 Impact on Thermal Charging by Insertion of Fins and Heat Pipe

Fins of high thermal conductive material are a cost-effective and efficient technique to increase the thermal charging rate [3]. Yang et al. [21] demonstrated that annular fins expedite the thermal capabilities of TES system. The fusion duration of PCM was diminished about 65% than that of without fins in their study by using annular fins. It stated that natural convection in PCM after melting is very pronounced to enhance the heat transport rate. Fusion time of PCM is decreased as number of fins increases up to a point after that it starts increases. The 0.0248 and 0.313 are optimal recommended value for ratio of thickness and gap between fins, ratio of gap between two fins, and length of tube, respectively. Mahood et al. [22] probed the consequences of fins positions on the liquification rate of PCM in the horizontal shell and tube type HX. When the fins are placed in the lower portion, below the horizontal axis (15° angle between fins) is most effective to decrease the melting time of PCM. This happened because all the fins directly improve the thermal conductivity in the region which has the lowest heat transport rate in the system. Diminishing the angle between the fins from 72° to 15° contribute to lower the fusion time of PCM. Karami et al. [3] probed the impact of perforated circular fins on LHTES capabilities of vertical shell and tube type HX. The total melting time slightly diminished about 7% than that of solid fins due to the expedition of buoyancy-driven convection flow by little impeding created through perforated circular fins. Bhagat et al. [23] probed the longitudinal fins geometric parameter incorporated with multiple tube in the PCM accommodated horizontally oriented shell by using Ansys Fluent. They accommodated the fins in both medium HTF and PCM. The main purpose of their research is to minimize the fluctuation in outlet HTF temperature for solar water heating. Fin's effectiveness is more in the case when fins accommodated in the both HTF and PCM than that of HTF. They recommended that thinner fins large in quantity is more advantageous than that of thicker fins small in quantity with constant volume of PCM. Nie et al. [24] numerically examined the impact of arrangement of longitudinal fins and other fins parameters in horizontally placed tube and shell model during successive thermal charging and discharging. They found an interesting result that total charging and discharging duration is diminished drastically by placing the fins uniformly in the container. On the contrary, the melting duration was reduced by accumulating all fins in the lower zone of the container but it showed a more adverse impact on the total solidification duration.

The heat pipe is a thermal device that enhanced the heat transport rate effectively in the LHTES system. The effective thermal conductivity of heat pipe is enormous than that of pure metals like copper, aluminum, etc. For Example, a heat pipe of copper with working fluid lithium can transfer the axial heat flux $10\text{--}20\text{ kW/cm}^2$ at the temperature of $1500\text{ }^\circ\text{C}$ [25]. Heat pipe can be assumed as a high thermal conductive rod during numerical simulation to minimize the numerical computational cost in place of evaporation and solidification model inside the heat pipe [26]. Mahdavi et al. [26] assumed heat pipe as a rod with effective thermal conductivity about 90 times of copper thermal conductivity. Hence, the heat pipe is a suitable medium to encounter the limitation of LHTES system as low heat flux. Motahar et al. [27] placed a vertical heat pipe in a vertical shell containing PCM to expedite the heat transport rate from the heat source which is placed at the base of PCM shell. It stated that when the heat source temperature increased by $15\text{ }^\circ\text{C}$, then the melting time decreases by 53% by the heat pipe than that of the tube. Sharif et al. [28] simulated the thermal performance of an energy storage vessel (vertical cylinder) with heat pipe as charging unit and compared the result with HTF tube in place of the heat pipe. The heat pipe is more effective in terms of the melting time of PCM than that of tube. The effectiveness of heat pipe is more pronounced with the enhancement of condenser length and diameter of heat pipe. Researchers recommended the heat pipe to enhance the liquefaction rate in LHTES system. Mahdavi et al. [26] numerically probed the impact of heat pipe on the thermal charging of PCM containing nanoparticle packed in the shell and tube type HX by Ansys Fluent. The shell was vertically oriented, and the heat pipe was horizontally placed in PCM considering the tube as heat source. Insertion of one, two, three, and four heat pipes reduced the melting time about 40%, 61.2%, 76%, and 83%, respectively. It showed that impact of heat pipe is not proportional pronounced as number of heat pipe increased.

2.6 Comparative Studies of Thermal Charging in Containers

The conical shell and tube system (horizontal orientation) reveal a better performance in terms of the thermal charging rate than that of the horizontal cylindrical shell and tube model by enhancing the convection mode [15]. Spherical container exhibits low volume to surface area ratio which increases the effective heat transport area than that of the non-spherical vessel. A spherical container is good for packing in LHTES bed system [5]. The orientation of the rectangular container is drastically affecting the charging rate of PCM LHTES system. Magnification of the height to width ratio of a rectangular container reveals the higher melting rate of PCM [29]. Researchers stated that natural convection in the PCM expedites the heat transport rate than that initial pure conduction [29]. Rectangular vessel for PCM storage demands the half of melting time than that of a spherical vessel for the same volume and heat convey area between the heat convey fluid and the vessel wall [30]. Zivkovic et al. recommended to use a rectangular vessel instead of a spherical vessel [30]. Vyshak et al. [31] stated that a cylindrical shell and tube model are required the least charging time for the

same energy accumulation than that of a rectangular and cylindrical vessel. In the shell and tube HX, the optimal shell to tube radius ratio was found to minimize the total duration of thermal energy accumulation and maximize thermal energy capacity by the Seddegh et al. [32]. It stated that the ratio is 5.4 in the above conditions. The number of tubes and their position in the shell has a markable impact on the fusion rate. The tube near bottom of horizontal shell could enhance the fusion rate of PCM [33]. Tube and shell-type HX is good for small and medium size applications due to high energy efficiency (more than 70%) [34]. The melting rate is going to decrease as container height is increased. Horizontal PCM container reveals a high melting rate and low charging time in all the type [34].

3 Conclusion

Shell and tube HX is the most studied HX for PCM LHTES system. Researches have successfully used the heat pipe, fins, multiple tubes, a conical tube, and a helical tube to expedite the heat convey rate between HTF and PCM. Heat pipe in the PCM is very effective to boost the heat convey rate than that of other methods due to high effective thermal conductivity. There are very limited comparative studies available which compare the performance and effectiveness of the different type of PCM container/HX. It is required to critical analysis and compared the melting gradient, melting time, solid–liquid front movement and mode of heat convey, etc., for different types of PCM container/HX to decide the most promising HX. Further, cost is also an important factor for small and medium size LHTES applications during commercialization. Researchers have successfully used nanoparticle to enhance the thermal charging rate of LHTES. But it creates a further burden on the cost of LHTES system. Hence, it is beneficial to optimize the geometric parameter to enhance the thermal charging rate and thermal capacity of LHTES. It is also found in some cases that the geometrics parameter which enhances the thermal charging performance have an adverse effect on the thermal discharging stage or freezing operation.

References

1. Sattari H, Mohebbi A et al (2017) CFD simulation of melting process of phase change materials (PCMs) in a spherical capsule. *Int J Refrig* 73:209–218
2. Kalapala L, Devanuri J (2019) Parametric investigation to assess the melt fraction and melting time for a latent heat storage material based vertical shell and tube heat exchanger. *Sol Energy* 193:360–371
3. Karami R, Kamkari B (2020) Experimental investigation of the effect of perforated fins on thermal performance enhancement of vertical shell and tube latent heat energy storage systems. *Energy Convers Manage* 210:112679
4. Tan F (2008) Constrained and unconstrained melting inside a sphere. *Int Commun Heat Mass Transfer* 35:466–475

5. Li W, Li S et al (2017) Numerical study on melt fraction during melting of phase change material inside a sphere. *Int J Hydrogen Energy* 42:18232–18239
6. Kamkari B, Shokouhmand H (2014) Experimental investigation of the effect of inclination angle on convection-driven melting of phase change material in a rectangular enclosure. *Int J Heat Mass Transf* 72:186–200
7. Kamkari B, Shokouhmand H (2014) Experimental investigation of phase change material melting in rectangular enclosures with horizontal partial fins. *Int J Heat Mass Transf* 78:839–851
8. Haddad Z, Iachachene F (2019) Melting characteristics of organic phase change material in a wavy trapezoidal cavity. *J Mol Liquids*, 112132
9. Seddegh S, Wang X et al (2016) A comparative study of thermal behaviour of a horizontal and vertical shell-and-tube energy storage using phase change materials. *Appl Therm Eng* 93:348–358
10. Mahdi M, Mahood H et al (2019) Numerical study on the effect of the location of the phase change material in a concentric double pipe latent heat thermal energy storage unit. *Thermal Sci Eng Progr* 11:40–49
11. Bechiri M, Mansouri K et al (2019) Study of heat and fluid flow during melting of PCM inside vertical cylindrical tube. *Int J Therm Sci* 135:235–246
12. Saraswat A, Bhattacharjee R et al (2017) Investigation of diffusional transport of heat and its enhancement. *Appl Therm Eng* 111:1611–1621
13. Joybari M, Seddegh S et al (2019) Experimental investigation of multiple tube heat transfer enhancement in a vertical cylindrical latent heat thermal energy storage system. *Renew Energy* 140:234–244
14. Hosseini M, Rahimi M et al (2014) Experimental and computational evolution of a shell and tube heat exchanger as a PCM thermal storage system. *Int Commun Heat Mass Transfer* 50:128–136
15. Sodhi G, Jaiswal A et al (2019) Investigation of charging and discharging characteristics of a horizontal conical shell and tube latent thermal energy storage device. *Energy Convers Manage* 188:381–397
16. Al I, Khanna S et al (2019) An experimental and numerical study on the effect of inclination angle of phase change materials thermal energy storage system. *J Energy Storage* 23:57–68
17. Mahdi Mustafa S, Mahood Hameed B et al (2019) Experimental study on the melting behavior of a phase change material in a conical coil latent heat thermal energy storage unit. *Appl Therm Eng* 11:40–49
18. Mao Q, Liu N et al (2019) A novel shell-and-tube thermal energy storage tank: Modeling and investigations of thermal performance. *Appl Therm Eng* 159:113964
19. Seddegh S, Cao F et al (2017) Comparison of heat transfer between cylindrical and conical vertical shell-and-tube LHTES systems. *Appl Therm Eng*
20. Mahdi M, Mahdi J et al (2020) Improved PCM melting in a thermal energy storage system of double-pipe helical-coil tube. *Energy Convers Manage* 203:112238
21. Yang X, Lu Z et al (2017) Thermal performance of a shell-and-tube latent heat thermal energy storage unit: Role of annular fins. *Appl Energy* 202:558–570
22. Mahood H, Mahdi M et al (2020) Numerical investigation on the effect of fin design on the melting of phase change material in a horizontal shell and tube thermal energy storage. *J Energy Storage* 29:101331
23. Bhagat K, Prabhakar M et al (2018) Estimation of thermal performance and design optimization of finned multitube latent heat thermal energy storage. *J Energy Storage* 19:135–144
24. Nie C, Deng S et al (2020) Numerical investigation of PCM in a TES unit with fins: consecutive charging and discharging. *J Energy Storage* 29:101319
25. Reay D, Kew P et al (2013) Heat pipes: theory, design and applications. Butterworth Heinemann
26. Mahdavi M, Tiari S et al (2020) A numerical study on the combined effect of dispersed nanoparticles and embedded heat pipes on melting and solidification of a shell and tube latent heat thermal energy storage system. *J Energy Storage* 27:101086
27. Motahar S, Khodabandeh R et al (2016) Experimental study on the melting and solidification of a phase change material enhanced by heat pipe. *Int Commun Heat Mass Transfer* 73:1–6

28. Sharifi N, Wang S et al (2012) Heat pipe-assisted melting of a phase change material. *Int J Heat Mass Transf* 55:3458–3469
29. Fadl M, Eames P (2019) A comparative study of the effect of varying wall heat flux on melting characteristics of phase change material RT44HC in rectangular test cells. *Int J Heat Mass Transf* 141:731–747
30. Zivkovic B, Fujii I (2001) Analysis of isothermal phase change of phase change material within rectangular and cylindrical containers. *Sol Energy* 70:51–61
31. Vyshak N, Jilani G (2007) Numerical analysis of latent heat thermal energy storage system. *Energy Convers Manage* 48:2161–2168
32. Seddegh S, Wang X (2017) Investigation of the effect of geometric and operating parameters on thermal behavior of vertical shell-and-tube latent heat energy storage systems. *Energy* 137:69–82
33. Esapour M, Hosseini M (2016) Numerical study on geometrical specifications and operational parameters of multi-tube heat storage systems. *Appl Therm Eng* 109:351–363
34. Zayed M, Zhao J et al (2020) Recent progress in phase change materials storage containers: geometries, design considerations and heat transfer improvement methods. *J Energy Storage* 30:101341

Generation of a Versatile Discharge Formula for Multiple Parshall Flumes Using a Regression Technique



D. Saran and N. K. Tiwari 

Abstract Parshall flumes (PFs) and modified Parshall flumes (MPFs) are specially designed devices that are commonly used for the measurement of discharge in open channels. They are widely used for the measurement of sewage flow, industrial discharge, seepage in dams, etc. These are given preference over weirs because of their ability to measure higher flow rates, self-cleaning capability as well as low head loss as compared to weirs. In the present study, 1 PF and 1 MPF of throat width 2.54 cm and 3.18 cm were studied under no-slope and positive longitudinal slope conditions by observing the depth of water at a specific point in each flume at different discharge values. An attempt was made to generate a versatile discharge formula that can be used for both the Parshall flumes. This formula was generated using multivariate regression applied with the help of the `mvregress` command present in Statistics and Machine Learning Toolbox™ in MATLAB. The predictive capability of this formula was analyzed with the help of common statistical indices, i.e., coefficient of correlation (CC) and root-mean-square error (RMSE). It was found that the formula predicted highly accurate discharge corresponding to the given depth of water, which was indicated by the fact that the values of CC and RMSE as yielded by the formula on the testing data set were 0.976 and 0.338, respectively.

Keywords Parshall flumes · Longitudinal slope · Discharge formula · Multivariate regression

1 Introduction

With the ever-increasing value of water, the importance of accurate measurement of water supplied to the farms has also increased [1]. Inaccurate measurements may lead to an insufficient supply of water, which acts as an obstruction in the full growth of crops, ultimately causing huge losses to the farmer [2].

D. Saran (✉) · N. K. Tiwari
NIT Kurukshetra, Kurukshetra, Haryana 136119, India

© The Author(s), under exclusive license to Springer Nature Singapore Pte Ltd. 2022
K. Govindan et al. (eds.), *Advances in Mechanical and Materials Technology*,
Lecture Notes in Mechanical Engineering,
https://doi.org/10.1007/978-981-16-2794-1_104

1197

Initially, weirs were used for the fulfillment of this purpose. However, with the passage of time, several problems were encountered in its use, most prominent being the constant blockage of weirs due to the presence of debris in the water passing through the weir. Fixing this problem required regular cleaning of weirs, resulting to a loss in its popularity [3].

The solution to this problem arrived in the form of Parshall flume. Invented by Ralph L. Parshall in 1928, it was actually an improvised form of Venturi flume. The improvisations involved reducing the angle of converging and diverging sidewalls; however, the chief modification was the inclusion of a “drop” on the floor of the throat of the flume [4, 5]. The presence of this drop accelerated the flow of water through the flume to such an extent that the initial subcritical flow ultimately changed to supercritical flow. This supercritical flow, possessing high velocity, prevented the accumulation of debris in the flume, thereby eliminating the need for regular inspection of flumes [6]. Further, error-free measurement of discharge required only a single head reading at a particular point in the flume [2, 4, 7, 8]. Figure 1 illustrates the detailed sketch of Parshall flume.

Numerous studies have been done by different investigators all over the world with the sole motive of providing user-oriented formulae for calculating flow rate through Parshall flumes of different sizes. Abt et al. [9] evaluated the effects of longitudinal settlement on the flow rate formula for a 7.62 cm Parshall flume and consequently prescribed a new formula taking into account the effects of settlement. Eventually, Abt et al. [10] extrapolated this research on the same Parshall flume;

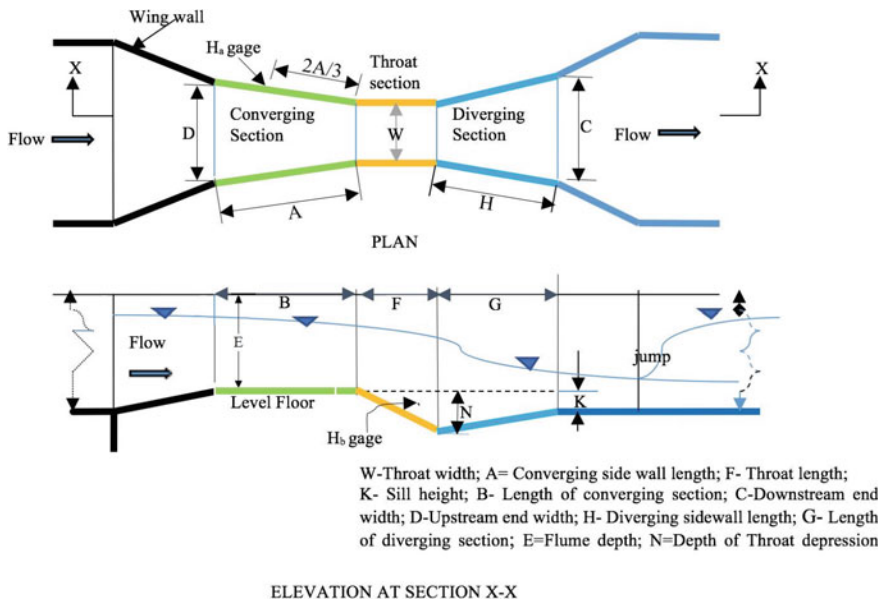


Fig. 1 Sketch of Parshall flume

however, this time the effects of cross-slopes were taken into account. Following this was the work done by Genovez et al. [11], which was performed on Parshall flumes possessing throat width dimensions 30.5 cm and 61 cm, respectively. In this case, the consequences of longitudinal slopes, cross-slopes, and combination of both lateral and longitudinal slopes were studied, with corrections being formulated for each anomaly. The outcomes of this study were then collated with the results produced by similar tests conducted on Parshall flumes of throat width 2.54 cm, 5.08 cm, and 7.62 cm. In due course of time, renewed interest was shown by Abt et al. [12], and experiments were run on 30.5 cm Parshall flume by simulating varying slopes with the added presence of submergence conditions. Here, two correction coefficients were formulated, one regarding cross-slopes and the other regarding submergence. Enhanced experiments were performed by Abt et al. [13] on a variety of Parshall flumes, i.e., 2.54 cm, 5.08 cm, 7.62 cm, 30.4 cm, and 61 cm throat size Parshall flumes, with each flume facing longitudinal settlement, lateral settlement as well as submergence conditions. Accordingly, different correction factors were given to address each abnormality. Heiner et al. [14] conducted experiments on Parshall flume of throat width 61 cm and studied the outcomes of the inaccurate location of staff gauge, in addition to the absence and erroneous design of inlet wing walls on the flow rate formula of the respective flume. Suitable correction factors were prescribed for each oddity.

Regression techniques have been used greatly to develop prediction models in the study of Parshall flumes. Abt et al. [9, 10, 12, 13] and Genovez et al. [11] have successfully implemented linear regression techniques as well as multiple variable regression techniques for the prediction of flow rate correction factors and formulation of new discharge formulae for Parshall flumes.

In the current study, a discharge rating formula has been created by applying multivariate linear regression on the obtained experimental data set. This was done using the `mvregress` command present in MATLAB. The formula generated using this technique can be used to find the discharge passing through the 2.54 cm standard Parshall flume as well as the 3.18 cm modified Parshall flume.

Originality/value: Generation of a versatile discharge formula has been conducted in this study. In all the previous works, there has been little application of regression techniques in the analysis of Parshall flumes. In fact, the application of the regression techniques was done only on standard Parshall flumes. However, this paper involves the application of regression technique not only on standard Parshall flume but also on modified Parshall flume in the quest of creating a discharge rating formula with the help of multivariate linear regression.

2 Proposed Regression Technique

Regression analysis is a method in statistics which is used in finding the trends in data. This is achieved by the regression analysis by giving the user a mathematical function or a curve establishing a relation between the criterion (dependent) variable and the predictor (independent) variable. The mathematical equation given by the regression can make the “best guess” of the dependent variable corresponding to a given value of independent variables. This equation is known as the regression equation, and the curve representing this regression equation is known as the regression line.

One of the most commonly used regression techniques is linear regression. It has been named so because the regression equation obtained using this technique is always linear. Consequently, the curve representing this equation is always a straight line of the type:

$$Y = a + mX$$

where:

- $Y =$ dependent variable
- $X =$ independent variable
- $m =$ slope of regression line, and
- $a =$ intercept on y-axis.

Linear regression itself is of two types: simple linear regression and multiple linear regression. Simple linear regression involves the challenge of establishing a relationship between an independent variable and a corresponding dependent variable. However, when the problem involves the presence of two or more independent variables, then the relationship between the predictor variables and the criterion variable is established using multiple linear regression.

2.1 *Multivariate Linear Regression*

Multivariate regression involves establishing a relationship between multiple responses (dependent) and multiple predictor (independent) variables. This is different from multiple linear regression, which involves the determination of the relationship between a single response variable and multiple predictor variables. As a result, multivariate linear regression involves expressing a vector consisting of dependent variables as a linear combination of a matrix consisting of independent variables and a vector consisting of error terms possessing multivariate normal distribution.

The multivariate regression problems of the type:

$$y_i = X_i\beta + \varepsilon_i, \varepsilon_i \sim \text{MVN}_d(0, \Sigma)$$

where:

- y_i denotes response vector,
- X_i denotes predictor matrix,
- β denotes coefficient vector, and
- ε_i denotes error vector following multivariate normal distribution

can be solved using the command `mvregress` present in Statistics and Machine Learning Toolbox™ in MATLAB.

3 Experimental Program

A standard Parshall flume possessing width 2.54 cm along with a modified Parshall flume possessing width 3.18 cm were made using an acrylic plastic sheet. The dimensions of both the flumes used in the present study have been stated in Table 1. The complete inflow of water through the flumes was achieved by constructing wing walls at the entrance as well as the exit of the flumes.

Both the flumes were installed in a 4.14-m-long, 0.3048-m-wide, and 0.3048-m-deep standard recirculating channel on an individual basis. The maximum discharge achievable through the channel was approximately 6 l/s. Connected to this channel was a recirculating closed device, which provided a constant supply of water to the channel by repetitively extracting water from a storage tank 1.27 m long, 0.635 m wide, and 0.635 m deep. A Cipoletti weir was installed at the downstream end of the channel, to measure actual discharge passing through the channel. The value of actual discharge was measured with the help of the formula [15]:

$$Q = 3.367LH^{\frac{3}{2}}$$

where:

- $L =$ Weir length (ft.)
- $H =$ Head (ft.), and
- $Q =$ Discharge (cfs).

In metric units, this formula takes the form:

Table 1 Dimensions of Parshall flume and modified Parshall flume

S. No.	Model	Throat width of the model (W) cm	Throat length of the model (F) cm	Sill height of the model (K) cm
1	Parshall Flume	2.54	7.62	1.91
2	Modified Parshall flume	3.18	8.57	1.98

$$Q = 1.857LH^{3/2}$$

where:

- $L =$ Weir length (m)
- $H =$ Head (m), and
- $Q =$ Discharge (m^3/s).

The Cipoletti weir used for experiments was found to possess weir length (L) = 0.142 m; as a result, the formula used boiled down to:

$$Q = \left(0.263694H^{3/2}\right) \times 1000$$

where:

- $H =$ Head (m) and
- $Q =$ Discharge (l/s).

The discharge through the channel was adjusted with the aid of a flow regulating valve. The schematic view of experimentation along with the view of the model utilized in this study has been shown in Fig. 2a, b.

Simulation of longitudinal settlements was achieved by the construction of wooden planks and their subsequent installation under the upstream section of both the flumes. This led to the formation of a longitudinal differential settlement between the inlet and discharge sections of the flume. A chain of 128 tests was carried out,

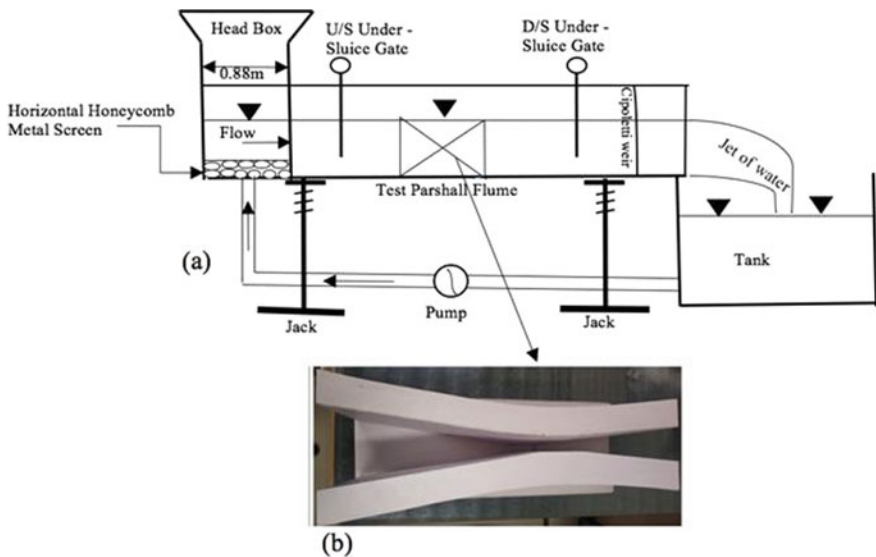


Fig. 2 a Schematic view of experimentation. b Typical view of the model utilized

with the discharge varying from 0.304 to 4.936 l/s. Longitudinal flume slopes of 0, 2.1, 4.2, and 6.3% were examined, with 32 tests conducted under each slope.

The same procedure was followed for performing all 128 tests. After the installation of the Parshall flume at the target slope, the flow was launched into the channel. The flow took about 15 minutes after it was initiated to attain a steady flow. Subsequently, the depth of water was measured (H_a) using a pointer gauge possessing least count 0.01 mm. H_a refers to the head of water, 2/3rd upstream the crest of the flume. This depth was always measured considering the floor of the converging part of the flume as zero elevation. The point of measuring H_a has been depicted in Fig. 1. Subsequently, the discharge through the flume was increased, and the same process was repeated. After completing all the tests on a particular slope, the slope was increased to the new value, and the same process was repeated. After completing all the tests on one flume, another constructed flume was installed after removing the previous flume from the channel, and the process was repeated. With the values of actual discharge and the corresponding values of H_a for all the 128 tests noted, this complete data set was bifurcated into a training data set (containing 89 observations) and testing data set (containing 39 observations). Finally, multivariate linear regression was applied to the training data set and its accuracy was checked on the testing data set.

3.1 Application of Multivariate Linear Regression

The fundamental equation used for the purpose of discharge measurement using Parshall flumes is:

$$Q = K H_a^n$$

where:

- Q = Discharge
- H_a = Depth of Water at the primary point of measurement
- K = Flume discharge constant, and
- n = Discharge exponent.

We aim to find the values of K and n using the obtained experimental data set. Taking log on both sides of the equation:

$$\log_{10} Q = \log_{10} K + n \log_{10} H_a$$

Now, we have 89 values of Q and corresponding 89 values of H_a in training data. These values can be used to form 89 equations, as follows:

$$\begin{aligned}
 \log_{10} Q_1 &= \log_{10} K + n \log_{10} H_{a1} \\
 \log_{10} Q_2 &= \log_{10} K + n \log_{10} H_{a2} \\
 \log_{10} Q_3 &= \log_{10} K + n \log_{10} H_{a3} \\
 &\vdots \\
 \log_{10} Q_{89} &= \log_{10} K + n \log_{10} H_{a89}
 \end{aligned}$$

This set of equations can be written in matrix form as:

$$\begin{pmatrix} \log_{10} Q_1 \\ \log_{10} Q_2 \\ \log_{10} Q_3 \\ \vdots \\ \log_{10} Q_{89} \end{pmatrix} = \begin{pmatrix} 1 & \log_{10} H_{a1} \\ 1 & \log_{10} H_{a2} \\ 1 & \log_{10} H_{a3} \\ \vdots & \vdots \\ 1 & \log_{10} H_{a89} \end{pmatrix} \begin{pmatrix} \log_{10} K \\ n \end{pmatrix}$$

Applying the mvregress command enables us to input all the values of Q and H_a and in return obtain the value of $\log_{10} K$ and n as output. The value of $\log_{10} K$ finally gives us the value of K .

3.2 Data Set

A total of 128 observations were utilized in this study. The data set was randomly divided into a training data set consisting of 89 observations and a testing data set consisting of 39 observations. The input parameters were discharge (Q in lps) and primary depth reading (H_a in cm), while the output parameters were K (flume discharge constant) and n (discharge exponent). The important features of the training data set as well as the testing data set have been given in Table 2.

Table 2 Features of training and testing data set

Parameter	Training		Testing	
	Q	H_a	Q	H_a
Unit	Lps	Cm	Lps	Cm
Min	0.304	3.66	0.304	3.62
Max	4.936	21.86	4.936	20.63
Mean	2.961112	14.12944	2.755615	13.45538
Std. deviation	1.594163	5.546569	1.429559	4.931254
Median	3.494	15.34	2.704	13.15
Kurtosis	-1.20383	-1.07908	-1.12136	-0.9382
Skewness	-0.37739	-0.45261	-0.18812	-0.32986

3.3 Statistical Parameters Used for Performance Evaluation

The predictive capability of the discharge formula created using multivariate linear regression was analyzed using two prevalent statistical parameters, namely coefficient of correlation (CC) and root-mean-square error (RMSE) as yielded by this formula on testing data set.

Mathematically:

$$CC = \frac{N(\sum HF) - (\sum H)(\sum F)}{\sqrt{N(\sum H^2) - (\sum H)^2} \sqrt{N(\sum F^2) - (\sum F)^2}}$$

$$RMSE = \sqrt{\frac{1}{N} \sum_{i=1}^N (H - F)^2}$$

where:

- N = No. of observations
- H = Observed values, and
- F = Predicted values.

4 Results and Discussion

Application of multivariate linear regression on the training data set yielded us the following discharge formula:

$$Q = 0.0246H_a^{1.7742}$$

where:

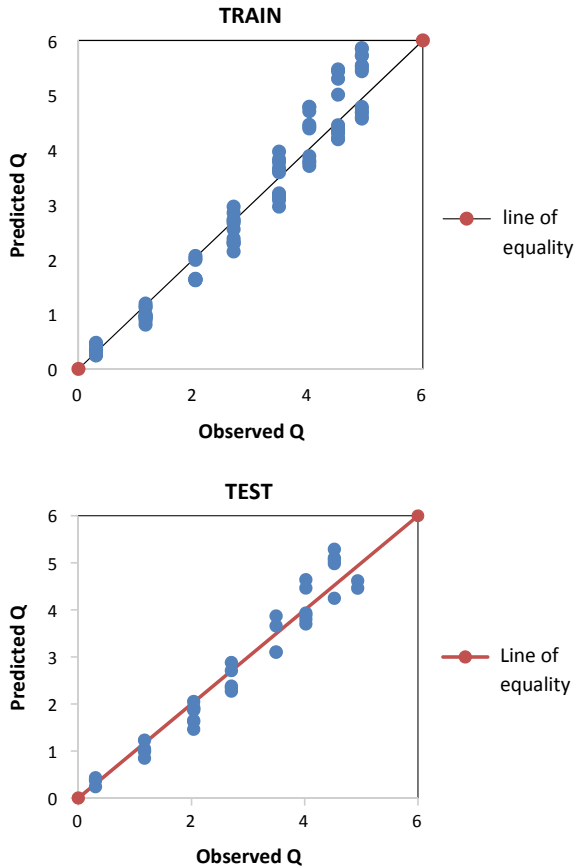
- Q = Discharge (lps) and
- H_a = Flow depth at primary point of measurement.

The application of this formula on testing data yielded $CC = 0.976$ and $RMSE = 0.338$, respectively. This has been further depicted in Fig. 3.

5 Conclusion

This paper explores the ability of a multivariate linear regression technique in the generation of a discharge rating formula applicable to both, a standard Parshall flume of throat width 2.54 cm and a modified Parshall flume of throat width 3.18 cm. The formula generated was:

Fig. 3 Observed and predicted values of Q using multivariate linear regression on training and testing data set



$$Q = 0.0246H_a^{1.7742}$$

The value of $CC = 0.976$ and $RMSE = 0.338$ further shows that this formula can be used to directly find the discharge when using the aforementioned flumes.

Finally, it can be deduced from this study that regression techniques are promising modeling approaches and should be encouraged and further used in various problems associated with water resources engineering.

References

1. Skogerboe GV, Hyatt ML, England JD, Johnson JR (1966) Measuring water with Parshall flumes
2. Parshall RL (1928) Improved Venturi flume, The. CER; 47/52-54
3. Saran D, Tiwari NK, Ranjan S, Parshall Flumes: a review

4. Parshall RL (1950) Measuring water in irrigation channels with Parshall flumes and small weirs. Circular (the United States. Department of Agriculture); no 843
5. Cone VM (1917) The venturi flume. US Government Printing Office
6. Kilpatrick FA, Schneider VR (1983) Use of flumes in measuring discharge. US Government Printing Office
7. Parshall RL (1953) Parshall flumes of large size. Bulletin (Colorado Agricultural and Mechanical College. Extension Service); 426A
8. Robinson AR (1957) Parshall measuring flumes of small sizes. Technical bul.(Colorado Agricultural Experiment Station); 61
9. Abt SR, Thompson K, Staker K (1989) Discharge correction for longitudinal settlement of Parshall flumes. Trans ASAE 32(5):1541–1544
10. Abt SR, Staker KJ (1990) Rating correction for lateral settlement of Parshall flumes. J Irrig Drain Eng 116(6):797–803
11. Genovez A, Abt S, Florentin B, Garton A (1993) Correction for settlement of Parshall flume. J Irrig Drain Eng 119(6):1081–1091
12. Abt S, Genovez A, Florentin B (1994) Correction for settlement in submerged Parshall flumes. J Irrig Drain Eng 120(3):676–682
13. Abt SR, Bradley Florentin C, Genovez A, Ruth BC (1995) Settlement and submergence adjustments for Parshall flume. J Irrig Drain Eng 121(5):317–321
14. Savage BM, Heiner B, Barfuss SL (2014) Parshall flume discharge correction coefficients through modelling. In: Proceedings of the Institution of Civil Engineers-Water Management, vol 167, no 5. Thomas Telford Ltd., pp 279–287
15. Horton RE (1906) Weir experiments, coefficients, and formulas, vol 16. US Government Printing Office

A Review on Bone Regeneration via Porosity Development Using Smart Manufacturing Techniques



Mahesh Chaudhary, Jinesh Kumar Jain, and Toshit Jain

Abstract Biomaterials are the materials that may be in natural or synthetic, lifeless or alive, and usually made of various components that interact with biological systems. Biomaterials are generally used in medical application to replace or augment a natural function. Additive manufacturing methods are used to create a part or prototype of a 3D structure in a layer-by-layer form directly by computer-aided design (CAD). Porosity in biomaterials improves biocompatibility and helps in cell ingrowth, but decreases physical properties due to the increase in surface area per unit volume which reduces the mechanical strength of the scaffold. In this review, the porosity of titanium alloy is increased by the hydrogen trapped technique using TiH_2 and Ti solution by using selective laser sintering (SLS) or selective laser melting (SLM). The density of the scaffold is increased by pre-sintering and then post-processing with hot isostatic pressing technique.

Keywords Additive manufacturing · 3D printing · Biomaterials compatibility · Biocomposites · Bioprinting · Tissue engineering · Bone tissue scaffold · Bone regeneration · Porosity enrichment · Hap scaffold · Ti alloy scaffold

1 Introduction

Life expectancy in humans is increased due to upgrading in health care, but because of the natural body functioning of osteoporosis density of bones moderates. The most successful procedure for replacing or converting that damaged bone part is total hip replacement using bio-inert as input materials. Development of porous implants reduces shielding stress and thus enhancing osteointegration and increasing the working durability and stability. Therefore, the primary aim is to develop computational relational characteristics between its structure, porosity, and in mechanical properties of selected material, configuration, and shape of the scaffold by MATLAB

M. Chaudhary (✉) · J. K. Jain · T. Jain
Department of Mechanical Engineering, Malaviya National Institute of Technology, Jaipur
302017, India
e-mail: 2019ppe5370@mnit.ac.in

© The Author(s), under exclusive license to Springer Nature Singapore Pte Ltd. 2022
K. Govindan et al. (eds.), *Advances in Mechanical and Materials Technology*,
Lecture Notes in Mechanical Engineering,
https://doi.org/10.1007/978-981-16-2794-1_105

1209

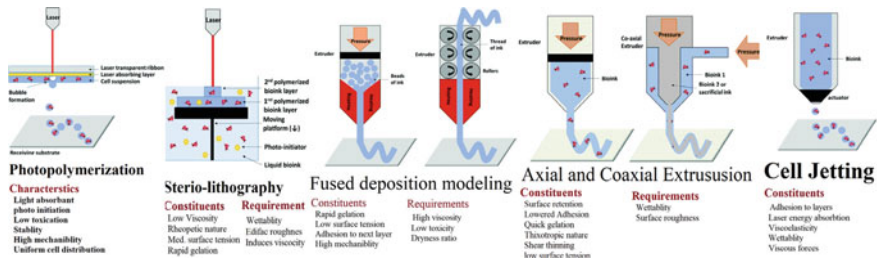


Fig. 1 AM technologies and material constituents

and Hyperworks using elasticity tensors in different sorts of bones and can be weighted using altered multipliers of body-centered cubic (BCC) and crystal structure [1, 2] prior taken to act in scaffold design. Later, design control of such tissue scaffolds with gradient modulus and homogenization techniques can be optimized with other topology optimization structures. Their analytical equation can be characterized by varied parameters of porosity, effective modulus, and evaluation of their analytical properties. The different types of materials properties and fabrication techniques are elaborated (Fig. 1) with their possibilities and type of deposition.

Hydroxyapatite (HAp) scaffolds are mainly used in implants, but its applications are limited due to limited mechanical properties and workability. Thus, nanocrystalline hydroxyapatite (nHAp) [1, 3] is compounded with numerous bioactive polymers for the generation of higher porous composite polymers applied in osteoinduction for orthopedic surgeries. Another technique is to redistribute natural bone by cladding/layering with glass and ceramic scaffolds to simulate composition and configuration in biological scaffold bond, minerals, or activation of genes to mimic bone regrowth.

Thus, such desired properties of polymers can be evaluated using the aforementioned computational approach by providing various composites, characterization, and reliability to use in the desired application. Later, fabrication of samples of selected compositions is done using the additive manufacturing approach (using selective laser sintering and direct laser melt sintering (DLMS)), and later, selection of scaffold for particular operation can be done by considering their biodegradability [4, 5] and biocompatibility accomplishments through in vitro and in vivo tests [6, 7].

Two different structures, known as cancellous and cortical bone, make osseous tissue, known as a bone. Cancellous [8] is the inner part of the bone spongy with 50–90% volume porosity. The dense outer layer of bone, i.e., cortical bone, has less than 10% volume porosity. For continuous ingrowth of bone tissue, porosity in a scaffold plays an important role. To transport nutrients and molecules to inner parts of a scaffold, open and interconnected pores facilitate cell ingrowth, vascularization, and waste material removal. Varying pore parameters can influence higher porosity increased surface area per unit volume and the biodegradation kinetics [9] of scaffolds. For bone formation, 100 and 150 μm are the minimum sizes, enhancing bone formation, and vascularization pore size should be larger than 300 μm [10–12].

The permeability and the mechanical properties of the nutrients to the scaffold are controlled by the pore volume (Table 1).

There are varieties of methods to prepare porous bone scaffolds with multiple material composition and techniques [17, 18]. Some of those used extensively are solvent casting, thermal-induced phase separation, particle/salt leaching, chemical/gas forming, freeze-drying, and foam gel. Porosity and pore volume decide the quality and rate of bone integration. For enhancing bone ingrowth and osseointegration [19, 20], large pores and high porosity are required. To determine the effectiveness of the porosity, structure of the pores concerning each other is another important factor. The pores either contain dead ends or interconnection. Porogens are added to introduce interconnecting macroporosity such as H_2O_2 , naphthalene, polymeric progen, or the foaming method. The sintering program or sintering temperature decides the microporosity. CaP [21–23] sintered at 1000 °C shows significantly higher porosity than that sintered at 1200 °C and a dramatic change in crystal size. Interconnected pores in CaP are advantageous in comparison to biomaterials containing dead-end pores. With the increase in pore volume, porosity increases and

Table 1 Biomedical materials [13–16]

Material composition	Abbreviation/representation	Potential applicability
Ti-based alloys	CP·Ti	Bone support and fixation
	Ti-6Al-4V	Stent development, synthetic valve fastening
	Ti-6Al-7Nb	Dental-based, knee-type joint, hip joints
	Ti-5Al-2.5Fe	Spinal-related implants
	Ti-15-Zr-4Nb-2Ta-0.2Pd	Dental based
	Ti-29Nb ₁₃ Ta _{4,6} Zr	Dental based
	83 to 7%; Ti13% to 17% Zr (Roxio lid)	Dental based
SS steel	316.L	Joint replacement, surgical tools, dentals, hip joints
Cobalt chromium matrix	Co-Cr-Mo, Co-Ni-Cr-Mo	Artificial valve, bone support and fixation, dental based joint replacement, hip-based joint
Smart alloys	Ni-Ti	Medullary cavity, heart stents
Polymers	PMMA, PE, PEEK	Dental applications, articular cartilage, hip joint bearing, knee joints
Zirconium-based bioglasses	SiO ₂ ; CaO; Na ₂ O; P ₂ O ₅ Zirconia	Dental applications, orthopedic implants, porous implants, dental applications
Alumina-based hydroxyapatite	Al ₂ O ₃	Dental uses
	Ca ₅ (PO ₄) ₃ (OH)	Dental applications, implant coating material

its biocompatibility also increases, but the mechanical property of the scaffold will decrease.

1.1 Metallic Biomaterials

Different additive manufacturing techniques are used to manufacture metallic biomaterials used as biomedical implants. Titanium- and cobalt-based materials are the primary materials used as biomaterials for medical implants. For biomedical applications, titanium and its alloy are prevalent materials due to their excellent biocompatibility and have extraordinary fatigue strength and resistance to corrosion. Other high strength-to-weight ratio makes part lighter than other material. Load-bearing implants such as hip joint or knee joint are made of titanium alloy due to its excellent load-bearing property. Titanium does not react with the body environment and provides excellent biocompatibility in cell ingrowth. Another alloy of titanium, Ti6Al4V [24, 25], is widely used in the biomedical application for their excellent load-bearing capability and biocompatibility.

2 Methodology

2.1 Porosity Creation Methods for Titanium

Hydrogen is a pore-forming agent, or we can say porogen due to its bubble-forming nature. Thus, trapped hydrogen gas will act as a porogen. When TiH_2 and Ti are mixed, the heat input during laser processing decomposes TiH_2 while releasing hydrogen gas. With an increase in TiH_2 , porosity will increase. A high degree of porosity was achieved using a mixture of TiH_2 and Ti having 40 wt% Ti, which will give a pore size of 200 to 500 mm at a laser power of 1000 W. SLM technique is used to manufacture a porous Ti structure similar to cancellous bone.

3D fiber deposition is the method of processing the Ti-based structure. A slurry was created using 0.5% aqueous methylcellulose, and Ti64 alloy powder solution was pushed to plotter machine through a syringe. The 3D scaffold was formed by layer-by-layer deposition of this solution and sintered at 1200 °C for two hours. Different square- and rectangular-shaped pore sizes in ranging from 200 to 800 mm with porosities ranging from 39 to 68% are achieved.

Porous and dense Ti-based materials are manufactured for biomedical applications by selective laser melting (SLM) or selective laser sintering (SLS). Ti6Al4V first sintered by a laser source and then hot isostatic pressing for improving the density up to 90% and more significant than this. Here we are replicating the developed scaffolds (Fig. 2) via simulated software online thereby using laser sintering methods

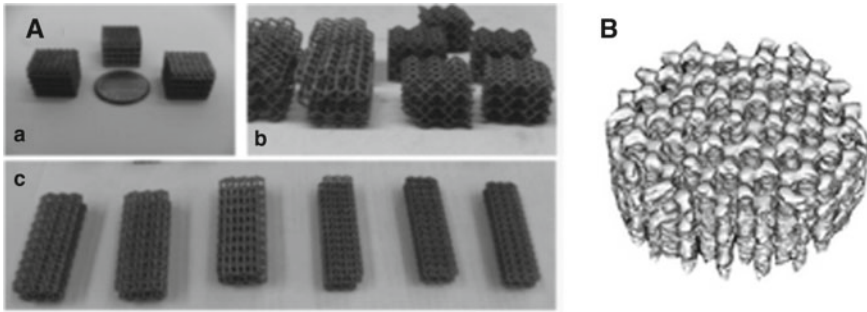


Fig. 2 **a** Ti-6Al-4V structures developed via S.L.S. [26, 27] and **b** meshed Ti scaffold fabricated using D.L.M.S. [28, 29]

for providing better suitability and desired responses in scaffolds. This will help us in making fabrication ease, thus providing better porous designs and linkages.

With the utilization of the selective laser sintering method, a net-shaped structure with controlled density can be manufactured. The properties of designed scaffolds can be contributed to the machine inputs. Thereafter, the laser properties can be adjusted, and alloy compositions can be made with defined parameters for desired responses.

Thus for the development of scaffolds of different constituents and materials, the research needs to undergo taking various parameters and approaches with suitable pore sizes and proportions. This approach will be done via different metallographic consults and research articles. Thus, the fabrication of various Ti-based alloy microstructures with the jetting-based composition is described below. This approach will provide us an intrinsic idea about how selection of composition will be prevalent and suited for particular application of techniques. All microstructures are taken at 500 μm scale except for rBMSC (ii) which is evaluated on 100 μm scale (Fig. 3).

There are also many researches conducted by researchers in this area and find much submissive to share for further selection of composition and type of structure to be developed. Please find the research accumulated by different researchers published in many research articles. The table consists of their names along with the research they have gone through with different approaches and quantified with suited feedbacks in their articles.

Review by previous researches

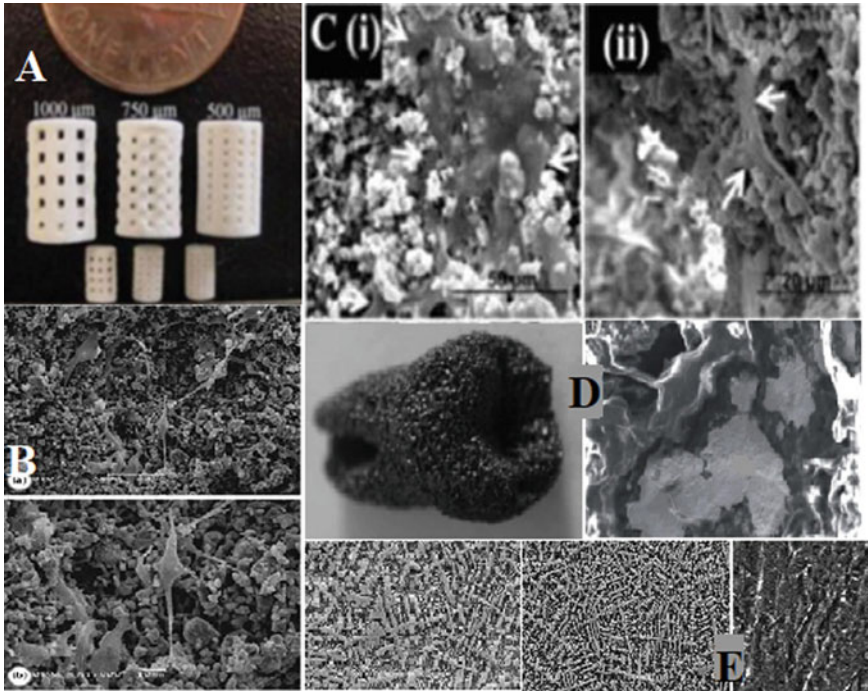


Fig. 3 **a** Binder jet polymer scaffolds, varying dimensions, and switched pore sizes (P.S), **b** biocompatibility of rBMSC scaffolds, **c** cell morphology on 500 μm P.S scaffolds, **d** SLM-based NiTi porous implant, and **e** multi-functional A.M. μ-structure of TiC, TiB, and Ti-pure scaffolds [28, 30–32]

S. No.	Researchers	Year	Base material	Support material	Technique used	Remarks
1	Hench [33]	2006	Silicate bioactive glass	(Si-OH) (CHA) (ACP)	3D glass-forming SiO ₂ with CaO and Na ₂ O	<ul style="list-style-type: none"> • Compositional features in 45S5's bioactivity • Osteoblasts (bone-regenerative gels) would form collagens • Perplexing for envisaging its living effects
2	Vallet-Regi [34]	2004	Phosphate bioactive glass	P2O ₅ glass-forming network	3D glass-forming SiO ₂ with CaO and Na ₂ O	<ul style="list-style-type: none"> • Strong chemical affinity toward the bone • Constituent ions available in organic, mineral bone phase • Possessing added clinical potentials toward restorable materials
3	Georg Hettich [35]	2019	Calcium phosphate (CaP)	Polyethyl methacrylate (PMMA)	Extrusion-based 3D printing	<ul style="list-style-type: none"> • CaP bone defects mainly focus scaffold, not considering their mechanical structures • Macroporous-TCP granules consisting with their different porosity <p>They modify the mechanical stability in bone tissues with granule withdrawal</p>

(continued)

(continued)

S. No.	Researchers	Year	Base material	Support material	Technique used	Remarks
4	Victoria Bruno [36]	2019	Solid titanium (Ti6Al4V ELI)	Bone mineral density (BMD) Polyurethane foam	Selective laser melting (SLM)	<ul style="list-style-type: none"> Force-displacement curves decoded for structures endured during linearity Physiological loading of samples evaluated at a crosshead Divulge deviations under the stiffness of implants Superior alterations detected through the latter imitations Natural osseointegration via designing functionally sorted meshes
5	Miranda [37]	2016	Ti6Al4V-HA	N/A	Hot pressing technique FGM design approach	<ul style="list-style-type: none"> Creates mingling with hot pressing effectiveness for production HA bioactivity shows the Ti6Al4V matrix with better alliance
6	Daniel Sundh [38]	2015	Transiliac crest biopsies	N/A	Tibia S.C. fat	<ul style="list-style-type: none"> Distinct parts of adipose tissue linked along BMSI through cortical microstructures of bone Tibia fats were initiate as autonomous of covariates

(continued)

(continued)

S. No.	Researchers	Year	Base material	Support material	Technique used	Remarks
7	Sybele Saska [39]	2017	BC-COL nanocomposites	Bacteria cellulose (B.C.) Collagens and appetites (Ap) Osteogenic growing peptides (O.G.P.) C-terminal-based pentapeptides (C.P.)	Carbodiimide-mediated coupling SEM FTIR P-NMR	<ul style="list-style-type: none"> The nanocomposite is based on bacteria-based cellulose studies, collagen development, appetite formation, and their osteogenic-based peptides <i>In situ</i> inclusion of apatite-based formation in bone-edifice apatite O.G.P. peptides prompt for regeneration of osteoblastic phenotypes This nanocomposite determines for non-cytotoxic, gene-toxic or maybe mutagenic effects
8	Yoon Shin Park [40]	2014	Extracellular matrix (ECM) Collagen-binding motif (CBM)	Osteocalcin (OCN) protein CBM-peptide-treated group (OVX.LP) estradiol-treated group (OVX-E)	Ovariectomized (OVX) mice	<ul style="list-style-type: none"> CBM peptides can be effectively used in persuading osteogenesis while reducing adipogenesis CBM peptide acts as a potential therapeutic mediator performing osteoporosis

(continued)

(continued)

S. No.	Researchers	Year	Base material	Support material	Technique used	Remarks
9	Nathaniel Hoguebe [23]	2018	self-assembling peptide (SAP) KFE-RDG	Matrix stiffness RGD (Arg-Gly-Asp) concentration	lipid vacuoles PPAR γ -2 expression	<ul style="list-style-type: none"> The density of cell binding and surrounding stiffness progressively acts as key regulators under the cell functional characteristics Binding sites and gel stiffness are swayed via cell dispersion and their separation
10	Min Sii Kang [41]	2016	Mesoporous bioactive glass nanospheres (MBNs)	FGF2 FGF18	Electrospinning Fibrous morphology	<ul style="list-style-type: none"> FGF2 and FGF18 were intended to endorse cell mitosis and angiogenesis Possessing good loading efficiency through protein molecules This novel therapeutic scaffolds are confined being possible space developing bone-regenerative 3-D matrix

3 Conclusion

- Porosity in biomaterials plays an important role in the biocompatibility of such compositions within living body's fluidic environment like their bloodstream and tissues present there.
- The various additive manufacturing techniques are utilized to create porous structure, and critical health issues can be accomplished by its capabilities.
- Development of customized implants with the emergence of AM technology and improvement in medical sector.
- Titanium cobalt and steel are some metals which are widely used in biomedical application.
- Materials comprising of polymers, composites, ceramics, and alloys with good tribology properties, mechanical strength along with their resistivity to erosion to improve biocompatibility can be advised to use for fabrication.
- Biodegradability and long-term response can be added to such fabricated implants, improving durability and balance with neighboring bones for lasting functionality.

References

1. Rogowska-Tylman J et al (2019) In vivo and in vitro study of a novel nanohydroxyapatite sonocoated scaffolds for enhanced bone regeneration. *Mater Sci Eng C Mater Biol Appl* 99:669–684
2. Pek YS, Gao S, Arshad MS, Leck KJ, Ying JY (2008) Porous collagen-apatite nanocomposite foams as bone regeneration scaffolds. *Biomaterials* 29(32):4300–4305
3. Sun F, Zhou H, Lee J (2011) Various preparation methods of highly porous hydroxyapatite/polymer nanoscale biocomposites for bone regeneration. *Acta Biomater* 7(11):3813–3828
4. Bornapour M, Muja N, Shum-Tim D, Cerruti M, Pegguleryuz M (2013) Biocompatibility and biodegradability of Mg–Sr alloys: The formation of Sr-substituted hydroxyapatite. *Acta Biomater* 9(2):5319–5330
5. Yoshikawa H, Myoui A (2005) Bone tissue engineering with porous hydroxyapatite ceramics. *J Artif Organs* 8(3):131–136
6. Gopinathan J, Noh I (2018) Recent trends in bioinks for 3D printing. *Biomater Res* 22:11
7. Ouyang L, Yao R, Zhao Y, Sun W (2016) Effect of bioink properties on printability and cell viability for 3D bioplotting of embryonic stem cells. *Biofabrication* 8(3):035020
8. Rosenberger RE, Fink C, Bale RJ, El Attal R, Muhlbacher R, Hoser C (2006) Computer-assisted minimally invasive treatment of osteochondrosis dissecans of the talus. *Oper Orthop Traumatol* 18(4):300–316
9. Ahlfeld T et al (2017) Development of a clay based bioink for 3D cell printing for skeletal application. *Biofabrication* 9(3):034103
10. Peak CW, Stein J, Gold KA, Gaharwar AK (2018) Nanoengineered colloidal Inks for 3D bioprinting. *Langmuir* 34(3):917–925
11. Wilson SA, Cross LM, Peak CW, Gaharwar AK (2017) Shear-thinning and thermo-reversible nanoengineered Inks for 3D bioprinting. *ACS Appl Mater Interfaces* 9(50):43449–43458
12. Guvendiren M, Molde J, Soares RM, Kohn J (2016) Designing biomaterials for 3D printing. *ACS Biomater Sci Eng* 2(10):1679–1693

13. Vu AA, Robertson SF, Ke D, Bandyopadhyay A, Bose S (2019) Mechanical and biological properties of ZnO, SiO₂, and Ag₂O doped plasma sprayed hydroxyapatite coating for orthopaedic and dental applications. *Acta Biomater* 92:325–335
14. Bose S, Ke D, Sahasrabudhe H, Bandyopadhyay A (2018) Additive manufacturing of biomaterials. *Prog Mater Sci* 93:45–111
15. Koch L et al (2018) Laser bioprinting of human induced pluripotent stem cells—the effect of printing and biomaterials on cell survival, pluripotency, and differentiation. *Biofabrication* 10(3):035005
16. Wu G et al (2018) Elastic polyurethane bearing pendant TGF-beta1 affinity peptide for potential tissue engineering applications. *Mater Sci Eng C Mater Biol Appl* 83:67–77
17. Shim JH et al (2017) Porosity effect of 3D-printed polycaprolactone membranes on calvarial defect model for guided bone regeneration. *Biomed Mater* 13(1):015014
18. Taniguchi N et al (2016) Effect of pore size on bone ingrowth into porous titanium implants fabricated by additive manufacturing: An in vivo experiment. *Mater Sci Eng, C* 59:690–701
19. Bose S, Banerjee D, Shivaram A, Tarafder S, Bandyopadhyay A (2018) Calcium phosphate coated 3D printed porous titanium with nanoscale surface modification for orthopedic and dental applications. *Mater Des* 151:102–112
20. Cohen DJ et al (2017) Performance of laser sintered Ti-6Al-4V implants with bone-inspired porosity and micro/nanoscale surface roughness in the rabbit femur. *Biomed Mater* 12(2):025021
21. Ahlfeld T et al (2018) Bioprinting of mineralized constructs utilizing multichannel plotting of a self-setting calcium phosphate cement and a cell-laden bioink. *Biofabrication* 10(4):045002
22. Chimene D et al (2018) Nanoengineered ionic-covalent entanglement (NICE) bioinks for 3D bioprinting. *ACS Appl Mater Interfaces* 10(12):9957–9968
23. Hogrebe NJ et al (2018) Independent control of matrix adhesiveness and stiffness within a 3D self-assembling peptide hydrogel. *Acta Biomater* 70:110–119
24. Ke D, Vu AA, Bandyopadhyay A, Bose S (2019) Compositionally graded doped hydroxyapatite coating on titanium using laser and plasma spray deposition for bone implants. *Acta Biomater* 84:414–423
25. Sahasrabudhe H, Bandyopadhyay A (2018) In situ reactive multi-material Ti6Al4V-calcium phosphate-nitride coatings for bio-tribological applications. *J Mech Behav Biomed Mater* 85:1–11
26. Fally M et al (2018) Photopolymerizable nanoparticle-polymer composite materials for light and neutron beam manipulations. Presented at the Proceedings of the 6th International Conference on Photonics, Optics and Laser Technology
27. Asri RIM et al (2017) Corrosion and surface modification on biocompatible metals: a review. *Mater Sci Eng C Mater Biol Appl* 77:1261–1274
28. Ran Q et al (2018) Osteogenesis of 3D printed porous Ti6Al4V implants with different pore sizes. *J Mech Behav Biomed Mater* 84:1–11
29. Fahmy-Garcia S et al (2018) Novel in situ gelling hydrogels loaded with recombinant collagen peptide microspheres as a slow-release system induce ectopic bone formation. *Adv Healthc Mater* 7(21):e1800507
30. Yin J, Yan M, Wang Y, Fu J, Suo H (2018) 3D Bioprinting of Low-concentration cell-laden gelatin methacrylate (GelMA) bioinks with a two-step cross-linking strategy. *ACS Appl Mater Interfaces* 10(8):6849–6857
31. Wang L, Kang J, Sun C, Li D, Cao Y, Jin Z (2017) Mapping porous microstructures to yield desired mechanical properties for application in 3D printed bone scaffolds and orthopaedic implants. *Mater Des* 133:62–68
32. Jones JR, Hench LL (2003) Regeneration of trabecular bone using porous ceramics. *Curr Opin Solid State Mater Sci* 7(4–5):301–307
33. Vallet-Regi M, González-Calbet JM (2004) Calcium phosphates as substitution of bone tissues. *Progr Solid State Chem* 32(1–2):1–31
34. Hettich G et al (2019) Calcium phosphate bone graft substitutes with high mechanical load capacity and high degree of interconnecting porosity. *Materials (Basel)* 12(21)

35. Bruno V (2019) The effects of porosity in selective laser melted titanium interbody cages and bone mineral density on subsidence: a biomechanical study. *BioMechanical Engineering*
36. Miranda G et al (2016) Design of Ti6Al4V-HA composites produced by hot pressing for biomedical applications. *Mater Des* 108:488–493
37. Sundh D, Rudang R, Zoulakis M, Nilsson AG, Darelid A, Lorentzon M (2016) A High amount of local adipose tissue is associated with high cortical porosity and low bone material strength in older women. *J Bone Miner Res* 31(4):749–757
38. Saska S et al (2017) Nanocellulose-collagen-apatite composite associated with osteogenic growth peptide for bone regeneration. *Int J Biol Macromol* 103:467–476
39. Park YS et al (2014) Selective osteogenesis by a synthetic mineral inducing peptide for the treatment of osteoporosis. *Biomaterials* 35(37):9747–9754
40. Kang MS, Kim JH, Singh RK, Jang JH, Kim HW (2015) Therapeutic-designed electrospun bone scaffolds: mesoporous bioactive nanocarriers in hollow fiber composites to sequentially deliver dual growth factors. *Acta Biomater* 16:103–116
41. Min Z, Huixue W, Yujie Z, Lixin J, Hai H, Yufang Z (2016) Synthesis of monodispersed mesoporous bioactive glass nanospheres for bone repair. *Mater Lett* (171):259–262

Various Methods of Metal Transfer in the Welding Process



Vinod Kumar Aswal and Jinesh Kumar Jain

Abstract The transfer of molten metal droplets from the electrode to the weld pool or work surface is considered as a metal transfer. The metal transfer makes a vital role in the formation of the weld pool. The size and shape of the droplet and the rate of transfer depend on the various factors of power source and welding power characteristics. These parameters mainly depend on the forces which are responsible for the metal transfer. There are two generous forces act on the droplet, i.e., aid metal transfer force, and the other one is retarding force. The various methods of metal transfer, i.e., globular transfer, spray transfer, short-circuit transfer, CMT, and their causes and affecting parameters have been reviewed in this article. The novel technique to control the metal transfer in different welding processes and with the help of double wire double-pulse GMAW, pulsed laser enhancing in short circuit transfer and underwater flux-cored wet welding as also discussed and observed that surface tension force, gravitational force and electromagnetic force play an important role in the formation and detachment of the droplet, and these forces can be controlled by the use of suitable polarity, current and a suitable power source. The pulsed metal transfer process, the overall time period during the formation and detachment of the metal droplet at the tip of the electrode, during the detachment period, facilitate the ODPP transfer to control welding parameters. Two dissimilar joints of Ti-Fe and other scan are also done by altering the temperature using the variable polarity CMT process.

Keywords Double wire double pulse GMAW · Underwater flux-cored wet welding · Metal transfer · WAAM · Laser arc welding

V. K. Aswal · J. K. Jain (✉)

Department of Mechanical Engineering, Malaviya National Institute of Technology, Jaipur, India
e-mail: jineshjain.mech@mnit.ac.in

1 Introduction

Welding is a fabrication process in which two materials are joining together through various processes. The welding process has been used in a wide range of applications such as ships, building construction, pipelines, nuclear power plants, boilers, aircraft, automobiles and railroads. There are some new technologies introduced in the field of welding such as using double filler wire, laser arc, etc. For producing good quality of the weld, using weld parameters makes a huge impact. In the microstructure study of the weld pool, the metal transfer makes a significant impact. There are several methods of metal transfer such as short circuit metal transfer, globular transfer, spray transfer, bridging metal transfer and cold metal transfer. Globular metal transfer process having a low current and larger droplet size is compared to electrode diameter. This process is frequently includes more spatters, So, the globular metal transfer is mostly used in those parts which does not make any impact in terms of product applications. In spray metal transfer, welding current is high and metal droplet size is lesser than electrode diameter. This process producing a stable arc with greater welding efficiency and is mostly used for thick plates. The short circuit metal transfer is a contact type in which the droplet touches the workpiece surface. This process needs low heat input and is mostly used for thin plates. These metal transfer methods affect many parameters such as penetration, the stability of the arc, production of spatter and porosity in the weld bead. The metal transfer mostly depends on various parameters such as type of polarity, welding current, welding voltage and the diameter of the electrode. To analyze the metal transfer phenomena, various studies have been attempted by researchers. Zhang et al. [1] observed the behavior of droplet transfer at the constant current power source and measured the weld pool geometry with a decrease in droplet size, and faster metal transfer gave uniform bead appearance. Ma et al. [2] studied the droplet transfer in the ultrasonic-assisted GMAW process through a mathematical model and observed the deformation of a droplet from the electrode and compared it with the conventional GMAW process. Rios et al. [3] observed the metal transfer behavior in plasma wire arc additive manufacturing and steady metal transfer attained with the convex weld pool because it reduces unwanted fleeting. Zhao et al. [4] studied the behavior of metal transfer in pulsed GMAW through a mathematical model and observed that pulsing variables significantly affected the metal transfer properties, and pulse using the maximum current but short duration of time results in prolonging pendant drop and quick detachment. Chen et al. [5] studied the behavior of metal droplet transfer in underwater flux-cored wet welding and observed that arc stability of welding downstream is always better than upstream welding. In this article, the behavior of weld pool with different metal transfer methods in various welding processes and also in some advancement in welding processes such as double-wire double-pulse GMAW, high-current super-TIG welding process, pulse-enhanced short circuit metal transfer welding process and variable polarity CMT process are discussed.

2 Methods of Metal Transfer

There are mainly three types of metal transfer considered in conventional metal arc welding.

2.1 Free Flight Metal Transfer

In this method, the gravitation force dominates over the other forces of metal transfer. Metal drops get detached from the electrode, pass through the arc and fall on the job. According to the effect of welding parameters, this mode of metal transfer is categorized into three types:

Globular metal transfer

This process occurs at a low welding current and having a larger arc length. In this process, metal droplets form at the electrode tip and grow until the force due to gravity surpasses the surface tension force. The molten droplet is large enough to be detached from the wire electrode and passes through an arc and falls on the weld pool. The droplet diameter is around double the diameter of the electrode (as shown in Fig. 1a). This process does not produce good weld bead geometry and occurs spatters frequently. This process is generally used for heavier thickness plates. The number of drop transfers in one sec is very less around 1/10 drop per second [6].

Spray metal transfer

The spray metal transfer is called for the spray of small metal droplets (as shown in Fig. 1b). Welding current density is higher than the globular metal transfer. High welding current density brings in a larger pinch force and a higher melting rate.

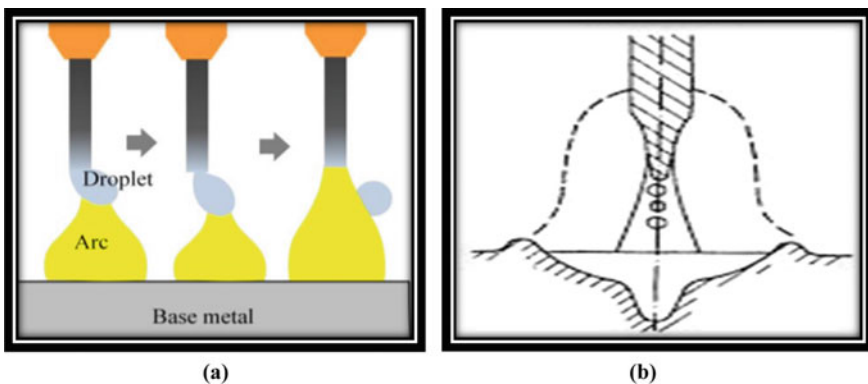


Fig. 1 Schematic diagram of **a** globular metal transfer process [7] and **b** spray metal transfer process [8]

Metal droplets formed rapidly at the electrode tip and pinched off quickly. The size of the droplets is very small. High welding current increases temperature that lowers the surface tension force. The rate of drop transfer is much higher than the globular transfer. In this process, the diameter of the droplet is smaller than the electrode diameter. This process occurs at high voltage. In this process, very few spatters are produced and mostly used in thick plates in the flat and horizontal positions [9].

Jet type

In this case, the electrode end becomes tapered and a jet of drops comes out from the electrode.

2.2 Contact Transfer

In this method, the arc is generated by touch and withdrawal of the electrode. This is also categorized into two types:

Bridging metal transfer

In this process, the wire electrode is exposed to a lower short circuit current during the contact drop pool. For metal transfer, the driving force is surface tension force and decreasing the impact of pinch effect in drop separation from electrode tip (as shown in Fig. 2). This process produced a uniform weld bead because of no generation of spatters. Constant current power source at a higher inductance level is generally used in this process. This process can be properly used to join thin metal sheets [10].

Short-circuiting transfer

Here the arcing end of the electrode starts melting, develops a spherical shape and makes contact with the molten metal pool in the base metal, and gets detached from

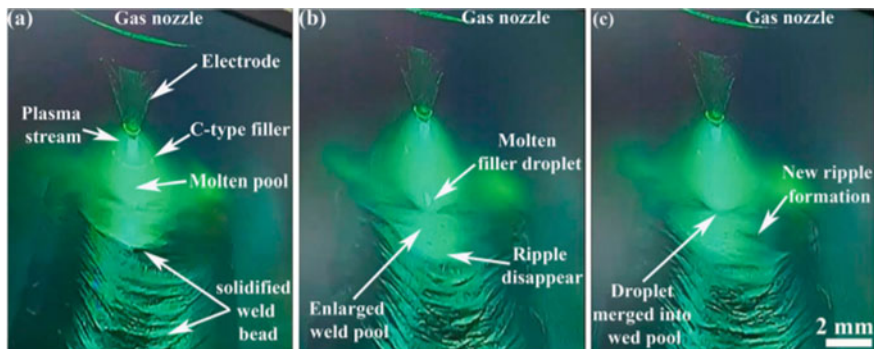


Fig. 2 Schematic diagram of bridging metal transfer: **a** droplet formation from C-type filler material; **b** droplet traveling toward weld pool; **c** droplet detachment on the molten pool [11]

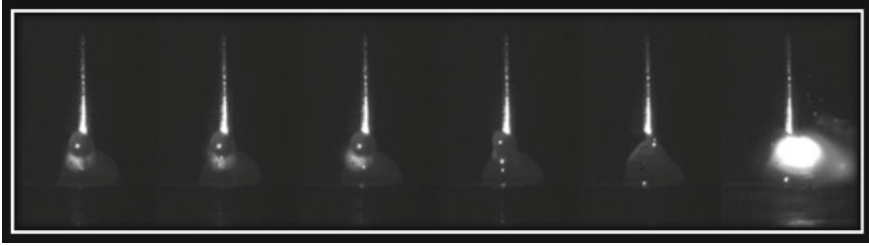


Fig. 3 Short circuit metal transfer in GMAW at low current application [2]

the electrode (as shown in Fig. 3). The hanging drop touches the joint area of the workpiece surface, the circuit is shorted, and the arc extinguishes. The electrode pinch effect increases due to an increase in current during shorting, neck formation quickens and ultimately quickens, and ultimately, the drops get detached from the electrode. The moment drop detaches from the electrode the circuit again opens, and the arc gets reignited. Normal short circuiting ranges from 20 to 200 per second. The short-circuiting frequency mainly depends on electrode wire diameter and arc voltage. As with the increase in wire diameter and welding voltage, the short circuit frequency starts decreasing [9].

Cold metal transfer (CMT)

CMT is a customized GMAW process based on the short circuit metal transfer process. CMT process differs from the conventional GMAW only by the type of metal droplet method not previously encountered. In the CMT process, when the electrode tip makes contact with the molten pool, the welding torch is reversed by the controller. In this process, spatters are not generated, and as soon as the droplet transfer is done, the arc is again burnt and with the preset current value electrode fed. According to the application, the CMT process can be divided into two variances such as welding of similar metal and welding of dissimilar metal [12, 13]. CMT with variable polarity welding process is used to provide better gap bridging ability, increases deposition rate and reduced heat input and joining of two dissimilar metals can be done by altering the temperature using the variable polarity CMT process [14].

2.3 Slag Protected Transfer

The metal transfer in SAW is similar to the one observed with bare wire electrodes as in GMAW. The droplet after detachment is either projected directly into the weld pool or is flung sideways. In the latter case, the droplet touches the wall of the flux cavity that surrounds the arc and slides along with it to the weld pool. This results in a slower rate of metal transfer. It is known as ‘flux-wall guided transfer’ and, for the obvious reasons, results in enhanced metal-slag reactions. Slag protected transfer

also takes place in the case of electro slag welding, wherein there is no solid-wall flux cavity, but the electrode melts continuously in a pool of high-temperature molten slag. In the case of FCAW, droplets are enveloped by molten slag, but the transfer is similar to that observed in GMAW [15].

3 Observations in Different Approaches

3.1 *The Behavior of Metal Transfer by Using Double-Wire Double-Pulse GMAW Process*

Metal transfer process during double-wire double-pulse GMAW is used with double pulse synchronous (DPS) and double pulse alternating (DPA) using a rapid computerized camera (1000 FPS). The metal transfer happened as one drop per pulse (ODPP) during welding. Double-wire GMAW consists of tandem GMAW and twin-wire GMAW, which are used to increase material deposition efficiency and travel speed. The welding of aluminum advances from pulsed globular to pulsed spray to pulsed streaming transfer has been seen in GMAW-P of 1.2 mm 4047 aluminum. Weld bead produces without defects like undercuts and humps. To control the current waveform, originally a novel double-pulse technique has been proposed based on low-frequency modulation using a high-frequency single phase.

Two types of pulses can be used to generate periodic strong and weak pulses:

- (a) Achieving ODPP at high frequency
- (b) Stirring the pool at a low frequency.

Stirring action is used to reduce porosity, grain refinement and improve the microstructure performance of weld bead geometry [16].

Wire took care of two discrete feeders and metal transfer observed by the rapid computerized camera. Bright arc light was efficiently filtered by using the principle of polarized light. Picture of metal transfer was caught at 1000 FPS, went through a SCSI data bus and transmitted to a computer. The laser path system involved a semiconductor laser (wavelength: 650 nm; power: 50 MW; spot diameter: 2 mm), beam expanding cylinder and an image-forming system. The droplet offset distance and wire diameter of the images were measured in the AutoCAD software (AutoCAD 2016, Autodesk), and the ratio of the actual to photographic wire diameter was calculated to get the actual droplet to offset distance based on the wire diameter (1.2 mm). Digital oscilloscope is used to record current and voltage signals. Leading and trailing voltages are attained between individuals' output terminals of the power suppliers, and leading and trailing currents are detected by two separate Hall effect sensors. Weld sample is obtained by wire electrode cutting and cleaning by abrasive paper, and corrosive testing is done by 4% HNO₃. The base material for this study is Q235 low-carbon steel (dimensions of 600 × 100 × 6). The filler material is H08Mn2SiA (diameter of 1.2 mm), shielding gas (argon) having flow rate around

20L/min, travel speed 13 mm/s, leading and trailing wire feed rate 100 mm/sec and 120 mm/sec, numbers of high-frequency strong and weak pulse 12 and 10. Spray transfer mode technique was used in this. Droplet offset distance was more prominent in DPS than DPA that will result in penetration deeper in DPA, so stable ODPP spray transfer is easier to attain in the DPA phase [17].

3.2 The Behavior of Metal Transfer in Underwater Flux-Cored Wet Welding Process

The impacts of flow rate and direction on metal transfer mode and molten pool shape in underwater wet flux-cored wet welding processes were studied. The electric signal outcomes are demonstrated, and the stability of the FCWW process is reduced by increasing the flow rate. In this experiment, two droplet transfer methods were introduced, i.e., globular repelled transfer and surface tension transfer method [18].

The substrate used in this process was Q235 mild steel which has a size of $200 \times 60 \times 18$ mm and filler wire having a composition of $\text{TiO}_2\text{-CaF}_2\text{-CaO-SiO}_2$, having 1.6 mm diameter with help of direct current reverse polarity having current 200 amp, voltage 32 V, traveling speed 2 mm/sec, wire extension 20 mm. In globular repelled transfer mode, arc voltage increases from 28.3 to 62.4 V, and welding current decreases from 276.9 to 21.7 A. In surface tension transfer mode, welding voltage reduces from 30.10 to 25.20 V, and current increases from 133.20 to 287.50 amp, and as the flow rate increases, the percentage of GRTM increases and STTM decreases. When the flow was in escapable, for decreasing the spatters during welding direction of welding should be upstream [19].

3.3 The Behavior of Metal Transfer on 3Cr12 Stainless Steel by GMAW Process

The behavior of droplet transfer on 3cr12 stainless steel was studied. The weld should be done in the butt joint. The modification in welding positions will affect the transfer modes partially due to the effect of gravity. Mode of metal transfer used in this globular and spray transfer in vertical up and vertical down. The base material is 3Cr12 stainless steel and wire electrode A5.9ER309L with a diameter of 1 mm. Shielding gas had a flow rate of 15–20 L/min, voltage 15–35 V and welding current 100–350 A [20].

The yield strength and ultimate tensile strength of spray transfer were lower than the globular transfer in the downward direction, while the percentage extension and percentage deduction in the area of spray transfer were higher than the globular transfer in the downward direction. The globular transfer had enhanced microstructural properties in the upward direction compared to the downward direction. The

globular down hand had better mechanical properties than the spray down hand. Globular vertical up had better mechanical properties than globular vertical down. Due to high heat input, welding in the vertical position (downward, upward and overhead) could not be performed in the spray transfer process. Heat input is 1 kJ/mm for a better outcome in grain development that is increasingly articulated in the HAZ [21].

3.4 The Behavior of Metal Transfer in the GMAW Process

Droplet size formed during GMAW is anticipated by static force balance theory and instability theory as a function of current. For the pinch instability phenomenon to happen, that is fluid metal should be in the form of a cylinder which is at a higher condition of free energy than a relating liquid metal sphere. Metal transfer with steel electrode shielded with Ar 2% O₂ shows steadily transition from globular to projected spray projected by the streaming transfer mode. The static force balance theory can anticipate the droplet size in the globular transfer range, but it diverges in spray transfer, and the cause of the deviation is geometry change of electrode due to taper formation at the electrode tip. If the taper is not formed, then we can expect the droplet size very accurately in spray transfer, which appeared in pulse current welding. Pinch instability theory neglects to clarify the impact of the electrode extension or of changes in shielding gas on metal transfer mode [22] (Table 1).

4 Conclusion

Review of the mode of metal transfer in various processes is discussed here. The main conclusions of this study are:

- In the CMT process, two dissimilar joints of Ti-Fe and others can also be done by altering the temperature using the variable polarity CMT process. With the decrease in the ratio of positive-to-negative electrode, penetration, weld pool temperature and the amount of Ti₅Si₃ decline as high heat input is provided to the deposited wire.
- Electrode polarity also affected the metal transfer, and in DCRP polarity, globular repelled metal transfer and in DCSP polarity, spray transfer mode were observed. DCSP produced higher arc stability and fewer weld spatters.
- In the laser arc hybrid welding process, with an increase in arc energy, the metal transfer changes from short circuit to a combination of short circuit and globular transfer and further followed by a spray transfer process.
- In the FCWW process, due to high heat input, welding in a vertical position (in downward, upward and overhead) could not be performed in the spray

Table 1 Mode of metal transfer for different welding processes

S. No.	Name of researchers	Year	Base material	Filler material	Mode of metal transfer	Effect on welded joint	Remarks
1	Ma et al. [2]	2019	Q235 low-carbon steel	H08Mn2SiA wire of 1.2 mm diameter	Globular metal transfer mode	In the ultrasonic-assisted GMAW process, an additional force was introduced during droplet transfer. This force is the transverse shearing force of the ultrasonic vibration on the metal droplet, increases the droplet transfer rate The detachment of metal droplets is measured through MATLAB software, and the droplet size decreases during the transition period	FLUENT software, a 2D non-axisymmetric mathematical model of ultrasonic-assisted GMAW droplet transfer is recognized For calculating the droplet size, MATLAB software is used

(continued)

Table 1 (continued)

S. No.	Name of researchers	Year	Base material	Filler material	Mode of metal transfer	Effect on welded joint	Remarks
2	Chen et al. [5]	2018	Q235 mild steel	TiO ₂ -CaF ₂ -CaO-SiO ₂	Globular metal transfer, surface tension, metal transfer	Arc stability of downstream was always better than upstream With increasing the heat dissipation, the flow rate increases, results in decreasing the temperature of the arc and deeper penetration	Using direct current reverse polarity, By using welding upstream and downstream, the behavior of droplet transfer is observed

(continued)

Table 1 (continued)

S. No.	Name of researchers	Year	Base material	Filler material	Mode of metal transfer	Effect on welded joint	Remarks
3	Xu et al. [7]	2020	304 stainless steel	CaF ₂ - Al ₂ O ₃ filler wire	Globular repelled, surface tension and spatter like metal transfer process	Droplets of hollow sphere type, having smaller gravitational force, producing spatter like droplet during underwater wet welding These hollow droplets having smaller gravitational force, the repulsive force more, result in the arc broken easily The metal droplet detaches from the electrode and results in spatters in the weld bead	The underwater wet welding process is used in which molten metal droplet having a hollow cavity introduces
4	Jun et al. [11]	2019	ASTM A283 steel plate	ER 100S-6 C-type filler wire	Bridging metal transfer process	The metal deposition rate was increased in super-TIG welding as compared to conventional GTAW In this process, a good weld bead is generated	In high-current super-TIG welding, a C-type filler wire is used which minimizes the molten pool depression Direct current electrode negative polarity was used

(continued)

Table 1 (continued)

S. No.	Name of researchers	Year	Base material	Filler material	Mode of metal transfer	Effect on welded joint	Remarks
5	Derekar et al. [23]	2020	Al-Mg-Mn Alloy	Solid wire ER5183	CMT and pulsed MIG	The pulsed metal inert gas having more hydrogen contains than cold metal transfer because of high energy of arc gives hotter melt pool and slower cooling rate Low heat input gives a higher total pore volume fraction in the pulsed metal transfer	The experiment was analyzed by varying various conditions: Interlayer temperature Heat input Dwell time
6	Balasubramanian et al. [24]	2020	Ti, Al, Mg and stainless steel substrate	CuSi ₃ electrode	Cold metal transfer mode	By reducing over weld in the weld area, welding efficiency increases If the weld joint area provided maximum heat input, then the weld joint having maximum tensile strength Grain structure is unaffected in the CMT process	Two dissimilar metals are joined, and the behavior of the weld pool is observed

(continued)

Table 1 (continued)

S. No.	Name of researchers	Year	Base material	Filler material	Mode of metal transfer	Effect on welded joint	Remarks
7	Cai et al. [25]	2020	5A06 aluminum alloy	5183 aluminum alloys	Short circuit and globular metal transfer process	<p>The penetration is affected by the mode of metal transfer</p> <p>When the flow rate of He increases, penetration first increases, then decreases, and finally increases</p> <p>Short-circuiting frequency increases with an increasing flow rate of He</p> <p>In shielding gas, if He was used current increased but if Ar was used current decreased</p>	<p>When Ar is supplied, metal transfer is globular, while He is supplied, metal transfer mode is a short circuit</p> <p>Direct current electrode positive polarity is used</p>

(continued)

Table 1 (continued)

S. No.	Name of researchers	Year	Base material	Filler material	Mode of metal transfer	Effect on welded joint	Remarks
8	Chen et al. [26]	2020	Mild steel plate	ER70S-6 wire	Short circuit metal transfer mode Spray transfer mode	The drop deflection is avoided by the use of double-sided laser-driven metal transfer, and if a single laser is used due to the small size of the metal droplet drop deflection is large The double-sided metal transfer increases metal transfer frequency, even at a very low current	A single-side and double-side laser metal transfer processes are used The constant current power supply is used The metal droplet transfer is done by laser recoil force
9	Panchenko et al. [27]	2020	5056 aluminum alloy substrate	Al-Mg-Mn filler wire	Short circuit transfer mode	An increase in travel speed provides an increment in the ductile and tensile properties of the weld metal	With the help of this process, thin and thick metals can be welded

(continued)

Table 1 (continued)

S. No.	Name of researchers	Year	Base material	Filler material	Mode of metal transfer	Effect on welded joint	Remarks
10	Singh et al. [28]	2020	Aluminum (AA5052) and steel (DP780)	Aluminum-based silicon-enriched filler (AlSi5)	Combination of cold metal transfer mode and pulsed metal inert gas (CMT + P)	<p>Because of reducing the fluidity of wire, with an increase in Al sheet size, the weld joint wettability is decreased</p> <p>This process produces a good weld bead with stable arc formation, spatters free and higher wettability</p> <p>By increasing the wire feed rate, significant improvement in wettability of joint is observed</p>	CMT with a pulsed process is used to weld two dissimilar metals (Al and steel) with varying Al sheet thickness through a lap joint

(continued)

Table 1 (continued)

S. No.	Name of researchers	Year	Base material	Filler material	Mode of metal transfer	Effect on welded joint	Remarks
11	Zhang et al. [29]	2020	6061 aluminum alloy	ER4043 filler metal	Cold metal transfer mode	By decreasing the positive-to-negative electrode ratio, the maximum value of the negative cycle is lower Because of higher heat input, with an increase in positive duty cycles, grain size increases The microhardness in the fusion zone and HAZ was increased with positive duty cycle and tensile strength initially increased but decreased after attained a certain limit	CMT with variable polarity welding process is used which gives better gap bridging ability, increases deposition rate, and reducing heat input With help of electrode positive-to-electrode negative ratio, behavior of welding parameters was observed

(continued)

Table 1 (continued)

S. No.	Name of researchers	Year	Base material	Filler material	Mode of metal transfer	Effect on welded joint	Remarks
12	Zhang et al. [30]	2020	Mild steel (Q235) plates	A5.20 E71 T wire	Globular repelled transfer mode Spray transfer mode	DCSP produced higher arc stability and fewer weld spatters In DCSP, the electromagnetic force is used to transfer metal droplets and the necking appeared easily In DCRP, EMF retarded metal transfer	The self-shielded FCAW process with DCSP and DCRP was observed In DCRP polarity, globular repelled transfer mode is performed and in DCSP polarity, spray transfer mode is observed
13	Mou et al. [31]	2020	Ti-6Al-4V and stainless steel	ERCuSi-A wire	Cold metal transfer mode	Two dissimilar joints of Ti-Fe and others can also be done by altering the temperature using the variable polarity CMT process With decreases in electrode positive-to-negative ratio, the penetration and weld pool temperature decrease	CMT with variable polarity welding process is used, and with help of electrode positive-to-electrode negative ratio, behavior of welding parameters was observed

(continued)

Table 1 (continued)

S. No.	Name of researchers	Year	Base material	Filler material	Mode of metal transfer	Effect on welded joint	Remarks
14	Liu et al. [32]	2020	6061 Al alloy	ER4043	CMT + P metal transfer mode	There is a variation in the behavior of microstructure observed in thick wall section to thin wall section for both CMT and CMT + P processes The longitudinal tensile strength of the thin wall section is higher as compared to the transverse tensile strength	WAAM of Al alloy is carried out with CMT + P process

(continued)

Table 1 (continued)

S. No.	Name of researchers	Year	Base material	Filler material	Mode of metal transfer	Effect on welded joint	Remarks
15	Huang et al. [33]	2019	Al6061 T6 base plate	ER 4047	Globular repelled and spray metal transfer process	Bypass current increment helps droplets to attach with the electrode and take more time to detach from the electrode In constant power source, by increasing bypass current, metal transfer rate increases, droplet diameter reduces and results in a variation of EMF	Effect of bypass current in GMAW process studied The constant current power supply is used
16	Sravanthi et al. [34]	2019	5052 Al Alloy with mild steel	BA404Al wire diameter 1.3 mm	Cold metal transfer mode	The presence of Fe-Si-Al IMC layer enhanced the hardness of weld bead of mild steel, and the matrix results in increasing localized corrosion	Al ₃ F ₃ Si ₂ , Al ₃ FeSi, FeAl, Fe ₂ Al ₅ intermetallic compounds are found With the help of nitric acid solution, two dissimilar metals are joined through metal inert gas brazing

(continued)

Table 1 (continued)

S. No.	Name of researchers	Year	Base material	Filler material	Mode of metal transfer	Effect on welded joint	Remarks
17	Hao et al. [35]	2019	TC4 + ST16 wire	CuSi ₃ electrode	Globular metal transfer mode	The diffusion of Si and Ti into the ST16 workpiece facilitates solution strengthening and at the interface and increases hardness	Ti ₂ Cu, TiCu, AlCu ₂ Ti electrode and TiCo ₂ IMC were found

(continued)

Table 1 (continued)

S. No.	Name of researchers	Year	Base material	Filler material	Mode of metal transfer	Effect on welded joint	Remarks
18	Jia et al. [36]	2019	Aluminum alloy	ER2319 aluminum alloy wire	Pulsed laser short circuit, spray and globular metal transfer	The globular transfer and short circuit stability to a stable ODPP spray transfer The laser recoil force helps in the detachment of droplets. Hence, increases the short-circuiting frequency The frequency of metal transfer increases by decreasing weld spatters The amount of heat input decreases with the addition of a pulsed laser	In pulsed mode, IPG YLS 4000 laser fiber was used There is an angle of 45 degrees between the torch and laser direction
19	Wu et al. [37]	2019	Q235 low-carbon steel	H08Mn2SiA	Spray transfer mode	By using DPA, phase penetration is deeper and we got a well-pronounced weld bead	Observed by DPS and DPA

(continued)

Table 1 (continued)

S. No.	Name of researchers	Year	Base material	Filler material	Mode of metal transfer	Effect on welded joint	Remarks
20	Madyira et al. [38]	2019	3Cr12 stainless steel	A5.9ER309L	Globular transfer mode Spray transfer mode	Due to high heat input, welding in a vertical position (downward, upward and overhead) could not be performed in the spray transfer process Globular down hand has high mechanical properties High mechanical properties are shown by globular vertical up compared to vertical down	Butt weld joint, using vertical welding up and down

(continued)

Table 1 (continued)

S. No.	Name of researchers	Year	Base material	Filler material	Mode of metal transfer	Effect on welded joint	Remarks
21	Teixeira et al. [39]	2019	AISI 1020 carbon steel plates	AWS ER70S-6 wires	Globular repelled and spray transfer process	There is a problem in small diameter electrode wire due to arc stability, results in spatters occurs, this issue mostly arises in CO ₂ shielding gas. For CO ₂ shielding gas, interchange did not happen from globular to spray metal transfer because of transition current increases. An increase in transition current with electrode diameter and in addition to O ₂ in Ar from globular to spray transfer method	GMAW process with DCRP is used and for different electrode diameters and different shielding gas, the behavior of metal transfer process and weld bead shape measured

(continued)

Table 1 (continued)

S. No.	Name of researchers	Year	Base material	Filler material	Mode of metal transfer	Effect on welded joint	Remarks
22	Zhang et al. [40]	2018	Q235 steel	ER50-6-type wire	Globular metal transfer mode	In BC-TWIAW, dilution rate decreases and deposition rate increases as compared to conventional GMAW	The bypass current technique with a tandem electrode is used to increase penetration
23	Valensi et al. [41]	2018	Alloy made up of Al, Ti, Zr	70S, AS26, G002, LZX23	Spray metal transfer process	With a decrease in Si content, welding parameter increases, but arc stability increases to a certain limit Adding of Zr gives higher conductivity in spray metal transfer The addition of alkali allows for a stable arc in the spray metal transfer method	Microstructure behavior of welding electrode wire composition is studied in GMAW process with DCEP polarity The constant current power source is used

(continued)

Table 1 (continued)

S. No.	Name of researchers	Year	Base material	Filler material	Mode of metal transfer	Effect on welded joint	Remarks
24	Liu et al. [42]	2018	High-strength (ARL 4460) steel plates	ASS filler wire	Short circuit, globular, spray, and projected metal transfer	By increases current, spray transfer is achieved from the projected transfer process In the laser metal active gas process, the arc is compressed by laser plasma, which leads to increasing electromagnetic resistance, which changes the droplet shape and decreases the transition frequency	The behavior of the weld pool was studied by various metal transfer processes through laser metal active gas hybrid welding process

(continued)

Table 1 (continued)

S. No.	Name of researchers	Year	Base material	Filler material	Mode of metal transfer	Effect on welded joint	Remarks
25	Cho et al. [43]	2020	V-groove joint	AWS5 electrode wire	Spray transfer mode Flux wall metal transfer	In the spray transfer method, the droplet detached to the V-groove joint at a very high speed. Thus, the energy of droplet detachment melts the joint area and results in deeper penetration and a narrow weld bead	The SAW process at low current is used to analyze the weld pool behavior In this process, the CFD model for guided metal transfer is introduced
26	Yang Lei et al. [44]	2017	AA6061-T6	ER 4043 electrode wire	CMT mode Pulsed mode	CMT method produces very few weld defects such as partial tearing and gives better weld bead shape In bottom welding, the heat dissipation rate increases and results in small HAZ	Three welding metal transfer methods are used to observe the behavior of the weld pool

(continued)

Table 1 (continued)

S. No.	Name of researchers	Year	Base material	Filler material	Mode of metal transfer	Effect on welded joint	Remarks
27	Pang et al. [45]	2016	AA6061 T6 base plate	ER 4043	Short-circuiting transfer CMT + P transfer mode	Penetration is decreased with an increase in the number of CMT short circuit. Maximum penetration is observed by the pulses process with an increased number of pulses There is no spattering in CMT + P process for all the welding variables	The CMT with pulses metal transfer method is used
28	Li et al. [46]	2016	Q235 steel	H08Mn2SiA wire	Short circuit, globular and spray metal transfer	With increasing arc energy, short circuit metal transfer changes to a combination of short circuit and globular metal transfer, then followed by a spray transfer process	Metal transfer behavior is studied by laser arc hybrid welding process This process is mostly used for welding thick plates

(continued)

Table 1 (continued)

S. No.	Name of researchers	Year	Base material	Filler material	Mode of metal transfer	Effect on welded joint	Remarks
29	Dutra J Carlos et al. [47]	2015	5083H116	5183 and 5087 filler wire	CMT + P transfer mode	The microstructural properties of weld bead increase in 5087 electrode wire in terms of tensile strength	The behavior of wire electrode in welding of Al alloy is studied through CMT with pulse metal transfer
30	Sun et al [48]	2015	Ti-6Al-4V Alloy	As base metal	Short circuit metal transfer	The frequency of droplet transfer increases with the wire feed rate and decreasing inductance correction	The CMT process is used with low heat input, and in this experiment, droplet contacts with weld pool and return gives droplet transfer in short circuit transfer mode
31.	Mez et al. [49]	2015	Zn-coated S235 steel sheet and Al alloy	4043 (AlSi5) Al alloy	Short-circuiting metal transfer mode with variable frequency	The decrease in drop weight deposited during each short circuit and an increase in short circuit frequency Welding of Al and steel provides good weld bead	The CMT process is used to weld the Zn-coated steel with Al alloy through a lap joint

(continued)

Table 1 (continued)

S. No.	Name of researchers	Year	Base material	Filler material	Mode of metal transfer	Effect on welded joint	Remarks
32	Feng et al. [50]	2009	Thin aluminum sheets	AlSi5 alloy wire	Short circuit metal transfer mode	At low heat input, the CMT process decreases deflection of thin sheets and producing spatters free weld bead For pure Al, shows gap bridging ability at low heat input	Three phases are introduced by decreasing the heat input and current in droplet transfer such as short-circuiting, highest current and background current phase

transfer process, and high mechanical properties are shown by globular vertical up compared to vertical down.

- In both phases DPS and DPA, ODPP spray transfer was attained. But it was easier to attain with the DPA phase because droplet offset distance was lesser in the DPA phase which results in penetration which was significantly deeper.
- The surface tension force, the gravitational force and EMF make a significant impact in the formation and detachment of the droplet and which can be controlled by the use of suitable polarity, current and a suitable power source.
- In submerged arc welding plate and electrode, melting efficiency is reciprocal to each other. By increasing electrode extension and current electrode melting efficiency increases, and it declines with electrode diameter and voltage.

The joining of dissimilar metals having large fusion temperature differences is still a critical problem. The different metallurgical constraints in the welding of dissimilar metal are a great challenge for the researcher. The CMT plays a crucial role to satisfy the dissimilar metal conditions up to some extent but still having more research space to work out to satisfy these constraints.

References

1. Zhang X, Gao H, Zhang G (2020) Current-independent metal transfer by utilizing droplet resonance in gas metal arc welding. *J Mater Process Technol*, 279
2. Ma G, Liu J, Yu L, Hong L, He Y (2020) Numerical simulation of droplet transfer process in ultrasonic-assisted MIG welding. *Sci Technol Weld Joining* 25(3):179–189
3. Rios S, Colegrove PA, Williams SW (2018) Metal transfer modes in plasma wire + arc additive manufacture. *J Mater Process Tech*
4. Zhao Y, Lee P-S, Chung H (2019) Effect of pulsing parameters on drop transfer dynamics and heat transfer behavior in pulsed gas metal arc welding. *Int J Heat Mass Transf* 129(1):1110–1122
5. Chen H, Guo N, Shi X, Du Y, Feng J, Wang G (2018) Effect of water flow on the arc stability and metal transfer in underwater flux-cored wet welding. *J Manuf Processes*, 3103–3115
6. Fan HG, Kovacevic R (1999) Droplet formation, detachment, and impingement on the molten pool in gas metal arc welding. *Metal Mater Trans B* 30:791–801
7. Xu c, Guo N, Zhang X, Chen H, Fu Y, Zhou L (2020) Internal characteristic of droplet and its influence on the underwater wet welding process stability. *J Mater Process Technol*, 280
8. https://www.weldability-sif.com/media/docs/Intro_MIG_Welding.pdf
9. Singhal TS, Jain JK (2020) GMAW cladding on metals to impart anti-corrosiveness: Machine, processes and materials. *Mater Today: Proc* 26(6):2432–2441
10. Węglowski M (2008) Effect of welding current on metal transfer in GMAW. *Arch Mater Sci Eng* 33:49–56
11. Jun JH, Park JH, Cheepu M, Cho SM (2020) Observation and analysis of metal transfer phenomena for high-current super-TIG welding process. *Sci Technol Weld Join* 25(2):106–111
12. Furukawa K (2006) New CMT arc welding process – welding of steel to aluminium dissimilar metals and welding of super-thin aluminium sheets. *Weld Int* 20(6):440–445
13. Pickin CG, Young K (2006) Evaluation of cold metal transfer (CMT) process for welding aluminium alloy. *Sci Technol Weld Joining* 11(5):583–585
14. Sonia P (2019) Review on heat and mass transfer in submerged arc welding (SAW) and gas metal arc welding (GMAW). *Int J Eng Adv Technol*, 8:503–512
15. Jain A, Sonia P, Kumari S, Pushp P (2020) Study of intermetallic compound (IMC) formed in welding of steel with magnesium: a review. *Mater Today: Proc* 26(2):1159–1166

16. Subramaniam S, White DR, Jones JE, Lyons DW (1998) Droplet transfer in pulsed gas metal arc welding of aluminium. *Weld J*
17. Wu K, Yin T, Ding N (2018) Effect of phase on the behavior of metal transfer in double-wire pulsed GMAW. *Int J Adv Manuf Technol* 97:3777–3789
18. Guo N, Yunlong Fu, Wang Y, Yongpeng Du, Feng J, Deng Z (2017) Effects of welding velocity on metal transfer mode and weld morphology in underwater flux-cored wire welding. *J Mater Process Technol* 239:103–112
19. Guo N, Wang M, Du Y, Guo W, Feng J (2015) Metal transfer in underwater flux-cored wire wet welding at shallow water depth. *Mater Lett* 144:90–92
20. Sonia P, Jain JK, Saxena KK (2020) Influence of severe metal forming processes on microstructure and mechanical properties of Mg alloys. *Adv Mater Process Technol*
21. Ibrahim IA, Mohamat SA, Amir A, Ghalib A (2012) the effect of gas metal arc welding (GMAW) processes on different welding parameters. *Procedia Eng* 41:1502–1506
22. Kim YS, Eager TW (1993) Analysis of metal transfer in gasmetal arc welding
23. Derekar KS, Addison A, Joshi SS (2020) Effect of pulsed metal inert gas (pulsed-MIG) and cold metal transfer (CMT) techniques on hydrogen dissolution in wire arc additive manufacturing (WAAM) of aluminium. *Int J Adv Manuf Technol* 107:311–331
24. Balasubramanian M, Choudary MV, Nagaraja A, Sai KOC (2020) Cold metal transfer process— a review. *Mater Today: Proc*
25. Cai X, Lin S, Wang B, Dai H, Fan C, Yang C (2020) Droplet transfer and weld formation of MIG welding with Ar-He alternating gas for aluminum alloy. *J Manuf Process* 49:94–101
26. Chen SJ, Jia YZ, Xiao J (2020) Double-sided pulsed laser driven metal transfer in GMAW. *J Manuf Process* 49:196–203
27. Panchenko O, Kurushkin D, Mushnikov I, Khismatullin A, Popovich A (2020) A high-performance WAAM process for Al–Mg–Mn using controlled short-circuiting metal transfer at increased wire feed rate and increased travel speed. *Mater Des* 195:1–11
28. Singh J, Arora KS, Shukla DK (2020) Lap weld-brazing of aluminium to steel using novel cold metal transfer process. *J Mater Process Technol*, 283
29. Zhang P, Li G, Yan H et al (2020) Effect of positive/negative electrode ratio on cold metal transfer welding of 6061 aluminum alloy. *Int J Adv Manuf Technol* 106:1453–1464. <https://doi.org/10.1007/s00170-019-04705-y>
30. Zhang H, Shi Y, Gu Y, Xie J, Li C (2020) Effects of electrode polarity on the droplet transfer mode in self-shielded flux-cored arc welding. *J Manuf Process* 58:478–488
31. Mou G, Hua X, Shen C, Wang W (2020) Effects of thermal distribution strategy on a Ti-6Al-4V/304L dissimilar joint fabricated using the variable polarity cold metal transfer arc-brazing method. *Mater Des* 191
32. Liu Z-Q et al (2020) Wire and arc additive manufacturing of 4043 Al alloy using a cold metal transfer method, *International Journal of Minerals. Metall Mater* 27(6):783–791
33. Huang J, Pan W, Yang W, Cheng Xue Yu, Shi DF (2020) The influence of bypass current on metal transfer in dual-bypass gas metal arc welding. *J Manuf Process* 38:179–186
34. Sravanthi SS, Acharyya SG, Phani Prabhakar KV, Padmanabham G (2019) Integrity of 5052 Al-mild steel dissimilar welds fabricated using MIG-brazing and cold metal transfer in nitric acid medium. *J Mater Process Technol* 268:97–106
35. Hao X, Dong H, Li P, Xia Y (2019) Dissimilar joining of TC4 alloy to ST16 steel by GTAW. *J Manuf Process* 37:413–417
36. Jia YZ, Xiao J, Chen SJ, Huang WH (2019) Pulsed laser enhanced metal transfer of aluminum alloy in GMAW. *Opt Lasers Eng* 121:29–36
37. Kaiyuan Wu, Cao X, Yin T, Zeng M, Liang Z (2019) Metal transfer process and properties of double-wire double pulsed gas metal arc welding. *J Manuf Process* 44:367–375
38. Madyira DM, Kaymakci A, Nkwanyana N (2019) The Effect of Metal Transfer Modes on Mechanical Properties of 3CR12 Stainless Steel. *Canadian Society of Mechanical Engineering*
39. Teixeira GS, Mazzaferro JAE (2019) GMA welding metal transfer mode study by high-speed imaging and electrical signal acquisition. *J Braz Soc Mech Sci Eng* 41:315

40. Zhang Z, Dongting Wu, Zou Y (2018) Effect of bypass coupling on droplet transfer in twin-wire indirect arc welding. *J Mater Process Technol* 262:123–130
41. Valensi F, Pellerin N, Pellerin S et al (2018) Influence of Wire Initial Composition on Anode Microstructure and on Metal Transfer Mode in GMAW: Noteworthy Role of Alkali Elements. *Plasma Chem Plasma Process* 38:177–205
42. Liu S, Zhang F, Dong S, Zhang H, Liu F (2018) Characteristics analysis of droplet transfer in laser-MAG hybrid welding process. *Int J Heat Mass Transf* 121:805–811
43. Cho D-W, Kiran DV, Na S-J (2017) Analysis of molten pool behavior by flux-wall guided metal transfer in low-current submerged arc welding process. *Int J Heat Mass Transf* 110:104–112
44. Lei HY, Li YB, Carlson BE (2017) Cold metal transfer spot welding of 1 mm thick AA6061-T6. *J Manuf Process* 28(1):209–219
45. Pang J, Shengsun Hu, Shen J, Wang P, Liang Y (2016) Arc characteristics and metal transfer behavior of CMT+P welding process. *J Mater Process Technol* 238:212–217
46. Li R, Yue J, Sun R et al (2016) A study of droplet transfer behavior in ultra-narrow gap laser arc hybrid welding. *Int J Adv Manuf Technol* 87:2997–3008
47. Carlos DJ, Henrique Gonçalves SR, Martinello SB, Cleber M, Estevam AO (2015) Metallurgical characterization of the 5083H116 aluminum alloy welded with the cold metal transfer process and two different wire-electrodes. *Weld World* 59(6)
48. Sun Z, Lv Y, Xu B, Liu Y, Lin J, Wang K (2015) Investigation of droplet transfer behaviours in cold metal transfer (CMT) process on welding Ti-6Al-4V alloy. *Int J Adv Manuf Technol* 8(9):2007–2014
49. Mezrag B, Deschaux-Beaume F, Benachour M (2015) Control of mass and heat transfer for steel/aluminium joining using Cold Metal Transfer process. *Sci Technol Weld Join* 20(3):189–198
50. Feng J, Zhang H, He P (2009) The CMT short-circuiting metal transfer process and its use in thin aluminium sheets welding. *Mater Des* 30(5):1850–1852

A Comparative Analysis of Different Algorithms for Optimizing Cutting Force Components in Turning Stainless Steel



Toukir Ahmed , Ferdous Al Rafi , and Shahed Mahmud 

Abstract Improved turning performance is critical for higher-quality goods to be manufactured and costs to be reduced. The aim of this paper is to determine the optimal cutting parameters that minimize the net force in turning AISI 201 stainless steel using different mathematical optimization algorithms. Spindle speed, feed, depth of cut, and workpiece diameter were selected as machining parameters. L_{16} Taguchi design of experiments was employed which include four factors and four levels. In addition, regression models were developed to estimate cutting forces. Then, several mathematical optimization algorithms were used to find the optimal parameters that minimize the net force. The algorithms employed in this paper were brute-force algorithm, genetic algorithm, SHGO algorithm, and basin-hopping algorithm. These algorithms were able to find optimal solutions to a set of equations with bounds and constraints. Both deterministic and non-deterministic techniques were used in these algorithms to achieve the optimized value. The optimal parameters in this investigation were cutting speed 245 rpm, feed 0.17 mm/rev, depth of cut 0.2 mm. and workpiece diameter 19.1 mm.

Keywords Turning · Machining parameter · Cutting force · Optimization · Genetic algorithm

T. Ahmed (✉) · S. Mahmud
Department of Industrial & Production Engineering, Rajshahi University of Engineering & Technology, Rajshahi 6204, Bangladesh
e-mail: toukir.ahmed@ipe.ruet.ac.bd

S. Mahmud
e-mail: shahed.mahmud@ipe.ruet.ac.bd

F. Al Rafi
Department of Civil Engineering, Bangladesh University of Engineering & Technology, Dhaka 1205, Bangladesh
e-mail: ferdousalrafi@ug.ce.buet.ac.bd

1 Introduction

Turning is the process of using a cutting tool such as a lathe to manufacture parts of a particular size and shape out of materials such as metal. The forces created by the cutting tool impact the cutting process and finished product quality greatly. The performance of the workpiece is primarily affected by the conditions of the turning process. It is possible to approximate the characteristics of the workpiece using mathematical models by carefully controlling the process variables. Mathematical optimization algorithms can be utilized to find the best parameters of the empirical model for optimizing a particular response factor. Many studies have been published over the years that analyze the effects of various turning parameters and the optimization of cutting force parameters.

Gupta et al. [1] used particle swarm optimization with teaching learning-based optimization to optimize the machining parameters for turning Inconel 800 grade nickel alloy. There are also numerous studies where genetic algorithm [2–7] performed well for optimizing machining parameters. Several studies use a desirability function [8–10] for multi-objective optimization. Some have experimented using methods based on neural networks and fuzzy systems [11–13]. Singaravel et al. [14] experimented with entropy measurement method and optimized response factors using multi-objective optimization by ratio analysis (MOORA). Gray relational analysis [15–20] is another popular method for optimizing multiple parameters at once. Tamizharasan et al. [21] found optimal turning conditions using design of experiments and by analyzing audible acoustic signals. They used simulated annealing algorithm and regression analysis for finding the optimal values. Sahali et al. [22] used P-NSGA-II, a type of genetic algorithm, to solve multi-objective optimization problems for turning parameters. In the dry turning of Inconel of 718 employing coated inserts, Ramanujan et al. [23] analyzed optimization modeling and trimming parameters. The experiment was on the basis of Taguchi's L_9 orthogonal array, and turning operation was performed at different stages of cutting parameters to test the output factors.

Although a large amount of work has been focused on optimizing cutting conditions for cutting force components and surface roughness using different grades of steel, there are no works that discuss optimizing cutting parameters for the turning of AISI 201 grade stainless steel utilizing empirical models and mathematical optimization algorithms. In this research, experiments were done using AISI 201 steel. The cutting forces were estimated with a regression model, and optimal cutting parameters were found using mathematical optimization routines.

2 Setup of Experiment

2.1 Workpiece and Material of Cutting Tool

AISI stainless steel (201 grade) was used as a workpiece in the experiment which includes carbon (max 0.15%), silicon (max 0.75%), manganese (5.5–7.5%), phosphorus (max 0.06%), sulfur (max 0.03%), nickel (3.5–5.5%), chromium (16–18%), and nitrogen (max 0.25%) [24]. For the procedure, carbide (cemented) cutting tool insert was used. Cemented carbide is a material which is durable enough that is commonly used in cutting machining equipment, as well as many manufacturing fields.

2.2 Experiment Design

In order to create relations between the parameters of machining, the Taguchi method was used. Four main processing parameters were defined including spindle speed (N), feed (f), depth of cut (ap), and workpiece diameter (D) in this experiment. The four levels of each machining parameter are shown in Table 1.

The current study describes the relation of the input N, f, ap , and D and the output factor Z as

$$Z = \zeta(N, f, ap, D) \tag{1}$$

where ζ represents response function. The tangential (F_t), axial (F_a), and radial (F_r) forces are the selected response factors in the current study. The machining parameters along with the values of output variables for all experimental runs are illustrated in Table 2.

Figure 1a, b shows the workpiece and cutting tool used for the experimentation. Cutting force was measured by dynamometer which is shown in Fig. 1c. For higher resolution, an L_{16} OA was selected for experimentation. The analyses were conducted on the basis of L_{16} OA.

Table 1 Selection of cutting parameters

Cutting parameters	Level-1	Level-2	Level-3	Level-4
N (rpm)	245	490	650	800
f (mm/rev)	0.12	0.14	0.16	0.18
ap (mm)	0.20	0.30	0.40	0.50
D (mm)	19.10	24.00	31.75	40.00

Table 2 Design of experiments

Run N°	Machining parameters				Responses		
	N	F	ap	D	F_t	F_a	F_r
1	245	0.16	0.2	19.10	0.06	0.02	0.07
2	245	0.12	0.3	24.00	0.16	0.10	0.15
3	245	0.14	0.4	31.75	0.09	0.04	0.12
4	245	0.18	0.5	40.00	0.32	0.15	0.29
5	490	0.16	0.3	31.75	0.12	0.05	0.15
6	490	0.12	0.2	40.00	0.10	0.06	0.16
7	490	0.14	0.5	19.10	0.08	0.04	0.09
8	490	0.18	0.4	24.00	0.19	0.09	0.19
9	650	0.16	0.4	40.00	0.19	0.09	0.12
10	650	0.12	0.5	31.75	0.06	0.04	0.09
11	650	0.14	0.2	24.00	0.05	0.04	0.08
12	650	0.18	0.3	19.10	0.04	0.02	0.07
13	800	0.16	0.5	24.00	0.02	0.12	0.17
14	800	0.12	0.4	19.10	0.04	0.03	0.06
15	800	0.14	0.3	40.00	0.12	0.07	0.19
16	800	0.18	0.2	31.75	0.03	0.01	0.07



(a) Work Piece



(b) Cutting Tool



(c) Dynamometer

Fig. 1 Workpiece, cutting tool, and device used in the investigation

3 Results and Discussion

3.1 Regression Analysis

The cutting forces can be approximated using various mathematical models. In this study, regression models were chosen for their simplicity and their ability to generalize well to unseen data. Three regression models were created from the experimental

data. Their coefficients of determination (R^2) are 92.31%, 90.95%, and 86.88% for the three forces [25]. The cutting force components are estimated using the turning parameters as input.

3.2 Parameter Optimization

In the current study, the goal is to minimize the cutting force components to improve machining performance. To achieve this, an objective function must be defined to decrease all three force components. In this situation, the objective function is the net cutting force. As the three forces are perpendicular to each other, the net force can be calculated using the principles of mechanics [26].

$$F_{\text{net}} = \sqrt{F_t^2 + F_a^2 + F_r^2}$$

The three component forces are approximated by three regression models. Since the optimization will be based on these regression models built on experimental data, the variables were bounded by the lowest and highest values of the experimental values. Variables were bounded because it could not be guaranteed that the empirical models will give accurate results for input parameters that are outside the range of values these models were fitted on.

$$N \in [245, 900], f \in [0.12, 0.2], ap \in [0.2, 0.5], D \in [18, 50]$$

Moreover, there was also a minimum bound on the three component forces F_t , F_a , and F_r . This was done because the lowest force recorded experimentally was 0.01

$$F_t > 0.01, F_a > 0.01, F_r > 0.01$$

With these constraints, four algorithms were employed to optimize the cutting force parameters: brute-force algorithm, simplicial homology global optimization (SHGO) algorithm, genetic algorithm, and *basin-hopping* algorithm.

Brute-force Algorithm. In the brute-force algorithm, all possible candidates for the solution are evaluated and the best one is chosen [27]. However, it is not feasible to evaluate all possible parameters in a reasonable amount of time. So, only the parameters in Table 1 were considered part of the solution space. Considering all possible combinations of the parameters in Table 1, there are 256 unique sets of parameter combinations available. After evaluating all these sets, the optimal set was chosen given the constraints. The results obtained by the brute-force algorithm are shown in Table 3.

Table 3 Optimized parameters obtained by different algorithms

Algorithm	N (rpm)	F (mm/rev)	ap (mm)	D (mm)	F_t (KN)	F_a (KN)	F_r (KN)	F_{net} (KN)
Brute-force	245.0	0.18	0.2	19.1	0.008865	0.05266	0.0603	0.080546
SHGO	900.0	0.12	0.35	18.0	0.0112	0.07538	0.04723	0.08966
Genetic algorithm	280.3	0.187	0.2212	18.14	0.01005	0.05073	0.06672	0.08442
Basin-hopping	245.0	0.180	0.2	18.0	0.01	0.05041	0.06094	0.07972

SHGO. Simplicial homology algorithm is a general-purpose global optimization algorithm [28]. It is a powerful algorithm capable of finding global minima or maxima of a function. It works even with black box functions; i.e., it does not require knowing the structure of the function it optimizes. So, it is suited for finding optimal parameters of complex models developed using empirical data. An implementation of the algorithm can be found in the SciPy library [29] in the Python programming language. The default configurations were used to find the optimal parameters. The results are shown in Table 3.

Genetic Algorithm. The genetic algorithm works on the principles of natural selection from the theory of evolution. A set of factors generate candidate solutions. Based on a fitness metric, it evaluates the candidate solutions. Then, the selected factors recombine and reproduce to create new sets of candidate solutions. Over many generations, the algorithm slowly converges to the optimal solution. This algorithm can be utilized to solve many different types of problems. It can also be used to find the global minima of a function with constraints. An implementation of the algorithm can be found in the genetic algorithm library [30] in the Python programming language. The number of generations the algorithm would run was set at 3000. The other configurations were left at their default values. The results are shown in Table 3.

Basin-hopping. Basin-hopping is a stochastic global optimization algorithm [31]. It runs perturbations on the acquired solutions based on Monte Carlo methods in a single iteration and uses a second optimization algorithm for finding the local minima again. It is a versatile algorithm capable of handling functions with many local minima. An implementation of the algorithm can be found in the SciPy library in the Python programming language.

The number of iterations for the algorithm was set at 100. The second optimization algorithm was set to trust-constr in SciPy, as this algorithm is capable of finding minima with bounds and constraints. The results are shown in Table 3.

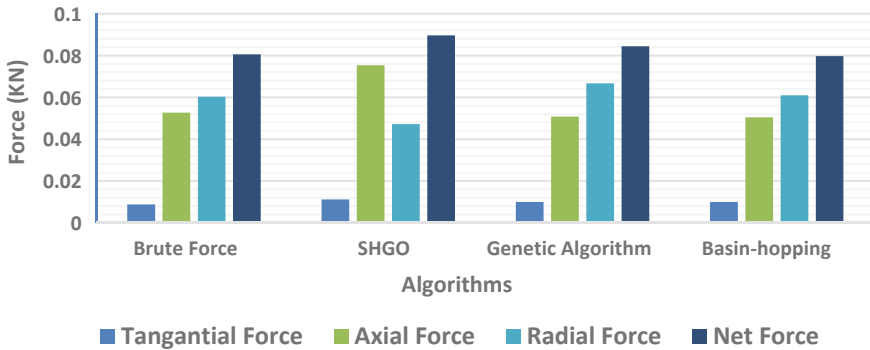


Fig. 2 Comparison of different algorithms for minimizing all forces

4 Result Analysis

From the data, it can be seen that the best parameters were determined by basin-hopping algorithm. And the optimal parameters are cutting speed 245 rpm, feed 0.18 mm/rev, depth of cut 0.2 mm, and workpiece diameter 18 mm. Basin-hopping algorithm provides the best overall result across all three cutting force components, as seen in Fig. 2.

Brute-force algorithm also performs sufficiently after basin-hopping. However, it is a very computationally expensive algorithm. This method may not be suitable in other applications.

SHGO also produces acceptable results. This algorithm is the fastest of the four. SHGO is rather well suited for optimizing functions with low dimensionality, as it is in this study. The optimized net force from SHGO is about 0.01 kN lower than the lowest net force estimated from all other algorithms.

Genetic algorithm performs adequately. It is worth mentioning that while genetic algorithm is powerful, it takes many generations for it to produce optimal results. In general, it performs slower than basin-hopping and SHGO but it does not give better results than these two algorithms.

It is worth mentioning that there is a significant difference from the lowest two performing algorithms to the highest two performing algorithms. This fact is better highlighted in Fig. 3, where only the optimal net force determined by the algorithms is shown.

5 Conclusions

In this study, experiments were conducted on turning AISI 201 grade steel with a cemented carbide cutting tool. The experiment design was employed on the basis of the principles of the Taguchi method. Then, regression models were developed based

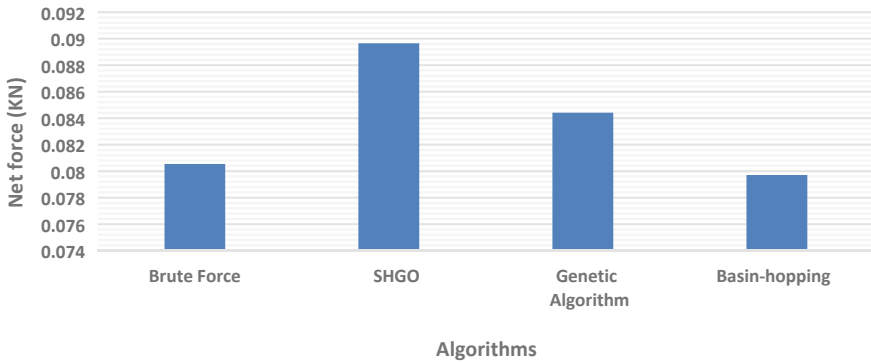


Fig. 3 Comparison of different algorithms for minimizing net force

on experimental data. Then using the empirical models, optimal cutting parameters were determined. Several conclusions can be drawn from the experiment. Firstly, in the turning of AISI 201 stainless steel, cutting speed 245 rpm, feed 0.17 mm/rev, depth of cut 0.2 mm, and workpiece diameter 19.1 mm are appropriate for minimizing the net cutting force. Secondly, basin-hopping algorithm is the best overall performing algorithm for optimization. It can also be observed that regression models for approximating workpiece response factors can be developed and be utilized for further analysis. More sophisticated models can be developed using artificial neural networks and decision trees. They can also be used with mathematical optimization algorithms to determine ideal conditions for the turning process. The performance of these models can be investigated in a future study.

References

1. Gupta MK, Mia M, Pruncu CI et al (2019) Parametric optimization and process capability analysis for machining of nickel-based superalloy. *Int J Adv Manuf Technol* 102:3995–4009. <https://doi.org/10.1007/s00170-019-03453-3>
2. Sahoo P (2011) Optimization of turning parameters for surface roughness using RSM and GA. *Adv Prod Eng Manag* 6(3)
3. Mia M, Grzegorz K, Radoslaw M, Szymon W (2019) Intelligent optimization of hard-turning parameters using evolutionary algorithms for smart manufacturing. *Materials* 12:879. <https://doi.org/10.3390/ma12060879>
4. Radovanović M (2019) Multi-objective optimization of multi-pass turning AISI 1064 steel. *Int J Adv Manuf Technol* 100:87–100. <https://doi.org/10.1007/s00170-018-2689-z>
5. Changle T, Zhou G, Zhang J, Chao Z (2019) Optimization of cutting parameters considering tool wear conditions in low-carbon manufacturing environment. *J Clean Prod* 226. <https://doi.org/10.1016/j.jclepro.2019.04.113>
6. Mia M, Dhar NR (2019) Prediction and optimization by using SVR, RSM and GA in hard turning of tempered AISI 1060 steel under effective cooling condition. *Neural Comput Appl* 31:2349–2370. <https://doi.org/10.1007/s00521-017-3192-4>

7. Laouissi A, Yallese MA, Belbah A et al (2019) Investigation, modeling, and optimization of cutting parameters in turning of gray cast iron using coated and uncoated silicon nitride ceramic tools. Based on ANN, RSM, and GA optimization. *Int J Adv Manuf Technol* 101:523–548. <https://doi.org/10.1007/s00170-018-2931-8>
8. Saidi R, Fathallah BB, Mabrouki T et al (2019) Modeling and optimization of the turning parameters of cobalt alloy (Stellite 6) based on RSM and desirability function. *Int J Adv Manuf Technol* 100:2945–2968. <https://doi.org/10.1007/s00170-018-2816-x>
9. Azizi MW, Belhadi S, Yallese MA et al (2012) Surface roughness and cutting forces modeling for optimization of machining condition in finish hard turning of AISI 52100 steel. *J Mech Sci Technol* 26:4105–4114. <https://doi.org/10.1007/s12206-012-0885-6>
10. Singh BK, Mondal B, Mandal N (2016) Machinability evaluation and desirability function optimization of turning parameters for Cr₂O₃ doped zirconia toughened alumina (Cr-ZTA) cutting insert in high speed machining of steel. *Ceram Int* 42(2):3338–3350. <https://doi.org/10.1016/j.ceramint.2015.10.128>
11. Shivakoti I, Kibria G, Pradhan P, Pradhan B, Sharma A (2018) ANFIS based prediction and parametric analysis during turning operation of stainless steel 202. *Mater Manuf Process* 34:1–10. <https://doi.org/10.1080/10426914.2018.1512134>
12. Le Chau N, Nguyen M, Dao T et al (2019) An effective approach of adaptive neuro-fuzzy inference system-integrated teaching learning-based optimization for use in machining optimization of S45C CNC turning. *Optim Eng* 20:811–832. <https://doi.org/10.1007/s11081-018-09418-x>
13. Pathak H, Das S, Doley R, Kashyap S (2020) Optimization of cutting parameters for AISI H13 tool steel by Taguchi method and artificial neural network. In: *Deep learning and neural networks*, pp 531–551. <https://doi.org/10.4018/978-1-7998-0414-7.ch030>
14. Singaravel B, Selvaraj T, Vinodh S (2016) Multi-objective optimization of turning parameters using the combined moora and entropy method. *T Can Soc Mech Eng* 40(1):101–111. <https://doi.org/10.1139/tcsme-2016-0008>
15. Thakur A, Manna A, Samir S (2020) Multi-response optimization of turning parameters during machining of EN-24 steel with SiC nanofluids based minimum quantity lubrication. *SILICON* 12:71–85. <https://doi.org/10.1007/s12633-019-00102-y>
16. Angappan P, Selvaraj T (2017) Optimisation of turning parameters for surface integrity properties on incoloy 800H superalloy using cryogenically treated multilayer CVD coated tool. *Surf Rev Lett* 26. <https://doi.org/10.1142/S0218625X18501391>
17. Vasudevan H et al (2019) Optimization of machining parameters in the turning operation of Inconel 825 using grey relation analysis: ICIMA 2018. https://doi.org/10.1007/978-981-13-2490-1_37
18. Younas M, Jaffery SHI, Khan M et al (2019) Multi-objective optimization for sustainable turning Ti6Al4V alloy using grey relational analysis (GRA) based on analytic hierarchy process (AHP). *Int J Adv Manuf Technol* 105:1175–1188. <https://doi.org/10.1007/s00170-019-04299-5>
19. Umamaheswarrao P, Rajub DR, Sumanc KNS, Sankar BR (2018) Multi objective optimization of process parameters for hard turning of AISI 52100 steel using Hybrid GRA-PCA. *Procedia Comput Sci*. <https://doi.org/10.1016/j.procs.2018.07.129>
20. Ahilan C, Kumanan S, Sivakumar N (2010) Application of grey based Taguchi method in multi-response optimization of turning process. *Adv Prod Eng Manag* 5(3):171–180
21. Tamizharasan T, Barnabas JK, Pakkirisamy V (2012) Optimization of turning parameters by using design of experiments and simulated annealing algorithm based on audible acoustic emission signals. *Proc Inst Mech Eng Part B: J Eng Manuf* 226(7):1159–1173. <https://doi.org/10.1177/0954405412442779>
22. Sahali MA, Belaidi I, Serra R (2016) New approach for robust multi-objective optimization of turning parameters using probabilistic genetic algorithm. *Int J Adv Manuf Tech* 83(5–8):1265–1279. <https://doi.org/10.1007/s00170-015-7526-z>
23. Ramanujan R, Venkatesan P, Saxena V, Joseph P (2014) Modeling and Optimization of Cutting Parameters in Dry Turning of Inconel 718 Using Coated Carbide Inserts. *Int Con Adv Manuf Mat Eng* 5:2550–2559. <https://doi.org/10.1016/j.mspro.2014.07.508>

24. Luo HS, Zhao C (2013) Low temperature salt bath hardening of AISI 201 austenitic stainless steel. *Phys Procedia* 50:38–42. <https://doi.org/10.1016/j.phpro.2013.11.008>
25. Ahmed T, Mollick N, Mahmud S, Ahmad T (2020) Analysis of effects of machining parameter on cutting force components in turning AISI 201 stainless steel using cemented carbide cutting tool insert. *Mater Today Proc.* <https://doi.org/10.1016/j.matpr.2020.11.416>
26. Taylor JR (2005) *Classical mechanics*. University Science Books
27. Bernstein DJ (2005) Understanding brute force. In: Workshop record of ECRYPT STVL workshop on symmetric key encryption, eSTREAM report, vol 36
28. Endres SC, Sandrock C, Focke WW (2018) A simplicial homology algorithm for Lipschitz optimisation. *J Global Optim* 72(2):181–217
29. Virtanen P, Gommers R, Oliphant TE et al (2020) SciPy 1.0: Fundamental Algorithms for Scientific Computing in Python. *Nat Methods* 17:261–272. <https://doi.org/10.1038/s41592-019-0686-2>
30. Genetic algorithm, <https://github.com/rmsolgi/geneticalgorithm>. Accessed 20 Aug 2020
31. Wales DJ, Doye JPK (1997) Global optimization by Basin-Hopping and the lowest energy structures of Lennard-Jones clusters containing up to 110 atoms. *J Phys Chem A* 101:5111. <https://doi.org/10.1021/jp970984n>

Computer Modelling of Loading-Induced Fluid Motion in 3D Osteon Model



Naman Sharma and Rakesh Kumar

Abstract The present study develops a fluid–structure interaction model of the three-dimensional osteon model within the bone tissue using ANSYS Fluent workbench. The effect of fluid motion and wall shear stress over the osteon model has been analysed using FSI model. The osteon model was subjected to a cantilever load (trapezoidal loading waveform of 5 N). The fluid wall shear and the velocity of streamlines are simulated. Further, it has been noticed that the fluid velocity and the wall shear stress are maximum in the similar zone. The outcomes of this study provide a better mechanism to understand the under lying phenomena occurs during the physiological loading on osteon network within the bone matrix.

Keywords Osteon model · Fluid motion · Fluid–structure interaction · Bone adaptation

1 Introduction

Physiological loading on bone may improve the bone health [1–3]. Experimental studies reported that the low magnitude cycle loading is beneficial in maintaining and regulating the desired health of bone tissue. For example, load bearing exercise [2], walking [5], jumping [12], etc., have a strong influence in preventing bone loss and promoting health of bone tissue. This physical activity (mechanical loading) causes canalicular fluid to flow. Fluid motion across the osteocytes network regulates the osteogenic activities [9]. Previous studies [4, 10, 11] on bone adaptation have noticed that whenever loading is applied on bone tissue, fluid flows through the osteon network due to cytoskeleton deformation. This deformation induces pore-pressure

N. Sharma

Department of Mechanical and Manufacturing Engineering, Manipal Institute of Technology, Udupi, Karnataka 576104, India

R. Kumar (✉)

Department of Mechanical Engineering, Manipal University, Jaipur, Rajasthan 303007, India
e-mail: kumar.rakesh@jaipur.manipal.edu

gradient which causes wall shear stress in the pericellular space of the lacunar–canalicular system and induces a drag force on the bone matrix. This stimulates a biological response in osteocytes. However, it remains unclear how canalicular fluid and osteon network interaction perceives under the effect physiological loading. A very few studies in the literature attempted to address this solid (bone/cell) and fluid (canalicular/interstitial fluid) domain interaction.

The present study attempts to investigate the environment how fluid encounters the osteon network that led it to deformations. Interaction of flowing fluid with the bone cell (osteocyte) also causes changes in the fluid flow properties such as velocity, streamline and fluid shear stress. However, the deformation of the osteon may depend upon the properties of the material, pore-pressure and velocity. In actual structure, it may vary from quite small to very high. The previous studies have reported that the poromechanical properties such as permeability and porosity may vary with age, location and tissue segments. Porosity and permeability also decide the amount of fluid which is allowed through the pores [1, 6, 7]. During the interaction of fluid with osteon model, it induces a wall shear stress. This wall shear stress on osteocytes cell process is responsible for osteogenesis, i.e. new bone formation. The interaction of solid bone and fluid during physiological loading can be captured through two-way fluid–structure interaction model. The outcome of this work may further be extended in designing better biomechanical strategies to enhance fluid flow in order to improve osteogenic activities in bone tissue.

2 Material and Methods

2.1 Computer Model

A 3D idealized osteon structure is designed using the software CATIA V6.0 as shown in Fig. 1. Osteon is depicted as a hollow cylinder having a network of osteocyte interconnected circumferentially and radially to each other with cylindrical channels known as canaliculi. Osteocytes are designed as elliptical structures. The model is assumed as a linear, elastic and isotropic material. A cantilever bending load [8] is applied on one end of the osteon structure and is fixed on the other. We have used the system coupling module available in ANSYS Multiphysics to combine two different physics, which is utilized to reproduce the interface between the osteon boundary and fluid motion. Fluid movement under the impact of applied loading pattern is investigated.

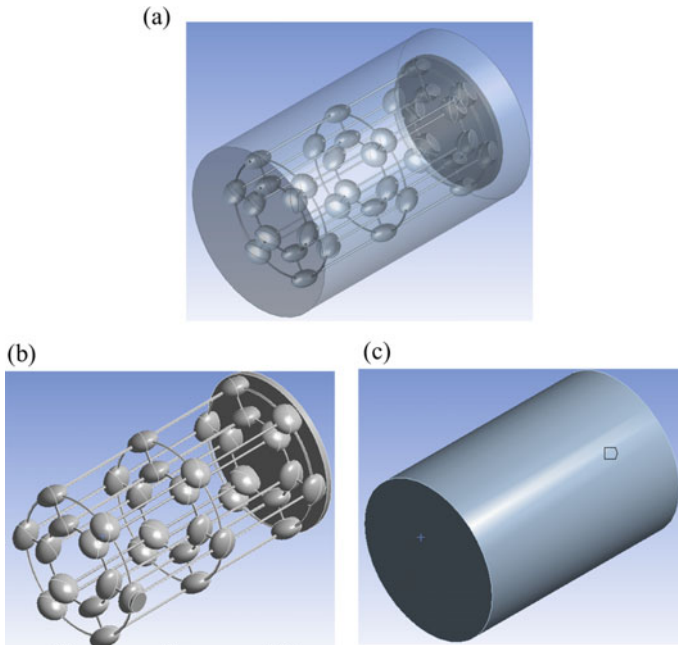


Fig. 1 **a** Idealized geometry of 3D osteon with solid domain and fluid domain, **b** solid domain of osteon model and **c** fluid domain geometry around osteon model

2.2 Mesh Characteristics

Both the fluid and solid domains of the geometry were meshed before performing the simulation (Fig. 2). Free meshing was done for both the domain of osteon model. Total number of nodes and elements for osteon model was 982,359 and 2,616,057, respectively. However, for the fluid domain the total nodes and element was about 570,212 and 2,758,961, respectively. The skewness and aspect ratio assessments were also performed to enhance the results as it prevents the node to move (Tables 1 and 2). Generally, skewness is defined as the ratio of internal angles of the element and the angles of the ideal element of the same volume. The value of skewness was minimum in solid and fluid domain.

2.3 Boundary Condition

In two-way FSI, the impact of interaction between streaming fluid and solid is analysed at the same time. Both fluid and solid structures were combined using the system coupling. The system coupling is shown in Fig. 3 which combines the transient structural analysis and fluent. In two-way fluid–structure interaction, multiphysics both

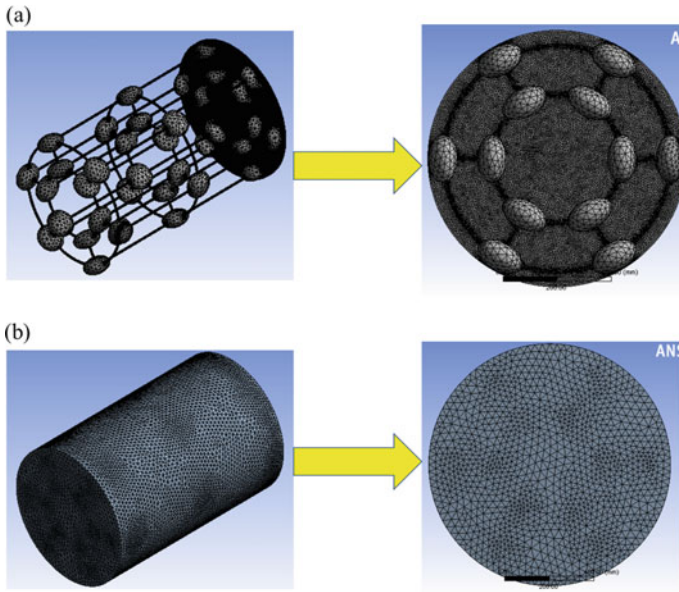


Fig. 2 a Mesh for solid domain (osteon model), b Mesh for fluid domain

Table 1 Skewness and aspect ratio metrics in osteon model

Solid domain			Fluid domain		
Quality metric	Skewness	Aspect ratio	Quality metric	Skewness	Aspect ratio
Minimum	4.4058×10^{-5}	1.1617	Minimum	1.8328×10^{-6}	1.1579
Maximum	0.95947	14.086	Maximum	0.84756	10.227
Average	0.26487	1.9093	Average	0.33778	2.0771

Table 2 Parameters used in fluid domain (pores)

Inlet	Velocity = 6×10^{-6} m/s
Outlet	Pressure (Gauge) = 0 bar
Wall	Stationary, No slip
Permeability	2.111×10^{-21} m ² in all directions
Porosity	0.5

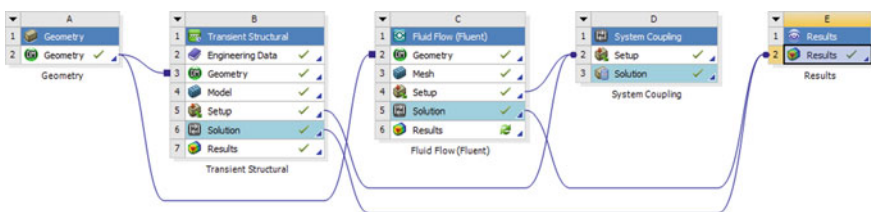


Fig. 3 Representation of two-way FSI in ANSYS Workbench

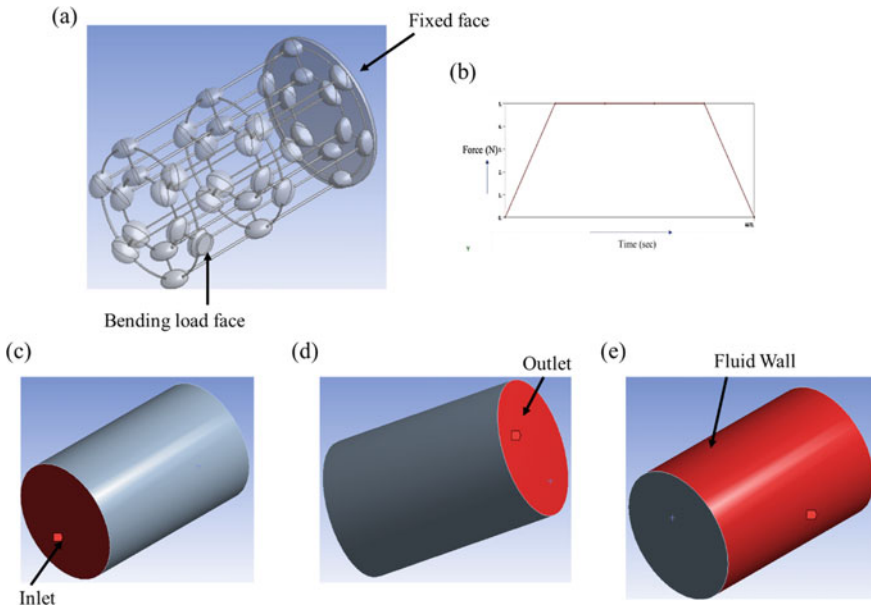


Fig. 4 Cantilever bending model of osteon model with their representation for solid and fluid domain (a, c, d and e) and b represents loading regimen

the system is solved separately and then coupled simultaneously until equilibrium is reached. Two-way data transfers are allowed in which one source is a transient structural analysis and the FLUENT fluid flow, and the case is vice versa in other data transfers (Fig. 4).

3 Result and Discussion

3.1 Fluid Motion

Fluid–structure interaction analysis was used to analyse the interaction between fluid and solid domain. Basically, the pattern of fluid flow can be shown using streamlines (Fig. 5). The maximum velocity was 3.94×10^{-5} m/s. It can be found that the velocity of the streamlines is around the same due to the very low velocity of the fluid (6×10^{-6} m/s). It is likewise perceptible that fluid flow velocity magnitude increases with increase in axial position and is greatest at the fixed point. At the end of the channel where the pores merged reflux phenomena is observed. In this model, we have not varied the micromechanical properties. Nevertheless, these limitations will be addressed in future.

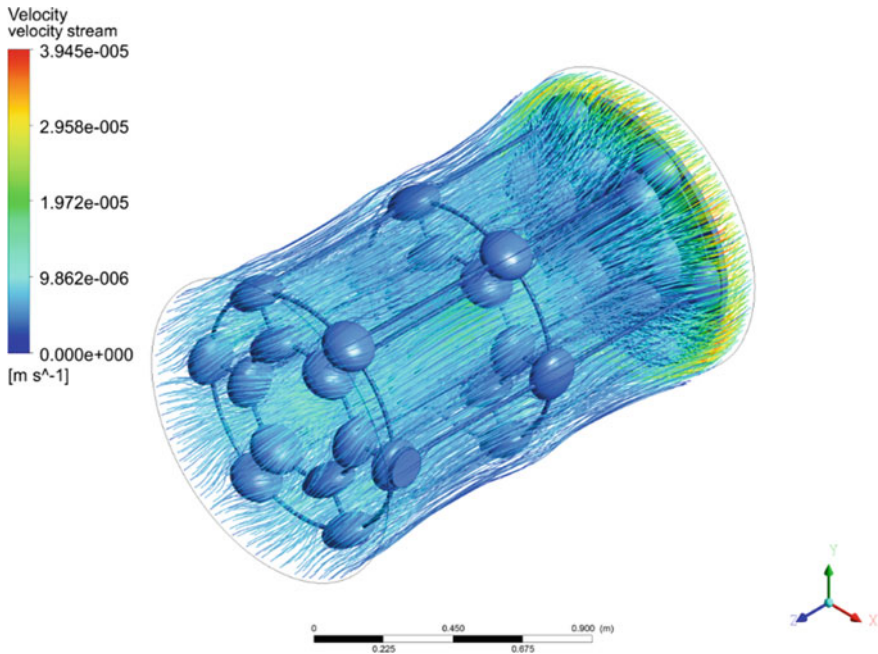


Fig. 5 Velocity streamline in case of bending load on osteocyte model

3.2 Wall Shear

In Fig. 6, wall shear stress due to bending is shown in statistic. The wall shear pattern can be noted to be almost identical to the streamlines of fluid velocity. In such areas where the fluid motion is highest, wall shear pressure is also highest. High shear is discovered because the velocity gradient increases due to maximum velocity, which is exactly proportional to the shear impact.

4 Conclusion

The current research is an effort to identify the interaction of solid osteocyte network and fluid–structure. Fluid wall shear stress is responsible for the new bone formation. Fluid velocities produced by the network of osteon depend on the boundary condition applied to the domain of fluid. The result indicates that the fluid flow profiles are affected by this irregular bone wall pore surface.

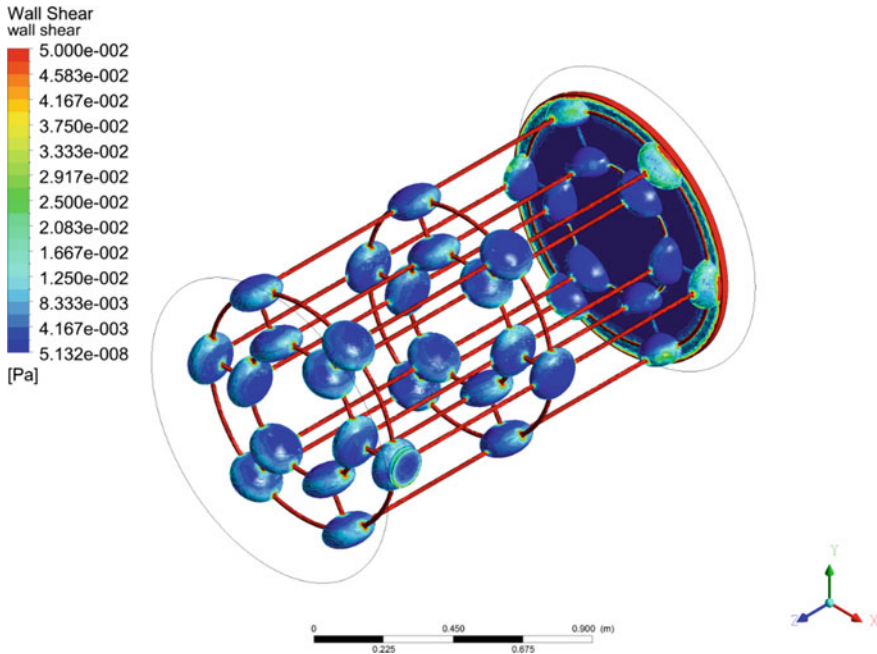


Fig. 6 Wall shear in case of bending

References

1. Carriero A, Pereira A, Wilson A, Castagno S, Javaheri B, Pitsillides A, Marenzana M, Shefelbine S (2018) Spatial relationship between bone formation and mechanical stimulus within cortical bone: Combining 3D fluorochrome mapping and poroelastic finite element modelling. *Bone Rep* 8:72–80
2. Dalsky GP, Stocke KS, Ehsani AA, Slatopolsky E, Lee WC, Birge SJ (1988) Weight-bearing exercise training and lumbar bone mineral content in postmenopausal women. *Ann Intern Med* 108:824–828
3. Khan K, McKay H, Kannus P, Wark J, Bailey D, Bennell K (2001) Physical activity and bone health. *Human Kinetics*
4. Kumar R, Tiwari AK, Tripathi D, Shrivastava NV, Nizam F (2019) Canalicular fluid flow induced by loading waveforms: A comparative analysis. *J Theor Biol* 471:59–73
5. Palombaro KM (2005) Effects of walking-only interventions on bone mineral density at various skeletal sites: a meta-analysis. *J Geriatr Phys Ther* 28:102–107
6. Pereira AF, Javaheri B, Pitsillides A, Shefelbine S (2015) Predicting cortical bone adaptation to axial loading in the mouse tibia. *J R Soc Interface* 12:20150590
7. Pereira AF, Shefelbine SJ (2014) The influence of load repetition in bone mechanotransduction using poroelastic finite-element models: the impact of permeability. *Biomech Model Mechanobiol* 13:215–225
8. Srinivasan S, Weimer DA, Agans SC, Bain SD, Gross TS (2002) Low-magnitude mechanical loading becomes osteogenic when rest is inserted between each load cycle. *J Bone Miner Res* 17(9):1613–1620
9. Tate MLK (2003) “Whither flows the fluid in bone?” An osteocyte’s perspective. *J Biomech* 36:1409–1424

10. Tiwari AK, Kumar R, Tripathi D, Badhyal S (2018) In silico modeling of bone adaptation to rest-inserted loading: strain energy density versus fluid flow as stimulus. *J Theor Biol* 446:110–127
11. Tiwari AK, Prasad J (2016) Computer modelling of bone's adaptation: the role of normal strain, shear strain and fluid flow. *Biomech Model Mechanobiol*, 1–16. <https://doi.org/10.1007/s10237-016-0824-z>
12. Umemura Y, Ishiko T, Tsujimoto H, Miura H, Mokushi N, Suzuki H (1995) Effects of jump training on bone hypertrophy in young and old rats. *Int J Sports Med* 16:364–367

Influence of Ultra-low Temperature Treatments on the Slurry Erosion Performance of Stainless Steel-316L



Munish Kumar, Hazoor Singh Sidhu, and Buta Singh Sidhu

Abstract In this research work, the stainless steel (SS) used for the fabrication of under-water parts in hydro-power plants was cryo-treated at different ultra-low temperatures, i.e. $-80\text{ }^{\circ}\text{C}$ and $-196\text{ }^{\circ}\text{C}$. The influence of such cryo-treatments on the silt erosion performance of SS-316L was investigated by conducting silt erosion tests on a self-fabricated jet model silt erosion trial apparatus. The tests were regulated for distinct operating parameters at two levels. It was found that the cryogenic treatments significantly affect the silt erosion performance of stainless steel samples. Scanning-electron-microscopy (SEM) and optical microscopy (OM) tests were done to examine the microstructural changes resulted after cryo-treatments. SEM results endorse the existence of residual austenite in the untreated steel. However, this residual aust. disappears after such cryo-treatments. XRD diffraction techniques were also used to investigate the various phase changes caused by low-temperature treatments. It was concluded that the samples, cryogenically treated at $-196\text{ }^{\circ}\text{C}$ exhibits the highest resistance against silt erosion followed by the one treated at $-80\text{ }^{\circ}\text{C}$. The untreated samples of SS-316L showed the least resistance against silt erosion. This upgradation in wear strength of cryogenically processed samples was further related to the metallurgical changes observed after cryogenic treatment.

Keywords Silt erosion · Shallow-cryogenic-treatment (SCT) · Deep-cryogenic-treatment (DCT) · Aust. (aust.) · Mart. (mart.) · Stainless steel (SS) · Impact velocity (IV) · Impingement angle (IA) · Stand-off distance (SOD) · Scanning-electron-microscopy (SEM) · X-ray-diffraction (XRD) · Optical microscopy (OM)

M. Kumar (✉)

Department of Mechanical Engineering, Government Polytechnic College, Bathinda, Punjab 151001, India

H. Singh Sidhu

Department of Mechanical Engineering, Yadavindra College of Engineering, Talwandi Sabo, Punjab 151002, India

B. Singh Sidhu

Department of Mechanical Engineering, Maharaja Ranjit Singh University, Bathinda, Punjab 151001, India

1 Introduction

The depletion of the material's surface, when some solid particles entrained in the water impinges on it, is a kind of silt erosion [1]. The silt erosion is a critical problem in engineering projects such as impellers, runners, centrifugal pumps, other under-water rotating parts, gates, and valves [2, 3]. Rate of erosion is greatly affected by the factors viz. impingement angle, the impact velocity of hard grains attacking the surface, grain size, slurry concentration and stand-off distance [3]. The investigators [2–4] have suggested many ways to control silt erosion problems such as thermal spray coatings. Investigators used different types of coatings, i.e. laser clad NiCoCrFeAl₃ coatings, tungsten coatings, Ni–20Cr₂O₃ coatings, detonation gun spray coatings, Ni–40Al₂O₃ coatings, NiCr and stellite-6 coatings, to upgrade the wear strength of turbine-steels. These coatings proved very effective to control the erosion wear performance of steels. The enormous expenses related to these coatings and limited life of coatings demands for some substitutes to control the erosion wear. Soleimany et al. [6] investigated the microstructure and wear performance of tool steels after D.C.T and found that the wear performance of tool steel escalates by 36% after D.C.T. In another work conducted by Bensely et al. [7], it was found that S.C.T and D.C.T escalates the wear strength of an En353 steel more than 80%. In their work, the authors correlated these facts with the metallurgical refinements in the microstructure of steel after cryogenic treatment (CT). Das et al. [8] in one of their work endorsed the upgradation in erosion wear of tool steels after D.C.T. The author accredited this upgradation to the conversion of residual Aust. to Mart., better precipitation of small carbides, homogenized and stress-free microstructure, diminution of residual aust. proportion and low-temperature refinement of mart. Barron et al. [9] studied that after CT greater amount of residual aust. was revamped, and the amount of mart. was intensified. Based on the previous published work, it was anticipated that the advantages of CT can be explored further to examine the impact of ultra-low-temperature treatments on the silt erosion performance of SS-316L.

2 Experimentation

2.1 Material Collection and Sample-Fabrication

For the research work, SS-316L was the preferred material because of its wide applications in the hydro-power plants. The material was procured from Bombay Steels, Ludhiana. The procured material was in the form of a steel sheet of 5 mm thickness. The cubical samples of 25 mm × 25 mm were fabricated with the assistance of wire cut electric-discharge-machine. Formerly, the samples were polished with silt-papers of different numbers [10, 11]. The element-content of SS-316L utilized in this work was assessed at the IAP, Ludhiana. Table 1 presents the composition of SS-316 grade. The element composition was performed at a temperature of 24

Table 1 Element content of SS 316L grade (wt. percentage)

C	Si	Mn	Ni	P	Cr	Mo	Fe
0.02	0.37	1.35	10.20	0.039	16.12	2.06	Bal

°C and relative humidity between 45 and 60 by spark emission spectroscopy analysis on a spectrometer BAIRD, DV6, USA. Microhardness test of samples was performed using Vickers method with MicroWiZhard Mitutoyo 810-352E hardness testing device (Japan) with 300 g load [12].

2.2 Cryogenic Treatments of Fabricated Samples

“The whole procedure of cryogenic treatment involves Austenitizing-Quenching-Cryogenic Treatment-Tempering” [13]. Two modes of cryogenic treatments were practiced, depending upon the temperature ranges as presented in Fig. 1.

- (a) *Shallow-Cryogenic-Treatment (S.C.T)*: For S.C.T, the austenitized-quenched SS-316L samples were rapidly cooled at $-80\text{ }^{\circ}\text{C}$ for 24 h succeeded by tempering at $150\text{ }^{\circ}\text{C}$ for 10 h and eventually bringing to room temperature.
- (b) *Deep-Cryogenic-Treatment (D.C.T)*: For D.C.T, the austenitized and quenched SS-316L specimens were rapidly cooled at $-196\text{ }^{\circ}\text{C}$ for 24 h succeeded by tempering at $150\text{ }^{\circ}\text{C}$ for 10 h and eventually bringing to room temperature.

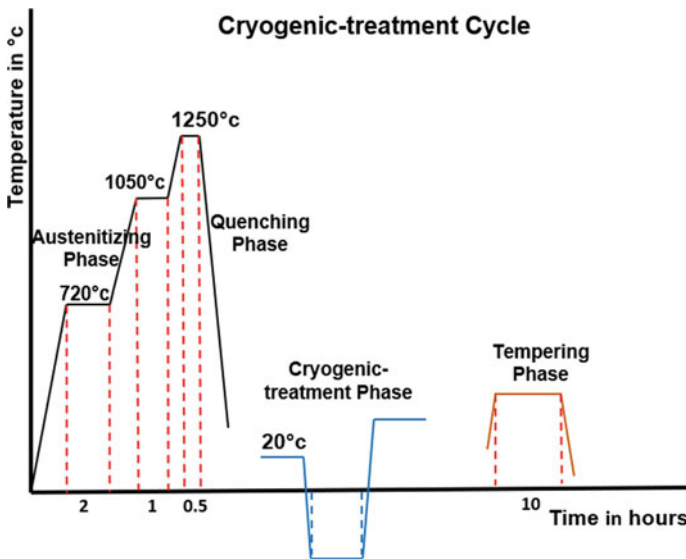


Fig. 1 Graphic-presentation of Cryogenic-heat-treatment cycle

2.3 Formation of Slurry

The silt used for experimentation work was collected from Sirhind canal Rupnagar in Ropar, India. Further, the silt was dried at 40 °C for 12 h. Later, the sieve examination of dried silt was performed to attain distinct sized silt particles. The proposed average particle size of 300 μm was attained by mixing the distinct sized silt particles in relevant ratio. The particle size dispersion graph is illustrated in Fig. 2. The calculated proportion of silt was then blended in the filtered water to obtain a slurry concentration of 10,000 ppm. The structure of silt particles under SEM is illustrated in Fig. 3. The particle size and slurry concentration considered in this work are adopted following the published work of many authors [1–5].

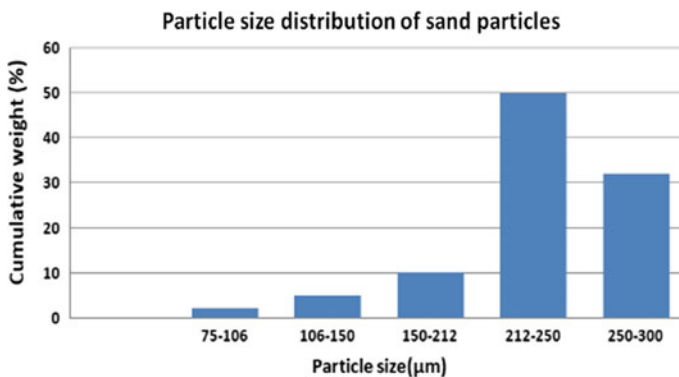


Fig. 2 Particle size distribution of silt grains

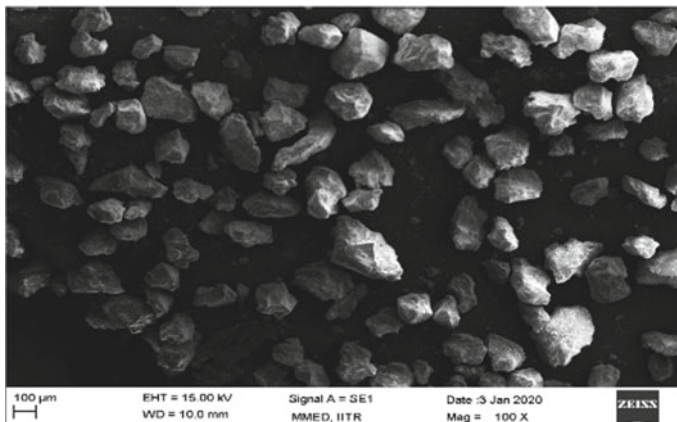


Fig. 3 SEM image of silt grains

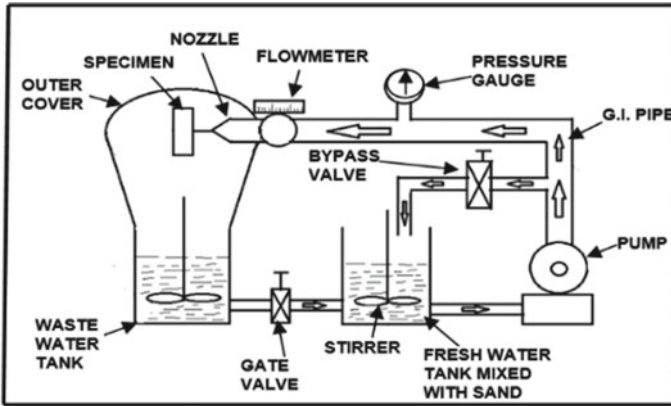


Fig. 4 Sketch of a silt erosion testing apparatus [12]

2.4 Layout of Silt Erosion Test Rig (Jet Type)

A silt erosion test apparatus was self-fabricated following the A.S.T.M standard G-73 [14]. As illustrated in Fig. 4, it consists of a pump, nozzle, pressure gauge, water chambers, and a sample fixture arrangement. The calculated amount of silt was blended in the fresh-water chamber. The pump ejects the pressurized sludge from the fresh-water chamber in the direction of targeted sample. The position of the nozzle was adjusted, so that the slurry jet impinges at the preferred position on the sample. After impinging upon the targeted specimen, the sludge gets collected in the waste-water chamber. The fixture holding the sample can also be adjusted up to 180° of rotational and 100 mm of linear motion to change I.A and the SOD, respectively. To prevent the deposition of silt in the chambers, stirrers were installed in both the chambers. The nozzle of diameter 4.09 mm was fabricated from tungsten carbide material to control its erosion. There was a deflection valve on the main water-line for the alteration of I.V. For each experiment, the mass of each worn-out sample was weighted after every 15 min. The total duration of each experiment was 120 min. The silt was replenished after every 30 min.

2.5 Experimental Proposal

The experimental work was conducted according to A.S.T.M G-73 typical procedure [14]. From the previous published work, it was found that the elements, i.e. I.V, I.A, SOD are the factors that significantly affect erosion wear. With reference to the literature facts, three parameters were chosen carefully for experimentation. Individual parameter has two distinct levels as illustrated in Table 2. During experimentation work, other parameters, i.e. slurry concentration and average grain size

Table 2 Parameters at distinct levels

Parameters	Vel	IA	SOD
Level I	5.76	30	10
Level II	14.32	60	50

Vel.—Velocity of hard grains in m/s

IA—Impingement angle in degrees

SOD—Stand-off distance in mm (from the nozzle tip to targeted specimen)

Table 3 Taguchi-L4 experimental design

Parameters and their levels			
Exp. No.	m/s	Degrees	mm
E 1	I	I	I
E 2	I	II	II
E 3	II	I	II
E 4	II	II	I

were maintained at of 10,000 ppm and 300 μ m, respectively. The Taguchi-L4 array was preferred for experimental design to reduce the number of experimental runs. Table 3 illustrates the total number of experiments to be performed following Taguchi L4 analysis.

3 Results and Explanation

3.1 Description of Microstructure

The SEM inspection of the untreated (UT), S.C.T and D.C.T samples is illustrated in Fig. 5. From the superficial SEM of UT specimen, the presence of residual aust. was detected from the appearance of white areas. The amount of residual aust. seems to be declined after S.C.T as presented in Fig. 5b. It was noticed that with the reduction

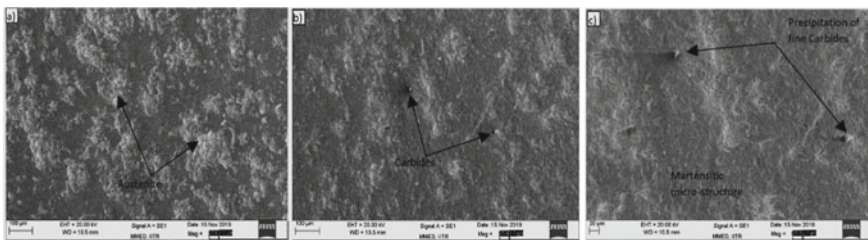


Fig. 5 Microstructure of samples under SEM analysis: **a** UT sample, **b** S.C.T sample, **c** D.C.T

in residual aust., there was a precipitation of fine carbides at various sites. These facts have also been proved by many authors [8–13, 15–21]. The microstructure of D.C.T samples was exposed in Fig. 5c. It can be observed that the white areas reported as aust., completely disappears from the surface and the microstructure seems to be more uniform and compact as compared to UT and S.C.T samples. The precipitation of fine carbides and homogenized microstructure after D.C.T may be because of crystal lattice shrinkage. After D.C.T, the crystal lattice shrinkage drives the carbon particles to spread out to adjacent disruptions and flaws. Furthermore, some new disruptions are also formed because of the variation in the thermic-contraction of aust. and mart. In a work carried out by Amini et al. [21], a 6% rise in the vol-percentage of small carbides was observed after D.C.T. In another work by Soleimany et al. [6] on H11 tool steel, a 6.4% and 58.2% increase in the vol-percentage of carbide was reported after S.C.T and D.C.T, respectively. The image analysing software has been used to compute the mean values of the vol-percentage of the carbides.

3.2 Optical Microscopy Analysis

The optical microscopy was done to visualize the grain boundaries and precipitation of fine carbides in the microstructure. Figure 6a–c illustrates the optical microscopy of the UT, S.C.T and D.C.T samples, respectively. It was noticed from Fig. 6a, the microstructure consists of large grain boundaries with no evidence of carbides. Figure 6b, c acknowledges the refinement of microstructure and an increase in the vol-percentage of carbides for S.C.T and D.C.T samples. Binzhou et al. [13] examined the influence of CT on carburized steel and observed more than 13.6% rise in the vol-percentage of carbides after S.C.T and D.C.T. These facts are also supported by the researchers [21–25].

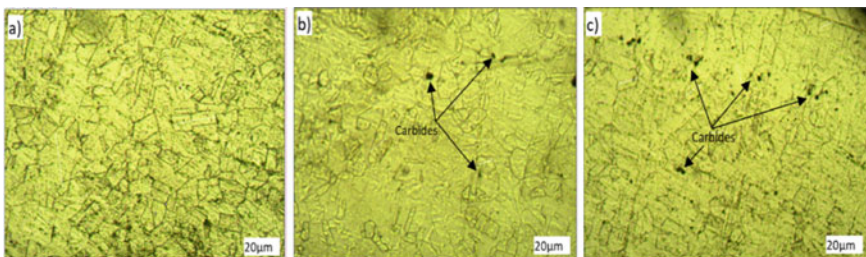


Fig. 6 Microstructure of samples under optical microscopy: **a** UT sample, **b** S.C.T sample, **c** D.C.T sample

3.3 X.R.D Examination

“The X-ray diffraction outlines were presented for the crests of the crystallographic planes corresponding to residual aust. and mart. along with 2θ limit. XRD outlines validate the existence of residual aust. in the UT steel” [1] but extreme sharp points of mart. were noticeable in the outlines of S.C.T and D.C.T samples as illustrated in Fig. 7. According to the images, the amount of residual aust. in D.C.T samples was least as compared to UT and S.C.T samples. This reduction in residual aust. after D.C.T has been inspected by many authors [16–25]. The quantity of residual aust. was identified by A.S.T.M E-975 typical exercise for X.R.D examination as per Eq. 1:

$$V_\gamma = \left[\frac{(1 - V_c)(I_\gamma/R_\gamma)}{(I_\alpha/R_\alpha)} + (I_\gamma/R_\gamma) \right] \tag{1}$$

“where the percentages of residual aust. and carbides are typically represented by V_γ and V_c , respectively. The intensity per angular diffraction peak (hkl) in the aust. and mart. phases is elucidated by the symbols I_γ and I_α , respectively, and the aust. and mart. constants are illustrated by the symbols R_γ and R_α , respectively” [12]. A similar approach was followed by Soleimany et al. [6] for the estimation of residual aust.

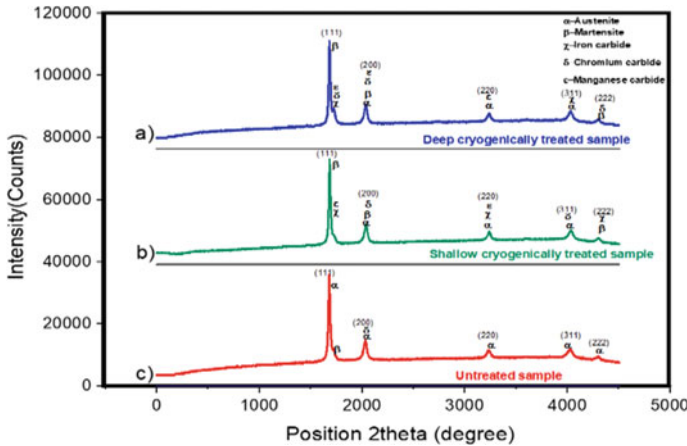


Fig. 7 X-ray diffraction image uncovering the distinct phases and carbides in **a** UT sample, **b** S.C.T sample, **c** D.C.T sample

Table 4 Microhardness (HV) of 316L SS after different heat treatments [1]

Action	HV	HRC
UT	261 ± 5	28 ± 0.5
S.C. T	291 ± 4	32 ± 0.4
D.C. T	312 ± 4	34 ± 0.4

3.4 Examination of Microhardness

The microhardness of S.C.T and D.C.T samples has increased by 11–20% against UT samples as presented in Table 4. The enhancement of hardness maybe because of the diminution of the residual aust. or refinement of microstructure after CT. The increase in hardness was more for D.C.T in comparison with S.C.T. This was related to the complete alteration of residual aust. into mart. and evolution of a better number of carbides in D.C.T samples.

3.5 Slurry Erosion Performance

The slurry erosion behaviour of UT, S.C.T and D.C.T steel samples were inspected on a self-fabricated silt erosion testing apparatus. Each experiment was performed five times, and the mean values were considered for the erosion results. Figure 8 presents the trend of cumulative mass loss (CML) against time for UT, S.C.T and D.C.T samples. The plot between CML and time was drawn against the mean values of erosion results. From the erosion results, it was observed that initially, the CML was less, but after an average time of 60 min, the mass loss suddenly rises. This was attributed to the fact that during the initial hours, erodent particles skids on the furbished steel samples and was unable to erode the targeted surface. Over time, the targeted surface gets rough and would be more prone to erosion wear. The maximum erosion occurred under an impact velocity of 14.32 m/s, impingement angle of 60°, stand-off distance of 10 mm and minimum erosion occurred under an impact velocity

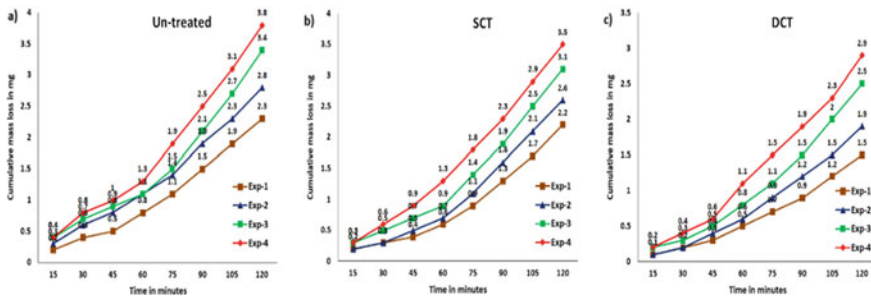


Fig. 8 CML versus time for a UT, b S.C.T and c D.C.T samples under distinct testing conditions

of 5.76 m/s, impingement angle of 30°, stand-off distance of 10 mm. It was also identified that at closer stand-off distances from the impact zone, the erosion wear was marginally higher in comparison with far stand-off distances. This may be attributed to the fact that at closer stand-off distances, the silt grains attacking the material would not disperse and strikes the surface collectively on the targeted surface with more impact force causing deep craters. These facts are very much similar to the work performed by Grewal et al. [3]. The erosion wear was extremely noticeable at sharp velocities. This trend might be accredited to the rise in kinetic-energy of silt grains entrained in the slurry. Similar facts were also endorsed by the authors [1–5, 26]. It was also noticed that the erosion wear was maximum at an impingement angle of 60° for all velocities. The possible reason for this may be that at large rake angles, the substantial-removal is in the form of crater lips or platelets or by plastic deformation. At 60° of impingement angle, the silt grains present in the fluid jet attack the surface tangentially and normally. The tangential component (aligned with the surface of the sample) has a cutting or shearing effect, whereas the normal component damages the material by repeated impacts or plastic deformation. These facts are very well supported by many authors [1–5, 27, 28].

Nevertheless, it was noticed that the CML for S.C.T and D.C.T samples was less against UT samples. This may be accredited to immense hardness and homogenous microstructure of cryogenically treated steel. Further, the erosion resistance of D.C.T samples was maximum, followed by S.C.T samples. This trend of erosion wear may be accredited to the almost complete elimination of residual aust. and better distribution of fine carbides after D.C.T. Amini et al. [21] observed similar facts in one of their work.

3.6 Performance of UT, S.C.T and D.C.T Samples Under Distinct Testing Conditions

To assess the erosion trends of UT and cryogenically treated samples, a bar-chart for CML versus time was drawn as illustrated in Fig. 9. It was observed that the maximum erosion resulted under test run 4 at an I.V of 14.32 m/s, I.A of 60°, SOD of 10 mm. The erosion wear was cut down by 7.8% after S.C.T and 23.6% after D.C.T. This may be accredited to the remarkable instabilities in the microstructure caused after cryogenic treatments and precipitation of small carbides at various locations. The authors [8–13, 20–23] proposed the same trends in their work.

3.7 SEM Examination of Worn Material

To determine the erosion process at distinct testing conditions, the worn-out surfaces were investigated under SEM as illustrated in Fig. 10. At testing conditions configured

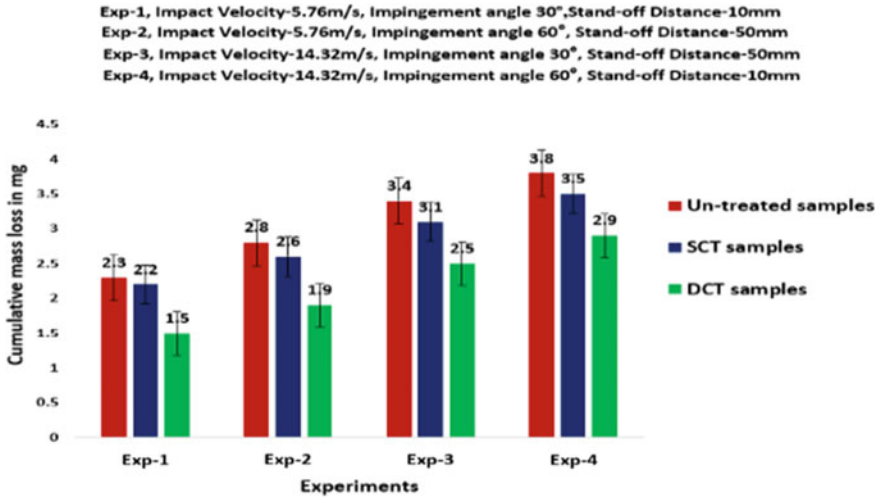


Fig. 9 Variation of CML w.r.t time for distinct samples underwork at various testing conditions

in experiment no-1, the worn-out surface of the UT, S.C.T and D.C.T samples is illustrated in Fig. 10 (a1), (a2), (a3). It was detected that the worn-out surfaces showed the existence of ploughing marks. Furthermore, signs of chip formation were also seen. These findings are also proposed by many authors [2–5]. According to the published work, at low rake angles, the material separation occurs in the form of small chips and cutting. At testing conditions configured in experiment no-2, the worn-out surface of the UT, S.C.T and D.C.T samples is illustrated in Fig. 10 (b1), (b2), (b3). The worn-out surface was comprised of cutting and ploughing marks with the formation of fragments at some locations. This may be attributed to the fact that at high rake angles, the material is removed in the form of fragments or lip formation. Increase in stand-off distance from 10 to 50 mm has resulted in a very marginal increase in the size of craters. Work conducted by Grewal et al. [3] suggested that the concept of revolution in the erosion process w.r.t SOD. The author concluded that distant from the collision zone results in the expansion of crater areas resulting in higher erosion. And moving far away beyond the limit, diminishes the power of collisions resulting in a reduction of erosion. Figure 10 (c1), (c2), (c3) shows the worn-out surface of UT, S.C.T and D.C.T samples examined at testing conditions configured in experiment no-3. Increase in the impact velocity from 5.76 m/s to 14.32 m/s has resulted in the formation of intense cavities on the steel surface and promotes the formation of platelets and chips. The worn-out surface also showed wear marks. Figure 10 (d1), (d2), (d3) shows the worn-out surface of UT, S.C.T and D.C.T samples examined at testing conditions configured in experiment no-4. There were signs of micro-chipping and deep craters on the worn-out surfaces. Tiny pores were also observed at some locations. Such a mechanism of material removal has also been supported by many authors [1–5, 27, 28].

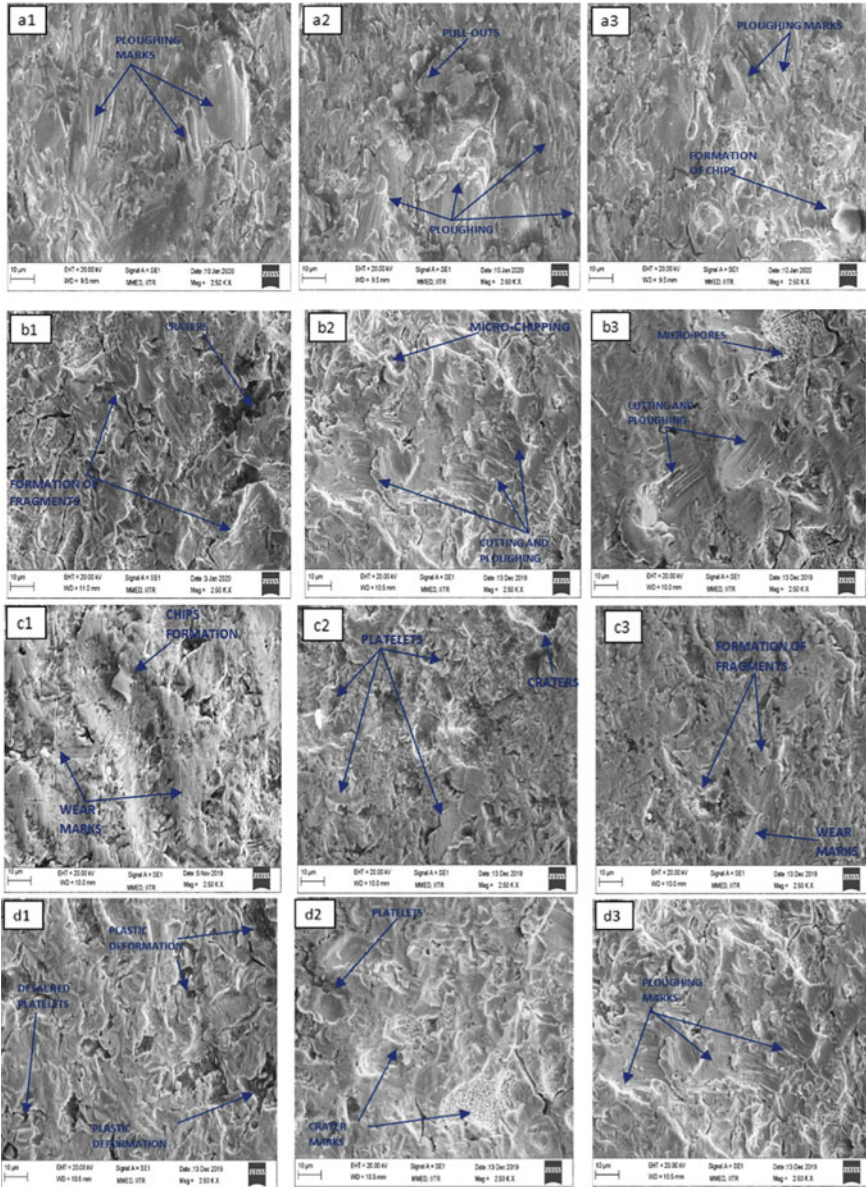


Fig. 10 SEM images of worn-out samples (a1) UT, (a2) S.C.T, (a3) D.C.T samples at testing conditions configured in experiment no-1 (b1) UT, (b2) S.C.T, (b3) D.C.T at testing conditions configured in experiment no-2 (c1) UT, (c2) S.C.T, (c3) D.C.T at testing conditions configured in experiment no-3 (d1) UT, (d2) S.C.T, (d3) D.C.T at testing conditions configured in experiment no-4

4 Conclusions

1. The cryogenic treatments conducted at ultra-low temperatures up to (-196°C) produces very valuable results to enhance the wear strength of SS-316L.
2. The erosion wear was found more significant at high impingement angles. This may be because at high rake angles the silt particles entrapped in the slurry strikes the targeted surface with more intensity.
3. Scanning-electron-microscopy and optical microscopy endorse the existence of residual aust. in the microstructure of UT steel samples. However, this residual aust. seems to be diminished after S.C.T and completely disappears after D.C.T with the precipitation of very fine carbides at various locations.
4. The variation of stand-off distance from the impact zone has a rare significance to affect the erosion performance of steel.
5. SEM investigation suggested that the prominent mechanism of material demolition was micro-cutting and ploughing at 30° of impact angles; however, a mixed phenomenon was found in case 60° of impact angle. Along with ploughing marks, the formation of crater lips and platelets was found at 60° of impingement angle.
6. D.C.T samples impart maximum resistance against erosion, followed by S.C.T samples. This trend of erosion wear may be attributed to the almost complete elimination of residual aust. and more homogenous microstructure of D.C.T samples.

Acknowledgements The authors wish to acknowledge with sincere thanks for the support rendered by Metallurgy Department I.I.T Roorkee and the Central University of Punjab in carrying testing work in this research. The keen encouragement and moral support rendered by the workshop department of Yadavindra College of Engineering, Talwandi Sabo, to complete the present research work.

References

1. Kumar Goyal D, Singh H, Kumar H, Sahni V (2012) Silt erosion behaviour of HVOF sprayed WC-10Co-4Cr and $\text{Al}_2\text{O}_3+13\text{TiO}_2$ coatings on a turbine steel. *Wear* 289:46–57
2. Nandre BD, Desale GR (2018) Work the effect of impact angle on silt erosion wear of four different ductile materials. *Mater Today Proc* 5:7561–7570
3. Grewal HS, Agrawal A, Singh H (2013) Silt erosion mechanism of hydro-turbine steel: Effect of operating parameters. *Tribol Lett* 52:287–303
4. Bansal A et al (2020) Erosive wear behaviour of HVOF-sprayed Ni-20Cr₂O₃ coating on pipeline materials. *Int J Refract Met Hard Mater* 92:105332
5. Shivamurthy RC, Kamaraj M, Nagarajan R, Shariff SM, Padmanabham G (2010) Silt erosion characteristics and erosive wear mechanisms of Co-based and Ni-based coatings formed by laser surface alloying. *Metall. Mater Trans A Phys Metall Mater Sci* 41:470–486
6. Soleimany J, Ghayour H, Amini K, Gharavi F (2019) The effect of deep cryogenic treatment on microstructure and wear behavior of H11 tool steel. *Phys Met Metallogr* 120:888–897

7. Bensely A, Prabhakaran A, Mohan Lal D, Nagarajan G (2005) Enhancing the wear strength of case carburized steel (En 353) by cryogenic treatment. *Cryogenics* 45:747–754
8. Das D, Ray KK (2012) On the mechanism of wear strength enhancement of tool steels by deep cryogenic treatment. *Philos Mag Lett* 92:295–303
9. Barron RF (1982) Cryogenic treatment of metals to improve wear strength. *Cryogenics* 22:409–413
10. Mohan Lal D, Renganarayanan S, Kalanidhi A (2001) Cryogenic treatment to augment wear strength of tool and die steels. *Cryogenics* 41:149–155
11. Hu F, Wu K, Peter HD, Shirzadi A (2014) A. Refinement of retained aust. in super-bainitic steel by a deep cryogenic treatment. *ISIJ Int* 54:222–226.
12. Kumar M, Sidhu HS, Sidhu BS (2020) Effect of different operating parameters on the silt erosion behavior of cryo-treated hydro-turbine steel. *Mater Today Proc* 28:1429–1438
13. Li B, Li C, Wang Y, Jin X (2018) Effect of cryogenic treatment on microstructure and wear strength of carburized 20CrNi2MoV steel. *Metals (Basel)* 8
14. Hinton R (1987) Interlaboratory evaluation of ASTM practice for X-ray determination of retained aust. in steel with near-random crystallographic orientation (e 975). *J Test Eval* 15:95–100
15. Alava LA, Artola G, Guinea I, Muro M (2017) On the influence of cryogenic steps on heat treatment processes. *Mater Perform Charact* 6
16. Jia G, Liubiao C, Kaixuan G, Junjie W (2015) A cryogenic treatment system for treating large rolls. *Phys Procedia* 67:367–372
17. Zhu YZ, Yin ZM, Zhou Y, Lei QF, Fang WS (2008) Effects of cryogenic treatment on mechanical properties and microstructure of Fe-Cr-Mo-Ni-C-Co alloy. *J Cent South Univ Technol (English Ed)* 15:454–458
18. Mahmudi R, Ghasemi HM, Faradji HR (2008) Effects of cryogenic treatments on mechanical properties and wear behaviour of high-speed steel M2. *Int Heat Treat Surf Eng* 2:162–166
19. Collins DN (2008) Cryogenic treatment deep cryogenic treatment of tool steels: a review. *Int Heat Treatment Surf Eng* 2:147–149
20. Molinari A, Pellizzari M, Gialanella S, Straffellini G, Stiasny KH (2001) Effect of deep cryogenic treatment on the mechanical properties of tool steels. *J Mater Process Technol* 118:350–355
21. Amini K, Nategh S, Shafyei A (2010) Influence of different cryotreatments on tribological behavior of 80CrMo12 5 cold work tool steel. *Mater Des* 31:4666–4675
22. Yan N, Di H, Misra RDK, Huang H, Li Y (2019) Enhancing aust. stability in a new medium-Mn steel by combining deep cryogenic treatment and intercritical annealing: an experimental and theoretical work. *Mater Sci Eng A* 753:11–21
23. Kumar P, Chattopadhyay K, Chakrabarty I (2014) Effect of sub-critical tempering and deep cryogenic treatment on silt erosion of Cr-Mn-Cu white cast irons. *ISIJ Int* 54:2294–2301
24. Han LL, Lin CM, Shih YS (2013) Corrosion resistance of ASSAB stavax ESR SS by heat and cold treatment. *Mater Trans* 54:833–838
25. Su YY, Chiu LH, Chen FS, Lin SC, Pan YT (2014) Residual stresses and dimensional changes related to the lattice parameter changes of heat-treated JIS SKD 11 tool steels. *Mater Trans* 55:831–837
26. Tan KS, Wood RJK, Stokes KR (2003) The silt erosion behaviour of high velocity oxy-fuel (HVOF) sprayed aluminium bronze coatings. *Wear* 255:195–205
27. Goyal DK, Singh H, Kumar H (2019) Characterization and accelerated erosion testing of WC-Co-Cr- and CoNiCrAlY-coated CA6NM turbine steel. *J Therm Spray Technol* 28:1363–1378
28. Sharma V, Kaur M, Bhandari S (2019) Development and characterization of high-velocity flame sprayed Ni/TiO₂/Al₂O₃ coatings on hydro turbine steel. *J Therm Spray Technol* 28:1379–1401

Performance, Combustion, and Emission Characteristics of Diesel Engine Using Low-Temperature Combustion



R. T. Sarathbabu, M. Kannan, R. Balaji, and Ashish Selokar

Abstract In developing countries, including India, biodiesel extracted from invalid feedstuffs such as Mahua, Jatropha, and Pongamia has been shown to be a viable alternative. The findings of the power output investigation and then the emission characteristics of Mahua biodiesel engines are discussed in this research. In this analysis, Mahua biodiesel and diesel blends of different proportions were packed analyzed against the output of diesel fuel and analyzed by means of a single diesel engine cylinder. The heat capacity, fuel consumption by brake, exhaust gas temperature, Co, Hc, No, and smoke releases are investigated. The main motto of present study of experiment is to improve the performance and reduced the exhaust emission characteristics of the compression ignition engine fuelled by mahua oil biodiesel fuel mixtures with low heat rejection (LHR) by coating of ceramic on engine parts and low-temperature combustion (LTC) done by EGR method, thus finding the optimum biodiesel blends for the diesel engine. This research studies focus on optimum NO_x reduction ratio and observed the performance, combustion and emission characteristics of diesel engine using low-temperature combustion with modified LTC + LHR engine and 5% ethanol blends. This study performs on improving efficient performance, combustion, and emission characteristics of diesel engine observation.

Keywords Low-temperature combustion (LTC) · Diesel engine · Biodiesel blend · Combustion analysis · Exhaust gas recirculation (EGR)

R. T. Sarathbabu

Department of Mechanical Engineering, Mother Theresa Institute of Engineering and Technology, Palamaner 517408, India

M. Kannan

Department of Mechanical Engineering, KCG College of Technology, Chennai, India

R. Balaji

Department of Mechanical Engineering, Hindustan Institute of Technology and Science, Chennai 603103, India

A. Selokar (✉)

Department of Physics, Mohsinbhai Zaveri Mahavidyalaya, Desaiganj (Wadsa), Maharashtra 441207, India

1 Introduction

The effect of exhaust gas recirculation (EGR), direct injection pressure, and injection frequency mostly on output of a typical fuel injection rail engine fuelled through fungus biodiesel. Authors conducted the experiments on the basis of the entire factorial design [1]. Mathematical models based on the surface response methodology were applied to determine the characteristics of the engine [2]. The surface response study shows that the thermal of 10oBTDC and 900 bar resulted in higher thermal brake performance and lower emissions of smoke, carbon monoxide, hydrocarbon, and nitrogen oxides [3]. Under certain two phases, with greater peak pressure and heat release rate, the ignition delay and the combustion duration were small. A research on the efficiency of the diesel engine using the exhaust gas recirculation system operated by mahua biodiesel has been conducted [4]. The authors focused on determining the effects on exhaust gas temperature (EGT), fuel consumption (SFC), and exhaust emissions (CO, NO_x, UHC, and CO₂) of EGR and mahua biodiesel. At a static engine speed of 2500 rpm at maximum load, the research method using an EGR multi-cylinder diesel engine and the simulation work utilizing diesel were carried out [5]. The findings have shown that mahua biodiesel has dramatically increased fuel consumption, strengthened NO_x, and significantly decreased certain emissions from predicted and measured works, namely CO, CO₂, and unburned hydrocarbon (UHC) [6]. Researchers are performed an investigational analysis on a 4-stroke direct injection, water-cooled DI diesel engine run by pure mahua biodiesel while using diaphragm EGR [7]. Author calculated the engine power output and exhaust emissions, mostly NO_x by using both EGR and biodiesel [8]. Experiments have been performed in a stable state in which unmodified diesel has been used by way of fuel. Analysis results display that the EGR and palm biodiesel in diesel engine reduced brake power output, reduced engine torque and enlarged fuel consumption, reduced NO_x, and marginally increased other emissions, such as CO₂, CO, and particulate matter. A most powerful and effective of these engines were its ceramic-coated engine [9]. Present investigation mostly on ceramic-coated engine has been carried out to increase thermal performance in biodiesel activities. Though, the solitary drawback in this technique is additional NO_x emissions owing to more exhaust gas temperature [10]. Hence, more NO_x emission must overcome by using another modification, which is implemented in this research work called low-temperature combustion (LTC). It is used to decrease NO_x emissions in the compression ignition engine by re-circulating the engine's exhaust gas back into the air intake system by using the EGR valve [11]. The typical LTC system implemented in a compression ignition engine, particularly this system has been used to reduce NO_x emissions in the biodiesel-fuelled diesel engine [12]. There are two modifications in LTC techniques that have been applied to a diesel engine to overcome the disadvantage of using biodiesel in the engine. During combustion, the exhaust temperature of the engine decreases with the cylinder pressure and the heat release rate of the engine. In current paper, the research concerns the use of mahua biodiesel and its combination of fuel in a stationary diesel engine. Experimentations are conducted to examine the

combustion, performance, and emission behavior of compression ignition engine and different blending combinations of mahua oil biodiesel and pure diesel under LTC processing.

2 Experimental Setup

The experiment with the modification of engine by coating Low Heat Rejection (LHR) material to improve efficiency and to reduce engine heat loss [1]. In this particular method, however, the emission of NO_x increases due to high exhausts gas temperature while using B20 Blend. This experiment is to implement the LTC method through the EGR process, varying from 5 to 20% LTC ratio. It is used fuel for experimentation which is pure diesel in spite of B20 blend. Because the properties of B20 are closer to those of diesel, as stated in Table 1. The LTC system is used to regulate NO_x emissions by reducing oxygen content in the engine cylinder. The temperature of the flame of the combustion chamber is reduced. This part of result besides discussion deals the same diesel engine's performance, combustion, and emission parameters impacts with an implementation of LTC concept by using different proportions of EGR to identify suitable LTC ratio for getting reasonable exhaust emission and engine efficiency.

2.1 Low-Temperature Combustion (LTC)

By changing low temperature combustion setting for experiment, diesel was used as a fuel for engine running. LTC controls the exhaust gas to flow the engine inlet with the different ratios using control valves and to determine the optimum NO_x reduction ratio. The optimum three phases were compared to the phase IV experiment with the modified LTC+LHR engine and 5% ethanol blends. Figure 1 demonstrates the setup of the experimental LTC engine.

For all four types of experiments conducted in the present research, a sole cylinder, straight injection, compression ignition, and four-stroke diesel engine was used. The electrical dynamometer was used to vary the loads of the experimental engine by the controller. The engine's speed was kept steady at 1500 rpm [8]. Thermocouples were being used for calculating the temperature of the exhaust gas. Engine's exhaust emission has been measured using the analyzer. The smoke analyzer was set in the engine for monitoring the emission levels. All experimental measurements were taken only after stability in the operation of the engine was achieved.

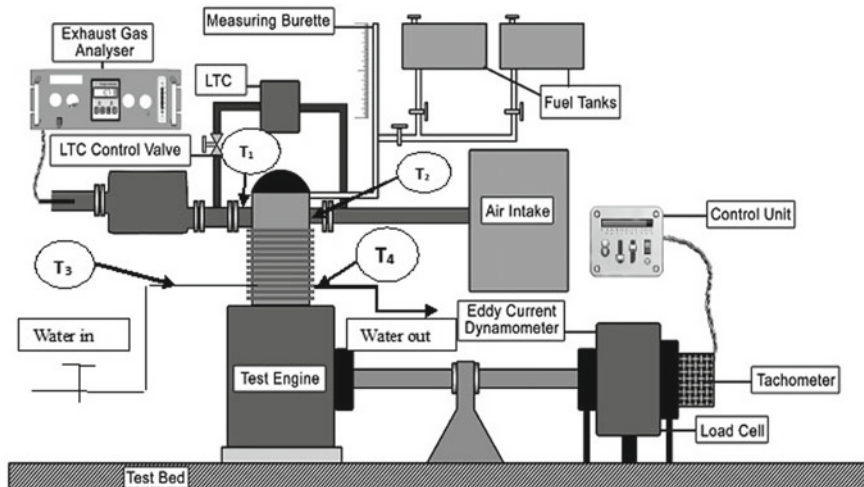


Fig. 1 Experimental engine setup with LTC

2.2 Mahua Biodiesel Properties

The physiochemical properties of mahua oil, crude oil, and biodiesel fuel blends were determined by using standards of ASTM. Different types of biodiesel fuel blends have been prepared [9], and their volumetric proportions remain recorded trendy Table 1.

The mahua biodiesel blends of calorific value were calculated by using ASTM standard of D240 used to determine the liquid and gas fuel temperature of combustion. The fuel blend density was determined by the D4052 ASTM standard, and a standard method for determining fuel properties was used with a digital density meter to specify the values, including density, relative density, and specific liquid gravity. Heating biodiesel blends at 45 °C as per standard of ASTM D445 referred to calculate the kinematic viscosity, followed by the determination of the kinematic viscosity of transparent and opaque liquids. Thus, the experimental investigation on mahua biodiesel in the diesel engine using LTC has been drawn in a graphs, and the results have been effectively explored.

Table 1 Blends of mahua biodiesel properties

Property	Mahua Oil	MOME	Diesel	D80/B20	D75/B20/E5
Density (kg/m ³)	960	880	850	860	869
Kinematic viscosity (CSt)	24.58	3.98	3.52	3.62	3.49
Flash point (°C)	232	208	49	80	77
Calorific value (MJ/kg)	36	37	42	38	40
Cetane number	45	47	53	51.2	51

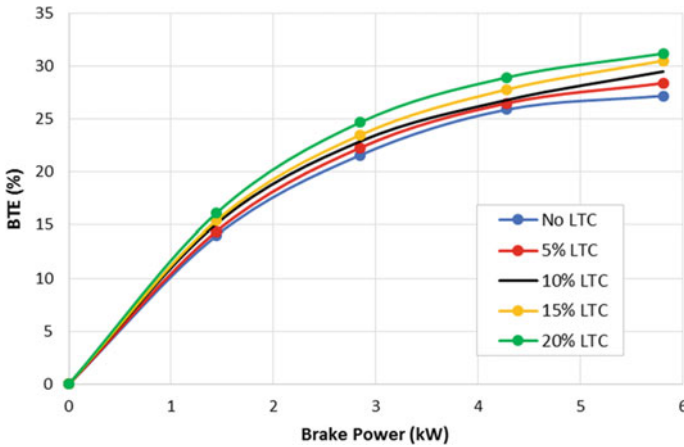


Fig. 2 BTE versus BP for different LTC ratios

3 Results

3.1 Effect of Brake Thermal Efficiency

BTE is the ratio of the real brake action to the sum of fuel energy each cycle. BTE depends upon the heating value of the fuel. Figure 2 indicates the different ratios of the LTC to the brake power of the BTE. The engine's BTE increases with the LTC ratio also increase.

For diesel fuel operation, at the maximum load of BTE is 27.2% for no LTC, then, 31.19% for 20% LTC. From Fig. 2, it is seen that the efficiency variation for no LTC is much lower when compared to the LTC engine at a minimum brake power. By extreme brake power (full load), BTE of 20% LTC is increased by approximately 12.8% compared to the diesel engine without LTC. During the suction stroke, the fuel-air mixture is lean [12]. Then the LTC proportions were increased by reducing the air-fuel ratio to the stoichiometric ratio [9], resulting with increased brake power.

3.2 Effect of Brake Specific Energy Consumption (BSEC)

It is usually desirable to have a lower BSEC value, which illustrates that an engine uses less fuel to produce the same amount of work. Figure 3 indicates the different ratios of the LTC to the brake power of the BSEC [9]. The BSEC of the engine decreases as the LTC ratio increases. From the figure, it clearly understood that the increase of brake power of an engine BSEC gradually decreased in all LTC ratios of diesel fuel.

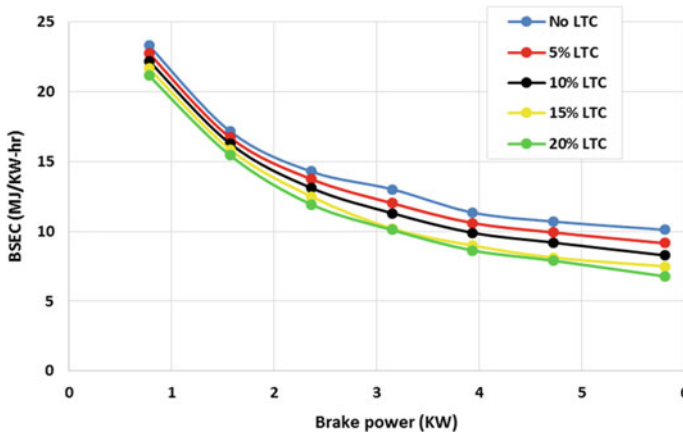


Fig. 3 BSEC versus brake power for different LTC ratios

Around 6.2% of engine, BSEC reduces by increasing LTC ratios for compared conventional (no LTC) engine. At the engine’s maximum brake power, the brake specific energy consumption of 20% LTC decreased by approximately 32.93%.

[6] compared to the diesel engine with no LTC. The decrease in BSEC with LTC is due to the rise in intake charge temperature, which accelerates the level of fuel combustion [3] also found comparable results during the operation of the reduced ignition four-stroke single-cylinder diesel engine.

3.3 Effect of Exhaust Gas Temperature

Figure 4 indicates the difference of the exhaust gas temperature (EGT) trendy various LTC proportions. The findings show that the exhaust gas temperature decreases by increasing in the LTC proportions. This is caused by the partial availability of oxygen, which decreases the maximum temperature of combustion in the engine cylinder. The lowest exhaust gas temperature of 296.7 °C [3] was shown by the 20% LTC, and the lowest value is recorded in the experiment.

3.4 Effect of In-Cylinder Pressure

Figure 5 shows the peak pressure trend of various LTC proportions. The peak pressure can be seen to decrease with an increase in the LTC proportions. This is attributed to a decline in combustion due to a decrease in the supply of renewed air. Lowest peak pressure is obtained in 20% LTC was 62.3 bar, while the maximum peak pressure

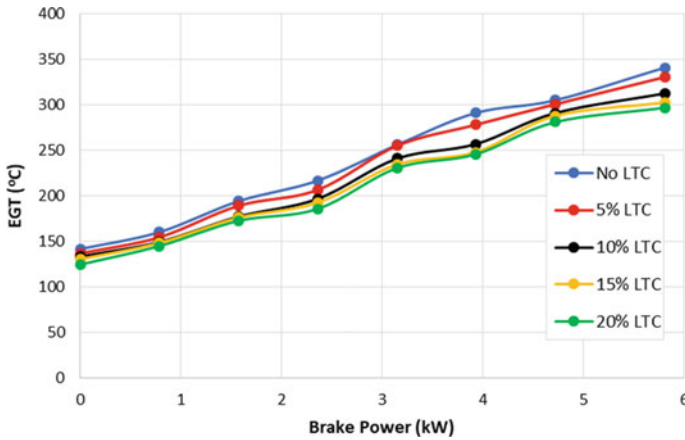


Fig. 4 Exhaust gas temperature versus BP for different LTC ratios

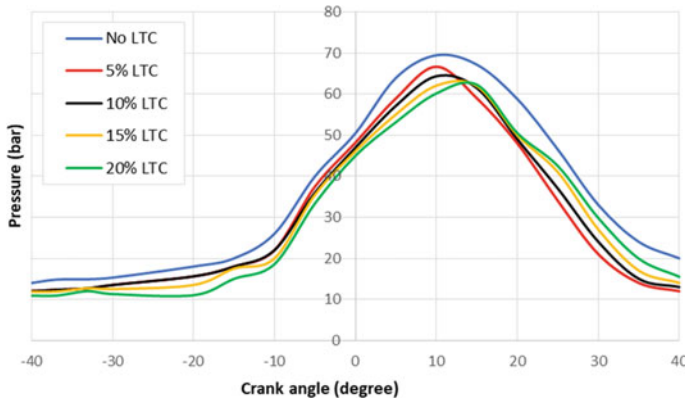


Fig. 5 In-cylinder pressure versus crank angle for various LTC ratios

for diesel with no LTC was 69.5 bar [6]. The peak pressure is reduced by 10.25% because of the occurrence of LTC.

3.5 Effect of Heat Release

Figure 6 demonstrates the heat release behavior of the engine in various LTC proportions. With an increase in LTC ratios, maximum heat release was reduced. Owing to the small amount of fresh oxygen available in the combustion process, the heat release decreased with increased LTC levels [6]. The maximum heat release of 20%

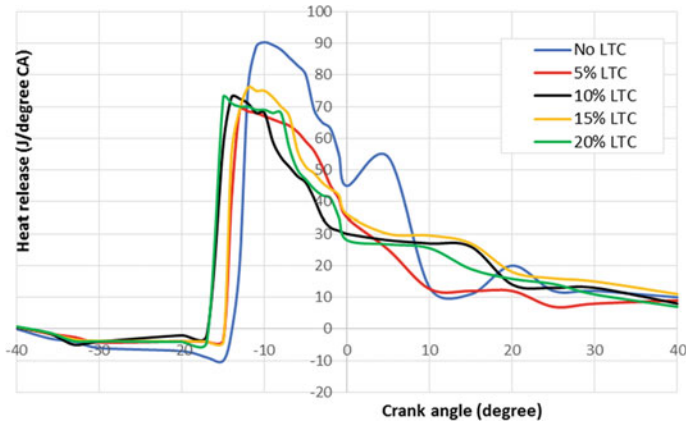


Fig. 6 Heat release rate versus crank angle for different LTC ratios

LTC is 73 J/°CA, which was 23% lower peak heat release than the pure diesel with no LTC.

3.6 Effect of Ignition Delay

Figure 7 indicates the engine ignition delay with reference to the brake power at various loads at different LTC ratios. Ignition delay in all LTC ratios can be seen as decreasing with load increases. The ignition delay at no load of 20% LTC is higher than other LTC ratios. Fuel aligned with automatic and proper atomization is the main

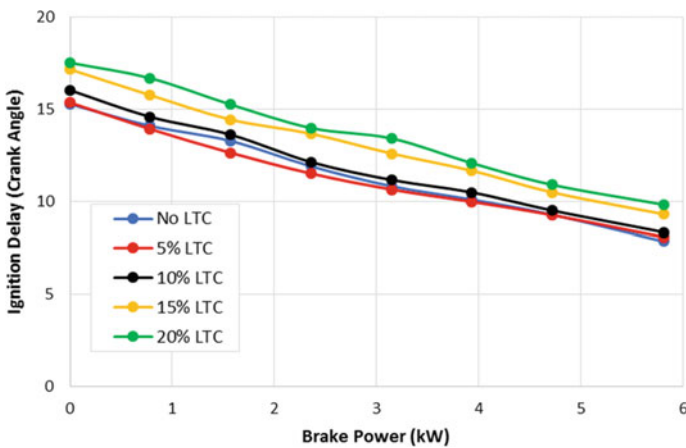


Fig. 7 Ignition delay versus brake power for different LTC ratios

point to reduce the ignition delay in an engine. The ignition delay increases when both LTCs decline [9]. However, 15% of the LTC showed a small delay increase, which is suitable for minimal impairment of diesel engine performance and operation.

3.7 Emission of HC and CO

Figures 8 and 9 illustrate the variation in the emissions of unburned hydrocarbon and carbon monoxides from brake power at different LTC ratios. From these figures, hydrocarbon and carbon monoxide emissions are clearly understood to increase with increased LTC. Figure 8, at the minimum and maximum load condition, 20%LTC engine increased the hydrocarbon emission around 25.6% and 27% compared to

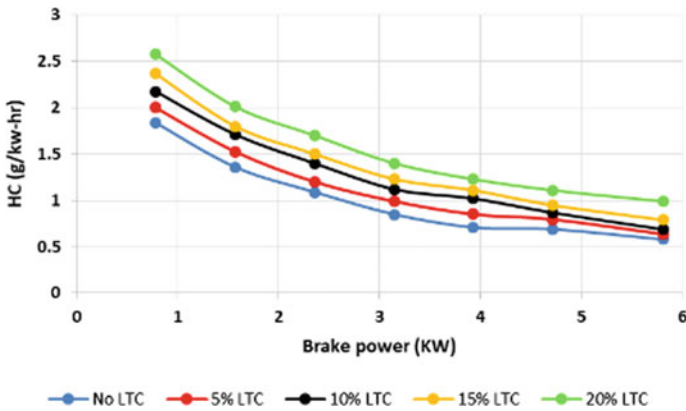


Fig. 8 Unburned HC versus BP for various LTC ratios

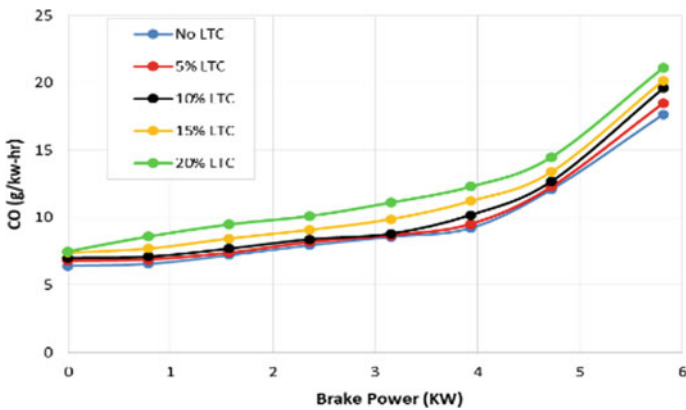


Fig. 9 CO versus BP for various LTC ratios

the diesel engine with no LTC [11]. Likewise, emissions of carbon monoxide (CO Fig. 9) increased by 7% and 16.38% at a minimum and maximum load during LTC operation [7], respectively. This shows that HC emissions tend to increase with a reduction in fuel oxygen content.

The reduction of excess oxygen concentration results in the rich mixtures of fuel-air at various locations in the ignition space. Process of burning depends on advanced the stoichiometric ratio, important to emissions of hydrocarbons and carbon monoxide. Lean mixtures are tougher to ignite at part loads because of the occurrence of heterogeneous mixtures that lead to higher hydrocarbon and carbon monoxide emissions.

3.8 Effect of CO₂ Emissions

The CO₂ emission has analyzed only in these sections of results and discussions because implementation of LTC by using a varying percentage of EGR does not supply the sufficient oxygen content for the engine combustion process. Figure 10 illustrates the difference in CO₂ emissions relative to brake power at various LTC ratios. Since CO₂ has a higher specific heat performance, the peak temperature of the cylinder decreases due to combustion process heat absorber [10].

From Fig. 10, diesel with no LTC attained highest CO₂ emission compared to other LTC ratio of diesel when increasing LTC ratio that led to reducing the CO₂ emissions [9]. At the lowest and highest brake power, the CO₂ emission of the 20%LTC engine is reduced by roughly 8.57% and 12.90% likened to diesel engine via no LTC. Because of the high LTC ratio, the extreme combustion temperature

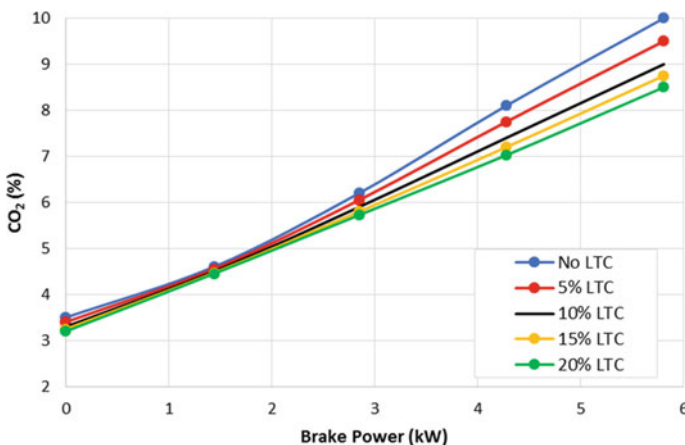


Fig. 10 CO₂ emission versus BP for different LTC ratios

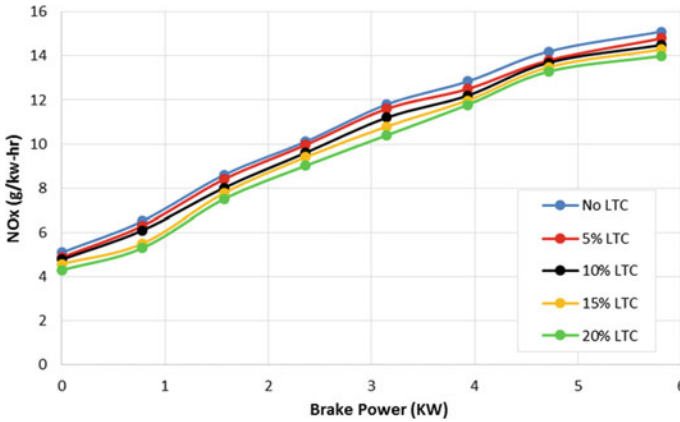


Fig. 11 Oxides of nitrogen versus brake power for various LTC ratios

is reduced. In addition to reducing CO_2 emissions during the combustion process, contemporary engine cylinders have a reduced oxygen content of LTC ratio.

3.9 Effect of NO_x Emission

Figure 11 illustrates the nitrogen oxides (NO_x) emissions with brake power at various LTC proportions. NO_x emissions are observed to decrease with an increase in the LTC ratio at lower and higher engine loads. At maximum load, NO_x emissions can decrease by about 7.8% for 20% of the LTC ratio. For the LTC ratio of 5%, 10% and 15% [2], the NO_x emission reduced by around 2.02%, 4.13%, and 5.59%, compared to with no LTC engine. The decrease of NO_x emissions is because of the support of an inert gas containing a three-atom molecule [7] such as CO_2 , H_2O , etc. Furthermore, combustion temperature reduced through an increase in the LTC ratio due to an increase in inert mass in the chamber of the combustion.

3.10 Effect of Smoke Emission

The exhaust gas of particulate matter was measured by using exhaust gases smoke opacity. Smoke emission impacts to the different LTC ratios shown in Fig. 12. The composition of the smoke opacity of the exhaust gas upsurges by means of LTC ratio rises. For 100% load, the CO_2 emission of 20% of the LTC motor decreased by approximately 10.34% compared to the diesel engine without LTC. This is because low-temperature combustion reduces the oxygen availability required for fuel combustion, leading to fairly incomplete combustion and also increases the

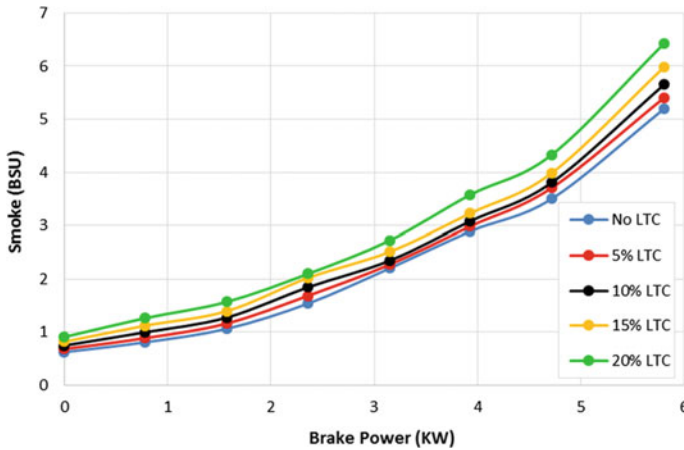


Fig. 12 Smoke emission versus BP for different LTC ratios

formulation of particulate matter [4]. Compared to no LTC, the 5% LTC ratios, 10%, 15%, and 20% LTC generate 4.03%, 8.84%, 15.2%, and 18.12% more smoke at maximum load than similar.

4 Discussion

An experiment of diesel engine with LTC was performed on the conventional diesel engine with modification of a LTC system. The engine fuelled with pure diesel varies LTC proportions from 0 to 20%. The results of the experiment were concluded the following,

- Experiments have shown that increasing the LTC percentage increases the engine's brake thermal efficiency in all load conditions. The increase difference is more at full loads than at low loads.
- Specific engine energy consumption fueled by diesel decrease with an LTC percentage increase overall loads. Compared to higher loads at lower loads, the fuel consumption rate decreases. The engine brake power has not been affected, and the entire LTC ratio remains the same. It was seen that nitrogen oxides reduced dramatically by using LTC. The increase in the LTC percentage reduces the emission of NO_x more due to the reduction of the engine's exhaust gas temperature through LTC.
- In LTC, engine emissions of CO and HC slightly increased. Because LTC ratios increasing, it has stoichiometric combustion due to reducing oxygen content while the suction stroke. So that increased the HC and CO emission, mainly owing to excess air reduced in addition that lowering combustion temperature.

- CO and HC emissions of 15% LTC were acceptable, and the optimum proportion was selected for testing the B20 blend in the LHR engine.

5 Conclusion

On this experiment, LTC modifications were implemented in a diesel engine with varying LTC ratios (0%, 5%, 10%, 15% and 20%) of diesel fuel. This method is mainly used for reducing the NO_x emission and meanwhile improving the efficiency of engine through recirculation of exhaust gas. It decreases facing high NO_x emission by using biodiesel mixtures.

Associated toward diesel, the 15% LTC's BTE 12.2% high, BSEC is 25.8% less, EGT is 11.2% less, HC is 36.2% high, CO is 14.2% high, NO_x is 5.3% less, and smoke is 15.1% more.

From these results and discussions, the observations indicate that 15% of LTC is best compared to other LTC ratios. Due to the low temperature inside the cylinder, the NO_x is reduced. But CO and HC increased by 14.2%, which is negligible.

References

1. Garud V, Bhoite S, Patil S, Ghadage S, Gaikwad N, Kute D, Sivakumar G (2017) 'Performance and Combustion Characteristics of Thermal Barrier Coated (YSZ) Low Heat Rejection Diesel Engine. *Materials Today: Proceedings* 4(2):188–194
2. Gavudhama Karunanidhi S, Balakrishnan N, Subba Rao G (2014) CFD studies of combustion in direct injection single cylinder diesel engine using non-premixed combustion model. *Int J Eng Res Appl* 4(7):68–73
3. Hawi M, Kiplimo R, Ndiritu H (2015) Smart grid and renewable energy effect of exhaust gas recirculation on performance and emission characteristics of a diesel-piloted biogas engine, vol 6, pp 49–58
4. Işcan B, Aydın H (2012) Improving the usability of vegetable oils as a fuel in a Low Heat Rejection diesel engine. *Fuel Process Technol* 98:59–64
5. Barabás I, Todoruț I-A (2011) Utilization of biodiesel-diesel-ethanol blends in CI engine, *Biodiesel-Quality, Emissions and By-Products*, Montero G (ed). ISBN: 978-953-307-784-0
6. Jaichandar S, Tamilporai P (2003) Low heat Rejection Engines—an overview. *SAE Technical Paper*, vol 724
7. Kannan M, Karthikeyan R, Deepanraj B, Baskaran R (2014) Feasibility and performance study of turpentine fueled DI diesel engine operated under HCCI combustion mode. *J Mech Sci Technol* 28(2):729–737
8. Karthikeyan B, Srithar K (2011) Performance characteristics of a glow plug assisted Low Heat Rejection diesel engine using ethanol. *Appl Energy* 88(1):323–329
9. Khandal SV, Banapurmath NR, Gaitonde VN (2017) Effect of exhaust gas recirculation, fuel injection pressure and injection timing on the performance of common rail direct injection engine powered with honge biodiesel (BHO)'. *Energy* 139:828–841
10. Krishna MVSM, Rao VVRS, Reddy TTK, Murthy PVK (2014) Comparative studies on performance evaluation of di diesel engine with high grade Low Heat Rejection combustion chamber with carbureted alcohols and crude jatropha oil. *Renew Sustain Energy Rev* 36:1–19

11. Kumar AN, Brahma K, Srinivas P, Narayana K (2018) Some experimental studies on effect of exhaust-gas recirculation on performance and emission characteristics of a compression-ignition engine fuelled with diesel and lemon-peel oil blends. *Mater Today Proc* 5(2):6138–6148
12. Kumar RS, Loganathan M, Gunasekaran EJ (2015) Performance, emission and combustion characteristics of CI engine fuelled with diesel and hydrogen. *Front Energy* 9(4):486–494

A Review on Machining Potential of Composite Materials During Abrasive Water Jet Machining



Anil Kumar Dahiya, B. K. Bhuyan, and Shailendra Kumar

Abstract Abrasive water jet machining (AWJM) is a latest mechanical-based hybrid machining process which is extensively used in industries like aerospace, automobile, nuclear and construction for machining of electrically conductive as well as non-conductive materials by impact of high-speed water with mixture of abrasive particles on workpiece surface. Composite materials are prominent amongst the advanced engineering materials these days, and their machining is a very challenging job for such industries, owing to their anisotropic as well as non-homogeneous nature. In this paper, a literature study is carried out for analysing the impact of process variables on performance characteristics of AWJM considering their viability of machinability potential for composite materials like carbon fibre-reinforced polymers (CFRPs) and glass fibre-reinforced polymers (GFRPs) along with major findings. Moreover, this study also gives insight on the research future scope in AWJM of CFRP and GFRP composites.

Keywords AWJM · CFRP · GFRP · Surface roughness · Kerf characteristics · Delamination

1 Introduction

Composites are macroscopical combinations of more than one distinct material to manufacture a better amalgamation of properties from all integrant than those of the individual components used alone. Reinforcement and matrix are the two constituents of composite materials. The reinforcement enhances the strength and stiffness in

A. K. Dahiya (✉)
FET-MRIIRS, Faridabad, India

Department of MAE, MAIT, Rohini, New Delhi, India

B. K. Bhuyan
Department of Mechanical Engineering, FET-MRIIRS, Faridabad, India

S. Kumar
Department of Mechanical Engineering, SVNIT, Surat, India

composites as it is harder and stronger than the matrix. The composites are classified on the basis of matrix constituents like organic matrix composites (OMCs), metal matrix composites and ceramic matrix composites. OMCs are further classified as polymer matrix and carbon matrix composites. Advantages of composite materials include high fatigue and toughness, high strength and stiffness, high temperature wear and oxidation resistance, low density, light weight, etc. [1]. Due to these superior specific properties, composite materials are used universally in applications which require high performance and they are custom-built to meet these ever-increasing challenges in today's world [2]. The major applications of composites include aerospace, automotive, construction, marine goods, sporting goods and infrastructure. In advanced composite materials, properties are tailored to achieve the balance for a given range of applications [3]. In present days, machining of composite materials is playing a major role for the modern industries and also a challenging job for proving its quality of machining prospective. There are various traditional and non-traditional machining operations that were initiated by various researchers to progress its quality of machining in a better manner.

In non-traditional machining processes, the recently developed machining process is AWJM which is widely used in the manufacturing industry for cutting, turning, drilling, threading, milling, cleaning and hybrid machining. It uses the high kinetic energy of a water jet mixed with abrasive for removal of material. The high-speed water jet along with abrasive particles impinges on workpiece's surface to erode the desired amount of material. In comparison with conventional machining processes, heat generated on the workpiece is negligible. Some more advantages of AWJM process are high speed and multi-directional cutting capability, less setup time, high cutting efficiency, ability to cut complex shapes, low deformation stresses, no cutting fluid required, no toxic fume generation or hazardous waste, etc. In comparison with traditional machining processes, AWJM is found to be a more environment-friendly process of removing material [4, 5]. Various process parameters of AWJM are hydraulic pressure, abrasive mass flow rate (AMFR), abrasive particle material and size, orifice size, focusing tube diameter and length, traverse rate, stand-off distance (SOD) and inclination angle. The major quality characteristics are attainable depth of cut, kerf geometry, surface finish and delamination. The following sections have thoroughly explicated the working principle, critical machining potential on composite materials, influence of process variables on responses and imperative analysis of AWJM along with reports the major scope of further research gaps in this area.

2 Working Principle of AWJM

Machining of composites is challenging, and it is difficult to cut and make holes in composite materials without damaging its surface with conventional machining due to fibre orientation (continuous fibre), heterogeneous nature, superior mechanical properties, anisotropy, high cutting temperature, matrix cracking, high cutting force

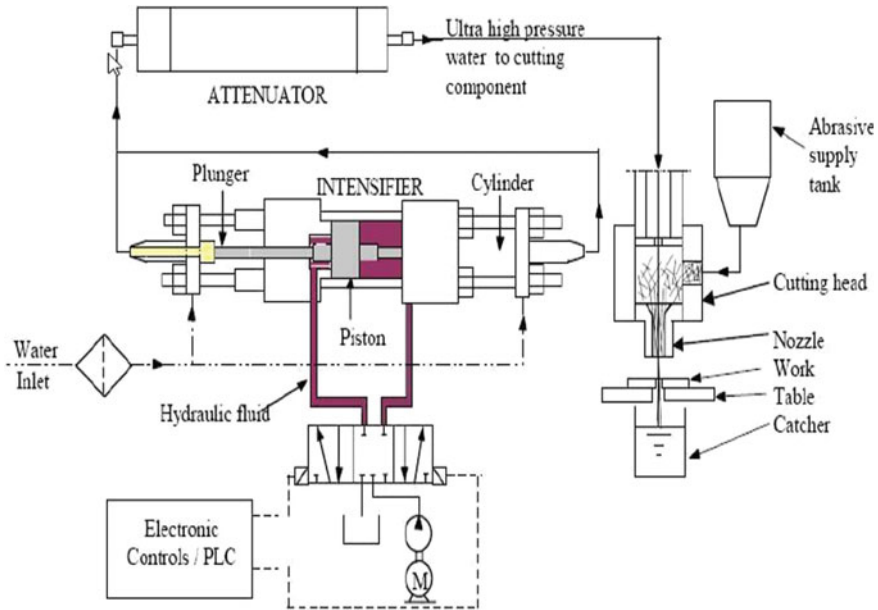


Fig. 1 Diagram of AWJM [10]

and excessive tool wear. Non-conventional machining processes like EDM, USM, laser and laser-assisted machining, WJM and AWJM may become the most practical method for machining the composites, advanced ceramic materials, granite, marble and glass [6]. AWJM has advantage over traditional machining such as negligible increase in temperature as water acts as coolant and absorbs heat generated during the process, no cutting force between workpiece and machine, no deformation and vibrations, higher production rate [7], environment-friendly as no fumes and vapours generated and minimum tool wear. For getting the maximum advantages of AWJM, the process parameters should be optimized. Even the complex shapes can be machined with better surface finish using AWJM, which is widely used in industries [8, 9]. Diagrammatic representation of AWJM is shown in Fig. 1.

3 Study of Composite Materials During AWJM

Many researchers have investigated the machinability characteristics of CFRP and GFRP composites through cutting performance measures like surface finish, kerf geometry, delamination, metal removal rate (MRR), etc. For example, surface roughness and kerf taper were investigated by Ramulu and Arola [11] for establishing effect of different parameters on graphite/epoxy laminate composite with AWJM, and they reported that kerf width is affected with stand-off distance (SOD). Kerf taper

and surface roughness of glass/epoxy composites were investigated by Shanmugam et al. [12] using Taguchi technique and ANOVA, and they concluded that for surface roughness hydraulic pressure and AMFR and SOD, abrasive material and traverse rate are significant factors for kerf taper. Siva Prasad and Chaitanya [13] investigated to determine the surface quality and dimensional accuracy of hole of 8-mm-thick sheet with 8-mm and 10-mm diameter hole of glass fibre-reinforced polymer (GFRP) and found that surface roughness and dimensional accuracy are influenced due to fibre orientation and SOD. Alberdi et al. [14] experimentally explored the machinability index and other process parameters for kerf taper and surface roughness of CFRP and fibre reinforced polymers (FRP) with AWJM. The machinability index of composite materials is much higher than that of metals. Hejjaji et al. [15] experimentally investigate influence of various machining parameters on MRR, machined surface quality, type of damages such as carters, broken fibre and abrasive particle embedment, and their impact was investigated on carbon/epoxy composite. Phapale et al. [16] examined impact of water pressure and SOD on delamination in AWJ drilling of CFRP composites, and no delamination was observed at low hydraulic pressure, SOD and AMFR and compared the surface roughness of drilled holes with various delamination techniques. Irina Wong et al. [17] studied and concluded that SOD and traverse rate are the major factors of minimization of kerf ratio and for minimum delamination abrasive flow rate and traverse speed are dominating factors in hybrid carbon/glass fibre reinforcement polymers using AWJM. Uthayakumar et al. [18] investigated the MRR and kerf taper on twill weaved carbon fibre-reinforced polyester composite with AWJ machining and concluded that MRR is mainly affected by traverse speed (95.11%) and by SOD (4.14%) and kerf taper depends upon SOD (66.7%), traverse speed (21.27%) and hydraulic pressure (1.52%). Dhanawade et al. [19] experimentally carried out the impact of different variable parameters of AWJM on carbon epoxy composite and revealed that there is increase in kerf taper and surface roughness when hydraulic pressure is decreased while traverse speed is increased. El-Hofy et al. [20] outlined that kerf width decreases with decrease in hydraulic pressure and SOD and increases with feed rate while surface quality decreases with low hydraulic pressure, high feed rate and high SOD in multi-directional CFRP laminates on AWJM and concluded with the help of process cost model that AWJM may be cheaper than milling. Dhanawade and Kumar [21] experimentally investigated the surface roughness and kerf characteristics of carbon epoxy composite with AWJ machining, and a predictive model was developed and suggested to evaluate surface roughness and kerf characteristics. It was concluded that as traverse speed decreases and water pressure increases, surface roughness improves on fibre-reinforced composites with AWJ machining by Vigneshwaran et al. [22]. Melentiev and Fang [23] examined various machining operations, technological advantages and current challenges of AWJM in various types of industries and studied the effect of nozzle wear with other processing parameters like SOD, traverse rate, hydraulic pressure and AMFR on machined surface. Doreswamy et al. [24] in his research investigated kerf width on graphite-filled GFRP composites to assess the impact of various process parameters like operating hydraulic pressure, SOD, feed rate and abrasive concentration using AWJM. A model has been developed by

optimizing the various process parameters for kerf width and concludes that water pressure, SOD and feed rate are dominating factors for kerf width. Morphology study was made on glass/epoxy composites, and scanning electron microscope (SEM) is used for optimizing variable parameters to make the machine surface free from delamination. Taguchi technique and ANOVA were used for optimizing the process parameters to investigate its surface roughness with AWJM. Abrasive type, traverse rate, and SOD were found to be the substantial factors for surface quality by Azmir and Ahsan [25]. Azmir and Ahsan [26] studied the glass/epoxy composite laminate for process parameters like kerf taper and surface roughness with AWJM. Taguchi's technique and ANOVA were used to evaluate impact of machining parameters on surface roughness and kerf taper and concluded that for surface roughness, hydraulic pressure and AMFR and for kerf taper SOD, type of abrasive material and traverse rate were most substantial factors. Process parameters like traverse speed, AMFR, water pressure and SOD were optimized for surface roughness and kerf taper of hybrid composite laminates using AWJM by Selvam et al. [27]. Taper angle and surface roughness were studied by Mayuet Ares et al. [28] on CFRP composites with AWJM, and they revealed that to obtain minimum taper angle and surface roughness SOD (between 1.5 and 3.0 mm), TFR around 300 mm/min and AMFR must be high. Alejandro Sambruno et al. [29] optimized the process parameters for kerf taper of carbon fibre-reinforced thermoplastic (CFRTP) with AWJM and concluded that combination of parameters to minimize the kerf taper is hydraulic pressure—3400 bar, feed rate—100 mm/min and AMFR—340 g/min. Thakur et al. [30] experimentally investigated delamination at jet entry and exit of drilled hole of hybrid carbon/glass composite with AWJM and concluded that delamination at jet entrance and exit of drilled hole decreases with decrease in SOD and traverse rate. Most significant factors for entry and exit were traverse rate and SOD. Delamination of CFRP has been analysed by Mayuet et al. [31] on stereoscopic optical microscopy (SOM) and SEM technique with AWJM. Mechanical and physical properties have been studied of natural glass fibre reinforcement polymer composite by Sanjay et al. [32]. Banon et al. [33] experimented to optimize the process parameters for surface quality using RSM of carbon fibre-reinforced thermoplastic plastic (CFRTP) matrix composite with AWJM. The optimized values for surface roughness were: hydraulic pressure—250 Mpa, TR—300 mm/min, AMFR—170 g/min. Kerf taper and surface roughness of glass–vinyl ester composite have been investigated by Armağan et al. [34] with AWJM, and they concluded that SOD is the main substantial factor for surface roughness and kerf geometry. Due to the large abrasive grain size, surface finish of AWJM is poor as compared to other hybrid machining processes [35, 36].

4 Parametric Analysis of AWJM

The work done by researchers in the area of cutting performance, optimization and modelling of AWJM process of CFRP and GFRP composites is summarized in this paper. It is concluded from the literature study that machined surface quality depends

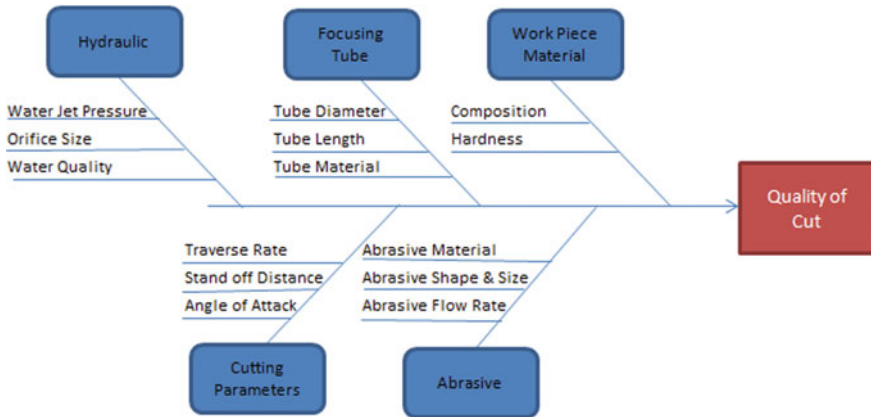


Fig. 2 Process parameter of AWJM

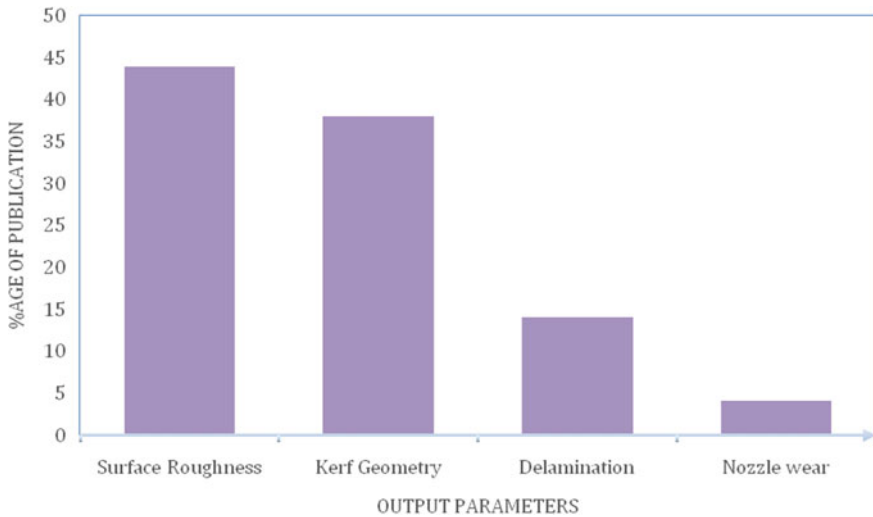


Fig. 3 Percentage of publications on output parameters reviewed in this report

upon various variable parameters like hydraulic pressure, SOD, traverse speed, AMFR, etc. Hence, proper process parameters should be selected for machining of these composite materials. Various process parameters are exhibited in Fig. 2.

From the last few years, AWJ machining process is extensively used in industries for machining, cutting and drilling of composites. Research over the last two decades in this area shows some improvement in the use of AWJM technique for machining, cutting and drilling of composites. Most of the researchers included in this report have investigated the performance of CFRP and GFRP composite materials with

AWJM based on various parameters like surface finish, kerf geometry, delamination and nozzle wear, etc., as shown in Fig. 3. But very less researchers have been applying their efforts to investigate nozzle wear and MRR in AWJM of composites.

Even though AWJM is widely used in the machining of these composites, very less work is found on optimization of AWJM process parameters for its effective use. Few researchers worked on optimization of process parameters, but they optimized 1 or 2 process parameters of AWJM. It is also found that very less research efforts have been applied in modelling of process parameters with AWJM. Few researchers have successfully tried to develop predictive models for delamination, depth of jet penetration and cut.

5 Critical Analysis

Many researchers have worked and reported the impact of various variable parameters on kerf characteristics, surface quality and delamination of CFRP and GFRP with AWJM. Further, but very less effort has been applied to investigate MRR, fibre pull-out and nozzle wear of CFRP and GFRP composites. The major work related to effect of process parameters on CRPF and GFRP with AWJM is summarized in Table 1.

6 Conclusion

This paper presented the study of CFRP and GFRP composite materials during the AWJM process. It was realized that for machining of these composites, AWJM was the most suitable and practical machining process. Moreover, the review of the research work on CFRP and GFRP composites with AWJM was summarized by various researchers. From the last few years of investigation, it obviously represents the trends of several process parameters like hydraulic pressure, SOD, traverse speed, AMFR, abrasive particle size on machining parameters, namely surface roughness, kerf characteristics, MRR during the machining and drilling of AWJM process. It also revealed that more efforts are required to study the nozzle errors, delamination, MRR, fibre pull-out and abrasive embedment during AWJM of CFRP and GFRP composites. So, more work is required to be done in this field. In addition, it also identified the further research ability for AWJM process.

Table 1 Summary of key research work related to influence of process parameters on CFRP and GFRP

Researcher(s)	Material	Process parameters	Output parameters	Abrasives	Findings	Scope of further work
Siva Prasad and Chaitanya [13]	GFRP	Pressure—125, 175, 225 and 275 Mpa, SOD—1.5, 2.5 and 3.5 mm, AMFR—200, 300, 400 and 600 g/min, fibre orientation—0°, 45° and 90°	Surface roughness and dimensional accuracy of hole		Main factors are SOD and fibre orientation which affect the surface roughness and dimensional accuracy	Other machining parameters
Hejjaji et al. [15]	Carbon fibre-reinforced composite (unidirectional laminate of size 300 X300mm)	Nozzle diameter—1.016 mm, tube length—76 mm, orifice diameter—0.3302 mm, TR—4, 8 and 12 m/min, SOD—50, 100 and 150 mm, scan step—0.5, 1 and 1.5 mm, abrasive mass flow rate—0.34 kg/min	Influence of damage (crater volume and ridge)	Garnet sand and grit size 120	In milling of composites, crater formation is mainly affected by jet pressure	Other machining parameters
Phapale et al. [16]	CFRP	Water pressure—1000, 2000 and 3000 bar, AMFR—5.4, 8.88 and 9.7 g/s, SOD—1, 2 and 3 mm	Delamination and surface roughness of drilled hole	Garnet—80 mesh	Dominant factors for delamination are SOD and water pressure	Kerf geometry
Irina Wong [17]	Hybrid fibre-reinforced polymer composites	Jet angle—90°, AMFR—120, 360 and 600 g/min, water pressure—2000, 2600 and 3200 bar, SOD—2, 6 and 8 mm, TR—1000, 1750 and 2500 mm/min	Kerf ratio and delamination	Garnet—80 mesh	Process parameters like water pressure and SOD are optimized	Investigation on surface roughness and MRR

(continued)

Table 1 (continued)

Researcher(s)	Material	Process parameters	Output parameters	Abrasives	Findings	Scope of further work
Uthayakumar et al. [18]	Carbon fibre-reinforced polyester composite	Water pressure—168, 216 and 264 Mpa, TR—5, 15 and 25 mm/min, SOD—1, 2 and 3 mm	MRR and kerf	Garnet—80 mesh	Major influencing parameters for MRR are traverse speed and for kerf are by SOD, traverse speed and water pressure	Investigation on delamination
Dhanawade et al. [19]	Carbon epoxy composite	SOD—1, 2, 3, 4 and 5 mm, water pressure—100, 130, 160, 190 and 220 Mpa, TR—50, 75, 100, 125 and 150 mm/min, AFMR—0, 100, 200, 300 and 400 g/min	Kerf taper and surface roughness	Garnet—80 mesh	Hydraulic pressure and TS influence kerf taper and surface roughness	MRR and delamination
El-Hofy et al. [20]	Multi-directional CFRP laminates	Jet pressure—100 and 350 Mpa, SOD—2 and 4 mm, Feed rate—50 and 150 mm/min	Kerf width, machinability and surface characteristics	Garnet—80 mesh	High hydraulic pressure, small SOD and high feed rate and for better surface quality high hydraulic pressure, small SOD, and low feed rate are recommended	Investigation on MRR and delamination

(continued)

Table 1 (continued)

Researcher(s)	Material	Process parameters	Output parameters	Abrasives	Findings	Scope of further work
Dhanawade et al. [21]	Carbon epoxy composite	SOD—1,2,3,4 and 5 mm, hydraulic pressure—100, 130, 160, 190 and 220 Mpa, TR—50, 75, 100, 125 and 150 mm/min, AFMR—0, 100, 200, 300 and 400 g/min	Surface roughness	Garnet—80 mesh	Decrease in hydraulic pressure and AMFR and increase in SOD and traverse rate increase surface roughness	Investigation on MRR and delamination
Doreswamy et al. [24]	Graphite/glass/epoxy composite (graphite 200 μm)	Hydraulic pressure—90, 120 and 150 Mpa, SOD—1, 3 and 5 mm, concentration of abrasive 6,10 and 14wt.%, feed rate—75, 100 and 125 mm/min,	Kerf width	Garnet—80 mesh	For kerf width feed rate, hydraulic pressure and SOD are significant factors	Investigation on surface roughness, MRR and delamination
Azmir and Ahsan [25]	Glass/epoxy composite laminate	Hydraulic pressure—138, 207 and 276 Mpa, AMFR—2.5, 5 and 7.5 g/s, SOD—1.5, 3 and 4.5 mm, TR—1.5, 3 and 4.5 mm/s, cutting orientation—0°, 22.5° and 45°	Surface roughness	Garnet and aluminium oxide—80 mesh	AMFR and hydraulic pressure are the most significant factors for surface roughness	Investigation on other machining parameters—MRR and kerf geometry

(continued)

Table 1 (continued)

Researcher(s)	Material	Process parameters	Output parameters	Abrasives	Findings	Scope of further work
Aznir and Ahsan [26]	Glass/epoxy composite laminate	Hydraulic pressure—137.9, 206.9 and 275.8 Mpa, AMFR—2.5, 5 and 7.5 g/s, SOD—1.5, 3 and 4.5 mm, TR—1.5, 3 and 4.5 mm/s, cutting orientation—0°, 22.5° and 45°	Surface roughness and kerf taper	Garnet and aluminium oxide—80 mesh	For surface roughness AMFR and hydraulic pressure and for kerf taper SOD, type of abrasive material and TR are the most significant factors	Investigation on delamination and MRR
Selvam et al. [27]	Hybrid composite laminate (E—glass fabric, carbon fabric)	Traverse rate—100, 150 and 150 mm/min, hydraulic pressure—200, 250 and 300 Mpa, AMFR—300, 400 and 500 g/min, SOD—1, 2 and 3 mm	Surface roughness and kerf taper	Garnet—80 mesh	Surface roughness directionally proportional to TS and kerf taper will be minimum with higher value of TR and hydraulic pressure	MRR and delamination

(continued)

Table 1 (continued)

Researcher(s)	Material	Process parameters	Output parameters	Abrasives	Findings	Scope of further work
Sambruno et al. [29]	Carbon fibre-reinforced thermoplastic (CFRTP)	Hydraulic pressure—1200, 2500 and 3400 bar, Feed rate—100, 300 and 500 mm/min, AMFR—170, 225 and 340 g/min, SOD—2.5 mm, orifice diameter—0.3 mm, focusing tube diameter/length—0.8/94.7 mm	Kerf taper	Garnet—120 mesh	Most significant factors are jet pressure and feed rate	Delamination and surface quality
Thakur [30]	Hybrid carbon I/glass composite	Hydraulic pressure—96 and 302 Mpa, traverse rate—72, 144 and 216 mm/min, SOD—1, 2 and 3 mm, nozzle diameter—0.76 mm, AMFR—300 g/ min	Delamination at jet entrance and exit of hole	Garnet—80 mesh	Major substantial factors are traverse rate and SOD	Kerf characteristic and surface quality
Mayuet et al. [31]	CFRP	Feed rate—300, 900, 1500 and 2100 m/min, SOD—1.5, 3 and 4.5 mm, AMFR—300 and 600 g/min, orifice diameter—0.3048, nozzle diameter/length—0.8/94.7 mm, water pressure—450 Mpa	Delamination	Garnet—80 mesh	Abrasive is the main influencing parameter for delamination	MRR and surface roughness

(continued)

Table 1 (continued)

Researcher(s)	Material	Process parameters	Output parameters	Abrasives	Findings	Scope of further work
Bañon et al. [33]	Carbon fibre-reinforced thermoplastic (low melting point)	Hydraulic pressure—120, 250 and 340 Mpa, traverse rate—100, 300 and 500 mm/min, AMFR—170, 225 and 340 g/min, nozzle diameter/length—0.8 mm/94.7 mm, orifice diameter—0.3 mm	Surface quality	Garnet—120 mesh	Surface quality influenced by abrasive material and hydraulic pressure	Kerf taper, MRR and delamination
Armağan et al. [34]	Glass-vinyl ester composite	Hydraulic pressure—260, 290 and 320 Mpa, traverse rate—8, 25 and 4 mm/s, AMFR—200, 250 and 350 g/min, SOD—5, 7 and 10 mm, nozzle diameter 10.2 mm, fibre orientation—0, -45°, 90° and +45°, material thickness—18, 28 and 38 mm	Kerf width at top and surface roughness	Garnet—80 mesh	Kerf width is highly affected by SOD and surface roughness affected by SOD, hydraulic pressure and traverse rate	MRR and delamination

References

1. Komanduri R (1997) Machining of fibre-reinforced composites. *Mach Sci Technol* 11:113–152
2. Campbell FC (2010) Introduction to Composite Materials, Structural Composite, Materials. ASM International, New York
3. Chawla N, Chawla KK (2013) Metal matrix composites. Springer, New York
4. Korat MM, Acharya GD (2014) A review on current research and development in abrasive water jet machining. *Int J Eng Res Appl* 41:423–432
5. Momber AW, Kovacevic R (1998) Principles of abrasive water jet machining. Springer Science & Business Media, Berlin
6. Mohamed H (1989) An investigation of milling with abrasive-waterjets. *J Eng Ind* 111(2):158–166
7. Mohamed H (1987) Turning with abrasive-water jets—a first investigation. *J Eng Ind* 109(4):281–290
8. Jain VK (2007) Advanced machining processes. Allied Publishers Private Limited, New Delhi
9. Pandey PC, Shan HS (1980) Modern machining processes. Tata McGraw Hill, New Delhi
10. Shahverdi H, Zohoor M, Mousavi SM (2011) Numerical simulation of abrasive water jet cutting process using the SPH and ALE methods. *Int J Adv Design Manuf Technol* 5(1):43–50
11. Ramulu M, Arola D (1996) The influence of abrasive water jet cutting conditions on the surface quality of graphite/epoxy laminates. *Int J Mach Tools Manuf* 34:295–313
12. Shanmugam DK, Nguyen T, Wang J (2008) A study of delamination on graphite/epoxy composites in abrasive water jet machining. *Compos A Appl Sci Manuf* 39:923–929
13. Siva Prasad K, Chaitanya G (2020) Experimental study on surface roughness and dimensional accuracy of hole machining process on GFRP composites using abrasive water jet technique. *Mater Today Proc* 23(3):651–658
14. Alberdi A, Suárez T, Artaza GA, Escobar-Palafox KR (2013) Composite cutting with abrasive water jet. *Procedia Eng* 63:421–429
15. Hejjaji A, Zitoune R, Crouzeix L, LeRoux S, Collombet F (2017) Surface and machining induced damage characterization of abrasive water jet milled carbon/epoxy composite specimens and their impact on tensile behaviour. *Wear* 376–377:1356–1364
16. Phapale K, Singh R, Patil S, Singh RKP (2016) Delamination characterization and comparative assessment of delamination control techniques in abrasive water jet drilling of CFRP. *Procedia Manuf* 5:521–535
17. Irina Wong MM, Azmi A, Lee CC, Mansor AF (2018) Kerf taper and delamination damage minimization of FRP hybrid composites under abrasive water-jet machining. *Int J Adv Manuf Technol* 94:1727–1744
18. Uthayakumar M, Vigneshwaran S, Adam Khan M, Slota A, Ahmad SJ (2019) Abrasive water jet machining performance on carbon epoxy composite. *Int J Innov Technol Exploring Eng* 9(2)
19. Dhanawade A, Kumar S, Kalmekar RV (2016) Abrasive Water Jet Machining of Carbon Epoxy Composite. *Def Sci J* 66(5):522–528
20. El-Hofy M, Helmy MO, Escobar-Palafox G, Kerrigan K, Scaife R, El-Hofy H (2018) Abrasive water jet machining of multidirectional CFRP laminates. *Procedia CIRP* 68:535–540
21. Dhanawade A, Kumar S (2017) Experimental study of delamination and kerf geometry of carbon epoxy composite machined by abrasive water jet. *J Compos Mater* 51(24):3373–3390
22. Vigneshwaran S, Uthayakumar M, Arumugaprabu V (2018) Abrasive water jet machining of fiber-reinforced composite materials. *J Reinf Plast Compos* 37(4):230–237
23. Melentiev R, Fang F (2018) Recent advances and challenges of abrasive jet machining. *CIRP J Manuf Sci Technol* 22:1–20
24. Doreswamy D, Shivamurthy B, Anjaiah D, Sharma NY (2015) An investigation of abrasive water jet machining on graphite/glass/epoxy composite. *Int J Manuf Eng* 2:1–11
25. Azmir M, Ahsan A (2008) Investigation on glass/epoxy composite surfaces machined by abrasive water jet machining. *J Mater Process Technol* 198:122–128

26. Azmir MA, Ahsan AK (2009) A study of abrasive water jet machining process on glass/epoxy composite laminate. *J Mater Process Technol* 209(20):6168–6173
27. Selvam R, Karunamoorthy L, Arunkumar N (2017) Investigation on performance of abrasive water jet in machining hybrid composites. *Mater Manuf Processes* 32(6):700–706
28. MayuetAres PF, Mata FG, Ponce MB, Gómez JS (2019) Defect analysis and detection of cutting regions in CFRP machining using AWJM. *Materials* 12(24):1–15
29. Sambruno A, Bañon F, Salguero J, Simonet B, Batista M (2019) Kerf Taper defect minimization based on abrasive waterjet machining of low thickness thermoplastic carbon fiber composites C/TPU. *Materials* 12(24):1–17
30. Thakur RK, Singh KK, Ramkumar J (2020) Delamination analysis and hole quality of hybrid FRP composite using abrasive water jet machining. *Mater Today Proc*. <https://doi.org/10.1016/j.matpr.2020.04.056>
31. Mayuet PF, Girot F, Lamikiz A, Fernández-Vidal SR, Salguero J, Marcos M (2015) SOM/SEM based characterization of internal delaminations of CFRP samples machined by AWJM. *Procedia Eng* 132:693–700
32. Sanjay MR, Arpitha GR, Yogesha B (2015) Study on mechanical properties of natural - glass fibre reinforced polymer hybrid composites: a review. *Mater Today Proc* 2(4–5):2959–2967
33. Bañon F, Sambruno A, Batista M, Simonet B, Salguero J (2020) Study of the surface quality of carbon fiber–reinforced thermoplastic matrix composite (CFRTP) machined by abrasive water jet (AWJM). *Int J Adv Manuf Technol* 107:3299–3313
34. Armağan M, Arici AA (2017) Cutting performance of glass-vinyl ester composite by abrasive water jet. *J Mater Manuf Processes* 32(15):1715–1722
35. Bhuyan BK, Gupta L, Garg C (2020) Design and development of tabletop electrochemical grinding setup. *Mater Today Proc* 21(3):1479–1482
36. Khattri K, Choudhary G, Bhuyan BK, Selokar A (2018) A review on parametric analysis of magnetic abrasive machining process. In: *IOP Conf Ser Mater Sci Eng* 330(1):1–9

Theoretical and Experimental Estimation of Material Removal Rate of Electric-Spark Diamond Grinding of Difficult-To-Cut Materials



Kumar Bhartendu, S. K. Jha, and B. K. Bhuyan

Abstract Electric-spark diamond grinding (ESDG) is a advanced hybrid cutting process where grinding is performed in presence of electric sparks or in other words, this machining process is combination of electric sparks and diamond grinding simultaneously. During the machining process, work piece is subjected to continuous emission of high-speed Electrons and mechanical abrasion of diamond grains simultaneously and synergistically. This paper paves a way to develop theoretical aspects of the spark assisted diamond grinding. This paper models material removal mechanism based on certain assumptions based on the first principle of process physics of material removal mechanism due to conventional grinding and Electric-spark machining. The ESGD set-up was designed and fabricated and the experiments were carried out on tungsten carbide tips. Material removal rate is co-related with key input meters such as pulse current, gap voltage, active grain density, pulse on time, grinding wheel velocity and duty cycle. Three different equations have been developed imitating three different idealized conditions. Three constants characterize the proportionality between Material removal rate and key process parameters. These constants were estimated using experimental data. Levenberg Marquardt algorithm was employed for estimation of these constants. Further, developed equation was compared against experimental data for validation.

Keywords ESGD · Material removal rate · Mathematical modelling · Material removal rate [MRR] · Inter-electrode gap [IEG]

1 Introduction

As a result of developments in the domain of advanced material, many advanced materials with higher quality even at high temperatures, high durability and

K. Bhartendu (✉) · S. K. Jha
Netaji Subhas Institute of Technology, University of Delhi, New Delhi, India

B. K. Bhuyan
Manav Rachna International Institute of Research and Studies, Faridabad, India

phenomenal wear obstruction are built up. In their processing, these characteristics pose a new challenge in machining extremely complex designs like turbine blades or machining blind cavities with conventional machining processes is almost impossible [1]. Moreover, journey for improvement of the machining cycle while taking focal points and limiting its constituent's restriction prompts the advancement of hybrid machining innovation. The term "hybrid process" can be applied to as various production process types with different active operating concepts such as ultrasonic aided grinding, laser guided drilling etc. [2]. This paper work is based on one of those hybrid manufacturing process, i.e. diamond grinding in combination with electric-discharge machining.

1.1 Diamond Grinding in Presence of Electro Sparks

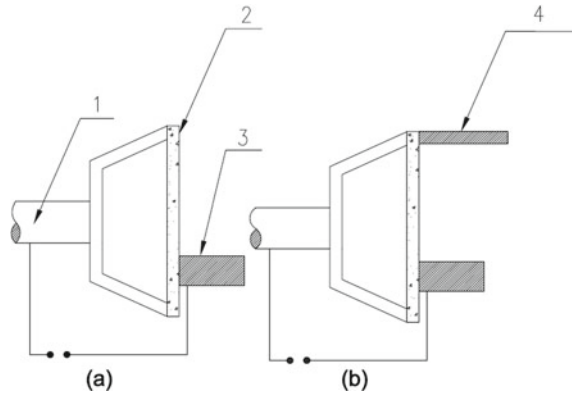
The idea behind this technique is that diamond grinding is the most widely used method for machining hard-to-cut materials out of all traditional machining processes. However the wheel is exposed to glazing and loading during the machining of materials with diamond abrasives grinding tool and to preserve the sharpness of the wheel, this wheel need to be passed with dressing operation. It is therefore highly desirable to ensure the consistent dressing without interruption of the operation [3]. This method is known by different names in the existing literature, such as Kozak's Abrasive Electric- Discharge Grinding (AEDG) [4]. Similarly, these processes were named by Jain [5], Lee [6] called this as Electric-discharge diamond grinding while Ahn [6] named it as In-process Electric-discharge dressing.

1. Grinding wheel spindle as seen by (1)
2. The grinding wheel is labelled by (2)
3. Work piece is labelled by (3)
4. Distinct Electrode for dressing is labelled by (4).

In the first configuration, the work piece is central to the electrical system, i.e. the grinding wheel and the wheel dressing area coexists, the work piece solely functions as a dressing electrode shown in Fig. 1a. The work piece is subjected to the combined action under mechanical erosion and thermal work soften by electric spark, respectively. During the thermal softening, the associated grinding force and required power are drastically diminish, resulting in improved wheel efficiency. Although the set-up is simple, this design may witness the wear of diamond abrasives, since it avoids independent optimization of the dressing and grinding processes. This concept is being incorporated in the current work.

In the second method, a different electrode is utilized for electric-discharge dressing of the wheel periphery beyond the grinding region, i.e. the work piece gets isolated from the electrical circuit. The benefit of this setup is that cleaner grinding can be done without too much thermal effects. Another benefit of this method is that independent grinding and wheel dressing optimization can be achieved conveniently relative to the first setup.

Fig. 1 Configuration of electric-spark diamond grinding [7]



As the material removal mechanism of the in-process dressing technique is based on the machining of electrical sparks. Thus, in a working space, a charging voltage is used to create a plasma channel between the work piece and the electrode. A large electrical current in the form of electric spark flows between the electrode and the work piece gap eliminates the metallic bonding material for effective dressing of the wheel. There is a possibility of occurrence of raining out valuable diamond abrasives and in order to prevent this, 67% of the diamond abrasives should be firmly protected by a metallic bonded diamond wheel. As a result, 33% the diamond abrasives is optimally subjected to grinding operation [8].

2 Mathematical Modelling

Owing to the dynamic behaviour of the grinding operation, the basic approach for predicting material removal during grinding is probabilistic in nature. This article has established an empirical probabilistic modelling for electric-sparks-aided diamond grinding. As grinding is unpredictable, the grinding process is probabilistic in nature, whereas the sparking is deterministic in nature.

2.1 MRR During Grinding

Typically, the grinding operation is distinguished by its kinematic condition and grains structure and their orientation, such as grains size, grains density of the grinding wheels, grains distributions on the grinding wheels surfaces integrity as well as wheels velocity, table feed rate and cutting depths. If the peripheral locations of the abrasives grains are random, there is requirement for random probability density function that integrate all grains interactions with the work piece in the disposal of the

stock. Thus, the uncut chips thickness is believed to obey the Rayleigh's probability density functions.

The probability distributions functions is applied to the uncut chips thickness during grinding and is purported to be Rayleigh's probability density functions [9–11]. Rayleigh probability density function have the same form to that of log normal functions used by Konig and Lortz [12] when grinding with a autonomous benefit over log-normal, it can be distinguished by a single estimation parameter.

“Rayleigh probability density function” [13] is stated as follows:

$$f(t) = \begin{cases} 0, & t < 0 \\ \frac{t}{c^2} e^{-\frac{t^2}{2c^2}}, & t \geq 0 \end{cases} \quad (1)$$

Here ‘ t ’ is the uncut chip thickness is essentially the extent of the involvement of the active grains to be indulged in the removal of the material and ‘ c ’ is the probability density function parameter. The shape of an uncut chip is believed to be a parabolic circular arc. So there is the estimated values and variances of the aforementioned equation.

$$\mu(t) = \sqrt{\frac{\pi}{2}} \alpha = 1.2533\alpha \quad (2)$$

$$v(t) = \left(2 - \frac{\pi}{2}\right) \alpha^2 \quad (3)$$

Assuming chip cross-sectional to be circular arc. Then expected chip cross-section will be

$$\mu(A_c) = \frac{\pi}{2} E(t^2) \quad (4)$$

Similarly, total area of the affiancing in grinding zone is given by

$$\mu(A_t) = N * \mu(A_c) = N * \frac{\pi}{2} \mu(t^2) \quad (5)$$

where, at any time, N is the number of active cutting points.

$$N = b * l_c * C$$

Here b is the wheel width, l_c is contact length and C is number of active abrasives grain per unit area of the wheel topography. Assuming uniform volume, the total estimated occupied area multiplied by the speed of the wheel gives the rate of material removal as-

$$\text{MRR} = \mu(A_c) * S_g = b * l_c * C * \frac{\pi}{2} * \mu(t^2) * S_g \quad (6)$$

As stated by Malkin [14], the contact length is $l_c = \sqrt{c * D_g}$.
Calculation for $E(t^2)$

$$\mu(t^2) = \int_0^{\infty} t^2 * f(t) dt = \int_0^{\infty} \frac{t^3}{\alpha^2} e^{-\frac{t^2}{2\alpha^2}} dt = 2\alpha^2 \quad (7)$$

Assuming that t_m is the typical chip thickness for the computation of the parameter α . Mean thickness of the chips as stated by Malkin [15].

$$\mu(t) = t_m$$

$$t_m = \frac{t_{\max}}{2} = \frac{1}{2} * \sqrt{\frac{4}{C.r} * \left(\frac{V_w}{S_g}\right) * \sqrt{\frac{c}{D_g}}} \quad (8)$$

The value of r is taken as 4 in the present analysis as the grooves shape is believed to be the parabolic circular arcs [14]. Then

$$\frac{t_m}{1.2533} = \alpha \quad (9)$$

MRR during Electric-Spark Machining: Material removal from the work piece material in the form of a crater in the electrical-spark phase during melting and vaporisation under the action of high frequency electrical sparks. It is thought that the shape of the craters is a hemispheric pyramid. Crater dimensions are believed to be in proportion to the energy produced by the sparks. Thus,

$$h_c = K_1 * Q^n \text{ and } d_c = K_2 * Q^n \quad (10)$$

where h_c is crater depth and d_c is crater diameter.

And Spark energy S is given by

$$S = V * I * t_{on} \quad (11)$$

The volume of the crater is provided by the hemispheric domes.

$$V_c = \frac{\pi}{6} * h_c * \left(\frac{3}{4} * d_c^2 + h_c^2\right) \quad (12)$$

Simplifying above equations

$$V_c = \frac{\pi}{6} * K_1 * K_3 * (V * I * t_{on})^{3n} \quad (13)$$

MRR in single spark can be written as-

$$\text{MRR} = V_c * f * \eta \quad (14)$$

where f is frequency and η is efficiency

$$f = K_4 * \frac{1}{t_{\text{on}} + t_{\text{off}}} \quad (15)$$

Then,

$$\text{MRR} = \frac{\pi}{6} * K_1 * K_3 * K_4 * (V * I * t_{\text{on}})^{3n} * \frac{1}{t_{\text{on}} + t_{\text{off}}} * \eta \quad (16)$$

Assuming 100% efficiency and putting D_c as duty cycle into the equation

$$\text{MRR} = \frac{\pi}{6} * K_1 * K_3 * K_4 * (V * I)^{3n} * t^{3n-1} * D_c * \eta \quad (17)$$

$$\text{MRR} = \frac{\pi}{6} * K_5 * (V * I)^{3n} * t^{3n-1} * D_c \quad (18)$$

Therefore,

$$\text{MRR} = \Upsilon * (V * I)^{3n} * t^{3n-1} * D_c \quad (19)$$

Here K_1, K_2, K_3, K_4, K_5 are constants and again Υ is constant of proportionality.

MRR during combined grinding and Electric-spark machining: In this method, the material removal rate is presumed to be a weighted sum of grinding and sparks action close to [16]. In this operation, inter electrode gap (IEG) plays a significant part in stock removal efficiency, When IEG is less than the highest protruding height then grinding process will dominate whereas if IEG is equals to highest protruding height then both process will take part in stock removal but when IEG is greater than protruding heights, stock removal will by spark only. Therefore MRR estimation can be modelled into three cases.

MRR during grinding operation: When the protruding height of abrasive grains is more than the IEG, grinding operation will prevail than sparking and stock removal due to sparking is remarkably lower than grinding process. Thus, MRR is given-

$$\text{MRR}_{\text{Total}} = \text{MRR}_{\text{Grinding}} = b * \sqrt{a * D_g} * C * \frac{\pi}{2} * \mu(t^2) * S_g \quad (20)$$

Assuming that the cutting depth is directly proportional to the dimensions of the crater and the height of the crater is also proportional to the sparking energy-

$$\text{MRR}_{\text{Total}} = \beta * b * \sqrt{V * I * t_{\text{on}} * D_c * D_g} * C * \alpha^2 * S_g \quad (21)$$

where β is the proportionality constant.

MRR during sparking action only: If the protruding height is comparatively smaller than IEG, then stock removal will take place mainly due to sparking.

$$MRR_{\text{Total}} = MRR_{\text{Spark}} = \Upsilon * (V * I)^{3n} * t_{\text{on}}^{3n-1} * D_c \quad (22)$$

MRR during combined grinding and sparking: If the protruding height of the abrasives grains is commensurate to IEG, higher frequency sparking actions thermally loosens the work piece while grinding operation cuts softer work piece. Therefore, MRR is given by their cumulative results.

$$MRR_{\text{Total}} = MRR_{\text{Grinding}} + MRR_{\text{Spark}}$$

$$MRR_{\text{Total}} = \Upsilon * (V * I)^{3n} * t_{\text{on}}^{3n-1} * D_c + \beta * b * \sqrt{V * I * t_{\text{on}} * D_c * D_g * C * \alpha^2 * S_g} \quad (23)$$

Thus, the MRR is given by three distinct Eq. (24) in three distinct machining conditions.

$$MRR = \begin{cases} \beta * b * \sqrt{V * I * t_{\text{on}} * D_c * D_g * C * \alpha^2 * S_g} \\ \Upsilon * (V * I)^{3n} * t_{\text{on}}^{3n-1} * D_c \\ \Upsilon * (V * I)^{3n} * t_{\text{on}}^{3n-1} * D_c + \beta * b * \sqrt{V * I * t_{\text{on}} * D_c * D_g * C * \alpha^2 * S_g} \end{cases} \quad (24)$$

3 Experimental Study of ESDG and Methodology

The grinding set-up was attached on Electronica (ENC 35 model) die sinking Electric Discharge Machining machine that will be used to perform experiments. The actual photograph of the experimental set up and grounded work piece is shown in Fig. 2.

The EDDG set-up will consist of a copper-bond diamond grinding wheel, motor, shaft, a belt pulley system along with bearing (6203). The metal (copper) bonded diamond wheel will be retrofitted with the ram of EDM machine through fabricated attachment and the servo mechanism of the ZNC i.e. Z-axis is numeric controlled. The ZNC 35 EDM machine will be used to maintain the required IEG between the two Electrodes i.e. copper bonded diamond wheel and the flat work piece. The wheel specifications of copper bonded diamond wheel is given in Table 1. A DC electric motor of 0.24 HP and 3000 rpm will be used to drive the grinding wheel through an EN 24 grade steel shaft with help of a belt pulley system. The work piece will be mounted on the machine table using the fixture and will be dipped in the dielectric medium i.e. EDM oil which primarily consists of paraffin hydrocarbons oil (Table 2).

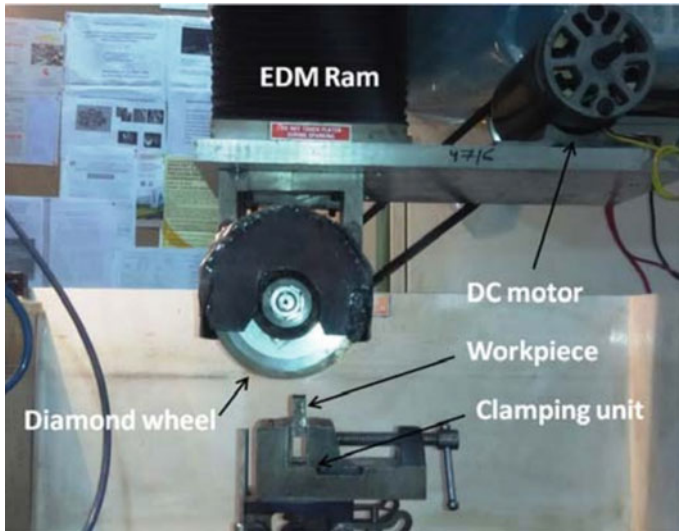


Fig. 2 Experimental setup [17]

Table 1 Metal bonded diamond abrasives grinding wheel specifications

Description	Specifications
Wheel diameter	100 mm
Bore diameter	32 mm
Thickness	6.3 mm
Bonding material	Copper
Grit size	100/120
Abrasives	Diamond
Concentration	C75
Depth of abrasives	5 mm

Table 2 Work piece material characteristics

Description	Specifications
Dimensions	34 × 10 × 19 mm
Tungsten carbide tips	Rapicut premium
WC	92%
Co	8%
Hardness	1260 HV30
Density	14.69 gm/cc

3.1 Evaluation of Parameters

A few experiments have been carried out in order to obtain an apprehension of the material removal mechanism. Tables 3, 4 and 5 show the processing conditions for MRR for grinding operation, combined grinding and sparking and sparking, respectively.

For estimation of β , Υ and n , “R—statistical software employing minpack.lm package is utilized. For finding the constants, non-linear least square minimization based on Levenberg Marquardt algorithm” [18] is employed with experimental dataset as shown Table 6.

After knowing β , it is used to calculate the remaining parameters in the final equation as alike processing conditions were used and the same has been shown in Table 6. For validation established model, another six experiments were conducted under alike processing conditions (Fig. 3).

Table 3 Processing conditions during grinding operation

S. No.	Depth of cut (μm)	Current (A)	Pulse on time (μs)	Duty cycle	Frequency (kHz)	Grinding wheel velocity (m/s)	Active grain density per 100 mm^2	MRR (mm^3/min)
1	5	38	23	0.8	22	30	2200	584.2
2	15	30	7.6	0.4	66	30	8500	580.6
3	15	35	11	0.8	44	40	3800	631.4
4	10	30	7.6	0.4	66	30	2200	534.7
5	15	35	11	0.6	44	40	3800	657.3
6	5	30	7.6	0.4	66	30	8500	556.6

Table 4 Processing conditions during combined grinding and sparking

S. No.	Depth of cut (μm)	Current (A)	Pulse on time (μs)	Duty cycle	Frequency (kHz)	Grinding wheel velocity (m/s)	Active grain density per 100 mm^2	MRR (mm^3/min)
1	5	38	23	0.4	22	50	2200	825.3
2	15	38	23	0.6	22	30	2200	850.6
3	15	38	23	0.4	22	50	8500	739.2
4	15	38	23	0.8	22	50	2200	1373.2
5	15	30	7.6	0.4	66	50	8500	942.8
6	15	30	7.6	0.8	66	50	2200	745.9

Table 5 Processing condition during sparking action

S. No	Depth of cut (μm)	Current (A)	Pulse on time (μs)	Duty cycle	Frequency (kHz)	Grinding wheel velocity (m/s)	Active grain density per 100 mm^2	MRR (mm^3/min)
1	5	38	23	0.6	22	30	85	314.4
2	5	30	7.6	0.6	66	30	85	374.1
3	5	30	11	0.6	66	30	22	398.5
4	5	38	7.6	0.8	22	50	85	458.6
5	5	30	11	0.6	66	50	85	377.2
6	5	30	7.6	0.6	66	50	22	431.8

Table 6 Constant parameters

Parameter	Estimated	Standard errors	<i>T</i> ratio	<i>P</i> -Value
β	2.4836	0.1994	13.661	1.3×10^{-12}
γ	1.3796	0.09612	14.35	2.96×10^{-6}
<i>n</i>	0.28	0.04107	6.64	0.00117

4 Results and Analysis

In ESDG, stock removal during grinding happens only when the IEG is lower than the protruding height of the abrasive grains. Hence, from a realistic view, however, only a fraction of the abrasive are used in the stock removal mechanism. For the validity of mathematical modelling, experimental results were compared with theoretical value extracted from the mathematical modelling. Table 7 and Fig. 4 are showing the disparity between experimental and theoretical evaluation in all the mentioned cases based on IEG. The highest absolute error was estimated to be 2.47%.

From Fig. 5, can be found that the MRR is the combined addition of stock removal during grinding and stock removal during sparking action. For a rise in the duty cycle, the stock removal is raised sharper in the ESDG process relative to grinding or sparking separately, which could be due to the long thermal softening time of the work piece. Therefore, stock removal during grinding has a remarkable endowment.

From Fig. 6, sparking action is shown dominant where increased current contributes to higher pulses energy, which results in higher material removal rates. But very high pulse energy will induce rainfall of precious diamond abrasives which is undesirable.

From Fig. 7, it can be concluded that the reduction of abrasives grain with aggressive cutting increases dramatically when more and more aggressive grains engage in the process of MRR.

It can be concluded from Fig. 8 that the rate of material removal increases with an increase of pulse on time. This is because higher pulse on time will lead to

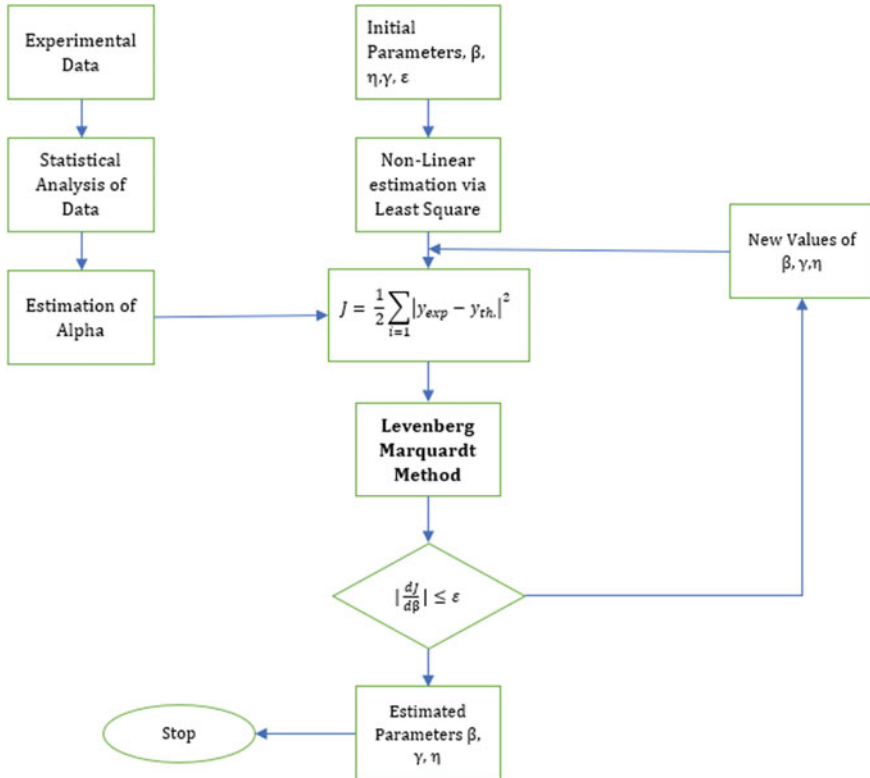


Fig. 3 Algorithm for estimating the parameters

longer durations of thermal softening, and hence greater volume of material becomes softened.

As it can be seen from Fig. 9, that rate of material removal is increasing with an increase in wheel velocity for tungsten carbide tips which is consistent with ceramic material grinding [10], as more grain would be involved in cutting operations.

It can be concluded from Fig. 10, alpha decreases dramatically with an increase in the active grain density. Alpha is the shape parameter in Rayleigh’s probability distributions that depends on the active grains densities, cutting depths, grinding wheel’s speed and chip thickness ratios.

5 Conclusions

- A mathematical framework based on the first theory of process physics of ESDG machining of tungsten carbide tips is developed in this study. A mathematical modelling was divided into three idealized settings, demonstrating

Table 7 Comparison between experimental and theoretical results

S. No.	Surface grain density per mm ²	Voltage	Current	Duty cycle	Pulse on time (μ s)	MRR _{EDM} (mm ³ /min)	MRR _{Grind} (mm ³ /min)	MRR _{Exp} (mm ³ /min)	Abs. error in percentage
<i>When grinding is dominant</i>									
1	3800	60	30	0.4	7.6	216.4272	531.9546	520.9	2.12
2	3800	60	35	0.4	11	232.1959	553.0031	562.5	1.68
<i>When EDM and grinding both prominent</i>									
3	3800	60	35	0.4	11	232.1959	553.0031	794.1	1.12
4	2200	60	35	0.6	11	348.2939	392.1139	751.2	1.43
<i>When EDM is prominent</i>									
5	8500	80	38	0.8	23	563.0935	1977.554	550.50	2.37
6	3800	80	38	0.8	23	422.3201	765.6383	432.56	2.36

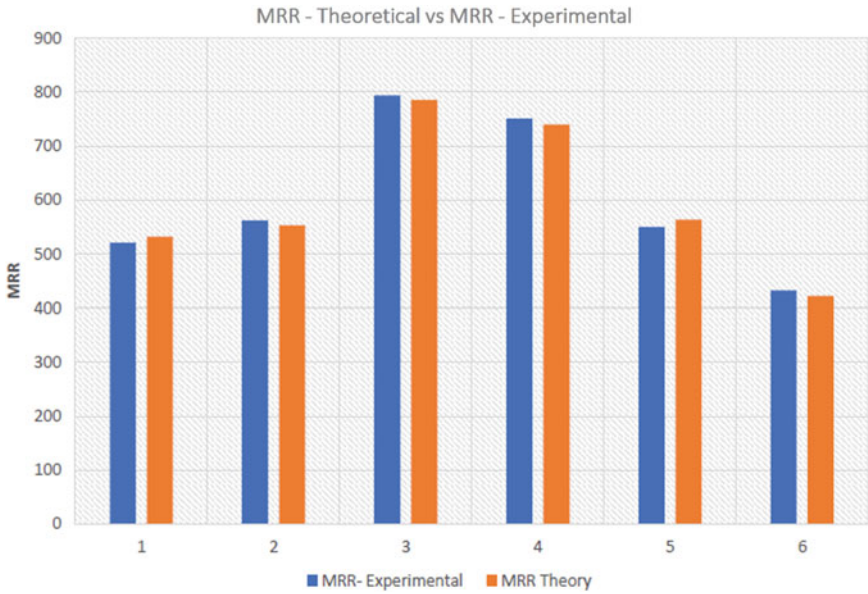


Fig. 4 Comparison between theoretical versus experimental values

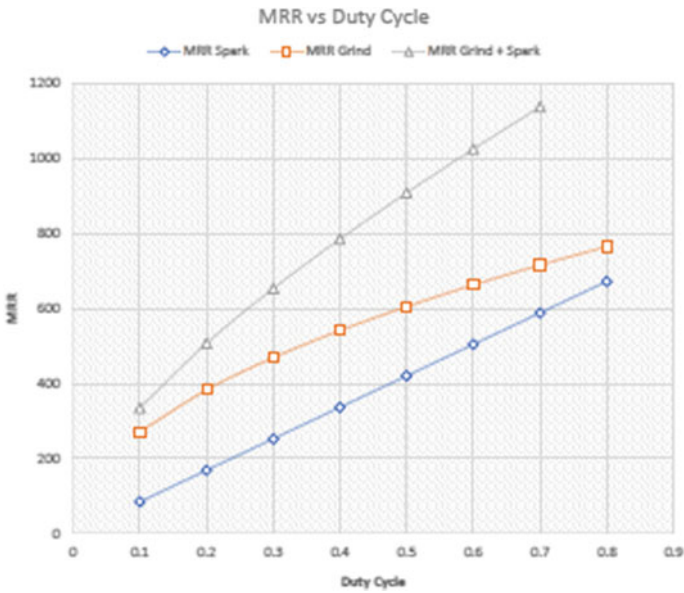


Fig. 5 Variation between MRR and duty cycle

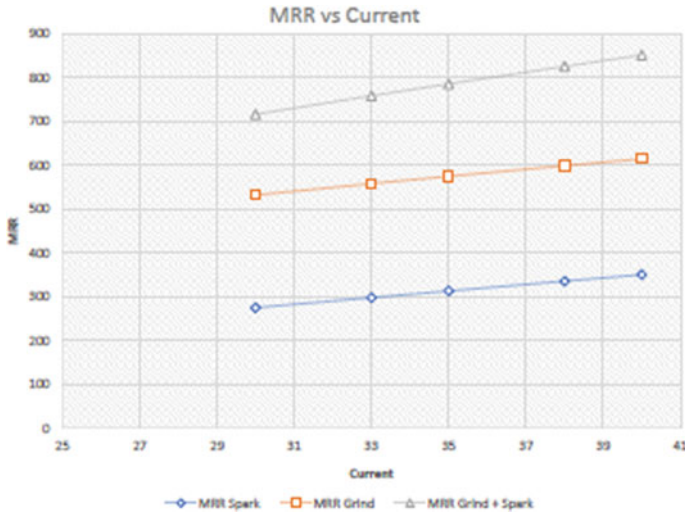


Fig. 6 Variation between MRR and discharge current

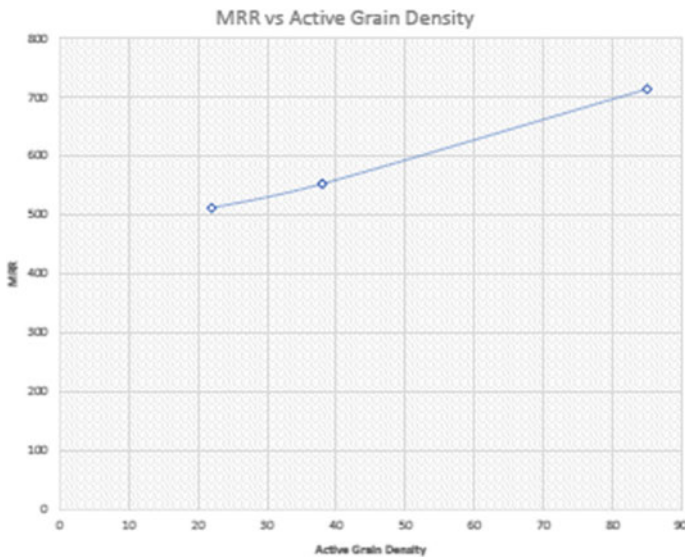


Fig. 7 Relation between MRR and active grain density

pure grinding, pure electric-spark machining and weighted mixture of the two. The method of grinding and spark machining overlaps one another in the cycle of material removal. The mathematical model developed is validated by necessary experiments. We can see from the validation table that the mean variance is below 2.37% of the experimental values. This variance can be ascribed to the hypotheses

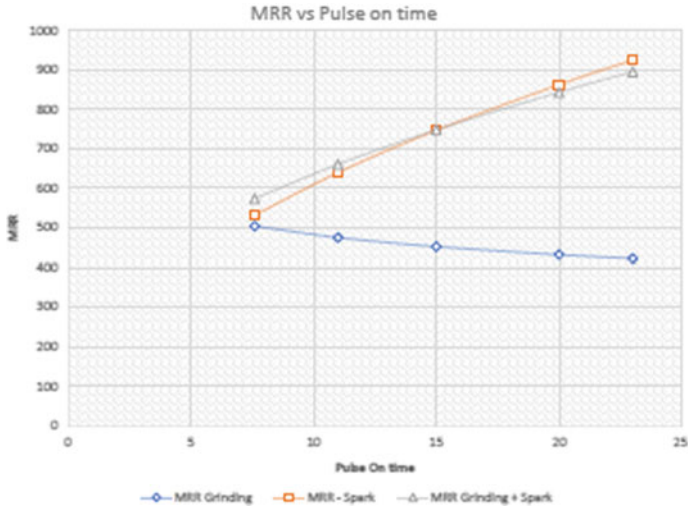


Fig. 8 Relation between MRR and pulse on Time

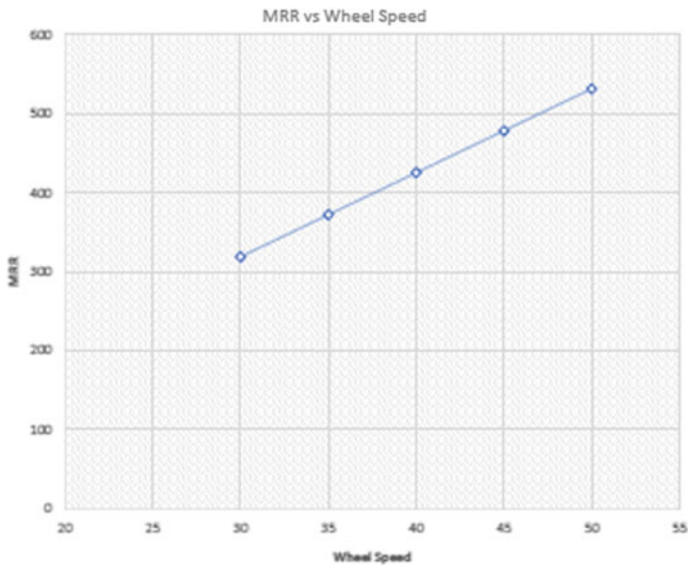


Fig. 9 MRR variation with wheel speed

of experimental error and simulation. This model can be extended by conducting experiments and finding for the constants for various materials.

- On the basis obtained mathematical models, it can be deduced that in ESDG material removal mechanism is a weighted summation of individual material removal from both sparking and grinding action.

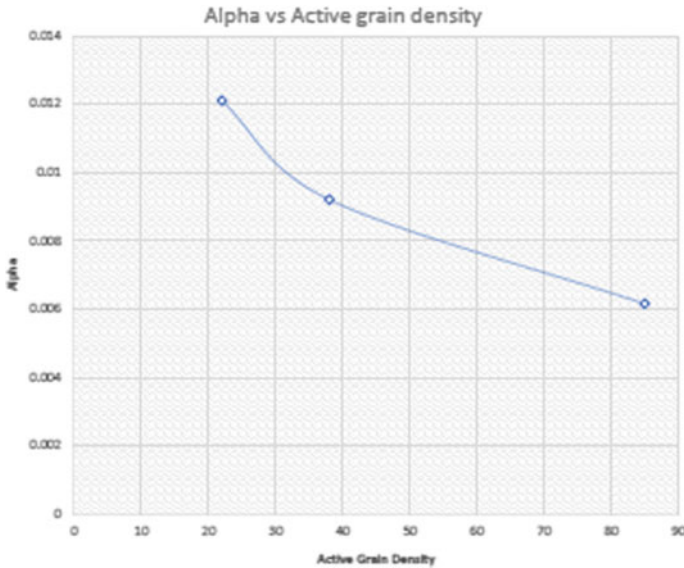


Fig. 10 Alpha variation with active grain density

- Higher MRR takes place as a contrast of diamond grinding and spark machining from both the literature analysis and the mathematical model.
- The union of electric-sparking and diamond grinding could be used to process hard-to-cut materials productively. The machining efficiency is remarkably higher as compared to sparking and diamond grinding.
- The MRR has increased with increasing pulse-on time, current and duty cycle. However, higher setting of these parameters will lead to raining out of abrasive grains that will lead to the supremacy of spark action in the process of material removal mechanism.
- All inclusive, the mathematical model and actual data set forecasted the material removal to be under 3% absolute error.

6 Future Scope

- The optimum process parameter configuration for the maximum material removal rate with the best surface quality is desired.
- Specific diamond consumption may also be controlled in the process with respect to optimizing the amount of material removal. For this, it is possible to use classical and heuristic optimization methods.
- Furthermore, considering this analysis as a basis for finding correlation effect on different parameters and incorporation in mathematical model, such as table feed rate, different grinding forces with MRR, an extension is possible.

- In this study we neglected the grinding zone recasting effect. With recasting effect in place a different model can also be established.
- In conjunction with sparking, thermal simulation and analysis can be carried out to measure the effects of heat-affected zone.

References

1. Ghosh A, Mallik AK (2010) Manufacturing science, 2nd edn. Affiliated East–West Press Private Limited
2. Jain VK (2008) Advanced (non-traditional) machining processes. In: Davim JP (ed) Editor machining: fundamentals and recent advances. Springer, London, pp299–327
3. Wegener K et al (2011) Conditioning and monitoring of grinding wheels. CIRP Ann 60(2):757–777
4. Kozak J (2002) Abrasive electric discharge grinding (AEDG) of advanced materials, vol. 2, pp 83–101
5. Koshy P, Jain VK, Lal GK (1996) Mechanism of material removal in electrical discharge diamond grinding. Int J Mach Tools Manuf 36(10):1173–1185
6. Lee E-S, Ahn S-O (1999) Precision surface grinding of Mn–Zn ferrite with in-process Electric-discharge dressing (IEDD). Int J Mach Tools Manuf 39(10):1655–1671
7. Koshy P, Jain VK, Lal GK Grinding of cemented carbide with electrical spark assistance
8. Koshy P et al (1997) Stochastic simulation approach to modelling diamondwheel topography 37(6):751–761
9. Agarwal S et al (2017) An analytical chip thickness model for performance assessment in silicon carbide grinding. Procedia Manuf 10:298–306
10. Agarwal S, Venkateswara Rao P (2010) Modeling and prediction of surface roughness in ceramic grinding. Int J Mach Tools Manuf 50(12): 1065–1076
11. Younis MA, Alawi H (1984) Probabilistic analysis of the surface grinding process. Trans Can Soc Mech Eng 8(4):208–213
12. Tönshoff H et al (1992) Modelling and simulation of grinding processes 41(2):677–688
13. Siddiqui MJJ ROTNBOS (1964) Sec. D, statistical inference for rayleigh distributions 68(9):1007
14. Malkin S, Guo C (2008) Grinding technology, theory and applications of machining with abrasives, 2nd edn. Industrial Press
15. Jha SK (1992) Pobisheniye Rabotospovnoschi Almaznikh Krugov Pychyom Stabilizatsii Uslovii Vzaimodeistviya Ekh s Obrabativayemim Materialom. Kharkov State Polytechnical University, Kharkov, Ukraine
16. Satyarthi MK, Pandey PM (2013) Modeling of material removal rate in electric discharge grinding process. Int J Mach Tools Manuf 74:65–73
17. Unune DR, Nirala CK, Mali HS (2018) ANN-NSGA-II dual approach for modelling and optimization in abrasive mixed electric discharge diamond grinding of monel K-500. Eng Sci Technol Int J
18. Srivastava AK, Sri Ram K, Lal GK (1985) A new technique for evaluating wheel loading. Int J Mach Tool Des Res 25(1):33–38

An Inverse Technique to Estimate the Heat Flux of a Slab with Transient Heat Conduction



Siddhartha Gollamudi and Pradeep S. Jakkareddy

Abstract The present work concerns the application of Artificial Neural Networks (ANN) and Genetic Algorithm (GA)-based inverse technique on a transient heat transfer problem. The proposed methodology has been demonstrated on a two-dimensional heat slab to estimate linearly varying heat flux constants using space–time temperature response. Initial temperatures and thermophysical properties are assigned. Different heat flux is specified at the right and bottom surfaces of the slab. The input–output (heat flux–temperature) data set of the slab is obtained using MATLAB [1]. This is used to train the ANN network, which acts as a proxy model. The synthetic experimental temperature data set are generated from the analytical method. In the inverse problem, the GA is employed to generate the samples and minimize the objective function to estimate the constants (S_1 and S_2) of the heat flux function $Q = S(t)$. The robustness of the methodology is examined for different noise levels.

1 Introduction

Transient conduction is a widely observed phenomenon in many engineering problems, where the heat transfer is dependent on time. It plays a pivotal role in analyzing space re-entry capsules, piping design, and temperature measuring devices. In the two-dimensional (2D) transient equation, the temperature distribution is a function of X -coordinate, Y -coordinate, and time. To solve the problems of the above kind, we need to have initial and boundary conditions. But, in many practical scenarios, the problem is ill-defined, making it challenging to model and obtain a numerical result. Also, the analytical approach becomes difficult due to the complex nature of the transient phenomena. To solve such problems, inverse techniques are beneficial. Inverse heat transfer methods can be used to determine heat flux and temperatures on

S. Gollamudi · P. S. Jakkareddy (✉)
Department of Mechanical Engineering, Amrita School of Engineering, Bengaluru, Amrita
Vishwa Vidyapeetham 560035, India
e-mail: js_pradeep@blr.amrita.edu

an inaccessible surface of a wall by measuring the boundary's temperature on accessible areas. The inverse technique may be an alternative for the traditionally used experimental techniques and reconstruct various unknown parameters like heat flux, temperatures, thermophysical properties, etc. Data-driven inverse methods find their application in the medical field [2]. Nakaumra et al. [3] proposed an inverse technique to predict the unknown heat fluxes, which are pivotal for determining the thermal load and stresses on atmospheric re-entry capsules. Frackowiak et al. [4] have developed an inverse technique of the cooling of gas turbine blades. An iterative algorithm has been employed to find out the porous media's porosity, used in cooling channels of the turbine blades. Duda [5] reconstructed the physics behind the formation of a convective boundary layer in a stem header to verify an inverse model. The unknown boundary conditions were obtained from the temperature distribution on the steam header. The model was validated by comparing the temperature profile obtained from the inverse calculation and experimental measurement. The same author [6] illustrated the use of stochastic search methods to solve a multi-dimensional heat transfer model using FEM to find out the unknown boundary conditions. Huang et al. [7] adopted the conjugate-gradient search algorithm to formulate an inverse solution to determine the unknown boundary conditions for a three-dimensional heat transfer problem on an irregular body. The effects of measurement errors on the inverse model were discussed, and the model was experimentally validated. Many of the inverse procedures involve FEM calculations. This makes the process time-consuming and computationally expensive. Since the FEM subroutine has to be followed for every search iteration. Surrogate methods like artificial neural networks are employed to overcome this shortcoming. Although the use of FEM is not eliminated but is restricted to a limited number. Chidambaram et al. [8] elucidated GA-ANN coupled methods to find optimal geometry for a fin configuration. A surrogate model and GA were employed to determine the optimal fin parameter. GA was again employed to find out the optimal number of neurons in the neural network. Zhu et al. [9] estimated the wall fluxes on a triangular wall. Using the experimentally measured temperatures from the domain, an inverse model was formulated to estimate the wall heat fluxes. The model was optimized using the conjugate-gradient method. Jakkareddy et al. [10] presented a surrogate model used to calculate the spatially varying heat transfer coefficient on a flat plate on which heat sources are mounted on a flat plate. Xi et al. [11] explained the ANN-GA method to optimize the stem-cooled ribbed channels to achieve maximum performance. Vakili [12] discussed the results of 1D, 2D, and 3D steady-state and transient problems using the PSO algorithm. Suraj et al. [13] discussed the alternative way to solve an inverse problem to detect hot spots and estimate the strength of heat flux in the flat plate. Based on the literature review, it is clear that there is a scope for applying inverse techniques for transient heat transfer problems. In the present study, an ANN-GA methodology is built to estimate the constants of the linear heat flux function of a slab using space-time temperature data.

2 An Overview of the ANN-GA-Based Inverse Methodology

In the present study, the inverse problem comprises of four sections, which are as follows:

1. Forward Model: The data generated from any sampling technique is input to the forward model. The forward model is a set of governing equations of a transient heat conduction problem, which is solved using an analytical method in the present case.
2. Surrogate Model: The data obtained using the forward model is used to create a proxy model using an artificial neural network to decrease the computational cost and time.
3. Parameter Estimation: Using a neural network and genetic algorithm, the measured and the simulated transient temperature response is minimized in the least square sense to estimate the constants S_1 and S_2 of heat flux function $Q(t)$.
4. Inferences: The effect of time steps and noise on the estimation is studied.

3 Forward Model

Two-dimensional transient heat conduction through a slab with dimensions of width $b = 0.1$ m and height of $d = 0.05$ m is shown in Fig. 1. The left and bottom surface of the slab is set to an adiabatic condition. The heat flux $Q1 = S_1(t)$ and $Q2 = S_2(t)$ are assigned at the right and top surface of the geometry. S_1 and S_2 are the constants of heat flux. The linear nature of the heating process can occur in practice during a

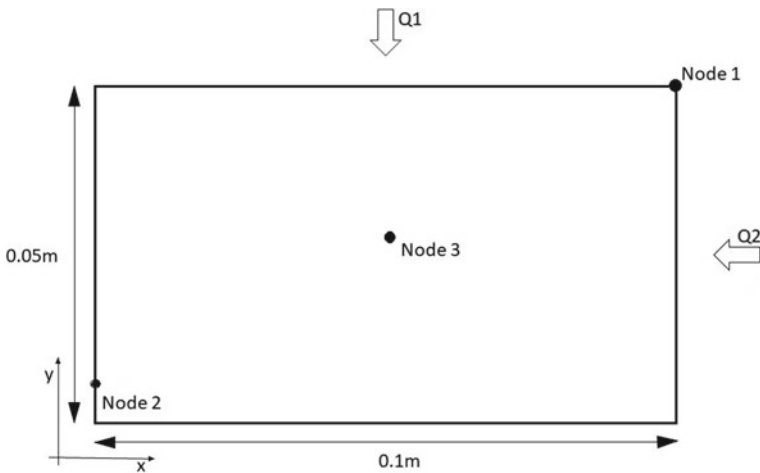


Fig. 1 Geometry of the slab

start-up procedure of a furnace. The initial temperature of the slab is constant and equals T_0 . Thermal conductivity and thermal diffusivity of the slab are $40 \text{ W/m}^2 \text{ K}$ and $4 \times 10^6 \text{ m}^2/\text{s}$, respectively.

The assumptions and the governing equations of the transient heat conduction slab are as follows:

1. Two-dimensional heat transfer.
2. The heat fluxes applied at the boundary of the slab are a linear function of time.
3. Thermophysical properties are independent of temperature changes.

$$\frac{\partial^2 T}{\partial x^2} + \frac{\partial^2 T}{\partial x^2} = \frac{\partial T}{\partial t} \frac{1}{\alpha} \tag{1}$$

$$k \frac{dt}{dx} \Big|_{x=0} = 0 \tag{2}$$

$$k \frac{dt}{dx} \Big|_{x=b} = S_1(t) \tag{3}$$

$$k \frac{dt}{dy} \Big|_{y=0} = 0 \tag{4}$$

$$k \frac{dt}{dy} \Big|_{y=d} = S_2(t) \tag{5}$$

The transient heat conduction Eq. (1) is solved by the method of superposition. Applying the necessary boundary conditions to Eqs. (2–5), the solution turns out to be,

$$T(x, y, t) = T_0 + \frac{1}{12} \frac{S_1 b^3}{k\alpha} \left[\begin{aligned} &6\left(\frac{\alpha t}{b^2} + \frac{x^2}{2b^2}\right) - \left(\frac{x^2}{b^2} + \frac{1}{2}\right) \\ &-2\frac{\alpha t}{b^2} + \frac{29}{69} - \frac{24}{\pi^2} \sum_{n=1}^{\infty} \frac{(-1)^{n+1}}{n^4} \cos\left(\frac{n\pi x}{b}\right) \exp\left(\frac{-n^2\pi^2\alpha t}{b^2}\right) \end{aligned} \right] \\ + \frac{1}{12} \frac{S_2 d^3}{k\alpha} \left[\begin{aligned} &\left(6\frac{\alpha t}{d^2} + \frac{y^2}{2d^2}\right) - \left(\frac{y^2}{d^2} + \frac{1}{2}\right) \\ &-2\frac{\alpha t}{d^2} + \frac{29}{d^2} - \frac{24}{\pi^2} \sum_{n=1}^{\infty} \frac{(-1)^{n+1}}{n^4} \cos\left(\frac{n\pi y}{d}\right) \exp\left(\frac{-n^2\pi^2\alpha t}{d^2}\right) \end{aligned} \right] \tag{6}$$

where ‘ k ’ is the thermal conductivity, α is the thermal diffusivity, ‘ x ’ and ‘ y ’ represent the coordinate of temperature measuring point in the domain, and ‘ t ’ represents flow time. The two-heat flux of varying intensities specified at the boundary surface is input to get the temperature–time response at three locations, as shown in Fig. 1, and the distance from the origin concerning x – y coordinates are given in Table 1. The temperature locations are chosen such that there is a temperature difference of a minimum of $1 \text{ }^\circ\text{C}$ from one location to another. Equation (6) is solved for a

Table 1 Temperature locations of a slab

S. No.	X-coordinate	Y-coordinate
1	0.1	0.05
2	0.05	0.025
3	0	0.0125

flow time of 1500 s with a step size of 50 s. Both S_1 and S_2 range from 10 to 100. Equations (1)–(6) are solved using [1].

4 Surrogate Model

Simulations of the forward model are repeatedly required in the ANN-GA-based estimation procedure. To ease the computational intensity, artificial neural network is employed as a surrogate for the forward model. ANN comprises the input layer, a group of hidden layers, and output layers. Neural networks have interconnected processing junctions known as neurons, which take the weighted input sets and gives the required output. Each layer consists of neurons that are connected to the neurons of the preceding and the subsequent layers [14]. The input and output data set decides the number of neurons in the hidden layer [15]. Figure 2 shows the typical architecture

Fig. 2 Typical single layer ANN architecture

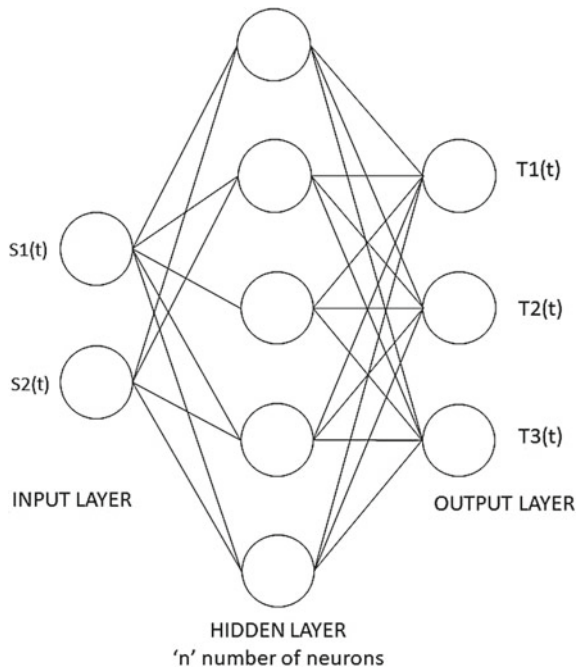


Table 2 Neuron independence study

S. No.	No. of neurons	Mean relative error
1	1	3.4629
2	2	1.6328
3	3	0.9882
4	4	0.7995
5	5	0.1280
6	10	0.0142
7	15	0.0031
8	20	0.0020
9	25	0.0022

of a neural network. The neural network used in the present study is based on the feed-forward backpropagation network. In the feed-forward backpropagation neural network, the input layer's input and output functions, the single hidden layer, and the final output layer are calculated. The Levenberg–Marquardt algorithm is used to train the network, in which the weights are updated according to the learning rate and given to the network until the estimation error is minimized, and this is called the backpropagation step. The tan-sigmoid function is employed to correlate the inputs and the outputs. S_1 and S_2 are the inputs and temperature time responses are the outputs. Out of the 2900 data sets obtained, 70% are used for training, 15% are used for validation, and 15% are for testing. Validation is done to avoid overfitting of data. To select the number of neurons required in the hidden layer is determined by the neuron independence study. (see Table 2). Table 2 clearly shows that there is no appreciable improvement in the mean relative error beyond 20 neurons.

The performance parameter mean relative error (MRE) is as follows:

$$MRE = \frac{\sum_{i=1}^N |T_{Ann} - T_{sim}|}{T_{sim} N} \quad (7)$$

5 Inverse Method

The procedure to solve the inverse problem using the ANN-GA method is shown in Fig. 3. In the inverse problem, the least square function of measured T_{meas} and simulated temperature responses T_{sim} have to be minimized to estimate the two unknown constants of heat flux $S_1(t)$ and $S_2(t)$.

$$R^2 = \sum_{i=1}^N (T_{sim} - T_{meas})^2 \quad (8)$$

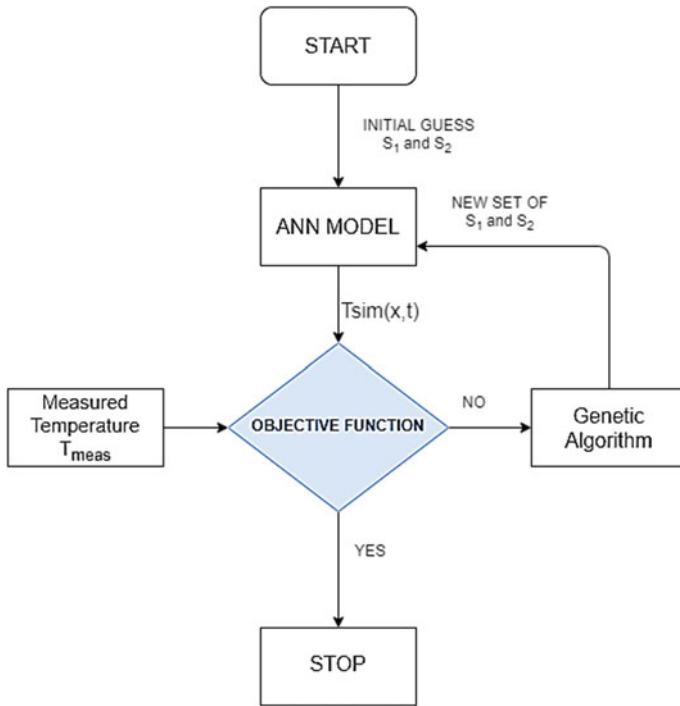


Fig. 3 ANN-GA procedure, the objective function is defined as follows: $\sum_{i=1}^N (T_{sim} - T_{meas})^2 < 10^{-6}$.

T_{sim} is the simulated data obtained from the ANN model, and T_{meas} are the synthetic temperature dataset at three different locations obtained using an analytical method for a given heat flux as input. If R^2 is within the specified error range of 10^{-6} , then the iteration stops; else runs in a loop till the criteria are satisfied. The GA is a population-based stochastic search method [15]. The reason for choosing GA in the present study is its capability to efficiently handle nonlinear equations and not get trapped in local minima/maxima. GA starts with a randomly generated population of initial solutions. The fitness value (objective function) is evaluated for each solution in the population. The various parameters, like reproduction, crossover, mutation, etc., are employed to modify and improve the population of solutions as the number of generations increases. The genetic algorithm's output is input to the artificial neural network, and the loop continues until the error falls below the desired value. Finally, it arrives at the best fit. A mutation rate of 0.1 and a two-point crossover function is used for mating samples at a rate of 0.8.

6 Results and Discussion

In this work, the main objective is to determine the unknown constants, S_1 and S_2 , of linear time-dependent heat flux $Q(t)$ boundary conditions of a slab using ANN-GA-based inverse technique. Transient temperature histories at three locations in the slab are repeatedly obtained by the ANN proxy model for a given set of S_1 and S_2 samples generated in the range of 0–100 using a genetic algorithm. The synthetic temperature data obtained for a given set of heat flux constants by the analytical method is considered as measured temperature. The parameter estimation results for a different set of S_1 , and S_2 are shown in Table 3. Since we have the luxury of knowing the constants of actual heat flux in the present case of surrogate parameter estimation, the comparison between actual and estimated values is shown in Table 3, and both the values seem to agree. The estimated heat flux set has an average standard deviation of 0.068, 0.183 and 0.233, respectively. The convergence histories of the heat flux ($S_1 S_2$), (35 55), (25 43), (61 77) are shown in Figs. 4, 5, and 6.

Table 3 Estimated constants of $Q1(t)$ and $Q2(t)$

S. No	Actual S_1	Actual S_2	Estimated S_1	Estimated S_2	Average standard deviation
1	35	55	35.01	55.087	0.068
2	25	43	24.84	42.687	0.183
3	61	77	61.12	77.21	0.223

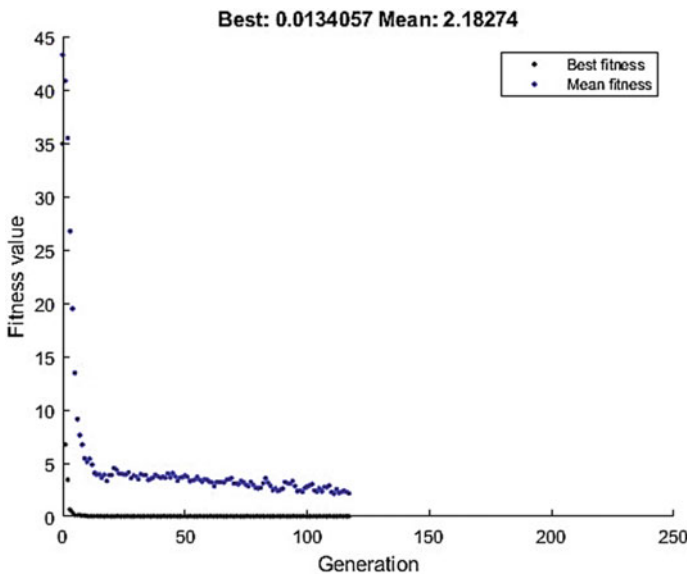


Fig. 4 Fitness values versus the number of generations to estimate heat flux constants (35 55)

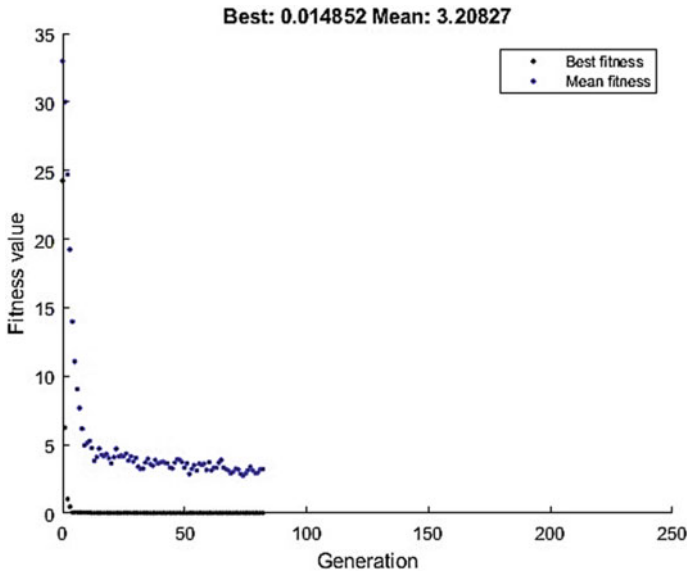


Fig. 5 Fitness values versus the number of generations to estimate heat flux constants (25 43)

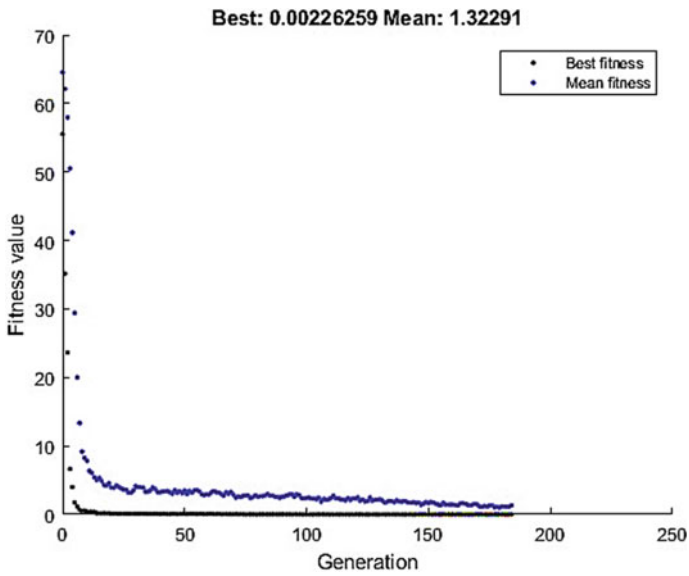


Fig. 6 Fitness values versus the number of generations to estimate heat flux constants (61 77)

The effect of the number of time steps for estimating the parameters S_1 and S_2 is studied. If we do not measure temperature for a sufficient number of time steps, the proposed ANN-GA-based inverse method can converge at a different value than the actual one, as there is always a possibility of obtaining a closer temperature profile to the measured one for different heat flux combination. The heat flux constants estimated for a varying time step is shown in Fig. 7. One can observe that as the number of time steps is very less, i.e., in the range of 1–8, there is a considerable variation in the estimated values. As the number of timesteps increases, say beyond 15, the heat flux values reach stationarity. The effect of noise on the estimation of S_1 and S_2 are shown in Table 4. It is observed that as the noise in the temperature increases, the standard error in the estimates increases. This is due to the rise of the uncertainty of temperature responses. Even with increased error in the temperature

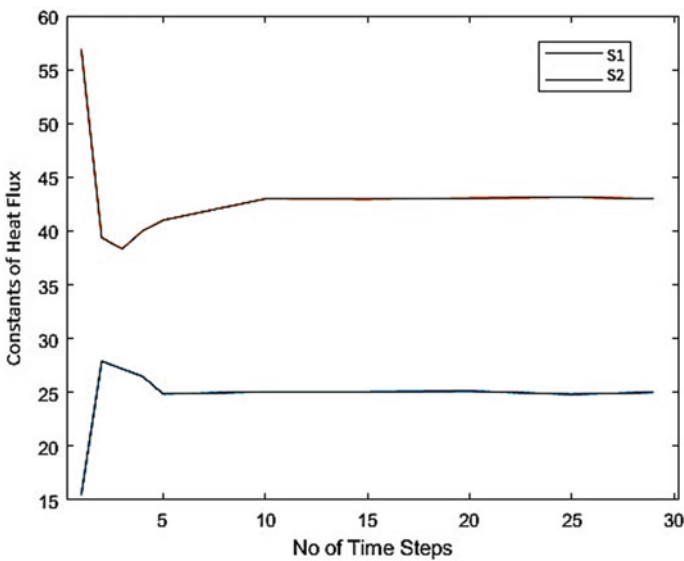


Fig. 7 Effect of the number of time steps for estimating constants of heat flux (25 43)

Table 4 Error independence study

S.No.	%Error	Estimated S_1	Estimated S_2	Standard deviation
1	0.1	34.91	55.23	0.112
2	0.2	35.12	54.89	0.080
3	0.3	35.61	54.23	0.487
4	0.5	34.76	54.51	0.257
5	0.8	34.80	56.08	0.452
6	1.0	34.29	56.56	0.801
7	2.0	34.90	52.87	0.788

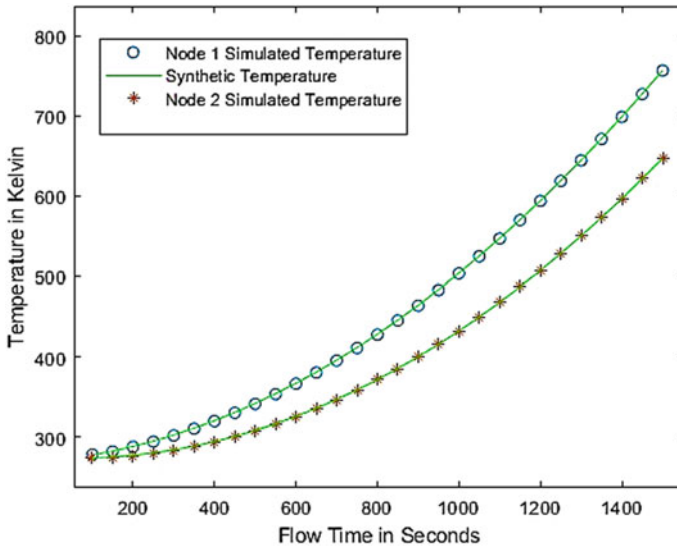


Fig. 8 Comparison of simulated and measured transient temperature response at node 1 and node 2 of the slab for the heat flux constants of 35 and 55

input, the proposed ANN-GA-based inverse method can give the best estimate of S_1 and S_2 . Thereby demonstrates the robustness of the methodology developed.

To validate the results obtained from the ANN-GA-based inverse method. The estimated constant S_1 and S_2 of $Q_1(t)$ and $Q_2(t)$, i.e., 35 and 55 are input to CFD simulation [16] to get the temperature responses. The simulated and synthetic measured space time–temperature data for a flow time of the 1500 s with a time step of 50 s at nodes 1 and 2 are compared, and the same is shown in Fig. 8. From Fig. 8, we can observe that both the results are found to be in good agreement. The difference between the two is 0.83%. Thus, it proves the capability of the proposed ANN-GA inverse method.

7 Conclusions

In the present study, a transient slab with unknown heat fluxes was determined using the proposed ANN-GA-based inverse technique. The estimated constants of linear heat flux function $Q(t)$ were S_1 : 35.01, 24.84, 61.12, and S_2 : 55.09, 42.69, 77.21. The temperature obtained from the estimated heat flux [$Q_1 = 35t$, $Q_2 = 55t$] was in agreement with the CFD simulation with a 0.83% error. Thus, it validates the inverse technique developed in the current study. The standard deviation of the estimates for heat flux constants ($S_1 = 35$, $S_2 = 55$) were 0.007 and 0.065. By adding errors up to 1% to the synthetic temperature data for estimated parameters S_1 and S_2 were

found to be reasonable. So the proposed inverse methodology is stable. The present work's novelty is building a robust ANN-GA inverse algorithm to accelerate the process of estimating the parameters in the transient heat transfer systems without compromising its accuracy.

References

1. MATLAB (2019a). MathWorks Inc. USA
2. Nedungadi P, Iyer A, Gutjahr G, Bhaskar J, Pillai AB (2018) Data-driven methods for advancing precision. *Oncol Curr Pharmacol Rep* 4:145–156
3. Nakamura T, Kamimura Y, Igawa H, Morino Y (2014) Inverse analysis for transient thermal load identification and application to aerodynamic heating on atmospheric reentry capsule. *Aerosp Sci Technol* 38:48–55
4. Frąckowiak A, CiaŁkowski M, Von Wolfersdorf J (2006) Numerical solution of a two-dimensional inverse heat transfer problem in gas turbine blade cooling. *Arch Thermodyn* 27:1–8
5. Duda P (2015) Numerical and experimental verification of two methods for solving an inverse heat conduction problem. *Int J Heat Mass Transf* 84:1101–1112
6. Duda P (2016) A general method for solving transient multidimensional inverse heat transfer problems. *Int J Heat Mass Transf* 93:665–673
7. Huang CH, Wang SP (1999) A three-dimensional inverse heat conduction problem in estimating surface heat flux by conjugate gradient method. *Int J Heat Mass Transf* 42:3387–3403
8. Chidambaram B, Ravichandran M, Seshadri A, Muniyandi V (2017) Computational heat transfer analysis and genetic algorithm-artificial neural network-genetic algorithm-based multi-objective optimization of rectangular perforated plate fins. *IEEE Trans Components, Packag Manuf Technol* 7:208–216
9. Zhu Y, Liu B, Jiang PX, Fu T, Lei Y (2017) Inverse heat conduction problem for estimating heat flux on a triangular wall. *J Thermophys Heat Transf* 31(1):205–210
10. Jakkareddy PS, Balaji C (2017) Estimation of spatially varying heat transfer coefficient from a flat plate with flush mounted heat sources using Bayesian inference. *J Phys Conf Ser* 745(3)
11. Xi L, Gao J, Xu L, Zhao Z, Li Y (2018) Study on heat transfer performance of steam-cooled ribbed channel using neural networks and genetic algorithms. *Int J Heat Mass Transf* 127:1110–1123
12. Vakili S, Gadala MS (2009) Effectiveness and efficiency of particle swarm optimization technique in inverse heat conduction analysis. *Numer Heat Transf Part B Fundam* 56(2):119–141
13. Kumar S, Jakkareddy PS, Balaji C (2020) A novel method to detect hot spots and estimate strengths of discrete heat sources using liquid crystal thermography. *Int J Therm Sci* 154:106377
14. Demuth H, Beale M (2002) *Neural network toolbox—for use with MATLAB*
15. Jakkareddy PS, Balaji C (2017) A methodology to determine boundary conditions from forced convection experiments using liquid crystal thermography. *Heat Mass Transf* 53(2):519–535
16. Ansys fluent, ANSYS Inc, USA, 2019

A Numerical Approach to Find Distinct Mechanisms of a Planar Kinematic Chain Using Linkage Coordinates



Vinjamuri Venkata Kamesh, V. Srinivasa Rao, D. V. S. S. V. Prasad,
and P. S. Ranjit

Abstract In a planar kinematic chain, different mechanisms are possible when on link's mobility is restricted by fixing it. These mechanisms obtained are called as inversions. In the present paper, a numerical approach is proposed which is based on new concept defined as 'linkage coordinates' related to connectivity of a link in a closed planar kinematic chain. The proposed method is tested on various linkages (8, 9, 10) with varying degree of freedom (DoF) for which identified inversions are in correlation with earlier results in the literature. The proposed method can be applied to analyze other characteristics of kinematic chains with higher linkages and higher DoF. 8-link 1-DoF completed results are presented in the results section of the paper.

Keywords Effective connectivity · Distinct mechanism · Linkage

V. V. Kamesh (✉) · P. S. Ranjit
Aditya Engineering College(A), Surampalem, East Godavari Dist., Andhra Pradesh, India

V. Srinivasa Rao
Raghu Engineering College(A), Dakamarri, Visakhapatnam Dist., Andhra Pradesh, India

D. V. S. S. V. Prasad
Aditya College of Engineering, Surampalem, East Godavari Dist., Andhra Pradesh, India

1 Introduction

1.1 Literature Review

In the type synthesis of planar kinematic chains, identification of distinct mechanisms is an important task. Finding the inversions is an essential part in fixing the grounding link and input links when a kinematic chain. The links of a kinematic chain can be binary, ternary, quaternary, etc. The connectivity of a link is the number of other links to which the link is connected. When one of the link is grounded, its mobility is fully restricted. Also, the mobility of all the links which are connected to it is also restricted partially. The links which are having the same functional behavior are said to form one distinct mechanism or inversion.

Rao and Raju [1] inherited the concept of hamming number from digital communication theory to identify isomorphism and inversions by forming hamming strings. Kui and Qing [2] developed adjacent-chain table (ACT) by which topological characteristics among links can be found easily. Rao [3] proposed fuzzy logic to assess topological characteristics of kinematic chains in which connectivity of link is calculated as a fuzzy element. Hasan et al. [4] proposed a method based on weighted physical connectivity matrix [WPCM] of a K-chain. The two structural invariants, namely sum of absolute characteristic polynomial coefficients and maximum absolute value of characteristic polynomial coefficient, are calculated and used as the identification numbers of the kinematic chains to find the inversions. Mohammad et al. [5] used extended adjacent matrix using graph theory to find the inversions. Sanyal used joint connectivity [6] and link-joint connectivity [7] approaches to find isomorphism and inversions of planar k-chains. Bal et al. [8] proposed a new method using link invariant functions based on distance matrix and loops of a kinematic chain. The functions generate a set of structural invariants capable of detecting distinct links of a kinematic chain and isomorphism. Hasan [9] used weighted physical connectivity [WPCM] matrix as a tool to find inversions of k-chains. Rizvi [10] used eigenvalues of adjacency matrix to find inversions. Rai [11] used distance concept in graph theory to find inversions. Shukla and Sanyal [12] proposed 'gradient' concept to identify isomorphism and to find inversions of planar k-chains. Kamesh [13] proposed a novel algorithm based on adjacency of each link mixed with the 'degree of vertex' concept in graph theory. Distinct kinematic mechanisms or inversions are found for 8-link 1-degree of freedom kinematic chains. Kamesh and Prasad [14] used 'link polynomial' to find distinct inversions.

In this paper, a novel concept is proposed as ‘linkage coordinates’ to identify inversions using connectivity of a link as primary constituent in the algorithm. The functioning of all the links which are not connected to grounded link directly is analyzed.

2 Algorithm Proposed to Find Distinct Mechanisms

Few linkage parameters are defined in the proposed algorithm to find inversions. They are explained in the next subsections.

Residual Linkage (R.L)

It is defined as the linkage that remained after removing the grounded link and its connected links from the kinematic chain. For example, if a ternary link is grounded, this link and its attached three other links will be removed from the kinematic chain. The remaining linkage will become open and divided into parts.

Effective Connectivity (E.C)

It is the modified connectivity of the link in the residual linkage. The calculation of effective connectivity is based on the number of connected joints to the link.

$$\begin{aligned} \text{Effective connectivity} &= \text{Original connectivity of link (if it has all connected joints)} \\ &= \frac{\text{Number of connected joints}}{\text{Original connectivity of link}} \text{ (if it has unconnected joints)} \end{aligned}$$

Ex: If a ternary link is having all joints connected, its effective connectivity will be 3. If it has 1 unconnected joint, its effective connectivity will be 2/3. If it has two unconnected joints, its EC will be 1/3.

In a similar way, effective connectivity of all other links can be calculated.

Attached Linkage of a link (AL)

It is defined as the summation of all effective connectivities of links attached in the residual linkage.

Detached Linkage of a link (DL)

It is defined as the summation of original connectivities of links which are detached from the link under consideration.

Total Attached Linkage (TAL)

It is defined as the summation of all the attached linkages in a residual linkage.

Total Detached Linkage (TDL)

It is defined as the summation of all the detached linkages in a residual linkage.

Linkage Coordinates (LC)

For a particular link, the values total attached linkage and total detached linkage are considered to be 'linkage coordinates' (LC). These linkage coordinates are the decision parameters to find the distinct inversions.

3 Decision Rule to Find the Distinct Mechanisms

All the links having similar linkage coordinates (LC) are said to have similar functional behavior, i.e., same inversion.

4 Steps in the Proposed Algorithm

The various steps in the proposed algorithm to find the distinct inversions are as under.

- Step 1 Select link 1 in the kinematic chain under consideration. Remove link 1 and all its connected links from the chain to form residual linkage.
- Step 2 In the residual linkage of link 1, calculate attached linkage (AL) and detached linkage (DL) for every link according to the defined rules.
- Step 3 Calculate total attached linkage (TAL) and total detached linkage (TDL) which are 'linkage coordinates' of link 1.
- Step 4 Steps 1–3 are repeated for all the links in the kinematic chain.
- Step 5 Compare the linkage coordinates of all links of K-chain.
- Step 6. According to decision rule in Sect. 3, the links which are having same linkage coordinates are declared to be of same inversion.

5 Illustrative Example for the Proposed Algorithm

Consider an 8-link 1-DoF kinematic chain (Chain 10) from Appendix as shown in Fig. 1.

Application of Proposed Algorithm for Chain 10.

- Step 1 For link 1, the residual linkage will be obtained after removing link 1 and its adjacent links (2, 6) attached to it. The residual linkage is shown in Fig. 2

Fig. 1 Chain 10

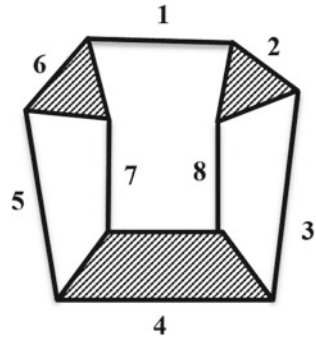
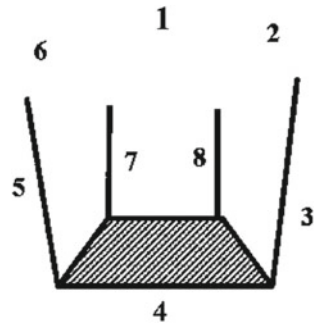


Fig. 2 Residual linkage



Step 2 The attached linkage (AL) and detached linkage (DL) of all the links in the residual linkage according to defined rules are calculated and shown in Table 1.

Table 1 Attached linkage and detached linkage values of links in residual linkage of link 1

Link	Adjacent links	Attached linkage	Detached linkage
3	Link 2 and link 4	4 (link 4 is fully connected)	3 (link 2, ternary link is removed from k-chain)
4	Link 3, link 5, link 7, and link 8	$\frac{1}{2} + \frac{1}{2} + \frac{1}{2} + \frac{1}{2} = 2$ (all the four links are having one connected joint)	–
5	Link 4 and link 6	4 (link 4 is fully connected)	3 (link 6, ternary link is removed from k-chain)
7	Link 4 and link 6	4 (link 4 is fully connected)	3 (link 6, ternary link is removed from k-chain)
8	Link 2 and link 4	4 (link 4 is fully connected)	3 (link 2, ternary link is removed from k-chain)
		Attached linkage of link 1 = $4 + 2 + 4 + 4 + 4 = 18$	Detached linkage of link 1 = $3 + 3 + 3 + 3 = 12$

- Step 3 The linkage coordinates of link 1 are found to be 18 and 12 from step 2.
- Step 4 Steps 1–3 are repeated for all the links in the kinematic chain.
The ‘linkage coordinates’ of all the links are shown in Table 2.
- Step 5 After comparing the linkage coordinates of all links of K-chain, using the decision rule in Sect. 3, the links which are having same linkage coordinates are identified as four combinations as (1), (2, 6), (3, 5, 7, 8), and (4).
- Step 6 The four combinations obtained in step 5 are declared as four distinct mechanisms or inversions for kinematic chain under consideration.

6 Results

The proposed algorithm is applied on different linkage with varying degree of freedom (DOF), i.e., 8-link 1-DOF, 9-link 2-DOF, 10-link 3-DOF, and 10-link 1-DOF. Proposed method results 71, 254, 684, and 1834 inversions for the above cases, respectively. Complete results of 8-link 1-DOF distinct kinematic chains (16 number) shown in Appendix (Table 3).

7 Conclusion

The proposed algorithm based on connectivity is very efficient and easy to understand. The method is having very less computations. It can be applied for higher linkage and varying DOF. All the results obtained by this method are same with the available literature [7–11]. By this method, inversions of any planar kinematic chain can be found easily. The proposed method can also be programmed.

Table 2 Linkage coordinates of all the links of kinematic chain in Fig. 1

Link	Attached linkage values								Detached linkage values								Linkage coordinates of links	
	2	3	4	5	6	7	8	1	2	3	4	5	6	7	8	Total attached linkage	Total detached linkage	
1																18.00	12.00	
1	0	4	2	4	0	4	4	0	0	3	0	3	0	3	3	18.00	18.00	
2	0	0	4	1.17	4	1.17	0	0	0	0	4	0	2	0	0	10.33	6.00	
3	0	0	0	3	1.5	3	0	3	0	0	0	4	0	4	7	10.50	18.00	
4	0.67	2	0	0	2	0	0	0	4	0	0	0	4	0	0	4.67	8.00	
5	3	1.5	3	0	0	0	3	3	0	4	0	0	0	7	4	10.50	18.00	
6	0	4	1.17	4	0	0	1.17	0	2	0	4	0	0	0	0	10.33	6.00	
7	3	1.5	3	0	0	0	3	3	0	4	0	7	0	0	4	10.50	18.00	
8	3	0	0	0	3	1.5	3	0	0	7	0	4	0	4	0	10.50	18.00	

Table 3 Distinct mechanisms of 8-link 1-DOF K-chains

Chain number	Link number	Linkage coordinates		Distinct mechanisms	Number of inversions
		Total attached linkage (TAL)	Total detached linkage (TDL)		
1	1	4.83	14	(1, 2, 5, 6), (3, 4, 7, 8)	2
	2	4.83	14		
	3	18.67	8		
	4	18.67	8		
	5	4.83	14		
	6	4.83	14		
	7	18.67	8		
	8	18.67	8		
2	1	1.83	14	(1, 2, 3, 6), (4, 5, 7, 8)	2
	2	1.83	14		
	3	1.83	14		
	4	12	8		
	5	12	8		
	6	1.83	14		
	7	12	8		
	8	12	8		
3	1	3.67	10	(1), (2), (3), (4), (5), (6), (7), (8)	8
	2	7.67	12		
	3	6.50	10		
	4	2.33	14		

(continued)

Table 3 (continued)

Chain number	Link number	Linkage coordinates		Distinct mechanisms	Number of inversions
		Total attached linkage (TAL)	Total detached linkage (TDL)		
	5	12	8		
	6	16.17	8		
	7	1.83	14		
	8	10.17	12		
4	1	10.33	10	(1, 4), (2, 8), (3, 7), (5, 6)	4
	2	4.83	14		
	3	10.17	12		
	4	10.33	10		
	5	16.17	8		
	6	16.17	8		
	7	10.17	12		
	8	4.83	14		
5	1	18.67	8	(1, 2), (3, 7), (4, 6), (5, 8)	4
	2	18.67	8		
	3	2.33	14		
	4	6.17	10		
	5	10.67	12		
	6	6.17	10		
	7	2.33	14		

(continued)

Table 3 (continued)

Chain number	Link number	Linkage coordinates		Distinct mechanisms	Number of inversions
		Total attached linkage (TAL)	Total detached linkage (TDL)		
6	8	10.67	12		
	1	16.17	8		5
	2	16.17	8		
	3	6.17	10		
	4	14.33	12		
	5	8.67	10		
	6	14.33	12		
	7	6.17	10		
8	1	18			
7	1	8	6		6
	2	11.83	12		
	3	6.17	10		
	4	14.33	12		
	5	6.17	10		
	6	11.83	12		
	7	7.67	12		
	8	2.33	14		
8	1	10.67	12		2
	2	10.33	10	(1, 4, 7, 8), (2, 3, 5, 6)	

(continued)

Table 3 (continued)

Chain number	Link number	Linkage coordinates		Distinct mechanisms	Number of inversions
		Total attached linkage (TAL)	Total detached linkage (TDL)		
9	3	10.33	10	(1, 3, 4, 8), (2, 5, 6, 7)	2
	4	10.67	12		
	5	10.33	10		
	6	10.33	10		
	7	10.67	12		
	8	10.67	12		
	1	3.67	10		
	2	7.67	12		
10	3	3.67	10	(1), (2, 6), (3, 5, 7, 8), (4)	4
	4	3.67	10		
	5	7.67	12		
	6	7.67	12		
	7	7.67	12		
	8	3.67	10		
	1	18	12		
	2	10.33	6		
3	10.50	18			
4	4.67	8			
5	10.50	18			

(continued)

Table 3 (continued)

Chain number	Link number	Linkage coordinates		Distinct mechanisms	Number of inversions
		Total attached linkage (TAL)	Total detached linkage (TDL)		
	6	10.33	6		
	7	10.50	18		
	8	10.50	18		
11	1	2.17	8	(1), (2, 8), (3), (4), (5), (6), (7)	7
	2	6.33	18		
	3	6	10		
	4	3.75	10		
	5	12.08	8		
	6	11.83	14		
	7	3.33	18		
	8	6.33	18		
12	1	0.83	12	(1), (2), (3), (4), (5), (6), (7, 8)	7
	2	14.33	14		
	3	18.50	8		
	4	2.33	16		
	5	7.75	12		
	6	10.50	6		
	7	6.33	18		
	8	6.33	18		

(continued)

Table 3 (continued)

Chain number	Link number	Linkage coordinates		Distinct mechanisms	Number of inversions
		Total attached linkage (TAL)	Total detached linkage (TDL)		
13	1	0.83	12	(1), (2), (3), (4), (5), (6), (7), (8)	8
	2	7.67	14		
	3	12.08	8		
	4	6	10		
	5	1	20		
	6	14.33	8		
	7	12.33	10		
	8	5.83	18		
14	1	0	16	1, (2, 8), (3, 7), (4, 6), 5	5
	2	10.17	10		
	3	18.50	8		
	4	4.83	16		
	5	10	12		
	6	4.83	16		
	7	18.50	8		
	8	10.17	10		
15	1	0	18	(1, 4), (2, 3, 5, 6, 7, 8)	2
	2	10	14		
	3	10	14		

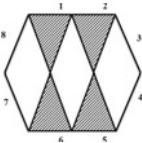
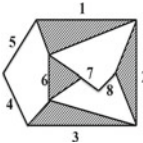
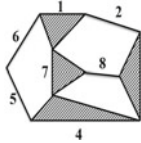
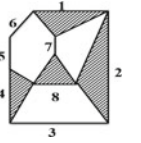
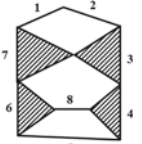
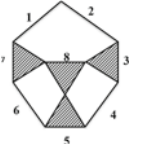
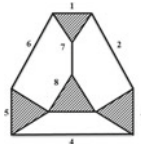
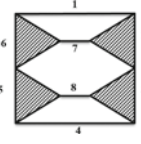
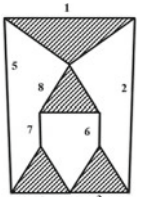
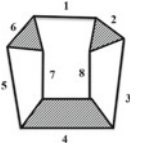
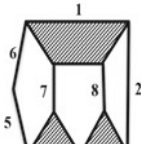
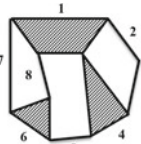
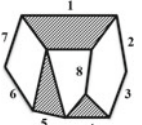
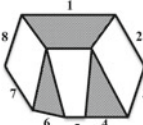
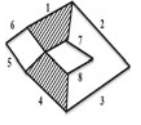
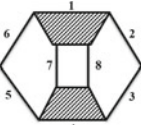
(continued)

Table 3 (continued)

Chain number	Link number	Linkage coordinates		Distinct mechanisms	Number of inversions
		Total attached linkage (TAL)	Total detached linkage (TDL)		
16	4	0	18	(1, 4), (2, 3, 5, 6), (7, 8)	3
	5	10	14		
	6	10	14		
	7	10	14		
	8	10	14		
	1	2	8		
	2	7.75	14		
	3	7.75	14		
Total number of inversions	4	2	8		71
	5	7.75	14		
	6	7.75	14		
	7	2	24		
	8	2	24		
	1	2	8		
	2	7.75	14		
	3	7.75	14		

Appendix

Distinct chains 8-link 1-DOF (16 no.)

			
Chain 1	Chain 2	Chain 3	Chain 4
			
Chain 5	Chain 6	Chain 7	Chain 8
			
Chain 9	Chain 10	Chain 11	Chain 12
			
Chain 13	Chain 14	Chain 15	Chain 16

References

1. Rao AC, Varada Raju D (1991) Application of the hamming number technique to detect isomorphism among kinematic chains and inversions. *Mech Mach Theory* 26(1):55–75
2. Kui CJ, Qing CW (1994) Identification of Isomorphism among kinematic chains and inversions using link's adjacent-chain-table. *Mech Mach Theory* 29(1):53–58
3. Rao AC (2000) Application of fuzzy logic for the study of isomorphism, inversions, symmetry, parallelism and mobility in kinematic chains. *Mech Mach Theory* 35:1103–1116
4. Ali H, Khan RA, Dargar AK (2007) Isomorphism and inversions of kinematic chains up to 10-Links. In: 13th national conference on mechanisms and machines (NaCoMM07), IISc, Bangalore, India

5. Mohammad A, Khan RA, Agrawal VP (2007) Identification of kinematic chains and distinct mechanisms using extended adjacency matrix. *Proc IMechE Part C J Mech Eng Sci* 221:81–88
6. Bedi GS, Sanyal S (2010) Joint connectivity: a new approach for detection of isomorphism and inversions of planar kinematic chains. *J Inst Eng (India)* 90:23–26
7. Sanyal S (2011) Structural identification of distinct inversions of planar kinematic chains. *IJUM Eng J* 85–92
8. Bal JS, Deshmukh PB, Jagadeesh A (2013) Link invariant functions and detection of isomorphism and inversions of kinematic chains. In: *Proceedings of the 1st international and 16th national conference on machines and mechanisms (iNaCoMM2013)*, IIT Roorkee, India
9. Hasan A (2013) Determination of the distinct mechanisms from a given kinematic chain. *i-Manager's J Mech Eng* 3(3):8–14. <https://doi.org/10.26634/jme.3.3.2366>
10. Rizvi SSH, Hasan A, Khan RA (2016) An efficient algorithm for distinct inversions and isomorphism detection in kinematic chains. *Persp Sci* 8:251–253
11. Rai RK, Punjabi S (2017) An elusive method to identify isomorphism and inversions of kinematic chains and mechanisms. *Indian J Sci Technol* 10(18):1–13
12. Shukla A, Sanyal S (2017) Gradient method for identification of isomorphism of planar kinematic chains. *Aust J Mech Eng*. <https://doi.org/10.1080/14484846.2017.1374815>
13. Kamesh VV (2018) A novel algorithm to find distinct mechanisms of a planar kinematic chain. *Int J Innov Res Explor* 5(2):27–31
14. Kamesh VV, Prasad DVSSSV (2020) A novel algorithm to find distinct mechanisms of a kinematic chain using link polynomial. In: *Proceedings of the national conference on recent technologies in engineering and basic sciences-2020 (NCRTEBS-2020)*. BVC Engineering College(A), Odalarevu, AP

Multi-objective Optimization of Machining Parameters in μ -EDM Drilling of SS317L Using Novel JAYA and TLBO Algorithms



V. Rajashekar and Shivraj Narayan Yeole 

Abstract Micro-electric discharge machining is a non-conventional electrothermal process used to produce microfeatures with precision and accuracy on difficult-to-cut materials. Efforts are made all over the globe for making the μ -EDM process robust for application through optimization. An attempt has been made to optimize the machining parameters of μ -EDM process using JAYA, teaching-learning-based optimization and novel multi-objective optimization techniques. To assess the performance of these algorithms, the results are compared with particle swarm optimization technique. The work focused on drilling of high-aspect-ratio microholes using brass electrode of 290 μm on Stainless Steel 317L (SS317L) as base material and deionized water as dielectric in an advanced EDM drill machine while minimizing surface roughness and overcut simultaneously. Optimum condition was produced at pulse-on time of 3.0776 μs , current of 1 A, servo voltage of 3 V and gap voltage of 30 V. JAYA algorithm produced optimum condition in a smaller number of generations compared to TLBO and PSO. Results showed that JAYA, TLBO and PSO are effective tools to obtain optimum condition for input parameters.

Keywords μ -EDM · Micromachining · MOO · TLBO · JAYA · PSO

Nomenclature

EDM	Electric discharge machining
μ -EDM	Micro-EDM
I_p	Current (A)
T_{on}	Pulse-on time (μs)
SV	Servo voltage (V)
GV	Gap voltage (V)

V. Rajashekar · S. N. Yeole (✉)

VNR Vignana Jyothi Institute of Engineering and Technology, Hyderabad, Telangana 500090, India

e-mail: shivrajyeole@vnrvjiet.in

SOO	Single-objective optimization
TLBO	Teaching-learning-based optimization
OC	Overcut (μm)
SR	Surface roughness (μm)
ANOVA	Analysis of variance
PSO	Particle swarm optimization
RSM	Response surface methodology
MOO	Multi-objective optimization

1 Introduction

Micromachining is a progressive technology employed in the creation of miniaturized components in the range of 1–999 μm dimensions. μ -EDM process has been prominently used for achieving precise and accurate miniaturized components [1]. μ -EDM is fundamentally similar to EDM process but with minor variation. Series of rapid spark discharges between tool and work which are immersed in dielectric remove the material. Initially, the dielectric medium is non-conductive and becomes conductive upon breakdown of dielectric strength. This happens because of the electrodes nearing each other, resulting in sparks between workpiece and tool, thereby removing material due to melting and evaporation process [2, 3]. Injection nozzles, spinneret holes and biomedical filters are some of the examples where μ -EDM holes are drilled successfully [3–5]. However, robustness of the process in terms of optimization is yet to be arrived. Optimization is an effective tool to utilize existing resources to improve productivity and quality and reduce cost and time [6].

Mohammad et al. and Ramversingh et al. have attempted to drill high-aspect-ratio holes using μ -EDM [7, 8]. Somashekhar et al. employed artificial neural network (ANN) in μ -EDM process for optimization [9]. Kalipada and Himanshu performed MOO using TLBO technique [10]. Lingxuan et al. utilized multi-objective genetic algorithm in μ -EDM process [11]. Manivannan and Pradeep have optimized μ -EDM process using TOPSIS [12].

Problem Definition: μ -EDM drilling is a well-established process for microdrilling of high-aspect-ratio holes with high accuracy and precision. Efficiency of MOO tools has been proved in different processes. But researchers have considered either high aspect ratio or MOO as the criteria for optimization, but combination of these is an open gap to work upon in μ -EDM. Hence, this paper presents high-aspect-ratio microdrilling of holes on difficult-to-cut material SS317L and MOO of parameters simultaneously. Novel MOO algorithms like TLBO [13] and JAYA [14] were employed and then compared with established PSO technique.

2 Experimentation

Advanced EDM drill machine (Make: Electronica, India) was used for drilling microholes with I_p , T_{on} , pulse-off time (T_{off}), SV and GV as input variables.

Materials: Power plants and chemical industries deal with continuous flow of liquids. Materials like SS317L that have high corrosion resistance and can sustain high temperatures are recommendable [15]. Table 1 depicts chemical composition of SS317L material. Electrode material used was tubular brass of 290 μm diameter and length 400 mm due to its effectiveness in μ -EDM [3]. Figures 1 and 2 represent specimen of rectangular cross section with 110 mm \times 10 mm \times 5 mm.

For each experiment, a separate electrode was used because of erosion of electrode. Depth of hole was kept 5 mm to achieve high aspect ratio of 17.24.

Table 1 Chemical composition of SS317L

Element	C	Mn	Si	S	P	Cr	Ni	Mo	Fe
Concentration (%)	0.03	1.88	0.27	0.01	0.008	18.67	11.52	3.22	64.392

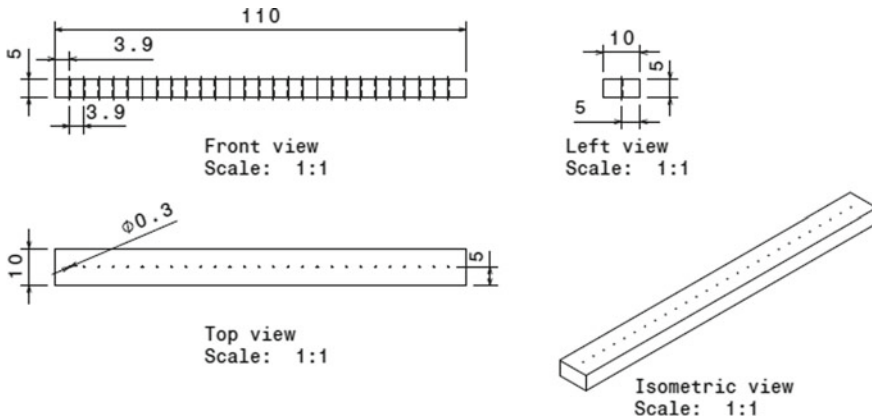


Fig. 1 Specimen dimensions

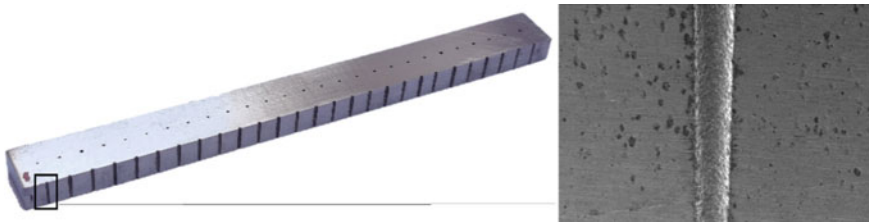


Fig. 2 Drilled workpiece with SEM image

Table 2 Input variables' range

Variables\range	Low	Medium	High
T_{on}	2	4	6
I_p	1	2	3
SV	3	4	5
GV	30	40	50

Input variables: Input variables considered are I_p , T_{on} , SV and V as these have been found to influence μ -EDM [2, 3, 6–10]. Ranges of each parameter are determined by performing trial experimentation.

Experimental Design: Experiments were designed using RSM-based Box–Behnken design (BBD) so as to identify relationship between response and input variables [16]. BBD experimental design consisted of 27 experiments based on four variables at three levels as shown in Table 2. MINITAB 19 statistical software was used for creating design. Experiments were performed, and response variables calculated are shown in Table 3.

Response variables: SR has major role in corrosive resistance, i.e., lower SR provides late corrosion. Hence, SR has been chosen as output parameter along with overcut as lesser OC is recommended; it was measured using Eq. 1 [17].

$$OC = \frac{|D_e - D_h|}{2} \quad (1)$$

where D_e —diameter of electrode (mm), D_h —average DOH at entry and exit (mm) and h —depth of hole. DOH was measured from SEM images as shown in Fig. 3.

SR was measured using CCI non-contact surface profiler on the split microholes drilled by placing two pieces together as shown in Fig. 2.

3 Results and Discussion

3.1 RSM Analysis for OC

According to experimental design, responses are evaluated as shown in Table 4. Second-order polynomial equation was developed by calculating the regression coefficients for OC. Regression equation for OC is shown in Eq. 2.

$$\begin{aligned}
 OC = & -134.4 + (0.65 * T_{on}) + (64.5 * I_p) + (123.1 * SV) \\
 & - (5.50 * GV) + (3.758 * T_{on} * T_{on}) + (6.03 * I_p * I_p) - (7.74 * SV * SV) \\
 & + (0.1492 * GV * GV) - (5.37 * T_{on} * I_p) - (5.04 * T_{on} * SV) \\
 & + (0.043 * T_{on} * GV) - (2.96 * I_p * SV) - (1.242 * I_p * GV) - (0.954 * SV * GV) \quad (2)
 \end{aligned}$$

Table 3 Design of experiments and response variables

S. No.	T_{on}	I_p	SV	GV	OC (μm)	SR (μm)
1	2	1	4	40	73.03611	10.9423
2	6	1	4	40	105.625	11.9335
3	2	3	4	40	110.3589	12.2567
4	6	3	4	40	100.00231	12.6527
5	4	2	3	30	72.108	11.2597
6	4	2	5	30	84.2356	12.1655
7	4	2	3	50	101.5821	12.1491
8	4	2	5	50	75.5655	12.7921
9	2	2	4	30	109.5341	11.0123
10	6	2	4	30	106.6708	12.0679
11	2	2	4	50	108.6404	12.1323
12	6	2	4	50	109.2292	12.4639
13	4	1	3	40	72.17769	11.2076
14	4	3	3	40	85.9993	12.2556
15	4	1	5	40	73.65247	12.0132
16	4	3	5	40	75.6252	12.9988
17	2	2	3	40	70.6167	11.0757
18	6	2	3	40	99.29836	12.1501
19	2	2	5	40	84.0724	12.2309
20	6	2	5	40	72.4295	12.5437
21	4	1	4	30	74.263	10.8593
22	4	3	4	30	109.1456	12.4583
23	4	1	4	50	106.2052	12.1995
24	4	3	4	50	91.4027	12.6341
25	4	2	4	40	77.3285	11.8876
26	4	2	4	40	78.3698	11.8876
27	4	2	4	40	73.3698	11.8876

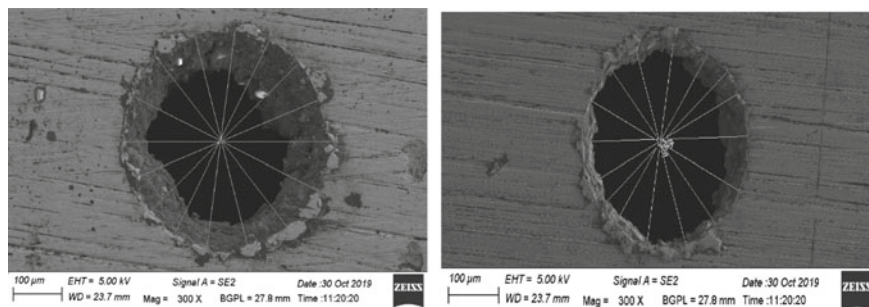
**Fig. 3** Calculation of hole diameters at entry and exit positions

Table 4 ANOVA before backward elimination

Source	DF	Adj SS	Adj MS	F-value	P-value
Model	14	5896.42	421.17	19.81	0.000 (Significant)
Linear	4	715.85	178.96	8.42	0.002
T_{on}	1	114.06	114.06	5.36	0.039
I_p	1	380.53	380.53	17.89	0.001
SV	1	109.21	109.21	5.14	0.043
GV	1	112.05	112.05	5.27	0.041
Square	4	3294.00	823.50	38.72	0.000
$T_{on} * T_{on}$	1	1205.29	1205.29	56.68	0.000
$I_p * I_p$	1	193.96	193.96	9.12	0.011
SV * SV	1	319.16	319.16	15.01	0.002
GV * GV	1	1186.69	1186.69	55.80	0.000
2-way interaction	6	1886.57	314.43	14.79	0.000
$T_{on} * I_p$	1	461.08	461.08	21.68	0.001
$T_{on} * SV$	1	406.52	406.52	19.12	0.001
$T_{on} * GV$	1	2.98	2.98	0.14	0.715
$I_p * SV$	1	35.10	35.10	1.65	0.223
$I_p * GV$	1	617.15	617.15	29.02	0.000
SV * GV	1	363.75	363.75	17.10	0.001
Error	12	255.19	21.27		
Lack-of-fit	10	241.27	24.13	3.47	0.245 (Not significant)
Pure error	2	13.92	6.96		
Total	26	6151.61			

ANOVA was performed on the data. Table 5 shows that the model has a P -value < 0.1 indicating significance and lack-of-fit P -value > 0.1 indicating insignificance. The developed model has prominent effect on responses. Confidence level (R^2) of model was 95.85%. Larger F -value and smaller P -values indicated that corresponding coefficients are prominently significant [18]. $T_{on} * GV$ and $I_p * SV$ were found to be insignificant and removed by using backward elimination process (BEP) and modified model as shown in Eq. 3.

$$\begin{aligned}
 OC = & -117.6 + (2.37 * T_{on}) + (52.7 * I_p) + (117.2 * SV) - (5.33 * GV) \\
 & + (3.758 * T_{on} * T_{on}) + (6.03 * I_p * I_p) - (7.74 * SV * SV) \\
 & + (0.1492 * GV * GV) - (5.37 * T_{on} * I_p) - (5.04 * T_{on} * SV) \\
 & - (1.242 * I_p * GV) - (0.954 * SV * GV)
 \end{aligned} \tag{3}$$

Table 6 shows ANOVA of modified model indicating improvement in F -value to 23.21 as compared to 19.81 (Table 5). R^2 of modified model was 95.23%.

Table 5 ANOVA after backward elimination

Source	DF	Adj SS	Adj MS	F-value	P-value
Model	12	5858.34	488.20	23.31	0.000 (Significant)
Linear	4	715.85	178.96	8.54	0.001
T_{on}	1	114.06	114.06	5.45	0.035
I_p	1	380.53	380.53	18.17	0.001
SV	1	109.21	109.21	5.21	0.039
GV	1	112.05	112.05	5.35	0.036
Square	4	3294.00	823.50	39.31	0.000
$T_{on} * T_{on}$	1	1205.29	1205.29	57.54	0.000
$I_p * I_p$	1	193.96	193.96	9.26	0.009
SV * SV	1	319.16	319.16	15.24	0.002
GV * GV	1	1186.69	1186.69	56.65	0.000
2-way interaction	4	1848.49	462.12	22.06	0.000
$T_{on} * I_p$	1	461.08	461.08	22.01	0.000
$T_{on} * SV$	1	406.52	406.52	19.41	0.001
$I_p * GV$	1	617.15	617.15	29.46	0.000
SV * GV	1	363.75	363.75	17.36	0.001
Error	14	293.27	20.95		
Lack-of-fit	12	279.35	23.28	3.35	0.253 (Not significant)
Pure error	2	13.92	6.96		
Total	26	6151.61			

Effect of parameters on OC: Figure 4 shows impact of pulse parameters on OC during microhole drilling on SS317L material. OC initially decreased with increase of T_{on} and GV later increased with increase of T_{on} and GV because of extension of the plasma channel which appeared to be more severe in areas around the tool. OC was noted to initially decrease, but later increase with higher I_p . Such activity was due to less energy dissipation at lower I_p , which rose steadily with increase in I_p . From 3 to 4 V of SV, OC increased, and from 4 to 5 V of SV, OC decreased. At 5 V, holes were produced with less OC.

3.2 RSM Analysis for SR

Equation 4 represents the second-order polynomial equation for SR.

$$\begin{aligned}
 SR = & 35.53 - (3.760 * T_{on}) - (1.745 * I_p) - (1.534 * SV) - (0.5161 * GV) \\
 & + (0.3322 * T_{on} * T_{on}) - (0.1581 * I_p * I_p) - (0.0485 * SV * SV)
 \end{aligned}$$

Table 6 ANOVA before elimination of not-significant variables

Source	DF	Adj SS	Adj MS	F-value	P-value
Model	14	17.4922	1.24945	23.89	0.000 (Significant)
Linear	4	1.7605	0.44012	8.41	0.002
T_{on}	1	0.2707	0.27073	5.18	0.042
I_p	1	0.2064	0.20642	3.95	0.070
SV	1	0.8222	0.82225	15.72	0.002
GV	1	0.4611	0.46107	8.81	0.012
Square	4	13.1243	3.28107	62.72	0.000
$T_{on} * T_{on}$	1	9.4149	9.41489	179.98	0.000
$I_p * I_p$	1	0.1334	0.13338	2.55	0.136
SV * SV	1	0.0126	0.01257	0.24	0.633
GV * GV	1	1.7339	1.73386	33.15	0.000
2-way interaction	6	2.6075	0.43458	8.31	0.001
$T_{on} * I_p$	1	1.8285	1.82853	34.96	0.000
$T_{on} * SV$	1	0.0994	0.09935	1.90	0.193
$T_{on} * GV$	1	0.0013	0.00130	0.02	0.877
$I_p * SV$	1	0.5075	0.50754	9.70	0.009
$I_p * GV$	1	0.0705	0.07050	1.35	0.268
SV * GV	1	0.1002	0.10024	1.92	0.191
Error	12	0.6277	0.05231		
Lack-of-fit	10	0.6073	0.06073	5.95	0.152 (Not significant)
Pure error	2	0.0204	0.01021		
Total	26	18.1200			

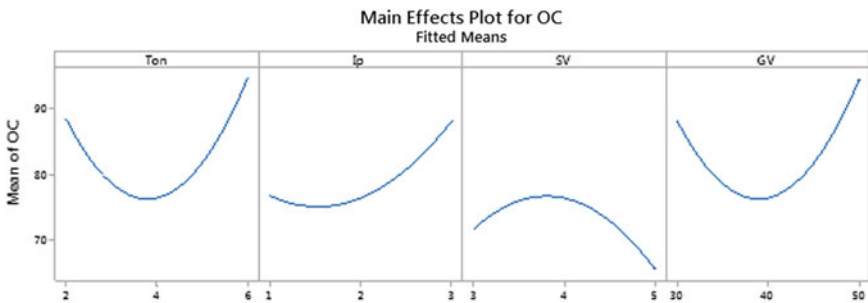


Fig. 4 Main effect plots for OC

$$\begin{aligned}
 &+ (0.005702 * GV * GV) + (0.3381 * T_{on} * I_p) + (0.0788 * T_{on} * SV) \\
 &+ (0.00090 * T_{on} * GV) + (0.356 * I_p * SV) \\
 &- (0.0133 * I_p * GV) + (0.0158 * SV * GV)
 \end{aligned} \tag{4}$$

Significance of data was determined by ANOVA and presented in Table 7. Model was found to be significant and lack-of-fit insignificant, so model indicated prominent effect on responses. R^2 of model was 96.54%. Terms $I_p * I_p$, $SV * SV$, $T_{on} * SV$, $T_{on} * GV$, $I_p * GV$ and $SV * GV$ were found to be insignificant and removed by using BEP and modified model as shown in Eq. 5.

$$\begin{aligned}
 SR = &34.96 - (3.512 * T_{on}) - (2.908 * I_p) - (0.974 * SV) \\
 &- (0.5171 * GV) + (0.3451 * T_{on} * T_{on}) \\
 &+ (0.00621 * GV * GV) \\
 &+ (0.3381 * T_{on} * I_p) + (0.356 * I_p * SV)
 \end{aligned} \tag{5}$$

Table 8 shows ANOVA of modified model. F-value improved to 37.23 compared to 23.89 (Table 7). R^2 of modified model was 94.30%.

Effect of parameters on SR: Figure 5 shows influence of process parameters on SR. SR initially decreased with increase of T_{on} and GV, later increased with increase in T_{on} and GV due to concentration of debris in microhole. SR was noted to initially

Table 7 ANOVA after elimination of not-significant variables

Source	DF	Adj SS	Adj MS	F-value	P-value
Model	8	17.0874	2.1359	37.23	0.000 (Significant)
Linear	4	1.7605	0.4401	7.67	0.001
T_{on}	1	0.2707	0.2707	4.72	0.043
I_p	1	0.2064	0.2064	3.60	0.074
SV	1	0.8222	0.8222	14.33	0.001
GV	1	0.4611	0.4611	8.04	0.011
Square	2	12.9908	6.4954	113.23	0.000
$T_{on} * T_{on}$	1	12.1937	12.1937	212.56	0.000
GV * GV	1	2.4748	2.4748	43.14	0.000
2-way interaction	2	2.3361	1.1680	20.36	0.000
$T_{on} * I_p$	1	1.8285	1.8285	31.87	0.000
$I_p * SV$	1	0.5075	0.5075	8.85	0.008
Error	18	1.0326	0.0574		
Lack-of-fit	16	1.0122	0.0633	6.20	0.148 (Not significant)
Pure error	2	0.0204	0.0102		
Total	26	18.1200			

Table 8 Optimization tables using JAYA, TLBO and PSO

Iteration	Z-value using JAYA	Z-value using TLBO	Z-value using PSO
1	4.325	4.2257	4.7359
5	4.2186	4.2187	4.3694
7	4.2186	4.2186	4.2543
10	4.2186	4.2186	4.2186
50	4.2186	4.2186	4.2186

Bold value indicates the MOO (Multi-Objective Optimization) function Z value (4.2186) obtained in 5th iteration of JAYA algorithm, 7th iteration of TLBO algorithm and 10th iteration of PSO algorithm

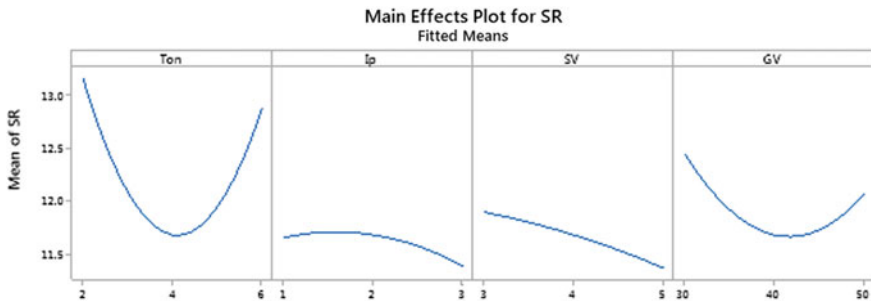


Fig. 5 Main effect plots for SR

increase but later decrease with higher I_p . This can be attributed to less energy dissipation at lower I_p , which decreases steadily with more I_p rise. From 3 to 5 V of SV, SR depicted decreasing trend. At 5 V, holes were produced with less SR.

3.3 Formulation of MOO Function:

Two objectives (minimum OC and minimum SR) were considered concurrently for MOO. The function was formulated using weighted sum method for converting individual objectives into SOO function as per equation [16].

$$Z = W1 * \left(\frac{OC}{OC(\min)} \right) + W2 * \left(\frac{SR}{SR(\min)} \right) \tag{6}$$

where W1 and W2 are weights of factors, and SR (min) and OC (min) are minimum values of each objective. These are optimized values of each objective. Equal weights are used for each objective on the basis of applications of SS317L, where corrosive resistance is important (chemical containers and biomedical implants [18]). On the

other hand, μ -EDM process has wide variety applications (fuel injection nozzles, [3–5]), where OC should minimum. Weights of each objective are calculated by analytical hierarchy process (AHP), weights are $W1 = 0.5$ and $W2 = 0.5$, and after each objective optimization, optimum values are OC (min) = 52.0894 μm and SR (min) = 11.0497 μm ; normalized MOO function (Z) is as given in Eq. 7.

$$\begin{aligned}
 Z = & 0.4730378 - (0.138154741 * T_{\text{on}}) + (0.372545424 * I_{\text{p}}) \\
 & + (1.080171397 * SV) + (0.027462578 * GV) \\
 & + (0.051876915 * T_{\text{on}} * T_{\text{on}}) + (0.057871259 * I_{\text{p}} * I_{\text{p}}) \\
 & - (0.074282512 * SV * SV) + (0.00171486 * GV * GV) \\
 & - (0.036047244 * T_{\text{on}} * I_{\text{p}}) - (0.048370008 * T_{\text{on}} * SV) \\
 & + (0.016309925 * I_{\text{p}} * SV) - (0.011919752 * I_{\text{p}} * GV) \\
 & - (0.009155751 * SV * GV)
 \end{aligned} \tag{7}$$

Teaching-Learning-Based Optimization (TLBO): R. Venkata Rao developed TLBO algorithm [13] based on the concept of classroom. It has two segments, i.e., teacher and learner, respectively. Teacher tries to improve average performance of class n teachers' phase, whereas in learners' phase, learners improve their performance by interacting among themselves [13]. TLBO flowchart is represented in Fig. 6.

JAYA algorithm: R. Venkata Rao developed JAYA algorithm (2016) by modifying variables using an equation in single step [14]. JAYA algorithm flowchart is depicted in Fig. 7.

Equation 7 was taken as the MO fitness function for TLBO and JAYA algorithms, and lower and upper limits were retained as in experimentation. MATLAB R2019a was used for creating the TLBO and JAYA codes. Population was taken as 27, number of design variables as 4 and number of iterations as 50 for both algorithms. Optimum condition was obtained at T_{on} of 3.077 μs , I_{p} of 1 A, SV of 3 V and GV of 30 V. MOO fitness function (Z) value at optimum condition was 4.2186 in case of both algorithms, as shown in Table 8.

Particle Swarm Optimization (PSO): For comparing performance of TLBO and JAYA algorithms with an established algorithm, PSO [19] was employed using same MO fitness function Z (Eq. 7). Code for PSO was created using MATLAB R2019a. Same inputs were used as that of previous case. Optimum condition was obtained at T_{on} of 3.0776 μs , I_{p} of 1 V, SV of 3 V and GV of 30 V at 10th iteration. MOO function value (Z) was shown in Table 8.

It was found that JAYA and TLBO algorithms produced optimum condition in a smaller number of iterations as compared to that of PSO thereby proving the efficiency of the novel algorithms. JAYA algorithm was found to be the most efficient among the three algorithms. OC and SR values obtained at the optimum condition are shown in Table 9.

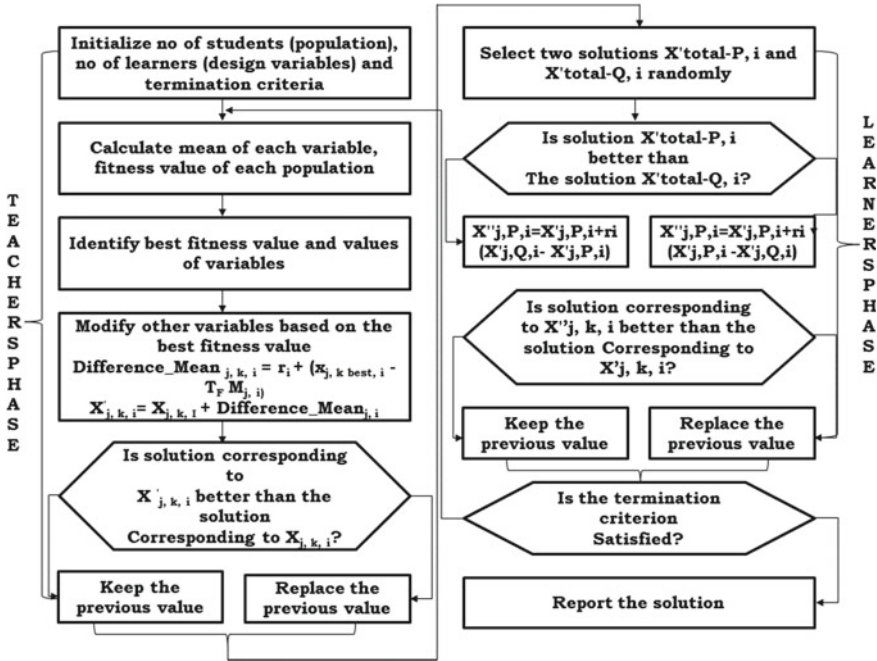


Fig. 6 Flowchart of TLBO algorithm. Source Venkata Rao, p. 21 [13]

4 Conclusions

The current research work aimed at simultaneous minimization of OC and SR in microhole drilling of SS317L using μ -EDM process. Experimentation was carried out using BBD of RSM with input design variables as T_{on} , I_p , SV and GV. Quadratic expression for OC and SR was generated using RSM. Significant and not-significant factors were identified using ANOVA. It was observed that overcut was influenced by T_{on} , I_p , SV and GV, whereas surface roughness was highly influenced by T_{on} and GV as compared to I_p and SV. Weighted sum approach was employed for combining OC and SR functions into a single function. AHP process was used to check correctness of weights. Combined objective function was optimized using TLBO, JAYA and PSO algorithms. The optimum condition was obtained at 3.0776 μ s of T_{on} , 1 A of I_p , 3 V of SV and 30 V of GV. At this MO optimum condition, fitness function value of OC was 54.1047 μ m and SR was 13.79335 μ m. TLBO and JAYA algorithms gave the optimum condition in a smaller number of iterations as compared to PSO. JAYA algorithm has good convergence rate and less complexity compared to other two algorithms, TLBO and PSO.

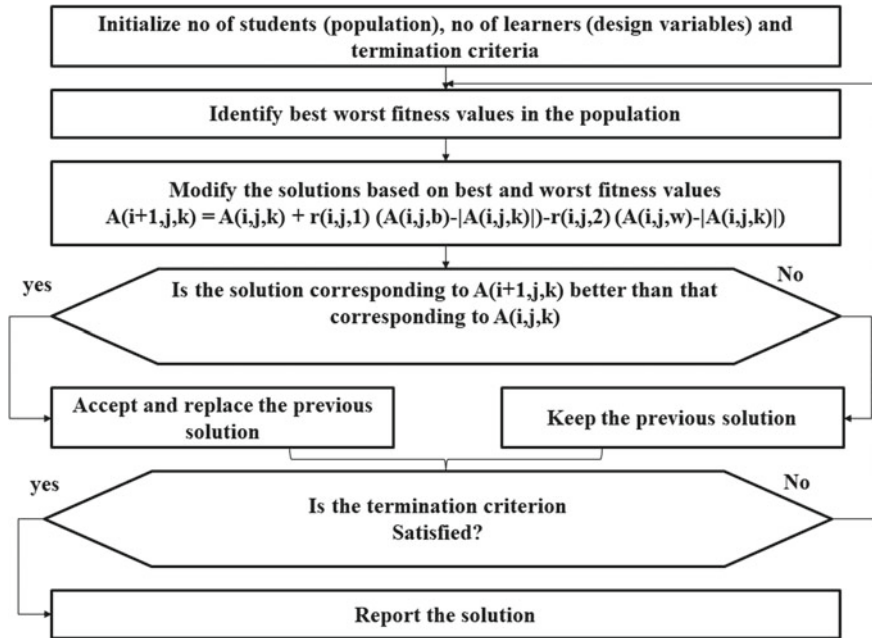


Fig. 7 Flowchart of JAYA algorithm. Source Venkata Rao, p. 17 [14]

Table 9 OC and SR at optimum condition

Design variable	T_{on}	I_p	SV	GV	OC (μm)	SR (μm)
Optimum condition	3.0776	1	3	30	54.1047	13.79335

Acknowledgements Authors convey their appreciation to S.N.R.M. EDM Drill works, Balanagar, Hyderabad, for valuable assistance and support in carrying out experiments. Sincere appreciation to ARCI Balapur, Hyderabad, for allowing to use their facilities. Finally, authors acknowledge the support of all faculty and students who were involved in direct or indirect completion of research work.

References

- Masuzawa T, Tönshoff HK (1997) Three-dimensional micromachining by machine tools. CIRP Ann 46(2):621–628
- Shivraj Narayan Y, Nagabhushana Ramesh N, Balu Naik B, Ramya A (2018) Pulse parameter characterization in microdrilling of maraging steel 300 alloy. In: Li B et al (eds) Characterization of minerals, metals, and materials 2018. TMS 2018, pp 387–398
- Oliaei SNB, Jahan MP, Perveen A (2019) Micro-EDM Drilling. In: Kibria G, Jahan M, Bhattacharyya B (eds) Micro-electrical discharge machining processes. Materials forming, machining and tribology. Springer, Singapore

4. Jahan MP, Wong YS, Rahman M (2010) A comparative experimental investigation of deep-hole micro-EDM drilling capability for cemented carbide (WC-Co) against austenitic stainless steel (SUS 304). *Int J Adv Manuf Technol* 46:1145–1160
5. Masuzawa T (2000) State of the art of micromachining. *CIRP Ann* 49(2):473–488
6. Mukherjee I, Kumar Ray P (2006) A review of optimization techniques in metal cutting processes. *Comput Ind Eng* 50:15–34
7. Ali MY, Rahman B, Adnan N (2016) High aspect ratio micro-EDM drilling with nano surface finish. In: Yacob N, Mohamed M, Megat Hanafiah M (eds) *Regional conference on science, technology and social sciences*. Springer, Singapore
8. Ramversingh A, Pradeep (2020) EDM of high aspect ratio micro-holes on Ti-6Al-4V alloy by synchronizing energy interactions. *Mater Manuf Process* 1–16
9. Somashekhar KP, Ramachandran N, Jose M (2010) Optimization of material removal rate in micro-EDM using artificial neural network and genetic algorithms. *Mater Manuf Process* 25:467–475
10. Maity K, Himanshu (2018) ANN modelling and Elitist teaching learning approach for multi-objective optimization of μ -EDM. *J Intell Manuf* 29:1599–1616
11. Zhang L, Jia Z, Wang F et al (2010) A hybrid model using supporting vector machine and multi-objective genetic algorithm for processing parameters optimization in micro-EDM. *Int J Adv Manuf Technol* 51:575–586
12. Manivannan R, Kumar MP (2016) Multi-response optimization of micro-EDM process parameters on AISI304 steel using TOPSIS. *J Mech Sci Technol* 30:137–144
13. Rao RV (2016) Teaching-learning-based optimization algorithm. In: *Teaching learning based optimization algorithm*. Springer, Cham
14. Rao RV (2019) *Jaya: an advanced optimization algorithm and its engineering applications*. Springer International Publishing, Cham
15. Groyzman A (2017) Corrosion failures and solutions at units. In: *Corrosion problems and solutions in oil refining and petrochemical industry. Topics in safety, risk, reliability and quality*, vol 32. Springer, Cham
16. Sahu N, Andhare A (2019) Multiobjective optimization for improving machinability of Ti-6Al-4V using RSM and advanced algorithms. *J Comput Des Eng* 6:1–12
17. Jahan M, Yoke S, Rahman (2010) A comparative experimental investigation of deep-hole micro-EDM drilling capability for cemented carbide (WC-Co) against austenitic stainless steel (SUS 304). *Int J Adv Manuf Tech* 46:1145–1116
18. Wang M, Li W, You C, Wang Qi, Zeng X, Chen M (2017) Triboelectric nanogenerator based on 317L stainless steel and ethyl cellulose for biomedical applications. *RSC Adv* 7(11):6772–6779
19. Lee Kwang Y, Jong-Bae P (2006) Application of particle swarm optimization to economic dispatch problem: advantages and disadvantages. In: *2006 IEEE PES power systems conference and exposition*. IEEE, pp 188–192

Effect of Inelasticity on Buckling of Axially Compressed Cylindrical Shell



Ishita 

Abstract The idea behind this research is that in experiments, we cannot separate plasticity of a material, but in FEA software we can. FE models are developed such that their buckling load according to classical theory is higher than yield point. It is first analyzed with linear elastic material model and then linear elastic-nonlinear plastic, and results are compared to study effects of plasticity. Material model is developed by using nonlinear kinematic hardening equations for 2024 T3 alloy of aluminum at room temperature (25 °C). To find inelastic critical buckling loads, an iterative method related to reduced modulus theory is tried for three different shell thickness, though it was a failure. The results of analysis show that there is an expected reduction of buckling load when plasticity is considered which in some cases could be about nine times of further reduction when imperfections are considered, so there is a need for a better theoretical model which would consider plasticity. The idea is maybe by studying inelastic load values we could get some insight on how to deal with theoretical equations or what kind of results should come.

Keywords Buckling · Inelastic · Finite element analysis

1 Introduction

This paper presents research into inelastic buckling of cylindrical shells under static axial compressive loads. This type of structure is found in launch vehicles, rockets, etc. Slope of load-displacement curve represents stiffness of the component, and negative stiffness is an indication of instability in the system (load decreases as deflection increases). One of the major design considerations in cylindrical shells is their stability under static axial loading, especially if loads are near buckling points, very small disturbance can make structure unstable and force it to change from one equilibrium configuration to another of a different nature suddenly. In stable structures, when load is released after first buckling, system may regain its shape

Ishita (✉)

Delhi Technological University, Shahbad Daulatpur village, Rohini, Delhi 110042, India

© The Author(s), under exclusive license to Springer Nature Singapore Pte Ltd. 2022

1377

K. Govindan et al. (eds.), *Advances in Mechanical and Materials Technology*,

Lecture Notes in Mechanical Engineering,

https://doi.org/10.1007/978-981-16-2794-1_116

but for unstable structures, there is no turning back. In load deflection curves, peak represents unstable, valleys stable, and saddle points neutral equilibrium.

The classical theories refer to buckling in elastic range and do not take plasticity and yielding into account. To consider plasticity, reduced modulus theories are used where elastic modulus is replaced by an equivalent modulus to take plasticity into account. But this is not completely right as buckling of shells is highly local phenomenon as explained later in regards to Eq. (1), and it is possible that though globally structure has not buckled, locally a section of it has crossed yielding stresses due to deformation if not loading. The formulas in classical theories highly overestimate the buckling loads, and in real life, there could be external disturbances or stress concentration at points as well. Shells have membrane stiffness which are a lot greater than bending, and if this membrane strain energy has to be released as equivalent bending stiffness energy, the shell will deform drastically. So there is a possibility of yielding at multiple points in prebuckling and postbuckling range which would affect the buckling load.

Donnel [1] in 1936 developed a large deformation theory which could develop formulations, which would take into account effect of initial geometric imperfections. He did not measure initial deflections in tests, but it was shown that most of the differences in theory and results can be explained if it is assumed that initial deflections are in the form of double harmonic series (eg-Sin A * Cos B). The Eigen modes calculated are in the same form, and this explains using them to seed imperfections during analysis. Karman and Tsien in 1940 showed that large discrepancies between test and theory in some shell structures are related to highly unstable post buckling behavior. Koiter [2] developed general theory for elastic stability of systems in his doctoral thesis in 1945. He developed theories in postbuckling particularly initial postbuckling and connected buckling to stability of structures. Batdorf [3] in 1947 in his National Advisory Committee of Aeronautics (NACA) report presented modified uncoupled form of Donnel's equation for equilibrium of thin shells, which made calculations easier for different boundary conditions, and on ignoring higher order terms, a simplified formulas could be derived for different loading cases (Eq. (1) for axial loading). There is discussion on Batdorf parameter Z which is related to geometry of structure. Later in 1960 Weingarten, Seide and Morgan published a collection of experimental results which combined with Donnel's equations were base for NASA SP-8007 guideline [4] published and revised in 1960's. The guideline basically gives knockdown factors which should be multiplied by loads calculated by classical theory (Donnel and Batdorf) to get design load for use, as one of the major drawback of classical theory is that it highly overestimates practical loads.

$$P_{cr} = \frac{2\pi}{\sqrt{3(1-\mu^2)}} Et^2 \text{ for } Z > 2.28 \quad (1)$$

$$Z = \frac{l^2}{Rt} (1-\mu^2)^{\frac{1}{2}}$$

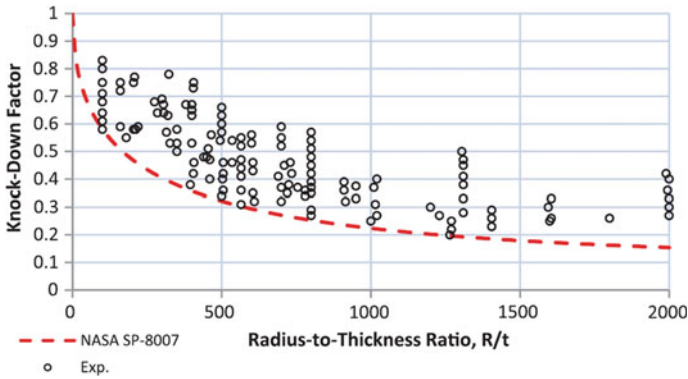


Fig. 1 Theoretical buckling load, and experimental results for different range of R/t ratio

where P_{cr} is critical buckling load, R is mean radius, t is thickness, l is length of cylinder, E is young’s modulus, and μ is Poisson’s ratio. As no length term is there in (1), it gives local buckling load. Knockdown factor is defined as ratio of actual buckling load P_{act} to theoretical P_{cr} , therefore value of one in Fig. 1 represents theoretical buckling load, and experimental results are shown for different range of R/t ratio. Equation (3) gives value for knockdown factor (Eq. 4).

$$\rho = \frac{P_{act}}{P_{cr}} \tag{2}$$

$$\rho = 1 - 0.901(1 - e^{-\phi}) \tag{3}$$

$$\phi = \frac{1}{16} \sqrt{\frac{R}{t}} \text{ for } \frac{R}{t} < 1500 \tag{4}$$

There are many factors responsible for discrepancy between theory and experiment like boundary conditions, initial geometric imperfections, plasticity and residual stresses, radius, and length of cylinder. Studying combination of these will tell the effects of each of them, which is now possible with computers; as in experiments, there is always a combination of parameters separating which is not practically possible. One such parameter is plasticity which could be easily removed or added in a software like ABAQUS as user can define material behavior.

From Eq. (1), we can see that ratio of buckling loads would be proportional to square of ratio of corresponding thickness for same material. It is checked if similar pattern is there for inelastic buckling, but it was rather a somewhat arithmetic progression with respect to thickness.

2 Material Model

Maximov et al. [5] developed constitutive models for 2024-T3 aluminum alloy at room and higher temperatures in order to be used in finite element analysis of cold hole working process. The material behavior in plastic range is described by nonlinear kinematic hardening model and verified with those of uniaxial tensile test. 2024-T3 aluminum alloy has a wide range of applications in aerospace industries for various structural shell type elements.

For this analysis in elastic region, linear behavior is considered, and for plastic region, a nonlinear model presented in [5] for 2024 T3 Al at different temperatures is used. Data is taken corresponding to room temperature (25 °C), and equations for kinematic hardening model are given as

$$\sigma^p = \frac{K}{\alpha} (1 - e^{-\alpha \varepsilon^p}) \quad (5)$$

$$\varepsilon^p = \varepsilon - \frac{\sigma_y}{E} \quad \sigma^p = \sigma - \sigma_y$$

where σ_y is true yield stress, K is kinematic hardening modulus, and α is a coefficient which defines rate of decrease of K with increase of the plastic deformation. Values of σ_y , K , and E at various temperatures with $\alpha = 10$ are given in [5]. For this analysis, these values at 25 °C are

$$\sigma_y = 369.47 \text{ MPa} \quad K = 2447.66 \text{ MPa} \quad E = 68563 \text{ MPa} \quad (6)$$

Stress–strain curve based on (5) and (6) is shown in Fig. 2.

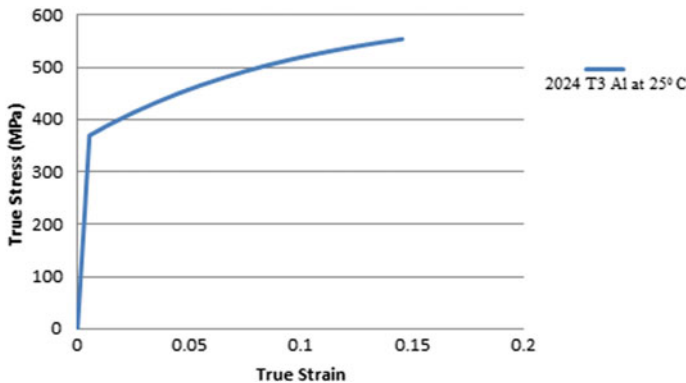


Fig. 2 True stress–strain curve for 2024 T3 aluminum alloy at 250 °C

3 Inelastic Buckling

In part four of an overview on shell buckling given by Brushnell [6], a rather thick aluminum cylinder under uniform axial deformation is discussed in which elastic–plastic buckle develops, and at later stages, it can be observed that deformations are concentrated at top end [4, 7] gives plasticity factors based on reduced modulus theory to be considered when buckling is in plastic range, but they do not give very accurate or at all a solution in all cases. Also these are for a range of t/R ratios, and one could create models for materials such that buckling loads are in plastic range according to classical theory and yet does not come in this t/R range.

An approximate solutions for inelastic buckling loads for axial compressions case are given in [4, 8, 7] for radius to thickness ratios such that there is chance of buckling to go into plastic range. In [7], the given range is $10 < \frac{R}{t} < 50$, although one of the ratios taken in this study is not in this range ($R = 100$ mm and $t = 1$ mm), but it is taken in a way that buckling stress falls between yielding and ultimate stresses for our material (2024 T3 Al) in uniaxial tensile test [8]. Then thickness of 2 and 3 mm are taken to compare which are in range, but results were still absurd.

A simple solution is provided in [7] to find inelastic stress (we can find load by multiplying it with $2\pi Rt$) for buckling as

$$\sigma_{cr|p} = \left(\frac{E_t E_s}{3(1 - \vartheta^2)} \right)^{1/2} \frac{t}{R} \tag{7}$$

where

$$E_s = \frac{\sigma}{\varepsilon} \quad E_t = \frac{d\sigma}{d\varepsilon}$$

$$\vartheta = \frac{1}{2} - \left(\frac{1}{2} - \mu \right) \frac{E_s}{E}$$

E_s and E_t are secant and tangent modulus, respectively, and are changing with stress, strain values on $\sigma - \varepsilon$ curve, therefore the solution of (7) is an iterative process. Let P be an assumed axial load then stress corresponding to it for pure axial compression will be $\sigma_a = \frac{P}{2\pi Rt}$, E_s and E_t are found corresponding to σ_a from $\sigma - \varepsilon$ curve, $\sigma_{cr|p}$ is calculated with these values and compared with assumed value σ_a , and if they are same, it is the solution if not another axial load is assumed till we get a solution. To find solution in this analysis, data points on stress–strain curve plotted in material modeling are taken as assumed values and critical stresses according to (7) were calculated (Table 1.), and it was found that this would not give a solution.

It can be seen from the table that values for critical stresses are not going to match. As critical stress is directly proportional to thickness, as we increase thickness, we will get in the range where this methods give some results (about 5 mm and above) but 2 mm is at boundary and 3 mm is clearly within the given range yet no results. Reference [7] did not take responsibility of accuracy of results.

Table 1 Iterative solution for buckling loads in plastic range

ϵ	$\sigma = \sigma_a$ (MPa)	$E_s = \frac{\sigma}{\epsilon}$ (MPa)	$E_t = \frac{d\sigma}{d\epsilon}$ (MPa)	σ_{cr} (MPa) t = 1 mm	σ_{cr} (MPa) t = 2 mm	σ_{cr} (MPa) t = 3 mm
0	0	68,563(E)	68,563(E)	419.34	838.68	1258.02
0.00538 (ϵ_y)	369.47	68,572.75	2447.7	79.2368	158.4736	237.7104
0.0054	369.47	68,420.37	2214.7	75.298	150.596	225.894
0.0154	392.7626	25,504.06	2004	45.8833	91.7666	137.6499
0.0254	413.8385	16,292.85	1813.3	35.3345	70.669	106.0035
0.0354	432.9089	12,229.06	1640.7	29.2934	58.5868	87.8802
0.0454	450.1644	9915.515	1484.6	25.1789	50.3578	75.5367
0.0554	465.7779	8407.543	1343.3	22.1054	44.2108	66.3162
0.0654	479.9056	7338.006	1215.5	19.6772	39.3544	59.0316
0.0754	492.6888	6534.334	1099.8	17.6848	35.3696	53.0544
0.0854	504.2555	5904.631	995.1	16.0067	32.0134	48.0201
0.0954	514.7216	5395.405	900.4	14.5663	29.1326	43.6989
0.1054	524.1916	4973.355	814.8	13.3125	26.625	39.9375
0.1154	532.7605	4616.642	737.2	12.2071	24.4142	36.6213
0.1254	540.5139	4310.318	667.1	11.2258	22.4516	33.6774
0.1354	547.5295	4043.792	603.6	10.3472	20.6944	31.0416
0.1454	553.8774	3809.336	2447.7	20.2311	40.4622	60.6933

4 FEM Analysis Results and Discussion

Three perfect thin cylindrical shells of radius 100 mm, length 200 mm, and thickness of 1, 2, and 3 mm is modeled in Abaqus 6.14. Aluminum alloy 2024 T3 is used with elastic modulus 68563 MPa (25 °C) and Poisson's ratio 0.33 for elastic model and for inelastic model stress–strain values from Table 1 are used as plastic material property. As Batdorf factors are greater than 2.28 in these cases, they are intermediate length cylinder. From classical theory, the buckling load is 263.47, 1053.91, and 2371.3 kN for shells of thickness 1 mm, 2 mm, and 3 mm, respectively. Cylinders are modeled with eight noded doubly curved shell element S8R5 having five degrees of freedom at each node and recommended for thin shell applications [9]. Boundary conditions are applied to the reference points tied to all the end nodes through rigid body tie constraint for convenience. Boundary conditions are clamped at both ends with one end free to move in axial direction.

Linear perturbation step is used to get first twenty Eigen modes in case of 1 mm thick shell which will later be used to seed imperfection with different imperfection amplitudes. Nonlinear (geometric nonlinearity is considered) analysis with static riks step is used to plot load versus end displacement curves for a perfect shell

(without any initial geometric imperfections) with (inelastic) and without (elastic) consideration of material nonlinearity in plastic range.

From Fig. 3a it can be observed that just by consideration of plastic data (for perfect shell), buckling load is reduced by 68.5 kN for 1 mm thick shell. It would further reduce when imperfections are considered. In Fig. 6, it can be seen that buckling load for imperfection size of 0.01 mm (1% thickness) buckling load is further decreased by 7.479 kN. It is quite clear that major decrease in buckling load from classical theory is due to plasticity rather than imperfections in this case. One could argue about imperfect shells with 10% imperfection amplitude should not be below NASA lower bound but that is quite high imperfection amplitude taken just to get some smooth curve to see postbuckling behavior.

In Fig. 4, deformation pattern for perfect elastic and inelastic shell is compared. It can be observed that when plasticity is considered deformations starts at ends where as it is in mid length when material nonlinearity is not considered. If we further compare it with Fig. 5 which shows a thick aluminum cylinder buckling into plastic range from an experiment, we can observe this similarity, though it was not pointed out in relation to plasticity by author [6]. It could be reasoned that due to clamping, there is stress concentration near ends. The material would cross yielding limit at points near ends earlier than at those further away or near mid length (Fig. 6).

From (1) if material, radius, and length are same and let P_e denote elastic load and P_{e1} , P_{e2} represent elastic load for t_1 , t_2 shell thickness, respectively, then

$$\frac{P_{e1}}{P_{e2}} = \left(\frac{t_1}{t_2}\right)^2 \quad (8)$$

Now let $t_1 = 1$ mm, $t_2 = 2$ mm, and $t_3 = 3$ mm and P_{i1} , P_{i2} represents inelastic loads. It could be seen from Table 2 that inelastic loads do not follow relation (8) in fact data follows more of an arithmetic progression with respect to thickness. On the other hand if one takes difference between elastic and inelastic buckling loads for each value of thickness, one might find a relation like (8) for different power. This study could be further extended with more data values to find some correlation.

5 Conclusion and Recommendation

1. There is a change in location of maximum lateral deformation from mid length to ends for perfect cylinders without and with plasticity considerations, respectively. It is recommended to study deformation patterns for different end conditions.
2. There was a case where drop in buckling load by consideration of plasticity for perfect body is higher than further drop due to imperfection. It is recommended to use this method of analysis for a lot of different material and geometric model combinations.

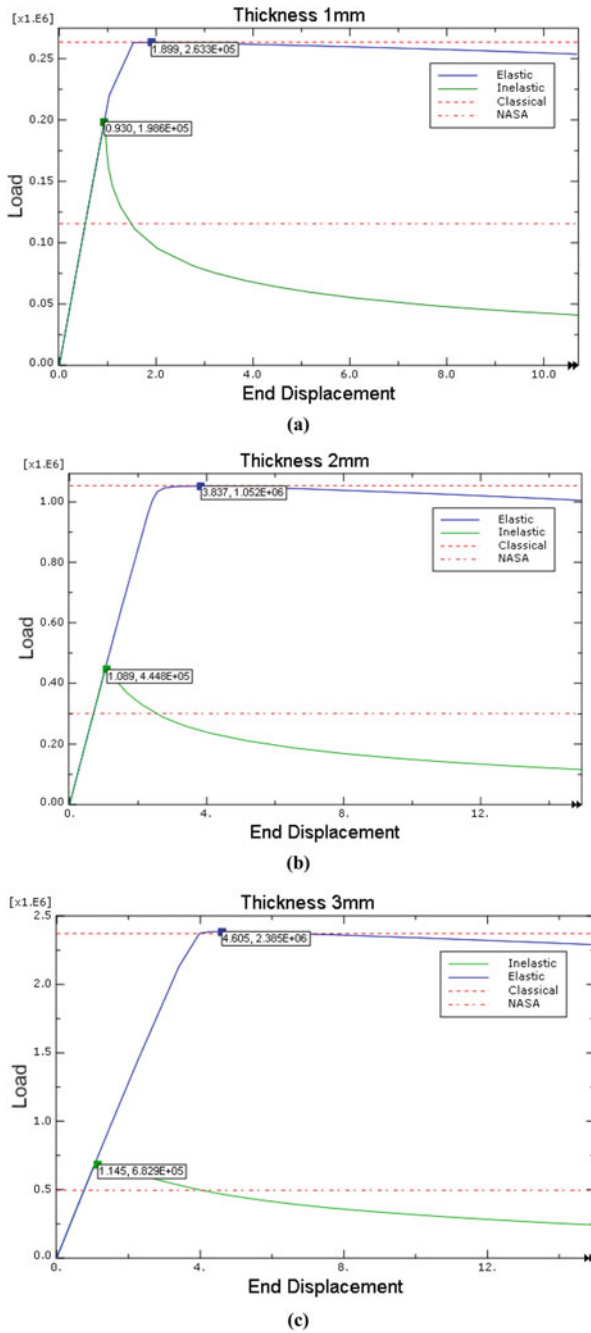


Fig. 3 Comparison of elastic and inelastic buckling for perfect shell of various thickness

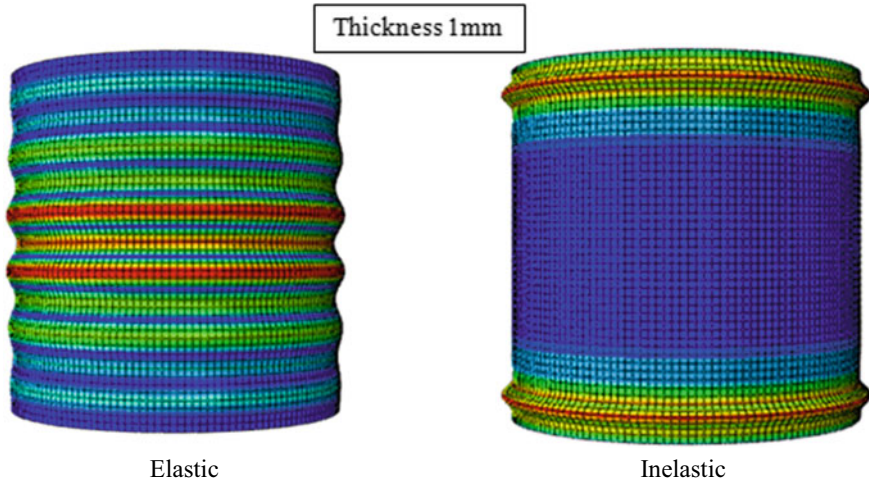


Fig. 4 Comparison of elastic and inelastic deformation pattern for perfect cylinder

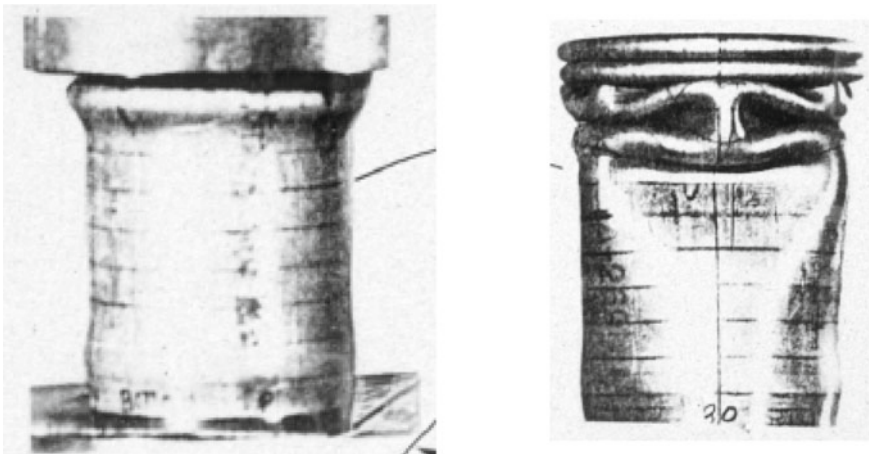


Fig. 5 Thick aluminum cylinder under uniform axial compression [6]

3. Though SP-8007 knockdowns are valid, the study indicate that a range of different values for same R/t ratio could be due to different material properties as well (elastic modulus of material does not affect knockdown factor as it is canceled out Eq. (2) but yield points could affect experimental output) other than random initial imperfections. This means following that guideline, one could be designing over safe structures with extra material mass, and this type of study might help us save material cost.
4. Ratio of elastic buckling loads is proportional to square of respective shell thickness if material and rest of the geometry is unchanged. Same is not true for

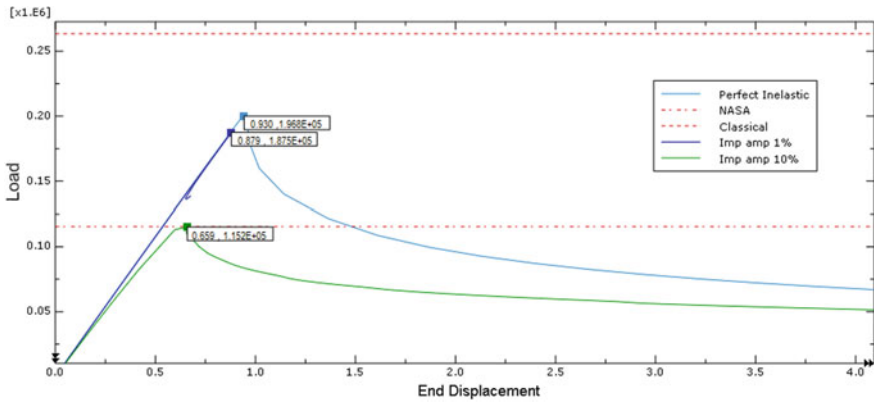


Fig. 6 Comparison of inelastic buckling for different imperfection amplitude

Table 2 Comparison of elastic and inelastic buckling loads for perfect shells

Thickness (mm)	Elastic load (P_e) in kN	Inelastic load(P_i) in kN
1	263.478	198.597
2	1053.915	444.839
3	2371.31	682.931

inelastic loads, in fact, they show somewhat an arithmetic progression patterns and difference in elastic and inelastic loads shows a higher order pattern. It is recommended to collect a lot more data to study it further for some correlation if any, it might give some insight for theoretical study.

References

1. Donnel LH. A new theory for buckling of thin cylinders under axial compression and bending, vol. 56. ASME. Akron OHIO, pp 795–806
2. Hutchinson JW, Koiter WT (1970) Postbuckling theory. Appl Mech Rev
3. Batdorf SB (1947) A Simplified method of elastic-stability analysis for thin cylindrical shells. NACA Report No. 874
4. Peterson JP, Seide P, Weingarten VI (1968) Buckling of thin-walled circular cylinders. Technical Report NASA SP-8007
5. Maximov JT et al (2014) Modeling of strain hardening and creep behavior of 2024T3 aluminium alloy at room and high temperatures. Comput Mater Sci 83:381–393
6. Bushnel D (1981) Buckling of shells-pitfall for designers. AIAA J 19(9):1183–1226
7. Griffin DS (1973) Inelastic and creep buckling of circular cylinders due to axial compression, bending, and twisting
8. Gerard G, Becker H (1957) Buckling of curved plates and shells. Handbook of structural stability part III, NACA TN, p 3738
9. Dassault Systemes Simulia Corp. Abaqus 6.14: Abaqus Benchmarks Guide

10. Timoshenko SP, Gere JM (1961) Theory of elastic stability, 2nd edn. McGraw-Hill, New York
11. Yoo CH, Lee SC (2011) Stability of structures-principles and applications. Elsevier publication
12. Dassault Systemes Simulia Corp. Abaqus 6.14: Abaqus Theory Guide
13. Dassault Systemes Simulia Corp. Abaqus 6.14: Abaqus Analysis User's Manual
14. Dassault Systemes Simulia Corp. Abaqus 6.14: Abaqus Example Problems Guide
15. Wagner HNR, Huhne C, Niemann S, Khakimova R (2017) Robust design criterion for axially loaded shells-simulation and validation. *Thin-Walled Struct* 115:154–167
16. Ye F. Local buckling analysis of thin-wall shell structures. Master thesis delft, University of Technology, 2 Nov 2015
17. Dassault Systemes Simulia Corp: Abaqus 6.14: Getting Started with Abaqus/CAE
18. Budiansky B (1974) Theory of buckling and postbuckling behaviour of elastic structure. *Adv Appl Mech*

Analysis of Shock Trains in an Isolator Model



Choraghe Shweta Laxman and S. R. Nagaraja

Abstract The dual mode engine is operated in scramjet mode in hypersonic flow and in ramjet mode in supersonic flow. Numerical simulation is carried out using ANSYS Fluent to study formation of shock trains in an isolator model. The isolator is the component placed between inlet and combustor of a dual mode engine. The isolator is used to increase the static pressure at inlet to the combustor. The interaction of reflected shock with the boundary layer results in bifurcation thus forming the shock train. The steady-state analysis is done for isolators having 6° and 15° ramp angles to study the shock trains formed inside the isolator. The analysis is carried out for different Mach numbers to observe the flow pattern and the pressure distribution. The peak pressure is about 3.78 times the free stream pressure for model with 6° ramp for Mach 5 and 15.5 times the free stream pressure for 15° ramp, for the same Mach number. For a given isolator model, the number of shock reflections increase with decrease in Mach number. In all cases, the pressure in the isolator increased as flow passes through a series of oblique shocks.

Keywords Shock train · Isolator · Dual mode engine · Scramjet · Ramjet · Hypersonic flow

1 Introduction

The two parameters on which thrust depends are the amount of mass flowing through the engine and the velocity of the gas [1]. As the fuel starts to combust, hot exhaust is released which is passed through the nozzle that accelerates the flow as a result of which thrust is produced. To sustain the continuous flow, the pressure at which combustion is happening should be maintained higher than the nozzle exit pressure. Depending on the process to generate this high pressure, two types, namely turbojet engines and dual mode engines are available. Compressor is responsible for the

C. Shweta Laxman · S. R. Nagaraja (✉)

Department of Mechanical Engineering, Amrita School of Engineering, Amrita Vishwa Vidyapeetham, Bengaluru, India
e-mail: sr_nagaraja@blr.amrita.edu

© The Author(s), under exclusive license to Springer Nature Singapore Pte Ltd. 2022
K. Govindan et al. (eds.), *Advances in Mechanical and Materials Technology*,
Lecture Notes in Mechanical Engineering,
https://doi.org/10.1007/978-981-16-2794-1_117

1389

generation of high pressure in turbojet engine, while shock waves are responsible for the generation of high pressure in ramjet and scramjet engines. The Ramjet and the Scramjet engines are the supersonic and hypersonic engines, respectively. The entering flow speed to the combustor differentiates the two engines. For the engine to start in ramjet and scramjet mode, an initial speed should be given to them as they cannot take off on their own. In the initial stages, the conventional engine, i.e., turbojet engine is capable of taking off the aircraft up to Mach number 3.5, after which the ramjet can operate between the speeds of Mach number 3.5–5, and in the later stages, the scramjet is used to operate on speeds of Mach number 5 and above.

Isolator is the crucial region in the operation of engine. Isolator is a component that is present between the inlet and the combustor so as to prevent the deviation of the separated region and the shock train outside the engine. It is a simple duct like structure with constant area. Shock wave is responsible for the generation of pressure gradient using the incoming supersonic flow. The interaction of normal shock with the boundary layer results in a series of repeated shocks thus forming continuous shock train also known as pseudo shock [2]. Scramjet inlet-isolator model to study the unstart as well as the started flow Hall [3] used the Navier–Stokes equations. The simulations are done for a freestream Mach number of 5. He has used SU2, an open-source CFD code developed at Stanford University, and both steady state and transient analysis are done. The dynamics of unstart are studied. The unstart is initiated through the use of an artificial body force, which mimicked a moveable flap used in the experiments. Wang et al. [4] have investigated the characteristics of the oblique shock train in upstream propagation. Generally, the shock train structure depends on the flow conditions, and depending on the flow pattern, the boundary layer interaction can also be classified into different categories. They observed the pattern of the flow and the pressure distribution by varying the throttling ratio. The Mach number plays a significant role in the interaction of the shock with the boundary layer. With the increase in the Mach number, the interaction becomes more and more significant. Xu et al. [5] have studied jumping characteristics of shock trains in an inlet-isolator with Mach 5. Numerically, studies have been carried out to find the trigger limits for shock train jumping. They have found that the separated flow forms local throat like shape. When the shock train jump occurs, there is very minimum contrail of the throat like shape. Wagner et al. [6] used a geometry where they have taken a compression ramp at the inlet with isolator being a long rectangular duct. Using a flap mechanism at the downstream end, they have obtained unstart in the isolator. An isolator model is used to experimentally investigate the unstart dynamics by mounting it on a Mach 5 wind tunnel. Tan et al. [7] have studied the behavior of the shock train using background waves in hypersonic isolator. The flow field of an isolator has shock train that contains both the expansion and compression waves known as background waves. In this analysis, they observed the presence of the complex waves both compression and expansion in the isolator. These complex waves cause the propagation of the shock train upwards thereby providing transverse pressure gradients and stream wise gradients.

Sekar et al. [8] have studied shock wave boundary layer interactions for 38.7° inlet ramp of a scramjet engine for an inlet Mach number of 5.96. They have solved

Navier–Stokes equations numerically. They have studied the formation of separation bubble due to shock wave impingement. Sekar et al. [9] have studied shock boundary layer interaction at inlet of scramjet engine for different ramp angles and for flow Mach number of 5. They have studied the effect of perforated wall on formation separation bubble. Emami et al. [10] have conducted cold flow experiments to study the performance inlet-isolator for ramjet/scramjet engine. They have varied isolator length, step height flow field parameters. Hariharan et al. [11] have studied effect of inlet Mach number and stagnation pressure in a supersonic combustor with a 10° wedge on the top wall of it. They observed that with the increase in Mach number, the oblique shock near the inlet moves down stream.

The paper is divided into four sections. Section 1 presents a brief report on existing literature. In Sect 2, the methodology adopted for simulation is reported followed by detailed analysis of results in Sect 3. Finally, the conclusions are presented in Sect 4, followed by references.

2 Computational Methodology and Implementation

The steady-state analysis is done in order to analyze the formation of shock trains inside an isolator. A major benefit of the computational results is the ability to see the entire flow, rather than be limited by a view window as in experiments. The model has been designed in the most appropriate way to facilitate the understanding of the working of isolator. Commercial CFD software ANSYS Fluent is used to study the formation of shock trains in the isolator for different Mach numbers and also the influence of inlet ramp angle in this process. The analysis is carried out by keeping inlet as pressure far field and outlet as pressure outlet with all the other walls as adiabatic walls. Two isolator models with 6° and 15° ramp angles at the inlet are considered. The height (*h*) of the isolator in both the cases is 25 mm. Figure 1 shows the geometry of the isolator with 6° ramp at inlet. The length of the constant area isolator is about 270 mm. The analysis is done for Mach numbers of 2, 3, and 5. The free stream pressure and temperature at inlet are 5.4 kPa and 55 K, respectively. The values of free stream pressure and temperature, isolator length, and height are chosen in order to compare the simulation results with experimental results of Wagner et al. [6]. Mesh independent studies are done by taking 0.5, 1.0, 1.5, and 3.0 mm mesh

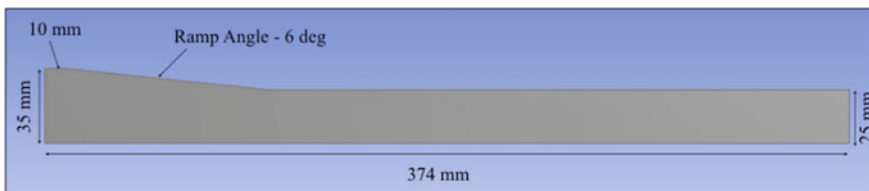


Fig. 1 Geometry of the inlet-isolator with 6° ramp angle

Table 1 Grid independent studies

Mesh size (mm)	P_{max}/P_{inf}
0.5	3.78
1.0	3.785
1.5	3.8
3.0	3.74

sizes. The pressure ratio P_{max}/P_{inf} is used as measure, where P_{max} is the largest static pressure on the bottom wall of the isolator and P_{inf} is the free stream pressure. For these studies, isolator with 6° ramp angle with flow Mach number of 5 is used. The results are as shown in Table 1. It can be seen that the values for 0.5 and 1.0 mm mesh are very close to each other, and hence, 1.0 mm mesh size is used for all calculations.

3 Results and Discussion

A fully started flow is analyzed in these simulations. Figures 2 and 3 show the pressure contours for Mach number $M = 5$ for isolator with inlet ramp angle of 6° and 15° , respectively. The oblique shock angles at the inlet match with theoretical values. Moreover, the oblique shock pattern obtained of 6° ramp angle is similar

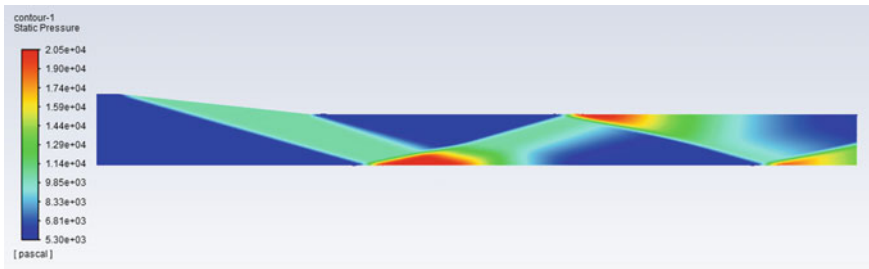


Fig. 2 Pressure contour for Mach number 5 with 6° ramp angle

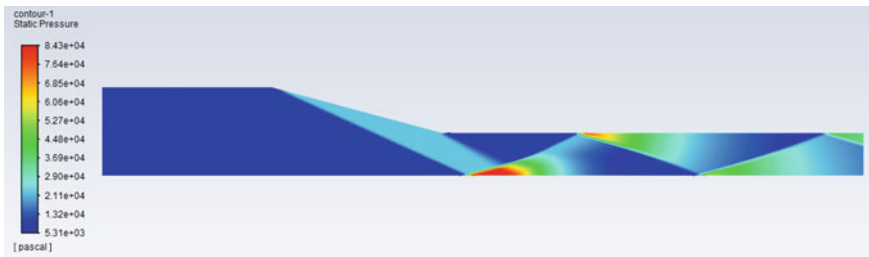


Fig. 3 Pressure contour for Mach number 5 with 15° ramp angle

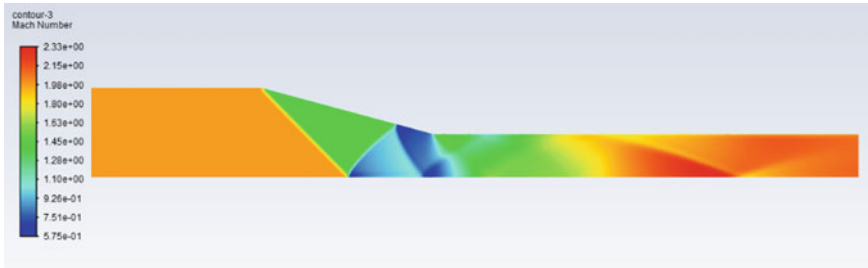


Fig. 4 Mach number contour for Mach number 2 with 15° ramp angle

to the experimental results obtained by Wagner et al. [6]. The number of shock reflections increases as the inlet ramp angle is increased and also as the Mach number is decreased for a given ramp angle. A number shocks for 6° and 15° ramp angles are 4 and 5, respectively, as can be seen from Figs. 2 and 3. A number of oblique shocks for isolator with 6° ramp for Mach numbers of 2, 3, and 5 are 13, 6, and 4, respectively. Similarly, for isolator with 15° ramp are 5 and 8 for $M = 3$ and 5. From Mach contour for isolator with 15° ramp angle and $M = 2$ (Fig. 4), it is difficult to determine the number of oblique shocks as the density and pressure gradients are not large. In this case, flow is subsonic at certain locations, whereas in all other cases considered flow was supersonic throughout. However, the flow slows down considerably as it passes through series of oblique shocks. In case of 15° ramp model, flow slows down from Mach 5 to approximately 3 (Fig. 5), for 6° ramp from Mach 5 to nearly Mach 4 and Mach 3 to nearly 2.5. In all these cases, the pressure is increased.

For $M = 5$ when the flow passes through the first shock, then the pressure jumps by approximately two times the free stream pressure. After detailed examination of the pressure distribution in the isolator for various Mach numbers, it is observed that after reflection high and low pressure region can be found on the walls of the isolator near the oblique shocks (Fig. 6). The high pressure regions are upstream of the shock and low pressure regions near the downstream of the shock.

The change in pressure on the bottom wall of the isolator is studied in detail. The normalized wall pressure is plotted against normalized distance x/h , where x represents distance from the inlet of the isolator and h represents the isolator’s height.

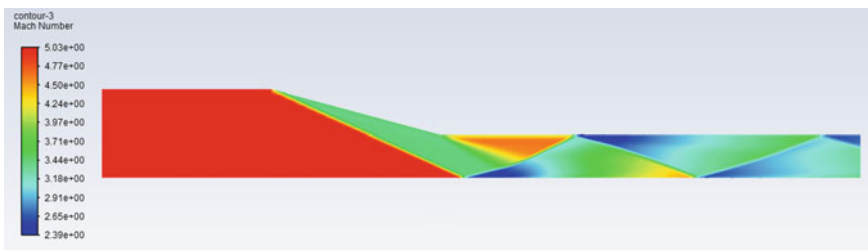


Fig. 5 Mach number contour for Mach number 5 with 15° ramp angle

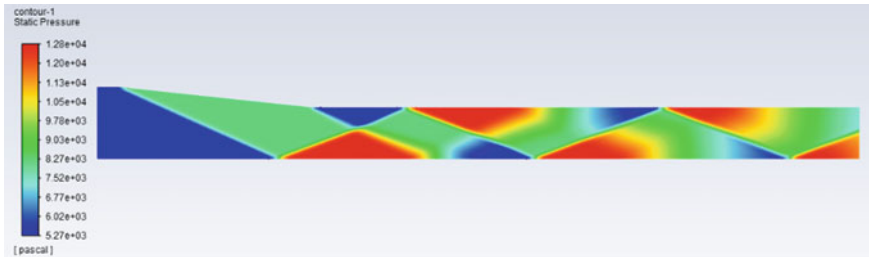


Fig. 6 Pressure contour for Mach number 3 with 6° ramp angle

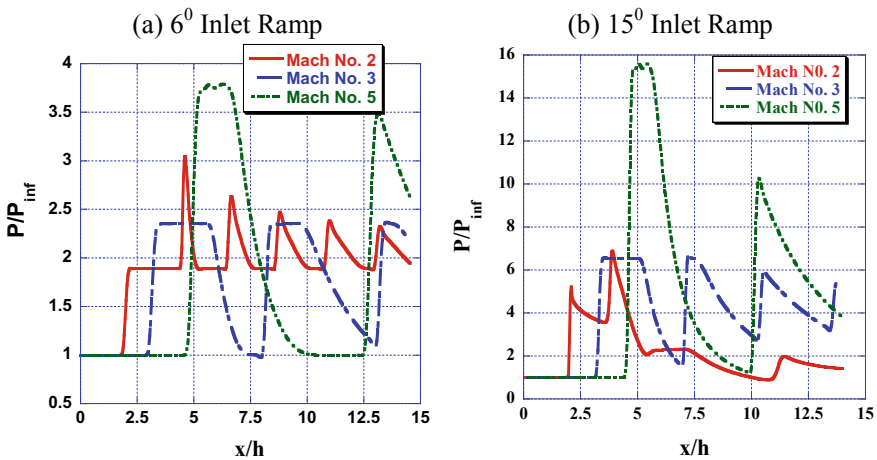
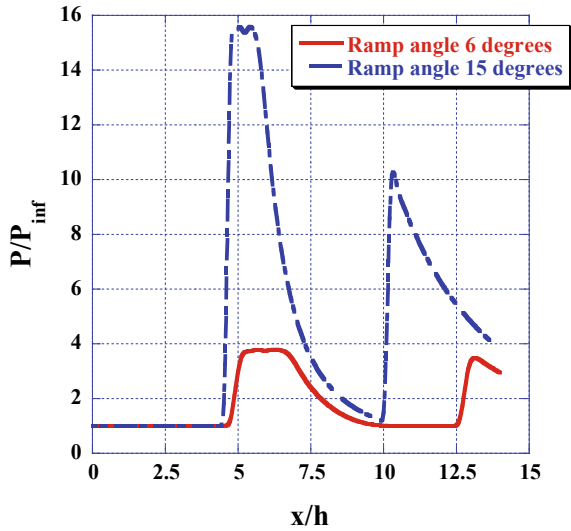


Fig. 7 Pressure distribution of started flow for isolator (a) with 6° inlet ramp and (b) with 15° inlet ramp

For both models of the isolator, the height is 25 mm. Figure 7 shows the change in pressure along the bottom wall of the isolator for different Mach numbers. In these figures, P represents the pressure on the bottom wall and P_{inf} the free stream pressure. As seen from Fig. 7a, the maximum pressure is about 3.78 times the free stream pressure for isolator with 6° ramp angle and $M = 5$. This value is close to that of the experimental values reported by Wagner et al. [6]. The pressure jumps when the flow passes through the shock impingement point and drops to nearly free stream value after each jump until another shock impingement point causes the pressure jump again. There is drastic increase in the peak pressure for isolator with 15° ramp, as seen from Fig. 7b for $M = 5$, the peak pressure is about 15.5 times the free stream pressure. This is due to larger angle of the first oblique shock at the entrance compared to 6° ramp model. For both models, the peak pressure decreases as for lower Mach numbers. There is significant drop in the peak pressure at the end of the isolator model. Figure 8 represents the variation of pressure for $M = 5$ for both the models. The first peak pressure occurs at x/h nearly equal to 5 for both the models,

Fig. 8 Pressure distribution of started flow for isolator with 6° and 15° inlet ramp for $M = 5$



whereas the second peak occurs at x/h nearly equal to 10 for 15° model and 13 for 6° model. This is due to smaller oblique shock angles for 6° model.

4 Conclusions

Computational analysis of shock train formation in an inlet-isolator model with different inlet ramp angles for different Mach number is done using ANSYS Fluent. The results obtained agreed closely with experimental results of Wagner et al. [6]. It is observed that the number of shock reflections is more for lower Mach numbers and smaller ramp angles. The peak pressure in the isolator increases with Mach number for a given model and also with increase ramp angle. The peak pressure is about 3.78 times the free stream pressure for model with 6° inlet ramp for $M = 5$ and 15.5 times the free stream pressure for model with 15° inlet ramp for $M = 5$. In all the cases investigated, the flow slows down as it passes through a series of oblique shocks thereby increasing the pressure.

References

1. National Aeronautics and Space Administration: Document on Ramjet Propulsion. <https://www.grc.nasa.gov/www/k-12/airplane/ramjet.html>
2. Gnani F, Zare-Behtash H, Kontis K (2016) Pseudo-shock waves and their interactions in high-speed intakes. Prog Aerosp Sci 82:36–56

3. Hall IA. Simulating scramjet behavior: unstart prediction in a supersonic, turbulent inlet-isolator duct flow. A thesis submitted to the faculty of Purdue University
4. Wang C, Xue L, Tian X (2017) Experimental characteristics of oblique shock train upstream propagation. *Chin J Aeronaut* 30(2):663–676
5. Xu K, Chang J, Li N, Zhaou W, Yu D (2018) Preliminary investigation of limits of shock train jumps in a hypersonic inlet-isolator. *Eur J Mech B Fluids* 72:664–675
6. Wagner JL, Yuceil KB, Clemens NT (2009) Experimental investigation of unstart in an inlet/isolator model in Mach 5 flow. *AIAA J* 47(6):1528–1542
7. Tan HJ, Sun S, Huang HX (2012) Behavior of shock trains in a hypersonic inlet/isolator model with complex background waves. *Exp Fluids* 53:1647–1661
8. Sekar KR, Jegadheeswaran S, Kannan R, Vadivelu P, Prasad G (2019) Numerical investigation of single ramp scramjet inlet characteristics at Mach number 5.96 due to shock wave–boundary layer interaction. In: Chandrasekhar U, Yang LJ, Gowthaman S (eds) *Innovative design, analysis and development practices in aerospace and automotive engineering (I-DAD 2018)*. Lecture notes in mechanical engineering. Springer. https://doi.org/10.1007/978-981-13-2697-4_20
9. Sekar KR, Jegadheeswaran S, Kannan R, Manigandan P (2019) Perforated wall in controlling the separation bubble due to shock wave–boundary layer interaction. *Int J Turbo Jet-Engines*. eISSN 2191-0332, ISSN 0334-0082 <https://doi.org/10.1515/tjj-2018-0048>
10. Emami S, Trexler CA, Auslender AH, Weidner JP (1995) Experimental investigation of inlet-combustor isolators for a dual-mode scramjet at a Mach number of 4. NASA technical paper 3502
11. Hariharan V, Velamati RK, Prathap C (2016) Investigation on supersonic combustion of hydrogen with variation of combustor inlet conditions. *Int J Hydrogen energy* xxx 1–9

Effect of Shear Work on Heat Transfer Characteristics of Gaseous Flow Between Two Micro-parallel Plates



Prathuk Balachandra Hegde and Hari Mohan Kushwaha

Abstract In this paper, efforts have been made to identify the influence of shear work on heat transfer behaviour of gas slip flow between two micro-parallel plates by imposing second-order slip velocity and temperature jump for constant heat flux case. The fluid flow is supposed as laminar, steady, incompressible and fully developed. The influence of rarefaction, viscous dissipation and shear work at plate walls has been considered. Closed-form expressions are derived for velocity profile, temperature distribution and the Nusselt number, which are depending on Knudsen, Brinkman and Prandtl numbers. A comparison and validation with then comparable class of a problem have been made, and a reasonably good consensus has been reached.

Keywords Nusselt number · Shear work · Temperature jump · Velocity slip

1 Introduction

The heat transfer behaviour of gaseous flow through micro-devices is of paramount importance in several scientific and industrial applications. This includes micro-fluidic devices (micro-heat exchangers, micro-valves, micro-sensors, etc.), cooling of electronic equipment and micro-systems for mixing [1, 2]. When gas flows through a micro-device, an important scaling effect called as rarefaction, and it affects heat transfer behaviour significantly. This is characterized by a non-dimensional number referred as Knudsen number ($Kn = \lambda/D_h$). The Knudsen number demarcates fluid flow into continuum, slip, transition and free molecular flow regimes [1]. In view of this, numerous authors have reported analytical, numerical and experimental studies in open literature. Earlier, Maslen [3] used thermal slip boundary condition to solve energy in a micro-channel. The author considered an additional term to the usual

P. B. Hegde · H. M. Kushwaha (✉)
Department of Mechanical Engineering, Amrita School of Engineering, Amrita Vishwa
Vidyapeetham, Bengaluru, India
e-mail: h_mohan@blr.amrita.edu

P. B. Hegde
e-mail: blenp2tse18008@bl.students.amrita.edu

© The Author(s), under exclusive license to Springer Nature Singapore Pte Ltd. 2022
K. Govindan et al. (eds.), *Advances in Mechanical and Materials Technology*,
Lecture Notes in Mechanical Engineering,
https://doi.org/10.1007/978-981-16-2794-1_118

1397

boundary condition to recompense shear work at wall. In recent years, numerous researchers examined the effect of shear work [4–8] on thermal behaviour of gas flow through small-size devices by imposing first-order boundary conditions [9–11] for CHF and CWT cases. The authors considered influence of various modelling parameters, rarefaction, axial conduction, inverse heat transfer and conjugate heat transfer [12–14]. They disclosed that shear work influences heat transfer characteristics considerably and neglecting shear work over/under predicts Nu in slip regime.

It is noticeable from literature that various studies are available that contemplate the influence of shear work along with first-order slip velocity and temperature jump. To the best of author’s knowledge, shear work along with second order and velocity slip has not been reported in literature extensively. Therefore, the authors took a cue from past study [15] and made an effort to derive analytical expressions for Nusselt number by imposing second-order slip velocity, temperature jump and shear work at wall for CHF case. A reasonably good consensus in open literature with the current investigation is reached.

2 Theoretical Analysis

Figure 1 elucidates a gaseous flow between two micro-parallel plates.

The momentum equation for the present configuration is

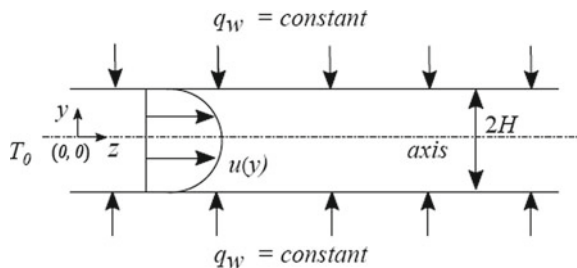
$$\frac{d}{dy} \left(\frac{du}{dy} \right) = \frac{1}{\mu} \frac{dp}{dz} \tag{1}$$

The energy equation is

$$u \frac{dT}{dz} = \alpha \left(\frac{\partial^2 T}{\partial y^2} + \frac{\partial^2 T}{\partial z^2} \right) + \frac{\mu}{\rho C_p} \left(\frac{\partial u}{\partial y} \right)^2 \tag{2}$$

The symmetry boundary condition at centreline is

Fig. 1 Schematic showing gas flow between micro-parallel plates



$$\left. \frac{du}{dy} \right|_{y=0} = 0 \tag{3}$$

The velocity slip boundary condition is

$$u = u_s = -B_v \left(\lambda \left. \frac{\partial u}{\partial y} \right|_{y=H} - \frac{\lambda^2}{2} \left. \frac{\partial^2 u}{\partial y^2} \right|_{y=H} \right) \tag{4}$$

where u_s is velocity of fluid at the wall and B_v is the constant parameter in terms of accommodation coefficients.

The fluid is assumed to enter the channel with constant temperature T_0 . The boundary conditions (symmetry at the centreline) associated with the Eq. (2) are

$$T(0, y) = T_0 \tag{5}$$

The symmetric boundary condition at centreline is

$$\left. \frac{\partial T}{\partial y} \right|_{y=0} = 0 \tag{6}$$

At large distance from the inlet, gas temperature eventually becomes constant

$$\left. \frac{\partial T}{\partial z} \right|_{z \rightarrow \infty} = 0 \tag{7}$$

Temperature jump boundary conditions are

$$T = T_w - \beta_T \frac{2\gamma}{(\gamma + 1) \text{Pr}} \left(\lambda \left. \frac{\partial T}{\partial y} \right|_{y=H} - \frac{\lambda^2}{2} \left. \frac{\partial^2 T}{\partial y^2} \right|_{y=H} \right) \tag{8}$$

where T_w is temperature of the fluid at wall and β_T is a constant parameter in terms of accommodation coefficients. The boundary condition with shear at wall [15] is

$$q_w = q_c - q_{sw} \Rightarrow k \left. \frac{\partial T}{\partial y} \right|_{y=H} + \mu u_s \left. \frac{\partial u}{\partial y} \right|_{y=H} \tag{9}$$

where q_c is heat conduction, q_{sw} is the shear work at the surface due to slipping fluid.

The velocity profile is derived by solving momentum Eq. (1) with the boundary conditions given by Eqs. (3) and (4),

$$u(y) = \frac{3}{2} \frac{u_m}{\left(1 + 3B_v \frac{4\lambda}{D_h} \left(1 - \left(\frac{2\lambda}{D_h} \right) \right) \right)} \left[1 + B_v \frac{8\lambda}{D_h} \left(1 - \left(\frac{2\lambda}{D_h} \right) \right) - \left(\frac{y}{H} \right)^2 \right] \tag{10}$$

where $\beta_v = \frac{2-\sigma_v}{\sigma_v}$, $u_m = \frac{-H^2}{3\mu} \frac{dP}{dz} (1 + 12\text{B}_v(\text{Kn} - 2\text{Kn}^2))$.
 Defining following dimensionless form

$$\eta = \frac{y}{H}, \text{Kn} = \frac{\lambda}{D_h} \tag{11}$$

The velocity profile can be re-written as

$$u(\eta) = \frac{3u_m(1 + 8\beta_v(\text{Kn} - 2\text{Kn}^2) - \eta^2)}{2(1 + 12\beta_v(\text{Kn} - 2\text{Kn}^2))} \tag{12}$$

Further, Eq. (12) can be written as

$$u(y) = \frac{3}{2} \frac{U_m}{C_2} (1 + 8C_1 - \eta^2) \tag{13}$$

where $C_1 = \beta_v * a$, $C_2 = 1 + 12C_1$, $a = (\text{Kn} - 2\text{Kn}^2)$.
 Defining the following dimensionless variables

$$\xi = \frac{z}{H}, \theta(\xi, \eta) = \frac{T - T_0}{qD_h/k} \tag{14}$$

The boundary conditions given by Eqs. (5)–(8) in non-dimensional form are

$$\theta(0, \eta) = 0 \tag{15}$$

$$\frac{\partial \theta}{\partial \eta}_{\eta=0} = 0 \tag{16}$$

$$\frac{\partial \theta}{\partial \xi}_{\xi \sim \infty} = 0 \tag{17}$$

$$\theta = \theta_w - \frac{8\gamma}{\gamma + 1} \frac{\beta_T}{\text{Pr}} \left[\text{Kn} \left(\frac{\partial \theta}{\partial \eta} \right)_{\eta=1} - 2\text{Kn}^2 \left(\frac{\partial^2 \theta}{\partial \eta^2} \right)_{\eta=1} \right] \tag{18}$$

The Eq. (9) in non-dimensional form is

$$q_w = q_c - q_{sw} \Rightarrow q_w \left(\frac{\partial \theta}{\partial \eta} \right)_{\eta=1} + \left(\frac{\mu u_s}{H} \left(\frac{\partial u}{\partial \eta} \right)_{\eta=1} \right) \tag{19}$$

The energy Eq. (2) in terms of ξ, η is

$$\frac{3P_e}{8C_2} (1 + 8C_1 - \eta^2) \frac{\partial \theta}{\partial \xi} = \frac{\partial^2 \theta}{\partial \xi^2} + \frac{\partial^2 \theta}{\partial \eta^2} + \frac{9\text{Br}_q}{C_2^2} \eta^2 \tag{20}$$

The non-dimensional parameters, Brinkman number (Br_q) and Peclet number (Pe), are

$$Br_q = \frac{\mu u_m^2}{q_w D_h}, Pe = \frac{u_m D_h}{\alpha} \tag{21}$$

here Re and Pr denote the Reynolds number and Prandtl number, respectively. Hence, it is understandable from Eq. (21), $Br_q > 0$ yields gas heating case while $Br_q < 0$ corresponds to gas cooling case.

The dimensionless temperature is obtained from energy Eq. (20), as

$$\begin{aligned} \theta(\eta) = \theta_w + \frac{3Pe}{8C_2} \frac{\partial \theta}{\partial \xi} \left(\frac{\eta^2}{2} + 4C_1 \eta^2 - \frac{\eta^4}{12} \right) + \frac{3Br_q}{4C_2^2} (1 - \eta^4) - \frac{3Pe}{8C_2} \frac{\partial \theta}{\partial \xi} \left(\frac{5}{12} + 4C_1 \right) \\ - 4C_3 \left[\left\{ \frac{Pe}{4} \frac{\partial \theta}{\partial \xi} - \frac{3Br_q}{C_2^2} \right\} - 2Kn \left\{ \frac{3PeC_1}{C_2} \frac{\partial \theta}{\partial \xi} - \frac{9Br_q}{C_2^2} \right\} \right] \end{aligned} \tag{22}$$

where $C_3 = \frac{2Kn\gamma}{Pr(\gamma+1)} \beta_T$.

The fluid mean temperature is

$$T_m = \frac{\int \rho u T dA}{\int \rho u dA} \tag{23}$$

The Eq. (23) in non-dimensional is

$$\theta_m = \frac{1}{u_m A} \int u \theta dA \tag{24}$$

The longitudinal bulk temperature gradient is

$$\frac{\partial T}{\partial z} = \frac{dT_m}{dz} \Rightarrow \frac{\partial \theta}{\partial \xi} \frac{q_w}{k} = \text{constant} \tag{25}$$

The mean temperature derivative is

$$\frac{dT_m}{dz} = \left[\frac{q_w P + \int_0^H \mu \left(\frac{\partial u}{\partial y} \right)^2 dy}{\dot{m} C_p} \right] \Rightarrow \frac{\partial \theta}{\partial \xi} \frac{q_w}{k} \tag{26}$$

where

$$\frac{\partial \theta}{\partial \xi} = \frac{q_w \Gamma}{\dot{m} C_p} \tag{27}$$

and

$$\Gamma = \left\{ \begin{array}{l} 1 + \frac{3Br_q}{C_2^2} \quad \text{Neglecting shear work} \\ 1 + \frac{3Br_q}{C_2^2} + \frac{36Br_q C_1}{C_2^3} \quad \text{Including shear work} \end{array} \right\} \quad (28)$$

From Eqs. (25), (26) and (28), we get

$$\begin{aligned} \theta_w - \theta_m = & \left\{ \frac{4\Gamma}{140C_2^2} (17 + 336C_1 + 1680C_1^2) - \frac{4Br_q}{35C_2^3} (6 + 63C_1) \right. \\ & \left. + 4C_3 \left[\left\{ \Gamma - \frac{3Br_q}{C_2^2} \right\} - 2Kn \left\{ \frac{12\Gamma C_1}{C_2} - \frac{9Br_q}{C_2^2} \right\} \right] \right\} \quad (29) \end{aligned}$$

The fully developed Nusselt number is

$$Nu_{Fd} = \frac{q_w D_h}{k(T_w - T_m)} \Rightarrow \frac{4}{\theta_w - \theta_m} \quad (30)$$

Substituting Eqs. (29) in (30) and simplifying, the fully developed Nusselt number is obtained as

$$\begin{aligned} Nu_{Fd} = & \left\{ \frac{\Gamma}{140C_2^2} (17 + 336C_1 + 1680C_1^2) - \frac{Br_q}{35C_2^3} (6 + 63C_1) \right. \\ & \left. C_1^* \left[\left\{ \Gamma - \frac{3Br_q}{C_2^2} \right\} - 2Kn \left\{ \frac{12\Gamma C_1}{C_2} - \frac{9Br_q}{C_2^2} \right\} \right] \right\} \quad (31) \end{aligned}$$

3 Results and Discussion

This investigation demonstrates the influence of shear on heat transfer behaviour of a gas flow between two micro-parallel plates by imposing constant heat flux condition.

The velocity slip and temperature jump boundary conditions are enforced at surface of plates. Consideration is given to the impact of viscous dissipation, rarefaction and shear work. For velocity profile, temperature distribution and Nusselt number, closed-form expressions are obtained. The non-dimensional velocity profile for different Kn values is shown in Fig. 2, which becomes flat with the increasing values of Kn. The significance of shear work on temperature profile has been illustrated in Fig. 3.

It emphasizes that shear work contributions predominate in increasing heat transfer rate for CHF case. It also narrates that with the increase in rarefaction, contribution of shear work increases. With second-order boundary condition, one can predict exact numerical values and clearly identify the contribution of each parameter on temperature distribution. Figure 4 demonstrates the variation of Nu with Kn for different Br_q .

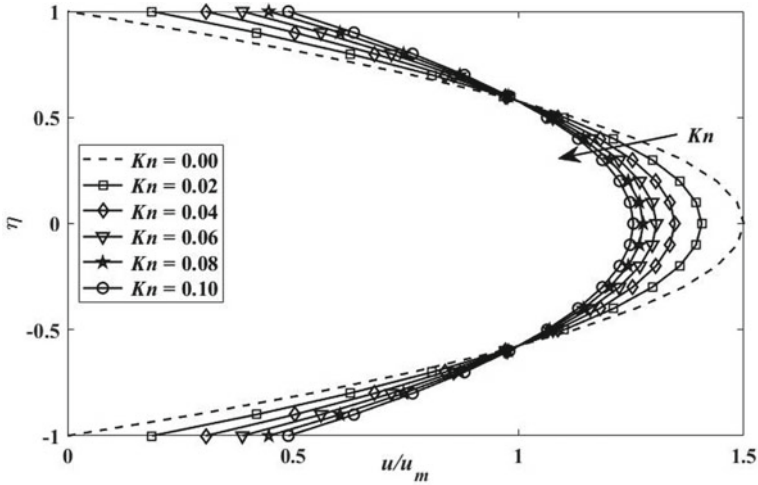


Fig. 2 Velocity profile for various Knudsen numbers

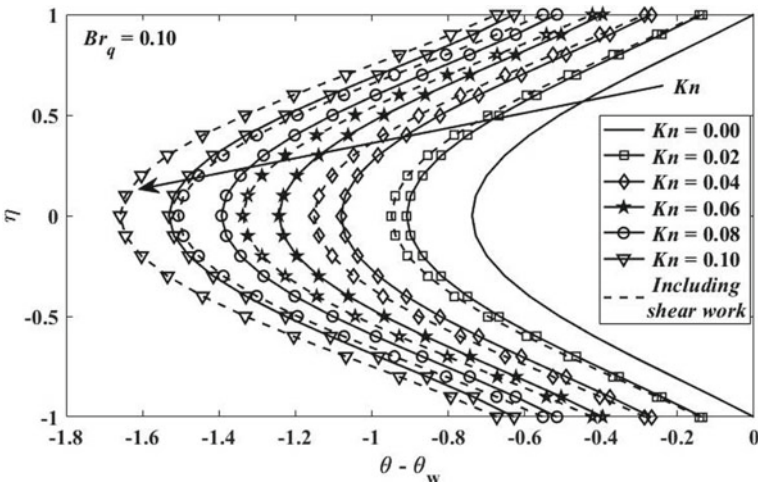


Fig. 3 Temperature profile for various Knudsen numbers

The contribution of sliding friction on heat transfer rate is clearly visible for both cooling and heating cases. The dotted and firm lines demonstrate, respectively, the cases of zero viscous dissipation and nonzero viscous dissipation. The relationship between Nusselt number and Kn is nonlinear for both positive and negative Br_q . It highlights that shear work is zero when Kn tends to zero, while it increases with the increase in Kn . For cases of gas cooling ($Br_q = -0.02$) and heating ($Br_q = 0.02$) respectively, the contribution of shear work in slip regime is found to be 16.30 and 13.90%. It is noticed that its contribution is more effective for higher values of Kn

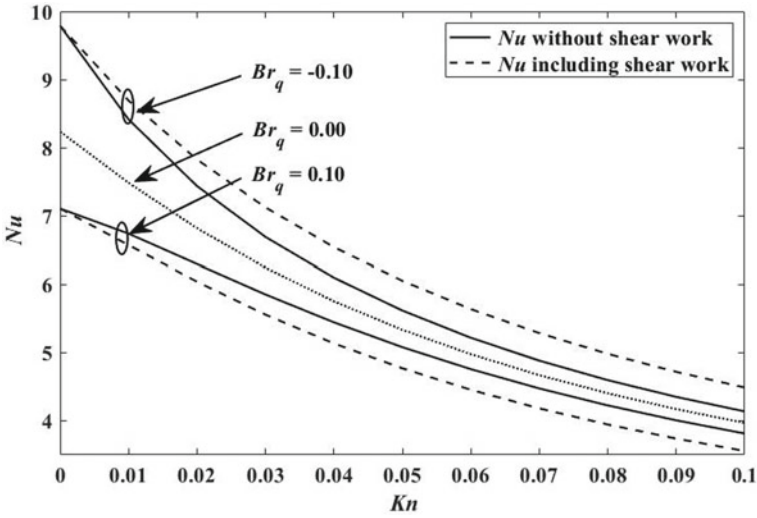


Fig. 4 Variation of Nu with Kn for CHF case

as compared to lower Kn values. The variation of fully developed Nu with Br_q is demonstrated in Fig. 5.

It indicates variation of Nu with Br_q excluding shear work and including shear work contribution on Nu with Br_q . Here, solid line highlights no shear work effect, whereas dashed line shows contribution of shear work. For a Kn value, a singularity is observed in Nu, due to reduced temperature differences between wall and bulk fluid. These singularities are found at a point where, due to viscous dissipation, wall heat

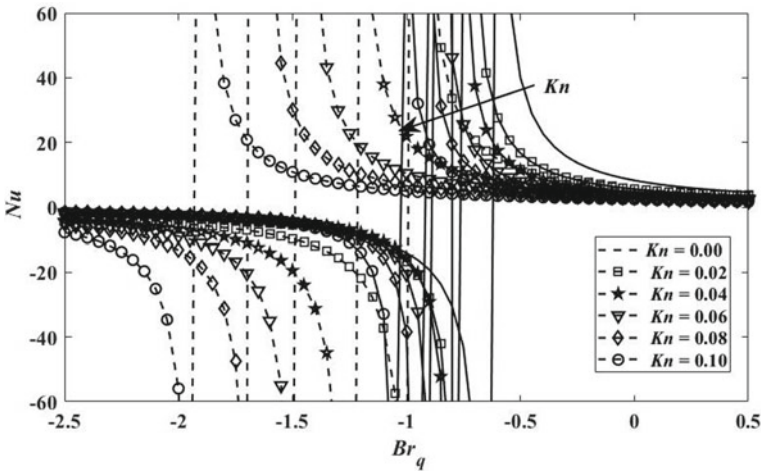


Fig. 5 Variation of Nusselt number with Br_q for CHF case

Table 1 Comparison of Nu for $Br_q = 0.01$; $Pr = 0.7$, without shear work for CHF case

Kn	Present analytical	Ref. [5]	Ref. [14]
0	8.2353	8.2353	8.2353
0.02	6.8185	6.8192	6.8192
0.04	5.7540	5.7242	5.7242
0.06	4.9779	4.8942	4.8942
0.08	4.4037	4.2569	4.2569
0.1	3.9690	3.7575	3.7575

flux and heat transfer equalize one another. At the point of singularity, asymptotic solution ($Br_q \rightarrow \infty, Nu \rightarrow 0$) is observed with increase in Brinkman number and vice versa. From Fig. 5, it is clear that due to the influence of shear work, position of singularity gets shifted towards negative axis with increase in Kn (i.e. singularity is attained at lesser Brinkman number). Hence, it is not continuous. It may also be noted that for gas cooling, shear work is responsible for an increase in Nu, and for heating, it decreases Nu. Compared to the heating, the effect of shear work is remarkable for cooling.

3.1 Comparison and Validation

In order to provide an understanding of shear work contribution on the surface of plates, the Nusselt number is derived for the case of with and/or without shear work. The obtained results are found to have reasonably a good agreement with earlier reported studies for no viscous dissipation ($Br_q = 0$) and no-slip ($Kn = 0$) conditions.

Table 1 shows comparison of Nu obtained by incorporating first- and second-order velocity slip and temperature jump conditions at surface of plates with existing studies. The results obtained are in good agreement with other studies. Table 2 shows that results predicted by utilizing second-order slip velocity and temperature jump conditions are less as compared to continuum value. It is because shear work makes

Table 2 Percentage difference of Nu with Kn at $Pr = 0.7$ and $Br_q = 0.01$

Kn	Conti...	I order	II order	$\frac{(P3-P2)}{P3}$	$\frac{(P1-P2)}{P1}$	$\frac{(P1-P3)}{P1}$
	P1	P2	P3			
0	8.235	8.1065	8.1065	0.0000	1.5599	1.5599
0.02	–	6.7514	6.7318	0.2909	18.0163	18.2541
0.04	–	5.6814	5.6855	0.0727	31.0091	30.9589
0.06	–	4.8639	4.9202	1.1439	40.9366	40.2531
0.08	–	4.2338	4.3532	2.7422	48.5878	47.1382
0.1	–	3.7391	3.9236	4.7032	54.5952	52.3543

Table 3 Percentage difference of Nu with Kn at Pr = 0.7 and Br_q = 0.001

Kn	Conti...	I order	II order	$\frac{(P3-P2)}{P3}$	$\frac{(P1-P2)}{P1}$	$\frac{(P1-P3)}{P1}$
	P1	P2	P3			
0	8.235	8.2222	8.2222	0.0000	0.1554	0.1554
0.02	–	6.8121	6.8097	0.0352	17.2793	17.3079
0.04	–	5.7195	5.7471	0.4792	30.5463	30.2119
0.06	–	4.8907	4.9721	1.6360	40.6104	39.6226
0.08	–	4.2541	4.3986	3.2847	48.3408	46.5863
0.1	–	3.7552	3.9645	5.2779	54.3993	51.8585

a substantial role near wall, and temperature jump reduces gradient near wall, which in turn decreases the heat transfer. For the Brinkman number (Br_q = 0.01) values, the difference in Nu between the continuum and first-order model is 54.5952%; between the continuum and second-order condition is 52.3543%; between first and second order is 4.7032%. Table 3 shows that percentage variation in Nu obtained by utilizing first- and second-order boundary conditions and Nu obtained from continuum case, for low viscous dissipation. Also, it reflects that shear work contribution is significant and unneglectable for low viscous dissipation. The percentage variation of first and second orders from continuum is 54.3993% and 51.8585%, respectively. With the rise in Kn for gas heating cases, the Nusselt number decreases and vice versa. It is noticed that the findings agree well with the similar class of problems [4, 8, 15–19].

4 Conclusions

The effect of slip is found to flatten velocity profile with increasing values of Kn. With the rise in Kn due to an increase in thermal resistance, which is caused by an increased temperature jump near wall, the Nusselt number decreases. The role of shear work near wall boundary is abruptly relative to the heat conduction, by increasing the rarefaction (i.e. with increasing Kn) at the surface. Even though the contribution is small/negligible near wall this effect is more substantial near the upper limit of slip region, which highlight present prediction. Hence, it should be considered in the calculation of total heat exchange with the walls, and in any case, it has no immediate impact on temperature field as it occurs at the boundary. The shear work contribution is more significant in case of gas cooling as compared to heating. The contribution of shear work is found to be significant for CHF condition, and over/underprediction of Nu mostly depends on Br_q and Kn. Hence, contribution of shear work is very much important while studying heat transfer behaviour at micro-scale, when viscous dissipation is considered and neglecting shear effect leads to imprecise results.

References

1. Agrawal A, Kushwaha HM, Jadhav RS (2020) *Microscale flow and heat transfer*. Springer, Berlin
2. Krishna VG, Dineshkumar L (2019) Numerical analysis on enhancement of heat transfer in micro-heat sink using dimpling surface. In: AIP conference proceedings, vol 2200. AIP Publishing LLC, p 020059
3. Maslen SH (1958) On heat transfer in slip flow. *J Aerosp Sci* 25(6):400–401
4. Kushwaha HM, Raj PB, Sahu SK (2017) Effect of shear work on the heat transfer characteristics of gaseous flows in microchannels. *Chem Eng Technol* 40(1):103–115
5. Haddout Y, Lahjomri J (2015) The extended Graetz problem for a gaseous slip flow in micropipe and parallel-plate microchannel with heating section of finite length: effects of axial conduction, viscous dissipation and pressure work. *Int J Heat Mass Transf* 80:673–687
6. Hong C, Asako Y (2010) Some considerations on thermal boundary condition of slip flow. *Int J Heat Mass Transf* 53(15):3075–3079
7. Sun Z, Jaluria Y (2012) Convective heat transfer in pressure-driven nitrogen slip flows in long microchannels: the effects of pressure work and viscous dissipation. *Int J Heat Mass Transf* 55(13):3488–3497
8. Ramadan K, Tlili I (2015) A numerical study of the extended Graetz problem in a microchannel with constant wall heat flux shear work effects on heat transfer. *J Mech* 31(6):733
9. Jeong H-E, Jeong J-T (2006) Extended Graetz problem including streamwise conduction and viscous dissipation in microchannel. *Int J Heat Mass Transf* 49(13):2151–2157
10. Aydin O, Avci M (2007) Analysis of laminar heat transfer in micro-Poiseuille flow. *Int J Therm Sci* 46(1):30–37
11. Hooman K (2007) Entropy generation for microscale forced convection: effects of different thermal boundary conditions, velocity slip, temperature jump, viscous dissipation, and duct geometry. *Int Commun Heat Mass Transfer* 34(8):945–957
12. Kumar S, Jakkareddy PS, Balaji C (2020) A novel method to detect hot spots and estimate strengths of discrete heat sources using liquid crystal thermography. *Int J Therm Sci* 154:106377
13. Jakkareddy PS, Balaji C (2018) A non-intrusive technique to determine the spatially varying heat transfer coefficients in a flat plate with flush mounted heat sources. *Int J Therm Sci* 131:144–159
14. Jakkareddy PS, Balaji C (2018) Estimation of local heat transfer coefficient from natural convection experiments using liquid crystal thermography and bayesian method. *Exp Thermal Fluid Sci* 97:458–467
15. Ramadan K (2016) The role of the shear work in microtube convective heat transfer: a comparative study. *J Heat Transfer* 138(1):011701
16. Nicolas X, Chenier E, Tchekiken C, Lauriat G (2018) Revisited analysis of gas convection and heat transfer in micro channels: influence of viscous stress power at wall on nusselt number. *Int J Thermal Sci* 134:565–584
17. Asako Y, Hong C (2018) Notes on factitious shear work of slip flow in a channel. *Int J Heat Mass Transf* 127:444–447
18. Asako Y, Hong C (2018) Letter to the editor: “shear work contribution to convective heat transfer of dilute gases in slip flow regime” (Vocale P, Morini GL, Spiga M, Colin S, 64 60–68 (2017)). *Eur J Mech B/Fluids* 72:301
19. Ramadan K (2019) Pressure work and viscous dissipation effects on heat transfer in a parallel-plate microchannel gas flow. *J Mech* 35(2):243–254

Prediction of Stable Cutting Range Using Local Mean Decomposition Merged with Statistical Approach



Pankaj Gupta, Bhagat Singh, and Yogesh Shrivastava

Abstract Regenerative chatter is responsible for loss in productivity during machining. Chatter is induced due to which waviness generates on the surface of the workpiece during machining. In modern manufacturing, intelligent machining is replacing the man-controlled machining. To achieve this objective, there is need for computational facilities and a newer algorithm to control the machining parameters before the incipient of chatter. In the present work, the authors have used the Al 6061-T6 workpiece and explored the chatter vibration during turning. The local mean decomposition (LMD) signal processing approach has been used to extract the chatter features of the acquired acoustic signal and statistical features have been studied. Chatter Index (CI) has been evaluated for influential product functions obtained from the LMD technique. The response surface methodology (RSM) has been adopted for better predictability of stable range at the low computational effort.

Keywords Chatter vibration · Stability analysis · Non-stationary signal processing · Response surface methodology · Al 6061-T6 · Chatter index

1 Introduction

During the turning of Al6061-T6, the waviness curves generate on the surface of the workpiece. During machining, in each subsequent pass of the tool on the workpiece, the chatter vibration regenerates. This relative motion between tool and work material is called chatter. The schematic representation of the wavy profile has been shown in Fig. 1.

Regenerative chatter is responsible for the loss in productivity during machining [1, 2]. Chatter vibration also generates exaggerated noise and reduces the machine tool and cutting tool life [3]. Thus, there is a need for computational facilities and a

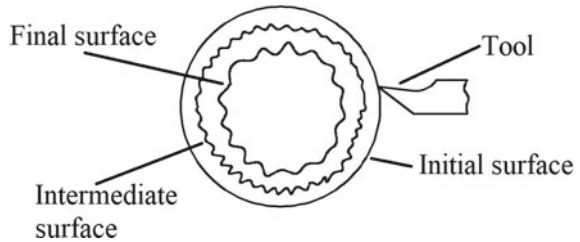
P. Gupta · B. Singh

Jaypee University of Engineering and Technology, Guna, Madhya Pradesh, India

Y. Shrivastava (✉)

Galgotias College of Engineering and Technology, Greater Noida, India

Fig. 1 Schematic representation of wavy profile



newer algorithm to control the machining parameters before the incipient of undesirable chatter vibrations. The unwanted noise is acquired using a microphone. The signal acquisition using a microphone sensor is most suitable and significant for chatter analysis. Researchers have found that the signal obtained from the microphone is a type of vibration signal which is nonlinear and non-stationary [3]. Analysis of the vibration signal indicates the presence of chatter. It serves as a direct indication of the intensity of chatter vibration and the impact on the surface quality of work material.

In recent times, researchers have used various chatter detection techniques for the analysis [4–6]. In these analyses, the peaks obtained are due to chatter frequencies, unwanted contaminations, and ambient sound. So, it is very important to remove these noise contents before processing using a suitable technique [7]. Some researchers used chatter detection methods based on time series using a recursive drawing process during titanium super alloy milling [8, 9]. Researchers have also extracted chatter features using ensemble empirical mode decomposition (EEMD) method [10–12] for ascertaining tool chatter features. They found that the EMD method is very effective in chatter analysis, but it is likely to face modal aliasing [13], which means that it is difficult to recognize the exact chatter band. In addition, sometimes performing Hilbert transform on the decomposition results of EMD, negative instantaneous frequency, and the end effects occur more prominently [14].

Hence, there is a need of technique, which can detect the occurrence of chatter onset or before its occurrence. Sensors play an important role in acquisition of chatter signal; microphone is one of them [9]. In recent development in the field of machining, advance sensors are replacing the space of machinist to control the cutting factors for stable machining. Researchers have used microphone to acquire audio signals during machining. The acquired audio signal is a vibration signal, which is used for non-destructive analysis. It is also reported that the acquired chatter signals contaminate with the ambient noise, which hinders the true nature of chatter features. The ambient noise mixed with the sound of turning and changed the true value of chatter frequencies. Authors have explored different signal processing techniques to remove the noise and get true chatter frequencies.

This problem has been solved to a large extent using local mean decomposition, developed by Smith [15]. LMD reduces the end effects during the decomposition and inhibits the over-enveloping phenomenon [16]. LMD has a better decomposition effect than the EMD. As any cutting factor value increases, the peak of the product

function on FFT will increase. Thus, the author used the absolute mean amplitude statistical parameter as chatter index (CI). Higher the value of CI signifies higher chatter vibration and leads to the bad surface quality of work material. Hence, from above, one may agree that the study on CI prediction with respect to the cutting factors cannot be ignored. This motivates the authors to use response surface methodology (RSM) for modeling prediction relation of surface quality of work material with cutting factors and CI.

2 Experimental Design

Experiments have been conducted on CNC lathe by varying the cutting factors: (d) mm = 0.2, 0.3, and 0.4, (n) rpm = 1000, 1500, and 2000, and (f) mm/min = 30, 35, and 40. The Carbide insert TTS04 cutting tool has been used for machining of AI-6061-T6 work material.

2.1 Experimental Setup

The experimental setup is consists of a CNC lathe, a microphone, a signal acquisition setup, a laptop to record signals using MATLAB software as shown in Fig. 2. The specification of the CNC lathe used for the experiments is shown in Table 1.

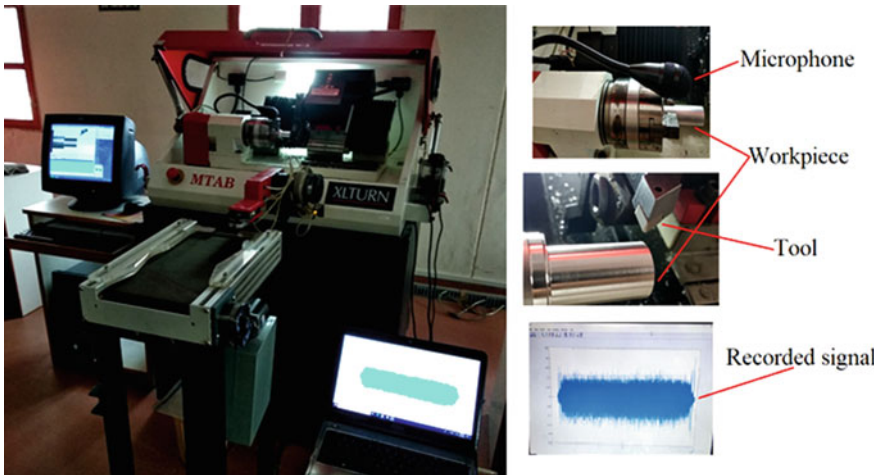


Fig. 2 Experimental setup

Table 1 Description of MTAB XL-TURN CNC lathe

Chuck size	Maximum turning diameter	Maximum turning length	Axes number	Overbed swing	Swing over cross slide	Space between centers from spindle face
100 mm	32 mm	120 mm	2	150 mm	50 mm	210 mm

2.2 Signal Acquisition

The signal acquisition using a microphone sensor is used for chatter analysis. The microphone received the noise-induced during turning and connected to the laptop. Through MATLAB software, acoustics signals have been acquired. The microphone needs to install carefully in the vicinity of the cutting tool and work material. One of the sample recorded signals is shown in Fig. 4.

3 Methodology

In order to develop a prediction model, cutting factors setting and acoustic signals are required. The cutting factors and acquisition of acoustic signals have already been described. FFT of acquired acoustic signals and corresponding surface quality of work material has been analyzed. In the analyses, the peaks obtained are due to chatter frequencies and also because of unwanted contaminations and ambient sound. So, it is very important to remove these noise contents before processing using a suitable technique. Authors have used local mean decomposition signal processing techniques to remove the unwanted noise and demodulate the acquired signals into product functions (PFs).

4 Local Mean Decomposition

Smith proposed the LMD signal processing technique [15]. The outlay of the LMD signal processing technique is shown in Fig. 3.

Further, chatter index has been evaluated for influential product function, obtained from the LMD technique. Moreover, using response surface methodology, the stability range has been predicted. The product function obtained using the LMD technique for one of the signals is shown in Fig. 4. In the figure, the FFT analysis is also shown for some of the PFs, in which scattered peaks represent the different chatter frequencies, obtained during turning. From Fig. 4, the chatter frequency of influential PF1 is 173.86 Hz at an amplitude 57.18 dB is obtained.

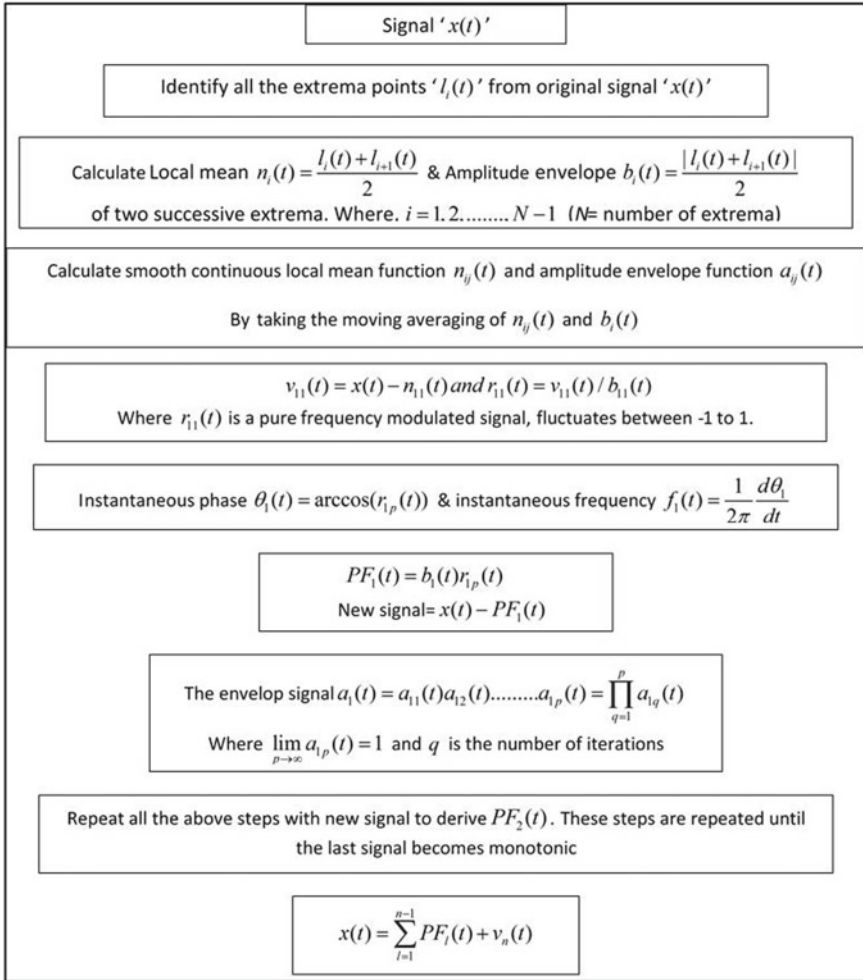


Fig. 3 Outlay of LMD signal processing technique

5 Prediction Model of Chatter Index

In the present analysis, the absolute mean amplitude has been considered as chatter index (CI), which reflects the severity of chatter [17–21]. The CI can be evaluated using Eq. (1). Higher the value of CI signifies higher chatter and leads to the bad surface quality of work material. Hence, authors have to use CI to develop the stability prediction model using response surface methodology (RSM) with cutting factors.

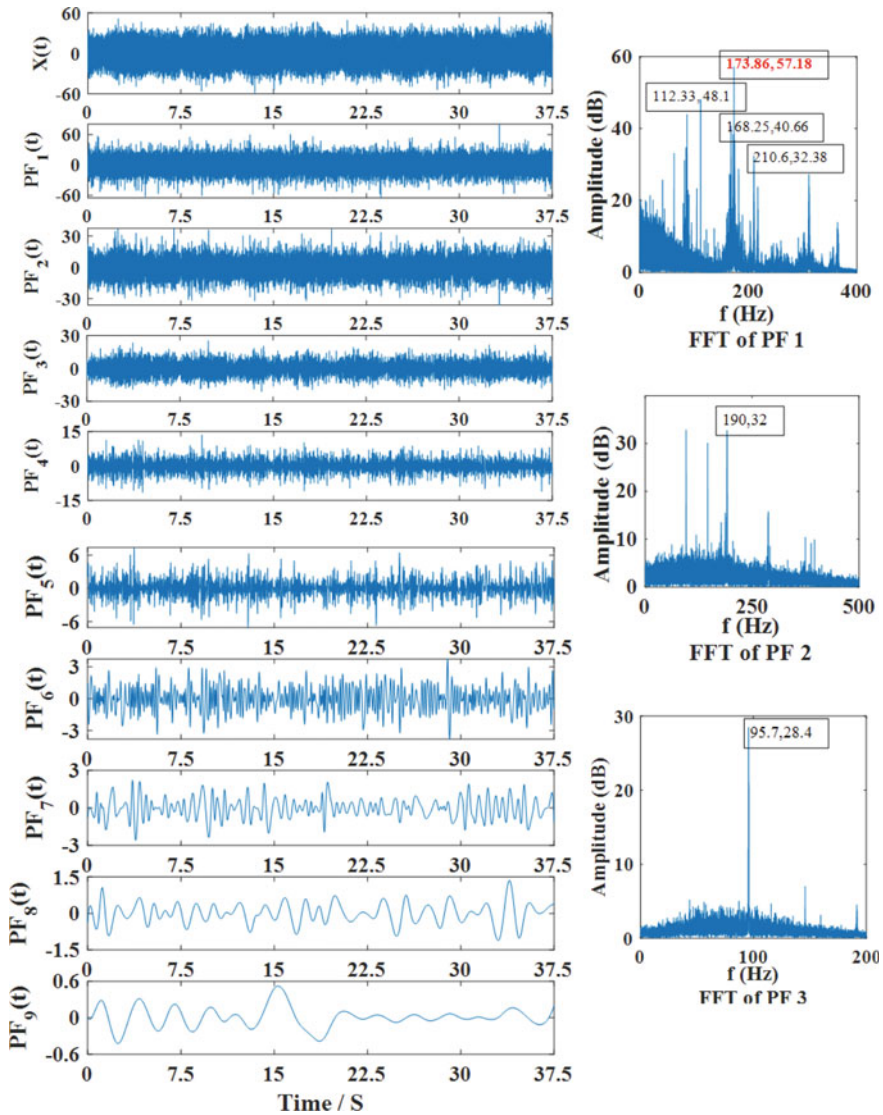


Fig. 4 PFs and FFTs of one of the acquired signal

$$CI = \frac{1}{L} \sum_{l=1}^L |x(t)| \tag{1}$$

‘ $|x(t)|$ ’ represents the absolute value of the signal’s amplitude, and the total sample size of signal is represented using ‘ L .’

The prediction model of chatter severity to discover the relative dependence of CI on input turning factors has been established using RSM [22]. The generated model is shown in Eq. (2).

$$\begin{aligned}
 \text{CI} = & 1.405 + 0.006 \times d + 0.930 \times n - 0.063 \times f \\
 & + 0.471 \times (d)^2 + 0.530 \times (n)^2 + 0.448 \times (f)^2 \\
 & - 0.014 \times (d) \times (n) + 0.215 \times (d) \times (f) \\
 & + 0.029 \times (n) \times (f)
 \end{aligned} \tag{2}$$

Validation of the prediction model

For validation of the developed prediction model, experimental CI values have been compared with different cutting factors. From the comparison, it has been found that the deviation is only 7.25%. The obtained surface topographies during machining at these aforementioned RSM validation experiments are also shown in Table 2.







6 Results and Discussion

To identify the comparative influence of input parameters on CI and to obtain a safe machining range pertaining to the minimum value of CI. From Fig. 5, it has been inferred that for minimum chatter, the depth of cut should be between 0.30 and 0.37 mm, and the value of spindle speed should be between 1000 and 1275 rpm when the feed rate is kept constant. Figure 6 inferred that at constant spindle speed the depth of cut should be between 0.30 and 0.36 mm, and the feed rate should be between 35.5 and 37.3 mm/min. Similarly, Fig. 7 shows the value of spindle speed should be between 1060 and 1300 rpm, and the feed rate should be between 35.5 and 37.3 mm/min at a constant depth of cut. Thus, the intersection of contours of Figs. 5, 6, and 7 combined shows that the value of a safe cutting zone should be as follows: Depth of cut ranges from 0.30 to 0.36 mm, spindle speed ranges from 1060 to 1275 rpm, and feed rate ranges from 35.5 to 37.3 mm/min.

It has been observed that spindle speed and depth of cut affect chatter more prominently as associated to feed rate. However, the feed rate is also an important parameter that needs to be selected properly for minimum chatter.

Intersections of these aforementioned zones have been done to govern a stable cutting range of input factors. The obtained stable cutting zone has been validated for carrying out more experiments, which is shown in Table 3. Table 3 also presents the value of CI obtained while machining at this given combination. In the validation experiments, performing turning operations considering the range of input process parameters are given and yielded that the CI values should be less than 1.52 for stable turning. Validation experiments show the significance of the proposed methodology.

Table 2 Surface topography

d (mm)	n (rpm)	f (mm/min)	Experimental CI	Predicted CI	% deviation	Surface topography
0.2	1000	40	1.42	1.60	12.20	
0.2	1500	30	2.73	2.60	5.01	
0.2	2000	40	3.38	3.54	4.84	
0.3	1000	35	1.03	1.01	2.39	
0.4	1000	40	1.92	2.07	7.58	
0.4	2000	40	3.55	3.96	11.48	
					Average % deviation of CI = 7.25	

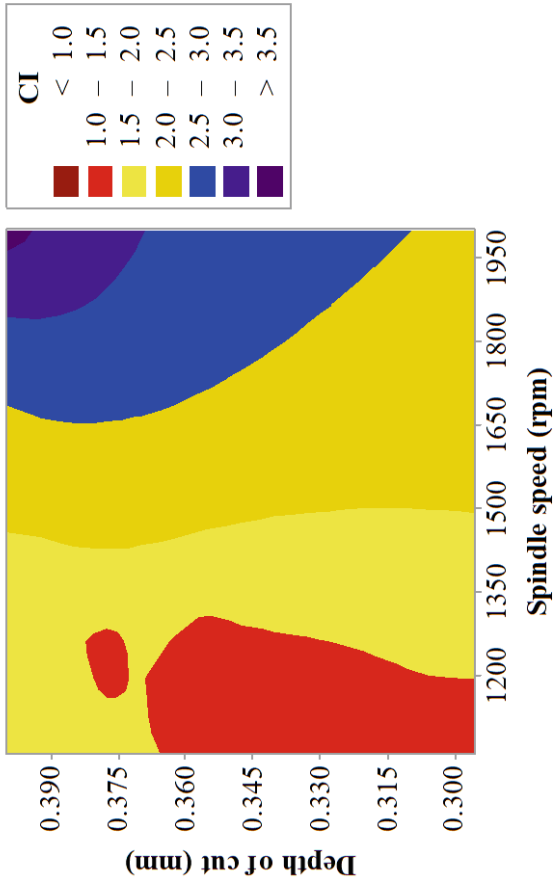


Fig. 5 Contour of CI with respect to (d) and (n)

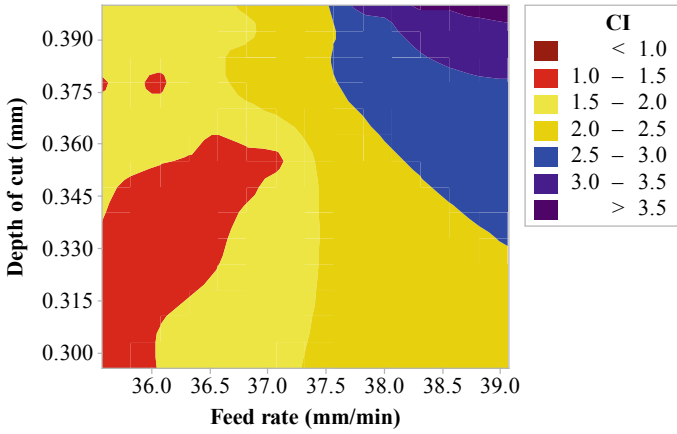


Fig. 6 Contour of CI with respect to (*d*) and (*f*)

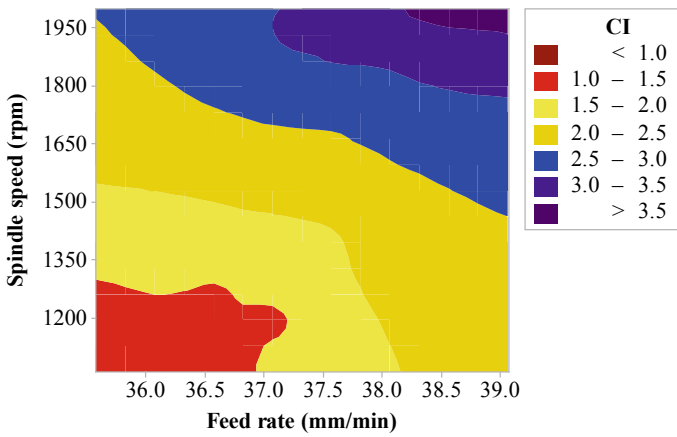


Fig. 7 Contour of CI with respect to (*n*) and (*f*)

Table 3 Validation experiments

<i>d</i> (mm)	<i>n</i> (rpm)	<i>f</i> (mm/min)	CI	Surface topography
0.35	1220	37	1.25	
0.36	1260	37.2	1.36	
0.37	1280	37.3	1.46	

7 Conclusions

In this paper, LMD signal processing approach has been used to extract the chatter features of the acquired acoustic signal. It shows that the LMD technique is efficient in removing unwanted noise. Further, the statistical features have been studied using chatter index (CI) and inferred that the CI can be used to represent the occurrence of chatter. The value of CI should be below 1.52 for stable turning. RSM has been attempted for better predictability of stable range at the low computational effort. The 7.25% percentage deviation of the prediction model shows the robustness of predictability. Moreover, it has been found that the stable cutting range for depth of cut is (0.30–0.36) mm, spindle speed is (1060–1275) rpm, and feed rate is (35.5–37.3) mm/min.

References

1. Wan M, Feng J, Ma Y-C et al (2017) Identification of milling process damping using operational modal analysis. *Int J Mach Tools Manuf* 122:120–131
2. Yang Y, Zhang W-H, Ma Y-C et al (2016) Chatter prediction for the peripheral milling of thin-walled workpieces with curved surfaces. *Int J Mach Tools Manuf* 109:36–48
3. Cao H, Yue Y, Chen X et al (2018) Chatter detection based on synchrosqueezing transform and statistical indicators in milling process. *Int J Adv Manuf Technol* 95:961–972
4. Liu C, Zhu L, Ni C (2017) The chatter identification in end milling based on combining EMD and WPD. *Int J Adv Manuf Technol* 91:3339–3348
5. Uekita M, Takaya Y (2017) Tool condition monitoring technique for deep-hole drilling of large components based on chatter identification in time–frequency domain. *Measurement* 103:199–207
6. Wei C-C, Liu M-K, Huang G-H (2016) Chatter identification of face milling operation via time-frequency and fourier analysis. *Int J Autom Smart Technol* 6:25–36
7. Zhang Z, Li H, Meng G et al (2016) Chatter detection in milling process based on the energy entropy of VMD and WPD. *Int J Mach Tools Manuf* 108:106–112
8. Rafal R, Pawel L, Krzysztof K et al (2015) Chatter identification methods on the basis of time series measured during titanium superalloy milling. *Int J Mech Sci* 99:196–207
9. Shrivastava Y, Singh B, Sharma AJMTP (2018) Identification of chatter in turning operation using WD and EMD 5:23917–23926
10. Zhao H, Sun M, Deng W et al (2017) A new feature extraction method based on EEMD and multi-scale fuzzy entropy for motor bearing. *Entropy* 19:14
11. Cao H, Zhou K, Chen X (2015) Chatter identification in end milling process based on EEMD and nonlinear dimensionless indicators. *Int J Mach Tools Manuf* 92:52–59
12. Huang NE, Shen Z, Long SR et al (1998) The empirical mode decomposition and the Hilbert spectrum for nonlinear and non-stationary time series analysis. *Proc Royal Soc London Series A: Math Phys Eng Sci* 454:903–995
13. Lian J, Liu Z, Wang H et al (2018) Adaptive variational mode decomposition method for signal processing based on mode characteristic. *Mech Syst Signal Process* 107:53–77
14. Sandoval S, Bredin M, De Leon PL (2018) Using linear prediction to mitigate end effects in empirical mode decomposition. In: 2018 IEEE global conference on signal and information processing (GlobalSIP). IEEE, pp 281–285
15. Smith JS (2005) The local mean decomposition and its application to EEG perception data. *J R Soc Interface* 2:443–454

16. Chen X, Yang Y (2017) De-noising for vibration signals based on local mean decomposition. In: IECON 2017–43rd annual conference of the IEEE industrial electronics society. IEEE, pp 3298–3303
17. Shrivastava Y, Singh B (2017) Possible way to diminish the effect of chatter in CNC turning based on EMD and ANN approaches. Arab J Sci Eng 43:4571–4591. <https://doi.org/10.1007/s13369-017-2993-1>
18. Shrivastava Y, Singh B (2017) Assessment of stable cutting zone in CNC turning based on empirical mode decomposition and genetic algorithm approach. Proc Inst Mech Eng C J Mech Eng Sci 232:3573–3594. <https://doi.org/10.1177/0954406217740163>
19. Shrivastava Y, Singh BJJOTBSOMS (2018) Estimation of stable cutting zone in turning based on empirical mode decomposition and statistical approach 40:77
20. Shrivastava Y, Singh B (2018) A comparative study of EMD and EEMD approaches for identifying chatter frequency in CNC turning. Eur J Mech A/Solids
21. Shrivastava Y, Singh B (2019) Online monitoring of tool chatter in turning based on ensemble empirical mode decomposition and Teager Filter. Trans Inst Meas Control 0142331219885511
22. Shrivastava Y, Singh B (2018) Estimation of stable cutting zone in turning based on empirical mode decomposition and statistical approach. J Braz Soc Mech Sci Eng 40:77

Thermoeconomic Analysis of Crossflow Printed Circuit Heat Exchanger



K. Manjunath

Abstract In this work, the economic analysis based on second law performance parameter, namely entropy generation number, is used to carry out parametric study of crossflow printed circuit heat exchanger (PCHE). Thermoeconomics involves two parts, namely cost associated with the investment of heat exchanger construction and material as capital cost. The other part is cost associated with operational irreversibilities losses in the heat exchanger. The advantage of using thermoeconomic analysis is that it incorporates all the second law thermodynamic irreversibilities occurring in the heat exchangers to provide realistic results. In this analysis, thermal design of PCHE is carried out considering the geometrical dimensions and operations parameters. Optimum values of PCHE dimensions are found out which provides lower thermoeconomic cost of operations which leads to conservation of energy.

Keywords Printed circuit heat exchanger · Entropy generation minimization · Economic analysis · Irreversibilities costs

Nomenclature

C_T	Thermoeconomic cost, \$/year;
N_{sh}	Heat transfer entropy generation number;
N_{sp}	Pressure drop entropy generation number;
PCHE	Printed circuit heat exchanger.

K. Manjunath (✉)

Department of Mechanical Engineering, Delhi Technological University, Bawana Road, New Delhi 110042, India

1 Introduction

Compactness of equipment is the new trend which is going to achieve not only weight reduction but also enhanced performance. Same is true in the case of heat exchangers, and there is a need of enhancing the heat transfer and reduction of size and weight. In the recent times, printed circuit heat exchangers are becoming popular in fulfilling above aspects of increasing the heat transfer duty and having very low size and low weight in comparison with conventional ones.

Irreversibilities losses happening in processes can be found out by second law thermodynamic analysis. The methods of second law of thermodynamics involve entropy generation and exergy analysis [1]. Extensive reviews of heat exchangers were carried out by [2] using method of second law analysis and constructal law. Manjunath and Kaushik [3] investigated constructal heat exchanger using thermoeconomics and entropy generation methods.

Printed circuit heat exchangers have been studied and analyzed by different investigators used for various applications. Various researches [4–18] have carried out their works on PCHE based on empirical correlations, parametric study, design optimization, investigations of flow configurations, comparison with conventional one, experimental, numerical, mathematical correlations, thermal and hydraulic performance analysis, different configurations for improvements, various designs of fluid paths and using different materials of constructions.

The manufacturing procedure of PCHE is as follows. The groove flow path on plates surface is photochemically etched. These plates are stacked one above the other and joined by diffusion bonding [19]. By the use of thermal soaking period resulting in grain growth, strong interface-free bond between the plates can be achieved. PCHEs have not only very high built strength but also have special capability to undergo very high operating pressures as high as 600 bar and withstand temperatures having from deep cryogenic and high up to 900 °C. Also, PCHE is having advantage of 75–80% compact in size, and weight is lower. It can withstand higher levels of vibrations and shock in comparison with conventional heat exchangers [20, 21]. PCHE produced by M/s. Heatric [19] is having compactness from 200 to 5000 m²/m³ and highest temperature capacity of 900 °C. It can have higher pressure capability up to 400 bar and results in effectiveness up to 0.97 as a unit. Usually, PCHEs are manufactured from special alloys materials such as hastelloy N, incoloy alloy 800H, inconel alloy 617, alloy 242, SiC (ceramic), along with stainless steel 316.

From the literature survey, it is found that the second law thermodynamic analysis has not been carried out for crossflow both unmixed fluids PCHE using thermoeconomics. So, there is a need to analyze this compact heat exchanger which has wider applications involving high temperature and pressure operations. In this work, economic analysis which incorporates the second law thermodynamic irreversibilities occurring in a system known as thermoeconomic is used as performance parameter. Also, another second law thermodynamic non-dimensional performance parameter, namely entropy generation number, used to analyze crossflow PCHE.

This entropy generation number consists of entropy generation because of heat transfer, pressure drop and imbalance irreversibility. The geometrical and operating parameters are studied along with thermoeconomic for thermal design of PCHE. Helium is considered as working fluid which is used for high-temperature heat transfer processes. The simulations program was written using the empirical formulae available in the open literatures which are established and validated experimentally.

2 Analysis

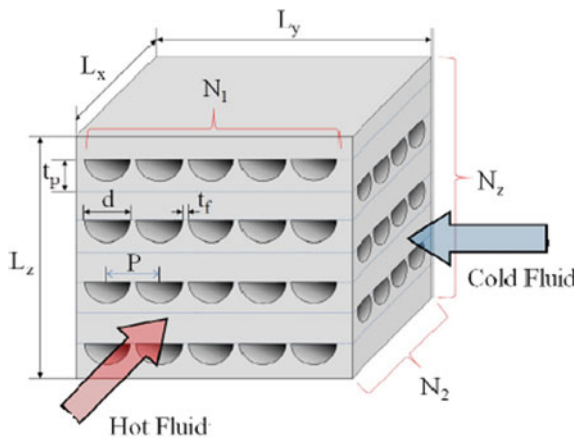
A crossflow PCHE having straight channels is shown in Fig. 1 [6]. The nomenclature of the PCHE flow path is mentioned as follows: diameter (semi-circular) = d , pitch = P , plate thickness = t_p , horizontal thickness = t_f , overall heat exchanger length = L_x , height = L_z , width = L_y , number of flow channels in hot side = N_1 , number of flow channels in cold side = N_2 and number of rows in cold and hot sides = N_z .

Some of the assumptions considered for the analysis are that the flow will be fully developed turbulent, the fluids flow pressure drop is assumed to be friction in constant cross section of tube only and pressure loss due to joints is neglected. The heat transfer between cold and hot streams is excellent, and fouling resistances are neglected [3].

2.1 Thermoeconomic Analysis

The overall (total) cost of PCHE is defined as the addition of investment (capital) cost and the irreversibility (operation) penalty costs [3].

Fig. 1 Crossflow PCHE configurations [6]



$$C_T = C_{\text{capital}} + C_{\text{Operation-penalty}}$$

$$C_T = C_E R_C \Phi + C_S H_R \dot{I} \quad (1)$$

Here, C_E is defined as the system cost taken as proportional to mass of the PCHE including the manufacturing cost. The operation maintenance factor will be Φ . C_S will be the cost in connection with irreversibilities (I) of the system. H_R = whole year hours of operations.

Also, the recovery factor is defined as

$$R_c = \frac{i_e(1 + i_e)^{l_c}}{(1 + i_e)^{l_c} - 1} \quad (2)$$

Here, i_e = interest rate and l_c = whole life of usage expressed in years.

2.2 Irreversibilities in PCHE

The irreversibility expression given by Gouy–Stodola formula is defined as product of reference temperature and entropy generation rate,

$$\dot{I} = T_o \dot{S}_{\text{gen}} \quad (3)$$

The entropy generation rate is expressed in terms of entropy generation number and minimum of heat capacity.

$$\dot{I} = T_o (N_s C_{\text{min}}) \quad (4)$$

where S_{gen} is entropy generation rate, T_o is the reference temperature, and C_{min} and N_s are defined further.

Heat capacity of heat exchanger is obtained by multiplying the specific heat and flow rate for both streams.

$$(\dot{m}c_p)_c = C_c \quad \text{and} \quad (\dot{m}c_p)_h = C_h \quad (5)$$

The heat capacity ratio is given as

$$C = \frac{C_{\text{max}}}{C_{\text{min}}} \quad (6)$$

where C_{max} = heat capacity (maximum), and C_{min} = heat capacity (minimum).

Here, in this analysis, defining $C_{\text{max}} = C_h$ and $C_{\text{min}} = C_c$,

$$C = \frac{C_h}{C_c} \quad (7)$$

The effectiveness of cross flow heat exchanger for both unmixed fluids is given as

$$\varepsilon = 1 - e^{-\left[\text{NTU}^{0.22} C \left\{ e^{\left(\frac{-\text{NTU}^{0.78}}{C} \right)} - 1 \right\} \right]} \quad (8)$$

Here, NTU is defined as

$$\text{NTU} = \frac{UA_s}{C_{\min}} \quad (9)$$

Here, U is defined in Eq. (14) and A_s = surface area obtained as [6]

$$A_s = \left(\frac{\pi d}{2} + d \right) L_x L_1 N_z = \left(\frac{\pi d}{2} + d \right) L_y L_2 N_z \quad (10)$$

The cold and hot streams numbers are defined as

$$N_1 d + (N_1 - 1) t_f = L_y \quad (11)$$

$$N_2 d + (N_2 - 1) t_f = L_x \quad (12)$$

The number of rows in cold and hot sides is given by

$$N_z = \frac{L_z}{2t_p} \quad (13)$$

The overall heat transfer coefficient is defined as

$$\frac{1}{U} = \frac{1}{h_c} + \frac{t}{k_{\text{wall}}} + \frac{1}{h_h} \quad (14)$$

where t is the plate thickness, k_{wall} = thermal conductivity of PCHE material, and h is the hot and cold channels heat transfer coefficients, respectively, defined as

$$h = \frac{\text{Nu}k}{d_e} \quad (15)$$

where k will be conductivity (thermal) of each stream, respectively.

The Nusselt number is defined for semi-circle fluid channel that can be expressed as [6]

$$\text{Nu} = 0.0228 \text{Re}^{0.8} \quad (16)$$

Here, Re = Reynolds number is expressed as

$$\text{Re} = \frac{\rho V d_e}{\mu} \quad (17)$$

where ρ = fluid density, V = fluid velocity, μ = fluid viscosity, and d_e = equivalent diameter is given as

$$d_e = \frac{\frac{\pi d^2}{2}}{\frac{\pi d^2}{2} + d} \quad (18)$$

The fluid velocity is given as

$$V = \frac{\dot{m}}{\rho A_c} \quad (19)$$

where A_c = channels cross-sectional area defined accordingly as

$$A_{c,c} = \frac{\pi d^2}{8} N_2 N_z \quad (20)$$

$$A_{c,h} = \frac{\pi d^2}{8} N_1 N_z \quad (21)$$

The heat transfer rate expressed as

$$Q = UA_s(T_{h,in} - T_{c,in}) \quad (22)$$

The heat exchanger pressure drop is expressed as

$$\Delta p = \frac{4fL\rho V^2}{2d_e} \quad (23)$$

where L = heat exchanger channel length, and f = friction factor for semi-circle fluid channel which is given as [6]

$$f = 0.478\text{Re}^{-0.26} \quad (24)$$

Entropy generation number is expressed as ratio of entropy generation rate and minimum heat capacity rate [1] as follows.

$$N_s = \frac{\dot{S}_{\text{gen}}}{C_{\text{min}}} \quad (25)$$

Above N_s equation is defined as the sum of heat transfer and pressure drop terms as

$$N_S = N_{S,\Delta T} + N_{S,\Delta P} \quad (26)$$

The entropy generation rate defined as [1]

$$\begin{aligned} \dot{S}_{\text{gen}} = & \left(\dot{m}c_p \right)_c \ln \left(\frac{T_{c,\text{out}}}{T_{c,\text{in}}} \right) + \left(\dot{m}c_p \right)_h \ln \left(\frac{T_{h,\text{out}}}{T_{h,\text{in}}} \right) \\ & - \left(\dot{m}R \right)_c \ln \left(\frac{P_{c,\text{out}}}{P_{c,\text{in}}} \right) - \left(\dot{m}R \right)_h \ln \left(\frac{P_{h,\text{out}}}{P_{h,\text{in}}} \right) \end{aligned} \quad (27)$$

Following the procedure provided in Ref. [1] finally the different terms of N_s are obtained as follows.

$$N_{S,\Delta T} = \ln \left[1 + \varepsilon \left(\frac{T_{h,\text{in}}}{T_{c,\text{in}}} - 1 \right) \right] + C \ln \left[1 - \frac{1}{C} \varepsilon \left(1 - \frac{T_{c,\text{in}}}{T_{h,\text{in}}} \right) \right] \quad (29)$$

$$N_{S,\Delta P} = \left[\left(\frac{R_c \Delta P}{C_{p,c} P_c} \right) + \left(\frac{R_h \Delta P}{C_{p,h} P_h} \right) \right] \quad (30)$$

3 Results and Discussion

The following input data of crossflow PCHE considered for the formulation and for generation of simulated results are as follows:

PCHE data [6]: channel diameter ($d = 0.003$ m), overall length ($L_x, L_y, L_z = 1$ m) (L_x varied for parametric study), channel pitch ($P = 0.0033$ m), thickness of plate (channel) ($t_p = 0.00317$ m) and horizontal thickness (channel) ($t_f = P - d$).

Operating data [22]: Helium is considered as working fluid which is used in high-temperature heat transfer. *Cold stream*: temperature (inlet, $T_{c,\text{in}} = 102$ °C), pressure (inlet, $P_{c,\text{in}} = 3$ MPa) and flow rate ($m_c = 100$ kg/s). *Hot stream*: temperature (inlet, $T_{h,\text{in}} = 494$ °C), pressure (inlet, $P_{h,\text{in}} = 7$ MPa) and flow rate ($m_h = 150$ kg/s).

Material data (hastealloy-N): conductivity, $k_{\text{wall}} = 23.5$ W/mK which is used as material for heat exchanger in high pressure and temperature operations in nuclear power plants [20, 21].

Thermoeconomic data: Equipment cost (C_E) can be defined as: $C_E =$ material mass \times material cost \times fabrication factor.

Material mass is defined as product of heat exchanger (volume) and material (density).

PCHE material cost [23] = 20 \$/kg (hastealloy-N), fabrication factor = 6.5 [20, 21] and density of heat exchanger material (ρ_m) = 8860 kg/m³ (hastealloy-N). (operation–maintenance) factor (ϕ) = 1.06, operation period (H_R) = (365 days/year \times 8 h/day) expressed as hours/year, technical life (l_c) = 20 years, interest rate (i_c) = 10% and cost of electricity (C_s) = 0.1 \$/kW h [3].

The simulations are carried out in EES software [24], and the outputs are obtained.

Figure 2 shows the variations of total cost (C_T) with the increase of length, width and height of heat exchanger. The thermoeconomic total cost is exhibiting minimum value for particular value of heat exchanger dimensions. This optimum value provides the most economical value for given input values of PCHE. Also, in the same figure, the variations of capital cost and operation penalty cost are shown. As the dimensions of PCHE increase, the capital cost increases while the operation penalty cost decreases. The sum of these two costs provided minimum optimum value of thermoeconomic total cost. The reasons for these results are presented in the next two figures.

Figures 3 and 4 present the behavior of entropy generation numbers of heat transfer (N_{sh}) and pressure drop (N_{sp}), respectively, for the increase of PCHE dimensions. There is decreasing trend of both N_{sh} and N_{sp} for increase of PCHE dimensions. This indicates that the losses due to irreversibilities will decrease for increase in dimensions. This is the reason for reducing trend of operation penalty cost as shown in Fig. 2.

Fig. 2 Thermoeconomic costs versus overall lengths of PCHE

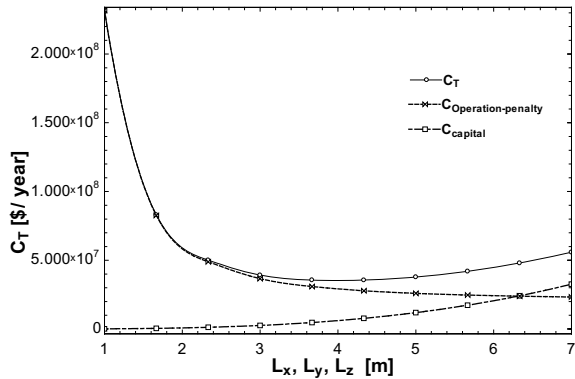


Fig. 3 Heat transfer entropy generation number versus overall lengths of PCHE

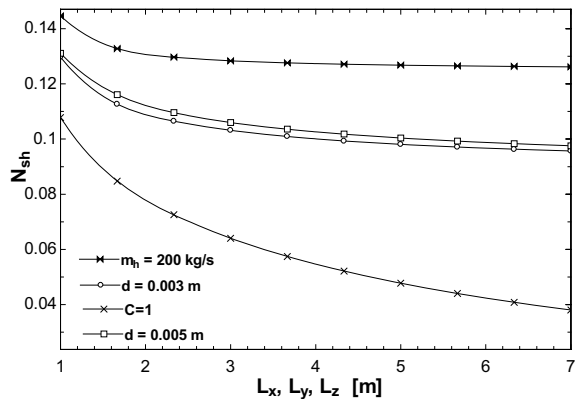
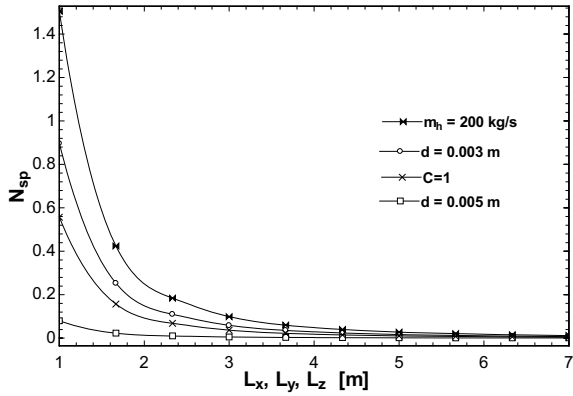


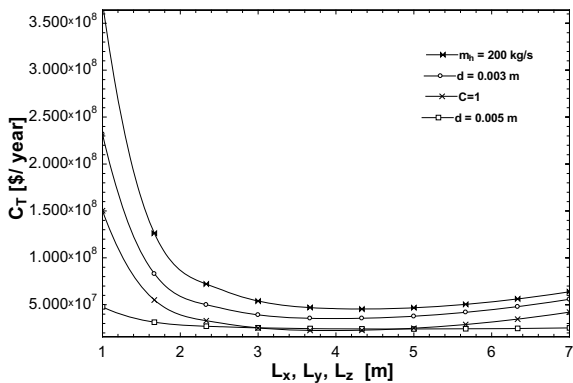
Fig. 4 Pressure drop entropy generation number versus overall lengths of PCHE



Also, Figs. 3 and 4 provide the trends of increase in channel diameter (d) from 0.003 to 0.005 m, increase of hot fluid (m_h) from 150 to 200 kg/s and when capacity rate ratio (C) = 1. When channel diameter increased, there is decrease in N_{sp} (because of reduction of pressure drop), while there is increase of N_{sh} (due to increase of surface area). As flow rate of hot fluid increases, both N_{sh} and N_{sp} increase due to increase of velocity (imbalance between the fluids) and pressure drop of working fluid. When $C = 1$, it will achieve a balanced heat exchanger. This will result in reduction of both N_{sh} and N_{sp} as there will be no imbalance irreversibility.

Figure 5 displays thermoeconomic cost (C_T) as mentioned in the above paragraph for different values of d , m_h and C for increase in the values of PCHE dimensions. C_T will initially decrease, attains minimum value and further increases. This will provide optimum values of geometrical and operating parameters for given inputs. When channel diameter increased, there is decrease in C_T value because of decrease in N_s value. As flow rate of hot fluid increases, there is increase in C_T value due to result in higher value of N_s . When $C = 1$, this will result in lower value of C_T due to reduction in imbalance irreversibility.

Fig. 5 Thermoeconomic cost versus overall lengths of PCHE



4 Conclusions

Thermo-economic cost analysis was carried out for crossflow printed circuit heat exchanger which is increasingly used in process industry and power generation sectors for its compact size, high performance and higher operating conditions. As compared to conventional economic analysis, thermo-economic considers the second law irreversibilities as penalty operation cost along with capital cost. These procedures will achieve in providing realistic geometrical and operating parameters in reducing not only costs but also entropy generation losses happening in the thermal systems. For the considered input values from the open literature, the optimum values of heat exchanger dimensions are found out for variations of important operating and geometrical parameters. This will result in achieving energy conservation in heat exchangers.

References

1. Bejan A (1996) Entropy generation minimization. CRS Press, Boca Raton
2. Manjunath K, Kaushik SC (2014) Second law thermodynamic study of heat exchangers: a review. *Renew Sustain Energy Rev* 1(40):348–374
3. Manjunath K, Kaushik SC (2014) Entropy generation and thermo-economic analysis of constructed heat exchanger. *Heat Transf Asian Res* 43(1):39–60
4. Serrano IP, Cantizano A, Linares JI, Moratilla BY (2014) Modeling and sizing of the heat exchangers of a new supercritical CO₂ Brayton power cycle for energy conversion for fusion reactors. *Fusion Eng Des* 1(89(9–10)):1905–1908
5. Lee SM, Kim KY (2014) A parametric study of the thermal-hydraulic performance of a zigzag printed circuit heat exchanger. *Heat Transf Eng* 2(35(13)):1192–2000
6. Yoon SJ, Sabharwall P, Kim ES (2014) Numerical study on crossflow printed circuit heat exchanger for advanced small modular reactors. *Int J Heat Mass Transf* 1(70):250–263
7. Lee SM, Kim KY (2015) Optimization of printed circuit heat exchanger using exergy analysis. *J Heat Transf* 1(137(6))
8. Meshram A, Jaiswal AK, Khivisara SD, Ortega JD, Ho C, Bapat R, Dutta P (2016) Modeling and analysis of a printed circuit heat exchanger for supercritical CO₂ power cycle applications. *Appl Therm Eng* 25(109):861–870
9. Jeon S, Baik YJ, Byon C, Kim W (2016) Thermal performance of heterogeneous PCHE for supercritical CO₂ energy cycle. *Int J Heat Mass Transf* 1(102):867–876
10. Chu WX, Li XH, Ma T, Chen YT, Wang QW (2017) Study on hydraulic and thermal performance of printed circuit heat transfer surface with distributed airfoil fins. *Appl Therm Eng* 5(114):1309–1318
11. Chen F, Zhang L, Huai X, Li J, Zhang H, Liu Z (2017) Comprehensive performance comparison of airfoil fin PCHEs with NACA 00XX series airfoil. *Nucl Eng Des* 15(315):42–50
12. Hinz JF, Nellis GF, Anderson MH (2017) Cost comparison of printed circuit heat exchanger to low cost periodic flow regenerator for use as recuperator in a s-CO₂ Brayton cycle. *Appl Energy* 15(208):1150–1161
13. Kim W, Baik YJ, Jeon S, Jeon D, Byon C (2017) A mathematical correlation for predicting the thermal performance of cross, parallel, and counterflow PCHEs. *Int J Heat Mass Transf* 1(106):1294–1302
14. Yoon SJ, O'Brien J, Chen M, Sabharwall P, Sun X (2017) Development and validation of Nusselt number and friction factor correlations for laminar flow in semi-circular zigzag channel of printed circuit heat exchanger. *Appl Therm Eng* 123:1327–1344

15. Zhao Z, Zhang X, Zhao K, Jiang P, Chen Y (2017) Numerical investigation on heat transfer and flow characteristics of supercritical nitrogen in a straight channel of printed circuit heat exchanger. *Appl Therm Eng* 5(126):717–729
16. Guo J, Huai X (2017) Performance analysis of printed circuit heat exchanger for supercritical carbon dioxide. *J Heat Transf* 1(139(6))
17. Manjunath K, Sharma OP, Kaushik SC (2020) Entropy generation and thermoeconomic analysis of printed circuit heat exchanger using different materials for supercritical CO₂ based waste heat recovery. *Mater Today: Proc* 1(21):1525–1532
18. Saeed M, Berrouk AS, Siddiqui MS, Awais AA (2020) Effect of printed circuit heat exchanger's different designs on the performance of supercritical carbon dioxide Brayton cycle. *Appl Thermal Eng* 1(179):115758
19. 'Heatric (2020) PCHE heat exchanger, internet website. <https://www.heatric.com>. Last accessed 18th Aug 2020
20. Ravindran P, Sabharwall P, Anderson NA (2010) Modeling a printed circuit heat exchanger with relap5–3d for the next generation nuclear plant. Office of scientific and technical information technical reports
21. Sabharwall P (2011) Feasibility study of secondary heat exchanger concepts for the advanced high temperature reactor. Idaho National Laboratory (INL)
22. Dewson SJ (2003) The development of high efficiency heat exchangers for helium gas cooled reactors. In: Proceedings 2003 international congress on advances in nuclear power plant (ICAPP'03), Cordoba, Spain, pp 3213
23. Cost of hastelloy-N for PCHE, internet website. <https://www.alibaba.com/trade/search>. Last accessed 20th Aug 2020
24. Klein SA (2008) EES, engineering equation solver, version 8.158, F Chart Software, Middleton, WI

A Comparative Study on the Performance of Energy Storage Systems for Hybrid Electric Vehicles



Kanchan Yadav and Sanjay Maurya

Abstract Energy storage is the focused area for the researchers and the academia; thus in this paper, the different energy storage technologies are discussed in detail. The main working principles for most of the ESS are explained by analyzing their attributes for different specifications. The emerging concepts in transportation raised the role of storage solutions, so it cannot be possible to specify any one storage solution that will be able to fulfill varying demands and performance characteristics; thus, different storage solutions are discussed. The comparison of different energy storage systems based on certain parameters like power, energy and efficiency demands is examined. The updated energy storage systems are also scrutinized along with their specifications for the electric vehicles. Finally, it is said that in this paper various electrical energy storage methods for the electric vehicles are discussed with their analysis so that this will help the readers to understand about the potential energy storage solutions for the electric vehicle, plug-in or hybrid electric vehicles. The model used in this analysis replaced the previous relationships in which ESS capacity is unpredicted.

Keywords ESS—energy storage system · ESS attributes · Key technologies · Hybrid electric vehicles · Energy demands

1 Introduction

We are very clear with the fact that the energy storage system is not the new thing, as we are using batteries since the early 1800. Various emerging concepts in the transportation and the increase in the usage for various hybrid, all-electric or plug-in vehicles are the main reason behind the significant role of ESS [1]. The demand

K. Yadav (✉) · S. Maurya
Department of Electrical Engineering, GLA University, Mathura, India
e-mail: kanchan.yadav@gla.ac.in

S. Maurya
e-mail: Sanjay.maurya@gla.ac.in

for the construction of new energy storage systems has been increased significantly when the more dynamic and cleaner grid requirement has come into existence and thus it led the policy makers to think about new and better solutions for the energy storage applications.

Basically, the purpose behind the storage of energy is to capture it and deliver this stored energy for the future usage. For the sustainable use of resources, the concern should be focused on environmental impacts of fossil fuels and various solutions for the energy storage systems. Thus, various characteristics of the ESS contribute to the performance of the hybrid vehicles [2]. With the involvement of energy storage, the intermittency of solar power and wind power has also been addressed and it can also be effective in reducing the need for building backup power plants. With the change in demand, how quickly the energy storage is able to respond shows the effectiveness of this facility. It is also dependent on several other factors which involve the rate at which energy loss occurs during the process of storage, the overall capacity of the energy storage systems and also on its quicker action during recharging.

Generally, the fossil fuel is the most used form of the energy. Their transportability and the practicality in stored form allow the control in energy supplied. If we look at the energy generation of other resources like solar and wind, then it clearly shows that they are intermittent sources and relied on the seasonal changes and environmental factors. In order to achieve improved efficiency and better power quality, these energy storage systems become the viable solution [3].

2 Selected ESS and SOC Estimation

There are many ways to store the energy, and each of them has their own pros and cons. The energy storage systems are looked upon with various view points by the researchers. These consideration points can be the use of ESS in power systems or the automotive applications. There is a debate in the automotive industry to select the ESS option for the HEV which is best suitable. There are a number of research practices happening so that these storage devices can be made available with the reduced cost, increased lifetime and the improved energy density [4, 5]. In the automotive applications they are used in electric vehicles, only battery electric vehicles or the hybrid electric vehicles with the combination of storage systems and can be fuel cell powered also. If we look at different technologies, then it covers various chemistries like lithium-ion, nickel–metal hydride, lead–acid, nickel–cadmium, Ni–Zn, fuel cell, ultra-capacitors or flywheels. In the current scenario, the developments are going on for various battery technologies, some are already available commercially in the market, while some are in the study struggling in the experimental observations [6]. For the sustainable energy generation taking long term in the view, the three important parameters that are generation, conversion and storage play a crucial role. The clean and efficient energy storage can be used as the strategy if we want to tackle this immense problem of sustainable energy economy [7].

The different storage technologies and their characteristics are observed so that it will serve the purpose to categorize and compare various ESSs and it can help in selecting the most appropriate type of ESS for the particular application [8]. Here is the schematic block diagram of the system’s configuration model. This block models the ESS as an SOC-dependent voltage in series with the SOC and current direction-dependent internal resistance. By assuming constant current A-h capacity, SOC is computed but limited in a way so that it can never exceed the minimum voltage level of the given ESS.

The most important parameter for the battery pack is its SOC which is defined as the ratio of current capacity $Q(t)$ to the nominal capacity Q_n . The maximum charge that can be stored is given by the nominal capacity and is given by the manufacturer itself, and thus we can define SOC as

$$SOC(t) = \frac{Q(t)}{Q_n} \tag{1}$$

The estimation of state of charge for different battery technologies is discussed in this paper, and various methods are illustrated systematically [9]. There are various SOC estimation methods as well that includes direct, bookkeeping, adaptive or the hybrid methods.

- (A) *Open-Circuit Voltage Method*—For this method, the OCV value at 0% SOC and 100% SOC needs to be known, then we can predict the SOC by estimating its open-circuit voltage, and then the battery OCV is calculated as

$$V_{OC}(t) = a_1 * SOC(t) + a_0 \tag{2}$$

- (B) *Terminal Voltage Method*—During battery discharging the terminal voltage drop due to internal impedance, thus its emf is taken as proportional to SOC.
- (C) *Coulomb Counting Method*—This method is most common for the SOC estimation. With the initial SOC value, the sate of charge at different time instants (t) is calculated by the following integration

$$SOC(t) = SOC_i + \frac{1}{3600} \frac{\eta_{bat}(i(t), T)}{Cap(T)} \int_{t_0}^t i(t) dt \tag{3}$$

where $Cap(T)$ is the capacity and $bat(i(t), T)$ is the columbic efficiency of the battery.

3 System Configuration and Description

In the energy storage block, the charge reservoir is the battery pack and then we will make the equivalent circuit by considering the remaining charge of reservoir as

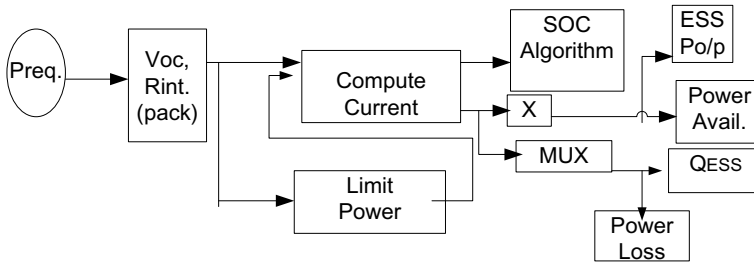


Fig. 1 Schematic block diagram of ESS model

the parameters of this circuit. The battery model is R_{int} which considers the charge contained by the ESS as the constant value, and it is subjected to the minimum voltage limit. After discharging, the battery replenishment gets affected by the coulombic efficiency. In order to evaluate the performance and state of health for the battery, internal resistance can be used to get the information. If there is a need to estimate the battery SOC, its open-circuit voltage can play an important role by considering the intrinsic characteristics of the battery technology [10]. The power which is given by the battery is limited to the maximum value which can be delivered by the equivalent circuit or which the controller is able to accept subjected to the minimum voltage requirements. After obtaining these values, the comparison is done in order to find that the changes occurred in the beginning and ending of cycle are not too large; thus in advisor, two methods are offered for this SOC balancing as it is very necessary during vehicle analysis [11] (Fig. 1).

ESS block represents the energy storage unit which contains the onboard energy for the modeled vehicle. With the power requests, this block provides the output battery power. During modeling, the charge gets reserved, the equivalent circuit accounts for the circuit parameters and the minimum voltage limit is subjected to the ESS. The charging parameters are limited to maximum voltage level, and the charge replenished in the ESS gets affected by the coulombic efficiency.

With the response of the SOC requirements, the ESS is modeled to fulfill the requirements of output available power. For computing the power loss, the i^2R and the coulombic efficiency losses are included. For the equivalent circuit, the V_{oc} and the R_{int} are taken as the linear functions of SOC. As the total power available is limited in the allowable range, thus in addition to V_{oc} , R_{int} actual power available is also taken as the variables for solving the quadratic equation. This quadratic equation is used for obtaining the circuit. The ESS current is used to update the effective SOC. Taking an example, we can say that if the incorrect SOC estimation takes place it can lead to the overcharged or the overdischarged battery and it will in turn damage the battery technology [12].

Maximum power available is also limited to certain parameters; the maximum power limit is obtained by

$$P = V_{\text{bus}} * \frac{V_{\text{oc}} - V_{\text{bus}}}{R} \quad (4)$$

where V_{bus} is either $V_{\text{OC}}/2$ or minimum battery voltage.

Power is given as

$$P = V * I \quad (5)$$

$$V = \frac{P}{I} \quad (6)$$

When we combine this power equation with the KVL, then it will yield

$$\frac{P}{I} = V_{\text{OC}} - (R * I) \quad (7)$$

By multiplying with I on both sides, the equation becomes

$$P = (V_{\text{OC}} * I) - RI^2 \quad (8)$$

Now the equation is solved in the block diagram

$$RI^2 - (V_{\text{OC}} * I) + P = 0 \quad (9)$$

The solution with lower voltage requirement is taken to produce the same amount of power. On charging, the maximum allowable voltage limit should not be exceeded and then the minimum raw current is calculated by

$$I = \frac{V_{\text{OC}} - V_{\text{max}}}{R} \quad (10)$$

For the prediction of the state of charge values for different battery technologies, the new SOC-based algorithm is proposed in the research which is based upon the back-stepping method by using the partial differential equations [13].

In order to estimate the SOC value with the coulombic efficiency, the discharging current is integrated over time. By investigating $\text{SOC}(t)$ from $i(t)$ integration and with the already estimated SOC values $\text{SOC}(t - 1)$, we can obtain the state of charge by

$$\text{SOC}(t) = \text{SOC}(t - 1) + i(t)Q_n \Delta t \quad (11)$$

In advisor, the SOC algorithm determines the residual capacity in amp-hrs charge unit. With the series of steps, this value is approximated, and during this estimation the coulombic efficiency and the maximum capacity remain the functions of temperature. The model used has the open-circuit voltage source and internal resistance. These parameters are proportional to the changes in the state of charge, temperature and

current direction [14]. With the average columbic efficiency estimation, the total effective amp-hr change is determined. For the initial SOC, nonzero Ah is used and then it is calculated by

$$SOC = \frac{C_{max} - Ah}{C_{max}} \tag{12}$$

where, Cmax is maximum capacity and Ah is amp-hr used.

Now the SOC is computed according to the power bus requirements, and the output has the available power. Thus here, the battery modeling is done with controlled voltage source which is taken in series with the constant resistance value [15].

4 Result and Discussion

In this section, we are going to present the schematic diagram of the model used for analysis and the comparison based on different attributes of the ESS. This analysis is done on ADVISOR with the following vehicle parameters (Table 1).

On the basis of above parameters, the different specifications for the selected ESS are tabulated and the analysis is also presented with their obtained characteristics (Table 2).

Table 1 Parameters for the analysis

Component	Parameter	Value
Vehicle	Veh_Cargo mass	136 kg
	Veh_Glider mass	592 kg
ESS Vnom	ESS_Pb	308
	ESS_Li-ion	267
	ESS_Ni-MH	335
	ESS_Ni-Zn	307
	ESS_Ni-Cad	159
	ESS_Ultra-cap	44

Table 2 Obtained ESS specifications

Parameters/ESS	VRLA	Li-ion	Ni-MH	Ni-Cad
Voltage (Max)	16.5	11.7	15.67	6.9
Voltage (Min)	9.5	6	9.13	5.9
Capacitive module	660	795	830	770
Effective res (off)	0.645	7.81	1.59	0.845
Effective res (on)	0.364	1.12	0.53	0.38

The analysis based on different characteristics is shown and illustrated with the following figures. The characteristic variation with state of charge is shown for four different ESS technologies, i.e., valve-regulated lead–acid battery, Li-ion battery, nickel–metal hydride and nickel–cadmium. In the result figures, the different characteristics like the SOC variation of the given ESS with the variation in the model parameters like internal resistance, and the efficiency, are analyzed by taking the four different ESS technologies. From Fig. 2a–d, the curves are shown for the internal resistance variation with the SOC. In Fig. 3a–d, the curves are given for the efficiency illustration.

In these figures, resistance variation with SOC is shown and we can notice that the larger changes are noticed in the nickel-based batteries. For nickel–metal hydride battery, the resistance level is highest when SOC is at lower level. We can say that just after the full charge, the higher battery performance cannot be achieved. Low internal resistance is the important factor needs to be noticed as it determines the run time in the large extent. During delivery, the power spikes require the lower resistance value and import the less restriction on the battery itself. The internal

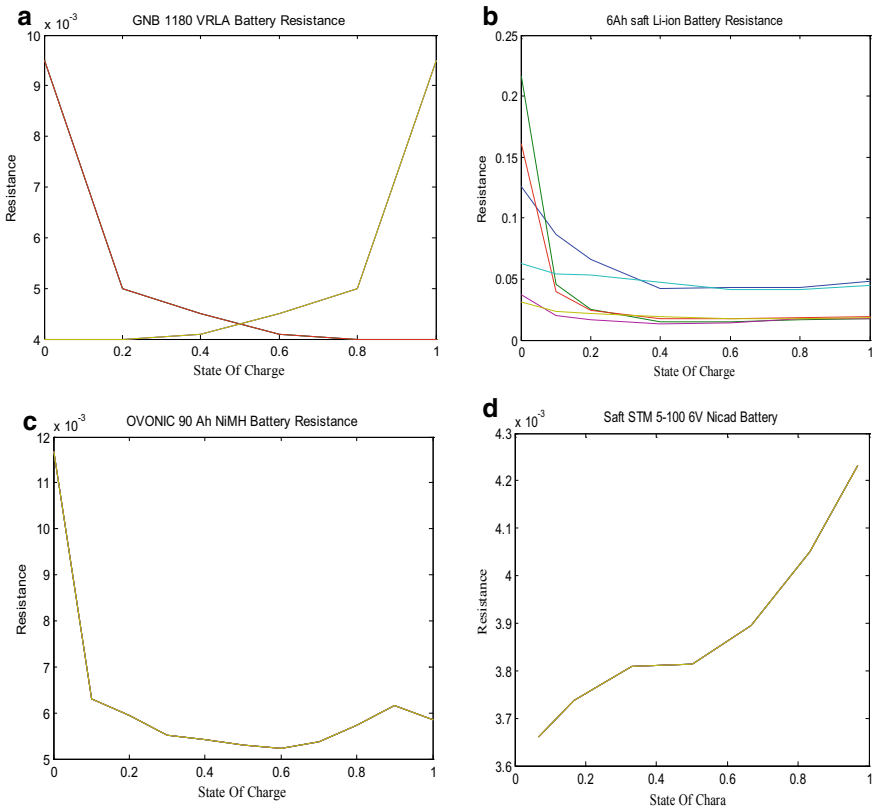


Fig. 2 State of Charge Variation with Resistance for a) VRLA b) Li-ion c) Ni-Mh d) NiCad

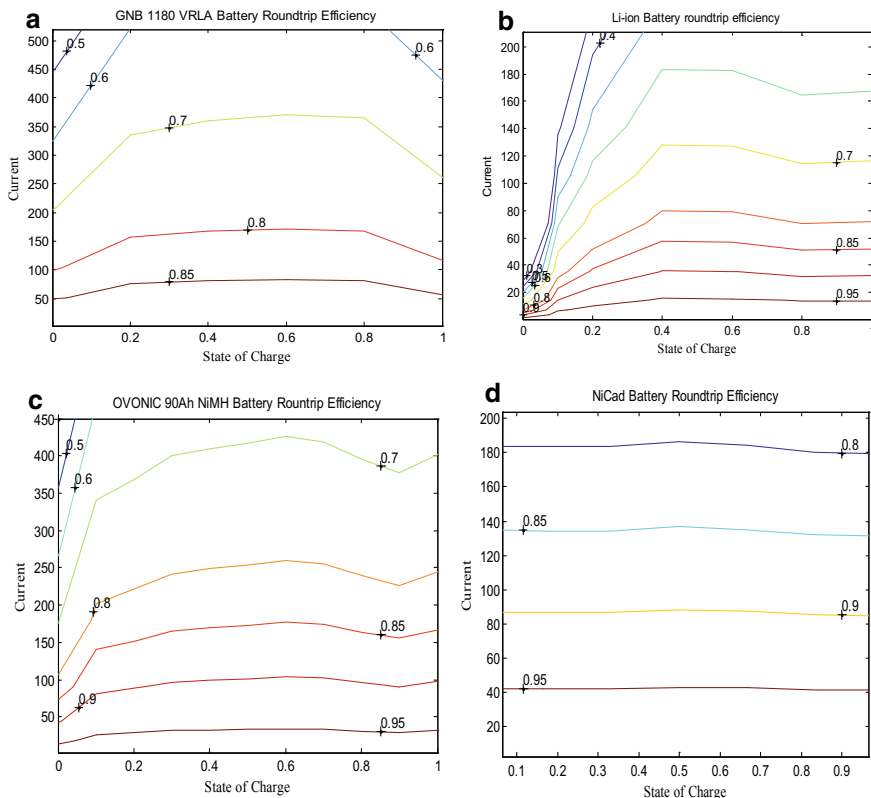


Fig. 3 State of Charge Variation with Current for a) VRLA b) Li-ion c) Ni-Mh d) NiCad

resistance value varies widely with the lower value for nickel–cadmium, the higher value for nickel–metal hydride and the moderate value for lithium-ion battery.

The critical factor defining the usefulness of the battery storage technology is the roundtrip efficiency which is illustrated in the above figures. In the charge efficiency characteristic, the Ni-MH battery is similar to Ni-cad one, as the efficiency is higher for 70% SOC and then it drops. The batteries’ ability to absorb charge is shown with the charge efficiency and has similarities with columbic efficiency. Comparing with lead–acid or lithium-ion batteries, nickel-based batteries are more complex to charge. For Li-ion battery, during a roundtrip it lost approximately 5% of energy; i.e., we can say that it has 95% roundtrip energy efficiency when compared with the lead–acid batteries in which the energy lost is approximately 20–25%. The technological and very innovative advancements are happening nowadays to boost the energy efficiency for the Li-ion battery storage. Thus, Li-ion batteries are often preferred more as compared to lead–acid due to their higher energy and power density. We can say that the storage with the higher roundtrip efficiency has the capability to retain more energy and be able to provide more power.

5 Conclusion

The energy storage technologies came in varieties, and the vehicles rely on them so it would be the fair perspective to select the best for the required application. The conventional lead–acid batteries are also proved for extreme reliability with low maintenance and have higher efficiency. Ni-Cad battery chemistry requires high charging rate and has low value of internal resistance, but at the same time it has higher level of discharge cycle. The advantageous attribute of longer cycle life and lower maintenance requirements makes it more suitable. It can be analyzed that its cycle life is dependent on the depth of discharge and has energy efficiency greater than 70%. Li-ion battery chemistry stores high amount of energy and makes the hybrid vehicles more attractive for them who have high horse power demand. Their use is newer, but due to their popular attributes like longer lifetime, quick recharging process, cost and weight effective thus becomes the best choice, and with the development of science and technology they have gained the mainstream. By analyzing the different ESSs, it can be concluded that in some or the other way if one ESS proves to be superior to the other but at the same time it does not contain the sufficient attributes to completely replace the existing one. Thus, the combination of ESS proves to be better way to use them effectively and take the automotive technologies to the viable mode.

References

1. Alahakoon S, Leksell M (2015) Emerging energy storage solutions for transportation—a review: an insight into road, rail, sea and air transportation applications. In: 2015 international conference on electrical systems for aircraft, railway, ship propulsion and road vehicles (ESARS). IEEE, pp 1–6
2. Kim B-H, Lee B-H, Jeong J-B, Shin D-H, Song H-S, Kim H-J (2009) A study on the performance of the improved energy storage system for mild hybrid vehicles. In: INTELEC 2009–31st international telecommunications energy conference. IEEE, pp 1–6
3. Farhadi M, Mohammed O (2015) Energy storage technologies for high-power applications. *IEEE Trans Ind Appl* 52(3):1953–1961
4. Williamson SS, Khaligh A, Oh SC, Emadi A (2005) Impact of energy storage device selection on the overall drive train efficiency and performance of heavy-duty hybrid vehicles. In: 2005 IEEE vehicle power and propulsion conference. IEEE, p 10
5. Chemali E, Preindl M, Malysz P, Emadi A (2016) Electrochemical and electrostatic energy storage and management systems for electric drive vehicles: state-of-the-art review and future trends. *IEEE J Emerg Sel Top Power Electron* 4(3):1117–1134
6. Divya KC, Østergaard J (2009) Battery energy storage technology for power systems—an overview. *Electr Power Syst Res* 79(4):511–520
7. Placke T, Kloepsch R, Dühnen S, Winter M (2017) Lithium ion, lithium metal, and alternative rechargeable battery technologies: the odyssey for high energy density. *J Solid State Electrochem* 21(7):1939–1964
8. Ibrahim H, Ilinca A, Perron J (2008) Energy storage systems—characteristics and comparisons. *Renew Sustain Energy Rev* 12(5):1221–1250
9. Xiong R, Cao J, Yu Q, He H, Sun F (2017) Critical review on the battery state of charge estimation methods for electric vehicles. *IEEE Access* 6:1832–1843

10. He H, Xiong R, Guo H (2012) Online estimation of model parameters and state-of-charge of LiFePO₄ batteries in electric vehicles. *Appl Energy* 89(1):413–420
11. Markel T, Brooker A, Hendricks T, Johnson V, Kelly K, Kramer B, O'Keefe M, Sprik S, Wipke K (2002) ADVISOR: a systems analysis tool for advanced vehicle modeling. *J Power Sources* 110(2):255–266
12. Peng S, Chen C, Shi H, Yao Z (2017) State of charge estimation of battery energy storage systems based on adaptive unscented Kalman filter with a noise statistics estimator. *IEEE Access* 5:13202–13212
13. Moura SJ, Chaturvedi NA, Krstic M (2012) PDE estimation techniques for advanced battery management systems—Part I: SOC estimation. In: 2012 American control conference (ACC). IEEE, pp 559–565
14. Johnson VH (2002) Battery performance models in ADVISOR. *J Power Sources* 110(2):321–329
15. Tremblay O, Dessaint L-A, Dekkiche A-I (2007) A generic battery model for the dynamic simulation of hybrid electric vehicles. In: 2007 IEEE vehicle power and propulsion conference. IEEE, pp 284–289

Parametric Analysis of Friction Stir Welding of Pure Copper



Deepak Kaushal and Akhilesh Kumar Choudhary

Abstract The present study aims to identify the ideal combination of process variables using Taguchi's method and to examine the impact of process variables which include shoulder diameter, feed, and tool rate on the properties of the pure copper FSW joints. Three H13 tools having shoulder diameter of 12 mm, 16 mm, and 20 mm, tool rate ranges from 600 to 1200 rpm, and welding speed ranges 50–100 mm/min were used for conducting the model calculation. The obtained results show that the tensile strength and hardness rise first to its maximum value with the increased in tool rate and shoulder diameter and then fall with further increase. At tool rate of 900 rpm, welding rate of 50 mm min⁻¹, and tool shoulder diameter of 16 mm, the joints fabricated shown high value of both TS and hardness. Tool shoulder diameter becomes visible to be the most significant variable from the results of ANOVA.

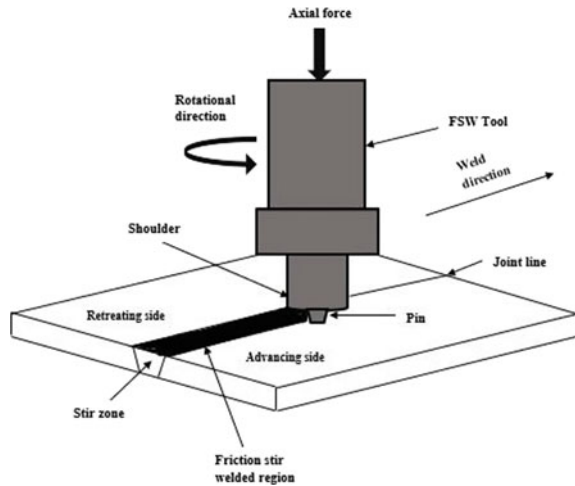
Keywords Copper · Friction stir welding · Shoulder diameter · Tool rate · Taguchi

1 Introduction

Friction stir welding was developed by Wayne Thomas at The Welding Institute (TWI) Limited in 1991, and it conquers a significant number of the issues related to non-pressure joining methods, for instance, solidification-related porosities, shrinkage, and distortion [1, 2]. FSW works through utilizing a non-consumable revolving tool that has, in particular, an intended pin and shoulder which is fed into the adjacent ends of the work-piece to be fused which are heavily clamped to restrict any movement of plates during welding. The shoulder of the rotating tool interacts with the plates, and due to friction among the tool and work material, the heat produced which plasticize the material and the pin rotating inside the joint mechanically mixes the softened material. Then, the tool is moved through the seam line to form a weld joint shown in Fig. 1 [1]. Azizi et al. [3] find that with increase in welding rate,

D. Kaushal · A. K. Choudhary (✉)
Mechanical Engineering Department, National Institute of Technology Hamirpur, Hamirpur,
Himachal Pradesh 177005, India
e-mail: akhilesh@nith.ac.in

Fig. 1 Graphical illustration of FS welding



the tensile strength, hardness, and elongation first increase to maximum and then fall. Pankaj Kumar et al. [4] investigated that increasing the tool rate maximizes the UTS and was decreased by increasing the welding speed. Lee and Jung [5] achieved flaw-free copper welds at tool rate of 1250 rpm and travel rate of 61 mm min⁻¹ with ultimate strength which was about 87% of the parent metal. Lina et al. [6] found that the FSW joint had 13.4% more strength than that of the GTAW joint, and the FSW joint had hardness 30 HV more prominent than that of the GTAW joint. The weld efficiency for GTAW was 79%, while for FSW, it was 92%. Avula et al. [7] investigated the fusing of copper alloy pieces by utilizing the friction stir joining process. The results show that the nugget zone exhibits finer grains than the parent material, and hardness at the SZ was more related to the base metal. The joint efficiency was about 94.03% of the parent material. Khodaverdizadeh et al. [8] found that weld plates had improved grain structure, which was joined by using the tool had a square pin profile and had superior mechanical properties than the plates which was joined by using the tool had a pin of threaded cylindrical shape. Liu et al. [9] observed that with increase in tool rotational speed, the tensile strength (TS) and elongation rise and then fall. Shen et al. [10] found that with increase in traverse rate, the size of grains at weld nugget zone (WNZ) rises and then falls, and the TS and elongation first increase and then decrease. Keivani et al. [11] studied the effect of increasing the pin angle resulted in enhancing the temperature nearby the seam line due to an increase in friction, and the effect of preheating shows no effect on the temperature dispersal along the seam line as a consequence of low generating heat during the welding process. Hwang et al. [12] examine the thermal behavior of pure copper experiencing FSW comprising butt configuration. The suitable temperatures for an effective FSW process were seen as between 460 and 530 °C. Suvarna Raju et al. [13] studied obtain defect-free copper welds with the optimum value of mechanical properties which were found at rate of 900 rpm and travel rate of 40 mm per minute. Nia and Shirazi [14] found that the impact toughness increases as the size

of grains decrease in the stir zone (SZ). Increasing the welding passes enhances the SZ properties, but weakens the HAZ and results in reducing the overall properties of the joint. Xue et al. [15] accomplish FSW with additional rapid cooling and found that at 400 rpm, the HAZ of the weld joint had nearly same microstructure as of parent material, and the yield strength (YS) of the seam was nearly equal to that of base metal. Nagamalleswara Rao et al. [16] found that at 900 rpm, the YS of joint was maximum using the cylindrical threaded tool than the taper threaded tool, and there is no impact of pin shape on the impact strength of the joint. Heidarzadeh et al. [17] found that welds created by tools having square and triangular profiles had better TS, and by enhancing the tool rotational rate, traverse rate and axial load resulted in raising the tensile strength to maximum value. Farrokhi et al. [18] analyzed the influence of different welding constraints and welding conditions and concluded that the underwater condition results in better grain structure than air condition, hardness of the seams was higher in both conditions, and the TS of the seams was higher in underwater condition than the air condition. The welding of copper and its alloys is difficult to accomplish through traditional joining process attributable to its superior melting point and superior conductivity which require high heat input and low welding speed. The FSW technique can be employed to overcome these problems. In this study, model calculation using Taguchi's method has been adopted to find the effect of process parameters on the tensile strength (TS) and hardness of copper welds.

2 Experimental Setup

In current work, copper plates having length of 120.0 mm, wide of 50.0 mm, and thickness of 3.0 mm were used. A fixture was designed and fabricated to assure the butt joint arrangement and also to ensure that plates do not slide while performing the experiments. Press plate mounting on the copper plates and tightened with nut bolt to prevent the plates from pulling up. Pilot test was performed utilizing the VMC milling center Chetak 55 MC.

Specifications of machine are listed below:

Machine weight	4000 kg.
Worktable	700 × 420 mm.
Power (spindle)	5.5/7.5 KW.
Speed (spindle)	60–6000 rpm.
Traverse X	510 mm.
Y	420 mm.
Z	470 mm.
Feed rate X, Y, and Z-axes	3–10,000 mm/min.
Power supply	3 phase 415 V, 50 Hz AC.

This machine uses a three-dimensional Cartesian coordinate system. The worktable consists of T-slots for holding the workpiece and fixture. The work table moves

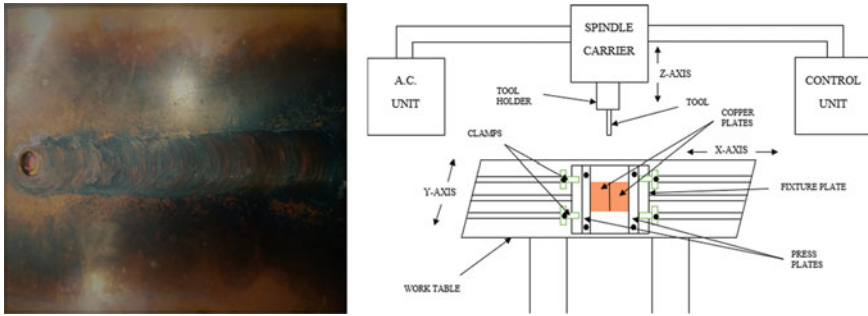


Fig. 2 Fabricated joint and experimental setup

in *xy*-plane, the *x*-axis provides left or right movement to the table, the forward and backward movement is provided by the *y*-axis, and the *z*-axis moves the spindle up and down. The control unit controls the movement of these axes through the motors attached to these parts of the machine. Figure 2 presents the snapshot of the made-up weld and experimental setup.

3 Material and Methodology

For the study, the 99% pure copper of 3 mm thickness plates have been used. The properties of experimental material are given in Table 1.

Three tools having different tool shoulder diameter 12 mm, 16 mm, and 20 mm were used. The process variables selected for this study are given in Table 2.

Table 1 Properties of experimental material

Density (g/cm ³)	Melting point (°C)	Thermal conductivity (W/m °C)	Hardness (HV)	Tensile strength (N/mm ²)
8.89	1083	394	102	272

Table 2 Operational parameters and their levels

Factor	Symbol	Levels		
		Low (-1)	Mid (0)	High (+1)
Tool rotational rate (rpm)	A	600	900	1200
Welding speed (mm/min)	B	50	75	100
Shoulder diameter (mm)	C	12	16	20

3.1 Taguchi's Method

Taguchi's method or robust design method was developed by Genichi Taguchi. It is an engineering technique to design a product or process that purposes at minimizing the variations and sensitivity to noise [19]. This includes several phases of development, directing, and estimating the outcomes of particularly planned tables named "orthogonal array" tests to consider whole constraint space through least quantity of runs to find the ideal stages of process variables [19]. Taguchi approach suggests the utilization of loss function which is at that point changed into a signal-to-noise ratio to amount the performance traits veering off from the ideal value, and afterward, for individual level of process variables, S/N ratio is assessed dependent on average S/N ratio response investigation, and superior S/N ratio is relating to well value distinctive independent of classification, and quality is assessed dependent on average S/N ratio response investigation, and larger S/N ratio is relating to improve execution characteristic irrespective of classification and quality. Since the main objective of this study is to maximize the properties of joints through ideal process parameters in FSW, larger is better characteristic has been adopted in this study.

For larger is better:

$$S/N = -10 \log_{10} \frac{1}{N} \sum_{i=1}^n \frac{1}{y_i^2} \quad (1)$$

where y_i is valued at i th test, n is the number of the test, and N is the total number of data points [20]. Table 3 shows the experimental output with input variables.

4 Result and Discussion

4.1 Effect of Process Parameters on Tensile Strength

The tensile strength is "larger is better" response characteristics, so the larger values are considered optimal for tensile strength. From results, it can be concluded that by rising the tool rate and tool shoulder diameter, the TS first rises to the maximum value and the falls with further rise equally in the rotational rate and diameter of shoulder. This is attributable to because by rising the tool rate, the grain size becomes coarse and results in low TS, and by increasing the diameter of tool shoulder, the large contact zone results in high frictional heat which further results in additional material flow and thus reduces the TS. The optimum setting of process variables for the TS is tool rotational speed (A_900), welding speed (B_50), and shoulder diameter (C_16) (Table 4). Table 5 gives the analysis of variance carried out for TS, and it specifies that the p-value of each factor is below 0.05; therefore, the model is statistically significant, and the analysis also shows that the tool shoulder diameter (C) is most

Table 3 Experimental output

Run	A: Tool rotational speed	B: Welding speed	C: Tool shoulder diameter	TS: Tensile strength	S/N ratio	H: Hardness	S/N ratio
1	600	50	12	239	47.568	73	37.266
2	600	50	16	253	48.062	82	38.276
3	600	50	20	246	47.819	77	37.730
4	600	75	12	236	47.458	71	37.025
5	600	75	16	248	47.889	79	37.953
6	600	75	20	240	47.604	74	37.385
7	600	100	12	226	47.082	70	36.902
8	600	100	16	238	47.532	71	37.025
9	600	100	20	230	47.235	72	37.147
10	900	50	12	239	47.568	75	37.501
11	900	50	16	258	48.232	91	39.181
12	900	50	20	246	47.819	82	38.276
13	900	75	12	232	47.310	76	37.616
14	900	75	16	252	48.028	93	39.370
15	900	75	20	238	47.532	73	37.266
16	900	100	12	231	47.272	71	37.025
17	900	100	16	248	47.889	78	37.842
18	900	100	20	235	47.421	70	36.902
19	1200	50	12	234	47.384	70	36.902
20	1200	50	16	249	47.924	79	37.953
21	1200	50	20	243	47.712	76	37.616
22	1200	75	12	227	47.121	72	37.147
23	1200	75	16	242	47.676	74	37.385
24	1200	75	20	235	47.421	71	37.025
25	1200	100	12	222	46.927	76	37.616
26	1200	100	16	237	47.495	73	37.266
27	1200	100	20	230	47.235	75	37.501

contributing factor with 52.64% contribution followed by feed (B) with 32.63%, and tool rotational rate (A) with 9.88% contribution.

Figure 3 shows main effect plots (a) TS and (b) means of S/N ratio. The mathematical equation developed for TS is given below:

$$\begin{aligned}
 \text{TS} = & 239.037 + 0.519A_{600} + 3.074A_{900} \\
 & - 3.593A_{1200} + 6.185B_{50} - 0.148B_{75} \\
 & - 6.037B_{100} - 7.259C_{12} + 8.185C_{16} - 0.926C_{20} \quad (2)
 \end{aligned}$$

Table 4 Response table. (a) S/N ratio and (b) means of TS

Level	A	B	C
(a) S/N ratio response table			
1	47.58	47.79	47.30
2	47.67	47.56	47.86
3	47.43	47.34	47.53
Delta	0.24	0.44	0.56
Rank	3	2	1
(b) Means response table			
1	239.6	245.2	231.8
2	242.1	238.9	247.2
3	235.4	233.0	238.1
Delta	6.7	12.2	15.4
Rank	3	2	1

Table 5 Analysis of variance

Source	dof	adjSS	adjMS	f-value	p-value
A	2	203.63	101.815	20.39	0.000
B	2	672.52	336.259	67.35	0.000
C	2	1084.96	542.481	108.66	0.000
Error	20	99.85	4.993		
Total	26	2060.96			

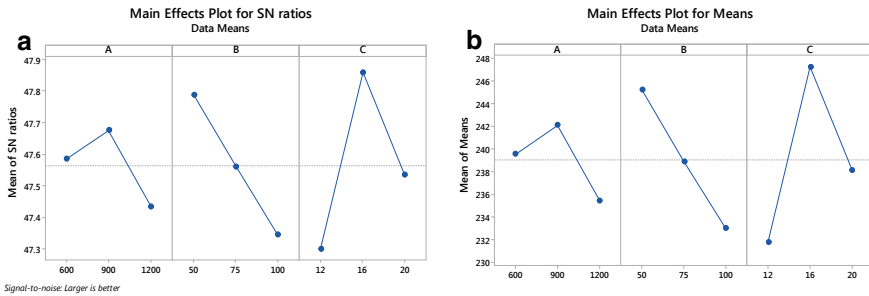


Fig. 3 Main effect plot. **a** TS and **b** means of S/N ratio

4.2 Effect of Process Parameters on Hardness

The plots in Fig. 5 show that through rise in the value of rotation of tool and diameter of shoulder, the value of hardness rises to its maximum value and then falls with more rise in the value of shoulder diameter and tool rate. The hardness declines by rising the

Table 6 Response table (a) *S/N* ratio and (b) means of hardness

Level	A	B	C
(a) <i>S/N</i> ratios response table			
1	37.41	37.86	37.22
2	37.89	37.57	38.03
3	37.38	37.25	37.43
Delta	0.51	0.61	0.81
Rank	3	2	1
(b) Means response table			
Level	A	B	C
1	74.33	78.33	72.67
2	78.78	75.89	80.00
3	74.00	72.89	74.44
Delta	4.78	5.44	7.33
Rank	3	2	1

Table 7 Analysis of variance

Source	dof	adjSS	adjMS	<i>f</i> -value	<i>p</i> -value
A	2	128.1	64.04	3.57	0.047
B	2	133.9	66.93	3.74	0.042
C	2	263.4	131.70	7.35	0.004
Error	20	358.3	17.91		
Total	26	883.6			

feed. The ideal settings of process variables for hardness are RMP (rotational speed) (A_900), welding speed (B_50), and shoulder diameter (C_16) (Table 6). ANOVA was completed for hardness which is given in Table 7. It indicates that the *p*-value for each factor is under 0.05; thus, the model is statistically significant, and the most contributing factor is shoulder diameter (29.80%) followed by feed (15.15%) and tool rate (14.50%).

The plots for residual versus order and normal probability are presented in Fig. 4 which shows that main effects plot for mean of hardness and *S/N* ratios of hardness. The regression Eq. (3) developed for hardness is given below:

$$\begin{aligned}
 \text{Hardness} = & 75.704 - 1.37A_{600} + 3.07A_{900} - 1.70A_{1200} \\
 & + 2.63B_{50} + 0.19B_{75} - 2.81B_{100} \\
 & - 3.04C_{12} + 4.30C_{16} - 1.26C_{20}
 \end{aligned} \tag{3}$$

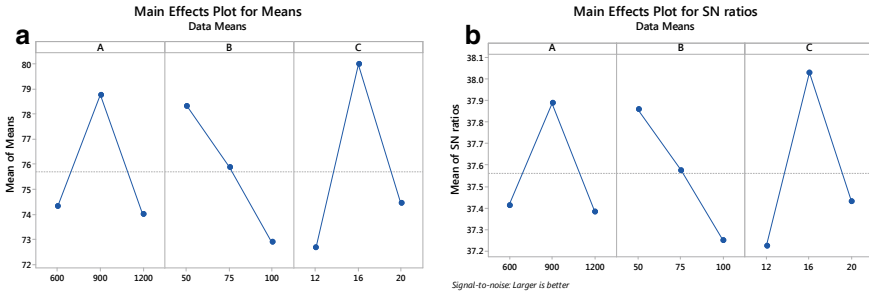


Fig. 4 Main effects plot for a mean of hardness and b S/N ratios of hardness

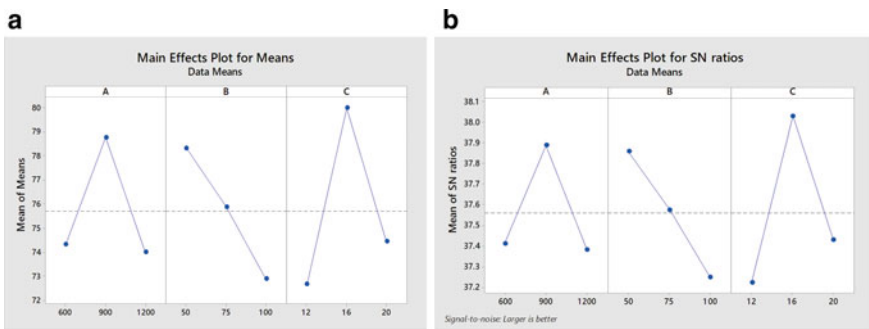


Fig. 5 Main effects plot for a mean of hardness and b S-N ratios of hardness

5 Conclusions

In the present research, a modeled analysis was led to detect the impact of different process variables which include tool shoulder diameter, tool rate, and feed on the joint properties of pure copper. The subsequent conclusions are made:

1. The ideal combination of process variables for TS was found using Taguchi’s method which are welding speed of 50 mm per min, tool rate of 900 rpm, and tool having 16 mm shoulder diameter.
2. From the outcomes of ANOVA for TS, it is found that the shoulder diameter is the utmost contributing variable with 52.64% contribution.
3. The ideal combinations of process variables for hardness are welding speed of 50 mm per min, tool rate of 900 rpm, and tool shoulder with 16 mm diameter.
4. For hardness, the ANOVA results specify that all three variables are found significant, and shoulder diameter is the most contributing factor with 29.80% contribution.
5. Increasing the tool rate and shoulder diameter resulted in increasing both tensile strength and hardness to maximum, and then, a decrease in both tensile strength and hardness occurred.

References

1. Mishra RS, Mahoney MW (2007) Friction stir welding and processing. ASM International, USA
2. Shtrikman MM (2008) Current state and development of friction stir welding. Part 3. Industrial application of friction stir welding. *Weld Int* 22:806–815
3. Azizi A, Barenji RV, Barenji AV, Hashemipour M (2016) Microstructure and mechanical properties of friction stir welded thick pure copper plates. *Int J Adv Manuf Technol* 86:1985–1995
4. Kumar P, Singh S, Singh G, Dua A (2016) Effect of process parameters on tensile strength of friction stir welded joint of pure copper. *IOSR J Mech Civ Eng (IOSR-JMCE)*. e-ISSN: 2278-1684, p-ISSN: 2320-334X
5. Lee W-B, Jung S-B (2004) The joint properties of copper by friction stir welding. *Mater Lett* 58:1041–1046
6. Lina J-W, Changa H-C, Wub M-H (2014) Comparison of mechanical properties of pure copper welded using friction stir welding and tungsten inert gas welding. *J Manuf Process* 16:296–304
7. Avula D, Raj Singh RK, Dwivedi DK, Mehta NK (2011) Effect of friction stir welding on microstructural and mechanical properties of copper alloy. *Int J Mech Mechatron Eng* 5(2)
8. Khodaverdizadeh H, Heidarzadeh A, Saeid T (2013) Effect of tool pin profile on microstructure and mechanical properties of friction stir welded pure copper joints. *Mater Des* 45:265–270
9. Liu HJ, Shen JJ, Huang YX, Kuang LY, Liu C, Li C (2009) Effect of tool rotation rate on microstructure and mechanical properties of friction stir welded copper. *Sci Technol Weld Joining* 14(6). <http://doi.org/10.1179/136217109X456951>
10. Shen JJ, Liu HJ, Cui F (2010) Effect of welding speed on microstructure and mechanical properties of friction stir welded copper. *Mater Des* 31:3937–3942
11. Keivani R, Bagheri B, Sharifi F, Ketabchi M, Abbasi M (2013) Effects of pin angle and preheating on temperature distribution during friction stir welding operation. *Trans Nonferrous Met Soc China* 23:2708–2713
12. Hwang YM, Fan PL, Lin CH (2010) Experimental study on friction stir welding of copper metals. *J Mater Process Technol* 210:1667–1672
13. Suvama Raju L, Kumar A, Rajendra Prasad S (2014) Microstructure and mechanical properties of friction stir welded pure copper. *Appl Mech Mater* 592–594:499–503
14. Nia AA, Shirazi A (2016) Effects of different friction stir welding conditions on the microstructure and mechanical properties of copper plates. *IJ Miner Metall Mater* 23(7):799
15. Xue P, Xiao BL, Zhang Q, Ma ZY (2011) Achieving friction stir welded pure copper joints with nearly equal strength to the parent metal via additional rapid cooling. *Scr Mater* 64:1051–1054
16. Nagamalleswara Rao A, Srinivas Naik L, Srinivas C (2017) Evaluation and impacts of tool profile and rotational speed on mechanical properties of friction stir welded copper 2200 alloy. *Mater Today Proc* 4:1225–1229
17. Heidarzadeh A, Saeid T, Khodaverdizadeh H, Mahmoudi A, Nazari E (2012) Establishing a mathematical model to predict the tensile strength of friction stir welded pure copper joints. The Minerals, Metals & Materials Society and ASM International. <http://doi.org/10.1007/s11663-012-9755-y>
18. Farrokhi H, Heidarzadeh A, Saeid T. Frictions stir welding of copper under different welding parameters and media. ISSN: 1362-1718 (Print) 1743-2936 (Online). Journal homepage: <https://www.tandfonline.com/loi/ystw20>
19. Roy RK (2001) Design of experiments using the Taguchi approach: 16 steps to product and process improvement. Wiley, Hoboken
20. Oktem H, Erzurumlu T, Erzincanli F (2006) Prediction of minimum surface roughness in end milling mold parts using neural network and genetic algorithm. *Mater Des* 27:735–744

Engineering and Ergonomics—An Important Aspect in Fruit Harvesting Systems



Suhail Nazir Wani, Sanjay Mohan, and Mohd. Kamal

Abstract Fruits are an integral part of all civilizations, and harvesting of them has always been a challenge. Fruits are subjected to damage while harvesting and persons involved also are subjected to various health issues. Growing of fruits has been a major component in most of the countries which even adds to the GDP of the nation. Scientists and researchers from various streams have been exploring the possibilities to enhance the growth and harvesting of fruits. Engineers and ergonomists, nowadays, are developing various alternative systems to safeguard the fruit and the persons involved in harvesting as this is influencing the productivity to a larger extent. This paper brings forth the past and recent happenings in the fruit harvesting systems, especially apple harvesting systems. The paper also focuses upon the shortcomings in the existing apple harvesting systems which are affecting the fruit harvesting setup as a whole. With this article, authors have tried to throw light on the existing harvesting systems and various possibilities to bring innovation in the existing systems.

Keywords Harvesting · Apple · Molybdenum (Mo) · Ergonomics · Productivity

1 Introduction

Harvesting has been of great concern since ancient times, and every civilization has tried to develop harvesting systems. The right time and right method of harvesting are very important as it affects overall productivity. The quality of the harvested item may be any crop; vegetable or fruit does not remain for long. This leads to decreased productivity if timely harvesting is not done. Moreover, if a poor harvesting system is being used, it may damage fruit or may cause some health issues to the worker. This also will result in decreased productivities. The harvesting also depends upon the type of crop, i.e. whether products are to be picked up in masses or individually.

S. N. Wani · S. Mohan (✉)

School of Mechanical Engineering, Shri Mata Vaishno Devi University, Katra, India

Mohd. Kamal

Faculty of Engineering, Universiti Malaysia Sabah, Kota Kinabalu, Sabah, Malaysia

Workers or labours carrying out harvesting have been a traditional methods which are still being followed in certain parts of the world. The conventional hand-harvesting method has made growers to stop or decrease their production as labour cost them three fourth of their investment. This conventional method involves lot of labours and time. Therefore, it becomes a necessity to optimize these variables such as method of harvesting, labours involved and timing for harvesting [1]. Picking of fresh fruits is a challenging job as they are more prone to damage, e.g. apples, mangoes, peaches, etc. Such fruits are picked up manually in most of the countries, and the picking cost holds a great percentage of the production cost. In the recent past, certain picking systems have been designed but have resulted in excessive fruit damage and health issues amongst the workers [2]. The past studies also revealed that due to musculoskeletal disorders during picking, labour productivity has decreased. The use of ladders and bucket while picking has resulted in odd postures which are not safe ergonomically, thus making labours prone to health issues. Absenteeism is one major component adding to decreased labour productivity due to health issues [3, 4]. Thus, there has been always an emergent need for reviewing the past developed harvesting systems so as to locate the shortcomings and develop a new harvesting system which will enhance the productivity and also provide easy and safe handling to the labours.

Various researchers have been associated with the evolution of apple plucking mechanisms. A lot of work has been carried out in the similar plucking mechanisms. Fresh fruit market has grown over the past decades and has taken the shape of a huge industry. Fruits such as apples, peaches, cherry and pear are grown in several parts of the world. The picking/plucking of apples has been carried out using the conventional way, i.e. manually apples are picked from the trees. With the growth of the apple orchards, picking is being carried out by hired labours nowadays which also adds to the expenditure. Figure 1 shows the traditional method of plucking which is being used even in present times to pluck apples. A lot of deliberations and innovations have been tried on apple picking in various countries; however, none of the innovation has been standardized. In present times, majority of the countries still follow manual plucking, and during manual picking, the fatigue occurring in workers is of prime concern for the experts. In certain countries, 55% of the total area is being used for apple cultivation which is roughly 150,000 ha of land, and thus, it is the biggest contributor to the state GDP. The growth of apple in India is mainly in the mountainous regions of Jammu and Kashmir, Himachal Pradesh and Uttaranchal. This fruit is grown at high altitudes of 4000–11,000 ft. Amongst the apple-growing states, Kashmir holds 67% of the total production of apples, 50% of which is exported to the other parts of the country and abroad [5, 6]. The height of the apple tree is in the range of 3–12 m and is full of dense twigs. The size of the apple is usually 5–9 cm in diameter, and is enriched with nutrients [7]. The involvement of labour and mechanization in apple harvesting has always been of great concern for the researchers as it directly affects the productivity. Sanders [8] reported difficulty in the plucking of apples from the trees. The authors also stressed upon the fact that there is no such system which can be treated as a wholesome substitute for the existing manual system of plucking. The possibility to pick the ripped fruit is more in manual system than any other system. Sichert [9] in his study



Fig. 1 Traditional method of apple picking/plucking

presented that apple picking in most of the places has been carried out manually, and there has been intensive requirement of labour, i.e. up to 215 h per hectare. This time spent in harvesting amounts goes up to 70% of the whole time involved in apple harvesting such as grading and transportation. The investigations have been carried out where authors [10] have discussed the demerits of poor mechanization in the process of apple harvesting. The authors have stressed upon the emergent need of mechanization in order to increase the productivity in the apple harvesting.

In this paper, authors have tried to discuss the ergonomic and engineering aspect of the existing harvesting systems. The drawbacks of the existing conventional harvesting system have also been focused upon. This paper would be an eye-opener for the researchers in developing a cost-effective and safe harvesting system for both labours and apples.

2 Conventional Apple Harvesting Systems

There are conventional apple harvesting systems which are still being used for apple picking. Figure 1 shows the conventional technique used to pluck apples. It is clearly visible from the figure that persons involved in apple plucking undergo musculoskeletal disorders due to unsafe postures. As prescribed by experts, following anthropometric measurements must be taken care of while performing any lifting or picking job [11, 12]. These measurements are:

1. The distance of hands from midpoints between ankles.

2. The height of hands to reach an object.
3. Frequency of picking.
4. The trunk rotation.
5. Load to be lifted
6. The type of grasp.

All the above-mentioned measurements if exceed the safe limit will result in musculoskeletal disorders amongst labours. This leads to decreased rate of picking and also labour absenteeism. It can be seen in Fig. 1 that the posture of persons for reaching apple is unsafe and will cause fatigue in arm and wrist. Moreover, standing posture with ladder is also not safe. In such postures, labour cannot focus on the job as he has to maintain stability and simultaneously pluck apple. This also results in damage of apple due to slip from the hands. These conventional systems have been explored by researchers, and newer systems have been proposed which were designed taking into account technology and safety. The systems have been discussed in the following section.

3 Ergonomics in Harvesting Systems

Ergonomics, an applied science, deals with the design and arrangement of machines with which humans are safe and comfortable. If the working environment is ergonomically designed, it will result in increased productivities, and nowadays, every Industry is going for ergonomically designed systems. With ergonomics, several health issues to which a worker is subjected can be resolved. Health issues amongst the workers associated with apple picking have also been of great concern [13, 14]. Poor styles of picking, old traditional ways, etc. have resulted in increased, labour cost, accidents, etc. Many researchers have worked upon the awkward postures in manual activities and accordingly have suggested various recommendations [15].

Many authors have studied the impact of repetitive activities on the workers involved in apple harvesting. These activities are carried out by the muscles of the hands, arms and shoulders [16, 17]. Further, the intense role of eyes and neck during such activities also results in fatigue. The author concluded that a repetitive activity which is quite common will call for low energy consumption; however, if the duration of the job is short and it is cyclic in nature, the worker will be subjected to musculoskeletal disorders. Researchers have investigated the injuries amongst apple harvesting workers due to their plucking methodology [18, 19]. A study was carried out to investigate for fatigue in the workers arm during apple harvesting, and results have revealed a significant amount of fatigue [20]. The researchers have been working on the problem of musculoskeletal disorders resulting due to odd-picking postures [21]. Earle-Richardson et al. [22] have proposed various designs in order to deal with odd working postures. The design of picking mechanisms was modified, e.g. shoulder straps and portable containers were proposed as a replacement for the existing baskets. The proposed modified designs resulted in the transfer

of back and neck load to shoulders [23]. As per Lomond and Côté [24], a large amount of energy is spent during apple plucking and in apple transportation. In addition, the workers carrying out apple harvesting are subjected to heavy loads on the spine, and disorders are developed in the limbs subjected to repetitive movements. The occupational hazards associated with physical strains were investigated through an experimental design [25]. The authors investigated various postures and oxygen intake of the workers during apple plucking. The experiments were carried out using a portable metabolimeter (COSMED), and Ovako working posture analysis system (OWAS) technique was used for assessing work postures. The results have shown that workers, both male and female, suffered from pains in dorsal and neck. It was observed that every worker was subjected to fatigue, and female workers seemed to be more tired during the harvesting. In a study, an investigation was carried out on ergonomic risk factors between the traditional method of apple plucking with ladders and a novel apple picking method with mobile platforms [26]. The main objective was to access the risk associated with the upper arm postures and the back during the picking process. The results revealed that the workers adopting the novel method of mobile platform are less exposed to postural disorders as compared to the traditional method.

4 Engineering in Harvesting Systems

A catching mechanism for collecting peaches which fall off from trees due to shaking had been developed. The authors [27] have fabricated and tested three types of catching systems, i.e. a pair of canvases, catching trailer and pair of canvases with direct discharge to boxes. The investigation revealed that 90% (average) of the fruits fell from the tress using hand-held shakers, and less than 2.4% of the fruits were severely damaged. The study revealed that harvesting rates per worker to increase with first two systems followed by the third system. El-Iraqi et al. [28] have developed a fruit picking mechanism where in telescopic pipe, fruit collection pipe and cutting mechanism were incorporated. The authors have used disc cutters associated with gasoline engine and electrical motor. Electrical scissors along with cutting edge hook were also used in this study. The results have revealed lowest injuries to the fruit during picking process. An overview was presented where the chronology of fruit harvesting systems from purely mechanical-based systems to automatic robotic harvesting systems has been discussed. The authors [29] have discussed the commonly mechanical harvesting systems such as limb shakers, air blast, canopy shaker and trunk shakers. They have elaborated the functioning of these systems along with the fruit removal efficiency and fruit injury. The authors have also elaborated automatic fruit harvesting systems such as various sensor-based mechanisms and robots. A cost-effective small-scale working mechanism to pick peach fruit was developed. The mechanism was designed considering minimum possible damage to the fruit while plucking [30]. The authors also investigated the effect of the system on the productivity of pickers, and the devised systems have shown fair

performance. Bakhtiari and Hematian [31] have developed a fruit picking system and conducted fruit harvesting with the developed system. The testing was carried out on 210 fruits, and it was found that except for 9%, rest of the fruits were picked by the system. The developed system has shown its effectiveness and also demonstrated possibility of using robots in harvesting of fruits with desired quality. Three types of mango pickers were investigated, namely the pull type, trigger type and modified trigger type equipped with a scissor blade controlled by steel wire to cut the stems. The findings have shown that against the picking capacity of 22 fruit/min with the conventional picking system, the pull and trigger type mechanisms have shown the picking capacity of 21 fruit/min and 12 fruit/min, respectively. Negligible damage to the mangoes while plucking was also reported by the authors [32]. Researchers have also highlighted the increasing labour cost in fresh fruit plucking. The authors have investigated the impact of the excitation position on the effectiveness in fruit plucking and also on the fruit injury using a hand-held limb shaker for harvesting sweet cherry [33]. From the results, it was concluded that fruit plucking efficiency may increase to 97% with less fruit injuries as compared to the previous plucking methodologies. Similar results have been reported by authors where labour cost accounts for 50% of annual expenditure of growers [34]. The technological advancements have also resulted in damage to the apples which are commonly referred as bruising. During picking of apples, bruising of apples takes place. This affects the quality of apple and thus decreases in the profitability. The bruising of apples during plucking has been investigated. Three zones of impact were finalized, i.e. middle to bottom, middle to top, middle to middle, and the study revealed that there will be no bruising if the impact force was less than 16 N. As per the investigation, up to 28 N and 53 N impact force, still 98% and 94% quality apples can be obtained [35]. Even after the development of many methodologies for apple picking, it is still evolving. Investigation carried out by many authors have reported in their work that harvesting apples was and still is a very challenging task. The mechanization in this sector is taking place at a very slow pace [36]. The labours have been taking care of apple harvesting, and cost of labour is also increasing day by day. This has given an impetus to researchers to focus more on cost-effective apple harvesting mechanisms. The studies carried out on automatic harvesting mechanisms, robots, etc. have revealed that there are certain drawbacks associated with these mechanisms, e.g. bruising of apples with automatic or semi-automatic mechanisms, high cost associated with robots. The article revealed the possibilities of developing cost-effective and efficient apple harvesting mechanisms.

5 Conclusion

The authors have intensely gone through the literature pertaining to the engineering and ergonomic issues of apple harvesting systems. The role of fruit growing, especially apple in raising the GDP of nation, has been discussed. Upon reviewing the literature, an emergent need for an efficient and cost-effective apple harvesting system has

been expressed. Although, there is no standard system developed for apple harvesting, growers in developing nations still prefer the conventional system of apple plucking. However, the authors have pointed out certain drawbacks in the conventional systems which are as mentioned below.

1. Risk associated with the balance of stairs. At times, stairs are adjusted again and again which results in wastage of effort and time.
2. Fatigue encountered in the persons involved in the process. Also the risk of falling from the stairs due to imbalance.
3. A huge risk encountered when man has to use both hands for plucking.
4. This process is time consuming.
5. No ergonomic principle applied during plucking.
6. Mostly, male members are involved in the process due to the risk and effort encountered.
7. Wrong way of plucking.
8. Person has also to hold a bucket or some container for gathering apples.
9. Ladder falls.
10. Bruising of apples.

These drawbacks, if worked upon, will bring a more safe and productive harvesting system.

References

1. Cargill BF, Marshall DE, Levin JH (1975) Harvesting cucumbers mechanically. Cooperative Extension Service, Michigan State University
2. Sarig Y (1993) Robotics of fruit harvesting: a state-of-the-art review. *J Agric Eng Res* 54(4):265–280
3. Benavides FG (2006) Ill health, social protection, labour relations, and sickness absence. *Occup Environ Med* 63(4):228–229
4. Brouwer WBF, Koopmanschap MA, Rutten FF (1999) Productivity losses without absence: measurement validation and empirical evidence. *Health Policy* 48(1):13–27
5. Malik ZA (2013) Assessment of apple production and marketing problems in Kashmir valley. *J Econ Soc Dev* 9(1):152–156
6. Malik ZA (2014) Economics of apple cultivation “with special reference to South Kashmir-India”. *Economics* 5(9)
7. Mittal S (2007) Can horticulture be a success story for India? Working paper, No. 197
8. Sanders KF (2005) Orange harvesting systems review. *Bio-systems engineering. Power Mach* 90(2):115–125
9. Sichert I, Heitkamper K, Schick M, Marbe-Sans D (2006) ART-Berichte. N 663: Arbeitswirtschaftliche Kennzahlen zur Tafelapfelproduktion
10. Dixit J, Sharma S, Ali M (2014) Present status, potential and future needs for mechanization of agricultural operations in Jammu and Kashmir state of India. *Agric Eng Int CIGR J* 16(3):87–96
11. Sharma SM, Singh S, Singh B, Javaid M, Asjad M (2016) Some investigations on low back pain amongst workers involved in lifting tasks. *Int J Procurement Manag* 9(6):659–683
12. Katoch V, Mohan S (2016) Design and fabrication of a safety frame for workers carrying out head lifting at construction sites. *J Eng Des Technol* 17:1250–1265

13. Dul J, De Vlaming PM, Munnik MJ (1996) A review of ISO and CEN standards on ergonomics. *Int J Ind Ergon* 17(3):291–297
14. Grandjean E, Hünting W (1997) Ergonomics of posture—review of various problems of standing and sitting posture. *Appl Ergon* 8(3):135–140
15. Ng YG, Bahri MTS, Mori MYI, Hashim Z (2013) Ergonomics observation: harvesting tasks at oil palm plantation. *J Occup Health* 13-0017
16. Muggleton JM, Allen R, Chappell PH (1999) Hand and arm injuries associated with repetitive manual work in industry: a review of disorders, risk factors and preventive measures. *Ergonomics* 42(5):714–739
17. Prussia SE (1985) Ergonomics of manual harvesting. *Appl Ergon* 16(3):209–215
18. Sakakibara H, Miyao M, Kondo TA, Yamada SY (1995) Overhead work and shoulder-neck pain in orchard farmers harvesting pears and apples. *Ergonomics* 38(4):700–706
19. Gilad I (1995) A methodology for functional ergonomics in repetitive work. *Int J Ind Ergon* 15(2):91–101
20. Earle-Richardson G, Jenkins PL, Strogatz D, Bell EM, May JJ (2006) Development and initial assessment of objective fatigue measures for apple harvest work. *Appl Ergon* 37(6):719–727
21. Fulmer S, Punnett L, Tucker Slingerland D, Earle-Richardson G (2002) Ergonomic exposures in apple harvesting: preliminary observations. *Am J Ind Med* 42(S2):3–9
22. Earle-Richardson G, Jenkins P, Fulmer S, Mason C, Burdick P, May J (2005) An ergonomic intervention to reduce back strain among apple harvest workers in New York State. *Appl Ergon* 36(3):327–334
23. Freivalds A, Park S, Lee C, Earle-Richardson G, Mason C, May JJ (2006) Effect of belt/bucket interface in apple harvesting. *Int J Ind Ergon* 36(11):1005–1010
24. Lomond KV, Côté JN (2011) Differences in posture–movement changes induced by repetitive arm motion in healthy and shoulder-injured individuals. *Clin Biomech* 26(2):123–129
25. Callea P, Zimbalatti G, Quendler E, Nimmerichter A, Bachl N, Bernardi B, Benalia S (2014) Occupational illnesses related to physical strains in apple harvesting. *Ann Agric Environ Med* 21(2)
26. Thamsuwan O, Johnson PW (2015) Comparing upper arm and back postural exposures between apple harvesting with ladders and mobile platform. In: *Proceedings of the human factors and ergonomics society annual meeting, Sept 2015, vol 59, no 1*. SAGE Publications, Los Angeles, pp 1252–1256
27. Torregrosa A, Martín B, García Brunton J, Bernad JJ (2008) Mechanical harvesting of processed peaches. *Appl Eng Agric* 24(6):723–729 (American Society of Agricultural and Biological Engineers)
28. El-Iraqi ME, Sharibim Y, El Khawaga SE (2010) Design and evaluation of mechanical aid tools for mango fruits harvesting. In: *The 17th annual conference of MISR society of agricultural engineering, vol 27, no 4*
29. Li P, Lee SH, Hsu HY (2011) Review on fruit harvesting method for potential use of automatic fruit harvesting systems. *Procedia Eng* 1(23):351–366
30. Hamam A, El-Iraqi ME, El Khawaga SE, Awais T (2011) Design and evaluation of mechanical picking head for peach fruits harvesting. *Egypt J Agric Res* 89(4)
31. Bakhtiari AA, Hematian A (2013) Design, fabrication and evaluation of a picking mechanism for fruit harvesting. *Indian J Agric Sci* 83(10):1027–1030
32. Roger CM, Cataytay JD, Aromin JA, Tuyogon RF (2016) Development of a mechanical mango fruit picker. In: *International symposium on tropical fruits*. Philippine Council for Agricultural Resources Research and Development Department. University of Southeastern Philippine Tagum-Mabini Campus
33. Zhou J, He L, Zhang Q, Karkee M (2014) Effect of excitation position of a handheld shaker on fruit removal efficiency and damage in mechanical harvesting of sweet cherry. *Biosyst Eng* 125:36–44
34. Caplan S, Tilt B, Hoheisel G, Baugher TA (2014) Specialty crop growers' perspectives on adopting new technologies. *Hort Technol* 24(1):81–87

35. Fu H, He L, Ma S, Karkee M, Chen D, Zhang Q, Wang S (2016) Bruise responses of apple-to-apple impact. *IFAC-PapersOnLine* 49(16):347–352
36. Zhang Z, Heinemann PH, Liu J, Baugher TA, Schupp JR (2016) The development of mechanical apple harvesting technology: a review. *Trans ASABE* 59(5):1165–1180

Emission Reduction from Diesel Engine Using Alkali Solution, and Carbon Black in Union with Catalytic Converter



Mohit Bhandwal  and R. K. Tyagi 

Abstract The catalytic converter is used to reduce the emission from the vehicles. Long run reduces the efficiency of the catalytic converter. Pollution is increasing due to the increase in the number of cars. The cars emit harmful gases. These gases are affecting human beings and the environment in different ways. CO, HC, SO_x, NO_x, and PM 2.5 are harmful emission present in the exhaust emission. A new novel device is introduced in this research to reduce diesel engine emissions. The device uses a freezer gel pack, carbon black, and alkali solution (NH₄OH), in association with the catalytic converter. For performing the experiments, an experimental setup is fabricated. For measuring the emission, AVL DIGAS 444 Automobile Exhaust Gas Analyzer is using a probe. NO_x is reducing by 63%, CO₂ by 70%, and PM2.5 by 99% with the use of the proposed novel system.

Keywords Carbon black · Catalytic converter · Alkali solution · Pollution

1 Introduction

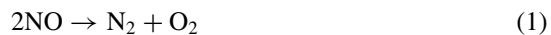
The world is changing very quickly. Many airborne diseases are spreading nowadays in the world. Different virus and bacteria are transmitting via air, but pollution is in itself enough to create a pandemic. Everyone is using cars worldwide, and it is increasing exponentially from 45 million to over 650 million. The rise is cars will be around 2 billion by 2021 [1]. Increase in the vehicles globally is impacting the environment. Due to this reason, it is crucial to focus on the area of exhaust emission [2]. The emission from the exhaust is very harmful to nature [3]. Carbon monoxide (CO), nitrous oxide gases (NO_x), unburned hydrocarbon (HC), sulfur oxides (HC), and particulate matter (PM) are the primary harmful pollutants from

M. Bhandwal (✉)
Amity University Tashkent, Tashkent, Uzbekistan
e-mail: mbhandwal@amity.edu

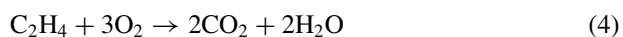
R. K. Tyagi
Amity University Noida, Noida, Uttar Pradesh, India

emission. Cars are the primary CO source in the urban areas contributing to half of all human-caused air pollutants [4]. The major sources of health problems like respiratory diseases, cancer, etc., are emissions [5]. The diesel engine produces large and harmful emission as compared to the petrol engine. Research is going on from past to present, and people invent the devices to reduce harmful emissions.

One invention is the catalytic converter, and it is found in all the vehicles nowadays. French engineer named Eugene Houdry invented the catalytic convertor. For reducing the exhaust emissions, catalytic converter is a beneficial device. Inside the catalytic converter, a chemical reaction occurs, which is reducing the harmful emission to less harmful emission [6–8]. The materials used inside are platinum, palladium, and rhodium, which are noble elements. These elements act as a catalyzer for the chemical reaction, and temperature plays a vital role in activating them. At a temperature range of 350–500 °C, the catalytic converter activates. Before the catalytic converter attains this temperature range, many harmful emissions are coming out from the exhaust. This is the cold start phase. Many researchers are preheating the catalytic convertor to reduce this cold start time and increasing its efficiency [9–11]. Equations 1 and 2 shows the reducing behavior of platinum and rhodium as a catalyst.



Equations 3 and 4 shows the reactions which are taking place in the second chamber. Platinum and palladium are acting as a catalyst for the oxidation in this chamber.



Long time running of cars decreases the effectiveness of the catalytic converter. In this research, a novel device is proposed, fitted in addition to the catalytic converter. An experimental setup of the proposed device and the catalytic converter is assembled. Effectiveness of the proposed device is known by comparing the results when the device is fitted and not fitted.

2 Experimental Setup

Figure 1 shows the proposed device is an association with the catalytic converter.

Figure 1b shows the experimental setup. Two layers of freezer gel are enfolding the engine exhaust pipe. The exhaust pipe is joining the aluminum alloy container, containing the black carbon particles of size equal to 0.8 μm. To avoid the converter's

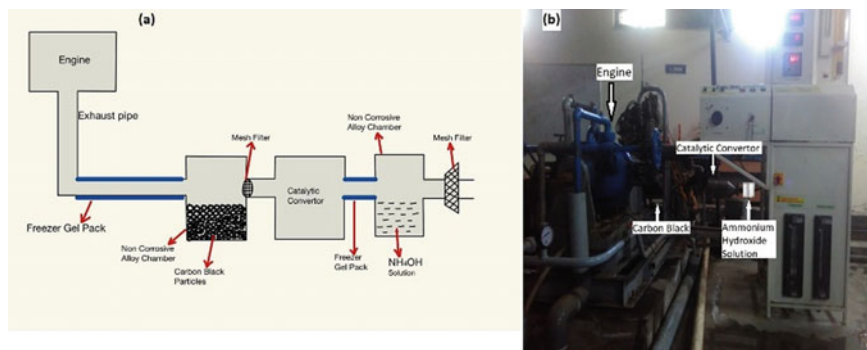


Fig. 1 a Line diagram, b experimental setup

choking, mesh filter of lattice size $0.5 \mu\text{m}$ is placed before the exhaust pipe is connected to the 3-way catalytic converter. One layer of freezer gel pack is again enfolding the exhaust pipe. This exhaust pipe is connecting to ammonium hydroxide solution (NH_4OH) contained in an aluminum chamber. At an exit also a mesh filter of lattice size of $0.8\text{-}\mu\text{m}$ is placed before the exhaust pipe exit. The exhaust gases are measured using the AVL DIGAS 444 Automobile Exhaust Gas Analyzer.

Nitrogen oxides are forming inside the combustion chamber when the reaction between O_2 and N_2 occurs at a temperature range of $1000\text{--}1200 \text{ }^\circ\text{C}$. Before the exhaust gases enter the chamber containing the carbon black, its temperature reduces up to $400 \text{ }^\circ\text{C}$ using the freeze gel pack (carboxymethyl cellulose and propylene glycol). The carbon black is reacting or absorbing with the oxygen gas and producing carbon–oxygen surface compounds that further decompose into CO_2 . More nitrous oxide gas is reducing into nitrogen gas because a higher concentration of oxygen is decreasing in the previous stage. All the HC and CO gets oxidize when passing through the 3-way catalytic converter.

Before entering the chamber of NH_4OH solution, the freezer gel pack reduces the exhaust gas temperature to $50\text{--}70 \text{ }^\circ\text{C}$. Ammonium carbonate ($(\text{NH}_4)_2\text{CO}_3$) is formed by absorbing CO_2 emitted from the convertor. The system, at the end, uses a mesh filter having lattice of $0.8 \mu\text{m}$ to stop fine particles producing from burning of fuel. Table 1 displays the engine specification, and Table 2 displays the 3-way catalytic convertor properties.

Table 1 Specification of engine used

Product	Research Engine test setup, 1 cylinder, 4 stroke, Multifuel, VCR, Code 240
Engine	Make Kirloskar, Single cylinder, 4 Stroke, water cooled, stroke 110 mm, bore 87.5 mm, 661 cc Diesel mode: 3.5 KW@1500 rpm, CR range 12–18, Injection Variation: 0–25 °C BTDC Petrol Mode: 4.5 KW@1500 rpm, Speed range 1200–1800 rpm, CR range 6–10

Table 2 Properties of the 3-way catalytic convertor

Temperature range, °C	100–650
Temperature gradient, °C	100–200
Space velocity, 1/h	30,000–150,000
Vibration acceleration, g	10–20

3 Result and Discussion

At different times of the day, the experiments are repeated, and the data were recorded and graphed. NO_x, CO₂, and PM 2.5 level in the exhaust decrease with the proposed device’s use. The comparison of the default system and the proposed novel system is shown in Figs. 2, 3, and 4. Figure 1 shows the NO_x level which decrease by 63%;

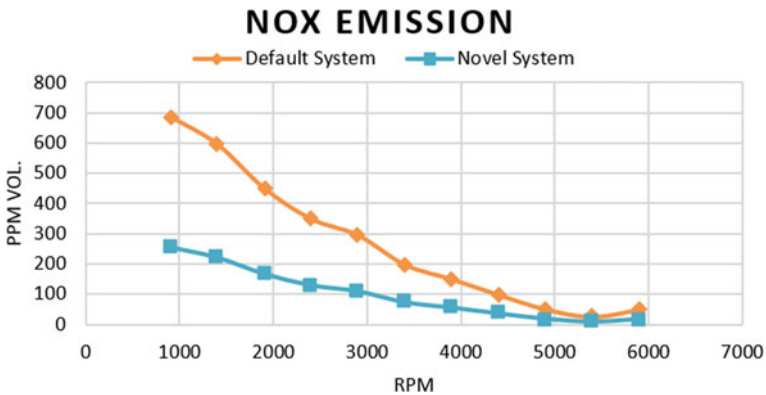


Fig. 2 NO_x emission comparison chart of novel device with the original system

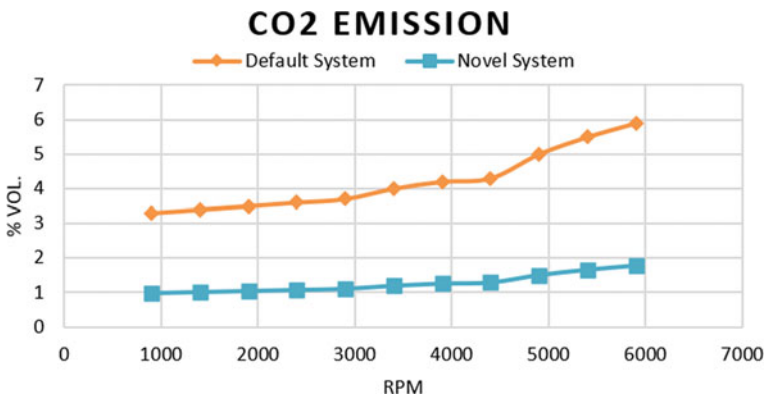


Fig. 3 CO₂ emission comparison chart of novel device with the original system

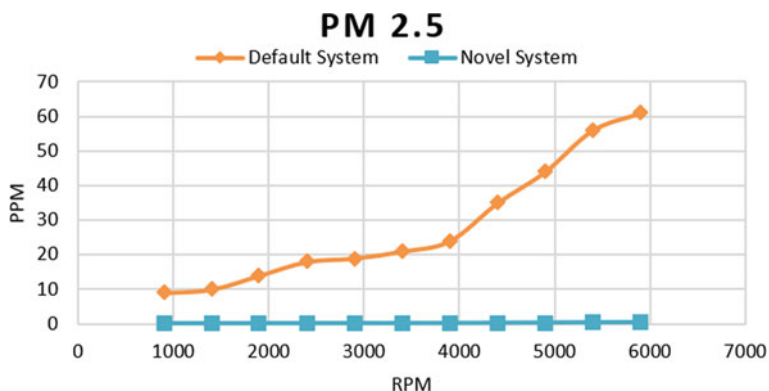


Fig. 4 PM 2.5 emission comparison chart of novel device with the original system

Fig. 2 shows CO₂ level which reduces by 70%, and Fig. 3 shows PM 2.5 level which decreases by 99%.

A proposed novel method is very efficient and effective as shown by the experimental result and fitting in the vehicles can reduce pollution.

References

1. Sperling D, Gordon D (2009) Two billion cars: driving toward sustainability. Oxford University Press, New York
2. Calvert JG, Heywood JB, Sawyer RF, Seinfeld JH (1993) Achieving acceptable air quality: some reflection on controlling vehicle emissions. *Science* 261:37–45
3. Heck RM, Farrauto RJ (2001) Automobile exhaust catalysts. *Appl Catal A* 221(1–2):443–457
4. Flachsbart PG, Howes JE, Mack GA, Rodes CE (1987) Carbon monoxide exposures of Washington commuters. *J Air Pollut Control Assoc* 37(2):135–142
5. US Department of Health Education and Welfare (1970) Air quality criterion for carbon monoxide. Washington, DC, pp 6–22
6. Wright M (2006) What exactly is a catalytic converter? About.com
7. http://autorepair.about.com/od/glossary/ss/how-it_catalyti.htm
8. Pundir BP (2007) Engine emissions pollutant formation and advances in control technology. Narosa Publishing House, New Delhi
9. Bera A, Hegde MS (2010) Recent advances in auto exhaust catalysis. *J Indian Inst Sci* 90(2):299–325
10. Houdry EJ, Ann (1956) Catalytic structure and composition. US Patent-US2742437, filed September 1952
11. Shelef M, McCabe RW (2000) Twenty-five years after introduction of automotive catalysts: what next? *Catal Today* 62:35–50